NASA SP-412

Apollo-Soyuz Test Project

Summary Science Report



Volume II

National Aeronautics and Space Administration

NASA SP-412

Apollo-Soyuz Test Project

Summary Science Report

Volume II
Earth Observations and Photography

Edited by
Farouk El-Baz and D. M. Warner
Smithsonian Institution

Prepared by
NASA Lyndon B. Johnson Space Center



Scientific and Technical Information Branch 1979
NATIONAL AERONAUTICS AND SPACE ADMINISTRATION
Washington, D.C.

NASA REVIEW BOARD

The material in this volume was compiled and edited by the Smithsonian Institution, under NASA contract NAS9-13831. This material was reviewed by a NASA Review Board at the Lyndon B. Johnson Space Center (JSC); board members were Richard R. Baldwin (Chairman), JSC; R. Thomas Giuli (ASTP Program Scientist), JSC; Harold Kernaghan, Kentron International, Inc.; W. Wilson Lauderdale, General Electric; and Lettie Reed, JSC.

In two volumes:

Volume I:	Astronomy, Earth Atmosphere and Gravity Field, Life Sciences, and Materials Processing
Volume II:	Earth Observations and Photography

Library of Congress Cataloging in Publication Data (Revised)

Lyndon B. Johnson Space Center.
Apollo-Soyuz Test Project.

(NASA SP ; 412)
Vol. 2 edited by F. El-Baz and D. M. Warner.
Includes bibliographical references.
CONTENTS: v. 1. Astronomy, earth atmosphere and gravity field, life sciences, and materials processing. –v. 2. Earth observations and photography.
1. Apollo-Soyuz Test Project. I. El-Baz, Farouk. II. Warner, Delia M. III. Title. IV. Series: United States. National Aeronautics and Space Administration. NASA SP ; 412.
TL788.4.L9 1977 500.5 77-11892

Foreword

International cooperation was the keynote of the Apollo-Soyuz Test Project. During the 3 years after the project was officially initiated by a U.S.-U.S.S.R. agreement on May 24, 1972, the great effort in coordination, communication, and integration culminated in the highly successful flight from July 15 to 24, 1975. The 9-day flight marked the first time that manned spacecraft of two nations met in space for joint engineering and scientific investigations.

The principal objective of the project was to develop a compatible docking system and rendezvous and crew transfer procedures that might be appropriate for future international manned space missions. Another important objective was the program of scientific investigations conducted during the mission. A science program was planned by NASA that made abundant use of the experiment opportunities afforded by the mission parameters and spacecraft capabilities.

In addition to five joint U.S.-U.S.S.R. experiments, the Apollo crewmen conducted 23 unilateral experiments. Two of these were provided by the Federal Republic of Germany — a further illustration of the international scope of the mission. Not only was scientific research served by this mission, but worldwide space-science awareness was promoted through extensive home television broadcasting and filming of flight experimentation and in-flight science demonstrations.

Volume I of this report discusses all the experiments except the Earth Observations and Photography Experiment. It provides detailed descriptions of the scientific concepts, experiment design and operation, and the scientific results of a year of postflight data analysis.

This document (Volume II) is devoted to the Earth Observations and Photography Experiment. To meet the objectives of this experiment, the U.S. crewmembers made visual observations and obtained photographs of the Earth. The team of investigators included scientists from several countries and from various fields of Earth science.

Earth observations from space rely primarily on the training of crewmembers as scientific observers. The spectrum of conducted observations and the usefulness of the documentary photographs attest to the effectiveness of "trained observers in space" as data gatherers. The scientific value of this experiment will contribute significantly to the planning of similar endeavors in future space flights.

CHESTER M. LEE
ASTP Program Director
GLYNN S. LUNNEY
ASTP Technical Director

Contents

	Page
SUMMARY OF SIGNIFICANT RESULTS *Farouk El-Baz, Delia M. Warner, and R. Thomas Giuli*	1
GEOLOGIC ANALYSIS OF ASTP PHOTOGRAPHS OF PARTS OF SOUTHERN CALIFORNIA *R. E. Powell and L. T. Silver*	9
MARDA FAULT ZONE AND THE OPENING OF THE RED SEA *Charles A. Wood*	29
EVALUATION OF SATELLITE IMAGES OF THE LEVANTINE RIFT ZONE *Richard M. Foose*	37
ANALYSIS OF SKYLAB AND ASTP PHOTOGRAPHS OF THE LEVANTINE (DEAD SEA) FAULT ZONE *W. R. Muehlberger, L. K. Goetz, and R. C. Belcher*	45
ANALYSIS AND SYNTHESIS OF SPACE IMAGERY OF THE SOUTHEASTERN-TURKEY/NORTHWESTERN-IRAN MOBILE BELT *Paul Dean Proctor, Douglas C. Melton, Jr., Ali Beken, and L. K. Abrams*	63
STRUCTURAL PATTERN OF THE NORTHERN PART OF THE EASTERN DESERT OF EGYPT *Mohamed A. Abdel-Rahman and Hassan A. El-Etr*	87
PHOTOLINEAMENTS IN THE ASTP STEREOSTRIP OF THE WESTERN DESERT OF EGYPT *Hassan A. El-Etr, Adel R. Moustafa, and Farouk El-Baz*	97
UTILIZATION OF ASTP PHOTOGRAPHS IN THE STUDY OF SMALL STRUCTURES IN ABU RAWÂSH AND WÂDI EL NATRÛN, EGYPT *Hassan A. El-Etr and Farouk El-Baz*	107
PHOTOTECTONIC ANALYSIS OF SOUTHEASTERN SPAIN FROM ASTP PHOTOGRAPHS AND LANDSAT IMAGES *Paul Dean Proctor, Kenneth B. Horrall, Douglas C. Melton, Jr., and David F. Thompson*	119

EAST-WEST PERVASIVE LINEAMENTS IN CENTRAL AND SOUTHEASTERN SPAIN 149
Mohamed A. Abdel-Rahman

PHOTOGEOLOGIC ANALYSIS OF ASTP PHOTOGRAPHS OF THE LAKE TORRENS-FLINDERS RANGES-LAKE BLANCHE AREA, SOUTH AUSTRALIA 157
Paul Dean Proctor and Robert Sickler

VOLCANIC LANDFORMS AND ASTROBLEMES 183
R. S. Dietz and J. F. McHone

RIACHÃO RING, BRAZIL: A POSSIBLE METEORITE CRATER DISCOVERED BY THE APOLLO ASTRONAUTS 193
J. F. McHone

COLOR ZONING IN THE WESTERN DESERT OF EGYPT 203
Farouk El-Baz and Hassan A. El-Etr

ORBITAL OBSERVATIONS OF SAND DISTRIBUTION IN THE WESTERN DESERT OF EGYPT 219
Ann W. Gifford, Delia M. Warner, and Farouk El-Baz

PRELIMINARY ANALYSIS OF COLOR VARIATIONS OF SAND DEPOSITS IN THE WESTERN DESERT OF EGYPT 237
Farouk El-Baz, Marie H. Slezak, and Ted A. Maxwell

TEMPORAL CHANGES AS DEPICTED ON ORBITAL PHOTOGRAPHS OF ARID REGIONS IN NORTH AFRICA 263
Marie H. Slezak and Farouk El-Baz

ASTP PHOTOGRAPHS OF SOUTHEASTERN ANGOLA 273
Delia M. Warner

COLOR OF DESERT SURFACES IN THE ARABIAN PENINSULA 285
Farouk El-Baz

MONTE DESERT OF SAN JUAN, ARGENTINA, AS PHOTOGRAPHED BY ASTP 301
Delia M. Warner and Farouk El-Baz

DUNES AND OTHER WINDFORMS OF CENTRAL AUSTRALIA (AND A COMPARISON WITH LINEAR DUNES ON THE MOENKOPI PLATEAU, ARIZONA) 319
C. S. Breed and W. J. Breed

DETERMINING PHOTOGRAPH LOCATIONS OVER OCEANS 359
S. McLafferty, M. Pryslak, and G. A. Maul

CONTENTS

INTERPRETING ASTP PHOTOGRAPHS OF THE OCEAN AND LOCATING THE AREA PHOTOGRAPHED (CASE STUDY OF THE GULF OF MEXICO) 371
G. A. Maul

VISUAL OBSERVATIONS OVER OCEANS 385
R. D. Terry

ANTIPODAL SEAS 409
Robert E. Stevenson

MALTESE FRONT AND STRAIT OF SICILY OCEAN PATTERN ANALYSIS 431
Daniel Jean Stanley

OCEAN COLOR OBSERVATIONS 441
C. S. Yentsch, W. Skea, J. C. Laird, and T. S. Hopkins

ANALYSIS OF WATER COLOR AS SEEN IN ORBITAL AND AERIAL PHOTOGRAPHS OF CAPE COD, NANTUCKET, AND MARTHA'S VINEYARD, MASSACHUSETTS 455
Tracey Tisdall and Farouk El-Baz

ASTP AT BARBADOS: MESOSCALE POOLS OF AMAZON RIVER WATER IN THE WESTERN TROPICAL ATLANTIC 481
G. Borstad

ESTIMATE OF TOTAL REFLECTANCE FROM THE ORINOCO RIVER OUTFLOW 499
C. S. Yentsch and Farouk El-Baz

OBSERVATIONS OF INTERNAL-WAVE SURFACE SIGNATURES IN ASTP PHOTOGRAPHS 505
John R. Apel

DETECTION OF A PROBABLE ANCESTRAL DELTA OF THE NILE RIVER 511
Mohamed A. Abdel-Rahman and Farouk El-Baz

SUSPENDED-SEDIMENT DISPERSAL PATTERNS OF RIVER DELTAS PHOTOGRAPHED BY ASTP 521
Ted A. Maxwell

USE OF APOLLO-SOYUZ PHOTOGRAPHS IN COASTAL STUDIES 531
M. T. El-Ashry

SOUTH AMERICAN RIVER MORPHOLOGY AND HYDROLOGY 545
R. K. Holz, V. R. Baker, S. M. Sutton, Jr., and M. M. Penteado-Orellana

SNOW HYDROLOGY STUDIES 595
M. D. Smallwood, C. J. Bowley, and J. C. Barnes

MESOSCALE CLOUD PATTERNS REVEALED BY ASTP PHOTOGRAPHS 617
P. G. Black

COMPARISON OF ASTRONAUT VISUAL COLOR OBSERVATIONS WITH ASTP PHOTOGRAPHS 635
Farouk El-Baz, Delia M. Warner, and Fred J. Anders

FILM SELECTION FOR THE EARTH OBSERVATIONS AND PHOTOGRAPHY EXPERIMENT 645
N. T. Lamar, H. E. Lockwood, and R. E. D'Alli

FILM EXPOSURE CALCULATIONS 655
H. E. Lockwood, Lincoln Perry, and R. W. Wolfe

ASTP PHOTOGRAPHIC FILM PROCESSING AND SENSITOMETRIC SUMMARY 663
H. E. Lockwood

PHOTOGRAMMETRIC ANALYSIS OF ASTP EARTH OBSERVATIONS EXPERIMENT DATA 667
C. W. Baker

APPENDIX A—GLOSSARY 675

APPENDIX B—ACRONYMS 691

Summary of Significant Results

Farouk El-Baz,[a†] Delia M. Warner,[a] and R. Thomas Giuli[b]

INTRODUCTION

During the Apollo-Soyuz Test Project (ASTP) of July 1975, 28 separate science and technology experiments were conducted by the Apollo crew. One of these, the Earth Observations and Photography Experiment, is the subject of this volume. The basic objective of the experiment was to utilize the special capabilities of trained observers (namely the three U.S. astronauts) in visually studying and photographing specific Earth features, processes, and phenomena. Areas were selected for visual observations and photography on the basis of their interest to specialists in the fields of geology, desert studies, oceanography, hydrology, and meteorology.

The success of the experiment is reflected in the plethora of excellent photographic and observational data acquired during the mission. These data, which include transcripts of astronaut observations and transparencies of more than 1400 70-mm photographs, were made available to the experiment team and other interested scientists. The reports included in this volume are the result of an extensive research program that drew investigators from government agencies, academic institutions, and research organizations in Australia, Barbados, Brazil, Canada, Egypt, India, Israel, Qatar, Turkey, and the United States.

In the last 10 years, scientists have become increasingly involved in monitoring Earth resources and in studying the processes and phenomena that affect the environment. Orbital photographs of the Earth have become important tools in such investigations. The great areal coverage of orbital photographs facilitates studies of regional relationships and of broad distributions. Orbital photographs also provide information on remote, inaccessible, and unexplored areas where they can be used for reconnaissance surveys.

To complement the photographic data, visual observations from Earth orbit are important because human observers can often see more color and textural variations than will be recorded on the most sensitive photographic film. This capability is related to the extensive dynamic range and color sensitivity of the eye and to the speed with which the eye/brain system can interpret what is seen and can distinguish what is significant. Moreover, one of the inherent advantages of visual observations is concerned with the ephemeral nature of many scientifically interesting features such as internal waves, which are only visible in sunglint for a very short period of time. Unlike unmanned satellites, trained human observers can easily locate, identify, describe, and photograph such "targets of opportunity," largely because the observers can exploit various degrees of obliqueness and Sun-elevation angles to scan the scene below.

The schedule for Earth observations and photography during ASTP called for three types of tasks: (1) visual observations of selected Earth features, (2) handheld-camera photography to document observations, and (3) stereo mapping photography of areas of significant scientific interest. To ensure the successful completion of these tasks, an extensive implementation effort, consisting of crew training, flight planning, and mission support, was initiated 1 year before the mission. A detailed report on the implementation

[a]National Air and Space Museum, Smithsonian Institution.

[b]NASA Lyndon B. Johnson Space Center.

[†]Principal Investigator.

effort has been published elsewhere;[1] a brief overview is given here.

The ASTP crewmembers devoted approximately 60 hours to attending lectures designed to familiarize them with the types of Earth features they would observe and photograph. These lectures were given by members of the Earth observations team, a group of specialists assembled to assist in the planning and execution of the experiment. Classroom lectures provided the crewmembers with background information on the basic fields of investigation (geology, desert studies, oceanography, hydrology, and meteorology) and familiarized them with the geography of areas scheduled for observations and photography.

Aircraft training flights, known as flyovers, gave the crewmembers practical experience in observing, describing, and photographing Earth features; the flyovers also provided practice in operational procedures such as handling cameras, lenses, film magazines, and the tape recorder. Seven different flyover exercises were planned and flown in California, Florida, southwestern and northwestern United States, and along the Gulf Coast and East Coast. For each of these flyovers, a visual observations book was prepared to show the flight route and the targets for observation and photography. The flyover exercises gave the ASTP crew valuable practice in selecting the optimum viewing conditions for specific features. For example, they found that high Sun angles were best for observing subtle color variations such as those marking plankton blooms in the ocean; on the other hand, low Sun angles enhanced relief and facilitated observations of geological features such as faults and fractures.

Because of the short duration of the ASTP mission (9 days), only a limited amount of time was available for the Earth Observations and Photography Experiment, and each target had to be specified ahead of time and scheduled in the ASTP Flight Plan. The selection of targets before the mission involved a number of considerations including the recommendations from members of the Earth observations team, the times available in the Flight Plan for the experiment and the locations of areas that would be overflown by the spacecraft during these times, and the optimum viewing conditions for each target.

The final site list consisted of 11 photographic mapping passes and 60 visual observation targets. The term "mapping pass" refers to vertical stereostrip photography acquired with a 70-mm Hasselblad data camera that was bracket mounted in a spacecraft window and used either a 60- or 100-mm lens. The Hasselblad data camera was equipped with an intervalometer that triggered the camera shutter every 10 seconds for the 60-mm lens and every 6.25 seconds for the 100-mm lens, thus providing 60-percent overlap between successive frames. These photographs could be studied stereoscopically, which provided a three-dimensional view and created an illusion of depth. In addition, the vertical photographs enabled the study of large-scale landforms and the preparation and correction of topographical base maps.

Visual observation targets were photographed with a handheld 70-mm Hasselblad reflex camera and a 35-mm Nikon camera. The Hasselblad camera used a 50- or 250-mm lens and was equipped with a single-lens reflex mechanism that permitted the astronaut to accurately aim the camera at the target. The 35-mm Nikon camera also incorporated through-the-lens light metering and a motorized film advance in addition to reflex viewing. The oblique photographs obtained with these cameras presented a perspective view more readily understood than a vertical view and were extremely useful for documenting visual observations and targets of opportunity.

In addition to the photographic equipment, the experiment flight package included visual observations aids designed to assist the astronauts in making the best use of the Flight Plan time allotted to the experiment. These aids consisted of the Earth Observations Book, the World Map Package, a color wheel, a ground scale, and an enlarging telescope.

During the ASTP mission, members of the Earth observations team provided technical support at the mission control center at NASA Lyndon B. Johnson Space Center. This real-time sup-

[1] El-Baz, Farouk: Astronaut Observations From the Apollo-Soyuz Mission. Vol. I of Smithsonian Studies in Air and Space, Smithsonian Institution Press (Washington, D.C.), 1977.

port was necessary (1) to ensure that any questions asked by the crewmembers could be answered immediately, (2) to monitor weather conditions so that cloud-covered targets could be rescheduled, and (3) to relay information on short-lived phenomena such as volcanic explosions, hurricanes, or outbreaks of red tide. The science support team also monitored numerous ground investigations conducted in support of the experiment and exchanged data between the crewmembers and the research parties. Concurrent aircraft flights, land investigations, and ocean surveys in many parts of the world were part of the largest ground-truth collection program conducted in support of any manned space mission. The data supplied by these surveys were used in the postmission analyses of ASTP observations and photography.

After the mission, the crewmembers attended debriefings to review the operational and scientific aspects of the experiment. These debriefings allowed the experiment team to more fully discuss the observations made by the crewmembers. Transcripts of these debriefings were made available to the teammembers and were used in the ASTP data analysis.

SIGNIFICANT RESULTS

In the following paragraphs, a summary is given of the significant results of the ASTP data analysis. The discussion is structured according to the fields of investigation including geology, desert studies, oceanography, hydrology, and meteorology.

Geology

In this volume, geological investigations may be grouped into two categories: (1) regional tectonic studies and (2) volcanic features and astroblemes. Most of the regional tectonic studies were concerned with identifying and mapping fault, fracture, and fold patterns as well as lithologic features. Other investigations pertained to the detection and identification of circular ground patterns that might be volcanic features or astroblemes (ancient meteorite-impact scars).

During ASTP, studies of global tectonic patterns included observations of southern California, the Red Sea/Levantine Rift zone, the Western Desert of Egypt, southern Spain, and South Australia. These photogeological investigations of regional tectonic settings profited by the extensive areal coverage of the ASTP data, which made it easy to trace large-scale fault and fold patterns and to perceive structural relationships. In addition, the color sensitivity and good resolution of the photographic film often allowed interpreters to make gross lithologic discriminations on the basis of subtle color and textural variations. Some of the most useful products of these investigations were geologic maps that presented all the pertinent details recognized and identified on the photographs and, in many cases, checked in the field.

The complex geology of the southwestern United States is, in part, the result of differential movement occurring between large parts of the Earth's crust known as the Pacific and American plates. This area of crustal fracturing is generally characterized by a northwest-southeast structural grain. Dominating the region is the northwest-trending San Andreas Fault, a transform fault along which large-scale horizontal motion occurs as a result of shear between the two plates. The geology of the area is further complicated by the intersection of an east-trending fracture zone, which is reflected in southern California by the Transverse Ranges.

A sequence of ASTP mapping photographs was obtained over the San Andreas Fault and the central Transverse Ranges in southern California. A study of the remarkably clear ASTP photographs facilitated the identification of many known structures and provided insights into previously unknown structural elements and patterns. Within and bounding the San Gabriel Mountains in the Transverse Ranges, a previously unrecognized pattern of east-northeast-trending lineaments and the lobate character of the mountain front were recognized. These observations offer new perspectives to possible interpretations of the San Gabriel Mountains, which may be a series of tectonically emplaced shingled slabs.

Geological investigations of the Red Sea/Levantine Rift zone during ASTP included observations and photography of the Afar Depression, the northwestern Gulf of Suez, the Levantine Rift, and southeastern Turkey/northwestern Iran.

Located at the junction of the Red Sea, the Gulf of Aden, and the East African Rift systems, the Afar Depression is a triple junction, an area of crustal separation and outward spreading in three directions. Early in this century, geologists first speculated that the remarkably similar shapes of the opposing coasts of the Red Sea and Gulf of Aden might indicate that Africa and Arabia were once a single continental block before crustal separation occurred. Since that time, geological, geophysical, and photographic evidence have provided further support for this hypothesis. According to modern plate tectonic theory, the northward translation and counterclockwise rotation of the Arabian plate away from the Afar spreading center resulted in the opening of the Red Sea and the Gulf of Aden, in the left-lateral strike-slip faulting along the Levantine Rift, and in the collision and subduction of the Arabian crustal plate beneath the Eurasian plate.

Geographically, the Afar Depression is a triangular region bounded on the west by the Ethiopian plateau, on the south by the Somali plateau, and on the east and northeast by the Red Sea and Gulf of Aden. When the original geographic positions of Africa and Arabia before separation are reconstructed, the Afar region is an area of overlap. Because of this, geologists generally agree that the Afar Depression is oceanic crust created since the breakup of the Afro-Arabian plate. For the most part, geologic data support this interpretation except for the anomalous occurrence of two old, nonvolcanic massifs, the Danakil Alps and the Aisha hills.

Paleomagnetic data have shown that the Danakil massif is a splinter of the Ethiopian plateau that has been rotated into Afar by the opening of the Red Sea. However, the position of the Aisha hills, which extend northward from the Somali escarpment, cannot be easily explained. The ASTP mapping photographs taken over the Afar region were studied and used to support a new interpretation for the occurrence of the Aisha hills. This theory states that the hills have moved north-northeastward to their present location by strike-slip movement along the Marda Fault zone, which stretches more than 900 km across the Horn of Africa. In this case, the ASTP photographs provided additional evidence to support a new model.

Farther north, over the western coast of the Gulf of Suez, ASTP photographs were studied in an investigation of regional structural patterns. Near-vertical and oblique ASTP photographs were used to identify faults; Landsat images were used for planimetric mapping; and aerial photographs were used to verify the mapped fault lines. The photographs showed that the area was characterized by a series of positive and negative fault blocks. On the ASTP photographs, three positive and two negative crustal blocks bounded by long east-northeast-trending faults could be identified. These results supported the theory that vertical tectonics were responsible for the development of the fault pattern in the area.

The northern extension of the Red Sea Rift is known as the Levantine Rift, a complex fault system extending from the Gulf of Aqaba northward into Turkey. It is a zone of left-lateral strike-slip faulting marking a transform plate boundary between Africa and Arabia. The southern part of the fault zone is characterized by a linear rift along which the Dead Sea and Sea of Galilee lie. Both Skylab and ASTP photographs were available for this part of the fault zone. Taken with different Sun angles and look directions, the photographs provided different types of information. It was found that vertical photographs were useful for synoptic, orthogonal mapping; low-Sun-angle photographs emphasized subtle structural and topographic variations; and oblique photographs provided regional views of fault systems.

Over the northern part of the Levantine Rift in Syria and Turkey, a vertical strip of ASTP mapping photographs produced a new structural interpretation that shows a splintering of the Levantine Rift zone northward toward the East Anatolian Fault zone in Turkey. This pattern was observed by the Apollo crewmembers who described the northern part of the Levantine Rift as a fan-shaped complex composed of three major curvilinear fractures.

In southeastern Turkey and northwestern Iran, ASTP photographs revealed complex structures that are probably also related to the motion of the Arabian plate away from the Afar spreading center. The general geologic setting of this area is characterized by two major tectonic blocks. The interface between the two blocks is paralleled by a major fold belt, slightly concave to the southwest. The structures in this area could be interpreted as resulting from the northward movement and subduction of the Arabian plate. In addition, a major strike-slip fault that was identified in the photographs probably corresponds to the Anatolian transform fault and suggests that plate movement may be continuing at the present time.

A number of mapping and handheld-camera photographs were taken over the Western Desert of Egypt. An investigation of lineaments displayed in these photographs provided information on the structural setting of the area. The ASTP findings were supplemented by collateral data such as Landsat images, aerial photographs, topographic and geologic maps, and field observations.

The northward movement of the African crustal plate has been used to explain the formation of the Sierra Nevadas in southern Spain. These mountains are related tectonically to the Rif Atlas in Morocco and represent the westernmost element of the Alpine orogenic belt. Excellent near-vertical ASTP photographs of southern Spain were used to identify and map lineaments and fold patterns. Analyses of these patterns revealed that they could be the result of compressional and tensional stresses. According to this model, a major compressional stress environment, generated by counterclockwise rotation of the Iberian Peninsula together with northward movement of the African plate, resulted in slowly closing jaws. Later relaxation of the stress field or a change in the direction of plate movement resulted in a tensional environment.

Apollo-Soyuz color photographs of the North Flinders Ranges in South Australia were analyzed to determine the characteristics of regional fold structures and to identify major folds, faults, and other lineaments. A good correlation between the photogeologic interpretations and geology on previously published geologic maps was found. Although remote, this area had already been extensively mapped by Australian geologists. However, if the ASTP photographs had been available earlier, they would have been a powerful tool for stratigraphic work, geologic mapping, and the interpretation of the large and complex structures of the region.

Terrestrial craters resulting from meteorite impacts are now known to have been more numerous than previously believed. These include relatively recent impact craters (e.g., Meteor Crater in Arizona) and ancient impact scars, or astroblemes (e.g., the Sudbury structure in Canada). During ASTP, a study was made of circular features in Brazil, Libya, and Mexico to increase our knowledge of the interaction of the Earth and meteorite bodies and to identify new areas for efficient ground exploration. The most significant result was the discovery of a new astrobleme in Brazil. Named the Riachão Ring after the nearest city, the feature was invisible on airborne radar and near-infrared satellite images. However, the circular structure, which is 4 km in diameter, was easily recognized and photographed by the orbiting astronauts. Based on this discovery of a probable meteorite impact crater, a field trip was conducted and samples collected which are being analyzed to assess this interpretation.

The ASTP astronauts also obtained excellent photographs of volcanic structures and observed an eruption of Mount Etna. In Mexico, a feature that had been previously identified as a possible meteorite-impact site was found to be a rhyolitic ash ring formed by a volcanic steam explosion.

Desert Studies

Photographs taken from Earth orbit provide a very practical means of studying remote, inaccessible, and unexplored desert regions. Because of their great areal coverage, these photographs are especially helpful in mapping regional patterns of sand distribution, in studying large-scale dune morphology, in determing the direction of sand movement, and in determining the location of areas where migrating dunes present a threat to cultivated land. In addition, the natural color of orbital photographs facilitates the detection of subtle color variations, which could provide infor-

mation on the chemical makeup and relative age of desert sands. For these reasons, desert studies were an important part of the Earth Observations and Photography Experiment, and excellent data were obtained of desert regions in Australia, Egypt, Argentina, Angola, and Arabia. The ASTP effort made a significant contribution in expanding the geological community's interest in desert investigations.

The ASTP mapping photographs of longitudinal dunes in the Strzelecki Desert of Australia reveal an increase in red color as the distance downwind from the source of sand increases. Reddened sands, due to iron-oxide coatings on individual grains, occur in deserts throughout the world, and the degree of reddening in sands of uniform aridity and source may be used to determine sequences of depositional events.

In Egypt, ASTP mapping and handheld-camera photographs showed regional and local color zones that were later checked in the field by a team of geologists from the Smithsonian Institution and Ain Shams University, Cairo, Egypt. In one photograph covering the desert just west of the Nile Delta, three distinct color zones were identified. These were correlated in the field with desert pavement, relatively active sand with sparse vegetation, and arable soil composed of quartz sand, clay, and calcium carbonate particles. The identification of the previously unknown extent of an arable zone west of the cultivated Nile Delta attests to the value of ASTP color photographs in desert studies.

A study was also made of sand distribution in the Western Desert to provide a descriptive basis for future desert studies in this area. The trends of dunes in the Western Desert generally veer in a clockwise direction around a center near Kufra Oasis in Libya. Dune orientations change from north-northwesterly in the northern desert to north-northeasterly in the south. The ASTP photographs revealed a distinct pattern of sand deposition and dune formation that was closely related to topography and prevailing wind patterns.

The ASTP data on Egypt were also used to study the feasibility of comparing orbital photographs taken in different years to detect temporal changes. The ASTP photographs of the Nile Delta and the Oweinat Mountain region were compared to Gemini and Apollo photographs of the same areas. West of the Nile Delta, an increase in vegetation of approximately 1108 km^2 in 10 years was identified. Near Oweinat Mountain, at the borders between Egypt, Libya and Sudan, it was found that sand patterns had shifted 2.5 km over a 6-year period.

In Argentina, ASTP photographs of the Monte Desert in southeastern San Juan Province revealed two unusual and little-known dune fields. These fields display complex dune patterns that are controlled by a number of factors including the rainfall, the underlying and surrounding topography, the wind regime, and the amount of sediment available. The ASTP observations resulted in Argentinian interest in performing in-depth studies of these areas.

Photographs in semiarid southeastern Angola revealed landforms that provide evidence of climatic change. Suspected karst features imply more humid conditions; whereas ancient eroded sand dunes indicate a more arid climate. Also, the ASTP photographs of Arabia showed reddened dunes oriented along the prevailing wind directions. These photographs were also used to distinguish the exposed rock surfaces on the basis of color and texture.

Oceanography

The ASTP astronauts collected a plethora of photographic and observational data in support of studies of the world's oceans. Orbital photographs have proved valuable in documenting large-scale ocean features and circulation patterns. Many of these features, such as ocean currents, are important to the shipping and fishing industries. Other features, such as large-scale cold water eddies, are important because they act as mechanisms of energy dispensation, in some cases as productive fisheries, and as hiding places for submarines because of their effect on sound waves. Color variations in ocean waters are also significant because accurate measurements of water color can help identify distinct ocean currents, eddies, and areas of biological productivity.

The ASTP crewmembers obtained a number of

excellent photographs over the world's oceans. However, the usefulness of some of these photographs was curtailed by the lack of information on their exact geographic positions. Therefore, to increase the scientific usefulness of these photographs, an effort was made to quantitatively define their locations. The methods used were based on photogrammetry, on a knowledge of the groundtracks of the spacecraft and the times during which the photographs were taken, and on a comparison with weather satellite imagery.

Visual observations were especially important in locating, identifying, describing, and photographing many ocean features, largely because many of these features are only visible under specific viewing conditions. For example, sunglint is especially helpful in studying water surface texture and in identifying internal waves. On the other hand, high Sun angles are useful in emphasizing subtle water-color variations that could mark current boundaries and upwelling areas.

Perhaps the most significant ocean observation was the recognition of the surface manifestations of internal waves off the coast of Thailand and the Strait of Gibraltar. Internal waves are little-understood ocean features similar to surface waves but orders of magnitude larger. They occur within the ocean at temperature or density discontinuities between water layers. Seen in sunglint, the scum lines often associated with internal waves facilitate their observation from space. Because observation periods are brief, many ocean features observed during ASTP were not visible in sunglint for more than 5 to 10 seconds. This emphasizes the importance of having trained observers who can rapidly recognize and photograph such targets of opportunity.

Photographs of the Sun's reflection also provided information on the texture of the sea surface. For example, a series of mapping photographs taken between Tunisia and Sicily included areas of sunglint. These areas revealed ocean surface phenomena related to turbulence, including possible internal waves. Photographs of the eastern Gulf of Mexico also documented patterns in the sunglint, which were interpreted as indicators of the cyclonic shear zone of the Gulf Loop Current.

The ASTP ocean photographs also revealed a wide variation in water color, which could be a function of Sun angle, water surface roughness, suspended sediments, water depth, and biological productivity. For example, around Cape Cod the natural color of the ASTP photographs enabled the recognition of light blue-green areas marking shoals and suspended sediments.

In South America, photographs and observations of the Orinoco River Delta showed discrete water-color zones that reflect the mixing of the sediment laden Orinoco outflow with the water of the tropical Atlantic. The ASTP crewmembers thought they could observe turbid water associated with the Orinoco outflow extending past the island of Barbados. To support these observations, the Bellairs Research Institute, McGill University, sponsored three cruises from Barbados in July 1975. Measurements and observations were made of sea state, water color, water temperature, salinity, chlorophyll content, cloud cover, and wind speed and direction. Analysis of these data suggested that the turbid waters observed by the crewmembers were actually related to successive passage of pools of brackish Amazon River water.

Hydrology

Hydrological investigations during ASTP included observations and photographs of major river deltas, of snow-cover patterns in the Cascades, and of South American river morphology.

Basically, river deltas are triangular-shaped alluvial deposits formed at the mouths of rivers. In the geologic record, ancient deltaic sediments are often a site of natural gas and oil accumulation, and an understanding of the growth of deltas might have applications in the future development of these resources.

One significant result of the ASTP data analysis was the detection of a probable ancestral delta of the Nile River. The ASTP photographs of northern Egypt revealed an extensive dark-colored and finely textured zone partially overlapped by the present Nile Delta. Extrapolation of the identified zone beyond the ASTP photographic coverage using a false-color Landsat mosaic indicated that

this zone forms part of a deltalike pattern and is most probably the late Eocene to early Miocene ancestral delta of the Nile River.

The ASTP photographs of the Fraser, Rhône, Orinoco, Yangtze, and Danube river deltas were also examined. These photographs reveal distinctive suspended sediment patterns that can be related to models of sedimentation in a deltaic environment. The study of these sediment plumes provided information on the short-term processes that dominate deltaic sedimentation—such as river inertia, buoyancy of suspended material, and frictional turbulence.

The ASTP photographs taken over the Amazon and Paraguay river basins showed a remarkable variation in the sizes and morphologies of various rivers. Channel widths, meander wavelengths, and other variables were measured from the photographs and were used to evaluate various empirical formulas for estimating the hydrologic properties of these rivers. This study revealed that these formulas, derived from studies of humid-temperate and semiarid streams, cannot explain the regime behavior of these complex tropical rivers.

The ASTP mission provided an excellent opportunity to observe and photograph snow cover on the Cascades and Olympic Mountains in Washington State. Accurate mapping of snow cover is important in predicting the volume of water reaching drainage systems for use in irrigation and the control of floods. Analysis of the ASTP data revealed that the most accurate snowline determinations were made by using photographs taken with the 250-mm lens. It was found that the availability of color, stereo photographs greatly facilitated interpretations of snowpack distribution, particularly with regard to delineating the very irregular snowline that is characteristic of the summer season.

Meteorology

The ASTP crewmembers were able to observe and photograph a number of interesting cloud patterns. Of special interest were photographs of ring clouds in the Pacific Ocean. Similar circular cloud patterns have previously been defined as atmospheric manifestations of cold-core eddies in the ocean. However, this study found that the features are associated with decaying maritime thunderstorms and are only atmospheric in nature.

CONCLUSIONS

The ASTP Earth Observations and Photography Experiment demonstrated the effectiveness of human observers in studying the Earth from orbit. This effectiveness is not only in verbal descriptions of observed features and phenomena, but in performance of high-quality documentary photography and in instantaneous determination of the most significant objects to study. The degree of effectiveness relies heavily on how well trained and well prepared the observer is.

An obvious feature of the research reports presented in this volume is the variety of the data used. The ASTP photographs from 70-mm and 35-mm cameras were used in conjunction with transcripts of real-time verbal descriptions and postmission debriefings. Also used were photographs from past manned missions such as Gemini, Apollo, and Skylab in addition to images from Landsat and weather satellites. Data from topographic maps, geologic maps, and bathymetric charts were integrated in the reports. Also, information gathered from mission-concurrent investigations such as aircraft photographic flights and oceanic vessel traverses was used. Finally, the data gathered during postmission field trips strengthened, in several cases, the photointerpretations. This variety of data helped establish the utility of spaceborne information in the various fields of study.

The variety of data is also accompanied by a variety in the style of scientific research. Because of the interdisciplinary nature of the experiment team and the data analysis program, most of the papers reflect the personal style of the research conducted. Therefore, some reports are largely descriptive, others are interpretive, and some are model dependent. This variety attests to the great variations in our knowledge of the Earth and to the many ways and means by which scientists attempt to answer questions about its features and phenomena.

Geologic Analysis of ASTP Photographs of Parts of Southern California

R. E. Powell[a] and L. T. Silver[a]

ABSTRACT

On July 16, 1975, the crew of the Apollo-Soyuz Test Project obtained a series of remarkably clear color stereoscopic photographs of the central Transverse Ranges and the Los Angeles Basin in southern California. These photographs are used to identify and interpret known geologic features of the Transverse Ranges, and to search for previously unrecognized features. High-altitude aerial photographs provide useful supplements to the orbital photographs.

Major well-known high-angle faults of the region (the San Andreas, San Gabriel, and San Jacinto faults) are clearly visible; low-angle faults, even if active, are less apparent. The sharpness of the visual definition of a fault zone, therefore, should not be used as an exclusive criterion for recency of activity. Conversely, pronounced topographic expression may be developed by preferential erosion along inactive fault zones. Vegetation can produce severe masking of originally strong lithologic contrasts.

Within and bounding the San Gabriel Mountains, current and recent fault breakage indicate a complex interplay of strike-slip and thrust fault movement. A previously unrecognized pattern of east-northeast-trending lineaments and the lobate character of the mountain front offer new perspectives to possible tectonic interpretations of this mountain range. They suggest the possibility that fault movement may represent a series of shingled slabs moving either in independent or in grouped increments, in response to compressive components across the Pacific/North America plate boundary.

INTRODUCTION

The Apollo-Soyuz Test Project (ASTP) on July 16, 1975, obtained a sequence of remarkably clear orbital photographs (AST-14-881 to AST-14-884) across the coast of southern California from Los Angeles into the Mojave Desert (fig. 1). These photographs provide a dramatic overview of the anomalous east-west (E-W) physiographic and structural features of a part of the Transverse Ranges province.

Physiographically, the Los Angeles Basin, the San Gabriel Valley, and the San Bernardino Valley, with flanking NW-trending ranges of hills (Palos Verdes, Whittier, and Puente hills), are abruptly truncated on the north by the E-W trending Santa Monica and San Gabriel mountains. East-west morphological trends are also seen to the north of the San Gabriel Mountains in the Soledad Basin and the Sierra Pelona, and to the north of the Santa Monica Mountains in the San Fernando Valley/Ventura Basin and the Santa Susana Mountains (figs. 2 and 3). The Santa Monica and Santa Susana mountains and the Ventura Basin appear on the margin of the photographs and will not be discussed because of the lack of adequate stereoscopic coverage.

A number of major structural features (the San Andreas, the San Gabriel, the San Francisquito, and the northern end of the San Jacinto fault zones) are strikingly delineated by their

[a]California Institute of Technology, Pasadena, California.

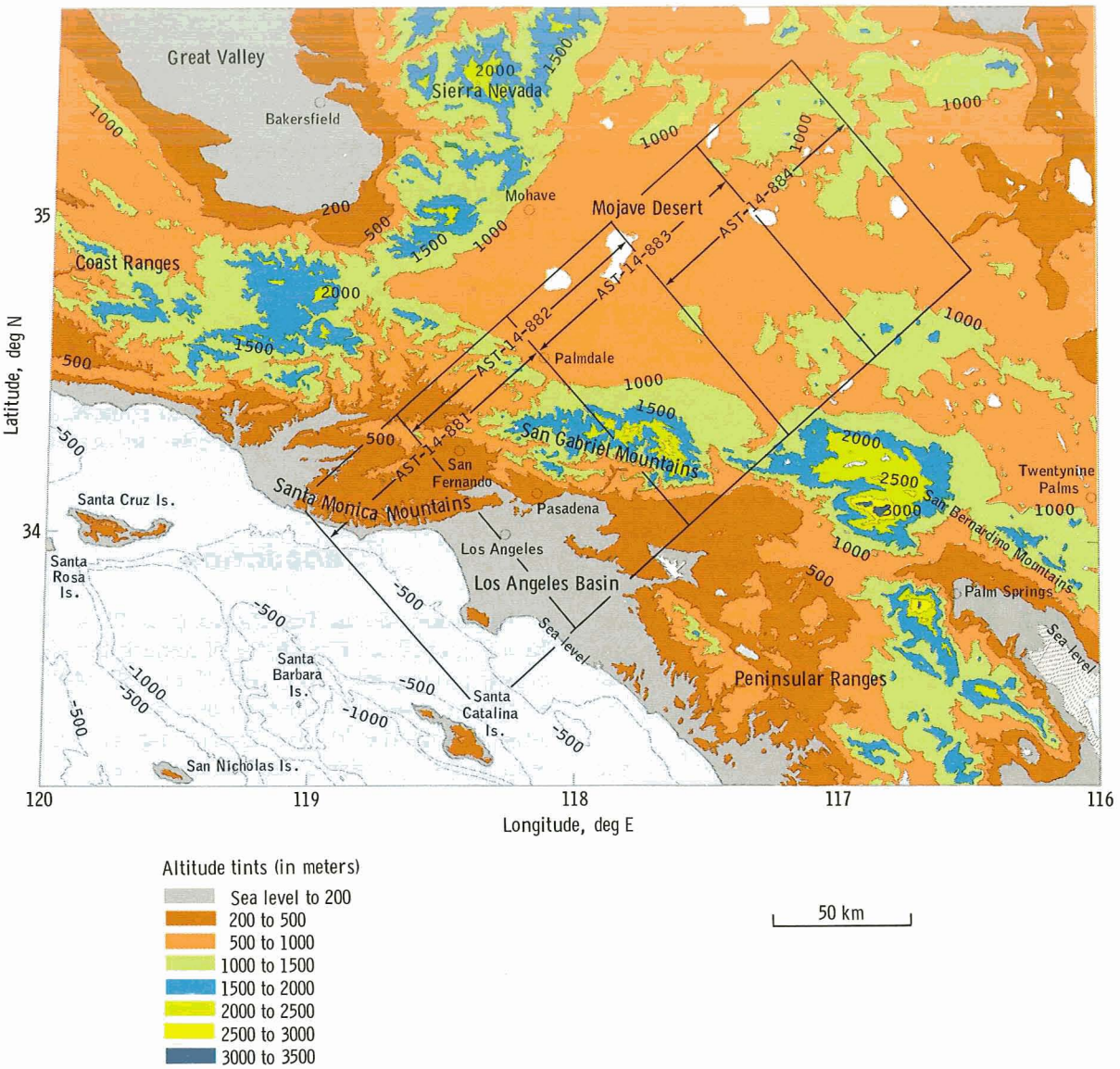


FIGURE 1.—Index map showing geographic coverage of the ASTP photographic sequence (AST-14-881 to AST-14-884) across the Los Angeles Basin, Transverse Ranges (including the Santa Monica, San Gabriel, and San Bernardino mountains), and Mojave Desert. The topography of the E-W trending Transverse Ranges transects the NW-SE trends of the Peninsular Ranges and offshore region to the south, and the Coast Ranges, Great Valley, and Sierra Nevada to the north.

topographic expression. Traces of other fault zones, such as the frontal Sierra Madre/Cucamonga, Santa Monica, Whittier, and Palos Verdes, are more diffuse trends that are marked topographically by conspicuous elevation changes (figs. 2 and 4).

Photointerpretation has been focused on the San Gabriel Mountains, for which stereoscopic ASTP coverage is available. The ASTP color photographs have been used in conjunction with partially coincidental high-altitude-aircraft color photographs, as well as some older low-altitude black-and-white aerial photographs, to identify and interpret known features of tectonic significance within and bounding the range. In addition, a search was made for possible unrecognized

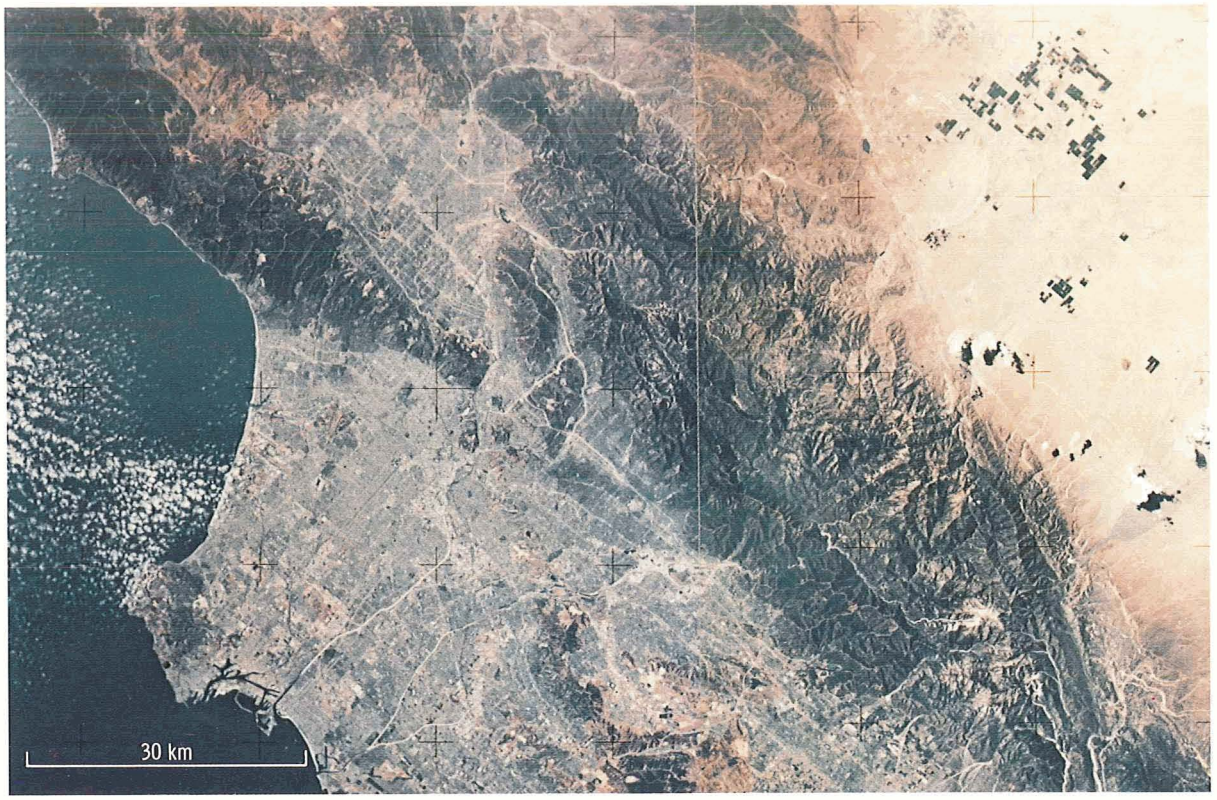


FIGURE 2.—Photomosaic of AST-14-881 and AST-14-882 covering the Los Angeles Basin and parts of the central Transverse Ranges and western Mojave Desert. The photographs were taken on July 16, 1975, by the ASTP crew.

features. The high-altitude support photography was flown by NASA in 1973.

Within the San Gabriel Mountains, the rugged chaparral-covered terrain has hindered surface geologic mapping in many areas and thus has restricted regional synthesis of structural elements within the range. Not only does the orbital sequence provide an overview of the range, but the exceptionally clear photographs provide ready identification of many known structures and insights into previously unknown structural elements and patterns. The ASTP photographs thus serve as an excellent framework for regional synthesis of fault and fracture patterns.

GEOLOGIC SETTING

The physiographic and geologic provinces of California are generally characterized by a NW-SE structural grain (fig. 5). Mountain ranges (Sierra Nevada, Coast Ranges, Peninsular Ranges) and valleys (Great Valley, Salton Trough/Gulf of California) extend for several hundreds of kilometers along NW-SE trends. The tectonic fabric is dominated by great NW-SE fault zones, including the San Andreas, Hayward, Calaveras, and Nacimiento faults in northern and central California; the San Andreas, San Gabriel, San Jacinto, Elsinore, Newport-Inglewood, and the Mojave Desert system of right-lateral faults in southern California (fig. 5).

In addition to faults, the tectonic grain is comprised of fold axes, elongate prisms of sedimentary rock, elongate batholiths, as well as elongate distributions of petrologic variations within the batholiths. Gravity and magnetic anomaly patterns reflect the trends of these structural and lithologic features. Some elements of this NW-SE grain represent current crustal activity; others have developed at various times since the early Mesozoic. The continental plate margin configura-

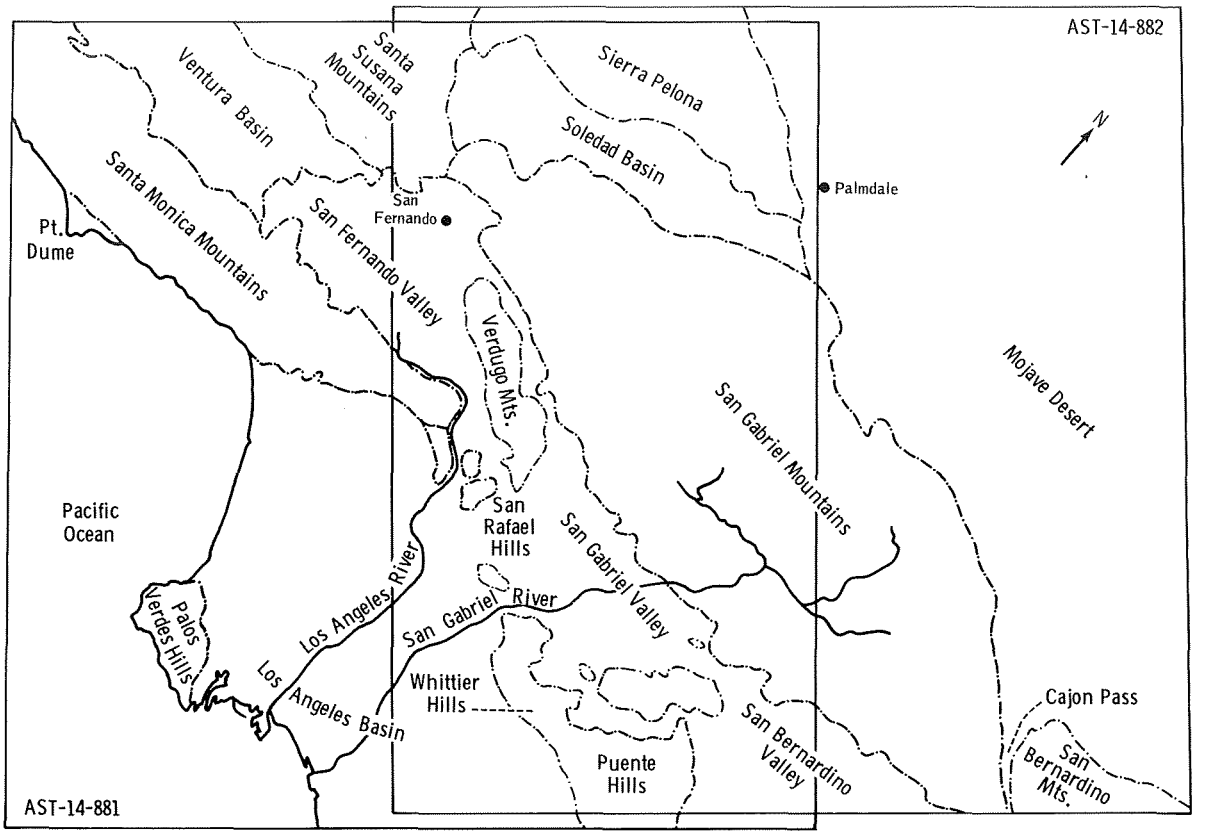


FIGURE 3.—Map identifying the major physiographic features of the Los Angeles Basin and E-W central Transverse Ranges that can be recognized on the photomosaic of AST-14-881 and AST-14-882 (fig. 2).

tion, which controlled the development of this grain, has probably existed for approximately 200 million years.

The E-W physiographic and geologic trends of the Transverse Ranges transect the predominant NW-SE grain of the continental margin (figs. 1 and 5). Morphologically, the E-W deflection is apparently left-lateral. The NW-SE physiography of the Peninsular Ranges is truncated northwestward by the E-W physiography of the Transverse Ranges and basins, which in turn is transitional northwestward into the NW-SE trend of the Coast Ranges (fig. 1). These relations are particularly apparent from the perspective of a space platform (fig. 4-3 in ref. 1).

Structural elements, including faults and folds, have an E-W orientation within the Transverse Ranges. Many of the faults (including the Big Pine, the Santa Ynez, and the Sylmar and Foothill Boulevard faults, which broke during the 1971 San Fernando earthquake) have documented left-lateral and reverse components of displacement. A set of lower to upper Miocene faults in Soledad Basin and in the San Gabriel Mountains (Vasquez Canyon, Mint Canyon, Agua Dulce Canyon, Pole Canyon, Magic Mountain, and Transmission Line faults) also displays left-lateral displacements.

Sedimentary basins within the Transverse Ranges (Ventura Basin, Soledad Basin, Lockwood Valley/southern Cuyama badlands) record a history of sediment accumulation in E-W troughs accompanied by N-S compressional deformation (E-W folds and reverse faults). The sedimentary rocks range in age from at least lower Miocene to Pleistocene.

The dynamic processes that have produced and maintained these anomalous ranges are not yet understood, but they have persisted or recurred

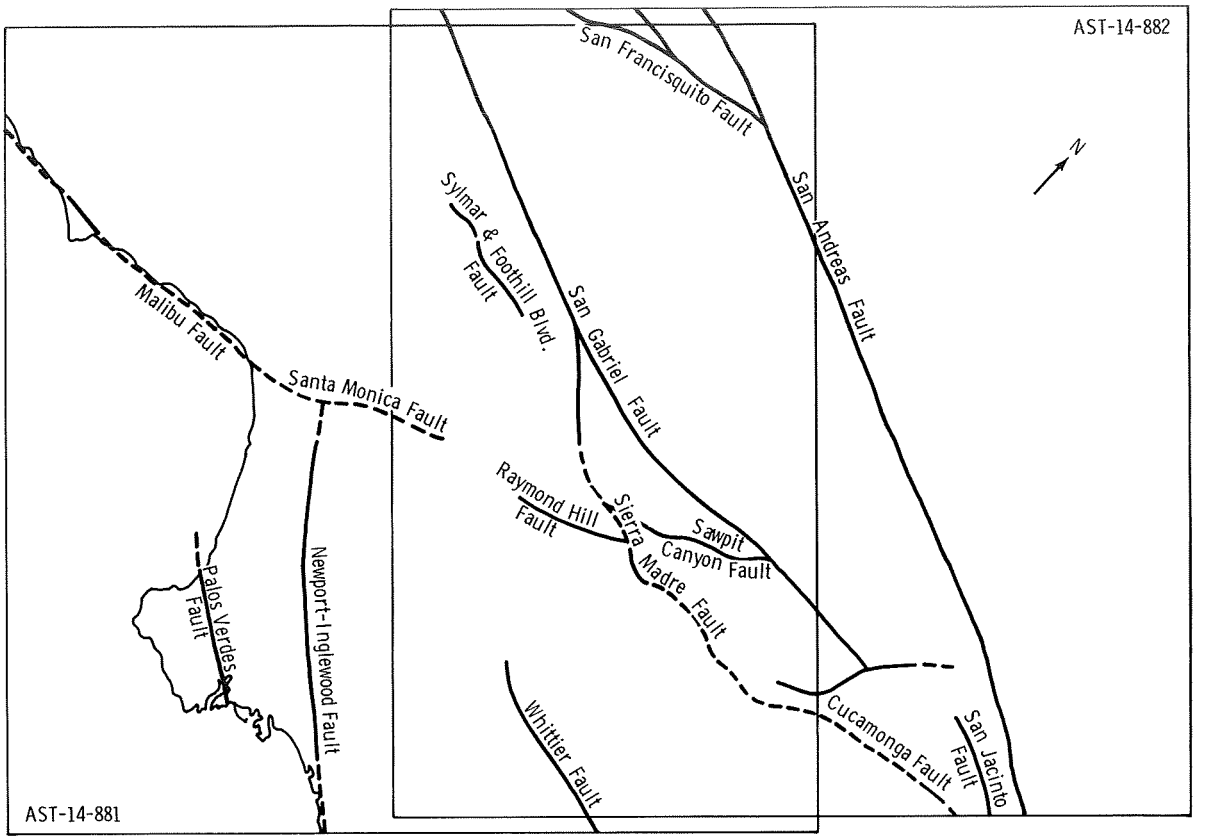


FIGURE 4.—Map showing location of the major faults that can be seen on the photomosaic of AST-14-881 and AST-14-882 (fig. 2). The San Andreas, San Gabriel, and San Jacinto faults are part of the right-lateral strike-slip system interpreted to represent the current boundary between the North American and Pacific crustal plates. The Malibu, Santa Monica, Sylmar and Foothill Boulevard, Raymond Hill, Sierra Madre, and Cucamonga faults are part of the system of left-lateral reverse faults that form the southern boundary of the Transverse Ranges. The San Fernando earthquake of February 9, 1971, broke the Earth's surface along the Sylmar and Foothill Boulevard Fault. The Newport-Inglewood, Palos Verdes, and Whittier faults are part of a system of high-angle faults with probable components of both vertical and right-lateral displacements.

through several millions, or perhaps tens of millions, of years. To reach an understanding of the Transverse Ranges will require the definition of spatial relationships of major structures and the establishment of the sequence of structural development. The ASTP photographs provide an excellent overview of many of these structures, and offer some suggestions as to their relative ages. The analysis of the ASTP photographs in the subsections entitled "Surficial Color Values of Geologic Units" and "Major Structural Lineaments" concentrates on the recognition and resolution of known geologic features. The subsection on ENE structural lineaments deals with previously unrecognized features and their relationships with known structures. The photointerpretive tectonic synthesis offers tentative models that integrate structural patterns with ground-established sequencing constraints.

SURFICIAL COLOR VALUES OF GEOLOGIC UNITS

Color variations on the ASTP photographs reflect changes in both the geologic units (i.e., lithology) and the surficial soils and vegetation. Attempts to map lithologies on the ASTP photographs were not consistently successful. Masking by vegetation in many instances concealed primary lithologic characteristics.

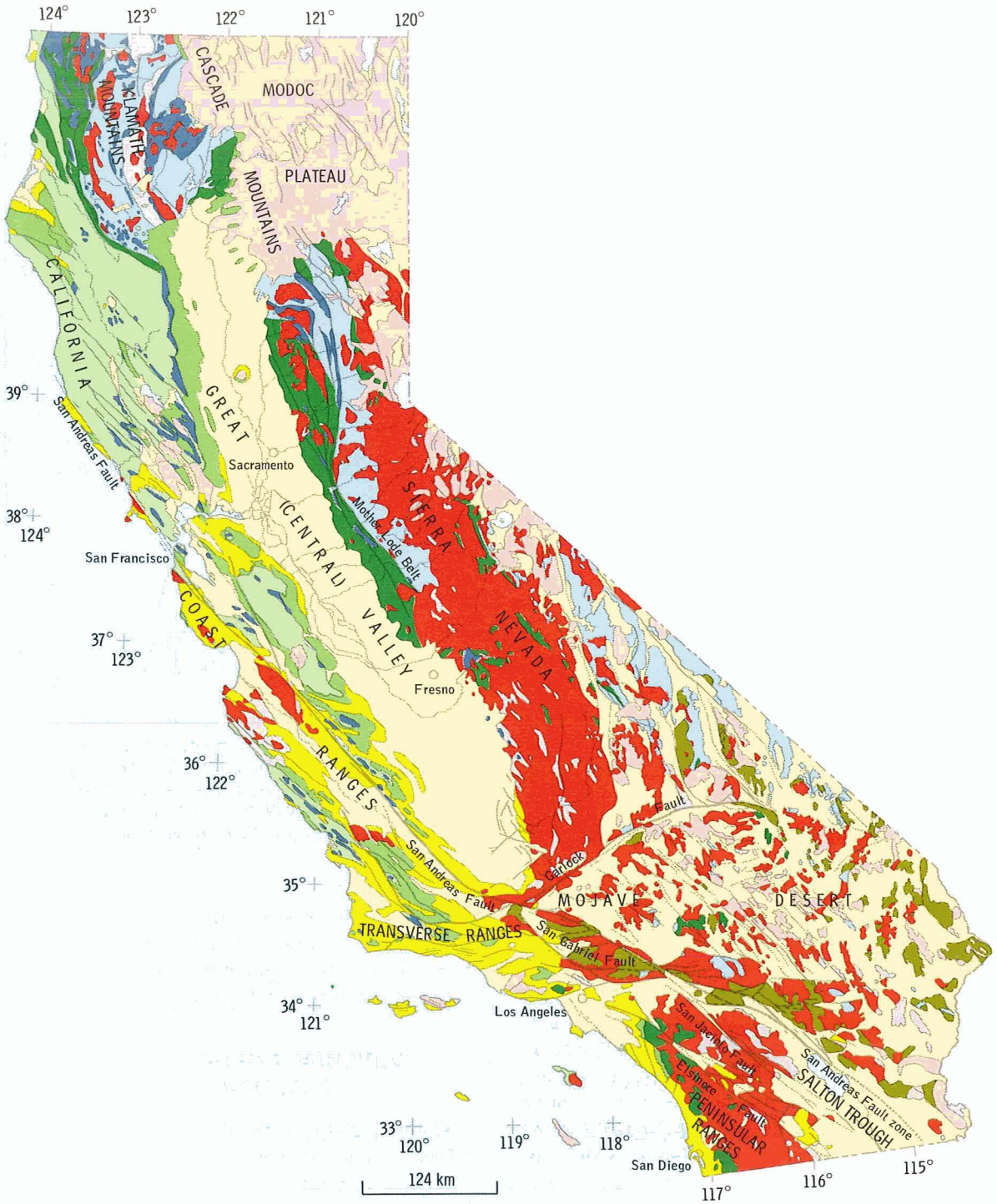
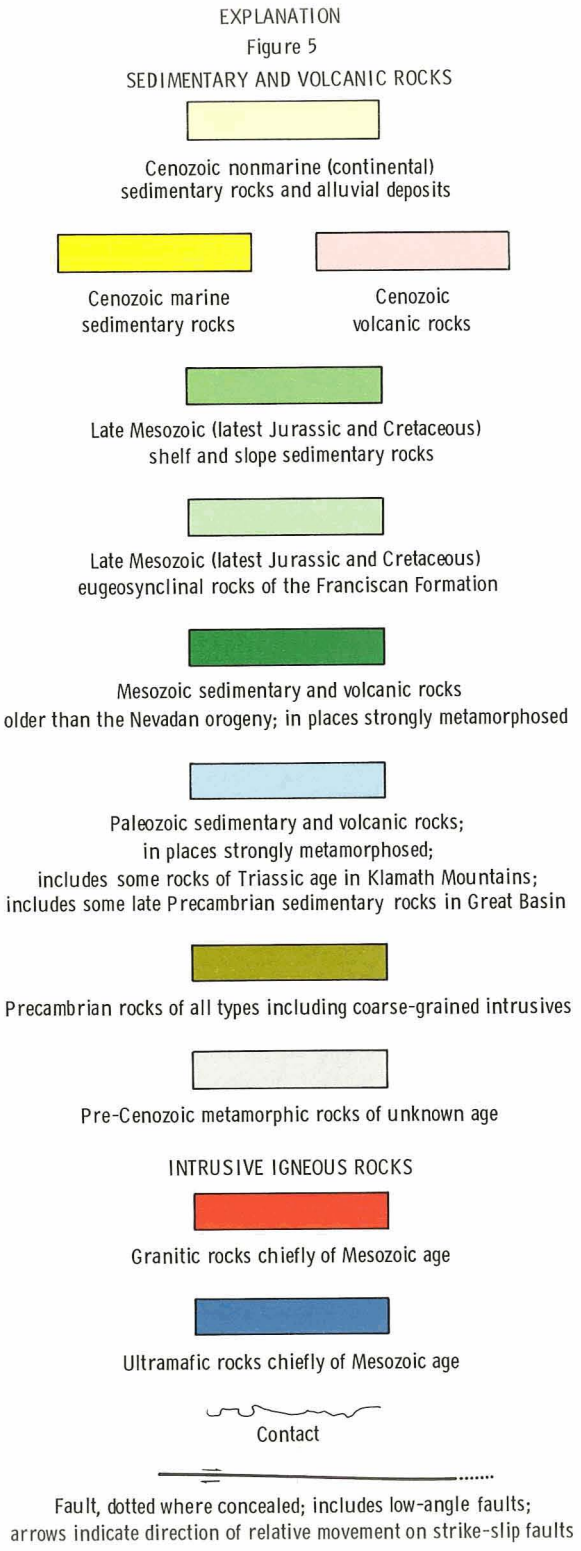


FIGURE 5.—Geologic map of California. The predominant NW-SE geologic trends in California are interrupted by the anomalous E-W trends within the Transverse Ranges. Explanation of map units appears on next page.



In figure 6, lithologic contacts were transferred from the geologic map of the San Gabriel Mountains (refs. 2 and 3). Comparison of color boundaries in the photograph (fig. 7) with the known geologic contacts reveals that the expected photographic contrast is usually not apparent. Discrepancies are greatest where heaviest vegetation occurs in a broad E-W belt along the southern side of the range. This vegetation distribution is a compound effect of increasing elevation into the range and the resultant orographic control on precipitation and climate. Although nearly the entire southern flank of the mountain range has been burned at least once in the recent history of the region, only the effects of the most recent forest fires seem to be visible on the ASTP photographs.

It is possible that, on the first-generation photographic coverage, more subtle indications of primary lithologic character may have been captured. This study was conducted on third- and fourth-generation transparencies and prints in which contrast and discrimination capability may have been reduced.

Atmospheric effects (haze and smog), which constitute frequent hindrances to successful high-altitude photography in this region, are slight to negligible in the mountain ranges in the ASTP photographs. Only a faint diffuseness appears over the piedmont valleys of San Fernando, San Gabriel, and San Bernardino.

MAJOR STRUCTURAL LINEAMENTS

Well-known structural features, especially high-angle faults and fractures, are strikingly visible on the ASTP photographs. Within and bounding the San Gabriel Mountains, several faults of the right-lateral San Andreas system form especially prominent lineaments (AST-14-881 to AST-14-883). These faults include the San Andreas, San Gabriel, San Jacinto, and Punchbowl faults (fig. 8). Notably less conspicuous is the steeply dipping segment of the Sierra Madre Fault zone between its intersection with the San Gabriel Fault and the south edge of the range.

Although major low-angle faults are not as prominent as the high-angle faults, they are iden-



FIGURE 6.—Map showing the location of geologic features on AST-14-882 (fig. 7). In places, the lineaments appear to bound or offset lithologic units; in other places, they appear to cross contacts with no offset. The geologic contacts and faults were identified, in part, with the aid of the Geologic Map of California (refs. 2 and 3).

tifiable with the aid of a geologic map. These faults include the range-front faults (Sylmar and Foothill Boulevard, Sierra Madre, and Cucamonga faults) and the Sawpit Canyon Fault and the Vincent thrust (figs. 4 and 6).

San Andreas Fault Zone

The main trace of the San Andreas Fault zone is the most striking lineament on the ASTP photographs (AST-14-882 and AST-14-883; figs. 7 and

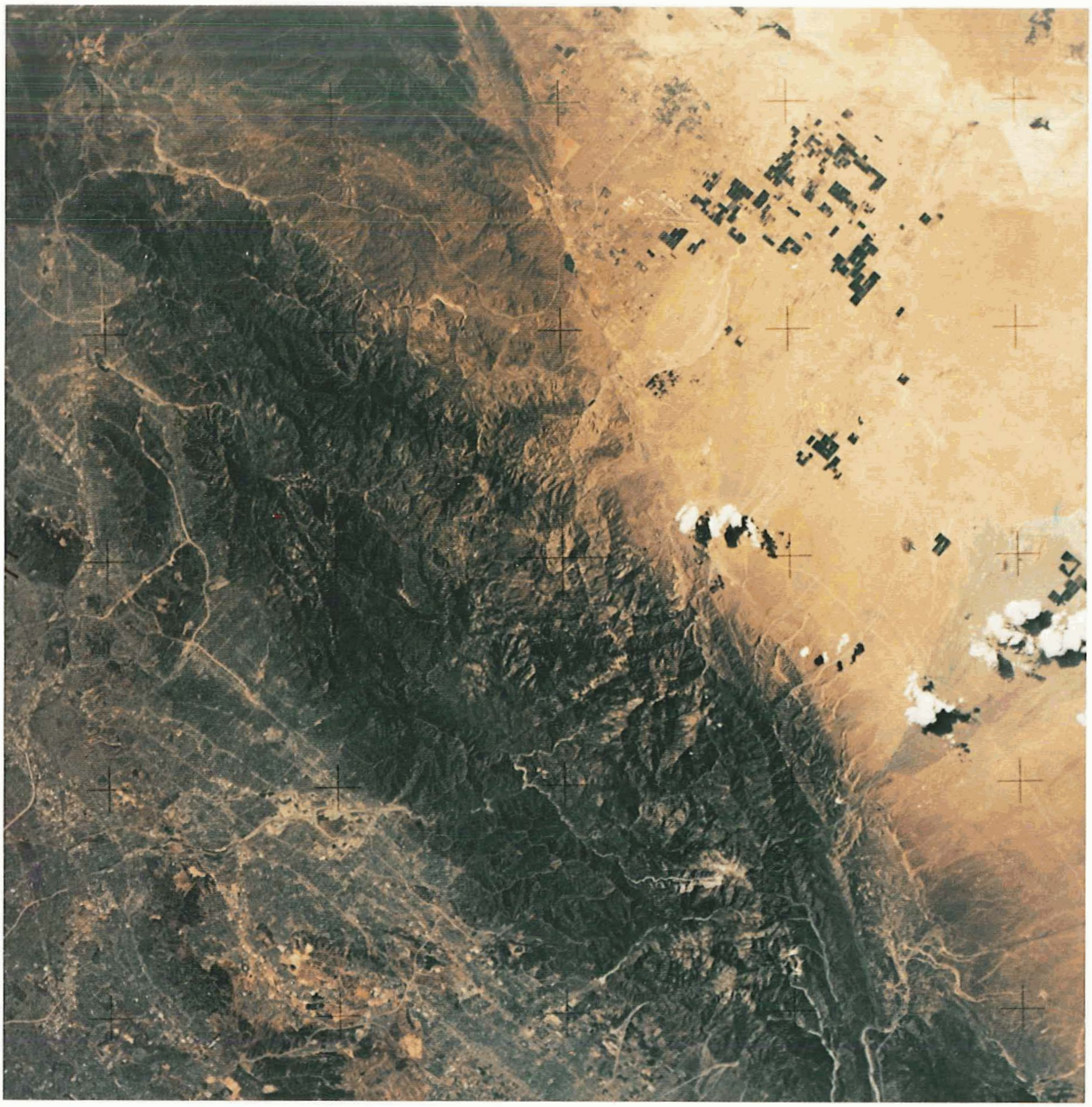


FIGURE 7.—Apollo-Soyuz photograph AST-14-882 covering the San Gabriel Mountains and parts of the Los Angeles Basin and Mojave Desert.

8). In a number of places its several anastomosing subsidiary traces can be seen distinctly. The photographic prominence of the San Andreas system is due in part to its recent disruption of existing topography and in part to preferential erosion along crushed zones that mark its trace. The lineament can clearly be traced through surficial alluvial material as well as bedrock.

Southeast of Palmdale an older trace (?) of the San Andreas Fault, the Punchbowl Fault, also forms a prominent lineament. Of course, the high-altitude aerial photographs (NASA/JSC 239-16-0097) provide greater detail on segments of the major features (figs. 9 to 11).

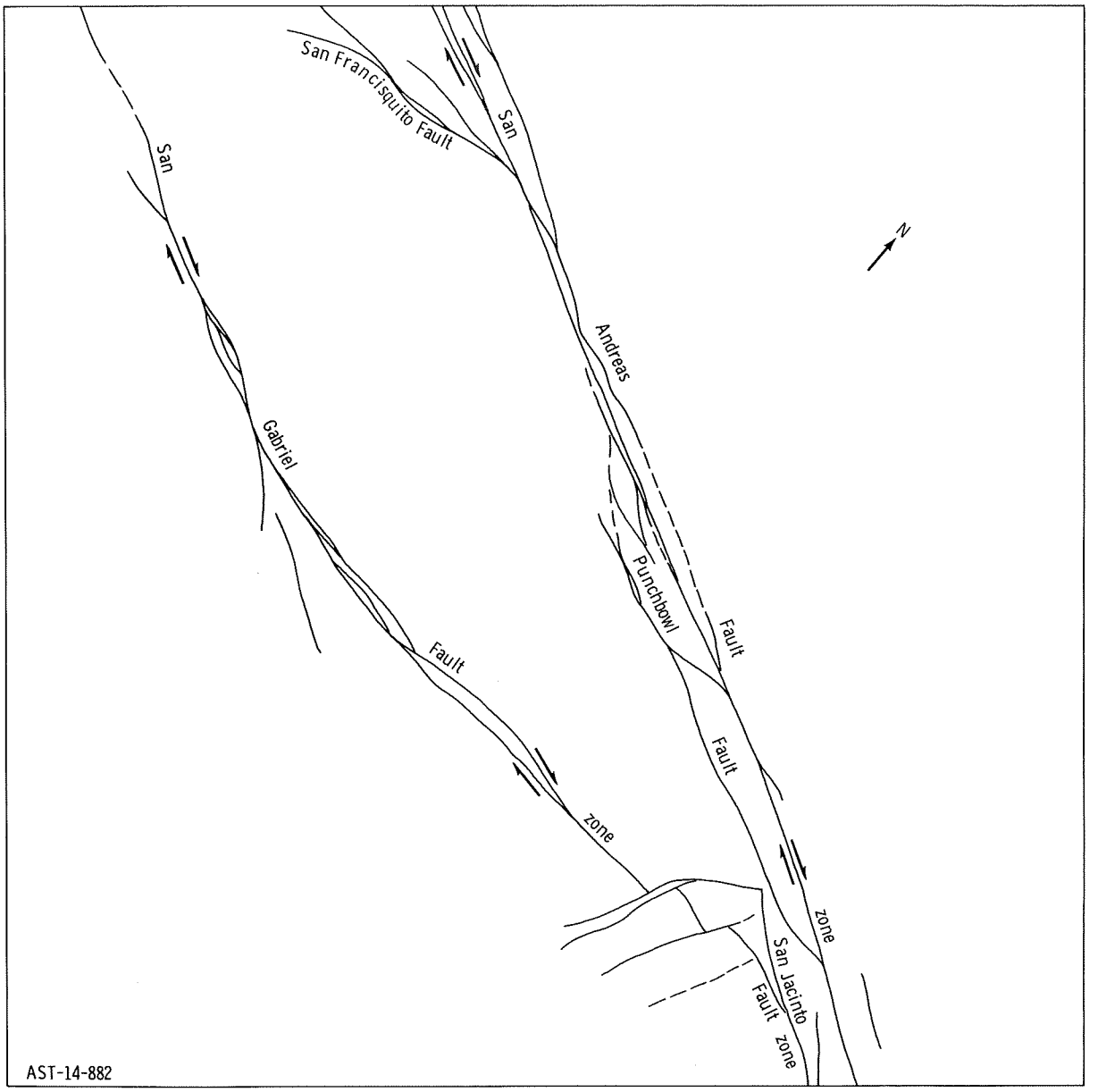


FIGURE 8.—Map showing location of NW-SE trending right-lateral strike-slip faults on AST-14-882 (fig. 7). The San Gabriel Fault may be an older strand of the San Andreas Fault. In a plate tectonic model, both fault zones appear to be the response to differential movement between the North American and Pacific plates.

San Jacinto Fault Zone

The northern end of the San Jacinto Fault, where it enters the San Gabriel Mountains from the San Bernardino Valley, forms a conspicuous lineament (figs. 7 and 8). Whether it intersects the San Andreas Fault is not clear; the resolution on the ASTP photographs is not sufficient to allow an interpretation of the manner in which the two faults merge. Unfortunately, the 1973 high-altitude aerial photographs do not cover the southeasternmost San Gabriel Mountains.

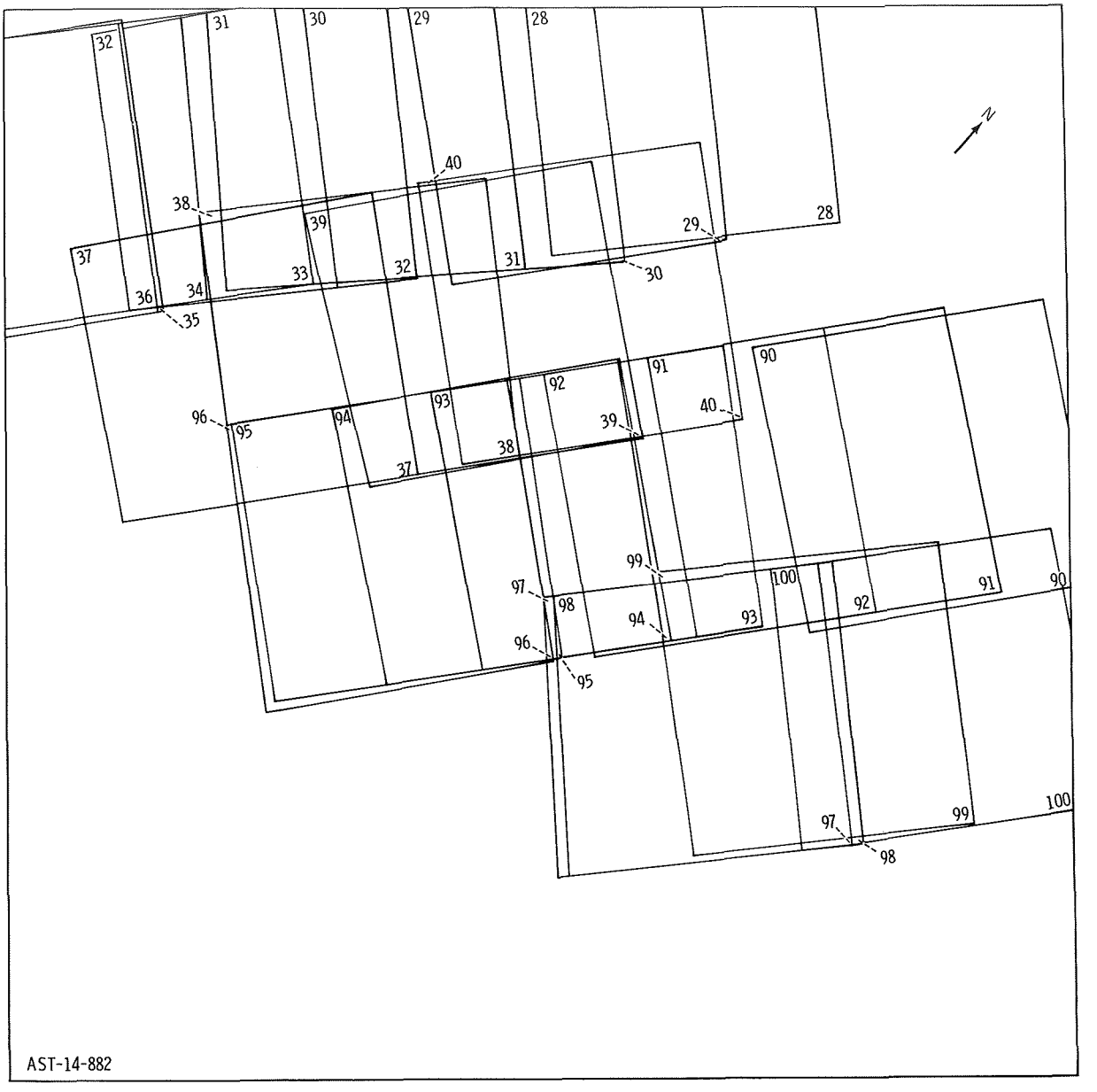


FIGURE 9.—Index map showing locations of NASA high-altitude aerial photographs (NASA/JSC 239-16-0028 to 0040 and 0090 to 0100) on ASTP photograph AST-14-882 (fig. 7). The aerial photographs were obtained by NASA in 1973.

On the ASTP photographs, the San Jacinto lineament appears to merge with the Punchbowl lineament. Surface geologic mapping apparently has eliminated that possibility (refs. 4 to 6). Other possible fault intersections and connections are suggested from study of the ASTP photographs and geologic maps, but they have not been tested in the field.

San Gabriel Fault Zone

The intersection of the San Gabriel and Sierra Madre fault zones in the southwestern San Gabriel Mountains approximately marks a change in trend of the trace of the San Gabriel Fault. The San Gabriel Fault extends 55 km to the east where it is truncated by a NE-trending left-lateral fault.

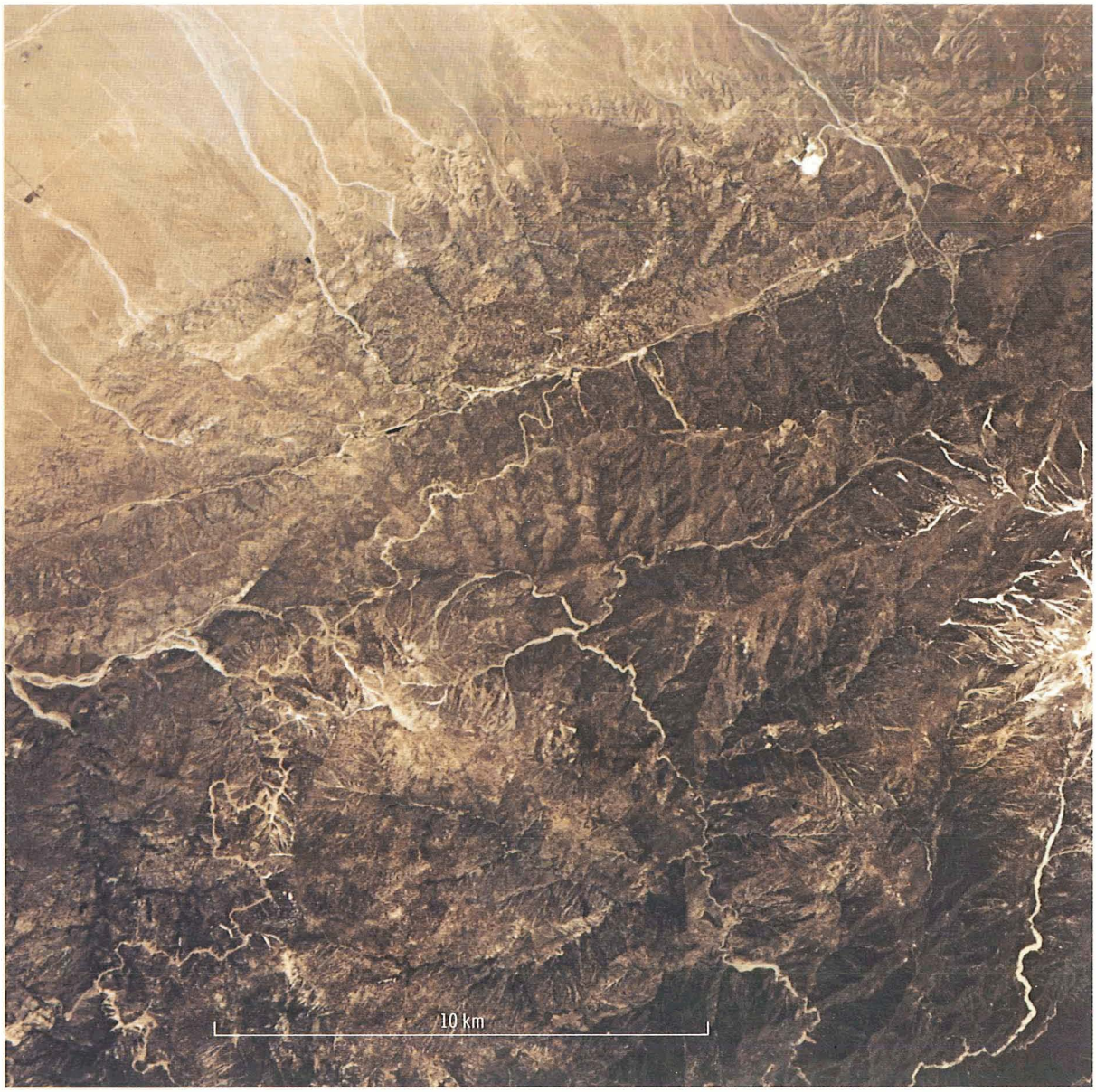


FIGURE 10.—One of a series of high-altitude aerial photographs obtained by NASA in 1973 (NASA/JSC 239-16-0097). See figure 9.

Offset plutonic and metamorphic lithologies along this eastern segment of the San Gabriel Fault record approximately 21 km of right-lateral displacement (refs. 2, 3, and 7). In part, these offset units are visible on the ASTP photographs (fig. 6).

Northwest of the intersection with the Sierra Madre Fault, the San Gabriel Fault can be traced 75 km, nearly to Frazier Mountain, where it is unconformably overlain by Plio-Pleistocene sediments of the upper Hungry Valley formation. The magnitude of displacement along this segment of the fault has not been conclusively demonstrated, but Crowell (refs. 8 to 10) has presented arguments for a cumulative Miocene to Plio-Pleistocene right-lateral offset of 60 km. Within the San Gabriel Mountains, the northwest seg-

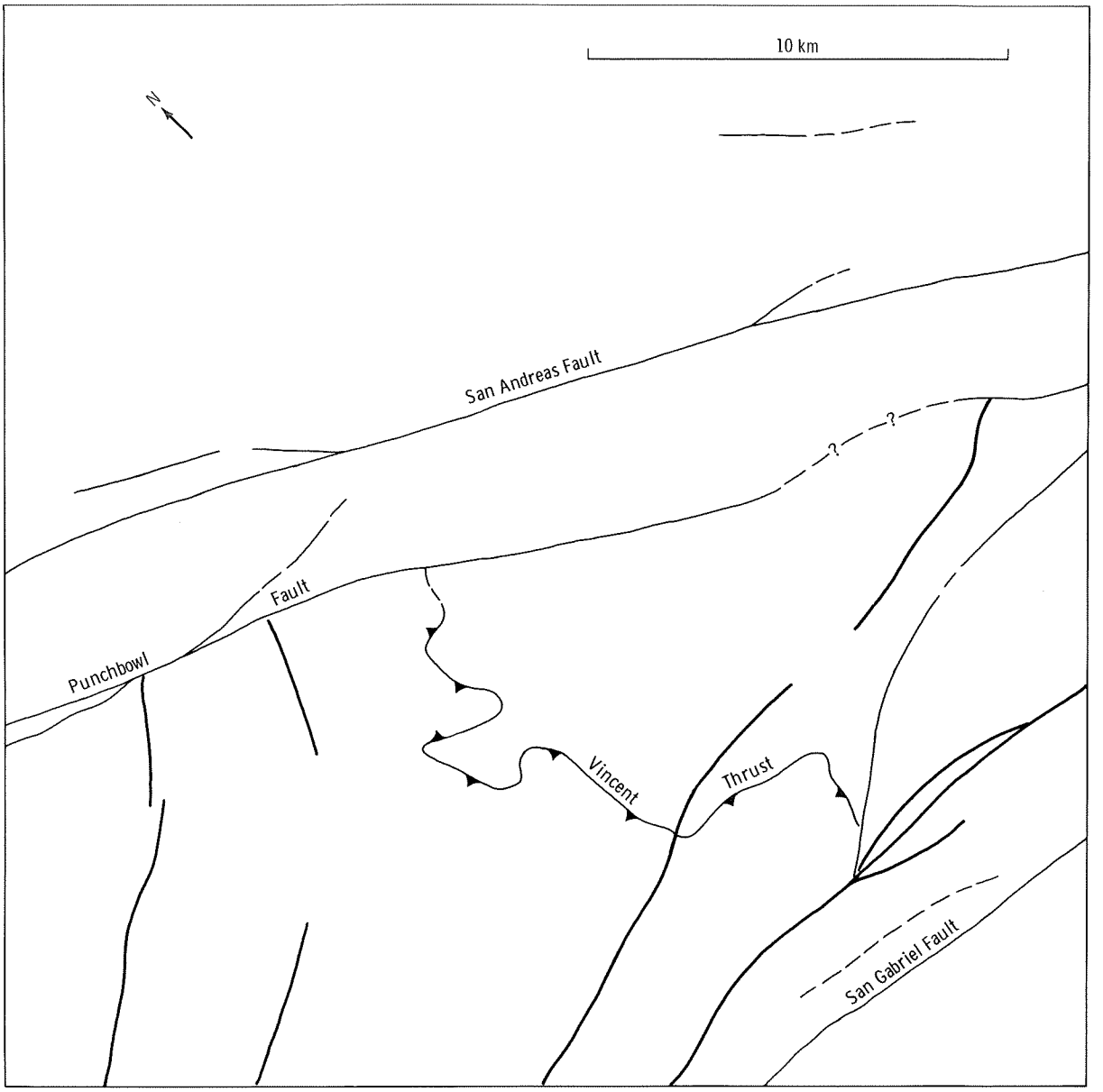


FIGURE 11.—Map showing the faults (solid and dashed lines) and lineaments (bold-solid lines) that can be recognized on NASA/JSC 239-16-0097 (fig. 10). The high-altitude aerial photographs provide greater detail on segments of the major geologic features. Some of the ENE lineaments of the ASTP photographs appear to be discontinuous composites of shorter lineaments on the aerial photographs.

ment of the San Gabriel Fault truncates Paleocene, Miocene, Pliocene, and Plio-Pleistocene sedimentary rocks as well as crystalline basement ranging in age from Precambrian to Cretaceous (refs. 2, 3, 11, and 12). The eastern segment of the fault has only been observed to cut the crystalline rocks. The San Gabriel Fault zone is not seismically active, yet much of its trace is nearly as conspicuous as that of the San Andreas Fault. The lineament must be due entirely to preferential erosion along the fault plane. This observation indicates that striking

photolinearity should not be the sole criterion for recognizing *active* faults.

Figure 6 shows some anastomosing lineaments visible on the ASTP photographs of the San Gabriel Fault zone that have not previously been mapped. These lineaments probably are branches of the fault, but field verification is necessary.

Current interpretations tend to accommodate the difference in displacement along the two segments of the San Gabriel Fault by the transfer of 39 km of right-lateral offset to the diverging Sierra Madre Fault zone. The high-angle segment of the Sierra Madre Fault zone, where it crosses the frontal ridge of the San Gabriel Mountains, is not an especially prominent lineament on either the ASTP photographs or the high-altitude aerial photographs. The contrast between the subdued expression of the Sierra Madre Fault and the striking photolineaments of the other strike-slip faults raises the possibility that this part of the Sierra Madre Fault zone is not a major tectonic feature. Indeed, the authors' field reconnaissance and the published geologic maps indicate that, unlike the San Gabriel Fault, no major lithologic change has been identified across the Sierra Madre Fault zone. Neither published geologic maps nor the fault's appearance on the ASTP photographs require or support a displacement of 39 km along this segment of the Sierra Madre Fault.

Subparallel to the Sierra Madre Fault zone, a pronounced lineament is strikingly visible on the ASTP photographs and discernible on both the high- and low-altitude aerial photographs. Initially, it was thought that this lineament might represent a more significant break than the steeply dipping segment of the Sierra Madre Fault zone. Field reconnaissance, however, has shown that although the lineament does represent a fracture or series of fractures, the horizontal component of displacement is small.

Frontal Sierra Madre and Cucamonga Fault System

The south front of the San Gabriel Mountains forms an impressive escarpment, 1.5 to 2.5 km high, that stretches a distance of 110 km from Cajon Pass on the east to San Fernando on the west. The slopes are generally over-steepened and reflect active uplift and southward translation of the range along thrust faults that dip northward. The actual traces of this fault system are not discernible on the ASTP photographs (AST-14-882 and AST-14-883; fig. 6).

The frontal Sierra Madre Fault system is dominantly a lower angle (dip) fault zone than the San Andreas, San Jacinto, and San Gabriel fault zones. A more irregular trace is to be expected. In detail, the San Gabriel mountain front has a lobate pattern to it (AST-14-882 and AST-14-883; figs. 6 and 12), which is consistent with the shallow northward dip of its controlling faults. The range front (southwest of the San Gabriel Fault) appears in the orbital photographs to be a composite of shingled lobes, which may represent a series of stacked allochthonous slabs (fig. 12).

The frontal fault system is an active feature. Crystalline rocks are thrust over alluvium along the entire front of the range. The San Fernando earthquake (February 9, 1971) broke along the western end of this system on the Sylmar and Foothill Boulevard faults. The San Fernando earthquake affected two of the lobes shown in figure 12. It is plausible that the frontal fault system episodically relieves strain with breakage and earthquakes that result in the southwest movement of one or more lobes.

The San Gabriel Mountains front is arcuate with a changing general trend; nearly east-west from Cajon Pass to the San Gabriel River; southeast-northwest from the San Gabriel River to San Fernando. The NW-SE segment parallels the northwest-trending San Rafael Hills/Verdugo Mountains. The E-W segment forms part of an extended lineament that also incorporates the prominent south flank of the Santa Monica Mountains and the more subdued Raymond Fault and the south end of the Verdugo Mountains. The lineament extends westward from Cajon Pass to Point Dume and beyond (figs. 1 to 4). It may represent a string of coalescing large lobes consisting of the San Gabriel Mountains, the Santa Monica Mountains, and the Santa Cruz and Santa Rosa islands (figs. 1, 5, and 12).

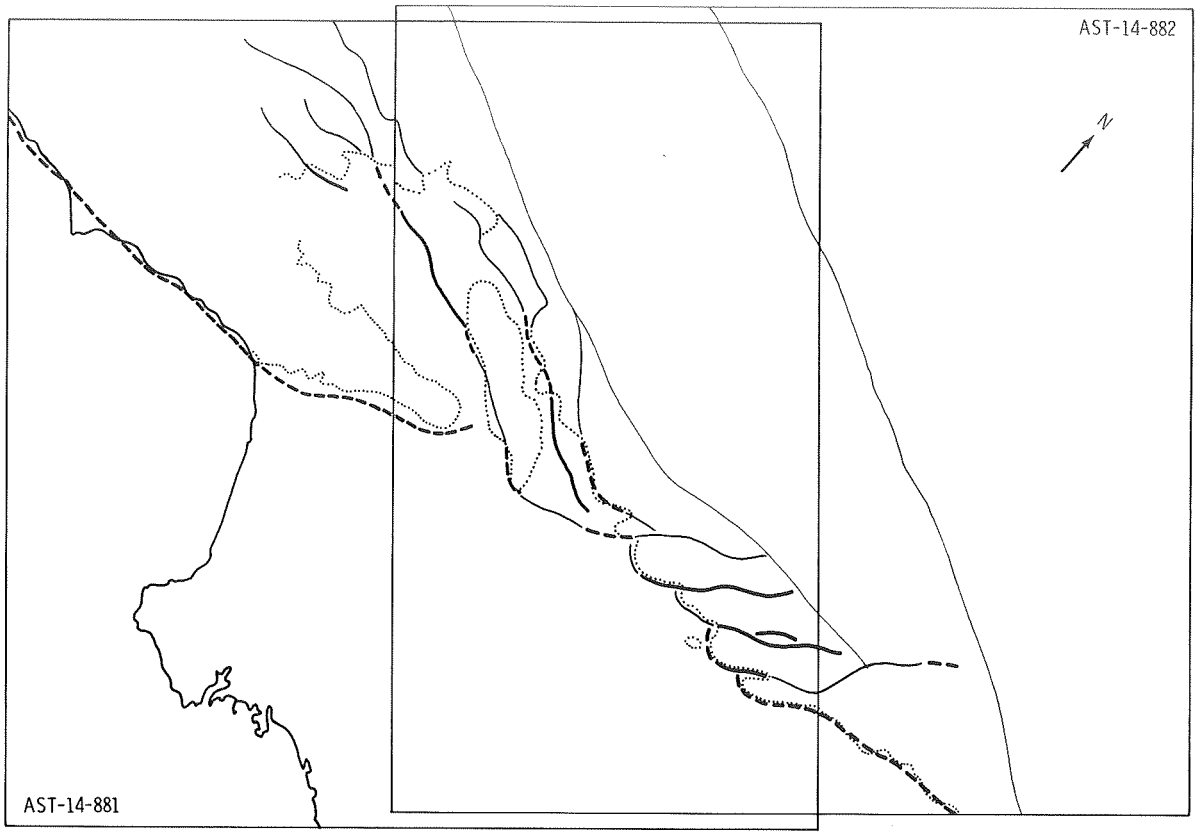


FIGURE 12.—Map showing the lobate nature of the south front of the San Gabriel Mountains. The bedrock-alluvium contact (dotted lines), which represents an abrupt topographic change in slope, displays elements of the lobe pattern. Previously mapped faults (dashed lines) and photointerpreted faults of this study (bold solid lines) appear to control the lobes.

EAST-NORTHEAST STRUCTURAL LINEAMENTS OF THE SAN GABRIEL MOUNTAINS

The Soledad Basin and the northwestern San Gabriel Mountains are cut by several known ENE-WSW trending faults each with left-lateral displacement measured in kilometers. These faults include the Vasquez Canyon, Mint Canyon, Agua Dulce Canyon, Pole Canyon, Magic Mountain, and Transmission Line faults (figs. 6 and 13). Where faults of this set cut the sedimentary section of Soledad Basin, several of them can be shown to be lower to upper Miocene in age. The faults in Soledad Basin are difficult to discern in the ASTP photographs, probably because of low relief within the basin. The faults in the mountains appear to have been topographically emphasized by preferential erosion. Where the faults cut the Precambrian anorthosite(white)/gabbro(dark) contact, left-lateral separation can be seen on the ASTP photographs (figs. 7 and 6). In the southeasternmost San Gabriel Mountains there is a younger set of NE-trending left-lateral faults that cut Miocene plutons as well as the San Gabriel Fault, which was active until Plio-Pleistocene time.

The ASTP photographs reveal a previously unrecognized analogous system of fractures in the intervening parts of the range, representing its largest areal extent. A set of arcuate lineaments that trend ENE-WSW to NE-SW appears to splay eastward from the San Gabriel Fault zone (AST-14-881 to AST-14-883; figs. 6 and 13). Only

fragmental elements of this lineament pattern have previously been mapped as faults (fig. 6). These lineaments appear to be through-going and pervasive on the orbital photographs. Examination of the high-altitude aerial photographs suggests, however, that many of these lineaments may consist of several shorter linear features rather than a single continuous lineament (figs. 10 and 11). Topographically, the lineaments correspond to alined streams, alined saddles and cols, and pronounced linear changes in elevation.

The lineament set occurs geographically between the sets of left-lateral faults previously mentioned. The lineaments may include, in part, elements of both fault sets. In general, though, the lineaments show greater similarity to the older fault set. Neither the lower Miocene fault set nor this lineament set cut the San Gabriel Fault. Both either merge with or are obliquely truncated by the San Gabriel Fault. These lineaments have been recognized only in the block between the San Gabriel and San Andreas faults. They may be present as a distinct set to the south between the San Gabriel and Sierra Madre faults, but, if so, conditions for erosional emphasis of the lineaments have not been favorable.

Photointerpretive evidence for the sense or magnitude of displacement along the lineaments is ambiguous. In places they appear to offset or bound lithologic units left-laterally; in other places they appear to cross contacts with no offset (fig. 6). The tectonic significance of the set of ENE lineaments is not yet fully understood. Many of the traces are in rugged terrain with almost no accessibility; necessary additional field studies will proceed slowly.

PHOTOINTERPRETIVE TECTONIC SYNTHESIS

There are at least two plausible models into which the ENE fault and lineament patterns fit. One model relates the ENE features to the same stress field as the San Gabriel Fault. In this model, the ENE lineaments and left-lateral faults would be a conjugate secondary set of fractures to the right-lateral San Gabriel Fault. The left-lateral faults began somewhat earlier than the San Gabriel Fault. A period of time followed in the upper Miocene during which both the left-lateral and San Gabriel faults were probably active. It is also possible, if the ENE lineaments actually are part of the ENE left-lateral fault set, that the fractures appearing progressively toward the southeast are such that their activity overlaps more in time with that of the San Gabriel Fault. This model is appealing because the trends of the ENE faults and lineaments appear to merge with the San Gabriel Fault rather than butt against it as they do against the clearly younger San Andreas Fault zone.

The alternative model, which is not mutually exclusive with the first model, treats the crystalline complex of the San Gabriel Mountains, along with some of its volcanic and sedimentary cover, as an allochthonous slab or slabs. Geological and geophysical evidence suggests that the exposed parts of the San Gabriel Mountains may be a series of tectonically emplaced slabs (refs. 13 and 14). These allochthonous slabs have been sliced by the San Gabriel and San Andreas fault zone. If this model is essentially correct, then systematic fracture patterns might be expected to develop within a slab as it responds to forces of emplacement and later disruption. Possibly the ENE fault and lineament pattern represents the brittle tectonic response of crystalline slabs emplaced near the Earth's surface, under the peculiar conditions of a transform plate boundary (San Andreas Fault) across which some compressive lithospheric forces are transmitted. The observation that the ENE fracture pattern seems limited to the area northeast of the San Gabriel Fault may mean that the fracture developed within only one of the slabs. For this model, the ENE lineament pattern may be younger than if it were related to the first model.

The plausible sources for the crystalline rocks of the San Gabriel Mountains are east of the San Andreas Fault, some 250 km to the southeast in the vicinity of the Orocopia and Chocolate mountains in Riverside County. Thus, initial horizontal displacement of the San Gabriel Mountains slabs must have occurred at least 4 to 5 million years ago (ref. 15). Subsequent translation along the San Andreas Fault has been accompanied by continued apparent thrusting, which reflects components of compressive force related to ongoing shear along the master fault.

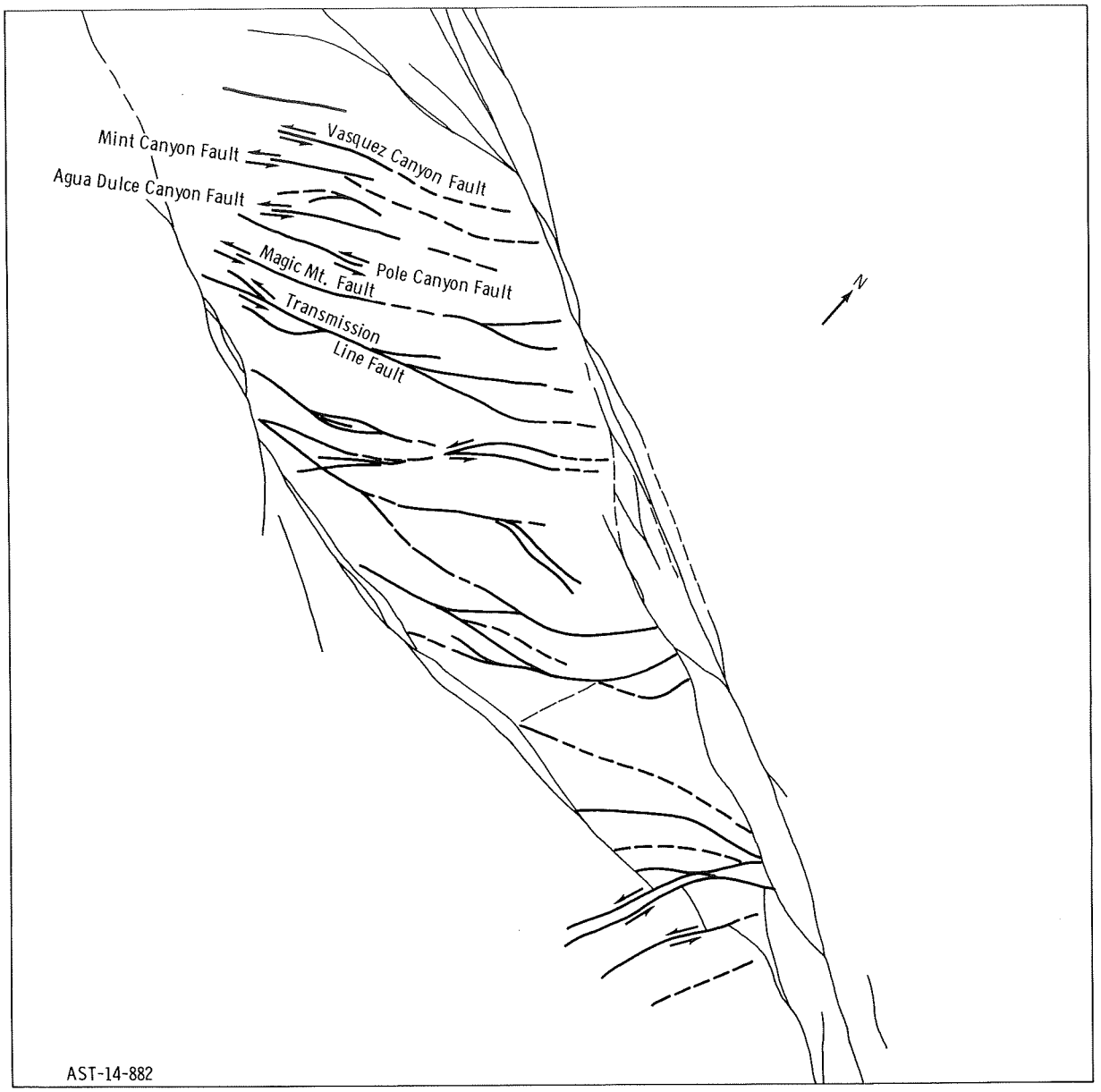


FIGURE 13.—Map showing ENE- to NE-trending faults and lineaments (bold-solid lines) superimposed on the NW-SE fault pattern of figure 8 (medium-weight lines). The ENE-trending system of faults and lineaments has been recognized only in the crustal block between the San Gabriel and San Andreas faults. The timing of their movement seems to overlap that of the San Gabriel Fault. The ENE faults may represent a secondary, conjugate response to the same crustal stress system which produced the San Gabriel Fault.

The lobate nature of the San Gabriel Mountains front (fig. 12) is consistent with the slab model for the emplacement of the range. In terms of presently understood distributions, geologic units of differing lithologies and ages seem to lie within separate shingles of the major lobes. Verification of the lobes as mapped in figure 12, as well as sequence and timing of emplacement of the lobes and of shingles within lobes, must be accomplished by ground studies.

At present, it is not possible to demonstrate whether either of the alternatives discussed previously comes close to representing the tectonic emplacement of the San Gabriel Mountains. If field work confirms the existence of the ENE fracture pattern and of shingled lobate slabs along the range front as mapped on the ASTP photographs, then any satisfactory tectonic model for the Transverse Ranges must account for these structural elements. The concept of shingled lobes of allochthonous slabs offers a powerful new perspective with which to view the tectonic evolution of the San Gabriel Mountains in particular and of the Transverse Ranges in general.

CONCLUSIONS

1. The San Gabriel Mountains front and, by analogy, the south front of the entire Transverse Ranges may be an expression of the lobate emplacement of stacked allochthonous slabs of crustal material transferred from across the North American plate boundary. The tectonic and mechanical implications of such a model offer an exciting new perspective in the tectonic emplacement of the San Gabriel Mountains. The lobate geometry may relate to the manner in which strain is released in ground breakage and earthquakes along the frontal fault system.

2. A previously unrecognized pattern of lineaments has been identified on the ASTP photographs. The lineament set may represent a significant extension of a known set of left-lateral faults.

3. The segment of the Sierra Madre Fault zone from its intersection in the San Gabriel Fault southward to the mountain front does not show the conspicuous photolinearity, surface expression, or crush zone commensurate with a proposed right-lateral displacement of nearly 40 km.

4. Criteria for assessing fault activity and earthquake potential on orbital photographs must be applied with caution. High-angle (steeply dipping) faults form more sharply defined photolineaments than low-angle faults, independent of recency of activity. The prominence of lineaments formed by high-angle faults is not necessarily related to the recency of activity (compare the San Andreas and San Gabriel fault lineaments on the ASTP photographs). Such factors as the width and intensity of fracturing in the crush zone and the relief with respect to drainage base level may be more significant.

5. Even moderate vegetation cover in a semiarid environment masks underlying contrasts in rock and soil types.

6. In general, the color high-altitude aerial photographs were useful for providing more detailed views of those features observed on the orbital photographs.

ACKNOWLEDGMENTS

This work was performed under Smithsonian Institution Grant PC6-22330 as a subcontract of NASA contract NAS9-13831. This is contribution number 2938 of the Division of Geological and Planetary Sciences, California Institute of Technology, Pasadena, California.

REFERENCES

1. Silver, L. T.; Anderson, T. H.; Conway, C. M.; Murray, J. D.; and Powell, R. E.: Geological Features of Southwestern North America. Sec. 4 of Skylab Explores the Earth, NASA SP-380, 1977, pp. 89-135.

2. Jennings, C. W.; and Strand, R. G.: Geologic Map of California. Olaf P. Jenkins edition, Los Angeles Sheet (scale 1:250 000), Calif. Div. Mines and Geol., 1969.

3. Rogers, T. H.: Geologic Map of California. Olaf P. Jenkins edition, San Bernardino Sheet (scale 1:250 000), Calif. Div. Mines and Geol., 1967.

4. Morton, D. M.: Synopsis of the Geology of the Eastern San Gabriel Mountains, Southern California. San Andreas Fault in Southern California, a Guide to San Andreas Fault From Mexico to Carrizo Plain, John C. Crowell, ed., Calif. Div. Mines and Geol. Spec. Rep., no. 118, 1975, pp. 170-176.

5. Dibblee, Thomas W., Jr.: Displacements on the San Andreas Fault System in the San Gabriel, San Bernardino, and San Jacinto Mountains, Southern California. Proc. Conf. on Geol. Problems of San Andreas Fault System, William R. Dickinson and Arthur Grantz, eds., Stanford Univ., 1968, pp. 260-278.

6. Dibblee, T.: Regional Geologic Map of San Andreas and Related Faults in Eastern San Gabriel Mountains, San Bernardino Mountains, Western San Jacinto Mountains and Vicinity. U.S. Geol. Survey Open-File Map (scale 1:250 000), 1970.

7. Ehlig, P. L.: Displacement Along the San Gabriel Fault, San Gabriel Mountains, Southern California (abstract). Geol. Soc. America Program Annual Meetings, San Francisco, 1966, p. 60.

8. Crowell, John C.: Geology of the Hungry Valley Area, Southern California. Bull. American Assoc. Petr. Geol., vol. 34, no. 8, Aug. 1950, pp. 1623-1646.

9. Crowell, John C.: Displacement Along the San Andreas Fault, California. Geol. Soc. America Spec. Paper, no. 71, 1962.

10. Crowell, John C.: The San Andreas Fault in Southern California. San Andreas Fault in Southern California, A Guide to San Andreas Fault From Mexico to Carrizo Plain, John C. Crowell, ed., Calif. Div. Mines and Geol. Spec. Rep., no. 118, 1975, pp. 7-27.

11. Silver, L. T.; McKinney, C. R.; Deutsch, S.; and Bolinger, J.: Precambrian Age Determinations in the Western San Gabriel Mountains, California. J. Geol., vol. 71, 1963, pp. 196-214.

12. Silver, L. T.: Problems of Crystalline Rocks of the Transverse Ranges. Geol. Soc. America, Abstracts with Programs, vol. 3, 1971, pp. 193-194.

13. Ehlig, Perry Lawrence: Geology of the Mount Baldy Region of the San Gabriel Mountains, California. Ph. D. dissertation, Univ. of Calif. at Los Angeles, 1958.

14. Carter, Bruce; and Silver, Leon T.: Structure and Petrology of the San Gabriel Anorthosite-Syenite Body, California. Sec. 2 of the 24th International Geol. Cong., Montreal, 1972, pp. 303-311.

15. Larson, R. L.; Menard, H. W.; and Smith, S. M.: Gulf of California: A Result of Ocean-Floor Spreading and Transform Faulting. Science, vol. 161, no. 3843, Aug. 1968, pp. 781-784.

Marda Fault Zone and the Opening of the Red Sea

Charles A. Wood[a]

ABSTRACT

According to plate tectonic theory, Africa and Arabia were a single continental block before the Red Sea spreading center separated them. The Afar region of Ethiopia is an area of overlap in palinspastic closings of the Red Sea, and thus Afar must be recently created crust. Geologic data support this interpretation except for two old, nonvolcanic massifs—the Danakil Alps and the Aisha hills. Paleomagnetic evidence shows that the Danakil Alps are a sliver of the Ethiopian plateau rotated into Afar by the opening of the Red Sea. It is here proposed that the Aisha hills have moved north-northwestward into their present position by strike-slip movement along the Marda Fault zone, a major fault belt extending more than 900 km across the Horn of Africa. Geological, geophysical, and photographic evidence are presented to support this hypothesis, and obvious problems are pointed out.

INTRODUCTION

Since the early Gemini missions, space photographs have provided clear synoptic views of inhospitable and inaccessible regions that are of critical importance in understanding the geological evolution of the Earth. Nowhere is this better illustrated than in the Horn of Africa, a previously little-known area made important by the recognition of its plate tectonics setting. The general structure of Ethiopia, Somalia, and Arabia has been mapped by using Landsat images (refs. 1 and 2). Apollo, Skylab, and now Apollo-Soyuz Test Project (ASTP) photographs provide additional coverage for detailed study of selected regions. From these resources and recent geologic studies, a new theory for the opening of the Red Sea is presented.

OVERLAPPING PLATES

Wegener and other early proponents of continental drift recognized the remarkably similar shapes of the opposing coasts of the Red Sea and Gulf of Aden, and more than 50 years later, McKenzie et al. (ref. 3) applied the postulates of plate tectonics to quantitatively reconstruct the history of the separation of Africa from Arabia. A provocative consequence of such a reconstruction was the realization that the Afar Depression of Ethiopia (a triangular region at the confluence of the Red Sea, the Gulf of Aden, and the East African Rift Valley (fig. 1; refs. 4 and 5)) must have been created since the breakup of the Afro-Arabian plate. Based on this theory and other geological and geophysical constraints, a model is emerging in which Afar is interpreted as a mosaic of block fault-attenuated continental slabs (ref. 6) and intervening intrusions/extrusions of oceanic crust (ref. 7).

A major problem for this interpretation is that two old, nonvolcanic massifs—the Danakil Alps and the Aisha hills—occur in the overlap zone of Afar. Both blocks are composed of Precambrian gneisses and schists and Mesozoic limestones and sandstones similar to pre-rift rocks found on the Ethiopian and Somali plateaus (ref. 4). Paleomagnetic data (ref. 8) show that the Danakil Alps have rotated approximately 20° to 30° coun-

[a]Brown University, Providence, Rhode Island.

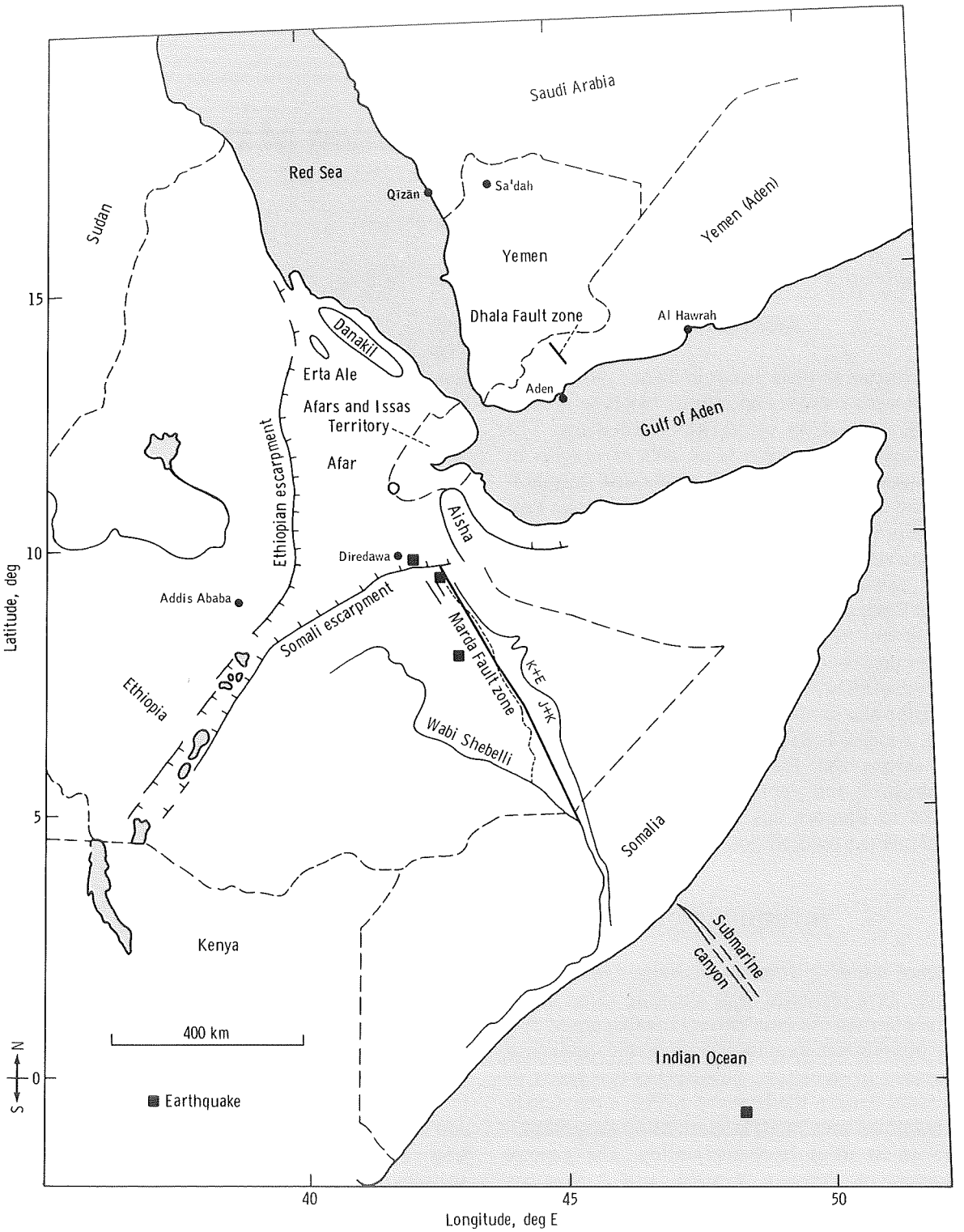


FIGURE 1.—Map of the Marda Fault zone (MFZ) and related structures, based on the maps of Merla et al. (ref. 4) and the U.S. Geological Survey and the Arabian-American Oil Co. (ref. 5) J=Jurassic, K=Cretaceous, E=Eocene.

terclockwise since the early Miocene, and thus are a splinter of the Ethiopian plateau pulled into Afar by the opening of the Red Sea (ref. 9).

There is no comparably simple way to explain the position of the Aisha hills, which extend northward from the Somali escarpment. Arabia could not have occupied Afar, nor could the Red Sea have been completely closed (as indicated by paleomagnetic results; ref. 10), if the Aisha hills were always in their present position. Mohr (refs. 11 and 12) proposed that the Aisha block originated in the Ethiopian rift funnel (approximately 9.5° N, 40.5° E) and moved eastward as a continuation of the Danakil Alps. Approximately 4 million years ago, according to this model, the Danakil and Aisha blocks were separated by a resurgence of sea-floor spreading that affected the Red Sea. If this theory were correct, the southern margin of Afar should be a shear zone, and the Aisha hills would probably be covered by Oligocene to Miocene volcanics such as those that form the Ethiopian plateau. Neither of these consequences is supported by field evidence. Additionally, geologic mapping by Black et al. (ref. 13) demonstrated that the Aisha region is an integral part of the Afar floor that has been affected by regional uplift. Furthermore, gravity data show a 20-km-thick crust under the northern end of the Aisha block. To the south, the crust thickens and apparently shares a continuous root with the Somali plateau (ref. 14).

AISHA AND THE MFZ

An alternative history for the Aisha block—and a speculation on its position prior to moving into the void caused by the separation of Arabia from Africa—is provided by the Marda Fault zone (MFZ). Initially recognized as a northwest-southeast alinement of basaltic vents on the Somali plateau (ref. 15), the MFZ is now believed to extend more than 900 km across Ethiopia and Somalia in line with the Red Sea coast, and is thus a major structural element in the Horn of Africa (ref. 16). Broad zones of crushed and rotated country rocks suggest that this feature is a major wrench fault with large-scale transcurrent movements (ref. 17), and Morton (ref. 18) has speculated that left-lateral displacement of at least 110 km may have occurred. The fault zone is associated with large-amplitude Bouguer gravity anomalies, and opposite sides of the zone have different gravity characteristics (ref. 19).

The MFZ generally coincides with a linear lithologic boundary that extends across the Somali plateau to the Indian Ocean. West of the MFZ are Jurassic to Cretaceous limestones and gypsums, whereas younger Cretaceous sandstones and Tertiary limestones and evaporites occur to the east (ref. 4). The abruptness of this boundary, and the seismic and gravity evidence for significantly different thicknesses of Jurassic limestones on either side of the MFZ (ref. 19), suggest that there has been a vertical component to movement along the fault, with the eastern side having subsided during the Cretaceous. Indeed, the intersection of the fault zone with the Somali escarpment coincides with an abrupt change in the elevation of the escarpment; to the west it is higher than 2 km, but to the east it is lower.

Mohr (ref. 1) noted that recent faulting and volcanism on the floor of Afar are alined with the MFZ. One such lava field occurs at the foot of the Somali escarpment, northeast of Diredawa. This field has not been studied in detail, but according to reconnaissance mapping, it is composed of Miocene-Pleistocene basaltic and rhyolitic flows (ref. 4). On the opposite side of the floor of Afar, a larger volcanic complex also lies along the extrapolated MFZ; this region is shown quite clearly in ASTP photographs (figs. 2(a) and 2(b); ref. 20). The Alayta axial range (the largest volcanic complex in Afar) is the most important feature lying along the projected MFZ, but an unnamed zone of intense faulting and recent fissural volcanism just south of Alayta also trends in the Marda direction (fig. 2). Alayta is an elongated basaltic-trachytic shield volcano surrounded by a broad apron of basaltic lava flows, the most recent of which was emplaced in 1907 (ref. 21). The volcanic field south of Alayta has been mapped as basaltic and is intensely cut by NNW-SSE (MFZ trend) fissures (ref. 20).

This evidence for recent volcanism and fissuring along the MFZ trend in Afar is complemented by the distribution of earthquake epicenters on the Somali plateau. Little seismic activity has been

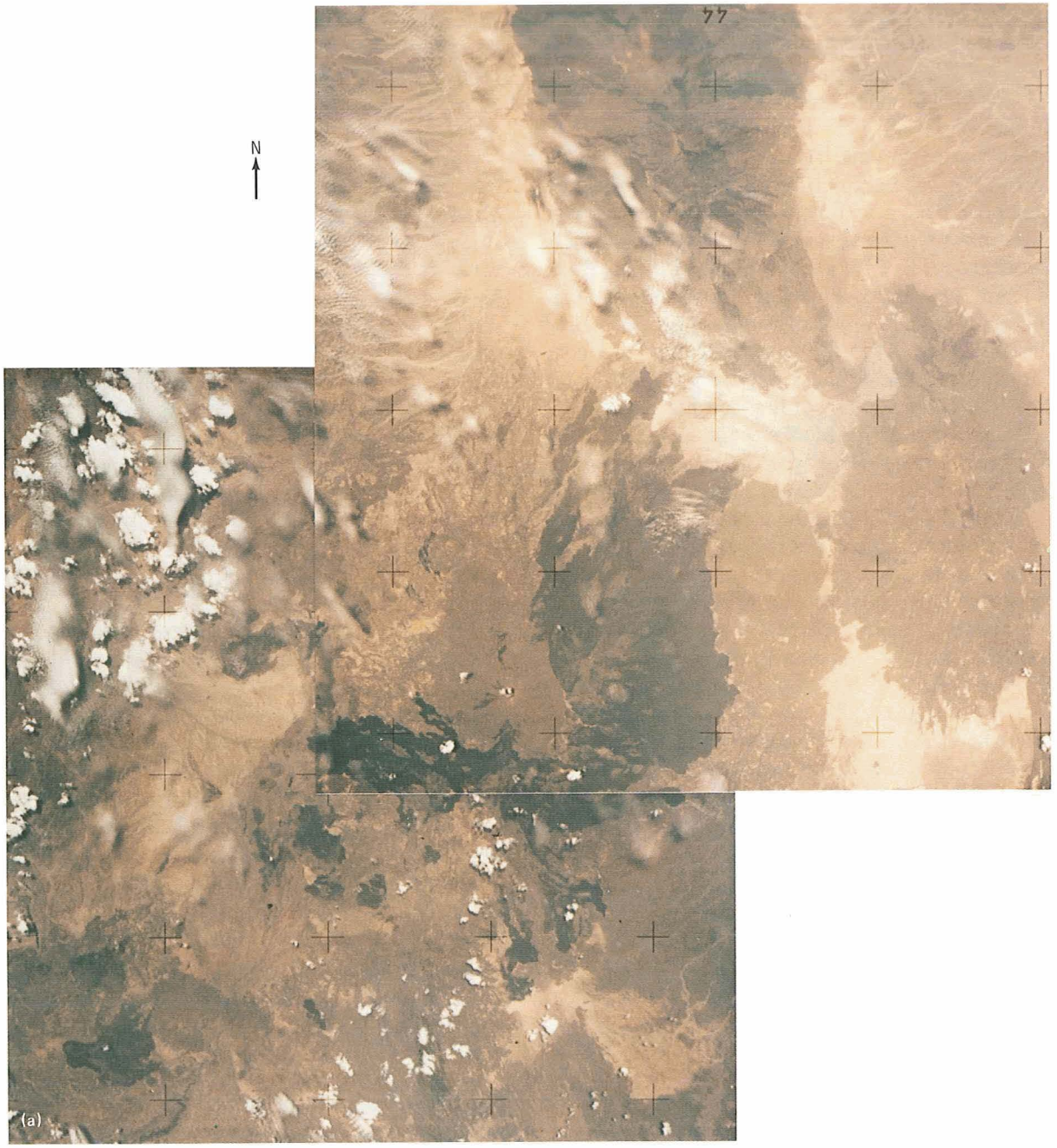


FIGURE 2.—Volcanic complexes in Afar, which are alined along the MFZ trend. (a) Mosaic of two ASTP photographs (AST-14-942 and AST-14-943). (b) Map (based on ref. 20) showing the geology of the area.

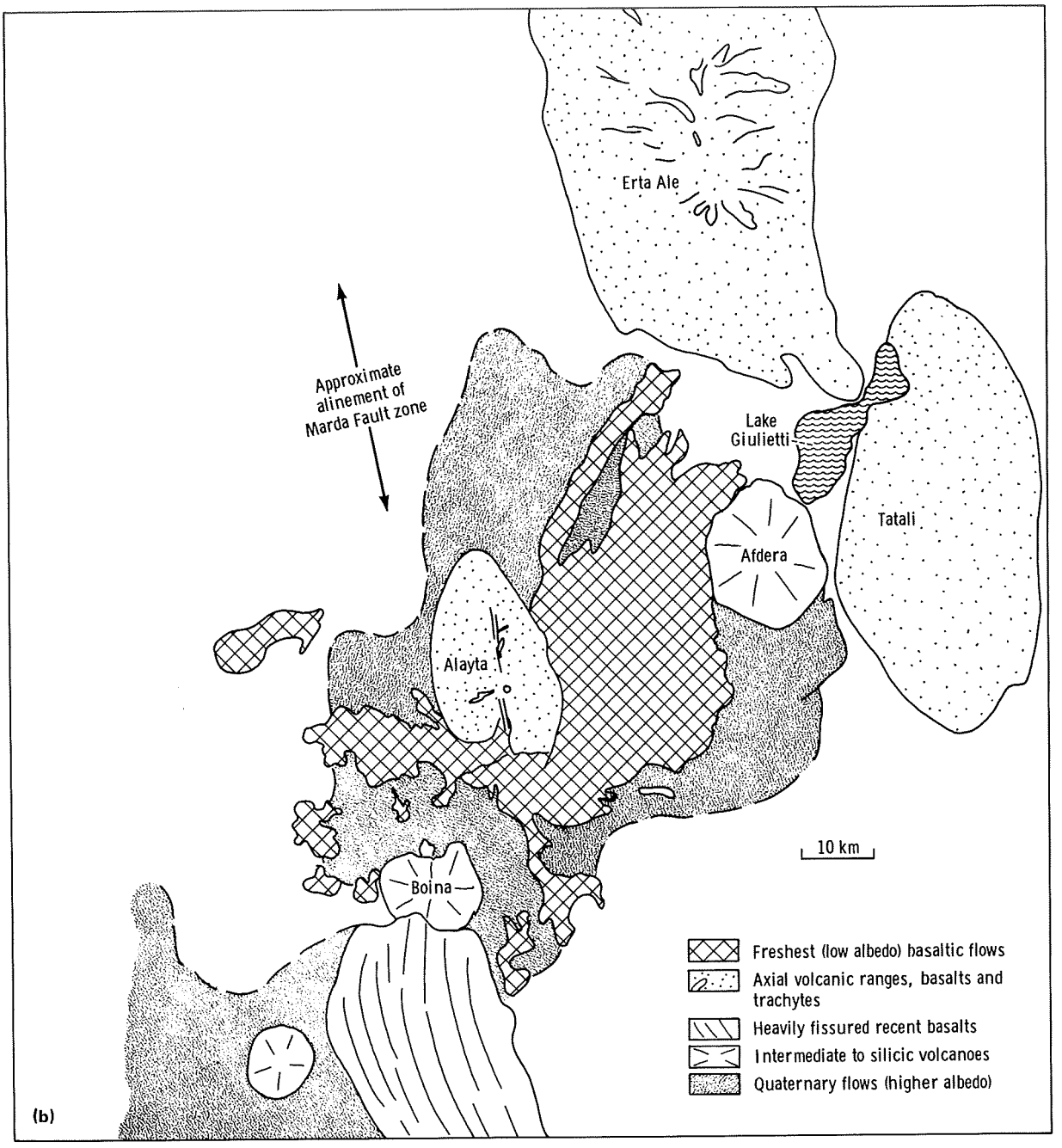


FIGURE 2.—Concluded.

recorded from this area, but three of the six earthquakes reported by Gouin (ref. 22) lie near the MFZ and the others are displaced only 30 to 110 km west of the fault zone. Thus, the MFZ appears to exert a continuing influence on tectonism.

These geological and geophysical observations support the interpretation of the MFZ as part of a major fracture zone extending from Suez, down the west coast of the Red Sea, through Somalia, to the Indian Ocean. Indications of early movement along most of the zone of weakness from Suez southward come from Garson and Krs (ref. 23), who proposed that 75 to 80 km of left-lateral movement occurred along a proto-Red-Sea fracture during Late Cretaceous to Eocene time in association with the initial opening of the Gulf of Aden. Concomitant spreading along the African rift valley would be required to accommodate symmetric opening of the Gulf of Aden (unless the spreading axis moved at half the spreading rate), but geologic evidence does not permit sufficient rift spreading (ref. 24). However, hypothesized movement along the MFZ obviates the need for rift opening, and implies that an equal amount of offset (75 to 80 km) occurred in a right-lateral sense. Thus, early opening of the Gulf of Aden would produce left-lateral strike-slip movement along the Ethiopian escarpment facing the Red Sea, as suggested by Morton (ref. 18) and Garson and Krs (ref. 23), and right-lateral movement along the MFZ, as envisaged by Purcell (ref. 16).

The present projection of the Aisha hills into Afar means that there must have been left-lateral movement along the MFZ since the breakup of the Afro-Arabian shield perhaps 25 million years ago (ref. 25). This movement would have been a minimum of approximately 50 km, the amount that Aisha currently blocks closure of the Red Sea. Nonetheless, to accommodate this motion, a 50-km closing of the Gulf of Aden must have occurred. This is at variance with present understanding of the history of the Gulf of Aden, but the possible activity of a proto-Gulf is little known and open to reinterpretation (e.g., refs. 10 and 26).

A reconstruction of the possible geometry of the Somali escarpment before the postulated movement along the MFZ is shown in figure 3. A left-lateral displacement of 110 km moves the Aisha region completely out of the path of predrift Arabia, and also realines Precambrian outcrops along a continuous east-west trend. The movement does not rotate or move the Aisha region relative to the adjacent Precambrian escarpment, in agreement with gravity evidence of a shared root (ref. 14). Paleomagnetic data showing no displacement of the Somali plate relative to the Nubian plate (ref. 27) were based on lavas from west of the MFZ; the present reconstruction predicts that old lavas east of the fault should have a slightly displaced pole of rotation.

POSSIBLE MFZ STRUCTURES IN YEMEN AND THE INDIAN OCEAN

If the MFZ does represent an ancient fracture that sheared the Horn of Africa during the late Cretaceous/early Tertiary, then there should be northwest-southeast-trending fractures in Yemen. Assuming nearly complete closure of the Red Sea and the Gulf of Aden, the continuation of the MFZ through Arabia should parallel a line between somewhere east of Aden (45° E, 14° N) and Qīzān (42.5° E, 17° N). Most of this region is covered by younger volcanics or sediments (ref. 5), but Landsat images show one possible MFZ-related fracture: the Dhala Fault zone (45° E, 13.5° N) of Mohr (ref. 1), which truncates east-west-trending Precambrian metamorphic rocks. The Dhala Fault zone, and other fractures visible through windows in the overlying volcanics, are somewhat misalined with respect to the expected MFZ trend, but uncertainty in the fit of Arabia against Africa may account for part of the misalinement. Farther east on the Arabian peninsula there is a major fracture zone that parallels the MFZ. An *en echelon* series of northwest-southeast faults extends from Al Hawrah on the Gulf of Aden coast through Sa'dah in northern Yemen, separating Jurassic and Precambrian rocks from Quaternary deposits. Although this lineament does not coincide with the MFZ on a reconstruction of the Afro-Arabian plate, it is interesting to note that it does overlie the present Red Sea coast of Afar.

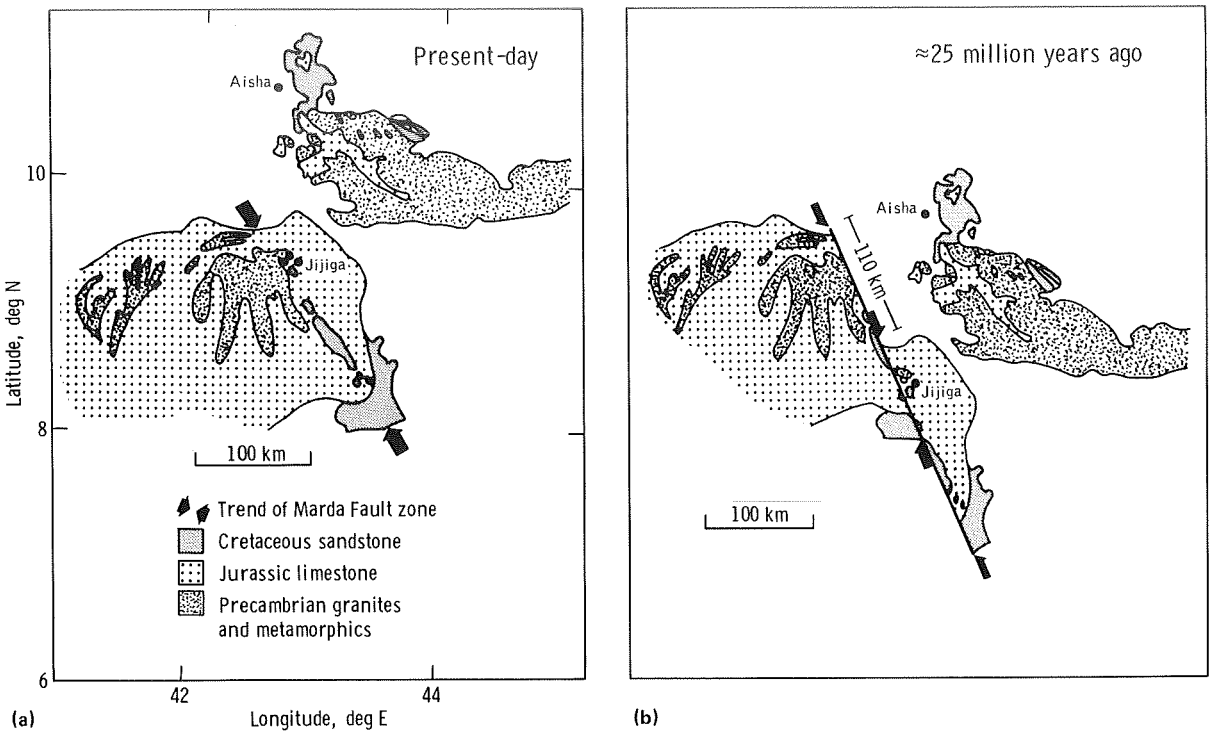


FIGURE 3.—Geological relationships of the Aisha region. (a) Schematic map of present relationships (simplified from Merla et al., ref. 4). (b) Possible reconstruction of original positions of blocks approximately 25 million years ago, prior to the separation of the Afro-Arabian plate.

If the MFZ is a wrench fault, its continuation should be visible under the Indian Ocean. Topography on the Indian Ocean floor (ref. 28, p. 10) does not reveal any continuation of the MFZ; however, this may be due to the more than 2-km-thick sediment blanket on the sea floor off Eastern Africa (ref. 28, p. 118). Some minor signs of the possible continuation of the MFZ do exist. A submarine canyon that is not fed by a present-day river extends from near the prolongation of the MFZ on the Somali coast to approximately 250 km into the Indian Ocean (ref. 28, p. 144). Also on line with the MFZ is the only earthquake recorded off the coast of East Africa that is not associated with major oceanic lineaments. Thus, there are a few tantalizing Indian Ocean alinements that lend support to the theory that the MFZ is a major wrench fault whose movements may account for the present location of the Aisha hills.

ACKNOWLEDGMENT

The author thanks Paul Mohr for his invigorating discussions and encouragement.

REFERENCES

1. Mohr, P. A.: Mapping of the Major Structures of the African Rift System. Final Report. Special Rep. 361, Smithsonian Astrophysical Observatory (Cambridge, Mass.), 1974.

2. Kronberg, P.; Schönfeld, M.; Günther, R.; and Tsombos, P.: ERTS-1 Data on the Geology and Tectonics of the Afar/Ethiopia and Adjacent Regions. Afar Depression of Ethiopia, A. Pilger and A. Rösler, eds., Inter-Union Commission on Geodynamics, Scientific Rep. 14, 1975, pp. 19-27.

3. McKenzie, D. P.; Davies, D.; and Molnar, P.: Plate Tectonics of the Red Sea and East Africa. Nature, vol. 226, Apr. 18, 1970, pp. 243-248.

4. Merla, G.; Abbate, E.; Canuti, P.; Sagri, M.; and Tacconi, P.: Geologic Map of Ethiopia and Somalia, CNR (Consiglio Nazionale Delle Ricerche) (Italy), 1973.

5. Geologic Map of the Arabian Peninsula. U.S. Geol. Survey Miscellaneous Geol. Investigations Map I-270 A, Scale 1:2 000 000, 1963.

6. Morton, W. H.; and Black, R.: Crustal Attenuation in Afar. Afar Depression of Ethiopia, A. Pilger and A. Rösler, eds., Inter-Union Commission on Geodynamics, Scientific Rep. 14, 1975, pp. 55-64.

7. Barberi, F.; and Varet, J.: Recent Volcanic Units of Afar and Their Structural Significance. Afar Depression of Ethiopia, A. Pilger and A. Rösler, eds., Inter-Union Commission on Geodynamics, Scientific Rep. 14, 1975, pp. 174-177.

8. Burek, Peter J.: Paleomagnetic Evidence for an Anti-Clockwise Rotation of the Danakil Alps, Ethiopia. EOS, vol. 51, no. 4, 1970, p. 271.

9. Laughton, A. S.: The Gulf of Aden in Relation to the Red Sea and the Afar Depression of Ethiopia. The World Rift System, T. N. Irvine, ed., Geol. Survey of Canada Paper 66-14, 1965, pp. 78-97.

10. Girdler, R. W.; and Styles, P.: Two Stage Red Sea Floor Spreading. Nature, vol. 247, Jan. 4, 1974, pp. 7-11.

11. Mohr, P. A.: Surface Structure and Plate Tectonics of Afar. Tectonophysics, vol. 15, no. 1/2, 1972, pp. 3-18.

12. Mohr, P. A.: Structural Setting and Evolution of Afar. Afar Depression of Ethiopia, A. Pilger and A. Rösler, eds., Inter-Union Commission on Geodynamics, Scientific Rep. 14, 1975, pp. 27-37.

13. Black, R.; Morton, W. H.; and Varet, J.: New Data on Afar Tectonics. Nature, vol. 240 (Physical Sciences), 1972, pp. 170-173.

14. Makris, J.; Menzel, H.; Zimmerman, J.; and Gouin, P.: Gravity Field and Crustal Structure of North Ethiopia. Afar Depression of Ethiopia, A. Pilger and A. Rösler, eds., Inter-Union Commission on Geodynamics, Scientific Rep. 14, 1975, pp. 135-144.

15. Gouin, P.; and Mohr, P. A.: Gravity Traverses in Ethiopia. Interim Report. Bull. Geophys. Obs. (Addis Ababa), no. 12, 1968, pp. 27-56.

16. Purcell, P. G.: The Marda Fault Zone, Ethiopia. Nature, vol. 261, June 17, 1976, pp. 569-571.

17. Black, R.; Morton, W. H.; and Hailu, Tsegaye: Early Structures Around the Afar Triple Junction. Nature, vol. 248, Apr. 5, 1974, pp. 496-497.

18. Morton, W. H.: A Major Wrench Fault in Ethiopia. Ann. Rep. Dept. of Geology, Haile Sellassie I Univ., 1974, pp. 24-25.

19. Purcell, P. G.: Gravity Anomalies Over the Marda Fault Zone. Bull. Geophys. Obs. (Addis Ababa), vol. 15, 1975, pp. 133-140.

20. CNRS-CNR (Centre National de la Recherche Scientifique/Consiglio Nazionale Delle Ricerche): Geological Map of the Danakil Depression (1:500 000) (Paris).

21. CNR-CNRS (Consiglio Nazionale Delle Ricerche/Centre National de la Recherche Scientifique) Afar Team: Geology of Northern Afar (Ethiopia). Revue de Géographie Physique et de Géologic Dynamique 15, pp. 443-490.

22. Gouin, P.: Earthquake History of Ethiopia. Bull. Geophys. Obs. (Addis Ababa), vol. 16 (in press).

23. Garson, Magnus S.; and Krs, Miroslav: Geophysical and Geological Evidence of the Relationship of Red Sea Transverse Tectonics to Ancient Fractures. Bull. Geol. Soc. America, vol. 87, no. 2, Feb. 1976, pp. 169-181.

24. Mohr, P. A.: The Afar Triple Junction and Sea-Floor Spreading. J. Geophys. Res., vol. 75, Dec. 10, 1970, pp. 7340-7352.

25. Barberi, F.; Borsi, S.; et al.: Evolution of the Danakil Depression (Afar, Ethiopia) in Light of Radiometric Age Determinations. J. Geol., vol. 80, no. 6, 1972, pp. 720-729.

26. Laughton, A. S.; Whitmarsh, R. B.; and Jones, M. T.: The Evolution of the Gulf of Aden. Phil. Trans. Roy. Soc. London, Ser. A, vol. 267, 1970, pp. 227-266.

27. Schult, A.: Paleomagnetic Results From the Ethiopian Southeastern Plateau and the Danakil Block. Afar Depression of Ethiopia, A. Pilger and A. Rösler, eds., Inter-Union Commission on Geodynamics, Scientific Rep. 14, 1975, pp. 80-84.

28. International Indian Ocean Expedition: Geological-Geophysical Atlas of the Indian Ocean. Academy of Sciences of the U.S.S.R., 1975.

Evaluation of Satellite Images of the Levantine Rift Zone

Richard M. Foose[a]

ABSTRACT

Structural and lithologic features along the Levantine Rift zone were mapped using satellite images from three sources: Landsat, Skylab, and Apollo-Soyuz. The accuracy and completeness of these maps were checked during January 1977 on a field trip from the southern end of the Gulf of Elat to the Israeli-Syrian border. Specific structural features and regional tectonic relationships along the zone were clearly displayed on all images. In certain instances, the oblique photographs from Apollo-Soyuz were superior; but, in most cases, the vertical images from Landsat provided more complete and accurate relationships. The analysis of tectonic features mapped on space images concurrent with geologic mapping in the field provides an improved basis for understanding the tectonic evolution of large regions.

INTRODUCTION

The primary objective of this report is to evaluate the effectiveness of satellite imagery as a tool for understanding the tectonic evolution of a region. A detailed technical report by Muehlberger et al. with a more extensive discussion of the Levantine Rift zone is included elsewhere in this publication. (See section entitled "Analysis of Skylab and ASTP Photographs of the Levantine (Dead Sea) Fault Zone.")

Field investigations in the Levantine Rift zone were conducted from January 2 to 12, 1977, by W. R. Muehlberger and this author in the company of Raphael Freund of the Hebrew University in Jerusalem. Freund's model (ref. 1) of the geology and structural development of this zone is widely known and accepted by most geologists. From January 12 to 15, discussions concerning the northern end of the Levantine Rift zone were held with Turkish geologists.

BACKGROUND

The author has performed numerous field studies along parts of the Levantine and Red Sea/East Africa Rift zones (Egypt (1962); Uganda, Kenya, and Tanzania (1965 and 1966); Lebanon and Syria (1969 and 1973); Israel (1973); and Saudi Arabia (1976)). The present field study was performed in Israel (January 1977).

Since the early 1960's, the author has been studying the tectonic framework of the Mediterranean Basin. Since 1973, this study has included using Landsat images and Skylab Earth Resources Experiment Package (EREP) photographs as tools for understanding the tectonic framework and crustal evolution of the Mediterranean region (refs. 2 to 5). Of course, an extensive body of research literature dealing with the geology of the Levantine Rift zone has been published; however, it is not the purpose of this brief report to summarize or cite that literature.

In a small country like Israel, where there are many geologists and where the rock exposures are good, the country has been extensively mapped. Therefore, there is less likelihood of actually discovering significant unmapped structures from

[a]Amherst College.

the analysis of satellite images. However, the opportunity for careful comparison of structures detected on these images with structures shown on existing geologic maps is excellent.

APPLICATION OF SATELLITE IMAGE STUDIES TO THE LEVANTINE RIFT ZONE

Shortly after Landsat-1 was launched in July 1972, many geologists became interested in correlating lineaments observed on satellite images with structural features known from surface mapping, particularly in well-known tectonic regions of the Earth such as the Levantine Rift zone. As part of his research on the tectonic framework of the Mediterranean Basin, the author prepared a map of structural lineaments of this zone in 1973 (ref. 2). A more recent map (ref. 3), showing the major structural features along this zone and in adjacent regions of southern Turkey and Cyprus, is presented in figure 1. This map, prepared from Landsat images, was used during the field study. Before the fieldwork, other single-image tracing maps were prepared using Skylab and Apollo-Soyuz Test Project (ASTP) photographs for all the Levantine Rift zone in Israel.

As a consequence of these preparations and of Freund's field assistance, it was possible to perform effective ground investigations in a relatively short time. It was also possible to concurrently evaluate the effectiveness of the different types of images and to establish constraints and limitations on their use.

Originally, the following five steps were outlined for establishing the usefulness of satellite imagery as a geological tool.

1. Establish which geologic features can and which cannot be seen on the photographs.
2. Establish the large-scale boundaries of the rift zone.
3. Determine which features can be traced across the rift zone.
4. Determine whether unknown megastructures exist that may increase understanding of the tectonic history of the area.
5. Determine the usefulness of such imagery in attempting to solve specific problems.

The preceding steps have been evaluated comparatively with respect to Landsat, Skylab, and ASTP images, and the results are shown in table I.

Most of the important faults, the major fold axes, and the lithologic contacts are observable on all the images, but the Skylab photographs are superior. The large-scale boundaries of the rift zone may be established on all images, but they are clearer on Skylab and Landsat images than on ASTP photographs. Figure 2 is an ASTP photograph showing the major structural features of the Levantine Rift zone in northern Israel and in Lebanon. The most evident feature is the linear, almost north-south-trending fault between the Dead Sea and the Sea of Galilee. North of this area, the main fault trace seems to split into a fan-shaped pattern trending northeast.

The features that can be traced across the rift zone are usually lithologic contacts or rapid changes in lithology. It probably would be possible to match any large faults that would be displaced across the zone, but most of the large faults in the rift zone are parallel or subparallel to the zone itself. Outstanding examples of matching lithologic contacts are (1) Precambrian crystalline rocks with younger Cambrian, Mesozoic, and Tertiary sedimentary rocks, and (2) Neogene basaltic lavas with Tertiary sedimentary rocks. These changes are best seen in Skylab photographs, but they can also be seen in ASTP photographs (fig. 2).

In Israel, no unknown or previously unmapped megastructures were revealed on any of the images. However, as noted earlier, the quality and technical detail of geologic mapping in Israel are very good. Some small lineaments previously identified on Landsat images have been checked in the field by Israeli geologists and found to be newly identified faults, but such discoveries have been limited to smaller structures. In northern Lebanon and in Syria, there are some large lineaments that curve away from the main rift zone toward the northeast and east. These are not shown on published geologic maps of Syria, and they may indeed represent megastructures not previously known (fig. 2). Farther north in Turkey, the northeast-trending structural junction of the Levantine Rift zone with the East Anatolia Fault zone is well shown on both Landsat images and ASTP photographs. In summary, megastructures are well displayed on satellite images. In

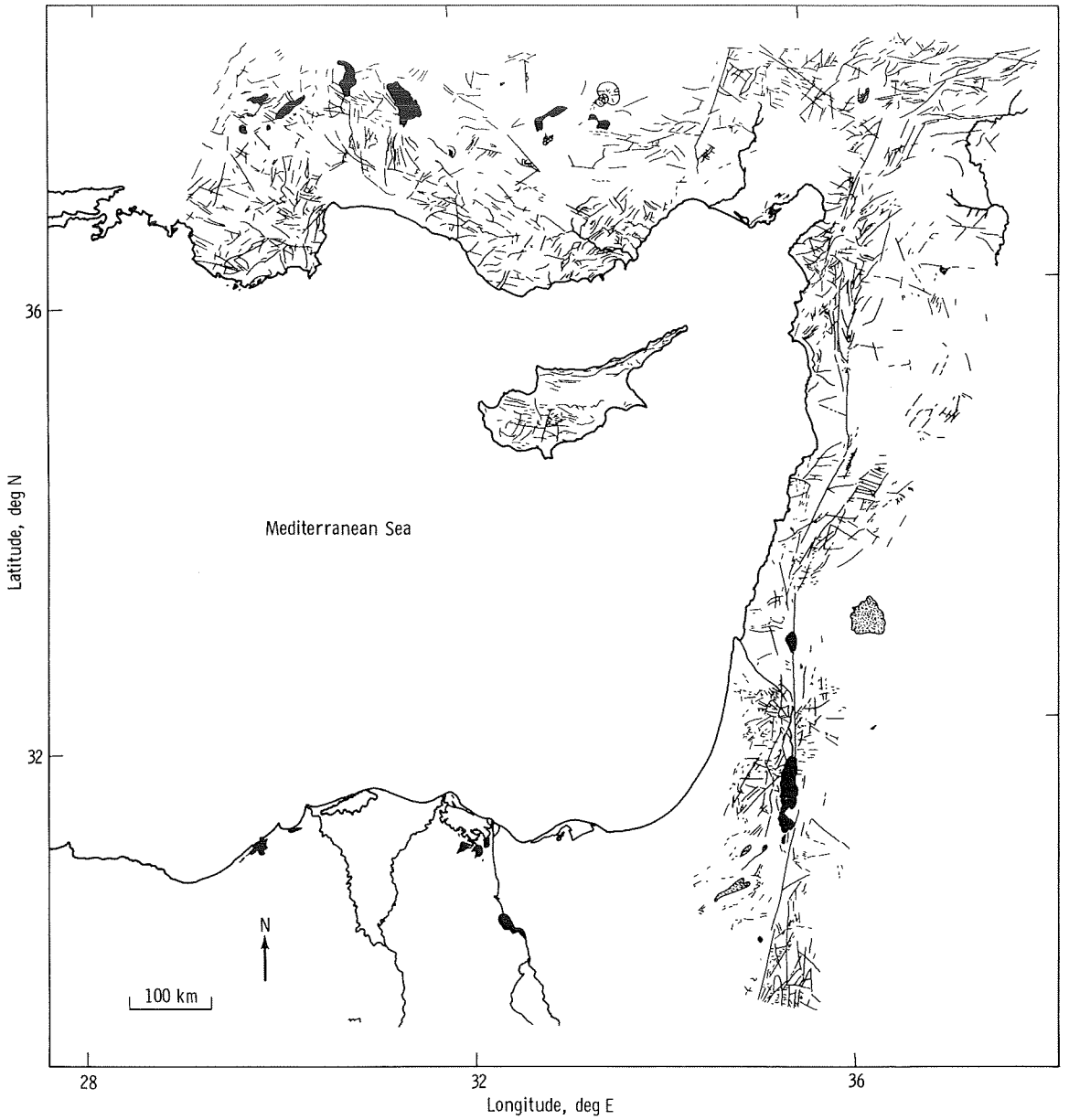


FIGURE 1.—Linear elements of the eastern Mediterranean region as observed on Landsat images.

areas where little prior geologic mapping has been done, there is little doubt that such structures could be seen and understood by skilled interpreters of space imagery.

The usefulness of satellite images in solving geologic problems in the area of the Levantine Rift zone (such as changes in structural style from one place to another; comparisons of tectonic shape, trend, and detail; and the reasons for both large- and small-scale structural relationships in specific places) is very great. The ability to observe faults, shear zones, some fold axes, major lithologic boundaries, sedimentary facies changes, geomorphic "grain," vegetative patterns, and changes in moisture content of soil, and to see each of these in relation to the others within a

TABLE I.—Evaluation of the Effectiveness of Different Types of Satellite Imagery for Geologic Applications

Geologic features visible on images	*Establishment of larger scale boundaries of rift zone*	*Identification of matching lithologic features across zone*	*Identification of previously unknown megastructures*	*Usefulness of images for solving geologic problems*
		Landsat		
Features: 1. All major faults 2. All faults of >5 km strike length 3. Major fold axes 4. Major lithologic boundaries	Clearly established	1. Precambrian crystalline rocks with sediments 2. Neogene basalts with sediments Established	None in Israel[a] but greatly improved observation of regional relations	Main value stems from: 1. Very clear regional relations 2. Guide to key areas for field visitation[b]
Evaluation: Very good	Excellent	Good	Excellent	Excellent
		Skylab (EREP)		
Features: 1. All major faults 2. All faults of >5 km strike length 3. Major fold axes 4. Major lithologic boundaries	Clearly established	Clearly established	Not identified	Not applicable
Evaluation: Superior	Superior	Very good	Excellent	Excellent
		ASTP		
Features: 1. All major faults 2. Some faults of >5 km strike length 3. Some fold axes 4. Most major lithologic boundaries	Well established	Established	Not identified	Not applicable
Evaluation: Fair to good	Very good	Fair to good	Good	Good to very good

[a]Possibly some in Syria. (See text.)
[b]See text.



FIGURE 2.—Major structural features of the Levantine Rift zone in northern Israel and in Lebanon. Two large areas of late Cenozoic basalts are shown with stippling (AST-9-561).

large area is indeed a powerful tool. However, one must emphasize that the main value of satellite imagery is the geometric accuracy and the clarity with which regional relationships are displayed in a much larger area than one could ever hope to study effectively on the ground. The images provide the geologist with a superior guide to key areas that should be visited in the field. The ultimate solution of a geologic problem, however, depends upon the geologist in the field, but his ability to solve the problem is enhanced by the visual clarity of the regional details that may be seen on the imagery. In this regard, ASTP photographs are less satisfactory than Skylab and Landsat images, primarily because the photographic quality and resolution are not as good.

LINEAMENT ANALYSIS

To use the data available on satellite imagery involves the analysis of lineaments. This is a relatively new and potentially powerful tool for the tectonic study of major areas such as the Levantine Rift zone. Attempts have been and are being made to develop objective approaches to the collection, handling, and interpretation of lineament data. Podwysocki et al. (ref. 6) have described one approach to this problem.

During research on the Mediterranean Basin, a computer program was developed for processing all the data on lineaments collected from Landsat images. Lineament shape, length, and orientation are of particular importance. Details of the procedures involved in collecting and manipulating the data have been described by Foose and Brigham (ref. 5). The procedures enable analysis of lineament data (shape, length, and orientation) so that the nature of the stress field within a major morphotectonic unit of the crust is understood. These procedures have been applied to tectonic studies of the Tyrrhenian, Adriatic, and Aegean basins of the Mediterranean, and preliminary results have been published (ref. 2). An important constraint on the space images used is that they must be vertical.

SUMMARY AND CONCLUSIONS

Skylab and ASTP photographs and Landsat images were used prior to and during field study of the Levantine Rift zone in Israel to identify individual structures and to study tectonic relationships. The quality and scale of the Skylab (EREP) photographs were superior to the others.

Constraints that apply to all space images and to their effective use include Sun angle, cloud cover, and obliquity. There was little difficulty with respect to Sun angle or cloud cover on the images of the Levantine Rift zone. The ASTP photographs were occasionally superior to the others because of different angles of obliquity.

Those features best displayed were, of course, linear (i.e., faults, rifts, joint systems, fold axes) and structurally controlled topographic features (mountain crests and valleys). Also well displayed were sediment-filled basins (Dead Sea, Galilee, and Hula basins) and sedimentary veneer-covered areas (Israel coastal plain). Circular features, particularly late Pleistocene and Holocene volcanic cones and craters, were displayed with excellent resolution (25 to 30 m for Skylab).

Because of the excellence of geologic mapping in Israel, it is not possible to say that the subjective use of space images would lead to the formulation of a tectonic evolutionary history different from or superior to that postulated by Freund (ref. 1). However, the clarity of the regional tectonic relationships displayed on all the images is such that the critical scrutiny of his conclusions and the possibility of making suggestions for modifying them are clearly enhanced.

Finally, there is the potential for performing a more objective analysis of the lineament data on Landsat and/or Skylab images of the Levantine Rift zone. This analysis could materially add to understanding of the structural relationships in specific parts of the rift zone and of the tectonic evolution of the entire rift zone. In this way, the space images would have significant value.

ACKNOWLEDGMENTS

The fieldwork in Israel was performed with William R. Muehlberger, University of Texas, and with Raphael Freund, Hebrew University of Jerusalem. Freund made all logistical arrangements for the fieldwork and was the source of extensive unpublished geological information.

This work was performed under Smithsonian Institution Grant PC70-3963 as a subcontract of NASA contract NAS9-13831.

REFERENCES

1. Freund, R.: A Model of the Structural Development of Israel and Adjacent Areas Since Upper Cretaceous Times. Geol. Mag., vol. 102, no. 3, 1965, pp. 189-205.

2. Foose, R. M.: ERTS Satellite Photography as a Tool for Tectonic Investigations in the Mediterranean Basin. XXIV Congres de Commission Internationale pour l'Exploration Scientifique de la Mer Mediterranee, Monaco, vol. 22, 1974, pp. 91-94.

3. Foose, R. M.: Structural Lineaments and Tectonics of the Mediterranean Basin. XXV Congres de Commission Internationale pour l'Exploration Scientifique de la Mer Mediterranee, Split, vol. 23, 1976.

4. Foose, R. M.: Structural Lineaments and Tectonics of the Mediterranean Basin. Structural History of the Mediterranean Basins, B. Biju-Duval and L. Montadert, eds., Editions Technip (Paris), 1977, pp. 221-232.

5. Foose, R. M.; and Brigham, R.: Interpreting the Genetic Character of Structural Lineaments in the Mediterranean Basin. Paper presented at Second International Conference on the New Basement Tectonics, University of Delaware, July 1976.

6. Podwysocki, M. H.; Moik, J. G.; and Shoup, W. C.: Quantification of Geologic Lineaments by Manual and Machine Processing Techniques—Landsat Satellites—Mapping/Geological Faults. NASA TM X-70951, 1975.

Analysis of Skylab and ASTP Photographs of the Levantine (Dead Sea) Fault Zone

W. R. Muehlberger,[a] L. K. Goetz,[a] and R. C. Belcher[a]

ABSTRACT

The Dead Sea Rift (fault) zone marks a transform plate boundary between the African and Arabian plates. Geologic evidence from offset geologic boundaries along the fault zone and from magnetic anomalies in the Red Sea demonstrates that the opening of the Red Sea and slip along the Dead Sea Fault zone occurred in two phases. The first phase, 48 to 34 million years ago, accounts for 60 km of left slip, and the present active phase accounts for another 40 to 45 km of left slip.

Space photographs show fracture and fold patterns and offsets of surficial structures. Many of the identified offset geological boundaries are only demonstrable by means of cross-section or subsurface mapping. Skylab handheld-camera photographs of the Sinai Peninsula and vicinity show a prominent linear, not previously recognized on either Landsat imagery or conventional aerial photography, that is offset approximately 105 km. This line may represent the outer boundary of extensional phenomena associated with the opening of the Red Sea.

Several sets of photographs with different Sun angles and look directions are available for the fault zone between the Dead Sea and southern Lebanon. These photographs demonstrate (1) the utility of vertical photography for synoptic, orthogonal mapping, (2) the difference in interpretability of high- and low-Sun-angle photography (i.e., low Sun angle emphasizes subtle structural and topographic variations), and (3) the utility of oblique, handheld-camera photographs, which emphasize the linearity or sudden, sharp bends of otherwise linear features.

The strip of Apollo-Soyuz mapping photographs of northwestern Syria and adjacent Turkey produces a structural interpretation that differs from previously published surface maps. The new interpretation shows a splintering of the Dead Sea Fault zone northward toward the East Anatolian Fault zone. This splintering has deranged modern drainage systems, which indicates that this region is tectonically active and that these faults constitute a major earthquake hazard.

INTRODUCTION

According to plate tectonic theory, the Dead Sea Rift zone is a transform boundary between the African and Arabian plates. This zone extends from the Gulf of Aqaba northward to the East Anatolian Fault at the Taurus Mountains in southern Turkey (fig. 1). Several authors have concluded that strike-slip movement, which began during the Eocene epoch, totals approximately 105 km, with 45 km occurring during the Pleistocene and Recent epochs (refs. 1 to 6). Other authors attribute the origin of the Dead Sea Rift zone to extensional movements with a minor or late strike-slip component (refs. 7 to 13), or a combination of both (ref. 14).

Manned-spacecraft photographs of the area were studied to evaluate the usefulness of such photographs in geological research and to establish the present-day tectonic style of the rift zone. Lineaments on the photographs were mapped and

[a]University of Texas at Austin.

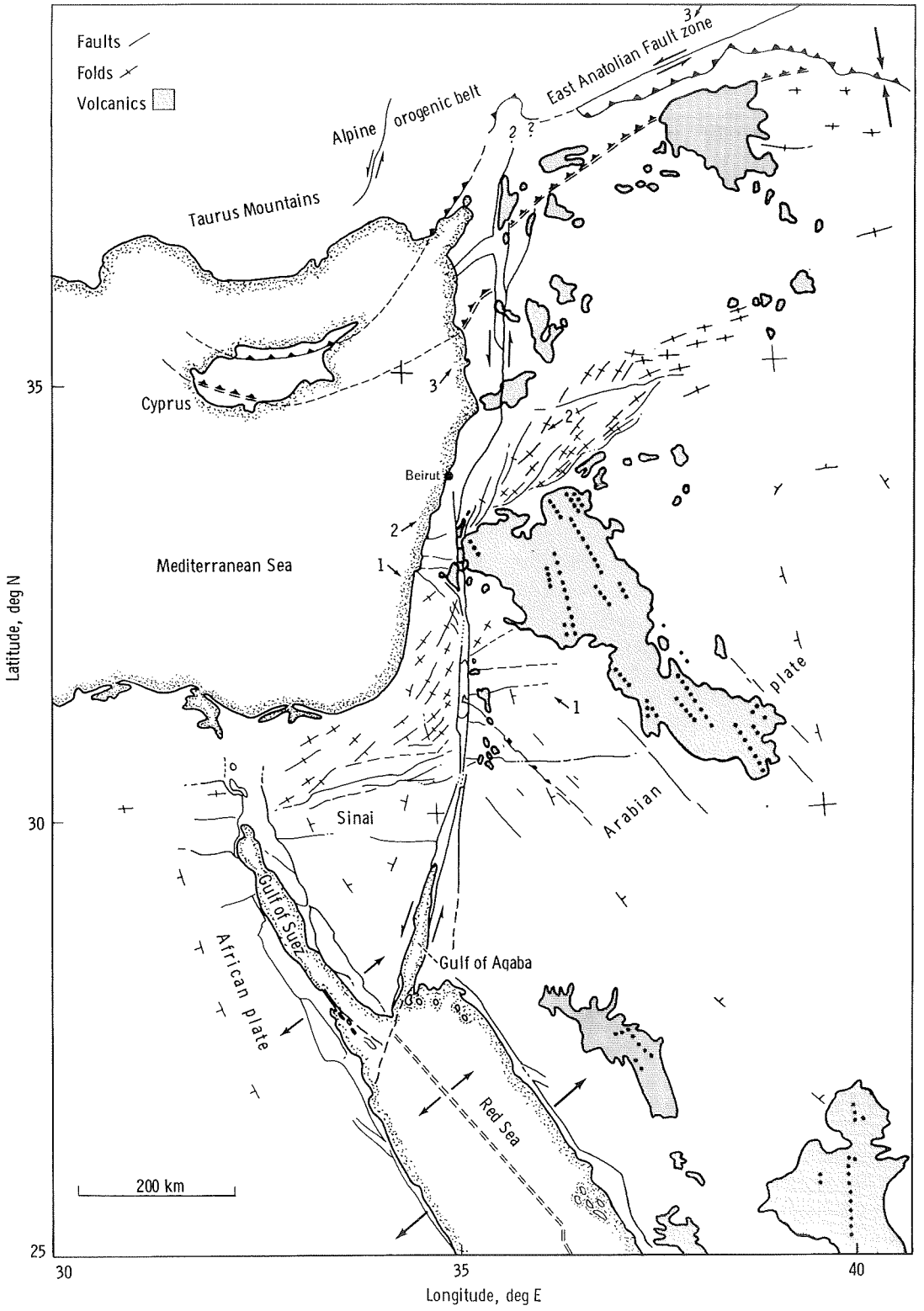

Faults
Folds
Volcanics
Alpine orogenic belt
East Anatolian Fault zone
Taurus Mountains
Cyprus
Beirut
Mediterranean Sea
Sinai
Gulf of Suez
Gulf of Aqaba
African plate
Arabian plate
Red Sea
200 km
Latitude, deg N
Longitude, deg E
25
30
35
40

FIGURE 1.—General setting of the Dead Sea Rift (from Freund and Garfunkel, ref. 6). Oblique to nearly vertical photographs from the Skylab and Apollo-Soyuz missions provide coverage from the Sinai Peninsula to the Sea of Galilee (near "1"). More distant, oblique views cover this region up to the latitude of "3," including a westward view at the latitude of "3." Vertical mapping passes were made on Skylab 3 at "1," and on Apollo-Soyuz at "2" and "3." Parts of this region have been covered by earlier missions, but the photographs were not specifically studied for this project.

grouped into three categories as follows: (1) lineaments marking a definite break in topography were denoted by solid lines with tick marks on the lower downthrown side, (2) lineaments marking a definite boundary, but across which a difference in topography could be detected, were denoted by solid lines, and (3) lineaments marking a vague boundary, usually a color change, were denoted by dashed lines. Although all mapped lineaments supposedly represent faults or major fracture zones, some of the mapped lineaments may actually be features such as vegetation changes, erosional escarpments, and dune fronts.

REGIONAL ANALYSIS

The direction of movement and the timing of displacements along the Dead Sea Fault zone have been subjects of discussion since geologists first began investigating this region. An excellent historical review of the principal arguments about whether this zone represents rifting, ramping, or left-hand shear is provided by Freund et al. (ref. 15). The work of Freund and associates, in conjunction with studies of the opening of the Red Sea (ref. 5), shows that the Dead Sea Fault zone has had two periods of left-hand strike-slip motion. The early phase, consisting of 60 km of left slip and previously dated only as pre-Miocene from the Dead Sea region, was shown to be upper Eocene to early Oligocene (48 to 34 million years ago) and to coincide with the initial rifting of the Red Sea and the Gulf of Suez. The present phase began approximately 4.5 million years ago and has accumulated an additional 40 to 45 km of slip.

Many of the geological features that are displaced laterally across the fault zone cannot be seen on space photographs, but can be detected only by reconstruction in cross sections of lateral variations of geologic units. The principal features to be recognized on the photographs are displaced faults and folds, and patterns of structures that demonstrate the sense of slip (rectangular or rhomb-shaped grabens, displaced stream segments, fault scarps, and other physiographic anomalies). The structures and patterns seen on these photographs are best explained by invoking major left-hand strike-slip movement.

The only surface features that do not easily match those of Freund et al. (ref. 3) consist of the offset Miocene rivers in the Dead Sea Region. A comparison of their figure and Skylab photograph SL4-194-7260 shows that the rivers can be correlated, but only by geologists familiar with the area. A study of the photograph shows that principal river systems east of the Dead Sea are deeply incised into the plateau because their local base level, the Dead Sea rhomb graben, has dropped below sea level. However, those west of the Dead Sea are not incised, but have instead been beheaded. These rivers are difficult to detect on the photograph. Remnants of the Miocene river deposits of the "Rotem River" are identifiable as lighter brown areas west of the southern end of the Dead Sea and north and west of the breached oval cores of two prominent anticlines.

The valley occupied by the Dead Sea Fault zone is subdivided into a series of blocks. The shape of the blocks is rhombic, and the direction of elongation is parallel to the major bounding faults of the zone (i.e., along faults that trend slightly east of the main direction of elongation of the valley). The Dead Sea lies within one of the rhomb-shaped depressions. This depression, formed during the first period of fault movement, lies to the south and has been completely filled so that only the southern and western scarps are still visible 60 km south of the Dead Sea. To the north, the Sea of Galilee and the Hula Depression lie in topographic lows caused by the opening of a younger rhomb graben.

DESCRIPTION OF AREAS STUDIED

Linears observable on the Skylab and Apollo-Soyuz photographs are described in this section.

Sinai Peninsula to the Dead Sea

The linears shown in figure 2 were mapped twice from an uncontrolled mosaic of three Skylab 4 photographs and were repeatable. Figure 3 is a high-oblique Apollo-Soyuz photograph that shows most of the area covered in figure 2. Comparison with published literature shows similar linear patterns, particularly near the Gulf of Aqaba (Eilat). The frequency of individual occurrence of the strikes of these linears was plotted in 5° intervals (fig. 4). Length was not considered. The area was divided into four subregions as follows: Area I, east-southeast of the Dead Sea; Area II, northeast of the Gulf of Aqaba; Area III, west of the Gulf of Aqaba; and Area IV, east of the Gulf of Aqaba. All areas have a prominent north-trending maximum, which is roughly parallel to the rift. In addition, the linears have the following maximums: 90° W, 60° W, north-south, 30° E, and 60° E. The Sinai Peninsula (Area III) has additional important trends of 45° W, 15° E, and 60° E. The similarity of trends in the Sinai Peninsula and northeast of Eilat is striking.

From south to north along the eastern side of the rift, the dominant trend shifts from mostly northeast, to northeast and northwest, to mostly northwest. At the southern end, northwest-trending linears are nearly absent to the east of the Gulf of Aqaba, whereas they are dominant in the Sinai Peninsula. The northwestward trend in the Sinai Peninsula, and in parallel structures farther north, is parallel to the Gulf of Suez and may be related to that earlier rifting stage.

No large horizontal displacements are obvious from an analysis of these photographs. Where offsets of linears are found, they usually show a

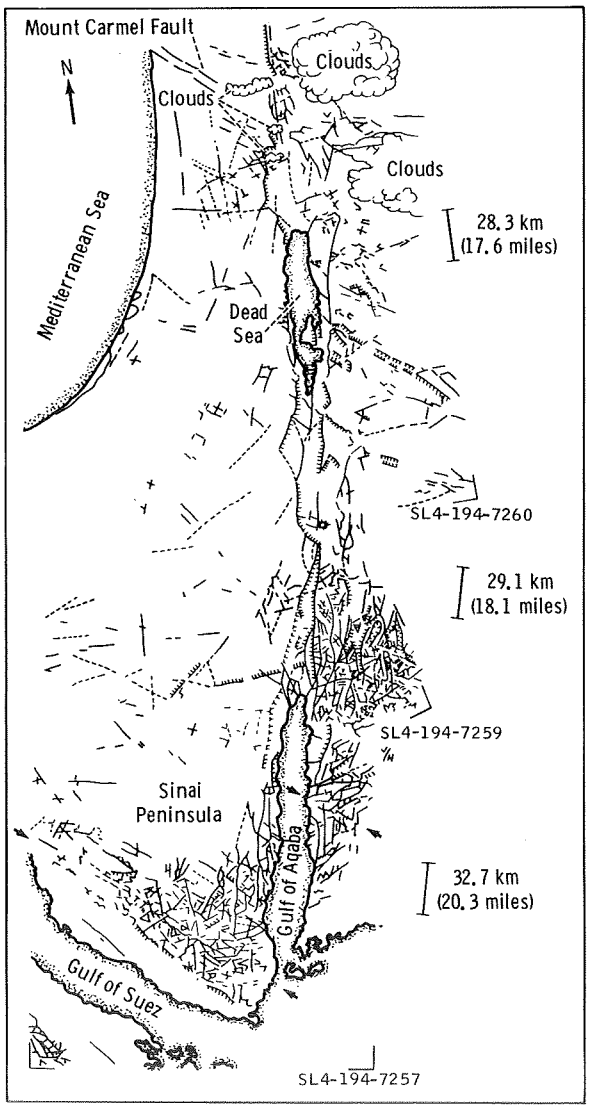


FIGURE 2.—This lineament map from the Mount Carmel Fault zone to the southern tip of the Sinai Peninsula was derived from an uncontrolled mosaic of NASA photographs SL-194-7257, SL4-194-7259, and SL4-194-7260. Scales given for photographs were determined along the Dead Sea Fault zone. The southern photograph is approximately 10 percent smaller than the central photograph, which, in turn, is 5 percent smaller than the northern photograph. There is slight east-west foreshortening across each photograph because of the westward tilt of the handheld 35-mm camera. Lineaments shown are straight river segments, escarpments, and sharp color (geologic) boundaries. Solid lines represent easily identified linears with visible escarpment (ticks on downthrown side); dashed lines represent alinements suggestive of a through-going feature. Arrows give location of a newly recognized lineament; the offset of this line from the line indicated by the lower arrows matches that demonstrated by other geologic lines for the strike-slip movement of the Dead Sea Fault zone.

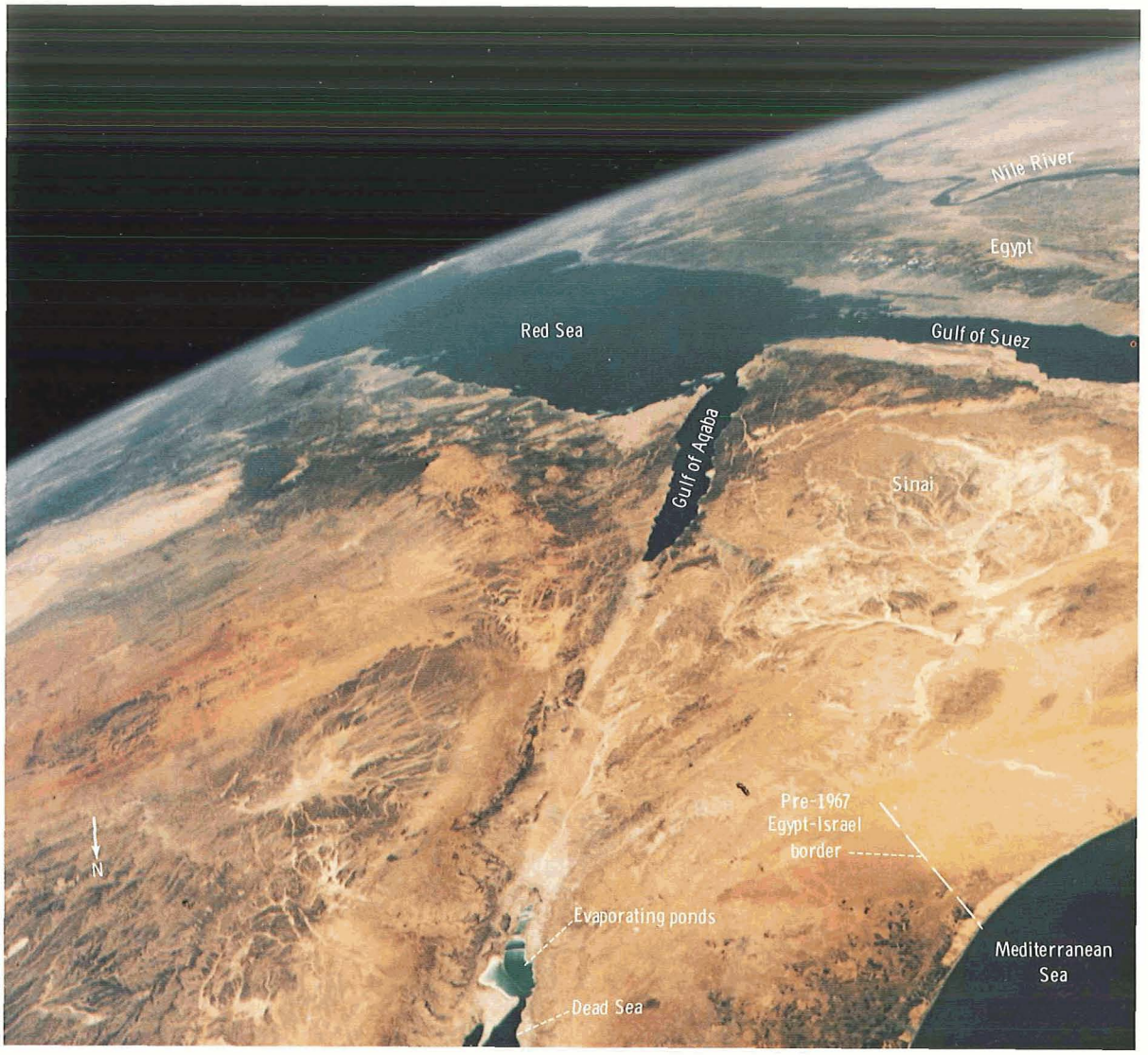


FIGURE 3.—Apollo-Soyuz photograph (AST-9-560) showing view southward across the Sinai and northern Red Sea region. The graben (pull apart) origin of the Gulf of Suez is suggested by the linear bands of contrasting color parallel to the gulf that mark prominent faults. The Gulf of Aqaba and the narrow valley that extends northward to the Dead Sea mark the southern segment of the Dead Sea Fault zone; its strike-slip origin (Arabian side moving north relative to the Sinai side) is shown by (1) the long, straight fault extending from the eastern margin of the Dead Sea to the western margin at the head of the Gulf of Aqaba, (2) angular corners of the gulf that match shape along opposite shores, and (3) curved structures (dragged?) against the fault zone near the Dead Sea. The dark region bordering the Red Sea is composed of Precambrian rocks; the oval areas are intrusives. Long, linear sand streaks and dunes (left center) show that the prevailing wind is from the Red Sea to the east across Arabia.

left separation (slip?) if they strike north or northeast and a right separation (slip?) if they strike west-northwest. This finding is consistent with an interpretation of the Dead Sea Fault zone as one of left lateral slip. A line visible on these photographs, but not recognized on Landsat imagery or on the ground,[1] extends southeastward from the midpoint of the eastern shore of the Gulf

[1] R. Freund, personal communication, January 1977.

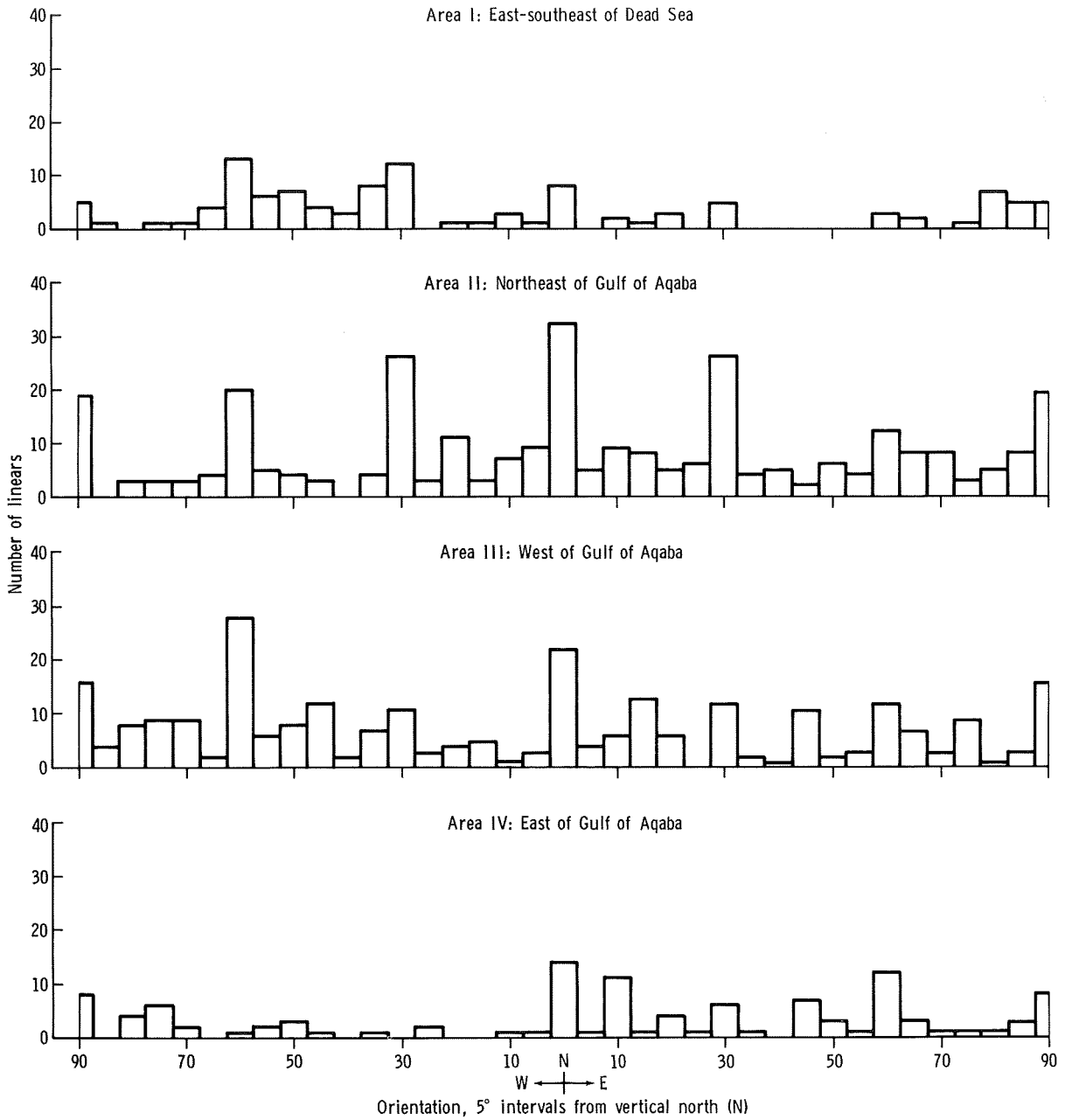


FIGURE 4.—Histogram of the orientation of linears in selected areas of figure 2. Area I: region east and south of the Dead Sea on Skylab photograph SL4-194-7260. Area II: region east and north of the head of the Gulf of Aqaba on Skylab photograph SL4-194-7259. Area III: southern half of Sinai Peninsula on Skylab photograph SL4-194-7257. Area IV: region east of the Gulf of Aqaba on Skylab photograph SL4-194-7257. Orientation of maximums is slightly distorted because of the camera tilt; at most, this tilt is less than 5°. Linears are plotted by 5° intervals. The overall trend of the Gulf of Aqaba and the main valley as far as the southern end of the Dead Sea is N15°E (fig. 1). The prominent trends that lie along this alinement are either north or N30°E.

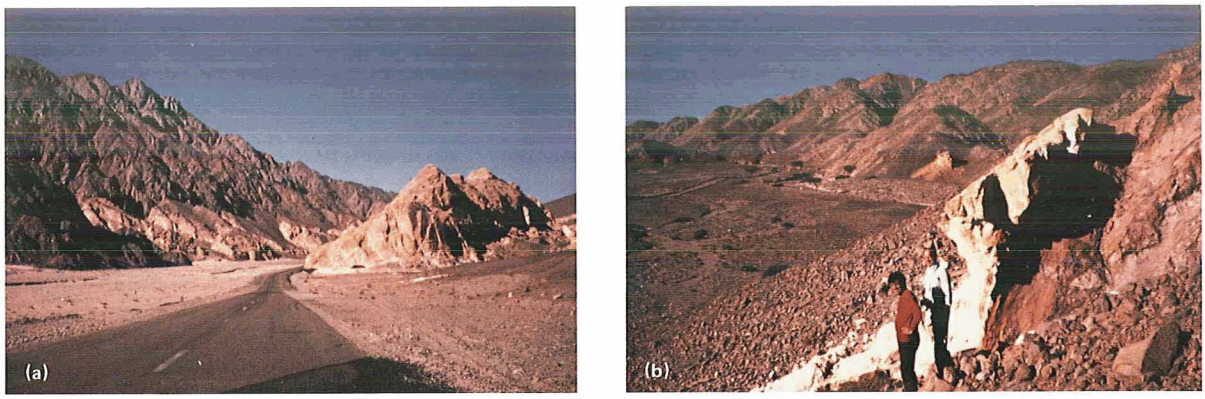


FIGURE 5.—Bir Zhair rhomb graben located approximately 50 km south of Eilat along the eastern side of the Sinai Peninsula. (a) Western border fault: dark Precambrian rocks (left) against downdropped, light-colored Cambrian sandstone. (b) Eastern border fault: Precambrian rocks (right) against downdropped Cambrian sandstone. In middle distance is the northern end of the rhomb. The total strike-slip movement needed to produce this rhomb is 3 km.

of Aqaba and matches a similar-trending line in the southern Sinai Peninsula. The offset of these lines is approximately the distance demonstrated by many other geologic lines for the slip of the Dead Sea Fault zone. One interpretation of this line is that it is a fault marking the eastern margin of crustal attenuation for the Red Sea.

Small rhomb-shaped grabens containing wedges of sedimentary rocks between walls of dark Precambrian rocks exist along many of the gently curved faults that parallel the Gulf of Aqaba. Freund et al. (ref. 15) show that movement along this anastomosing system is necessary to close the Gulf of Aqaba. Most of these grabens can be identified on the photographs, some with difficulty. The largest and easiest to identify reaches the coast of the Gulf of Aqaba at a reentrant angle approximately 10 km south of the city of Eilat (at the head of the gulf). The smaller ones are slightly lighter colored rhomb-shaped depressions along the linear depression representing the fault zone. Figure 5 shows ground views of one of these grabens, which is visible only as a tiny, light-colored patch on Skylab photographs.

The amount and direction of present-day motion along the fault zone in the Gulf of Aqaba can only be inferred from the photographs because the active faults are below sea level. The general direction can be derived by the major bends in the shoreline of the southern gulf. This implies motion along faults that cut obliquely across the gulf rather than along the gently curved anastomosing faults of the earlier movement (ref. 6). Offset of the shoreline edges is 50 km, whereas the actual displacement along the submarine scarps is approximately 40 km. Because the gulf resulted from this later movement, the earlier slip direction must have been closer to the overall trend of the fault zone.

Northward from the head of the Gulf of Aqaba to the Dead Sea, the valley narrows and then opens. The narrow portion, near the midpoint, marks the southern end of the Dead Sea depression, a long, rhomb-shaped graben. The Dead Sea occupies the depression developed during the present movement period; the earlier depression immediately to the south has been filled by sedimentation.

Figure 6 is given for comparison with the northern segment of figure 2. Although the scale of the figures is approximately the same, the high Sun angle of the photograph washes out the surface lineaments in figure 6 so that only the most prominent ones are recognized. The principal lineaments visible are the main scarps along the Dead Sea Fault zone and the high Mount Carmel

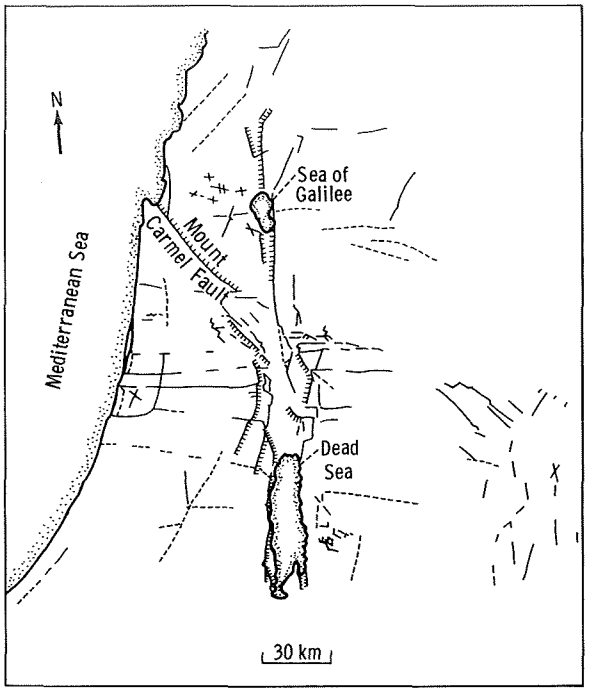


FIGURE 6.—Lineaments visible on NASA photograph SL3-122-2621. Scale is slightly smaller than the corresponding area on figure 2 but is almost identical to that of the Sinai region in figure 2. The difference in lineaments mapped is the result of different Sun angles between the two photographs.

Fault. Figure 7 shows visible lineaments from high-resolution Skylab Earth Resources Experiment Package (EREP) photographs. East and south of the Sea of Galilee is a band in which a myriad of short segments normal to the Dead Sea Fault zone are observed. Only the bounding linears are shown in the figure.

Figures 2 and 6 show different sets of linears that are visible between the Dead and Mediterranean Seas, including a number of linears perpendicular to the coast. Where these intersect the coast, the shoreline is offset to the right. Similar offsets can be seen in the graben walls north of the Dead Sea. These may be the southern continuation of the normal faults described by Freund (ref. 16) in the Galilee region that demonstrate north-south extension. If so, then each of these faults is downthrown to the north, and displacement increases to the east toward the Dead Sea Fault zone. In contrast, figure 2 for the same region reveals apparent conjugate pairs that appear to be bisected by the east-trending faults.

Figures 2, 6, and 7 can be compared with the recently published lineament map of Israel (ref. 17), in which various types of lineaments are distinguished and whether they have been identified on the ground is noted. The fact that this map contains more detail than that in figures 2, 6, and 7 may reflect the familiarity of the authors with the region. Figures 2 and 6 are derived from 70- and 35-mm handheld-camera photographs, whereas figure 7 is compiled from an EREP photograph. The detail of figure 7 demonstrates that with higher resolution and stereoscopic study, the amount of useful geological data that can be extracted is significantly improved. The combination of an EREP-type camera system with a trained observer for aiming should produce a wealth of useful and pertinent data for the problems that are being studied from space.

Sea of Galilee Area

Within the area surrounding the Sea of Galilee, the dominant structural trends are northwest and north (figs. 6 and 7). Secondary trends are north-northwest, north-northeast, and northeast.

The rift valley contains numerous north-trending faults. The eastern side of the valley is an abrupt wall, well marked by long, linear fault traces. In contrast, the western side of the valley is poorly defined and consists of several curved fault traces. The western side is also obscured by the presence of many northwest-trending faults, especially west of the Sea of Galilee. The eastern side is covered by Pleistocene and Recent basalts from the N30°W-trending line of volcanoes that cap the Golan Heights.

The southwestern part of the area is broken by numerous faults trending approximately north to N20°W. This trend is disturbed by a prominent graben trending approximately N20°E that truncates most of the faults (ref. 6).

In the north, the transition from the Sea of Galilee to the Hula Depression is marked by numerous west- and northwest-trending faults. The southern end of the Hula Depression is indistinct and obscured by northwest-trending faults as

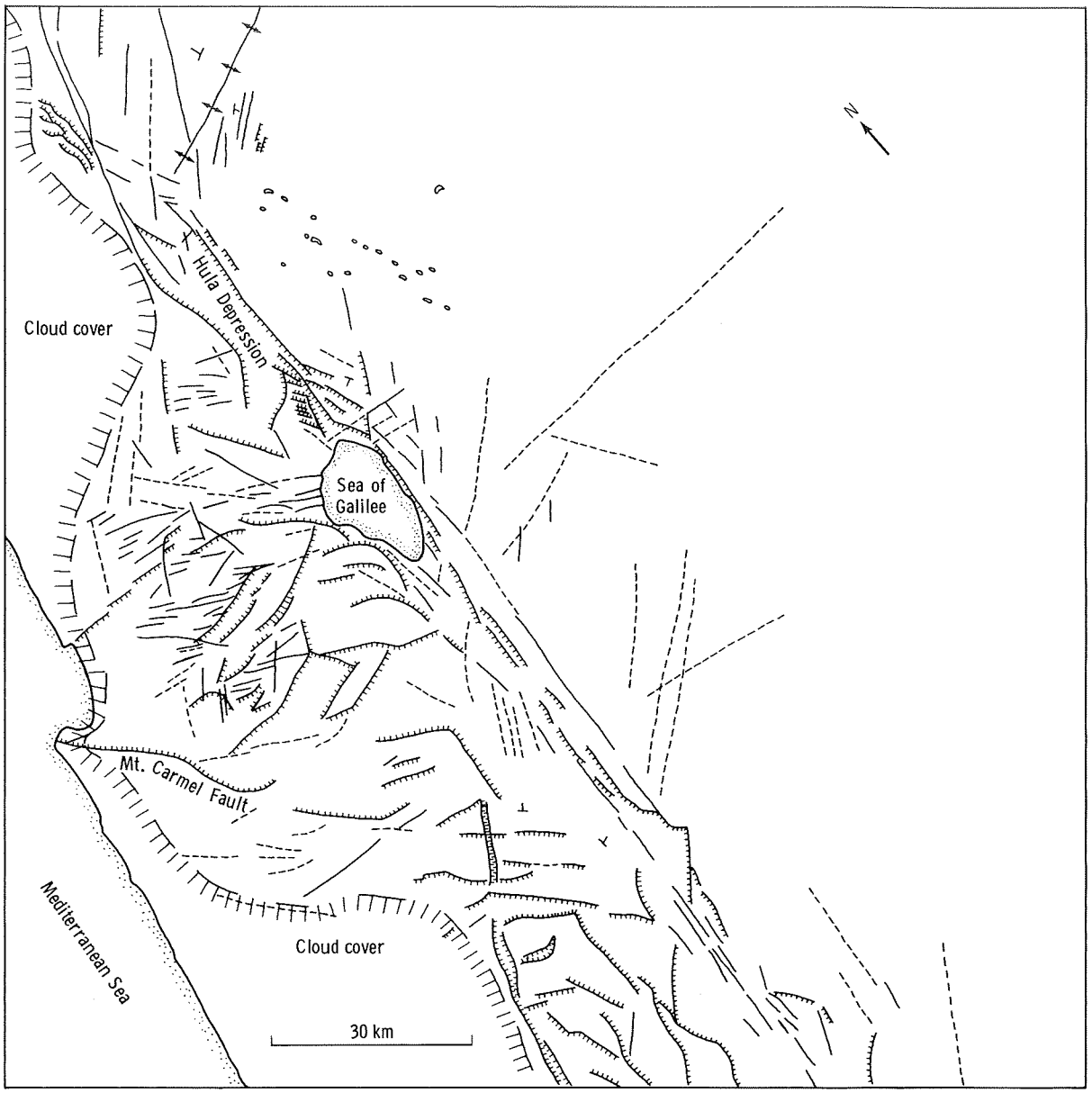


FIGURE 7.—Lineaments visible on NASA photograph SL3-46-209, taken with the color camera of the high-resolution EREP camera system. Solid lines represent prominent linears with scarps; solid lines with ticks represent discontinuous linears; ovals and circles delineate volcanoes surmounting the Golan Heights; and the solid line with arrows shows crest of anticline along Mount Hermon.

well as by faults that trend approximately N70°W. Within the Hula Depression, the western side is prominently marked by bounding faults rather than the eastern side, which becomes indistinct near the anti-Lebanon folds.

The most complicated structural zone is that west of the Sea of Galilee. The area is bounded on the south by the Mount Carmel Fault zone and on the north by an east-west line at the southern end of the Hula Depression. There are four major fault

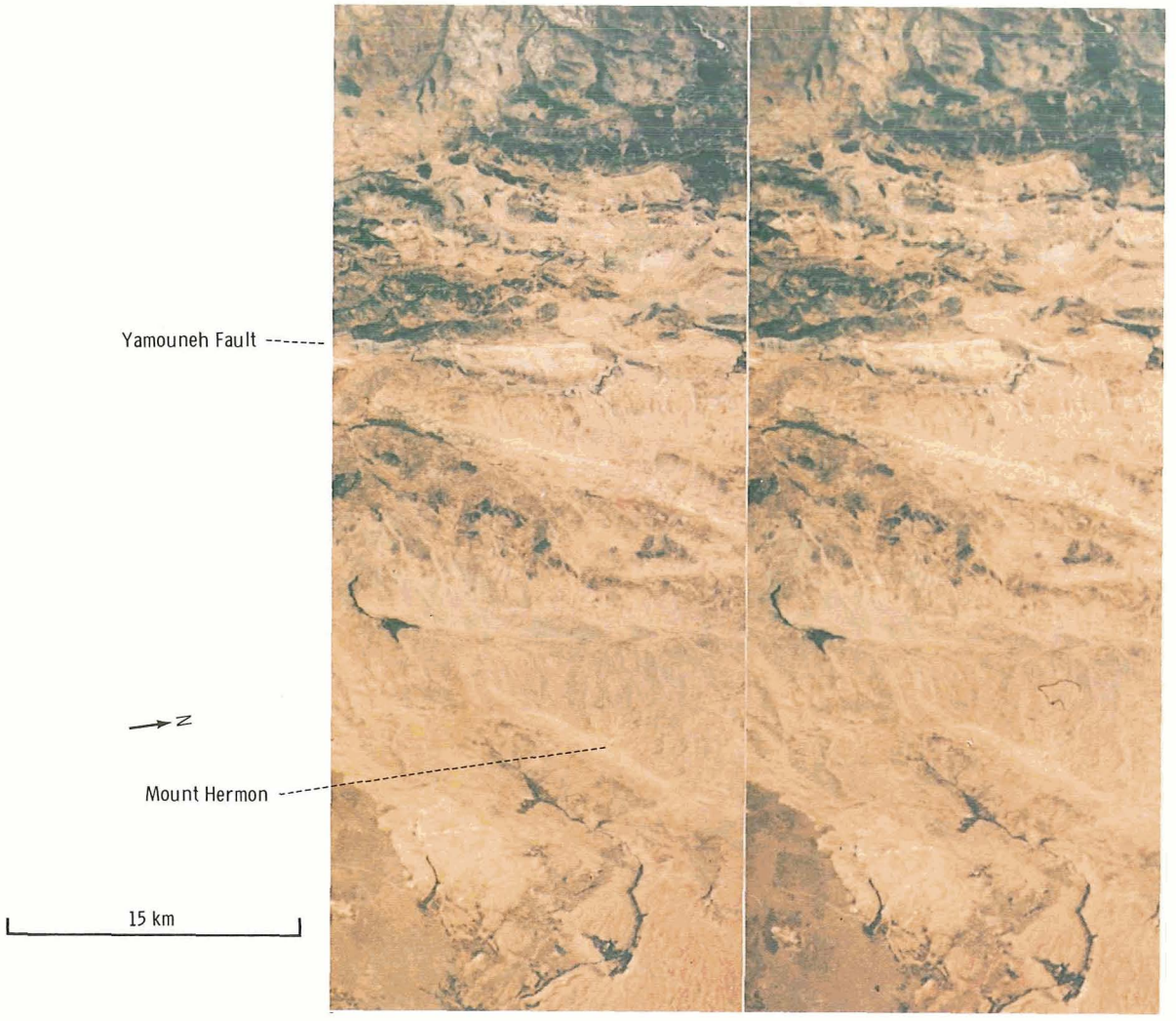


FIGURE 8.—*Stereopair* (AST-2-141 and AST-2-142) showing the Yamouneh Fault in the Lebanese Fault zone near the Israel-Lebanon border. Details are shown in figure 9.

trends within this area: (1) N60°W, (2) N45°W, (3) N20°E, and (4) N45°E. The greatest fault density is found within an east-west band along the latitude of the Sea of Galilee. The Sea of Galilee occupies the common junction of all fault trends in this area. Freund (ref. 16) demonstrated that this region has extended parallel to the Dead Sea Fault zone, and the extension decreases away from the fault zone.

A peculiar aspect of this area is the relatively undeformed appearance of the region east of the rift zone in comparison to the highly deformed western side. This characteristic is probably the result of young volcanic cover from the N30°W-trending line of volcanoes along the Golan Heights.

Hula Depression (Israel) to Bekaa Valley (Lebanon)

The area covered in Apollo-Soyuz frames AST-2-141 and AST-2-142 (fig. 8) includes the first major bend in strike and several major depressions: the Hula Depression, the Ayun Depression, and the Bekaa Valley. The Bekaa

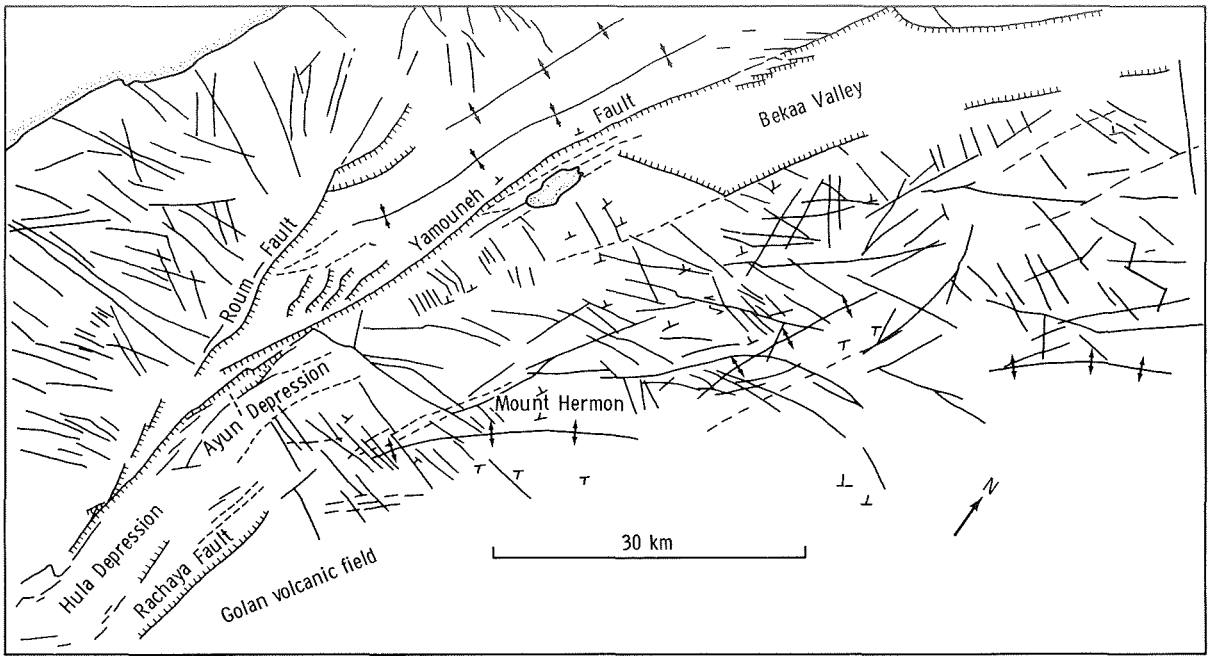


FIGURE 9.—Linears visible on a photomosaic of frames AST-2-141 to AST-2-143 with prominent structures named. (See fig. 8.) The Roum Fault can be seen to terminate toward Beirut (upper left center). The triangular region between the Roum and Yamouneh Faults appears to be a wedge that has been moved parallel to the Roum Fault (a strike-slip fault that decreases displacement to the north) and extended along the Yamouneh Fault. The high Sun angle makes some linears very difficult to study except under stereoscopic viewing. The southern part of this mosaic (Hula Depression, Golan Heights, Mount Hermon) also appears on figure 7, which is derived from low-Sun-angle and higher resolution photography. Both sets of photographs were taken in a mapping attitude; therefore, they make a good comparison study. A good camera system and shadows make for remarkably useful stereoscopic analysis!

Valley appears to be a half graben, being bounded on the western side by the Yamouneh Fault.

The southwestern side of the rift zone exhibits a high fault density, which decreases to the northeast. The major fault trends are approximately N60°W, N45°W, N45°E, and N60°E. These trends are truncated by the north-trending Roum Fault, which diverges from the major rift zone and curves to the northwest toward Beirut, Lebanon. Several major step faults trending in the same direction as this diverging fault are present along the rift zone a short distance to the north. Most of the faults in the southwestern part of this area exhibit trends similar to the fault trends in the complex region west of the Sea of Galilee.

Just to the north of the previously mentioned step faults, the major through-going fault (Yamouneh) truncates the eastern flank of a syncline formed on the western side of the rift zone. The area east of the rift zone contains the anti-Lebanon folds and associated faults. The dominant structure on this side is a westward-dipping monocline. As the strata in the monocline approach the rift zone, they dip beneath alluvial fill to form the eastern edge of the Bekaa Valley.

Figure 9 shows the major lineaments of an excellent stereo set of photographs (AST-2-141 to AST-2-143) that covers the major bend and apparent trifurcation of the Dead Sea Fault zone in southern Lebanon. The Roum Fault can be seen to die out toward Beirut. No faults can be seen to continue along this trend toward the Mediterranean coast. Several investigators (e.g., ref. 12) used such a fault to terminate the Dead Sea Fault zone at this latitude. If such a fault exists, it has since been covered by the Cretaceous rocks of this region and was not reactivated during either period of slip along the Dead Sea Fault zone.

The Yamouneh Fault is the most prominent linear feature on the photographs. At its southern end, where it makes a bend from the Dead Sea trend along the Hula and Ayun Depressions, it appears to break into a series of segments rather than being a continuous fault. The Litani River flows through this bend and leaves it at right angles to the zone. It is the only river along the entire rift, until the intersection of the rift with the Alpine trends in southern Turkey, that leaves the fault zone and empties into the Mediterranean Sea. All other rivers in the rift end in lakes that occupy rhomb grabens formed during the present period of rifting.

A comparison of the photographs taken on the Apollo-Soyuz mission with those from Skylab (SL3-46-208 and SL3-46-209) that cover this bend and the Hula Depression shows the contrast between high Sun angle with no shadows (Apollo-Soyuz) and low Sun angle with shadows. The shadows in the Skylab photographs enhance small changes in relief. A good example of this enhancement is the series of faults in the wedge between the Roum and Yamouneh Faults. Each of these small faults forms a shallow "S" shape with the eastern side down. Each is at a small angle to the Yamouneh Fault, and displacement is consistent with a left-hand strike-slip displacement along the Yamouneh Fault. The Litani River takes advantage of these tilted fault blocks to step westward out of the main rift zone to the Roum Fault. It exits from the Roum Fault by way of a major east-trending fault zone.

Astronaut descriptions and observations of this region during the Apollo-Soyuz mission confirm that the Yamouneh Fault continues to the north, where it makes a bend and parallels the Mediterranean coast into Turkey. The other faults that trend more easterly end in "a lot of jumbled country" according to the command module pilot, and the most easterly fault dies out as it approaches a river.

A series of south-looking oblique photographs taken on this mission (AST-9-559 to AST-9-564) illustrates the remarkable bends of the zone, the straightness of the intervening segments, and the segmentation of the Galilee region (fig. 10). Cloud cover over much of Lebanon, however, prevents the recognition of its segmentation.

Study of figure 9 together with the schematic geometrical model of Freund et al. (ref. 15, p. 122) demonstrates the plausibility of the model, which uses the many faults that cross Lebanon and terminate against the Yamouneh Fault as the mechanism of rotation and elongation of coastal Lebanon. With this model, the net slip in Syria north of Lebanon where the fault has passed the next bend has been reduced from 105 to 80 km. The model requires a 10° counterclockwise rotation of each segment. Recent paleomagnetic data (ref. 18) suggest a greater rotation of almost 35°. If the paleomagnetic data prove rotation of the fault blocks, then the slip to the north might be considerably less than the 70 km suggested by Freund et al. (ref. 15, p. 123) for the northern offset of the southern boundary of the ophiolites of northern Syria and adjacent Turkey. A lesser displacement would fit better with the results of a study by Arpat and Saroglu (ref. 19) that shows 22 and 27 km of left slip on the northeast-trending East Anatolian Fault, the northern termination of the Dead Sea Fault zone; the displacements are on Miocene and Mesozoic units, respectively.

Northwestern Syria and Adjacent Turkey

The intersection of the Lebanese Fault zone and the Alpine ophiolite belt is shown in figure 11. The Apollo-Soyuz flight line continues northeastward to Elazig and Diyarbakir, Turkey, but the 60-percent cloud cover in the photographs from Gaziantep, Turkey, eastward limits geologic interpretation. This flight line was taken in a vertical mapping attitude and provides stereoscopic coverage at a scale of 1:1 000 000 with 23- by 23-cm prints. Figure 12 is a stereotriplet of these Apollo-Soyuz mapping photographs.

Geologic maps available for this region are those of Dubertret (ref. 20). The maps consist of a 1:500 000 geologic map that covers most of the area shown in figure 11, and a 1:200 000 map north of latitude 36°00′ N and west of longitude 37°00′ E. The published maps show the major geologic map units and principal faults, each of which can be recognized on the photographs. Figure 11 delineates the faults and associated lesser fractures (also faults?) of this region. The

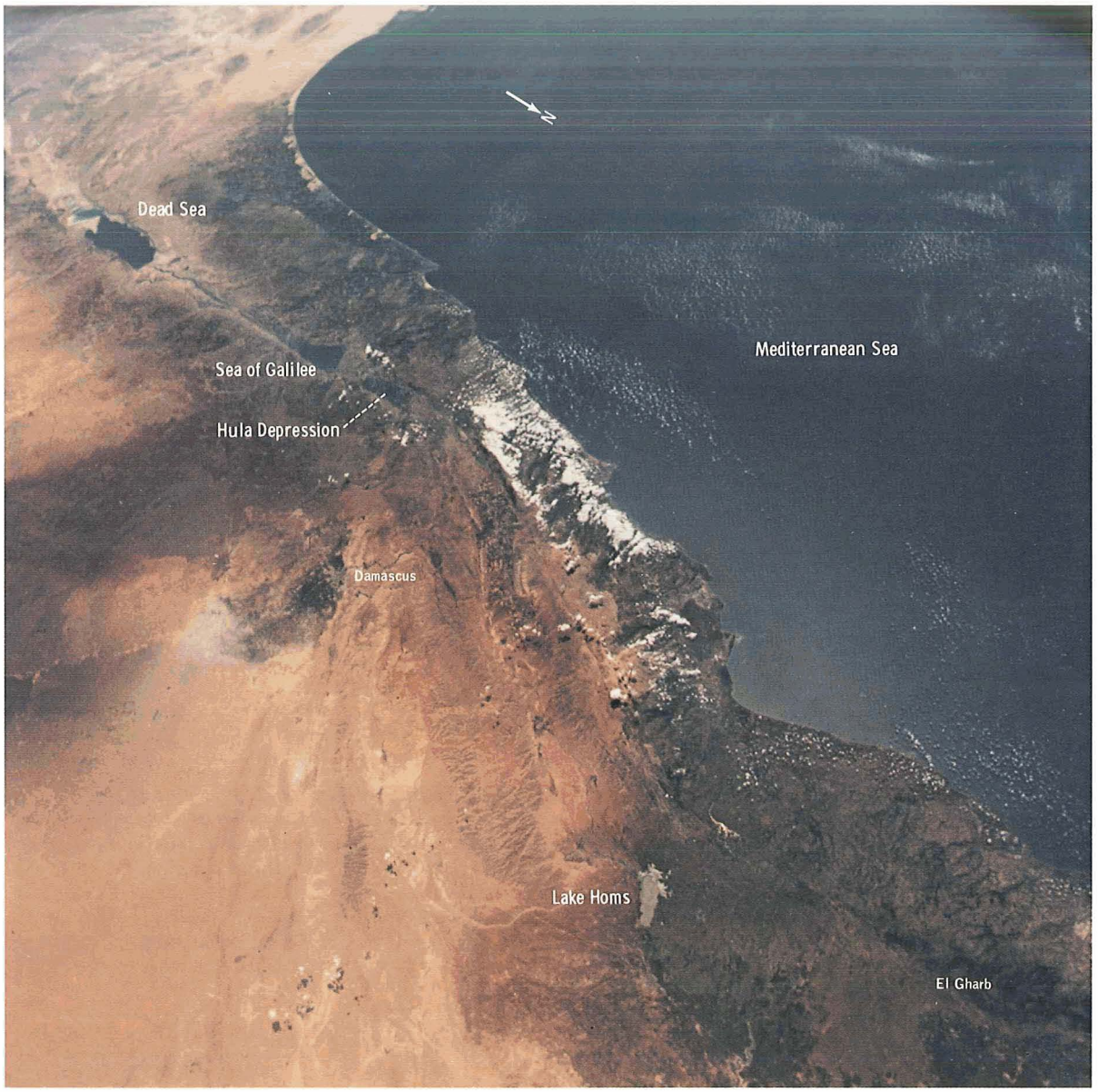


FIGURE 10.—Apollo-Soyuz photograph (AST-9-564) showing the view southward along the Lebanese Fault zone from the Dead Sea (upper left) to the Gharb region of northwestern Syria (lower right) (figs. 8 and 11 to 13). Sharp bends in the fault zone show well because of the obliquity of view; examples are a minor change in strike at the Dead Sea (upper left), a major bend and bifurcation near the Hula Depression (upper center) (figs. 8 and 9), and a major bend and associated volcanic field (lower right center) near Lake Homs. The dark area (left center) is a cultivated region surrounding Damascus.

pattern as seen from this synoptic photography is different from that found in Dubertret (ref. 20). The entire pattern of figure 11 is understandable if left-hand strike-slip movement along the Yamouneh Fault is of large magnitude and if the Arabian block is splintering as it is forced into the boundary of the Turkey block. The Gharb is a large rhomb graben with a succession of smaller ones between it and the fault east of Afrin. The depression at Ed Dâna is much more complicated

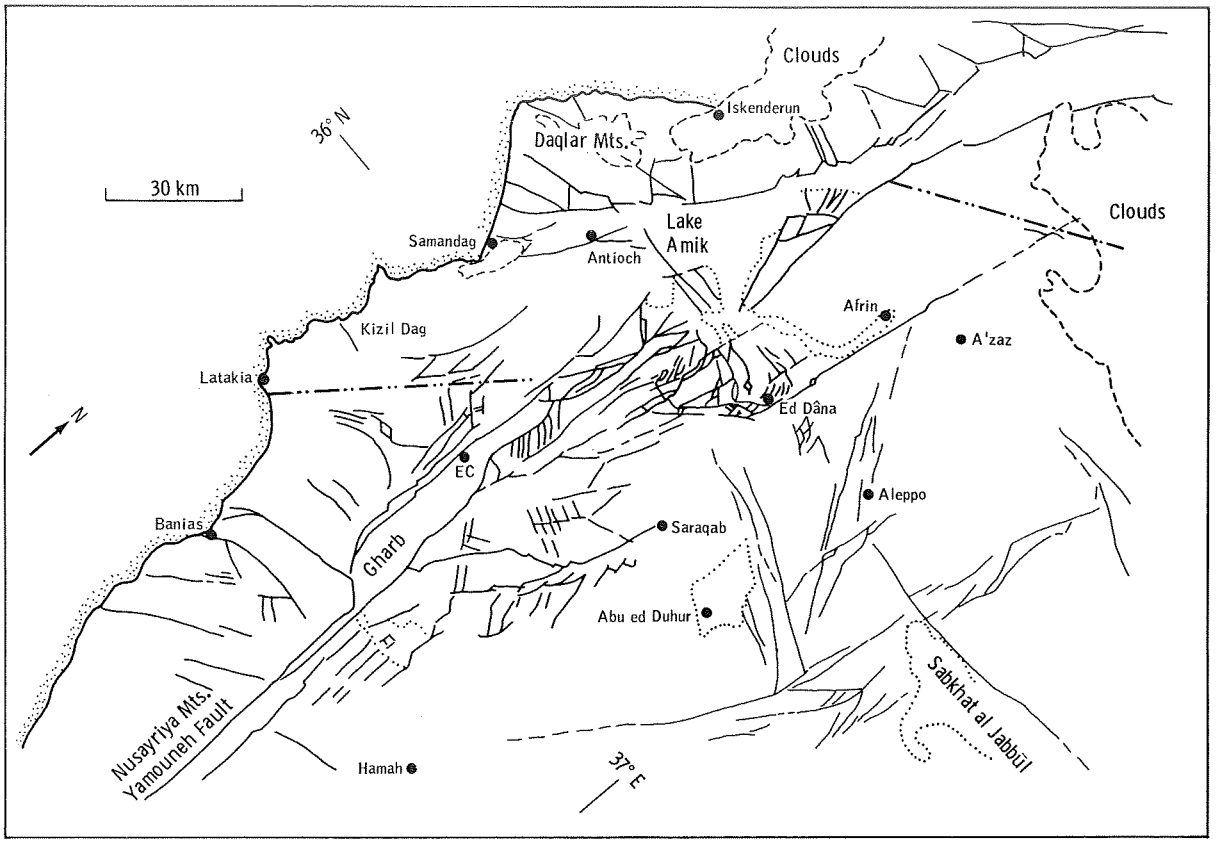


FIGURE 11.—Linears seen on photographs AST-16-1266 to AST-16-1270. Major linears observed on the photographs are faults on the maps of Dubertret (ref. 20). Other linears shown in this figure are most probably faults as well. This region includes the splaying of the Dead Sea Fault zone from a single major fault, the Yamouneh Fault, northward into at least three major segments: (1) north of Lake Amik (probable northward continuation of the Yamouneh Fault); (2) the intricate system of rhomb grabens and splaying between Ech Chourgour (EC) and Ed Dâna to where a single major fracture is identifiable that continues past Afrin and under the cloud cover at the edge of the map; and (3) the zone that extends from near Hamah northward and east of Aleppo and which is interrupted by major bands of west- and northwest-trending fault systems near Abu ed Duhur, Aleppo, and Sabkhat al Jabbūl. Dash double-dot line marks southern boundary of ophiolite belt as shown in Freund et al. (ref. 15, p. 123).

than can be seen at this scale, but its pattern probably resembles that shown on a larger scale for this region.

Other major linear trends associated with closed depressions, such as those near Antioch, Abu ed Duhur, and Sabkhat al Jabbūl, show that the Arabian block is splintering, and movements along these faults can be expected to occur again.

The trend of the Daqlar Mountains shows a significant bend to the north at the latitude of Iskenderun. This bend can be attributed to drag produced as the northward continuation of the Yamouneh Fault pushes north along the boundary. This is similar to the fault segmentation of Lebanon and the rotation of these segments counterclockwise in response to the northward shove of the Arabian block.

FIGURE 12.—Stereotriplet of northwestern Syria and adjacent Turkey (AST-16-1267 to AST-16-1269). Fracture pattern of this region is shown in figure 11. →

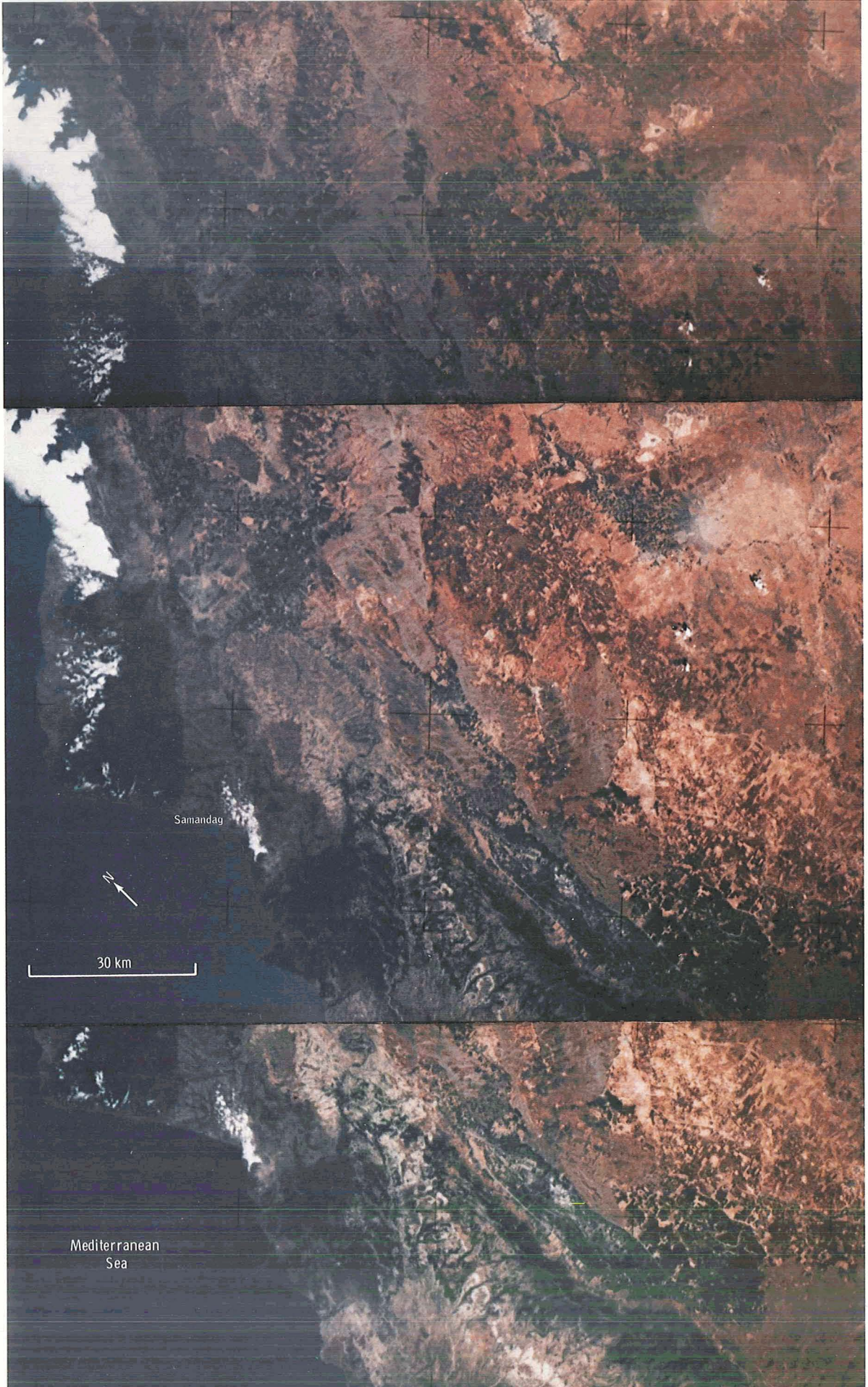

Samandag
N
30 km
Mediterranean
Sea



FIGURE 13.—View westward across El Gharb, a cultivated region along rhomb-shaped graben in the Lebanese Fault zone (i.e., prominent escarpment is facing viewer) on the Orontes ('Asi) River, northwestern Syria (AST-1-52). Northeastern tip of Cyprus is visible at upper left. Vertical view of this region can be seen in figure 12 (AST-16-1267 to AST-16-1269 stereotriplet). The prominent bend in the fault trace (southern end of rhomb-shaped graben) is foreshortened in this view because of look direction.

Slip along the Yamouneh Fault in this area has been estimated by Freund et al. (ref. 15) to be 70 km as measured by the offset of the southern boundary of ophiolites. Freund used the Dubertret (ref. 21) 1:1 000 000 map as his source. Depending on how measurements are made (along or diagonally up the valley), the measured offset can be as small as 30 km.

An oblique view westward of the Gharb (fig. 13) shows how the height of the fault scarp grows rapidly northward into the southwestern corner of the Gharb. East of the Yamouneh Fault, the ter-

rain is differentially downwarped northward by a series of subparallel faults, many of which can be identified by angular corners to the cultivated valley.

Freund et al. (ref. 15) show the Gharb valley as a rhomb graben and use its length as a measure of slip (70 km) along the Dead Sea Rift in this region. Dubertret (ref. 20) shows the fault that forms the west wall of the Gharb as terminating in southern Turkey. Field study of this region in June 1977 by Muehlberger with geologists of the Mineral Research and Exploration Institute (Maden Tetkik Arama (MTA) Enst. of Ankara, Turkey) shows that Dubertret is correct. Thus, the western border fault of the Gharb valley must be considered as another splinter or splay from the main Dead Sea Rift system of faults that extends across northwestern Syria and adjacent Turkey.

CONCLUSIONS

Astronaut observations and handheld-camera photographs are useful for confirming suspected trends of fault lines and for identifying the fractures.

Handheld-camera photographs have a unique advantage of being oriented in the direction necessary to show the linearity or sharp bends of fault zones. These photographs emphasize the features so that the pattern is easier to demonstrate or understand.

Photographs taken at various Sun angles emphasize different features or different sets of lineaments. These differences are apparent when comparing sets of photographs that are available for the Dead Sea, Sea of Galilee, and Hula Depression regions.

Apollo-Soyuz photographs taken in the vertical mapping attitude over northwestern Syria and adjacent Turkey permitted a stereoscopic study of fault scarps (fig. 12). The pattern of these scarps is different from that shown in earlier publications and shows a splintering northward of the Dead Sea Fault zone as it approaches the East Anatolian Fault of Turkey. This splintering has deranged modern drainage systems, which indicates that this region is tectonically active and that these faults constitute a major earthquake hazard. Further analysis of the fault patterns documented by the Apollo-Soyuz photographs could be used to develop a seismic risk map of this region.

Each type of camera and lens combination produced different quality photographs for interpretation. By far the best quality is that available from the Skylab EREP camera system. If this equipment had been available to document astronaut observations during the Apollo-Soyuz mission, then more detailed analyses would have been possible than could be done with either the 70-mm Hasselblad or 35-mm Nikon cameras that were used for handheld-camera photography.

ACKNOWLEDGMENTS

This work was performed under Smithsonian Institution Grant PC6-22302 as a subcontract of NASA contract NAS9-13831. Muehlberger acknowledges the expert guidance of Raphael Freund (Hebrew University, Jerusalem) during a tour of the Israel segment of the fault zone, and the discussions with Esen Arpat and colleagues (Basic Research Division, Mineral Research and Exploration Institute (Maden Tetkik Arama (MTA) Enst.) of Ankara, Turkey) concerning the tectonics of Turkey and the relationships of the Lebanese Fault zone to the East Anatolian Fault.

REFERENCES

1. Quennell, A. M.: Tectonics of the Dead Sea Rift. International Geological Congress, 20th, 1956, African Geological Surveys. Associacion de Servicios Geologicos Africanos, 1959, pp. 385-403.

2. Freund, R.: A Model of the Structural Development of Israel and Adjacent Areas Since Upper Cretaceous Times. Geol. Mag., vol. 102, no. 3, 1965, pp. 189-205.

3. Freund, Raphael; Zak, Israel; and Garfunkel, Zwi: Age and Rate of the Sinistral Movement Along the Dead Sea Rift. Nature, vol. 220, Oct. 19, 1968, pp. 253-255.

4. Roberts, D. G.: Structural Evolution of the Rift Zones in the Middle East. Nature, vol. 223, July 5, 1969, pp. 55-57.

5. Girdler, R. W.; and Styles, P.: Two Stage Red Sea Floor Spreading. Nature, vol. 247, Jan. 4, 1974, pp. 7-11.

6. Freund, R.; and Garfunkel, Z.: Guidebook to Excursion Along the Dead Sea Rift. Hebrew University (Jerusalem), 1976.

7. De Sitter, L. U.: Structural Development of the Arabian Shield in Palestine. Geol. Mijnbouw, vol. 41, 1962, pp. 116-124.

8. Dubertret, L.: Review of Structural Geology of the Red Sea and Surrounding Areas. Phil. Trans. Roy. Soc. London, Ser. A, vol. 267, no. 1181, Oct. 29, 1970, pp. 9-20.

9. Picard, Leo: Further Reflections on Graben Tectonics in the Levant. Graben Problems, Proceedings of an International Rift Symposium, Karlsruhe, West Germany, Oct. 10-12, 1968, J. H. Illies and St. Mueller, eds., E. Schweizerbart'sche Verlagsbuchhandlung (Stuttgart), 1970, pp. 249-267.

10. Bender, F.: Über das Alter und die Entstehungsgeschichte des Jordan grabens am Beispiel seines Südabschnittes (Wâdi 'Araba, Jordanien). Geol. Jahrb., vol. 86, 1968, pp. 177-196. (Conclusions summarized in discussion (pp. 127-129) of ref. 15.)

11. Illies, Henning: Die Grossen Gräben; Harmonische Strukturen in einer Disharmonisch Struierten Erdkruste (The Major Rift Systems; Harmonic Structures in a Disharmonically Structured Crust). Geol. Rundschau, vol. 59, no. 2, 1970, pp. 528-552.

12. Illies, J. H.: Intraplate Tectonics in Stable Europe as Related to Plate Tectonics in the Alpine System. Geol. Rundschau, vol. 64, no. 3, 1975, pp. 677-699.

13. Beydoun, Z. R.: Petroleum Prospects of Lebanon; Reevaluation. Bull. American Assoc. Petr. Geol., vol. 61, no. 1, 1977, pp. 43-64.

14. Vroman, A. J.: Is a Compromise Between the Theories of Tension and of Shear for the Origin of the Jordan-Dead Sea Trench Possible? Israel J. Earth Sci., vol. 22, no. 3, 1973, pp. 141-156.

15. Freund, R.; Garfunkel, Z.; et al.: The Shear Along the Dead Sea Rift. Phil. Trans. Roy. Soc. London, Ser. A, vol. 267, no. 1181, Oct. 29, 1970, pp. 107-130.

16. Freund, R.: The Geometry of Faulting in the Galilee. Israel J. Earth Sci., vol. 19, nos. 3-4, 1970, pp. 117-140.

17. Arkin, Y.; and Bartov, Y.: Lineament Map of Israel Observed on Satellite Imagery. Scale 1:500 000, Geological Survey of Israel, 1976.

18. Gregor, C. B.; Mertzman, S.; Nairn, A. E. M.; and Negendank, J.: The Paleomagnetism of Some Mesozoic and Cenozoic Volcanic Rocks From the Lebanon. Tectonophysics, vol. 21, 1974, pp. 375-395.

19. Arpat, Esen; and Saroglu, Fuat: The East Anatolian Fault System; Thoughts on its Development. Bull. Mineral Res. Exploration Inst. Turkey, Foreign Ed., no. 78, 1972, pp. 33-39.

20. Dubertret, L.: Géologie des roches vertes du Nord — Ouest de la Syrie et du Hatay (Turquie). Notes Mém. Moyen-Orient, vol. 6, 1955, pp. 5-224.

21. Dubertret, L.: Carte géologique du Liban, Syrie et bordure de pays voisins, au 1:1 000 000. Mus. d'Hist. Natur. (Paris), 1962.

Analysis and Synthesis of Space Imagery of the Southeastern-Turkey/Northwestern-Iran Mobile Belt

Paul Dean Proctor,[a] Douglas C. Melton, Jr.,[a] Ali Beken,[b] and L. K. Abrams[a]

ABSTRACT

Apollo-Soyuz photographs and Landsat images covering approximately 500 000 km² of eastern Turkey and northwestern Iran were analyzed for major geologic features. The general tectonic setting of the study area is formed by a northward-trending, tonguelike subsurface projection of the Arabian shield to the west, a shelf zone to the east, and a part of the Tauride orogenic belt to the north. The interface between the shelf and the Taurides is a distinctive fold-thrust zone. This zone extends 700 km westward across the mapped area. The allochthon on the north consists of one or more thrust sheets. The rocks of the allochthon include a core of metamorphic units thrust over Tertiary sediments; this total rock mass has been thrust southward over the autochthonous fold and shelf zone.

The shelf zone includes rocks of Precambrian, lower and upper Paleozoic, Mesozoic, and Cenozoic age. To the south, these units are flat to gently inclined. Northward, they are cast into open folds of northwesterly to westerly trend. The intensity of folding increases northward, asymmetry develops, and overturning to the south with some reverse faulting occurs near the interface with the thrust zone. This fold belt is approximately 200 km wide, and it extends both west and east of the mapped area. Strike-slip faults and some small reverse and thrust faults occur within this province. Younger volcanic rocks and sediments cover part of the fold belt on the west.

A thrust zone bounds the allochthon on the south and parallels the fold belt of the autochthon. The allochthon is made up of one or more thrust plates. Large folds, generally of westerly trend, occur southeast of Lake Van, and those of northeasterly trend occur near Kars in the northwestern part of the region. Transverse faults, some thrusts, some unknown curvilinear lineaments, and a well-developed northwesterly lineament that probably represents the Anatolian transform fault are visible on the photographs and images. Younger features on the allochthon include extensive volcanic flows, impressively large volcanic cones, including Mount Ararat and Süphan Dağı, and well-defined volcanic craters, some of which are arranged in linear form.

Regional stresses resulted in two major tectonic blocks (the autochthon and the allochthon) and in associated internal structures. A prominent fold belt, slightly concave to the southwest, parallels the interface between the blocks and is genetically related to them. Movement of the allochthon was southward over the fold belt. Possible causes for these structures include (1) a rising root zone with a stress field directed southward, (2) an uplifted, east-west-elongated mass with gravity slide potential northward and southward, and (3) a northward-moving platform subducted beneath the Tauride zone. The thrust zones, the asymmetric folds, and related faults suggest a southward-directed stress or, conversely, a northward movement of the African-Arabian plate. Results include (1) subduction of part of the Arabian shield,

[a]University of Missouri at Rolla.

[b]Middle Eastern Technical University, Ankara, Turkey.

(2) synchronous development of an overlying fold belt, (3) underthrusting of the Tauride allochthon, (4) ophiolitic intrusions, and (5) intermediate to acidic volcanism on the allochthon to the north. Plate movement may be continuing at the present and may be expressed by displacement on the Anatolian transform fault as a result of a modest change in the regional stress direction.

Ground-truth investigations would confirm, modify, or refute the interpreted structures and possible causes. The use of Apollo-Soyuz photographs and Landsat images together with ground-truth investigations would enable preliminary tectonic analysis of this large region.

INTRODUCTION

Apollo-Soyuz photographs and Landsat images of eastern Turkey and northwestern Iran were analyzed for major geologic features. The principal objective of this study was to synthesize these data into a meaningful regional tectonic map. In addition, the structural characteristics of the platform zone, of the fold belt zone, and of a possible allochthonous block were analyzed, described, and related to the regional geologic setting. Lineaments, folds, and faults on both the allochthon and the autochthon were identified, and their possible application to petroleum exploration was considered. Ground-truth investigations were recommended for some critical areas in the region to confirm, modify, or refute interpretations made in this report.

Apollo-Soyuz Test Project (ASTP) photographs covering parts of eastern Turkey, northern Syria and Iraq, northwestern Iran, and the U.S.S.R. were used in this study. (Landsat images of the same general area were also used to enhance the geologic analysis and interpretation.) In general, the study area is bounded by longitudes 39°30′ and 48°00′ E and by latitudes 35°00′ and 41°30′ N, and comprises more than 500 000 km^2 (fig. 1).

In this region, an allochthonous block is overthrust onto the foreland fold belt of the Taurides. (The Taurus Range is a westward extension of the Zagros Mountains of Iran. It separates southeastern Turkey from the Anatolian Plateau to the north.) In the mapped region, volcanic rocks partly cover complex fold and fault structures of the allochthon.

Geographically, the region is almost centrally located in relation to the Arabian (Persian) Gulf to the south, the Mediterranean Sea to the west, the Caspian Sea to the east, and the Black Sea to the north. For the most part, the region is quite mountainous. Two prominent mountain peaks are Mount Ararat (Büyük Ağri Dagi) with a summit elevation of 5185 m and Süphan Dağı at 4434 m.

Several major rivers have headwaters in the region, including the Tigris, the Euphrates, the Little Zab, the Great Zab, and the Aras. Major lakes are Lake Van in Turkey, Lake Urmia in Iran, and Lake Sevan in the U.S.S.R. Principal cities within or adjacent to the area are Tabrīz, Iran; Yerevan, U.S.S.R.; Kirkūk and Mosul, Iraq; and Diyarbakir, Van, and Erzurum, Turkey.

The basic materials used in the study were 10 ASTP color photographs (18- by 18-cm format) and 10 ASTP color transparencies (5.5- by 5.5-cm format) of central and eastern Turkey. These were supplemented by Landsat images acquired on different dates but covering the same general region. The specific ASTP photographs and Landsat images used are listed in table I. The reconnaissance geologic maps of Turkey, issued as individual 1:500 000-scale geologic maps, some with accompanying texts, were valuable source materials. Citations to these are made in the text. A geologic manuscript pertaining to a part of the area[1] was used for some geologic details. Brinkmann's recent book on the geology of Turkey (ref. 1) was also most useful.

REGIONAL GEOLOGIC SETTING

Turkey is in the eastern part of the Alpine fold belt. Brinkmann (ref. 1) and Ilhan (ref. 2) suggest that the Alpidic orogenies, which affected almost all of Turkey, were initiated in the Mesozoic and have continued to the present. (The term

[1]Ismail Ozkaya and Paul Dean Proctor: Mio-Eugeosynclinal Thrust Interface and Related Petroleum Implications, Sason-Baykan Area, Southeastern Turkey. Bull. American Assoc. Petr. Geol., in revision, 1977.

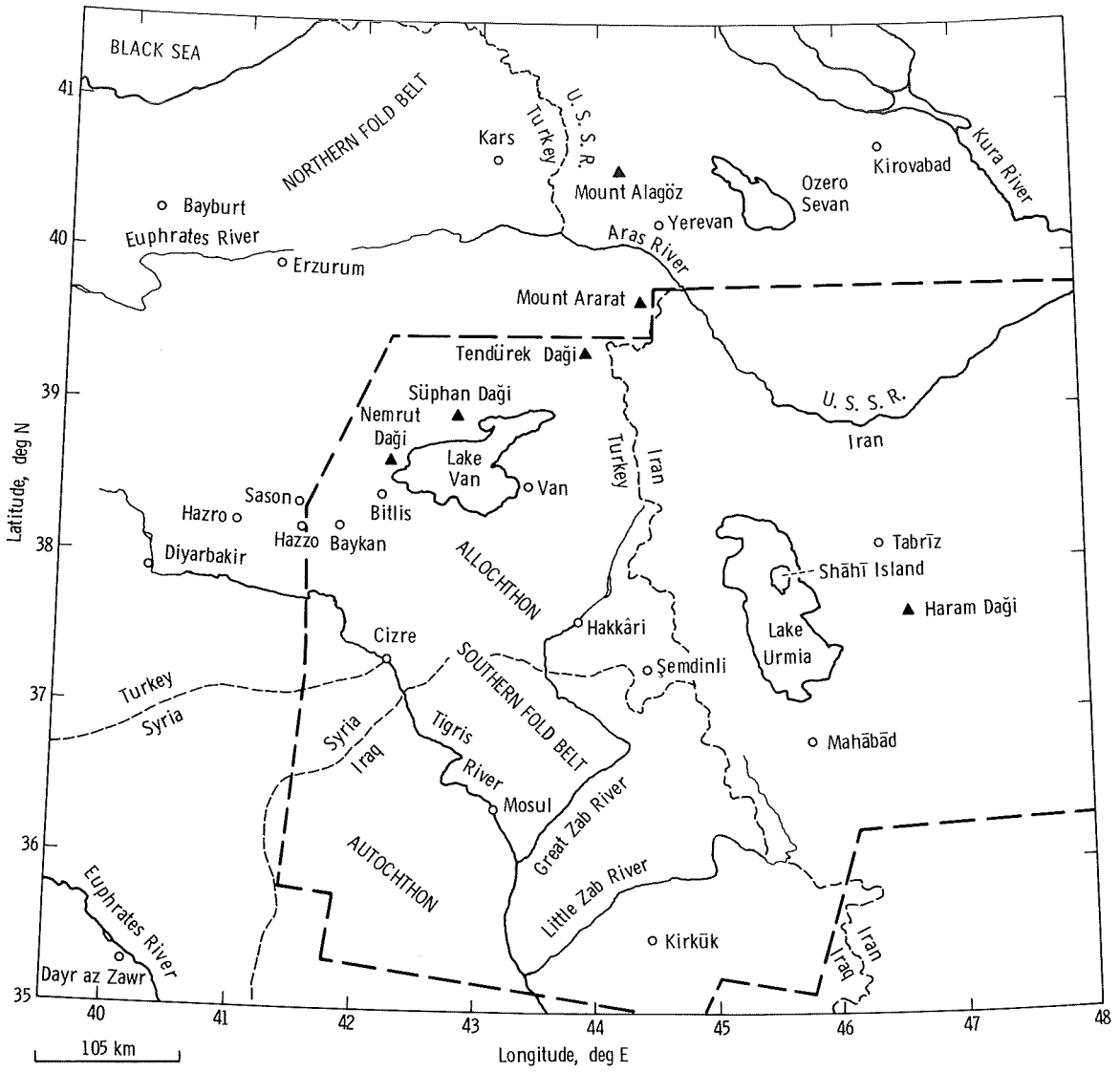


FIGURE 1.—Index map of study area, with approximate ASTP coverage indicated by heavy dashed line.

"Alpidic" is used in the manner of Brinkmann (ref. 1). He differentiates between the earlier, relatively minor Caledonian and Variscan mountain building events and the subsequent Alpidic event.) Structural evidence of Paleozoic orogenies, such as the Caledonian and the Variscan, has largely been obliterated by more recent Alpidic orogenies (ref. 2). According to Ilhan (ref. 2, pp. 159-161), the Turkish part of the Alpine belt consists of two segments, the southern and the northern Anatolian fold belts (fig. 2; ref. 3). These have European counterparts. The southern Anatolian fold belt includes the Taurus Mountains, which join the southern Alps, the Apennines, and the Zagros Mountains of Iran to form the "Dinaride" and "Hellenic" branch of the Alpine fold belt. The northern Anatolides join the northern Alps, the Carpathians, the Balkans, and the northern Iranian ranges to form the "Alpide" branch of the Alpine fold belt.

TABLE I.—Space Imagery Used in the Study

(a) ASTP photographs

Frame no.	*Quality; conditions*
AST-24-1978	Good central, poor peripheral; cloud cover
AST-24-1979	Good central
AST-24-1980	Good to fair; peripheral haze and cloud cover
AST-24-1981	Fair; hazy, some cloud cover
AST-24-1982	Fair; hazy
AST-24-1983	Fair; hazy
AST-24-1984	Fair; restricted view, hazy
AST-24-1985	Poor; hazy, extensive cloud cover
AST-24-1986	Poor; hazy, extensive cloud cover
AST-24-1987	Poor; hazy

(b) Landsat images

Date	*Frame no.*	*Bands*	*Quality; conditions*
July 14, 1973	E-1356-07181	7	Good
Dec. 29, 1972	E-1139-07130	5,7	Good
Dec. 26, 1972	E-1156-07071	7	Poor
July 18, 1975	E-2169-06494	7	Fair
Aug. 19, 1975	E-2209-07111	4,5,7	Good
Nov. 22, 1972	E-1122-07182	4,5,7	Fair; snow cover higher elevation
Nov. 21, 1972	E-1121-07124	7	Fair; much snow cover, mountains
June 25, 1975	E-2134-06550	4,5,7	Excellent; some cloud cover
Aug. 15, 1975	E-2205-06482	4,5,7	Good; some cloud cover northeast
Apr. 16, 1975	E-2084-07173	7	Fair; approximately 50 percent snow cover
Sept. 6, 1975	E-2227-07104	7	Good
Nov. 22, 1972	E-1122-07180	4,5,7	Poor; much snow cover
July 13, 1973	E-1355-07114	4,5,7	Excellent
Dec. 26, 1972	E-1156-07062	7	Poor; snow cover
Dec. 24, 1973	E-1519-07200	4,5,7	Poor; all snow cover
Nov. 22, 1972	E-1122-07173	4,5,7	Poor to fair; snow cover

A crystalline massif of intermediate composition occurs in western and central Turkey and separates the northern and southern Anatolian fold belts. These belts nearly converge in eastern Turkey and are separated only by a tectonic scar characterized by a thin zone of greenstones and sediments. These belts diverge again in northwestern Iran.

According to Ozkaya and Proctor,[2] the two Anatolian fold zones correspond to a past geosynclinal couple on each side of the hinterland. The northern couple is proximal to the Baltic shield, and the southern couple is adjacent to the Arabian shield. The part of the buried Arabian shield that lies within southeastern Turkey corresponds to the borderfolds region.

The general tectonic setting of the ASTP study area is formed by a northward-trending, tonguelike subsurface projection of the Arabian shield to the west, a shelf zone to the east, and a part of the Tauride orogenic belt to the north. The boundary between the shelf and the Taurides is marked by an extensive fold-thrust zone. The zone of allochthonous rocks extends from southeast of Hakkâri, Turkey, to Iskenderun, Turkey, which is more than 300 km west of the study area. The allochthon consists of geosynclinal sediments and metamorphic units thrust southward over the shelf zone. The allochthonous mass narrows westward and is tangential to the subsurface Arabian shield; the western part of the fold-thrust zone is characterized by submarine igneous activity, flysch deposition, metamorphism, and acid intrusions.[3] Rock units of the zone range in age from Precambrian to Pleistocene (fig. 3). Deformation occurred in the Tauride orogenic belt and was of greater intensity there than on the shelf to the south, where only minor folding and faulting took place.

Stratigraphy of the Autochthon

A brief description of the stratigraphy and the structure of the autochthon and the allochthon is presented as background for the interpretive study. Some of the data are from a geologic

[2,3] Ibid.

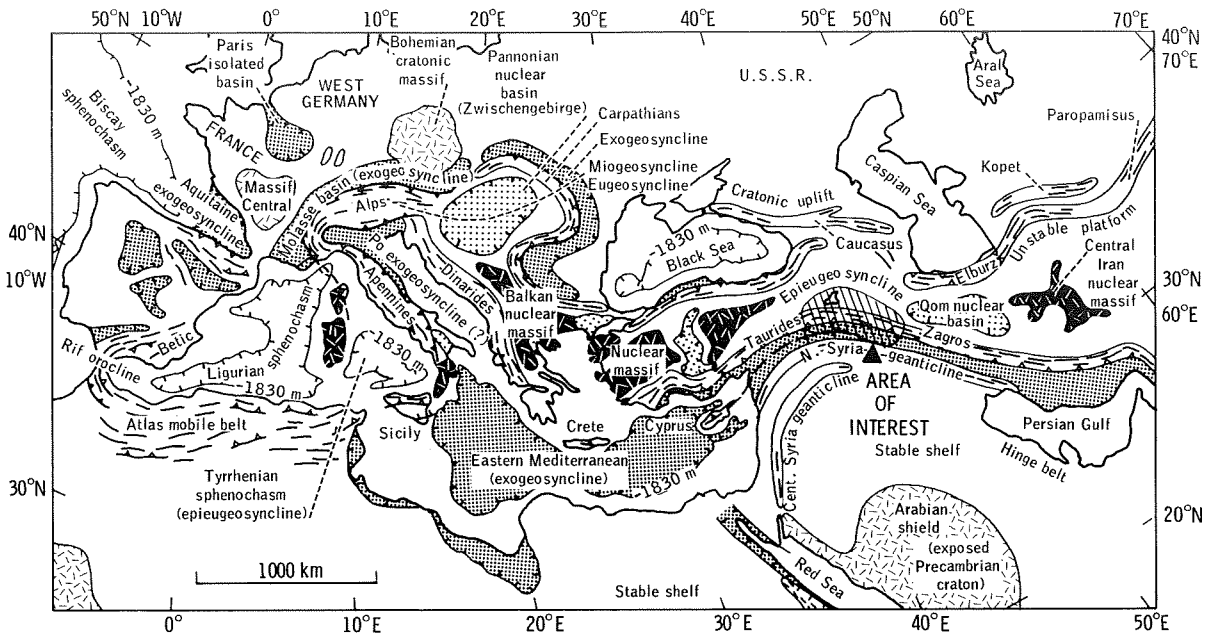


FIGURE 2.—Tectonic index map of Eurasia showing location of area of photogeologic study (after ref. 3).

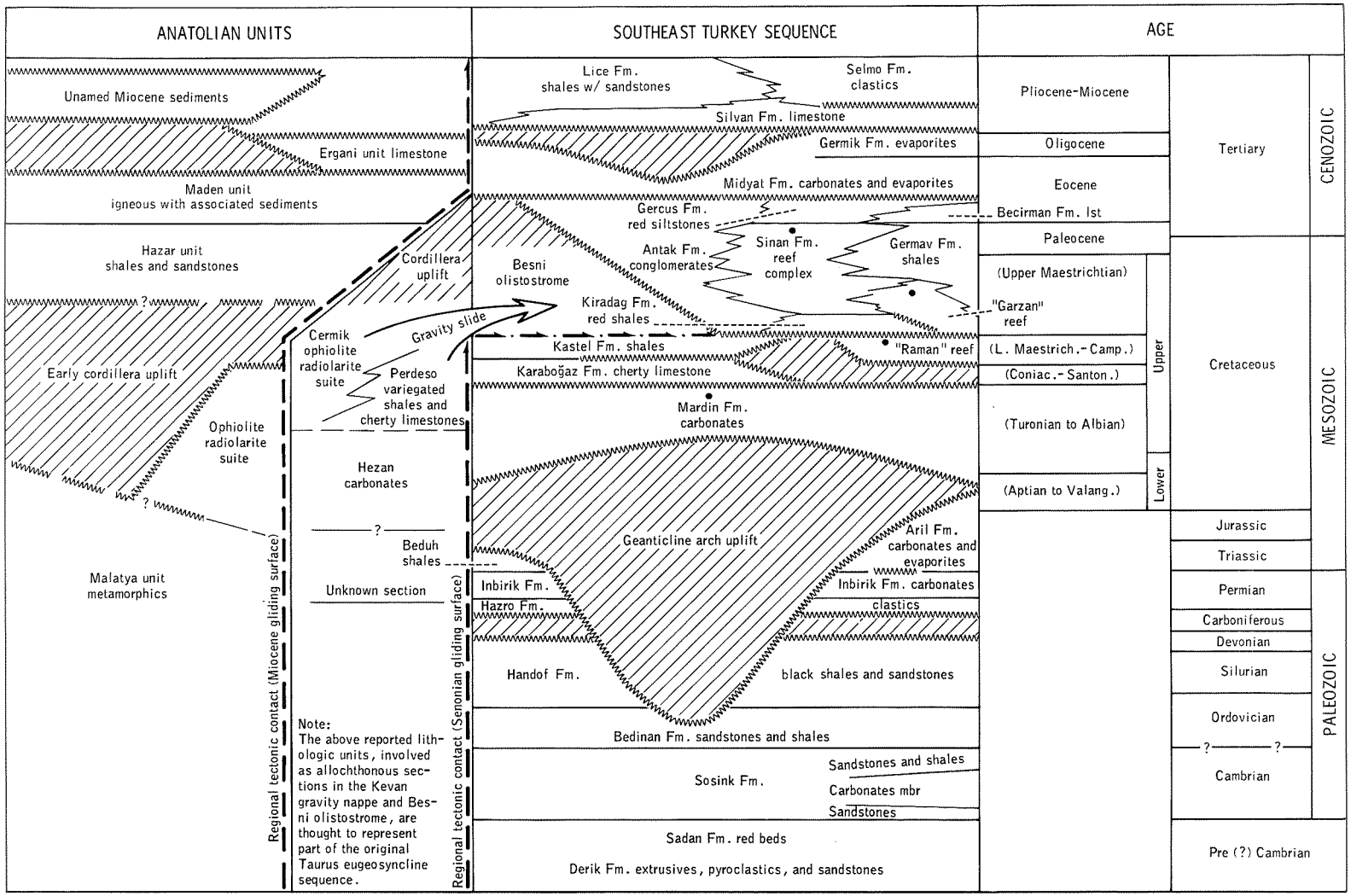
manuscript by the senior author and his Turkish colleague, Ismail Özkaya.[4]

The Paleozoic section of the autochthon can be divided into two major cycles (fig. 3). The first cycle is Cambrian to Devonian and comprises "basal transgressive clastics which, after a carbonate sedimentation, were overlapped by shallow marine Cambrian-Ordovician clastics" (ref. 4, p. 1913). This sequence grades upward into a shale sequence (Silurian), which represents the basinal phase of the cycle. The second Paleozoic cycle of sedimentation is represented by an upper Paleozoic section that "displays an interfingering of sub-continental, littoral, and shallow marine sediments" (ref. 4, p. 1920). Mesozoic sedimentation also consisted of two cycles separated by a regional unconformity at the base of the Cretaceous Mardin Formation (ref. 4, p. 1920). Cenozoic stratigraphy is not easily separated from the Mesozoic, but "locally a hiatus seems to occur between the Upper Cretaceous and Paleocene sediments" (ref. 4, p. 1921).

The following stratigraphic summary is mainly from Rigo de Righi and Cortesini (ref. 4). The oldest unit exposed in the study area is the Precambrian Derik Formation, a 2000-m-thick succession of extrusives, pyroclastics, and sedimentary clastic rocks. Also probably of Precambrian age is the 300-m-thick Sadan Formation composed of polygenetic conglomerates and sandstones. The Paleozoic section is represented by the Sosink Formation of sandstones, shales, siltstones, and carbonates (1950 m); the Bedinan Formation of fine-grained clastics (700 m); and the Handof Formation, a shale section (900 m). The upper Paleozoic is typified by the Hazro clastics (150 m) and the Inbirik Formation of carbonate rocks (250 m).

The Mesozoic sequence of the autochthon contains a thick carbonate-evaporite series including the Aril Formation, a 1000-m-thick Triassic-Jurassic unit, and the Beduh Formation, a 170-m-thick sequence of shales and quartzose sandstones. These are overlain by the Cretaceous Mardin Formation (750 m), an extensively dolomitized reefoid limestone. The Upper Cretaceous Karaboğaz Formation (100 m), a cherty blue marl, unconformably overlies the Mardin Limestone. This, in turn, is capped by a 350- to 600-m sequence of calcareous shales and

[4]Ibid.



Abbreviations: Fm. formation; w/ with; lst limestone; L. Maestrich. lower Maestrichtian; Camp. Campanian; Coniac. Coniacian; Santon. Santonian; Valang. Valanginian; mbr member

FIGURE 3.—Schematic stratigraphic section of southern Turkey (after ref. 4).

graywacke-type sandstones of the Kastel Formation (ref. 4, p. 1921). Red beds of the Upper Cretaceous-Eocene Antak Formation complete the succession. Ozkaya and Proctor[5] state that the "Raman reefs, Kiradag and Germav shales with Sinan and Garzan reef limestone intercalations and the uppermost Gercus red clastics constitute the Upper Cretaceous-Lower Eocene deposits of the southern shelf zone."

The limestones of the Midyat Formation (600 m) lie upon the red-bed clastics. The carbonate rocks of the Midyat are overlain by the evaporites of the Germik Formation. A reefoid carbonate, the Silvan Formation (50 to 100 m thick) lies upon the Germik Formation. At approximately the same depositional time of the Silvan, continental sediments of the Selmo Formation were being deposited (ref. 4, p. 1922). A thick (1000 to 1500 m) sequence of subgraywacke sandstones and shales makes up the flysch deposits of the Lice Formation. Continental clastics of the Lahti Formation, a 400- to 500-m-thick Plio-Pleistocene unit, locally overlie the Selmo Formation unconformably, and an equivalent clastic sequence overlies the Lice Formation.[6]

Stratigraphy of the Allochthon

The allochthon is composed of a high-grade metamorphic core and of a low-grade metamorphic cover (ref. 5). In the Sason-Baykan area, "low-grade metamorphic rocks occur as a 1000- to 1500-m thick massive plate thrust over geosynclinal sediments. The sequence of the allochthon in this area is chlorite schists, quartzites, calc-schists and crystalline limestones repeated by thrust faulting."[7] Non-metamorphosed sediments, graywackes, marls, serpentinites, silicified rocks, and spilites occur as intrathrust layers. According to Ozkaya and Proctor,[8] a "lower thrust plate of uniform green marls, shales and graywackes and an upper plate of red marls, clastics, flysch, serpentinites and spilites constitute the allochthonous Tertiary section between the underlying autochthonous block and the overlying metamorphic plates."

[5,6,7,8] Ibid.

The Lice Formation (1100 m), an Oligocene-Miocene succession of marls, graywackes, conglomerates, and spilites, makes up the lower thrust plate. The middle thrust plate, at least in the Sason-Baykan area of Turkey, is composed of the Baykan Group, a 2000-m sequence of the Yazpinar, Sason, and Melefan Formations. The Yazpinar Formation consists of a clastic series, a biomicrite unit, and a marl sequence; the Sason Formation is a flysch unit containing graywackes and shales; the Melefan Formation contains marls, mudstones, black micrite and sandy intrasparite beds, and a clastic unit as well as extensive spilites.[9]

Structures of the Autochthon

The most notable structural features of the autochthon are elongate anticlines. These tend to follow the trend of the thrust boundary. Broad uplifts related to faulting, and some transverse faults, are also present.

The first appearance of elongate anticlines more or less defines the boundary between the foreland and the fold belt (fig. 4). Rigo de Righi and Cortesini suggest that the Tertiary sediments are generally draped over fault blocks, which have displaced deeper, more competent beds (ref. 4, p. 1928); "These features are characterized by a strong relief, generally with a closure of several hundred meters, definite asymmetry, and a slight disharmony. Moreover, the steep southern flanks normally are affected by high-angle (50°-60°) reverse faults involving at depth the Mardin carbonate section . . ."

The folds within the belt trend nearly east-west and form a well-developed concavity toward the Arabian shield. The decrease in intensity of folding toward the south, the asymmetry of the folds with steeper limbs on the south, and the southward-displaced thrust sheets all imply a principal stress environment of north-south orientation. Ozkaya and Proctor[10] note that "The increase in intensity of deformation northward suggests a gradual increase in the magnitude of the stress in this direction towards the orogenic zone."

[9,10] Ibid.

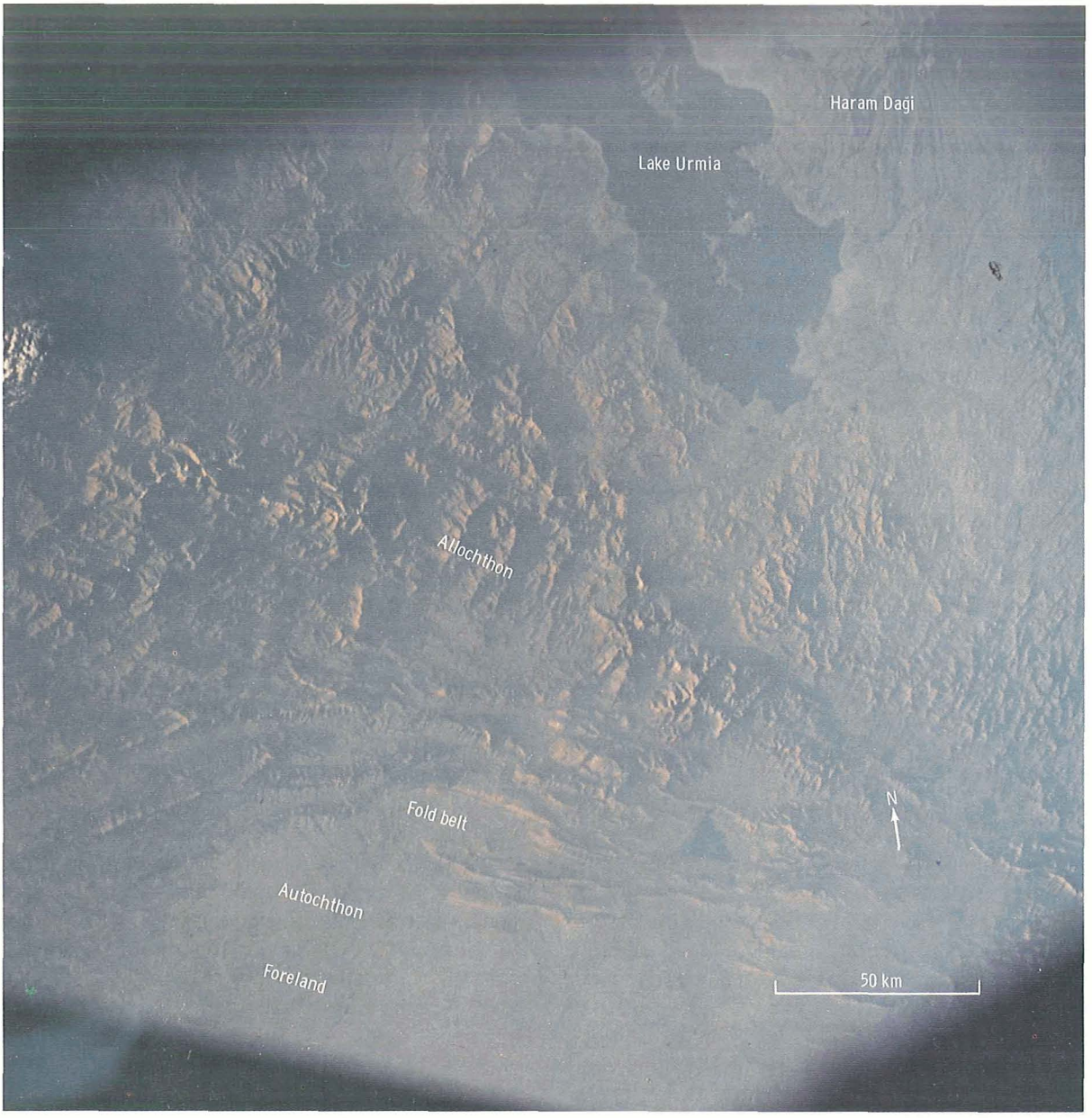


FIGURE 4.—ASTP photograph showing boundary between the allochthon and the fold belt and the transition to the relatively undisturbed foreland. Lake Urmia is at upper right, and Haram Dağı, the volcanic mountain, is to the east of the lake (AST-24-1982).

Structures of the Allochthon

Using the Sason-Baykan area as an example, it is concluded that the allochthon consists of four major thrust sheets. The thrust faults between these sheets are the Lice, the Baykan, the Sason, and the Kale from the bottom upwards.[11] Each of the thrust faults is essentially horizontal, and a common front zone roughly follows the hinge zone (the boundary between a stable region and a

[11] Ibid.

region affected by upward or downward movement). The Lice, Baykan, and Sason thrust faults formed at the end of the Miocene.[12] Displacement of the Kale thrust sheet by the Sason thrust fault suggests that the former thrust possibly occurred in Paleocene or Oligocene time. Ozkaya and Proctor[13] note that the age of associated sediments is not sufficiently conclusive to specifically date the development of the Kale thrust fault.

Interplate structural features, such as imbricate faults and tight asymmetrical folds, are present. These do not extend either upward or downward through the plate. Ozkaya and Proctor also record a number of conjugate northwest and northeast vertical faults, and some east-west and north-south normal faults within the allochthonous and autochthonous blocks.

PHOTOGEOLOGIC ANALYSIS

Photogeologic analysis reveals four fairly distinct geologic provinces: (1) a fold belt province south of the Tauride thrust zone (fig. 4), (2) the allochthon of the Taurides, (3) an area of volcanic rocks mainly in the central part of the study area, and (4) a northern fold belt of the Pontides. Geologic structures of different types are present in different degrees from one province to another (fig. 5).

Southern Fold Belt Province

The southern fold belt province is bounded on the north by the allochthon province. Southward, the fold belt gradually merges into the less folded shelf zone of the Arabian shield. The fold belt reaches a maximum width of approximately 200 km in the central area and narrows westward. The overall zone is slightly concave to the southwest as shown in figure 6.

Prominent structural features of the fold belt are the numerous elongate, topographically expressed northwesterly to westerly trending folds. Individual folds are typically asymmetric with the steeper limb on the south. Fold dimensions vary, but the longest strike length measured between the topographically expressed structural depressions is approximately 110 km. Structurally, the individual fold lengths are much longer. The wavelengths are also variable, but are generally less than 12 km for the largest. Smaller folds approximate an 11-km strike length and a 5-km wavelength. Limbs on the folds are inclined from a few degrees to very steep and are locally overturned to the south. Some reverse faults, transverse faults, and longitudinal faults cut the fold structures.

In the central and eastern part of the fold belt province, a series of fold culminations occurs along three northeasterly oriented belts. This characteristic suggests possible cross folds of a regional nature that are almost at right angles to the main fold belt.

In the far western part of the region, the fold belt is partly covered by younger volcanic rocks and sediments. In the central and western part, the allochthonous plate overrides part of the fold belt, an indication that the belt extends an unknown distance beneath the allochthon. An example of such structure is illustrated in the interpretive geologic map of a small part of the fold belt and allochthon (fig. 7). The Landsat image of the area is shown in figure 8.

Some strike-slip, normal, and imbricate thrust faults are recognized within this province. Lineaments of unknown origin are also visible in the images. Most of these lineaments parallel the trend of the fold belt. Some, however, are discordant to the structural grain of the area. They probably represent fracture zones within the rock units.

In the far eastern part of the province, some major structural features with well-developed radial drainage and fine-grained rock texture occur. These features are mainly along the axial parts of large anticlinal folds. Their size, their discordant character, and the fine texture of their rocks all suggest unexposed forceful intrusive bodies or sedimentary diapirs. The latter explanation is favored because of the lack of volcanic rocks in the immediate area and because of the absence of igneous plutons in the fold areas of the autochthon.

[12,13] Ibid.

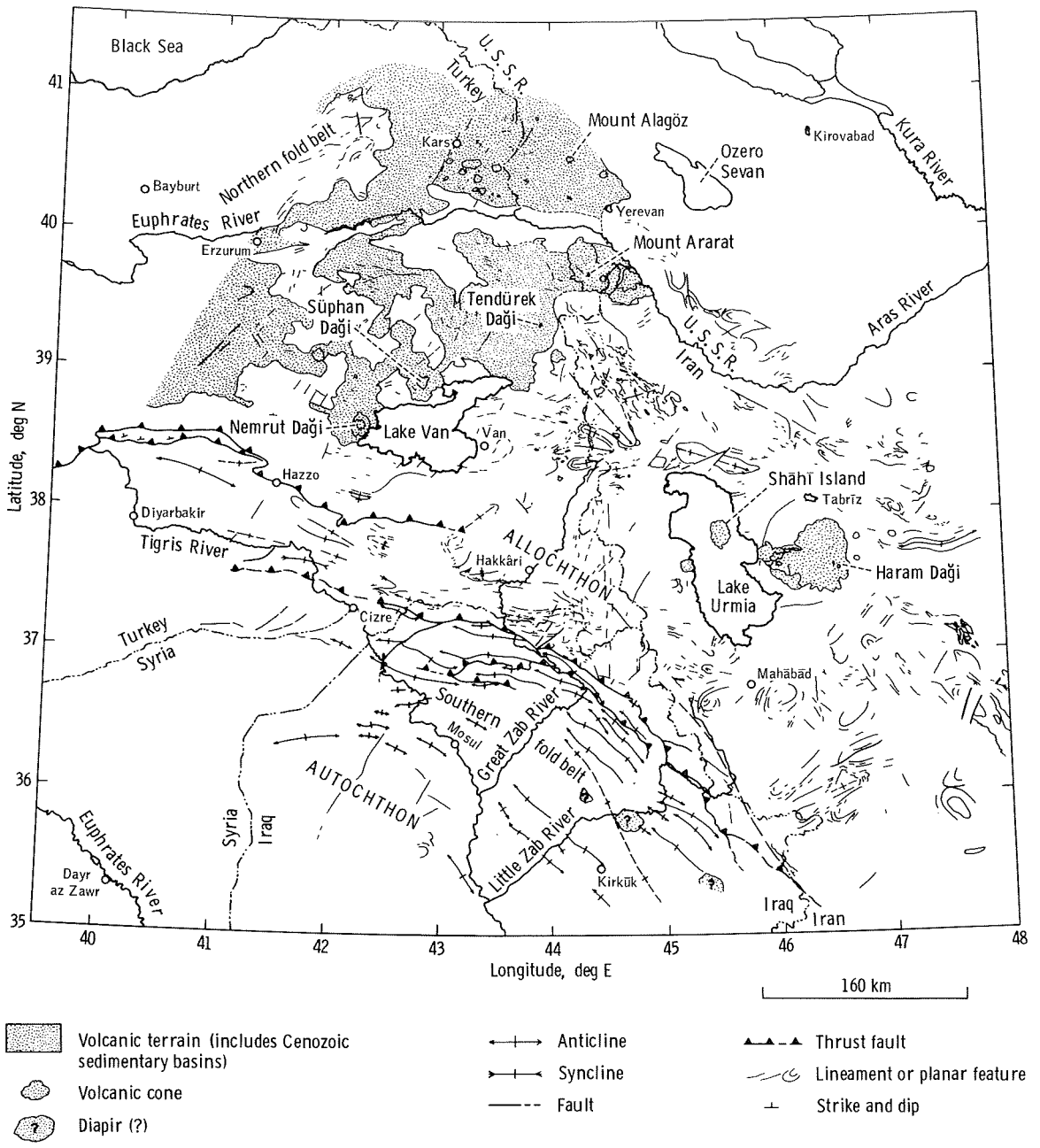


FIGURE 5.—Interpretive phototectonic map of southeastern Turkey, northern Iraq, and northwestern Iran.

Allochthon

The allochthon is bounded on the south by a thrust zone and by the fold belt. The thrust zone roughly parallels the trend of the folds in the fold belt and is continuous over the entire length of the region studied. The southeastern part of the allochthon interfaces with a northwesterly trending lineament near the southern part of the mapped area. This lineament is continuous to the northwest for approximately 190 km. It is divergent from the thrust zone in the south, but to



FIGURE 6.—Landsat image of a part of the study area showing the concave nature of the southern fold belt (E-1139-07130).

the north, it tends to parallel the thrust zone. Its continuity and linearity suggest the trace of a strike-slip fault.

The thrust boundary of the allochthon south of Lake Van and Lake Urmia trends westward. Several thrust sheets occur in this area. These definitely override large anticlines of the fold belt. The thrust sheets range from 10 to 30 km in width and are as much as 100 km long. Strike-slip faults are also associated with these thrust sheets and are transverse to them.

Two possible thrusts occur north of Cizre, Turkey. One is approximately 10 km north of Cizre; it bears westward for approximately 100

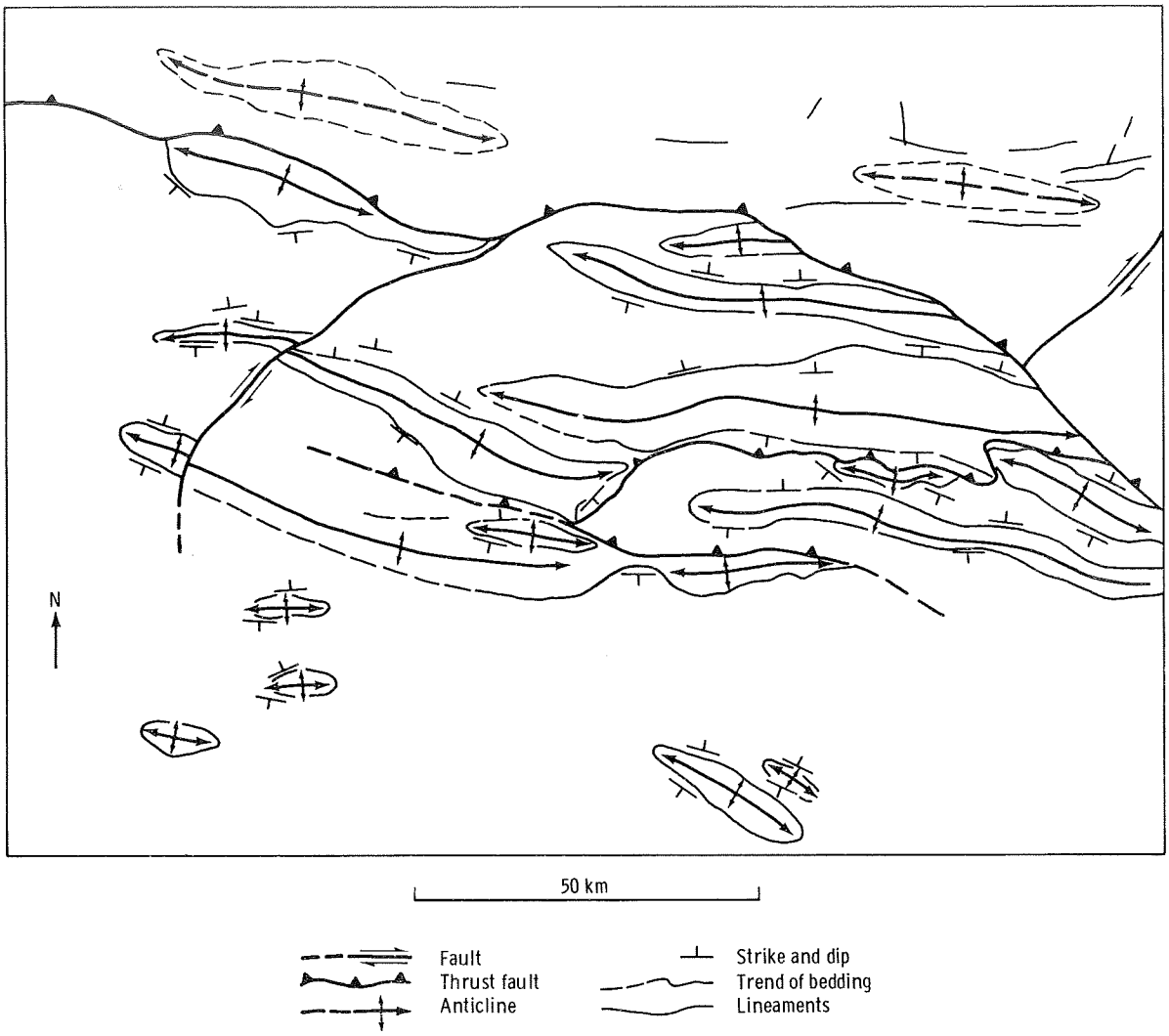


FIGURE 7.—Photogeologic map of a part of the autochthon north of Mosul, Iraq.

km. Volcanic rocks cover parts of the area to the southwest of this thrust boundary. To the east, the thrust zone interfaces directly with the fold belt province.

The second possible thrust, generally trending westward, occurs 70 km north of Cizre. Major salients and recesses in the vicinity of large synclines and anticlines, respectively, suggest that the thrust plane may be partly folded and that the effects of erosion are now defining these folded areas. The thrust also continues eastward, but it is not easily identified on the images beyond a 75-km distance into the allochthon.

Approximately 80 km southwest of Bitlis, the thrust boundary of the allochthon continues westward as a single fault zone. North of the Hazro uplift, a second thrust sheet appears. This block is approximately 10 km in exposed width and approximately 20 km in length. It joins with the main thrust fault at both ends.

Another distinctive characteristic of the allochthon is a group of somewhat elongate curved to circular linear patterns in the southeastern part of the allochthonous block. These curvilinear features have a northwest orientation. They could represent domes and/or basins within

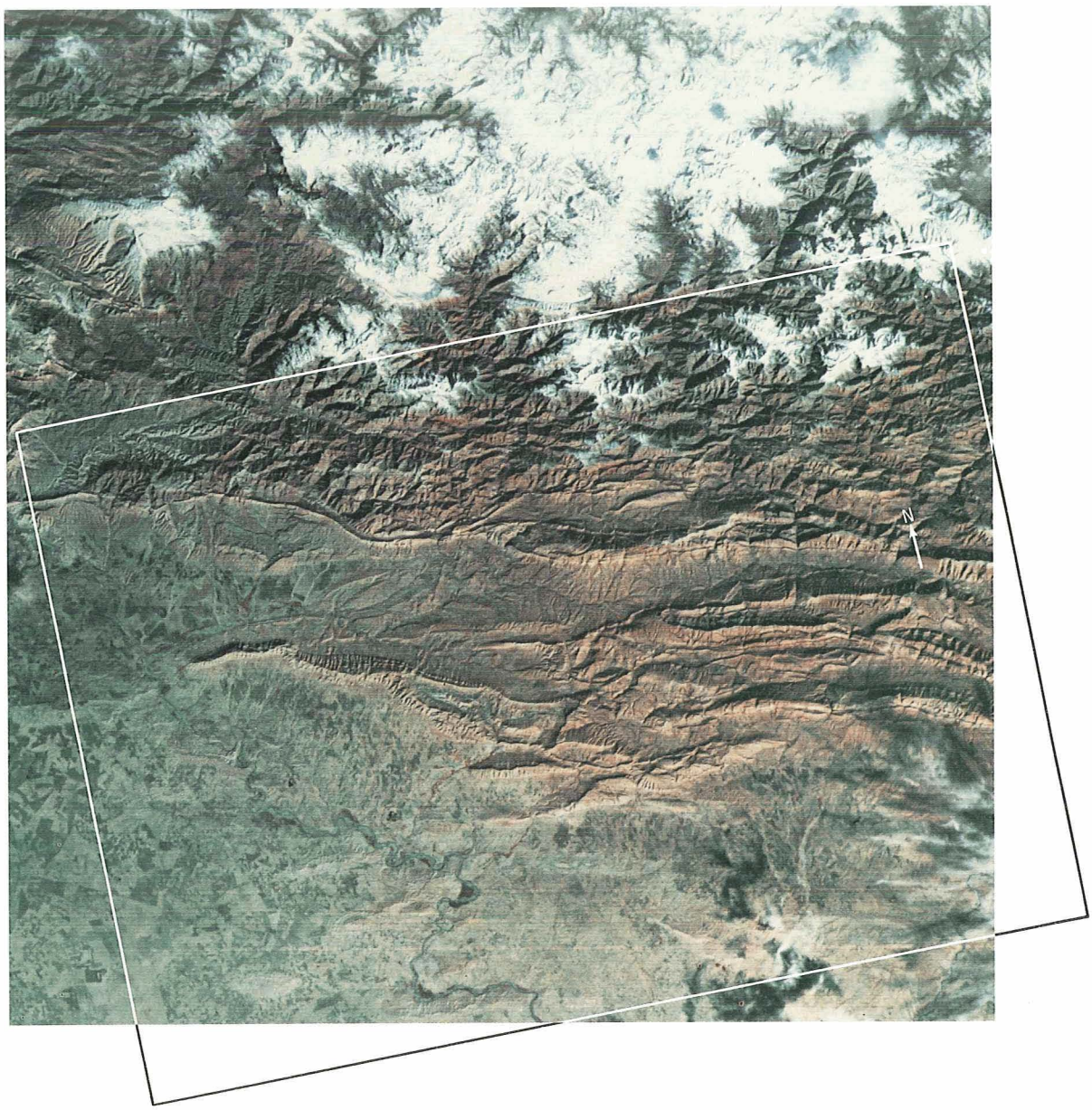


FIGURE 8.—Landsat image of a part of the southern fold belt. Outlined area corresponds to the photogeologic map of figure 7 (E-1122-07182).

the tectonic block. Locally, they are partly truncated by younger alluvial sediments.

Well-expressed northerly and westerly trending lineaments occur between Lake Van and Lake Urmia. South of Lake Urmia, lineaments and some layered structures trend mainly northeasterly. North of the lake, the trends are mainly northwesterly.

Between Lake Van and Lake Urmia, an unusual textural pattern occurs in the exposed rock units. This pattern is characterized by bodies of rock that range in size from isolated and dis-

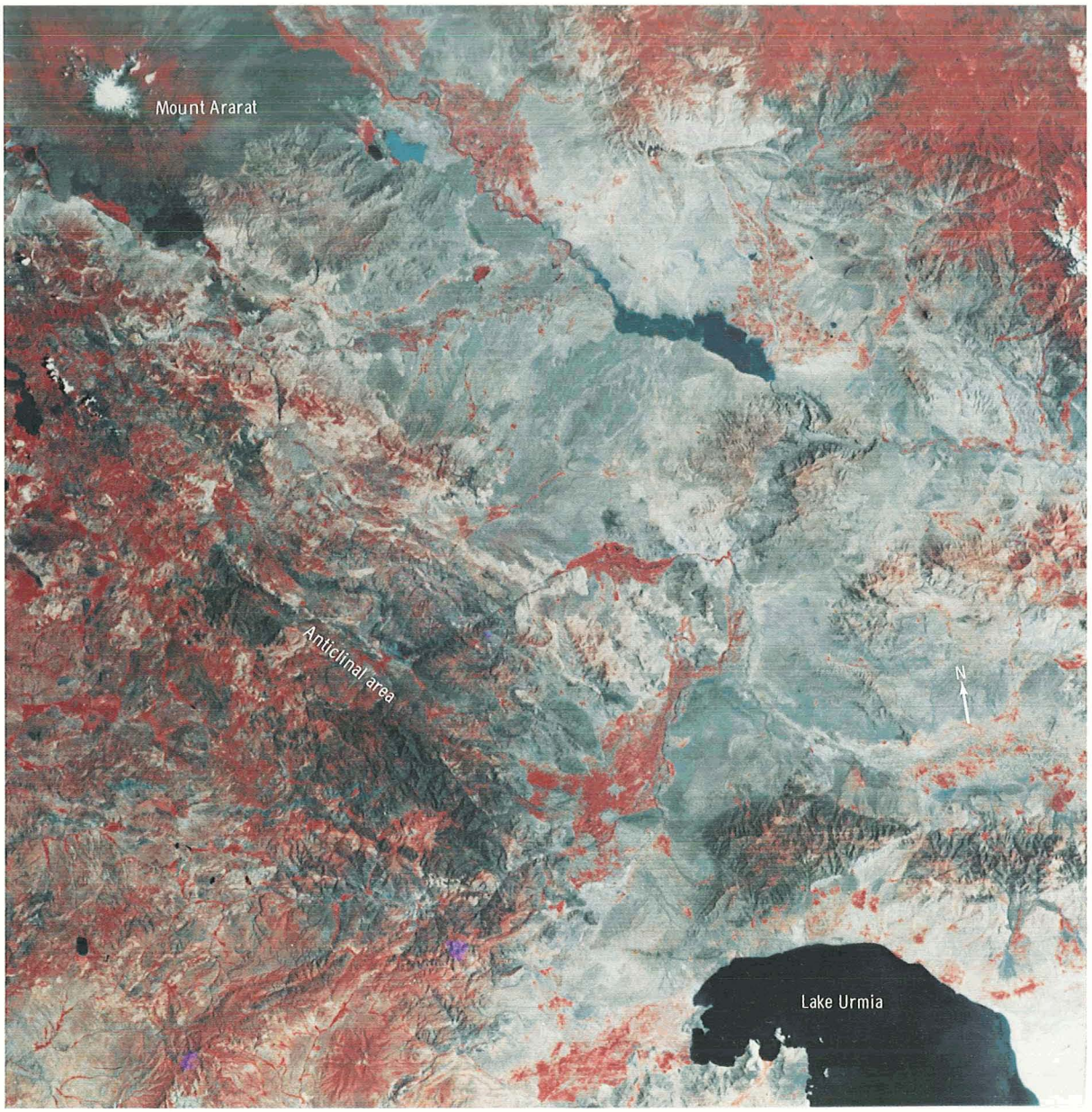


FIGURE 9.—Landsat image of the area north and west of Lake Urmia, showing a major anticline and an area of possible mélange. Mount Ararat is in the extreme northwestern part of the image (E-1355-07114).

crete masses to large connected bodies. These large bodies are composed of a light-toned resistant rock with a linear to random pattern within a darker, finer grained, mainly nonlayered rock matrix. The layered to fragmented character of these light-toned masses in the darker matrix is strongly suggestive of a mélange. Such rock units are known to occur north of Diyarbakir in the allochthon.

Just north and northwest of Lake Urmia, the mélange is involved in a large anticline and several smaller subsidiary folds. The major anticline is approximately 35 km wide and as much as 100 km in exposed length. The subsidiary folds

are much smaller, but they generally have parallel axial trends. The major anticline plunges eastward to form a large depression along its axis. This same fold reappears as a faulted culmination north of Lake Urmia as depicted in figure 9.

Although the resolution of the images in the eastern area is not the best, geologic structures do appear to be more abundant on the allochthonous block in this area. Much additional work and field checks would be required to resolve these structures. Lineaments are of general westerly trend; curvilinear structures suggest large folds of similar trend.

Northern Fold Belt

Of the four geologic terrains observed, the northern fold belt is the most poorly defined on the images. Poor ground resolution as a result of adverse weather conditions at the time the image was taken added to the difficulties of photographic analysis in this region.

The region is northwest of Lake Van and west of the volcanic rock area centered about Kars, Turkey. Here, layered structures and lineaments trend northeasterly. These structures probably represent folded, layered rock units. Although recognition of the layered character of the rock units is possible, the poor image resolution permits only the identification of a fold belt of northeasterly trend.

Volcanic Terrain

Extensive cover of Tertiary and younger volcanic rock is quite common in parts of the region. This type of terrain is identifiable, and the boundaries are fairly well defined.

Three main centers of volcanic activity are indicated: (1) an area centered around Tabrīz, Iran, (2) a volcanic rock area north and west of Lake Van, Turkey, and (3) an area of volcanic rock near Kars, Turkey. (See fig. 5.) Some extensive volcanic rock cover also occurs west of Diyarbakir, Turkey, in the southwestern part of the region on the autochthon and just west of the mapped area.

The Tabrīz, Iran, volcanic area is the smallest of the three. It centers about a large volcanic cone, Haram Dăgi (Kūh-e Sahand) (3700 m), south of Tabrīz and on the eastern shore of Lake Urmia. This complex of flows and volcanic cones is approximately 42 km wide and approximately 75 km long. The volcanic area is clearly shown in figure 10.

A very long, discontinuous, circular lineament is peripheral to the main volcanic complex south and west of Tabrīz. This feature may represent a peripheral subsidence fault related to the volcanic field. Within this volcanic terrain, at least four different volcanic rock units are identifiable on the images.

Several small volcanic cones are readily visible in the area. These occur both within the main volcanic complex and east-southeast of Tabrīz. Associated with the cones are volcanic flows that range from 2 to 7 km in diameter.

Two other features, interpreted as volcanic cones and associated volcanic rock, occur west of the main volcanic complex. One is Shāhī Island in Lake Urmia. This island is approximately 15 by 22 km in size. The other probable volcanic cone and its associated flows are on the west-central shore of Lake Urmia. These features are approximately 10 km in diameter.

The greatest areal extent of volcanic terrain is immediately north-northwest of Lake Van, Turkey. Altinli et al. (ref. 6) describe various volcanic rock types within this region and identify abundant basalt, dolerite, andesite, spilite, and porphyrite. Less abundant are tuffs, agglomerates, breccias, rhyolite, and dacite.

North-northwest of Lake Van, some prominent volcanic cones appear to be related to lineaments, which, in this area, follow the well-known regmatic pattern of the Earth. The best developed of the lineaments in this region is a northeasterly set. One of these lineaments is regional in character and is traceable for more than 225 km. Four distinctive volcanic cones along it are described by Altinli et al. (ref. 6): Mount Nemrut, Süphan Dağı, Tendürek Dağı, and Mount Ararat.

Nemrut Dağı (2400 m) is just west of Lake Van and has the characteristic shape of a young volcano. Its large crater is occupied by a lake, and small parasitic cones occur on the southern flank.



FIGURE 10.—Landsat image of Haram Dağı and Lake Urmia in northwestern Iran. Arrow indicates parasitic cone on western flank of Haram Dağı (E-2134-06550).

Süphan Dağı (4434 m) is 60 km northeast of Nemrut Dağı and 15 km north of Lake Van. This conspicuous mountain has several parasitic cones and a crater as shown in figure 11. Altinli et al. (ref. 6) suggest that it is a stratovolcano composed mainly of andesite and obsidian.

Tendürek Dağı (3313 m) is 50 km northeast of Lake Van. Two cones make up the peak area, and a small lake occupies a crater zone. The main mass is reported as andesitic in composition. Earlier eruptions included Peléan flows and basalt flows, then andesite and late basalt capping. Cinder

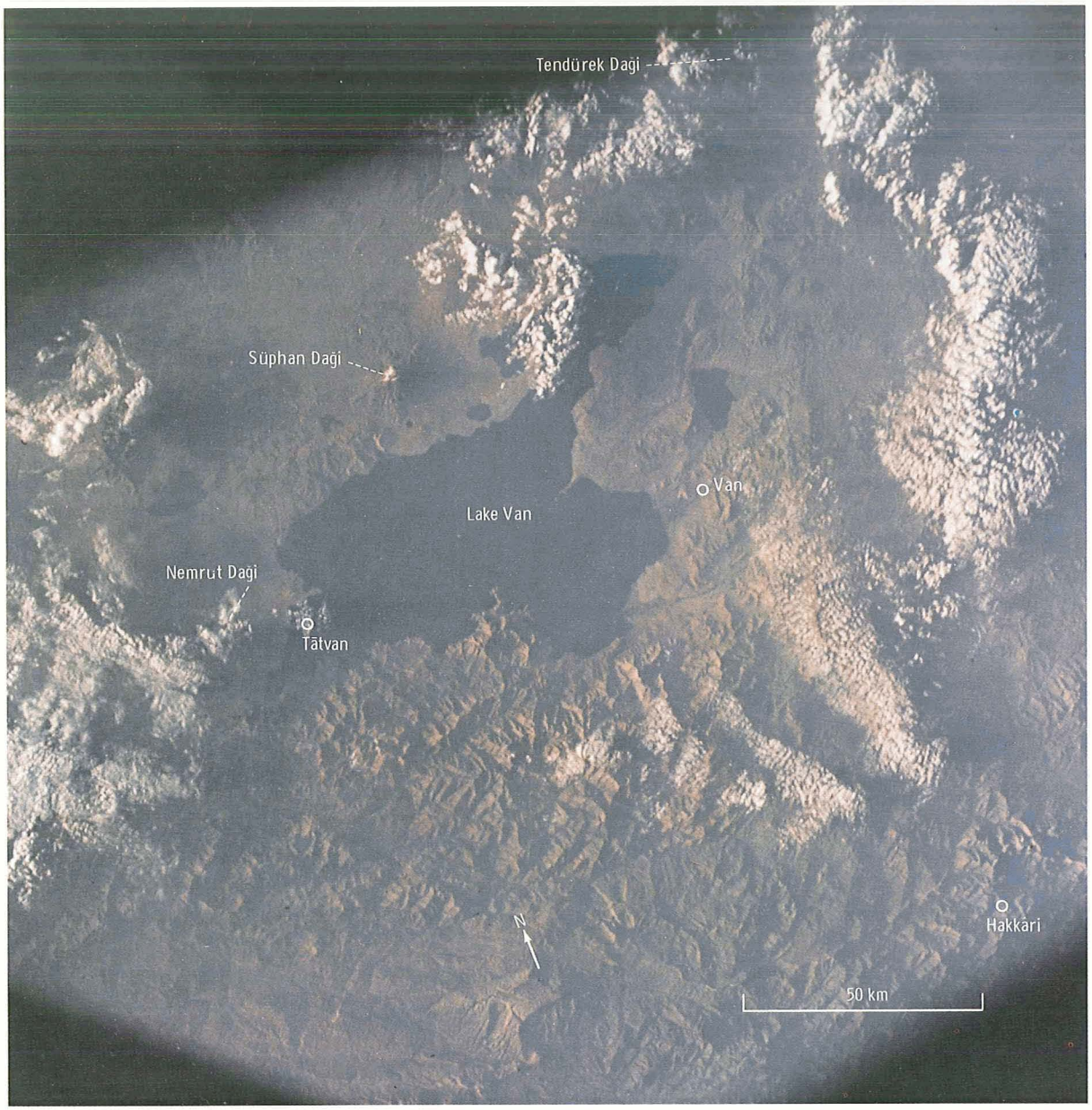


FIGURE 11.—ASTP photograph of volcanic area north of Lake Van showing the volcano Süphan Dağı. Nemrut Dağı, another volcano in the area, is situated at the western end of Lake Van and is partly obscured by cloud cover. Tendürek Dağı, a third volcanic peak, is in the northern part of the image (AST-24-1979).

cones, spatter cones, mounds, and other volcanic features suggest relatively recent volcanic activity (ref. 6).

Mount Ararat (5185 m) is 100 km northeast of Lake Van (fig. 9). Of Biblical fame, this beautiful volcanic mountain rises several thousand meters above the surrounding valley floors. It is a compound stratovolcano made up of Great Ararat (Büyük Ağri Dağı) and Little Ararat (Bücük Ağri Dağı). Unlike the other peaks of this chain, Mount Ararat does not have a defined crater. Altinli et al. (ref. 6) report andesitic lava as the

main rock type with flank eruptions of basalt. Parasitic cones occur along radial fissures.

Little Ararat (3925 m) is some 12 km southeast of the main peak and is considered a separate volcano. Lavas and interlayered breccias, lapilli, and tuffs make this a stratovolcano also.

East of these volcanic peaks, the associated volcanic rock distribution and some of the parasitic cones are readily visible on the images. These features are shown in figure 5.

Extensive volcanic rock cover also occurs in the area around Kars, Turkey. This volcanic terrain extends west of the town and also east into the U.S.S.R. The high volcanic peak of Mount Alagöz (4095 m) is within this volcanic field. Several other volcanic cones and associated volcanic rocks are also present. The largest of the smaller ones is 6 by 15 km, and the smallest less than 1 km in diameter. The associated effusive material of Mount Alagöz covers an area of approximately 40 by 32 km.

The age of volcanism in the Kars area (ref. 7) ranges from Upper Cretaceous on the west to Tertiary in the central part and Neogene in the eastern part. Basalt, dolerite, andesite, spilite, porphyrite, tuff, agglomerate, and breccia are the common rock types. Erentöz and Ketin (ref. 7, pp. 38-46) observe that volcanism continued from the Upper Cretaceous to the Quaternary.

TECTONIC ANALYSIS

Major tectonic units, lineaments, and planar structures visible on the small-scale color ASTP photographs and Landsat images indicate that regional stresses resulted in two major tectonic blocks and associated structures (fig. 5). These include a well-developed autochthon with visible foreland fold structures, as well as an allochthonous block with associated internal structures and a partial volcanic rock cover.

A distinctive and easily identifiable fold belt province etched out by erosion occurs on the autochthon. The individual folds are of long linear extent, have definite culminations and depressions, and are locally cut by both transverse and longitudinal faults. The fold belt province extends the full 700-km distance of the mapped area. The fold zone is slightly concave to the southwest and shows asymmetry for individual folds within it, with steeper limbs on the south. Small thrust and/or reverse faults locally cut the folds. The fold belt tends to be parallel, and in places is tangential, to a well-developed thrust zone, which forms the interface with the overriding allochthonous block.

Locally, the allochthonous block is characterized by internal folds, faults, and lineaments. In general, these features tend to parallel the trend of the underlying thrust faults and folds, but local and major variations from this trend are present. The resistance of the rock units within the allochthon to erosion and weathering makes the distinction of individual units difficult. Most of the block is mountainous. Layered structures permit resolution of major folds, of some distinctive and long lineaments, and of an extensive cover of volcanic rocks. The last shows volcanic cones, craters, calderas, and parasitic cones that are little affected by erosive processes and apparently of recent geologic age.

The parallelism of the fold belt on the autochthon, of the thrust zone, and of some major internal structures in the allochthon is strong evidence for a common causative force. The concavity of the fold-thrust zone to the southwest suggests that a directed tectonic stress formed this large recess. The presence of ophiolitic masses along the thrust zone suggests a deep internal source for these materials. Possible mélange units and a long period of volcanic activity, as expressed in the volcanic terrain, are also indications of a region of tectonism.

At least three major stress environments are possible for the region: (1) a rising root zone with directed stresses southward, (2) a rising area in the central region with gravity slide potential northward and southward from this elongate upland area, and (3) northward motion and subduction of a plate beneath the Tauride zone (fig. 12).

The photogeologic data do not yield convincing evidence of large gravity slide masses from a relatively high upland zone. Source areas for gravity slides and lineaments related to such source areas are absent or, if present, are now covered by extensive volcanic material. The thrust zones and the underlying folded rocks suggest a southward-directed stress, which could have resulted in the

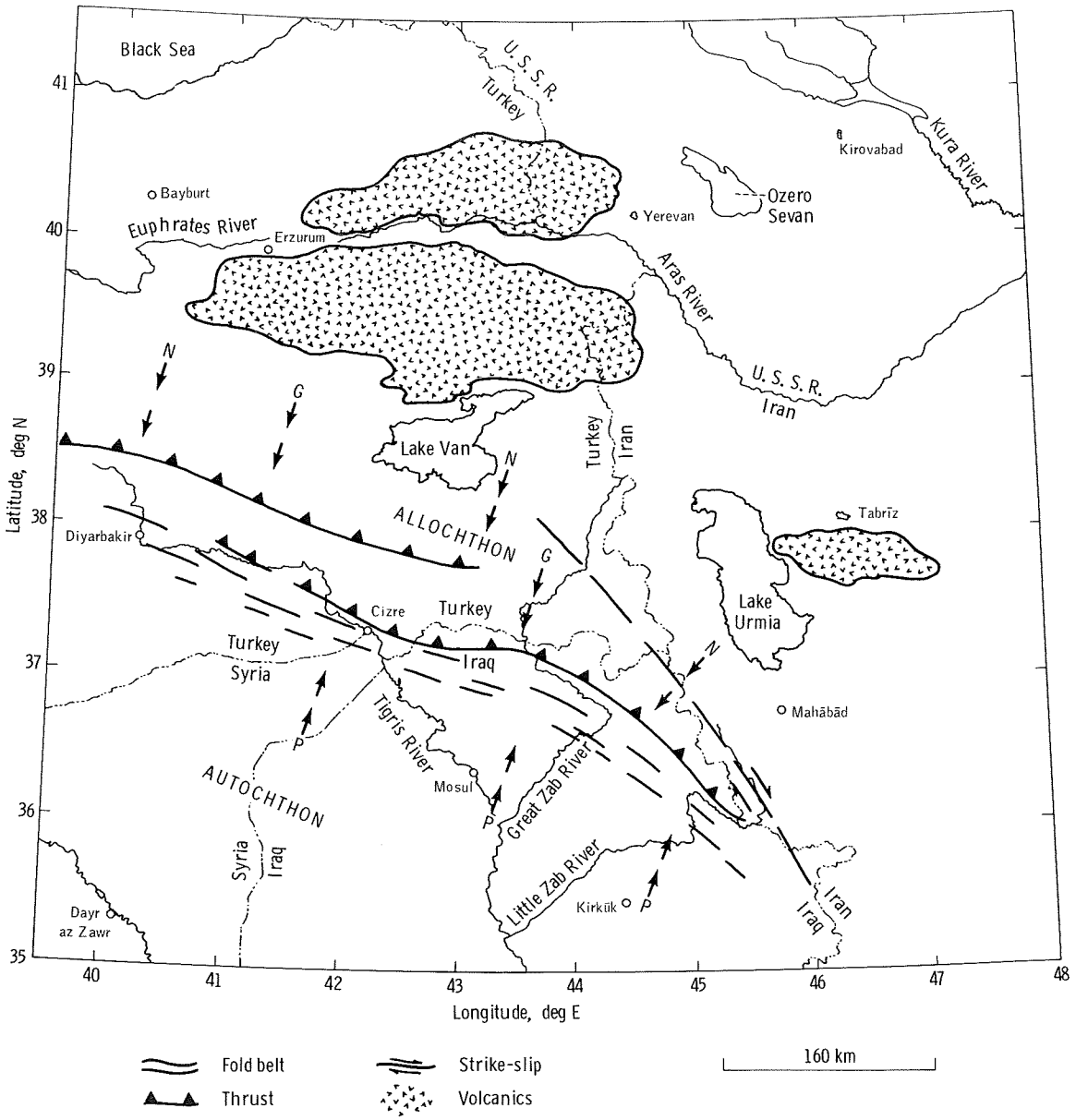


FIGURE 12.—Schematic map of possible stress fields of southeastern Turkey and northwestern Iran, showing directions for nappes (N), gravity slides (G), and plates (P).

thrusts and the asymmetrical folds and transverse faults.

Brinkmann (ref. 1), Ilhan (ref. 2), and others suggest that the initiation of the Tauride fold zone began in the Mesozoic. Indeed, first Alpidic tectogenesis was in Triassic time (ref. 1) and corresponds to the first northward movement of the African-Arabian plate and to the subduction of oceanic crust that was moved northward in front of it (ref. 8). This movement continued throughout Mesozoic time and into the Cenozoic, with intermittent motion possibly corresponding to different phases of the Alpidic tectogenesis. The northward tectonic stresses and the related

plate movement resulted in the subduction of the African-Arabian plate. Resultant structures were the development of the overlying fold belt province of the Taurides, the associated east-west thrust sheets and subsidiary strike-slip faults, ophiolitic intrusions, and basic to rhyolitic flows on the allochthon.

Innocenti et al. (ref. 9) relate the structural features and volcanism of eastern Turkey to the interaction of continental plates. They indicate that the impingement of the Arabian plate on the Anatolian and Iranian plates has produced "conspicuous fragmentation and development of conjugated structures trending at 45° to the main compressive stress." The association of calc-alkaline volcanics with alkaline volcanics is interpreted by Innocenti et al. (ref. 9) as being related to the subduction of the Arabian plate beneath the Anatolian and Iranian plates. The alkaline volcanism is the result of "lithospheric fragmentation due to the divergent motion of the Anatolian and Iranian microplates."

The previously discussed structural and tectonic features, when considered with the much broader regional tectonics of a northward-moving Arabian shield plate, give credence to the plate tectonic concept as a possible origin for this portion of a continent-wide fold-thrust zone. That the movement is continuing to the present is suggested by the strike-slip fault in the southeastern part of the region (i.e., this feature probably corresponds to the Anatolian transform fault), and by the postulated folding of the thrust plane and displacement by even more recent faulting.

The relatively young, and still active, strike-slip fault suggests a change in the mechanical response of the Turkish and Iranian plates to the northward-acting stresses, or possibly a modest change in the stress direction itself.

Dietz and Holden (ref. 10) suggest that the Tethyan Sea was closed in Upper Cretaceous and that the African-Arabian plate was brought in contact with the Eurasian plate. In Miocene time, the Arabian-Syrian plate began to separate from the African plate (ref. 11). This movement subjected the Turkish and Iranian microplates to new stresses. It is reasonable to assume that this counterclockwise movement of the Arabian-Syrian subcontinental mass resulted in the observed borderfolds and the major strike-slip fault of this region.

PROPOSED GROUND-TRUTH CHECKS

Complex structural and stratigraphic relationships occur in at least six different areas of the region. Ground-truth investigation (GTI) of these areas is needed. The selected areas relate either to long lineaments, the origins of which are not clear, or to large structures not identifiable on the images. The areas of the proposed GTI's are illustrated in figure 13.

The first GTI (GTI-1) is on the allochthon between Lake Van and Lake Urmia and north of Lake Urmia. In the western part of the GTI-1A area, lineaments and layered structures on the images suggest two anticlines. The larger one could have a wavelength of as much as 35 km and a strike length of 100 km or more. The large fold strikes northwesterly. The smaller fold to the south strikes east-northeasterly. The layering and inclinations of the fold areas suggest that they converge toward the east.

Another probable anticline is visible approximately 50 km south of the city of Van (GTI-1B). This structure may represent a continuation to the southwest of the smaller of the two northern upfolds to the east. Each of the fold structures noted has dark-colored massive rock units overlain by a mélange-like rock unit of extensive areal distribution. The GTI should result in confirmation or modification of the structural interpretation and should enable evaluation of the possible mélange unit for this part of the region.

In the eastern part of the GTI-1A area, the depression zone eastward along the axial trace of the major fold should also be checked in the field. Dark-colored units are exposed to the east of the depression in a culmination-like structure of 60 km or more strike length just north of Lake Urmia.

The second GTI area (GTI-2) is between Cizre and Şemdinli, Turkey, on the autochthonous block. Lineaments and some planar structures in the finely dissected autochthon suggest anticlinal

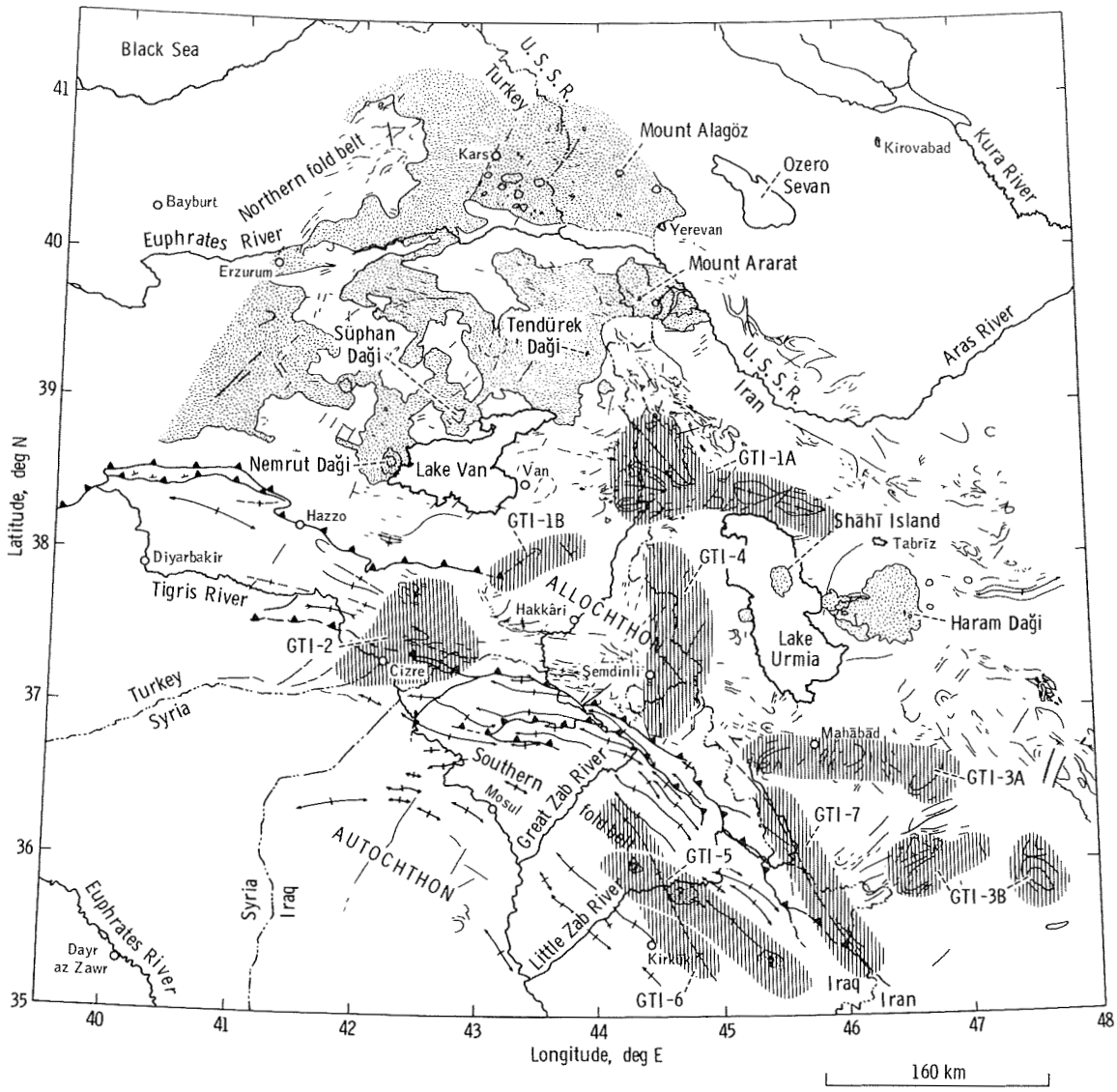


FIGURE 13.—Index map of proposed ground-truth investigations in southeastern Turkey, northern Iraq, and northwestern Iran. (See fig. 5 for explanation of geologic symbols.)

folds. The central part of a west-trending anticline is approximately 70 km west of the Great Zab River (fig. 13).

At GTI-2, the validity of the fold structures should be determined. Are these anticlines pre-allochthon, syn-allochthon, or post-allochthon? Finally, is the stratigraphy of the autochthonous block near the thrust interface favorable as a source and reservoir rock for petroleum occurrences? Confirmation of such favorable stratigraphy in the exposed autochthon would be most significant in the search for underlying structures in the covered autochthon, which could have petroleum potential.

Lineaments and some planar structures in the GTI-3 area south of Mahābād, Iran, suggest several large southwest-trending anticlines, some domes, and faults. In much of this allochthonous

area, bedding attitudes are not easily identifiable from the images.

Domelike structures occur in the area of Mahābād, Iran, approximately 25 km east and west of the town (GTI-3A), and large probable anticlines occur some 95 km southeast of the city (GTI-3B). By means of GTI-3, the presence of the folds, the existence of a possible major fault, and the age of the folded rocks should be confirmed or refuted. Each evaluation would assist in a better understanding of the structure, the stratigraphy, and the economic potential of the allochthon.

The area of GTI-4, approximately west of Lake Urmia, has a pair of northward-trending lineaments somewhat discontinuous over a 140-km strike length. These lineaments could represent strike-slip faults. The GTI-4 would confirm the character of the lineaments, whether faults or joints, and if faults, the type of displacement and the relationship to the allochthon and autochthon.

Two other areas, GTI-5 and GTI-6, are on the autochthon. The GTI-5 area includes a set of three roughly circular features alined northwesterly. These are indicated by radial drainage and a slight tonal variation in the underlying rock units. The structures occur north, northeast, and east of Kirkūk, Iraq. The smallest of the three is approximately 50 km north, the largest approximately 40 km northeast, and the third approximately 95 km east of the city. At GTI-5, the presence of the three possible sedimentary diapirs would be confirmed or refuted. Hopefully, the type of intrusion, the interface characteristics, the nature of the circular features (igneous or diapiric), the structural setting, and the age of the rock units would also be determined.

The GTI-6 area is also on the autochthon. Here, a large, somewhat discontinuous anticline appears to have a longitudinal extent of approximately 130 km. This major structure is in the same area as the intrusive masses noted previously. Indeed, the fold axis can be traced between the two northern bodies. At GTI-6, the upfold would be confirmed or refuted, the relationship of the fold axis to the possible intrusive centers would be checked, and a possible explanation for the spatial relationships would be established.

The GTI-7 area is selected to check the interface characteristics of the thrust zone and the very prominent northwest-trending lineament of probable strike-slip origin. The latter could be a continuation of the Anatolian Fault. The results of the ground investigation should confirm or refute the presence of a major strike-slip fault, demonstrate the age relationships between the lineament and the thrust zone, and yield data on the structural characteristics of the interface zone.

The proposed GTI's of selected areas would require a minimum period of 30 field days. A field party of at least two, one with language capability for the region (i.e., Turkish, Persian, Arabic), would be required for the field studies.

CONCLUSIONS

Photogeologic analysis of the region of southeastern Turkey and northwestern Iran reveals three major geological terrains: an autochthonous block of mildly to intensely folded layered rocks; an allochthonous block of older, more uniform, and probably more resistant, layered to massive rocks, with associated folds and faults and some lineaments of unknown origin; and, finally, a volcanic terrain, which covers large areas of the allochthonous block. Young volcanic cones, some impressively high such as Mount Ararat (5185 m), rise above the general level of the volcanic terrain. Younger sediments and Quaternary alluvium cover other parts of the area.

Tectonic analysis suggests that gravity sliding, a southward-moving nappe, or plate intersections and related phenomena are possible modes of origin for the three terrains. Of these, the plate tectonic theory appears most reasonable. This theory involves a counterclockwise motion of the Arabian shield plate and subduction of that plate under the Turkish-Iranian microplate. The consequences of the plate motions and interactions are foreland folding of the autochthonous block and overthrusting of the allochthon with some folding and faulting. Possibly synchronous with the plate movements were some ophiolitic intrusions, and intermediate to rhyolitic with less basaltic volcanism on the allochthon. This igneous activity occurred over a long time interval. Most recent volcanism is expressed as shield volcanoes, stratovolcanoes, some parasitic cones, and crater

and caldera development. Some volcanic peaks now rise well above the general terrain. Four of these, including Mount Ararat, occur along a major northeast-trending lineament.

Finally, a prominent and well-developed northwest-trending lineament, on the allochthon in the southeastern part of the region, trends toward Lake Van. This structure interfaces southward with the thrust zone. To the northwest, it probably becomes the Anatolian strike-slip or transform fault. This area has had continuous seismic activity, some disastrous, within recent time.

Although no rock ages are identified on the map of this 500 000-km^2 region, the tectonic features and smaller structures represent a reasonable geologic synthesis of major features of the area. The geological interpretations give encouragement that petroleum accumulations might possibly occur beneath the allochthonous block if structural and stratigraphic conditions are favorable in the autochthon. To confirm or refute that possibility, and to enhance the interpretations of other tectonic and structural features, ground-truth investigations are proposed.

ACKNOWLEDGMENTS

This work was performed under Smithsonian Institutuion Grant PC6-22279 as a subcontract of NASA contract NAS9-13831.

REFERENCES

1. Brinkmann, Roland (Irene Woodall, transl.): Geology of Turkey. Encke (Stuttgart), 1976.

2. Ilhan, Emin: The Structural Features of Turkey. Geology and History of Turkey, Annual Field Conf. no. 13, A. S. Campbell, ed., Petrol. Explor. Soc. Libya (Tripoli), 1971, pp. 159-170.

3. Badgley, Peter C.: Structural and Tectonic Principles. Harper and Row (New York), 1965.

4. Rigo de Righi, M.; and Cortesini, A.: Gravity Tectonics in Foothills Structure Belt of Southeast Turkey. Bull. American Assoc. Petr. Geol., vol. 48, no. 12, 1964, pp. 1911-1937.

5. Yilmaz, O.: Étude pétrographique et géochronologique de la region de Cacas (partie méridionale de massif de Bitlis, Turquie). Ph. D. dissertation, Universite Scientifique et Medical de Grenoble, France, 1971.

6. Altinli, I. Enver; Pamir, Hamit N.; and Erentöz, Cahit: Explanatory Text of the Geological Map of Turkey, Van. Mineral Res. Exploration Inst. (Ankara, Turkey), 1964.

7. Erentöz, Cahit; and Ketin, Ihsan: Explanatory Text of the Geological Map of Turkey, Kars. Mineral Res. Exploration Inst. (Ankara, Turkey), 1974.

8. Dewey, John F.; and Bird, John M.: Mountain Belts and the New Global Tectonics. J. Geophys. Res., vol. 75, no. 14, 1970, pp. 2625-2645.

9. Innocenti, F.; Mazzuoli, R.; et al.: Evolution of the Volcanism in the Area of Interaction Between the Arabian, Anatolian and Iranian Plates (Lake Van, Eastern Turkey). J. Volcanol. & Geothermal Res., vol. 1, 1976, pp. 103-112.

10. Dietz, Robert S.; and Holden, John C.: Reconstruction of Pangaea: Breakup and Dispersion of Continents, Permian to Present. J. Geophys. Res., vol. 75, no. 26, 1970, pp. 4939-4956.

11. Glen, William: Continental Drift and Plate Tectonics. Charles E. Merrill Publishing Co. (Columbus, Ohio), 1975.

Structural Pattern of the Northern Part of the Eastern Desert of Egypt

Mohamed A. Abdel-Rahman[a] *and Hassan A. El-Etr*[a]

ABSTRACT

Apollo-Soyuz color photographs of the northern part of the Eastern Desert of Egypt were excellent for regional structural mapping because of their color fidelity and large areal coverage. The oblique Apollo-Soyuz photographs were used for the identification of faults, whereas enlarged Landsat images were used for planimetric mapping. Aerial photographs were also examined to verify the mapped fault lines, and it was revealed that several of the lines detected on Apollo-Soyuz photographs were, in fact, zones of narrowly spaced, parallel faults.

The faults in this area, which are predominantly gravity (normal) faults, have produced a series of positive and negative fault blocks. Three positive and two negative blocks were identified. These blocks, arranged from south to north, are known as Southern Galala Plateau, Wâdi 'Araba, Northern Galala Plateau, Wâdi Akheidir, and Gebel Ataqa. The blocks are separated by long east-northeast-trending faults. One of these east-northeast faults extended from the Gulf of Suez to the Nile Valley and was discovered for the first time by analyzing Apollo-Soyuz photographs. The density of faults within the study area varied appreciably, and the Gebel Ataqa block appears to be the most tectonically active. In this highly faulted block, abundant basaltic exposures occurred along major fault lines and near fault intersections.

To a great extent, fault trends in the study area resembled the overall structural grain of the Egyptian Eastern Desert, in which both northwest and east-northeast trends are pervasive. However, a clockwise swing of approximately 12° was calculated between the northern part of the Eastern Desert (the present study area) and the remainder of the Eastern Desert.

The results of this investigation support the contention that vertical tectonics were responsible for the development of the fault pattern of the area, whereas the applicability of the tangential compression model cannot be substantiated.

INTRODUCTION

Excellent photographs of the northern part of the Eastern Desert of Egypt were obtained during the Apollo-Soyuz Test Project (ASTP) mission. The scarcity of vegetation, the absence of clouds, and the color sensitivity of the film were probably the main factors contributing to the good results. In addition, the high altitude of the photography accentuated the regional appearance of geological features, particularly geological structures such as faults.

The study area encompasses approximately 30 000 km^2 bounded by latitudes 28°35′ and 30°20′ north, by the Gulf of Suez on the east, and by the Nile River on the west. The study of the structural pattern of this particular area was initiated because of the availability of ASTP color photographs and was motivated by the tectonic complexity of the area and the economic potential of the area, especially petroleum resources.

Six ASTP photographs (table I) were used to trace the structural pattern of the area. In addition to variations in areal coverage and angle of tilt be-

[a]Ain Shams University, Cairo, Egypt.

tween the photographs, the ease with which structures could be detected varied appreciably from one photograph to another. This variation is attributed to Sun angle and to the orientation of tilt in relation to the orientation of structures.

A large number of faults were identified on ASTP photographs without magnification; others were detected by using a lens with 4× magnification. Because of the variations in obliquity and scale of the ASTP photographs, compilation of identical structures required the use of a planimetric base map prepared from Landsat band 7 images. Every identified fault line was transferred onto two enlarged Landsat images at a scale of 1:250 000. This stage was followed by another stage in which 1:100 000-scale aerial photomosaics and 1:40 000-scale aerial photographs were used to verify the structural lines detected on the ASTP photographs. The process of verification indicated that narrowly spaced, parallel faults appeared on the space photographs as one fault line and that two alined faults might appear on the space photograph as one fault line. Because the mapping process involved the use of both ASTP color photographs and Landsat band 7 images, it was possible to compare the clarity of structures on both mediums. The Landsat images were superior to the ASTP photographs in showing the fault lines that encompassed drainage anomalies along or across their strikes. Otherwise, the clarity of relief, the natural bedrock colors, and the absence of flaws (linear electronic runs) in the ASTP photographs made them a better tool for structural mapping.

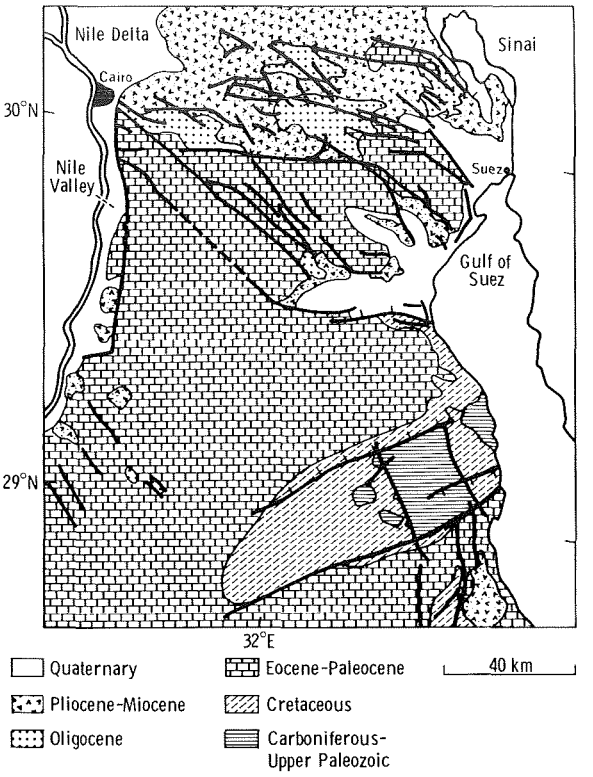


FIGURE 1.—Geological map of the study area (simplified from ref. 1).

Most of the rock outcrops in the study area belong to the Eocene-Paleocene limestones (fig. 1). Latitude 30° north roughly divides the area into two stratigraphically distinct regions. To the south of this line, the main rock outcrops are the Eocene-Paleocene limestones, massive Mesozoic

TABLE I.—ASTP Photographs of the Eastern Desert

Frame no.	*Center coordinates*	*Tilt*	*Lens, mm*	*Sun angle, deg*	*Exposure*
AST-2-138	29°20′ N, 32°20′ E	Near vertical	250	78	Excellent
AST-2-139	29°30′ N, 32°20′ E	Near vertical	250	78	Excellent
AST-9-555	30°10′ N, 31°10′ E	Low oblique	50	78	Excellent
AST-9-556	30°10′ N, 31°15′ E	Low oblique	50	78	Excellent
AST-9-557	30°10′ N, 31°25′ E	Low oblique	50	78	Fair
AST-31-2633	30°30′ N, 33°20′ E	Low oblique	35	78	Overexposed

and Paleozoic rocks occurring mainly in Wâdi 'Araba, and a few scattered outcrops of Oligocene and Miocene rocks. North of latitude 30° north, the surface exposures are distinctly younger, and Pliocene, Miocene, and Oligocene rocks form the major rock exposures.

STRUCTURAL UNITS

Faults identified on ASTP photographs are shown in figure 2. To keep the boundaries of the study area simple, faults in a small section not covered by the ASTP photographs were mapped from Landsat images.

Approximately 120 fault lines are identified in the area; most are clearly gravity faults. The density and length of faults show appreciable spatial and orientational variations. Thus, the area west of Suez (Gebel Ataqa block) is characterized by the maximum density of faults, whereas the southwestern corner of the study area contains the least number of faults. In addition, the east-northeast faults are remarkably longer than those of any other fault trend.

The spatial distribution of the mapped faults (fig. 2) reveals the following characteristics: (1) the east-northeast transverse faults are basically more pronounced in the vicinity of the Gulf of Suez and die out westward, (2) the northwest faults do not show spatial clustering as they exist throughout the area, and (3) the north-south faults mainly characterize the eastern escarpment of the Nile Valley. In addition, a fault line that occupies a long section of the Nile River channel and terminates south of Cairo has the same north-south trend. For the majority of these faults, the downthrown side is westward toward the Nile Valley.

The east-northeast faults divide the study area into five transverse blocks (figs. 2, 3(a), and 3(b)). Three of these blocks, designated a, b, and c, are structural highs representing the Southern Galala Plateau, the Northern Galala Plateau, and the Gebel Ataqa block, respectively. The two structural lows, designated d and e, represent Wâdi 'Araba and Wâdi Akheidir, respectively. Intrablock faulting is numerous and creates subblocks of various dimensions and alinements. This type of faulting has the highest density in the Gebel Ataqa block (c), in which basalt exposures are abundant.

The amount of displacement along the gravity faults bounding the blocks is maximum on the Gulf of Suez side. Most of the block-bounding faults terminate westward. Both positive blocks of the Northern Galala (b) and the Southern Galala (a) Plateaus are characterized by a series of step faults on their eastern sides. The faults have a northwesterly trend, and their downthrown sides are toward the Gulf of Suez. Fault spacing is relatively wider in the Southern Galala Plateau than in the Northern Galala Plateau. In contrast, the Gebel Ataqa block (c) has a unique structural pattern. Although this block is also affected by step faulting, its main feature is the abundance of uplifted and depressed subblocks.

The structural pattern of Wâdi 'Araba (block d), as presented in figure 2, differs significantly from the pattern shown in the Geological Map of Egypt (fig. 1; ref. 1). The main differences are as follows.

1. Wâdi 'Araba appears to be a graben in figure 2, although it is defined by the Geological Survey of Egypt as a horst. In fact, Wâdi 'Araba is a stratigraphic horst bounded by well-defined east-northeast transverse faults; however, it is also a longitudinal topographic depression (wadi) that appears as a grabenlike structure when mapped photogeologically. Wâdi 'Araba represents an unsolved problem regarding the relationships among its stratigraphy, structure, and topography. A likely explanation of the origin of Wâdi 'Araba could be related to the reversal of the direction of displacement on the same fault lines.

2. The Geological Map of Egypt shows several localized faults that divide Wâdi 'Araba into a series of positive and negative subblocks. These faults, which were delineated through a stratigraphic study and were not detected on the ASTP photographs (figs. 3 and 4), caused Carboniferous rocks to crop out. This particular exposure is of special interest in the geology of Egypt because it is one of only two surface exposures of rocks of that age (ref. 2).

The negative block of Wâdi Akheidir (block e) is a wedge-shaped graben in which smaller horsts and grabens are developed. The faults bounding

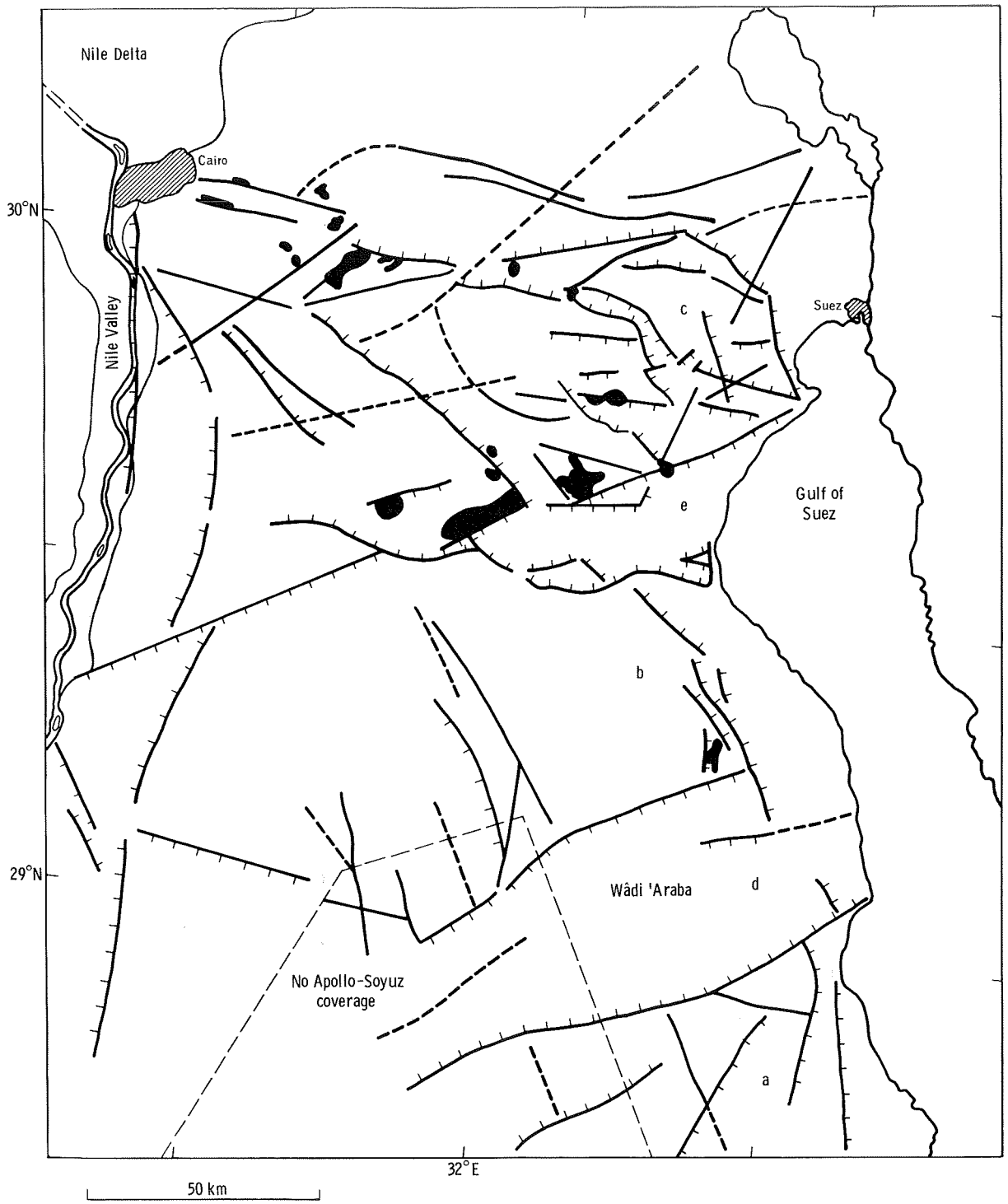


FIGURE 2.—Fault pattern detected on ASTP photographs. Black areas indicate basaltic exposures. The designators are as follows: a, Southern Galala Plateau; b, Northern Galala Plateau; c, Gebel Ataqa block; d, Wâdi 'Araba; and e, Wâdi Akheidir.

the Wâdi Akheidir graben converge westward. The fault zone, which extends between the Gulf of Suez and the Nile River and separates the Wâdi Akheidir graben (block e) from the Gebel Ataqa horst (block c), was identified and mapped for the first time as part of this study. This fault zone (figs. 2 and 4) localizes the largest basaltic exposures of the area along its central sector where it intersects with diagonal faults.

FAULT TRENDS

The frequency distributions of fault trends on the Geological Map of Egypt (fig. 1; ref. 1) and of fault trends mapped from the ASTP photographs (fig. 2) are presented in figures 5 and 6, respectively. Each distribution was statistically analyzed to determine the orientation of significant peaks using the Poisson distribution (ref. 3). Figure 5 indicates that faults presented on the Geological Map of Egypt show a significant northwesterly trend (N35°W to N68°W) and a marginally nonsignificant peak (at the 95-percent-probability level) of east-west trend. The histogram of fault trends detected on ASTP photographs (fig. 6) indicates, however, two statistically significant trends: first, a combined east-northeast and east-west trend ranging in orientation between N65°E and east-west; and second, a very narrow and less predominant northwesterly trend ranging between N30°W and N35°W.

A comparison of figure 1 with figure 2 and figure 5 with figure 6 indicates the following.

1. The number of faults detected on ASTP photographs and verified on aerial photographs is approximately double the number of faults shown on the Geological Map of Egypt.

2. Many of the ASTP-identified faults correspond, at least in part, with faults on the geological map.

3. The sense of displacement was determined for a substantial number of ASTP-identified faults. Their number far exceeds that illustrated in figure 1.

4. Despite the numerous faults identified in the Northern Galala Plateau (block b) and in Wâdi Akheidir (block e), the geological map does not show any faults in these blocks.

5. Fault trends depicted in figures 5 and 6 differ appreciably. All the faults on the geological map trend northwestward, with the exception of the east-northeast faults bounding Wâdi 'Araba and the east-west faults along the road between Cairo and Suez. The northwesterly fault trend clearly swings westward from the recognized Gulf of Suez trend (refs. 2 and 4). In contrast, the fault pattern detected on ASTP photographs shows that the east-northeast and east-west trends appear to be the most important structural trends in the area, followed by the Gulf of Suez trend.

DISCUSSION

The present investigation has added new geological information and substantiated some published arguments regarding the tectonic framework of the northern part of the Eastern Desert of Egypt. The findings reported here represent two aspects: (1) a photointerpretation aspect that relates to the identification of structural features; and (2) an analytical aspect, in which the tectonic framework of the region is examined in light of the mapped fault pattern.

Photointerpretation Aspects

1. The clarity and good resolution of ASTP photographs facilitated the detection and mapping of the regional fault pattern. Most of the faults were identified using a magnifying lens.

2. Comparison between figures 1, 3(a), and 3(b) indicated that the colors of the ASTP photographs were very useful for detecting lithological variations.

3. Because ASTP photographs were oblique, Landsat images were used as base maps for the planimetric plotting of structures. However, obliquity was useful because it accentuated the appearance of faults and, therefore, made their detection relatively easy.

4. The use of aerial photographs to verify the ASTP-detected fault lines indicated that space photographs cannot be used as a substitute for aerial photographs. The best results, however, are obtained when both large-scale and small-scale

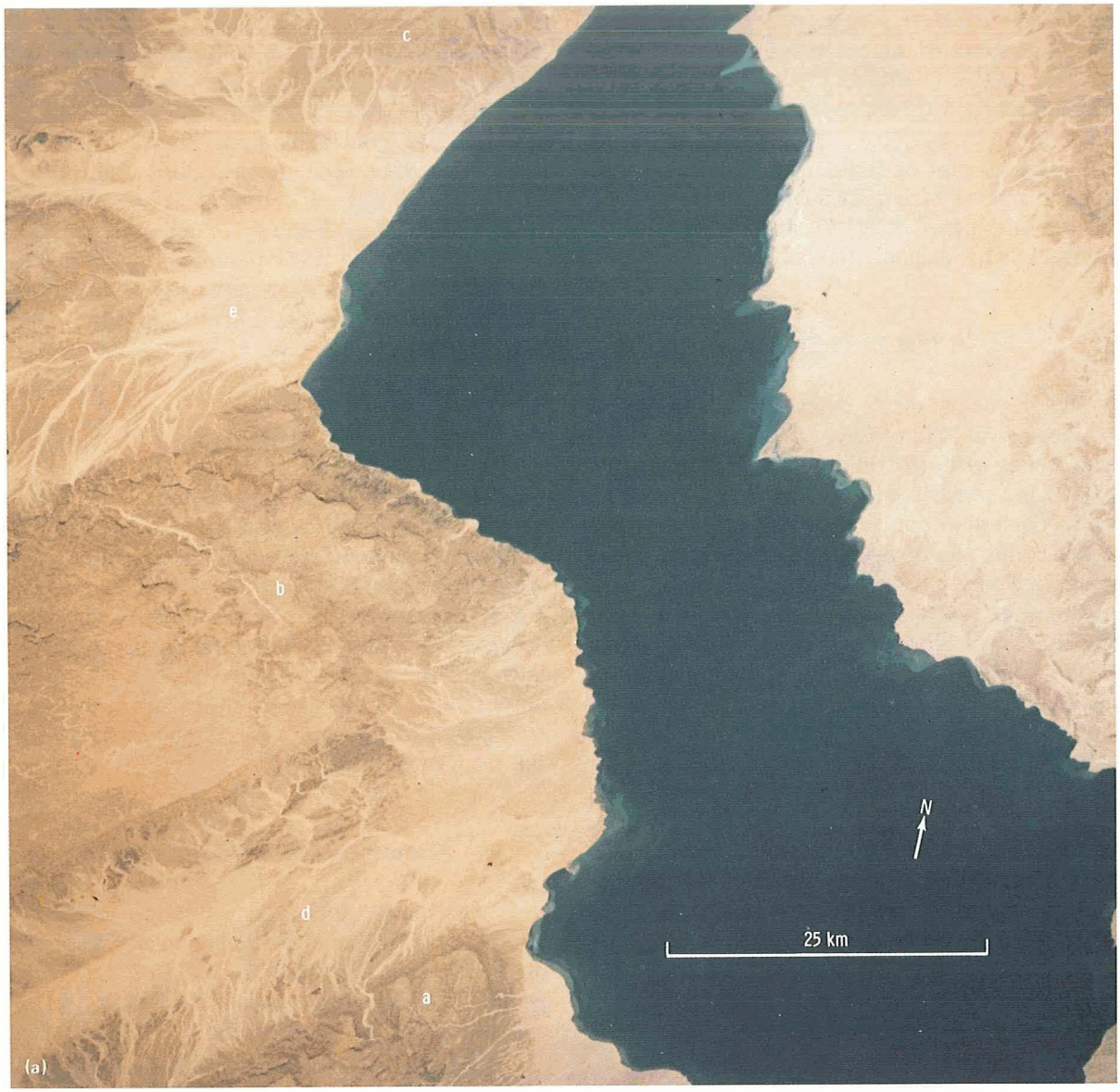


FIGURE 3.—Apollo-Soyuz photographs showing the east-northeast transverse blocks. The designators are defined in figure 2. (a) The southern part of the Gulf of Suez region (AST-2-138). (b) The northern part of the Gulf of Suez region (AST-2-139).

photographs are used. Many of the ASTP-detected faults are, in fact, fault zones encompassing narrowly spaced fault lines. The space photographs, because they are smaller scale than the aerial photographs, are not useful for identifying very small details, but they are very useful for mapping the continuity and linear extensions of fault lines.

5. The ASTP photographs revealed several fault lines that were not detected in any previous study. Probably the most significant of these is an east-northeast-trending fault zone that extends, transversely, from the Gulf of Suez to the Nile Valley (fig. 4). Along this fault zone, the largest basaltic occurrences were extruded.

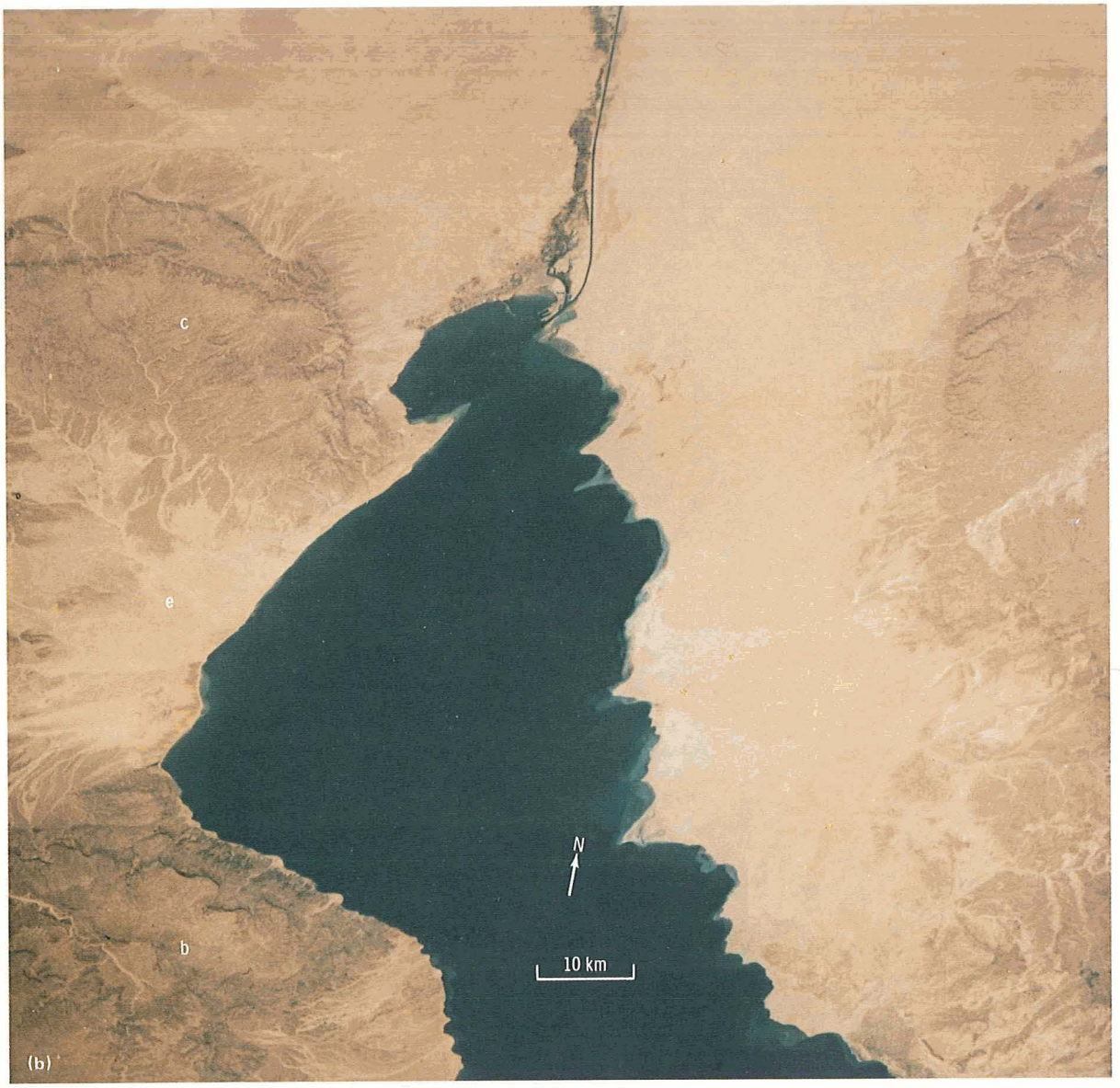


FIGURE 3.—Concluded.

Analytical Aspects

1. The study area is affected by three fault trends, one of which (the east-west trend) is most pronounced along the area of the Cairo-Suez road (almost alined with latitude 30° north), whereas the other two trends (the east-northeast and northwest trends) are spatially more dispersed.

2. The orientations of the east-northeast and northwest fault trends are shifted approximately 12° in a clockwise direction from the calculated positions of corresponding peaks of the structural grain of the Eastern Desert of Egypt (ref. 5). This swing in structural trends might indicate the pres-

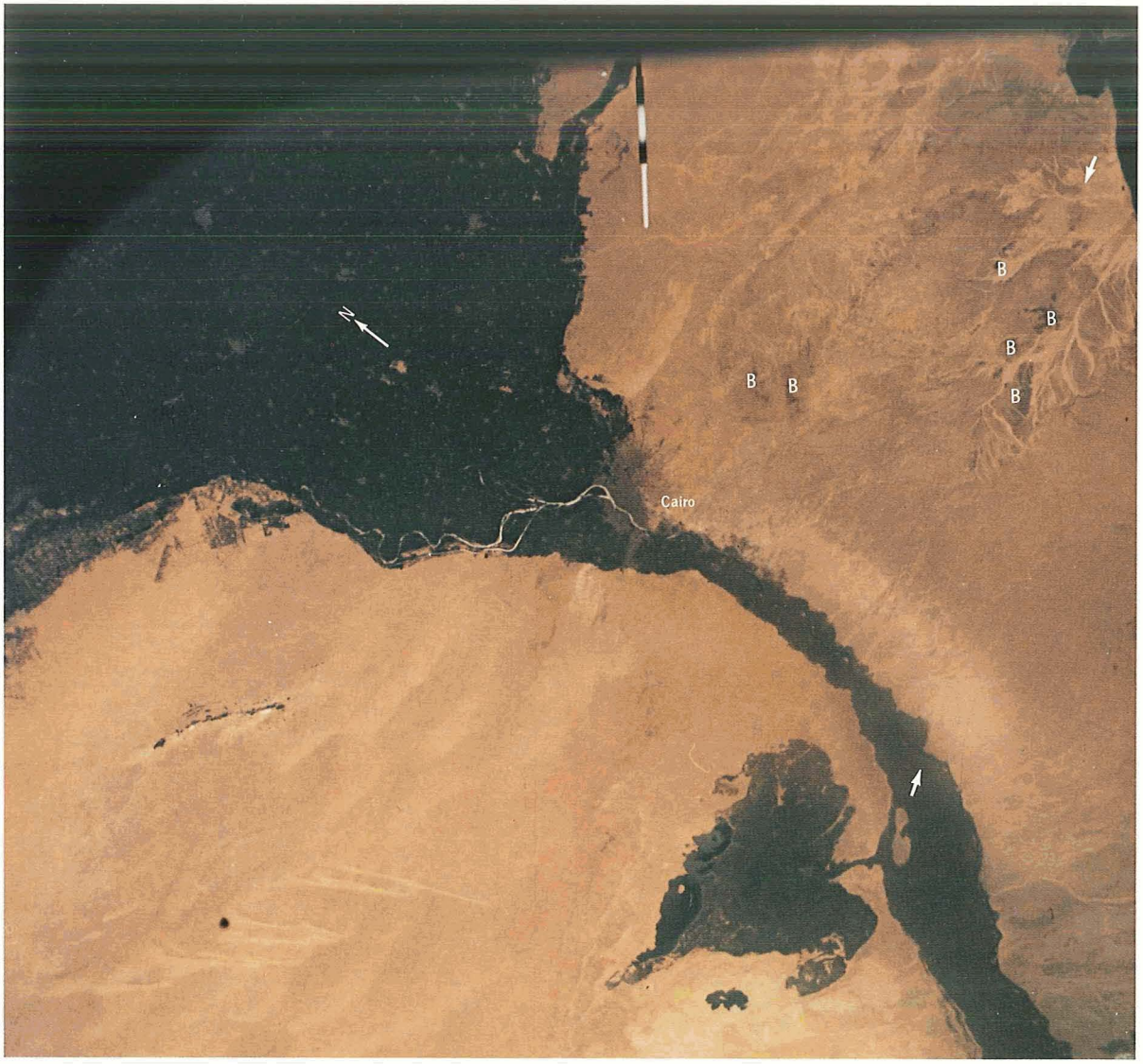


FIGURE 4.—Oblique photograph of the Nile Delta and the northern part of the Eastern Desert of Egypt (AST-9-555). Arrows indicate an east-northeast fault zone along which basalts are localized. The letter "B" symbolizes basalts.

ence of hinge zones along which large blocks were rotated horizontally during their vertical uplifting. A similar observation was noted in the block-faulted Esh Mellaha Range (ref. 6).

3. The east-northeast fault trend has long been neglected as one of the most important structural trends in the Eastern Desert of Egypt. In a recent photogeologic study (ref. 5), it was indicated that although this trend was significantly present in all the time-rock units of the Eastern Desert, it was more significantly affiliated with the basement rocks. Recent studies based on the interpretation of both geophysical and photogeological data have indicated the predominance of east-northeast deep-seated tectonic zones in the Eastern Desert of Egypt (refs. 7 and 8).

4. The studies of Tromp (ref. 9), Krs et al. (ref. 7), El-Etr et al. (ref. 10), Garson and Krs (ref. 8), and Abdel-Rahman and El-Etr (ref. 5) clearly indicated that the east-northeast trend is a basement trend. Figure 2 indicates, however, that the east-northeast faults do not hold any particular age relationship with the other faults. In some places, the east-northeast faults are displaced by other faults, whereas in other locations, they displace other faults. It appears, therefore, that these fault lines may have been propagated upward from the basement rocks episodically and are inconsistently reactivated at different times.

5. The structural pattern of Egypt in general (ref. 4) and that of the Gulf of Suez area were believed to be a result of horizontal compression. Riad (ref. 11) and Meshref et al. (ref. 12) used Bouguer gravity maps to study the structural pattern of the Gulf of Suez region. Despite the similarity of the techniques used, they arrived at different interpretations. Thus, Riad (ref. 11) predicted a number of northwest shear zones, whereas Meshref et al. (ref. 12) suggested three major tectonic shear zones trending north-northeast and cutting across the Gulf of Suez. Despite the obvious contradiction in the two interpretations, both investigators adopted the model of tangential compression of Moody and Hill (ref. 13). Tromp (ref. 9), Heybrock (ref. 14), El-Etr and Abdel-Rahman (refs. 6 and 10), El-Etr and Yousif (ref. 15), and Garson and Krs (ref. 8), among many others, have stressed the block-faulting phenomenon in the Eastern Desert of Egypt. The fault pattern of the study area (fig. 2) was dominated by block faulting, suggesting that vertical uplift was the main force that created the present fault pattern.

6. The model of tangential compression oriented at N10°W (ref. 4), although it may be applicable to some areas in Egypt, is not adequate for the study area. In addition to failing to account for the block-faulting phenomenon, fault orientations expected under this model were not observed either in the present study area or in the Eastern Desert of Egypt as a whole (ref. 5). For example, no predominant faults were observed with an orientation of approximately N15°E, which was an essential trend of wrench faults in this model. Moreover, faults having the N35°W orientation were all found to be gravity faults with no detectable strike-slip components. Nevertheless, the presence of a limited strike-slip component along any fault need not indicate compressional origin. Anderson (ref. 16) proved mathematically that horizontal movement might develop during the gravity-faulting mechanism. Thrusting is another important criterion for tangential compression and is not documented in the study area. Briefly, the opinion of Heybrock (ref. 14), that there is no single observation that might point to a compressional or lateral movement, is hereby supported.

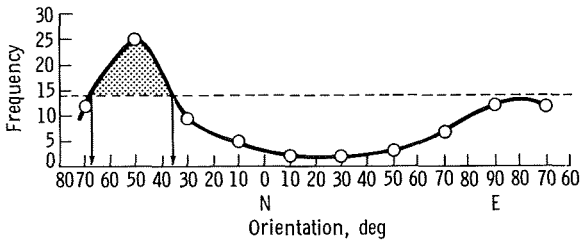


FIGURE 5.—The frequency distribution of fault trends included on the Geological Map of Egypt (ref. 1). The shaded area represents the significant peak at 95-percent probability; the dashed line is the minimum limit for a significant peak.

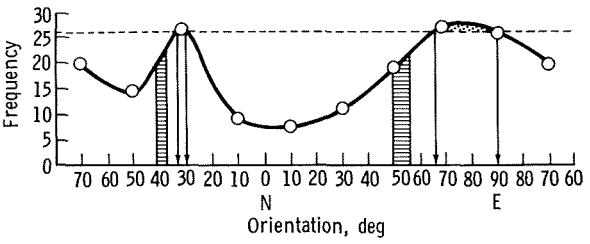


FIGURE 6.—The frequency distribution of fault trends detected on ASTP photographs. The dashed line is the minimum limit for a significant peak, and the shaded areas represent the significant peak at 95-percent probability. The peak limits of the Eastern Desert structural grain are indicated by the hatched areas.

REFERENCES

1. Geological Map of Egypt, Scale 1:2 000 000. Geological Survey of Egypt, 1971.

2. Said, Rushdi: The Geology of Egypt. Elsevier Pub. Co. (Amsterdam), 1962.

3. Hay, A. M.; and Abdel-Rahman, M. A.: Use of Chi-Square for the Identification of Peaks in Orientation Data: A Comment. Bull. Geol. Soc. America, vol. 85, Dec. 1974, pp. 1963-1965.

4. Youssef, Mourad I.: Structural Pattern of Egypt and Its Interpretation. Bull. American Assoc. Petr. Geol., vol. 52, no. 4, Apr. 1968, pp. 601-614.

5. Abdel-Rahman, M. A.; and El-Etr, H. A.: The Orientation Characteristics of the Structural Grain of the Eastern Desert of Egypt. Paper presented at Symposium on the Evolution and Mineralization of the Arabian-Nubian Shield, Inst. Applied Geol. (Jeddah, Saudi Arabia), 1978.

6. El-Etr, H. A.; and Abdel-Rahman, M. A.: Photogeology of the Esh Mellaha Range, Gulf of Suez District, Egypt. Proc. Egyptian Acad. Sci., vol. 26, 1973, pp. 37-44.

7. Krs, M.; Soliman, A. A. H.; and Amin, A. H.: Geophysical Phenomena Over Deep-Seated Tectonic Zones in Southern Part of Eastern Desert of Egypt. Ann. Geol. Surv. Egypt, vol. 3, 1973, pp. 125-138.

8. Garson, Magnus S.; and Krs, Miroslav: Geophysical and Geological Evidence of the Relationship of Red Sea Transverse Tectonics to Ancient Fractures. Bull. Geol. Soc. America, vol. 87, no. 2, Feb. 1976, pp. 169-181.

9. Tromp, S. W.: Blockfolding Phenomena in the Middle East. Geol. Mijnbouw, vol. 11, no. 9, 1949, pp. 273-278.

10. El-Etr, H. A.; Abdallah, A. M.; and Abdel-Rahman, M. A.: Dike Distribution Analysis in the Southern Part of the Gulf of Suez Region, Egypt. Afar Between Continental and Oceanic Rifting, Vol. 2, A. Pilger and A. Roesler, eds., Naegele u. Obermiller (Stuttgart), 1976, pp. 144-148.

11. Riad, S.: Shear Zones in North Egypt Interpreted From Gravity Data. Int. Atomic Energy Agency and UNESCO Pub., 1975.

12. Meshref, W. M.; Refai, E. M.; and Abdel-Baki, S. H.: Structural Pattern of the Gulf of Suez and Its Oil Potentialities. 5th Explor. Seminar (Cairo, Egypt), 1976.

13. Moody, John Drummond; and Hill, Melvin James: Wrench-Fault Tectonics. Bull. Geol. Soc. America, vol. 67, no. 9, Sept. 1956, pp. 1207-1246.

14. Heybrock, F.: The Red Sea Miocene Evaporite Basin. Salt Basins Around Africa. Inst. Petr. (London), 1965, pp. 17-40.

15. El-Etr, H. A.; and Yousif, M. S. M.: Airphoto Lineations of Wâdi 'Araba Area, Gulf of Suez Region, Egypt. Paper presented at Second International Conference on the New Basement Tectonics, University of Delaware, July 1976.

16. Anderson, E. M.: The Dynamics of Faulting and Dyke Formation, With Application to Britain. Second ed. Oliver and Boyd (Edinburgh), 1951.

Photolineaments in the ASTP Stereostrip of the Western Desert of Egypt

Hassan A. El-Etr,[a] Adel R. Moustafa,[a] and Farouk El-Baz[b†]

ABSTRACT

This paper deals with the study of photolineaments displayed on the Apollo-Soyuz stereostrip covering part of the Western Desert of Egypt. Photolineaments abound in the study area and are easily distinguished on the color photographs. Many of these photolineaments, which are soil-tonal or topographic alinements, are probably the surface expressions of faults or fractures. Others are most likely related to erosional escarpments at formational boundaries. Photolineaments in the Western Desert occurred most frequently in two regions: the Baharîya/Sitra region and the Qattara Depression/Wâdi el Natrûn region. The area between these two regions is probably blanketed by unconsolidated rock and/or active sand sheets. From this study, it is believed that there are two preferred regional orientations of the photolineaments: east-northeast to east-west and northwest to west-northwest.

A comparison of the detectability of photolineaments on Apollo-Soyuz photographs and Landsat images was made. Virtually all of the photolineaments detected on Landsat images (black-and-white as well as false-color composites) were also detected on Apollo-Soyuz photographs of the same scale and approximately the same resolution. In this study, the drawbacks of Apollo-Soyuz photographs include (1) the low base/height ratio, which limited the effective stereovision; (2) the high Sun-elevation angle, which limited the shadows required to easily identify linear features; and (3) the overexposure of the central parts of the frames, particularly over the Great Sand Sea. Recommendations are made to remedy this on future Earth-orbital photographic missions.

INTRODUCTION

As a primary objective of the Earth Observations and Photography Experiment on the Apollo-Soyuz Test Project (ASTP), a strip of 15 vertical photographs was taken over the Western Desert of Egypt. This strip was acquired from an altitude of approximately 220 km with a bracket-mounted 70-mm Hasselblad data camera using a 60-mm lens. The strip is oriented in a northeasterly direction, and it extends for approximately 1000 km from east of the Egyptian-Libyan border, near latitude 26°30′ N, to the Nile Delta near latitude 31°30′ N. The width of this strip is approximately 200 km.

The ASTP photographic strip is bounded on the northwestern side by the Sitra Depression and the northeastern part of the Qattara Depression; it reaches the Mediterranean Sea east of El 'Alamein. The southeastern side of the strip is bounded by the northwestern edge of the Farâfra and Baharîya oases; it extends across the Nile Delta south of Tanta and crosses the Mediterranean coast just west of Port Said. This report pertains to data obtained from 9 of the 15 photographs covering the stretch extending from northwestern Farâfra to west of the Nile Delta. The

[a]Ain Shams University, Cairo, Egypt.

[b]National Air and Space Museum, Smithsonian Institution.

[†]Principal Investigator.

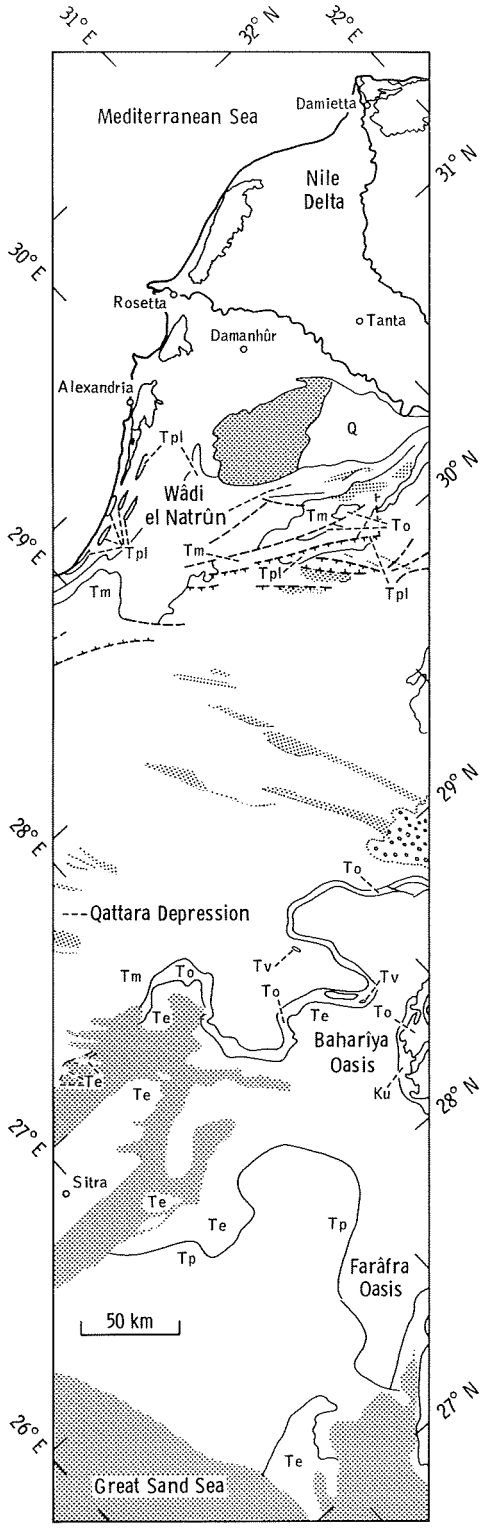


FIGURE 1.—Geological map of the Western Desert region covered by ASTP photographs and studied in this report (from ref. 1).

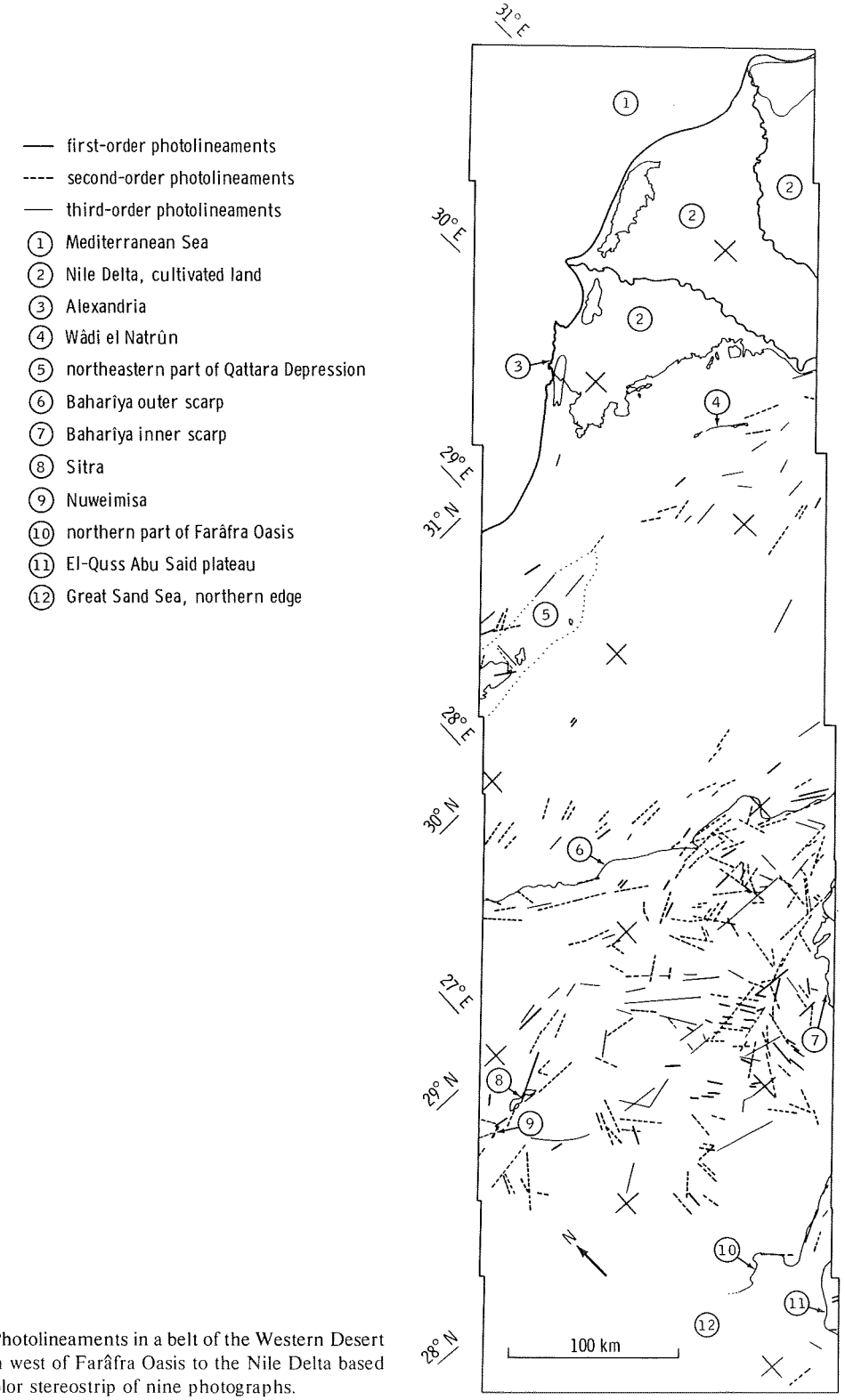


FIGURE 2.—Photolineaments in a belt of the Western Desert extending from west of Farâfra Oasis to the Nile Delta based on an ASTP color stereostrip of nine photographs.

photographs across the Great Sand Sea were not studied because they were overexposed.

The geology of this area is not well known (fig. 1; ref. 1). In general terms, the Western Desert is characterized by thick beds of sedimentary rocks that dip gently to the north and that decrease in age from south to north. Detailed geological and structural maps exist only for the northern part of the area (ref. 2). The southern half of the area is comparatively unexplored. For this reason, the study of the ASTP photographs supplemented by Landsat images could add much to our knowledge of the structural setting of the area.

PHOTOLINEAMENTS

Photolineament (ref. 3) is a term that has been used to describe natural linear features of any length that appear on photographs. This definition includes topographic, physiographic (straight stream segments), lithologic, structural, vegetational, and soil-tonal alinements, or any combinations thereof. More specifically, according to El-Etr (ref. 3), these lineaments may be subdivided and classified by length into megalineaments (>100 km), lineaments (100 to 10 km), macrolineaments (10 to 2 km), brachylineaments (2 km or less), and microlineaments (below the resolution limit of the unaided eye). The last three divisions may be referred to by the general term 'linear' (<10 km).

The advent of the space age has provided a new dimension to the study of photolineaments. Photographs obtained from Earth orbit provide a powerful tool for the direct identification of regional and super-regional structures. These structures become visible in a single space photograph as compared with aerial views that require mosaics of hundreds of aerial photographs. In addition, the orbital photographs enable correlations to be made between geographically separated structures.

The technique of quantitative analysis of photolineaments has previously been discussed and reviewed (ref. 4). Briefly, each photograph is viewed in eight different directions, four parallel to its sides and four diagonal to these. The light source remains fixed and is always high behind the analyst's left shoulder. The detected photolineaments are marked on the photographs using a grease pencil. Reliability orders are then assigned; the first order denotes the most pronounced photolineaments and the third order the most subtle.

The photolineament pattern is usually checked after several days to identify any linear features that may have been missed during earlier stages. During this checking stage, the reliability ordering is reevaluated.

Because the ASTP strip was taken with 60 percent overlap, successive photographs could be viewed stereoscopically. The stereoscopic viewing provided an additional capability to confirm both major and minor photolineaments.

The next phase of the study includes the compilation of the photolineaments on a map and their analysis. Each linear feature is annotated; its length in kilometers and its orientation (azimuth) in classes of 10° of arc are determined. Grid units are laid over the maps to count the number of photolineaments per unit area. Frequency curves are constructed for the number in percent (N%) and length in percent (L%) of photolineaments in each grid unit area. Gay's suggestions (ref. 5) for drawing frequency curves are followed. Also, the Poisson frequency distribution statistical method (ref. 6) is applied to test the significance of the peaks obtained at the 95-percent level and to show the areal variations in photolineament density.

Use of the previously described procedure led to the stereoscopic detection of 307 linear features (fig. 2), of which 135 rank as "lineaments" (10 km or longer) and 172 rank as "linears" (shorter than 10 km). Many of the photolineaments do not correspond to faults or structures shown on the 1971 geologic map of Egypt (compare figs. 1 and 2) (ref. 1).

As previously stated, the detected photolineaments were classified into three orders of reliability. Two hundred and fifty photolineaments belong to the first and second orders; 108 of these are lineaments and 142 are linears. The remaining photolineaments belong to the third order and include 27 lineaments and 30 linears. The orientation and length of these photolineaments per 10° classes of azimuth are included in table I.

The photolineament pattern shown in figure 2 includes a conspicuous concentration in the Baharîya/Sitra region and a less dense concentration in the Qattara Depression/Wâdi el Natrûn region. The areas in between are generally low in photolineament concentration. This low density is attributed to partial or total masking of bedrock exposures by unconsolidated sediments (mainly sand dunes, sand sheets, and "serir," or pebble-strewn desert plains). Another reason for the association of photolineaments and depressions such as Baharîya, Sitra, Qattara, and Wâdi el Natrûn may be that the depressions are structurally controlled.

Study of figure 2 shows that the photolineament patterns have prominent east-northeasterly and northwesterly trends. For a quantitative analysis of the frequencies of photolineament trends, six frequency curves were plotted (fig. 3). The Group I plots represent frequency curves of the numbers and lengths in percent of the selective field of first- and second-order photolineaments (I-1), the selective field of the third order (I-2), and the total field (first, second, and third order) photolineaments (I-3).

The peaks detected in plot I-1, in decreasing statistical significance, are ENE, NW, WNW, and NNE. Those detected in plot I-2 are more differentiated, with less background photolineament scattering, and are as follows: E-W, NW to WNW, and NNE. The average length of linear features of the third order is relatively more than that of linear features of the first and second orders. This difference seems plausible because the longer a photolineament is, the more subtle and complex its appearance on photographs; hence, its

TABLE I.—Photolineaments Detected in Area Covered by ASTP Stereostrip of Western Desert

(a) Northwesterly

Parameter (a)	*Photolineaments with orientation, deg, of—*								
	81-[b]90	*71-80*	*61-70*	*51-60*	*41-50*	*31-40*	*21-30*	*11-20*	*[c]0-10*
					First and second orders				
N.....	18	8	20	13	23	20	9	11	11
N, percent .	7.2	3.2	8.0	5.2	9.2	8.0	3.6	4.4	4.4
L, km	225.6	70.0	244.4	141.1	218.9	195.6	88.9	102.2	107.8
L, percent..	8.0	2.5	8.6	5.0	7.7	6.9	3.1	3.6	3.8
					Third order				
N.....	9	2	4	5	5	5	3	1	1
N, percent .	15.8	3.5	7.0	8.8	8.8	8.9	5.3	1.8	1.8
L, km	153.3	60.0	43.3	94.4	40.0	73.3	27.8	7.8	12.2
L, percent..	20.4	8.0	5.8	12.6	5.3	9.7	3.7	1.0	1.6
					Total				
N.....	27	10	24	18	28	25	12	12	12
N, percent .	8.8	3.3	7.9	5.9	9.1	8.1	3.9	3.9	3.9
L, km	378.9	130.0	287.7	235.5	258.9	268.9	116.7	110.0	120.0
L, percent..	10.6	3.6	8.0	6.6	7.2	7.5	3.3	3.1	3.3

[a]N = number of photolineaments; L = total length of photolineaments.
[b]90° = west.
[c]0° = north.

TABLE I.—Concluded

(b) Northeasterly

Parameter (a)	*Photolineaments with orientation, deg, of —*								
	[c]*0-10*	*11-20*	*21-30*	*31-40*	*41-50*	*51-60*	*61-70*	*71-80*	*81-*[d]*90*
					First and second orders				
N.....	13	8	10	8	4	10	11	28	25
N, percent .	5.2	3.2	4.0	3.2	1.6	4.0	4.4	11.2	10.0
L, km	175.6	88.9	113.3	101.1	38.9	115.6	160.0	348.9	298.9
L, percent .	6.2	3.1	4.0	3.6	1.4	4.1	5.6	12.3	10.5
					Third order				
N.....	2	1	-	-	2	2	2	5	8
N, percent .	3.5	1.8	-	-	3.5	3.5	3.5	8.9	14.0
L, km	14.4	4.4	-	-	26.7	40.0	15.6	57.8	81.1
L, percent .	1.9	0.6	-	-	3.5	5.3	2.1	7.7	10.8
					Total				
N.....	15	9	10	8	6	12	13	33	33
N, percent .	4.9	2.9	3.3	2.6	2.0	3.9	4.2	10.7	10.7
L, km	190.0	93.3	113.3	101.1	65.6	155.6	175.6	406.7	380.0
L, percent .	5.3	2.6	3.2	2.8	1.9	4.3	4.9	11.3	10.6

[a]N = number of photolineaments; L = total length of photolineaments.
[c]0° = north.
[d]90° = east.

(c) Grand total

Ordering	*Number*	*Length, km*
First and second	250	2835.7
Third	57	752.1
Total	307	3587.8

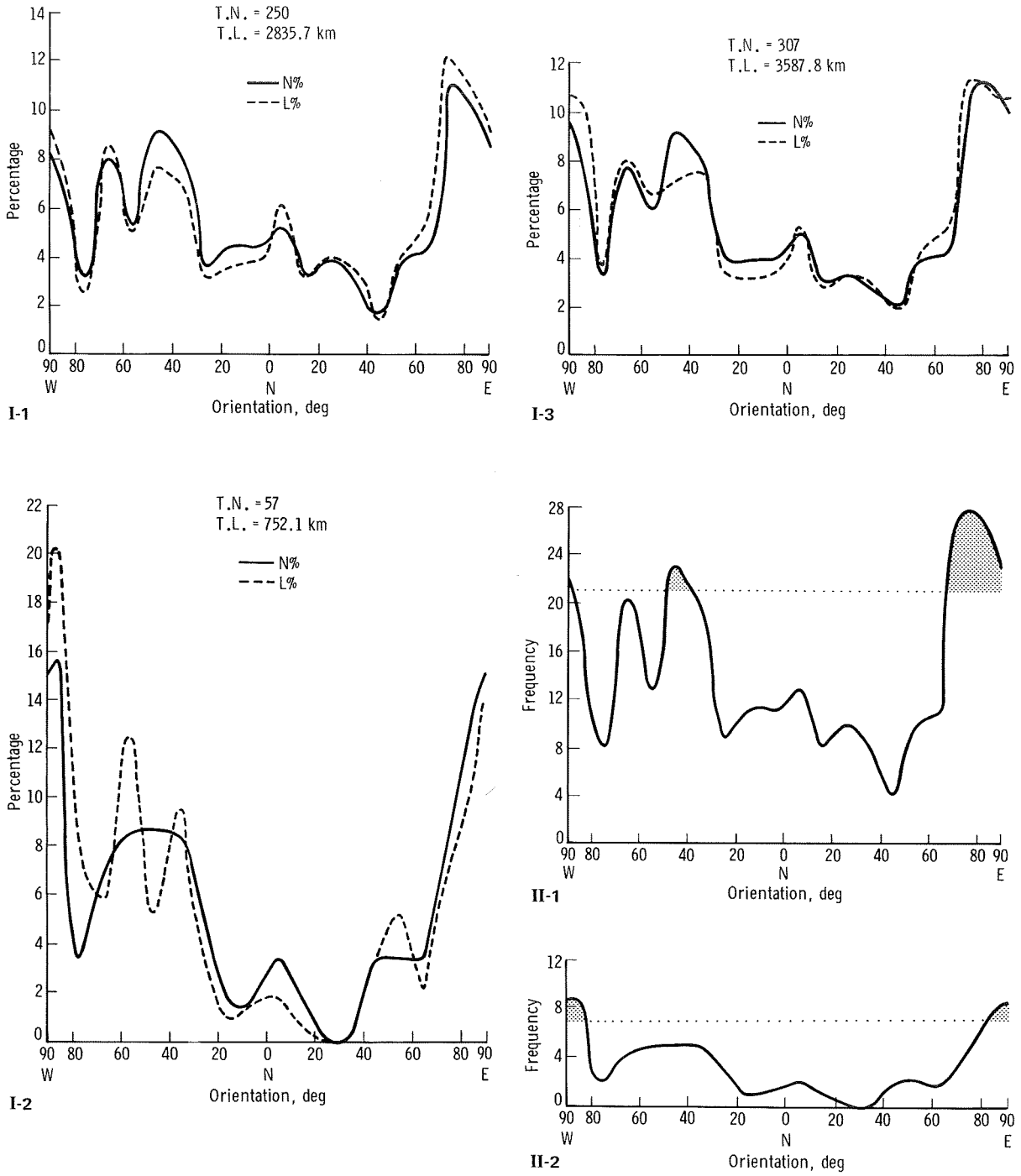


FIGURE 3.—Frequency curves of ASTP photolineaments in the area covered by the stereostrip. Diagrams in Group I are based on number in percent (N%) and length in percent (L%). Total numbers (T.N.) and total lengths (T.L.) are also given. Diagrams in Group II are based on the total number of photolineaments. Diagrams I-1 and II-1 include photolineaments of the first and second orders; diagrams I-2 and II-2 include photolineaments of the third order; and diagrams I-3 and II-3 are summations for photolineaments of the first, second, and third orders. Dotted horizontal lines in type II diagrams delimit the significant peaks calculated using the Poisson frequency distribution at the 95-percent significance level.

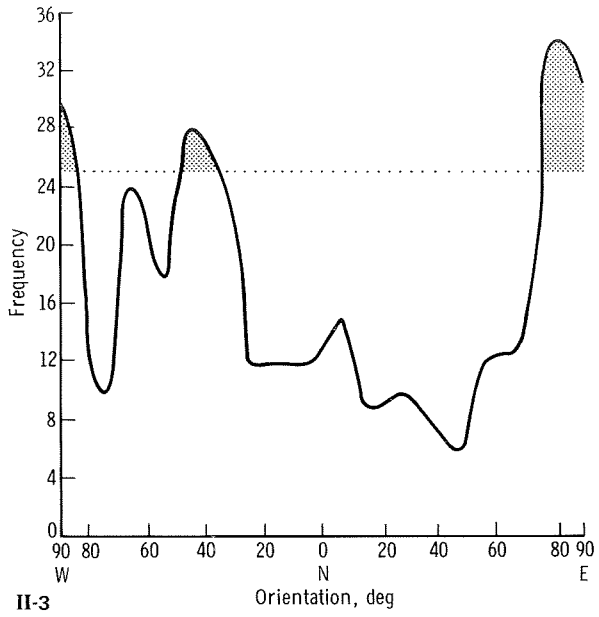


FIGURE 3.—Concluded.

low reliability ranking. It should be mentioned, however, that plot I-2 is based on a relatively smaller number of photolineaments (57) than that on which plot I-1 is based (250). Plot I-3 is a summation of plots I-1 and I-2. The peaks illustrated, in decreasing order, are ENE to E-W, NW to WNW, and NNE.

The azimuth-frequency distribution of the 307 linear features of the region was statistically tested using the Poisson frequency distribution (ref. 6). The Group II plots in figure 3 represent frequency curves based on actual numbers of photolineaments for first- and second-order photolineaments (II-1), third-order photolineaments (II-2), and their total field (II-3). The dotted horizontal line delimits the peaks that are significant at the 95-percent significance level. Diagram II-1 shows two such peaks, oriented ENE and NW. Diagram II-2, however, shows only one peak, oriented E-W (although split in two sectors). The summation diagram, II-3, shows the prominence of the regional trends ENE to E-W and NW to WNW; thus confirming the results obtained from the Group I frequency curves. It becomes evident, also, that the ENE trend is of local significance only.

DISCUSSION

Photolineaments were easily detected on the ASTP color photographs. Many of these photolineaments are probably the surface expressions of faults or fractures. Others are most likely related to erosional escarpments at formational boundaries. The photolineaments are mainly clustered in the Baharîya/Sitra region and the Qattara Depression/Wâdi el Natrûn region. The presence of photolineaments in these two regions seems to indicate that structural control played a part in the formation of the main depressions in the region. The absence of photolineaments between these two areas is attributed to partial or total masking of bedrock by unconsolidated material.

There is a specific preferred regional orientation of the photolineaments of the Western Desert of Egypt. These orientations are ENE to E-W and NW to WNW.

In the present study, virtually all photolineaments detected on Landsat images were also detected on the ASTP photographs. A few photolineaments detected on Landsat images were refuted, however, after a check of the ASTP photographs showed that they were superfluous lines related to imperceptible cloud alinements and the like. On the other hand, a few linear features detected on Landsat images are subtle or indistinct on their ASTP counterparts. This is attributed mainly to the broader electromagnetic spectrum involved in Landsat imagery (particularly the near-infrared band 7).

Being in natural colors, ASTP photographs are more easily interpreted than black-and-white photographs or single-band Landsat images. Alterations, weathering manifestations, and bedrock colors are the same as observed on the ground. This is a rather distinct advantage over multispectral false-color images, such as those produced by Landsat, which need a "mental translation" of each electronic color into the corresponding natural color.

The photographic texture is clear by comparison with the electronically assembled images of the Landsat type. Flaws in the linear electronic runs in Landsat images commonly occur and may be misidentified as natural linear features. For the

ASTP photographic strip, although stereovision was achieved using ordinary mirror stereoscopes, depth perception was rather limited because of the inherent low relief of the region; modification of the base/height ratio of stereophotographs may be deemed necessary to enhance the vertical exaggeration. The effective resolution of the stereostrip photographs needs to be increased; this need was particularly felt during field and aerial photographic checking of the dune forms in the region.

The ASTP photographs taken over the central Western Desert suffered from a high Sun-elevation angle and from the overexposure of the centers of some photographs. This characteristic is generally referred to as vignetting. More effective antivignetting filters should be used in future flights. Vignetting is a gradual reduction in density of parts of a photographic image caused by the stopping of some rays entering the lens (ref. 7). Thus, a lens mounting may interfere with the extremely oblique rays. An antivignetting filter is one that gradually decreases in density from the center toward the edges; it is used with aerial wide-angle lenses to produce a photograph of uniform density by reducing the overexposure of the photograph center.

ACKNOWLEDGMENTS

Part of the research was done in partial fulfillment of the requirements for the degree of Master of Science for the second author (ref. 8). The report was prepared under both the Ain Shams University/Smithsonian Institution joint research project and NASA contract NAS9-13831.

REFERENCES

1. Geological Map of Egypt, Scale 1:2 000 000. Geological Survey of Egypt, 1971.

2. Said, Rushdi: The Geology of Egypt. Elsevier Pub. Co. (Amsterdam), 1962.

3. El-Etr, H. A.: Proposed Terminology of Natural Linear Features. Proceedings of the First International Conference on the New Basement Tectonics, Utah Geol. Assoc., no. 5, 1976, pp. 480-489.

4. El-Etr, H. A.; and Abdel-Rahman, M. A.: Air Photo Lineations of the Southern Part of the Gulf of Suez Region, Egypt. Proceedings of the First International Conference on the New Basement Tectonics, Utah Geol. Assoc., no. 5, 1976, pp. 309-326.

5. Gay, S. Parker, Jr.: Standardization of Azimuthal Presentations. Proceedings of the First International Conference on the New Basement Tectonics, Utah Geol. Assoc., no. 5, 1976, pp. 499-500.

6. Hay, A. M.; and Abdel-Rahman, M. A.: Use of Chi-Square for the Identification of Peaks in Orientation Data: A Comment. Bull. Geol. Soc. America, vol. 85, Dec. 1974, pp. 1963-1965.

7. Smith, John T., Jr., ed.: Manual of Color Aerial Photography. American Soc. Photogram. (Arlington, Va.), 1968.

8. Moustafa, A. R.: Photogeology of the Central Western Desert, Egypt (With a Special Emphasis on Siwa and Bahariya Oases). M. S. Thesis, Ain Shams University (Cairo, Egypt), 1977.

Utilization of ASTP Photographs in the Study of Small Structures in Abu Rawâsh and Wâdi el Natrûn, Egypt

Hassan A. El-Etr [a] *and Farouk El-Baz* [b†]

ABSTRACT

This paper deals with a study of geologic structures using 8× enlargements of Apollo-Soyuz Test Project color photographs. The two study areas are Abu Rawâsh and Wâdi el Natrûn; both are in the northern part of the Western Desert of Egypt. Because the structures are small, aerial photographs were studied and field checks were made to verify the findings from Apollo-Soyuz photographs.

The Apollo-Soyuz photographs of Abu Rawâsh clearly show structural uplifts that brought white chalk deposits to the surface. The photographs also depict the distribution of dark volcanic rocks in the region and clearly delineate complex structures including several domes and plunging anticlines. Differences and similarities between these structures are clearly displayed in the Apollo-Soyuz photographs.

Wâdi el Natrûn is an elongate depression that is probably tectonic in origin. The Apollo-Soyuz photographs display its structures as well as the string of salt lakes within it. The natural color of these photographs enables distinction between these lakes on the basis of color. Natural color also enables recognition of the barren nature of the northern and southern extremities of the depression. The photographs also reveal that there is a potential for increasing the area of cultivated land on the eastern slope of the depression.

INTRODUCTION

Three sections in this volume describe the utility of Apollo-Soyuz Test Project (ASTP) photographs in regional studies of the Western Desert of Egypt. These reports address (1) photolineaments and major structures, (2) color zones and their geologic meaning, and (3) sand dunes and their distribution. A common aspect of these reports is the study of ASTP data and the extrapolation of observations to other parts of the Western Desert

In this section, the authors have investigated the utility of ASTP photographs of Egypt in detailed studies of small structures. The two areas selected for this investigation are just west of the Nile Delta in the northeastern part of the Western Desert (fig. 1). A common feature of the two areas is the difference in color between the structures of interest and the surrounding terrain. These two localities include the complex structures of the Abu Rawâsh area and the numerous lakes in a depression called Wâdi el Natrûn.

The ASTP crewmembers obtained photographs of these two areas with a handheld 70-mm camera. In addition, Wâdi el Natrûn was covered by photographs obtained with the bracket-mounted 70-mm mapping camera. The handheld-

[a] Ain Shams University, Cairo, Egypt.

[b] National Air and Space Museum, Smithsonian Institution.

[†] Principal Investigator.

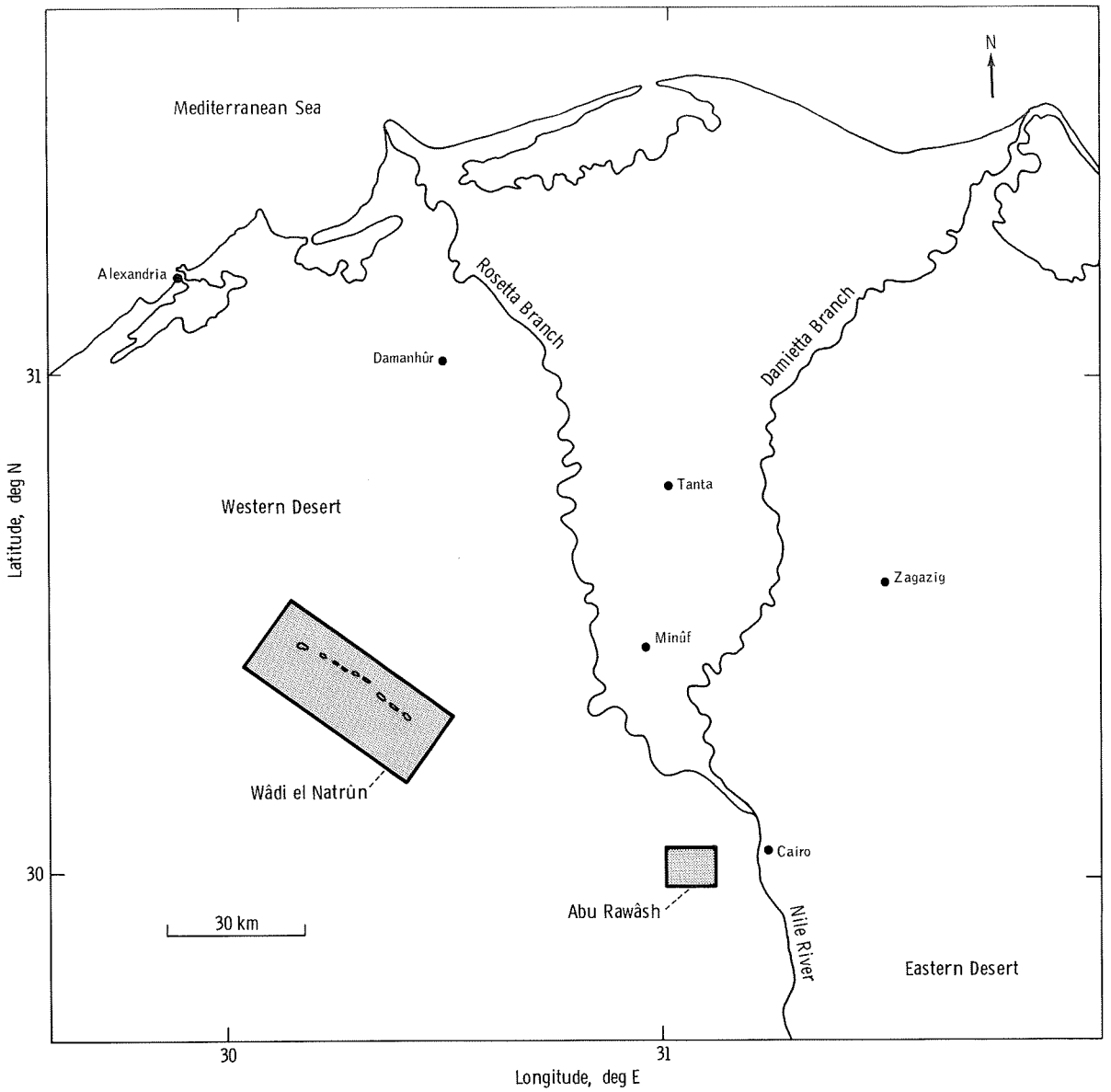


FIGURE 1.—Sketch map of the Nile Delta region showing the location of the two areas studied in this report, Abu Rawâsh and Wâdi el Natrûn.

camera photographs are low oblique, but this did not affect their use in photogeologic interpretation.

The structures portrayed on these photographs are small and cannot be easily studied on 1:1 000 000-scale (20 by 25 cm) photographic prints. For this reason, 8× enlargements were especially made from the original 70-mm film by the Photographic Technology Laboratory at the NASA Lyndon B. Johnson Space Center. These enlargements faithfully reproduced the color variations on the original film, which were important to the study.

It was important to make certain that the findings from the ASTP photographs were real and were not affected by inherent limitations in the

photographic prints. For this reason, available aerial photographs were studied and compared to the Earth-orbital photographs. Also, a field trip was made to the two areas to collect ground-truth information.

ABU RAWÂSH AREA

The ASTP photographs show an elliptical, light-toned area whose long axis is oriented in an east-northeast/west-southwest direction (e.g., fig. 2). This area is known as the Abu Rawâsh uplift; it is characterized by exposures of Upper Cretaceous chalky white limestone that are easily demarked from the surrounding buff-tinted plain. This plain is strewn with sand and gravel of Oligocene to lower Miocene age and underlain by Eocene limestones that are exposed farther south in the Pyramids plateau.

The occurrence of Cretaceous rocks at Abu Rawâsh is rather significant in Egyptian geology because it represents an inlier of older rocks. This is the only location at this latitude where Cretaceous rocks are exposed on the surface of the Western Desert. The occurrence of Cretaceous outcrops owes its existence to folding and faulting that took place during the Upper Cretaceous (ref. 1).

Several authors have reported on the geology of this district, particularly Faris (ref. 2) and Jux (ref. 3). Figure 3 (ref. 1) is a detailed geologic map of the district. Comparison between this map and the ASTP photograph (fig. 2(a)) shows how the size and shape (geometry) of the Abu Rawâsh structure are clearly and accurately expressed on the space photograph.

In addition to the main structure, the ASTP photograph (fig. 2(a)) shows several east-northeasterly elongated dark patches that are spatially related to the Abu Rawâsh structure. Field study indicated that these patches are Tertiary (Oligocene) basalt extrusions (refs. 4 and 5) and/or related hydrothermally indurated ferruginous quartzitic grits. Volcanic activity was probably guided by regional fractures of an east-northeasterly orientation. Such a relationship is not evident from the geologic map (fig. 3), because of its limited coverage. However, the relationship of volcanism to regional fractures was particularly emphasized through the use of the ASTP photographs.

In detail, the field-based geologic map (fig. 3) shows eight geologic units; namely: Cenomanian sandstones, marls, and shales (unit 1), Turonian limestones (unit 2), Santonian Plicatula limestones (unit 3), Campanian to Maestrichtian chalk (unit 4), Eocene limestones and sandy limestones (unit 5), Oligocene basalt (unit 6), Oligocene to lower Miocene fluviatile sands and gravels (unit 7), and wadi alluvium (unit 8). On the ASTP photographs, the units that are easily discerned are unit 1, a moderately dark-toned unit; units 2 through 5, which are very light toned; unit 6, which is grayish; and units 7 and 8, which are more yellow.

Unit 1 is exposed in the eastern and southern parts of the study area, and units 2 through 5 form the main part of the uplift. These latter units are not easily differentiated on the space photograph. On the ground, they are distinguished by paleontologic rather than lithologic criteria. Thus, the number of mappable rock units on the space photograph may be reduced to four (figs. 2(a) and 2(b)). These four units are easily recognizable and their contacts are readily discernible.

From these observations, it is recommended that geologic mapping be based on distinct rock units as much as possible so as to benefit from the capabilities of space (and complementary aerial) photography. Subdivision of these rock units may be performed at a later time for relatively small districts of particular interest on the basis of paleontologic (or generally stratigraphic) grounds; i.e., on the basis of time-rock units.

Figures 4(a) and 4(b) show the main structures of the Abu Rawâsh uplift, as portrayed on aerial photographs. The aerial photomosaic shows several structures, particularly El Hassana dome, El Ghigiga dome, the Sudr el Khamis plunging syncline, and the Wâdi el Talun plunging anticline. Faults modify these fold structures to varying degrees. The ASTP photographs (figs. 2(a) and 2(b)) also show virtually all of these structures. They are discerned through the bedding traces of the exposures of the limestone and sandstone units (fig. 3, units 2 through 5 and unit 1, respectively). The photographic texture of

the bedding traces is enhanced by the presence of yellowish-peach-tinted wadi alluvium (unit 8). The drainage network of the district is evidently highly dependent on the lithologies and structures present.

Figure 2(b) shows the structures identified on the space photographs of the district. The difference in size between El Hassana dome and El Ghigiga dome is quite evident on the ASTP photograph (fig. 2(a)), although it is indistinct on the geologic map (fig. 3). In addition, the similarity in style of these structures is clear on the space photograph. The plunging Sudr el Khamis syncline and Wâdi el Talun anticline are also similar in structural style, but are markedly distinct from the aforementioned domes. Disharmony of the overall structural pattern of the region is thus revealed in the space photographs. This was not perceived from the previously published geologic map (fig. 3).

To substantiate the findings from the ASTP data, the more detailed aerial photographs (scale 1:20 000) were studied stereoscopically. From this study (figs. 4(a) and 4(b)), it became evident that (1) the fold structures of Abu Rawâsh uplift are disharmonious; (2) the prominent faults dislocating these folds are the longitudinal and transverse type; (3) some bedding plane displacement is locally manifested; e.g., in El Ghigiga structure; (4) diapiric mobilization occurred in the relatively incompetent horizons; e.g., in the Sudr el Khamis and El Ghigiga structures; and (5) the actuating mechanism is probably complicated, and the maximum stresses are believed to be of vertical internal origin. The incompetent character of the oldest exposed (Cenomanian) sandstones and marls of the district is probably of prime significance in determining the disharmonic structural style referred to earlier. It must be stated that geophysical investigations (ref. 6) support the contention that the Abu Rawâsh uplift is deep-rooted and expresses a basement high, the actuating faults of which may possibly have subcrustal extensions.

From this part of the study, it is evident that structural interpretations, even of a complicated region, may be performed satisfactorily with space photographs as augmented by the use of selected aerial photographs and by field checking.

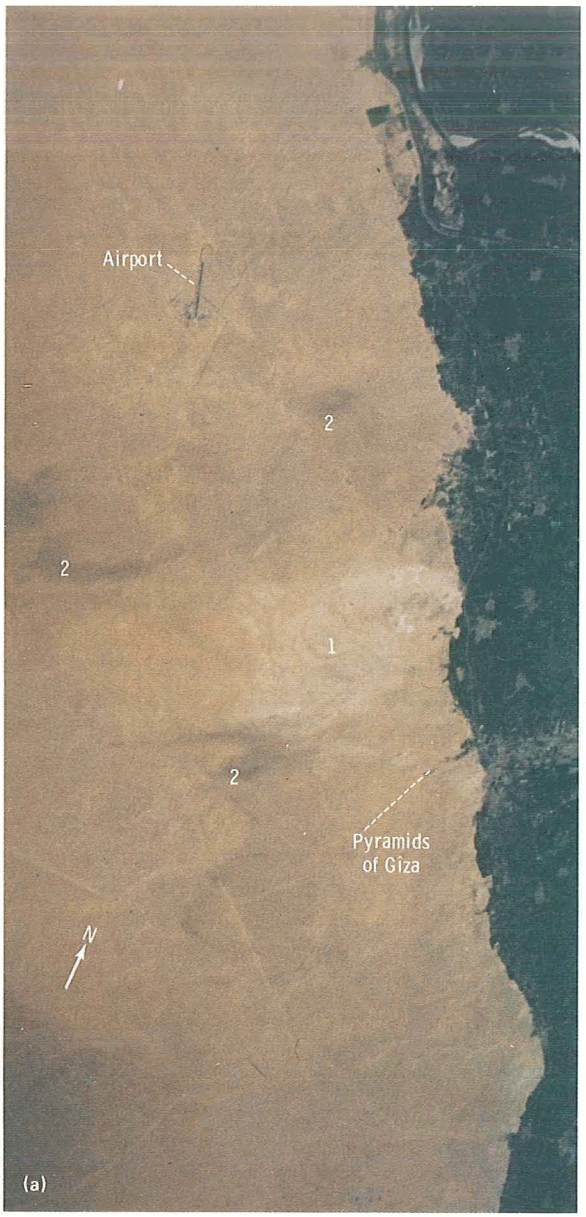


FIGURE 2.—Orbital photograph detail of Abu Rawâsh. (a) Part of ASTP photograph AST-2-136 showing the Abu Rawâsh area west of the Nile Delta. The dark green-gray color on the right edge represents vegetation and the shades of dark earthy gold are those of desert formations. Note the whitish color in the area of folded and faulted structures (1) and the dark-gray color of eroded basalt exposures (2). (b) Drawing of an enlargement of part of the area illustrated in figure 2(a). Within the light-toned area, dashed lines indicate structural elements, arrows give direction of plunge of folds, and solid lines indicate faults. Shaded areas are covered by debris from volcanic (basaltic) intrusions in the otherwise sedimentary surface.

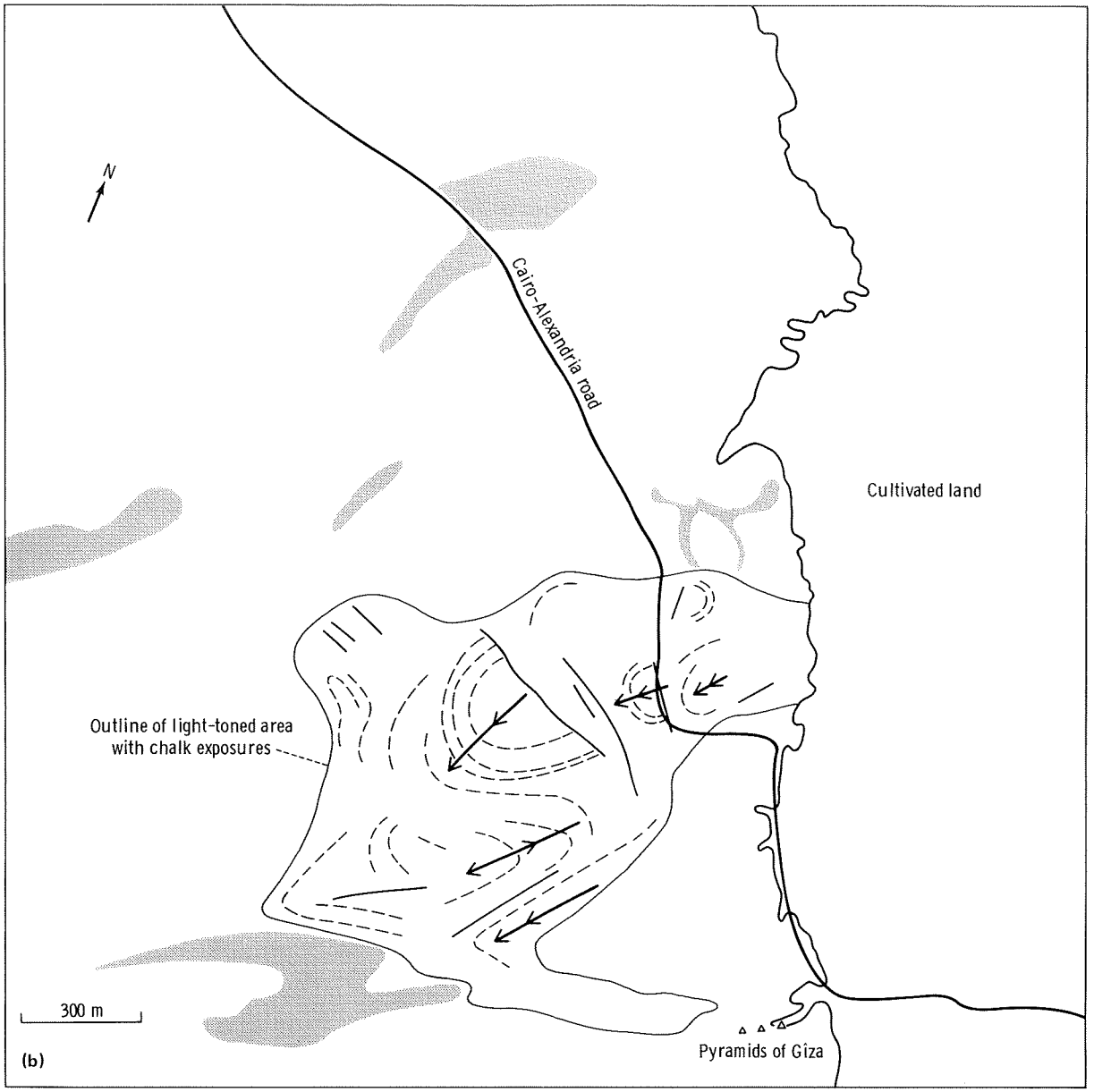


FIGURE 2.—Concluded.

WÂDI EL NATRÛN

The Apollo astronauts photographed a northwesterly elongated, linear depression approximately 40 km west of the Nile Delta. The depression is known as Wâdi el Natrûn; it extends for some 60 km and has an average width of 10 km (ref. 7). The lowest point of this wadi (valley) is approximately 23 m below sea level, and the central lowland is generally 50 m below the level of the surrounding plain.

On the ASTP photographs (e.g., fig. 5), the northern and southern extremities of this physiographic feature are lighter yellow than the

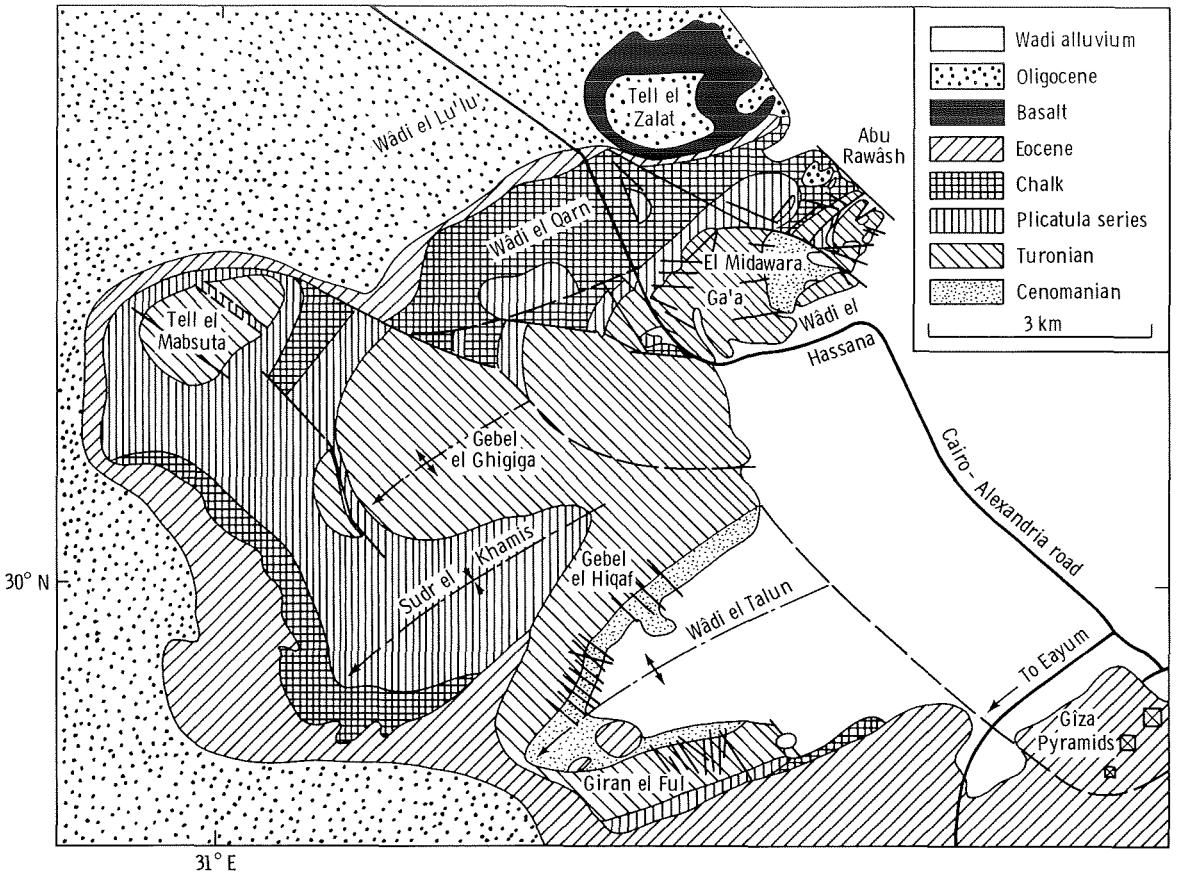


FIGURE 3.—Geologic map of the Abu Rawâsh area (ref. 1, p. 198).

surrounding desert plain. The smooth texture of each end is due to the fact that they are covered by drifting sands. Because of this covering, these extremities are essentially barren. The central part of the depression, however, shows a series of colors; the dark, mottled strips and patches denote vegetation, and the white, brownish-red, and dark-blue patches are soda lakes and associated saline deposits. These salt deposits were known to the ancient Egyptians and were commonly referred to as "natron," or soda salt. In pharaonic times, the natron was in common use and was used in cooking, bleaching linen, and manufacturing glass and glaze. In addition, natron was extensively used in medical works, in purification ceremonies, and in mummification (ref. 8).

The Wâdi el Natrûn region is covered by Quaternary lakebeds and old alluvial deposits of sand and gravel. These deposits were laid down when the sea encroached north of the depression and the Nile River flowed through the area. The lake deposits and alluvium are underlain by sedimentary rocks of Pleistocene and Pliocene age that consist of sand and gravel interbedded with thin layers of clay (ref. 1). These, in turn, are underlain by sandstones, shales, and limestones of Miocene age; basalts underlain by sandstones and shales of Oligocene age; and Eocene and Cretaceous limestones.

The main morphotectonic subdivisions of this region have previously been well studied and mapped (ref. 7). On the eastern side of the depression, a series of gravel terraces is present. These are recognized as old Nile terraces and are cultivated. The ASTP photograph (fig. 5) shows three such cultivated terraces extending for several

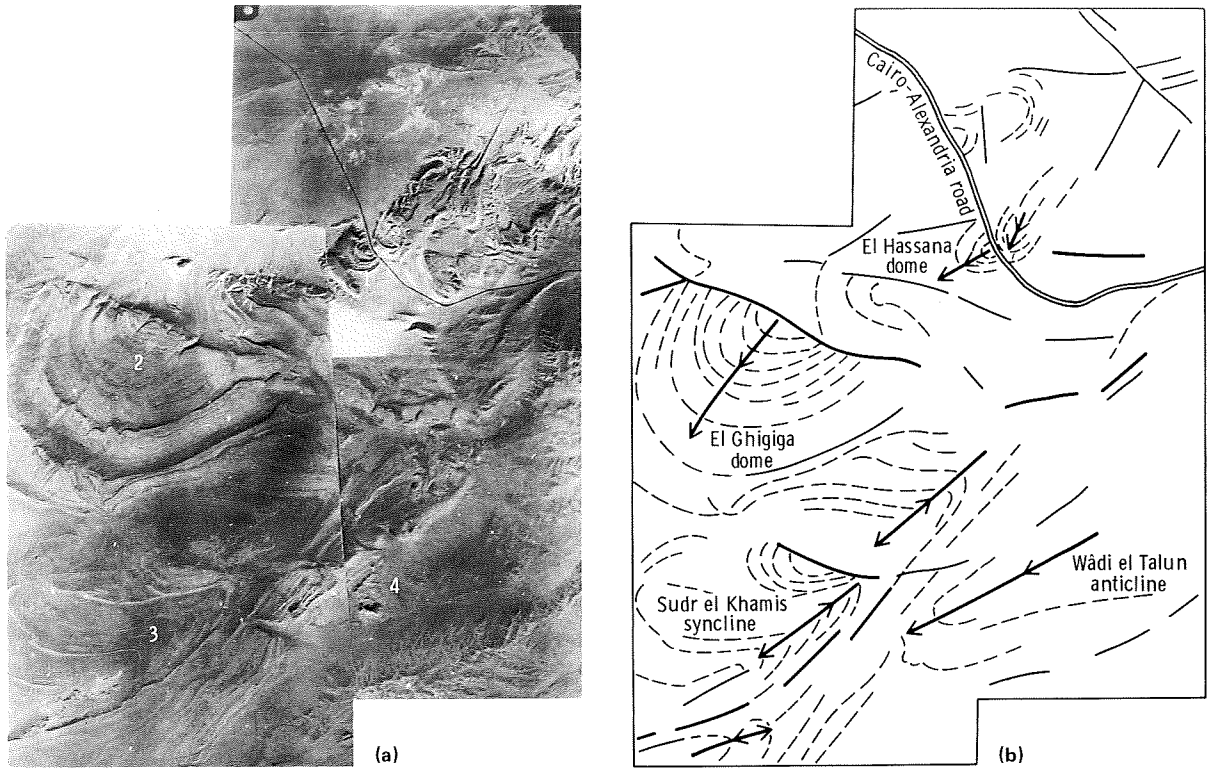


FIGURE 4.—Aerial photograph detail of Abu Rawâsh. (a) Aerial photographs showing the complex structures in the Abu Rawâsh area: (1) El Hassana dome, (2) El Ghigiga dome, (3) Sudr el Khamis plunging syncline, and (4) Wâdi el Talun plunging anticline. (b) Drawing of the structures displayed in the aerial photographs shown in figure 4(a). Solid lines indicate faults; dashed lines, fold boundaries; and arrows, fold plunge directions.

kilometers near the north-central part of the depression. Irrigation on these terraces depends on underground water that is pumped from deep aquifers. This water has moderate to good irrigation qualities. On the central lowland of the wadi, cultivation is mainly concentrated on the eastern side and extends for approximately 30 km. Here, irrigation depends on the shallow subsurface water present 1 or 2 m below the surface. This water is generally saline.

Because of their color sensitivity, the ASTP photographs are well suited to study the numerous lakes within the depression (fig. 5). These soda lakes are mainly confined to the western side of the central lowland of the depression. Some 20 lakes are present, the largest of which is approximately 2.5 km^2 in area. The main lakes are illustrated in figure 6. These lakes are generally asymmetric. Their longer axes are on the eastern side; their other sides commonly taper to the west. Smaller lakes are merely arms of the larger ones that have been cut off by drifting sands. Such small lakes dry up partly or wholly in the summer (ref. 9).

The water levels of the Wâdi el Natrûn lakes generally show seasonal fluctuations. A number of freshwater springs flow energetically all year round from the bottom of some of these lakes, particularly near their northeasterly sides (ref. 9). The source of water in the lakes is accordingly believed to be due partly to seepage along faults of ground water from deep aquifers, and partly to infiltration from the Nile through porous and permeable shallow sandy sediments. On the western side of the depression, the presence of some "fossil" surface-drainage lines denotes earlier sur-

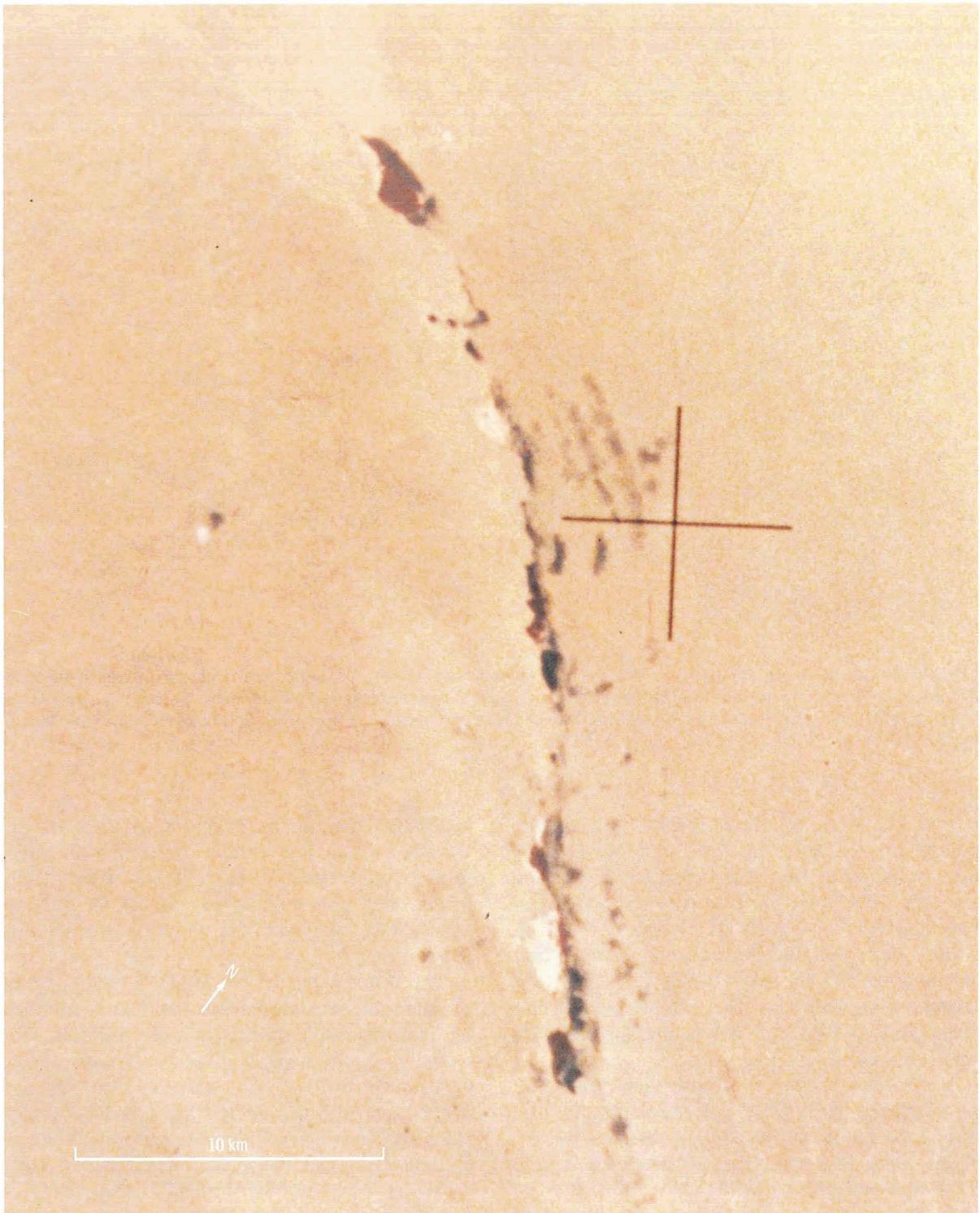


FIGURE 5.—Enlargement of ASTP photograph AST-16-1256 showing Wâdi el Natrûn and its numerous median lakes. The color of the lakes is a function of chemistry, salinity, and bacterial content.

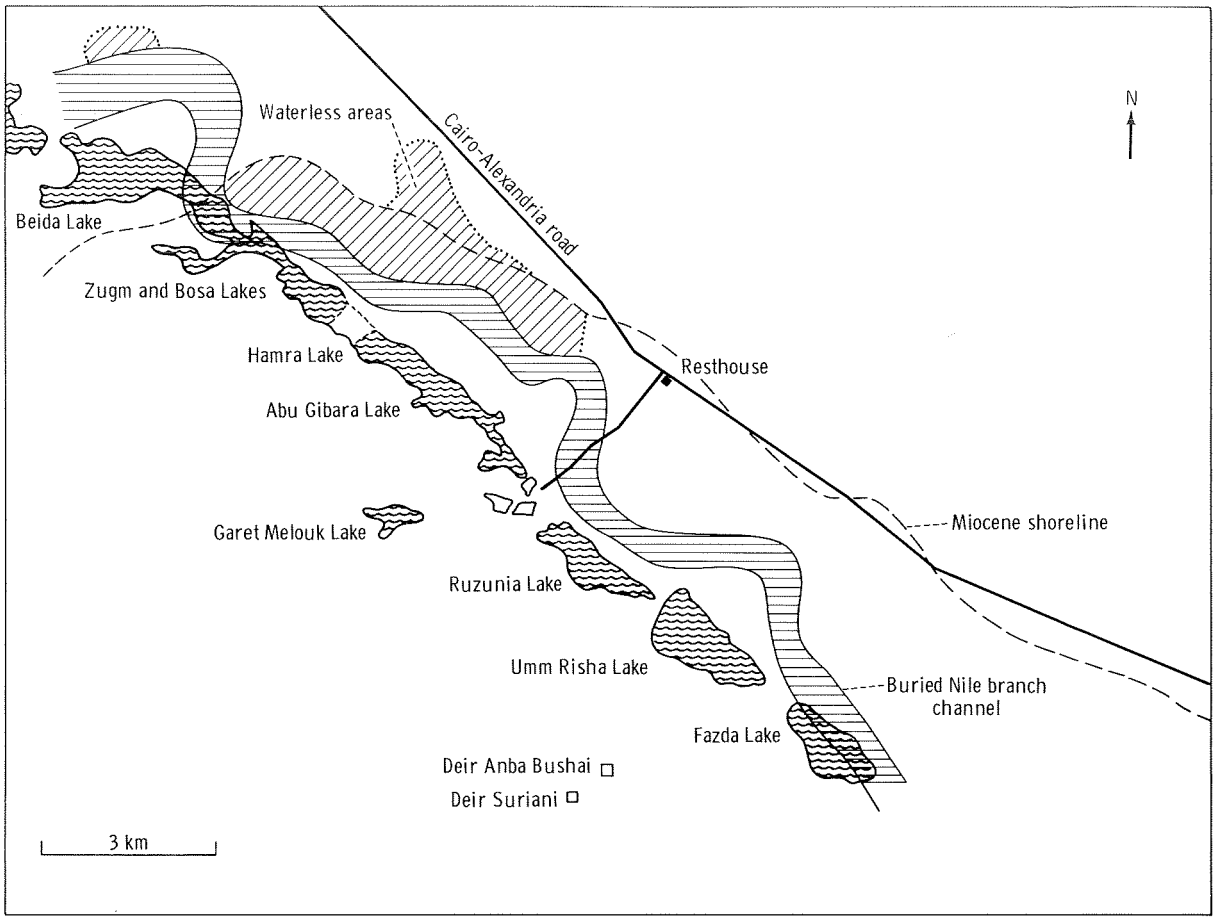


FIGURE 6.—Sketch map of part of Wâdi el Natrûn showing the old course of a Nile River branch, the Miocene shoreline, and the shape of lakes within the depression (courtesy of A. Shata).

face runoff contributions to the lakes in pluvial periods (fig. 7). These drainage tributaries are also clear on the ASTP photograph (fig. 5). Present-day water runoff is small and averages approximately 33 mm/year.

Along the bottom and rims of the lakes, saline deposits are common. They are presently in the process of formation. The main salts are chlorides, carbonates, and sulfates of sodium. The most abundant minerals (ref. 10) are halite (NaCl), thenardite (Na_2SO_4), trona ($NaHCO_3 \cdot Na_2CO_3 \cdot 2H_2O$), burkeite ($2NA_2SO_4 \cdot Na_2CO_3$), hanksite ($Na_{22}KCl(CO_3)_2(SO_4)_9$), sylvite (KCl), and aphthitalite ($(K, Na)_3Na(SO_4)_2$). The quantities of such salts and the relative abundance of the different constituent minerals are variable in the different lakes.

The color of water in the lakes is mostly pinkish- to violet-red (fig. 8), although some lakes are lighter in color. The water itself is generally alkaline (pH 9 and more), and dissolved salts may reach a density of 200 g/liter. The reddish color has been attributed by some authors to the existence of a type of small crustacean named *Artemia salina*, whose color changes from green during life to red after death (ref. 9). Other authors argue, however, that such crustaceans are not commonly present throughout the year but the deep water color is. For this reason, they attribute the color to the presence of cocci-type bacteria instead (ref. 9). Such bacteria are known to exhibit a red coloration and grow abundantly in the lakes. These bacteria seem to be sensitive to the water salinity and consequently their increase causes deeper water

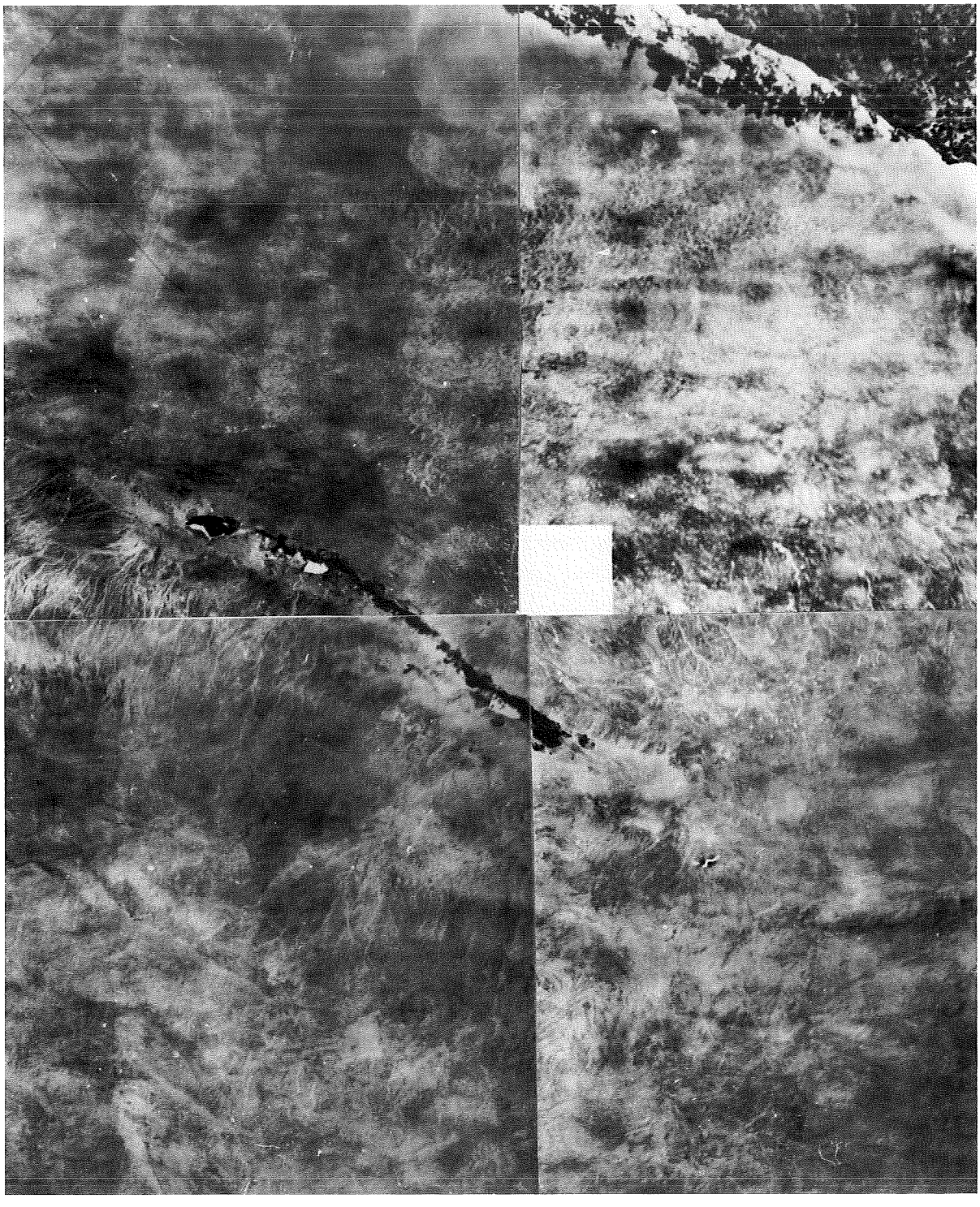


FIGURE 7.—Mosaic of four aerial photographs of the Wâdi el Natrûn region. North is at the top. The dark region in the upper right corner is part of the vegetated Nile Delta. The narrow black region represents the lakes and vegetation within the Natrûn depression. To the west, a complex drainage network of dry valleys is clearly visible.

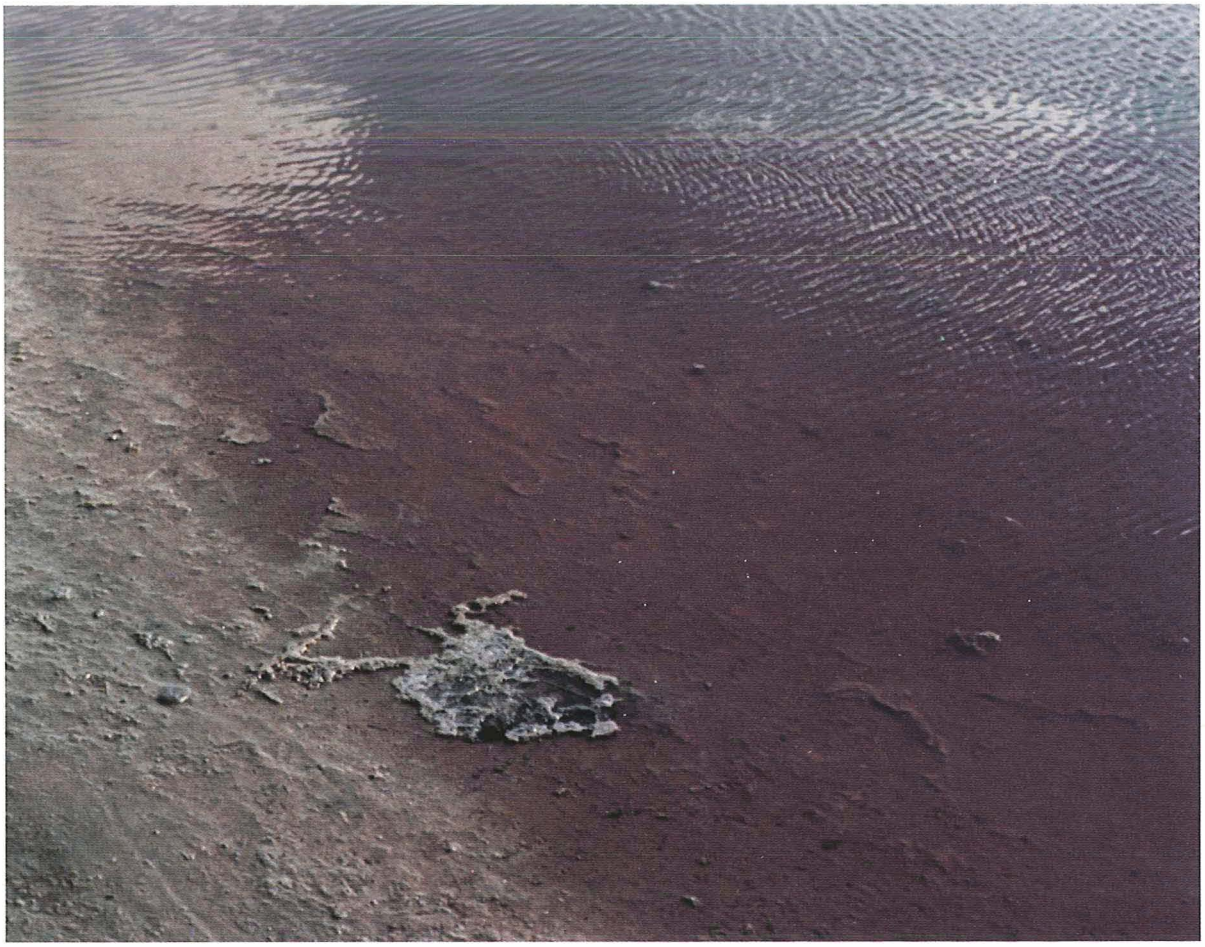


FIGURE 8.—A crust of pinkish-white salt in the process of formation at the edge of Ruzunia Lake in the middle of Wâdi el Natrûn. The purple-brown color of the water is similar to that described and photographed by the Skylab 4 and the ASTP astronauts in the northern half of the Great Salt Lake in Utah (ref. 11). The salt layers in this region display a pink color (photograph by Farouk El-Baz).

coloration. On space and aerial photographs, this color may be taken as an indicator of the degree of salinity. This situation is somewhat similar to that of Utah's Great Salt Lake whose northern, more saline half is redder than its southern half because of the presence of algae (ref. 11).

In addition, the deposition of salts in the Wâdi el Natrûn lakes is believed to be biochemically controlled. If this proves to be true, the abundance of bacteria will reflect the more favorable sites of deposition in the different lakes or parts of lakes. This, in turn, may enhance salt mining exploration and exploitation.

Based on the authors' photogeologic studies and field observations, the Wâdi el Natrûn is believed to have been formed by tectonic (fault) initiation, developed by water (fluvial) erosion in pluvial (Pleistocene) periods, and modified by later (sub-Recent) arid deflation. The tectonic phase is evidenced by the linear contrast in fresh to brackish water input on the eastern and western sides of the depression. This water is more abundant on the eastern side and nurtures all vegetation in the region. The concentration of saline lakes on the western side and the presence of freshwater springs in the bottom of some of them, particularly on their northeasterly sides, add evidence. The tectonic phase is further substantiated by regional geophysical studies (ref. 12), which emphasize the deep nature of the depression. The

actuating faults (or fault) are believed to be deep seated (basement) extensions. Block faulting is probably a common structural style in the basement. As stated earlier, the role of fluvial erosion is evidenced by the "fossil" drainage network on the western side of the depression (fig. 7), and the role of wind deflation is attested by present-day wind manifestations.

The Wâdi el Natrûn region is economically important for two reasons: because of its potential for farming and for soda salts mining. This study of ASTP photographs shows that there is a strong possibility of increasing the cultivated lands on the eastern slopes of the depression. In addition, the study outlines the total dimensions of the depression and points to the barren nature of its northern and southern extremities due to desertification. The contribution of this study to the improvement of the salt mining operations in the region will be the subject of a future study that will involve the size-shape distribution of the lakes, their detailed spatial distribution and control, and a correlation between their chemistry, bacterial content (water coloration), and salt deposition.

ACKNOWLEDGMENTS

The authors wish to thank the Military Survey of Egypt for providing aerial photographs for this study. This paper was prepared in part under a joint research project between Ain Shams University and the Smithsonian Institution, and in part under NASA contract NAS9-13831.

REFERENCES

1. Said, Rushdi: The Geology of Egypt. Elsevier Pub. Co. (Amsterdam), 1962.

2. Faris, Mohammad Ibrahim: Contribution to the Stratigraphy of Abu Rauwash and the History of the Upper Cretaceous in Egypt. Bull. Fac. Sci., Fouad I Univ., Cairo, no. 27, 1948, pp. 221-239.

3. Jux, Ulrich: Zur Geologie des Kreidegebietes von Abu Roasch bei Kairo. Neues Jahrb. Geol. Palaeontol., Abhandl., Bd. 100, Heft 2, 1954, pp. 159-207.

4. Andrew, Gerald: The Late Tertiary Igneous Rocks of Egypt; Field Relations. Bull. Fac. Sci., Egyptian Univ., no. 10, 1937, pp. 1-60.

5. El-Hinnawi, Essam E.; and Maksoud, M. A. Abdel: Petrography of Cenozoic Volcanic Rocks of Egypt (UAR). Geol. Rundschau, vol. 57, no. 3, 1968, pp. 879-890.

6. Bayoumi, A. I.; and El-Gamili, M.: An Attempt for the Estimation of the Basement Depths in the Northern Western Desert of Egypt. U.A.R. Bulletin of Science and Technology, Asyut University, vol. 12, part II, 1969, pp. 129-141.

7. Shata, A.; and El-Fayoumy, I.: Geomorphological and Morphopedological Aspects of the Region West of the Nile Delta With Special Reference to Wadi El-Natrun Area. Bull. Inst. Desert, Egypte, vol. 17, no. 1, 1967, pp. 1-28.

8. Locus, A.: Ancient Egyptian Materials and Industries, 3rd ed., Arnold (London), 1948.

9. Darwish, M. H.: Geology and Mineralogy of the Saline Deposits of Wadi El-Natrun, Egypt, U.A.R. M.Sc. Thesis, Ain Shams University, Cairo, 1965.

10. Hilmy, M. E.; and Darwish, M. H.: Mineralogy of the Saline Deposits From Wadi El-Natrun, Egypt, U.A.R. Proceedings of the Fifth Arab Science Congress, Baghdad, Part II, 1966, pp. 441-453.

11. El-Baz, Farouk: Astronaut Observations From the Apollo-Soyuz Mission. Vol. I of Smithsonian Studies in Air and Space, Smithsonian Institution Press (Washington, D.C.), 1977.

12. Bayoumi, A.; and Ahmed, A. S.: Structural Interpretation of Geophysical Anomalies in Qatrani-Natrun Area, Northern Western Desert of U.A.R. Proceedings of the Sixth Arab Science Congress, Damascus, Part 4, 1969, pp. 209-222.

Phototectonic Analysis of Southeastern Spain From ASTP Photographs and Landsat Images

Paul Dean Proctor,[a] Kenneth B. Horrall,[a] Douglas C. Melton, Jr.,[a] and David F. Thompson[a]

ABSTRACT

The Alpine orogenic belt of Spain and the Atlas orogenic belt of Morocco constitute a tectonically significant part of southwestern Europe and northern Africa. The area is within a possible hinge-zone between the geotectonic plates of Eurasia and Africa.

The Betic Cordillera, the westernmost element of the Alpine orogenic belt, occurs in southeastern Spain. It is bounded on the northwest by the Iberian Meseta, a stable block of Hercynian basement rocks. The Betic Cordillera is divided into (1) the Guadalquivir Basin, composed of sediments of Neogene to Quaternary age and occurring immediately southeast of the Iberian Meseta; (2) the Prebetic zone of Triassic rocks east-northeast of the Guadalquivir Basin; (3) the disharmonically folded Subbetic zone of Triassic rocks southeast of the Prebetic zone; and (4) the intensely folded and faulted Betic zone of mostly crystalline core rock of Paleozoic and Mesozoic ages southeast of the Subbetic zone. The Betic zone, the main subdivision of the Betic Cordillera, is divided into three main subzones: the Sierra Nevada Betic, the Alpujarrides, and the Málaga Betic. The Rondaïdes, once considered a locally divergent unit, may now represent a westerly extension of the Alpujarrides. The generally accepted tectonic succession places the Sierra Nevada at the lowest position, followed upwards by the Alpujarrides-Rondaïdes and the Málaga Betic.

The Iberian and Catalanides mountain systems occur northeast of the Betic Cordillera of southeastern Spain. These systems consist of an irregular network of mountain ranges separated by an equally irregular set of grabens. Hercynian basement rocks crop out in the middle of the chain and are covered on the flanks by a sequence of epicontinental rocks of Mesozoic, and locally, Eocene age. The graben zones are sites of strong continental Neogene sedimentation.

Studies of Apollo-Soyuz Test Project photographs and Landsat images of southeastern Spain reveal four major tectonic provinces: (1) an unfolded to slightly disturbed reentrant northeast of Cádiz, (2) a broadly folded and somewhat faulted area of sedimentary rocks north and west of Alicante, (3) an area of intensely folded and faulted rocks in southeastern Spain, and (4) a less-studied northwesterly trending series of older folds and rocks northwest of the Guadalquivir River. These four well-defined tectonic provinces appear to correspond respectively to (1) the Guadalquivir Basin, (2) the Iberian and Catalanides mountain systems, (3) the Betic Cordillera, and (4) a part of the Iberian Meseta of southwestern Spain.

Within the region, three orders of folds are recognized (first, second, and third). First-order folds are scores of kilometers across and up to hundreds of kilometers in length. The north flank of the largest first-order fold trends along the southern coast of Spain and bends sharply southward at the Strait of Gibraltar. Landsat images strongly suggest that this first-order fold continues south of the Strait of Gibraltar as a mountain system called the "Rif." Second-order folds are components of the first-order group and con-

[a]University of Missouri at Rolla.

sist of anticlinoria and synclinoria. Third-order folds are individual anticlines and synclines of much smaller dimensions than the other two orders.

Lineaments of southeastern Spain are classified according to size into first-order lineaments and second-order lineaments. First-order lineaments have lengths up to 200 km and widths up to 12 km. Second-order lineaments are more abundant than the first-order group, but are much smaller and appear more like lines than like bands on the imagery. Two different systems of lineaments are present in southeastern Spain: (1) a north-south and east-west system and (2) an acute-angle system approximately diagonal to the first-order group. The first system, or regmatic shear pattern, is represented primarily by first-order lineaments.

Folds and faults of the region are the result of compressional and tensional stresses. A major compressional stress environment, generated by a counterclockwise rotation of the Iberian Peninsula together with a more rapidly, northerly, counterclockwise-moving African plate, resulted in slowly closing jaws. Between these, a series of folds, thrust faults, gravity slides, and other shear phenomena developed. Later relaxation of the stress field, or change in the direction of plate movement, resulted in a tensional environment with synchronous normal faulting.

The repetitive north-south and east-west lineaments may be caused by crustal tidal forces. The diagonal system, with the acute angle southward, may be related to principal northerly acting stresses. Local variations in the diagonal pattern may have resulted from differences in rock unit competencies.

Ground-truth checks at selected parts of the region would materially assist in confirming, modifying, or refuting some of the interpreted tectonic features.

INTRODUCTION

Location

An area of Spain, extending approximately from Valencia in the east to the Strait of Gibraltar in the south and bounded approximately by the Hercynian uplands of the Iberian Meseta, was studied by using space imagery. This area, a tectonically significant part of southwestern Europe, includes the Betic Cordillera and parts of the Iberian chain and the Catalanide Mountains of Spain, as well as part of the Rif of northern Africa (fig. 1; ref. 1).

Purpose and Scope

The Alpine orogenic belt of Spain is particularly significant because it is located in the area of a possible hinge-zone interaction between the geotectonic plates of Eurasia and Africa. The tectonic characteristics of southeastern Spain were analyzed with space imagery. These data were used to test two basic assumptions concerning (1) a direct structural relationship between the Alpine orogenic belt of Spain and the Atlas orogenic belt of Morocco and (2) the genetic relationship between the geotectonic patterns of southeastern Spain and the tectonic reaction between Eurasia and northernmost Africa during continental drift.

Space photographs are particularly amenable to this type of investigation. According to Rowan (ref. 2, p. 393), three aspects of the Landsat multispectral scanner subsystem (MSS) and the Landsat-1 orbital geometry combine to make the resulting images unique and especially useful for geologic interpretation. These aspects are (1) the synoptic view of large areas, (2) the spatially registered multispectral radiometry, and (3) the repetitive imaging, which provides data over a period of time. The first aspect was the most valuable in this study. Landsat images and Apollo-Soyuz Test Project (ASTP) color photographs of southeastern Spain presented a unique view of major geologic structures and some unsuspected ones—especially large lineaments.

Source of Research Materials

Two sets of data were used in this investigation: (1) the ASTP oblique color photographs (range of scales for an approximately 18- by 18-cm image area was from 1:4 420 000 to 1:4 480 000) and (2) Landsat vertical images (scale of an 18.5-

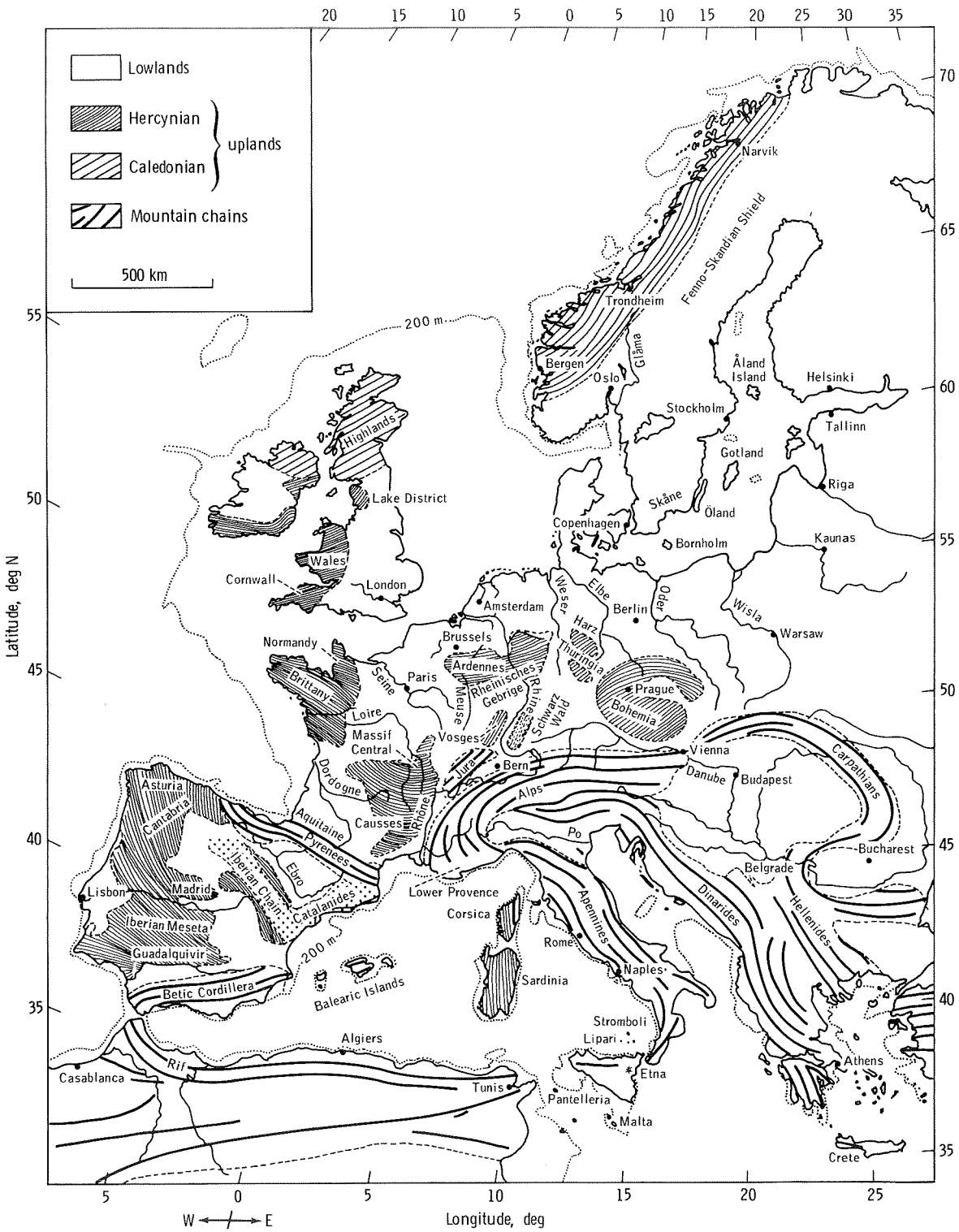


FIGURE 1.—Generalized tectonic map of western Europe showing the relationship of the Alpine orogenic belt of southeastern Spain to the Iberian Meseta (modified from Rutten, ref. 1).

by 18.5-cm image area was 1:1 000 000). All the Landsat images used in this study were black-and-white except for one false-color composite. The black-and-white images recorded band 7 (near-infrared), whereas the false-color image recorded band 4 (green), band 5 (red), and band 7 (near-infrared). These bands range in electromagnetic wavelength as follows: band 4 (0.5 to 0.6 μm), band 5 (0.6 to 0.7 μm), and band 7 (0.8 to 1.1 μm).

Photographic interpretation was, at times, checked against three geologic maps: (1) Seismic-Structural Map of the Iberian Peninsula, Balearic Islands, and Canary Islands published by the Geological and Mining Institute of Spain and the Geographical and Cadastral Institute (ref. 3), (2) International Geologic Map Number A6 (ref. 4), and (3) International Geologic Map Number B6 (ref. 5). The most helpful literature source was "The Geology of Western Europe" by M. G. Rutten (ref. 1). The following discussion on the geologic setting of southern Spain is largely a summary from Rutten's book.

GEOLOGIC SETTING

Alpine Europe includes those regions folded during the Alpine orogeny and extends across the southern part of the continent along the northern shore of the Mediterranean Sea (fig. 1). Along the southern shore of the Mediterranean, its African counterpart (the Atlas Mountain system) extends across the northern parts of Morocco, Algeria, and Tunisia.

The westernmost element of the Alpine orogenic belt occurs in southern and southeastern Spain in the Betic Cordillera (fig. 1). This cordillera, some 500 km long by 100 km wide, trends eastward from Cádiz and Gibraltar on the west, and more or less parallels the southern coast of Spain. At its eastern end, the belt enters the Mediterranean Sea between Cartagena and Alicante. Eastward from Spain, the Betic Cordillera can be correlated with the Balearic Islands, particularly the island of Mallorca. Eastern Corsica also belongs to the Alpine belt. However, Rutten (ref. 1, p. 172) notes that the structural connections are not clear either westward to the Balearic Islands or northward to the French Alps.

The Pyrenees of northern Spain are another element of Alpine Europe. These mountains trend almost east-west along the border between Spain and France. Many features of the Pyrenees mountain chain can be traced eastward along the Mediterranean Sea into southern France. These structures continue across the Rhône graben into Lower Provence, an area which was also folded primarily during the Pyrenean phase of the Alpine orogeny (ref. 1, p. 172).

Between the Betic Cordillera in southern Spain and the Pyrenees in the north, several smaller Alpine chains occur. These are of the Jura Mountains type. One, the Catalanides, occurs along the Mediterranean coast and trends southwest from Barcelona. Another, the Iberian chain, borders the Ebro River basin on the south and trends generally northwest (fig. 1).

Betic Cordillera

Although the Betic Cordillera forms an element of the Alpine orogenic belt, it differs from the Alps proper in several ways. A major difference is the topography. Rutten (ref. 1, p. 392) summarizes this difference:

> Topographically, this area is occupied not by a system of elongated mountain chains, but by a more or less irregular mosaic of individual sierras, high and steep, but rather short, separated by quite extensive plateaus, both high and low. . . . This topography of an irregular network of smaller individual sierras alternating with plateaus is due to the development of younger, Neogene, intramontane basins. Instead of the larger external, more or less continuous, molasse basins of the Alps, the Betic Cordillera is characterized by these smaller, internal and discontinuous molasse basins.

Main Divisions

The Betic Cordillera is divided into various units based mainly on geologic structure (fig. 2; refs. 1 and 6). South of the Iberian Meseta lies the

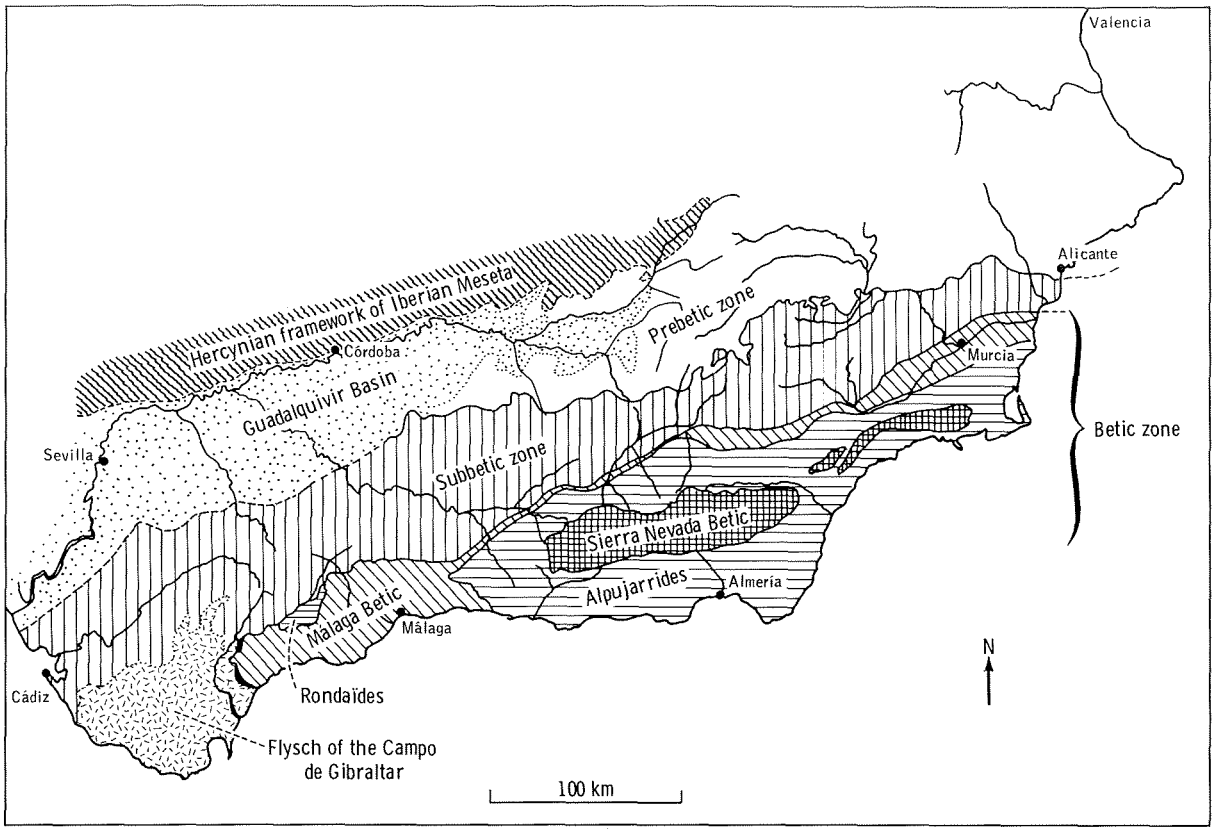


FIGURE 2.—Generalized map of the Betic Cordillera showing the main divisions (modified from Fallot, ref. 6; in Rutten, ref. 1).

Guadalquivir Basin. Shallowing in an easterly direction, the basin is replaced by an area of epicontinental cover resting on Triassic rocks; in this area tectonic forces have produced small, irregular structures. This zone, the Prebetic, probably continues westward beneath the Guadalquivir Basin.

South of the Prebetic zone lies the Subbetic zone. This division, according to Rutten (ref. 1, p. 393), is the northernmost zone of the Betic Cordillera. The Subbetic is subdivided into a northern subzone, the Subbetic *sensu stricto*, and a southern subzone, the Pénibetic.

The Betic zone, the main division of the Betic Cordillera, is south of the Subbetic. This unit is subdivided into three main subzones: The Málaga Betic, the Alpujarrides, and the Sierra Nevada Betic. Further subzones include the divergent Rondaïdes in the western part of the Betic Cordillera and, still further west, the flysch region of the Campo de Gibraltar (ref. 1, p. 394).

Stratigraphy and Structure

As in the Alps proper, there is a striking difference between the external part of the Betic Cordillera, the Subbetic, and the internal part, the Betic. Rutten (ref. 1, p. 394) records:

> The Subbetic consists of epidermis-type structures, sheared off over the evaporites of the Triassic in Germanic facies. The main nappe system of the Betic, on the other hand, the Alpujarrides, is characterized by geosynclinal Triassic in Alpine facies. Moreover, in both the Alpujarrides and in the Málaga Betic the pre-Alpine basement has become incorporated into the Alpine structures. In contrast to the two units mentioned, the Sierra Nevada Betic is in the main formed by a monotonous series of mica schists, several kilometers thick.

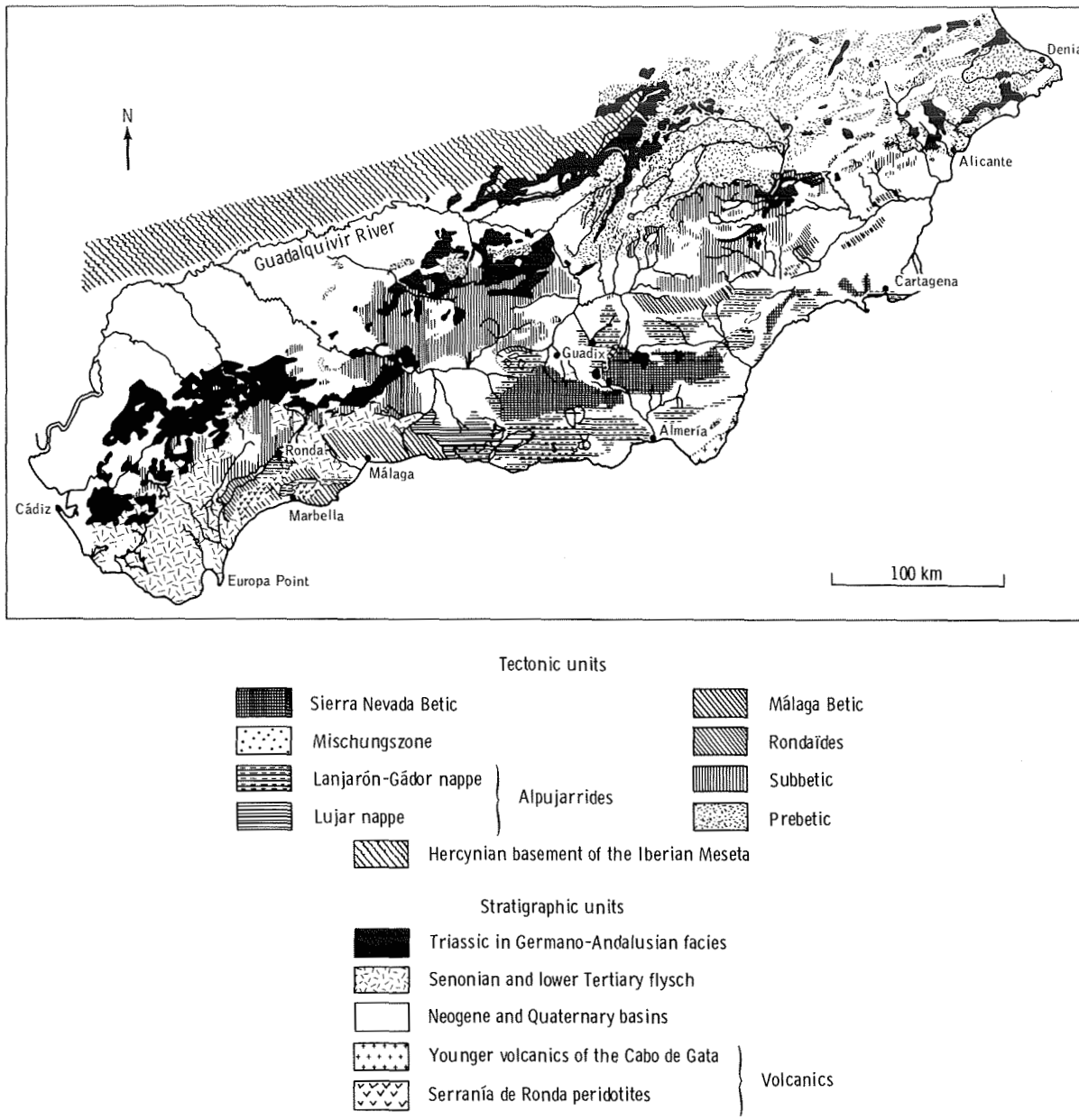


FIGURE 3.—Generalized structural and stratigraphic map of the Betic Cordillera (after Fallot, ref. 6; in Rutten, ref. 1).

Subbetic zone.—The disharmonically folded structures of the Subbetic zone are sheared off over the evaporites of the Triassic Germano-Andalusian facies. This facies, a variant of the "Germanic facies" (a largely continental, red-bed facies of the European Triassic System), occurs over much of Spain (fig. 3; refs. 1 and 6).

The development of a thick sequence of gypsum beds in the lower part of the Germano-Andalusian facies is very important tectonically, because these beds serve as a décollement zone and locally may develop strong salt tectonics.

The epidermis structures are characterized by a relatively thin carbonate series of late Mesozoic

age formed in an epicontinental environment, which extended into the early Tertiary period (ref. 1, pp. 395-397).

Betic zone.—The units of the Betic zone (the Málaga Betic, the Alpujarrides, and the Sierra Nevada Betic) may each consist of a number of individual nappes. The Rondaïdes, formerly considered a locally divergent unit, are now believed to possibly represent a more important element. Some investigators suggest they may form a major subzone and even represent the westerly extension of the Alpujarrides. The most generally accepted tectonic succession places the Sierra Nevada at the lowest position, followed successively upwards by the Alpujarrides-Rondaïdes and the Málaga Betic (ref. 1, pp. 397-398).

1. Málaga Betic: The Málaga Betic subzone has a stratigraphy characterized by the predominance of pre-Alpine rocks, which consist of an older sequence of high-grade metamorphic rocks including schists, gneisses, and marbles as well as a younger sequence of weakly metamorphosed clastic metasediments containing fossils ranging in age from Silurian to Carboniferous.

Post-Hercynian rocks start with the transgression of the Buntsandstein Stage followed by individual complexes of the younger Mesozoic. Widespread sedimentation did not start until the Late Cretaceous and the early Tertiary when it resulted in the deposition of the flysch sediments (ref. 1, p. 398).

The geographical extent of the Málaga Betic subzone is unusual (figs. 2 and 3) (ref. 1, p. 398). Two hypotheses have been proposed to explain the shape of the thin zone of the Malága Betic that extends northeast along the northern border of the Betic zone. The first, proposed by M. Blumenthal (according to Rutten, ref. 1) maintains that the southwestern area of the Málaga Betic dips into the Mediterranean Sea. From the Mediterranean, the nappes are believed to be overthrusted northward and to override all the Betic zone and, in its frontal part, even a substantial area of the Subbetic zone (fig. 4). Recently, however, MacGillavry et al. (refs. 7 and 8) have proposed that the thin zone of the Málaga Betic is subautochthonous and represents a root-zone scar from which elements have been overthrust in a southerly direction over the Alpujarrides (fig. 5; refs. 1 and 9).

According to Rutten (ref. 1, p. 399), the second hypothesis on the tectonics of the Málaga Betic assumes an earlier northward thrust during the early Oligocene-Miocene to form the Alpujarrides, followed by a southward thrust of the Málaga Betic over the Alpujarrides during later Oligocene-Miocene. During early Miocene-Pliocene, the Subbetic zone then underwent a

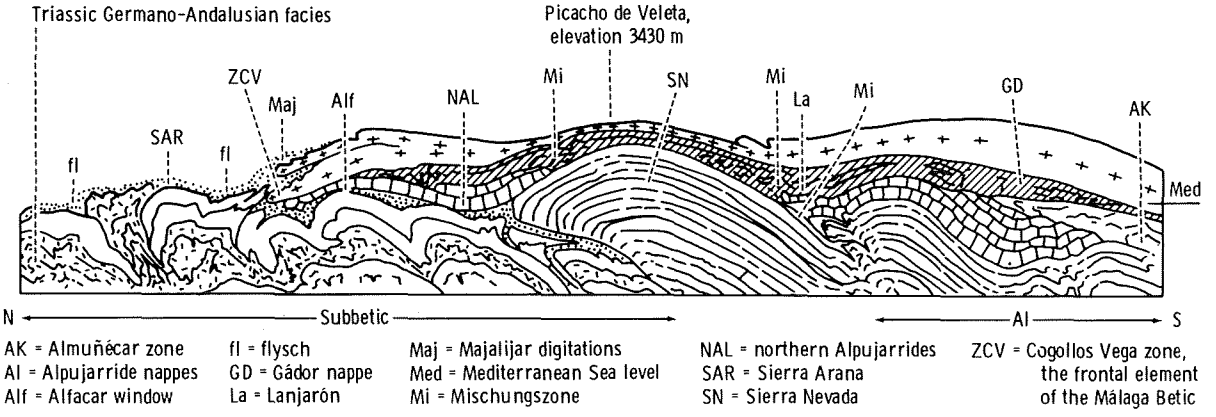


FIGURE 4.—Structure section through the western part of the Betic Cordillera showing the Málaga Betic (elongated crosses) overriding other tectonic units (after M. Blumenthal; in Fallot, ref. 6, and in Rutten, ref. 1).

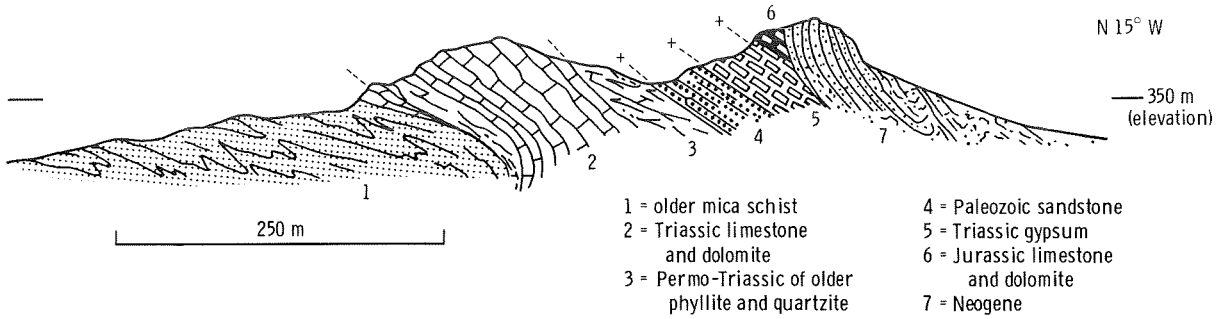


FIGURE 5.—Structure section through the Cerro del Medio, western Sierra Cabrera, southeasterly part of the Betic, showing small elements of the Málaga Betic (4, 6) pinched in the Alpujarrides (1 to 3 and 5); an argument for a southerly thrust of the Málaga Betic (after Rondeel, ref. 9; in Rutten, ref. 1).

northward thrust. Rutten (ref. 1, p. 399) disagrees with this interpretation:

> Such a sequence of orogenetic movements is, to my mind, difficult to visualize. Such interpretation may well be another result of a too strict an application of the facies concept of the classic picture of the Alps.

2. Alpujarrides: The Alpujarrides subzone is composed of two distinct rock sequences, an older and a younger. When only one sequence crops out in a particular nappe, it is usually the younger one—this having been sheared off from the older.

The older sequence consists mainly of medium-grade schists with intercalated marbles. Although earlier literature has always indicated the age of the older rocks to be Paleozoic, Egeler (ref. 10) assumes a pre-Silurian age on the evidence of lithofacial resemblance of some intermediate graywackes in the Alpujarrides to the Paleozoic rocks of the Málaga Betic.

The younger sequence is composed mainly of massive, predominantly dolomitic limestones. Its lithology and fossils of Middle and Late Triassic age suggest a close relationship with the Triassic Alpine facies. Deposition of the younger rocks began with a gypsiferous shale horizon of Werfenian age, over which the décollement of the still younger rocks of the Alpujarrides occurs. Rocks younger than Triassic age have not been found in the Alpujarrides (ref. 1, pp. 399-400).

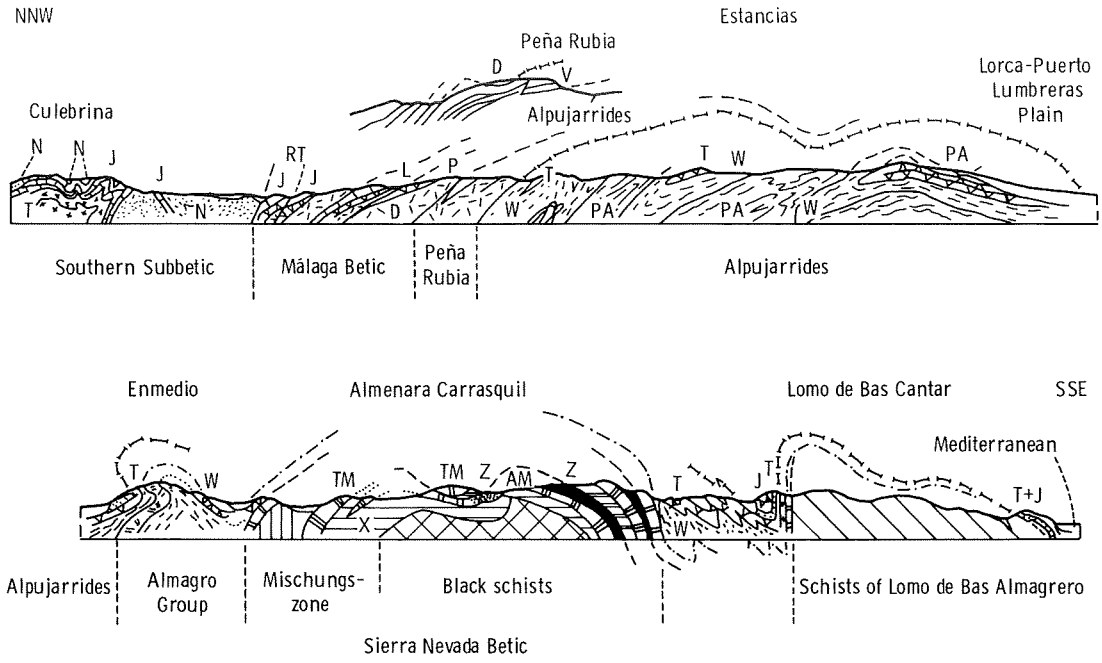
The Alpujarrides have been strongly faulted and folded. Numerous major overthrusts are present, and a first division into three nappes was made by H. A. Brouwer and his group (Rutten, ref. 1, p. 400). From high to low, these nappes are the Guajar nappe, the Lanjarón-Gádor nappe, and the Lujar nappe. However, Rutten (ref. 1, p. 400) states: "Not everybody has agreed, and moreover, recent work has proved the structure of the Alpujarrides to be much more complicated than had originally been thought."

A recent cross section of the Sierra Nevada Betic, showing the Alpujarrides developed both to the north and to the south, is illustrated in figure 6 (refs. 1 and 11).

According to Durand Delga and Fontboté (ref. 12), the main period of diastrophism occurred in either late Oligocene or early Miocene.

3. Sierra Nevada Betic: The lithology of the Sierra Nevada Betic subzone is extremely uniform. It consists of a lower, very thick, monotonous sequence of mica schists covered by rocks of the Mischungszone. The structure of the subzone, however, is not so uniform. Although the Sierra Nevada itself forms a single doubly plunging anticlinorium, the more easterly units of the Sierra Nevada Betic, from the Sierra de los Filabres on, have been subjected to strong tectonization.

The lower sequence of the Sierra Nevada Betic exhibits mesozonal metamorphism. Only sandy intercalations break the monotony of the 4-km-thick mica schist sequence (fig. 7; refs. 1 and 12). Although the age of the sequence is unknown, it must be pre-Silurian based on an extension of the lithostratigraphic correlation between the Málaga Betic crystalline rocks and the Alpujarrides (ref. 1, pp. 402-403).



Southern Subbetic
N = Upper Cretaceous-lower Tertiary
J = Jurassic
T = Triassic

Málaga Betic
J = Middle and Upper Jurassic and lower Tertiary
RT = Permo-Triassic and Triassic
L = Upper Triassic and Liassic
D = Devonian-Carboniferous
P = Permo-Triassic

Complex unit of Peña Rubia
V = Permo-Triassic

Alpujarrides
T = Middle and Upper Triassic
W = Permian and Werfenian
PA = older schists

Sierra Nevada Betic
TM = Triassic marble
AM = amphibolites and prasinites
X = mica schists
Z = garnet schists

FIGURE 6.—Structure section through the Betic Cordillera across the Sierra Nevada. The upper section is the northern continuation of the lower section (after Fernex, ref. 11; in Rutten, ref. 1).

The younger upper sequence, the Mischungszone, forms a thin envelope around the core of the older schists in the Sierra Nevada *sensu stricto*. The envelope thickens eastward, reaching thicknesses of approximately 1 km. How much of this can be attributed to tectonic repetition is unknown.

Mischungszone, meaning "mixed zone," is an apt term for this younger sequence because it contains a number of rock types. Mica schists are again the most abundant rocks, but these show transitions toward albitic gneiss. Hence, the younger schists are more feldspathic than the older schists. Of minor importance volumetrically, but very important for petrogenesis, are the intercalations of marble and even of gypsum (ref. 1, pp. 403-404).

Rutten (ref. 1, p. 405) maintains that most investigators believe the Mischungszone is the metamorphosed Germano-Andalusian facies of Triassic age. The large gradation of the original facies (from fully marine to saline, to evaporite, to continental) could explain the varied suite of rocks in the Mischungszone. This interpretation is important for two reasons. The dating of the Mischungszone as Triassic would prove mesozonal Alpine metamorphism. Also, this would mean that the Sierra Nevada Betic was in the area of the Germano-Andalusian facies during the time of deposition.

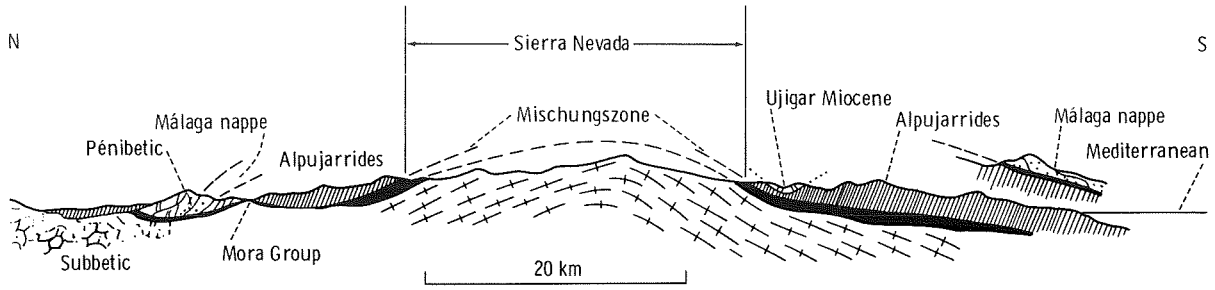


FIGURE 7.—Structure section through the Betic zone across the Sierra Nevada, showing the older lower sequence of mica schist and the younger upper Mischungszone (after Durand Delga and Fontboté, ref. 12; in Rutten, ref. 1).

The strong diastrophism in the Sierra de los Filabres and farther east is comparable to that of the Alpujarride nappes (fig. 8; refs. 1 and 13). Because of this, Egeler (ref. 10) and other investigators assume the existence of a lower nappe system in the Betic zone that they named "Nevada-Filabrides." This interpretation suggests that the Sierra Nevada Betic is not autochthonous. However, Rutten, in agreement with Fallot (refs. 6 and 14), finds no evidence for nappe structures in the Sierra Nevada. Rather, the mountain range resembles descriptions of migmatite domes and may therefore be autochthonous. The increased structural disturbance of the Sierra de los Filabres

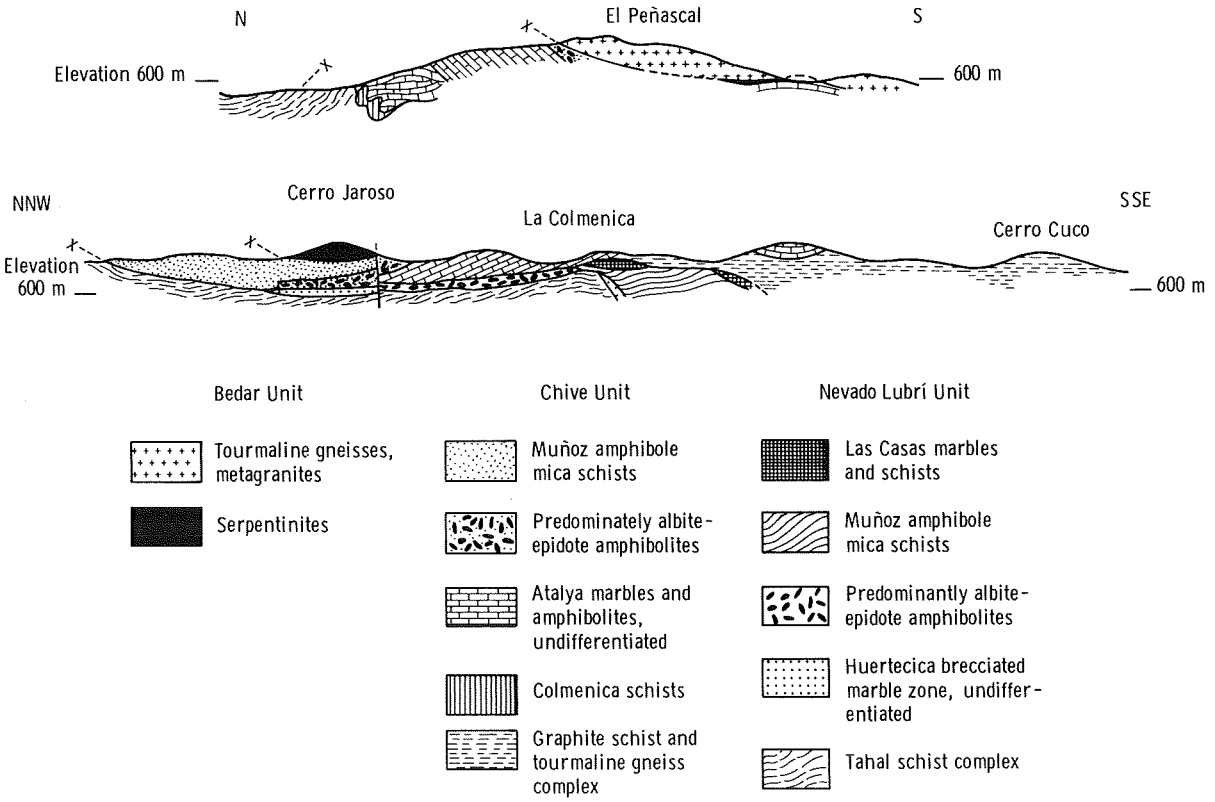


FIGURE 8.—Structure sections through the Sierra de los Filabres showing the strong diastrophism of the easterly elements of the Sierra Nevada Betic (after Nijhuis, ref. 13; in Rutten, ref. 1).

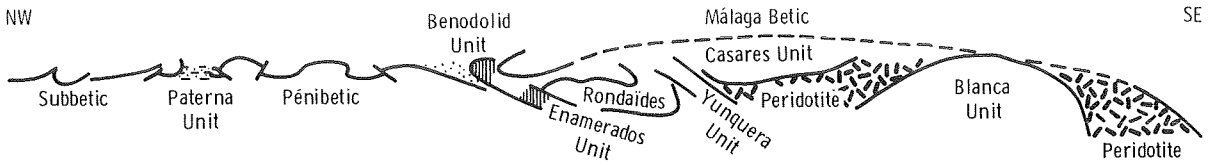


FIGURE 9.—Structure section of westerly part of the Betic Cordillera, showing relation between the Subbetic and the Rondaïdes and Málaga units of the Betic (after Hoeppener et al., refs. 15 and 16; in Rutten, ref. 1).

and more easterly units may imply parautochthonous movements (ref. 1, pp. 405-406).

4. Rondaïdes: The Rondaïdes subzone, a divergent unit of the western Betic zone (figs. 2 and 3), resembles the Alpujarrides and has been classified with this unit. Because of the complex structure of the Rondaïdes (fig. 9; refs. 1, 15, and 16), it is often confused with elements of the overlying Málaga Betic. Through the recent investigation of R. Hoeppener and others (refs. 15 and 16), it has now become customary to refer to the Rondaïdes as a separate subzone of the Betic.

The restricted stratigraphy of the Rondaïdes consists only of Upper Triassic and Lower Jurassic rocks. The Triassic consists of massive Norian Stage dolomites, more than 1 km thick. These rocks represent the upper part of the Alpine facies and are therefore comparable to the Alpujarrides stratigraphy. The Jurassic System is represented only by the lower part of the Lias Series. This sequence is developed as several hundreds of meters of marls and limestones intercalated with "cargneules" (porous dolomites that are related to the deposition of evaporite facies and which normally occur in the Triassic System) (ref. 1, pp. 400-402).

Extensive masses of peridotite occur in the same area as the Rondaïdes, and these masses constitute another divergent unit (fig. 3). They were formerly placed in the Málaga Betic, but recently Hoeppener et al. (refs. 15 and 16) have included them in the Alpujarrides. Figure 9 shows their puzzling position.

5. Strait of Gibraltar: Alpine geologists have speculated for approximately 50 years on how to connect the Alpine orogenic belt of Spain, the Mediterranean islands, and North Africa with the Apennines and Alps proper (fig. 10; refs. 1 and 6). Investigators were especially interested in the westernmost connection across the Strait of Gibraltar. Rutten (ref. 1, p. 406) queries:

> Is this young feature a graben cutting across the former continuation of the Betic Cordillera, curving southwards into Morocco? Or does the Betic Cordillera continue westwards, to be cut off by the Atlantic?

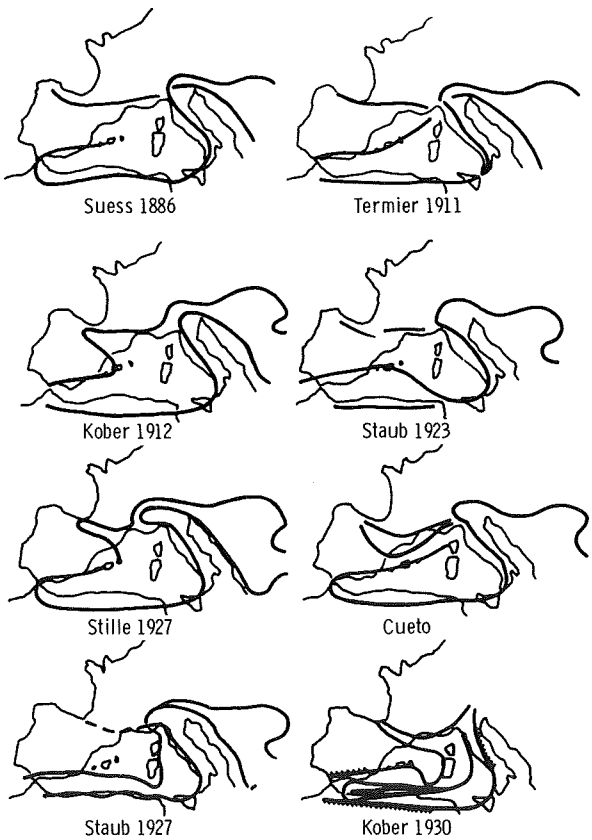


FIGURE 10.—Various interpretations of the connections between elements of the Alpine chain around the western Mediterranean Sea, as proposed by major Alpine geologists (after Fallot, ref. 6; in Rutten, ref. 1).

In the opinion of Durand Delga et al. (ref. 17), a north-south-trending fold belt occurs south of the Strait of Gibraltar (fig. 11; refs. 1, 15, and 16). This belt, called the "Rif," forms a separate orogenic unit and is not directly related to the more southerly, east-west-trending Atlas Mountains. The Rif strongly resembles part of the external elements of the Betic Cordillera and, to a lesser extent, the Málaga Betic.

Despite the similarities between the Rif and the Betic Cordillera, Fallot, according to Rutten (ref. 1), maintained that the differences between them were so important as to exclude the possibility that they formerly formed one single, curved orogenic belt. However, Rutten (ref. 1, p. 407) states:

> Recent research in the Campo de Gibraltar, in the Subbetic, and in the western part of the Rif has brought out more and more points of resemblance. Today all authors seem to consider the Rif to be the continuation of the Betic Cordillera. . . . This indicates a young, post-orogenetic age for the present Straits of Gibraltar. It must be kept in mind, however, that in the Rif only the "higher" elements of the Betic Cordillera, are exposed. Only the Subbetic and the highest element of the Betic, the Málaga Betic, are represented in the Rif. The axial dip, found in the Betic Cordillera westwards of the Sierra Nevada, evidently continues into the Rif.

Iberian and Catalanides Mountain Systems

The Iberian and Catalanide mountain systems consist of an irregular network of mountain ranges and have been variously interpreted as major orogenic belts comparable to the Alps proper. The Hercynian basement crops out in the middle of the chain and is covered by a series of epicontinental units of Mesozoic and, locally, Eocene age. An equally irregular set of grabens separates the positive elements; and these grabens are sites of strong, continental, Neogene sedimentation. Pliocene-Pleistocene epeirogeny followed all previous events (ref. 1, pp. 407-408).

Stratigraphy

The Triassic Germano-Andalusian facies is well developed in both the Iberian and Catalanide chains. In Catalonia, the Muschelkalk Stage predominates, and several gypsiferous horizons are present throughout the sequence. As in the Subbetic division, these horizons probably serve as décollement zones.

The Jurassic and Cretaceous systems, as well as the Eocene Series, are mainly represented by a carbonate facies. However, at the transition from Jurassic to Cretaceous, there was a period of regression resulting in extensive areas above sea level. This led to the deposition of the continental Wealden facies (fig. 12; ref. 18) (ref. 1, pp. 408-409).

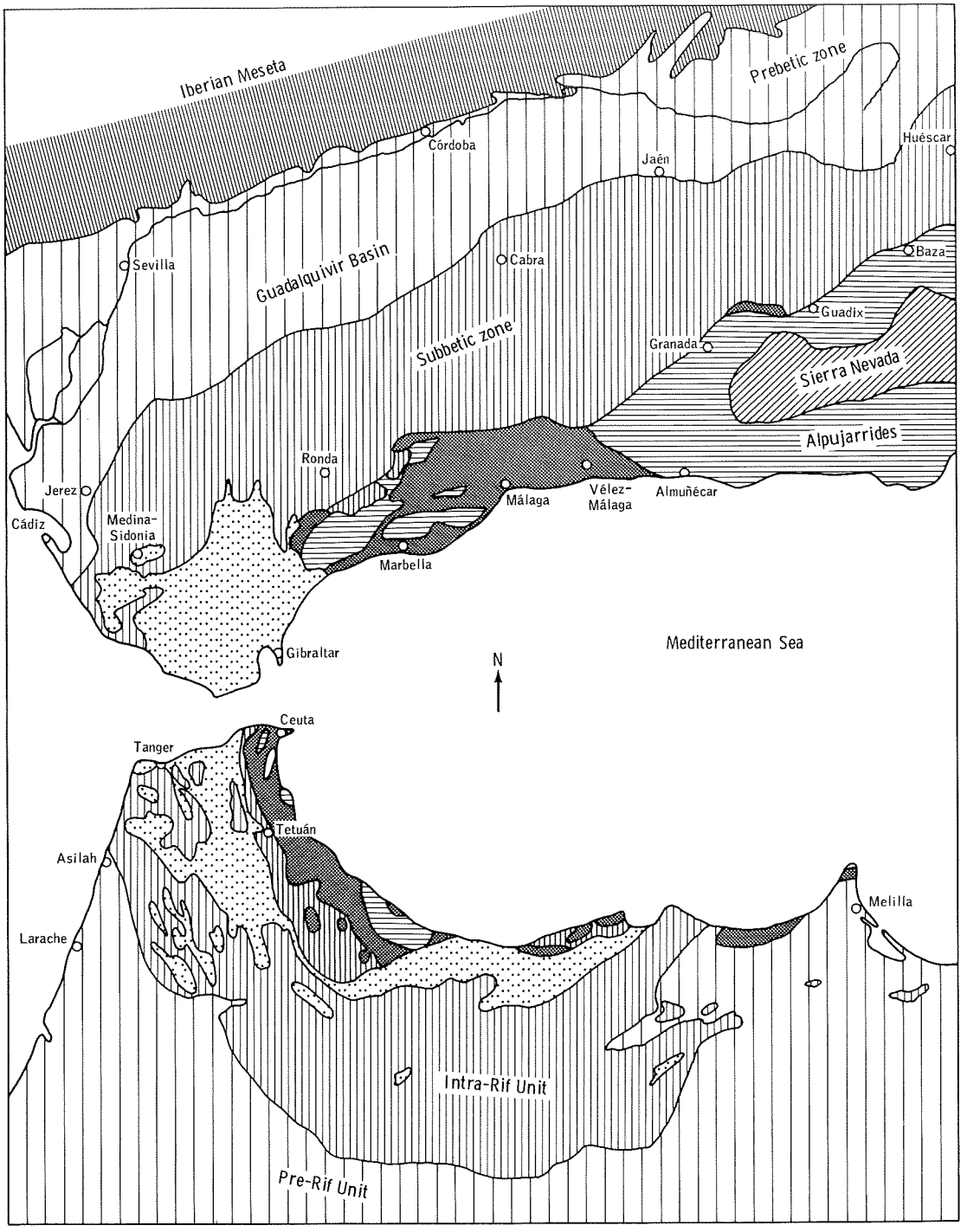
As in the southern border of the Aquitanian Basin and the northern marginal areas of the Pyrenees, the rate of subsidence and the facies deposited vary strongly, both temporally and spatially. Subsidence of a given area and its sedimentational history are not related; nor is there a relationship to later block faulting, which led to the Alpine orogeny.

This characteristic is apparent in the two basins of especially strong sedimentation at either end of the Iberian chain (i.e., the Sierra de los Cameros and the Maestrazgo). These former basins were independently subsiding at approximately the same time. This subsidence of the basins is indicated by the development of their sedimentary stages; the Sierra de los Cameros has a continental Wealden facies, whereas the Maestrazgo has a marine Urgo-Aptian facies.

Structure

The geologic structure of the Iberian and Catalanide mountain systems is characterized by irregularity (fig. 12). Large numbers of short structures are more or less alined but, nevertheless, show an extremely irregular pattern. Rutten

FIGURE 11.—Generalized map of the western Betic Cordillera and of the Rif, showing the main divisions (after Hoeppener et al., refs. 15 and 16; in Rutten, ref. 1). →


Iberian Meseta
Prebetic zone
Córdoba
Jaén
Huéscar
Sevilla
Guadalquivir Basin
Cabra
Baza
Guadix
Granada
Subbetic zone
Sierra Nevada
Alpujarrides
Ronda
Jerez
Málaga
Vélez-Málaga
Almuñécar
Cádiz
Medina-Sidonia
Marbella
Gibraltar
Mediterranean Sea
N
Ceuta
Tanger
Tetuán
Asilah
Melilla
Larache
Intra-Rif Unit
Pre-Rif Unit
Hercynian basement of the Iberian Meseta
Prebetic, Pre-Rif, and Postorogenic sediments
Subbetic and Intra-Rif
Flysch of the Campo de Gibraltar and of the Ultra-Rif
Rondaides
Sierra Nevada Betic
50 km
Alpujarrides
Málaga Betic

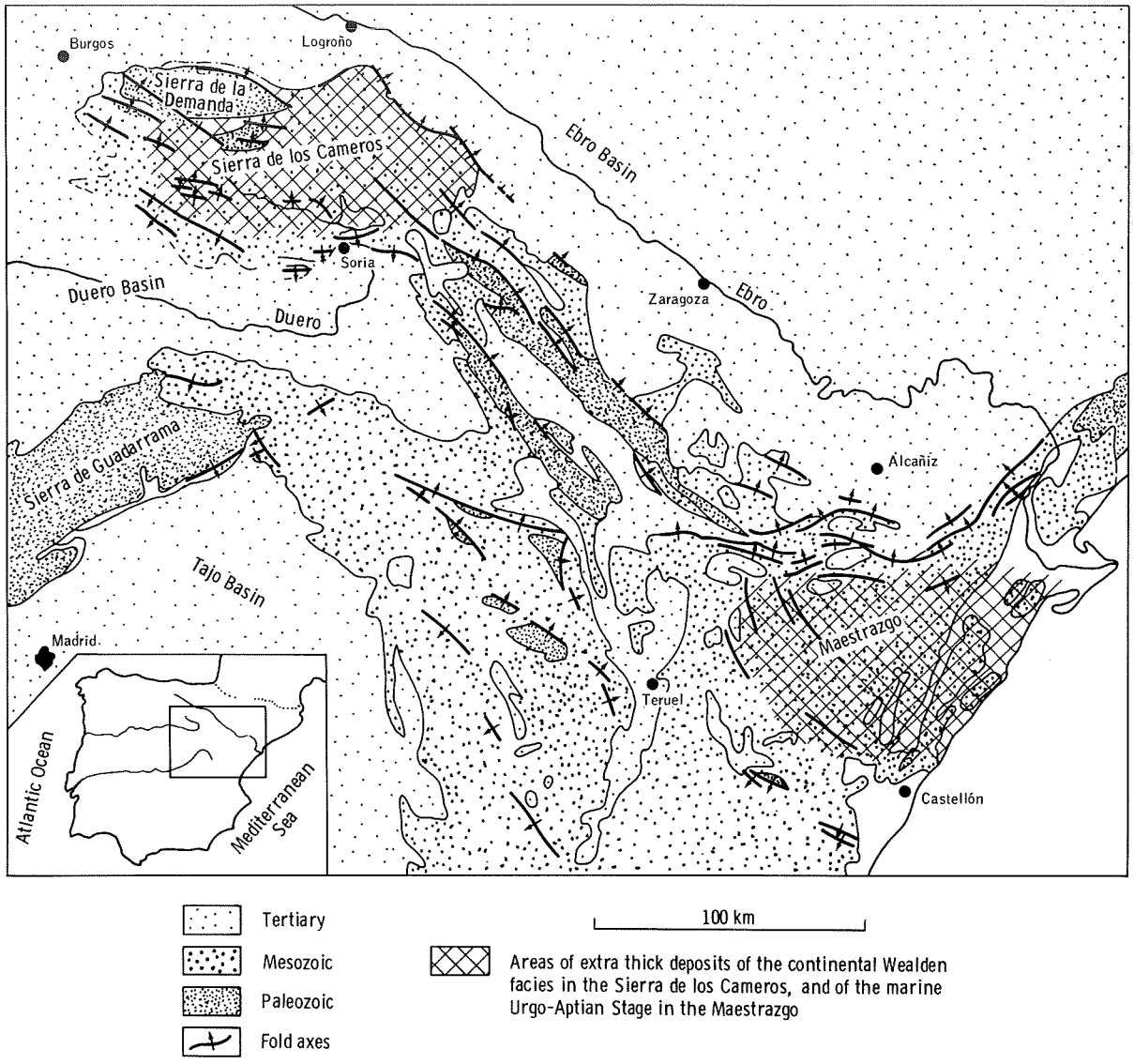


FIGURE 12.—Generalized tectonic map of the Iberian chain, showing the irregular distribution of fold axes (after Brinkmann, ref. 18; in Rutten, ref. 1).

(ref. 1, p. 411) describes this pattern as follows:

> The "en échelon" arrangement often acquires a habit which is more reminiscent of the shape of a braided river, than that of a fold belt. . . . More or less horizontal plateau areas, structurally situated either high or low, alternate with narrow, normally strongly asymmetric, folds, which show strong along-the-strike variation.

The basement normally crops out in certain areas of the topographically higher horizontal-to-subhorizontal plateaus of the Catalanides. The Buntsandstein Stage invariably overlies the Hercynian basement and, together with the basement and its thin cover of Buntsandstein, shows only block faulting and tilting characteristics by irregular movement. Beneath the lowest gypsum horizon of the Buntsandstein, the beds are horizontal or only slightly dipping. On the other

hand, higher elements of the sequence have folding of the epidermis type (ref. 19).

Concerning the disharmonic folding, Rutten (ref. 1, p. 412) states, "It seems to me that the folding of the epidermis is due either to gravitational sliding of epidermis blocks from rising areas, or to a draping over faults in the basement."

Figure 13 (refs. 1 and 20) shows a miniature example of such draping, the "Branden einer Deckenstirn," i.e., the break of a tectonic front.

PHOTOTECTONIC ANALYSIS

At least four distinct tectonic provinces are recognizable in the study area (figs. 14 and 15). These include (1) an unfolded to slightly disturbed reentrant northeast of Cádiz that trends northeasterly and probably consists of younger sediments and valley fill, (2) a broadly folded and somewhat faulted area of sedimentary rocks north and west of Alicante, (3) a zone of intense folding and thrusting and of probable crystalline core rock in the mountainous southern part of the region near Loja-Purchena-Lorca, and (4) an area, only partly studied, but of uniquely different fold trends and of probably older rocks, northwest of the Guadalquivir River. These four well-defined provinces probably correspond roughly to (1) the Guadalquivir Basin, (2) the Catalanides-Iberian chains, (3) the Betic Cordillera, and (4) a part of the Iberian Meseta of southwestern Spain.

The complex structures of the Betic and Subbetic zones of southeast Spain are convincingly revealed on the ASTP photographs and on the supplemental Landsat images (figs. 16, 17, and

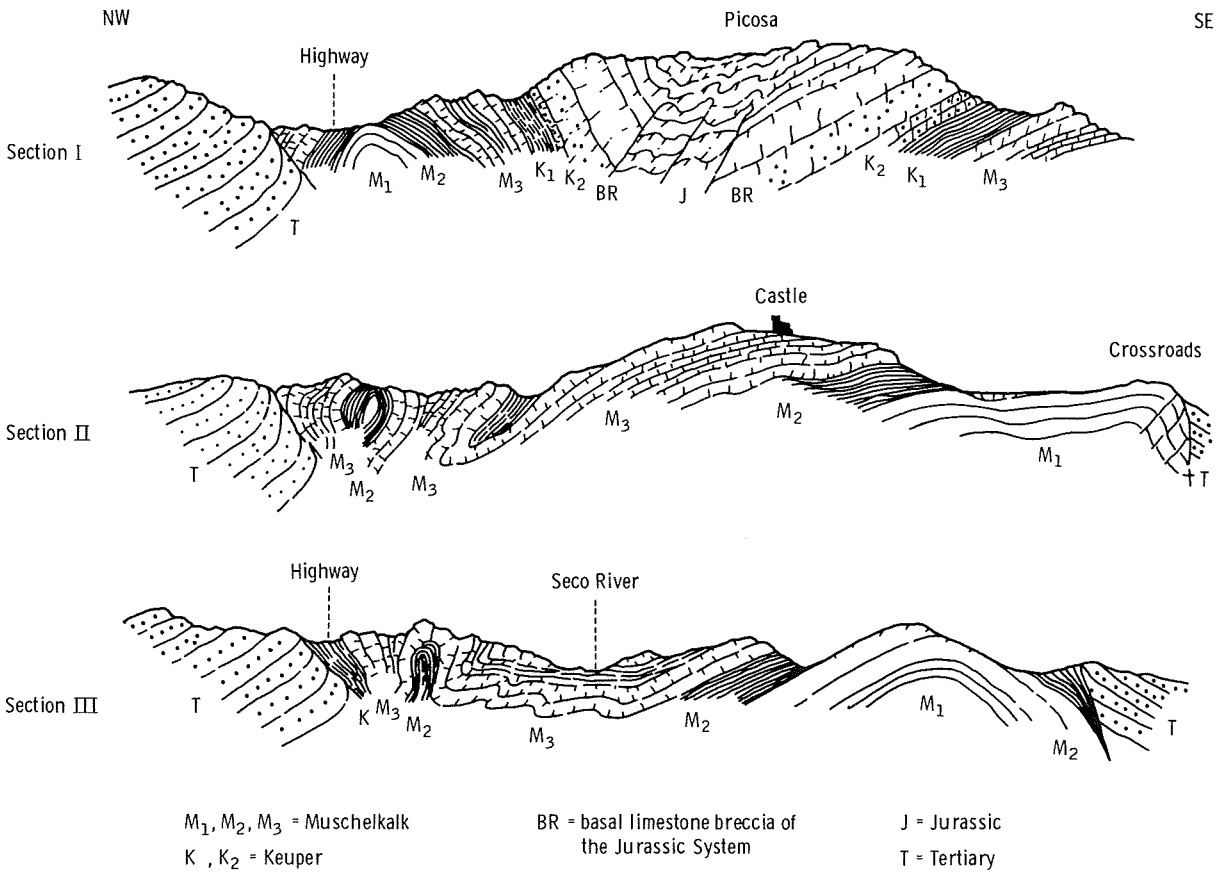


FIGURE 13.—Three structure sections through the Camposines structure in the Catalanides. This is a miniature example of the "Branden einer Deckenstirn" (after Virgili, ref. 20; in Rutten, ref. 1).

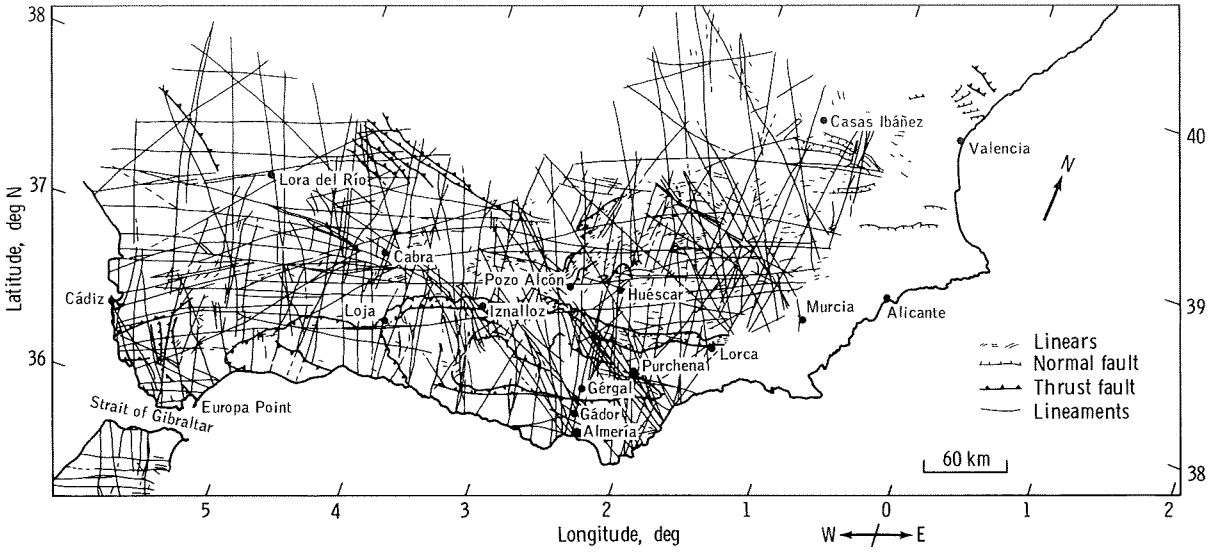


FIGURE 14.—Photointerpretive tectonic map of southeastern Spain showing linears, faults, lineaments.

18). Well-defined linears probably represent traces of bedding and planar structures of other rock units. These features help to define noses and general axial positions of numerous folds in the region. At least three orders of fold dimensions are present. Normal faults and thrust faults are also identified on the images. Of less certain origin, but abundant and well defined, are at least two prominent systems of lineaments.

Fold Orders

Three orders of fold dimensions are shown on the tectonic map of the area (fig. 15). These occur in three of the four tectonic provinces previously noted. The first-order folds are similar to oroclines (ref. 21), in which fold mountain belts are strongly bent or curved in plan view. In this region, such folded-fold belts are on the order of

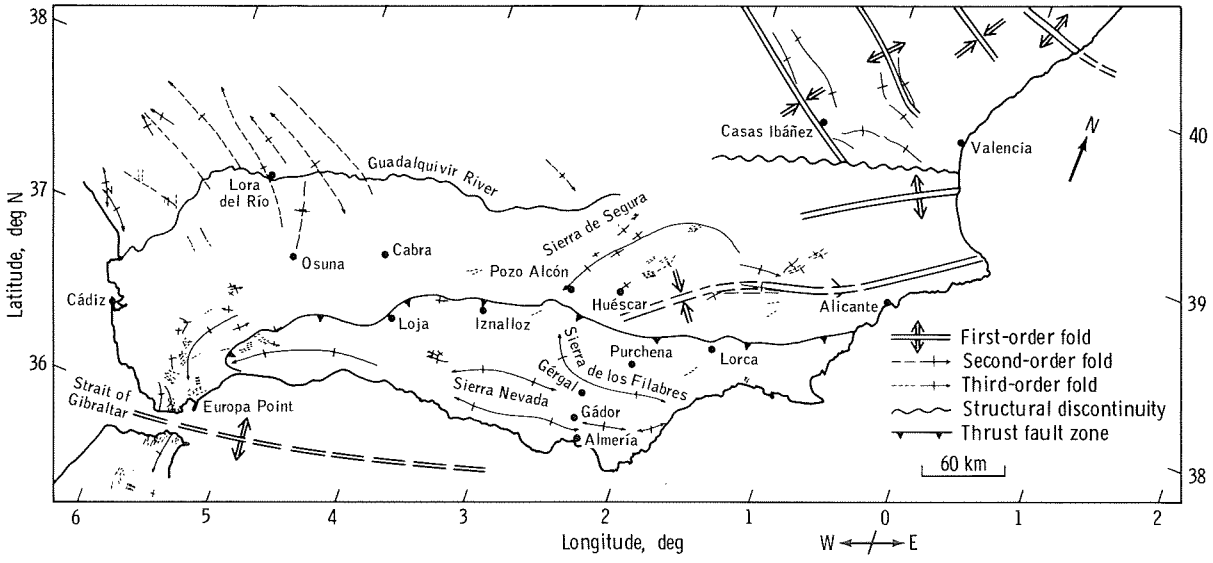


FIGURE 15.—Photointerpretive tectonic map of southeastern Spain showing fold axes.

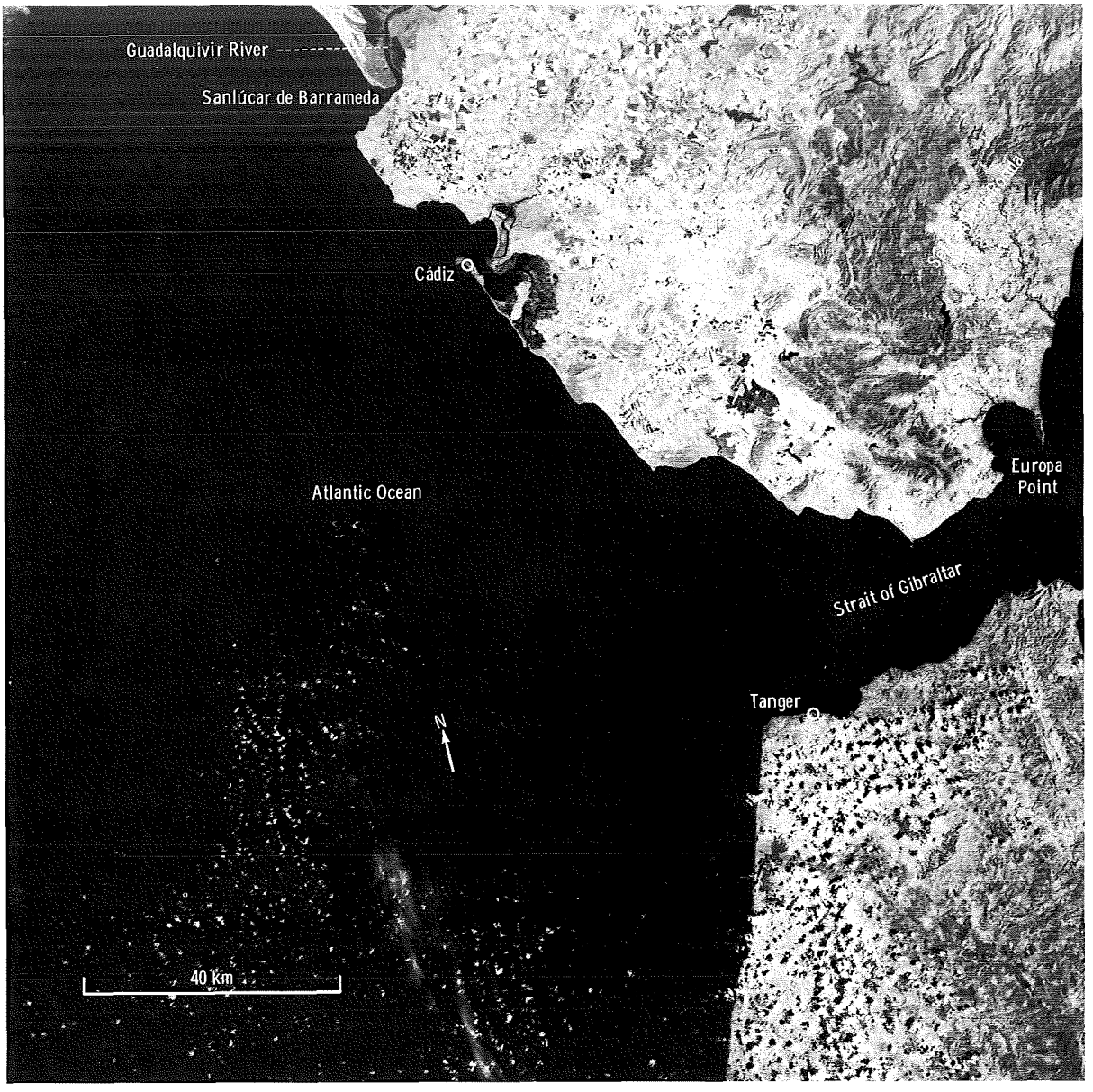


FIGURE 16.—Landsat vertical black-and-white image of the Strait of Gibraltar showing the western nose of the largest first-order fold of southeastern Spain trending sharply southward toward the Rif mountain system of northern Africa. Note the indications of faulting suggested by the straight boundaries of coasts of Spain and Morocco (E-1246-10341-7).

70 km in width and up to hundreds of kilometers in axial length.

Second-order folds consist of anticlinoria and synclinoria of essentially parallel folds. These fold zones are a component of the first-order folds.

Single anticlines and synclines comprise the third-order fold type. These fold zones range from many kilometers in axial length to a few kilometers in length or less. These could be further subdivided, but the subdivisions would be unresolvable at the map scale considered.

The dimension of the region, while large, is marginal in permitting classification of an even higher or larger fold order than first-order. Several

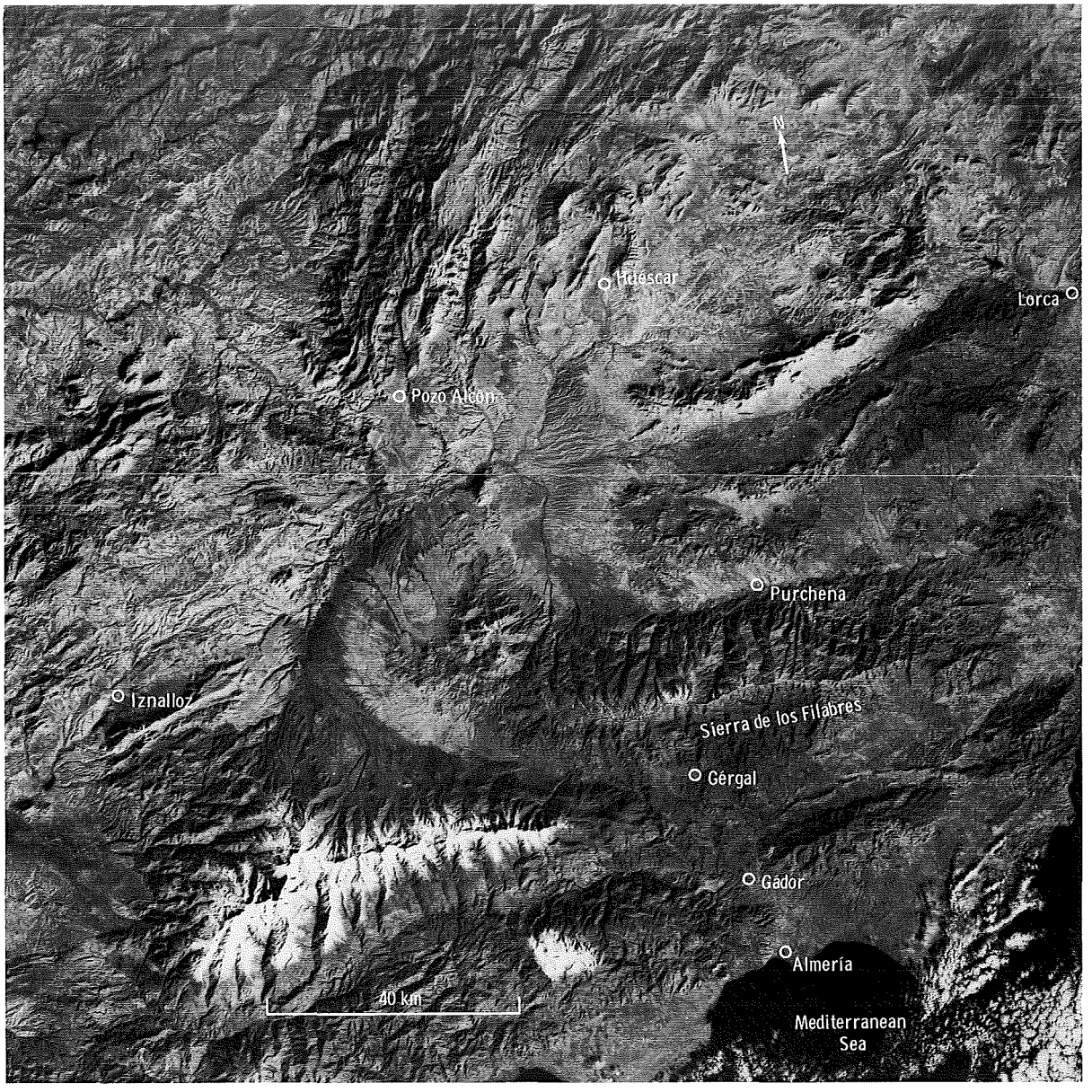


FIGURE 17.—Landsat vertical black-and-white image of the southeastern corner of Spain showing the large first-order fold near the village of Huéscar. Note the prominent northwest-trending lineaments northeast and southwest of the village of Gérgal and also the distinctive lineament trending northeast from Huéscar (E-1550-10174-7).

investigators (ref. 1, p. 406) have considered the very large sinuous fold belts comprising the orogenic belts of the Pyrenees, Apennines, Atlas, and other ranges of southern Europe and northern Africa (fig. 10). These folds grade into the first-order fold type.

First-Order Folds

For the study area, at least seven first-order folds are identified. The largest first-order fold trends along the southern coast of Spain from Europa Point, just north of the Strait of Gibraltar,

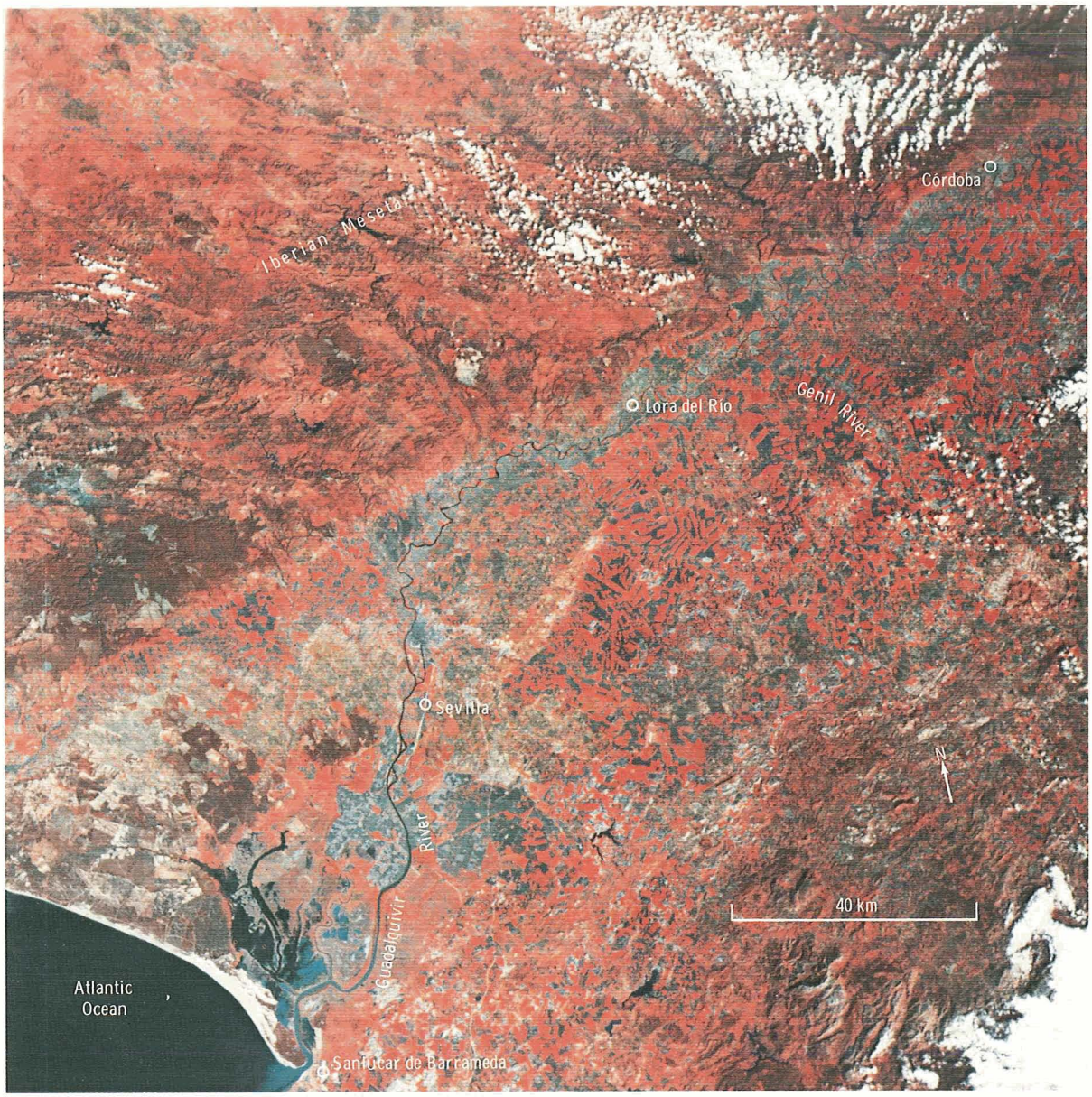


FIGURE 18.—Landsat vertical false-color image of the drainage basin of the Guadalquivir River northeast of Cádiz. Note the tonal and pattern suggestions of fold extensions from the Iberian Meseta into the Guadalquivir Basin; also the prominent physiographic discontinuity between the river basin and the Iberian Meseta. Several other prominent east- and northeast-trending lineaments are also present (E-1228-10334).

eastward and includes the Serranía de Ronda, Sierra Nevadas, Sierra de los Filabres, and other ranges of southern Spain. The belt extends eastward under the sea beyond Almería.

North of the Strait of Gibraltar, numerous folds of west-southwest trend bend sharply southward (fig. 16). These folds and related second-order folds cross the Strait of Gibraltar and become part of the Rif of northern Africa. Both regional geologic and tectonic maps indicate that these folds bend sharply eastward and become part of the Atlas orogenic belt of the African continent

(figs. 1 and 11). The older crystalline rocks exposed in this folded zone of southern Spain are indicative that this major first-order fold zone is antiformal in nature.

The village of Huéscar, Spain, is immediately northwest of the axis of another first-order fold (figs. 15 and 17). This fold is somewhat modified by faulting and is smaller than other first-order folds. Linears and fold axes bend sharply around the nose of the folded-fold zone. The broad axial zone trends slightly north of east for well over 150 km. The width of the first-order fold belt exceeds 70 km. A fold of similar trend lies 35 km south-southeast of Valencia.

Four first-order folds occur west and north of Valencia. Though these are not as well expressed, the Seismic and Structural Map of Spain (ref. 3) substantiates the imagery interpretation. An antiformal first-order fold appears to be present northwest of Valencia where the fold belt changes from an eastward to northwestward trend. This fold zone is continuous for several score kilometers. The other first-order folds occur just beyond the map boundary to the north of Valencia. Here the northernmost fold belt of northwesterly trend turns eastward into the sea.

Second-Order Folds

Second-order folds are of much smaller size than the first-order folds. Indeed, these are a component part of the first-order group. A fold belt consisting of anticlinoria and synclinoria comprises the second-order folds shown on the map (fig. 15). These are, in fact, the limbs of the larger first-order folds.

Although the second-order folds are shown as a single line symbol on the map, they actually represent several parallel anticlinal and synclinal folds. The large upfolds of the Sierra de Segura, the Sierra de los Filabres, and the Sierra Nevada are representative of the second-order fold. These fold zones extend more than 100 km in length and may be 10 or more kilometers in width.

Such second-order folds are believed to be present in the Iberian Meseta to the northwest. The imagery suggests a system of northwesterly trending second-order folds of up to 100 or more kilometers in strike length and major axes 10 or more kilometers apart. The uniqueness of this system of folds is their relatively consistent northwesterly trend with little or no tendency to develop into first-order folds. There is a slight suggestion, from tonal and pattern differences observable on the images, that some renewed movement on these fold zones has slightly affected younger sediments in the province along the Guadalquivir River. In particular, the color composite Landsat image shows a relatively clear outline of what may be a very broad northwesterly-trending doubly-plunging fold buried under the younger rocks. The eastern flank of the fold appears to be the locus of a strike valley for the Genil River (figs. 15 and 18).

Third-Order Folds

The third-order folds are single anticlines and/or synclines. Generally only a few kilometers in strike length, some third-order folds do extend to 70 km or more. These are abundant throughout the region. Perhaps their best expression is in the area north of Alicante and also to the west near Huéscar.

Faults

Both thrust faults and normal faults occur in the region (fig. 14). The thrust faults, described in the literature and on geologic maps, are well expressed on the Landsat images in the southern part of the Betic Cordillera. They are also present near Pozo Alcón and northward. Others are visible far to the west and just north of the Strait of Gibraltar in the vicinity of the first-order fold nose. Here and elsewhere there appears to be a general relationship between fold axis directions and the strikes of the thrust faults. Displacements along the thrust faults are not known, nor can they be determined directly from the images.

In the Sierra Nevada, prominent thrust faults occur both north and south of the range. The trend of the thrusts is generally east-west. At the western end of the Sierra Nevada the thrusts appear to converge. This suggests either a single

thrust zone underlying the mountain or an eroded drape thrust sheet over it.

Many normal faults, and possibly some reverse faults, are present in the region. The best expressed normal faults occur south of the Jucar River approximately 10 km south of Casas Ibáñez. Here a series of normal faults of similar strike result in at least three prominent grabenlike structures. One of these extends at least 50 km in strike length. Other normal faults occur to the southwest and have a similar strike. Some linear features on the map (fig. 14) may actually be faults of relatively steep dip. Lacking visible displacements, however, these structures have been identified as lineaments.

Lineaments

Two orders of lineaments are identified on the images (figs. 14 and 19). On the images, each of the first-order lineaments is characterized by a broad band of tonal difference and shows a distinctly elongate trend across the region (fig. 20). The first-order lineaments always contain narrower and shorter second-order lineaments.

As Hobbs (refs. 22 and 23) recognized earlier in the century, the first-order lineaments are composite features in both the structural and geomorphic sense. This composite nature has probably disguised many of the major lineaments locally, and they have therefore not been recognized in geological surveys.

The second-order lineaments are usually quite narrow and almost linelike in expression (figs. 17 and 18). These consist of similar tonal alinements of visible linear patterns in the exposed rock masses, but lack readily recognizable planar characteristics.

First-Order Lineaments

The larger and more prominent first-order lineaments, because of their size, are almost bandlike features. These are best demonstrated on the detailed interpretive map of southeast Spain (fig. 19). They are expressed on the ASTP color photographs by distinct tonal differences; either light tan to orange-brown bands or dark greenish-gray bands (fig. 20).

Invariably, these major lineaments are zones containing narrower, shorter lineaments. The major lineaments have lengths up to 200 km and widths up to 12 km. The most prominent first-order lineament in southeastern Spain is one that trends east-northeast from an area 4 km south of Huéscar. It has a width of up to 10 km and a length that extends across the width of southeast Spain (figs. 14 and 19).

First-order lineaments occur in at least five sets based on their strike: north-northeast, north-northwest, northwest, east-northeast, and west-northwest. These sets of lineaments suggest generalized north-south and east-west sets on which a northwest set is superimposed. The observed north-northeast lineament set may be the Rhinish lineament, which according to Pilger (ref. 24, p. 556), crosses Europe *en echelon* from Spain to Scandinavia.

Second-Order Lineaments

The second-order lineaments are abundant and locally quite conspicuous on Landsat images (figs. 17 and 18), but less well shown on ASTP color photographs. The second-order lineaments have shadowing of linear form on the images, alinement of vegetation, and may also follow straight portions of streams. They are expressed by similar tonal differences and by other linear characteristics such as fractures, angular drainage patterns, elongated lakes, and linear trends of topographic highs—particularly ridges.

The second-order lineaments are more abundant than the first-order lineaments, but are much smaller. Lengths range from approximately 20 km or less to 50 km. Widths are from fractions of a kilometer to approximately 1 km.

Major first-order lineaments always contain second-order lineaments. In at least three areas of southeastern Spain, second-order lineaments occur in large numbers and in relatively tight, sheaflike groups. Horsetail-like patterns are fairly common within these groups (figs. 14 and 19) and, indeed, they locally resemble, on a very large scale, the much smaller scale horsetail structures of the Butte mining district (ref. 25).

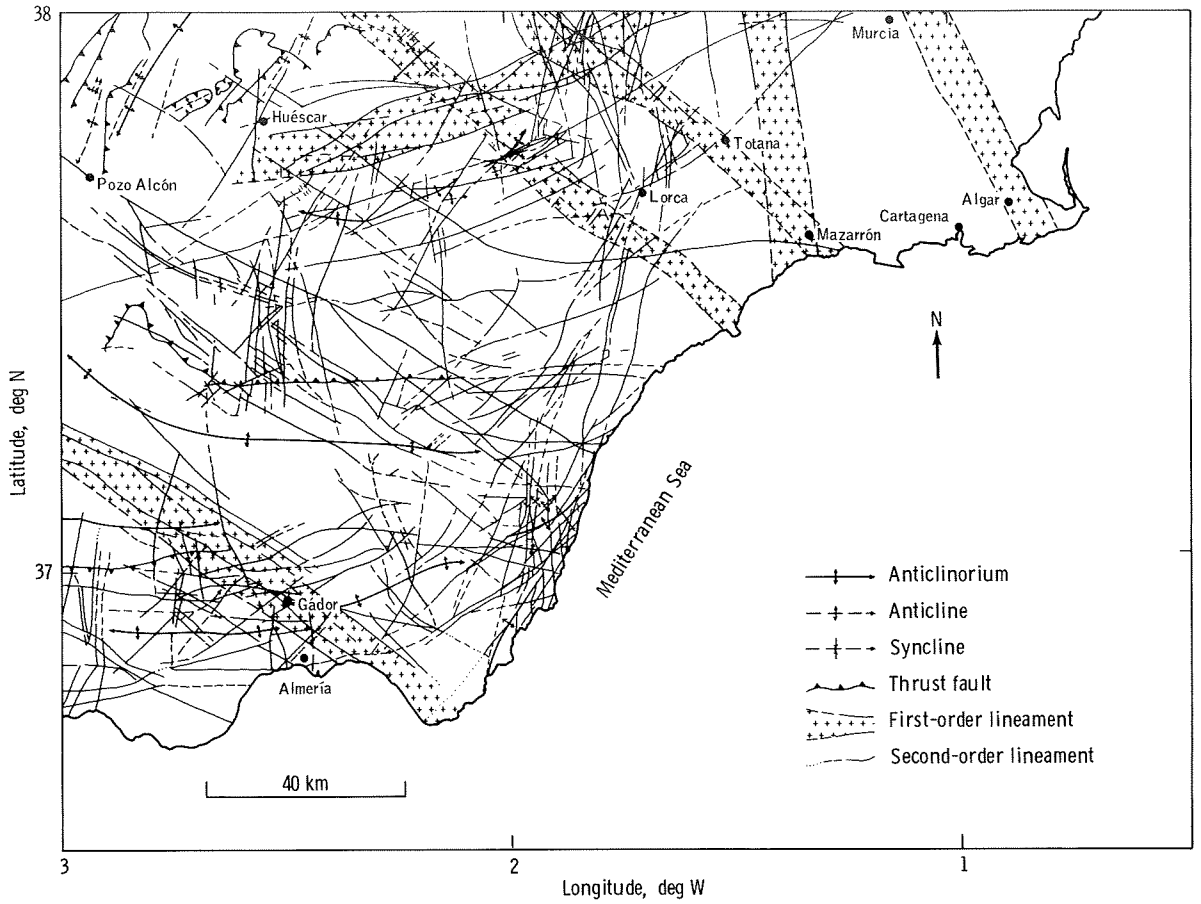


FIGURE 19.—Photointerpretative tectonic map of the southeastern Betic Cordillera.

Two dominant sets, a northwest and a northeast, characterize the second-order lineaments, although other trends are present. Examples of the northwest set and the horsetailing groups occur in the vicinities of Gádor, Purchena, Cabra, and Iznalloz as well as about 30 km north-northeast of Húescar. Good examples of the northeast set and associated horsetail types occur approximately 57 km north-northwest of Murcia.

TECTONIC INTERPRETATION

Folds

At least seven first-order folds are indicated in southeastern Spain (fig. 15). These features include the nose of a possible synform near Huéscar, a poorly recognized antiform northwest of Alicante, and a better developed synform west of Valencia. Other first-order folds occur north of Valencia. The largest first-order fold has a nose in the Strait of Gibraltar, and the northern limb parallels the southern coast of Spain. Each of the first-order folds trends generally westward; but, in detail, the southernmost fold zone trends generally east-west and the northernmost ones bear northwest. A structural discontinuity is apparently present between these two fold systems. The first-order fold zones are approximately 120 km across and have lengths measured in excess of 260 km (fig. 15).

The largest first-order fold, a type of orocline, consists of the Sierra de los Filabres, Sierra Nevada, Alpujarrides, Málaga nappe, and Rondaïdes of Spain; also the Rif and at least part of the

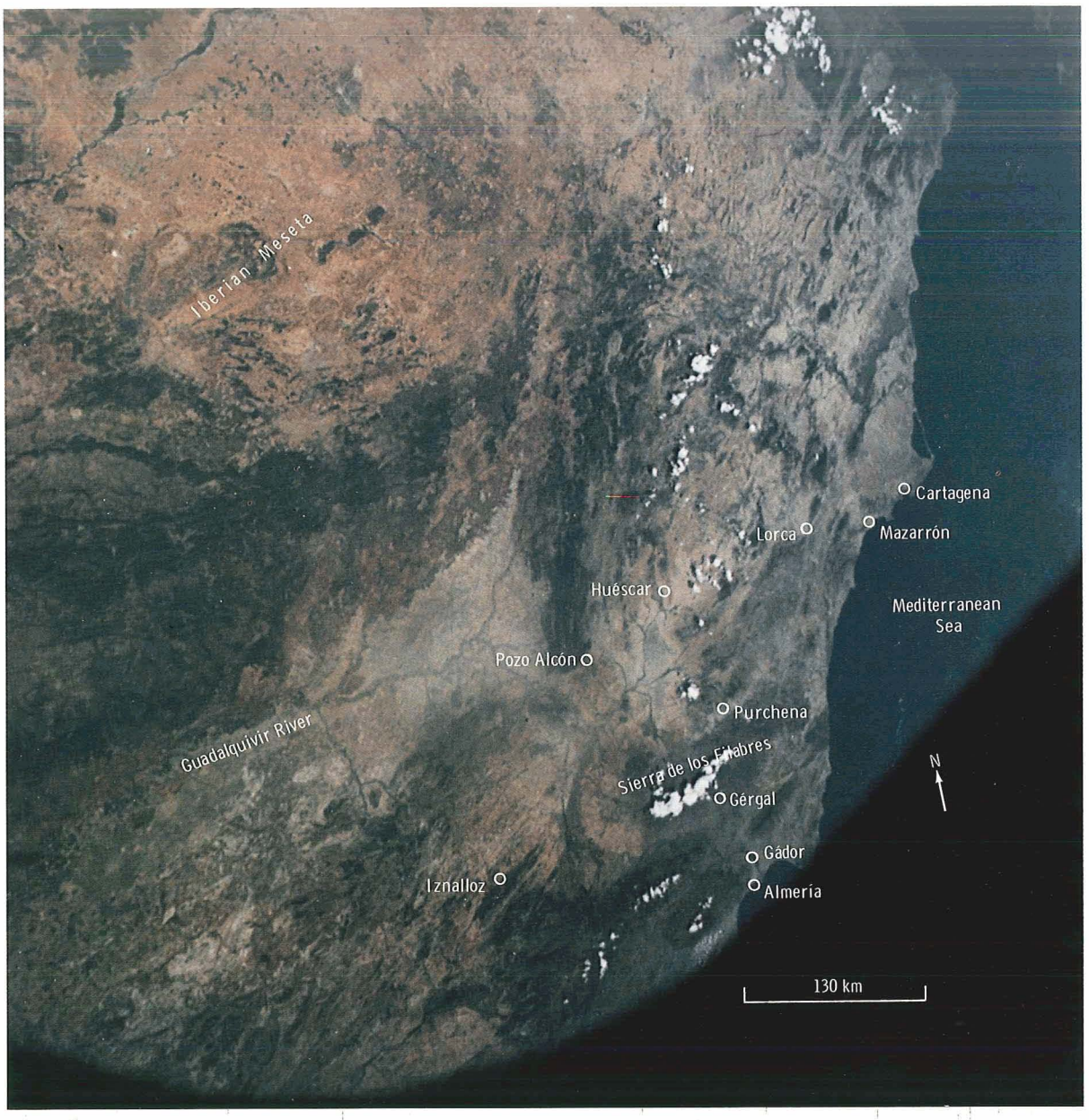


FIGURE 20.—An ASTP oblique color photograph of southeastern Spain showing the large light tan to orange-brown and dark greenish-gray bands interpreted as first-order lineaments (AST-27-2371).

Atlas range of Africa. The northern flank of this southernmost fold zone trends almost parallel to the east-trending southern coast of Spain. At its westernmost expression, the flank bends sharply southward, crosses the Strait of Gibraltar, continues into the Rif area (fig. 16), then bends eastward and becomes part of the Atlas range of north Africa (figs. 1 and 15).

Analysis of the images, photographs, and published research suggests that a major structural break occurs between the more crystalline Sierra-Nevada/Sierra-de-los-Filabres and the first-order

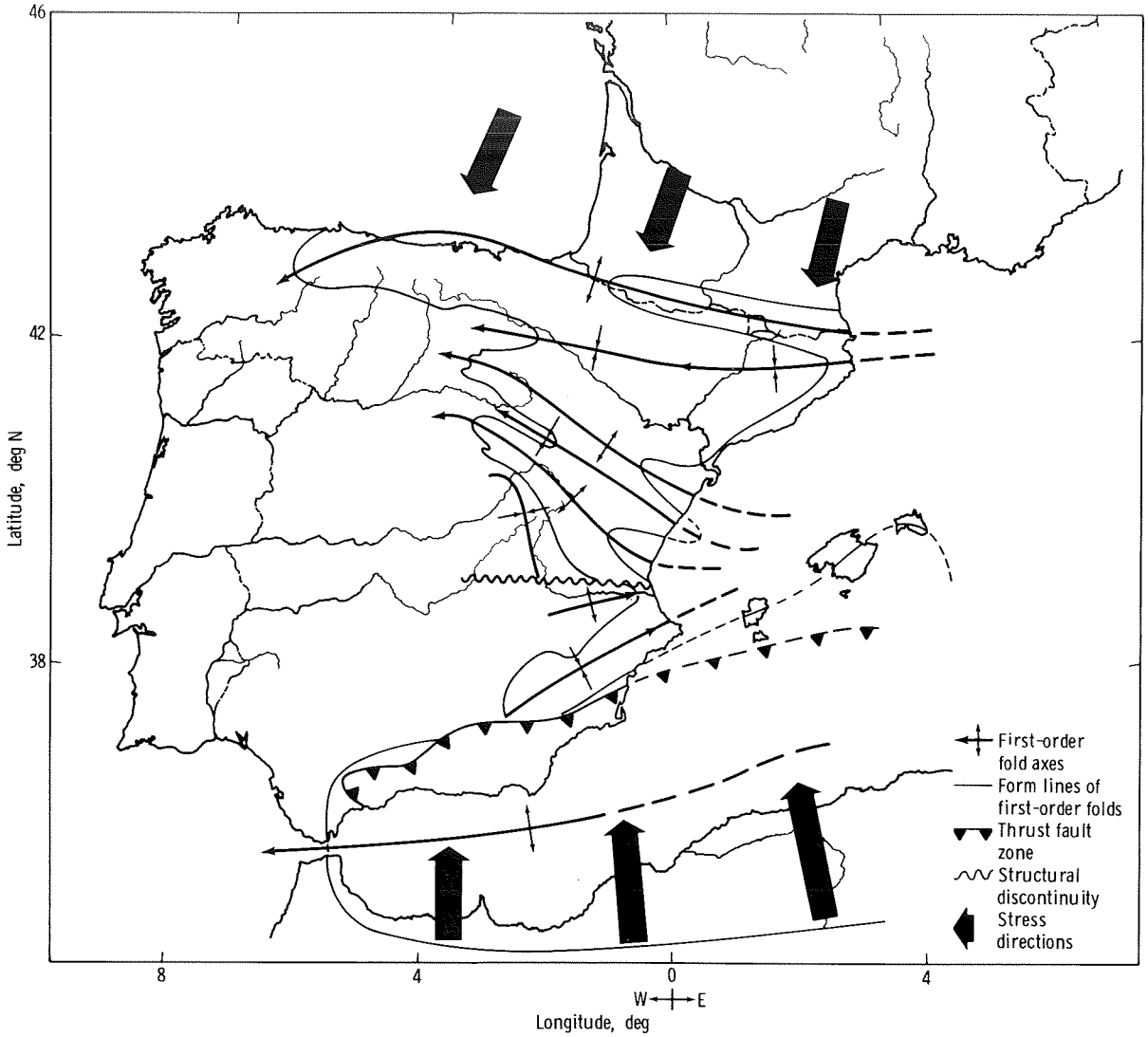


FIGURE 21.—Interpretive tectonic setting and stress environment for the first-order folds of Spain and part of north Africa.

synform of the Huéscar area to the north (figs. 14, 15, and 17). If this is true, then the first-order folds are more readily explained for this region.

Numerous geologists have considered and discussed the trends and possible connections of the Alpine fold belts of southern Europe and north Africa. Some of these possible relationships are suggested in the interpretations shown in figure 10 (Rutten, ref. 1). Of these, Stille's concept most reasonably matches the tectonic features now known.

This photointerpretation suggests that the Rif mountain system and the fold-ranges of southern Spain connect through an orocline across the Strait of Gibraltar (figs. 15 and 16). The northern part of the orocline, or major first-order fold, continues eastward into the Mediterranean. The studied images do not cover the Balearic Islands with sufficiently good resolution to define the structural grain. Freeman and Obrador (ref. 26), however, suggest that Mallorca and Menorca are on trend. They could be a part of the Betic struc-

tures in southern Spain. The main Betics could continue more eastward, then bend northward through Corsica, then trend westward as part of an orocline to become the Pyrenees of Spain and France (fig. 10).

The proposed model places the somewhat smaller first-order folds, noted earlier, between the megalimbs of the Pyrenees and the Betic Cordillera. These first-order fold zones are of large size, but they have the structural setting of megadrag folds caught between the northern, or Pyrenees, limb of the orocline and the southern limb or Betic Cordillera of southern Spain (fig. 21).

The time framework leading to these remarkably large Earth folds is not readily decipherable from the images. The tectonic features, however, pose some most interesting genetic possibilities. Assuming that continental drift and Earth plates are factual, the motion of the large African plate offers a logical source for the stress fields required to develop the known tectonic features expressed in the space images.

Dietz and Holden (ref. 27) suggest an early counterclockwise motion for the Iberian Peninsula at the end of Jurassic time, resulting in the formation of the Bay of Biscay; Africa, with more rapid counterclockwise motion, moved farther northward in its eastern part and tended to close the Tethyan seaway.

Later motion of the Iberian subplate to the southeast and the continued northward movement of the African plate may have provided a slow "jaw crusher" action of sufficient magnitude to develop the embryonic, major, first-order folds of the Atlas, Betic Cordillera, and Pyrenees mountain systems. Continued slow plate movement occurred. Erosion and deposition proceeded contemporaneously within the plate. The sedimentary rock section of southeastern Spain was caught between the slowly closing jaws of the larger Earth folds, and the rock section compressed. A series of smaller first-order folds developed together with thrust faults, probable gravity slides, and other shear phenomena under this stress environment. While simplistic in presentation, the plate-drift concept does give a basis for an explanation of these major Earth structures in southeastern Spain.

Faults

Under the postulated stress field noted here, the more competent rock units in the sedimentary rock section were thrust faulted, mainly northward. Décollements also developed in parts of the area. A major thrust zone probably developed between the Sierra-Nevada/Sierra-de-los-Filabres block and the first-order fold near Huéscar during the compressional stage of the orocline or major first-order fold development.

Tensional faults may have developed within the Strait of Gibraltar at a somewhat later time (figs. 14 and 16). Grabenlike structures also developed approximately 90 km northwest of Alicante. These fault structures trend mainly east-west and cut across compressional structures (fig. 14). These structures may have resulted from relaxation of the compressional stresses, or from a change in plate movement with tensional stresses dominating.

Lineaments

While the folds and thrust faults can possibly be explained by the genesis suggested, the numerous lineaments within this large region may have resulted from somewhat different stress conditions.

Two different systems of lineaments are recognized in the region: (1) a rectilinear system made up of generally northerly and easterly trending sets and (2) an acute angle system of almost diagonal character to the first group with the northwesterly trending set the most prominent, and a less developed northeasterly trending set.

The first-order lineaments extend scores to hundreds of kilometers in length across folded and unfolded terrain usually without visible disturbance of the folded or faulted structures, or of the lineaments themselves. Lack of apparent relationships to other known tectonic features is somewhat enigmatic.

The rectilinear system is well shown in figure 14 and also in the more detailed map of figure 19. Sonder (ref. 28) has called these repeating lineaments the "regmatic shear pattern." Four major trends have been recognized: northerly (merid-

ional), easterly (equatorial), northwesterly, and northeasterly. The latter are usually the more common, though not so in southeastern Spain.

Many authors have described the regmatic pattern of lineaments in various parts of the world. In North America, descriptions are provided by Mayo (ref. 29), Wisser for the Cordillera (ref. 30), Vernon for Florida (ref. 31), Fisk (ref. 32) for the lower Mississippi Valley, El-Etr (ref. 33) for southeast Missouri, and Kisvarsanyi (ref. 34) for the overall state of Missouri, among others. In Canada, Wilson (ref. 35), Blanchet (ref. 36), Mollard (refs. 37 and 38), and Haman (ref. 39) describe such features. In Europe, Umbgrove (ref. 40), Cloos (ref. 41), and Sonder (ref. 28) report on similar features, whereas Hills reports on lineaments from Australia (ref. 42). Sonder (ref. 28) also reports on the Atlantic and Mediterranean basins. Earlier, Vening Meinesz (ref. 43) suggested a worldwide shear net.

Mollard clearly outlines certain requisites for the development of regional lineament patterns including a great span of time, continuous simple mechanism extending downward many kilometers from the surficial materials, differential adjustments absent or small along lineaments, and a mechanism of worldwide extent, yet with possible greater local intensity.

Several theories have been proposed to explain lineament development, including displacement of the rotational poles in early Earth history (Vening Meinesz, ref. 43). Sonder (ref. 28) and Umbgrove (ref. 40) questioned the magnitude of the displacement of the Earth's rotational axis. Moody and Hill (ref. 44) suggest several types of stress responsible for the regmatic pattern: (1) subcrustal convection currents with preferred orientation acting in a meridional direction, (2) compressional stresses from diurnal rotation of the Earth, and (3) secular compression from cooling and contraction. They suggest large north-south components of stress and other forces.

P. H. Blanchet (from Colwell, ref. 45) points out that four stress fields are of primary importance: (1) north-south rotational stresses resulting from the departure of the Earth from a circular revolution about the Sun and resulting from the variation in the shape of the Earth, (2) east-west rotational stress from the tendency of certain annular segments of crust to migrate east faster than adjacent segments, (3) tidal stresses of significant repetitive nature, and (4) stresses caused by the difference in elasticity of the Earth's crust (approximately 20 to 30 percent less elasticity for the north-south direction than for the east-west direction).

Haman (ref. 46) suggests two general stress fields; i.e., internal or tectonic forces and external oscillatory forces or Earth tides. Internal forces should cause variations in the worldwide pattern. An external force should yield a rather similar worldwide pattern. The internal stress field can also be imposed upon the internally generated fracture systems.

In southeastern Spain, the almost rectilinear pattern strongly resembles the regmatic patterns just described. These do not depart too much from Vening Meinesz's (ref. 43) shear net. It does not follow, however, that his suggested origin is applicable.

Whatever the basic cause of the lineaments, they are not restricted in time or space in this region. The stress environment must have been generally uniform (with some local variations possible because of rock types) and continuous to the present. Only tidal forces appear to meet the requirements for the regmatic lineament pattern.

The sheaflike pattern of lineaments shows intersections of individual lineaments at less than 90°. The acute angle generally faces southward. This suggests a principal stress orientation northward. These lineaments could be shear fractures. Their abundance and location could be dependent on local rock competency and reaction to the stress field.

GROUND-TRUTH INVESTIGATIONS

The complexity of the geological terrain of southeastern Spain and the small scale of the images made interpretation difficult, and in some cases quite tenuous. The original maps presented in figures 14, 15, and 19 illustrate the observed geologic structures. Factual observations are the linears, or line/planar features, some faults, and the lineaments. The smaller fold axes and the positions of first-order fold axes are more in-

terpretive, but are based on the most rigorous observations.

For such a region of complex geology, ground-truth investigations of certain critical areas are recommended. Eight such areas have been selected for field review to confirm, modify, or refute the postulated geological interpretation.

1. In the Huéscar area, check the interpretation of a first-order fold nose in this area, and review field expression of a prominent first-order lineament just south of Huéscar. The lineament may represent part of the major structural discontinuity between the Huéscar block and the Sierra de los Filabres to the south. At the same time, review the closely spaced second-order lineaments in this area and their relationship to the westerly and northerly lineament sets.

2. Ground check the presumed thrust zone expressed from Lorca through Iznalloz.

3. In the area 28 km northeast of Gérgal, resolve the characteristics of the closely spaced lineaments and their relationship to the thrust zone. Are the lineaments actually strike-slip faults that displace the thrust fault? Resolution of these structures would have application to similar areas of lineaments such as near Gádor, Almería, Iznalloz, and other localities.

4. At Mazarrón, in the southeast part of the region, two first-order lineaments cross each other. At this intersection, several mines and/or prospects are shown on the base maps of the area. The field study would yield information on the makeup of the first-order lineaments, possibly determine the structural control of the mineral deposits, and define relationships, if any, to the lineaments.

5. In the northeastern part of the study area, grabenlike structures south of Casas Ibáñez need field review. Field investigations would confirm or refute the interpretation and would yield useful information on fold-fault relationships in the area. A field check should also be made of the regional character of the northwest-trending first-order fold that passes through the Casas Ibáñez area.

6. Southeast of Lora del Río, in the western part of the region, a southeasterly trending second-order fold of the Iberian Meseta appears to be expressed in the younger sediments of the Guadalquivir Basin. Similar expressions on the Landsat images occur east-northeast and west-southwest of Lora del Río. The field work would confirm or modify the concept of renewed upwarping in the area and provide a better understanding of the interface between the Iberian Meseta and younger sedimentary rock.

7. Very interesting and complex geology is present in the Strait of Gibraltar area. Folds, thrust faults, and possibly grabenlike faults occur on both the European and African sides of the strait. The field study would yield critical information on the character of the nose of the large orocline, or first-order fold. Details on the characteristics of second- and third-order folds could also be obtained. The interrelationships of the fold orders, thrust faults, and possible graben structures could also be resolved. Review of the African side of the first-order fold would test the proposed continuation of the Betic zone across the Strait of Gibraltar.

8. The Balearic, Sardinia, and Corsica islands may well hold the key to testing the validity of the proposed major first-order fold from the Pyrenees eastward, thence southward and southwesterly to join the Betic Cordillera of southeastern Spain. A more detailed photogeologic review of these islands followed by field investigations would yield significant data on the problem. Recent favorable developments in petroleum exploration in this region suggest that this area is one of high interest.

CONCLUSIONS

Analysis of ASTP color photographs and Landsat images of southeastern Spain reveals four major tectonic provinces: (1) an unfolded to slightly disturbed reentrant northeast of Cádiz, (2) a broadly folded and somewhat faulted area of sedimentary rocks north and west of Alicante, (3) intensely folded and faulted rocks in southernmost and southeastern Spain, and (4) a less-studied northwesterly-trending series of older folds and rocks northwest of the Guadalquivir River.

In the folded areas of southeast Spain, well-expressed linears help define noses and axial trends of folds. Three orders of folds are recognized (first, second, and third). The first-order

folds are scores of kilometers across and up to hundreds of kilometers in length. Second-order folds are components of the first-order group and consist of synclinoria and anticlinoria. Third-order folds are individual anticlines and synclines of much smaller dimension than the other two orders. Some first-order folds may be equivalent to major oroclines, such as one expressed by the Atlas/Rif/southern-Spain ranges. Associated with the fold orders are numerous thrust, shear, and tensional faults. Some décollements are also present in the region associated with evaporite-type rock units.

Rather distinctive and fairly well-developed systems of lineaments are omnipresent in the region. Each system includes two or more sets. First- and second-order lineaments are also identified and classified on the basis of size and continuity.

Folds and faults owe their origin to compressive and tensional stresses developed in the area. A major compressional stress environment generated by a counterclockwise-rotating Iberian subplate together with a more rapidly, northerly, counterclockwise-moving African plate resulted in slowly closing jaws. Between the two closing plates, a series of smaller first-order folds developed together with thrust faults and other shear phenomena. Later relaxation of the stress, or change in direction of plate movement, brought about a tensional environment; and normal and graben faulting occurred in the region. The Strait of Gibraltar shows characteristics of such faulting.

Lineaments of large (first-order) and smaller (second-order) size are abundantly present throughout the region. These lineaments cut across folded and unfolded terrain, and they show little or no visible disturbance of rock units or of other cross-cutting lineaments. A rectilinear pattern and a somewhat diagonal pattern are clearly visible.

Of numerous genetic theories suggested, the rectilinear pattern best relates to crustal tidal forces as the cause. The somewhat diagonal pattern, with an acute angle southward, may be the result of principal northerly acting stresses. Local variations in the diagonal pattern may have resulted from differences in rock unit competencies.

Ground-truth investigations are recommended to confirm, modify, or refute major interpretations of this regional study. Though the maps are interpretive, the basic data for the study area were obtained at a cost of approximately 4 cents per square kilometer. Actual time costs approximated 7 cents per square kilometer.

ACKNOWLEDGMENTS

This work was performed under Smithsonian Institution Grant PC6-22279 as a subcontract of NASA contract NAS9-13831.

REFERENCES

1. Rutten, M. G.: The Geology of Western Europe. Elsevier Publishing Co., 1969.

2. Rowan, Lawrence C.: Application of Satellites to Geologic Exploration. American Scientist, vol. 63, no. 4, 1975, pp. 393-403.

3. Mapa Sismoestructural de la Peninsula Iberica, Baleares y Canarias, scale 1:1 000 000. Inst. Geolog. Min. España & Inst. Geograf. Catastral (Madrid), 1966.

4. International Geologic Map of Europe 1:1 500 000, No. A6. International Geological Congress, Bundesanstalt für Bodenforschung, Germany, and UNESCO (Paris), 1973.

5. International Geologic Map of Europe 1:1 500 000, No. B6. International Geological Congress, Bundesanstalt für Bodenforschung, Germany, and UNESCO (Paris), 1973.

6. Fallot, Paul: Les Cordillères Bétiques. Estudios Geol. (Inst. Invest. Geol. "Lucas Mallada," Madrid), no. 8, 1948, pp. 83-172.

7. MacGillavry, H. J.: Speculations Based Upon a Comparison of the Stratigraphies of the Different Tectonic Units Between Vélez Rubio and Moratalla. Geol. Mijnbouw, vol. 43, no. 7, 1964, pp. 299-309.

8. MacGillavry, H. J.; Geel, T.; Roep, T. B.; and Soediono, H.: Further Notes on the Geology of Málaga, the Subbetic and the Zone Between These Two Units in the Region of Vélez Rubio (Southern Spain). Geol. Rundschau, vol. 53, 1964, pp. 233-259.

9. Rondeel, H.: Geological Investigations in the Western Sierra Cabrera and Adjoining Areas, Southeastern Spain. Thesis, Univ. Amsterdam, 1965.

10. Egeler, C. G.: On the Tectonics of the Eastern Betic Cordilleras (SE Spain). Geol. Rundschau, vol. 53, 1964, pp. 260-269.

11. Fernex, Francois: Essai de Corrélation des Unités Bétique sur la Transversale de Lorca-Aquilas. Geol. Mijnbouw, vol. 43, no. 7, 1964, pp. 326-330.

12. Durand Delga, Michel; and Fontboté, J. M.: Le Problème de l'âge des Nappes Alpujarrides d' Andalousie. Rev. Géog. Phys. Géol. Dyn., vol. 3, no. 4, 1960, pp. 181-187.

13. Nijhuis, H. J.: Plurifacial Alpine Metamorphism in the Southeastern Sierra de los Filabres, South of Lubrin, Southeast Spain. Thesis, Univ. Amsterdam, 1964.

14. Fallot, P.: Comparaison entre Cordillères Bétiques et Alpes Orientales. Bol. Soc. Real. Españ. Hist. Nat., Tormo Extraordinario 80 Aniv. Prof. Ed. Hernandez-Pacheco, 1954, pp. 259-279.

15. Hoeppener, R.; Hoppe, Peter; Dürr, Stefan H.; and Mollat, H.: Ein Querschnitt durch die Betischen Kordilleren bei Ronda (SW Spanien). Geol. Mijnbouw, vol. 43, no. 7, 1964, pp. 282-298.

16. Hoeppener, R.; Hoppe, P.; et al.: Über den Westlichen Abschnitt der Betischen Kordillere und Seine Beziehungen zum Gesamtorogen. Geol. Rundschau, vol. 53, 1964, pp. 269-296.

17. Durand Delga, M.; Hottinger, L.; et al.: Donneés Actuelles sur la Structure du Rif. Livre à la Mémmoire du Professeur Paul Fallot Consecré à l'évolution Paleogeographique et Structurale des Domaines Mediterranéen et Alpins D'Europe, Michel Durand Delga, ed., Geol. Soc. France (Paris), t. 2, 1962, pp. 399-422.

18. Brinkmann, Roland: Aperçu sur les Chaînes Ibériques du Nord de l'Espagne. Livre à la Mémmoire du Professeur Paul Fallot Consecré à l'évolution Paleogeographique et Structurale des Domaines Mediterranéen et Alpins D'Europe, Michel Durand Delga, ed., Geol. Soc. France (Paris), t. 1, 1962, pp. 291-300.

19. Riba, Oriol; and Ríos, J. M.: Observations sur la structure du Secteur Sud-ouest de la Chaîne Ibérique (Espagne). Livre à la Mémmoire du Professeur Paul Fallot Consecré à l'évolution Paleogeographique et Structurale des Domaines Mediterranéen et Alpins D'Europe, Michel Durand Delga, ed., Geol. Soc. France (Paris), t. 1, 1962, pp. 275-290.

20. Virgili, C.: El Triássico de los Catalánides. Bol. Inst. Geol. Minero Españ., vol. 69, 1958.

21. Carey, S. Warren: A Tectonic Approach to Continental Drift. Continental Drift: A Symposium, S. W. Carey, ed., Univ. of Tasmania (Hobart), 1958, pp. 177-355.

22. Hobbs, W. H.: Lineaments of the Atlantic Border Region. Bull. Geol. Soc. America, vol. 15, 1904, pp. 483-506.

23. Hobbs, W. H.: Repeating Patterns in the Relief and in the Structure of the Land. Bull. Geol. Soc. America, vol. 22, 1911, pp. 123-176.

24. Pilger, A.: The Importance of Lineaments in the Tectonic Evolution of the Earth's Crust and in the Occurrence of Ore Deposits in Middle Europe. Proceedings of the First International Conference on the New Basement Tectonics, Utah Geol. Assoc., no. 5, 1976, pp. 555-564.

25. Sales, R. H.: Ore Deposits of Butte, Montana. AIME Trans., vol. 46, 1914, pp. 3-109.

26. Freeman, Tom; and Obrador, Antonio: Is There a Structural Discordance Between Mallorca and Menorca? Tenth International Field Institute Guidebook: Spain, Tom Freeman and Antonio Obrador, directors, American Geol. Inst., 1971, pp. 149-152.

27. Dietz, Robert S.; and Holden, John C.: Reconstruction of Pangaea: Breakup and Dispersion of Continents, Permian to Present. J. Geophys. Res., vol. 75, no. 26, 1970, pp. 4939-4956.

28. Sonder, R. A.: Discussion of "Shear Patterns of the Earth's Crust" by F. A. Vening Meinesz. Trans. American Geophys. Union, vol. 28, no. 6, Dec. 1947, pp. 939-945.

29. Mayo, Evans Blakemore: Lineament Tectonics and Some Ore Districts of the Southwest. Mining Eng., vol. 10, no. 11, Nov. 1958, pp. 1169-1175.

30. Wisser, Edward Hollister: Deformation in the Cordilleran Region of Western United States. Colo. Sch. Mines Quart., vol. 52, no. 3, July 1957, pp. 53-73.

31. Vernon, Robert Orion: Geology of Citrus and Levy Counties, Florida. Fla. Geol. Surv. Bull., no. 33, 1951.

32. Fisk, Harold Norman: Geological Investigation of the Alluvial Valley of the Lower Mississippi River. U.S. Mississippi River Commission (Vicksburg, Miss.), Dec. 1, 1944.

33. El-Etr, Hassan A.: The Technique of Lineaments and Linears Analysis and Its Application in the Minerogenic Province of Southeast Missouri. Ph. D. dissertation, Univ. of Missouri at Rolla, 1967.

34. Kisvarsanyi, Geza; and Kisvarsanyi, Eva B.: Ortho-Polygonal Tectonic Patterns in the Exposed and Buried Precambrian Basement of Southeast Missouri. Proceedings of the First International Conference on the New Basement Tectonics, Utah Geol. Assoc., no. 5, 1976, pp. 169-182.

35. Wilson, J. Tuzo: Some Aspects of Geophysics in Canada With Special Reference to Structural Research in the Canadian Shield; Part 2, An Approach to the Structure of the Canadian Shield. Trans. American Geophys. Union, vol 29, no. 5, Oct. 1948, pp. 691-726.

36. Blanchet, P. H.: Development of Fracture Analysis as an Exploration Method. Bull. American Assoc. Petr. Geol., vol. 41, no. 8, 1957, pp. 1748-1759.

37. Mollard, John Douglas: Photogeophysics—Its Application in Petroleum Exploration Over the Glaciated Plains of Western Canada. Proceedings of Second Williston Basin Conference (Regina, Saskatchewan, Apr. 1958), Conrad Pub. Co. (Bismarck, N. Dak.), 1958, pp. 109-117.

38. Mollard, John Douglas: Aerial Mosaics Reveal Fracture Patterns on Surface Materials in Southern Saskatchewan and Manitoba. Oil in Canada, vol. 9, no. 40, Aug. 5, 1957, pp. 26-50.

39. Haman, P. J.: Geomechanics Applied to Fracture Analysis on Aerial Photographs. Calgary West Canadian Res. Pubs., series 2, no. 2, 1964.

40. Umbgrove, Johannes H. F.: The Pulse of the Earth. Second ed. Martinus Nihoff (The Hague), 1947, pp. 294-320.

41. Cloos, Hans: The Ancient European Basement Blocks—Preliminary Note. Trans. American Geophys. Union, vol. 29, no. 1, Feb. 1948, pp. 99-103.

42. Hills, E. Sherbon: A Contribution to the Morphotectonics of Australia. J. Geol. Soc. Australia, vol. 3, 1956, pp. 1-15.

43. Vening Meinesz, F. A.: Shear Patterns of the Earth's Crust. Trans. American Geophys. Union, vol. 28, no. 1, Feb. 1947, pp. 1-61.

44. Moody, John Drummond; and Hill, Melvin James: Wrench Fault Tectonics. Bull. Geol. Soc. America, vol. 67, no. 9, Sept. 1956, pp. 1207-1246.

45. Colwell, R. M.: Manual of Photographic Interpretation. American Soc. Photogram., 1960.

46. Haman, Peter J.: Lineament Analysis on Aerial Photographs Exemplified in the North Sturgeon Lake Area, Alberta. Calgary West Canadian Res. Pubs., series 2, no. 1, 1961.

East-West Pervasive Lineaments in Central and Southeastern Spain

Mohamed A. Abdel-Rahman[a]

ABSTRACT

The lineament pattern of central and southeastern Spain was detected on photographs taken during the Apollo-Soyuz mission. The obliquity of these photographs made possible the recognition of previously unnoticed structures. The true color of the photographs also aided in identifying the lineaments.

Statistical analysis indicated that the lineament pattern was not random and must be caused by geological factors. Three lineament trends were identified. In decreasing order of significance, these were east-west, northeast, and northwest. Faults in this region were traced from a geological map, and their strikes were analyzed and found to include two preferred orientations, a northeasterly trend and a west-northwesterly trend; the first trend was more prominent.

Despite the partial dissimilarity of the lineament and fault trends, significant numbers of lineaments were either approximately parallel or approximately orthogonal to faults. Similarly, significant numbers of lineaments were associated with fold-axis orientations either in a parallel manner or in an oblique manner at angles between 30° and 45°. Results suggest that (with the exception of the east-west lineaments) a significant number of the mapped lineaments represent linear structural features related to those present on the geological map.

The existence of major east/west-trending lineaments, however, is a new and valuable addition to the structural geology of the region. Their photographic expression, morphology, and length characteristics suggest that they may be deep-seated faults, initially developed as thrusts and tectonically related to the north-south phases of the tangential compression that developed the east-west folding and thrusting of the Pyrenees Mountains. An alternative hypothesis relates these lineaments to the regmatic shear pattern of the Earth's crust.

INTRODUCTION

The Earth Observations and Photography Experiment of the Apollo-Soyuz mission provided another valuable source of information on the regional scenery of the Earth. Although both manned and unmanned space missions have provided a multitude of space photographs, some of which cover the same areas, repeated orbital photography from different aspects and using various systems is very useful in Earth studies. Because spacecraft altitudes, camera types, film/filter combinations, lens resolutions and focal lengths, areal coverage, and photoacquisition times differed appreciably among the various missions and slightly within each mission, the availability of different space photographs and images of one area will aid the study of subtle Earth features and phenomena. In addition, repeated photography of the same area on one or several missions is very useful for the study of temporal changes.

In the investigation reported here, photographs taken during the Apollo-Soyuz Test Project (ASTP) were used to study the lineament pattern

[a]Ain Shams University, Cairo, Egypt.

of central and southeastern Spain. The study area has a trapezoidal shape and is delimited by latitudes 36°15′ and 41°10′ north and longitudes 6°05′ west and 0°45′ east. The area is covered by five ASTP photographs (AST-27-2369 to 2373) taken with a 50-mm lens. The first two photographs were taken from an altitude of 221 km; the other three were taken from 222 km. The five photographs were acquired by a handheld 70-mm camera at noontime, when the illumination was maximum and the Sun angle was high. Although all five color photographs were oblique, there were appreciable differences in their angle of tilt.

One of the best uses of orbital photography is the mapping of regional fault and lineament patterns. In this respect, the superiority of space photographs over ordinary aerial photographs is due to the very small scale of space photographs, which provides synoptic views of fault and lineament traces. Hamilton (ref. 1), among many others, provided numerous examples of faults and lineaments that were detected for the first time on space photographs.

The objectives of this study were (1) to map the lineament pattern of the area, (2) to investigate the relationship between the lineaments and the structures on the geological map (ref. 2), and (3) to compare the patterns of faults and lineaments and formulate a hypothesis regarding the origin of these lineaments. No emphasis was placed on examining the association between lineaments and time-rock units, because the majority of lineaments appeared to continue from one time-rock unit to another; thus, the spatial distribution and orientation of these lineaments have no strong affiliation to any one time-rock unit.

The stratigraphy of the study area is complex, and the areal extent of any one rock type is commonly limited. Most of the sedimentary, metamorphic, and igneous rocks that outcrop in Spain are represented in the study area (ref. 2).

METHODOLOGY

A photolineament is defined as a natural linear feature that is identified on space photographs and images and is distinguished from adjoining areas by a linear contrast in tone (color) and/or texture.

The use of oblique space photographs in mapping lineaments has some advantages and disadvantages. The main advantages are (1) that oblique photographs show a more familiar, perspective view than do vertical photographs, (2) that oblique photographs accentuate relief (although in a distorted manner), which commonly enhances the appearance of subtle linear features, and (3) that, by covering large areas, oblique photographs provide synoptic views of linear features. The main disadvantage, however, is that oblique photographs are difficult to use in planimetric mapping, because no one scale is applicable for the entire photograph and, therefore, distortions of form, size, and orientation are introduced.

The five ASTP photographs of southern Spain were examined individually to identify the lineament patterns appearing in each. Best results were obtained when the photographs were viewed obliquely at low angles, because this method intensified tonal contrasts by reducing the scale of the photographs in a direction parallel to the line of sight (ref. 3). A fixed light source was oriented behind the line of sight, and the photographs were continually rotated during the process of identifying lineaments.

It was noticed that the clarity of individual lineaments varied from one photograph to another. Because all photographs were oblique, it is likely that variations in the handheld-camera tilt angle could affect the clarity of lineaments on the photographs.

Because photographs AST-27-2369 and AST-27-2370 were taken from an altitude higher than that of the other three photographs, these two photographs covered larger areas. Photograph AST-27-2370 was used for mapping the lineaments, whereas frame AST-27-2369 was included in this paper for illustration (fig. 1).

Because there was no available facility to accurately transfer the lineament pattern from the oblique ASTP photograph to a planimetric map, a less accurate method was used. This method involved the following steps:

1. A planimetric base map showing the shoreline, locations of the major cities, and major



FIGURE 1.—An ASTP photograph of central and southeastern Spain showing the predominance of east-west lineaments (AST-27-2369).

drainage lines was prepared from the geological map of Spain (ref. 2).

2. The photograph on which the lineaments were annotated (AST-27-2370) was projected onto the planimetric base map using a projector. The base map was mounted on a table that was fixed only at its center and could tilt freely as much as 45° in any direction. In this way, the Apollo-Soyuz oblique photograph was projected on the base map so that the obliquity of the photograph was eliminated on the tilted table.

3. It was not possible to match the whole base map with the photograph by fixing the table at one single tilted position. Therefore, the matching process was performed separately for each part of the map at which the amount and direction of tilt

was readjusted. Thus, each section of the projected ASTP photograph was separately matched with the respective part of the planimetric base map, and the traced lineaments were transferred from the photograph's projection onto the map.

It is worth noting that, because of the inherent inaccuracy involved in the applied methodology, this method does not result in very accurate positioning of the lineaments on the map. Since the tilt of photograph AST-27-2370 was toward the south, the maximum distortion would be expected for lineaments alined north-south; conversely, distortions in the east-west alinements should be negligible.

DATA ANALYSIS

Figure 2 shows the faults and folds in the study area simplified from the geological map, also the lineaments identified from ASTP photographs. Examination of this figure reveals the following.

1. Neither uniformity of density nor orientation of structures is found in the study area. The

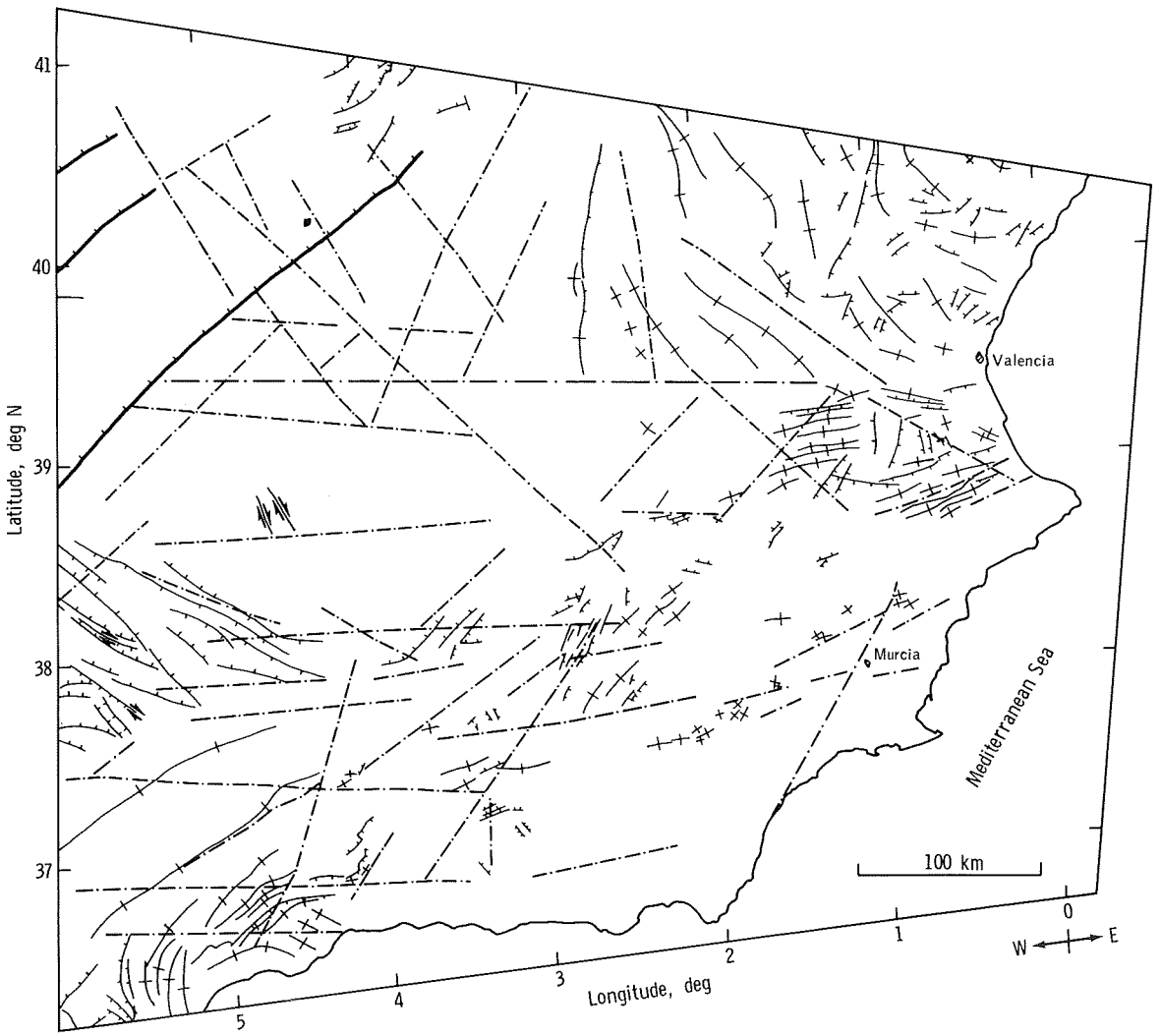


FIGURE 2.—Structural map of central and southeastern Spain as interpreted from frame AST-27-2370. Faults and folds from the geologic map (ref. 2) are shown, using conventional symbols, by thin solid lines. Faults that were also recognized as lineaments on the ASTP photographs are shown as thick solid lines. Other lineaments are shown as thick dashed lines.

northwestern part of the area is characterized by a few long, northeast (NE) trending faults without apparent folding. South and southwest of Valencia, narrow and linear belts of E-W folding are very prominent. The area near the intersection of latitude 38° north and longitude 5° west is characterized by a very dense pattern of NW thrusting. High folding intensity dominates the southwestern and northeastern corners of the study area.

2. Lineaments are also spatially variable in both density and length. In particular, most of the E-W trending lineaments are longer than the others.

3. No apparent association is seen between the density of faults and folds and the density of lineaments.

4. Where lineaments intersect, the angle of intersection commonly is approximately 45° or 90°.

5. The orientational relationships between faults and folds on the one hand and lineaments on the other hand are difficult to assess visually. However, it is clear that some lineaments are the linear continuation of mapped fault strikes. The majority of lineaments, however, are not exactly parallel or exactly orthogonal to fault strikes or fold axes.

The frequency distribution of trends for faults and lineaments, respectively, is shown in figures 3 and 4. Use of this type of graphical presentation of orientation data (the smooth-curve Cartesian histogram) was recommended by Gay (ref. 4). In addition, the statistical methodology of Hay and Abdel-Rahman (ref. 5) was used to identify the significant peaks in these frequency distributions. It was found that the frequency distributions of both faults and lineaments include significant peaks at the 95-percent significance level, and, accordingly, both distributions depart significantly from randomness. Two predominant fault trends are shown in figure 3: (1) a NE set that is significant at the 95-percent probability level and (2) a WNW set, mostly representing thrusts, having a statistical significance lower than 95 percent. The frequency distribution of lineament trends (fig. 4) reveals the presence of three main sets: an E-W set that is significant at the 95-percent probability level, a NE set that is also significant at the 95-percent level, and a NW set that is not significant at the 95-percent level.

Comparison of the orientation patterns of faults and lineaments (figs. 3 and 4) indicates that both patterns have a persistent NE trend, whereas the WNW-trending set of faults is not matched by lineaments. Instead, two sets of lineaments oriented E-W and NW were observed. Deductions regarding the relationship of folds, faults, and lineaments could be erroneous if based solely on the visual comparison of orientation patterns. A method that was especially designed for investigating the orientation association of variables (ref. 6) was used in the analysis reported here. To apply this method, the following procedures were followed:

1. On a 1:1 000 000-scale map of lineaments, faults, and folds, circles with radii equivalent to 10 km on the ground were drawn around the centers of random points plotted on the map using random number tables (ref. 7). Only circles that included at least part of a lineament and a fault

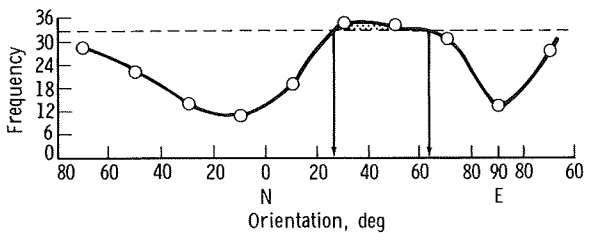


FIGURE 3.—The pattern of fault orientation in the study area. The shaded area is the significant peak at 95-percent probability level; the dashed line denotes the minimum limit for a significant peak.

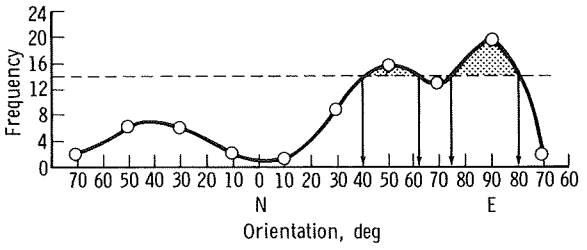


FIGURE 4.—The pattern of lineament orientation in the study area. The shaded area is the significant peak at 95-percent probability level; the dashed line denotes the minimum limit for a significant peak.

strike or a fold axis were used; the other circles were ignored.

2. The orientational maximum (mode) of the lineaments that lie within each sampling circle was determined as being equivalent to the orientation of the longest lineament in the circle. Similarly, the orientational maximums of fault strikes and fold axes were determined for each sampling circle.

3. The angular differences in orientation between lineaments and faults and between lineaments and folds were determined for each sampling circle using the orientational maximums calculated in item 2. Overall frequency plots of these angular differences are shown in figures 5 and 6, respectively. In any frequency plot of the angular difference in orientation, if the orientation of one variable changes randomly with a change in the other variable, the pattern of angular differences in orientation should approximate a random pattern under equiprobability. Hence, the degree of departure of the observed pattern of angular differences from the expected pattern of randomness under equiprobability was determined using the Poisson distribution function (ref. 6). The minimum frequency limit for a significant peak was calculated for each frequency plot at the 95-percent significance level.

Examination of figures 5 and 6 reveals that the orientation of lineaments and faults and of lineaments and folds is significantly different from a random association (within 10-km radii) at the 95-percent significance level. Positions of the significant peaks in figures 5 and 6 indicate the following: (1) There are significant associations of lineaments and faults with angular differences in orientation of 0° to 15° and 75° to 90°. (2) There are significant associations of lineaments and folds with angular differences in orientation of 0° to 15° and 30° to 45°.

If the angular difference in orientation of 0° to 15° is regarded as an indication of similarity in orientation, and if the 75° to 90° difference is accepted as indicative of orthogonality, it can be argued that statistically significant numbers of lineaments are either roughly parallel or orthogonal to fault strikes. Besides, statistically significant numbers of lineaments are either approximately parallel to fold-axis orientations or diverge from fold-axis orientation with an angular difference of 30° to 45°.

DISCUSSION

Analysis of lineament orientation patterns (fig. 4) indicated the presence of two significant peaks oriented NE and E-W and a NW peak that was significant only at a probability level lower than 95 percent. The NE lineament trend resembles the NE fault trend (fig. 3), whereas the NW lineament trend deviates northward from the WNW fault trend. The E-W set of lineaments, although the most prominent of all lineament trends, is not matched by the faults shown on the geological map (ref. 2). The only E-W structural elements

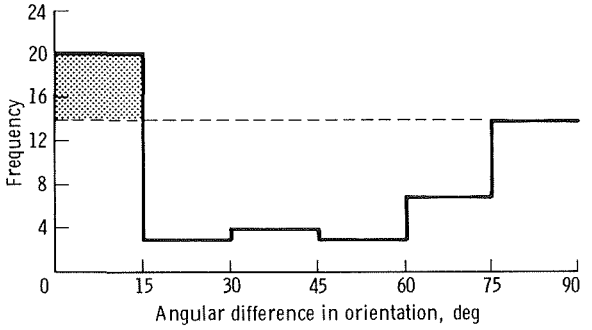


FIGURE 5.—The orientation relationship between faults and lineaments. The shaded area is the significant peak at 95-percent probability level; the dashed line denotes the minimum limit for a significant peak.

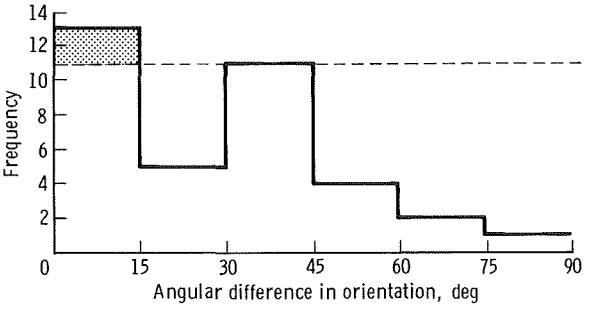


FIGURE 6.—The orientation relationship between folds and lineaments. The shaded area is the significant peak at 95-percent probability level; the dashed line denotes the minimum limit for a significant peak.

represented on the geological map are fold axes of relatively limited length.

Despite the partial dissimilarity of patterns, significant orientational associations were found between fault strikes and lineaments and between fold axes and lineaments. The associations were examined within a 10-km radius to account for possible shifts that might have occurred when lineaments were transferred onto the planimetric map (fig. 2). The group of lineaments that are similar in orientation to tensional faults is most probably the photographic expression of similar features. In addition, lineaments that are orthogonal to tensional fault trends may be tensional faults themselves since orthogonality of tensional trends is a likely phenomenon (ref. 8).

Most of the folds in the study area are linear and narrow, are arranged in a parallel manner within bundles, and are chiefly associated with thrust faulting. Such a type of folding could be attributed to tangential compression with a horizontal maximum-stress component. Lineaments that are similar in orientation to the fold axes in the area could be indicative of thrust faults. Lineaments that are spatially associated with folds and that are oblique to fold axes at angles of 30° to 45° resemble the strike-slip-fault orientation in relation to folds in Moody and Hill's (ref. 9) model. Previous studies in the Mula area of southeastern Spain (ref. 10) and in part of the Pyrenees district of northern Spain (ref. 11) have indicated that several lineaments identified from aerial photographs were structural lines of different orders and magnitude.

The E-W lineament trend, although predominant and statistically significant, is not readily explicable by the published structural pattern of the area. This trend, however, was mapped from Landsat imagery by Biju-Duval et al. (ref. 12) and was shown as a subsidiary lineament trend, whereas the NE lineaments were the most predominant.

Figure 1 shows some of the E-W trending lineaments on photograph AST-27-2369, some of which fall outside the boundaries of the study area. The photocharacteristics of these lineaments are as follows: (1) Most lineaments mark color differences alined in an anomalous manner and only a few lineaments mark linear textural anomalies. (2) The lineaments are mostly long and continuous. (3) Although the lineaments appear rectilinear on the small-scale photograph (fig. 1), detailed examination reveals their wavy character.

The distribution of the time-rock units of the area shows a few discontinuous contacts alined E-W, which appear to correspond to some of the E-W lineaments. This observation, together with the color contrast on both sides of most lineaments, strongly suggests that these E-W lineaments are (partly or totally) fault lines. The remarkably long and wavy character of lineaments was interpreted by Foose and Brigham (ref. 13) to indicate thrusting or gravity gliding. The remarkable length of these lineaments also indicates their great depth penetration.

Similar E-W trending long lineaments were reported in the United States by Saunders and Hicks (ref. 14) and were termed "regional lineaments." It is believed that these lineaments represent the surface expression of very old and deep-seated planes of weakness that divide the continental crust into blocks (ref. 14).

The exact nature of the E-W trending lineaments, which occupy an unfamiliar trend in the study area, may not be accurately clarified without detailed aerial-photograph interpretation and fieldwork. However, the remarkable length and areal persistence of these lineaments suggest that they may be related either to the regmatic shear pattern (ref. 15) or to a major tectonic event. The E-W folding of the Pyrenees Mountains, which was accentuated by north-south phases of tangential compression, should be regarded as one of the major tectonic events that were capable of initiating regional and pervasive structural lines oriented E-W.

REFERENCES

1. Hamilton, Warren: Recognition on Space Photographs of Structural Elements of Baja California. U.S. Geol. Survey Prof. Paper 718, 1971.

2. Mapa Sismoestructural de la Peninsula Iberica, Baleares y Canarias, scale 1:1 000 000. Inst. Geolog. Min. España & Inst. Geograf. Catastral (Madrid), 1966.

3. Tator, Benjamin Almon: Photo Interpretation in Geology. Manual of Photographic Interpretation, R. M. Colwell, ed., American Soc. Photogram., 1960, pp. 169-342.

4. Gay, S. Parker, Jr.: Standardization of Azimuthal Presentations. Proceedings of the First International Conference on the New Basement Tectonics, Utah Geol. Assoc., no. 5, 1976, pp. 499-500.

5. Hay, A. M.; and Abdel-Rahman, M. A.: Use of Chi-Square for the Identification of Peaks in Orientation Data: A Comment. Bull. Geol. Soc. America, vol. 85, Dec. 1974, pp. 1963-1965.

6. Abdel-Rahman, M. A.: A Statistical Method for Determining the Orientational Relationship Between Geological Variables. Paper presented at Second International Conference on the New Basement Tectonics, University of Delaware, July 1976.

7. Arkin, H.; and Colton, R. R.: Tables for Statisticians. Second ed. Barnes and Noble (New York), 1962.

8. De Sitter, L. U.: Structural Geology. Second ed. McGraw-Hill, 1964.

9. Moody, John Drummond; and Hill, Melvin James: Wrench-Fault Tectonics. Bull. Geol. Soc. America, vol. 67, no. 9, Sept. 1956, pp. 1207-1246.

10. Abdel-Rahman, M. A.; and Wright, R. L.: Airphoto Lineations, Joints, and Bedding in Part of the Southeast Spain. Paper presented at Second International Conference on the New Basement Tectonics, University of Delaware, July 1976.

11. Reener, J. G. A.: The Structural Significance of Lineaments in the Eastern Monsech Area, Province of Lerida, Spain. International Institute for Aerial Survey and Earth Sciences, B (45), 1968.

12. Biju-Duval, B.; Rivereau, J.-C.; Lomperein, C.; and Lopex, N.: Esquisse Photogeologique du Domaine Méditerranéen; Grands Traits Structuraux à Partir des Images du Satellite Landsat-1 (Photogeological Sketchmap of the Mediterranean Realm — Major Structural Features Determined From Landsat-1 Satellite Images.) Rev. Inst. Français Pet., vol. 31, no. 3, May-June 1976, pp. 365-400.

13. Foose, R. M.; and Brigham, R. H.: Interpreting the Genetic Character of Structural Lineaments in the Mediterranean Basin. Abstracts, Second International Conference on the New Basement Tectonics, University of Delaware, July 1976.

14. Saunders, D. F.; and Hicks, D. E.: Regional Geomorphic Lineaments on Satellite Imagery — Their Origin and Applications. Abstracts, Second International Conference on the New Basement Tectonics, University of Delaware, July 1976.

15. Sonder, R. A.: Discussion of "Shear Patterns of the Earth's Crust" by F. A. Vening Meinesz. Trans. American Geophys. Union, vol. 28, no. 6, Dec. 1947, pp. 939-945.

Photogeologic Analysis of ASTP Photographs of the Lake Torrens-Flinders Ranges-Lake Blanche Area, South Australia

Paul Dean Proctor[a] and Robert Sickler[a]

ABSTRACT

The Apollo-Soyuz Test Project color photographs of the area around the North Flinders Ranges in South Australia were photogeologically analyzed for stratigraphic characteristics, regional fold structures, faults, other lineaments, and basin features. Relatively unaltered thick Precambrian sedimentary rocks and minor volcanic rocks cover the crystalline rocks of the basement in this area. The folded sedimentary rocks expose one of the world's best records of Precambrian time from 1400 to 560 million years ago. Outliers of folded Cambrian and nonfolded Ordovician and Mesozoic rocks are also present. Tertiary sediments fill the basins and Quaternary deposits form low-angle slope deposits and are in drainage channels adjacent to the ranges. Sand dunes cover parts of the older rocks and younger sediments.

In the western part of the area is the Stuart Shelf, a plateau-like block of flat to gently inclined massive rock units. The Lake Torrens depressed block is to the east of the Stuart Shelf and is partly covered by outwash, playa lake deposits, and sand dunes, which rise gradually eastward to the Flinders Ranges. Gently to steeply inclined and regionally folded rock masses comprise the Flinders Ranges. Megafolds of tens of kilometers in length and with wavelengths as long as 8 km show complex fold patterns of rheid characteristics. The faults present are of easterly, northeasterly, and northerly trend. Some extend to 128 km in length and have displacements to 1000 m or more. Less well expressed faults occur along the eastern and western boundaries of the ranges. Lineaments mainly relate to drainage patterns and recognizable faults. Unique crosscutting bodies with features of intrusive rock, yet lacking uniform internal rock texture, crop out in numerous areas of the mountains. These may represent intrusive breccias.

The complex folds of the Flinders Ranges near Parachilna and Leigh Creek have an unusual bend eastward then southward and westward, forming a "U" concave westward. The overall fold zone of the ranges may have resulted from (1) primary compression as a result of a westward-directed stress field with a later imposed stress field of northerly direction; (2) a lateral stress of varying magnitude from the east directed against the geosynclinal sediments and an underlying subsurface prong of relatively unyielding Precambrian crystalline rocks; (3) an eastward-directed stress field modified by a very competent prong of older Precambrian crystalline rocks acting as a localized ram in the U region of the fold belt. Whichever cause, the regional geosynclinal belt appears to have been squeezed between microplate movements within the continental framework.

Fault patterns suggest either eastward- or westward-directed principal stress directions. Thrust faults east of the Copley area trend northward and dip eastward, suggesting a westward-directed stress field. The border faults are younger and outline the ranges by downfaulting of the Tertiary and Quaternary basins. Diapirs of intrusive breccia masses were actively eroded in Precambrian

[a]University of Missouri at Rolla.

times and developed during the orogenic cycle. Some may be related to older faults.

Continental drift may apply to the area. Permian glacial deposits, similar rocks in Africa, a major fold belt analogous to one in Antarctica, general continental margin matching geometrics, and shear pattern similarities (if Australia is rotated) all lend support to the theory. The presence of coals of Upper Triassic age indicates a breakup of the landmass much earlier than Cretaceous time.

The Apollo-Soyuz photographs are an excellent base for photogeologic analysis of broad areas of well-exposed rocks in desert terrains. Early applications would assist such studies in time and energy savings, accuracy, and economy.

INTRODUCTION

Location of the Study Area

The Lake Torrens-Lake Blanche area is in South Australia (fig. 1; ref. 1) between longitudes 137° and 140° E and latitudes 29° and 32° S. It is approximately 400 km north of Adelaide and covers approximately 77 700 km^2 (30 000 mi^2). The Apollo-Soyuz Test Project (ASTP) photographs used in this study cover parts of the Andamooka, Torrens, Copley, Parachilna, Marree, Callabonna, Curdimurka, and Frome 1° by 1.5° geologic quadrangle sheets of South Australia.

Physiographically, the study area is in a desert environment of plateaus, folded mountain ranges, broad alluvial plains, and several large playa lakes (fig. 2). The four major physiographic features include (1) the lake and/or playa lake lands of Lake Torrens and Lake Blanche, (2) a plateau area to the west of Lake Torrens, (3) a folded mountain range in the central part of the region, and (4) flanking, sloping plains between the mountain ranges and the lake basins.

Lake Torrens is approximately 34 m (112 ft) above sea level, more than 193 km (120 mi) in length, and as much as 40 km (25 mi) in width. It may once have been a northern extension of Spencer Gulf to the south. The Arcoona Plateau (also called the Andamooka Range) is west of Lake Torrens and rises 183 to 244 m (600 to 800 ft) above sea level. The Willouran Ranges lie to the northeast of Lake Torrens and rise to more than 305 m (1000 ft) above sea level. The Flinders Ranges occupy the area east of Lake Torrens. Here peaks rise to 1190 m (3903 ft) above sea level or approximately 1156 m (3792 ft) above Lake Torrens. Gorges have been cut through the resistant rocks that make up parts of these ranges. From the Flinders Ranges, alluvial plains extend downward to Lake Torrens to the west, Lake Blanche to the northeast, and Lake Frome to the east.

Low rainfall (approximately 12 to 20 cm annually), a mean annual temperature of approximately 292 K (65° F), a large diurnal temperature range, and a high evaporation rate characterize this region. As a general guide, maximum and minimum temperatures, averaged for a period of 7 years, are 298 K (77.1° F) and 285 K (53.9° F), respectively. Vegetation is sparse; saltbush on the tablelands, mulga scrub and saltbush in the sand dune areas, and some myall scrub and blue bush in the plains and flats (ref. 2) characterize the plant life. In gullies and large depressions, black oak is present. Native pines are also relatively widespread, together with some red gum and eucalyptus trees.

A railroad from the south passes through Copley and Marree and then goes westward and northward toward Alice Springs. Side tracks lead easterly from Marree and Lyndhurst. A main road parallels the railroad from south of Hawker, northward through Parachilna and northward to Marree. Other roads serve the area.

Purpose and Scope

Excellent ASTP color prints and transparencies of the North Flinders Ranges and the adjacent Lake Torrens-Lake Blanche basin areas of South Australia were analyzed to determine the characteristics of the regional fold structures. Major folds, faults, and other lineaments were identified. Tectonic patterns and their relationships to mobile belt-plate tectonics were examined. In addition, basin forms and features were analyzed

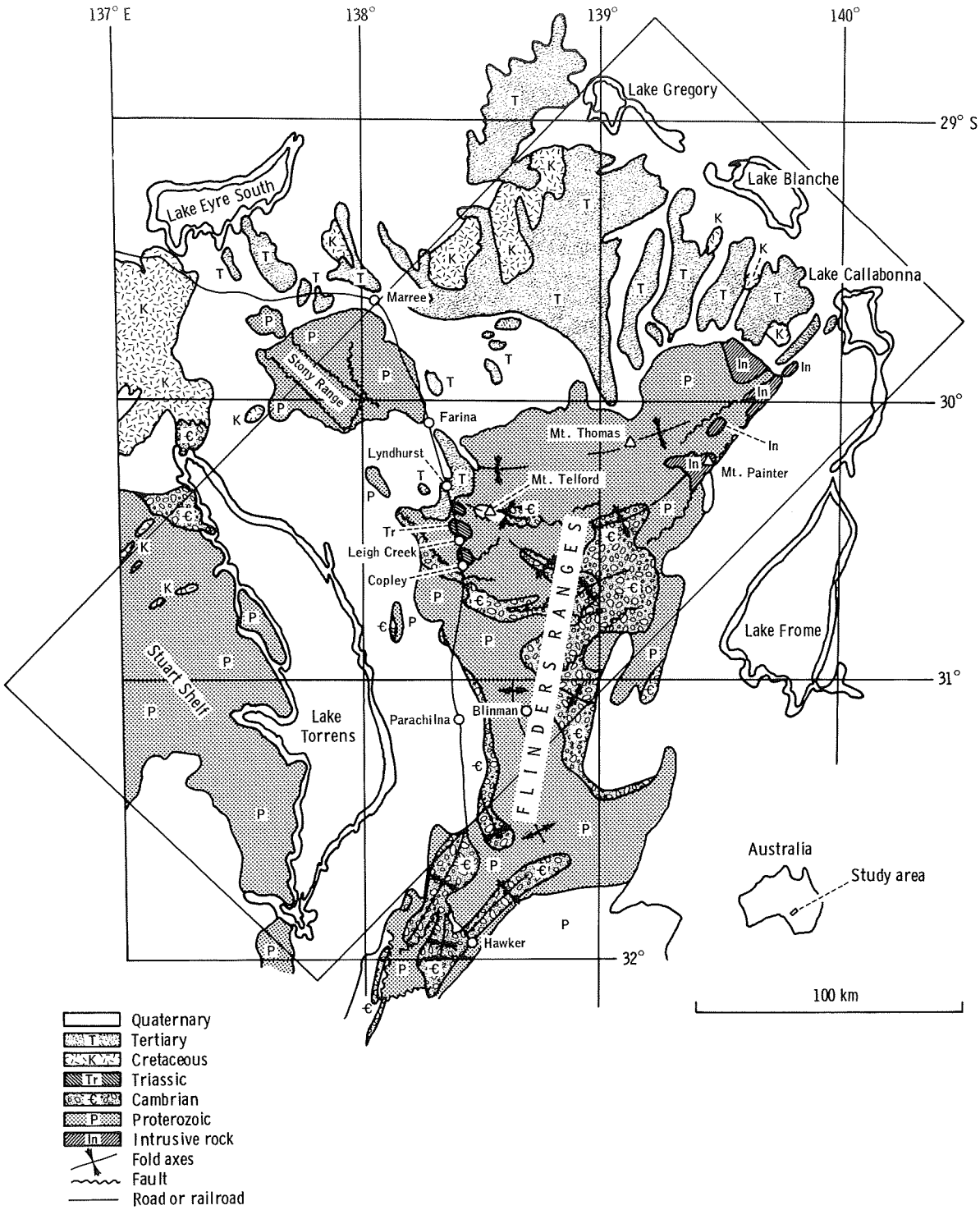


FIGURE 1.—Index map of the Lake Torrens-Flinders Ranges-Lake Blanche area, South Australia (modified from ref. 1). The area outlined is the area of study and of ASTP photographic coverage (AST-16-1129 to AST-16-1132).

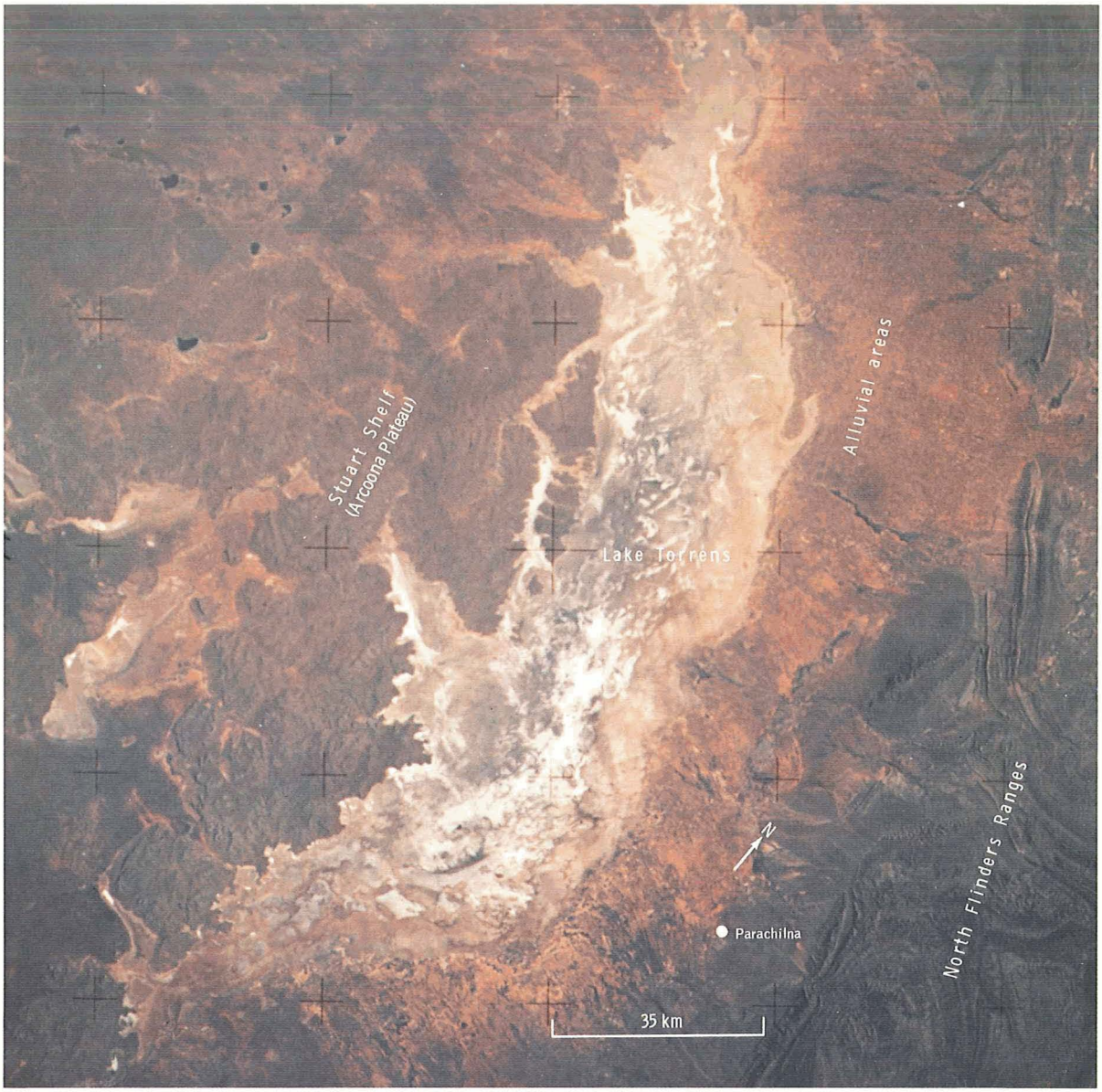


FIGURE 2.—ASTP photograph AST-16-1129 showing the characteristic physiographic features of the study area. Major features include Lake Torrens, the Stuart Shelf west of the lake, the folded mountains of the North Flinders Ranges, and the flanking, sloping plains between the mountains and the lake.

and related to the desert environment of the area. Possible rock types and the character of the widespread alluvial materials surrounding the bedrock areas were predicted. A product of this study was an interpretive photogeologic map covering the area of the ASTP photographs.

Sources of Information

The photographic data used in this study were transparencies and prints of AST-16-1129 to AST-16-1132, color prints of AST-16-1131 and AST-16-1132 enlarged to 36 by 36 cm, and three

ASTP strip mosaics of frames AST-16-1127 to AST-16-1134 enlarged to approximately 1:250 000 scale. After much of the photogeologic analysis was completed, published and preliminary 1:250 000-scale geologic maps of the Andamooka, Copley, Curdimurka, and Marree quadrangles of South Australia were received.

For such a relatively remote desert area, considerable geologic literature is available. For an in-depth review of the literature, the following reports include extensive reference lists useful for details of local stratigraphy, lithology, structure, and mineral occurrences within the region. The "Handbook of South Australian Geology" (ref. 3) is a basic reference for the regional geology. Within the specific area of investigation, the following references are pertinent: (1) the Marree 1:250 000-scale geologic map (ref. 4); (2) Johns' study (ref. 2) of the Andamooka-Torrens area; (3) Coats' study (ref. 5) of the Blinman Dome diapir; (4) the preliminary study of the Curdimurka area by Coats and Anaconda Australia (ref. 6); (5) the excellent geological map of the Copley quadrangle by Coats et al. (ref. 7); and (6) similar studies of the geology of the Parachilna area by Forbes (ref. 8), the Frome area by Callen and Coats (ref. 9), and the Torrens area by Johns et al. (ref. 10). Each of these geologic maps includes a concise description of the stratigraphy of the region, meaningful sketches of tectonic features, and one or more geologic cross-sections.

REGIONAL GEOLOGIC SETTING

The tectonic setting of the study area is suggested in figure 3 (ref. 11). Folded mountain ranges of northerly to northwesterly trend and a central easterly trend rise above alluvial plains and lake basins. The Great Artesian Basin of Australia is to the northeast, the Gawler Block is west and south, and the Murray Basin is to the south-southeast. The Darling lineament bounds the Murray Basin on the north.

The Flinders Ranges trend generally northward from Spencer Gulf to the town of Leigh Creek. The general geologic map of South Australia (ref. 3) indicates that the Flinders Ranges area is composed mainly of Proterozoic rocks with remnant outliers of Cambrian, some Permian, and Triassic rocks. Some granitic rocks occur in the far northeastern part of the Flinders Ranges (ref. 12). Large areas of undifferentiated Quaternary alluvium flank the Flinders Ranges on both the west and the east. These join across the northern part of the ranges east of Marree (fig. 1).

Stratigraphy of the Area

Thomson (ref. 13) described the Precambrian basement cover that comprises the Adelaide System of South Australia. A great belt of relatively unaltered Precambrian sediments, with local and minor occurrences of volcanic rocks, forms a cover over the older crystalline rocks of the basement. The thickest section is exposed in the Adelaide Geosyncline. This is now expressed as a fold belt extending through the northern Flinders Ranges and the Peake and Denison ranges northwest of the study area. Thomson (ref. 3, p. 49) points out that these rocks are "magnificently exposed." This is confirmed by the ASTP photographs. Because of the excellent Proterozoic rock exposures and the complete stratigraphic section, this area has achieved international recognition as a record of this part of Precambrian time. The time interval included in the rock units is from the base of the Cambrian (approximately 560 million years ago) to approximately 1400 million years ago.

Rocks of the Proterozoic, the Cambrian, a part of the Ordovician System, and the Mesozoic are exposed within the study area. All are partly covered by Tertiary and Quaternary semiconsolidated to unconsolidated sediments. Subsurface studies and surface mapping by others (refs. 14 and 15) indicate a buried basement composed of Precambrian metamorphic and igneous rocks as part of the Australian Precambrian shield. The shield is covered by unaltered Precambrian and younger rocks.

The Stuart Shelf, west of Lake Torrens, is underlain by a series of sediments, mainly undisturbed although some thrust faulting to the west is present. Eastward, more than 21 336 m (70 000 ft) of sediments of Proterozoic age were

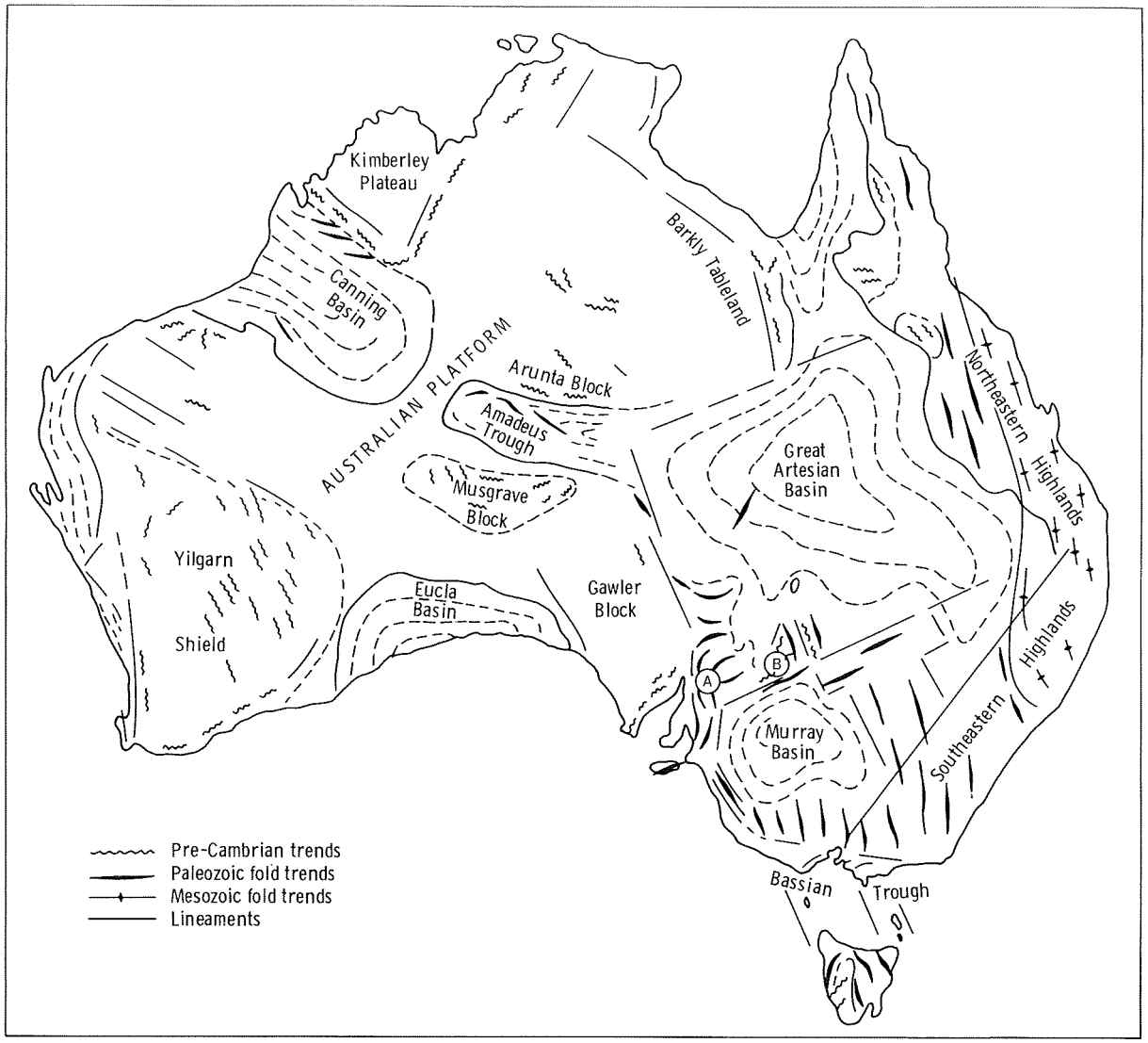


FIGURE 3.—Simplified tectonic map of Australia showing the Adelaidean fold belt (A) and the Darling lineament (B) near the study area (after ref. 11).

deposited in a great geosynclinal trough with the source area to the west. This trough extended from the present coastal area northward through the Flinders Ranges, and then northwest through the Peake and Denison ranges. The sediments, though very thick, were of shallow-water origin. Even glacial sediments, possibly derived from floating ice from a nearby icecap, are included. The Proterozoic in the Adelaide Geosyncline covers a timespan of approximately 840 million years (ref. 3).

The term "Adelaidean" is applied to the time interval of these sediments. The rock sequence has been subdivided into time units as shown in figure 4 (ref. 3). In the Lower Callanna beds totaling 3767 m (12 360 ft), rock units include quartzites, dolomites, volcanic rocks, and some sandstone and quartzite. Unconformably above are the Upper Callanna beds, 2134 m thick, made up of a basal conglomerate, phyllite, conglomerate, and ending with siltstone. The Burra Group, approximately 6186 m thick, is a major sedimen-

tary cycle beginning with a sandstone and followed by a dominantly carbonate-siltstone succession including sedimentary magnesite. Shallow-water clastics end the Burra Group. The Umberatana Group includes cycles of sedimentation and associated tillites that begin the sequence. This is covered by thick, shallow marine and continental sediments, and tillites terminate the group. Thickness ranges from 3657 to 4572 m. Tillites of similar age and succession have been recorded in central Africa. Remarkably uniform sedimentary conditions were extant for the Wilpena Group. This commences with a carbonate-siltstone sequence, followed by dominantly siltstone of shallow-water character and uppermost limestone and sandstone. In the Copley area, the Wilpena Group reaches 4876 m thickness. The Pound Quartzite is the youngest unit and forms "spectacular rugged ridges and domes" in the area (ref. 3, p. 78).

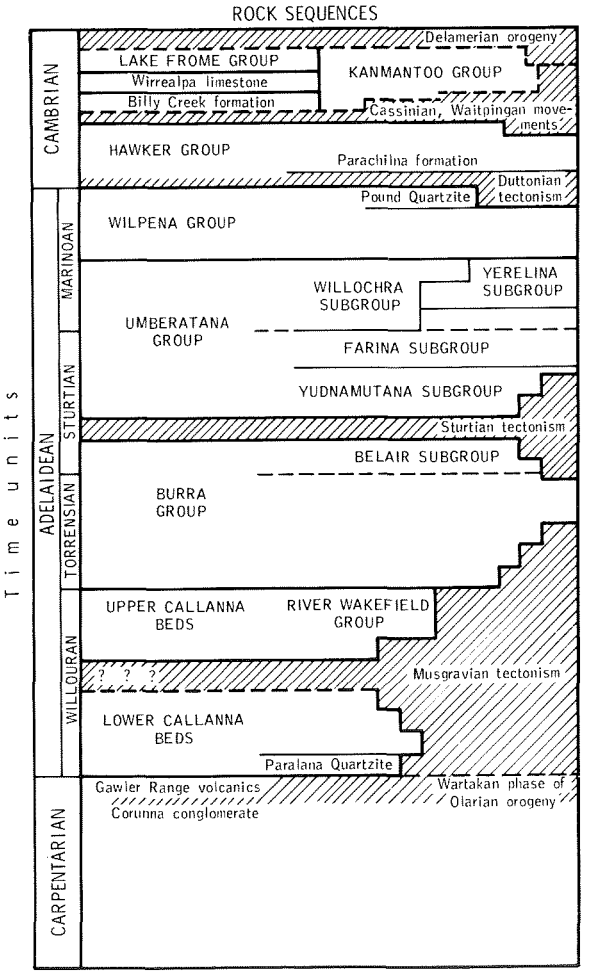


FIGURE 4.—Rock sequences in the Flinders Ranges, South Australia (after ref. 3).

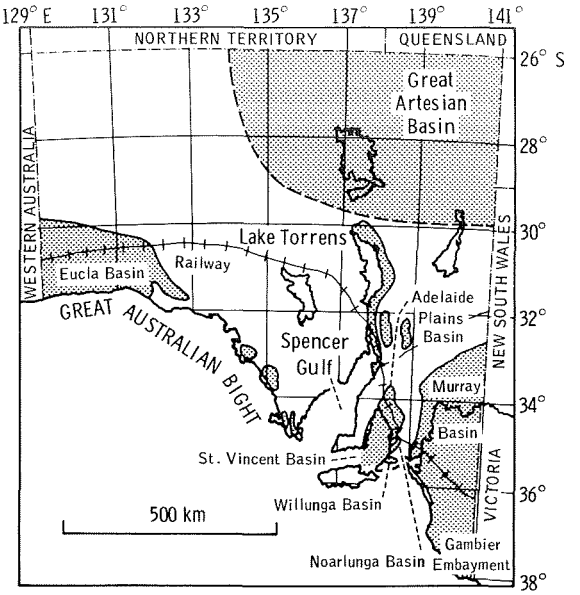


FIGURE 5.—Areas of Tertiary sedimentation in South Australia (after ref. 3).

In the Flinders Ranges, magnificent exposures of Cambrian rocks cap some of the rugged outcrops of the Precambrian Pound Quartzite, which they disconformably overlie. The Cambrian sediments were the last rock units deposited before the final deformation of the Adelaide Geosyncline. The Lower Cambrian units are characterized by a thick succession of dark-colored carbonates and shales. There were some red beds and then carbonates deposited, and in Middle to Late Cambrian time, a reversion to the red-bed environment occurred.

The Adelaide Geosyncline was transformed into a complex fold belt by Lower Ordovician time. This belt extended from at least the boundary of the present southern ocean to the northern border of South Australia. Although Ordovician rocks are absent in this area (except for some igneous rocks), subsurface occurrences are known to the north. The beds rest in strong angular un-

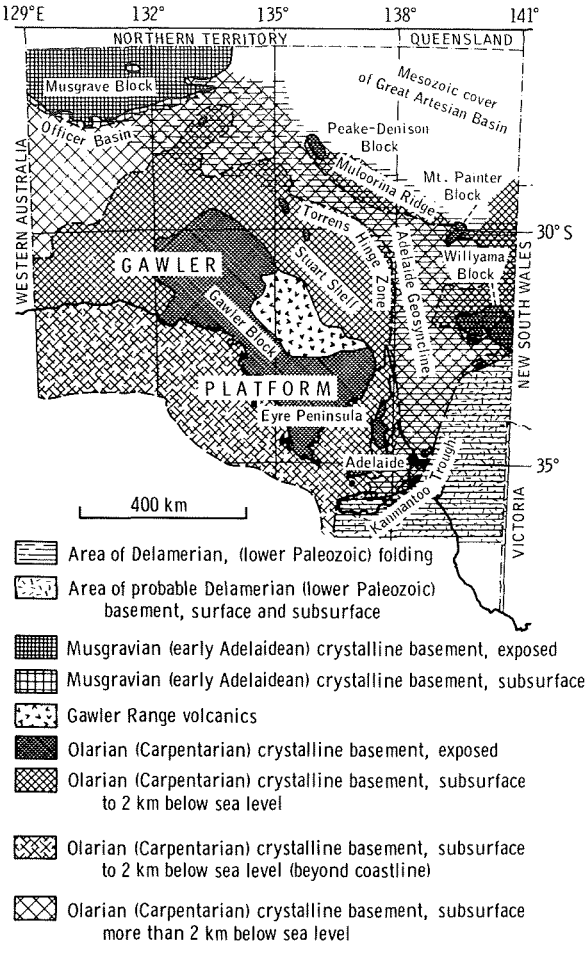


FIGURE 6.—Major tectonic units of South Australia (after ref. 3).

conformity with the underlying Precambrian rocks.

Mesozoic sediments are reported and include the Triassic Leigh Creek coal measures (more than 600 m thick) and Jurassic-Cretaceous sedimentary units of somewhat limited distribution within the area of this report. These beds are gently to moderately inclined and lie over the folded older rock units of Paleozoic age.

Tertiary sedimentation occurred in a series of sedimentary basins and embayments along the continental margin. One of these areas of sedimentation paralleled the eastern part of Lake Torrens and extended southward to Spencer Gulf (fig. 5; ref. 3). These sediments were mainly sands and silts, somewhat carbonaceous, and some lignitic beds and low-rank coal of early Tertiary time. Sandstones, conglomerates, silcrete-duricrust, and some shales are more characteristic of the Lake Torrens area.

Quaternary deposits form low-angle slope deposits; scree occurs in the bedrock areas; alluvium is in drainage channels and flood plains; and sand dunes cover rocks of older age and younger sediments in the area.

Tectonic Patterns and Regional Geology

Parkin (ref. 3) suggests that the crustal movements of the Australian shield in South Australia can be divided into three parts: the Gawler Platform, the Adelaide Geosyncline, and the Musgrave Block (fig. 6). He recognizes the Gawler Platform west of Lake Torrens as a stable block.

The Torrens Hinge Zone marks the transition between the Gawler Platform-Stuart Shelf and the Adelaide Geosyncline to the east. The second major tectonic feature, the Adelaide Geosyncline, was less stable and was downwarped and folded during Adelaidean (Proterozoic) and lower Paleozoic time (refs. 1 and 13). This feature is flanked on the east and north by basement rock in the Olary, Mount Painter, and Peake-Denison areas.

The great Musgrave Block to the northwest is the third major tectonic feature of the shield. It consists of exposed crystalline basement rocks and forms "part of the topographic backbone of the continent" (ref. 3). The Great Artesian Basin of Australia is east and northeast of this block.

Fracture patterns, faults, shears, and hinge lines (fig. 7) developed and remodeled the shield area (ref. 3). Some of the faults have been intermittently active since Proterozoic time. Thomson (ref. 16) suggests that productive metalliferous belts are related to part of this older fracture pattern.

The distinctive and complex variations in fold patterns suggest that the shield has undergone more than one cycle of folding and metamorphism. Yet, from a regional viewpoint, Parkin (ref. 3) suggests that an overall northeasterly trend is present in many of the fold belts within the shield in South Australia.

PHOTOGEOLOGIC ANALYSIS

Four major geologic terrains are apparent in the study area.

1. A conspicuous and well-exposed fold-mountain area that covers the central and southeastern part of the region between Lake Torrens on the southwest and Lake Blanche on the northeast.
2. Alluvial plains that slope down toward both Lake Torrens and Lake Blanche.
3. A plateau-like area that lies west of Lake Torrens.
4. Distinctive lake plains and/or playa areas characterized by Lake Torrens and Lake Blanche.

Within these geological terrains, the rock-sediment units are subdivided into indurated rock units and surficial materials mainly of a noncoherent type. The indurated units are further subdivided into nonlayered and layered rock units with nonlinear and linear outcrop patterns. The units with linear outcrop patterns consist of furrow-and-ridge formers and inclined and layered ridge formers. Several subdivisions are also suggested for the surficial materials.

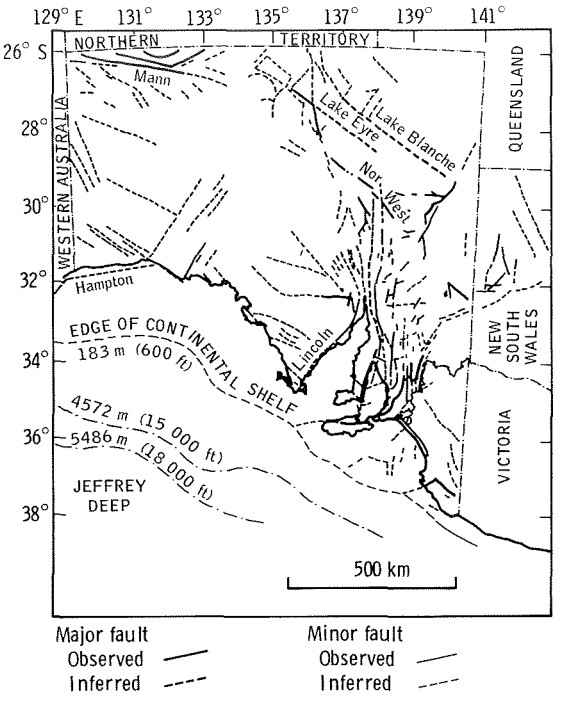


FIGURE 7.—Major faults and lineaments of South Australia (after ref. 3).

Layered and Nonlayered Rock Units With Nonlinear Outcrop Patterns

The layered-nonlayered group of rock units consists of two major types: (1) a massive, nonlinear, flat-lying, layered, probable sedimentary rock sequence and (2) a hill-and-valley forming rock unit. The first type occurs as massive layered units at the surface, lacks visible linearity in outcrop pattern, forms rolling hills, and develops drainage patterns that are mainly dendritic. The best exposed rock units of the group occur west of Lake Torrens and south of Andamooka. These rock units are resistant to erosion and form conspicuous outcrop areas (fig. 8). The hill-and-valley forming rock unit of nonlayered character erodes and weathers into a low-profile surface form. Imposed structures, most likely joints and some faults, are visible and tend to control the drainage pattern. Exposures of the unit occur west of Lake Torrens in the far corner of the mapped area (fig. 8), where as much as 1169 km^2 may be underlain by this rock unit.

Inclined and Layered Units With Linear Outcrop Patterns

Six rock units with layered characteristics and inclined attitudes were identified in the Flinders Ranges. These units are subdivided into furrow-and-ridge formers and inclined and layered linear units. These make up the main rock masses within the range.

Furrow-and-Ridge Formers

Of the furrow-and-ridge formers observed, four different types are recognized: (1) gentle-slope former, (2) steep-slope former, (3) stepped-slope former, and (4) moderate-slope former. The gentle-slope former consists of well-consolidated materials and develops somewhat U-shaped valleys and rounded ridges. Drainage patterns are dense pinnate-dendritic to dendritic. The probable composition of the rock unit is siltstone. The steep-slope former is characterized by a low ero-

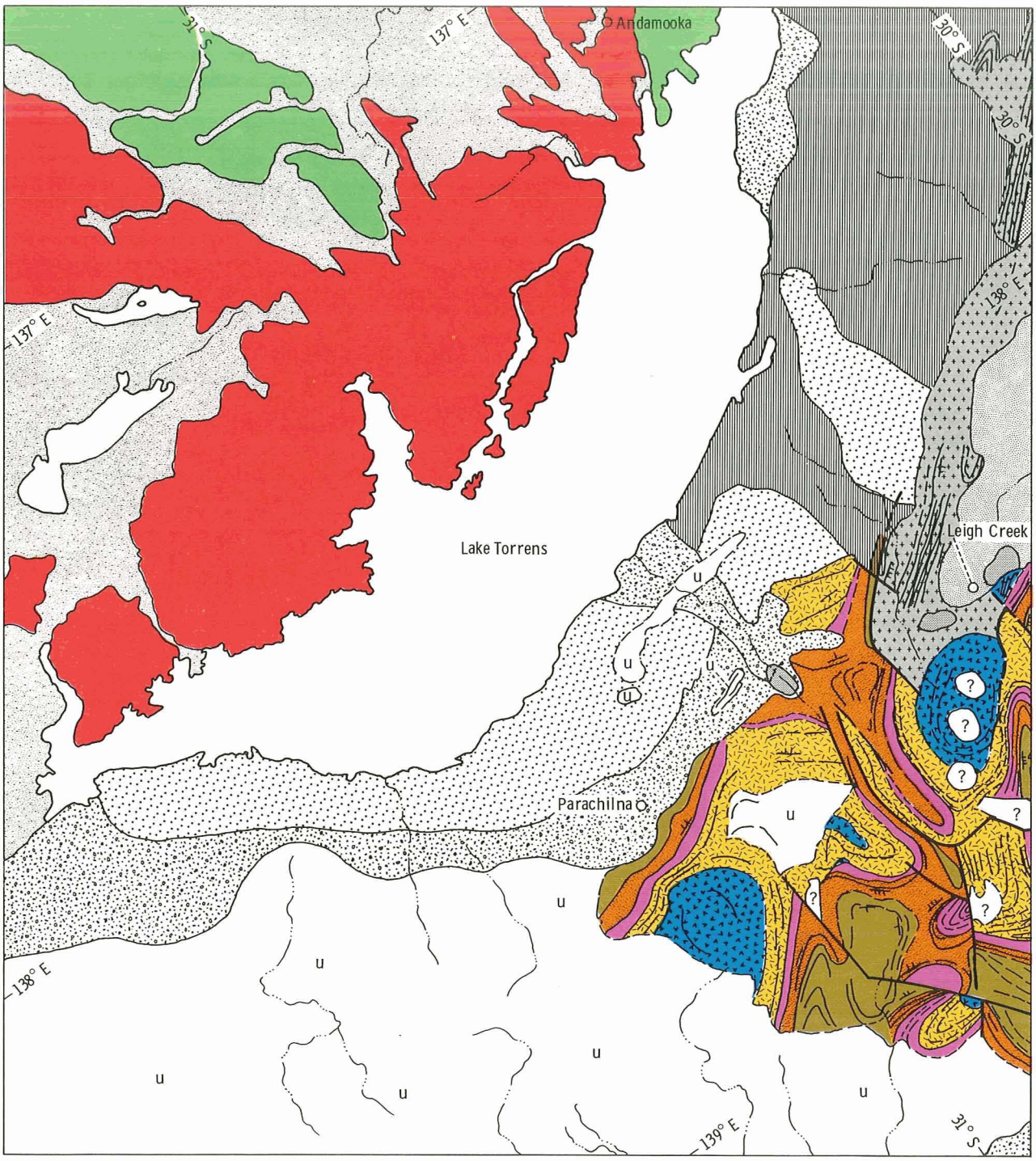


FIGURE 8.—Interpretive geologic map of Lake Torrens-Flinders Ranges and Lake Blanche region, South Australia. Explanation of map units is listed separately.

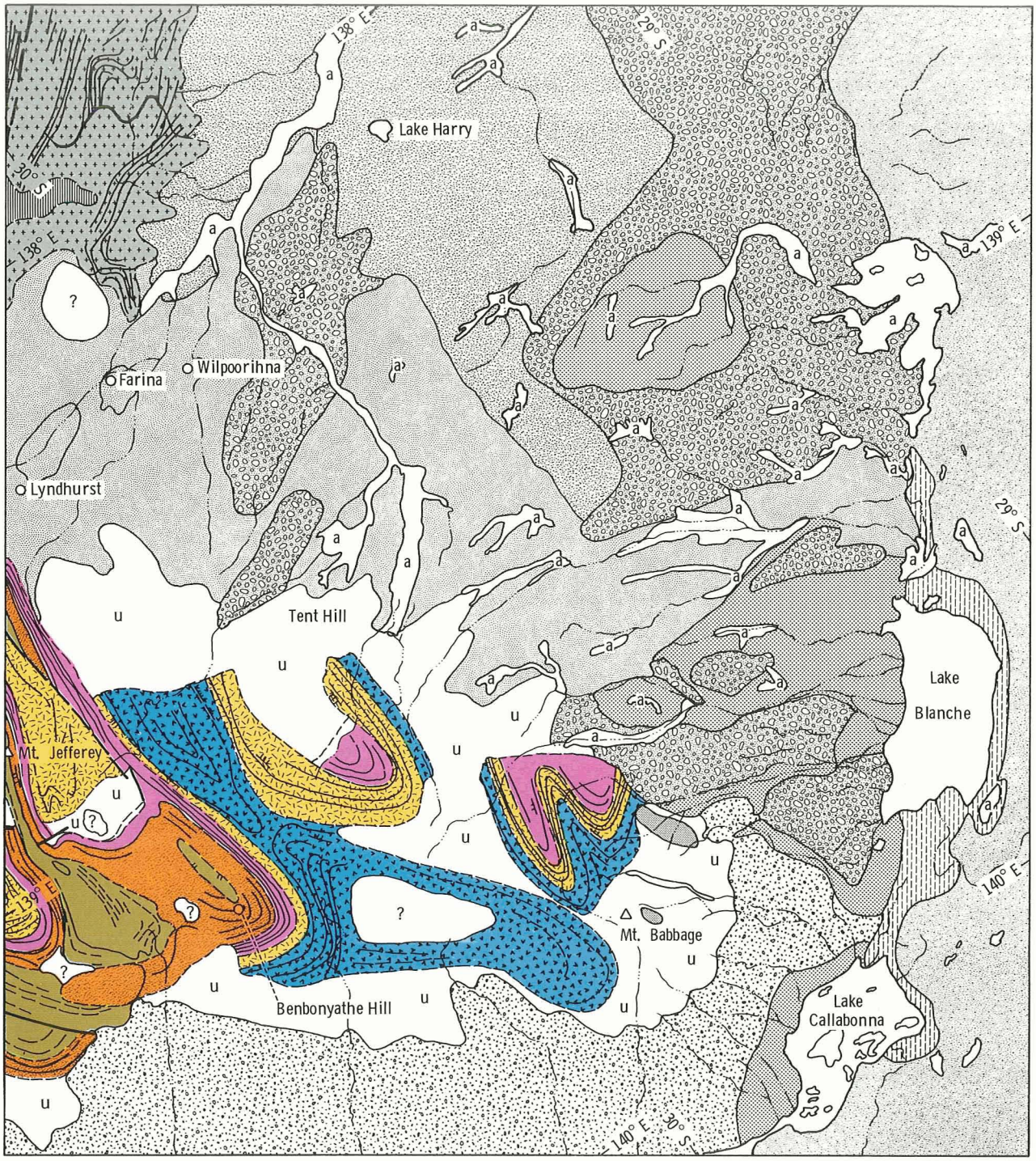


FIGURE 8.—Continued.

Explanation for figure 8

Rock units

Layered linear units - inclined

- Blocky ridge former — Steep-sided valleys, lack of normal tributaries, blocky valley patterns, lighter colors - CARBONATE ROCK
- Ridge former — Massive thick-bedded, asymmetrical to symmetrical ridges, well-defined V-patterns on slope, V-shaped valleys - SANDSTONE
- Step-ridge former — Interbedded carbonate and granular materials, blocky weathering, square ridges and benches (combined with unit above) - CARBONATE / SANDSTONE

Layered and nonlayered units - nonlinear

- Hill-and-valley former — Weathers to low profile, jointed, with joint blocks, linear drainage - IGNEOUS ROCK
- Bedrock former — Massive nonlinear, rolling hills with dendritic drainage - FLAT-LYING SEDIMENTARY ROCKS
- u — Undifferentiated bedrock
- ? — Nondefinitive bedrock

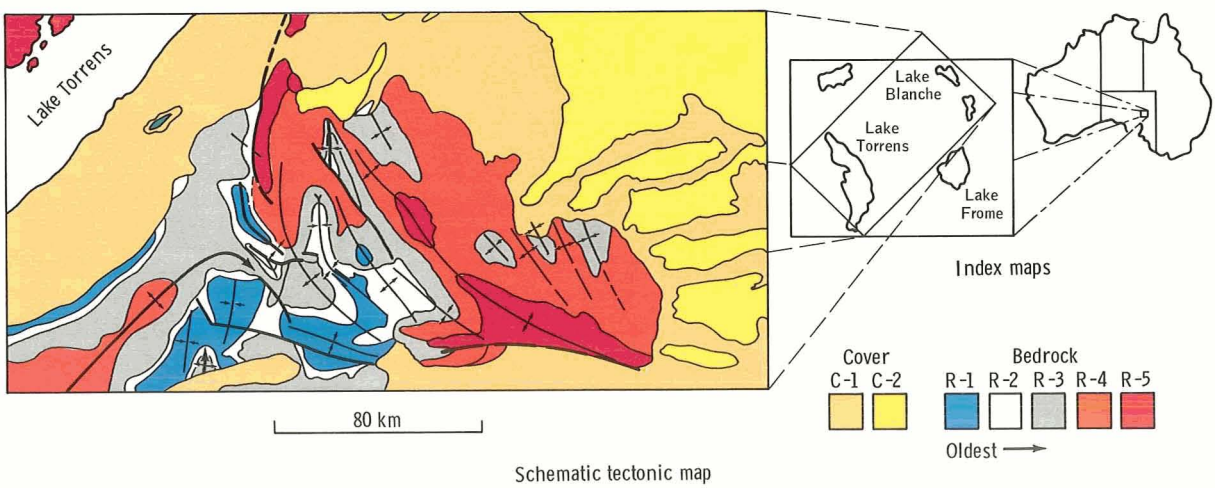
Furrow-and-ridge formers

- Stepped slope — Interbedded, fine-grained, layered weathering and soft ridges, much coarser-grained, dissected - SHALE / SANDSTONE
- Steep slope — Interbedded silts, fine-grained, low-erosion profile, well integrated, uniform drainage - SHALE / SILTSTONE
- Gentle slope — Well consolidated, forms U-shaped valleys, rounded ridges, steep undercuttings and sheetflow. Uniform, dense pinnate-dendritic / dendritic drainage - SILTSTONE / MUDSTONE
- Moderate slope — Well consolidated, forms string and fine ribbon banding. Shallow trellis and subparallel drainage - SHALE-SANDSTONE-CARBONATE

- Fault
- Gentle dip
- Moderate dip
- Steep dip
- Contact
- Bedding form line
- Stream
- Intermittent surface water area

Surficial materials	Surface expression
a	Duned sands and alluvium
	Areas of surface disturbance
	New secondary stringer deltas
	Top-set beds
	New outwash

Surficial materials	Surface expression
	Moderately consolidated outwash
	Bajada
	Old outwash, mottled texture, possibly duned
	New deltaic material, delta apron
	Soil former, consolidated, in final stage of erosion



Schematic tectonic map

FIGURE 8.—Concluded.

sion profile. The drainage pattern is well integrated and uniform. This rock unit may consist of fine-grained siltstones and shales. The stepped-slope former is a well-layered interbedded fine and coarse sedimentary unit. This forms soft-appearing ridges, is much dissected by erosion, and probably consists of a shale-sandstone sequence. The moderate-slope former of the furrow-and-ridge group consists of string-like and fine-ribbon erosional bands on the photographs. Shallow trellis and subparallel drainage patterns are characteristic of the unit. The probable rock composition is sandstone and carbonate.

Inclined and Layered Linear-Ridge Formers

Three distinct inclined and layered linear-ridge-former units crop out in the range: (1) a step-ridge former, (2) a blocky-ridge former, and (3) a ridge former of mainly symmetrical weathering habit. The step-ridge former has a blocky weathering habit and forms square-shaped ridges and benches. The composition is probably interbedded carbonate and granular materials equating to a possible sandstone-carbonate rock sequence. The blocky-ridge former yields steep-sided valleys and blocky valley patterns and is of lighter tone. Drainage patterns lack normal tributaries. The unit is interpreted as a carbonate rock. The ridge former is massive and thick bedded. The ridges formed are symmetrical to asymmetrical. Well-defined V-patterns develop on the dip slopes together with V-shaped valleys. The rock is believed to be a sandstone.

Surficial Materials

At least nine types of surficial materials are recognized in the region. These consist of consolidated sand dunes, soil former, delta-like aprons, old outwash materials often duned, bajada deposits, older and moderately consolidated outwash materials, new outwash detritus, top-set beds, new secondary stringer deltas, and areas of surface disturbance. These surficial materials flank the Flinders Ranges on the western and eastern sides and apparently form a crescent connection around the northern end of the ranges. The units are recognized by their surface expression, type and density of associated drainage patterns, and underlying coarse to fine-grained texture. These are shown on the map of the region (fig. 8).

Regional Tectonic Patterns

Regional tectonic patterns are based on the interpretation of linear and planar characteristics of the rock units. Planar attitudes are classified as gentle, moderate, or steep, wherever possible. From such interpretations and from actual photo-tracing of several well-defined rock units, large folds, faults, flat-lying rock units, and some non-linear massive rock units are identified.

The Flinders Ranges consist of a series of very broad and long anticlines and synclines of northerly and easterly trend (fig. 9). Wavelengths of individual folds range from 6 to 13 km. Imposed on the folds are faults of northwesterly and northeasterly trend. Other faults of northerly trend may bound the western border of the range.

Folds and Patterns

The Stuart Shelf in the far western part of the mapped area is a plateau-like block of flat to very gently dipping massive rock units (fig. 10). The Lake Torrens depressed block lies to the east and is mainly covered by outwash, sand dunes, and playa lake deposits. East of the broad alluvium-covered area is the western boundary of the Flinders Ranges. Here impressive rock units, gently to steeply inclined and regionally folded, crop out. The strong resistance of many of the rock units to weathering and erosion has resulted in conspicuously folded strike ridges. Less-resistant beds form well-developed valleys (fig. 9).

Although not all folds of the region are described, the size and character of some are most worthy of description. Those of more than 32 km strike length and 8 km wavelength are here termed megafolds. Just east of Parachilna, a megafold approaches 100 km axial length and almost 32 km wavelength and is well expressed by

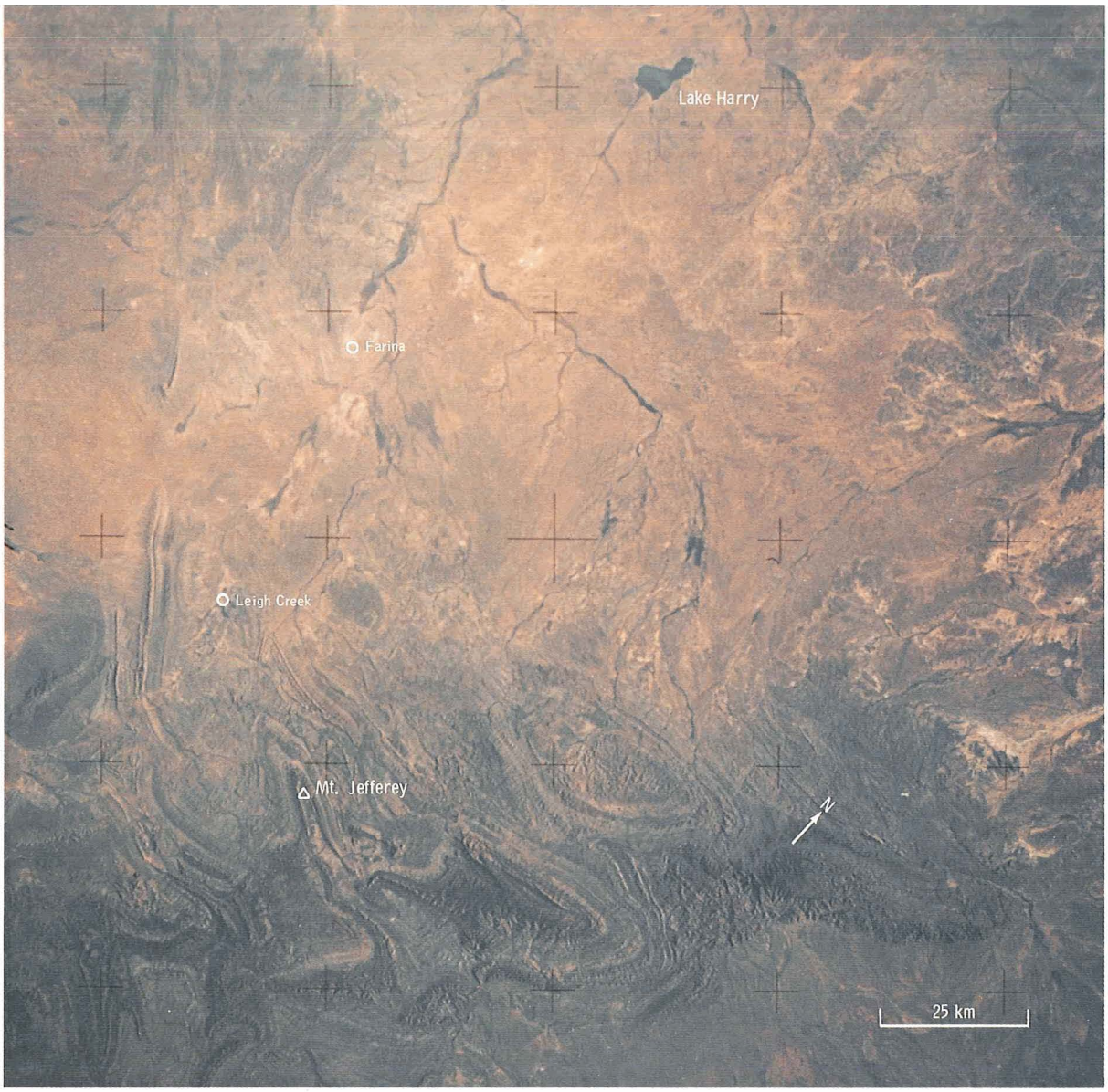


FIGURE 9.—ASTP photograph AST-16-1131 showing characteristics of fold structures in the North Flinders Ranges, South Australia.

a sedimentary series of alternating resistant and less-resistant beds. The inclination of the limbs of the fold is moderate. This megafold continues northward, then abruptly turns eastward for more than 40 km until it disappears beneath alluvial cover (fig. 10).

Thirty-two kilometers north and also east of Leigh Creek, at least five megafolds trend easterly and are transverse to the general trend of the Flinders Ranges. These megafolds are as much as 26 km across and at least 80 km in strike length. Smaller folds of 6- to 8-km length are superimposed on these megafolds.

The map patterns of the folds are complex. On a regional scale, they strikingly resemble the small-scale fold patterns expressed in the intricate

folding of primary slump structures in sedimentary rocks. On the megascale, however, the folds have bed continuity and are not intensely faulted. Flowage, or rheid behavior (ref. 17), of less-competent members from limbs into fold axial areas occurs at several localities. Examples are the synclinal noses near Mount Jefferey, Mount Thomas to the northeast, and a hill farther east. The megafolds appear to have developed under a heavy load over a long period of time under stress conditions. Yet the relatively short time interval between the folded Upper Cambrian sediments and the overlying essentially unfolded Ordovician rocks indicates that depth of burial and stress field may have been the major contributing causes for the observed folds.

Photogeologic examples of areas of rather intricate folding on a much smaller scale than the megafolds near Leigh Creek occur some 40 km northwest of the town. Here individual folds are approximately 7 km in wavelength and as much as 40 km in strike length. Although photographic resolution in this area is not good, the fold patterns do show rather extreme flow-fold behavior (fig. 11; refs. 6, 14, and 18).

Another example of the smaller scale fold characteristics is shown in the photointerpretive geologic map of the Mount Jefferey area (fig. 12; ref. 7). The map shows not only the flow-fold phenomena; it is also a comparison between mapping with photointerpretation of orbital photographs and mapping in the field using much larger scale photographs (ref. 7). The correspondence is relatively good. A rather involved fold-on-fold structure occurs just northeast of Mount Jefferey where a very tight anticline lies between two major synclines.

Faults

Several conspicuous faults cut the folded rocks of the Flinders Ranges. These faults trend easterly, northeasterly, and northerly. Other faults, though poorly defined on the photographs, probably occur along the boundaries of the ranges on the east near Lake Blanche and on the west near Lake Torrens.

Recognized faults extend to 128 km or more in strike length. Without distinctly correlatable beds, the direction of slip on these faults is unknown. However, the fact that some faulted folds, such as at Mount Telford (fig. 12), are much isolated from their parent fold suggests a slip displacement in thousands of meters.

A fault at least 80 km long bounds a major fold zone northwest of Leigh Creek. Here fold limbs are truncated on the northwest, and a long 3-km-wide strike ridge of steeply dipping beds trends southeastward toward Leigh Creek (figs. 10 and 11). Another faulted fold zone, approximately 20 km long and possibly of domal form, is now partly covered by outwash materials and lies to the east. Other faulted fold structures probably occur beneath the outwash sediments and playa lake deposits of Lake Torrens.

Crosscutting Bodies

Although the majority of the major folds are well expressed by the layered rocks on the ASTP photographs, several areas within the folds and on their flanks show other poorly developed structures. Some of these distinctly crosscut the layered units. Other such structures have unknown relationships to the bedding.

The crosscutting masses may represent intrusive rock areas, yet they lack the uniform rock texture expected of such bodies. Two such examples of crosscutting bodies occur approximately 38 km northeast of Leigh Creek and approximately 26 km north of Mount Jefferey. A similar, somewhat disturbed domed area also appears just east of Parachilna. Other such bodies have been observed in the area (ref. 5).

The crosscutting characteristics and the lack of uniform rock texture suggest some type of intrusive rock mass, possibly of breccia-like internal structure. This could be explained by igneous intrusive breccia, or by diapiric structures of sedimentary origin. The latter have been described for a large area within the Flinders Ranges. Figure 12 illustrates occurrences of diapir-like masses in the area of Mount Jefferey and their spatial relationship to folds and faults.

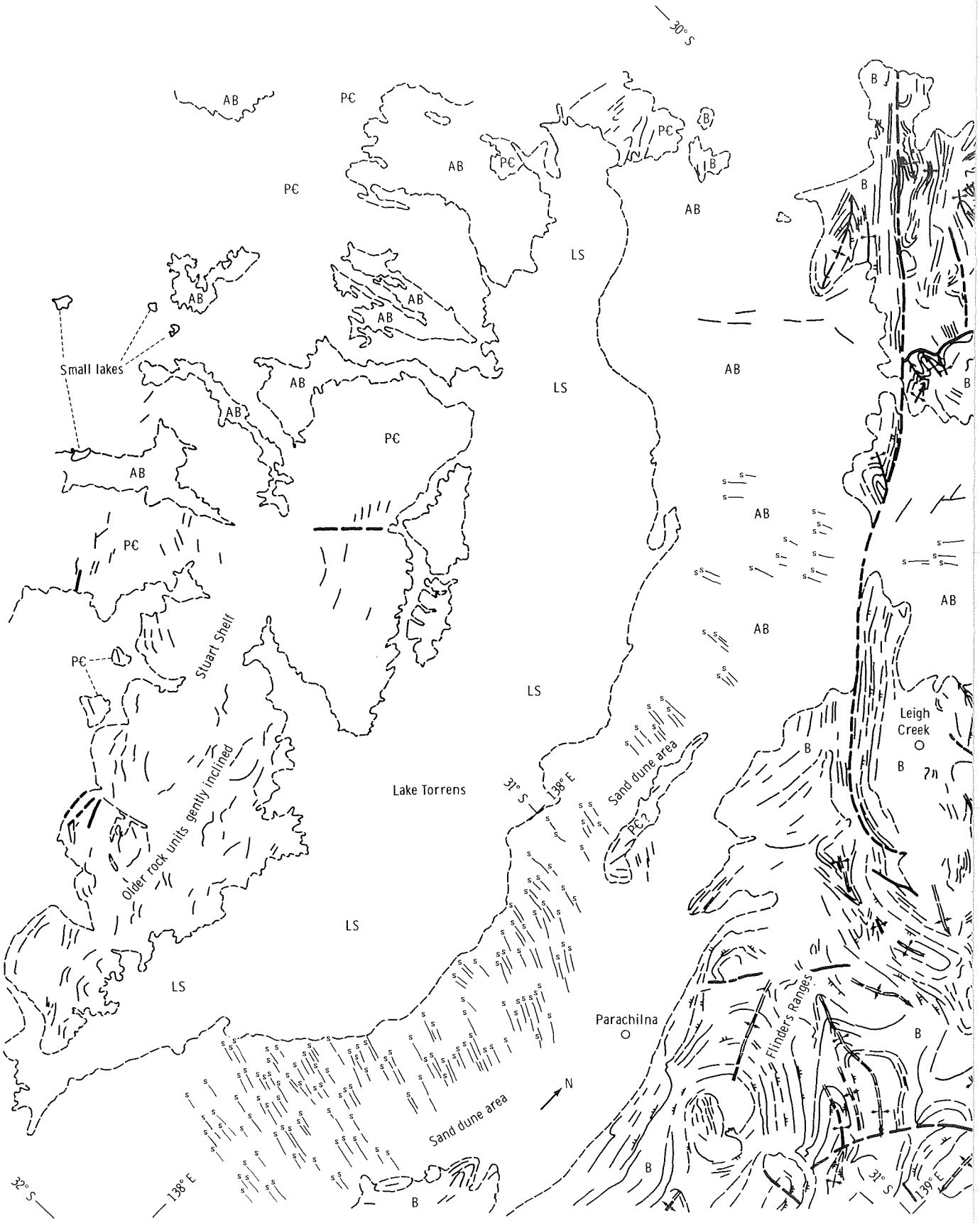


FIGURE 10.—Interpretive phototectonic map of the Lake Torrens-North Flinders Ranges-Lake Blanche area, South Australia (strip-mosaic base of ASTP photographs AST-16-1127 to AST-16-1134). Explanation of map units is listed separately.

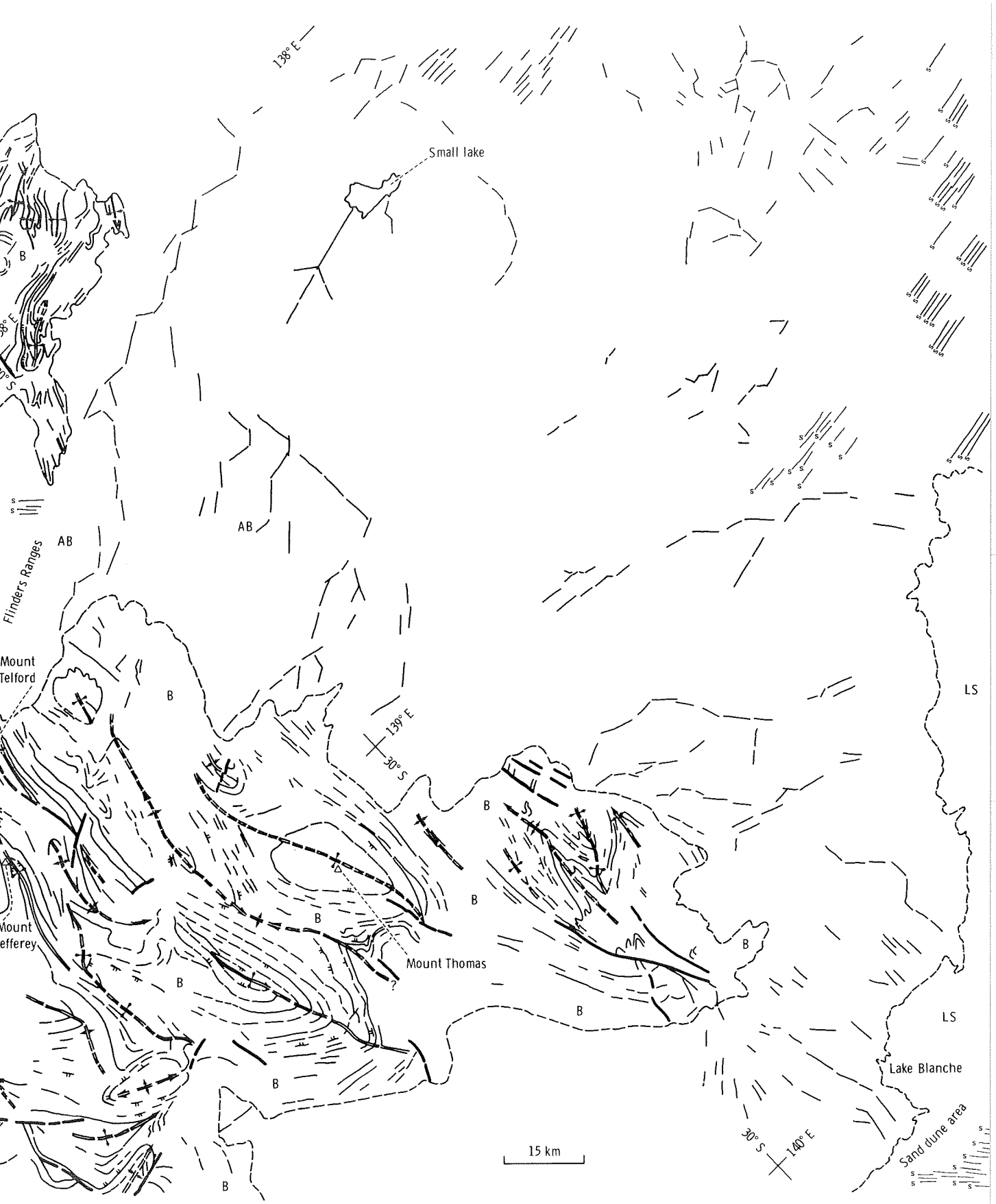


FIGURE 10.—Continued.

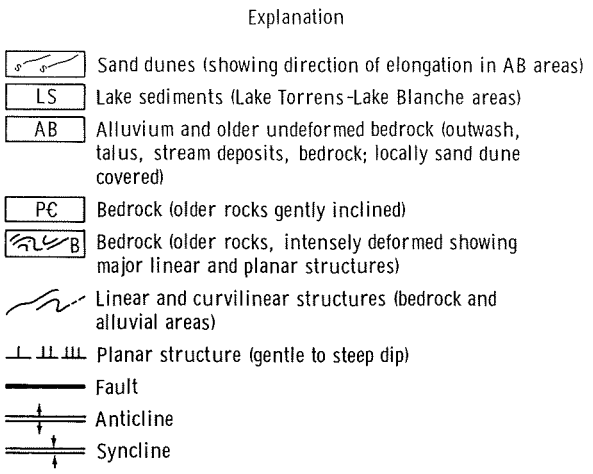


FIGURE 10.—Concluded.

Lineaments

Well-developed northerly and westerly trending patterns of drainage occur north of the Flinders Ranges. The drainage texture is coarse. The main stream trend is northerly for more than 60 km. A secondary stream set trends westerly. The second set, in turn, has several large tributaries of northerly trend. These distinctive and well-defined linear features suggest an underlying structural control. Less-conspicuous lineaments of northwesterly trend also occur in the area and are as long as 12 km. Bed offsets are not visible along these straight-line features. Other than the well-expressed linears of bedding, faults, and drainage, large-scale lineaments are not well expressed on the photographs.

TECTONIC ANALYSIS

Regional Setting

The North Flinders Ranges lie between the stable Gawler Block-Stuart Shelf on the west and the Willyama Block of similar Precambrian rocks on the east. Crystalline rocks of the Musgrave Block are exposed to the northwest (figs. 3 and 6). Northeast and southeast, respectively, of the Flinders Ranges are the Great Artesian and Murray Basins. These are separated by an eastward-projecting salient of Proterozoic rocks and by the Darling lineament (ref. 19).

The Stuart Shelf has a cover of flat to gently folded Proterozoic and Cambrian sediments that thicken rapidly east of the Torrens Hinge Zone. Toward the north, cover rocks of the shield thicken toward the Musgrave Block. Parkin (ref. 3) has summarized major stratigraphic and tectonic events of Precambrian time in the region (fig. 13).

The orogenic event that resulted in the fold mountains of the Flinders Ranges occurred in Late Cambrian time. It was an event of relatively short geologic timespan, because Early Ordovician rocks were deposited unconformably on Cambrian and older rocks in the region. These Ordovician rocks have been disturbed little since their original deposition.

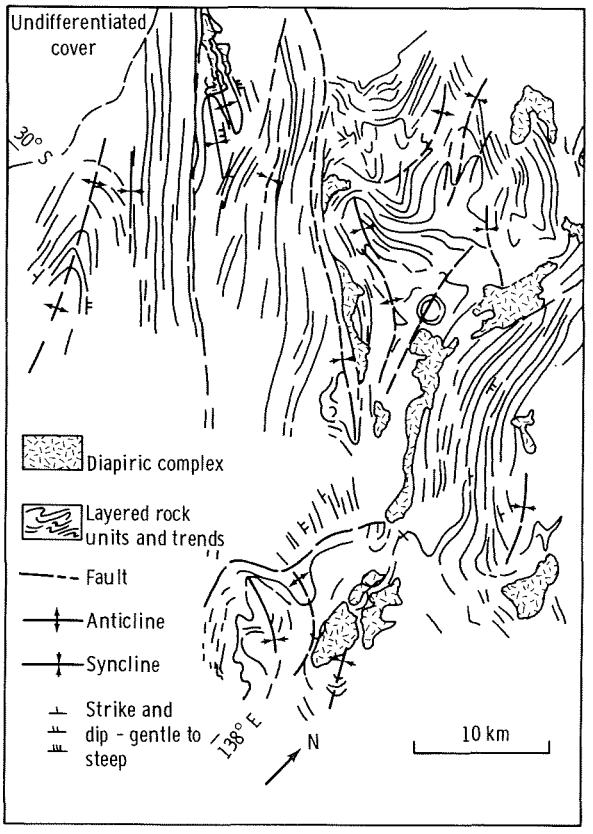


FIGURE 11.—Photogeologic analysis of the Marree area, South Australia (some data from refs. 6, 14, and 18).

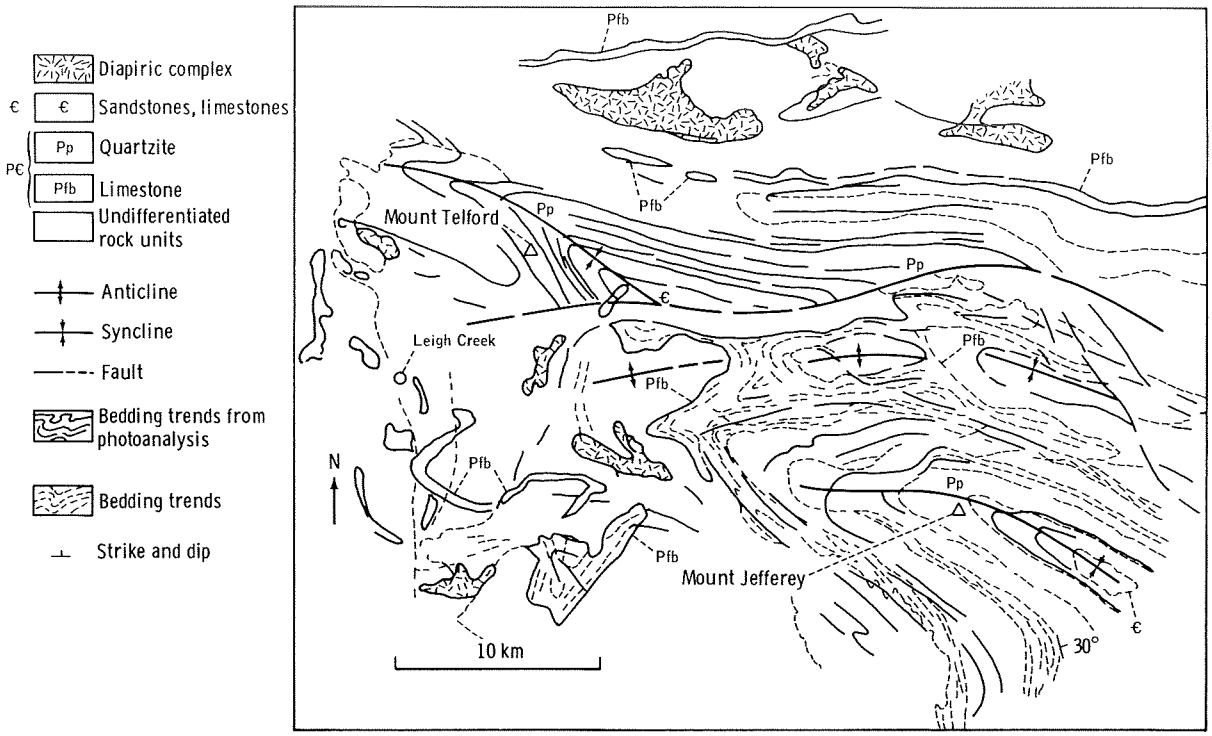


FIGURE 12.—Photogeologic analysis and map comparison of the Mount Jefferey area, Flinders Ranges, South Australia (partly after ref. 7).

Although not in the immediate area, some Devonian rocks have been identified in the deeper basins in the northern part of South Australia together with Permian marine sediments and rather extensive Permian glacial debris.

Upper Triassic terrestrial sediments, including coal measures, were deposited together with fluviatile and lacustrine sediments (ref. 3). Marine deposition occurred at the beginning of the Cretaceous, and by Late Cretaceous most of the basins were filled with sediments. Continental-type sedimentation gradually replaced the marine type. By Tertiary time, several important sedimentary basins and embayments had developed along the continental margin, such as Murray Basin, Saint Vincent Basin, and others (fig. 5). Tertiary sedimentation occurred within these basins and included the area east of Lake Torrens and southward to Spencer Gulf.

Tectonic movements resulted in the breakup of Tertiary basins of sedimentation (ref. 3) in late Miocene. These movements continued into the Quaternary as part of the Kosciuskan orogeny. As Parkin (ref. 3, p. 204) states: "The physiographic features we now know as Mount Lofty and Flinders Ranges, Lake Eyre and other inland depressions, . . . are all geologically young and are still being developed and modified."

Folding

Within the previously described time-geologic sequence, the layered rocks of the Flinders Ranges were folded into a series of mega-anticlines and megasynclines. In the Marree region, these folds trend generally northwesterly, but near Parachilna and Leigh Creek, there are very marked deflections to the east. Here the southern fold belt abruptly turns eastward through an almost right-angle bend. Farther north near Leigh Creek, the north to north-northwesterly fold belt turns southeasterly, then almost east for at least 112 km to where it is finally covered by younger

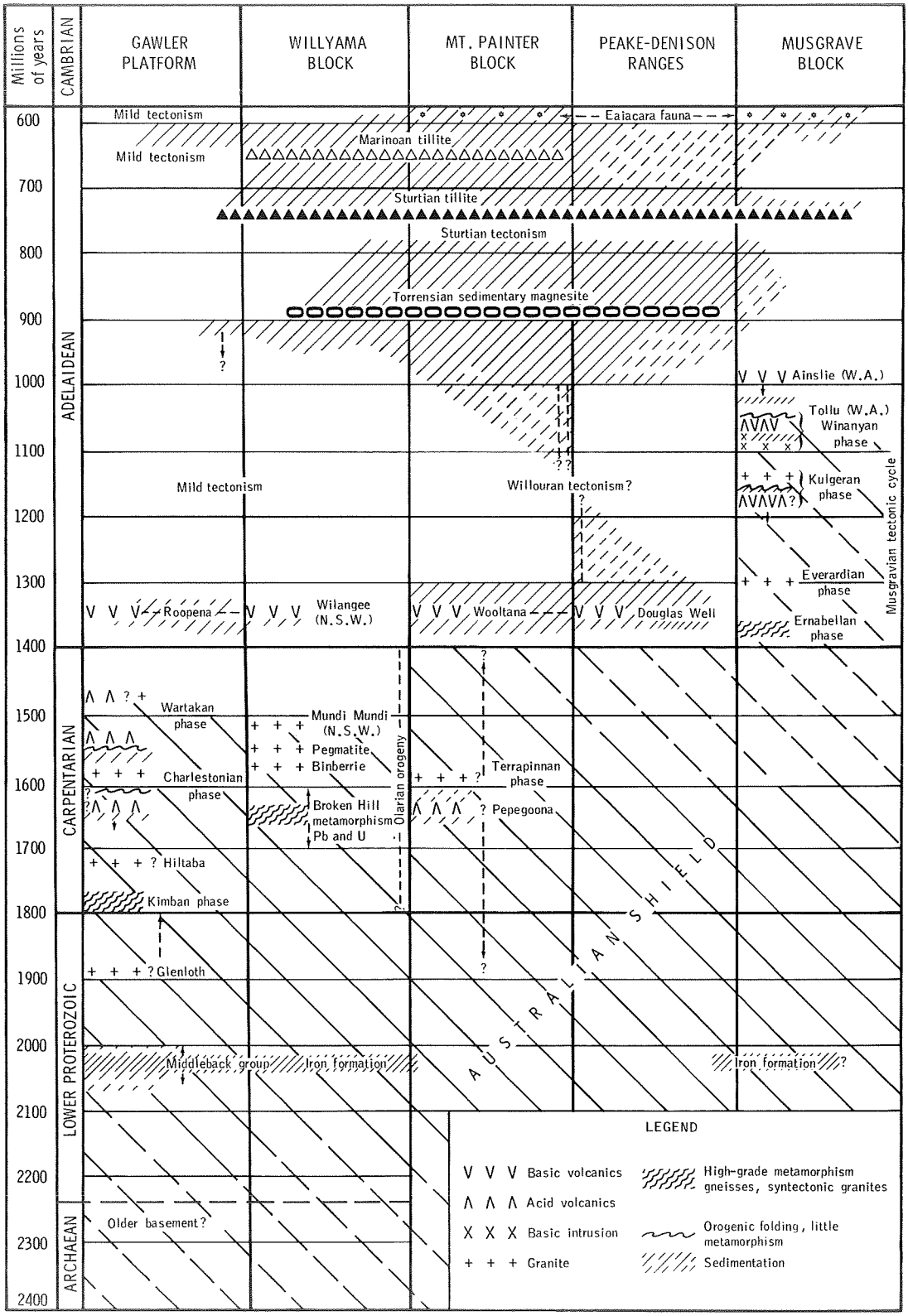

Millions of years
CAMBRIAN
GAWLER PLATFORM
WILLYAMA BLOCK
MT. PAINTER BLOCK
PEAKE-DENISON RANGES
MUSGRAVE BLOCK
600
700
800
900
1000
1100
1200
1300
1400
1500
1600
1700
1800
1900
2000
2100
2200
2300
2400
ADELAIDEAN
CARPENTARIAN
LOWER PROTEROZOIC
ARCHAEAN
Mild tectonism
Marinoan tillite
Mild tectonism
Ediacara fauna
Sturtian tillite
Sturtian tectonism
Torrensian sedimentary magnesite
Ainslie (W.A.)
Tollu (W.A.)
Winanyan phase
Kulgeran phase
Everardian phase
Ernabellan phase
Musgravian tectonic cycle
Mild tectonism
Willouran tectonism?
Roopena
Wilangee (N.S.W.)
Wooltana
Douglas Well
Wartakan phase
Charlestonian phase
Mundi Mundi (N.S.W.)
Pegmatite
Binberrie
Broken Hill metamorphism
Pb and U
Olarian orogeny
Terrapinnan phase
Pepegoona
Hiltaba
Kimban phase
Glenloth
Middleback group
Iron formation
Iron formation?
AUSTRALIAN SHIELD
Older basement?
LEGEND
Basic volcanics
Acid volcanics
Basic intrusion
Granite
High-grade metamorphism gneisses, syntectonic granites
Orogenic folding, little metamorphism
Sedimentation

FIGURE 13.—Major stratigraphic and tectonic events of Precambrian time, South Australia (after ref. 3).

basin sediments. Approximately 56 km southeast of Leigh Creek, the fold belt changes from an easterly to a roughly north-south bearing, to form the concave part of a broad U facing westward.

To the west of Leigh Creek across Lake Torrens, and just beyond the area of figure 8, broad open folds are lacking on the Stuart Shelf on the trend of the U-shaped fold complex.

At least three possible modes are suggested for the origin of this general pattern of folding in the Flinders Ranges: (1) primary compression-type folding by a westward-directed stress field with secondary folding imposed under different stress conditions; (2) lateral stress of varying magnitude from the east directed against the yielding geosynclinal sediments and against a subsurface prong of relatively unyielding Precambrian crystalline rocks around which the Proterozoic and Cambrian sediments were folded; and (3) an eastward-directed stress with a relatively stable prong of older Precambrian rocks acting as a localized ram in the U region of the fold belt. A fourth consideration could be a major buried shear zone in the area of the warped fold axes, such as now expressed in the Darling lineament to the east. That the folds are mainly not broken and displaced, but appear to be continuous and interrelated throughout this complex area, suggests a stress field that resulted in flow folds, rather than faulted folds. A subsurface resistant prong around which the flow folds developed may be a likely cause. Chamberlin and Shepard's (ref. 20) folding experiment with a directed ram yielded rather good curved folds of the type present in South Australia.

The source of the stress, whatever the type, was of regional character because the entire Adelaidean Geosyncline was affected. The interplate elongate geosynclinal basin may have been squeezed between the movements of the microplates of the continental mass (the Gawler-Musgrave blocks and the Murray-Great Artesian Basin blocks). Basement movement parallel to the Darling lineament may have effected the U-imposed fold zone on the linear folds of the Flinders Ranges.

Faulting

Faults are not spectacularly developed in this orogenic region of megafolds. Two prominent sets are recognized: a northeast set, best developed near Parachilna, and a less-abundant set of northwesterly trend near Leigh Creek. A third set, not readily visible on the photographs but most likely present, is a northerly set developed along the eastern and western margins of the Flinders Ranges. Movement on the latter resulted in the horst of Precambrian and Cambrian rocks above the lake plains. A major "crushed zone" of generally northerly trend is reported along the western side of Lake Torrens in the zone of the Torrens Hinge Zone (ref. 3, p. 220).

The northwest-northeast fault sets locally offset fold axes and limbs. Considering the magnitude of the folds in the area, the fault displacement is modest. Interpretation of the photographs does not permit quantitative displacements either in direction or amount. The known northwest-northeast faults within the Flinders Ranges on projection intersect each other at less than 90°. This intersecting set suggests shear fracture resulting from either an eastward- or westward-directed principal stress direction as noted previously.

Some thrust faults occur along the eastern part of the Copley area. Here the faults trend generally northward and dip eastward. The very long fault that extends from Leigh Creek northward has reverse fault movement and large southwesterly displacement. South of Leigh Creek, it resembles a thrust fault. Older beds of generally northeastward dip lie on the faulted southwest limb of a northwesterly striking anticline and part of a trough of a parallel trending syncline. These suggest a possible westward-directed stress.

The range border faults are relatively young features related to Tertiary tectonism. They were important in outlining the present Flinders Ranges by downfaulting of the Lake Torrens and Lake Blanche blocks.

Diapirs

Webb (ref. 21) observed that the breccia components of the diapirs were similar to rocks of the

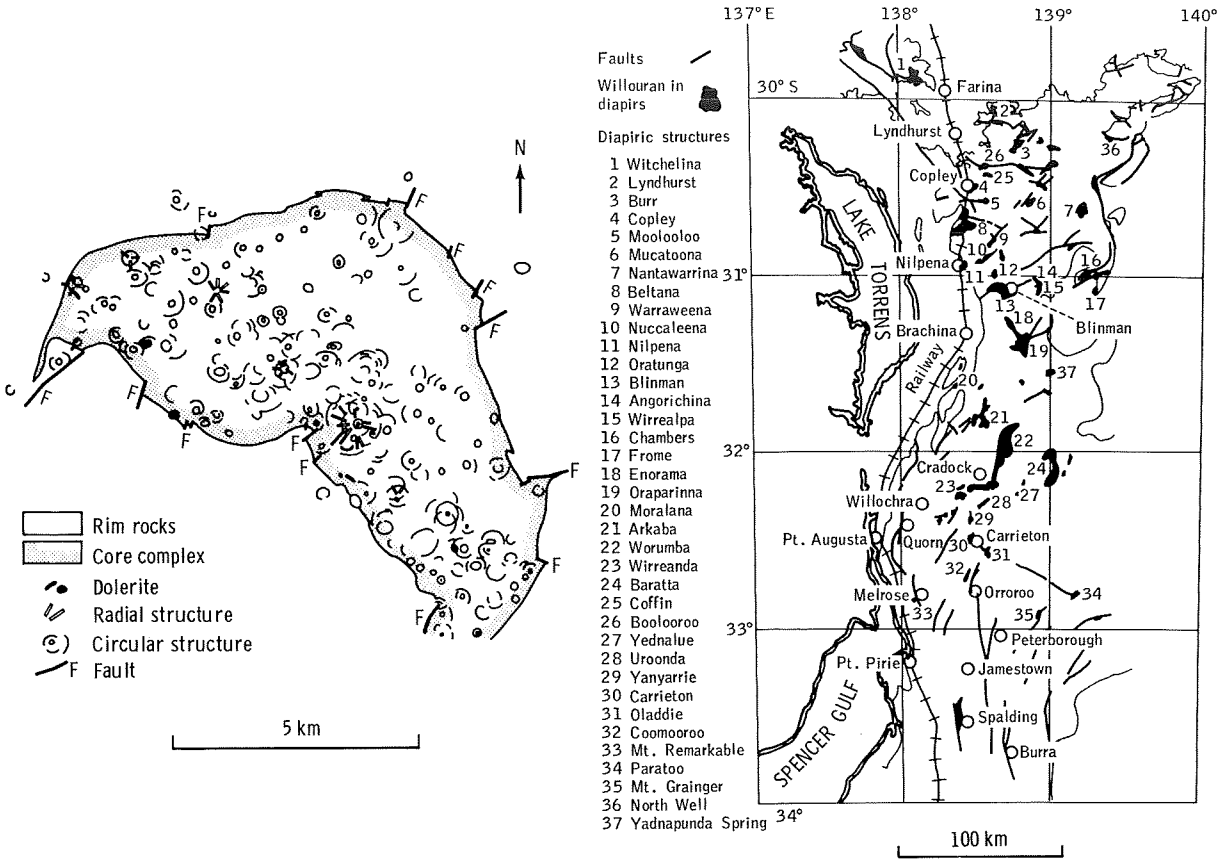


FIGURE 14.—Detail of the Blinman Dome diapir (after ref. 5) and index to diapirs in the Flinders Ranges, South Australia (after refs. 3 and 5).

Willouran Series lower in the stratigraphic section. From this, he and his colleague Von der Borch concluded that the breccia masses had been forcibly intruded into overlying sediments as piercement of diapiric structures. Coats (ref. 5) studied the Blinman Dome (fig. 14) in detail. This loaf-shaped body is approximately 14 km long and as much as 6 km across. He confirmed that it was of diapiric origin and observed that "tectonic crush zones" originally described in the Flinders Ranges were also of diapiric origin. Emplacement evidence suggests that intermittent diapirism occurred from pre-Sturtian to Cambrian times. Coats (ref. 5, p. 33) suggests that the imposed tectonic stresses on and the plastic behavior of Willouran rocks resulted in the diapirism. He does not directly relate them to orogenic activity at the end of Cambrian, recognizing that some diapirs were actively eroded in Sturtian (Precambrian) time.

The broad pattern of distribution of these structures and their close relationship to the general area of the Adelaidean Geosyncline lends support to Coats' theory of origin. The spatial relationship to folds and faults is probably more apparent than real. If this be so, then the diapirs were rock components involved in the orogeny at the end of Cambrian time.

Some unanswered questions exist for these intrusive masses; for example: How do you account for the common occurrence of igneous rocks in the diapirs? Why is the presence of mineral deposits of copper, silver, lead, and gold associated with the bodies? How do you account for the close spatial relationship of many of the diapirs to axial parts of the folds, which are

presumed to be of much later age than the diapirs?

Basin Development

The folding and faulting of early Paleozoic time was followed by basin development in parts of the region. The large Great Artesian and Murray Basins are examples. In the smaller Copley Basin near Leigh Creek, Upper Triassic coal measures more than 600 m thick accumulated in this local basin on the Precambrian and Cambrian rocks. The Triassic beds are flat to gently inclined and lie in strong unconformity with the underlying Cambrian-Precambrian folded rocks.

The larger and elongate Torrens-Blanche-Frome basins developed at a later date. Thick accumulation of Tertiary sediments occurred in these basins. These major tectonic features are now still active and prominent physiographic forms of South Australia.

Continental Drift and Plate Tectonics

Modern researchers lend strong support to the theory of Pangaea and its southern part, Gondwana, as land entities in the Permian (refs. 22 and 23) with Australia as a component part. The maps of Dietz and Holden (ref. 23) indicate that the postulated Permian position of part of South Australia (the area of concern in this paper) is south of the Antarctic circle. The evidence of Permian continental glaciation in South Australia as well as in the Indian subcontinent, South Africa, Brazil, and Antarctica, together with paleontological data, similar tectonic characteristics and rock types, paleomagnetism, and continental margin outlines, gives strong support to this concept. Crowell and Frakes (ref. 24) confirm evidence of a Permian ice age and show that glaciers grew and radiated from centers somewhat coincident to the positions of the Earth's magnetic pole at that time. Donn and Ewing (ref. 25), however, suggest that icecap buildup occurred where the Earth's rotational poles moved onto land or landlocked water bodies.

Less clear is the position of South Australia in Proterozoic time just before the development of the fold mountains of the Flinders Ranges. Glaciation in Sturtian (Precambrian) time together with distinct sedimentary cycles in South Australia and the similarities of rock types in central Africa pose the possibility that both continents were in a far south latitudinal position in at least part of Proterozoic time. If this be so, and if the breakup of Gondwana did not occur until post-Permian time (though Dietz and Holden (ref. 23) suggest that it occurred near the end of Cretaceous time), we must consider a tectonic setting that relates to both Antarctica and Australia. However, the presence of thick Upper Triassic coals in the Copley Basin of South Australia would not be expected in this part of Australia if this part of the continent was in a near 60° south latitude position in Jurassic and part of Cretaceous time. This suggests an earlier north and eastward movement of the Australian plate.

Badgley (ref. 19) suggests that the strong Precambrian lineaments of Australia are anomalous. He notes that if the continent is rotated clockwise more than 90°, the major lineaments more closely accord with known lineaments of other Precambrian areas of the world. Figure 15 shows his

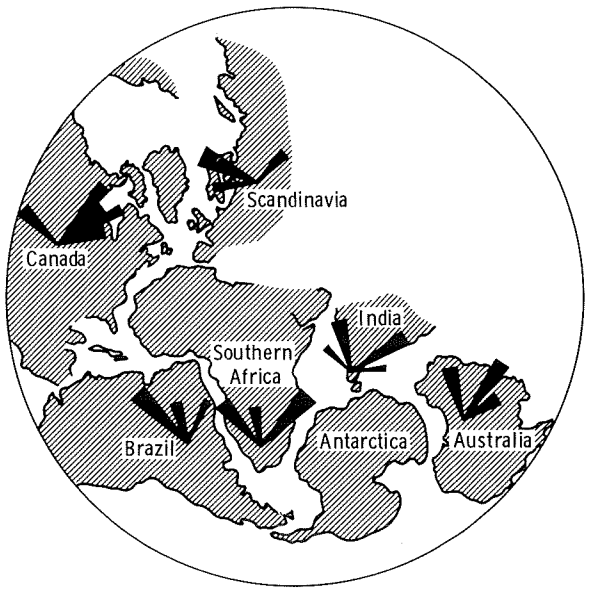


FIGURE 15.—Precontinental drift positions of continents showing major structural trends by rosettes (after ref. 19).

concept of the continents before continental drift. He suggests late Paleozoic as the time of breakup of the landmass.

If Australia was in the pre-breakup position in Gondwanaland, then the stresses acting on the Adelaide Geosyncline more closely approached a northerly direction than the easterly or westerly directions indicated by the present orientation of the continent. Additional details of rock types and structure of Antarctica and corresponding rock ages and ages for structures on the present South Australia coast are needed to confirm or modify the past tectonic setting of Proterozoic time.

GROUND-TRUTH CHECKS

If good geologic data were not already available, numerous ground check areas would have been proposed for this most interesting and complex region. The excellent 1:250 000-scale geologic maps of a major part of the area make such ground checks less necessary. Good correlation of photogeologic data and the geology on the geologic maps is readily apparent. Fold structures are correlatable; faults match well; even some of the nonlinear crosscutting features can be identified on the photographs and correlated with diapir-like masses shown on published geologic maps.

Surficial materials are identifiable and some field checks could be made to confirm or refute the nine types suggested. For this project, however, the cost of such checks is high in relation to the value that might be returned.

The excellent ASTP color photographs would have been a boon to the Australian geologists in the field had they been available at the time of the geologic mapping. Indeed, the maps presented here would have been an excellent working tool for stratigraphic work, geologic mapping, and interpretation of the large and complex structures of the region.

CONCLUSIONS

Exceptional ASTP color photographs of the Flinders Ranges and environs of South Australia permitted photogeologic analysis of general rock types, megafolds, folds, faults, and lineaments exposed in the area. Although formational units were not established, the photogeologic analysis did define various types of layered and nonlayered units, as well as several varieties of surficial materials.

Major folds occur in a thick sequence of sedimentary rocks of geosynclinal origin. The layered units show megafold structures extending scores of kilometers in length, folds of lesser dimensions up to a few kilometers in length, and small drag-like folds up to 2 km or so in size. Significantly, the generally northerly trending folds are warped strongly eastward near Leigh Creek and form an easterly trending series of megafolds and smaller folds. The fold belt turns southward for several kilometers, then westward and finally south again. This U-shaped fold on the northerly trending fold belt occurs in the thick sedimentary rock section.

The layered units are cut by northeasterly and northwesterly trending faults of several kilometers' strike length and up to a kilometer or more slip displacement. The type of slip displacement cannot be defined without ground-truth confirmation or correlative rock units across the fault interfaces. Poorly defined north-south faults outline the ranges. Lineaments, other than bedding and fracture types, relate to drainage patterns in the region. These may also have an underlying, but unknown, structural control.

Some nonlinear to roughly linear features cut the layered rock units. The structures have characteristics of intrusive masses. Known diapir-like bodies within the sedimentary rock sequence explain many of these not too well defined masses on the photographs.

The ASTP color photographs are exceptional in their resolution of stratigraphy and structures in this South Australian area.

The interpretive maps presented here would have been an excellent working base for stratigraphic and structural work in the region. Work already completed by the very competent geologists of South Australia confirms many of the features observed and adds details available only from a ground geologic study of the region.

Because of the exceptionally good regional geologic maps available, no ground-truth investigations are proposed for this area.

ACKNOWLEDGMENTS

This work was performed under Smithsonian Grant PC6-22279 as a subcontract of NASA contract NAS9-13831.

REFERENCES

1. Sprigg, R. C.: Sedimentation in the Adelaide Geosyncline and the Formation of the Continental Terrace. Sir Douglas Mawson Anniversary Volume, M. F. Glaessner and E. A. Rudd, eds., University of Adelaide (South Australia), 1952, pp. 153-159.

2. Johns, R. K.: Geology and Mineral Resources of the Andamooka-Torrens Area. Bull. no. 41, Geol. Surv., Dept. Mines, South Australia, 1968.

3. Parkin, L. W., ed.: Handbook of South Australian Geology. Geol. Surv., Dept. Mines, South Australia (Adelaide), 1969.

4. Forbes, B. G.: The Geology of the Marree 1:250 000 Map Area. Rept. Invest. no. 28, Geol. Surv., Dept. Mines, South Australia, 1966.

5. Coats, R. P.: The Geology and Mineralization of the Blinman Dome Diapir. Rept. Invest. no. 26, Geol. Surv., Dept. Mines, South Australia, 1964.

6. Coats, R. P.; and Anaconda Australia, Inc.: Curdimurka 1:250 000 Preliminary Geological Map. Geol. Surv., Dept. Mines, South Australia, 1970.

7. Coats, R. P., compiler: Copley 1:250 000 Geological Map. Geol. Surv., Dept. Mines, South Australia, 1973.

8. Forbes, B. G., compiler: Parachilna, South Australia, 1:250 000 Geological Series. Geol. Surv., Dept. Mines, South Australia, 1972.

9. Callen, R. A.; and Coats, R. P.: Frome 1:250 000 Geological Map. Geol. Surv., Dept. Mines, South Australia, 1975.

10. Johns, R. K.; Hiern, M. N.; et al.: Torrens 1:250 000 Geological Map. Geol. Surv., Dept. Mines, South Australia, 1964.

11. Hills, Edwin Sherbon: Elements of Structural Geology. John Wiley and Sons (New York), 1963.

12. Coats, R. P.; and Blissett, A. H.: Regional and Economic Geology of the Mount Painter Province, South Australia. Bull. no. 43, Geol. Surv., Dept. Mines, South Australia, 1971.

13. Thomson, B. P.: The Lower Boundary of the Adelaide System and Older Basement Relationships in South Australia. J. Geol. Soc. Australia, vol. 13, part 1, 1966, pp. 203-228.

14. Johns, R. K.; Hiern, M. N.; and Nixon, L. G.: Andamooka 1:250 000 Geological Map. Geol. Surv., Dept. Mines, South Australia, 1966.

15. Whitten, G. F.: Suggested Correlations of Iron Deposits in South Australia. Quart. Geol. Notes, Geol. Surv., Dept. Mines, South Australia, vol. 18, 1966, pp. 7-11.

16. Thomson, B. P.: Geology and Mineralization of South Australia. Geology of Australian Ore Deposits, Vol. 1. Eighth Comm. Min. Met. Congr., Australia, no. 2, 1965, pp. 270-284.

17. Carey, S. Warren: The Rheid Concept in Geotectonics. J. Geol. Soc. Australia, vol. 1, no. 1, 1954, pp. 67-117.

18. Forbes, B. G.; Coats, R. P.; Webb, B. P.; and Horwitz, R. C.: Marree 1:250 000 Geological Map. Geol. Surv., Dept. Mines, South Australia, 1965.

19. Badgley, Peter C.: Structural and Tectonic Principles. Harper and Row (New York), 1965.

20. Chamberlin, Rollin Thomas; and Shepard, F. P.: Some Experiments in Folding. J. Geol., vol. 31, no. 6, 1923, pp. 490-512.

21. Webb, B. P.: Diapiric Structures in the Flinders Ranges, South Australia. Trans. Roy. Soc. South Australia, vol. 75, 1960, pp. 97-114.

22. Carey, S. Warren: Continental Drift, A Symposium. Univ. of Tasmania (Hobart), 1958.

23. Dietz, Robert S.; and Holden, John C.: Reconstruction of Pangaea: Breakup and Dispersion of Continents, Permian to Present. J. Geophys. Res., vol. 75, no. 26, Sept. 10, 1970, pp. 4939-4956.

24. Crowell, John C.; and Frakes, Lawrence A.: Phanerozoic Glaciation and the Causes of the Ice Ages. American J. Sci., vol. 268, Mar. 1970, pp. 193-224.

25. Donn, William L.; and Ewing, Maurice: The Theory of An Ice-Free Arctic Ocean. Causes of Climatic Change. Proceedings of the 7th INQUA Congress, Vol. 5, 1968.

Volcanic Landforms and Astroblemes

R. S. Dietz[a] *and J. F. McHone*[b]

ABSTRACT

Apollo crewmembers, while searching for circular ground features, observed and photographed astroblemes (ancient impact scars) in Brazil and Libya, and volcanoes in Italy, the Galapagos Islands, and Mexico. The Brazilian site was previously unknown to impact scientists, and photographic measurements of the Libyan structure proved larger than measurements made by Earth-based investigators. Plumes of active volcanoes in Italy were traced great distances, and the inaccessible Galapagos Islands were viewed synoptically. In Mexico, a feature that had been previously identified as a possible meteorite impact site was found to be formed by a volcanic steam explosion.

INTRODUCTION

Before the Apollo-Soyuz Test Project (ASTP) mission, the Apollo astronauts were briefed on volcanic features and on astroblemes, which are geologically ancient meteorite impact scars. They were alerted to the possibility of observing and photographing plumes of active volcanoes and circular structures that might be astroblemes. Because of the exigencies of the mission, not all of the objectives were attained. Nonetheless, many excellent space photographs were acquired; five of the more spectacular examples are discussed in this report.

[a]Arizona State University, Tempe, Arizona.

[b]University of Illinois at Urbana-Champaign.

BRAZILIAN CIRCULAR STRUCTURE

Astroblemes are rare features on Earth, yet they are of unusual interest in astrogeology and planetology because they are terrestrial analogs of the impact craters that dominate the Moon, Mars, and Mercury. Among the circular structures scheduled for photography on ASTP were two astroblemes in Brazil: Serra da Cangalha in Goiás and Araguainha dome in Mato Grosso. Although these features were not photographed during the ASTP mission, a new unnamed circular structure only 45 km north-northeast of Serra da Cangalha was photographed (fig. 1).

This feature occurs in the State of Maranhão at latitude 07°43′ S and longitude 46°39′ W, and it is 4 km in diameter. It appears to be of a geomorphic and structural style similar to Serra da Cangalha. The newly found circular structure is almost certainly the central dome of an astrobleme. Because the dome diameter is generally one-third the diameter of the entire impact structure (a central dome surrounded by an annular depressed ring graben), the entire structure is presumably 12 km in diameter.

This feature can provisionally be termed the Riachão Ring, the name of the nearest prominent village 25 km to the north. This feature seems to be a highly probable meteorite impact scar and, together with the Serra da Cangalha, could represent a twin-impact event. The new structure is not that of a modern meteorite crater but rather of an ancient impact scar or astrobleme and is, hence, presumably a pre-Neogene event. In addition, the structural event affects the flat-lying Permian Pedra do Fogo Formation; therefore, the impact event occurred in post-Permian time. This formation is mainly arenaceous, but it contains flints

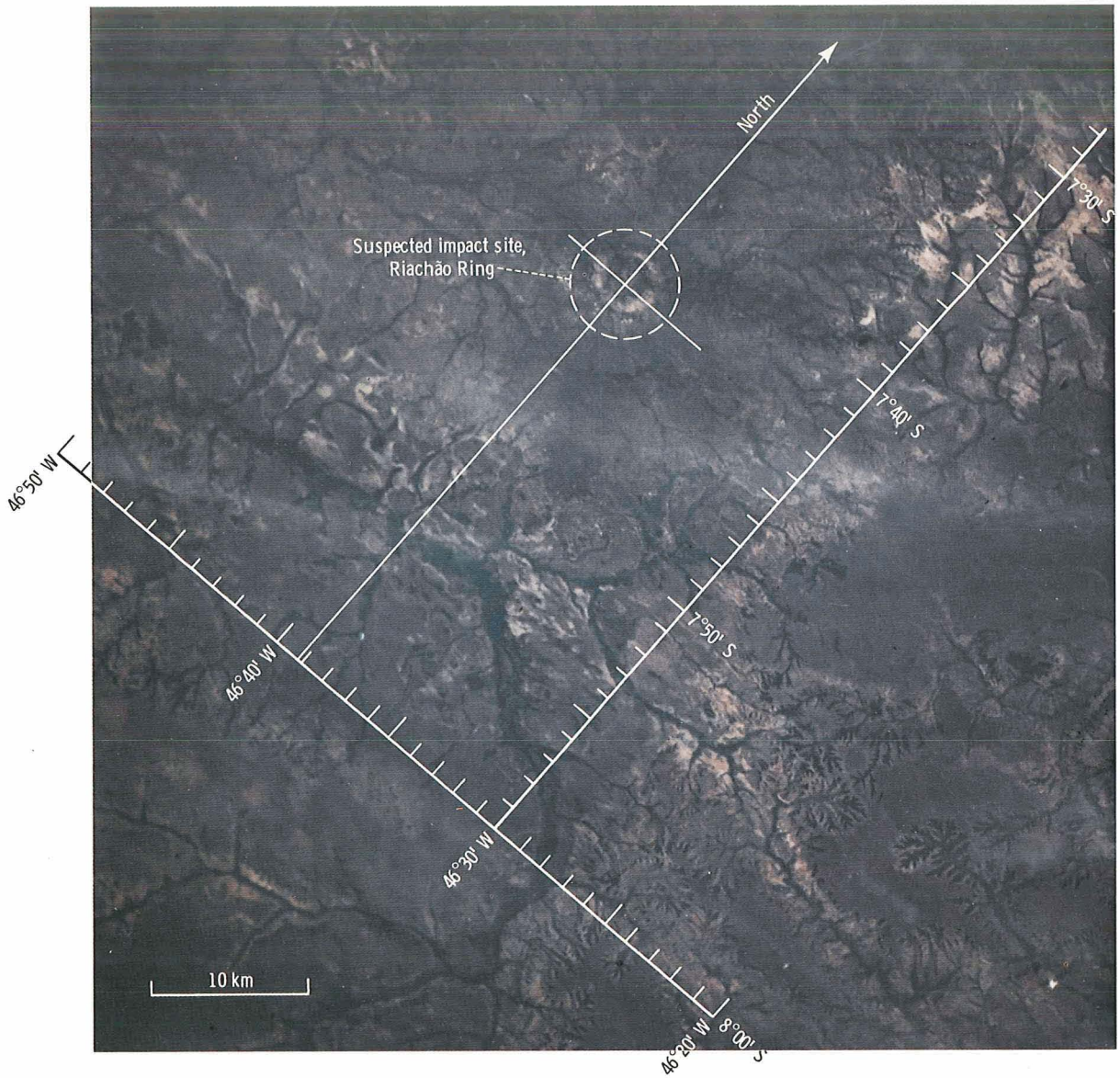


FIGURE 1.—The Riachão Ring structure in Brazil: the bleached ring of a probable ancient impact site or astrobleme in central Brazil. This domal structure interrupts regionally flat-lying beds as indicated by dendritic stream patterns. The haze is probably caused in part by slash and burn agronomy (AST-23-1931).

that weather out into the regolith, hence the name Pedra do Fogo or "fire stone." According to a Radar Mapping of the Amazon (RADAM) geologic map (scale 1:1 000 000) (ref. 1), the Riachão Ring is a dome entirely within the Permian Pedra do Fogo Formation, which is a complex unit consisting of sandstone, siltstone, shale with lenses of silex, and fossiliferous limestone and gypsum. Serra da Cangalha was recently studied in a field reconnaissance and interpreted as a probable astrobleme (ref. 2); at the time, the existence of a twin structure was not suspected. It seems likely that the Riachão structure is of the same origin. The results of a later field investigation of the Riachão Ring are discussed in another report in this publication (see section entitled

"Riachão Ring, Brazil: A Possible Meteorite Crater Discovered by the Apollo Astronauts"). It is quite possible that the Serra da Cangalha and the Riachão domes resulted from a dual impact; such multiple events are rather common among the Earth's known astroblemes.

A vertical aerial photograph of the Riachão structure confirms a domal structure for the entire ring with only a vague indication of a surrounding annular ring syncline. The authors believe that the dome consists of three formations: (1) a small central dome of resistant, light-colored rock with a central depressed dimple; (2) an annular ring of soft, topographically low, dark rock, which has been eroded by a stream that breaches the outer ring along the northwest quadrant; and (3) a high outer ring of resistant, light rock, which has been highly modified by agricultural activity such as small farms and extensive grazing. Although topographically high, the outer ring has only moderate relief; this is unlike Serra da Cangalha where the mountainous ring makes a natural corral breached by a single stream across which a barbed-wire fence has been erected.

The photographic acquisition from space of this newly found probable astrobleme is a significant accomplishment of the ASTP mission.

OASIS ASTROBLEME, KUFRA (LIBYA)

Figure 2 is part of the Sahara Desert in Libya, which was photographed during a mapping pass. The photograph reveals remarkable circular patterns that are strung together to seemingly create a giant insect, complete with antennae, but lacking the full complement of six legs. These circular patterns are, of course, vegetation patterns caused by huge rotating sprinklers at the Kufra Oasis in Libya.

For the purpose of this report, however, interest is aroused by the circular ring feature lying 115 km west-northwest of Kufra. The feature is an established astrobleme, discovered a few years ago by Martin (ref. 3) and recently described in detail by French et al. (ref. 4), who have provisionally named it the Oasis structure (latitude 24°35′ N and longitude 24°24′ E). Clearly visible on the ASTP photograph is the prominent central dome. 5.1 km in diameter. The dome is outlined by resistant, quaquaversally dipping beds that form a discontinuous series of hills approximately 100 m higher than the interior. In places, sandstones are intensely folded and possibly overturned, but the central part of the structure, where deformation should be most intense, is obscured by sand cover. French et al. (ref. 4) cite the overall diameter, including the surrounding ring graben, as 11.5 km, but the authors' study of Landsat images suggests an overall diameter of approximately 17 km. This outer ring is not readily apparent on the ASTP photograph. Shock metamorphic effects, especially planar structures in quartz, demonstrate that this is indeed an astrobleme. The structure can only be dated as post-Early Cretaceous, the age of the Nubian Sandstone, which is affected by the event. It has been speculated that the Oasis astrobleme could possibly be the site of origin of the highly siliceous Libyan glass, which is thought to have been generated by impact splash.

ERUPTION OF MOUNT ETNA

On July 24, 1975, the 3240-m-high Mount Etna was photographed in eruption while emitting a cloud of ash and steam visible to the east for approximately 200 km (fig. 3). East of the crater, cumulus clouds are generated apparently using the ash particles as condensation nuclei.

Mount Etna, a basaltic shield volcano 30 km across at its base, is the most active in all of Europe; more than 75 eruptions have been observed since Roman times. Its ash falls and lava flows have frequently caused damage to cities and crops. Volcanic ash layers are commonly found in sediment core samples taken from the Mediterranean Sea floor; the layers were dispersed from erupting centers such as Mount Etna.

The activity of Mount Etna is now closely monitored through the Italian-Belgian-sponsored International Volcanological Institute, which is located in Catania, Sicily, and which also maintains an observatory on the flanks of Mount Etna. The edifice of Etna has been entirely built up by eruptions from two craters; the presently active center is the volcano of Gibello. The volcanoes of Italy are due to a partial melting of a downgoing slab of

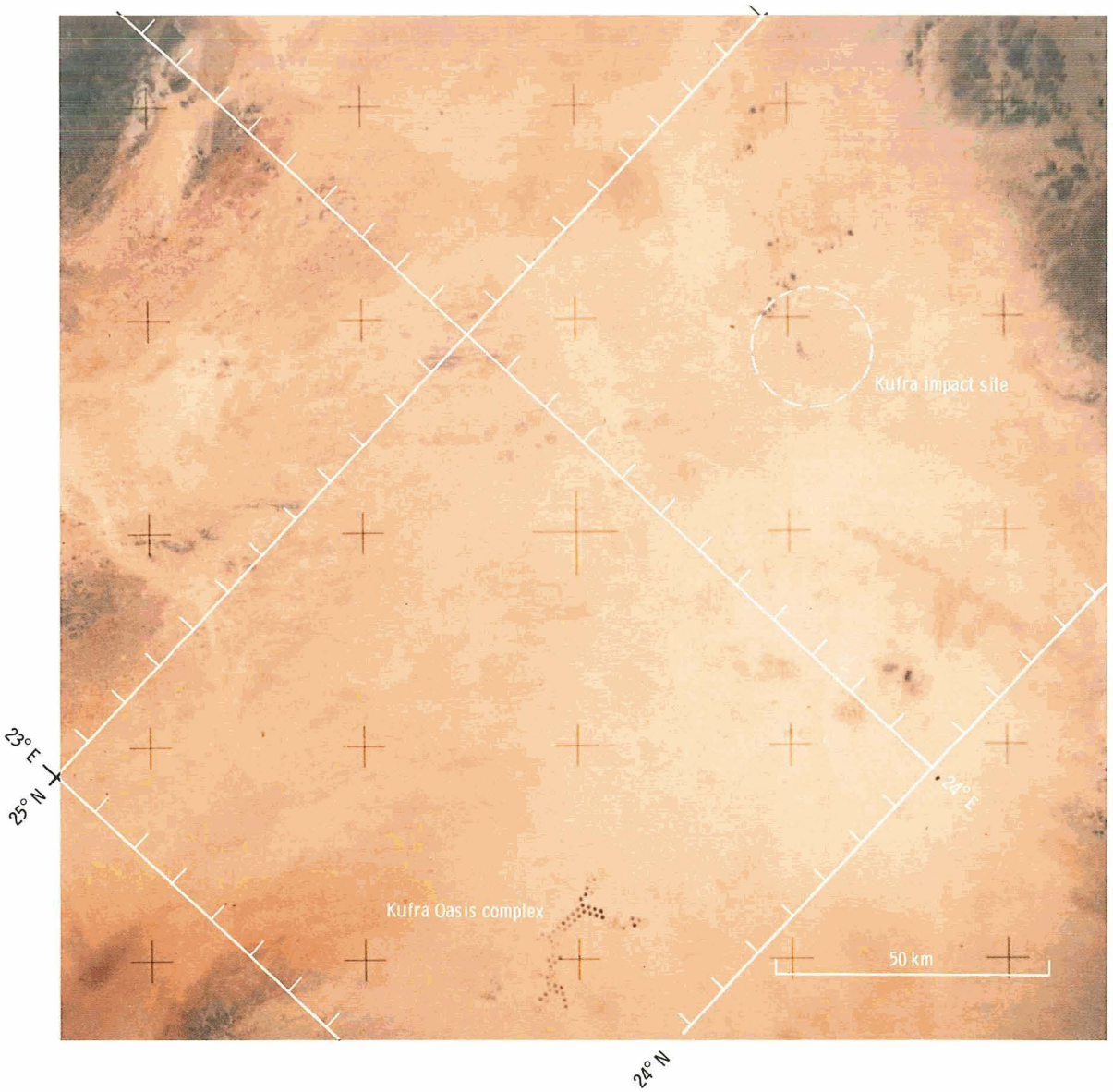


FIGURE 2.—Circular structure in Libya: the Oasis astrobleme (AST-16-1244).

lithosphere involved in the rotation of Sardinia and Corsica away from southern France, but the details of this scheme remain problematical.

Lying to the north of Sicily are the Lipari Islands (Eolie Islands), the southernmost of which is the site of Vulcano (the type-locality of volcanoes), which was last active in 1964. Immediately to the north of Vulcano, and forming a small projection to the island, is Volcanello, which was last active in 183 B.C. The northernmost member of the Lipari Islands is Stromboli. Its famous volcano can also be seen to be in moderate eruption, evidenced by a steam-and-ash cloud being carried eastward by the wind (fig. 3).

The cloud from Etna can be traced for approximately 200 km to the east, and is carried by an



FIGURE 3.—Southern Italy, Sicily, and Mount Etna. High-oblique color-infrared photograph looking southwestward and showing the southern tip of Italy and the entire island of Sicily (AST-13-835).

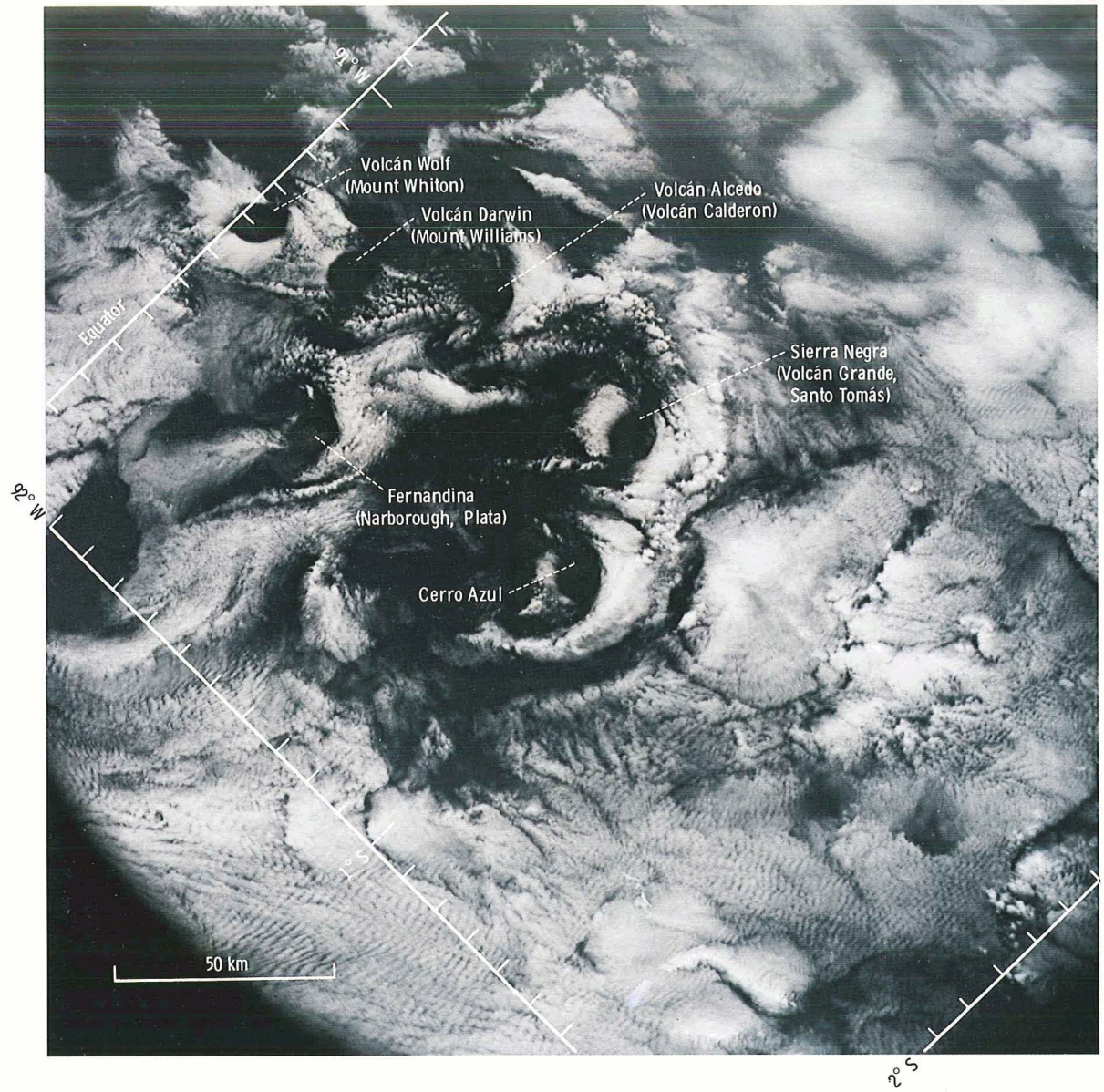


FIGURE 4.—Isla Fernandina and Isla Isabela, Galapagos Islands, with associated calderas. The unusual cloud patterns are related to the orographic effects of the islands intercepting the southeast trade winds (AST-19-1579).

east-setting wind. The plume disperses gradually, indicating little wind turbulence. A comparison of the Etna plume with that observed at Sakurajima (Japan) by the Skylab 4 crew (ref. 5) is of interest. The Etna plume appears somewhat more coherent, diffuses more regularly, and provides no evidence of a changing wind direction at higher altitude. Similar to the Sakurajima plume, the Etna plume does not appear to break through the tropopause and carry ash into the stratosphere; thus, the area of ash fallout remains limited. However, the usually inferred pattern of an ash fallout in an elliptical pattern along a linear axis seems an oversimplification.

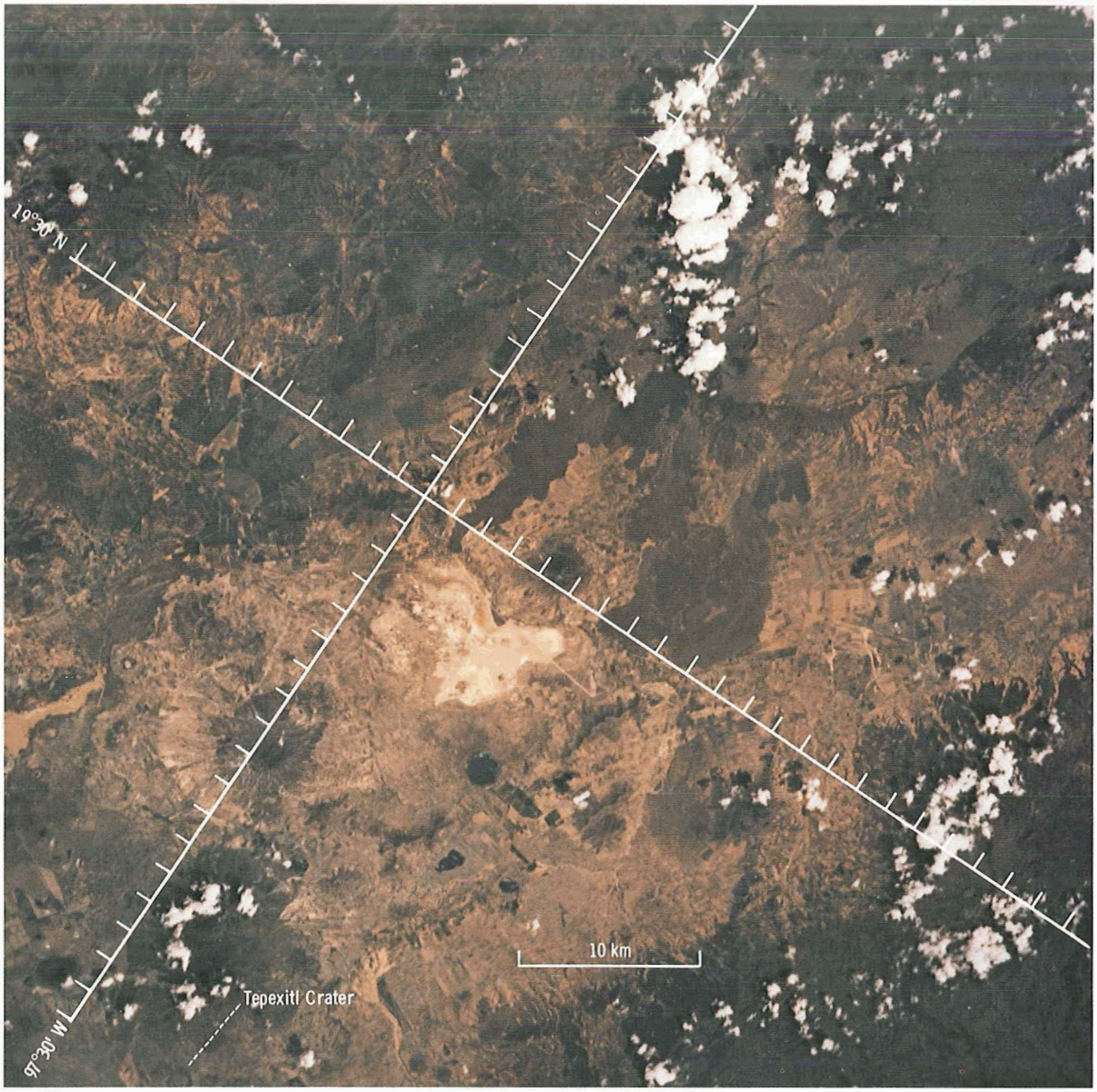


FIGURE 5.—The eastern end of the Transverse Volcanic Zone, Mexico (AST-24-2003).

GALAPAGOS VOLCANOES

Straddling the Equator in the eastern Pacific Ocean, the Galapagos Islands are wreathed in clouds under the influence of the southeast trade winds. Six volcanic craters project above the clouds in figure 4, one of several near-vertical photographs taken on July 24, 1975.

The two islands of Isla Isabela and Isla Fernandina offer an unusual opportunity for volcanic surveillance by spacecraft because they lie in a remote and uninhabited part of the world. The volcanoes are of the alkalic plume type with their magmas originating below the asthenosphere.

Eastward drift of the Nazca tectonic plate over the Galapagos hot spot largely confines modern volcanic activity to Isla Isabela and Isla Fernandina.

In terms of the amount of lava extruded, the Galapagos are possibly the third most important center of volcanic activity in the world, exceeded only by Hawaii and Iceland. Five of the six volcanoes of the Isla Isabela/Isla Fernandina complex have been active since 1948: Cerro Azul in 1959, Sierra Negra in 1953 and 1954, Alcedo in 1970, Wolf in 1948, and Fernandina last in 1972. In 1968, Fernandina sustained an essentially *en bloc* caldera subsidence of nearly 300 m, which is probably the most spectacular example of this phenomenon ever recorded. All these volcanoes are shield volcanoes with central calderas and are characterized by ring-injection lava dikes rather than radial dikes as in Hawaii (ref. 6).

TRANSVERSE VOLCANIC ZONE, MEXICO

Mexico is cut by the Transverse Volcanic Zone (TVZ), which dominates the geologic structure of the central region of that country. The TVZ trends east-west in contrast to the north-south Pacific "Ring of Fire" that margins the Pacific Ocean. The anomalous trend of the TVZ remains unexplained. The Apollo crewmen captured on film a remarkable view of the eastern end of this zone, revealing a wealth of volcanic features lying to the east of the city of Puebla (fig. 5).

Figure 5 covers a 70- by 70-km area at the eastern end of the TVZ and immediately to the northwest of 5700-m-high Orizaba Mountain, the grandest volcano in North America, last active in 1687. The region offers one of the finest displays of volcanic features anywhere in the world.

Among the features revealed are extensive lava flows, rhyolite domes, maars, diatremes, vitric ash rings, and volcanic collapse features. In the central part of the photograph, a dry playa is visible, the central remnant of an extensive lake that existed when the Spanish conquistadors arrived in North America. This shallow body of water was similar to Lake Texcoco occupied by the Aztecs in the Valley of Mexico. Extensive lakebeds and ash rings now remain as evidence of the abundant ground water used to generate phreatic (steam) explosions. The maturely dissected, sinuous ridges with sharp crest lines are Cretaceous limestone outcrops, which project through the younger volcanic and lacustrine sediments. Their wooded cover gives them a darker hue. None of the volcanic features displayed in this photograph have been active in historic time, but their geomorphic youth suggests that they cannot be more than several thousand years old. A volcanic structure, Tepexitl Crater, appearing in this view was recently studied in the field by Dietz. The feature had been previously suggested as a possible meteorite impact site (ref. 7), but field studies incontrovertibly demonstrate a volcanic origin. The crater is a rhyolitic ash ring formed by a series of phreatic explosions rather than by a meteorite impact (ref. 8). The ASTP photograph (fig. 5) has sufficient detail to firmly support the volcanic nature of the crater, thus making the field investigation unnecessary. Although a Landsat image of the same region was available and was used in connection with the field study, the details of the image were far inferior to those of the ASTP photograph; thus, the value of supplementing electronically transmitted space imagery with film photography is demonstrated.

CONCLUSION

Visual observers searching for circular terrestrial patterns during ASTP returned with photographs of meteorite impact sites and volcanoes. The vantage point of near space enabled the viewing of geologic features and supplied details previously unavailable to scientists. An undescribed astrobleme was found in Brazil, and a known impact site in the Libyan desert was confirmed to be larger than measured by ground explorers. Airborne ash plumes were traced great distances from erupting Italian volcanoes with little sign of high-altitude dispersion. The entire Galapagos volcanic island system could be viewed at one time. A circular feature in Mexico, previously suggested as an impact site, could clearly be seen to be associated with a series of volcanic steam explosion craters.

REFERENCES

1. Radar Mapping of the Amazon (Project RADAM) Geologic Map, sheet SB 23/24, Teresina-Jaguaribe, 1973.

2. Dietz, Robert S.; and French, Bevan M.: Two Probable Astroblemes in Brazil. Nature, vol. 244, Aug. 31, 1973, pp. 561-562.

3. Martin, A. J.: Possible Impact Structure in Southern Cyrenaica, Libya. Nature, vol. 223, Aug. 30, 1969, pp. 940-941.

4. French, Bevan M.; Underwood, James R., Jr.; and Fisk, Edward P.: Shock-Metamorphic Features in Two Meteorite Impact Structures, Southeastern Libya. Bull. Geol. Soc. America, vol. 85, no. 9, Sept. 1974, pp. 1425-1428.

5. Kaltenbach, J. L.; Lenoir, W. B.; et al.: Skylab 4 Visual Observations Project Report. NASA TM X-58142, 1974.

6. MacDonald, Gordon A.: Volcanoes. Prentice-Hall, Inc. (Englewood Cliffs, New Jersey), 1972.

7. Maupome, L.: Possible Meteorite Crater in Mexico. Rev. Mex. Astron. & Astrofis. (Mexico), vol. 1, no. 1, 1974, pp. 81-86.

8. Maupome, L.; Alvarez, R.; Kieffer, S.W.; and Dietz, R. S.: On the Terrestrial Origin of the Tepexitl Crater, Mexico. Meteoritics, vol. 10, no. 3, 1975, pp. 209-214.

Riachão Ring, Brazil: A Possible Meteorite Crater Discovered by the Apollo Astronauts

J. F. McHone[a]

ABSTRACT

In north-central Brazil, the Apollo crewmembers photographed a 4-km-wide circular ground pattern. Although the feature was not visible on airborne radar and in near-infrared satellite images, it was clearly seen from space in the visible part of the spectrum.

A ground reconnaissance of this location and of a second circular structure nearby strongly supports a meteoritic origin for both sites.

INTRODUCTION

Remote sensing of the solar system's inner planets and their satellites has shown that meteoritic-impact craters are the most ubiquitous of all planetary landforms. However, on Earth they are comparatively rare; their scarcity is due to geologic erasure by tectonic, depositional, and erosional forces and to previous misidentification as volcanic or diapiric features. In recent years, the search for terrestrial craters and their ancient remains (astroblemes) has been intensified, resulting in the discovery of more than 100 confirmed or suspected sites on Earth (refs. 1 and 2). Investigators examining Landsat and side-looking airborne radar (SLAR) images of Brazil have recently detected two astroblemes (fig. 1); Araguainha to the west of Brasília and Serra da Cangalha in northern Goiás (refs. 3 and 4). A third and previously unknown site, now designated as Riachão Ring, was observed and photographed (fig. 2) by Apollo crewmembers during the Apollo-Soyuz Test Project (ASTP).

The 12-km-wide Serra da Cangalha was originally selected for ASTP photography to learn more about the visual appearance of terrestrial astroblemes from space. The location and general appearance of Serra da Cangalha were known from a study of SLAR and Landsat images (figs. 3(a) and 3(b)). Because of the common occurrence of heavy clouds and agricultural smoke in the area, only the haze-penetrating near-infrared band-7 Landsat images (0.8 to 1.1 μm spectral response) were used to prepare a description of landmarks and easily identifiable features (fig. 3(b)). This description was used by astronaut observers in the Apollo spacecraft. Unlike most geological features, the previously unknown 4-km ring in the ASTP photograph is most prominent in the *visible* part of the spectrum. The ring was therefore not noticed in the premission examination of near-infrared and radar images, but it was clearly seen and consequently photographed by crewmembers of the Apollo spacecraft. The intended site, Serra da Cangalha, is somewhat difficult to detect in the visible part of the spectrum and lies 45 km to the southwest of Riachão Ring (fig. 3(c)).

In spite of earlier geologic expeditions to Serra da Cangalha (ref. 4), no petrographic evidence of meteoritic shock-loading had been recovered; identification of the feature as an astrobleme was

[a]University of Illinois at Urbana-Champaign.

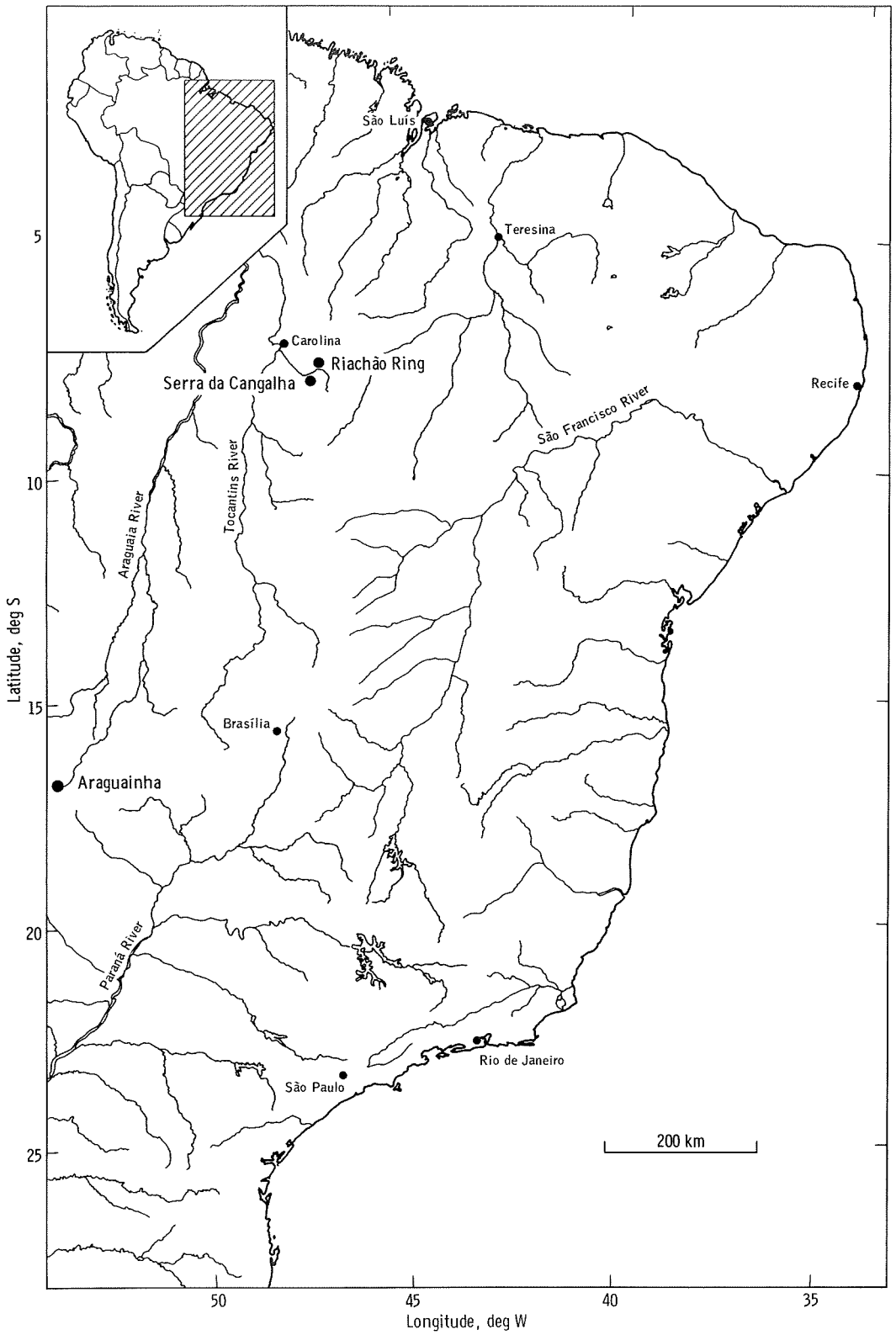

São Luís
Teresina
Carolina
Riachão Ring
Serra da Cangalha
Recife
São Francisco River
Tocantins River
Araguaia River
Brasília
Araguainha
Paraná River
Rio de Janeiro
São Paulo
200 km
5
10
15
20
25
Latitude, deg S
50
45
40
35
Longitude, deg W

FIGURE 1.—Map showing locations of three astroblemes in Brazil. The Riachão Ring was discovered by Apollo crewmembers while seeking the larger Serra da Cangalha.

based on a unique geomorphology in a nonvolcanic region. Discovery of the second nearby "ring structure" during ASTP prompted a ground reconnaissance of both features. In October 1976, a two-man NASA/INPE (Brazil's space agency, Instituto de Pesquisas Espacias) team successfully explored both sites on foot. Shatter cones, a distinct fracture pattern widely accepted by geologists as diagnostic of shock conditions (ref. 5), were recovered from Serra da Cangalha, thus confirming the meteoritic origin of this structure. Definitive shock criteria have not yet been detected in the samples recovered from the smaller structure, tentatively named the Riachão Ring; but the lithology, structure, and makeup of the exposed rocks strongly support an impact origin.

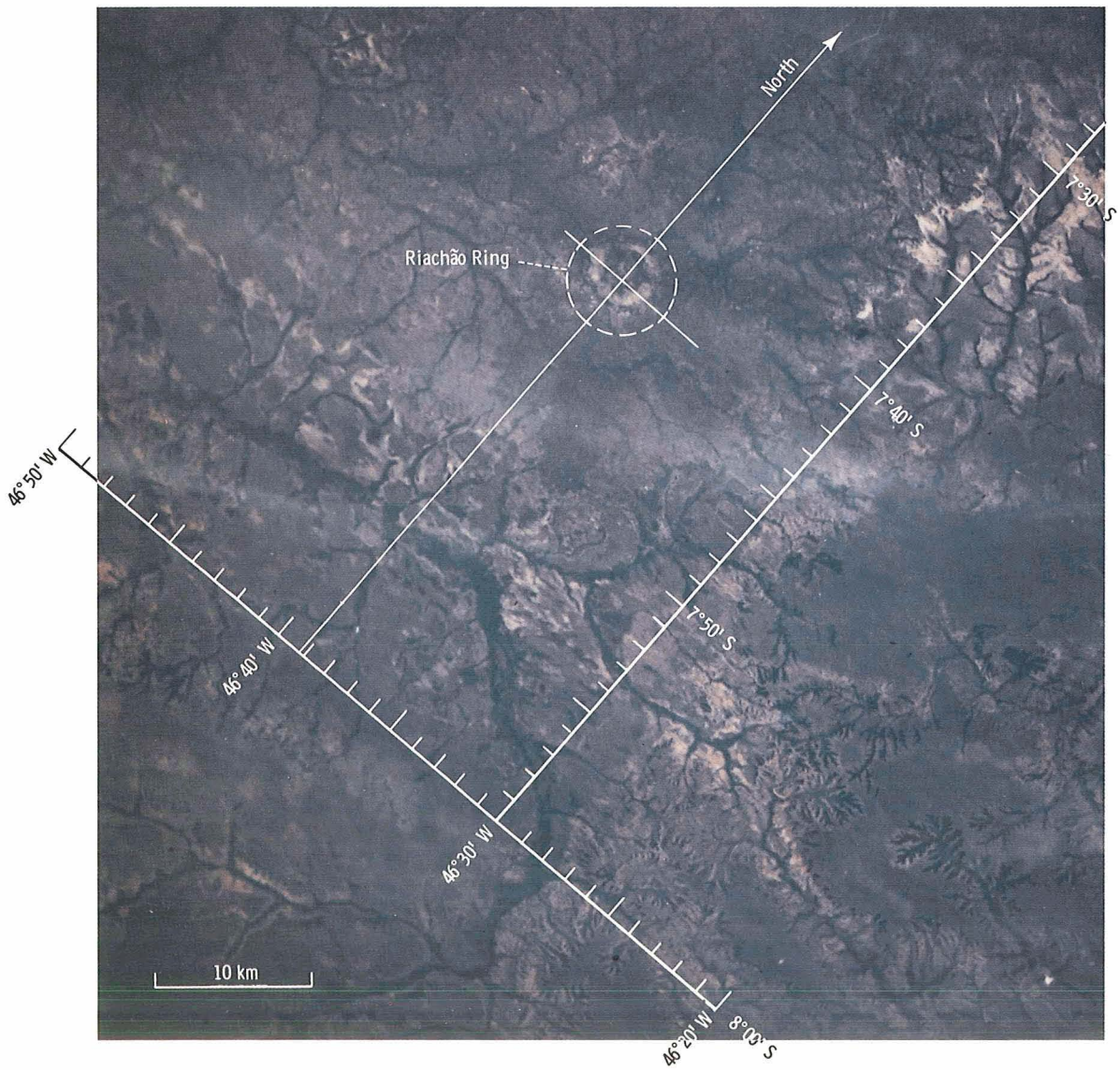


FIGURE 2.—The Riachão Ring as it appeared to visual observers onboard Apollo (AST-23-1931).

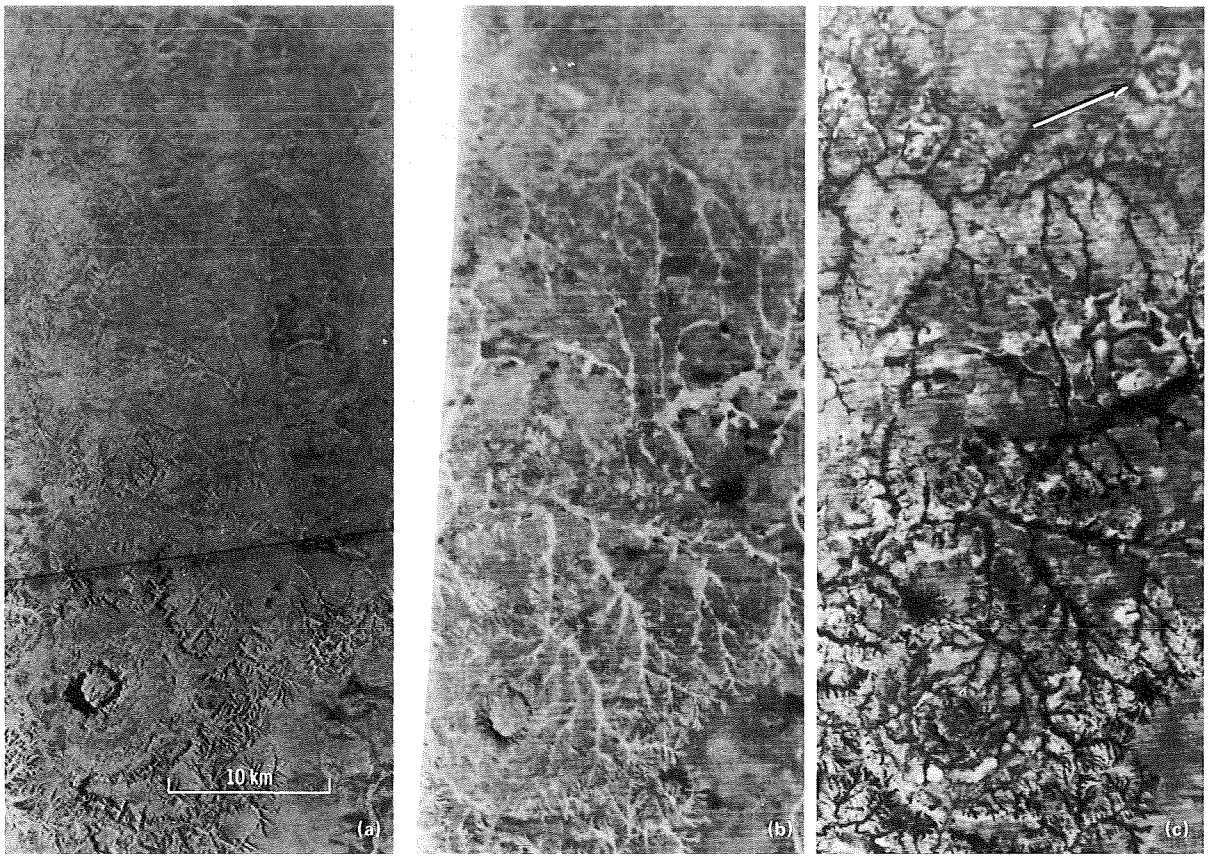


FIGURE 3.—Serra da Cangalha (lower left) and the Riachão Ring (upper right) as they appear on remote sensing imagery. (a) SLAR image in which the Riachão Ring is not visible. (Radar mapping of the Amazon (RADAM) mosaic sheets SC-23-V-A and SB-23-Y-C.) (b) Landsat infrared image in which Riachão Ring is still obscure (No. E-1374-12404-7). (c) Landsat image in visible part of spectrum; Serra da Cangalha is no longer so prominent a feature and Riachão Ring (arrow) is quite clear. (INPE image 275231-123413-5).

GEOLOGIC RESULTS

Maranhão Basin

Petroleum exploration in northern Brazil has defined a series of intracratonic basins containing great thicknesses of level-bedded sedimentary rocks. The Maranhão basin covers an area of more than a half million square kilometers and consists of Mesozoic and Paleozoic rocks up to 3 km thick (ref. 6). Parts of the southwestern section, including the region in which the Riachão Ring and Serra da Cangalha are situated, are presently being dissected by tributaries of the Tocantins River. The features themselves are actually embedded in the otherwise level strata; they are being etched out and enhanced by stream erosion. Tropical weathering conditions have produced a thick lateritic soil over much of the territory, and most surface rocks have deteriorated to clays and sands.

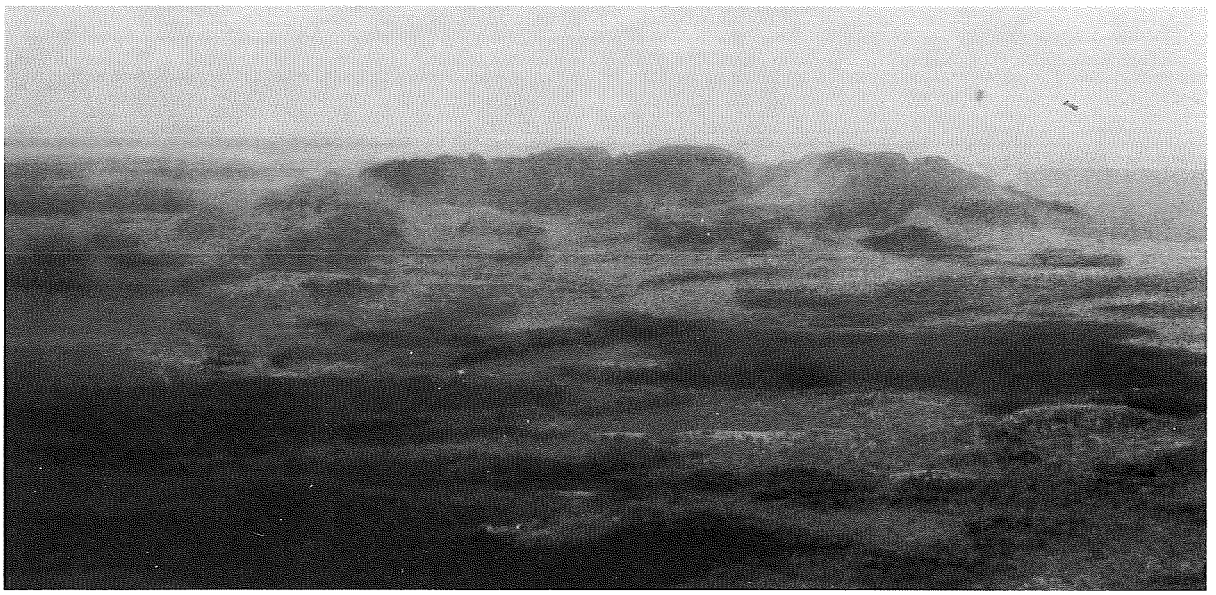


FIGURE 4.—Photograph showing the inner mountain ring at Serra da Cangalha.

At scattered localities in the basin, Jurassic basalt flows and diabases occur. No igneous rocks were encountered during the field investigation, and the nearest mapped exposures of basalt lie 50 km to the north of the study area (ref. 7).

Serra da Cangalha

The Serra da Cangalha structure is located at latitude 08°05′ S and longitude 46°52′ W. The entire structure (fig. 4) is a topographic and stratigraphic bull's-eye pattern. It is 12 km in diameter and is surrounded by the flat-lying Permian Pedra do Fogo Formation. The oldest rocks, Devonian Longa Shales, floor the heavily forested central bowl in vertically oriented beds. A Brazilian Government drilling expedition has cored three test wells to a depth of 200 m, but only the same vertical shales were encountered.

A ring of steep hills, 300 m in relief, surrounds the 3-km-wide central depression and is composed of steeply quaquaversal Mississippian marine clastics. A quartzite basal conglomerate is exposed along the base of the inside walls, and it is in the boulders of this conglomerate that shatter cones were discovered. Some of the rocks have a surface pattern of hairline fractures and will readily fracture at a blow from a heavy sledge, occasionally revealing unmistakable shatter-coned faces (fig. 5). Thin sections prepared from these boulders reveal the strongly fractured fabric of the individual grains of quartzite (fig. 6).

Scanning electron photomicrographs of the same samples reveal an abundance of minute spherules thought to be fused host rock preserved in the dilated fractures of the shatter cones (ref. 8).

Outside the ring of hills lies a 4-km-wide band of outward-dipping Pennsylvanian beds. The general attitude of the beds is concentric with the overall circularity of the structure, but the beds have been eroded to a level nearly 100 m below the flat-lying sediments of the countryside. Within the ring trough, exhumed resistant sandstone beds have weathered to remarkable fencelike slabs, which protrude from the sandy floor. Occasional cherty beds have accumulated buttresses of rubble resulting in annularly alined silicate-spined ridges tens of meters high and hundreds of meters in length (fig. 7). Numerous blocks of fossil wood occur in the rubble, indicating that the silicate

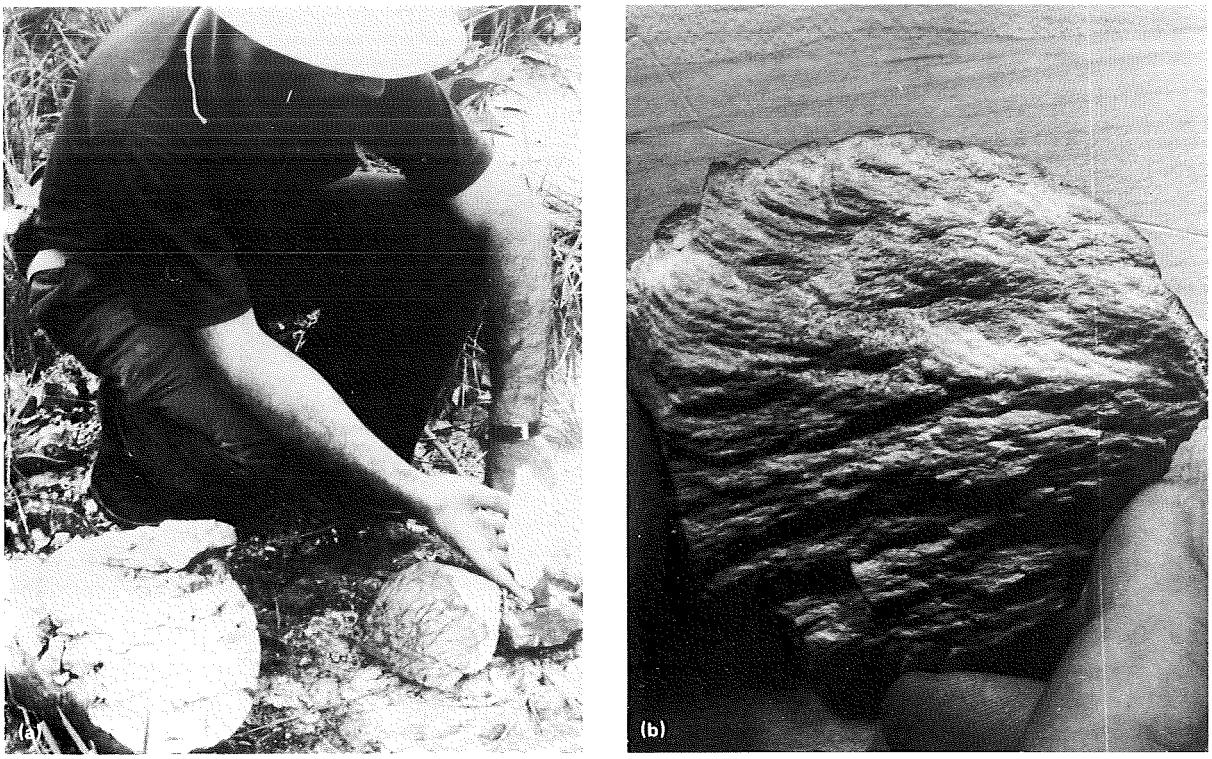


FIGURE 5.—Shatter cones at Serra da Cangalha. (a) Quartzite boulders with hairline cracks visible on their outer surfaces are easily fractured with a sledge. (b) Shatter cones from a broken boulder.

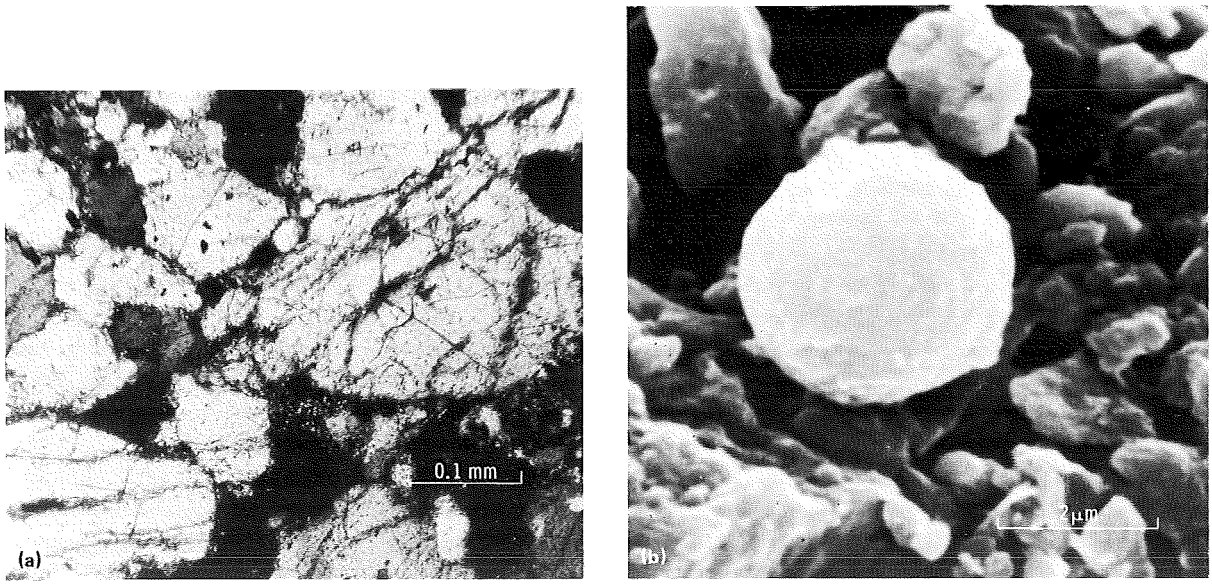


FIGURE 6.—Photomicrographs of Serra da Cangalha shatter-coned quartzite. (a) Optical thin-section of strongly fractured grains in cross-polarized light. (b) One of the numerous microspherules commonly detected in shatter-coned rocks by scanning electron microscopy. (Photograph courtesy of John Belk, Clemson University.)

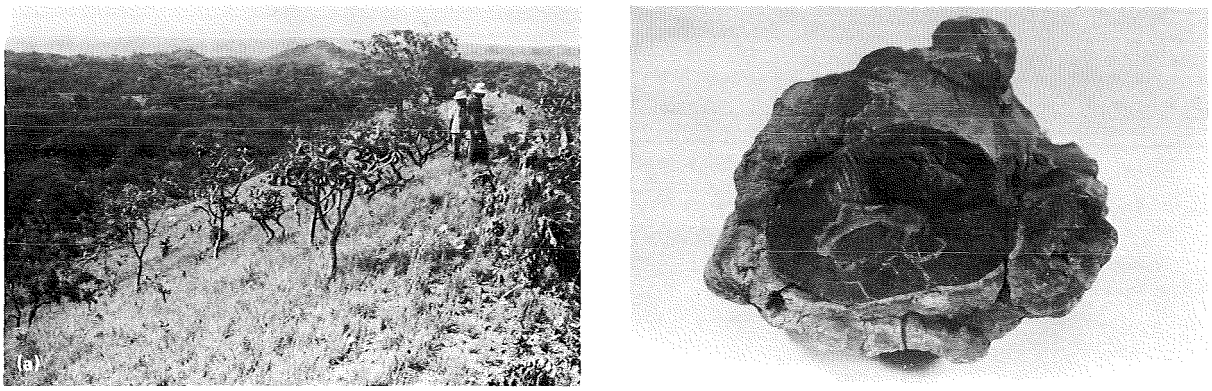


FIGURE 7.—Silicate-spined ridge circling Serra da Cangalha and a typical block of fossil wood from the ridge crests. (a) A silicate-spined ridge circling Serra da Cangalha; the same ridge can be seen as hillocks in the distance. (b) Block of fossil wood. Numerous blocks of fossil wood from the ridge crests indicate that the cores originated as flat beds and not as silicified fractures or voids.

material originated as horizontal surface beds rather than in the silicification of buried conical fractures.

The overall appearance and structure of Serra da Cangalha is quite similar to the verified astroblemes at Gosses Bluff, Australia, and Kufra, Libya (refs. 9 and 10).

Riachão Ring

The Riachão Ring is located at latitude 07°43′ S and longitude 46°39′ W. The bleached ring in figure 2 is a slightly elevated rim of unconsolidated sand. In an aerial photograph (fig. 8), the ring is almost invisible. Outside the ring lie the

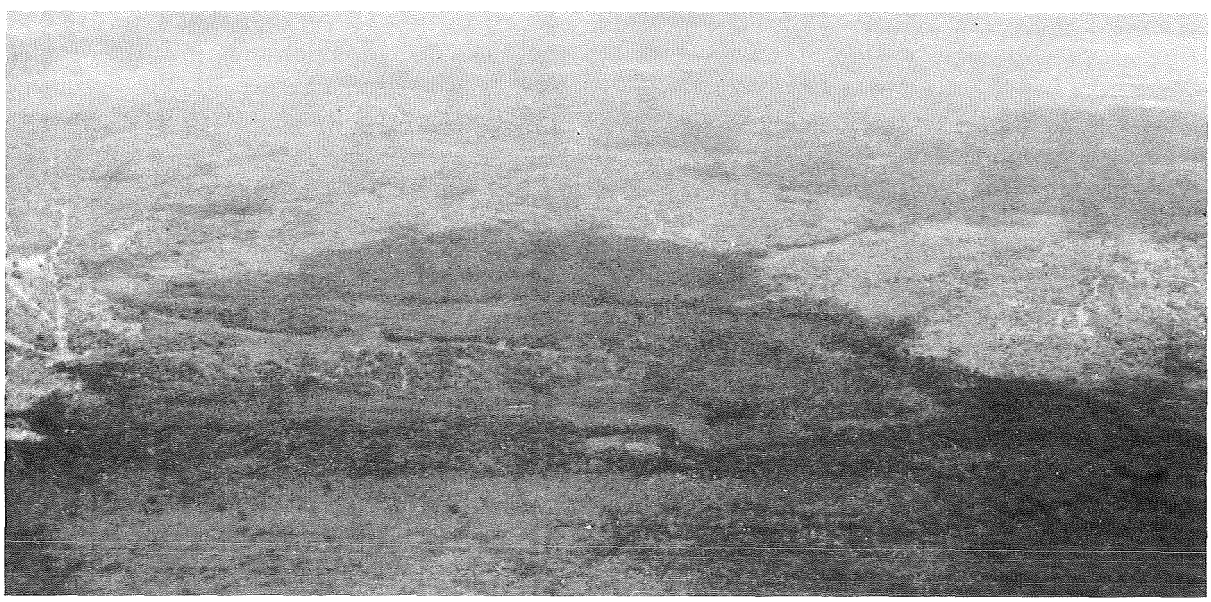


FIGURE 8.—Riachão Ring is barely visible in this aerial photograph taken from a small aircraft. Elevated outer rim is marked by trails, but the white sands are obscured by grass during the rainy season.

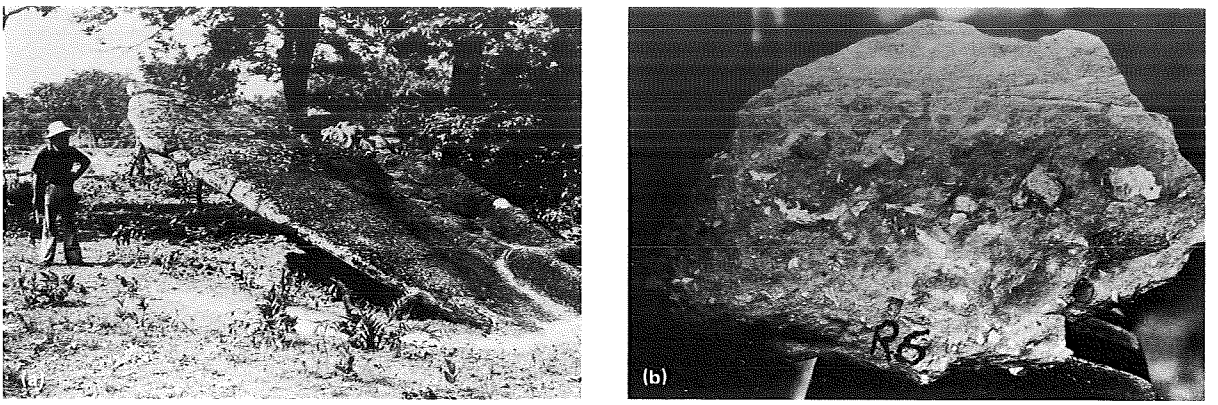


FIGURE 9.—Inclined slab of breccia and example of breccia fragment. (a) An inclined slab of breccia protruding from the Riachão Ring; slabs dip away from the center and occur only along the rim of the structure. (b) Fragment of the rim breccia indicating polymict sedimentary clasts and the overlying crossbedded sandstone.

same flat Permian rocks that surround the Serra da Cangalha structure to the southwest. Jutting from the sand at various rim locations are outward dipping slabs of polymict breccia (fig. 9) 20 to 40 cm in thickness. The breccia consists of angular clasts of sandstones enclosed in a granular matrix, and identifiable blocks of cross-bedded Triassic sandstone are in sharp contact both above and below the slabs. The white sands of the Riachão Ring are residual sands weathered from an annular body of friable sandstone, which has been partially shielded by a conical sheet of thin, resistant breccia. It is possible that the breccia slabs are the welded remains of an impact ejecta blanket. During preparation of thin sections of the breccias, the quartz grains had a marked tendency to fracture. Individual grains fractured into a regular pattern of perpendicular cracks in which spacing decreases as the sample thickness decreases. Such an effect is often noted near the edges of thin-section mounts of normal sandstones but rarely over an entire section. Apparently, there is some inherent pattern of weakness in the rocks from Riachão Ring, which is enhanced by the usual laboratory grinding technique (fig. 10).

The inner edge of the sand ring is bounded by a gentle annular valley of approximately 10-m relief. Dense jungle vegetation, the typical sign of shallow ground water for the region, occupies most of the trough and hampers geologic surveys.

In the center of the structure, chaotic blocks of deeply weathered Permian Motuca Sandstone are uplifted to an elevation of a few meters above the outer rim. The rocks of the central uplift burst into a fine powder when struck by a hammer (fig. 11). Under the microscope, rock particles appear as fractured subangular quartz grains approximately half the size of the grains from the outer ring rocks. At various locations in the center, beds have been tilted to a vertical attitude and tightly folded about a vertical axis. One such outcrop is referred to as the *cotovelo* or "elbow" by the local natives and serves as a convenient landmark (fig. 11). Similar features have been attributed to the centripetal inward rebound described for the astroblemes at Sierra Madera, Texas (ref. 11, p. 17), and Gosses Bluff, Australia (ref. 9, p. 1206).

Although no definitive petrographic evidence of impact shock has been detected to date in the samples, reconnaissance study has revealed several features that favor an extraterrestrial origin for the structure. A meteoritic impact origin for the Riachão Ring is strongly suggested by the highly circular pattern, the central uplift of chaotic blocks, the severely fractured nature of the rocks, and a raised circumferential rim capped by a thin polymict breccia in the absence of soluble carbonates or volcanics.

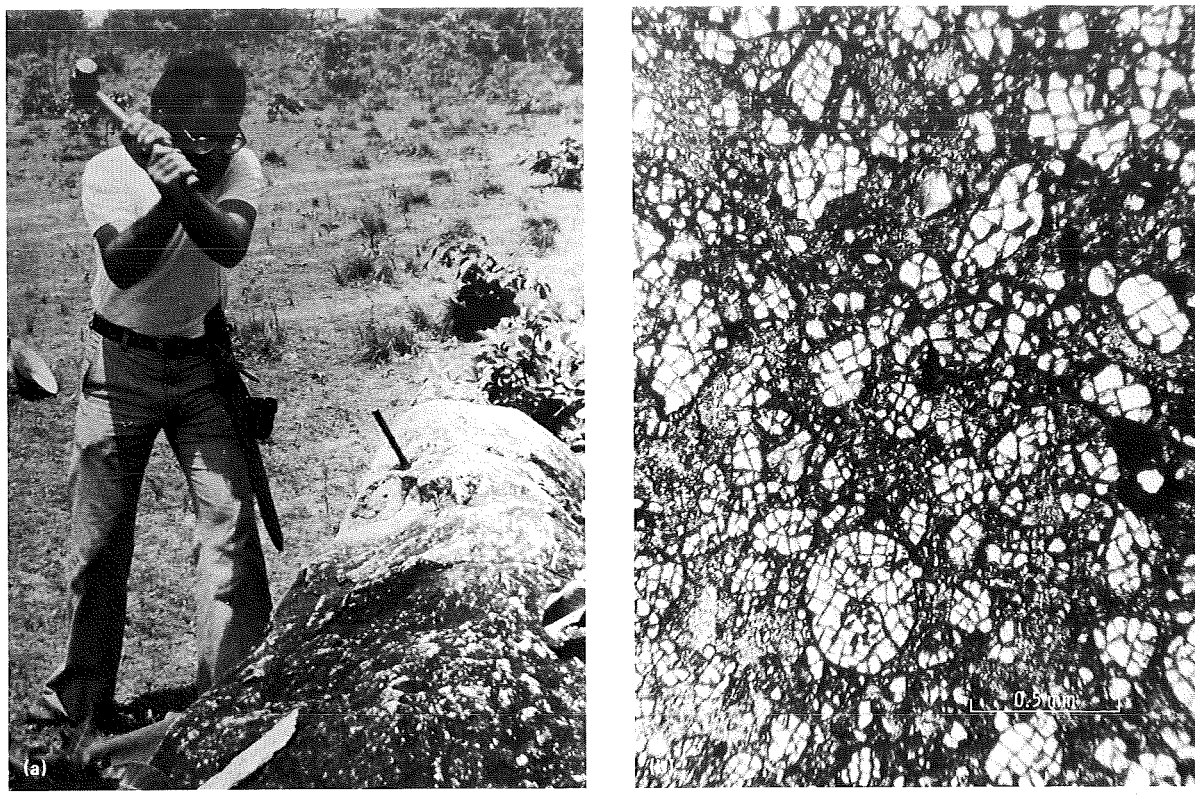


FIGURE 10.—Rim breccias at Riachão Ring are quite durable; quartz grains fracture into regular patterns. (a) Rim breccias resist sampling efforts. (b) During preparation of thin sections, quartz grains in the breccias tend to fracture into these regular patterns (transmitted plane-polarized light).

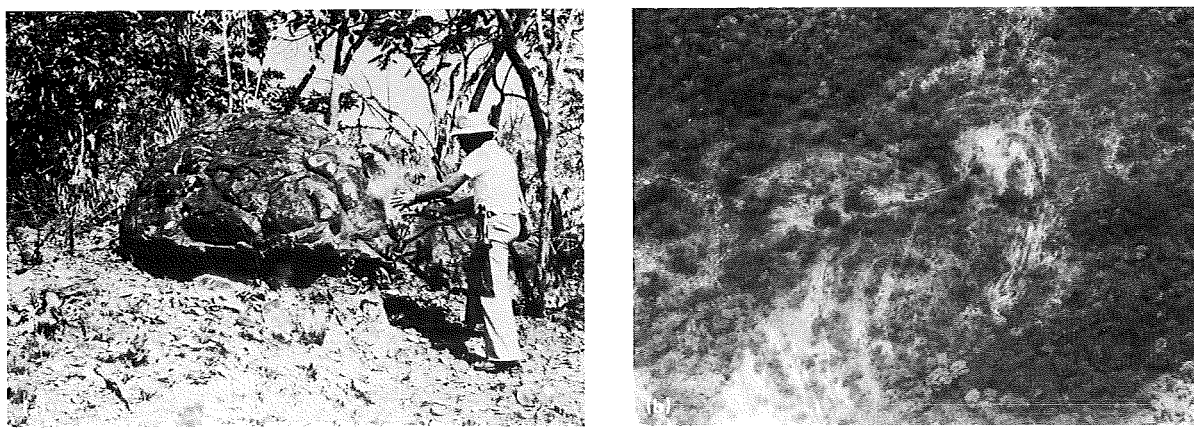


FIGURE 11.—Block of uplifted central rocks of Riachão Ring and aerial photograph of its center. (a) Blocks of uplifted central rocks burst into powder when struck by hammer. (b) Low-altitude aerial view of Riãchao Ring center; vertical beds tightly folded about a vertical axis are outlined by livestock trails.

CONCLUSION

Recent searches for terrestrial impact sites have stressed the use of remotely sensed data from nonvisible (radar, infrared) imagery. The crew of Apollo visually detected and photographed a possible meteorite crater in Brazil, which had not been prominently portrayed on infrared or radar scenes of the same area.

ACKNOWLEDGMENTS

The Brazilian ground expedition was made possible through courtesies extended by the national petroleum company, PETROBRAS; the national mineral resources company, Companhia de Pesquisa de Recursos Minerals (CPRM); and the Brazilian space agency INPE. Special appreciation is expressed to the INPE Department of Remote Sensing of Earth Resources and to their field geologist, Ubiritan Porto dos Santos who, for 2 months, was the author's guide and companion in the hinterlands of Brazil.

REFERENCES

1. Dence, M. R.: The Nature and Significance of Terrestrial Impact Structures. Sec. 15 of the Proc. 24th International Geol. Cong., Montreal, 1972, pp. 77-89.

2. Tsvetkov, V. I.; and Zotkin, I. T.: Searches for Meteorite Craters on the Earth. Astron. Vestnik, vol. 4, 1970, pp. 55-66.

3. Short, Nicholas M.; and Lowman, Paul D., Jr.: Earth Observations From Space: Outlook for the Geological Sciences. NASA TM X-70519, 1973.

4. Dietz, Robert S.; and French, Bevan M.: Two Probable Astroblemes in Brazil. Nature, vol. 244, Aug. 31, 1973, pp. 561-562.

5. Dietz, Robert S.: Meteorite Impact Suggested by Shatter Cones in Rock. Science, vol. 131, no. 3416, 1960, pp. 1781-1784.

6. Mesner, John C.; and Wooldridge, L. C. P.: Maranhão Paleozoic Basin and Cretaceous Coastal Basins, North Brazil. Bull. American Assoc. Petr. Geol., vol. 48, no. 9, 1964, pp. 1475-1512.

7. Ferreria, E. O.: Tectonic Map of Brazil. Dep. Nac. Prod. Min., Boletim No. 1, Rio de Janeiro, 1972.

8. Gay, N. C.: Spherules on Shatter Cone Surfaces From the Vredefort Structure, South Africa. Science, vol. 194, no. 4266, 1976, pp. 724-725.

9. Milton, D. J.; Barlow, B. C.; et al.: Gosses Bluff Impact Structure, Australia. Science, vol. 175, no. 4027, 1972, pp. 1199-1207.

10. French, Bevan M.; Underwood, James R., Jr.; and Fisk, Edward P.: Shock-Metamorphic Features in Two Meteorite Impact Structures, Southeastern Libya. Bull. Geol. Soc. America, vol. 85, no. 9, Sept. 1974, pp. 1425-1428.

11. Wilshire, H. G.; Offield, T. W.; Howard, K. A.; and Cummings, David: Geology of the Sierra Madera Cryptoexplosion Structure, Pecos County, Texas. U.S. Geol. Survey Prof. Paper 599-H, 1972.

Color Zoning in the Western Desert of Egypt

Farouk El-Baz[a†] *and Hassan A. El-Etr*[b]

ABSTRACT

The Western Desert of Egypt was selected for detailed study as a type locality of the north African desert environment. In addition to astronaut observations, 55 color photographs of Egypt were obtained during the Apollo-Soyuz mission using 70- and 35-mm cameras. These photographs showed regional and local color zones that were mapped and checked in the field.

On the regional scale, a stereostrip of 15 photographs shows the following color zones from southwest to northeast: (1) a rosy-peach zone of sandstone plains (zone A), (2) a grayish-brown or taupe zone of sandstone tablelands (zone B), (3) a dusty-peach or dark-yellow zone of sand in the Great Sand Sea (zone C), and (4) a yellowish-mauve to dark-gold zone of gravel plains west of the Nile Delta (zone D).

In one photograph west of the Nile Delta, distinct color zones have been correlated in the field with (1) desert pavement with relatively inactive sand that is mixed with dark, desert-varnished gravel; (2) yellow, relatively active sand with or without sparse vegetation, and with increased reddening toward the north; and (3) dark, arable soil with a mottled appearance that is composed of quartz sand, clay, and calcium carbonate particles. The photograph also shows yellow, active longitudinal sand dunes within the first zone.

The Apollo-Soyuz color data were used in the selection of areas for field investigations and in the extrapolation of knowledge to unphotographed areas of the Western Desert. One of the results, the mapping of an arable zone west of the Nile Delta, attests to the potential value of color photographs in desert study.

INTRODUCTION

One of the objectives of the Earth Observations and Photography Experiment on the Apollo-Soyuz Test Project (ASTP) was to study the desert environment (ref. 1). During the project, observations were made and photographs were obtained of eight major desert regions (ref. 2). The Western Desert of Egypt was selected for detailed study as a type locality of the north African deserts. Reasons for this selection are, first, the fact that this desert is comparatively well studied and, second, the accessibility of parts of it for field investigations by local members of the experiment team.

The Western Desert occupies 681 000 km^2 (262 930 mi^2; approximately the size of the State of Texas), or more than two-thirds the area of Egypt. It is basically a bedrock platform cluttered by sand fields that contain several varieties of sand dunes. The generally flat terrain is broken by several large enclosed or partly enclosed depressions and by the salient basement highs of the Oweinat region at the Egyptian-Libyan-Sudanese border (refs. 3 to 5).

Geological mapping of the study region has been accomplished by the Geological Survey of Egypt at scales of 1:1 000 000 in 1928 (ref. 6) and 1:2 000 000 in 1971 (ref. 7). For the more recent map, Gemini photographs provided data on the southwestern part of the Western Desert. Landsat images of the northern Western Desert have also

[a]National Air and Space Museum, Smithsonian Institution.

[b]Ain Shams University, Cairo, Egypt.

[†]Principal Investigator.

been used in the construction of geological, structural, and drainage maps at 1:1 000 000 scale (ref. 8). A few larger scale maps and reports of parts of the Western Desert are available; for example, Khârga and Dakhla Oases (e.g., refs. 9 and 10), Baharîya (ref. 11), Sîwa (ref. 12), and the Oweinat region and the southern Western Desert (refs. 5, 13, and 14). The geologic setting of the area west of the Nile Delta has been described in some detail by Shata and El-Fayoumy (ref. 15). This area, whose color zones are discussed in this report, has received much attention in the past two decades because of its land reclamation potential.

The ASTP photographs of the Western Desert were obtained from an altitude of approximately 220 km (136 mi.) with a 35-mm Nikon camera and two 70-mm Hasselblad cameras. One of the Hasselblad cameras was bracket-mounted and was equipped with an intervalometer and a reseau plate to provide stereo, mapping-quality photographs. The second camera had a single-lens reflex mechanism for handheld photography. Photographs with the bracket-mounted camera were taken with a color-sensitive film (SO-242) that was specifically selected for desert photography (ref. 1). Figure 1 illustrates the ground coverage for these photographs.

Deserts portray a variety of colors described by astronauts in orbit. With the knowledge that the color films used by the ASTP astronauts could not faithfully reproduce these natural colors, a wheel of Munsell color chips was used to quantify the observed colors (refs. 1 and 2). Details of the astronaut observations of desert terrain have been previously discussed (ref. 2). Also, the color wheel and its use are discussed in a separate section in this volume.

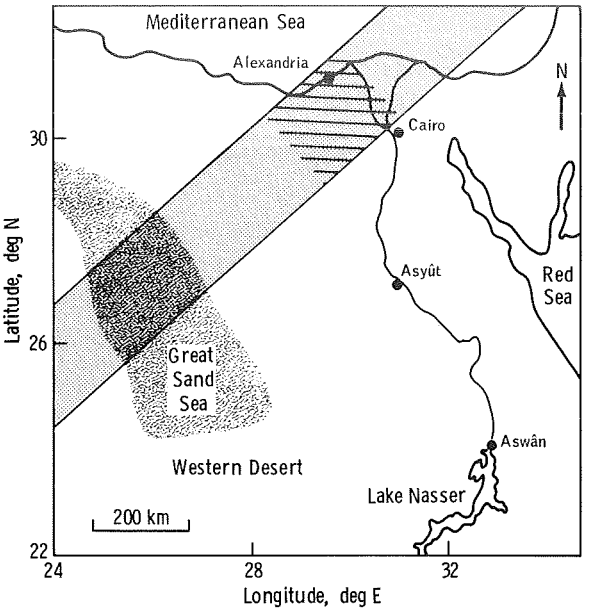


FIGURE 1.—Sketch map of Egypt showing the boundaries of photographic stereostrip coverage by the 70-mm bracket-mounted Hasselblad camera (stippled area), and the coverage of one frame west of the Nile Delta (lined square).

ORIGIN OF DESERT COLOR

Desert color is an indication of the composition of the outer surfaces of exposed rock and rock rubble. In addition to bright-yellow colors, the most widespread color in desert environments is red. Field investigations have shown that red color in desert sands is caused by the presence of hematite (iron oxide) coatings on individual grains. Reddened sands have been observed in deserts throughout the world, but their mode of formation is a matter of controversy (refs. 16 and 17).

There are two major hypotheses concerning the origin of the red color caused by hematite in desert sands. According to one hypothesis, the hematite is detrital, having been formed in lateritic soils of hot, humid climates and later transported to desert basins. Advocates of the second hypothesis contend that the hematite coating is postdepositional and results from the weathering of iron-bearing minerals.

Many reviews of this problem have been published (e.g., refs. 18 to 21). Although the origin of the red color is controversial, the fact that the red color increases with the flow of time has been established in many localities. For example, in the Algodones dunes, the intensity of sand color increases from north to south; 25 to 60 percent of the grains are hematite-coated, with maximum values occurring in the south (ref. 20, p. 611). Because the more southerly dunes are older, the degree of reddening may be used to determine the relative age of the sands.

Earth-orbital photographs have been used in the past to confirm field observations of desert color; for example, in the Namib Desert of South-West Africa. Here, the linear dunes have migrated from west to east along the coast of Namibia. As described by Logan (ref. 22), the sands farthest inland are much redder in color and are of greater age. Skylab 4 photographs of the same region show color zones in the dune sand. In these photographs, younger sands near the coast appear brighter than the redder zones farther inland (ref. 23). In addition, ASTP photographs of southern Australia were used to illustrate dune reddening as a function of increasing distance from the source. Photographs of the Lake Blanche area in the Sturt Desert and of the Lake Eyre region in the southern Simpson Desert show an increase in red color as the distance from the sand source increases (ref. 21).

COLOR ZONES IN ASTP PHOTOGRAPHS

Regional Color Zones

A strip of 15 ASTP stereophotographs of the Western Desert of Egypt (fig. 1) shows several color zones. Most of these zones have been correlated with known geological formations. Because successive photographs overlap by 60 percent, they can be used to study superposition relationships between these formations.

Figure 2 illustrates the four major color zones in the Western Desert as they are portrayed in ASTP photographs. Starting from the south end, these color zones are discussed in the following paragraphs.

Rosy-Peach Zone

The rosy-peach zone (zone A, Munsell 10R 7/4)[1] occupies the southwestern part of the Western Desert in which a sandstone succession ranging in age from Paleozoic to Upper Cretaceous is exposed. The upper part of the sequence is commonly referred to as the Nubian (or Nubia) Sandstone. However, Issawi (ref. 14) prefers to designate this formation as the "Gilf Sandstone."

The exposed sandstones in this region generally show variations in color, texture, and hardness. In the field (ref. 3), the color of the sandstone ranges from white to yellow to brownish red. Grain size commonly ranges from medium to coarse, and some horizons are conglomeratic. The rosy-peach color in the photographs represents sandstones that are poorly cemented. Such sandstones weather easily and their relief becomes fairly subdued; thus, they form low-lying isolated hillocks separated by broad sandy plains. These disintegrating sandstones are believed to be the main source of sands that feed the huge sand dunes of the Great Sand Sea to the north of this region.

Grayish-Brown or Taupe Zone

Prominences that lie northwest of the Gilf Kebîr Plateau display brownish or taupe colors (zone B, Munsell 10R 4/1). They characterize Paleozoic sandstone rocks similar to those exposed to the southwest, but they are much more indurated because of cementation by silica and/or iron oxides; high concentrations of iron oxide are common. In this zone, the sandstones are more weather-resistant and form distinct, elevated tablelands and cuestas. Desert-varnished chert gravel is also present in the general vicinity, and it contributes to the dark tone of the zone.

Dusty-Peach or Dark-Yellow Zone

The dusty-peach or dark-yellow color zone (zone C, Munsell 7.5YR 7/4) coincides with part of the Great Sand Sea. This mass of sand comprises an area of 111 370 km^2 (43 000 mi^2), or 340 times the area of the Algodones dunes of southeastern California. The ASTP photographs clearly show the difference in color between the linear or seif dunes of the Great Sand Sea and the redder and older sandstone rocks (fig. 3). Although there is a slight brightening of the sand color northward, this sand mass is essentially the same dusty-peach or dark-yellow color throughout the area.

[1]This and similar notations in this paper are the equivalent Munsell designations from reference 24.

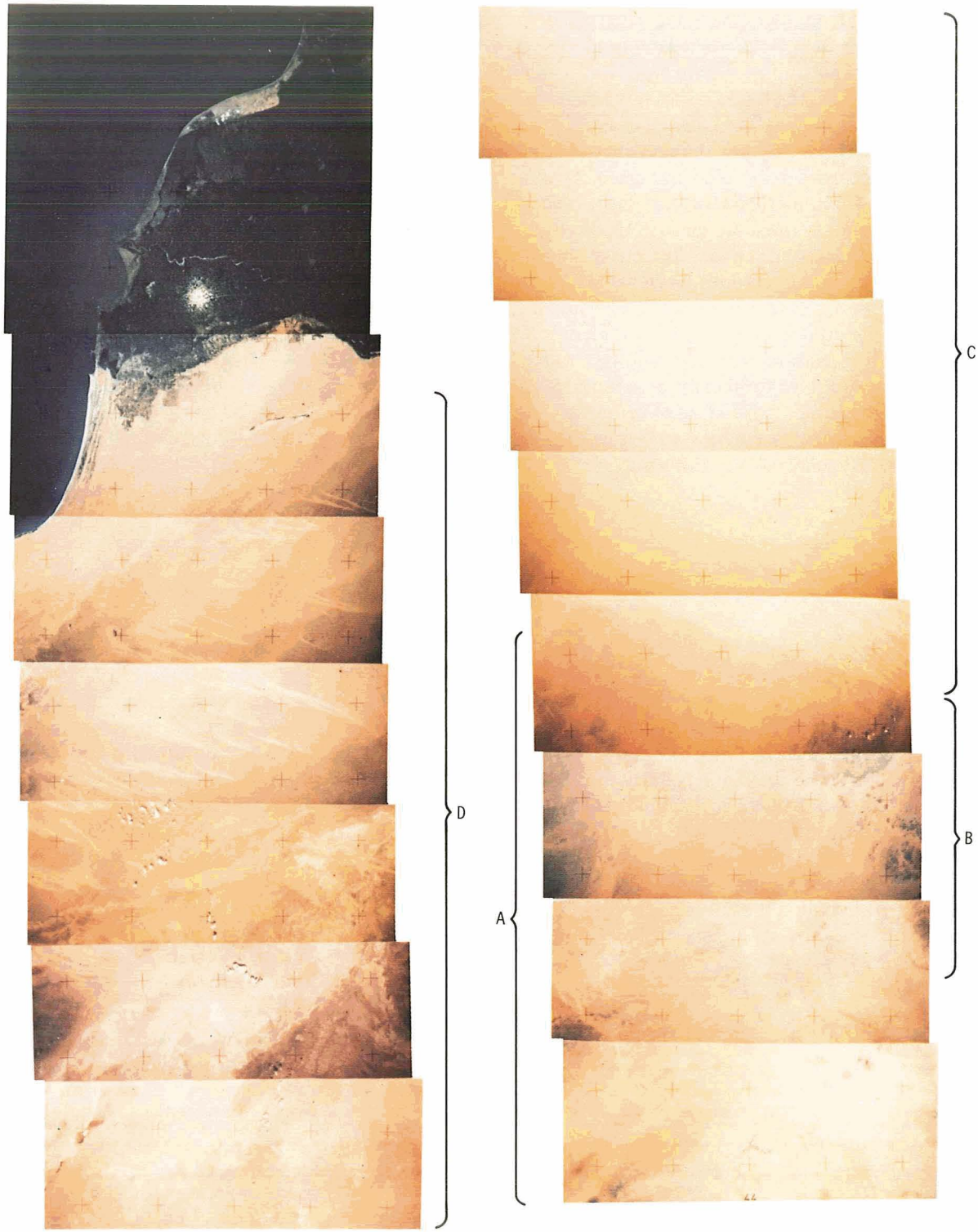


FIGURE 2.—Mosaic of 15 ASTP stereo photographs, taken using the bracket-mounted camera, of the Western Desert of Egypt. The lettered color zones are described in the text (AST-16-1245 through AST-16-1259).

Yellowish-Mauve to Dark-Gold Zone

The yellowish-mauve to dark-gold color zone (zone D, Munsell 10R 6/4 to 10YR 7/4) encompasses a very broad area from the Baharîya Depression to the area west of the Nile Delta. The exposed rocks are basically limestones with some purplish units that account for the mauve tint, particularly near the Baharîya Depression (ref. 11). Toward the northeast, the dark-gold color predominates.

Within this zone, the ASTP photographs depict numerous bright yellow-gold streaks. These streaks represent parallel belts of longitudinal sand dunes of a relatively young age. The young age of these dunes is supported by field observations of their migration patterns. Farther to the north, a color band that is nearest to the coast of the Mediterranean Sea is divided into a pink-yellow zone and a wedge-shaped area of mottled appearance. These local color zones are discussed in detail in the following section.

Color Zones West of the Nile Delta

The area of the Western Desert adjacent to the Nile Delta was selected for detailed study because a single ASTP photograph of this area depicts three distinct zones (figs. 4(a) and 4(b)). In addition, this region has received considerable attention recently because of its potential for development of arable land; wide tracts of it are now under reclamation using available surface water and ground water (ref. 15).

This region displays numerous examples of landforms typical of desert conditions. According to Shata and El-Fayoumy (ref. 15, p. 1), these conditions are characterized by the severe degradation of the surface (of both soil and plants), by the accumulation of dune sand deposits, by the presence of relict drainage features, and by the eventual domination of saline deposits and crust formation. The same authors also mention that these old drainage channelways are indicative of wetter climatic conditions in the past. The evidence for more humid conditions also includes extensive gravel plains with fossil wood and bone remains.

In considering these factors, and on the basis of its geological characteristics, this area was divided by Shata and El-Fayoumy (ref. 15) into five physiographic provinces. Boundaries of these provinces, however, do not correspond to the color zones in the ASTP photograph. Furthermore, the boundaries of these zones do not exactly match the boundaries of geological formations

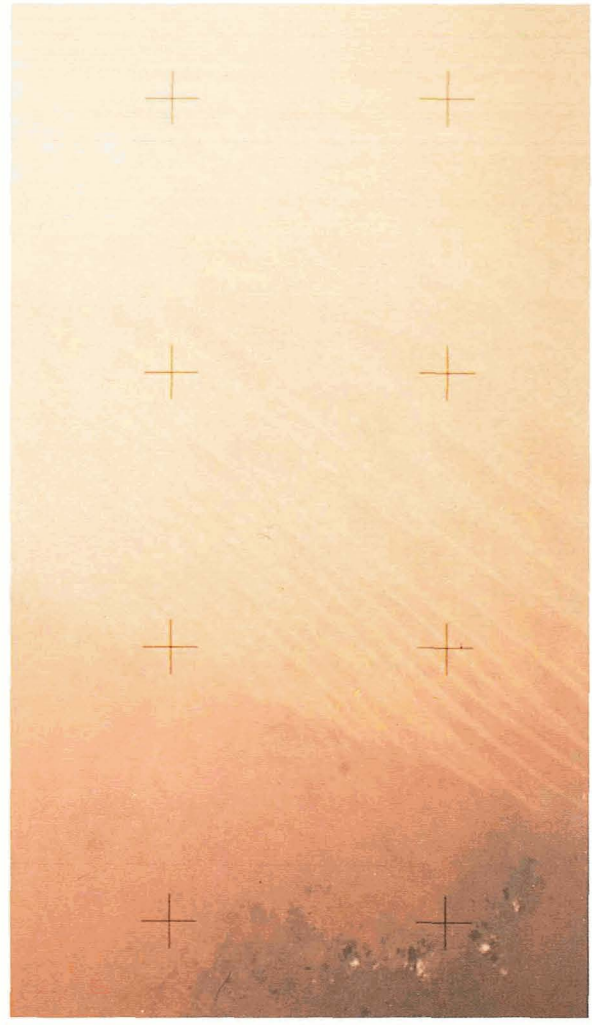


FIGURE 3.—A sharp color change is evident along the western boundary of the Great Sand Sea in the Western Desert. The rosy-peach color with a brownish tint in the lower part represents the Nubian Sandstone of the Gilf Kebîr region. The dusty-peach color with a dark-yellow tint in the upper half represents the younger sands of the Great Sand Sea. Individual dunes can be recognized near the boundary of the two color zones (AST-16-1247).

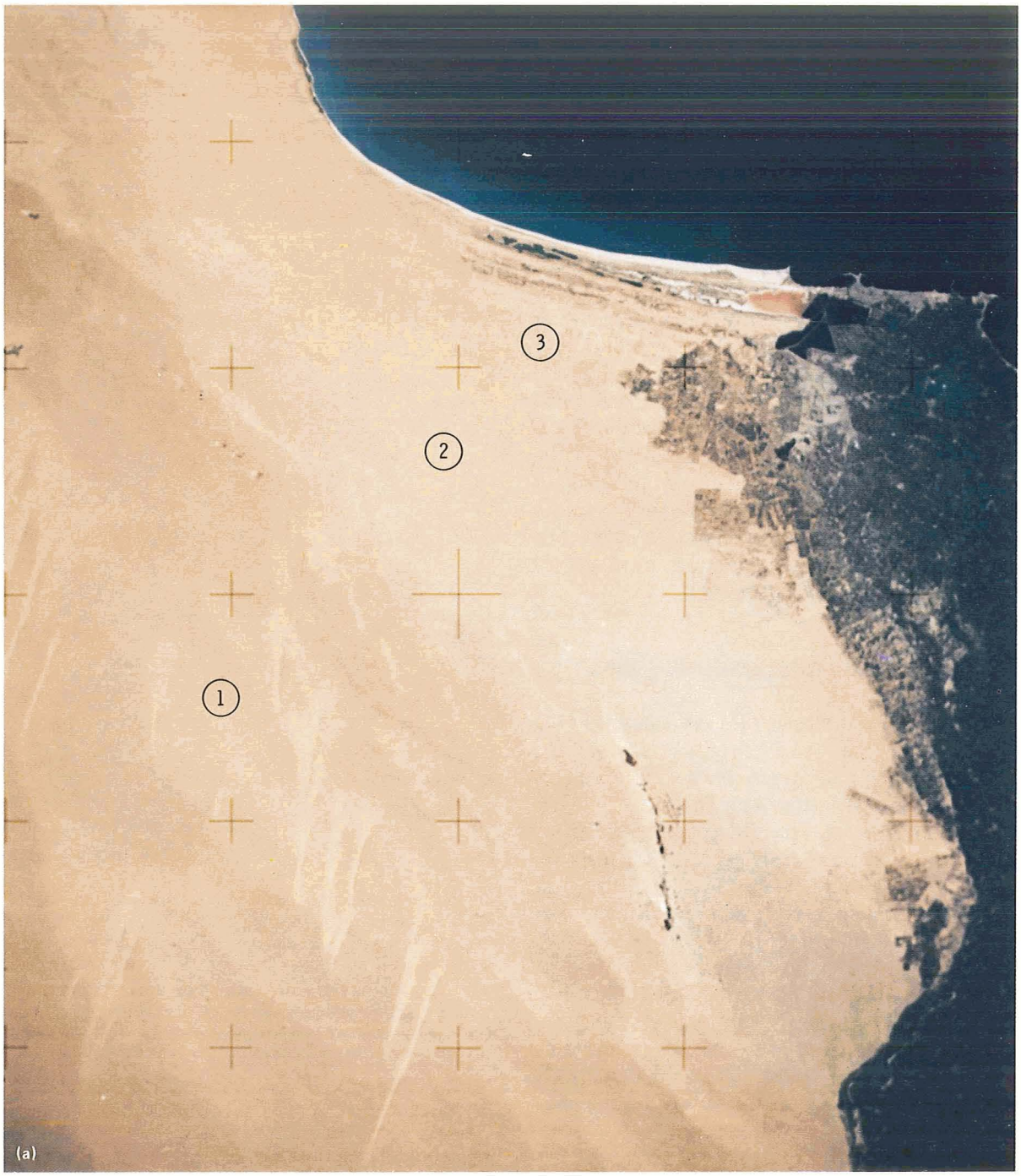
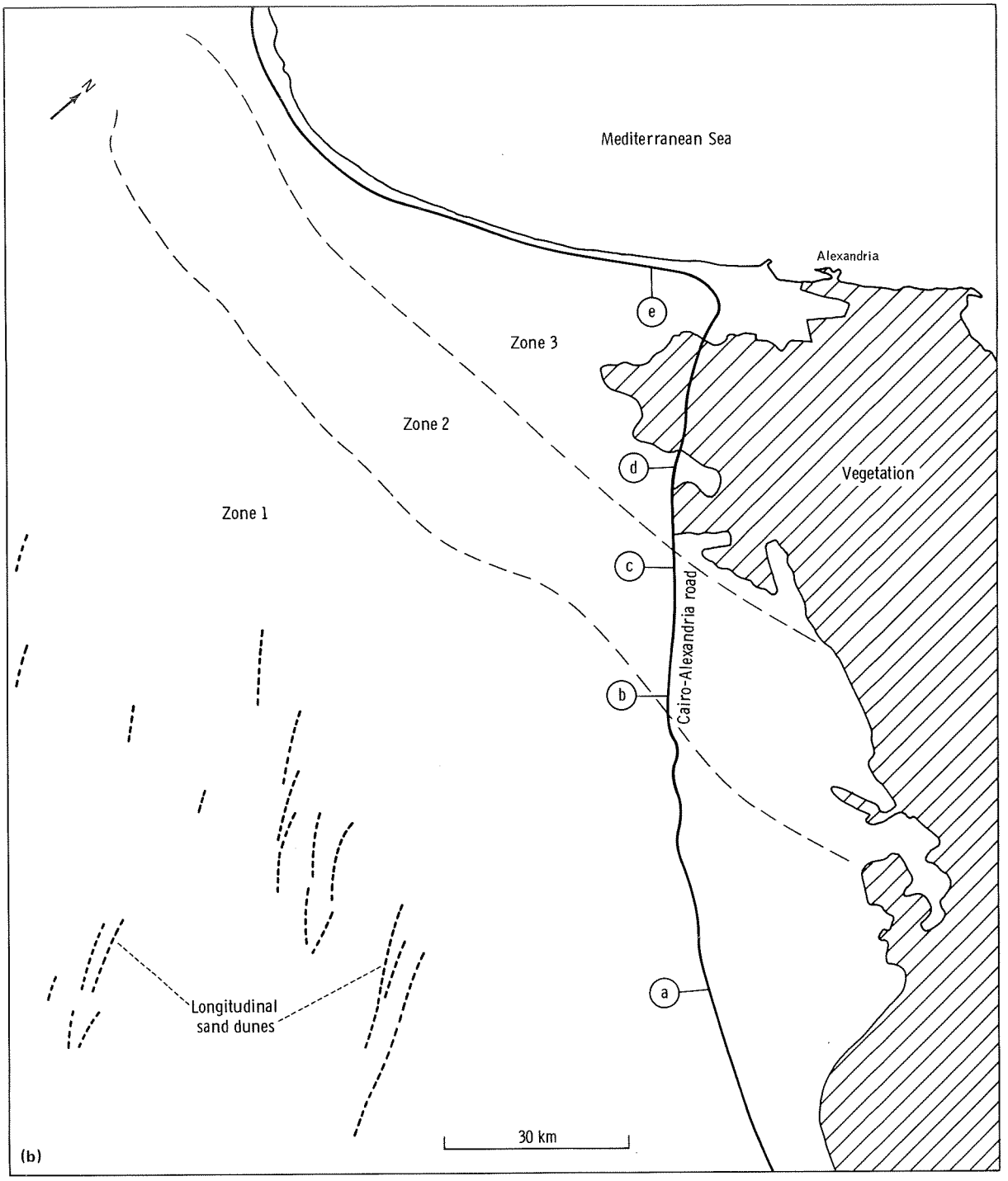


FIGURE 4.—Space photograph and sketch map of the Western Desert. (a) Three color zones in the area of the Western Desert of Egypt just west of the Nile Delta: (1) dark earthy-gold desert pavement with lighter colored patches and bright yellow-gold longitudinal dunes; (2) a pinkish-yellow zone representative of a sand sheet, with a red tint that increases toward the north; and (3) a dusty pinkish-gray, mottled area closer to the Mediterranean coast, with large ridges that parallel the seacoast (AST-16-1256).



(b) Sketch map of the area of the ASTP photograph in figure 4(a). Thick solid line indicates route of field investigation from Cairo to Alexandria and then west along the Mediterranean coast. Letters along the Cairo-Alexandria desert road show the location of surface photographs taken by the first author and illustrated as follows: "a" figure 5, "b" figure 6, "c" figure 7, "d" figure 8, and "e" figure 9.

(ref. 3), even those that are based on the interpretation of Landsat images (ref. 8). Accordingly, the boundaries of these provinces evidently need to be revised using the ASTP photographs.

To ascertain the cause of color change in these zones, the authors studied the terrain by traveling from Cairo in a northerly direction to Alexandria via a desert road that traversed all the color zones (fig. 4(b)). This paved road from Cairo to Alexandria is 211 km long. Frequent stops were made (every 5 to 10 km) to study the terrain adjacent to the road. The fieldwork confirmed the existence of three major zones that are essentially parallel and trend approximately in an east-west direction (fig. 4(a)). In each of the three zones, two distinct colors on the photograph were correlated with compositions of exposed sand and soil as discussed in the following paragraphs.

Southernmost Zone

The first zone encountered in the field was that located in the southwestern half of ASTP photograph AST-16-1256 (fig. 4(a), zone 1), which represents an area of more than 8000 km^2 (3100 mi^2). This zone extends along the road from Cairo to a point approximately 108 km south of Alexandria.

The color of this zone in the ASTP photograph is dark "earthy" gold (Munsell 10YR 7/4), with brighter yellow-gold patches. Field observations indicate that the zone is basically a desert pavement composed of sand mixed with dark pebbles (fig. 5). Most of these are desert-varnished; i.e., coated with a thin, glossy film of iron and possibly manganese oxides. The topography of this zone is not flat but rather rolling or undulating. The



FIGURE 5.—The wavy surface of the desert pavement west of the Nile Delta. Dark, desert-varnished pebbles are predominant on higher ground, whereas finer, light-colored sands fill most of the low areas. Dark, heavy mineral grains tend to be concentrated on the surface and contribute to the heterogeneity of the surface coloration of both highs and lows.

amount of gravel increases on higher areas, and the low areas are covered mostly with sand (fig. 5). These microrelief characteristics may have been produced by wind deflation. Variations in the distribution of dark pebbles are probably responsible for the patchy texture of this zone in the ASTP photograph.

The second, bright-yellow color in this zone is represented by longitudinal sand dunes (fig. 4(a)). These dunes are parallel to the prevailing wind direction and trend essentially S25°E. These dunes, 3 to 35 km in length, are disturbed by subsidiary winds creating aprons of sand that extend from the southern tips of the dunes in a S70°E to due east direction. Although these aprons have a great areal extent of as much as 40 by 5 km, they appear to have a thickness of only a few inches or less. This sheet of sand is substantial enough to change the color in the ASTP photograph from darker gold to brighter yellow.

Intermediate Zone

The intermediate zone in the ASTP photographs of the desert adjacent to the Nile Delta displays the brightest colors (fig. 4(a), zone 2). It is characterized by a pinkish-yellow color (Munsell 7.5YR 7/4) with a reddish tint that gradually intensifies toward the north.

This zone extends along the Cairo-Alexandria road from the 108-km marker to the 69-km marker. At the 108-km marker, two distinct differences were noticed between this zone and the southernmost zone. First, the sand appears to be active in this zone and forms ripples and sand shadows behind desert brush (fig. 6), whereas it is relatively inactive in the southernmost zone. Second, the surface is sparsely covered by vegetation in this intermediate zone, whereas it is densely covered by desert-varnished pebbles in the southernmost zone.

Driving northward, the authors observed that at the 104-km marker, the desert brush became smaller and darker. Eight kilometers farther, a marked increase in vegetation was noted, and 86 km from Alexandria, the sand showed a distinct increase in the red tint. Three kilometers farther, the authors visited a sand quarry (fig. 7), where the reddish sands are relatively pure and form a layer that is more than 3 m (10 ft) thick.

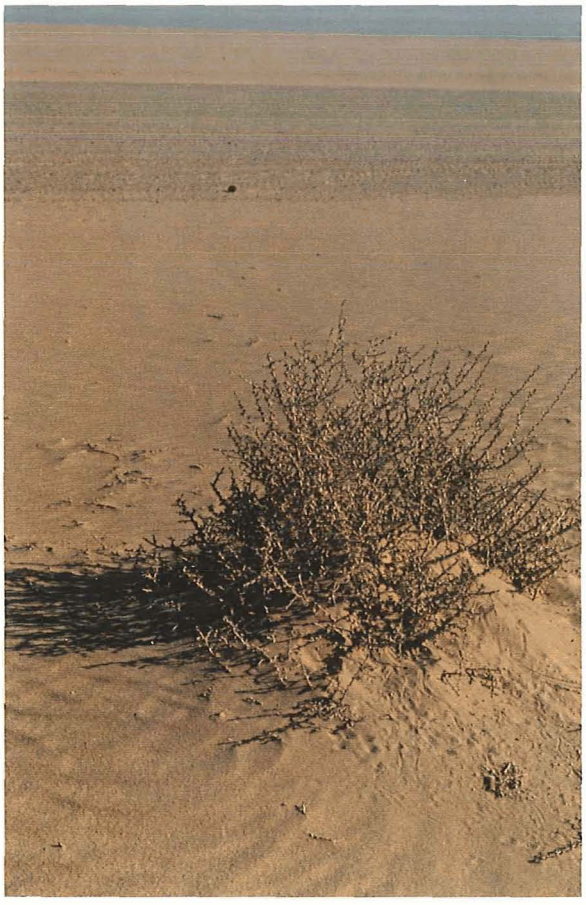


FIGURE 6.—Part of the sand sheet that constitutes the intermediate zone of coloration in ASTP photograph AST-16-1256. The fact that sand in this zone is active is indicated by two features in this photograph: first, the ripple marks, which suggest a wind direction from left to right; second, the sand shadow on the leeward side of a dry, dark-colored desert bush. Pencil near lower edge gives scale.

Northernmost Zone

The zone of color closest to the Mediterranean (fig. 4(a), zone 3) is subdivided into a belt parallel to the seacoast that displays bright white segments, and a larger area that is triangular in shape and shows a dusty pinkish-gray color (Munsell 7.5YR 7/2). The most obvious photo characteristic of this triangular area is its mottled texture.

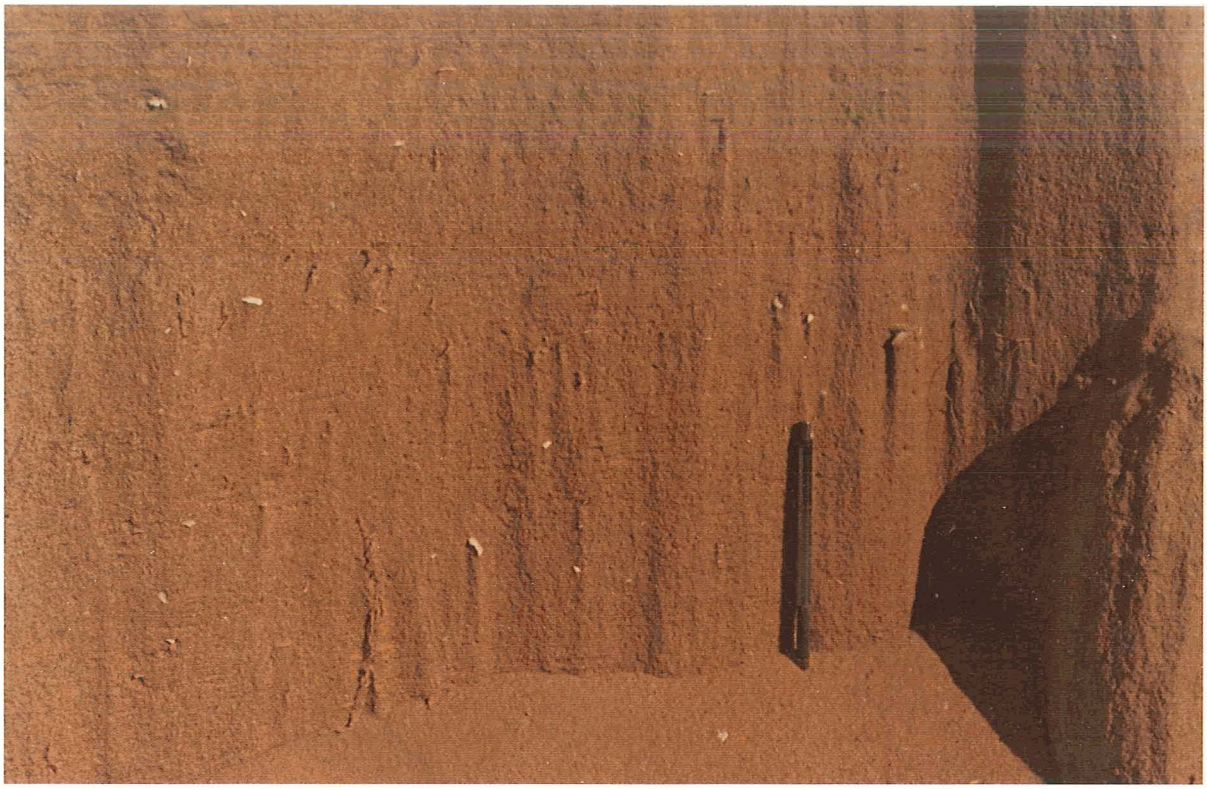


FIGURE 7.—Vertical cut in a quarry of reddish and relatively pure sand. Note subtle indications of horizontal bedding in this layer of very friable sand, which suggests accumulation during a long period of time under stable conditions. Vertical striations are hand-shovel marks produced during quarrying, in which no explosives are used. White particles are wind-transported calcareous rocks and fragments of shells. Pencil gives scale.

Field investigations indicated that the surface rock in the northernmost zone is covered by a soil composed of sand grains mixed with clay and calcium carbonate particles. This zone extends from the 69-km marker from Alexandria, where the soil is reasonably arable as evidenced by the apparent growth of natural vegetation. In places, the authors noticed mud cracks on level plains indicating the existence of conditions that allow the accumulation of rainwater on the surface before evaporation (fig. 8). The high percentage of clays was demonstrated in trenches dug in this soil. Figure 8 illustrates a small trench that was dug in this soil approximately 60 km from Alexandria. In this area, the authors encountered large limestone blocks partly buried in the soil; some of the limestones were concretionary in nature. It was also noticed that the flora is more varied and includes flowering plants. Small hillocks of marly composition also were observed. The surface of some of these is lighter in color than the interior. This phenomenon is probably due to a thin crust of salts, which developed after repeated evaporation of collected rainwater.

The fact that the land in this zone is arable is evident by the westward growth of land reclamation projects. Similar projects have been started at the boundary between the Nile Delta and the desert in the intermediate color zone (fig. 4(a)). However, very limited westward growth of vegetation is apparent in the more sandy zone.

The northernmost belt of land in the Western Desert just west of Alexandria displays distinct characteristics. Its most prominent feature is the existence of closely spaced ridges that parallel the Mediterranean coast. Dark patches along these ridges are caused by vegetation (fig. 4(a)). In the field, white-colored ridges were noticed, which are

composed of clastic oolitic carbonates (calcarenite). These ridges were observed approximately 32 km from Alexandria (fig. 9).

The preceding discussion shows how the combination of photogeologic interpretation and field investigation has resulted in a full understanding of desert color in one ASTP photograph. It must be stated that the true color of this photograph made possible the recognition of color zones. Also, although fieldwork was conducted along a single line (the Cairo-Alexandria desert road), the findings can be extrapolated to the whole area of the photograph and to larger areas, as indicated in the following discussion.

EXTRAPOLATION OF COLOR DATA

It was shown in the previous discussion that the ASTP photographs were extremely useful in delineating color zones in a strip of the Western Desert of Egypt. These color zones can also be distinguished in additional photographs taken with the handheld camera that was used by the astronauts to document their own observations of color variations.

However, the limited coverage of the ASTP photographs did not allow the extrapolation of color data to the whole Western Desert of Egypt. To do so, it was necessary to use Landsat data that constitute the only complete coverage. In recent years, studies of desert landscapes have been facilitated by the interpretation of Landsat data. For example, McKee and Breed (refs. 25 and 26) have used Landsat imagery to formulate a classification scheme for sand seas.

To allow the use of Landsat images in the extrapolation of ASTP data to larger areas, a false-color mosaic was prepared from these images. The mosaic comprised 70 images that cover the area of Egypt. It was attempted to produce false-color composites that simulate the true color of the ASTP photographs (fig. 10).

As an offshoot of the ASTP study, this mosaic is being used in a joint research project between the Smithsonian Institution and Ain Shams University, Cairo, with the authors of this paper as Co-Principal Investigators. An important aspect of this study is the correlation of the color zones depicted on the ASTP photographs and on the Landsat image mosaic.



FIGURE 8.—Trench made in dry mud of the arable zone near the Mediterranean Sea coast. The surface in the upper part of the photograph displays fine mud cracks. The trench in the lower part shows the cohesiveness of the soil. Pencil gives scale.

Preliminary investigations indicate that the mottled, dusty pinkish-gray zone (fig. 4(a)) continues along at least a part of the Mediterranean coast. In its westward continuation, it varies between 5 and 45 km in width. This is significant because the zone is made up of arable land. Additional support for its nature is shown in the Land-



FIGURE 9.—A longitudinal ridge of calcareous sand that parallels the Mediterranean coastline. The ridge is one of a group of east-northeast/west-southwest ridges that produce the linear pattern in the ASTP photograph shown in figure 4(a). Interridge areas contain darker, more fertile soil. Palm trees are approximately 30 m high.

sat mosaic by the red color, which indicates the presence of vegetation (fig. 10). The red color intensifies particularly in the northwestern corner of Egypt, which is at a higher altitude and, therefore, is exposed to somewhat wetter climate and is capable of supporting more vegetation.

CONCLUSIONS

The ASTP orbital photographs and astronaut observations, including the description of desert surface color, have provided valuable information on color variations in the Western Desert of Egypt. This information has been successfully used to pinpoint areas for field study in which color can be correlated with the composition of exposed desert soil.

The ASTP photographs confirm that older sands are redder. This is true on both regional and local scales. These photographs allow the recognition of areas of Egypt that can be reclaimed from the desert. The photographs also permitted the extrapolation of data to larger areas of the Western Desert of Egypt by the use of the Landsat false-color mosaic.

This study also indicates the limitations of both the ASTP photographs and the Landsat data. In Landsat images, color zones are not clearly obvious, even on false-color composites. However, it was possible to "calibrate" the Landsat image color with the ASTP true-color photographs. It was found that color photographs are more suitable for the study of desert color because (1) the photointerpreter does not have to translate mentally one color into another, as is necessary when working with Landsat false-color composites; (2) natural color photographs can be used as such, unlike Landsat data that require the support of a computer facility; and (3) use of true-color photographs saves both time and money; the cost of digitally enhancing Landsat data is prohibitive when compared to the cost of making a photographic print from a color negative.

Similarly, the ASTP photographs were found to have several adverse characteristics, which should

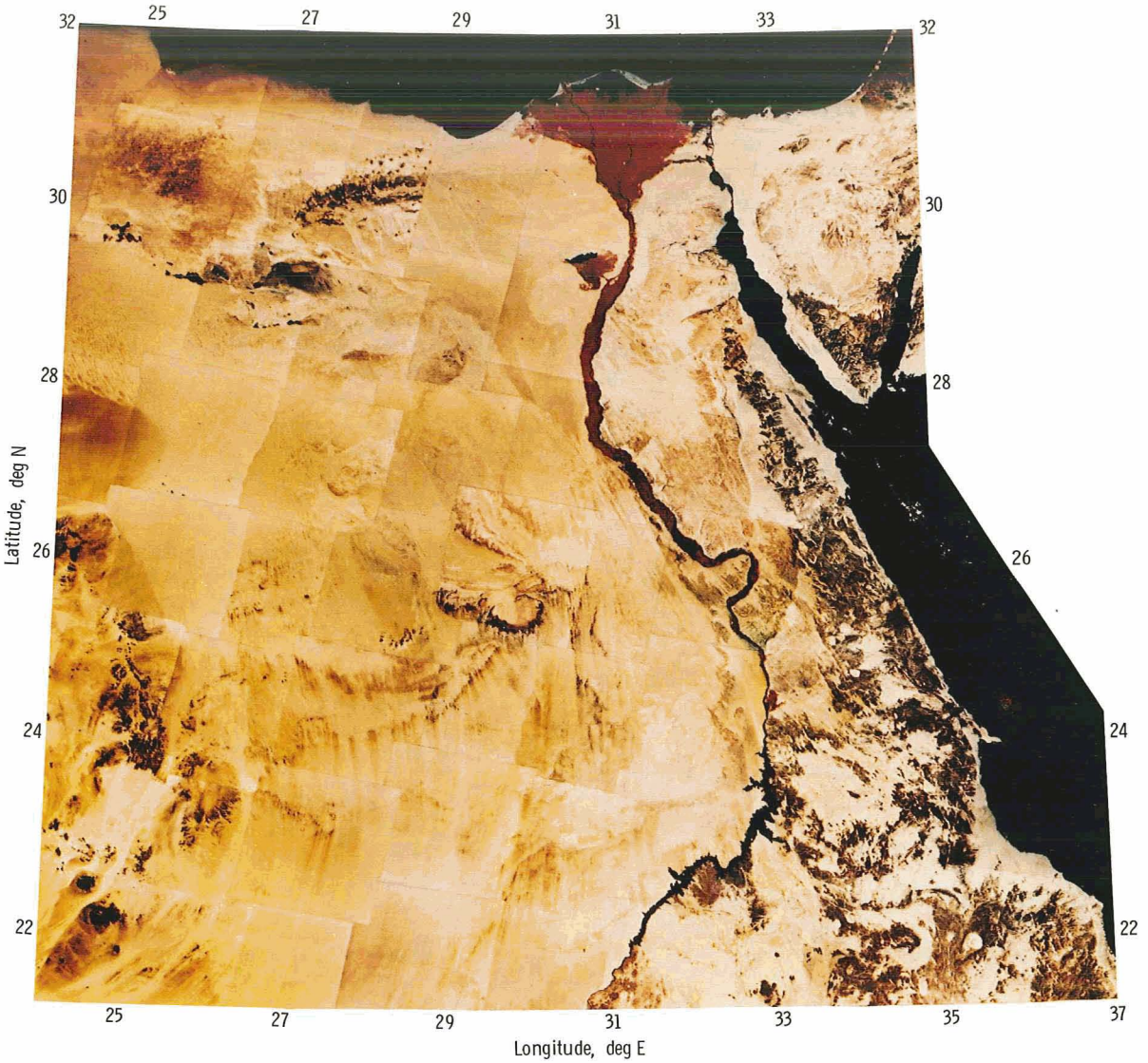


FIGURE 10.—Mosaic of false-color composites made from Landsat data. The color of unvegetated land areas on the composites approximates as closely as possible the color on ASTP photographs. Red color represents vegetation, and water appears black. Note the presence of red (vegetated) areas near the Mediterranean Sea at higher latitudes east and west of the Nile Delta. (Mosaic prepared by the General Electric Company for the Smithsonian Institution.)

be remedied in future photographs. Among these are (1) the centers of most photographs of the stereostrip are overexposed; therefore, more effective antivignetting filters should be used; (2) although stereovision was achieved using ordinary mirror stereoscopes, depth perception was rather limited because of the inherent low relief of the region; therefore, the stereo angle of photographic acquisition must be modified to enhance the vertical exaggeration; and (3) the effective resolution of the photographs should be increased.

Based on the authors' findings, it is strongly recommended that color photographs be obtained from Earth orbit in support of desert studies. However, attempts should be made to obtain high base/height ratio, natural color, and high-resolu-

tion photographs on future space missions. The need for such photographs becomes increasingly important when the worldwide concern for the desert environment and the process of desertification is considered. The large format camera, which is planned for use on the Space Shuttle, is believed to satisfy the necessary requirements.

ACKNOWLEDGMENTS

Apollo-Soyuz astronaut Vance D. Brand participated in assigning the descriptive terms for the color zones discussed in this paper. The fieldwork was organized with the help of a grant from Ain Shams University, Cairo, under a joint research project with the Smithsonian Foreign Currency Program. The authors wish to thank the Geological Survey of Egypt for providing support for the fieldwork. The paper was prepared under NASA contract NAS9-13831.

REFERENCES

1. El-Baz, Farouk; and Mitchell, D. A.: Earth Observations and Photography Experiment MA-136. Sec. 10 of the Apollo-Soyuz Test Project Preliminary Science Report, NASA TM X-58173, 1976.

2. El-Baz, Farouk: Astronaut Observations From the Apollo-Soyuz Mission. Vol. I of Smithsonian Studies in Air and Space, Smithsonian Institution Press (Washington, D.C.), 1977.

3. Said, Rushdi: The Geology of Egypt. Elsevier Pub. Co. (Amsterdam), 1962.

4. Burollet, Pierre Félix: Reconnaissance Géologique dans le Sud-est du Bassin de Kufra. Rev. Inst. Français Pétrole, vol. 18, no. 11, 1963, pp. 1537-1545.

5. El Ramly, M. F.: A New Geological Map for the Basement Rocks in the Eastern and South-Western Deserts of Egypt. Ann. Geol. Surv. Egypt, vol. 2, 1972, pp. 1-18.

6. Geological Map of Egypt, Scale 1:1 000 000. In Atlas of Egypt, Geological Survey of Egypt (Cairo), 1928.

7. Geological Map of Egypt, Scale 1:2 000 000. Geological Survey of Egypt, 1971.

8. El-Shazly, E. M.; et al.: Geologic Interpretation of Landsat Satellite Images for West Nile Delta Area, Egypt. Remote Sensing Research Project (Cairo), 1975.

9. Beadnell, H. J. L.: An Egyptian Oasis: An Account of the Oasis of Kharga in the Libyan Desert. Murray (London), 1909.

10. Hermina, Maurice H.; Ghobrial, M. G.; and Issawi, B.: The Geology of the Dakhla Area. United Arab Republic, Geol. Surv. & Min. Res. Dept., Cairo, 1961.

11. Said, Rushdi; and Issawi, Bahay: Geology of Northern Plateau, Bahariya Oasis, Egypt. UAR, Geol. Surv., Paper 29, 1964.

12. Gindy, Amin R.; and El Askary, M. A.: Stratigraphy, Structure, and Origin of Siwa Depression, Western Desert of Egypt. Bull. American Assoc. Petr. Geol., vol. 53, no. 3, 1969, pp. 603-625.

13. Sandford, Kenneth Stuart: Geological Observations on the Northwest Frontiers of the Anglo-Egyptian Sudan and the Adjoining Part of the Southern Libyan Desert. Quart. J. London Geol. Soc., vol. 91, no. 363, 1935, pp. 323-381.

14. Issawi, B.: Contribution to the Geology of Uweinate-Gilf Kebir Area, Western Desert, Egypt. Geol. Surv. Egypt Internal Report, 1973.

15. Shata, A.; and El-Fayoumy, I.: Geomorphological and Morphopedological Aspects of the Region West of the Nile Delta With Special Reference to Wadi El-Natrun Area. Bull. Inst. Desert, Egypt, vol. 17, no. 1, 1967, pp. 1-28.

16. Van Houten, Franklyn B.: Origin of Red Beds: A Review, 1961-1972. Ann. Rev. Earth & Planet. Sci., vol. 1, 1973, pp. 39-61.

17. Folk, Robert L.: Reddening of Desert Sands: Simpson Desert, N. T., Australia. J. Sediment. Petrol., vol. 46, no. 3, Sept. 1976, pp. 604-615.

18. Walker, Theodore R.: Formation of Red Beds in Modern and Ancient Deserts. Bull. Geol. Soc. America, vol. 78, no. 2, Mar. 1967, pp. 353-368.

19. Glennie, K. W.: Desert Sedimentary Environments. Developments in Sedimentology, vol. 14, Elsevier Pub. Co., 1970.

20. Norris, R.; and Norris, K.: Algodones Dunes of Southeastern California. Bull. Geol. Soc. America, vol. 72, 1961, pp. 605-620.

21. El-Baz, Farouk: The Meaning of Desert Color in Earth Orbital Photographs. Photogramm. Eng. & Remote Sens., vol. 44, no. 1, 1978, pp. 69-75.

22. Logan, R. F.: The Central Namib Desert, South West Africa. Natl. Acad. Sci./Natl. Res. Coun. Pub. 758, 1960.

23. McKee, Edwin D.; Breed, Carol S.; and Fryberger, Steven G.: Desert Sand Seas. Sec. 2 of Skylab Explores the Earth, NASA SP-380, 1977, pp. 5-47.

24. Munsell Book of Color. Munsell Color Company, Inc. (Baltimore, Md.), 1963.

25. McKee, Edwin D.; and Breed, Carol S.: An Investigation of Major Sand Seas in Desert Areas Throughout the World. Paper G6 in Third Earth Resources Technology Satellite-1 Symposium, Stanley C. Freden, Enrico P. Mercanti, and Margaret A. Becker, eds., vol. I, sec. A, NASA SP-351, 1974, pp. 665-679.

26. McKee, E. D.; and Breed, C. S.: Sand Seas of the World. ERTS-1, A New Window On Our Planet, R. S. Williams and W. D. Carter, eds., U.S. Geol. Survey Prof. Paper 929, 1976, pp. 81-88.

Orbital Observations of Sand Distribution in the Western Desert of Egypt

Ann W. Gifford,[a] Delia M. Warner,[a] and Farouk El-Baz[a†]

ABSTRACT

Apollo-Soyuz Test Project photographs of the Western Desert of Egypt were studied to discover the usefulness of orbital imagery in delineating sand deposits. A strip of Apollo-Soyuz mapping-camera photographs was used to map sand distribution patterns. Information from this strip was extrapolated to the rest of Egypt using a false-color mosaic of Landsat images.

Sand deposits in the Western Desert were divided into the following 12 areas for observation and discussion: (1) Wâdi el Natrûn, (2) Qattara, (3) Baharîya, (4) north Sitra, (5) south Sitra, (6) Great Sand Sea, (7) El-Quss Abu Said, (8) Farâfra, (9) Dakhla, (10) Khârga, (11) Oweinat, and (12) Faiyûm. Each area shows a distinct pattern of sand deposition and dune formation that is closely related to topography and wind patterns.

In general, the dunes of the Western Desert trend in a clockwise pattern around a center near Kufra Oasis in Libya. The dune orientations change from north-northwesterly in the northern desert to north-northeasterly in the south. The dunes are intimately associated with scarps that bound numerous depressions in the Western Desert. This relationship is believed to result from the interactions between sand-carrying winds and scarps and other topographic variations.

The sand distribution pattern also reveals areas where dune movement presents a threat to cultivated land. Examples of these areas are on the western side of the Nile Valley, where the Faiyûm dune field in particular is encroaching on fertile land, and in several of the Western Desert oases.

INTRODUCTION

Although as much as a third of the world's landmass can be called arid and as much as 20 percent has been classed as desert, only approximately 4 percent is actually covered by sand (refs. 1 and 2). The distribution of these sand deposits, whether single dunes, dune fields, sand drifts, or the more amorphous sand sheets, is a far from random phenomenon. The factors controlling the occurrence and morphology of sand deposits are complex; they include the wind direction, strength, and duration; the nature, extent, and rate of erosion at the sediment source; the distance from the source; the grain and fragment size; the underlying and surrounding topography; the nature of the surface (rough or smooth); the amount and type of vegetation; and the amount of rainfall (refs. 2 and 3). Although a number of studies have dealt with these factors, a thorough understanding of the mechanisms governing sand movement and deposition is still lacking.

Recently, though, the desertification of what were once arable lands has resulted in an increasing emphasis being placed on general desert studies. Because spreading sands are both a result of and an element in the process of desertification, two of the aims of these studies are (1) to map sand distribution and (2) to determine the direction of sand movement (ref. 4). For this investigation of sand distribution, the Western Desert of

[a]National Air and Space Museum, Smithsonian Institution.

[†]Principal Investigator.

Egypt was chosen because it contains a variety of desert landforms and because excellent photographs of it were obtained during the Apollo-Soyuz Test Project (ASTP).

During the past decade, orbital photography has emerged as a useful tool in the study of large, inaccessible, and remote desert regions. Because of their large regional coverage and their ability to depict temporal distributions, space photographs can provide a new way of observing features of the desert environment, particularly sand distribution. With this fact in mind, the ASTP Visual Observations Team selected photographic targets over eight desert regions including the Western Desert of Egypt (ref. 5).

The ASTP photographs of Egypt were studied to ascertain (1) the usefulness of orbital photographs and satellite images in mapping the distribution of sand deposits; (2) the types of images and the resolutions needed for such mapping; and (3) the varieties of fieldwork and other supporting data needed. The Western Desert of Egypt was studied using both ASTP photographs and Landsat images, which were complemented by collateral data in the form of aerial photographs, field observations, and ground photographs. In addition, attempts were made to correlate these various types of data for the purpose of determining the direction of sand movement and the provenance of the sand.

STUDY AREA

In the Western Desert, explorers and scientists working in various disciplines have "rubbed shoulders" for years in attempts to decipher secrets of the ancient past and also in performing field studies in geology, meteorology, and biology. Much of the basic research on dune classification and sand movement by wind has been performed in the Western Desert. Bagnold (ref. 6) did work there that led to his classic study of sand movement and dunes. Geological works include the pioneering studies of Ball (ref. 7), Beadnell (refs. 8 to 10), and Sandford (ref. 11), as well as more recent work (e.g., ref. 12).

Deserts have traditionally been remote places of mystery, and the Western Desert still retains this mystique, even though it is perhaps one of the best studied desert areas in the world. The Western Desert includes all the land in Egypt west of the Nile River (fig. 1). It has an area of 681 000 km^2, approximately 27 percent of which is actually covered by sand. It is essentially a low-elevation plateau consisting of expanses of rocky terrain interrupted by a series of scarp-bounded depressions and crossed in numerous places by parallel belts of sand dunes and extensive deposits of relatively flat sand sheets (ref. 12).

The regional geology of the Western Desert is characterized by great thicknesses of sedimentary rocks that dip gently to the north (ref. 12). Rocks exposed at the surface include the Cretaceous Nubian sandstone in the south; Cretaceous and Eocene limestones in the central part; and, farther north, Miocene marly limestones and calcareous sandstones. The great oases (Sîwa, Baharîya, Farâfra, Dakhla, and Khârga) are all located in scarp-bounded depressions that occur at the boundaries between these formations. The generally sedimentary character of the Western Desert plateau is disturbed in the southwestern corner of Egypt by a number of volcanic cones and by the plutonic massifs of Gebel Arkenu, Gebel Oweinat, and Gebel Kissu. Only the northeastern flanks of Gebel Oweinat are actually within Egypt; Gebel Arkenu lies in Libya and Gebel Kissu in Sudan.

PHOTOGRAPHIC DATA

The ASTP photographs of Egypt include (1) a strip of 15 overlapping mapping frames taken with a bracket-mounted 70-mm Hasselblad data camera (HDC) and (2) a series of 40 handheld-camera photographs taken with a 70-mm Hasselblad reflex camera and a 35-mm Nikon camera. A color-sensitive film (SO-242) especially selected for desert photography was used for the HDC mapping pass (ref. 5). The accurate depiction of color variations in deserts was regarded as essential because the color tones that delineate sand bodies could provide information on the chemical makeup and relative age of desert sands. (See section entitled "Color Zoning in the Western Desert of Egypt.") Additional informa-

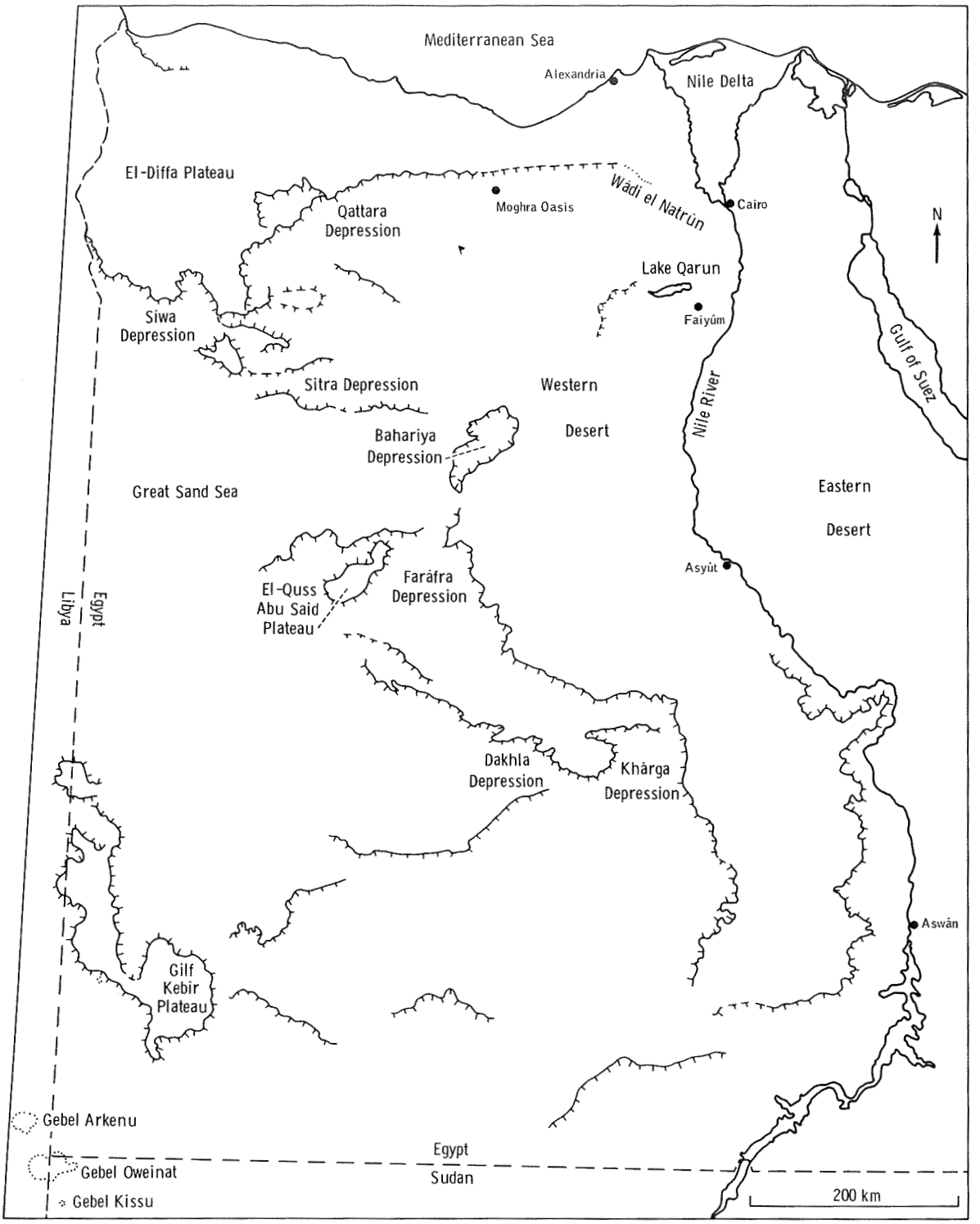


FIGURE 1.—Sketch map of the Western Desert of Egypt showing the location of features and places mentioned in the text.

tion on the ASTP photographs is given in NASA publication number TM 58218, a catalog of ASTP Earth photographs.

Figure 2 is a color mosaic of the ASTP mapping pass of Egypt. This mosaic extends from the Egyptian-Libyan border (latitude 26° N and longitude 25° E) to the Mediterranean Sea (latitude 32° N and longitude 31° E). A variety of desert landforms are clearly shown in these photographs. At the western end, a sharp color difference marks the boundary between the reddish gravel plains associated with the Gilf Kebîr sandstone plateau and the yellow sands of the Great Sand Sea. Within this sand sea, long linear dune features trending northwest-southeast are visible. Other sand features evident in these photographs include dune fields south and northeast of Sitra Depression, the northern limits of three dune belts bordering Baharîya Depression, and an extensive series of parallel dunes south of the northern scarp of Qattara Depression. In addition, the northeastern boundary of the Western Desert is easily distinguished by the contrast between the dark-green, fertile Nile Delta and the yellow, barren desert plain. In this area, an interesting pattern is revealed in the relation of sand deposits and cultivated land. West of the Nile Delta, the mottled sand/vegetation pattern is caused by an increase in cultivated land. (See section entitled "Temporal Changes as Depicted on Orbital Photographs of Arid Regions in North Africa.") As will be discussed later, this is in contrast to the situation 250 km south of the delta (cf. plate 2 in ref. 13), where a similar pattern is caused by dunes encroaching on the narrow strip of farmland bordering the Nile River.

Knowledge gained from studies of orbital photographs of one area can often be used for correlations with other spatially removed but geographically similar regions. To extend the usefulness of the ASTP data to the entire Western Desert, as well as to other desert regions of the world, an attempt was made to extrapolate from the orbital photographs to Landsat satellite images. A false-color mosaic of 65 Landsat images of Egypt was prepared (fig. 3). Each false-color image is a combination of band 4 (0.5 to 0.6 μm), band 5 (0.6 to 0.7 μm), and band 7 (0.8 to 1.1 μm) data. In these Landsat color composites, vegetation appears red; rocks and soils are shades of yellow and brown; deep, clear water is black; and sediment-laden water has blue tones. An effort was made to match the desert colors on the Landsat images with the colors on the ASTP photographs to facilitate the recognition of sand deposits. (See section entitled "Color Zoning in the Western Desert of Egypt.")

SAND DISTRIBUTION

The Landsat mosaic provided a useful photobase on which to map sand distribution for all of Egypt. Figure 4 is a thematic map showing the location of sand deposits in the Western Desert. This map was prepared from the Landsat mosaic and the ASTP photographs. A comparison of the usefulness of the two types of data will be discussed later.

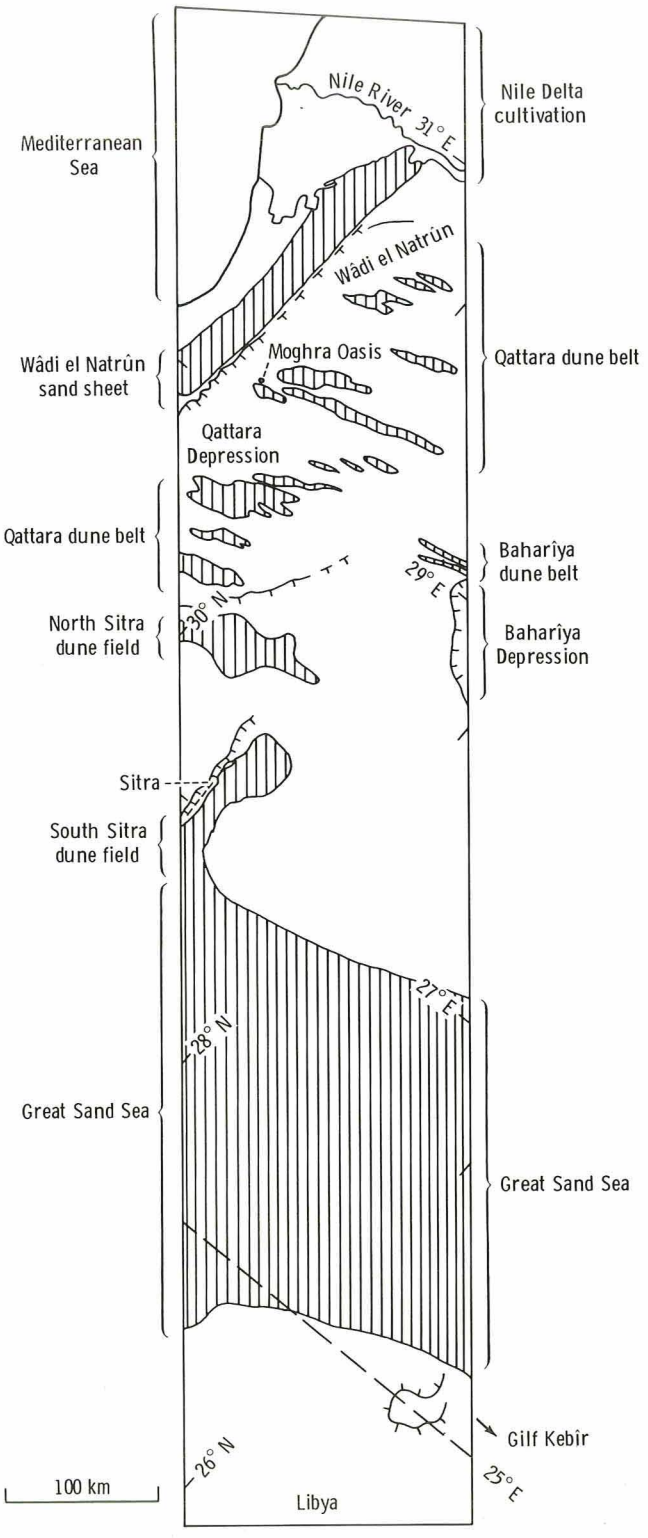
The pattern of sand distribution depicted in figure 4 reveals several distinctive features. Of particular interest is the orientation of the major dune trends. Ball (ref. 7, p. 128) points out that the dune trends in the Western Desert probably afford a very exact index to the general wind direction. The overall dune pattern is one of clockwise veering of trend around a point near Kufra Oasis in Libya (latitude 24.5° N, longitude 23° E). This pattern has already been documented (refs. 6, 7, and 14), and it implies a change in the prevailing wind direction from north-northwest in the northern desert to north-northeast in the southern desert near Gebel Oweinat.

Another interesting feature is the association of sand deposits and the depression-bounding escarpments previously described. Three types of relationships can be noted. First, in many places, sand dunes and sheets lie south of the east/west-trending scarps. In some areas, such as Qattara, Sitra, and Sîwa, there is a sand-free area at the foot of each scarp, and the sand deposits do not start until farther south. This can perhaps be attributed to the occurrence of wetlands (sebkhas) or lakes

FIGURE 2.—Area covered in the ASTP mapping pass over Egypt. (a) Color mosaic of ASTP photographs (AST-16-1246 to AST-16-1257). (b) Sketch map showing the major physiographic features. →



(a)


Nile River
31° E
Nile Delta cultivation
Mediterranean Sea
Wâdi el Natrûn
Wâdi el Natrûn sand sheet
Moghra Oasis
Qattara dune belt
Qattara Depression
Qattara dune belt
Baharîya dune belt
29° E
30° N
North Sitra dune field
Baharîya Depression
Sitra
South Sitra dune field
27° E
28° N
Great Sand Sea
Great Sand Sea
Gilf Kebîr
26° N
25° E
100 km
Libya

(b)

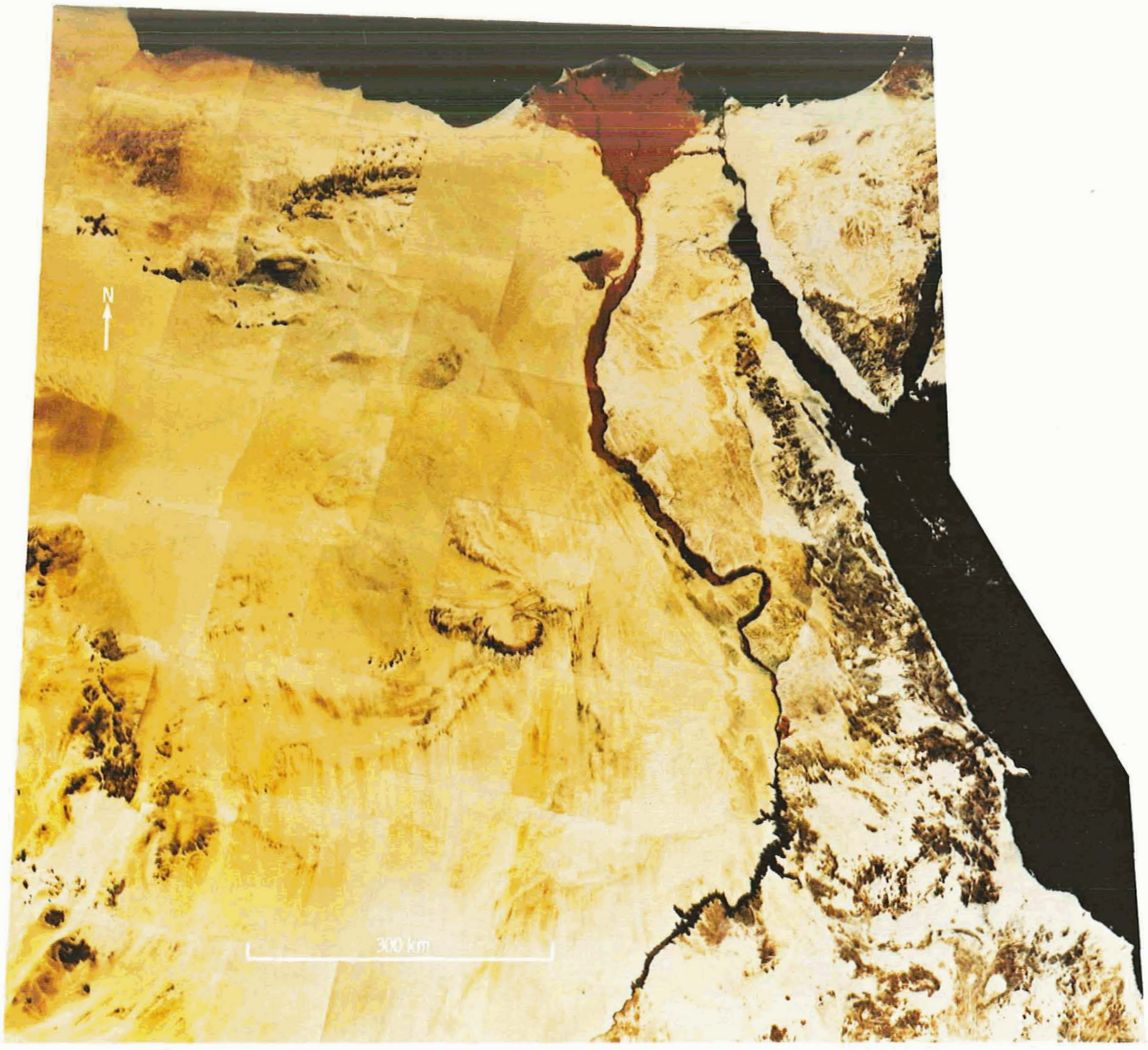


FIGURE 3.—False-color mosaic of 65 Landsat images of Egypt. (Prepared by the General Electric Company for the Smithsonian Institution.)

at the bases of the scarps; sand deposition does not occur until farther away, where it is dry enough for dunes to form. In other areas, it appears that the sand actually starts at the bases of the scarps. This mode of sand deposition can be attributed to a rapid decrease in the velocity of the prevailing northwesterly winds as they meet the scarps. This decrease is concomitant with a decrease in the sand-carrying capacity of the winds and results in sand deposition on descending slopes (ref. 15).

A second sand/scarp-related feature is seen where a large dune, a series of dunes, or a sand sheet is moving from one direction (usually from the north) and meets a scarp trending perpendicular (generally east-west) to the direction of sand movement. The effect of the scarp in this case is to break up the sand bodies and split the dunes into stringers, which sometimes recombine to continue as dunes downwind of the scarp. This is particularly true in the case of the Khârga scarp.

A third association of sand deposits and scarps

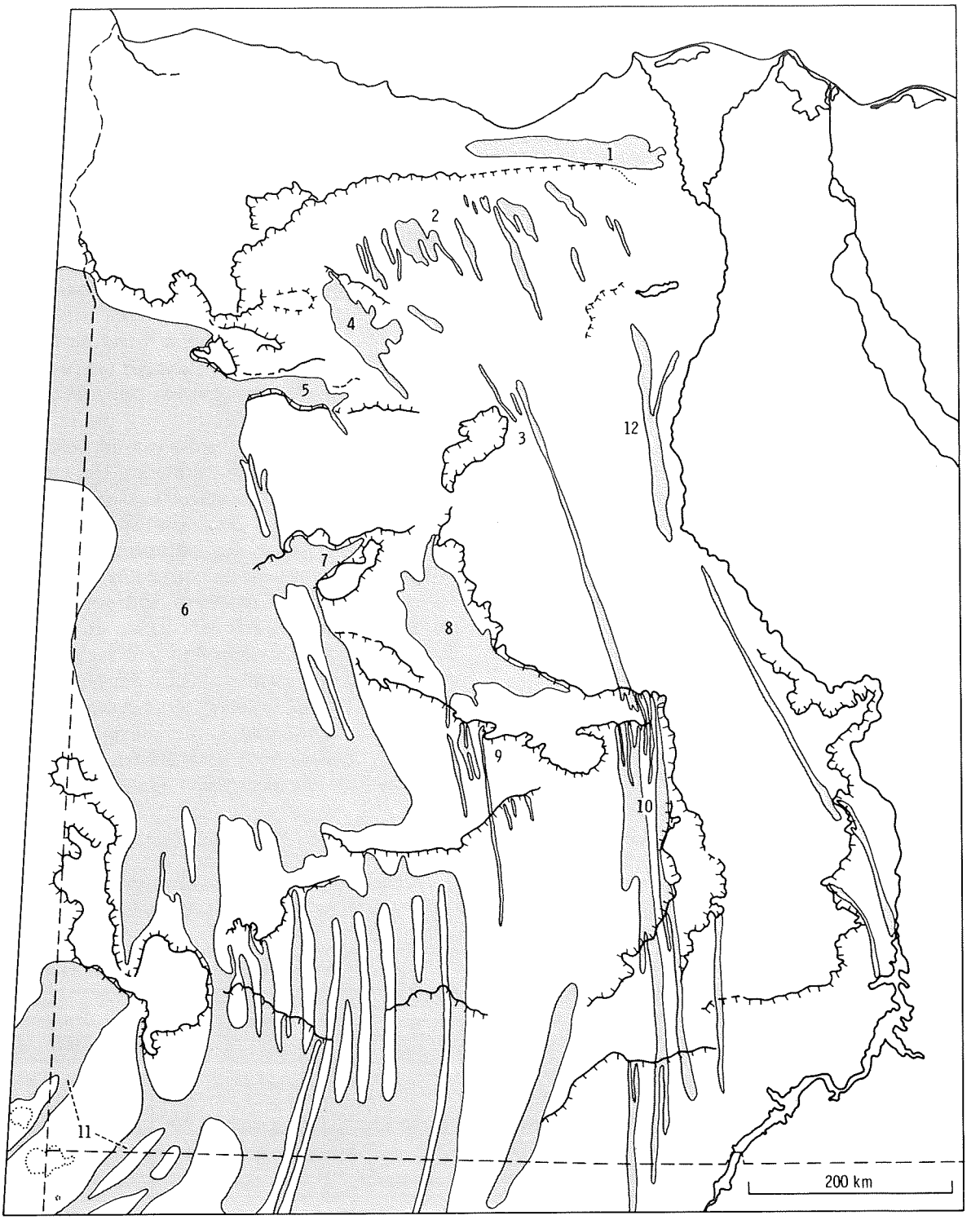


FIGURE 4.—Map showing the location of sand deposits in the Western Desert. These deposits are designated (1) Wâdi el Natrûn, (2) Qattara, (3) Baharîya, (4) north Sitra, (5) south Sitra, (6) Great Sand Sea, (7) El-Quss Abu Said, (8) Farâfra, (9) Dakhla, (10) Khârga, (11) Oweinat, and (12) Faiyûm.

occurs when a depression is enclosed not only on the north but also on the east and/or west by steep north/south-trending escarpments. Sand blown into the depression from the north is channeled southward. In the depression, the prevailing northerly winds and the north/south-trending scarps reinforce each other as factors in sand deposition.

Another type of relationship is seen in places where sand meets a rise in topography. This results in a change in the direction of sand movement. An example is seen in the Oweinat region, where the sand is diverted around protruding igneous masses that lie in the path of regional sand movement. Places where the topography rises more gently also seem to have the effect of halting or rerouting sand.

This study of sand distribution also helped pinpoint areas where moving sands constitute a threat to cultivated lands. The encroachment of dunes on fertile land represents a danger to the economy of Egypt, particularly because less than 4 percent of the land area of Egypt is presently cultivated; the rest is barren desert.

DISCUSSION OF SPECIFIC AREAS

The sand deposits mapped from ASTP photographs and Landsat images were divided into 12 areas for observation and discussion. These are designated (1) Wâdi el Natrûn, (2) Qattara, (3) Bahariya, (4) north Sitra, (5) south Sitra, (6) Great Sand Sea, (7) El-Quss Abu Said, (8) Farâfra, (9) Dakhla, (10) Khârga, (11) Oweinat, and (12) Faiyûm (fig. 4, table I). Areas 1 to 6, 11, and 12 were covered by ASTP photographs; supporting data in the form of Landsat images and aerial photographs provided information on the remaining areas.

Figure 5(a) is a mosaic of five ASTP mapping photographs showing the area between Sitra and the Nile River. Just west of the Nile Delta, three broad color zones in the desert can be seen; on a mosaic of Landsat images of the same area (fig. 5(b)), only two of these zones could be detected (ref. 13). (See section entitled "Color Zoning in the Western Desert of Egypt.") One of the color zones was tentatively identified as a sand sheet because of its bright yellow color and uniform tone (fig. 4). This sand sheet has been designated area 1, Wâdi el Natrûn. This zone runs roughly east-west and is approximately 22 km in width.

Aerial photographs of area 1 were examined to substantiate the ASTP findings. These photographs show a dune field northeast of Wâdi el Natrûn (fig. 6). The dunes are simple and compound crescentic forms; their slip faces indicate prevailing easterly winds and dune movement to the west. Near the outer western margin of the dune field, the dune forms dissipate into a sand sheet. The aerial photographs therefore confirm the ASTP interpretations, although the resolution of the orbital photographs was not sufficient to discern individual dunes.

Five other areas of sand dunes were depicted in the ASTP mapping strip; these are Qattara (area 2), Bahariya (area 3), north Sitra (area 4), south Sitra (area 5), and the Great Sand Sea (area 6). Unfortunately, some of the photographs over the Great Sand Sea were overexposed, and only dune forms near the northeastern and southwestern borders of area 6 could be identified. In areas 2 to 5, however, sand distribution and regional sand patterns were easily mapped and were found to be intimately related to topographic scarps.

Qattara Depression is bounded by a steep northern and western escarpment. The lowest elevations in the depression (134 m below sea

TABLE I.—Areal Extent of Major Sand Deposits in the Western Desert of Egypt

Dune belt designation	*Area, km²*
1. Wâdi el Natrûn	3 000
2. Qattara	18 000
3. Bahariya	4 500
4. North Sitra	4 000
5. South Sitra	2 100
6. Great Sand Sea	72 000
7. El-Quss Abu Said	800
8. Farâfra	10 000
9. Dakhla	2 700
10. Khârga	8 000
11. Oweinat	31 500
12. Faiyûm	2 400

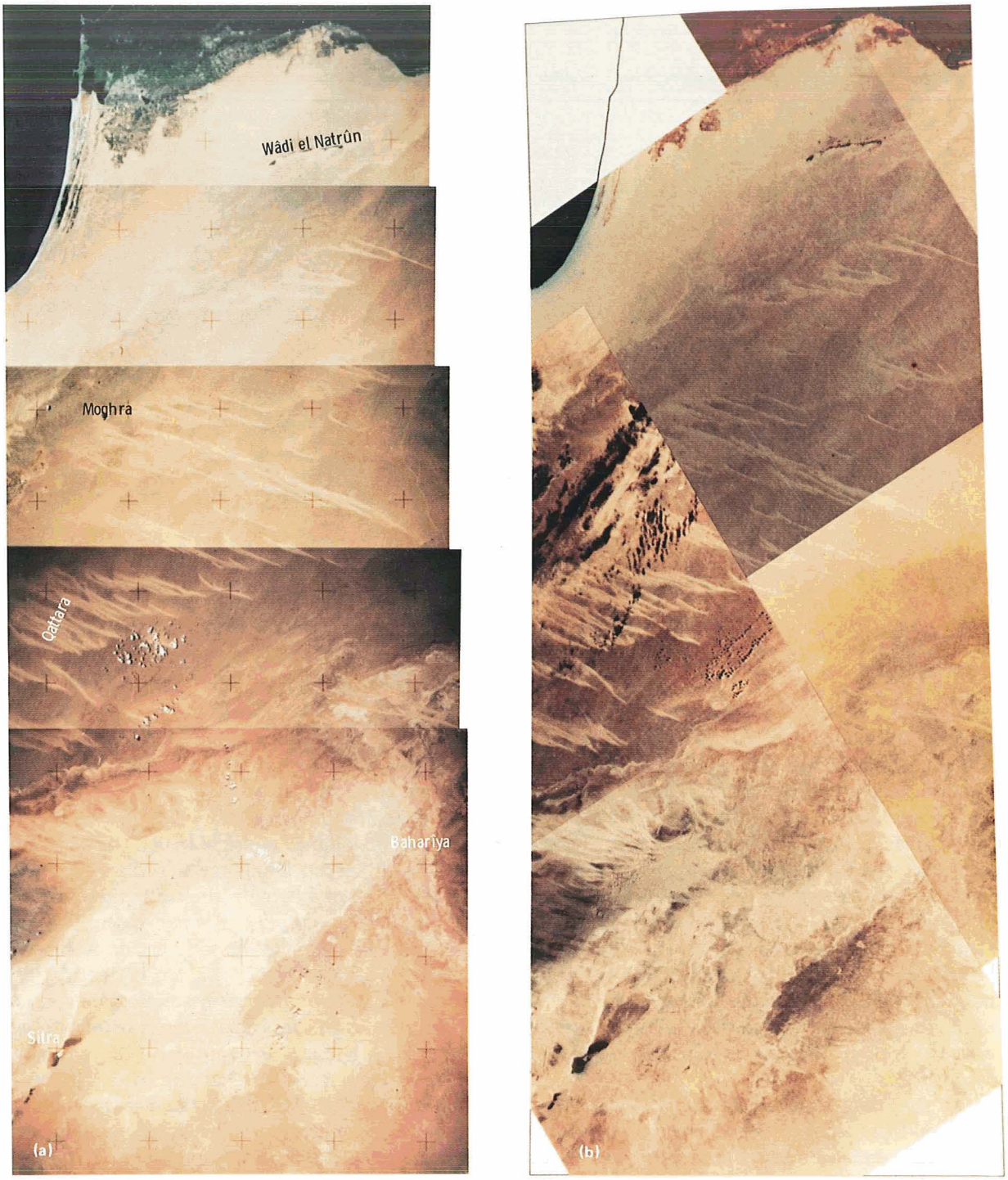


FIGURE 5.—Photomosaics of area between Sitra and the Nile River. (a) ASTP mapping photographs (AST-16-1252 to AST-16-1256). (b) Landsat false-color images.

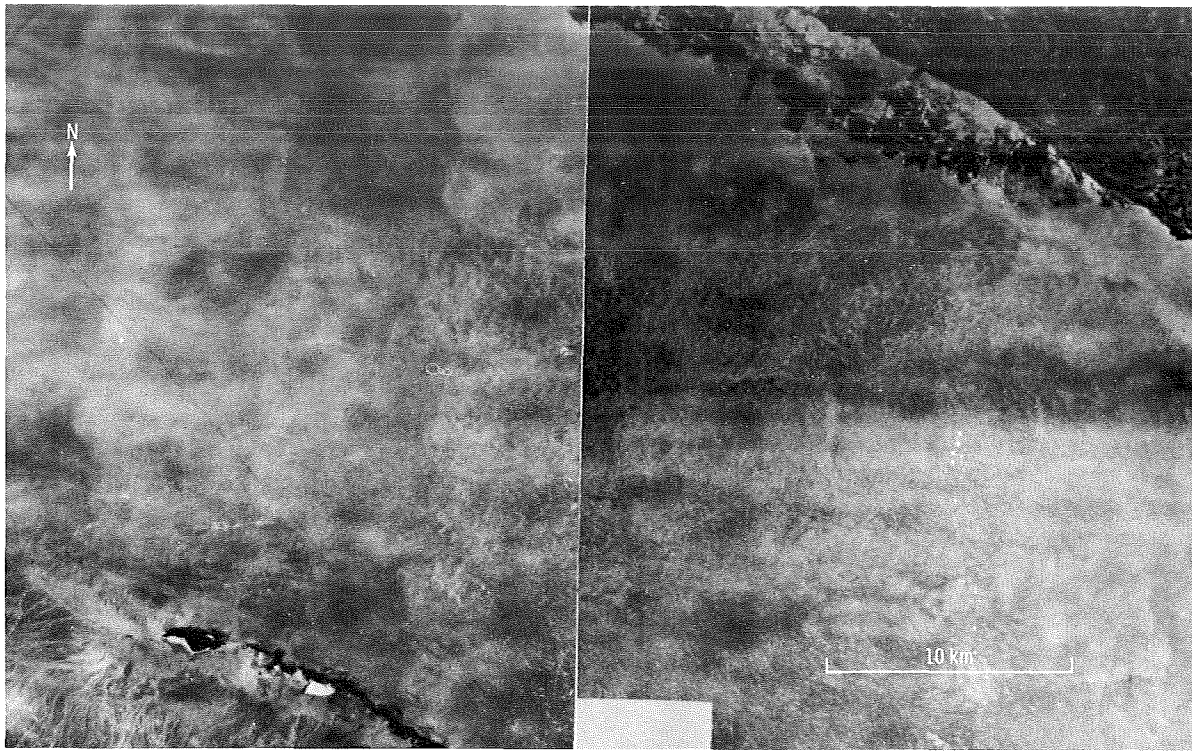


FIGURE 6.—Mosaic of two aerial photographs of the Wâdi el Natrûn area. Part of the Nile Delta is visible in the upper right corner. Wâdi el Natrûn is the elongated dark area in the lower left corner. A field of crescentic dune forms is visible northeast of Wâdi el Natrûn. (Photograph from the Military Survey, Egypt.)

level) are located at the foot of the northern scarp and are characterized by sebkhas. Toward the south and east, the depression is more open and its floor rises gradually to the general level of the desert surface (ref. 16). Because of this, the sea level contour is usually chosen to mark the southern and eastern limits of the depression on topographic maps. The northeastern border of Qattara is usually placed near Moghra Oasis, one of two oases within the depression. However, on the ASTP photographs, a continuation of the northern scarp, although poorly defined, can be traced at least to Wâdi el Natrûn, 140 km east of Moghra.

Large quantities of material have been removed from Qattara Depression by wind deflation, and sand-sized particles are blown to the south-southeast, where they are deposited as long chains of sand dunes (ref. 16). The Qattara dunes (area 2) begin south of the sebkhas and extend to the south-southeast; their lengths vary from 10 to 40 km (fig. 5(a)). The Qattara dunes have been referred to in the literature as seif dunes (ref. 17). They are characterized on the orbital photographs by diffuse northern ends and tapering southern termini. These dunes are subparallel, but they are not equally spaced along the desert surface. In fact, the ASTP photographs show that these dunes are clustered in bundles; in some cases, two or more dunes may join at the southern ends to produce a "spearhead" (ref. 18). Dune density increases to the west and, on the photographs, it is difficult to identify individual dunes within these westernmost bundles. In contrast, however, dunes in the eastern part of area 2 appear better defined. This variation within area 2 can perhaps be attributed to the effect of the northern Qattara scarp on the prevailing northwesterly winds. As the scarp increases in height to the west, crosswinds might become more prevalent. This possibility is confirmed by an examination of aerial photographs, which reveal crescentic forms concen-



FIGURE 7.—Aerial photograph of dunes in the western part of Qattara dune field. (Photograph from the Military Survey, Egypt.)

trated at the northern ends of these westernmost dunes (fig. 7). The orientation of these crescentic slip faces indicates crosswinds normal and oblique to the direction of the prevailing wind.

Baharîya Oasis lies 170 km southeast of Qattara in a scarp-enclosed depression excavated in a plateau of Eocene limestones (ref. 12). Details of the northern ends of three large dune belts north-

east of Baharîya (area 3) are revealed in the ASTP mapping strip (fig. 5(a)). The three dune belts are oriented south-southeast and are named Ghard Ghorabi, Ghard El-Qazzun, and Ghard Abu Muharik. The last dune belt is the longest measured dune line in Egypt, extending approximately 300 km from the northeastern tip of Baharîya Depression to Khârga Depression.

On ASTP photographs, the Baharîya dunes are similar in appearance to the Qattara dunes (fig. 5(a)); on a Landsat image of the same area, these dunes are much more difficult to distinguish (fig. 5(b)). To extend the ASTP data and to determine the southern limits of the Baharîya dunes, aerial photographs and Landsat images were examined. Aerial photographs indicate that to the southeast of Baharîya, the dunes diffuse into a broader belt of sand sheets and longitudinal dunes (ref. 18). On the corresponding Landsat images, it is extremely difficult to distinguish these sand deposits from the surrounding terrain on the basis of color. In this area, where the bedrock units have not been well mapped (ref. 19, p. 22), fieldwork is necessary to determine whether color variations are due to different bedrock units or to various ground coverings such as sand.

The north Sitra dune field (area 4) provides a good illustration of how dune form is influenced by local relief. Stereoscopic examination of two ASTP mapping photographs shows that the dune field is bounded on the west by a topographic high and on the northeast by a poorly defined scarp that marks the southern limit of Qattara Depression. The dunes do not start at the foot of the scarp (fig. 5(a)). For this reason, the dark mottled tones occurring at the base of the scarp have been interpreted as sebkhas. In the northern half of the dune field, long slightly curving dune forms seem to converge toward the south where a break in slope coincides with a change in dune form. Examination of a Landsat image of this area revealed a change in size, spacing, and orientation of dune forms at this break in slope (fig. 5(b)). In this case, the quality of the Landsat image was better than that of the ASTP photograph, a fact probably attributable to Sun elevation angle (37° for the Landsat image and 80° for the ASTP photograph).

The south Sitra dune field (area 5) lies in Sitra Depression, which is bounded on the north and south by east/west-trending scarps (fig. 5(a)). Lakes and sebkhas occur directly south of the northern scarp, and the dune field lies south of these wetlands. In this area, the identification of sand deposits was facilitated by the color contrast between the sand and the interdune surfaces. It seems likely that in the north Sitra and south Sitra dune fields, variations in topography increase the complexity of the wind regime. Both factors (topography and deviations in wind strength and direction) have an effect on dune geometry.

The western end of the south Sitra dune field grades into the Great Sand Sea (area 6). The Great Sand Sea is the largest dune field in Egypt. It begins just south of the oases that border the southern edge of El-Diffa Plateau in Libya and Egypt. The sand sea then continues south for 600 km before the dunes are deflected by the Gilf Kebîr Plateau and associated topographic highs. Although most of the ASTP mapping photographs of the Great Sand Sea were overexposed, linear seif dunes of tremendous lengths can be seen at the southern border of the sand sea. Landsat images provided more detail and revealed a change in form from large seif dunes with sinuous crests (called "whalebacks" by Bagnold, ref. 6) (fig. 8) in the northern part of the Great Sand Sea to narrow linear seifs in the south.

Areas 7 to 10 were not covered by ASTP photographs but were examined on Landsat images. These areas are similar to Qattara, Baharîya, and Sitra in that they provide further illustrations of the relationships between sand deposits and scarps.

Two dune belts occur in Farâfra Depression. Both a small field on the north side of El-Quss Abu Said Plateau (area 7) and a relatively large field filling a major part of the main depression (area 8) are visible on Landsat images, but dune forms cannot be well defined. The former field is interesting because the trend of its longitudinal dune forms is normal to the trend of the dunes in the Great Sand Sea, which borders the El-Quss Abu Said group on the west. The details of this dune field do not show well on Landsat images but are confirmed on aerial photographs. These photographs also reveal the interesting fact that these dunes converge and taper to the northeast and are more widely spaced to the southwest.



FIGURE 8.—Sinuous dunes at the northern edge of the Great Sand Sea. Top: numerous dunes that start at the southwesternmost edge of Sîwa Oasis. Bottom: view from the top of one of the sinuous dunes; the vehicle near the base of the dune gives scale. (Photographs by Farouk El-Baz.)

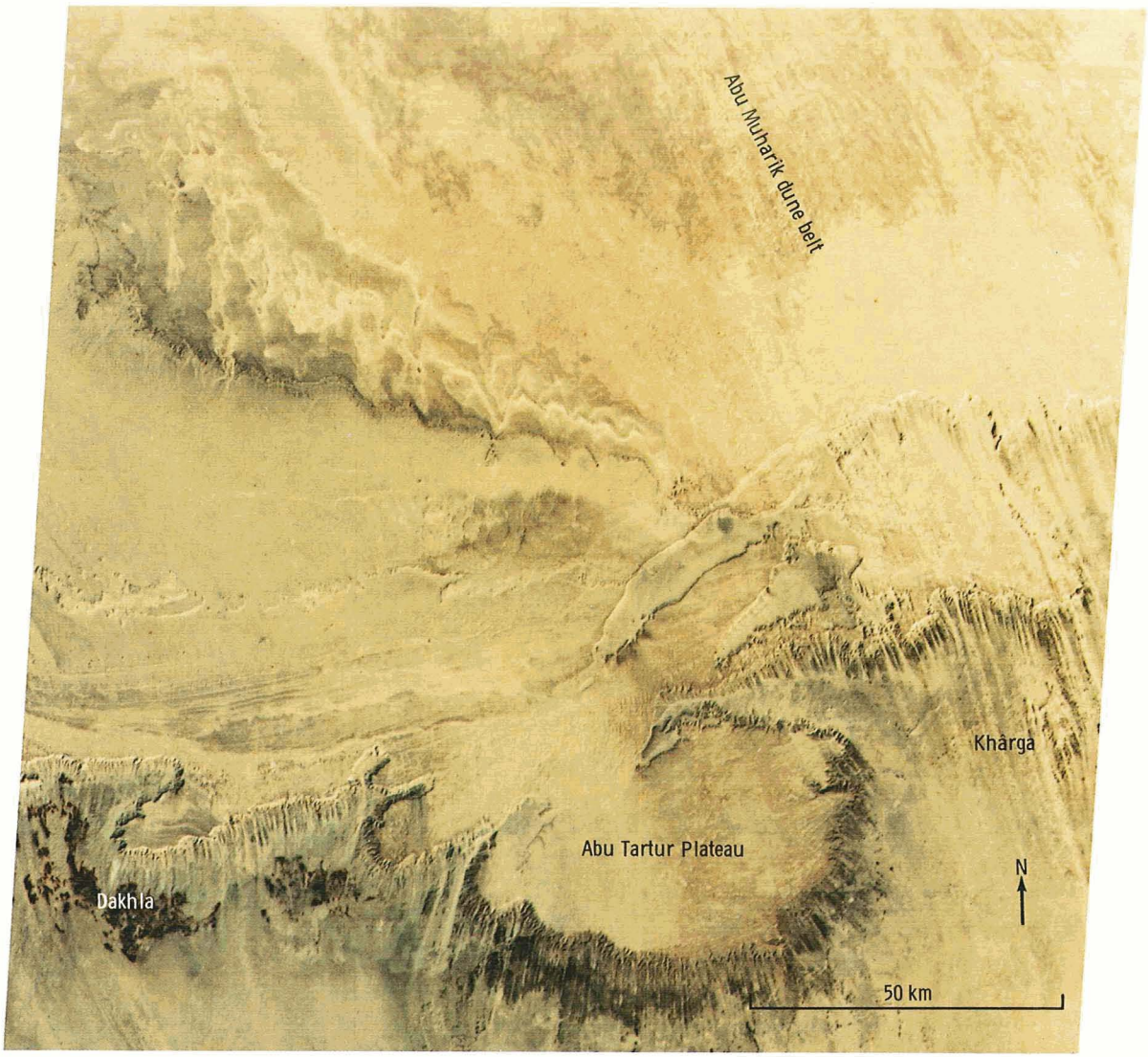


FIGURE 9.—Landsat false-color image of the Dakhla-Khârga area. Vegetated areas on the floor of these depressions appear in red tones (E-1165-08014).

Other dunes previously discussed (e.g., the Qattara dune bundles) converge to the southeast. The unusual patterns are probably attributable to wind deflection caused by the presence of scarps (ref. 19).

To the south, where the eastern north/south-trending Farâfra scarp veers to head east-west, the Farâfra dune field (area 8) spreads out to the east and south. Sand in the southern part of area 8 is channeled down the Dakhla scarp along wadis and then moves onto the flat floor of Dakhla Depression (fig. 9). Aerial photographs show that the Dakhla dunes (area 9) are barchans.

The occurrence of the barchan dunes in Khârga Depression (area 10) is similar to the situation in Dakhla. Sand is derived from the Abu Muharik dune field on the plateau north of Khârga Depression (fig. 9). The northern scarp is characterized by a number of remarkably linear sand-filled wadis that may be structurally controlled. A number of barchan chains begin at the mouths of these wadis and continue to move southward.

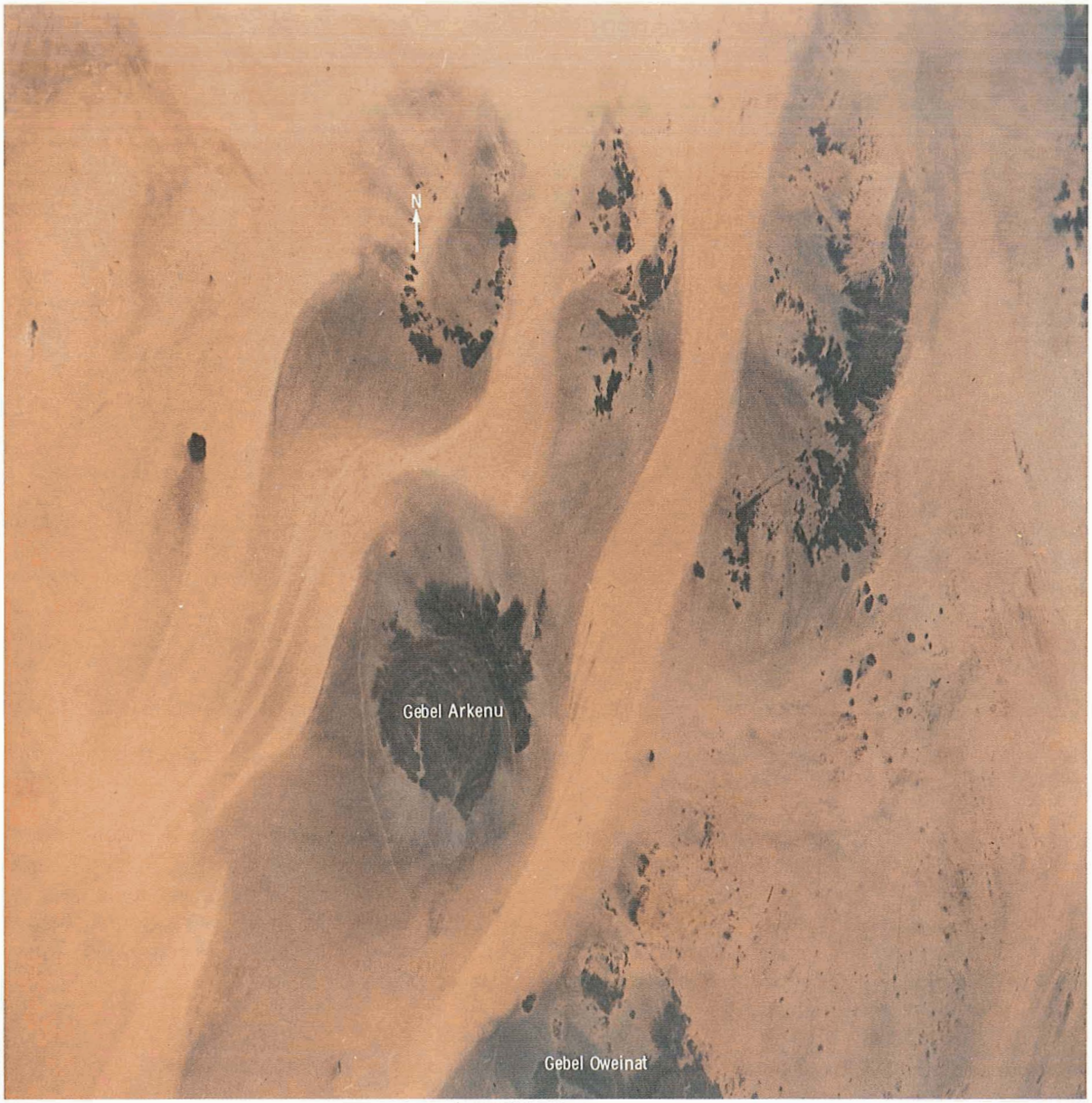


FIGURE 10.—Oblique ASTP photograph showing the patterns of sand distribution around topographic highs in the Oweinat region. Gebel Arkenu is approximately 15 by 20 km (AST-2-127).

Perhaps the best example of topographic control of sand deposits is in the area around Gebel Oweinat in the southwestern corner of Egypt (area 11). Excellent orbital photographs of this area are available (fig. 10). In the southwestern quadrant of the Western Desert, the prevailing wind direction becomes northeasterly; this is reflected by the major trends of sand movement and deposition. Another major feature in this area is the presence of several protruding topographic highs with sand-free areas on their leeward sides. Sand deflected around the hills and mountains



FIGURE 11.—Aerial view of sand dunes encroaching on the cultivated land of the Nile Valley south of Cairo. Direction of sand movement is indicated by arrow. (After El-Baz, ref. 20.)

coalesces downwind to form dunes and stringers of sand reaching into Sudan to the south and Libya to the west.

The areas discussed up until now have been studied to show the relationships between sand, wind, and topography. Of equal interest are areas where sand movement constitutes a threat to cultivated land. The problem of sand dune encroachment on vegetated land has lately been the subject of much concern (ref. 13). An excellent example of the advance of dunes onto farmland is shown by ASTP and Landsat images of the Faiyûm dune belt (area 12). These dunes begin on the floor of the flat desert surface southwest of Faiyûm and stretch south-southeastward until they meet the western border of the Nile Valley. As segments of the dune field come into contact with vegetated lands, they diffuse around patches of wetter ground and produce a spotty, frayed edge to the sand/vegetation border (fig. 11, ref. 20). Dune encroachment on cultivations is also observed in many of the Western Desert oases, particularly in Dakhla, Khârga, and Baharîya. This phenomenon shows up extremely well on Landsat false-color composites, where small vegetated spots appear as red islands in an ocean of yellow sand waves.

CONCLUSIONS

This study shows the usefulness of orbital images in mapping sand distribution patterns in the Western Desert of Egypt. The ASTP photographs and Landsat images were used to recognize and map the individual dunes, dune bundles, dune fields of various shapes and sizes, and relatively homogeneous sand sheets. However, the resolution and other qualities of these photographs and images fall short of allowing detailed study of the sand accumulations and their relationship to surrounding topography.

To enable clear delineation of dunes and other sand deposits from the surrounding bright sediments, orbital photographs must have the following characteristics:

1. Natural color: The brightness and the color of surface features are often important diagnostic characteristics in the recognition of sand deposits. Therefore, a highly color-sensitive film helps in the delineation of dunes and sand deposits. Also, variations in color within the same sand field or between different fields are usually meaningful (ref. 13). For these reasons, it is important to obtain a film record of the true colors of the surface.

2. Stereo overlap: Dune form is significant in determining prevailing wind directions and dune migration. Therefore, stereo coverage with the greatest possible vertical exaggeration is important to the study of sand distribution patterns.

3. High resolution: The resolutions of ASTP photographs (50 m at best) and Landsat images (80 m at best) are not adequate to clearly identify dunes and sand fields. The resolution required to achieve this identification is approximately 10 m.

4. Low-Sun-angle illumination: At relatively high Sun angles, the sand deposits appear washed out and it is very difficult to distinguish sand dunes from the surrounding sediments that appear equally bright. Low-Sun-angle illumination provides shadows that clearly delineate the dunes. A Sun angle of close to 30° is ideal for enhancing dune relief because this is approximately equal to the angle of repose of loose sand.

In the 1980's, the Space Shuttle will enable the acquisition of orbital photographs of the Earth by means of a 305-mm f/6 "large-format camera" that has a 40° by 74° field of view. This camera will provide an orthographic (vertical) perspective and large areal coverage. It will also provide stereoscopic photographs with as much as 80 percent overlap and high photographic resolution (10 to 20 m from a 260-km altitude).

The first Space Shuttle missions on which the large-format camera is used will have a relatively low orbital inclination of 28.5°. These missions will cover the Earth's equatorial regions and will thus be suitable for studying desert belts north of the Equator. This will enable a complete survey of the characteristics of sand accumulation to be made from Earth orbit.

Finally, in addition to detailed study of orbital photographs, subsidiary data are required. In the case of the ASTP photographs and Landsat images, both aerial photographs and field studies were necessary to clarify some of the orbital observations. With increased resolution of orbital images, aerial photographs and ground checks will be necessary in places to confirm the photogeologic interpretations.

ACKNOWLEDGMENTS

The fieldwork reported in this paper was made possible through the support of the Geology Department, Ain Shams University, Cairo, Egypt. The authors gained a better understanding of the sand distribution patterns and their controlling factors from discussions with Dr. Hassan El-Etr of that department. This work was done under NASA contract NAS9-13831.

REFERENCES

1. Petrov, M. P.: Deserts of the World. John Wiley & Sons (New York), 1976.

2. Holmes, Arthur: Principles of Physical Geology. Second ed. Ronald Press Co. (New York), 1965.

3. McKee, Edwin D.; and Breed, Carol S.: An Investigation of Major Sand Seas in Desert Areas Throughout the World. Paper G6 in Third Earth Resources Technology Satellite-1 Symposium, Stanley C. Freden, Enrico P. Mercanti, and Margaret A. Becker, eds., vol. I, sec. A, NASA SP-351, 1974, pp. 665-679.

4. Schechter, Joel: Desertification Processes and the Search for Solutions. Interdiscip. Sci. Rev., vol. 2, no. 1, 1977, pp. 36-54.

5. El-Baz, Farouk; and Mitchell, D. A.: Earth Observations and Photography Experiment MA-136. Sec. 10 of Apollo-Soyuz Test Project Preliminary Science Report, NASA TM X-58173, 1976.

6. Bagnold, Ralph Alger: The Physics of Blown Sand and Desert Dunes. Methuen (London), 1941.

7. Ball, John: Problems of the Libyan Desert. Geog. J., vol. 70, 1927, pp. 21-38, 105-128, 209-224.

8. Beadnell, Hugh J. L.: Dakhla Oasis: Its Topography and Geology. Egypt. Geol. Surv. Dept. (Cairo), 1901.

9. Beadnell, H. J. L.: An Egyptian Oasis: An Account of the Oasis of Kharga in the Libyan Desert. Murray (London), 1909.

10. Beadnell, H. J. L.: The Sand Dunes of the Libyan Desert. Geog. J., vol. 35, 1910, pp. 379-395.

11. Sandford, Kenneth Stuart: Geological Observations on the Northwest Frontiers of the Anglo-Egyptian Sudan and the Adjoining Part of the Southern Libyan Desert. Quart. J. London Geol. Soc., vol. 91, no. 363, 1935, pp. 323-381.

12. Said, Rushdi: The Geology of Egypt. Elsevier Pub. Co. (Amsterdam), 1962.

13. El-Baz, Farouk: The Meaning of Desert Color in Earth Orbital Photographs. Photogram. Eng. & Remote Sens., vol. 44, no. 1, 1978, pp. 69-75.

14. Wilson, Ian Gordon: Desert Sandflow Basins and a Model for the Origin of Ergs. Geog. J., vol. 137, pt. 2, June 1971, pp. 180-199.

15. Holm, Donald August: Desert Geomorphology in the Arabian Peninsula. Science, vol. 132, no. 3437, Nov. 1960, pp. 1369-1379.

16. Ball, John: The Qattara Depression of the Libyan Desert and the Possibility of Its Utilization for Power Production. Geog. J., London, vol. 82, no. 4, Oct. 1933, pp. 289-314.

17. Bagnold, Ralph Alger: Libyan Sands; Travel in a Dead World. Hodder and Stoughton (London), 1935.

18. Moustafa, A. R.: Photogeology of the Central Western Desert, Egypt (With a Special Emphasis on Siwa and Bahariya Oases). M.S. Thesis, Ain Shams University (Cairo, Egypt), 1977.

19. Said, Rushdi: Explanatory Notes to Accompany the Geological Map of Egypt. UAR, Geol. Surv., Paper 56, 1971.

20. El-Baz, Farouk: Expanding Desert Creates Grim Beauty But Also Threatens Crucial Cropland. Smithsonian Magazine, vol. 8, no. 3, 1977, pp. 34-41.

Preliminary Analysis of Color Variations of Sand Deposits in the Western Desert of Egypt

Farouk El-Baz,[a†] Marie H. Slezak,[a] and Ted A. Maxwell[a]

ABSTRACT

Astronaut observations and photographs of color variations in the Western Desert of Egypt are related to both iron oxide coatings on individual grains and the presence of locally derived material in the sand deposits. The results of four field trips, to Baharîya Oasis, Sîwa Oasis, Khârga and Dakhla Oases, and the Great Sand Sea, enable more detailed interpretations of colors photographed during the Apollo-Soyuz mission. The northern region of the Western Desert has the highest percentage of calcareous grains originating from local limestone outcrops. Samples from the central part of the Western Desert contain numerous iron-rich grains originating from the iron deposits of Baharîya and are locally enriched in shale fragments from the Dakhla Shale. Sands of the Great Sand Sea are relatively homogeneous, quartz-rich deposits that vary little in percentage of minor components. Although these results are preliminary, they indicate the need for more detailed field investigations of the causes of color variations; such investigations are currently underway.

INTRODUCTION

Visual observations made by the astronauts of the Apollo-Soyuz Test Project (ASTP) indicated that the colors of desert surfaces varied considerably from place to place (ref. 1). Both mapping- and handheld-camera photographs obtained on the same mission confirmed that these color variations abound on both regional and local scales. It was also shown that these color variations probably reflect compositional variations of the exposed surfaces (ref. 2). For these reasons, an investigation was planned to document the causes of color variations in sand deposits, which are an important component of desert surfaces.

The Western Desert of Egypt was selected for this study because (1) this desert was used as a test site for the investigation of variations in color as seen in ASTP photographs and (2) a team of Egyptian geologists served as team members of the ASTP Earth Observations and Photography Experiment and were able to plan and participate in the collection of field data.

This report must be considered as preliminary. The number of samples reported on here is only a fraction of the samples collected. Additional information is being gathered and analyzed by the research team members at Ain Shams University, Cairo, Egypt. This research is continuing under the auspices of a joint research project between Ain Shams University and the Smithsonian Institution.

GENERAL SETTING

The Western Desert of Egypt is a rocky platform of sandstones and limestones that is interrupted by seven major depressions and that is crossed by roughly north-south-trending parallel belts of sand dunes. The largest concentration of

[a]National Air and Space Museum, Smithsonian Institution.

[†]Principal Investigator.

dunes occupies the west-central part of the desert and is known as the Great Sand Sea (fig. 1). The origin of all these sand accumulations is not well known.

The largest of the depressions, the Qattara, measures approximately 300 km in length and averages 70 km in width. The depression includes the lowest point in the African continent, 134 m below sea level (ref. 3). Other depressions are smaller, but they enclose the habitable Sîwa, Faiyûm, Baharîya, Farâfra, Dakhla, and Khârga Oases (fig. 1).

The highest areas in the Western Desert of Egypt are in its southwestern corner and include Gilf Kebîr Plateau and Oweinat Mountain. Most of this region is more than 1000 m above sea level. The central and southeastern parts of the desert vary from 200 to 500 m above sea level, and the northwestern and northern parts of the desert reach a maximum elevation of 200 m (ref. 3).

This setting indicates a gentle slope of the terrain from south to north. This northward tilt supports the theory that the sand deposits originated from southern Egypt and northern Sudan. The most likely source for the sand is the Nubian Sandstone Formation (fig. 1). In past wetter climates, fluvial transport by the Nile River and other drainage systems would have been responsible for carrying sand grains from south to north. Also, in addition to the existing Nile Delta, the ancestral delta of the Nile may have contributed much to the accumulation of fluvial sands in the area between the present Nile Delta and the Qattara Depression (fig. 1). (See section entitled "Detection of a Probable Ancestral Delta of the Nile River.") After the fluvial deposition of the sand grains in the north, the winds carried them back southward in the numerous dune belts.

FIELDWORK

The ASTP mission occurred in July 1975. Following a preliminary review of the data, field excursions were planned to check some of the photographic interpretations of studied areas in the Western Desert of Egypt. The senior author took part in four trips that were conducted in the Western Desert. One trip was supported by the ASTP research project, and the rest were in part sponsored through the joint research program between Ain Shams University, Cairo, Egypt, and the Smithsonian Institution. A brief summary of these trips follows. (See fig. 2.)

Baharîya Oasis

The first field trip, conducted in April 1976, started at Cairo and followed the paved desert road to Baharîya Oasis and El-Gedida iron mines. The terrain from Cairo to Baharîya is basically a rocky desert plain with few prominences. Limestone rocks crop out approximately 90 km southwest of Cairo and continue to the Baharîya Depression. Any sand accumulations observed were predominantly sand shadows in the lee of limestone exposures.

The Qattara dunes are located midway between Cairo and Baharîya, and are composed of dune bundles that are very clearly exhibited on the ASTP photographs. In most cases, these bundles are composed of three to five longitudinal dunes that taper and converge at their southern termini (fig. 3). (See section entitled "Orbital Observations of Sand Distribution in the Western Desert of Egypt.")

Iron deposits abound in the Baharîya Oasis region and are mined at El-Gedida, where hematite occurs as a horizontal bed of considerable thickness (fig. 4). At El-Gedida and other areas in and around the Baharîya Depression, hematite and limonite are exposed on the surface. These occurrences are believed to be important because they provide a source of sand-size iron grains that are mixed with the sand in the Western Desert.

Sîwa Oasis

The field excursion to the Sîwa Oasis (fig. 2) was conducted in December 1976. Field checking of color zones seen in ASTP photographs was done on the 211-km-long desert road from Cairo to Alexandria. (See section entitled "Color Zoning in the Western Desert of Egypt.")

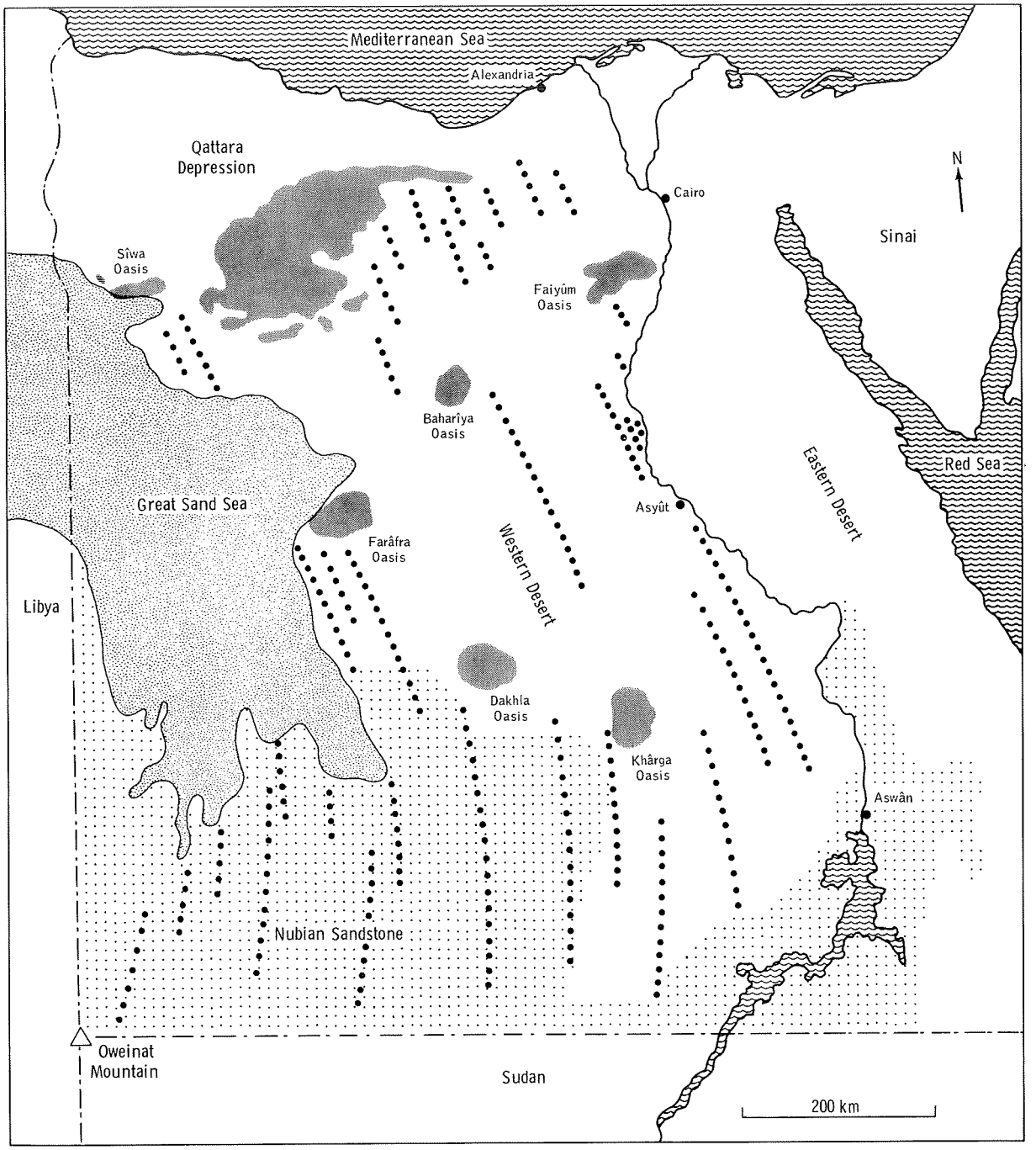


FIGURE 1.—Map of Egypt showing the distribution of depressions (dark areas) and sand dune belts (lines of dots) in the Western Desert. The Great Sand Sea occupies the west-central part of the desert. The Nubian Sandstone, the probable source of most of the sand, is exposed in the southern part of the desert.



FIGURE 2.—Mosaic of false-color Landsat images of Egypt showing color variations in the exposed rock and soil. The tracks of field excursions in the Western Desert are shown with solid lines. The dashed lines indicate the paths of visual observation overflights at 1 to 2 km altitude.

From Alexandria, the field team traveled along a 300-km-long coastal road to Mersa Matrûh, where the pavement ended. From this point, the drive followed a 300-km southwesterly track on unpaved road to Sîwa Oasis. The exposed rock was mostly limestone of Oligocene, Miocene, and Pliocene age. The Miocene limestone, locally known as the Marmarica Formation, is characterized by a reddish or pinkish color, and is fossiliferous, sandy, and highly brecciated (fig. 5). This limestone may be represented in the sand samples discussed in this paper by reddish-brown, calcareous sand-size grains.

South and southwest of Sîwa Oasis, the northern extremities of the Great Sand Sea were investigated (fig. 1). In this region, the dunes are noticeably smaller than those in the main part of the Great Sand Sea farther south. Unlike the longitudinal dunes photographed by ASTP crewmen in the southern part of the sand sea, the dunes near Sîwa are sinuous and form short curving arcs (fig. 6(a)).

The sand color southwest of the Sîwa region (fig. 6(a)) is light red. The reddish tint is made more distinctive by the gray color of the crystalline limestone that forms the rock exposures in the area (fig. 6(b)). However, the red color is not prevalent throughout. It appears to be most obvious on active sand surfaces, whereas inactive sand is lighter yellow in color (fig. 6(c) and 6(d)). This observation suggests the possibility of two different sources, although *in situ* reddening may also be important. The sands may have been of mixed origin to start with, or may have been dislodged from the rocky exposures in the area.

Following the investigation of the Sîwa area and sampling of the northern part of the Great Sand Sea, desert landforms were studied from an airplane. A flight was made from Sîwa 480 km eastward to Faiyûm Oasis and continued southward for approximately 260 km to Asyût (fig. 2). During this flight, the nature of the Qattara dune belts was studied in addition to the sand dunes of the Faiyûm area. Also, it was noticed that sand dunes were encroaching on farmland along the western boundary of the Nile Valley from Faiyûm to Asyût (ref. 4). This encroachment is dangerous to the economy of Egypt, a country where the farmland constitutes less then 4 percent of the total area.

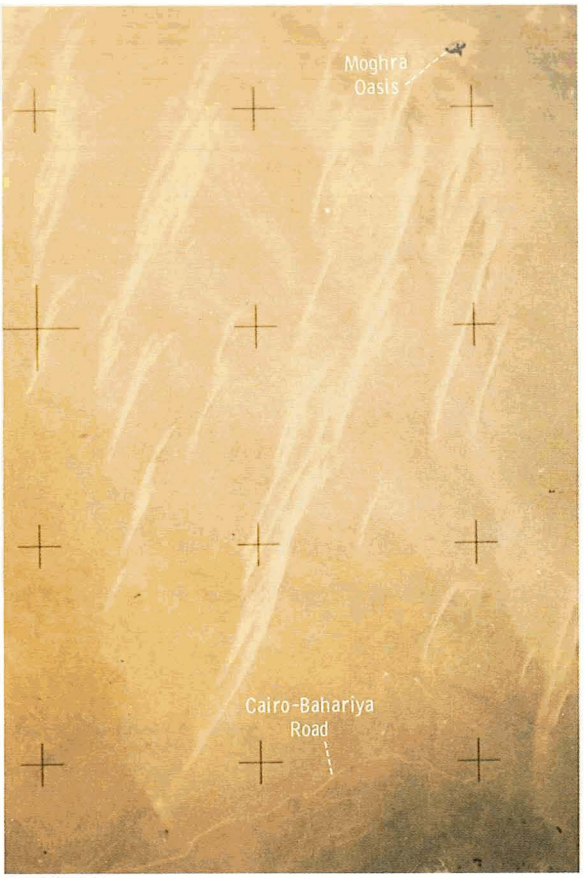


FIGURE 3.—ASTP photograph of longitudinal dune belts in the Qattara region. The southern tips of the dunes are migrating toward the Cairo-Bahariya Road (AST-16-1254).

Khârga and Dakhla Oases

A preliminary survey of Khârga and Dakhla Depressions was conducted in April 1977. After a flight from Cairo to Khârga, the field investigation was begun.



FIGURE 4.—View of the El-Gedida iron mine in the Baharîya Depression. Note that the red iron ore (hematite) occurs near the surface.



FIGURE 5.—An exposure of the pink-colored, concretionary, and argillaceous limestone north of Sîwa Oasis. Pencil at left center is 13 cm long.



FIGURE 6.—Sand color at the northern edge of the Great Sand Sea. (a) A cluster of sinuous dunes as seen from a hill west-southwest of Sîwa Oasis. (b) Reddish sand ripples around a dark-gray, crystalline limestone block. (c) The windward side of a dune that occurs on a limestone hill, approximately 20 m high. (d) The crest of the same dune showing reddish sand on the windward (right) side and a mixture of red and gray sand on the leeward (left) side. The mixing of the two colors is apparently caused by crosswinds on the leeward side, which form several intersecting ripples on the dune surface.

From Khârga, the field party drove north-northeast along a paved road, which was elevated in many places to block advancing dunes. Here, encroachment is so severe that new telephone poles had to be attached to the original ones. Pleistocene lacustrine deposits occur to the north where the road becomes level with the desert surface. These outcrops are consistently streamlined by wind erosion and are parallel in a north-south direction. Sand tails on the leeward side of most of these outcrops range in height from less than 0.3 m to 1.5 m. These forms are small-scale analogs of yardangs streamlined by the action of wind. The last stop north of Khârga was at an enormous compound barchan. The degree of compaction varies significantly from the base to the crest of this dune. Near the base of the dune, the sand was hard and closely packed, but in other places, our feet sank several centimeters into the sand. The desert surface in this area is characterized by low and widely spaced sand ridges and by a desert pavement of coarse rounded pebbles and stones.

The trip continued west along the Ghabari Road from Khârga to Dakhla. Just west of Khârga, there is a field of crescentic-shaped barchans. The first barchan, 1.3 km west of Khârga, had completely blocked the road so that a bypass road had to be constructed behind the dune. Barchans are the dominant form of dunes

within 20 km west of Khârga and frequently obstruct passage.

On aerial mosaics, the barchan belt west of Khârga is easily identified. The belt widens to the south, and the eastern side of the dune field is remarkably linear. Sand from the field appears to be derived from the plateau north of the scarp bounding the depression. These dunes are probably a continuation of the Abu Muharik dune field. The northern scarp is characterized by a number of parallel, linear wadis filled with sand. A number of barchan chains emanate from these wadis and continue to migrate southward. Fracture patterns in this area are generally east-west and north-south, and the prevailing wind direction is north-south. Therefore, it appears that in the Khârga area, fault and lineament trends control the distribution of sand.

Great Sand Sea

A field excursion was organized in December 1977 to investigate and sample the central part of the Great Sand Sea and to perform detailed studies in areas that were previously visited. This trip included visits to six oases in the Western Desert. It started in Cairo along the desert road to Faiyûm Oasis and then proceeded southward along the Nile Valley to Asyût.

From Asyût, a paved desert road was followed to Khârga Oasis and travel continued farther south on an unpaved road to Bârîs Oasis. The route then followed a westerly direction to Dakhla Oasis and from there to the eastern borders of the Great Sand Sea. From that point, the road followed a northeasterly trend through rugged desert terrain and numerous sand deposits toward Baharîya Oasis, and back to Cairo (fig. 2). Upon return, the odometers on the desert jeeps had registered nearly 3000 km.

The investigation of sand color on this trip included comparisons made with the ASTP color wheel. (See section entitled "Comparison of Astronaut Visual Color Observations With ASTP Photographs.") Wherever sand samples were collected, the color of sand was compared to the numbered color chips. In most instances, the color of the active face of a given dune was redder than the slip face (fig. 7).

SAMPLE ANALYSIS

Methods

Both grain size and lithologic components of 31 samples from the Western Desert of Egypt (fig. 8) and of 1 sample from the United Arab Emirates were analyzed. To more fully understand the color variations seen in ASTP photographs, these colors were compared to field and laboratory observations of sand color and texture. The bulk samples collected varied in weight from 61 to 617 g and averaged 305 g. Samples were split into two halves, and one half was sieved for 15 minutes on a Ro-Tap using standard mesh sieves at 0.25ϕ intervals. After sieving, each size fraction was weighed and recorded. Sediment size-frequency, cumulative-arithmetic (fig. 9), and cumulative-probability curves were plotted for each sample (ref. 5). The analysis of grain composition consisted of examining the second half of the bulk sample under a binocular microscope. In addition to the observation of physical characteristics using the binocular microscope, elemental analyses of randomly selected grains were performed with a scanning electron microscope (SEM). The SEM has an energy dispersive system equipped with a silicon-lithium detector and a multichannel analyzer, which includes a display calibrated for elements of atomic numbers 11 to 32. As a result, it was possible to perform elemental analyses of various grains and of specific areas or points on the grains. Individual grains were identified according to the following scheme, and visual estimates were made of the component percentages of each sample.

Classification Criteria

For this analysis, the components of the sand samples were grouped under the following classification: quartz, reddish-brown calcareous grains, shale, white calcareous grains (dolomitic limestone(?)), heavy minerals (glauconite, phosphates, and hornblende(?)), ferruginous grains (nodules, limonitic grains, and ferruginous sandstone grains), chalk, marl, gypsum, and calcite. The following criteria were used for identification of the components under the binocular

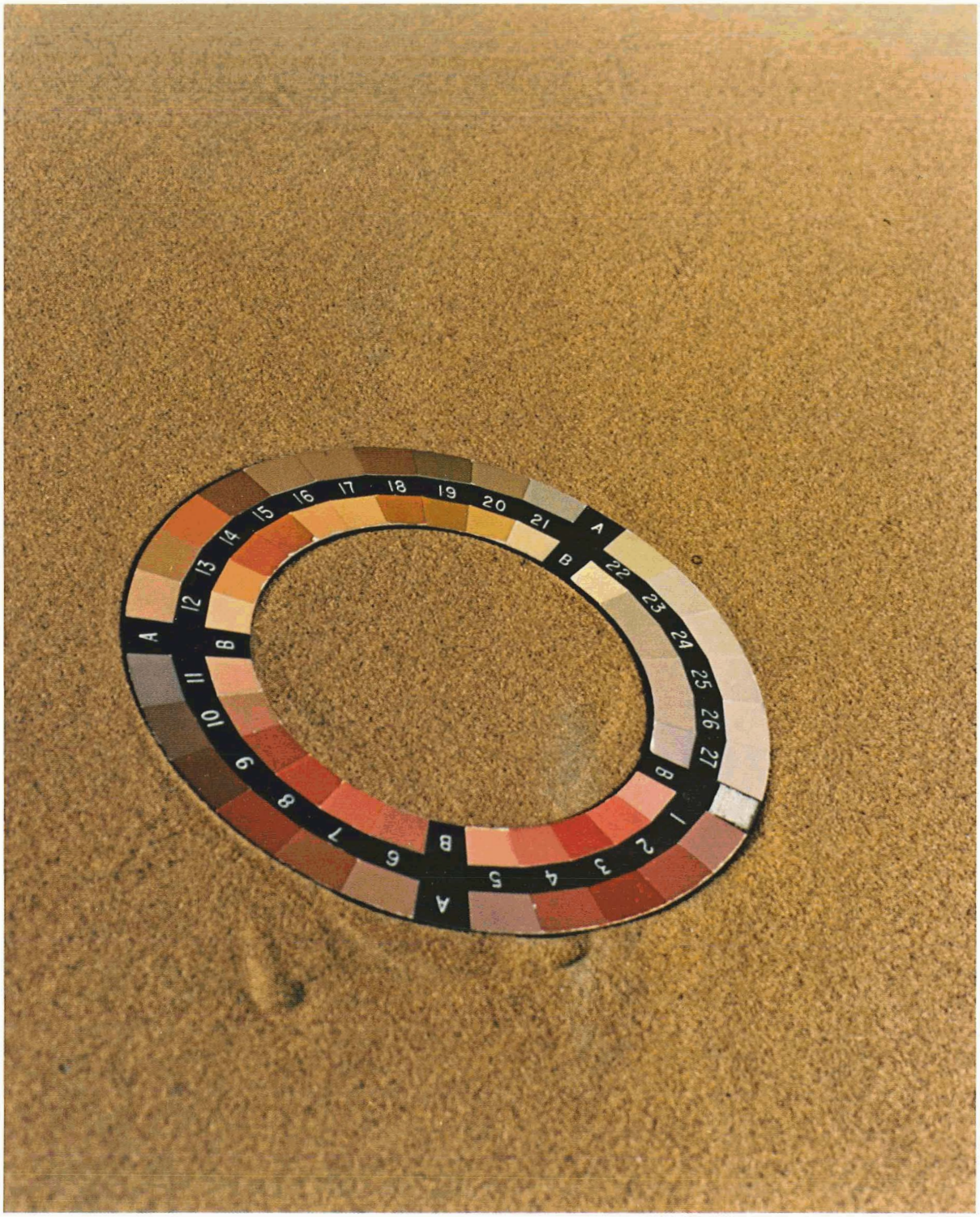


FIGURE 7.—The color wheel used by the ASTP astronauts in orbit is shown near the crest of a dune. The near field is part of the redder, windward side of the dune.

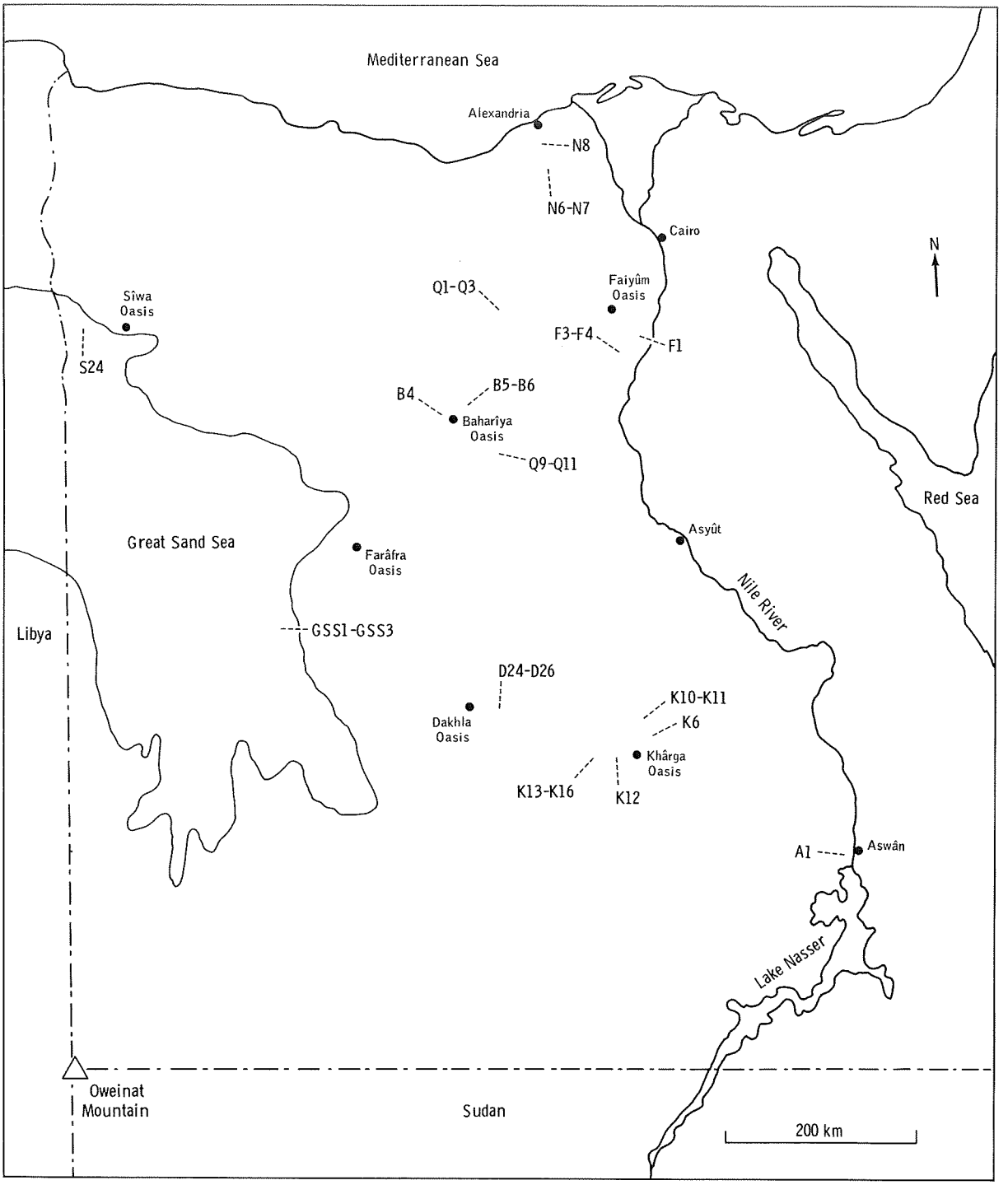


FIGURE 8.—Location of numbered sand samples collected by the senior author on four field trips.

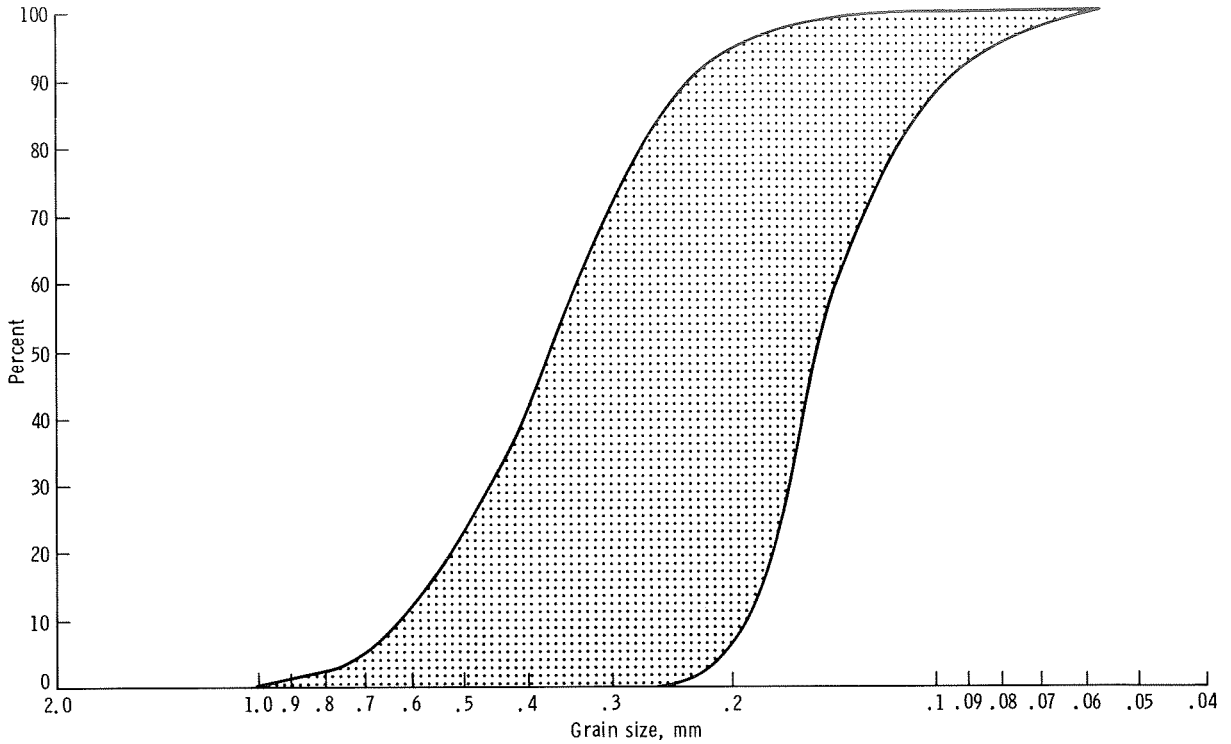


FIGURE 9.—Cumulative size frequency distribution representative of sand samples from the Western Desert. As shown by the steepness of the bounding curves, most samples are well to moderately well sorted.

microscope, supplemented by SEM analysis where noted.

1. *Quartz* was identified by glossy luster, translucence or transparence, lack of cleavage, conchoidal fracture, lack of color, frequent frosting and yellowing, and great hardness.

2. *Reddish-brown calcareous grains* were identified by reddish-brown color, very low hardness, minor crystallinity, and translucence. Supplemental SEM analysis indicates similar composition to white calcareous grains. These two sets of grains vary mainly in color.

3. *Shale* was identified by fissility and very low hardness, and by comparison with grains derived from an Esna Shale rock fragment, collected near Luxor.

4. *White calcareous grains* were identified by white color, very low hardness, minor crystallinity, and translucence, and by SEM analysis.

5. *Heavy minerals*

a. *Glauconite* was identified by high sphericity, bright- to dark-green color, very low hardness, and high polish, and by SEM analysis.

b. *Phosphates* were identified by comparison of the irregular habit, black color, and interior appearance of the grains with grains derived from a phosphate rock collected from a scarp midway between Dakhla and Khârga Oases.

c. *Hornblende(?)* was identified by SEM analysis.

6. *Ferruginous grains (nodules, limonitic grains, and ferruginous sandstone grains)* were identified by rounded habit and dark reddish-brown or orange color. The ferruginous sandstone grains are aggregates composed of fine angular quartz grains within an iron oxide matrix.

7. *Chalk* was identified by snow-white color and low hardness, and by SEM analysis; soft noncrystalline chalk and microcrystalline limestone have been included under this classification.

8. *Marl* was identified by brown to gray color, low hardness, calcareous composition, and lack of crystallinity. These grains are often composed of

very loosely compacted silt- and clay-size fragments.

9. *Gypsum* was identified by snow-white color and extremely low hardness, by SEM analysis, and by visual comparison with a gypsum and clayey rock fragment collected at Sîwa Oasis.

10. *Calcite grains* were identified by rhombohedral cleavage, lack of color, vitreous luster, and low hardness.

FIGURE 10.—Photomicrographs of sand grains of various compositions and shapes. (a) Quartz grain with frosted surface; light areas in pits on the surface (A and B) are hematite. (b) High magnification of area A showing minor crystallinity of iron oxides. (c) X-ray fluorescence spectrum of area B; highest peak is located at the iron (Fe) energy level. Other peaks are silicon (Si) and calcium (Ca). (d) Example of angular quartz grains which occur predominantly at smaller grain sizes. (e) Highly spherical glauconite grain. (f) Fissile shale grain. (g) Chalk grain. (h) Marl grain. →

SAMPLE CHARACTERISTICS

Texture and Composition

The mean grain size of most samples falls in the range of fine sand, and the size distribution for all samples is summarized in figure 9. As would be expected from these wind-deposited sands, most samples are well to moderately well sorted, and they generally contain less than 1 percent (by weight) silt and clay.

Because of the survey nature of this study, many local environments were sampled, and textural characteristics for individual samples are shown in table I. Preliminary analyses indicate some dependence on local environment; the crests and windward sides of barchans generally contain coarser grains, although there is no apparent difference in grain size on either side of longitudinal dunes.

Although most samples are composed of more than 50 percent quartz grains, the amount and type of other fragments is the result of local material. Samples from Baharîya, Khârga, and Dakhla Oases contain the largest amounts of local components, consisting of white and reddish-brown calcareous grains and shale. Because the individual sampling sites exert the greatest influence on components other than quartz, representative samples of exposed bedrock are used for comparison with sand samples.

The surface texture of individual grains is predominantly a function of lithology (fig. 10). As determined from high magnification (fig. 10(a)), quartz grains larger than 0.20 mm diameter are well rounded and have frosted surfaces. Iron oxides occur both within fractures of quartz grains and in protected hollows on the grain surfaces.

Sample Locations

Because of the regional distribution pattern of the sand deposits, the localities are divided into three parts: (1) the northern region of the Western Desert, including the area west of the Nile Valley (Wâdi el Natrûn), the Qattara dunes, and dunes southwest of the Faiyûm Oasis; (2) the central region, which includes the oases of Baharîya, Khârga, and Dakhla; and (3) the Great Sand Sea, including samples obtained south of Sîwa Oasis and southwest of Farâfra Oasis. Comparisons are made between the samples of the Great Sand Sea with those collected near Aswân in southern Egypt and from the eastern part of Ar Rub' al Khālī dunes in the United Arab Emirates.

Northern Region

Wâdi el Natrûn.—Samples at Wâdi el Natrûn were taken from a sand sheet that shows a bright pinkish-yellow color with a reddish tint on ASTP photographs (ref. 2). Samples N6 and N7 were taken from the same dune; sample N6 was collected from the more active, windward side, and sample N7 from the slip face.[1] Sample N8 was located in the color zone that appears as a dusty pinkish-gray area with mottled texture in ASTP photographs. (See section entitled "Color Zoning in the Western Desert of Egypt.") Field observations of this zone suggest that it has more clay and carbonate particles than the dune from which samples N6 and N7 were taken.

[1]Sample numbers are referred to throughout the text, and locations are indicated in figure 8.

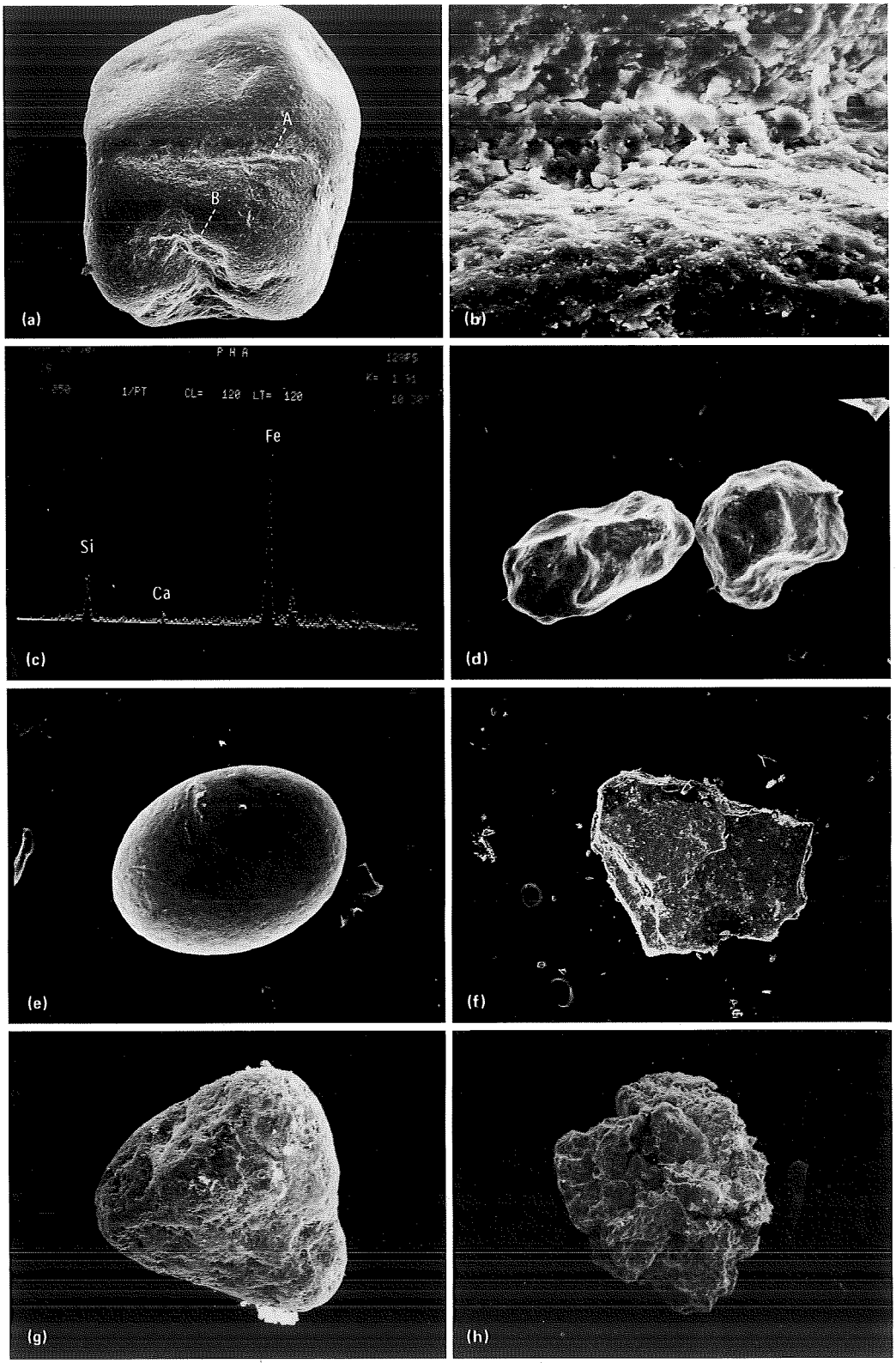

A
B
(a)
(b)
P H A
1/PT CL= 120 LT= 120
Fe
Si
Ca
(c)
(d)
(e)
(f)
(g)
(h)

TABLE I.—Summary of Size Analysis Data From Sediment Samples[a]

Sample number	*Environment*	*Mean grain Size*[b] Mz, ϕ *(mm)*	*Weight % silt and clay* ($< 4.0\,\phi$)	*Sorting*[c] σ_I, ϕ	*Skewness,*[d] SK_I	*Kurtosis,*[e] K_G	*Munsell color*[f]
			Wâdi El Natrûn				
N6	Windward side of dune	1.70 (0.32)[g]	1.79	(h)	(h)	(h)	10YR 6/6
N7	Slip face of dune	.40 (.75)[g]	8.27	(h)	(h)	(h)	10YR 6/6
N8	Sand sheet	2.60 (.17)[g]	25.68	(h)	(h)	(h)	10YR 6/4
			Qattara dunes				
Q1	Lee side of sand dome	2.30 (0.21)	0.72	0.47	+0.30	1.12	2.5Y 7/6
Q2	Windward side of sand dome	1.86 (.28)	.05	.55	−.13	1.43	2.5Y 7/6
Q3	Lee side of barchan	2.23 (.22)	1.23	.48	+.20	1.16	2.5Y 7/6
Q9	Base of longitudinal dune	2.06 (.24)	.19	.85	+.07	.93	2.5Y 7/4
Q10	Sinuous segment of longitudinal dune	1.18 (.44)	.01	.57	+.32	1.31	10YR 7/6
Q11	Crest of longitudinal dune	1.78 (.30)	.41	.56	+.81	.58	2.5Y 7/4
			Faiyûm Oasis				
F1	Sand sheet	0.39 (0.78)	0.84	0.56	+0.62	2.94	2.5Y 7/4
F3	Crest of dune	1.89 (.28)	.84	.56	+.46	1.54	2.5Y 7/4
F4	Slope of dune	1.80 (.29)	1.16	.54	+.53	1.45	2.5Y 6/4
			Bahariya Oasis				
B4	Crescentic dune	2.57 (0.17)	0.21	0.43	+0.15	0.87	2.5Y 7/4
B5	Crescentic dune	2.17 (.22)	.18	.42	+.24	1.98	2.5Y 7/6
B6	Crescentic dune	1.87 (.28)	.04	.43	+.29	1.36	2.5Y 7/6

[a]Equations for size relationships are from Folk (ref. 5).

[b]Graphic mean grain size: $Mz = (\phi 16 + \phi 50 + \phi 84)/3$

[c]Inclusive graphic standard deviation: $\sigma_I = \frac{\phi 84 - \phi 16}{4} + \frac{\phi 95 - \phi 5}{6.6}$

[d]Inclusive graphic skewness: $SK_I = \frac{\phi 16 + \phi 84 - 2(\phi 50)}{2(\phi 84 - \phi 16)} + \frac{\phi 5 + \phi 95 - 2(\phi 50)}{2(\phi 95 - \phi 5)}$

[e]Graphic kurtosis: $K_G = \frac{\phi 95 - \phi 5}{2.44(\phi 75 - \phi 25)}$

[f]Color of bulk sample from comparison with Munsell color chart (ref. 6).
[g]Median grain size ($\phi 50$) only.
[h]Small sample size did not allow more detailed analysis.

TABLE I.—Concluded

Sample number	*Environment*	*Mean grain Size*[b] Mz, ϕ *(mm)*	*Weight % silt and clay* ($< 4.0\,\phi$)	*Sorting*[c] σ_I, ϕ	*Skewness,*[d] SK_I	*Kurtosis,*[e] K_G	*Munsell color*[f]
			Khârga Oasis				
K6	Lee side of dune	2.51 (0.18)	1.57	0.67	+0.01	0.94	10YR 6/4
K10	Compound barchan	2.22 (.22)	.35	.77	+.12	.80	10YR 6/6
K11	Compound barchan	2.20 (.22)	.41	.76	+.25	.75	10YR 6/6
K12	Base of barchan	2.54 (.18)	.67	.56	−.04	.72	10YR 6/6
K13	Lee side of barchan	2.03 (.25)	.39	.77	−.01	.78	10YR 6/6
K14	Crest of arm of barchan	2.73 (.15)	.07	.28	+.13	1.06	10YR 6/4
K15	Crest of barchan	2.71 (.15)	.18	.34	+.01	1.02	10YR 6/4
K16	Windward base of barchan	1.54 (.35)	.08	.74	+.16	.94	10YR 6/6
			Dakhla Oasis				
D24	Base of barchan	2.50 (0.18)	1.11	0.83	−0.34	1.00	10YR 6/4
D25	Surface of barchan (dark sand streaks)	1.46 (.37)	.12	.53	+.07	1.10	10YR 6/4
D26	Barchan (predominant color)	1.71 (.31)	.09	.48	+.07	1.04	10YR 6/6
			Sîwa Oasis				
S24	Base of windward side of dune	0.70 (0.64)	<0.01	0.81	+0.75	1.38	10YR 6/6
			Great Sand Sea				
GSS1	Base of sinuous longitudinal dune	0.74 (0.60)	<0.01	0.45	+0.23	1.02	10YR 6/6
GSS2	Arm of sinuous longitudinal dune	1.82 (.29)	.11	.61	+.04	.99	10YR 6/6
GSS3	Crest of sinuous longitudinal dune	1.91 (.27)	.97	.39	+.14	1.33	10YR 6/6
			Aswân				
A1	Sand sheet at base of cliff	1.56 (0.35)	3.32	0.77	+0.39	1.54	10YR 6/6
			Ar Rub' al Khālī				
UAE1	Red sands at terminus of dune	2.61 (0.16)[g]	0.25	0.39	+0.07	0.91	7.5YR 5/6

Samples N6 and N7 are fairly clean sand. Similar to most of the other samples, N6 consists predominantly of quartz with minor amounts of white calcareous grains, reddish-brown calcareous grains, ferruginous grains (nodules and limonitic grains) and heavy minerals (fig. 11). The heavy minerals in all three samples have been tentatively identified as hornblende. Sample N7 differs from N6 in that it contains more heavy minerals, no calcareous grains, and fewer limonitic grains. The composition of these two samples is a direct result of the local environment, since the leeward side is better sorted compositionally and has a finer mean grain size than the windward side.

Field observations of the color zone from which sample N8 was taken are well substantiated by analysis of the sample. It differs from samples N6 and N7 by containing a higher percentage of calcareous marl grains, minor amounts of gypsum, chalk, and calcite(?) grains, and one or two fossils. In addition, this sample contains the largest amount (25 percent) of silt- and clay-size particles. The composition of this sample is likely influenced by local outcrops, particularly the "small hillocks of marly composition" that appear in this zone. (See section entitled "Color Zoning in the Western Desert of Egypt.")

Qattara dunes.—The Qattara dunes are three parallel belts of longitudinal dunes that cross the rocky, dark-colored desert platform southwest of the Nile Delta (figs. 1 and 2). The tips of some of these dunes have approached the Cairo-Bahariya Road and have even started blocking it (fig. 3). The southern termini of these dunes are characterized by numerous complex crescentic or sinuous dunes.

The southernmost tip is usually characterized by a gently sloping sand dome that is perfectly symmetrical (fig. 12). A clear color difference exists between the windward and the leeward sides of the dome and the crescentic dunes. The windward, more active side appears redder, whereas the leeward side is usually more gray in color.

The southern tip of the dune complex illustrated in figure 12 was sampled to see how much compositional variation exists in the sands at the terminal part of the dune, where mixing with materials from the surrounding terrain is at its maximum. Sample Q1 was taken from the leeward side of the sand dome, Q2 from the windward side of the same dome, and Q3 from the leeward side of the first barchanlike dune at the tip of the complex. The samples from the leeward sides of both the dome and the barchan are finer grained and contain more silt and clay than the sample from the windward side. However, there is no difference in bulk sample color between the leeward and windward sides. This discrepancy between field and laboratory color designation is not unexpected because samples are from the upper few centimeters, whereas the field color differences are due to a thin veneer of surface sand.

Samples Q1, Q2, and Q3 contain many different components (fig. 11). Sample Q1 consists predominantly of quartz and white calcareous grains, lesser amounts of reddish-brown calcareous grains, heavy minerals (glauconite and hornblende(?)), and ferruginous grains (nodules, limonitic grains, ferruginous sandstone), and contains very low amounts of chalk, marl, and shale.

The composition of sample Q2 is very similar to that of Q1; the ratios of the components of both samples are approximately the same. However, sample Q2 does not contain any shale or marl and has fewer ferruginous grains. Sample Q3 contains less quartz, more white and reddish-brown calcareous grains, and more heavy minerals than do samples Q1 and Q2. This sample also does not include shale or marl in its composition.

These three samples, however, are not characteristic of the longitudinal dunes of the Qattara dune bundles. One of these, known as Ghard Abu Muharik, extends from east of Bahariya Oasis in the north to the Khârga Depression in the south. Three samples were collected from its northern part: Q9 from the base of the dune, Q10 from the leeward side of a sinuous dune segment, and Q11 from the crest of the dune.

Samples Q9, Q10, and Q11 contain fairly high percentages of quartz, particularly Q9 and Q10 (fig. 11). Sample Q9 includes minor amounts of white calcareous grains, heavy minerals (glauconite), chalk, ferruginous grains, marl, and

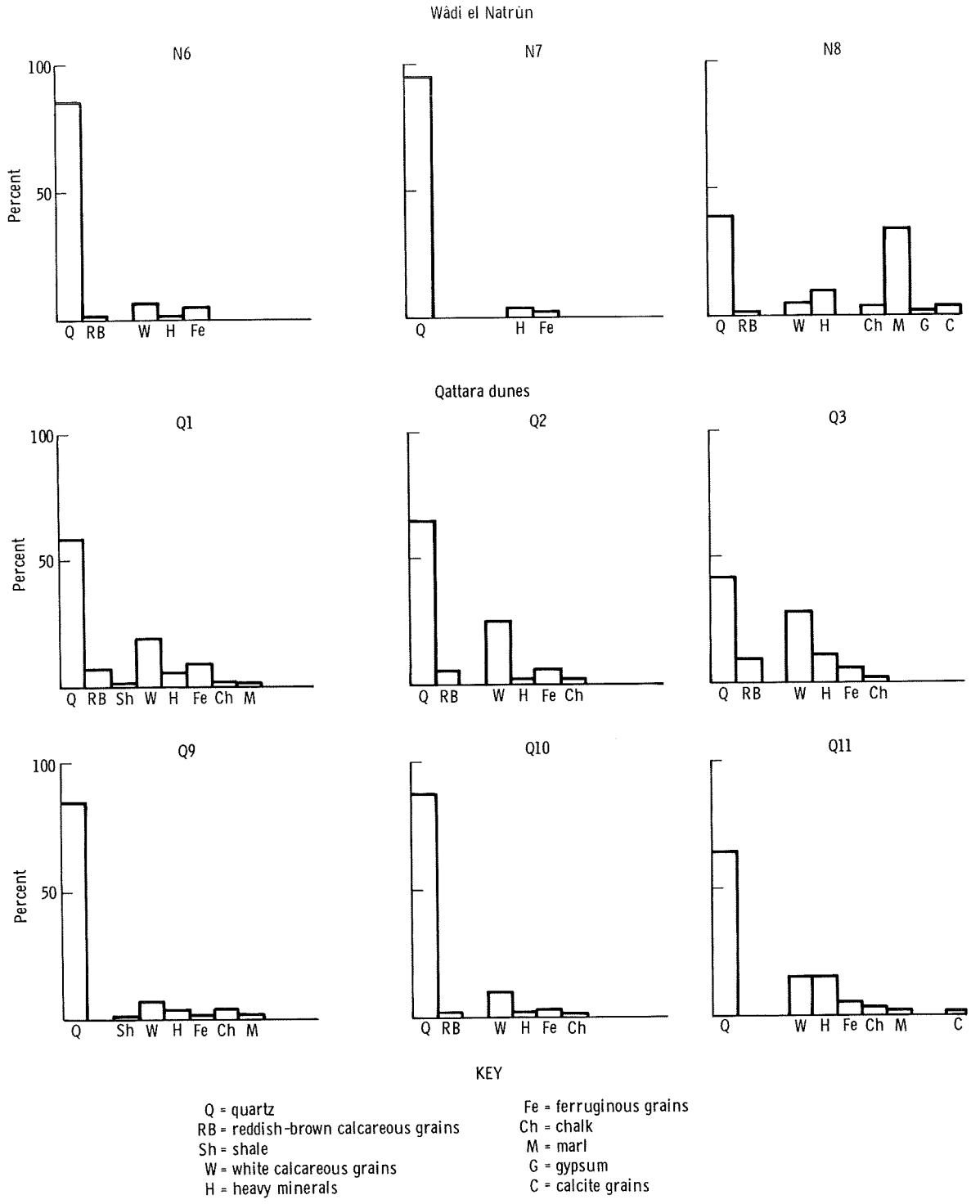
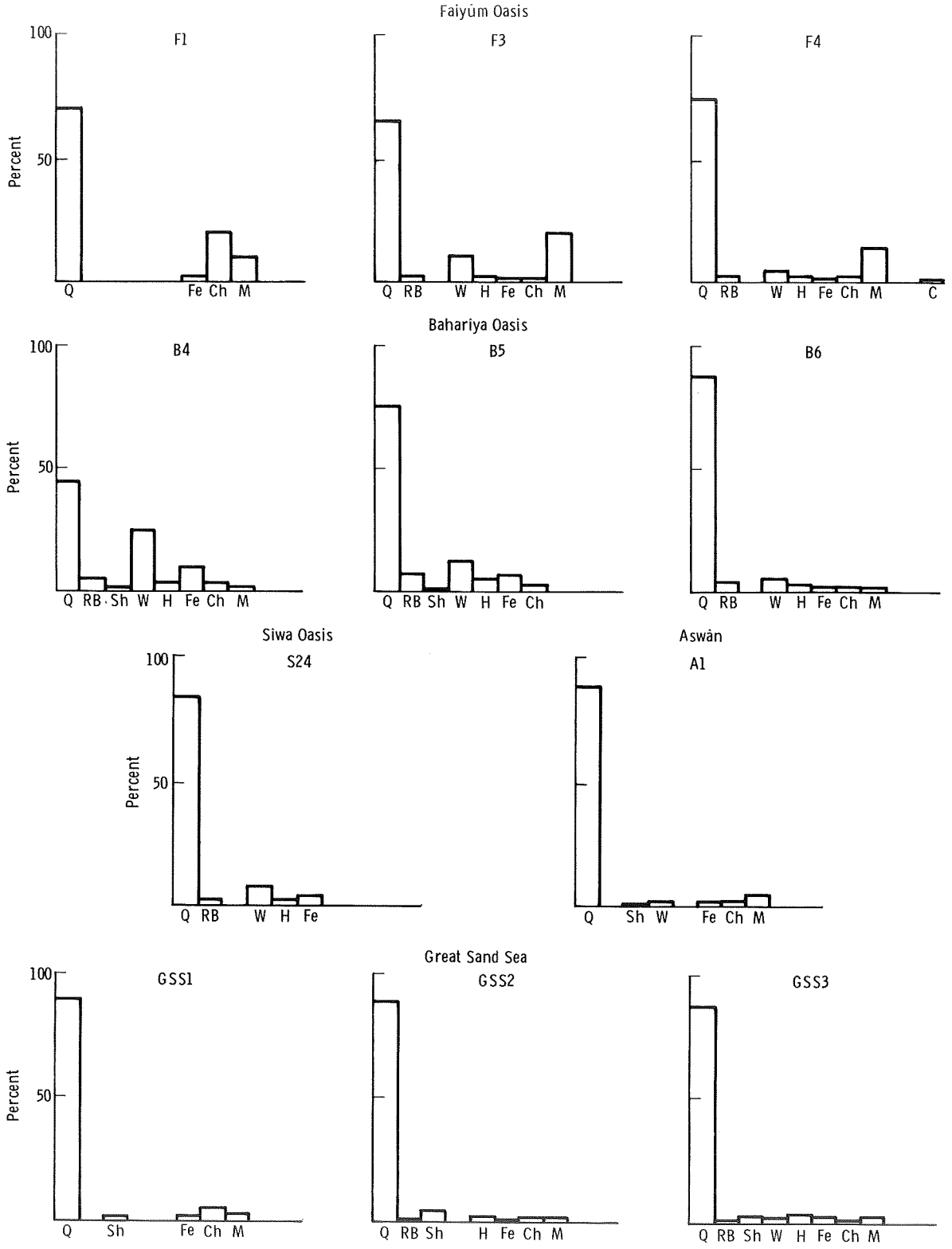
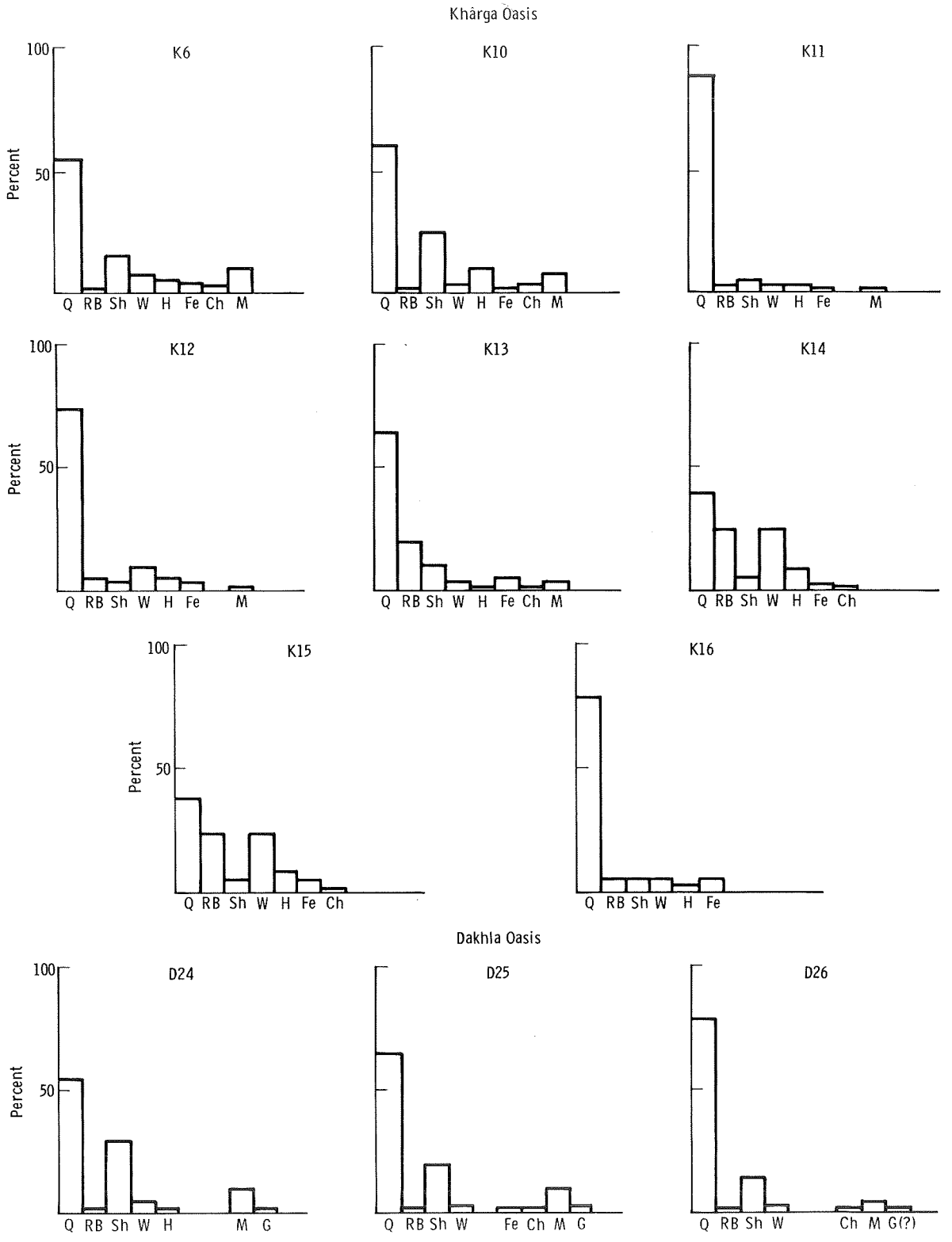


FIGURE 11.—Lithologic frequency histograms indicating visual estimates of individual components in the bulk sand samples. (Continued on following pages.)


Faiyum Oasis
F1
F3
F4
Bahariya Oasis
B4
B5
B6
Siwa Oasis
S24
Aswan
A1
Great Sand Sea
GSS1
GSS2
GSS3
Percent
100
50
Q
RB
Sh
W
H
Fe
Ch
M
C


Khârga Oasis
K6
K10
K11
K12
K13
K14
K15
K16
Dakhla Oasis
D24
D25
D26
Percent
100
50
Q RB Sh W H Fe Ch M
Q RB Sh W H Fe M
Q RB Sh W H Fe Ch
Q RB Sh W H Fe
Q RB Sh W H M G
Q RB Sh W Fe Ch M G
Q RB Sh W Ch M G(?)

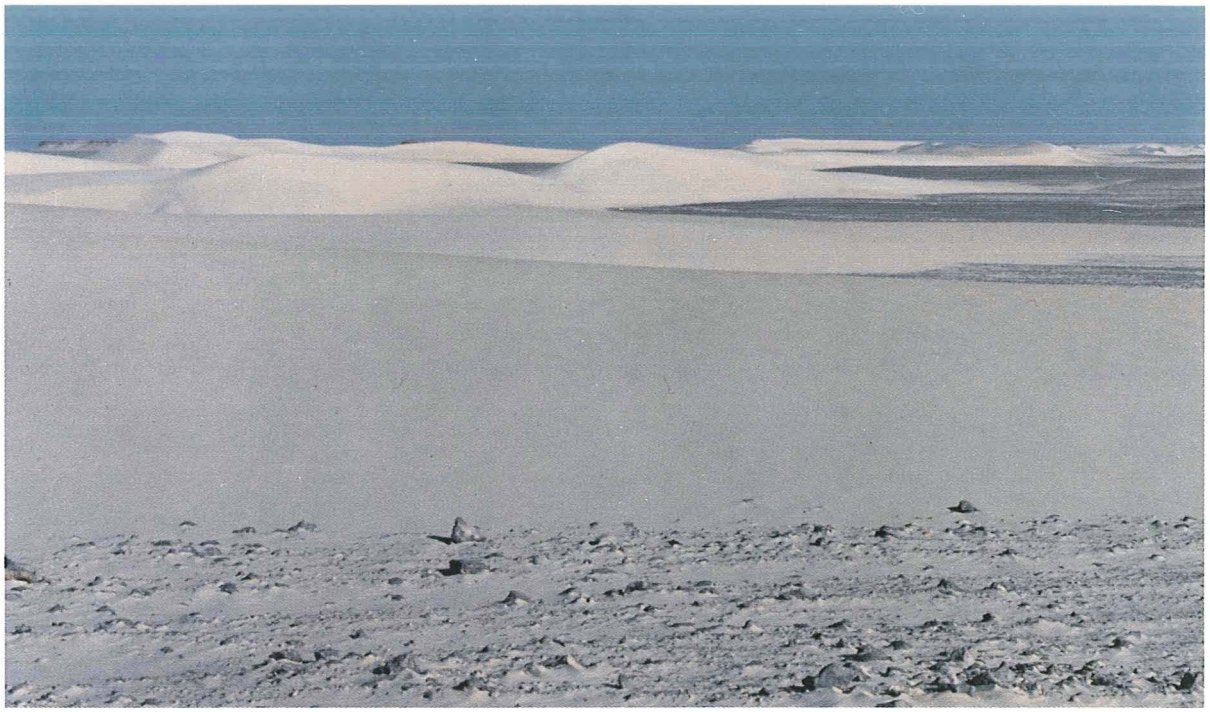


FIGURE 12.—View looking north from the southern tip of the longitudinal dunes photographed by the ASTP astronauts (fig. 3). The foreground of the photograph is occupied by a sand dome; dunes behind this dome are crescentic or complex barchan forms. The dark areas are covered by desert-varnished limestone and chert pebbles.

reddish-brown and green calcareous shale, which could possibly be traced to the variegated shales of El-Hefhuf and Baharîa Sandstone formations in Baharîya Oasis to the north (ref. 3).

Sample Q10 is fairly similar to Q9 in composition, differing mainly in the lack of shale and marl and in the addition of a very minor quantity of reddish-brown calcareous grains. Sample Q10 also contains slightly more white calcareous grains and one or two ferruginous basaltic grains, possibly derived from the dolerite intrusions of Baharîya Oasis (ref. 3).

Sample Q11 differs from both samples Q9 and Q10 by containing higher percentages of white calcareous grains and heavy minerals (mostly glauconite), a lower percentage of quartz, and approximately twice as many ferruginous grains (nodules, limonitic grains, and ferruginous sandstone). This sample also does not contain any reddish-brown calcareous grains or shale, but does include a few calcite grains.

The percentage of white calcareous grains increases from a low value in sample Q9 to a high value in sample Q11.

Faiyûm Oasis.—Sand accumulations abound south of the Faiyûm Oasis. There are two different types of deposits: sand sheets with gentle swells and longitudinal dunes at the beginning of the Wâdi el Ruwayân belt. Sample F1 was taken from a sand sheet that is grayish-yellow (21A on the color wheel (i.e., see section entitled "Comparison of Astronaut Visual Color Observations With ASTP Photographs"), or Munsell 10YR 7/4 (ref. 6)). The color observed in the field differs from that of the sample (see table I) because the field observation did not include deeper layers of sand.

Two other samples were collected from the sand of the northern part of the Wâdi el Ruwayân dunes. These dunes are enclosed by scarps made primarily of light-colored limestone with marly and chalky intercalations. Sample F3 was taken

from a dune crest and sample F4 from the slope of the same longitudinal dune. As expected from the rapidly shifting leeward and windward sides of a longitudinal dune, both crest and slope have approximately the same mean grain size and cannot be distinguished on the basis of textural characteristics. They also have almost identical compositions, as illustrated by samples F3 and F4, where the only major difference is the appearance of calcite grains in sample F4 (fig. 11). Both samples contain fairly high percentages of marl, presumably derived from the scarps enclosing the dunes.

Sample F1 also contains a high percentage of locally derived chalk as well as marl. Unlike samples F3 and F4, however, it does not contain any white or reddish-brown calcareous grains or heavy minerals. Basalt grains do appear in sample F1, however; they are probably derived from basalt dikes north of Faiyûm (ref. 3).

Central Region

Baharîya Oasis.—Numerous dunes occur within the Baharîya Depression. Because of human activity, many of the dunes have lost their original forms and have become either complex or subdued in shape. One sample (B4) was collected 8 km north of the village of El Bawîti and additional samples were taken 34 km (B5) and 37 km (B6) north of the village. Dune sand from which samples B5 and B6 were obtained appeared similar in both localities, although both sands were lighter in color than the sand from which sample B4 was taken. Based on the mechanical analyses, there is no difference in size characteristics among all three samples. Visual estimations of the bulk sample colors, however, do not support the field observations; sample B4 is lighter in color than either B5 or B6.

In the analysis, these three samples were found to vary considerably from each other (fig. 11). Sample B4 contains the lowest percentage of quartz and the highest percentages of ferruginous grains (nodules and ferruginous sandstone), white calcareous grains, and chalk. This sample also includes smaller amounts of heavy minerals (glauconite and hornblende(?)), shale, marl, and reddish-brown calcareous grains. The iron ore of Baharîya is very apparent in this sample as the probable source of the large percentage of ferruginous grains.

Sample B5 differs from sample B4 by containing more quartz, fewer white calcareous grains, and slightly fewer ferruginous grains and chalk. It does not include any marl. However, the two samples do contain approximately the same amount of grains tentatively identified as hornblende.

Sample B6 includes in its composition the highest percentage of quartz of the three samples and the lowest percentages of white calcareous grains, ferruginous grains, and heavy minerals. It also contains a very small amount of hornblende(?) and marl.

Khârga Oasis.—The Khârga Depression is elongate in a north-south direction and measures approximately 180 km in length. The habitable areas in the depression lie along a major fault (ref. 3), which is believed to have aided in bringing underground water closer to the surface.

The large longitudinal dunes that cross the limestone plateau north of Khârga divide into smaller dunes as they descend the northern scarp of the depression. These smaller dunes are usually barchans, although some longitudinal forms develop farther to the south.

At the road marker 218 km from Asyût, a large abandoned building is responsible for sand accumulation. Low sand mounds were found on both the windward and leeward sides of the building and within some of the roofless rooms. One sample (K6) was taken from the leeward side of a dune on the north (windward) side of the building. Farther north of Khârga, two samples (K10 and K11) were collected from an enormous compound barchan that is approaching a star-dune shape. Both samples of this barchan are almost identical in size characteristics and are consistent with the rapidly changing shape of the dune.

Just west of Khârga, samples were collected from a field of barchans that are progressively moving southward. One sand sample (K12) was taken 1.3 km west of Khârga near the base of a dune. A group of four sand samples (K13 to K16, fig. 13) was obtained at the last barchan blocking the road 21 km west of Khârga. Sample K13 was taken on the leeward side at the base of the barchan arm, K14 on top of the arm, K15 from the

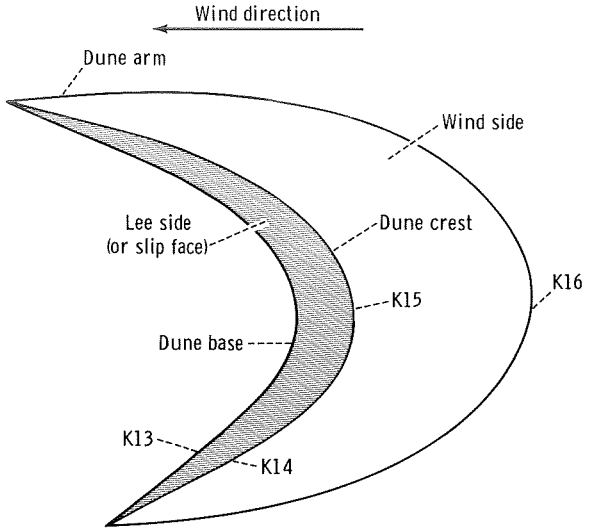


FIGURE 13.—Schematic illustration of the method used in sampling barchan dunes at Khârga and Dakhla Oases. Sample numbers are discussed in the text.

crest of the dune, and K16 from the base of the windward slope. Laboratory analyses indicate that the color of the two samples from the crest is slightly lighter than the color of those from the base of the windward and leeward slopes (10YR 6/4 versus 10YR 6/6; ref. 6). The sand size characteristics of this barchan, however, are consistent with those from Natrûn and Qattara in that the windward side is coarser grained.

All the samples from Khârga Oasis contain the same heavy minerals (glauconite, phosphates, and hornblende(?)) in only slightly varying amounts. Sample K6 is composed of quartz, fairly high percentages of shale and marl, and lesser amounts of white and reddish-brown calcareous grains, chalk, ferruginous grains (nodules and limonitic grains), heavy minerals, and a few fossils.

Samples K10 and K11 are very dissimilar despite the fact that they were collected from the same compound barchan. Sample K10 contains a lower percentage of quartz than does sample K11 and higher percentages of shale, heavy minerals, ferruginous grains (limonitic grains and ferruginous sandstone), and marl. Unlike sample K11, sample K10 includes a small percentage of chalk in its composition.

Of the four samples taken from the same barchan dune (K13 to K16), the samples from the base of the dune (K13 and K16) differ significantly from each other and also from those taken at the crest (K14 and K15). Sample K13 (from the leeward side of the dune) contains a higher percentage of quartz than samples K14 and K15 but a lower percentage than K16. It also includes the highest amount of shale, the lowest percentage of heavy minerals, and the only marl of the four samples. Samples K14 and K15 have virtually the same composition. Of these four samples, K14 and K15 contain the highest percentages of white and reddish-brown calcareous grains in equal amounts, and heavy minerals. They also include the lowest percentages of quartz. Sample K16 contains the lowest percentage of reddish-brown calcareous grains and does not contain any chalk.

Individual grains of the sand deposits in the Khârga Oasis can possibly be traced to formations that outcrop within the oasis and form the surrounding scarps. For example, the shale of the samples has been specifically identified as predominantly Dakhla Shale and minor Esna Shale by visual comparison with the grains derived from collected rock fragments and through published descriptions. The purple and variegated shales are also represented. Similar techniques were used to discover the source of other grains: the chalk grains are presumably derived from the chalk unit and the source of the phosphate grains would be phosphate beds, both of which outcrop within the oasis (ref. 3). Local outcrops therefore contribute significantly to the lithology of the sand deposits.

Dakhla Oasis.—Three sand samples were taken from a barchan blocking the road that connects Khârga and Dakhla Oases. By comparing its position on aerial photographs to its current position, it was found that this barchan has moved 30 m in 3 years. It is an unusual dune because of its poorly sorted sands (as observed in the field) and its mottled colors. Sample D24 was taken from the base of the dune where there was a predominance of calcareous sands. Sample D25 was collected from the black sand streaks on the surface, and sample D26 was obtained from the reddish-yellow sand representative of most of the dune.

Sample D24, from the base of the barchan, has a smaller mean grain size (2.5ϕ/0.18 mm) than do samples of the surface. It also is slightly gray in color, as is sample D25 (table I).

The microscopic analysis revealed that the three samples are very similar, even though minor differences do exist. All three samples contain relatively high percentages of predominantly gray shale, presumably derived mainly from the Dakhla Shale and to a lesser degree from the variegated shales and from shales in the phosphatic beds (ref. 3). This shale contributes significantly to the grayer colors of samples D24 and D25, as compared to sample D26. Sample D25, in particular, contains a high percentage of coarse shale. Phosphate grains, probably from the phosphate beds that outcrop in the oasis, were found in sample D24. Sample D25 contains the only ferruginous grains (nodules) observed in the three samples.

Great Sand Sea

Sîwa Oasis.—The sample numbered S24 was collected at the base of the reddish, windward side of the Sîwa Oasis dune illustrated in figure 6(c). It is a very clean sample composed of quartz, very minor amounts of white calcareous grains, and a few chert grains.

Great Sand Sea (southwest of Farâfra).—Samples of dune sand on the eastern margin of the Great Sand Sea were collected west of Abu Minqâr, 70 km southwest of Farâfra (fig. 2). Several gently sloping dunes occur in accumulations that resemble those described by Bagnold as "whalebacks." (See section entitled "Color Zoning in the Western Desert of Egypt.") All samples were collected from the first line of longitudinal, sharp-crested dunes that overlie these whaleback dunes.

Three samples are considered in this report: GSS1 was collected from the base of a sinuous dune, GSS2 from an arm of the same dune, and GSS3 from the dune crest. It is significant to note that these samples were taken from the uppermost few centimeters of sand (fig. 14). In this area, the sand grains that form the upper layer are redder than those beneath. The stratification is similar to that of a large dune field east of Farâfra Oasis in that alternating dark- and light-colored layers are present in both localities.



FIGURE 14.—Layering in a 30-cm-deep trench that was dug in dune sand of the Great Sand Sea. The surface ripples (top half of photograph) are made of sand that is redder than some of the layers below the surface. The scale is 15 cm long.

The three samples were found to be composed mostly of equal amounts of quartz. Differences were observed only in the lithology of the minor components. Reddish-brown calcareous grains and heavy minerals were not observed in sample GSS1, but were found in samples GSS2 and GSS3. Sample GSS1 also contains the lowest percentage of shale and the highest percentage of chalk. Sample GSS3 is the only sample including white calcareous grains in its composition.

Aswân

For comparison with the reddish sands of the Great Sand Sea, a sample collected just west of Aswân (fig. 2), near the base of a cliff, was studied. In this locality, the sand is close to its probable source, the Nubian Sandstone (fig. 1). However, the color of the bulk sample is the same as most of the samples from the Western Desert (fig. 15).

The composition of this sample does not vary significantly from that of other samples collected in the Western Desert. It is composed mainly of quartz, with minor amounts of shale, white calcareous grains, ferruginous grains (nodules and ferruginous sandstone), and marl. Several grains of weathered granite(?) were found in this sample and are presumed to be from the basement complex exposed in the nearby cliff.

Ar Rub' al Khālī Dunes

For additional comparison with the sands of the Great Sand Sea, one sample was collected from another typically red sand deposit in the United Arab Emirates. This dune sand occurs at the terminus of the great dunes of Ar Rub' al Khālī (The Empty Quarter) of the Arabian Peninsula. The sample, UAE1, was collected from a relatively low (10-m high) irregular dune mass that was stabilized by natural vegetation south of Abu Dhabi in the United Arab Emirates. The quartz of this sample is very vitreous as compared to the predominantly frosted quartz of the Western Desert of Egypt. The reddish color is due to extensive deposits of iron oxides on the surface of quartz grains.

SUMMARY

Color variations of the Western Desert observed and photographed by the ASTP astronauts can be related to minor compositional variations within the sand deposits. Although the origin of the sand is not well known, the Nubian Sandstone of southern Egypt may have provided a source for much of the sand. As a result of four field trips made to check photointerpretations of ASTP data, it was found that sand colors varied greatly on both local and regional scales. Most samples are composed of fine-sand-size grains, and are well to moderately well sorted; and these preliminary results also suggest a dependence on local sampling environment.

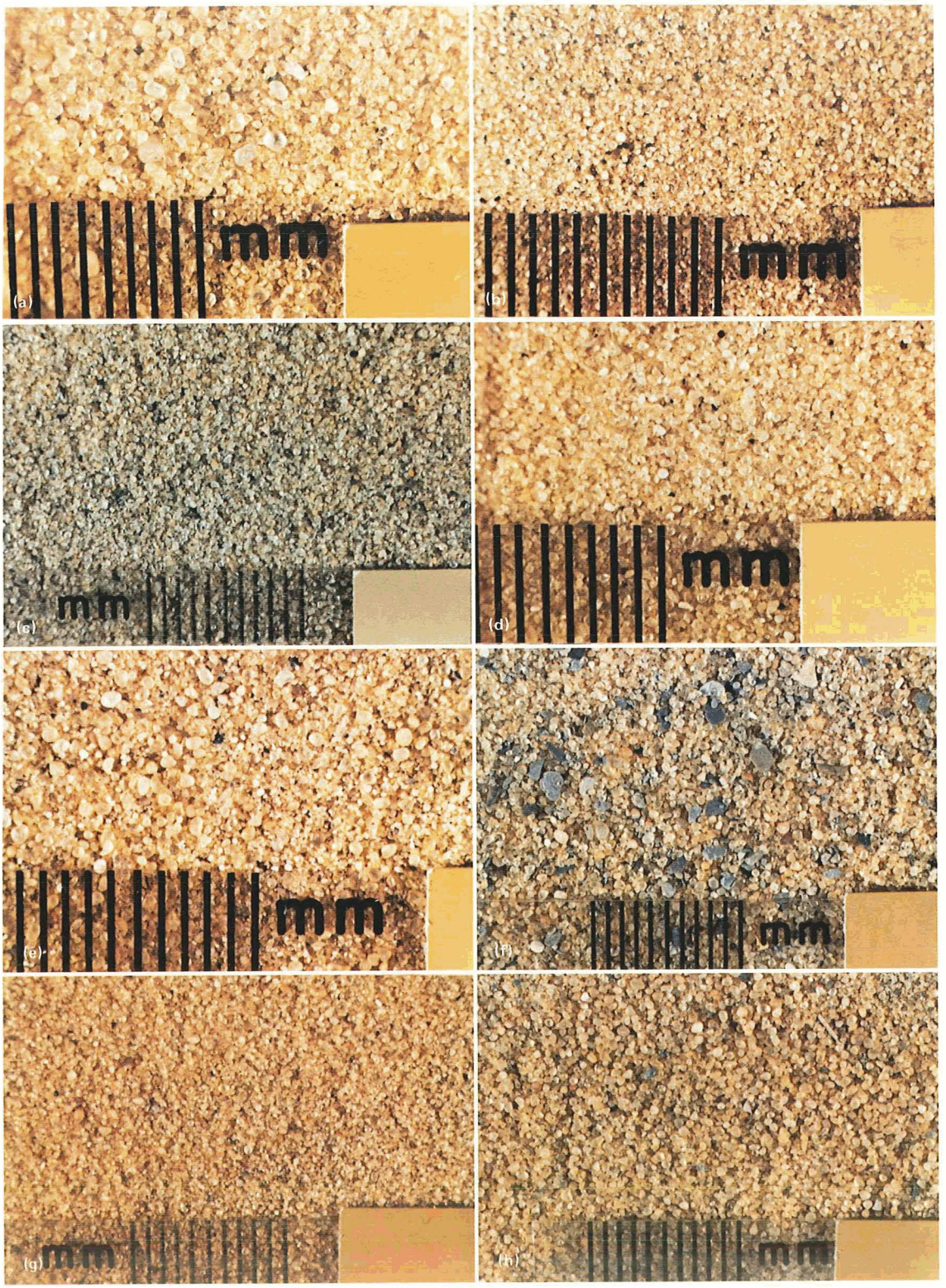
FIGURE 15.—Bulk sand samples representative of sand color variations in the Western Desert. (a) Sample N6 from sand sheet at Wâdi el Natrûn that appears bright pinkish-yellow on ASTP photographs. (b) Qattara sample Q3 from the leeward side of a barchan. (c) Sample F3 from the crest of a longitudinal dune at Faiyûm Oasis. (d) Baharîya sample B6 collected 37 km north of El Bawîti. (e) Khârga sample K13 from the leeward side of a barchan. (f) Dakhla sample D25 showing influence of local shale fragments (Dakhla Shale) on the sample color. (g) Sample GSS3 from a longitudinal dune in the Great Sand Sea. (h) Sample A1 from base of cliff in the Aswân area. →

Compositional variations in both field and laboratory studies indicate that the major color differences result from the influx of local material and variation in the more regional occurrence of light-colored calcareous fragments. The samples collected from the northern and central regions of the Western Desert are slightly lighter in color and less red than the samples from the Great Sand Sea region. This difference is due primarily to the large percentages of light-colored calcareous grains found in the northern and central samples. Locally, the ferruginous nodules and sandstones at Baharîya and the predominance of shale in Dakhla samples indicate the effect of local material.

Although these results are preliminary, three observations can be made on the basis of this analysis.

1. There is a discrepancy between the color of sand deposits noted by field investigation and that estimated from the bulk samples. This is primarily due to the sampling of sand layers deeper than the thin veneer that is responsible for the color as observed from Earth orbit. More detailed field investigations are currently being planned that will help to account for this source of color discrepancy.

2. The colors of bulk sand samples classified according to the Munsell color chart vary significantly, even within the same color designation. A


(a)
(b)
(c)
(d)
(e)
(f)
(g)
(h)

more detailed sand color chart for the Western Desert of Egypt is being investigated to provide more accurate ground truth for orbital data.

3. The results presented here suggest that both dune reddening with time and the addition of local material are important to color variations of sand deposits. More detailed field investigations must be made to determine the relative effect of each of these processes before remote observations can be extended to more widespread areas. This need is particularly important in anticipation of the detailed color photographs that will be available from the large format camera to be flown on the Space Shuttle in the next decade.

ACKNOWLEDGMENTS

Hassan A. El-Etr, Geology Department, Ain Shams University, helped to plan and conduct all field excursions. The Geological Survey of Egypt provided both technical expertise and vehicles for these investigations. The Egyptian Air Force generously provided the aircraft for observation and transport between locations in the Western Desert.

For mechanical analysis, the laboratories of the Sedimentological Laboratory of the Museum of Natural History, Smithsonian Institution, were used; the authors thank Diane Cobb for helping with these studies; the authors are also indebted to David George of the Geophysical Laboratory, Carnegie Institution of Washington, for his help in obtaining the SEM photographs and analyses.

This work was done under the Smithsonian Institution/Ain Shams University joint research project and under NASA contract NAS9-13831.

REFERENCES

1. El-Baz, Farouk: Astronaut Observations From the Apollo-Soyuz Mission. Vol. I of Smithsonian Studies in Air and Space, Smithsonian Institution Press (Washington, D.C.), 1977.

2. El-Baz, Farouk: The Meaning of Desert Color in Earth Orbital Photographs. Photogramm. Eng. & Remote Sens., vol. 44, no. 1, 1978, pp. 69-75.

3. Said, Rushdi: The Geology of Egypt. Elsevier Pub. Co. (Amsterdam), 1962.

4. El-Baz, Farouk: Expanding Desert Creates Grim Beauty But Also Threatens Crucial Cropland. Smithsonian Magazine, vol. 8, no. 3, 1977, pp. 34-41.

5. Folk, R. L.: Petrology of Sedimentary Rocks. Hemphill Pub. Co. (Austin, Tex.), 1974.

6. Munsell Book of Color. Munsell Color Company, Inc. (Baltimore, Md.), 1963.

Temporal Changes as Depicted on Orbital Photographs of Arid Regions in North Africa

Marie H. Slezak[a] *and Farouk El-Baz*[a†]

ABSTRACT

Processes typical of arid environments can be monitored from space by comparing orbital photographs taken over a period of years. Using the zoom transfer scope, it is possible to superimpose two photographs and detect changes occurring with time. Oblique photographs can be used, but best results are obtained with vertical or near-vertical photographs.

Changes observed by comparing the 1975 Apollo-Soyuz photographs with data from previous missions include (1) an increase in vegetation west of the Nile Delta of approximately 1108 km^2 in 10 years; (2) an average shift of 2.5 km over a 6-year period in the sand patterns of the Oweinat Mountain region at the borders between Egypt, Libya, and Sudan; and (3) a reduction in the water level of Lake Chad and dune encroachment upon the lake over a period of 9 years.

As a result of this investigation, it is concluded that studies of temporal changes in arid and other regions are facilitated when orbital photographs are vertical and are taken from similar altitudes.

INTRODUCTION

Photographs taken from space enable studies of temporal changes in dynamic processes by documenting these changes on a scale that is not possible in the field. Processes characteristic of arid environments are examined in this paper by comparing photographs taken during the Gemini, Apollo, Skylab, and Apollo-Soyuz missions.

The three processes considered in this paper include the following: (1) land reclamation, specifically on the western margin of the Nile River Delta in northern Egypt; (2) shifts in eolian sand patterns, as seen in the Oweinat Mountain region at the borders between Egypt, Libya, and Sudan; and (3) changes in lake boundaries, as in the example of Lake Chad in north-central Africa (fig. 1).

The comparison of photographs was facilitated by the use of the model ZT-4 zoom transfer scope (Bausch and Lomb). This instrument enables the projection of one photograph onto another, despite differences in obliquity and scale, by optically rotating, stretching, and enlarging the photographs. Only when they are vertical or near-vertical can entire photographs be overlaid. When using two photographs of varying scale and obliquity, it is necessary to continually adjust the photographs from area to area. By superimposing permanent features, it is possible to compare the area surrounding each feature by transposing details from one photograph onto another. The best technique when using oblique photographs is to fix three points, which form a triangle. This procedure will ensure that the transposition is correct in more than one direction. The zoom transfer scope can also be used to make accurate measurements by translating photographic data directly onto maps.

[a]National Air and Space Museum, Smithsonian Institution.

[†]Principal Investigator.

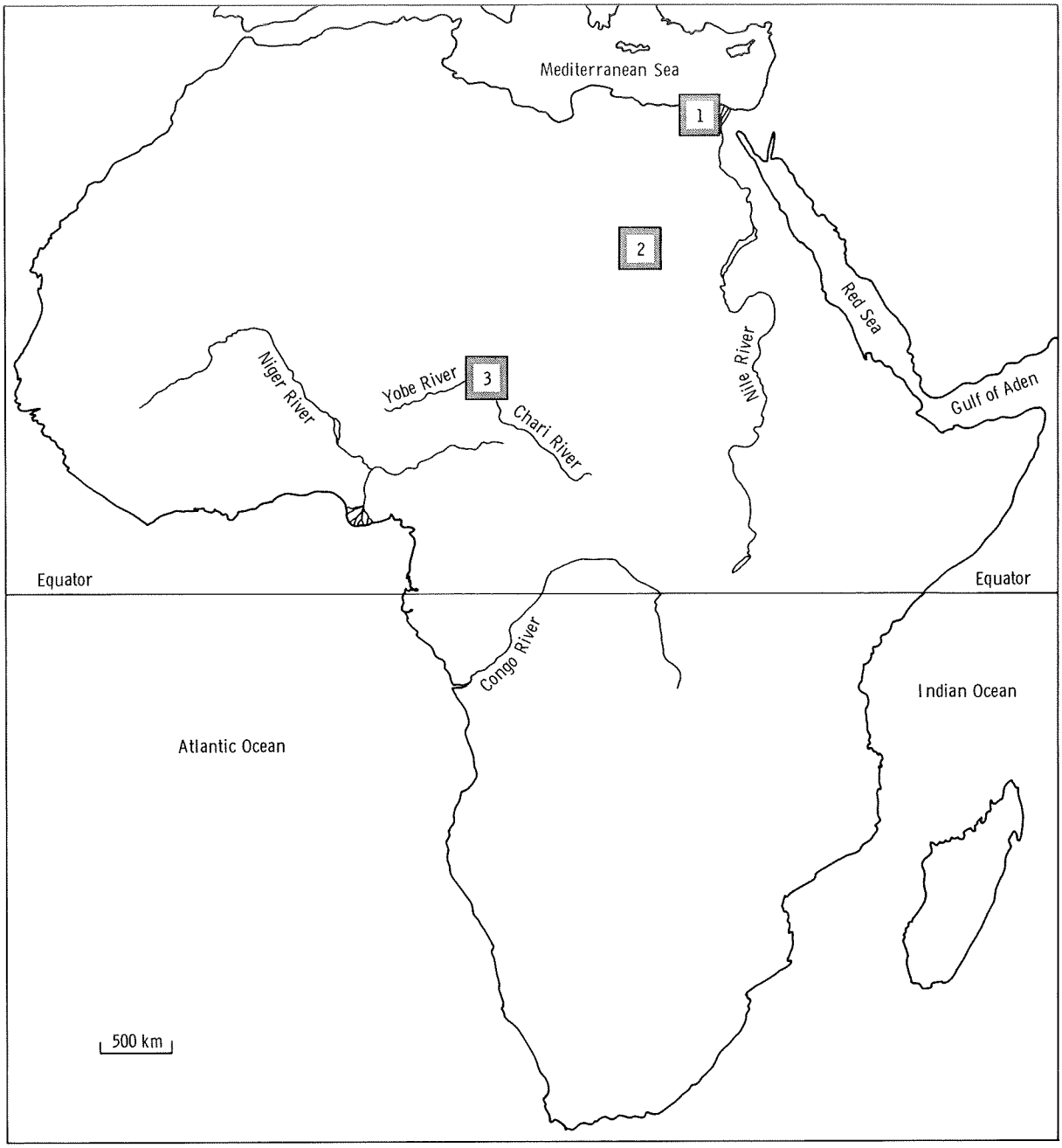


FIGURE 1.—Location of the three areas discussed in this paper: (1) Nile Delta, (2) Oweinat Mountain region, and (3) Lake Chad.

NILE DELTA

The total geographic area of Egypt is 999 735 km^2. Of this, only 3.5 to 4 percent of the land, or approximately 35 000 to 40 000 km^2, is under cultivation; the remainder is barren desert. Not all the cultivated land is highly productive, however. In 1968, 20 percent of the cultivated land was degraded by the salinity and alkalinity of the soil and by poor drainage (ref. 1).

The Nile Delta contains 60 percent of the cultivated land of the Egyptian Nile, or approximately 22 000 km^2. The existence of topographically depressed areas within and around the delta, in conjunction with irrigation, silty soil, and relatively small fluctuations in annual temperatures, makes this area suitable for cultivation. In fact, two or even three crops per year can be raised (ref. 2). With a numerically large and rapidly increasing population, one of Egypt's major concerns is food production. Thus, the amount of arable land is of great importance to that country, as it is to other countries with large populations.

In 1964, estimates were made that the scheduled 1970 completion of the Aswân High Dam on the Nile, 860 km south of Cairo, would increase the amount of land suitable for cultivation by approximately 5260 km^2. The dam would also permit the conversion of approximately 2833 km^2 of land from basin to perennial irrigation (ref. 1). The increase in cultivated land was planned to occur mainly in the sandy area west of the delta where more irrigation is necessary than within the delta or along the flood plain of the Nile itself (ref. 2).

The results of this program can easily be seen by comparing two photographs that were taken during the same season: a Gemini V photograph taken in 1965 (S65-45736), whose footprint is shown in figure 2, and an Apollo-Soyuz Test Project (ASTP) photograph taken in 1975 (AST-16-1257). The western margin of the Nile Delta, targeted for cultivation in 1964, was compared in these two photographs.

To overlay the two photographs, features such as the Nile River and roads were used. The outline of the westernmost limit of the vegetation was traced from the ASTP photograph onto the Gemini photograph (fig. 3). A significant amount of desert plain has been reclaimed and cultivated to varying degrees during the 10 years separating the two photographs. There are three distinct areas of vegetation increase: (1) the southernmost area, which is a thin zone parallel to the previously cultivated land, with approximately 186 km^2 of increased vegetation; (2) the central area consisting of two broad zones, with approximately 732 km^2 of increased vegetation; and (3) the northernmost area characterized by linear belts of vegetation that parallel the coast of the Mediterranean Sea, with an increase in vegetation of approximately 190 km^2.

The total increase in vegetation west of the Nile Delta is 1108 km^2. This represents approximately 111 km^2 per year of land reclaimed from the desert. It does not take into account vegetation, such as that marked with an "X" on figure 3, which appears sparse in the 1965 photograph and has grown more dense in the 1975 photograph.

This example shows that orbital photographs can be used to monitor and document the amount of land being denuded, being cultivated for the first time, or being rendered more fertile; and they can also be used to monitor the processes of desertification as well as land reclamation.

OWEINAT MOUNTAIN REGION

The Oweinat Mountain region is located at the boundaries of Egypt, Libya, and Sudan (fig. 4). This region is dominated by Precambrian or slightly younger mountains formed by ring-dike-type intrusions composed mainly of granites, syenites, and monzonites (refs. 3 and 4). Gebel Oweinat, 1934 m high, and Gebel Arkenu, 1435 m high, form the highest topographical barriers to the wind in this region, followed by Gebel Babein, 1104 m high, and Gebel el Bahri (fig. 4).

Between these mountains are streaks of wind-deposited active sand that is lighter in color than the rest of the region. Darker areas are presumed to be windswept zones and/or higher ground. South of Gebel Oweinat and Gebel Arkenu, where the deposition of the sand is not constrained by the mountains, the sand streaks become subdivided into individual seif dunes separated by areas of desert pavement.

This region was analyzed in an effort to determine the temporal changes that may have occurred between the time that an Apollo 9 photograph was taken in 1969 and the time ASTP photographs were taken in 1975. Special attention was given to sand streaks between the mountains to determine whether they had shifted laterally and whether the seif dunes south of the mountains had migrated in the direction of the prevail-

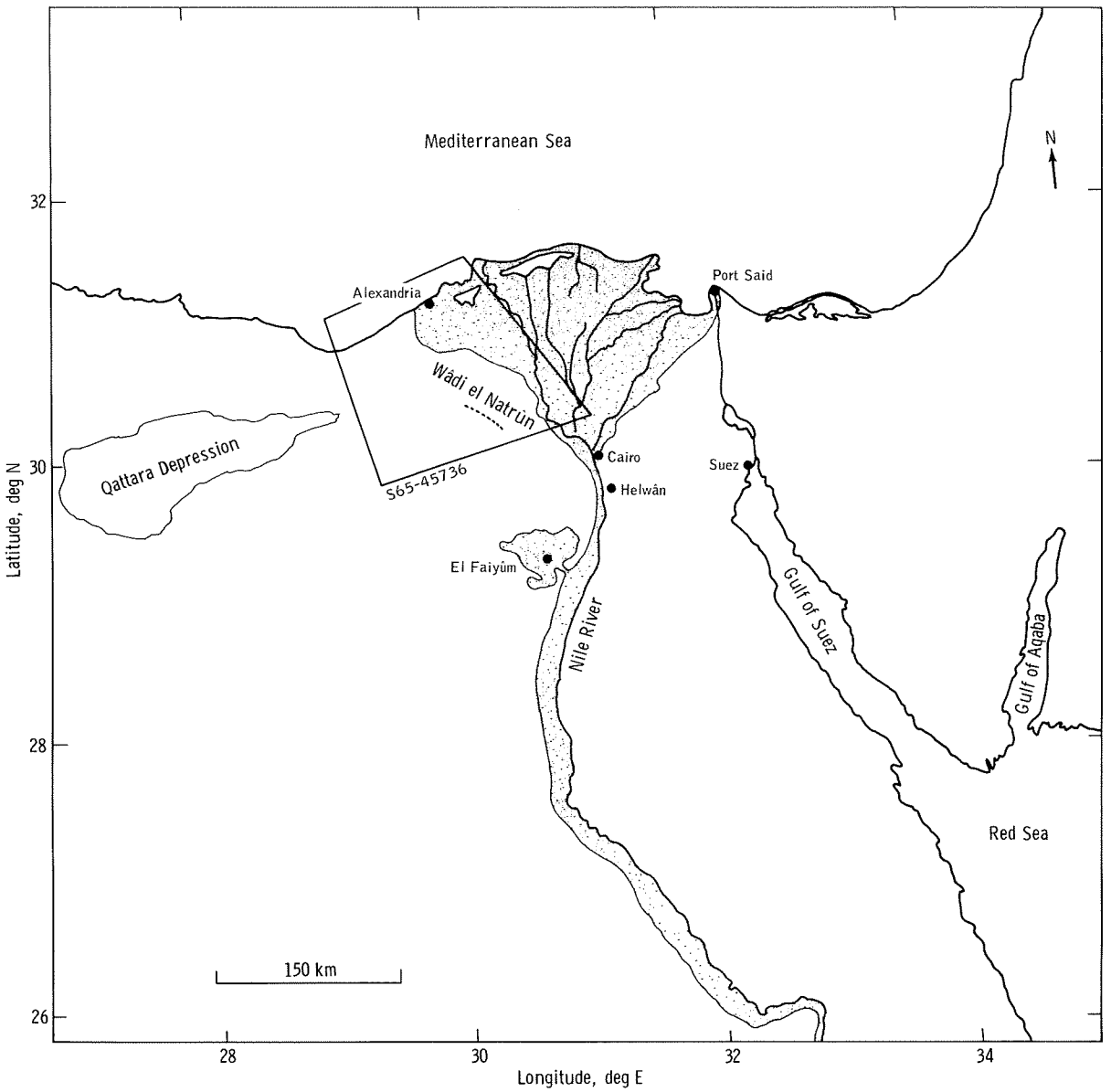


FIGURE 2.—Ground coverage of Gemini V photograph S65-45736 (fig. 3), west of the Nile Delta.

ing wind. In each instance, distances were measured.

The analysis consisted of transposing ASTP photographs AST-2-126, AST-2-127, AST-2-129, and AST-2-130 onto different sections of Apollo 9 photograph AS9-23-3533 and tracing the outlines of the 1975 sand streaks onto the 1969 photograph (fig. 4). The mountains were used as reference features in superimposing the photographs.

The orientation of the sand streaks is controlled by the prevailing north-northeasterly winds and by the deflecting influences of the mountains. North of Gebel Arkenu and Gebel Oweinat, the sand streaks are oriented north-

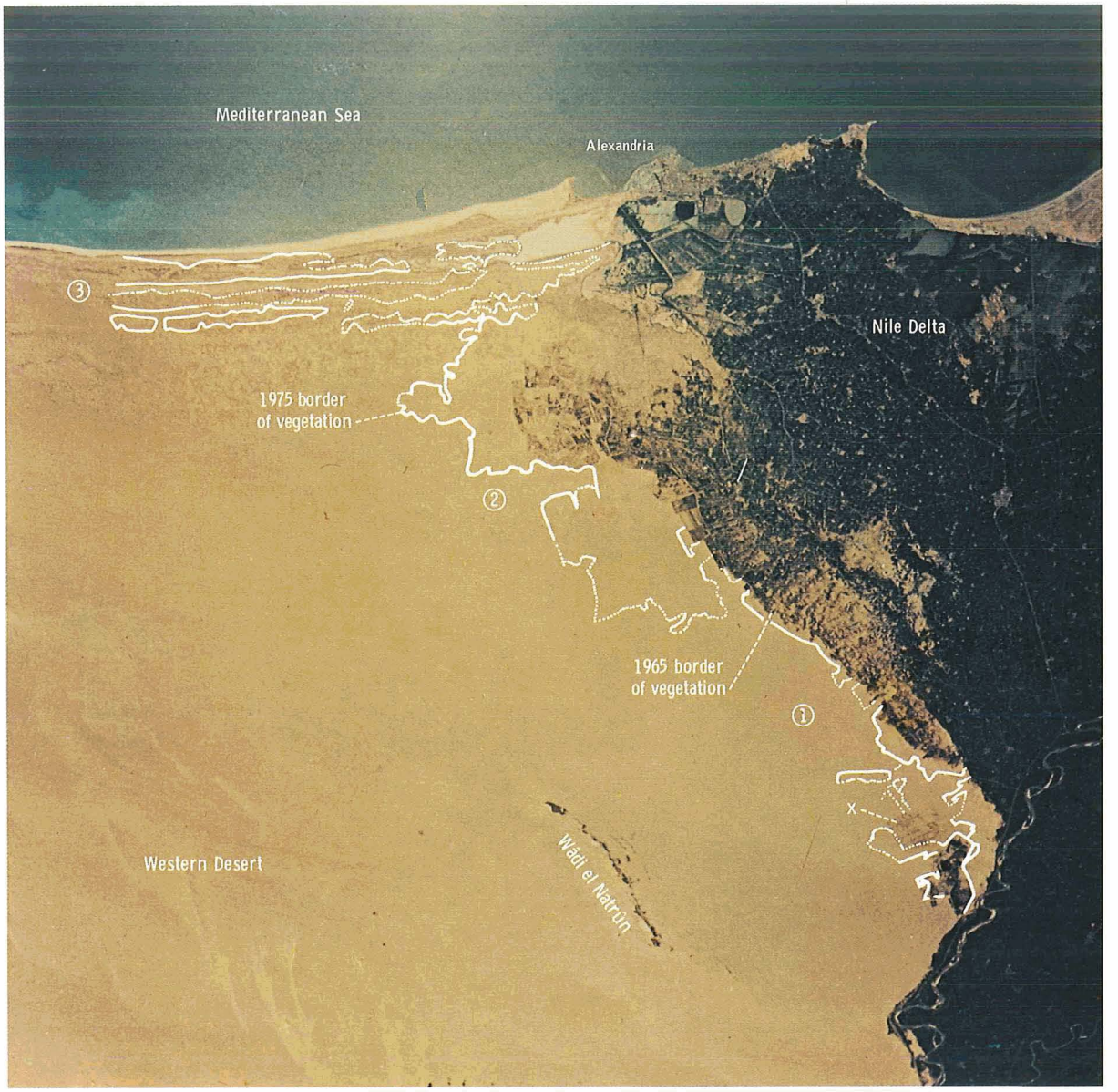


FIGURE 3.—Increase in vegetation at the western edge of the Nile Delta in 10 years. Drawn on Gemini photograph S65-45736 from ASTP photograph AST-16-1257. Dotted lines indicate sparse vegetation; solid lines represent dense vegetation. At area "X," vegetation appears denser in the 1975 photograph.

northeast to south-southwest, rotating to an east-northeast to west-southwest trend exhibited by the seif dunes south of the mountains. This is due, in part, to the general clockwise rotation of the prevailing wind direction and to the channeling of the wind between the mountains as illustrated in figure 4. Sand is deposited on the lowest ground between the mountains and on their windward slopes. Active sand is not found on the lee sides of the mountains; the leeward slopes are probably free of sand because of the lack of deposition.

In places such as the region directly west of Gebel Arkenu, the sand streaks consist of short, discontinuous longitudinal dunes, presumably

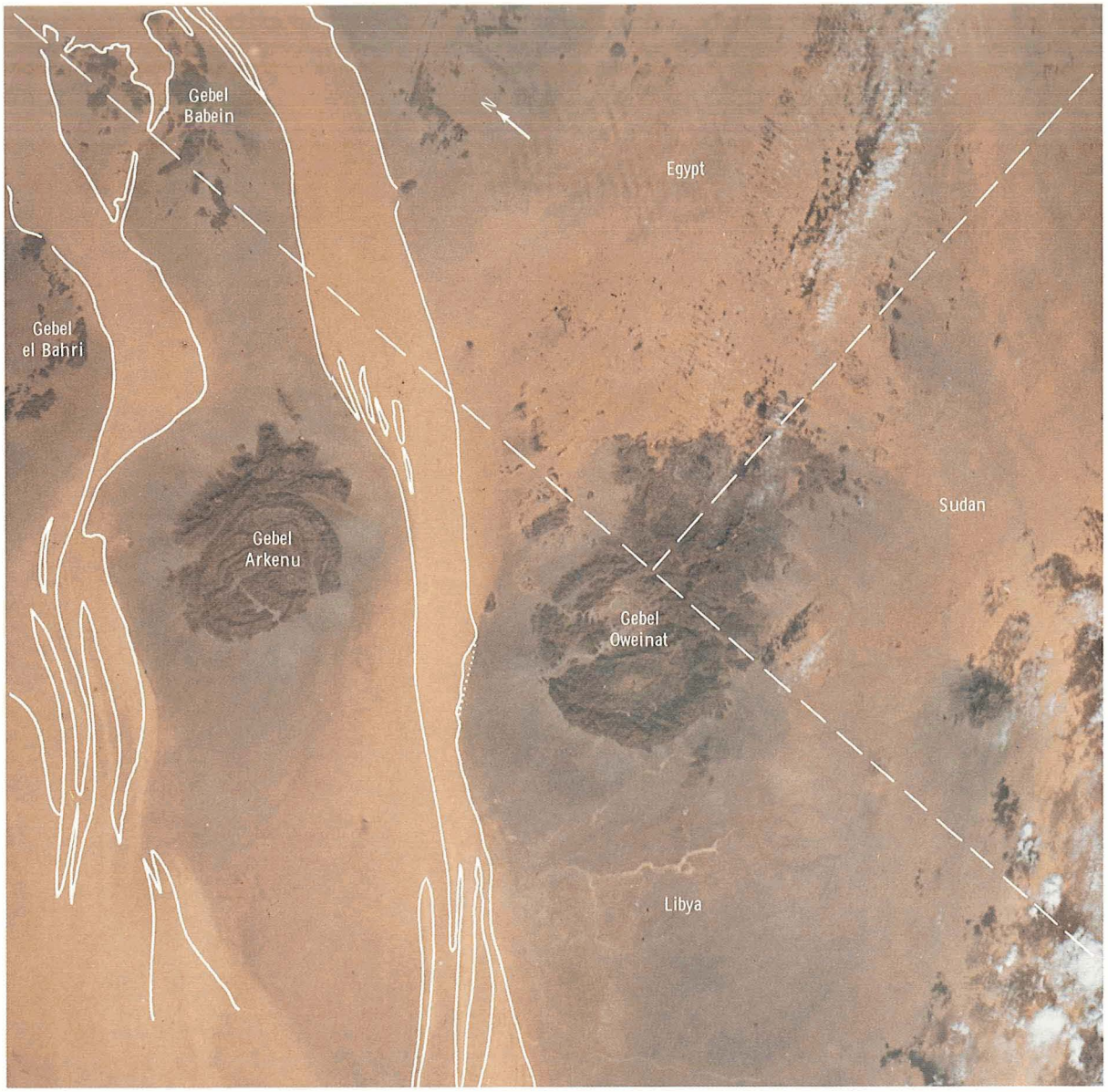


FIGURE 4.—Sand-streak boundaries transposed from 1975 ASTP photographs onto 1966 Apollo 9 photograph AS9-23-3533.

derived from fragmented seif dunes. This pattern of disrupted seif dunes also occurs to the southwest of Gebel Oweinat and appears to be characteristic of areas in which seif dunes meet a major obstacle (ref. 5).

From 1969 to 1975, it appears that consolidation of these longitudinal dunes occurred, as shown by the line drawn at "A" on figure 5, in which changes documented by the photographs are summarized. This line was easily seen on the ASTP photographs but could not be drawn on the Apollo 9 photograph. Dune consolidation is presumed to have occurred, thereby delineating the boundary between desert pavement and sand more clearly on the ASTP photographs than on the Apollo 9 photograph.

For the most part, the sand streaks of the Oweinat Mountain region have not been dis-

placed. However, there are sites at which differences can be seen. These are marked as "B," "C," "D," "E," and "F" on figure 5. At site B, the southern end of the seif dune has migrated 3 km to the northwest. The southern end of the dune at site C has also migrated to the northwest, but by 4 km, and at site D, the northern end of the dune has shifted to the northwest by 2 km. Site E presents a different situation in which the southwestern boundary of a sand streak has shifted 1 km to the north-northwest. At site F, the northern end of the seif dune has migrated 2.5 km to the southwest. Because the prevailing wind direction is to the southwest, the northwestern dune shifts can possibly be attributed to wind deflection by the mountains.

The average shifting distance of dunes in the Oweinat Mountain region is 2.5 km in 6 years, which is more than 400 m per year. This rate is higher than that estimated for longitudinal dunes in the northern part of the Western Desert of Egypt. In the latter area, comparison of ASTP and aerial photographs taken 22 years apart showed a southerly shift of 5.7 km, which is 260 m per year (ref. 6). However, it must be stated that the photographs covering the Oweinat Mountain region were particularly difficult to work with. When alining different features on the zoom transfer scope, equivalent results were not always obtained. The temporal change measurements discussed earlier represent the best results possible, but these should be viewed in light of the difficulty in transposing the photographs.

As illustrated by the example of the Oweinat Mountain region, orbital photographs can be used to observe temporal changes in patterns of sand distribution. Distances covered by these changes can be measured with reasonable accuracy, provided that the resolution of the photographs allows such measurements to be made.

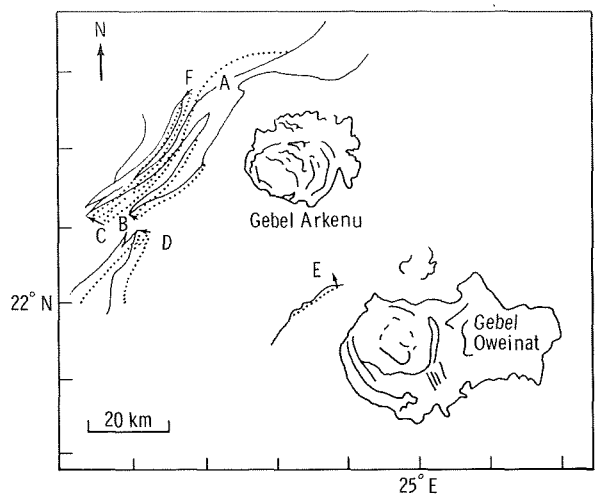


FIGURE 5.—Summary of sand boundary shifts over a 6-year period in the Oweinat Mountain region. Solid line outlines 1975 sand boundaries, dotted line indicates 1969 boundaries. Arrows at sites B, C, D, E, and F show the direction of sand movement.

LAKE CHAD

Lake Chad is situated at the junction of the borders of Niger, Nigeria, Cameroon, and Chad in north-central Africa (fig. 6). It is elongated in a northwest-southeast direction and consists of two basins partly separated by a barrier of sand dunes.

Lake Chad is extremely shallow, with the deepest water, 4.5 m, occurring in the northern basin (ref. 7). Sand dunes are irregularly distributed throughout approximately 85 percent of this basin. The dunes are elongate in shape and trend in a northerly and north-northwesterly direction. They have been measured to be less than 3 km in length (ref. 7). Sand dunes also form the eastern boundary of the southern basin.

Two rivers flow into Lake Chad. The Chari River supplies approximately 95 percent of the total fluvial discharge into the lake of 800 km^3 per year. The remaining 5 percent is supplied by the Yobe River (ref. 8). Rainfall adds approximately 80 km^3 to the lake annually (ref. 7).

Because no river outlet exists for the lake, water loss is due primarily to evaporation and secondarily to infiltration. The amount of water entering and leaving the system is not in equilibrium, resulting in fluctuations of water depth and lake boundaries. For example, from 1963 to 1971 the average level of the lake dropped by 2 m. Over a 3-year period of observation, the average volume decreased by 13 percent (ref. 8). Other factors contributing to the decrease in size of Lake Chad include the influx of sediment from the Yobe and Chari Rivers and of sand from the Sahara Desert (ref. 9).

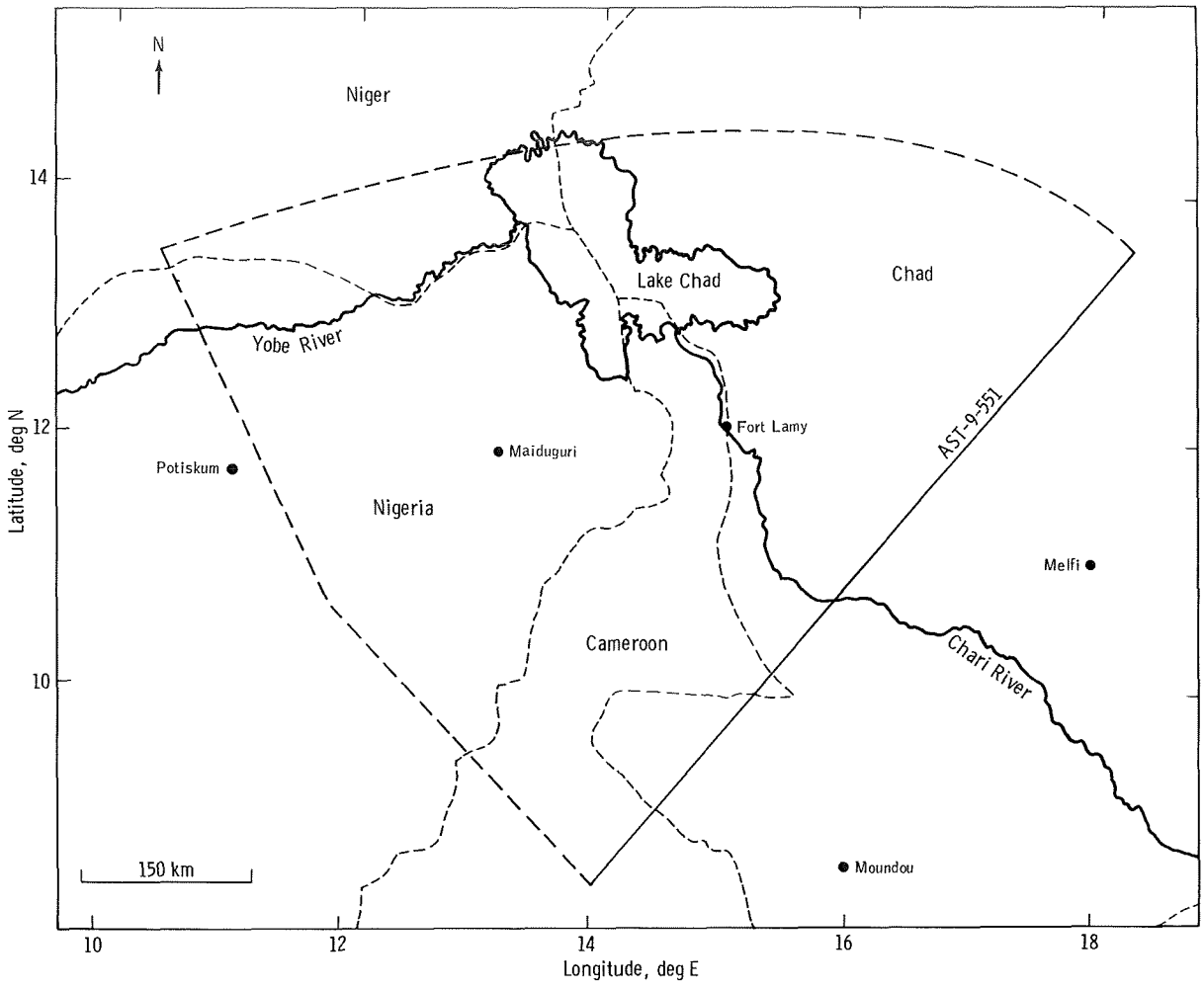


FIGURE 6.—Sketch showing the location of Lake Chad and the areal coverage of ASTP photograph AST-9-551.

An enlargement of ASTP photograph AST-9-551, taken in July 1975 (fig. 7(a)), and Gemini IX-A photograph S66-38444, taken in June 1966 (fig. 7(b)), were compared. Emphasis was placed on visible changes in Lake Chad as a result of the increasing aridity of the environment. Two main problems were considered: (1) Are there changes in the areal extent of dune fields in and around Lake Chad and have specific dunes migrated into it? (2) Is a change in water level visible and, if so, could this be due to dune encroachment upon the lake?

Because of the extreme obliquity of the ASTP photograph, the subsequent distorted geometry of Lake Chad, and the lack of relatively permanent features, the ASTP photograph could not be directly superimposed onto the Gemini IX-A photograph. Therefore, the comparison was made by constant referral from one photograph to the other, aided by Skylab 4 photographs SL4-194-7253 and SL4-138-3785 and Gemini VII photographs S65-63970 and S65-63969. Areas of noticeable change between 1966 and 1975 are marked on both figures 7(a) and 7(b) for easy comparison.

At site 1 (fig. 7(b)), two dune fields on the southeastern boundary of the lake are seen to be submerged. By 1975, these dune fields are the same color as the surrounding desert (fig. 7(a)) and have therefore emerged above the level of the

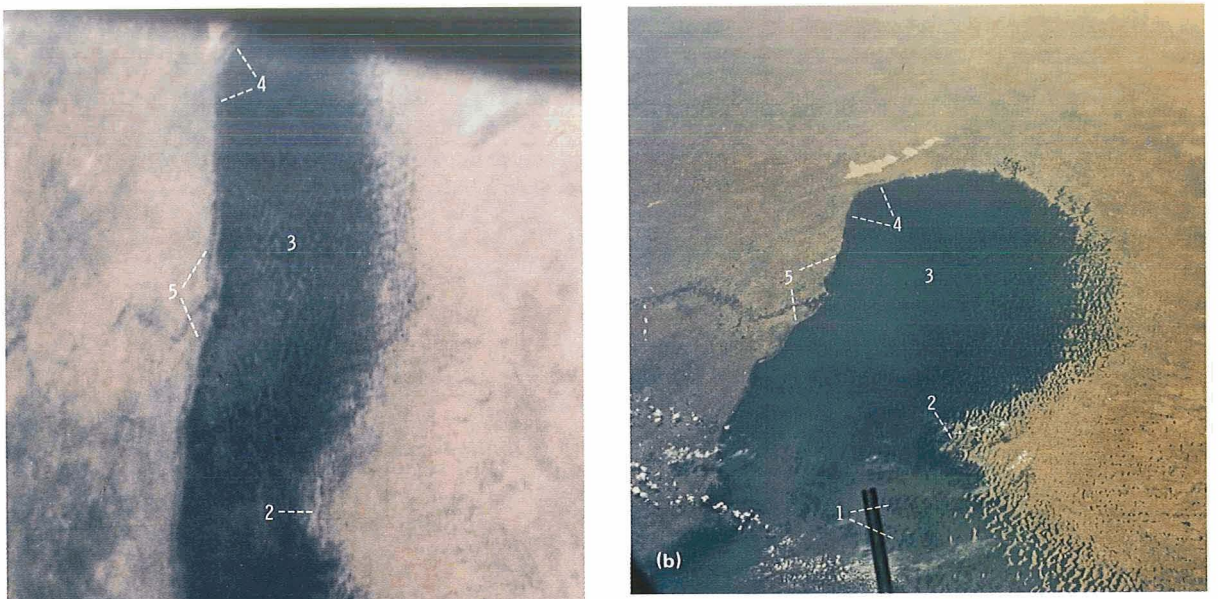


FIGURE 7.—Lake Chad. (a) Enlargement of the 1975 ASTP photograph AST-9-551 showing the northern and southern basins of Lake Chad. (b) The northern part of Lake Chad as depicted in Gemini IX-A photograph S66-38444, taken in 1966.

water. This clearly indicates a reduction in the water level of the lake since 1966. Another example of this phenomenon is seen at site 2 (figs. 7(a) and 7(b)), the east-central side of the lake, where the boundary between dunes and water is not as clearly defined in the ASTP photograph as it is in the Gemini photograph. Immediately west of this boundary, previously submerged dunes have appeared above the surface of the water in the 1975 photograph.

At site 3 (fig. 7(b)), the dunes within the northern basin in the Gemini photograph are largely submerged and appear to cover only approximately 60 percent of the basin as opposed to emerged dune coverage of approximately 85 percent in the ASTP photograph (fig. 7(a)). Several Gemini photographs were examined and none revealed the presence of submerged dunes as far to the west and southwest in the northern basin as seen in the ASTP photograph, although their presence could be hidden by the deeper water depicted in the Gemini photograph. The greater occurrence of dunes in the ASTP photographs could be attributed to the emergence of previously submerged dunes or to dune migration.

From June through September, the prevailing wind direction in the Lake Chad region is to the southwest, whereas from October through January, it is to the north and northeast (ref. 7). From the photographs, the dominant wind direction appears to be to the southwest. Dune migration would be facilitated by the gradual reduction in water level over time.

A second example of the effects of dune migration on Lake Chad can be seen at the northern and northwestern boundary of the lake, site 4 (fig. 7(b)). This boundary is very sharply defined in the Gemini photograph. Because it is not clearly visible in the ASTP photograph, Skylab photograph SL4-138-3785, taken in the winter of 1973, was used for clarification and comparison. In this photograph, the boundary appears encroached upon by sand dunes, thereby giving it a crenulated appearance. The sand dunes have caused the water at this site to recede 48.3 km in the past 30 years (ref. 10).

Parallel to the northwestern shoreline of the lake, at site 5 (fig. 7(a)), a blue line is clearly visible in the ASTP photograph. This line is not seen on the Gemini photograph. Therefore, it appears plausible that this line represents a former shoreline of the lake, existing at the time that the Gemini photograph was taken. By 1975, the areal extent of Lake Chad had diminished, leaving this line as evidence of its once greater extent.

From orbital photographs, a reduction in the water level of Lake Chad is clearly visible. Evidence consists of the emergence of previously submerged dunes and the presence of a former shoreline. Field studies of Lake Chad have shown that the lowering of the level of the lake is due to the decrease in both fluvial discharge and rainfall, which reflects the increasing aridity of the environment (ref. 7). Analysis of orbital photographs also suggests dune migration into the lake, especially in the northern basin. Because of the altitude at which these photographs were taken, particularly the ASTP photograph (fig. 7(a)), the resolution was not conducive to a detailed study of the migration of individual dunes.

CONCLUSION

As the three examples cited in this paper indicate, photographs taken from Earth orbit are valuable in monitoring changes within a given area over a period of years. For maximum benefit, vertical photographs taken from similar altitudes should be used. However, oblique photographs from varying altitudes can be useful if comparisons between photographs are done carefully.

REFERENCES

1. Holz, Robert K.: The Aswan High Dam. The Professional Geographer, vol. 20, no. 4, July 1968, pp. 231-237.

2. Hance, William A.: The United Arab Republic (Egypt). Chapter 8 in The Geography of Modern Africa, Columbia University Press (New York), 1964, pp. 119-141.

3. Burollet, Pierre Félix: Reconnaissance Géologique dans le Sud-est du Bassin de Kufra. Rev. Inst. Français Pétrole, vol. 18, no. 11, 1963, pp. 1537-1545.

4. Sandford, Kenneth Stuart: Geological Observations on the Northwest Frontiers of the Anglo-Egyptian Sudan and the Adjoining Part of the Southern Libyan Desert. Quart. J. London Geol. Soc., vol. 91, no. 363, 1935, pp. 323-381.

5. Williams, M. A. J.; and Hall, D. N.: Recent Expeditions to Libya From the Royal Military Academy, Sandhurst. Geog. J., vol. 131, part 4, 1965, pp. 482-501.

6. El-Baz, Farouk: Onslaught on the Nile; Shifting Dunes Threaten Egypt's Breadbasket. UNESCO Courier, June 1977, pp. 23-33.

7. Mothersill, John S.: Lake Chad: Geochemistry and Sedimentary Aspects of a Shallow Polymictic Lake. J. Sediment. Petrol., vol. 45, no. 1, Mar. 1975, pp. 295-309.

8. Carmouze, J. P.: Circulation Générale des Eaux Dans le Lac Tchad. Cahiers O.R.S.T.O.M., série Hydrobiologie, vol. 5, no, 3/4, 1971, pp. 191-212.

9. El-Baz, Farouk: Astronaut Observations From the Apollo-Soyuz Mission. Vol. I of Smithsonian Studies in Air and Space, Smithsonian Institution Press (Washington, D.C.), 1977.

10. Surtees, G.: Sahara Reclamation. World Crops, vol. 18, no. 2, June 1966, pp. 30-32.

ASTP Photographs of Southeastern Angola

Delia M. Warner[a]

ABSTRACT

Apollo-Soyuz photographs of southeastern Angola were studied to provide a preliminary description of landforms in this remote and sparsely populated region. These photographs were useful in distinguishing drainage patterns, lineament trends, rock types, and the distribution of unusual playa-like features.

The lineaments mapped correspond to stream channels that are straight for more than 5 km, to linear tonal variations that probably mark conspicuous changes in vegetation density or type, and to topographic lineaments that represent abrupt changes in relief. Three major trends were mapped: east-west, north-south, and northeast-southwest.

Clues to the origin and development of the playa-like features were found by a close examination of the photographs. This revealed (1) the occurrence of suspected karst features in the study area, (2) the association of east-west- and northeast-southwest-trending lineaments with the playas, and (3) the occurrence of ancient eolian deposits. The Angola features may have initially developed under more humid conditions as implied by solutional phenomena. Later, under arid conditions, wind deflation may have extended and maintained these forms.

[a]National Air and Space Museum, Smithsonian Institution.

INTRODUCTION

Since the advent of NASA's manned space program, orbital photographs of the Earth have been praised for their usefulness in providing information on remote, inaccessible, and unexplored areas. Because of their great regional coverage, orbital photographs present an effective format for the study of large-scale landforms and for the preparation of base maps. An opportunity to test this inference was provided by the Apollo-Soyuz Test Project (ASTP) photographs of part of southeastern Angola, a sparsely populated area for which little ground data exist.

The ASTP photographs revealed a semiarid region characterized by a generally flat, level plain on which the most conspicuous features were bright-toned playa-like depressions and remarkably straight north-south- and east-west-trending watercourses. The only departures from the relatively flat surface were low hills just east of the prominent north-south-trending Cuito River and a low-elevation limestone(?) plateau outlined by scalloped edges. The ASTP photographs of Angola were studied to provide a preliminary description of the landforms in this remote area, especially the playa-like features. One photograph in particular, AST-14-888, was studied in detail and used to prepare thematic maps.

ASTP PHOTOGRAPHS

The photographs of southeastern Angola were part of an ASTP mapping pass that extended approximately 5000 km from Angola (latitude 17°00′ south, longitude 18°40′ east) to Qatar on the Arabian Peninsula (latitude 26°00′ north,

longitude 51°30′ east). Although central Africa was cloud covered, the photographs of semiarid south-eastern Angola were cloud free, and image quality was excellent.

These photographs were taken on July 18, 1975, from an altitude of 224 km with the bracket-mounted 70-mm Hasselblad data camera. The 100-mm lens was used, and each frame covered 115 km on a side. Unfortunately, these photographs were not acquired with the normal 60 percent overlap planned for all ASTP mapping passes. Because the spacecraft was yawed 90°, stereo overlap occurred only in the lower-left and upper-right corners of the photographs. For the Angola photographs, this was not too critical because the landscape lacked the high relief necessary to provide a good stereo image for photographs taken from orbital altitudes.

STUDY AREA

The region covered in AST-14-888 (figs. 1 and 2) is situated along the northern edge of the Kalahari Desert. This desert, a generally featureless, relatively flat sand-covered plain with internal drainage, lies in a tectonic basin formed by epeirogenic movements of the African crystalline platform (refs. 1 to 3). The Kalahari Basin has been dry land since the Jurassic (ref. 4), and its surface is covered by Pleistocene sands underlain by the unusual Tertiary age Kalahari beds (refs. 5 and 6). These terrestrial deposits consist mainly of sandstones (ref. 5) as well as calcareous sandstones, conglomerates, marls, calcretes, and silcretes (ref. 7).

The generally flat or gently undulating surface of the Kalahari Desert is disturbed by the east-northeast- to northeast-trending Ghanzi Ridge along which Precambrian rocks crop out (refs. 2, 4, and 6; fig. 2). That part of the Kalahari Basin north of the Ghanzi Ridge has been referred to as the Barotse Basin (ref. 8), the Cubango Basin (ref. 2), the Okavango Basin (ref. 1), and simply the northern Kalahari Basin. In this report, the last designation will be used.

In southern Africa, the east-northeast to northeast trend followed by the Ghanzi Ridge is an important structural trend, which is related to Upper Proterozoic/Lower Paleozoic orogenic belts (ref. 9). Another important trend in this area is east-west (refs. 4 and 9). This trend is also related to the Upper Proterozoic/Lower Paleozoic structural pattern, which Clifford (ref. 9, p. 69) believes has strongly influenced later structural movements:

> Fault systems that developed in broad parallelism to, and were clearly controlled by, the overall trend of the Upper-Proterozoic-Lower-Paleozoic orogenic zones include . . . the east-west-trending faults of northern and north-western Southern Rhodesia; (and) post-Karoo faulting parallel to the northwest-trending segment of the Damara orogen and in the Kaokoveldt in South-West Africa . . .

As will be discussed later, a lineament map prepared from the ASTP Angola photographs revealed that the east-west and northeast-southwest trends were also important in the study area.

The northern Kalahari Basin is not truly desert but is semiarid savanna characterized by grassy plains with scattered trees. Wellington (ref. 10, p. 298) described the vegetation as mixed savanna including "trees of the genera *Acacia, Sclerocarya, Commiphora,* and *Hyphaene,* with *Hyparrhenia* and *Andropogon* as the dominant grasses."

Rainfall in the study area is approximately 76 cm/year (ref. 5); there are marked wet and dry seasons with most of the precipitation occurring in the summer from October to April. When the ASTP photographs were taken, winter drought conditions prevailed.

PHOTOINTERPRETATION

The detailed study of the ASTP photographs was accomplished with regular 20.5 cm by 25.5 cm color prints, with 4× Cibachrome enlargements of the original 70-mm film, and with a 1:250 000-scale color mosaic prepared by the Defense Mapping Agency Aerospace Center, Saint Louis, Missouri. The resolution and clarity of the Cibachrome prints was found to be superior.

Lineaments, which were probably the surface



FIGURE 1.—ASTP photograph of a remote and sparsely populated part of southeastern Angola (AST-14-888).

expressions of faults or fractures, were easily mapped from AST-14-888 (figs. 1 and 3). These lineaments correspond to stream channels that are straight for more than 5 km, to linear tonal variations that probably represent conspicuous changes in vegetation density or type, and to topographic lineaments that represent abrupt changes in relief.

For example, the courses followed by the rivers in AST-14-888 (fig. 1) suggest structural control and reveal two major trends, east-west and north-south. Figure 4 shows that the study area is characterized by a relatively coarse-textured rectangular drainage pattern. The watercourses in the eastern part drain into the Zambezi Basin; those in the west belong to the Kalahari drainage basin.

The major river in the study area is the Cuito River, which joins the Okavango River farther south and ultimately drains into the Okavango

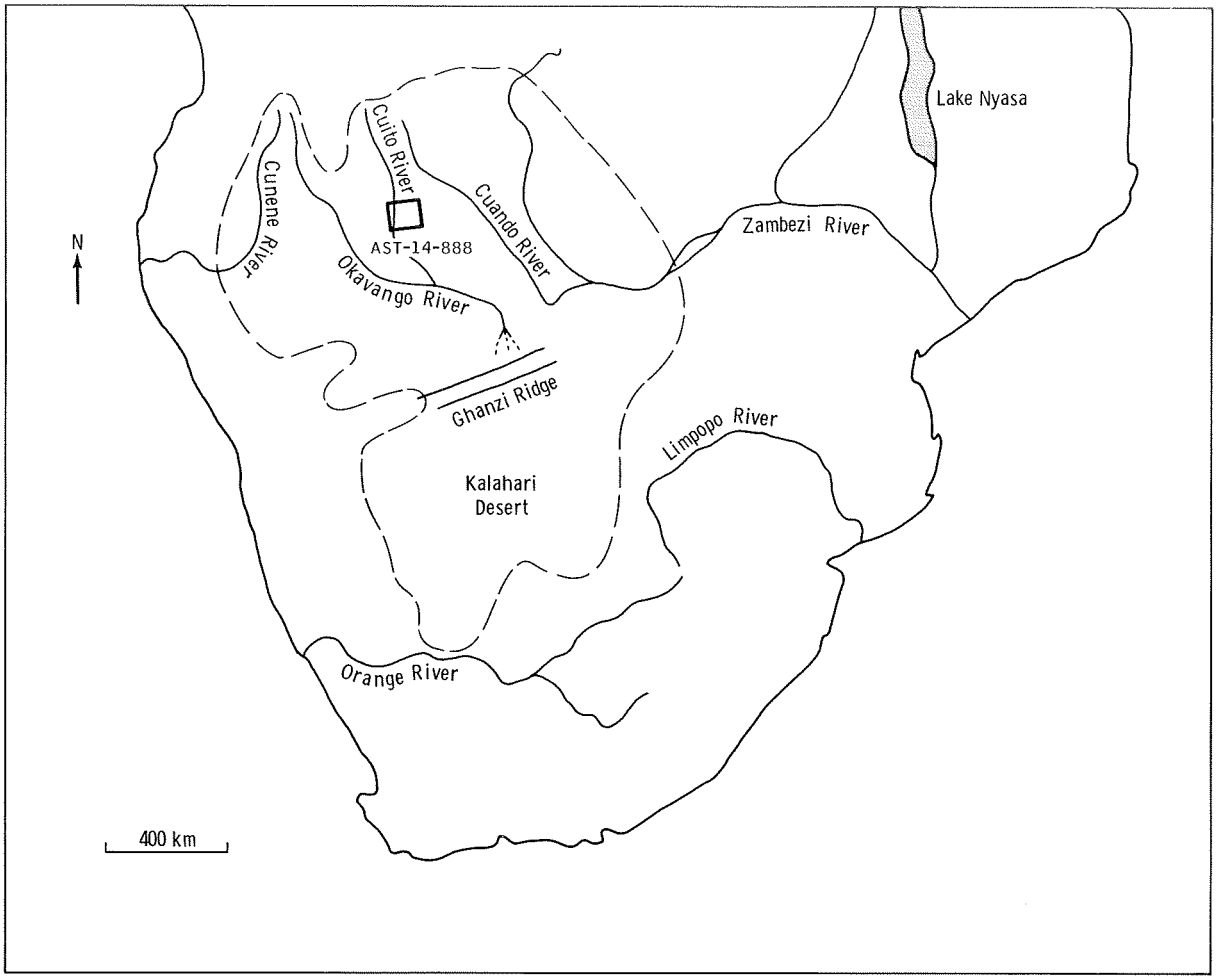


FIGURE 2.—Sketch of southern Africa showing the location of AST-14-888 (fig. 1). The Kalahari Basin, which is outlined by a dashed line, is divided into a northern and southern half by the east-northeast- to northeast-trending Ghanzi Ridge.

Swamp in the Kalahari Basin (fig. 2). In the ASTP photograph, the Cuito River flows down a remarkably straight north-south-trending valley, and meanders through a flood plain almost equal to the meander belt in width (fig. 1). Its tributaries, which trend generally east-west and exhibit right-angle bends, have straighter channel patterns and appear to flow through swampy stretches.

The east-west-trending watercourses in the eastern part of the study area (figs. 1, 2, and 4) drain into the Cuando River, which flows southeast and then east before joining the Zambezi above Victoria Falls. These straight and parallel streams appear to follow the east-west trend described by Dixey as one of two main structural trends in southern Africa (ref. 4).

Additional evidence for an east-west structural trend is provided by a prominent east-west-trending lineament that corresponds to an abrupt change in relief ("A" on figs. 1 and 3). North of the scarp, the surface is flat and level; to the south, hilly terrain is found. This lineament might be the surface expression of a fault.

A third lineament trend, northeast-southwest, was marked by subtle tonal variations that probably represent differences in vegetation density or type. As previously mentioned, this direction is

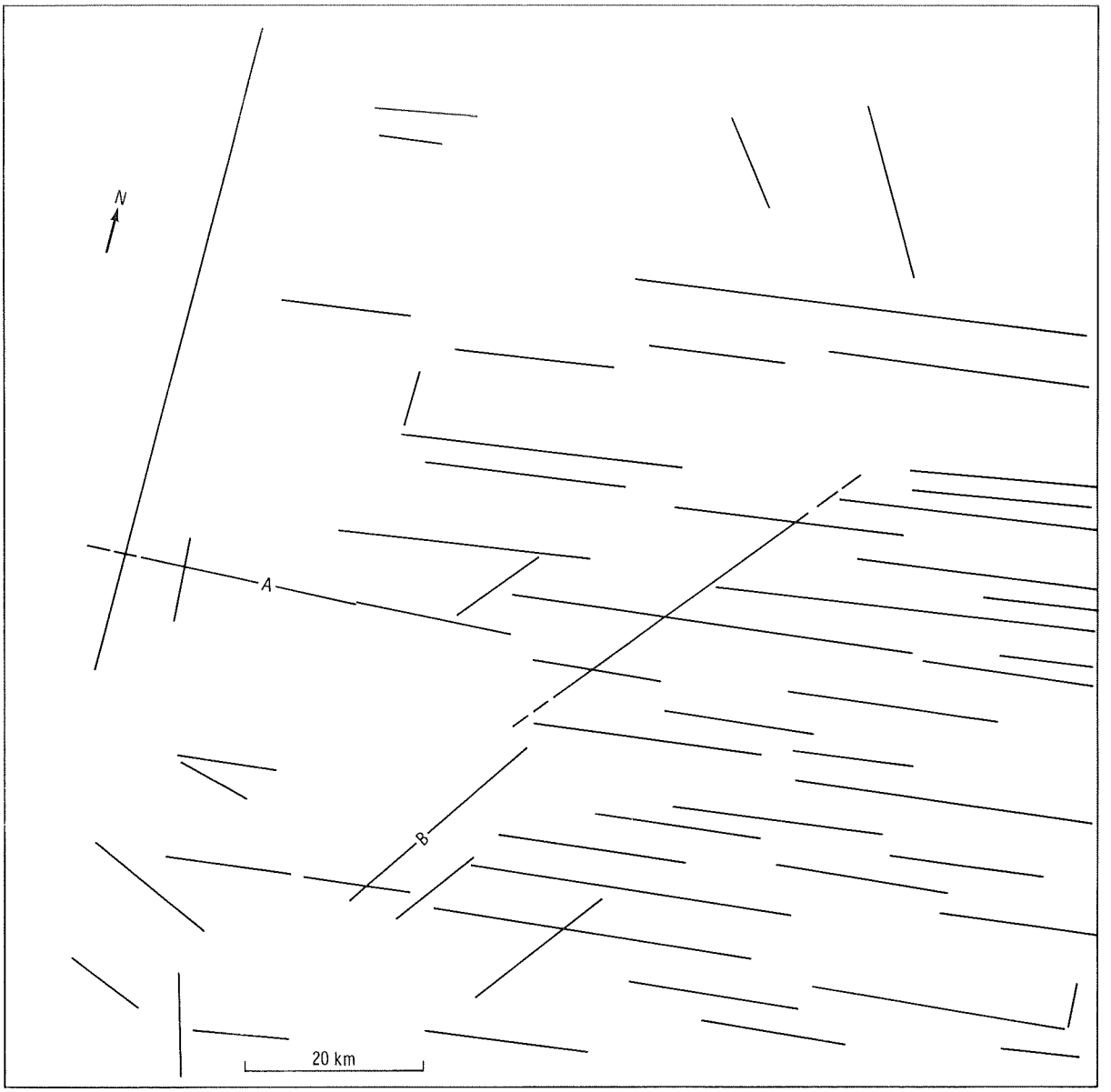


FIGURE 3.—Lineament trends mapped from AST-14-888 (fig. 1).

another important structural trend in southern Africa. The most prominent northeast-southwest lineament in AST-14-888 ("B" on figs. 1 and 3) is marked by a conspicuous color variation; the terrain is greener east of the lineament. It is noteworthy that springs or waterholes in this area are found at or near the intersections of the east-west- and northeast-southwest-trending lineaments. This might imply the presence of an aquifer tapped by faults or fractures that serve as paths for water movement.

In the southeastern corner of AST-14-888 (fig. 1), unusual bright-toned, flat-floored playa-like features are observed at the heads of and along the east-west-trending watercourses. The largest of these features ("C" on fig. 1) is approx-

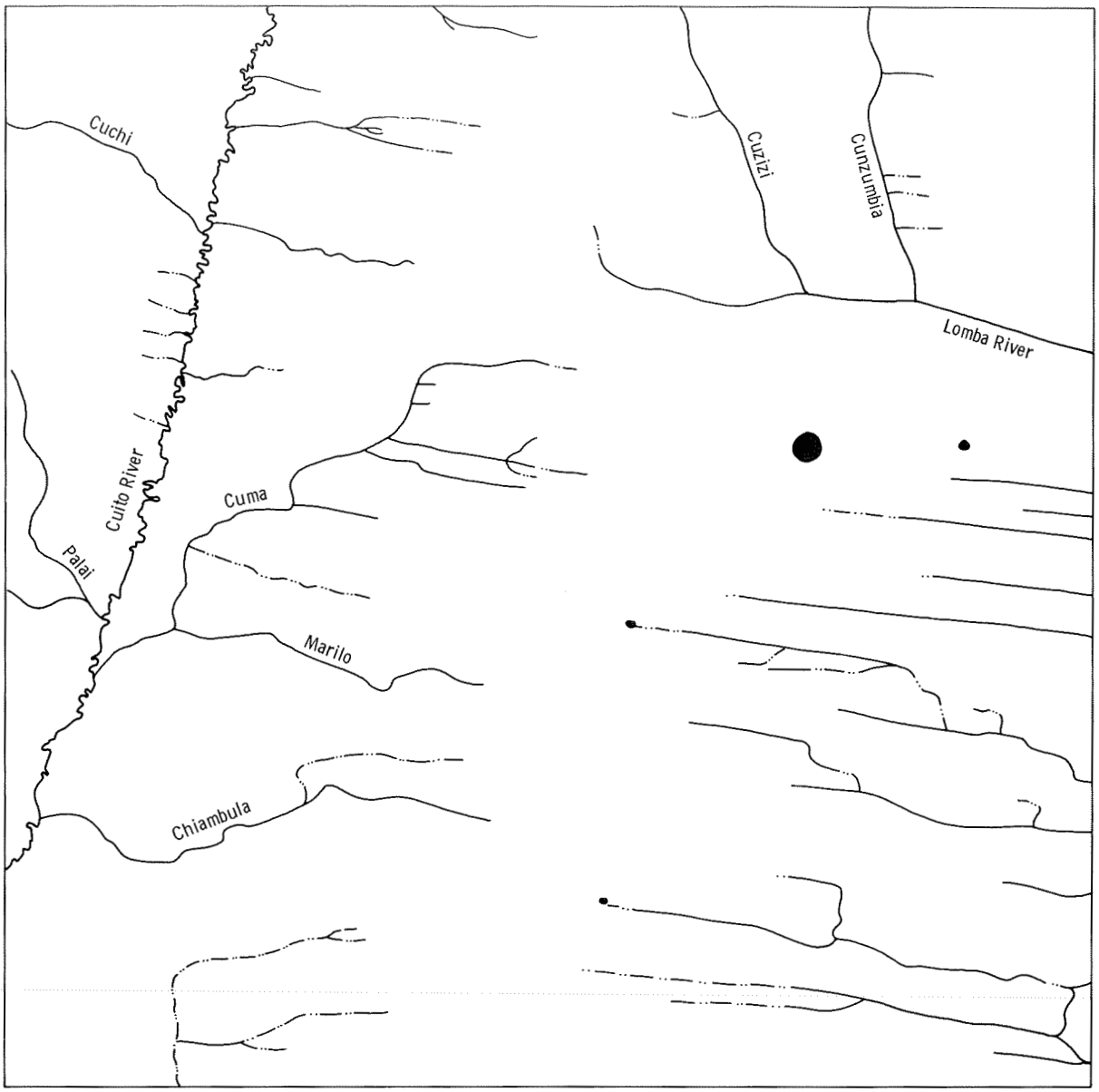


FIGURE 4.—Sketch of drainage patterns mapped from AST-14-888 (fig. 1). Dark areas mark waterholes.

imately 156 km^2. The term *playa* is generally used to describe flat-floored topographic depressions found at the lowest parts of enclosed arid drainage basins (refs. 11, p. 215, and 12, p. 1). Playa surfaces, which are periodically flooded and occupied by temporary lakes, are characterized by fine-grained sediments and are usually free of vegetation (ref. 11).

Although the Angola features resemble classical playas in many ways, they differ in one essential characteristic: They do not occur at the lowest part of an area of internal drainage. Instead, they are found at the heads of streams. However, in modern usage the term playa has been expanded



FIGURE 5.—Sketch showing the extent of suspected karst features in AST-14-888 (fig. 1).

to encompass "a variety of topographic depressions and desiccated former lakes that occur in the arid zone" (ref. 12, p. 1).

Another term that might apply to the Angola features is *dambo*. This term is used locally in southern Africa to describe "shallow saucer-shaped depressions" found where "streams rise in grassy treeless areas" (ref. 13, p. 15). Dambos are "wet or swampy during the rainy season but may dry out during the dry season from May to October" (ref. 13, p. 15).

A number of different theories have been proposed to explain the origin and development of depressions such as playas and dambos. These

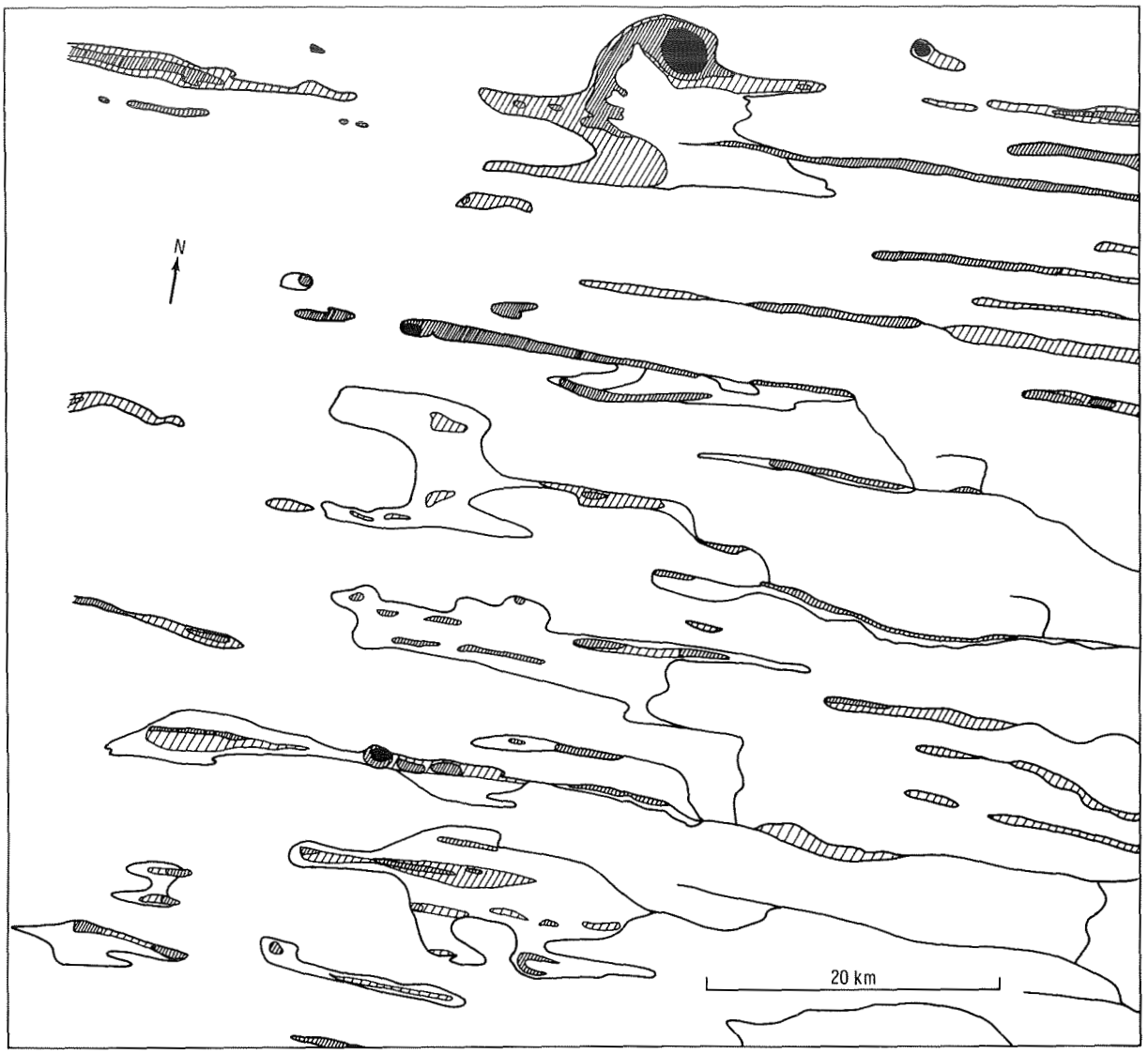


FIGURE 6.—Sketch showing the distribution of vegetation (hatch marks) on the playa-like features. Closer hatch marks indicate denser vegetation; water bodies are marked in black. (Drawn from an enlargement of AST-14-888.)

theories include wind deflation, solution, subsidence, scouring by animals, tectonic causes, and even meteorite impact (refs. 12 and 14). The close examination of ASTP photographs revealed a number of interesting features that might provide a clue to the origin and development of the Angola features.

The first feature is the observation of suspected karst features in the study area (fig. 5). These are topographic forms produced primarily by solution, usually of limestone or dolomite. Perhaps the most characteristic features of karst regions are sinkholes. Examples of features identified as sinkholes on the ASTP photographs are designated by points "D" and "E" in figure 1. The most prominent suspected karst feature in AST-14-888 (fig. 1) is a limestone(?) plateau outlined by scalloped edges. In addition, the circular outlines of waterholes associated with the playa-like features are suggestive of solution.

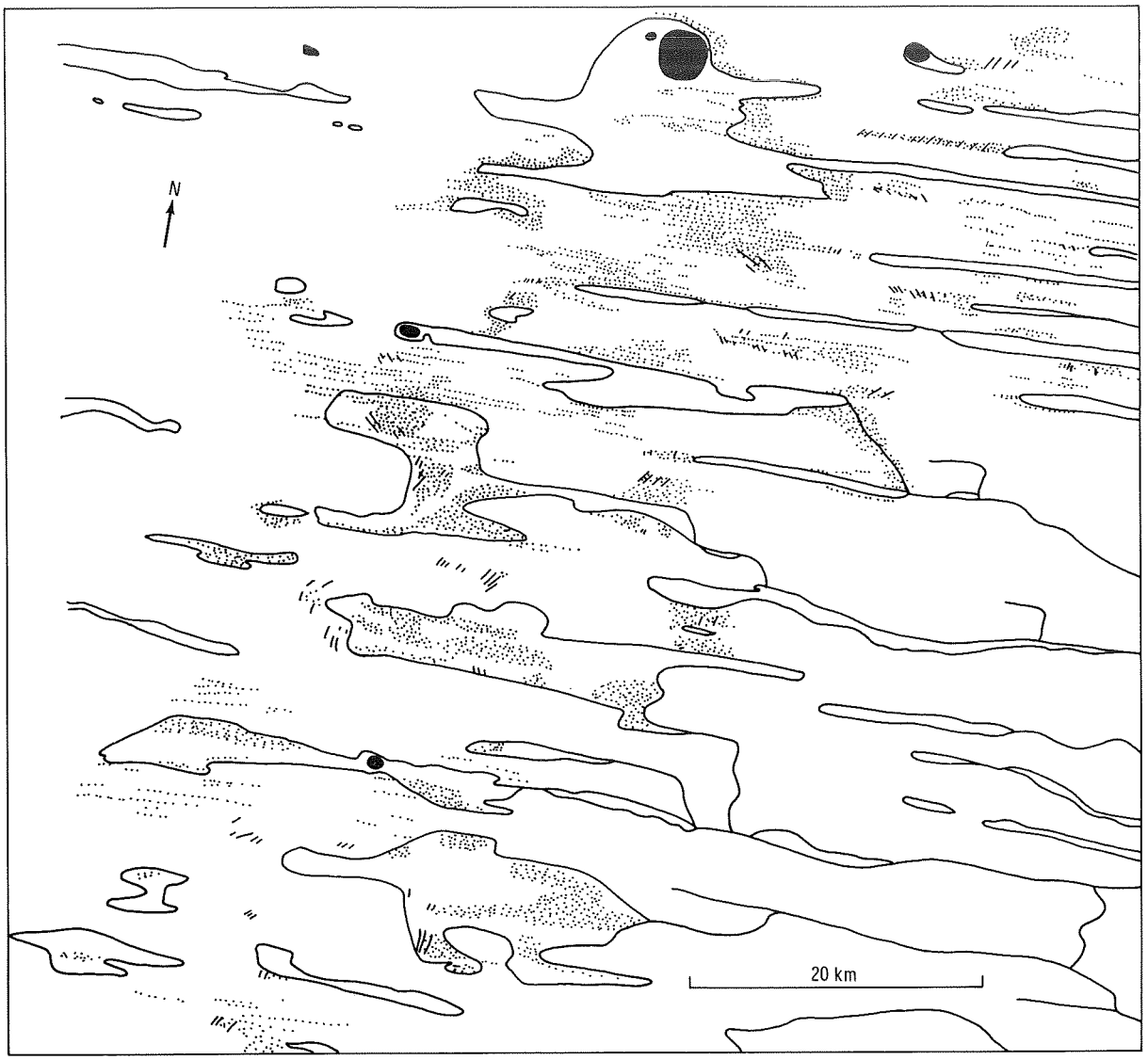


FIGURE 7.—Sketch showing the distribution of bright elongate streaks and areas (stippling) associated with the playas. Some of the streaks are composed of short parallel segments oriented oblique to or transverse to the east-west direction in which the streaks run. These features are probably ancient sand dunes that have been eroded by easterly or westerly winds. The trends of these dunes are indicated by thick lines. (Drawn from an enlargement of AST-14-888.)

Other interesting features are the angular elongate shapes of the playas and the occurrence of east-west-trending brown-colored streaks on the playa surfaces. In plan view, the Angola playas are elongate in an east-west direction, and their northern and southern boundaries are noticeably straight. In addition, the western edges of some of the features trend northeast-southwest. If these playas are partly the result of solution, east-west- and northeast-southwest-trending fractures probably controlled solution.

The surfaces of the playas are not uniformly colored. Instead, they exhibit marked tonal variations where the usually bright, white playa surfaces are crossed by elongate east-west-trending brown-colored streaks. These streaks were examined on two Landsat false-color composites of the study area. One Landsat image was taken dur-

ing the dry season in August 1973; the other was acquired during the rainy season in January 1973. Both of these images showed that the brown streaks were associated with vegetation. Figure 6 illustrates the distribution of patches of vegetation on the playas. The elongate east-west trend of these patches seems to provide evidence of faults or fractures that bring groundwater to the surface.

Another feature associated with the Angola playas appears on the ASTP photographs as narrow, elongate bright streaks (fig. 7). Closer examination of these streaks reveals that many of them are composed of short, parallel segments oriented oblique to or transverse to the east-west direction in which the streaks run. These features may be ancient calcreted(?) sand dunes that were later eroded by easterly or westerly winds. The existence of these probable eolian deposits seems to indicate that, in the past, climatic conditions in this area have been drier, vegetation has been sparser, and wind deflation might therefore have been an important factor in the development of the Angola playas. Other bright features associated with the playas exhibit a smooth texture and are probably saline deposits. The resolution of the photography was not sufficient to make an absolute distinction between all saline sediments and eolian deposits.

SUMMARY

The ASTP mapping photographs of part of southeastern Angola were useful in providing a preliminary description of landforms in this remote and sparsely populated area. Lineaments, drainage patterns, rock types, and the distribution of playa-like features were easily mapped.

Close examination of the photographs revealed a number of interesting features that might provide a clue to the origin of the unusual playa-like features. These included the occurrence of (1) suspected karst features, (2) east-west- and northeast-southwest-trending lineaments, and (3) ancient eolian deposits.

These aforementioned features indicate that the origin and development of the Angola playas cannot be attributed to one factor. However, it is likely that both solution and deflation had a role at different times. Both factors are associated with different climatic conditions. The Angola features may have initially developed under more humid conditions as implied by solutional phenomena. Later, under more arid conditions, wind deflation may have extended and maintained these forms. In addition, the prominent east-west and northeast-southwest structural trends probably affected the distribution of the playa-like features.

REFERENCES

1. Furon, Raymond: Geology of Africa (Translated by A. Hallam and L. A. Stevens.) Oliver and Boyd (Edinburgh and London), 1963.

2. Holmes, Arthur: Principles of Physical Geology, Second ed. Ronald Press Co. (New York), 1965.

3. Petrov, M. P.: Deserts of the World. (Translated from Russian by the Israel Program for Scientific Translations). Halsted Press, 1977.

4. Dixey, Frank: Some Aspects of the Geomorphology of Central and Southern Africa. Geol. Soc. of South Africa, Alex. L. du Toit Memorial Lectures No. 4, 1956.

5. Flint, Richard Foster: Pleistocene Climates in Eastern and Southern Africa. Bull. Geol. Soc. America, vol. 70, no. 3, 1959, pp. 343-374.

6. Haughton, Sidney Henry: The Stratigraphic History of Africa South of the Sahara. Oliver and Boyd (Edinburgh and London), 1963.

7. Boocock, C.; and Van Straten, O. J.: Notes on the Geology and Hydrogeology of the Central Kalahari Region, Bechuanaland Protectorate. Trans. Geol. Soc. South Africa, vol. 65, 1962, pp. 125-171.

8. McConnell, R. B.: Geological Development of the Rift System of Eastern Africa. Bull. Geol. Soc. America, vol. 83, 1972, pp. 2549-2572.

9. Clifford, Tom N.: The Damaran Episode in the Upper Proterozoic-Lower Paleozoic Structural History of Africa. Geol. Soc. America Special Paper No. 92, 1967.

10. Wellington, John H.: Southern Africa: A Geographical Study. Cambridge University Press, 1955.

11. Cooke, Ronald Urwick; and Warren, Andrew: Geomorphology in Deserts. University of California Press (Berkeley and Los Angeles), 1973.

12. Neal, James T., ed.: Playas and Dried Lakes. Benchmark Papers in Geology, vol. 20. Dowden, Hutchinson and Ross, Inc. (Stroudsburg, Pa.), 1975.

13. Mendelsohn, F., ed.: The Geology of the Northern Rhodesian Copperbelt. MacDonald (London), 1961.

14. Reeves, C. C., Jr.: Pluvial Lake Basins of West Texas. J. Geol., vol. 74, no. 3, 1966, pp. 269-291.

Color of Desert Surfaces in the Arabian Peninsula

Farouk El-Baz[a†]

ABSTRACT

The Arabian Peninsula was photographed during the Apollo-Soyuz mission with a stereostrip of 21 photographs starting at the Red Sea coast at west-central Yemen and ending at Qatar. These photographs sample all the major geologic and structural provinces of the peninsula. The natural color of the photographs enables the recognition of these provinces and the detailed study of some of their features.

Among the features discussed in this report are the Red Sea islands and the coastline at west-central Yemen; the red-colored plains that separate the Red Sea from the crystalline massifs of the Arabian shield; the structures, lineaments, and drainage patterns displayed by these igneous and metamorphic massifs; the various desert surfaces of the sedimentary interior; and the Dukhan anticline and eolian streaks in the Qatar Peninsula.

Detailed analysis of the Apollo-Soyuz photographs resulted in establishing the following facts: (1) available charts and maps can be updated using the orbital photographs, particularly of coastal zones; (2) geologic maps can be improved by use of the natural color photographs, which clearly delineate major geologic features and their characteristics; (3) the photographs can be used in characterizing sand fields and classifying dune forms; and (4) enlargements of the photographs can be useful in detailed studies of small areas, such as the city of Ad Dawḥah (Doha), Qatar, and its environs.

INTRODUCTION

Deserts may be defined as those arid areas of the Earth that receive less than 25 cm of rain per year. Although deserts occupy more than 20 percent of the land area of the Earth, information on their morphology is scanty and in some cases inadequate. Among the reasons for this limited knowledge of the Earth's deserts are their immense size and their remoteness and inaccessibility. These reasons make conventional surveys and detailed studies of desert regions impractical and costly.

Experience gained from the Gemini, Apollo, and Skylab missions indicated that orbital surveys of desert regions were very effective. Much new knowledge was gained from studying desert photographs obtained by the astronauts from Earth orbit (ref. 1). One factor that increased the effectiveness of orbital photographs was their natural color; desert surfaces are colorful and the colors are meaningful (ref. 2). Therefore, color photographs helped greatly in understanding desert morphology, in classifying sand dunes, and in evaluating eolian landforms (ref. 1).

For these reasons, photography of desert regions was one of the major objectives of the Earth Observations and Photography Experiment on the Apollo-Soyuz Test Project (ASTP). Excellent photographs were taken of the Arabian Peninsula, Argentina, Australia, and the North

[a]National Air and Space Museum, Smithsonian Institution.

[†]Principal Investigator.

African Sahara (ref. 3). This paper will discuss the ASTP photographic strip of the Arabian Peninsula (fig. 1) with emphasis on color variations in the terrain.

GENERAL SETTING

The Arabian Peninsula occupies the southwestern corner of Asia. It is bounded on the west by the Gulf of Aqaba and the Red Sea, on the south by the Arabian Sea, and on the east by the Gulf of Oman and the Arabian (Persian) Gulf. Its northern borders are common with southern Iraq and Jordan.

Politically, the Arabian Peninsula includes Saudi Arabia, Yemen, Southern Yemen, Oman, the United Arab Emirates (U.A.E.), Qatar, Bahrain, Kuwait (fig. 1), and several neutral zones, which are owned by more than one state.

The Arabian Peninsula is a great plateau of ancient crystalline rock, which is overlain by limestone and sandstone (ref. 4, p. 130). The crystalline rocks crop out, in the south and east, in a belt that parallels the Red Sea coast. The greatest height is achieved in southwestern Arabia, where the mountains are approximately 3700 m high (ref. 5).

The high coastal mountains of the Arabian Peninsula catch the little moisture that is carried by the passing winds; thus, the interior region is one of the most arid areas of the Earth. The precipitation in the interior of Arabia is less than 10 cm per year (ref. 4, p. 130). The extreme aridity of its interior is exemplified by the lack of any perennial streams and, hence, the lack of natural vegetation.

The basin-shaped interior consists of alternating steppe and desert landscapes. The Nafūd Desert in the north is connected with Ar Rub' al Khālī in the south by Ad Dahnā' Desert, a narrow sand corridor. Ar Rub' al Khālī, which means "The Empty Quarter," is the largest sand field in the world.

References to the geology of the Arabian Peninsula before the start of oil research in Saudi Arabia in 1933 are scarce. Camel trips across the interior escarpment by H. S. J. B. Philby, during World War I and later years, provided the first concrete evidence that marine rocks were extensively exposed in central Arabia (ref. 6, p. 2). Geological exploration entered a particularly interesting phase when the U.S. Geological Survey and the Arabian American Oil Company (Aramco) began a series of geologic-geographic maps covering most of the peninsula. To perform this task, which was begun in 1954, Saudi Arabia became one of the few countries in the world that was completely covered by high-altitude aerial photographs (ref. 6, p. 4).

Geological mapping started with the preparation of 1:500 000-scale maps compiled on topographic base maps of the same scale. From these maps, a geologic map was prepared at 1:2 000 000 scale and published in 1963 (ref. 7). To this day, the map remains a major source of geologic information on the Arabian Peninsula.

One image taken by the Nimbus-3 high resolution infrared (HRIR) scanner (0.7 to 1.3 μm) at 1:2 000 000 scale gives an excellent view of the general geology of the peninsula. The image shows that the rocks which parallel either side of the Red Sea are nearly identical. This is true since the Arabian shield is regarded by most geologists as being a continuation of the African shield and is now separated from it by the Red Sea rift (e.g., ref. 8).

The crystalline rocks that form the massifs of the Arabian shield are mostly Precambrian in age. Since Precambrian time, these massifs have been amazingly stable and subject only to gentle epeirogenic movements (ref. 6, p. 5). On these rigid peneplaned landmasses was deposited a thick sequence of continental and shallow water shelf sediments that dip gently to the north and east. The sediments are clearly depicted on the Nimbus-3 image (fig. 2) as occupying the central and eastern parts of the peninsula. The white areas in figure 2 appear to reflect thick sand accumulations that overlie the sedimentary rocks.

The major structural provinces of the Arabian Peninsula are shown in figure 3. The Arabian shield just east of the Red Sea coast is composed mainly of igneous and metamorphic rocks that are locally overlain by Cenozoic volcanics and Quaternary alluvial and eolian sediments (ref. 9).

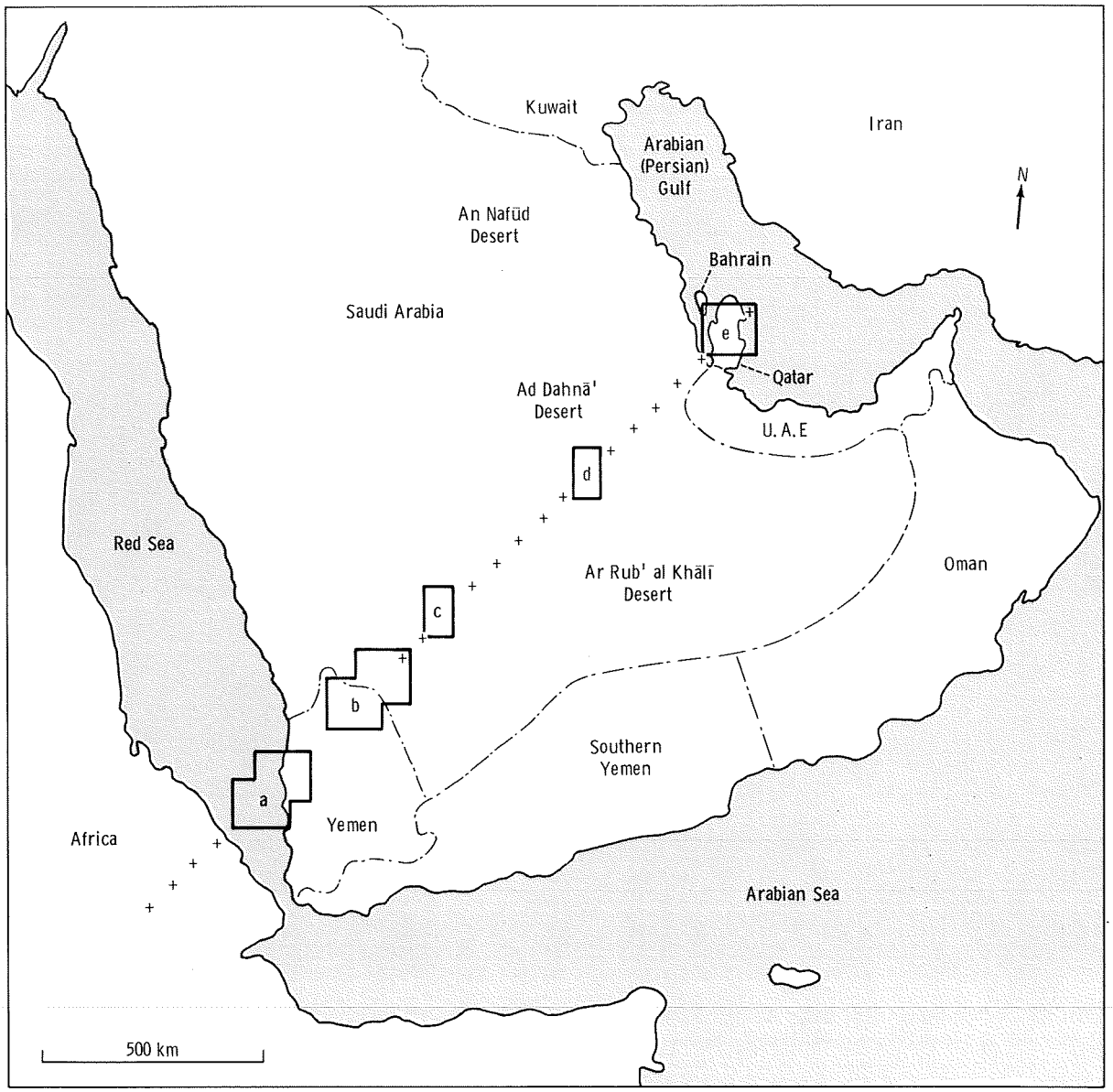


FIGURE 1.—Sketch map of the Arabian Peninsula showing the photographic strip obtained on the Apollo-Soyuz mission. Crosses show centers of the photographs, and the lettered areas show the locations of figures in this paper: "a," figure 4; "b," figure 6; "c," figure 7; "d," figure 8; and "e," figure 9.

It is interesting to note that the shape of the Arabian shield in this map (fig. 3) is almost identical to that on the Nimbus-3 image (fig. 2).

The interior homocline borders the Arabian shield and consists of eroded limestone, dolomite, shale, and sandstone. Dominating the exposed part of the homocline is a series of essentially parallel, west-facing, strike escarpments, each supported by a resistant limestone cap (ref. 6, p. 6). Sandstone and shale, which are less resistant to eolian weathering, floor intervening valleys and plains. Covering parts of the homocline are exten-

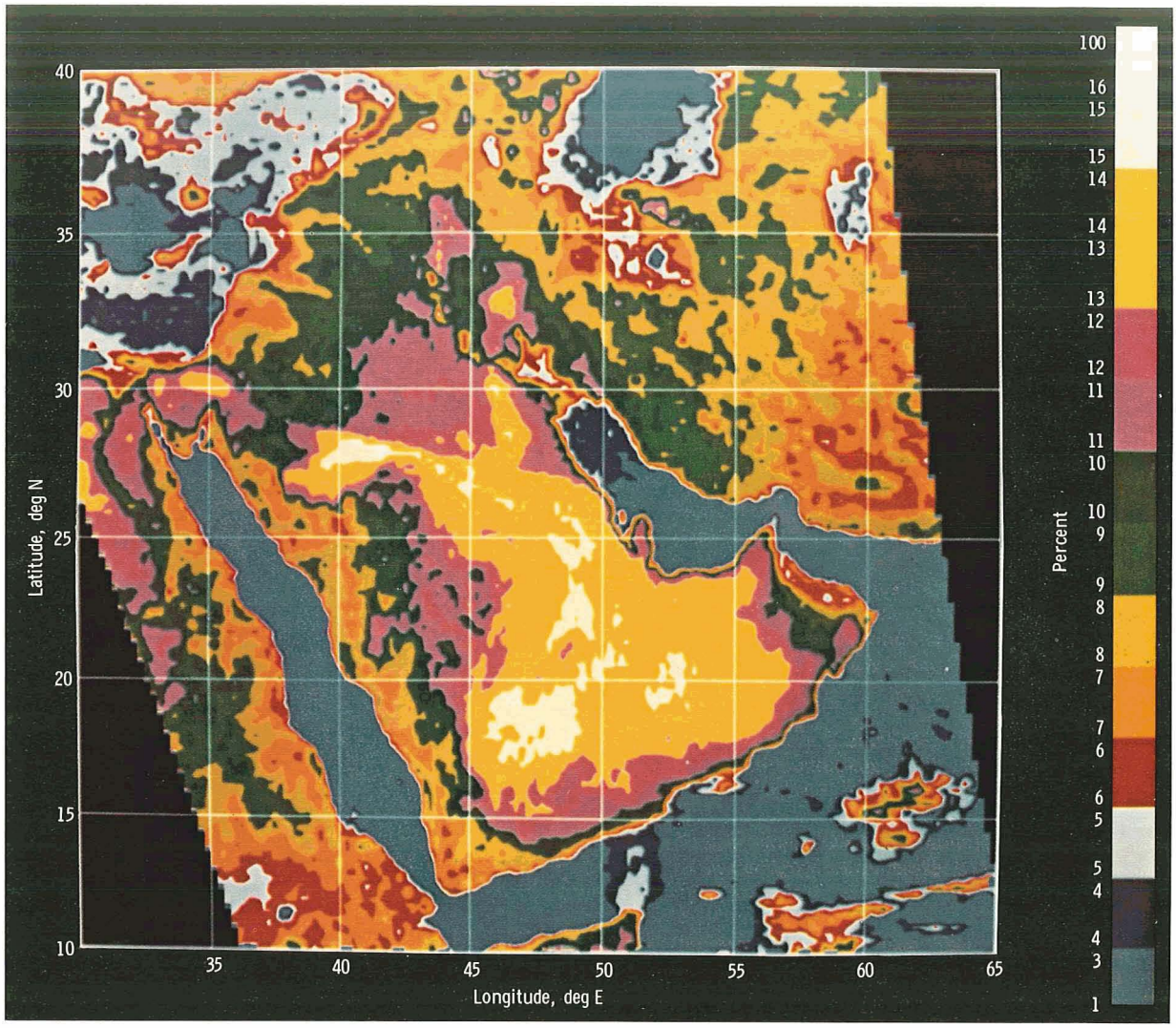


FIGURE 2.—Nimbus-3 HRIR image (0.7 to 1.3 μm) of the Arabian Peninsula obtained on June 6, 1969, 7:55 to 8:08 Greenwich mean time. The scale on the right edge shows the heat reflectance values of the various surface units (NASA 74-HC-156).

sive windblown eolian sands in An Nafūd and Ar Rub' al Khālī deserts, to the north and south, respectively. The Hadramaut plateau along the south is made up of limestone, shale, and marl strata with a dominant east-west drainage system, which is beautifully documented by Gemini IV photographs (ref. 10, pp. 19 to 21).

East of the homocline is a broad expanse of relatively low relief terrain in which older rocks are buried by Tertiary and younger deposits. Paleozoic and Mesozoic strata do not reappear at the surface until the Oman Mountains in the easternmost part of the peninsula (ref. 6, p. 6).

As stated previously, the major geologic and structural maps of the Arabian Peninsula show much similarity to the Nimbus-3 image (fig. 2). Similar comparisons were made between geologic maps of the peninsula and Nimbus-5 and Nimbus-6 data on microwave brightness temperatures (ref. 11). It is believed that comparisons of all such data may yield significant results. Perhaps the comparisons could be done digitally as in the

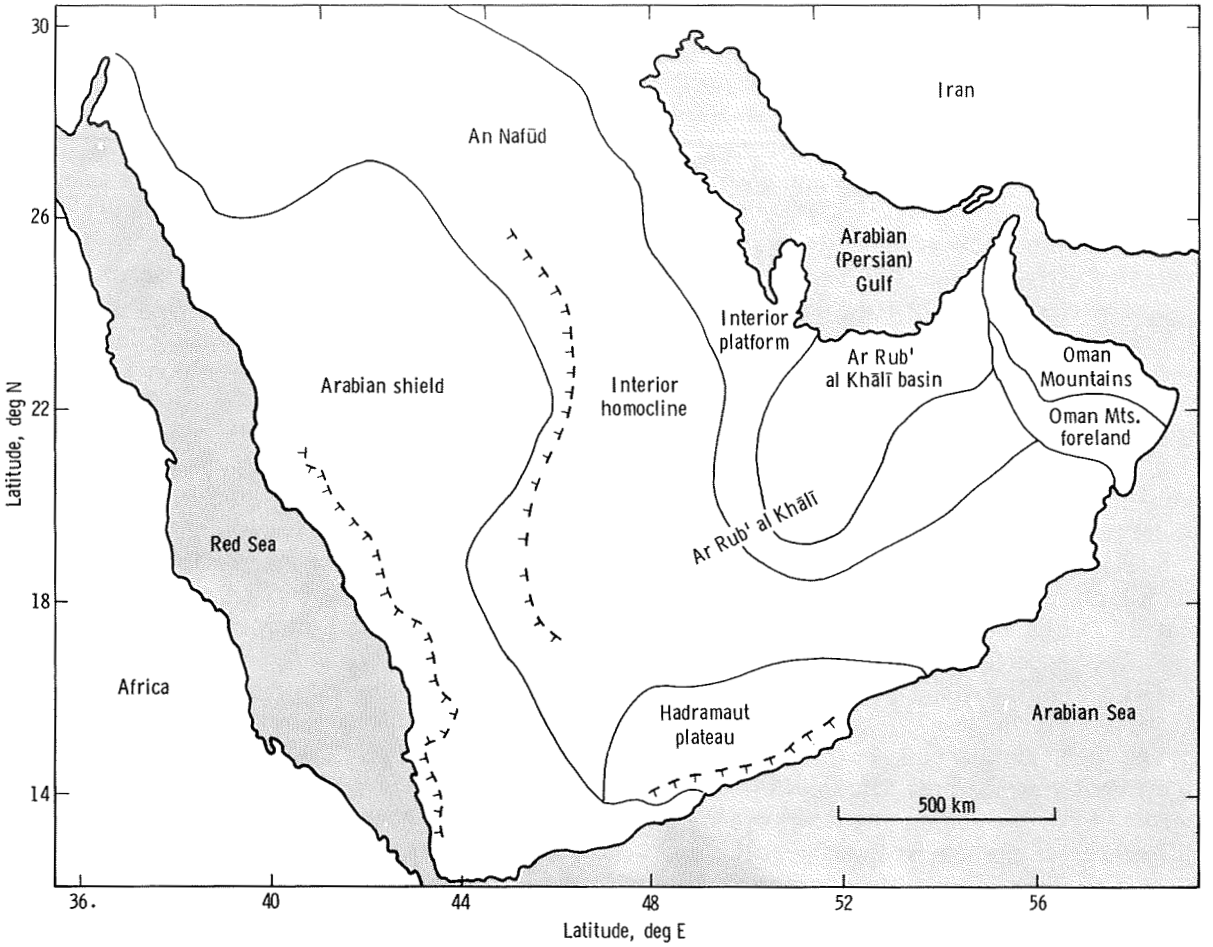


FIGURE 3.—Map showing structural provinces of Saudi Arabia and adjacent areas. Dashed lines indicate major escarpments. (Simplified from ref. 6, plate 2).

correlations of the Apollo lunar-orbital data with geologic maps at the U.S. Geological Survey, Flagstaff, Arizona (ref. 12).

COLOR ZONES IN ASTP PHOTOGRAPHS

Photographs of the Arabian Peninsula were obtained during the ASTP mission using the "black" Hasselblad camera on revolution 40 as part of photographic strip M5 (ref. 3). The photographic objectives of this strip were the Afar Triangle at the Horn of Africa, the structures bordering the Red Sea rift, the dune patterns in Ar Rub' al Khālī Desert, and the coastal processes at Doha, Qatar (ref. 13, p. 110).

The camera (with its 100-mm lens) was bracket-mounted in spacecraft window 5, and the intervalometer was set at 6.5-second intervals. This particular strip differed from other photographic strips on the Apollo-Soyuz mission; it was obtained with a difference of 90° in spacecraft yaw. This resulted in the reduction of overlap from 60 to 30 percent; the stereographic overlap covered the lower-left and upper-right corners of the photographs rather than being normal sidelap. (See stereopairs marked "a" and "b" in fig. 1.)

The ASTP crewmen obtained a total of 21 partial stereophotographs of the Arabian Peninsula

(fig. 1). The strip started at the southern end of the Red Sea off the coast of Yemen and continued in a northeasterly direction to the tip of the Qatar Peninsula (fig. 1). These excellent photographs cross all the major geologic and structural provinces of the Arabian Peninsula and clearly show the following:

1. The numerous islands, shoals, and coral reefs in the coastal waters of Yemen
2. The coastal strip of red-colored plains with numerous lighter colored alluvial fans
3. The rugged southern part of the Hijāz Mountains at the border between Yemen and Saudi Arabia
4. The eastern foothills of the Arabian shield with a major drainage pattern of east-trending wadis (valleys)
5. The numerous eolian landforms including sand dunes and color zones in Ar Rub' al Khālī and Ad Dahnā' deserts
6. The lineated limestone exposures in the eastern part of the Arabian Peninsula, particularly in Qatar

The ASTP photographs show color zones within many of these features. The color variations are believed to be caused by compositional differences of the exposed surfaces. Because of the apparent significance of geographical distributions, the color zones and variations thereof will be discussed separately for each of the following regions: (1) the Red Sea coast, (2) the mountainous west, (3) the sandy interior, and (4) the Qatar Peninsula.

Red Sea Coast

The first two photographs of the ASTP strip of the Arabian Peninsula clearly display the coastal features of west-central Yemen (fig. 4). The Red Sea coastline appears sharp and crisp in these photographs. Dark splotches near the coast are probably *sebkhas,* which are accumulations of silt, clay, and sand often with saline encrustations (ref. 5). The author has seen many larger *sebkhas* on the eastern edge of the Arabian Peninsula, which show the same photocharacteristics as these small features in the coastal areas of Yemen.

The natural color of the ASTP photographs helps delineate the flat coastal plains, which appear bright earthy-red in color (closest to 5A on the ASTP color wheel; Munsell 5R 6/6).[1] These plains appear much lighter in color than the foothills of the crystalline rocks of the Arabian shelf, which are more brown in color (fig. 4).

The coastal plains are dissected by east-west drainage patterns of wadis, valleys, or dry watercourses. The most distinctive of these is Wādī La'ah, which displays a dark course of the dry streambed. The dark color of the wadi and its delta-shaped alluvial fan is probably due to scant vegetation; it is somewhat darker than the color of *sebkhas* nearer the Red Sea coast. Other wadis, particularly north of La'ah, are marked by lighter colored, probably more sandy, alluvial fans.

West of the Yemen coastline, the ASTP photographs show numerous variations in the color of water. Somewhat murky, purplish-bluish-gray water colors dominate the coastal zone (color 48A on the ASTP color wheel; Munsell color 5PB 5/6). The water that surrounds some of the numerous islands, which probably reflects bottom topography, is more bluish-green (color 32A on the ASTP color wheel; Munsell color 2.5PB 5/6). The open seawater is deep purple-blue (color 45B on the ASTP color wheel; Munsell 2.5PB 5/6). A wake of one island on the left edge of figure 4 (Jabal at Tayr) trends in a southeasterly direction and appears darker than the surrounding seawater.

The ASTP photographs clearly display both the coastline and the boundaries of the islands. The photographs were compared with the Defense Mapping Agency charts of the region (Operational Navigation Charts ONC J6 and ONC K5). The comparison showed that these charts, at 1:1 000 000 scale, did not accurately depict the natural boundaries (fig. 5). The ASTP photographs can be used to update the maps by (1) correcting the coastline, particularly north of Al Luḥayyah; (2) changing the boundaries of many of the large islands, such as Takghash; (3) deleting some of the islands that do not appear in the photographs; (4) changing the positions of some of the islands; and (5) adding the islands that appear on the photographs but not on the charts.

[1]These and similar color notations are explained in the section of this volume entitled "Comparison of Astronaut Visual Color Observations with ASTP Photographs."

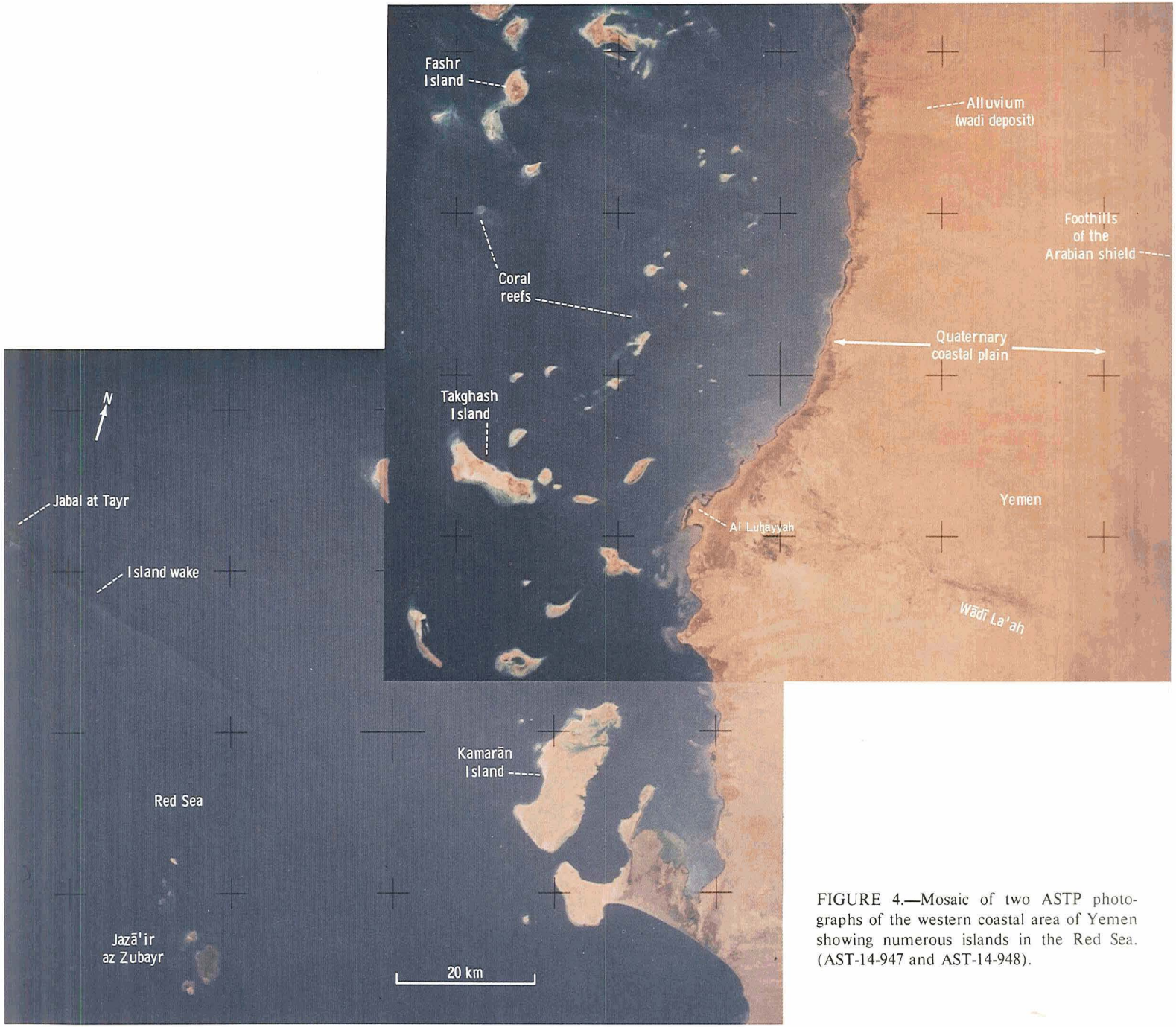


FIGURE 4.—Mosaic of two ASTP photographs of the western coastal area of Yemen showing numerous islands in the Red Sea. (AST-14-947 and AST-14-948).

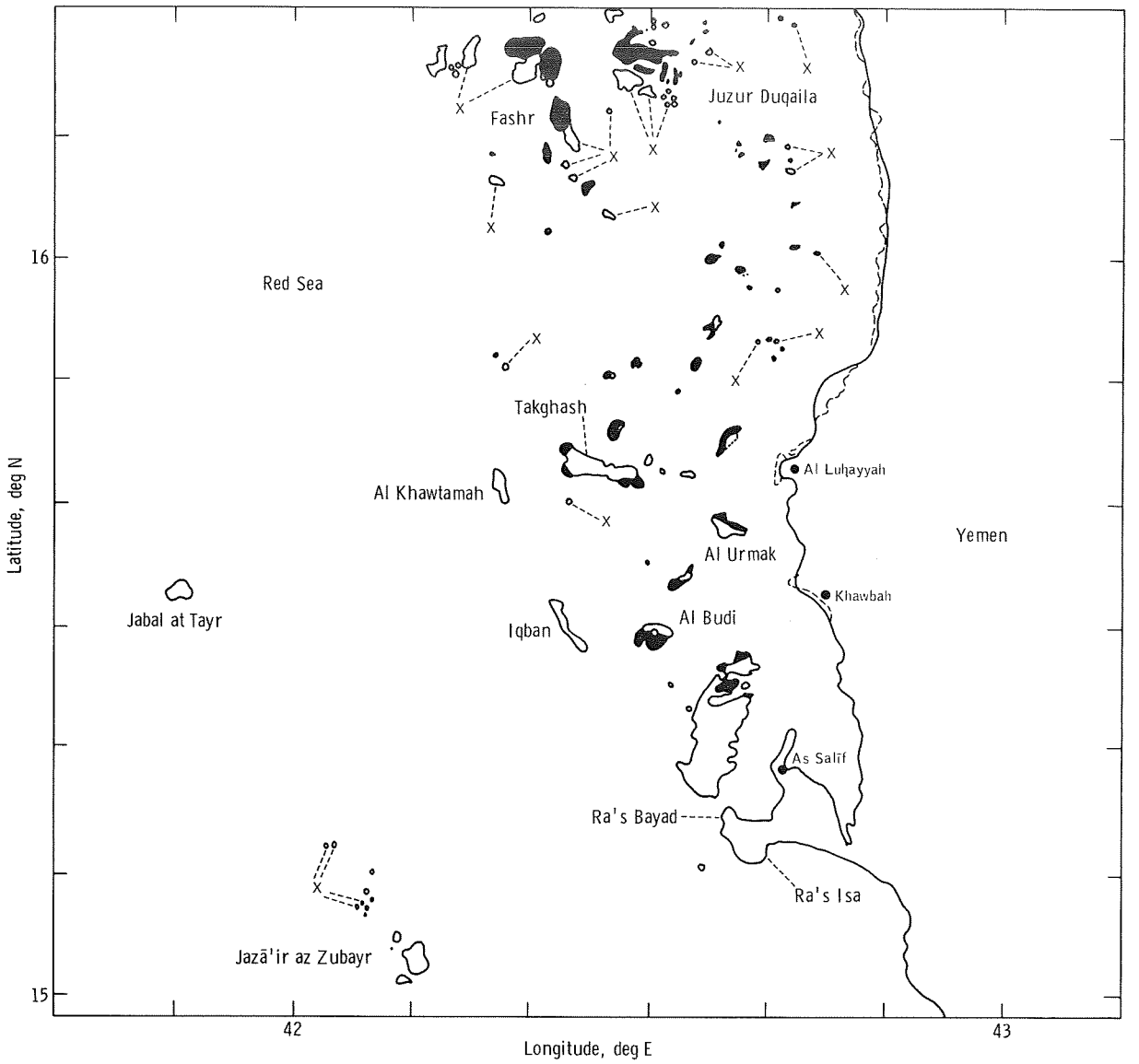


FIGURE 5.—Map of the coastal area of west-central Yemen based on Operational Navigation Charts ONC J6 and ONC K5. Dashed line at Khawbah and north of Al Luḥayyah marks the coastline as depicted on Apollo-Soyuz photographs. Black areas indicate corrections to island coastlines or locations of islands as seen on the ASTP photographs; islands marked by an "X" do not appear on these photographs.

Mountainous West

The ASTP stereophotographs clearly display the rugged nature of the high massifs of the Arabian shield. The color of these mountains is brownish-red (color 11A on the ASTP color wheel; Munsell color 10R 6/4). The structural grain in the photographed part is dominantly north-south. As shown in the central part of figure 6, numerous belts of north-south-trending lineaments abound. Intersecting this major trend are lineaments trending in a northeast-southwest direction and a few east-west-oriented lineaments. The latter are particularly emphasized by the wadis, which spread eastward from the mountains toward the low-lying desert surface.



FIGURE 6.—Mosaic of two Apollo-Soyuz photographs of the eastern part of the Arabian shield and adjacent desert surfaces. Dashed circular areas are granitic plugs (AST-14-951 and AST-14-952).

Circular features abound in the central part of the photographs illustrated in figure 6. The one that is divided by the border between Saudi Arabia and Yemen as well as all those north of that border are mapped as peralkaline granite (ref. 7). The U.S. Geological Survey map, however, does not show the structure south of the border in figure 6. The shape, color, and texture of this structure suggest that it is identical to the ones in Saudi Arabia. It is believed that it also is a circular plug of probable peralkaline granite composition. This interpretation is supported by the map of Grolier and Overstreet (ref. 14), who mapped the rocks in this area as granites.

The open desert east of the Arabian shield is shown in much lighter colors than the mountains. Although individual dunes are not distinct, the texture of the terrain suggests the existence of dunes, particularly in Ramlet Yam. The latter area lies between two major wadis, Habawna on the north and Najrān to the south (fig. 6). The wadi alluvium is grayish-white when compared to the yellowish-red color of the desert surface. The latter is much brighter in color (color 23A on the ASTP color wheel; Munsell color 2.5Y 8/6) than the surface of the coastal plains on the western side of the Arabian shield massifs.

Sandy Interior

As stated earlier, much of the interior of the Arabian Peninsula is occupied by sedimentary deserts. Approximately one-half of the sedimentary area is blanketed by eolian sand. Ar Rub' al Khālī is the largest sand field and occupies nearly 600 000 km^2. This desert was first explored by the English explorer Philby in 1932 (ref. 15). It covers much of the southern interior of the peninsula from the highlands of the Najd in the north to the Hadramaut plateau in the south. It slopes from an altitude of 1000 m in the west to near sea level in the east. Sand dunes of Ar Rub' al Khālī rise as high as 200 m in the southwest (ref. 4).

The ASTP photographs of Ar Rub' al Khālī Desert show some of these dunes. In one photograph, the dunes measure at least 100 km long. These dunes show a very regular wavelength, and they appear much redder than the limestone rock beneath (fig. 7). In the northwestern part of the desert, the dune sand is pinkish-red in color (color number 25A on the ASTP color wheel; Munsell color 2.5YR 8/4). As shown in the upper-left corner of figure 7, the dunes taper toward the west-facing interior escarpments.

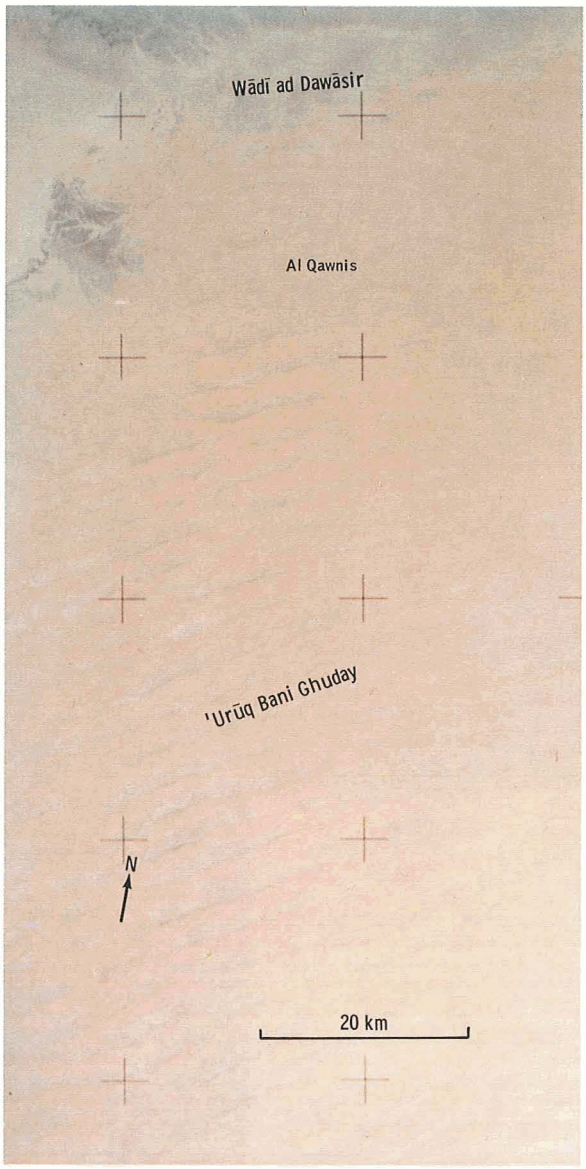


FIGURE 7.—Part of ASTP photograph showing the red-colored, nearly east-west-oriented dunes ('Urūq Bani Ghuday) at the northwestern edge of Ar Rub' al Khālī Desert, Saudi Arabia (AST-14-955).

North of Ar Rub' al Khālī, the ASTP photographic strip covers the sand dunes named 'Urūq ar Rumaylah. These appear to be continuations of Ar Rub' al Khālī dunes. However, instead of the near east-west orientations of 'Urūq Bani Ghuday of Ar Rub' al Khālī (fig. 7), the dunes of 'Urūq ar Rumaylah veer toward the northeast.

The deserts of Ar Rub' al Khālī in the south and An Nafūd in the north are connected by Ad Dahnā' Desert, which is a narrow corridor of sand, approximately 1300 km long. The Apollo-Soyuz photographs clearly depict this sand corridor because of its bright-red color (fig. 8). In the orbital photographs, the sedimentary rocks on either side of the sand corridor are light greenish-gray whereas the sand appears pinkish-red (color 26B on the ASTP color wheel; Munsell color 7.5R 8/4).

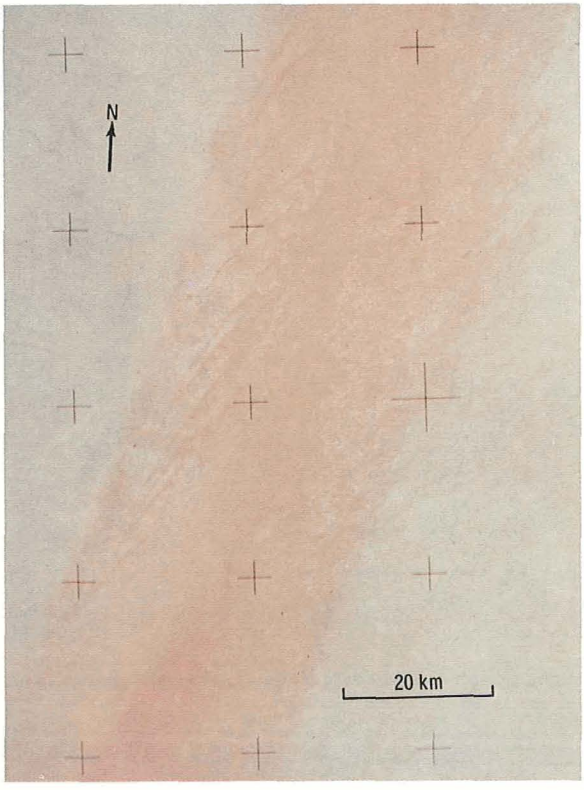


FIGURE 8.—Part of the red-colored Ad Dahnā' sand corridor (pinkish-red color), which connects the deserts of An Nafūd to the north and Ar Rub' al Khālī to the south. The Huraysan area to the west (left) of the sand corridor consists of limestone, dolomitic limestone, and dolomite. The formation east (right) of the sand is composed of sandstone, marl, and limestone. Note the fine drainage lines west of the sand corridor (part of Apollo-Soyuz photograph AST-14-961).

The ASTP photograph shown in figure 8 suggests a difference between the rocks exposed on either side of the sand deposit. The surface to the west (left side, Huraysan area) is darker in color and is dissected by fine drainage lines oriented in a nearly east-west direction. The rocks to the east (right side, Şummān area) are lighter in color with fewer drainage lines and with fine northeast to southwest lineaments.

This difference is reflected in the geologic map (ref. 7). According to this map, the rocks west of Ad Dahnā' belong to the Paleocene-age Umm ar Radhuma Formation. It is composed of limestone, dolomitic limestone, and dolomite (ref. 7). The rocks east of the sand belt are Miocene- to Pliocene-age sandstone, marl, and limestone strata.

Some color variations also occur within the sand zone itself (fig. 8). These may reflect thickness of sand cover and variations in dune morphology. For example, the eastern part of the sand field appears to contain numerous small complex dunes, with the interdune areas forming a dotted pattern. The central part of the red zone is smoother in texture and appears to have a relatively constant sand thickness. The western part of the sand field is characterized by relatively large dunes trending in a northeast-southwest direction. These variations in dune morphology and morphometry may be caused by topographic characteristics of the underlying terrain and their effects on the wind regime.

Qatar Peninsula

The Qatar Peninsula lies on the eastern shores of the Arabian Peninsula and occupies 11 400 km^2. It is largely a barren and rocky desert, with very little vegetation (fig. 9). The terrain is flat, and from field observations by the author, it consists mainly of fine-grained limestone that is crystalline or dolomitic and vuggy in many places. This limestone, which forms the major part of the peninsula, is lower Eocene in age and belongs to the Dammam and Rus Formations (ref. 7). It is

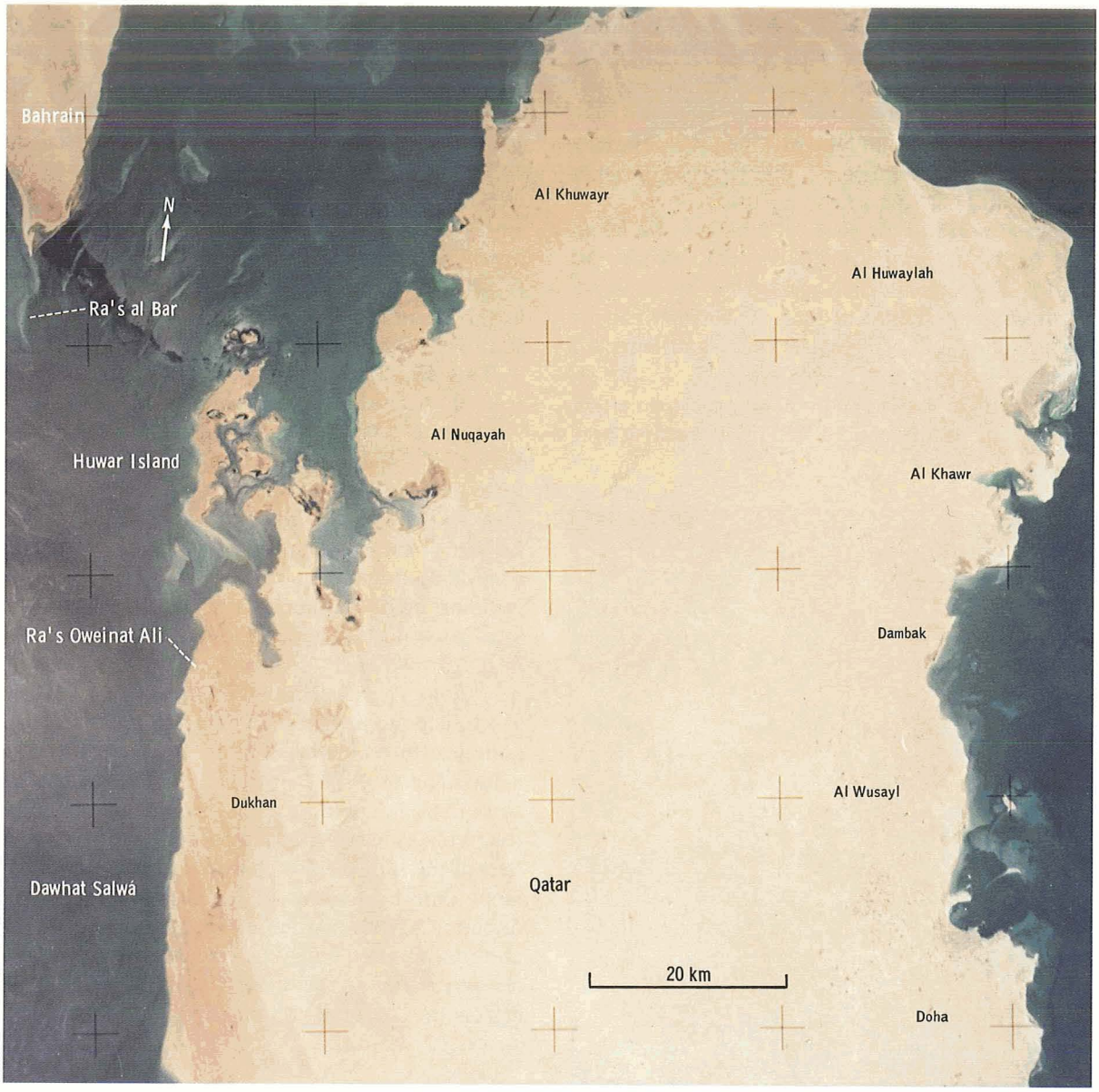


FIGURE 9.—The Qatar Peninsula as depicted in one Apollo-Soyuz photograph (AST-14-967). Note the shades of greenish-blue water that surround the coastline and reflect bottom topography.

overlain in the south and southwest by Eocene to Miocene marls and limestones and in the center by a cobble conglomerate of igneous, metamorphic, and sedimentary constituents. Sand deposits are limited to the south and southeast, where numerous barchan and complex dunes occur.

The ASTP photographs cover the northern two-thirds of the Qatar Peninsula. They clearly show the flat nature of most of the terrain; the only structurally high area on the western margin appears darker than the rest of the peninsula (fig. 9). This long, north-south-oriented rise is known as the Dukhan anticline. It parallels the

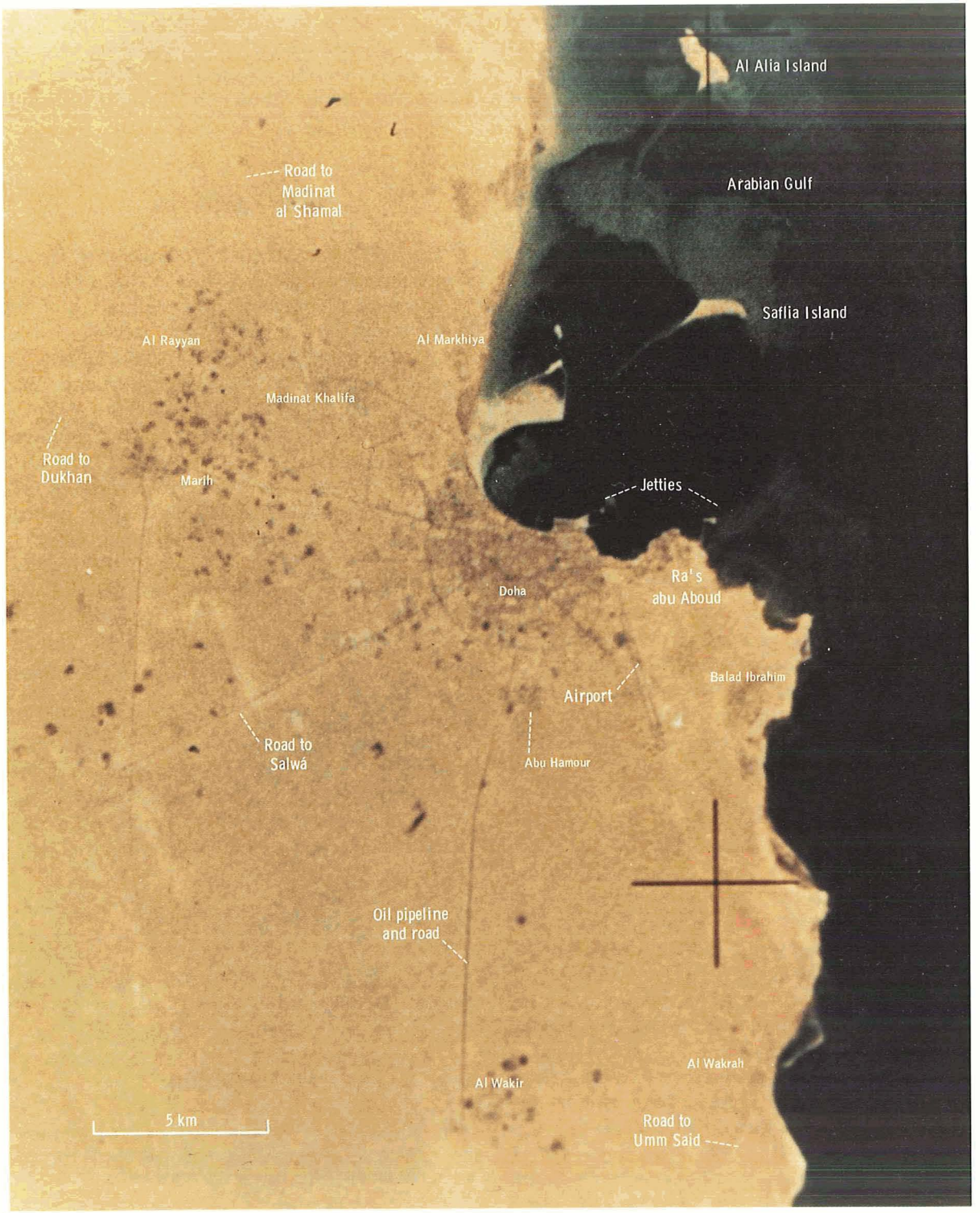


FIGURE 10.—Enlargement of the ASTP photograph in figure 9 showing details of the city of Doha and surrounding area, southeastern Qatar.

coastline of Dawhat Salwá and rises from it as a chain of hills approximately 100 m high. The anticline is approximately 55 km long and varies from 5 to 8 km wide. The anticline has previously been noticed on Landsat images by Grolier (ref. 16). It is interesting to note that this anticline houses the source of the major oilfield of Qatar.

The ASTP photographs clearly show numerous bright striations in the northern part of the Qatar Peninsula. These parallel streaks are reminiscent of the striations on San Miguel Island off the coast of California (ref. 13, p. 34). The brightest streak in figure 9 occurs between the cities of Al Huwaylah and Al Khawr. Other smaller streaks emanate from the northern and west-central coastlines of the peninsula.

The rocks in this streaked region, locally known as *barr Gatar*, consist of Tertiary carbonate rocks, which are undergoing strong wind erosion (ref. 16). These bright streaks consist of sand blown from the beaches along the northern shores and of particles eroded off the surface of the limestone plateau. The streaks trend north-northwest and taper toward the south-southeast. This direction indicates the trend of particle transport by the dominant northwesterly wind, the *shamal*. Based on field observations by the author, these streaks are the most likely source of the barchan and complex dunes that occur in the southeastern corner of the Qatar Peninsula, south of the capital city of Doha (fig. 9).

The natural color of the ASTP photograph helps to clearly delineate the coastline of the peninsula. It also helps to distinguish various color changes in the surrounding waters, which probably reflect bottom topography. Between Ra's al Bar at the southern tip of the island of Bahrain and Huwar Island west of the Qatar Peninsula, a dark band of water occurs. Its texture and dark color are reminiscent of island wakes (e.g., see fig. 4); however, its nature is not fully understood.

Some of the major features of the city of Doha were depicted in the ASTP photograph. An enlargement (10× the original negative) was made of the area to check the resolution as well as the color sensitivity of the photograph. The result is shown in figure 10. The enlargement clearly shows three circular beltways that ring the city. The Doha International Airport and all the major desert roads to the north, west, and south are clearly distinguished. At this scale (fig. 10), the photograph is useful to city planners. This attests to the color sensitivity as well as the resolution of the original ASTP photographs.

CONCLUSIONS

The ASTP stereostrip of photographs across the Arabian Peninsula shows all its major geologic and structural provinces. The natural color of these photographs enables the recognition of boundaries between the many surface units. It also enables detailed study of lineaments and drainage patterns in the massifs of the Arabian shield on the west, as well as dune patterns in the sandy interior plains.

The ASTP photographs are also useful in updating maps and charts, particularly of the coastal areas. They show that existing charts do not correctly portray the Red Sea islands off the coast of Yemen and their boundaries. Analysis of these photographs also resulted in the recognition of a circular granitic body in northern Yemen that had apparently been overlooked by geological mappers.

Based on the utility of these photographs, it is recommended that future Earth-orbital missions include the acquisition of stereographic, high-resolution photographs in natural color. These photographs will greatly aid in the study of vast desert regions such as the Arabian Peninsula.

ACKNOWLEDGMENT

This research was performed under NASA contract NAS9-13831.

REFERENCES

1. McKee, Edwin D.; Breed, Carol S.; and Fryberger, Steven G.: Desert Sand Seas. Sec. 2 of Skylab Explores the Earth, NASA SP-380, 1977, pp. 5-47.

2. El-Baz, Farouk: The Meaning of Desert Color in Earth Orbital Photographs. Photogramm. Eng. & Remote Sens., vol. 44, no. 1, 1978, pp. 69-75.

3. El-Baz, Farouk; and Mitchell, D. A.: Earth Observations and Photography Experiment MA-136. Sec. 10 of Apollo-Soyuz Test Project Preliminary Science Report, NASA TM X-58173, 1976.

4. Harris, William H.; and Levey, Judith S., eds.: The New Columbia Encyclopedia, Columbia University Press, 1975.

5. Map of the Arabian Peninsula, Scale 1:2 000 000. U.S. Geol. Survey Misc. Geol. Inv. Map I-270 B-2, 1965.

6. Powers, R. W.; Ramirez, L. F.; Redmond, C. D.; and Elberg, E. L., Jr.: Geology of the Arabian Peninsula—Sedimentary Geology of Saudi Arabia. U.S. Geol. Survey Prof. Paper 560-D, 1966.

7. Geological Map of the Arabian Peninsula, Scale 1:2 000 000, U.S. Geol. Survey Misc. Geol. Inv. Map I-270 A, 1963.

8. Muehlberger, W. R.; Gucwa, P. R.; Ritchie, A. W.; and Swanson, E. R.: Global Tectonics: Some Geologic Analyses of Observations and Photographs From Skylab. Sec. 3 of Skylab Explores the Earth. NASA SP-380, 1977, pp. 49-88.

9. Blodget, H. W.; Brown, G. F.; and Moik, J. G.: Geological Mapping in Northwestern Saudi Arabia Using Landsat Multispectral Techniques. NASA TM X-70961, 1975.

10. Earth Photographs from Gemini III, IV, and V. NASA SP-129, 1967.

11. Allison, Lewis J.: Geological Applications of Nimbus Radiation Data in the Middle East. NASA TM X-71207, 1976.

12. Eliason, Eric M.; and Soderblom, Laurence A.: An Array Processing System for Lunar Geochemical and Geophysical Data. Proceedings of the Eighth Lunar Science Conference, Geochim. et Cosmochim. Acta, Suppl. 8, Vol. 1, Pergamon Press, 1977, pp. 1163-1170.

13. El-Baz, Farouk: Astronaut Observations From the Apollo-Soyuz Mission. Vol. 1 of Smithsonian Studies in Air and Space, Smithsonian Institution Press (Washington, D. C.), 1977.

14. Grolier, M. J.; and Overstreet, W. C.: Preliminary Geologic Map of Region East of Sa'dah, Yemen Arab Republic (Landsat-1 Image No. 1117-06553), Scale 1:500 000. U.S. Geol. Survey, Open File Report 76-740, 1976.

15. Philby, H. St. John B.: The Empty Quarter. Henry Holt and Company (New York), 1933.

16. Grolier, M. J.: Interpretation of Landsat Images, Qatar. U.S. Geol. Survey, Open File Report 77-295, 1977.

Monte Desert of San Juan, Argentina, as Photographed by ASTP

Delia M. Warner[a] *and Farouk El-Baz*[a†]

ABSTRACT

Apollo-Soyuz photographs of the Monte Desert in southeastern San Juan, Argentina, were used for a reconnaissance survey of large-scale desert landforms. The Apollo-Soyuz color photographs were helpful in distinguishing lineaments and probable faults, drainage patterns, rock types, and soil-tonal variations. These photographs were especially useful in studying the distribution of sand deposits and large-scale dune morphology.

The photographs reveal that the physiographic setting of the study area is characterized by mountain-and-bolsón topography controlled mainly by faulting. Most of the lineaments detected on the photographs appear to correspond to faults, and some of them may provide evidence of recent fault movement in the area. Typical topographic features include barren, deeply dissected block mountains bordered by slopes of alluvial materials that descend to a flat-floored desert basin.

The most prominent features on the desert floor are two dune fields. The larger field lies south of the town of Vallecito and is approximately 1300 km^2; the smaller dune field is near the town of Marayes and is approximately 160 km^2.

In the southern part of the Vallecito dune field, draa-size complex ridges display steep western flanks and gently sloping eastern flanks. These ridges are diagonally crossed by smaller linear dunes. In the central part, draa-size crescentic dunes with elongated horns abound; these horns may be affected by a seasonal cross wind called the zonda. The complex array of transverse, longitudinal, and oblique elements displayed by the Vallecito dunes cannot easily be explained. These patterns may be controlled by changes in climate, underlying and surrounding topography, wind regime, amount of sediment available, and grain-size characteristics. It is recommended that fieldwork be conducted to establish the roles of these factors in the formation of the complex Vallecito dunes.

INTRODUCTION

Photographs taken from Earth orbit provide a very practical means of studying the vast desert environment. Because of their large areal coverage, these orbital photographs are especially helpful in mapping regional patterns of sand distribution, in studying large-scale dune morphology, and in determining the direction of sand movement (refs. 1 to 4). In addition, deserts are particularly suitable for orbital photography because the general lack of cloud cover over arid regions improves image quality and because the size, remoteness, and inaccessibility of many deserts make reconnaissance ground surveys difficult and costly. Such preliminary surveys, which would include the general descriptions of desert landforms and the selection of areas for detailed fieldwork, can easily be made with orbital photographs.

[a]National Air and Space Museum, Smithsonian Institution.

[†]Principal Investigator.

For these reasons, desert studies were an important part of the Earth Observations and Photography Experiment on the Apollo-Soyuz Test Project (ASTP), and excellent data were obtained of desert regions in many parts of the world (ref. 1). Of particular interest here are the ASTP data pertaining to part of the Monte Desert of Argentina. In this study, photographs and visual observations by the ASTP crewmembers are used to survey large-scale desert landforms of the Monte Desert. As part of the study, thematic maps of sand distribution are presented, and the morphology of large-scale dune forms is examined.

ASTP DATA

The ASTP photographs of Argentina include 11 photographs taken with a 70-mm Hasselblad reflex camera and 1 photograph taken with a 35-mm Nikon camera. The photographs were obtained shortly after sunrise on spacecraft revolution 73 (July 20, 1975) and on revolution 88 (July 21, 1975); the Sun-elevation angles were 20° and 15°, respectively. Both near-vertical and low-oblique Hasselblad photographs were taken, and the area covered by individual frames ranged between 2500 km^2 and 6400 km^2. In contrast, the Nikon photograph covered more than 30 000 km^2 (fig. 1).

For Argentina, the verbal data include the astronauts' comments on (1) the shape of a dune field in the Monte Desert, (2) the dune patterns within the same field, and (3) the relationship of these dunes to adjacent mountains. A transcript of the ASTP crewmembers' visual observations is in reference 2.

STUDY AREA

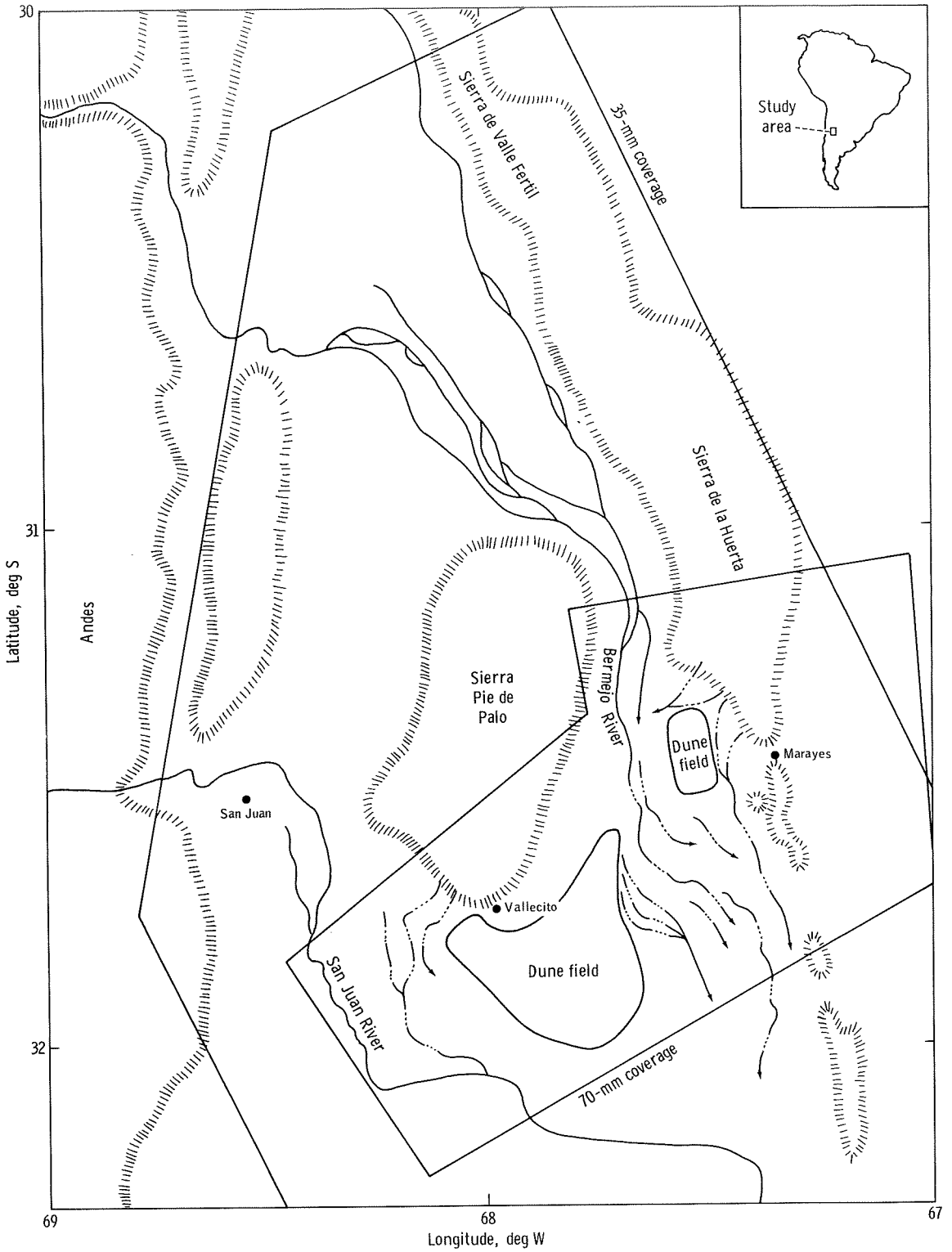
The ASTP photographs of Argentina provide an excellent regional view of desert landforms in part of the Monte Desert, a rainshadow desert lying along the eastern base of the Andes between latitudes 28° and 35° south (refs. 5 and 6). In this region, the high Andean Cordillera acts as an orographic barrier to moisture-laden easterly moving Pacific air; this brings heavy precipitation to the windward Chilean slopes, but the winds that descend the eastern leeward slopes are dry. The Monte Desert environment is characterized by flat-bottomed depressions that are often occupied by salt pans and that are usually bounded by high mountains (ref. 6).

The ASTP Hasselblad photographs only cover a small part of the Monte Desert in the southeastern corner of San Juan Province. The center of the study area is located at latitude 31°45′ south and longitude 67°45′ west (fig. 1).

Southeastern San Juan Province is one of the most arid parts of Argentina. According to meteorological records for its capital, San Juan City (31°36′ S, 68°33′ W), the mean annual precipitation averaged over a period of 20 years is only 84 mm (3.3 in.).[1] Temperatures vary annually between a mean maximum of 298.7 K (25.6° C) and a mean minimum of 283.2 K (10° C). Figure 2 shows the monthly values for mean maximum temperature, mean minimum temperature, and mean precipitation. According to these data, most of the rainfall in San Juan City occurs in the hot summer months (December through February) when evaporation is most intense. As a result, the amount of water available for runoff is small (ref. 7, p. 205). In fact, the only permanent streams in the study area (the San Juan and Bermejo Rivers) originate high in the Andes. Further evidence for the aridity of southeastern San Juan is provided by Burgos and Vidal (ref. 8) who calculate a mean annual potential evapotranspiration of approximately 900 mm and a mean annual water deficiency between 700 and 800 mm.

[1]Meteorological data for the city of San Juan were obtained from the National Climatic Center in Asheville, North Carolina.

FIGURE 1.—Sketch map of southeastern San Juan, Argentina, showing the boundaries of the ASTP photographic coverage with the 35-mm Nikon camera and the 70-mm Hasselblad camera. →


30
31
32
69
68
67
Latitude, deg S
Longitude, deg W
Andes
Sierra de Valle Fertil
35-mm coverage
Sierra de la Huerta
Sierra Pie de Palo
Bermejo River
Dune field
Marayes
San Juan
Vallecito
Dune field
San Juan River
70-mm coverage
Study area

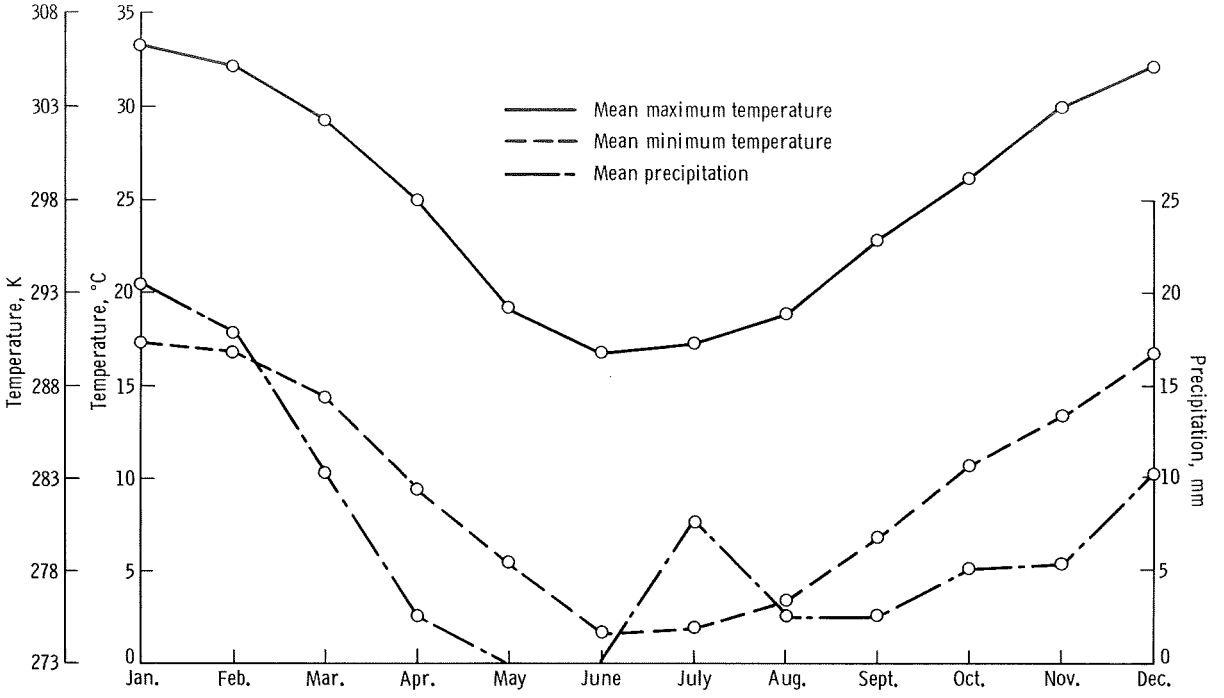


FIGURE 2.—Graph showing the monthly values for mean maximum temperature, mean minimum temperature, and mean precipitation for San Juan City. Meteorological data were obtained from the National Climatic Center in Asheville, North Carolina.

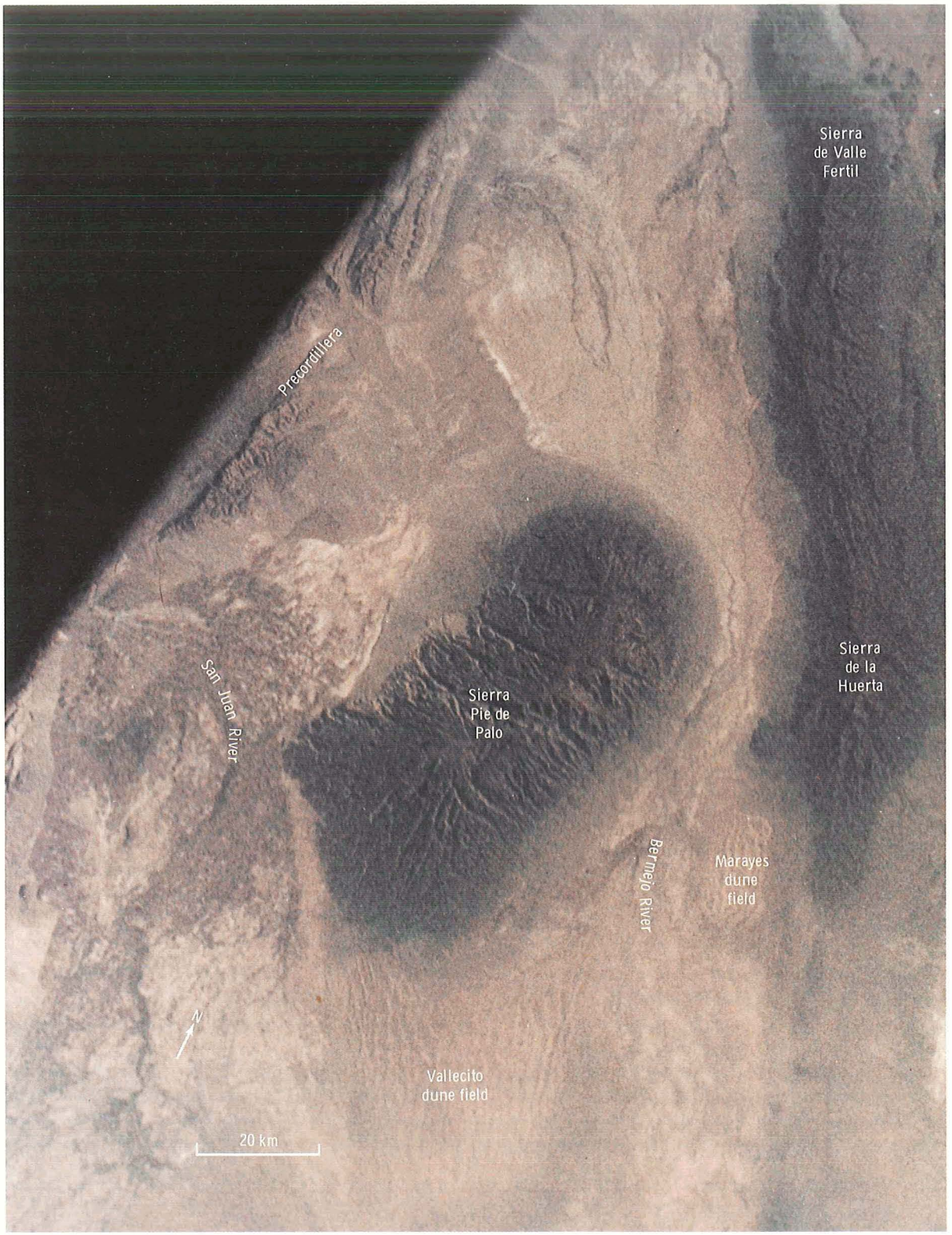
Meteorological data for San Juan City indicate that local surface winds are predominantly from the south. However, another noteworthy surface wind is the zonda, a warm, dry katabatic wind that descends the lee side of the Andes (ref. 9, p. 1156). Data on surface-wind velocity and direction reveal that in San Juan the zonda is a strong seasonal wind from the northwestern quarter occurring mainly from June through August. For these 3 months, the maximum winds observed over 6 years were from the west (20 m/sec in June), the northwest (20 m/sec in July), and the northwest (25 m/sec in August).

PHYSIOGRAPHIC SETTING

The physiographic setting of the study area is characterized by fingerlike, generally north-south-trending mountain ranges and deep alluvium-filled fault basins (ref. 7, p. 201). Within these basins, drainage is essentially endorheic, and playas often occupy the lowermost parts of the basin floors. This is known as mountain-and-bolsón topography and is similar to the basin-and-range physiographic province in the western United States. In southeastern San Juan, elevations range from 500 m on the desert floor to more than 2500 m in the mountains.

The ASTP photographs reveal the typical topographic features that distinguish the Argentinean mountain-and-bolsón landscape. Figure 3 is an ASTP Nikon photograph covering most of eastern San Juan. Although the quality of this photograph is poor, the major landforms are easily recognized. These landforms include barren, deeply dissected mountains bordered by slopes of alluvial materials that descend to a flat desert basin known as Travesía Bolsón. It is in-

FIGURE 3.—ASTP Nikon photograph showing some of the typical topographic features of southeastern San Juan, Argentina. These features include barren, deeply dissected block mountains encircled by slopes of alluvial materials. Slopes descend to a flat-floored desert basin on which the most conspicuous features are two dune fields (AST-11-679). →


Sierra
de Valle
Fertil
Precordillera
San Juan River
Sierra
Pie de
Palo
Sierra
de la
Huerta
Bermejo River
Marayes
dune
field
N
Vallecito
dune field
20 km

teresting to note that the only agricultural patterns distinguishable in this photograph are situated where the San Juan River comes down from the Andes and debouches onto the flat surface of Travesía Bolsón.

On the Nikon photograph (fig. 3), two different rock units can be distinguished on the basis of texture, color, and form. To the far west, rocks of the Precordillera comprise the first group and are characterized by their lighter tone and by their appearance as elongate asymmetric ridges of folded rocks. Rocks of the second group are darker in tone and have a massive appearance. These include the north-northeast trending Sierra Pie de Palo and the north-northwest trending Sierra de la Huerta, which rise more than 2500 m above the surrounding desert plain.

Sierra Pie de Palo and Sierra de la Huerta are structurally related to the Pampean Ranges, which are basically block mountains bounded by north-south-trending faults (refs. 7 and 10). They are composed of late Precambrian to early Paleozoic metamorphics and migmatites frequently intruded by plutonic rocks (ref. 10). The Pampean Ranges owe their present-day morphotectonic structure to block faulting and tilting in the Tertiary and Quaternary (refs. 10 and 11). The fact that tectonic activity in the study area persists to this day is attested by the occurrence of strong earthquakes; the city of San Juan was virtually destroyed by an earthquake on January 15, 1944. In addition, the tectonic nature of the landscape can be seen in the regional outlines of Sierra Pie de Palo and Sierra de la Huerta (fig. 3); these mountains have the appearance of tilted blocks bounded on their longer sides by roughly parallel faults.

Parts of Sierra Pie de Palo and Sierra de la Huerta were also photographed with the Hasselblad reflex camera. Although these photographs do not cover as large a geographic area as the Nikon photograph (fig. 1), they are superior in quality and resolution. For example, in figure 4 the topographic manifestations of faults and fractures are well displayed, and photolineaments can easily be mapped. This can, in part, be attributed to the relatively higher resolution of the Hasselblad photograph and to the low Sun-angle illumination, which accentuates relief.

When the photolineaments observed on the ASTP photographs were compared with faults on a published geologic map of the area (ref. 12), it was evident that a number of new features could be recognized (fig. 5). For example, in figure 4 three parallel lineaments that are visible along part of the eastern flank of Sierra Pie de Palo may be indicative of recent fault movement in the area. The most prominent lineament is marked by a sharp, linear contact between the mountain front and the alluvial slopes and by triangular facets that truncate mountain spurs ("A" in figs. 4 and 5). The other two lineaments, which occur toward the base of the alluvial slopes, run parallel to the mountain front. The topographically higher of these two lineaments ("B" in figs. 4 and 5) is on the lower alluvial slope and is distinguished by the sharp color difference between the gray alluvial sediments above the lineament and the lighter toned material below it. At the base of the slope, the lowermost lineament ("C" in figs. 4 and 5) appears to be a low scarp when viewed stereoscopically. This could be explained by a fault parallel to the mountain front, which was responsible for the exposure of previously buried sediments.

On and around Sierra de la Huerta, a number of lineaments that are probably the surface expressions of faults and fractures were also mapped from ASTP photographs. In figure 4, the most prominent feature is an almost north-south-trending lineament ("D" in figs. 4 and 5) cutting across the alluvial slopes bordering the western flank of Sierra de la Huerta. On the geologic map of San Juan (ref. 12), this feature is drawn as a fault (fig. 5). Between this fault and the mountain to the east, the ASTP photographs revealed deeply incised drainage channels ("E" in fig. 4); this entrenchment could be caused by tectonic uplift of the massif.

Another interesting feature depicted on the ASTP photographs is the dome-shaped rock body projecting from the main mass of Sierra de la Huerta ("F" in fig. 4). In plan view, this rock body

is elliptical, and on the photograph, it is similar in color to Sierra de la Huerta. Its eastern and western sides are parallel to major lineament trends in the area. Although its dome shape is suggestive of an intrusive origin, it may just be an inselberg whose outline is structurally controlled.

The mountains in the study area are entirely surrounded by slopes of alluvial materials. When infrequent rainstorms occur over the uplands, sediment-laden streams flow down the normally dry steep-sided mountain gorges and deposit most of their load when they encounter the sharp break in slope at the mountain front. The surfaces of the alluvial slopes are characterized by intricately branching systems of stream channels. The paths of these channels are largely controlled by slope, although in one area a rectangular drainage pattern indicates structural control ("G" in fig. 4). In addition, as discussed later, sand deposits have affected drainage patterns.

SAND DEPOSITS

Viewed from Earth orbit, eolian sand deposits have a characteristic appearance and distribution, which can be controlled by a number of factors such as the wind regime, rainfall, vegetation, sand supply, and topography (refs. 3, 4, and 13). On the ASTP photographs of San Juan Province, regional patterns of sand distribution and dune morphology were easily studied. For mapping sand deposits, the most important recognition elements were texture and color. Interpretations of dune morphology, on the other hand, relied on form and pattern and were facilitated by the low Sun-angle illumination (15° to 20°).

In southeastern San Juan, the alluvial slopes surrounding the mountains descend to the flat-floored Travesía Bolsón. This plain is slightly tilted to the east, and its surface is covered by sand dunes and fluviolacustrine deposits (ref. 14, p. 2689). On the floor of the bolsón, the most conspicuous features are two dune fields (fig. 6). The larger field lies south of the town of Vallecito (31°45′ S, 67°59′ W) and will be referred to as the "Vallecito" dune field. The smaller field will be designated the "Marayes" dune field after Marayes (31°29′ S, 67°22′ W), a town 12 km east of the dunes.

Vallecito Dune Field

In figure 6, the most prominent feature on the floor of Travesía Bolsón is the heart-shaped Vallecito dune field, which covers approximately 1300 km^2. On its northern margin, the dune field extends close to the base of Sierra Pie de Palo, which rises more than 2000 m above the surrounding plain. This northern margin is sharp and well-defined, and the boundary between the sand and the alluvial slopes bordering the mountain is easily distinguished. Stream channels descending the slopes are, for the most part, deflected around the dune field. However, some channels enter the field and, during occasional storms, probably wash into the north-central part of the field and flood interdune areas. It is likely that occasional runoff from the uplands has a part in controlling the northern margin of the Vallecito field.

To the west and east, the Vallecito dune field is surrounded by a flat desert plain with intermittent streams and sand deposits. On this plain, interesting patterns of sand distribution are revealed in the relationships between sand deposits, stream channels, cultivated lands, and topography. The nature and distribution of materials on the surface of Travesía Bolsón were interpreted from the ASTP Hasselblad photographs.

On the surface of Travesía Bolsón, immediately west of the Vallecito dunes, three kinds of surface deposits are recognized. One of these deposits is a highly reflective white material that may be a saline deposit. On the basis of color and texture, the other two kinds of deposits are interpreted as sand (figs. 7(a) and 7(b)). The first type of sand deposit is characterized by dark tan-colored sands and by dune forms. These windblown deposits are of wide extent and appear to pose a threat to cultivated lands. Because cultivation is limited by climate in this part of San Juan, irrigation is impor-

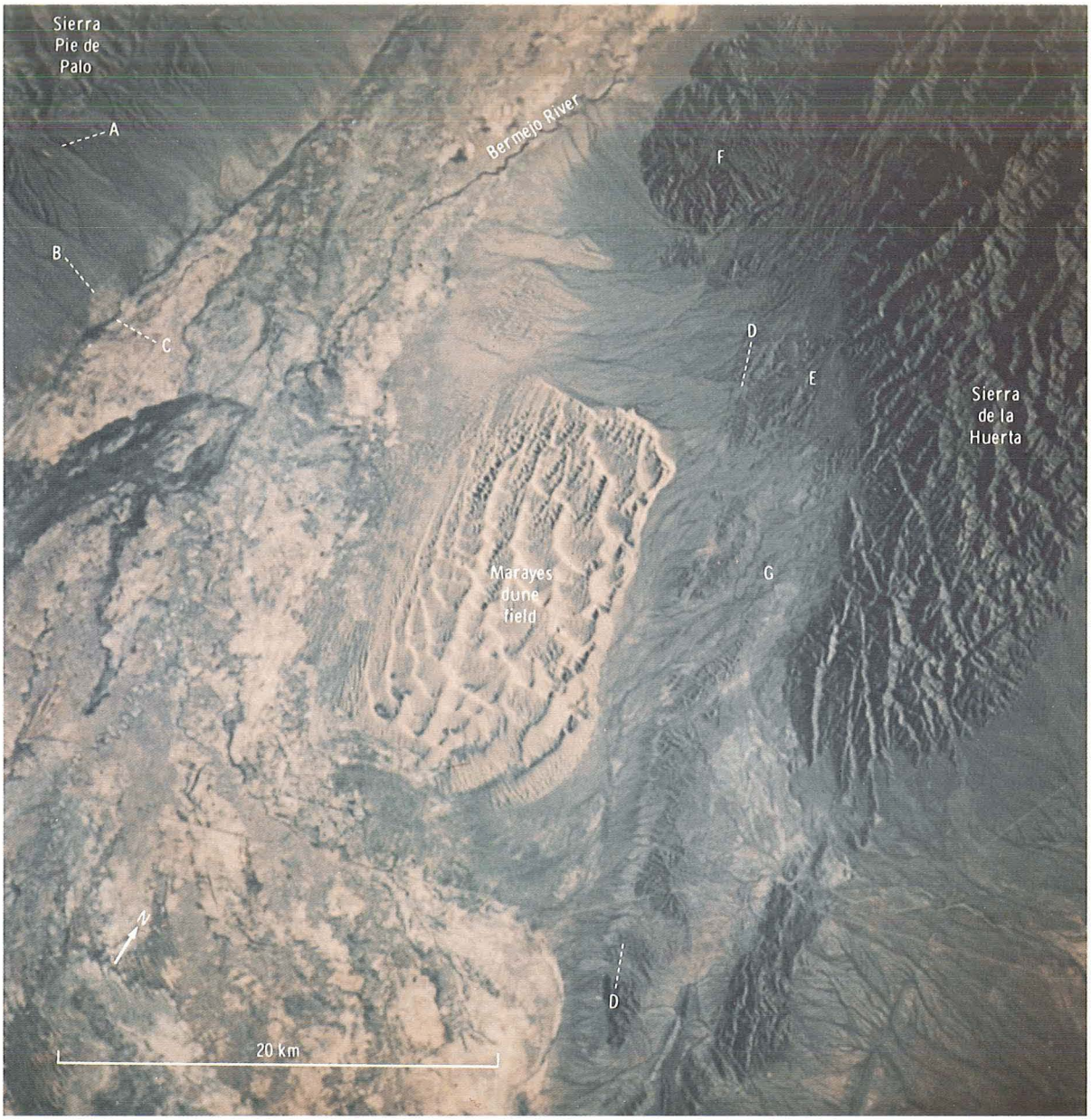


FIGURE 4.—ASTP Hasselblad photograph showing parts of Sierra Pie de Palo and Sierra de la Huerta. In this photograph, the topographic manifestations of faults and fractures are well displayed as photolineaments. Points "A" to "G" designate specific locations referred to in the text (AST-23-1913).

tant, and farmlands exist only along the western side of the basin where streams come down from the Andes. It is easy to imagine how the agricultural economy of this region could be adversely affected by strong southerly winds acting on the sandy soils and dunes (ref. 7).

The second type of sand deposit west of Vallecito dune field is of limited extent (fig. 7(b)). In plan view, these deposits are fan-shaped with an apex lying close to Sierra Pie de Palo and branches extending to the south and south-southeast. No dune forms are observable in these

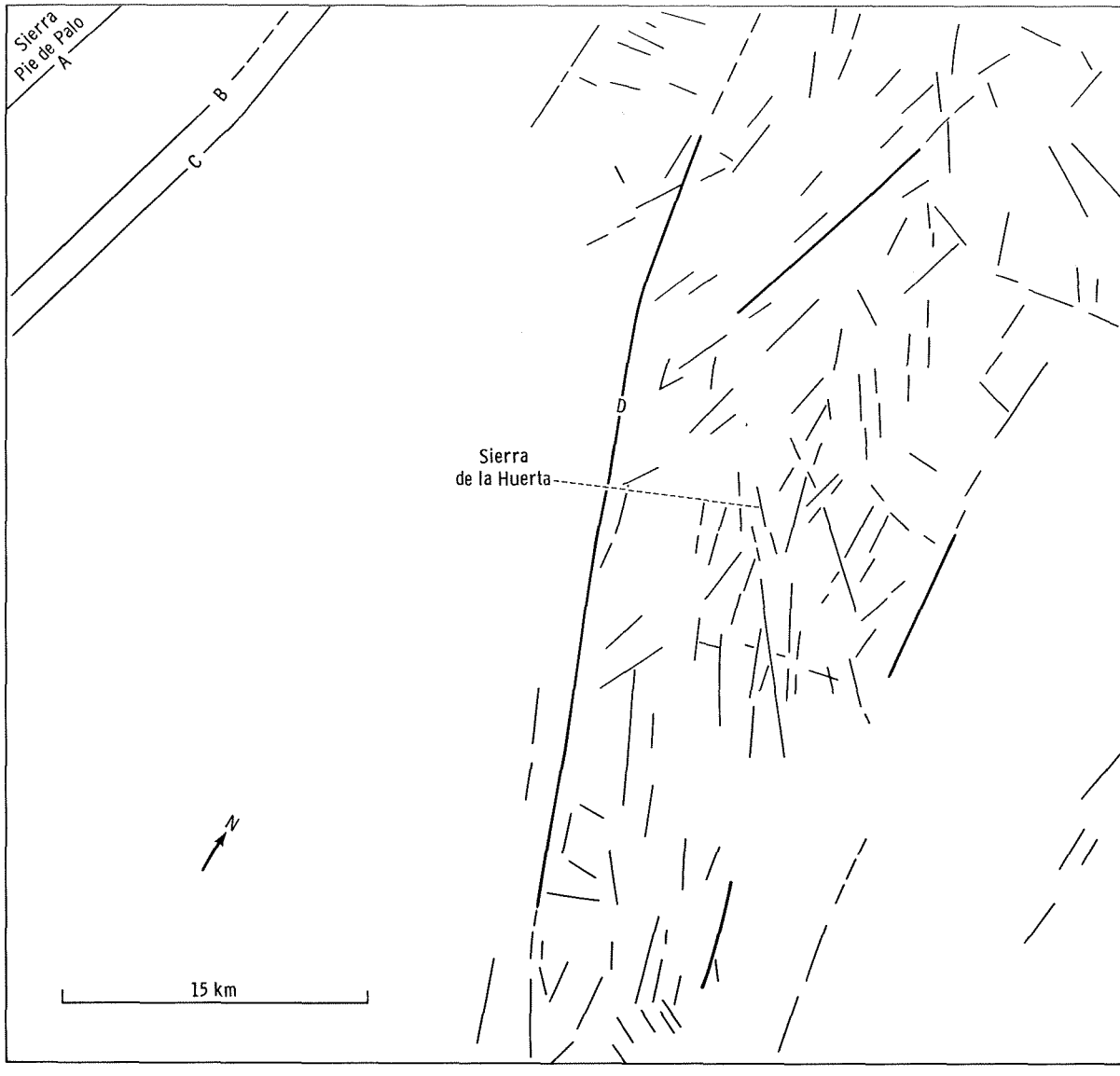


FIGURE 5.—Sketch showing photolineaments mapped from a 4× enlargement of AST-23-1913. Bold lines indicate lineaments drawn as faults on a published geologic map of San Juan (ref. 12). Points "A" to "D" designate lineaments referred to in the text.

deposits, and the sand is lighter in color than sands of the first type. These light-toned sand deposits appear to originate close to the southwestern flank of Sierra Pie de Palo.

Along the base of the mountain, a narrow band of the first type of sand occurs, and in places, it is breached by stream channels. It seems likely that, after an occasional heavy rainfall in the upland, runoff would rapidly move downslope along stream channels and wash away the windblown sand at the foot of the slope. The short-lived streams, after spreading out laterally across the plain, would soon deposit their load as they disappear. Therefore, the light-colored sand deposits may be the result of fluvial rather than eolian deposition.

East of the Vallecito dune field, the ASTP photographs reveal small linear dunes migrating

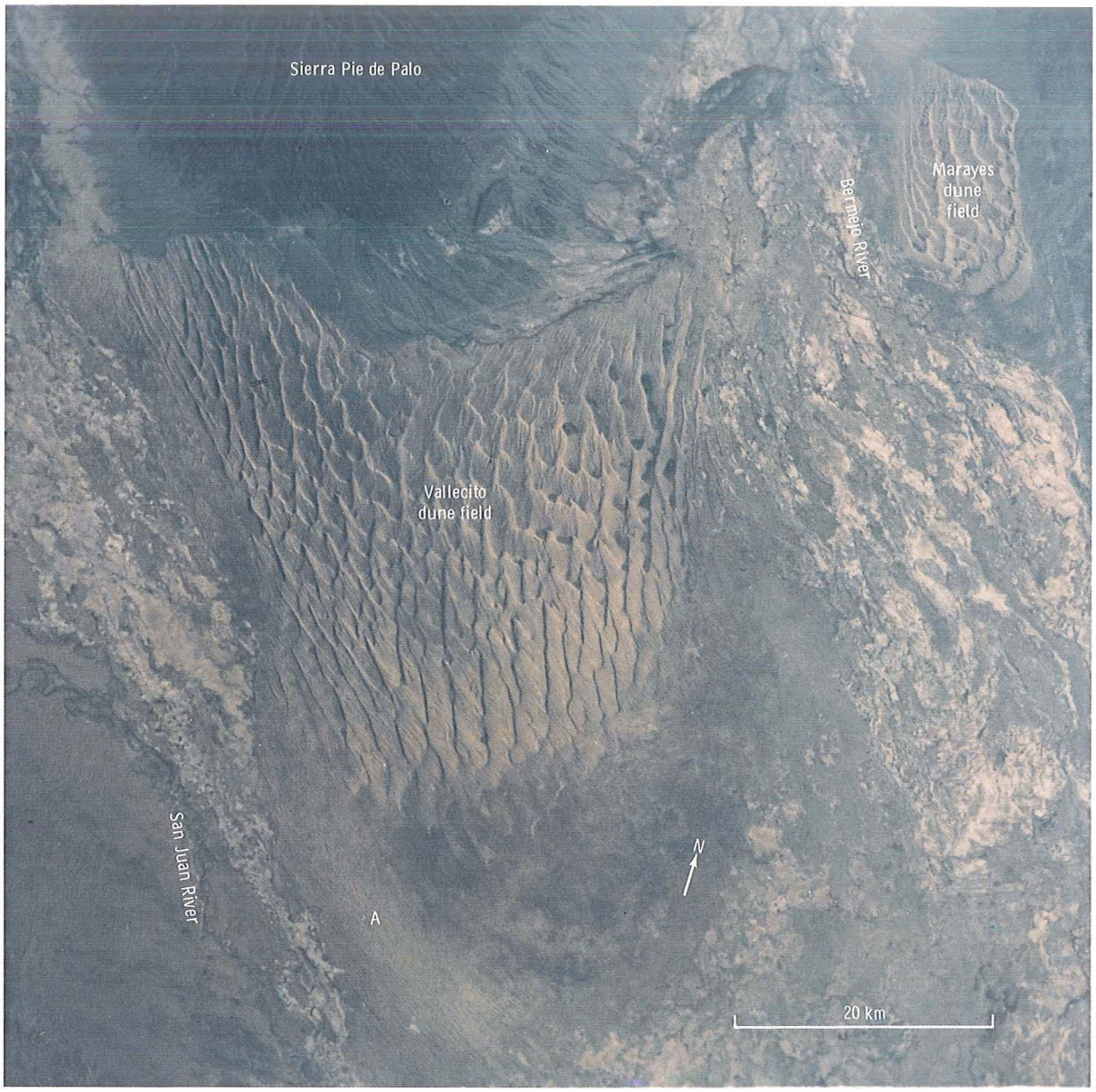


FIGURE 6.—ASTP Hasselblad photograph showing the complex sand dune patterns characterizing the Vallecito and Marayes dune fields (AST-27-2340). The letter "A" designates the location of narrow linear dunes referred to in the text.

toward and merging with the larger Vallecito field (figs. 6 and 8). The trends of these dunes veer in a clockwise manner from NW-SE to NNE-SSW. This change in trend is probably the result of a change in the prevailing wind pattern, which would be deflected by the protruding Sierra Pie de Palo. These linear dunes are generally less than 5 km long; their dune/interdune ratio is approximately 1:1; and some Y-junctions that open to the southeast are present. These dunes are probably longitudinal forms parallel to the prevailing wind direction. Outside the southwestern corner of the Vallecito field, similar linear dune forms occur ("A" in fig. 6), but the northwestward migra-

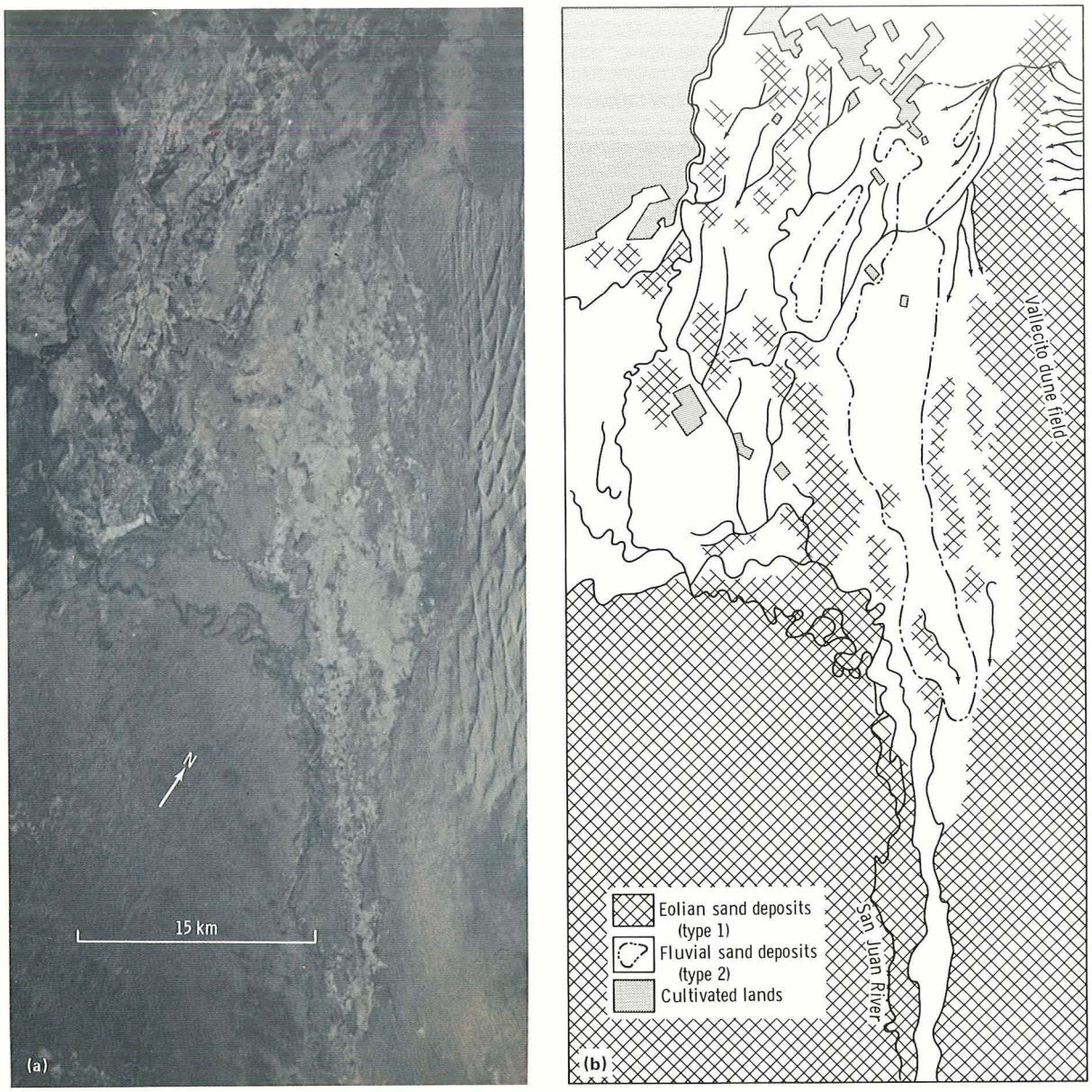


FIGURE 7.—Sand distribution west of the Vallecito dune field. (a) Part of Hasselblad photograph AST-23-1910 showing area covered by figure 7(b). (b) Sketch illustrating the relationship of sand deposits with stream channels and cultivated land. Two types of deposits are shown. The first type is probably eolian, but the second type of deposit may be fluvial.

tion of these dunes appears to be limited by a stream channel and a steep, narrow north-south-trending sand ridge.

In addition to the linear dune forms east of the Vallecito field, somewhat amorphous dark-colored sand deposits could also be discerned on the ASTP photographs. Figure 8 shows that the distribution of these deposits is intimately related to the subparallel drainage pattern. This type of drainage pattern can be attributed to either a pronounced regional slope or to parallel topographic features, which in this case would be the sand deposits (ref. 15). It is difficult to determine whether the sand distribution is governed by the

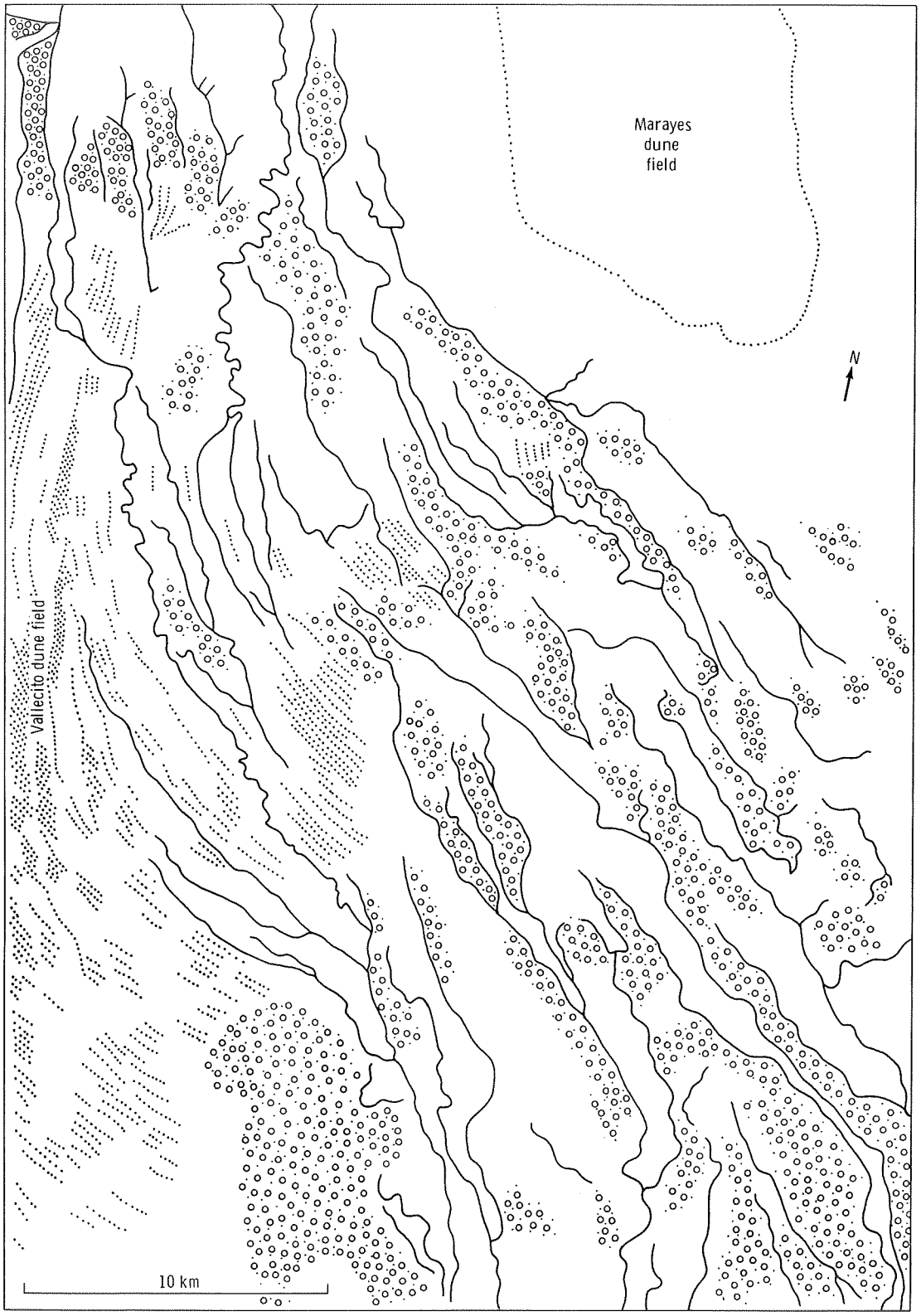

Marayes
dune
field
N
Vallecito dune field
10 km

FIGURE 8.—Sketch showing sand distribution east of the Vallecito dune field. Two types of eolian sand deposits are indicated: (1) narrow, linear dunes (dotted lines) and (2) amorphous dark-colored sands (circle and dot pattern). (Drawn from an enlargement of AST-27-2340, fig. 6.)

drainage pattern or whether the opposite case is true and the drainage pattern is controlled by the distribution of sand deposits.

The ASTP photographs reveal that the Vallecito dune field displays a fishscale pattern of numerous, irregular crescentic dunes and linear sand ridges. During postmission debriefings, the ASTP crewmembers described this unusual dune field as follows (ref. 2, p. 196):

> Okay, it's right over the edge of the Andes Mountains. Where the mountains end, there is a little area in between and those (dunes) start. And you could really see how they were crescents; it looked like maybe the head of a crescent would wash out, and it would tend to be a linear one with lineations on a side . . . .

Study of the ASTP photographs show two different size eolian bedforms within the Vallecito field (fig. 6). The major forms have wavelengths greater than 0.5 km and will be referred to as draa (ref. 16). The minor forms, which are migrating over the draa, are dunes. The existence of these draa-size bedforms implies a plentiful supply of sand, most of which is probably derived from the fluvio-lacustrine deposits of Travesía Bolsón.

In the southern part of the field, draa-size complex ridges display steep western flanks and gently sloping eastern flanks. The crests of these draa ridges are not absolutely straight, and they exhibit curved crescentic elements. These ridges appear to be complex combinations of linear and crescentic elements. The distance from crest to crest varies between 1 and 2.3 km, and small linear dunes are alined diagonally across the eastern slopes of the draa.

The central part of the Vallecito dune field is characterized by imbricated draa-size crescentic forms with elongated horns. In the western half of the field, the right-hand horn is the one that is usually elongated. This could be attributed to the action of an important crosswind, perhaps the seasonal zonda. Superposed on these draa forms is a finer pattern of parallel linear dunes whose trends are consistent with the trends of the elongated horns.

In the northwestern part of the field, sharp-crested narrow linear ridges 5 to 11 km long are characteristic. In the northeastern part, sand cover is incomplete, and the substrate is exposed in sand-free hollows. A decline in dune size is observed toward the northeastern and northwestern edges of the field. This is most likely a function of sand supply.

On orbital photographs, the Vallecito dune field presents a complex array of transverse, longitudinal, and oblique trends. These complex patterns can be attributed to a number of factors such as changes in climate, the underlying and surrounding topography, the wind regime, the amount of sediment available, and grain-size characteristics (ref. 13). The roles of each of these factors can only be determined through extensive and detailed fieldwork, although some inferences can be made about the wind regime from a study of ASTP photographs. This is done by analyzing dune trends and slipface orientations.

Probably the most important factor in determining dune form is the direction and strength of the wind in relation to the sand supply (ref. 17, p. 13; ref. 18). To provide further data on the wind regime in the study area, N-Summaries of surface-wind velocity and direction were obtained from the National Climatic Center in Asheville, North Carolina. These N-Summaries contain data on the percentage occurrence by velocity categories (e.g., 0.51 to 1.54 m/sec, 2.06 to 3.09 m/sec (1 to 3 knots, 4 to 6 knots) etc.) and by direction of surface winds at San Juan City. These data are plotted on circular histograms (called sand roses) according to the method described by McKee et al. (ref. 4) (fig. 9). To obtain a better idea of the distribution of winds capable of moving sand, only winds greater than 5.1 m/sec (10 knots) are used in the calculations. The sand roses in figure 9 show, by month, the potential movement of sand from 16 compass directions; the arrows point downdrift and indicate the hypothetical resultant direction of potential sand movement.

According to the wind data, the prevailing sand-moving winds at San Juan City are from the south, although strong seasonal winds (zonda) from the northwestern quarter occur from June through August. For San Juan City, the annual resultant direction of potential sand movement is toward approximately N5°E. At the Vallecito dune field, 60 km southeast of San Juan City, the dune patterns seem to indicate that the prevailing winds are from the south and southeast. In addition, the dominance of the right-oblique element in the western part of the field suggests the presence of an important crosswind, probably the seasonal zonda. This interpretation of wind regime is based on an analysis of (1) the trends of linear dune forms east of the Vallecito field and (2) the orientations of slipfaces on the crescentic draa forms within the dune field (fig. 10). It was assumed that the crescentic slipfaces were transverse to the prevailing winds and that the linear dunes were longitudinal and parallel to the wind direction.

The occurrence of a topographic obstruction (Sierra Pie de Palo) in the path of the prevailing sand-moving southerly and southeasterly winds has the effect of channeling the wind and diverting sand movement around the flanks of the mountain. However, most of the sand leaving the dune field and blowing around the mountain is probably carried back down to the south by intermittent streams, which soon dry up as they wander across the plain. For example, sand blown around the northeastern side of Sierra Pie de Palo may be channeled to the north along the valley

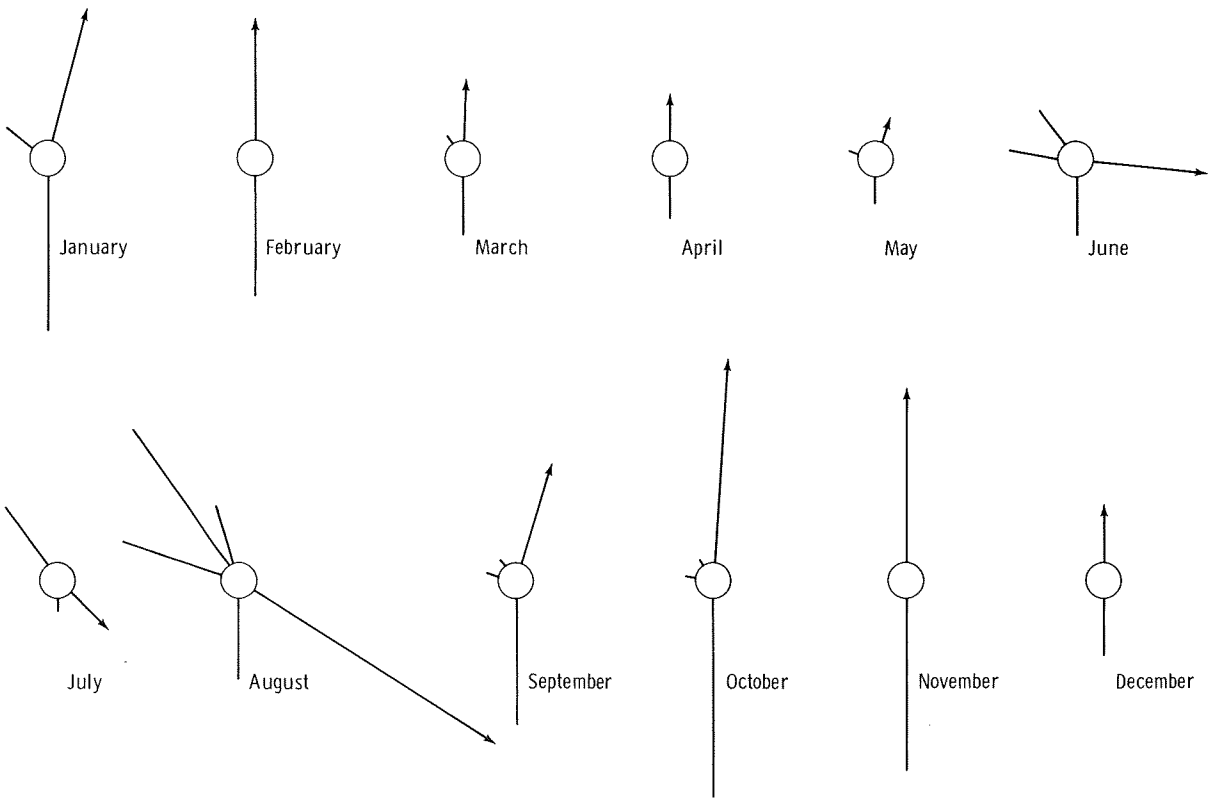


FIGURE 9.—Sand roses for San Juan City showing by month the potential movement of sand from 16 compass directions. Arrows point downdrift and indicate the resultant direction of potential sand movement. These diagrams show that the prevailing sand-moving winds at San Juan are from the south, although strong seasonal winds from the northwestern quarter occur from June through August.

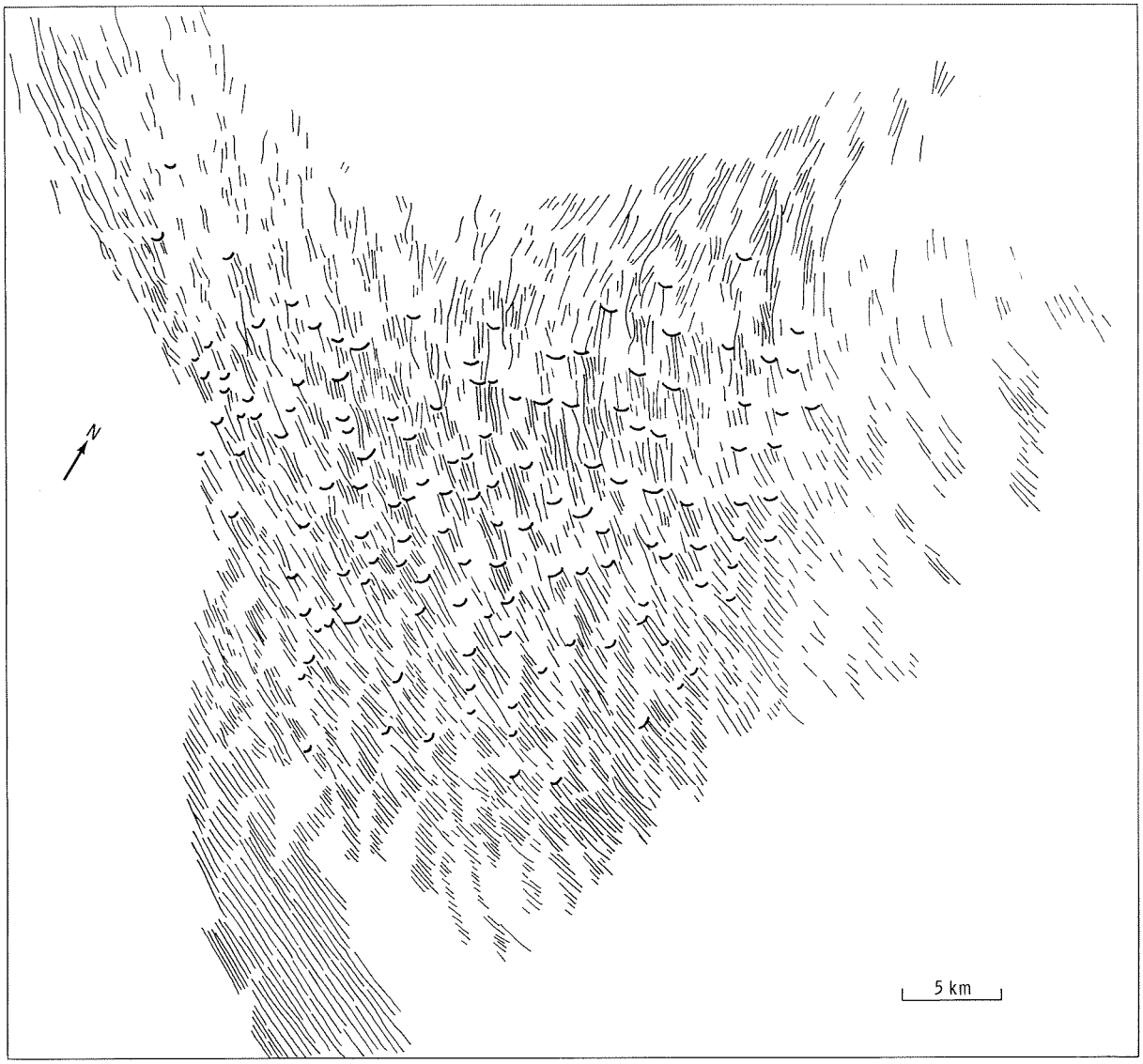


FIGURE 10.—Sketch showing draa-size crescentic elements (bold lines) and dune-size linear elements in and around the Vallecito dune field.

between Sierra Pie de Palo and Sierra de la Huerta. Some of this sand may blow into the Marayes dune field, approximately 25 km northeast of the Vallecito dunes. However, the migration of most of the sand is probably controlled by the Bermejo River, which flows down the valley. Sand may be carried to the south by any of the numerous channels into which the river subdivides. These channels spread out across the plain to the east and southeast of the Vallecito field and soon dry up and deposit their load. The sand may then, once again, be picked up by the wind and blown to the north.

Marayes Dune Field

The Marayes dune field (fig. 11(a)) lies at the foot of Sierra de la Huerta and occupies an area of approximately 160 km^2. The eastern margin of the



FIGURE 11.—The Marayes dune field. (a) Enlargement of part of AST-23-1913. (b) Sketch showing draa-size crescentic elements (bold lines) and dune-size linear elements. Circles indicate the locations of draa-size forms resembling star dunes.

field roughly parallels the 1000-m contour, and the field's rectangular shape is strongly influenced by bordering topographic highs. On the northern and eastern borders of the field, there is a sharp boundary between the sand and the alluvial slopes, and the dunes seem to have altered the courses of streams coming down from the mountain (fig. 11(b)). The western margin of the field is less well defined.

On ASTP photographs, the Marayes dunes are depicted as a complex network of crescentic and linear elements (fig. 11(b)). The most prominent features are the draa-size crescentic forms over which dune-size forms are superposed. The orientations of these crescentic forms, which are transverse to the effective winds, seem to indicate a predominantly bimodal regime of winds from the southeast and south. In the eastern part of the field, dune forms that resemble star dunes may indicate a more complex wind regime. These forms are found at the nodes in the draa patterns where three different trends meet (fig. 11(b)).

CONCLUSIONS

Color orbital photographs are useful in studies of arid environments. This is particularly true in distinguishing lineaments and probable faults, drainage patterns, rock types, and soil-tonal variations. These photographs are especially useful in studying the distribution of sand deposits and

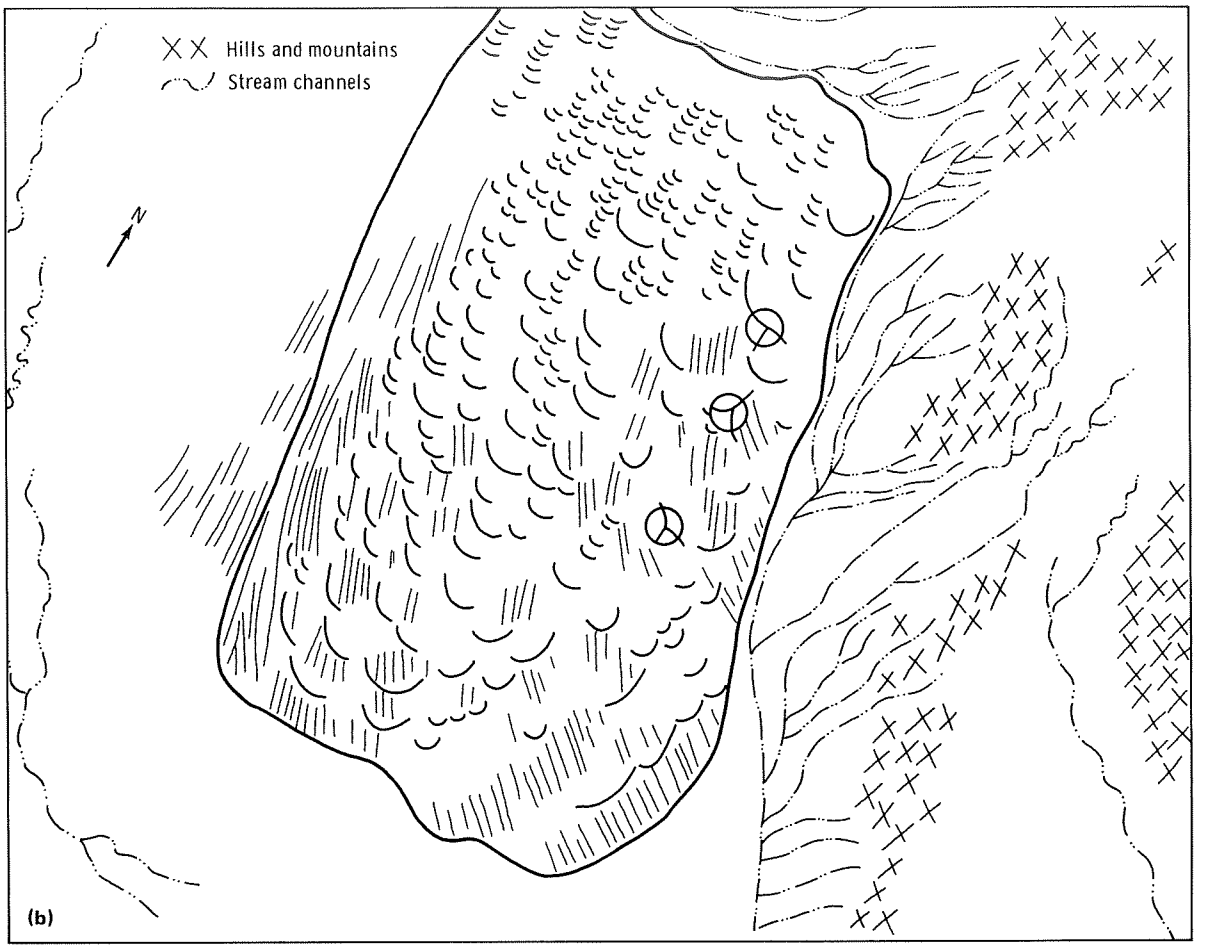


FIGURE 11.—Concluded.

large-scale dune morphology. Low Sun-elevation angles enhance the utility of the ASTP photographs, and it is recommended that additional color, low Sun-elevation photographs be taken of desert regions from Earth orbit.

The study of the two unusual dune fields in southeastern San Juan, Argentina, resulted in the recognition of complex dune patterns that are controlled by numerous factors. The ASTP photographs and preliminary results have been supplied by the authors to the Geological Survey Department of Argentina. It is recommended that field investigations be conducted to establish the relationships between the sand dune patterns and the underlying desert surface, the surrounding mountain highs, the amount of available sand, the grain size, and the local wind regime. Deciphering complex dune patterns such as those displayed by the Vallecito dunes will help in the study of other complex desert dunes. Field investigations would perhaps be best made in cooperation with Argentinean researchers whose understanding of the local geography and geology would be essential.

REFERENCES

1. El-Baz, Farouk; and Mitchell, D. A.: Earth Observations and Photography Experiment MA-136. Sec. 10 of Apollo-Soyuz Test Project Preliminary Science Report. NASA TM X-58173, 1976.

2. El-Baz, Farouk: Astronaut Observations From the Apollo-Soyuz Mission. Vol. I of Smithsonian Studies in Air and Space, Smithsonian Institution Press (Washington, D. C.), 1977.

3. McKee, Edwin D.; and Breed, Carol S.: An Investigation of Major Sand Seas in Desert Areas Throughout the World. Paper G6 in Third Earth Resources Technology Satellite-1 Symposium, Stanley C. Freden, Enrico P. Mercanti, and Margaret A. Becker, eds., vol. I, sec. A, NASA SP-351, 1974, pp. 665-679.

4. McKee, Edwin D.; Breed, Carol S.; and Fryberger, Steven G.: Desert Sand Seas. Sec. 2 of Skylab Explores the Earth, NASA SP-380, 1977, pp. 5-47.

5. Cornejo, Arturo: Resources of Arid South America. Arid Lands in Transition, Harold E. Dregne, ed., Publication No. 90, American Association for the Advancement of Science (Washington, D. C.), 1970, pp. 345-380.

6. McGinnies, William G.; Goldman, Bram J.; and Paylore, Patricia, eds.: Deserts of the World. University of Arizona Press, 1968.

7. Shanahan, Edward William: The Pampean Hinterland and the Pre-Cordilleras. South America. Methuen (London), 1959, Chapter XVI, pp. 201-216.

8. Burgos, J. J.; and Vidal, A. L.: The Climates of the Argentine Republic According to the New Thornthwaite Classification. Ann. Assoc. American Geog., Henry Madison Kendall, ed., vol. 41, 1951, pp. 237-263.

9. Fairbridge, Rhodes W.: The Encyclopedia of Atmospheric Sciences and Astrogeology. Encyclopedia of Earth Sciences Series, vol. II, Reinhold Publishing Corp., 1967.

10. Bonorino, F. González: Argentina. The Encyclopedia of World Regional Geology, Part 1, Rhodes W. Fairbridge, ed., Encyclopedia of Earth Sciences Series, vol. VIII, Dowden, Hutchinson & Ross, Inc. (Stroudsburg, Pa.), 1975, pp. 15-21.

11. Bailey, H. P.; Simpson, B. B.; and Vervoorst, F.: The Physical Environment: The Independent Variable. Chapter 2 in Convergent Evolution in Warm Deserts, Gordon H. Orians and Otto T. Solbrig, eds., Dowden, Hutchinson & Ross, Inc. (Stroudsburg, Pa.), 1977.

12. Argentina, Direccion General De Investigacion Y Desarrollo: Estudio de cuencas aluvionales en las provincias de San Juan y Mendoza. 1973, 4 volumes.

13. Cooke, Ronald U.; and Warren, Andrew: Geomorphology in Deserts. University of California Press, 1973.

14. Dessanti, Raúl: Geologic Outline of Natural Regions of Mendoza, Argentina. Bull. American Assoc. Petr. Geol., vol. 42, no. 11, 1958, pp. 2670-2691.

15. Feldman, Sandra; Harris, Stuart; and Fairbridge, Rhodes W.: Drainage Patterns. The Encyclopedia of Geomorphology, Rhodes W. Fairbridge, ed., Encyclopedia of Earth Sciences Series, vol. III, Reinhold Publishing Corp., 1968, p. 288.

16. Wilson, Ian G.: Aeolian Bedforms—Their Development and Origins. Sedimentology, vol. 19, no. 3/4, Dec. 1972, pp. 173-210.

17. Bigarella, João José: Eolian Environments: Their Characteristics, Recognition, and Importance. Recognition of Ancient Sedimentary Environments, J. Keith Rigby and Wm. Kenneth Hamblin, eds., Paleontologists and Mineralogists, Special Publication No. 16, 1972.

18. Holm, Donald August: Desert Geomorphology in the Arabian Peninsula. Science, vol. 132, no. 3437, Nov. 1960, pp. 1369-1379.

Dunes and Other Windforms of Central Australia (and a Comparison With Linear Dunes on the Moenkopi Plateau, Arizona)

C. S. Breed[a] *and W. J. Breed*[b]

ABSTRACT

Field examinations of sand dunes observed and photographed during the Apollo-Soyuz mission confirm that linear dunes of the sand-ridge variety can be reliably identified from space. Surface similarities of dune shapes and dune distribution patterns are matched by similarities of internal stratification, grain size distribution, slipface development, and relation to wind regimes. These relationships, which differ from those that have been reported in seif dunes, suggest that sand ridges and seifs are probably different varieties of longitudinal dunes that form in different wind regimes.

Internal structures of linear dunes that were examined in central Australia and in northern Arizona are mainly medium-scale, thin cross-beds or cross-laminae with dips commonly less than 20°. These layers occur in tabular and wedge-shaped sets bounded by planar erosion surfaces. The surfaces bounding the sets are commonly near-horizontal; the steeply crosscutting erosion surfaces characteristic of seif dunes are rare. Thin laminae occur as surface sets on all parts of the observed sand-ridge dunes, and these layers dip parallel to the dune surfaces.

Cores of many of the strongly reddened dunes in Australia are structureless, as are cores of the slightly reddish dunes on the Moenkopi Plateau, Arizona. Both the reddening and the lack of structure are interpreted as evidence of aging of dunes in semiarid, subaerial environments punctuated by occasional torrential rains and sheetfloods. A Pleistocene age is accepted by many workers for some of the linear dunes of central Australia, and it is also tentatively suggested for some of the linear dunes on the Moenkopi Plateau, Arizona.

The sand-ridge areas of the Simpson Desert, Australia, and the Moenkopi Plateau, Arizona, have wind regimes that are dominated by one strong, prevailing wind direction, but these wind regimes also include some seasonally bimodal sand-moving winds. Wind records and field evidence in both regions indicate seasonal shifts of effective winds, as well as a strong shepherding effect of the winds from the dominant quarter. The regional trends of the dunes in both regions are nearly parallel to these prevailing winds.

Differences between the internal structures, shapes, and distribution patterns of sand-ridge dunes and seif dunes may reflect differences in the duration of shifting winds. Such shifts are apparently seasonal in some areas of sand-ridge dunes, such as in central Australia and northern Arizona, but are reportedly diurnal in an area of seif dunes at Sabhā, Libya.

Wind erosion by deflation has produced streamlined hills and small ridges in soft sediments, including dune flanks and interdune corridors, and has modified some bedrock outcrops in central Australia. Some wind-grooving of the lower parts of dunes and of interdune corridors in the northwestern Simpson Desert is also sug-

[a]U.S. Geological Survey and Museum of Northern Arizona, Flagstaff, Arizona.

[b]Museum of Northern Arizona, Flagstaff, Arizona.

gested. It is believed that some of the sediments there are brought in by sheetfloods and then reworked by winds into an eolian veneer that includes cross-bedded sands on the crests of the dunes. In other areas, however, the dunes are wholly eolian constructional features superimposed on the gravel plains.

Astronauts aboard the Apollo spacecraft identified the same hue, chroma, and value of red sand in dunes of central Australia that ground survey teams found in the main body of the Simpson Desert. The close correspondence of space and ground color determinations is attributed to the presence of clear air over the desert and to the fact that, in both cases, the Munsell Color Chart was viewed in sunlight. Ground examination confirms that within each field of dunes, relative degrees of redness can help discern sequences of depositional events in that area (given a uniform sand supply and climatic zone). Regional variations in color, together with regional patterns of dune distribution, size, and shapes, can be well defined by trained observers from space. Reconnaissance from space is ideal for identifying key sites for field studies of specific geomorphic problems in remote desert regions.

INTRODUCTION

Apollo-Soyuz Test Project (ASTP) photographs and visual observations cover much of central Australia, including most of the Simpson Desert, Lake Eyre, Sturt's Stony Desert, the lower Cooper Creek channel country, and the Strzelecki Desert north of Lake Frome (fig. 1). This region, together with the Great Victoria and Great Sandy Deserts to the west, includes some of the most extensive arrays of linear (longitudinal) dunes on Earth, covering an area of approximately 1 000 000 km^2 (see table 1 in ref. 2). These patterns of unusually long, closely spaced linear dunes were described by the ASTP crew as "like hundreds of parallel road tracks" (ref. 3, p. 149). Linear dune patterns are uniform over great distances, and other types of dunes (such as barchanoid ridges) are rare. This region, together with the Kalahari Desert of southern Africa and the Moenkopi Plateau of Arizona, is thus one of the type areas for simple linear dunes observed from space (refs. 4 and 5).

PREVIOUS WORK

The origin, distribution, and general characteristics of these linear dunes, called "sand ridges" in Australia, have been studied by numerous workers, including Madigan (refs. 6 to 9), King (refs. 10 and 11), Wopfner and Twidale (ref. 12), Mabbutt (refs. 13 and 14), Mabbutt, Wooding, and Jennings (ref. 15), Mabbutt and Sullivan (ref. 16), Twidale (ref. 17), Folk (refs. 18 to 20), and others. In general, the Australian sand-ridge dunes have been considered identical to "seif" dunes. Seifs (from the Arabic word for sword or knife-edge) are sharp-crested, sinuous linear dunes and have been described from localities in the Egyptian sand seas (ref. 21, pp. 222-235 and 241-243), in the Libyan Desert (ref. 22), and in the Arabian deserts (ref. 23, pp. 89-95, 153-156, and fig. 79).

Recent work using measurements of dune lengths, widths, and wavelengths (measured from crest to crest) obtained from satellite images and aerial photographs (figs. 2 and 3) has resulted in a classification of eolian landforms (mainly dunes) based on their surface geometric forms (refs. 4, 5, and 24 to 28). However, comparisons of the scale ratios of linear dunes in Australia, Arizona, and Saudi Arabia (after Strahler, ref. 29) indicate a range of morphologic types among supposedly similar dunes. Differences are also evident in the pattern relationships among sand seas composed of linear dunes (table I(b)). These comparisons suggest that different varieties, the seif and the sand ridge, may be included in the general category of "longitudinal dunes," as first suggested by Price (ref. 30, pp. 462-463).

The usefulness of a system that identifies basic dune types and their varieties according to their surface geometry as viewed from space depends on the reliability of these shapes as indicators of certain internal structures. Structures such as cross-bedding are important to understanding the processes by which dunes of various types are formed, so that similar structures in ancient

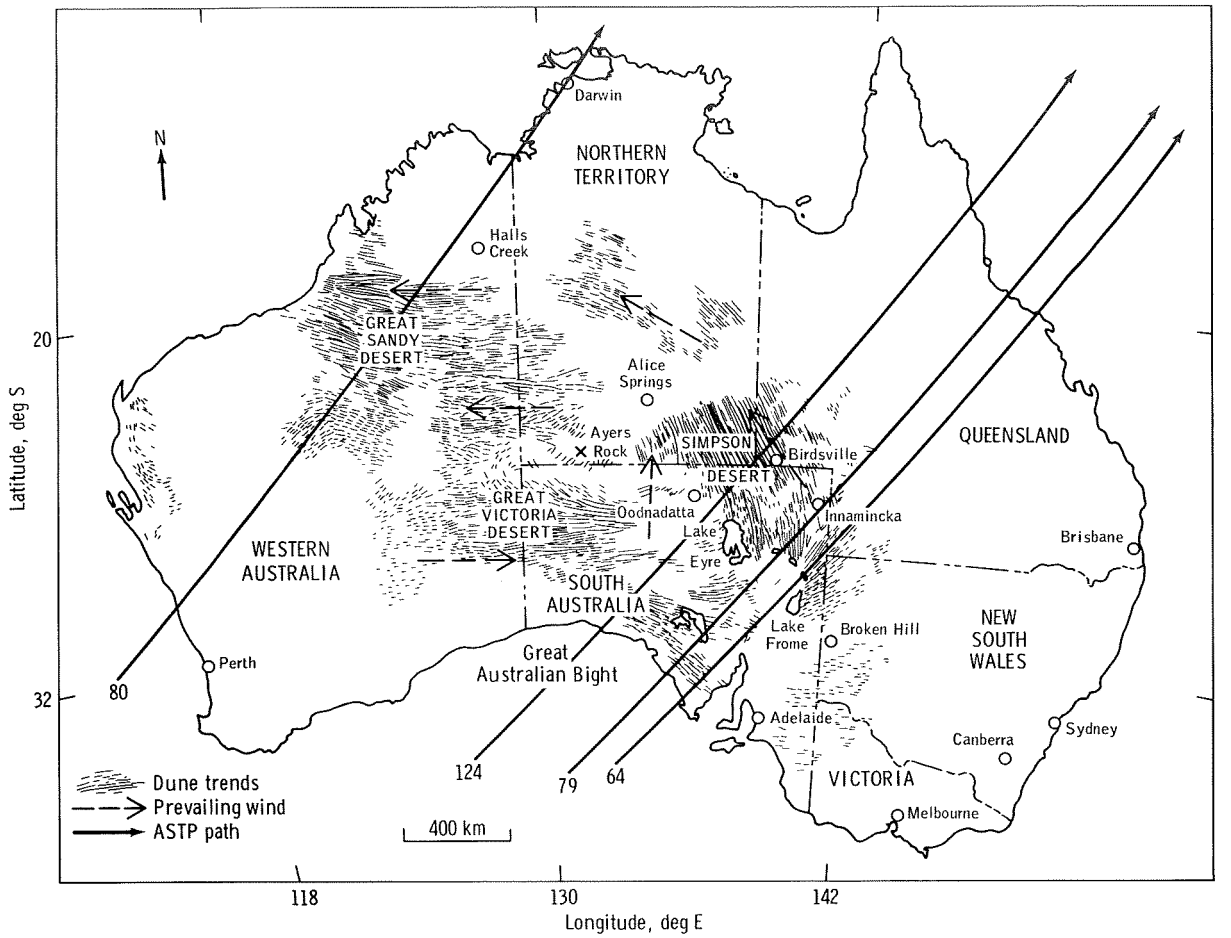


FIGURE 1.—Index map showing distribution of the Australian sand-ridge deserts (after Jennings, ref. 1) in relation to ASTP coverage. (Numbered arrows designate ASTP revolutions.)

sandstones can be correctly interpreted. Internal structures of simple barchans, transverse ridges, seifs, domes, stars, and parabolic dunes have been described (refs. 22 and 31 to 33) based on observations in western North America, Libya, and Saudi Arabia. Internal structures of the sand-ridge dunes of central Australia and of the Moenkopi Plateau, Arizona, however, have not been similarly described or compared with those of seifs.

Furthermore, the processes by which "longitudinal" dunes are formed remain controversial. The name connotes the lengthwise growth of a dune along an axis parallel to the direction of effective (sand-moving) winds. Some workers propose that longitudinal dunes are deposited in zones of low velocity between parallel horizontal helical vortices, which they believe develop in winds that blow along interdune corridors. Such helical currents might be set up by thermal instability in air blowing over hot deserts (refs. 15, 18, 19, 34, and 35) or in the lee of obstacles to windflow (ref. 17, pp. 88-98; ref. 21, pp. 191-195; and ref. 36, p. 122). Many workers believe that winds blowing from two alternate directions are necessary to produce the characteristic cross-bedded structures in linear dunes (ref. 21, p. 195; ref. 22, pp. 6-8), but others propose that these dunes are built in essentially unimodal wind regimes (refs. 18 and 19; ref. 23, pp. 89-92; ref. 36, p. 121). Studies of internal structures in

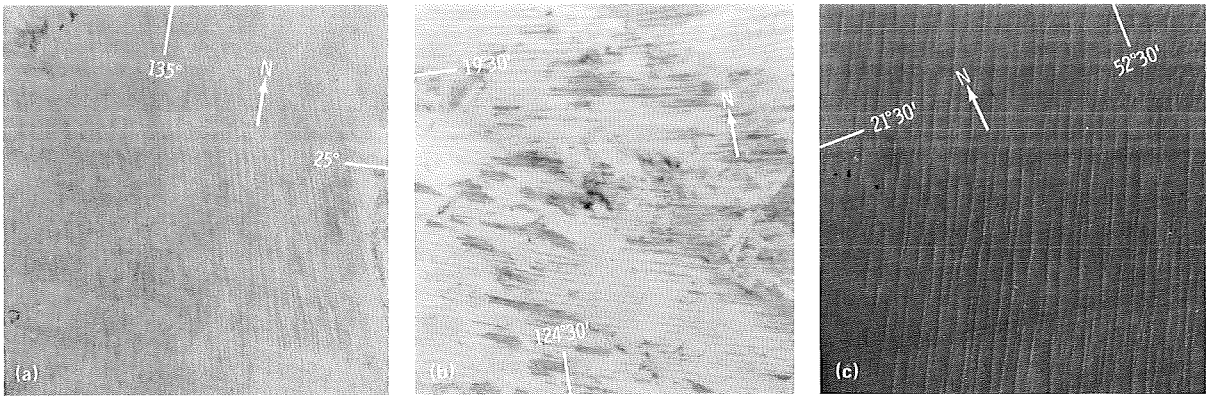


FIGURE 2.—Sample areas of Landsat-1 images from which measurements of linear dune length L, width W, and wavelength λ were made; each sample includes 2500 km^2. (a) Simpson Desert, Australia (includes the area of field studies, site A, near Andado Station). (b) Great Sandy Desert, Australia. (c) Ar Rub' al Khālī, Saudi Arabia.

more linear-type dunes may provide more information about processes of linear dune formation.

To examine the internal structures of linear dunes that were observed and photographed in Australia during the ASTP mission and to compare these features with published sections of seif dunes in Egyptian, Libyan, and Arabian sand seas, field investigations were made near Innamincka, South Australia, and in the Simpson Desert around Andado Station, Northern Territory, in September 1976 (fig. 4). For further comparison, linear dunes on the Moenkopi Plateau between Goldtooth and Gold Spring, Arizona, were examined in July and November 1976 and in February 1977 (fig. 3).

DUNE STUDIES IN SOUTH AUSTRALIA

General Setting

The southern part of the Simpson Desert is the lowest and the driest part of Australia, receiving an average annual rainfall of approximately 12.7 cm (5 in.) (ref. 37, p. 33). Lake Eyre (fig. 5) is a normally dry playa that occupies approximately 9360 km^2 and lies approximately 18 m below sea level (ref. 38, p. 3; ref. 39, p. 62). King (ref. 11, p. 104) attributed the origin of Lake Eyre entirely to wind deflation and compared the Lake Eyre basin to the Qattara Depression of Egypt. A more generally accepted theory (ref. 12, pp. 119-120) is that the Lake Eyre basin and the basins that contain other large playas such as Callabonna, Blanche, Gregory, and Frome (fig. 4) are, at least in part, structurally controlled.

Basement rocks in the region range in age from Precambrian to Permian and are overlain by a thick sequence of marine to lagoonal and lacustrine Mesozoic rocks that form the Great Artesian Basin. These strata are overlain by a thin veneer of continental sedimentary rocks of Tertiary age. Long periods of subaerial weathering during Tertiary time resulted in laterization of soils and silicification of the surface to a hard, resistant capping called "duricrust" in Australia. Erosional remnants of the duricrust now cap mesas and buttes around the margins of the Lake Eyre basin. A younger weathering profile associated with the present alluvial surface has produced a thick gypsum crust in Holocene sediments (ref. 12, pp. 128-130).

Dune sand mantles much of the region and is as much as 30 m (100 ft) thick in the center of the Simpson Desert (see table 1 in ref. 40) but thins to approximately 15 m (50 ft) at the northern (downwind) end of the sand sea (see table 3 in ref. 41). The age of the sand sea in central Australia is believed by some (ref. 17, pp. 101-102; ref. 42, p. 46) to be Holocene or latest Pleistocene but by many others (ref. 13, pp. 177-178; ref. 43, pp.

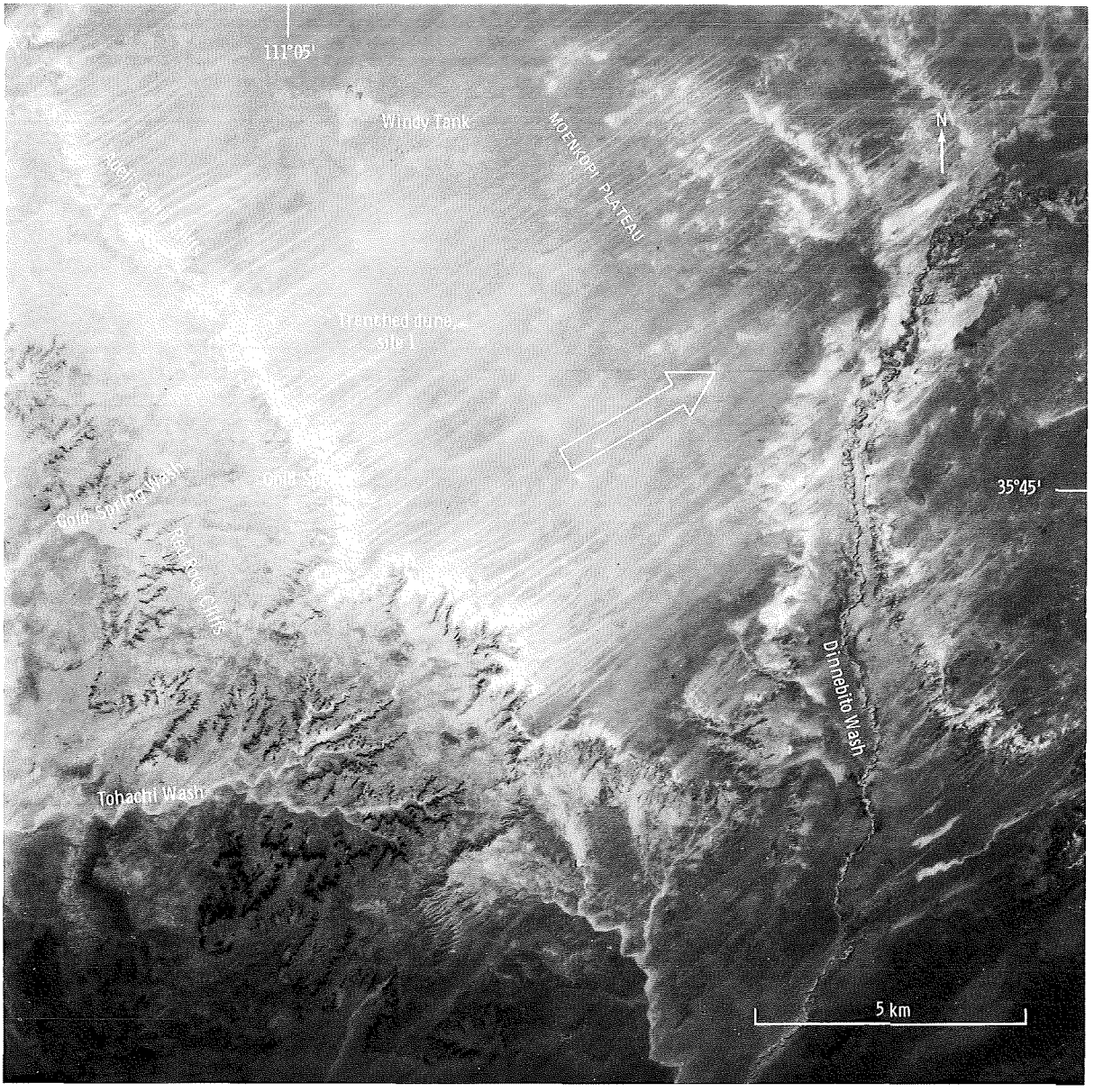


FIGURE 3.—Part of a high-altitude aerial photograph (NASA/JSC 236-28-0084) on which measurements were made of the length L, width W, and wavelength λ of linear dunes on the Moenkopi Plateau, Arizona. The large arrow shows the annual resultant direction of effective winds recorded at Winslow, Arizona, approximately 80 km southeast of Gold Spring.

615-616; ref. 44) to be considerably older. According to one hypothesis (ref. 44, p. 303), dune building in the arid center of Australia was "already well-advanced by 0.3 m.y." B.P. (before the present). The main dune-building episode in the South Australian deserts, according to this hypothesis, occurred between 17 500 and 16 000 years B.P. (coincident with the glacial maximum) and was followed by two Holocene episodes: one from 6000 to 3000 years B.P. and the other from 2000 years B.P. to the present (ref. 44, p. 279, fig. I, p. 284).

TABLE I.— Comparison of Pattern Relationships and Linear Dune Forms in Parts of Australia, Arizona, and Saudi Arabia

Comparisons are shown by dimensionless ratios derived from the measurements of mean dune lengths ($\bar{L}$), widths ($\bar{W}$), and wavelengths ($\bar{\lambda}$) on Landsat 1 and vertical aerial photographs. Comparison of the patterns (b) shows that the dunes in Australia and Arizona are characteristically very long relative to their widths ($\bar{L}/\bar{W}$ = nearly 100:1) and have very similar length-to-spacing relationships ($\bar{L}/\bar{\lambda}$ = about 25:1). The similarities of "growth habit" are particularly striking in view of the great disparity in the sizes (a) and geographic setting of the sand-ridge dunes in Australia and Arizona. In contrast, seif dunes in the northern Ar Rub' al Khālī, Saudi Arabia, are much shorter in relation to their mean widths ($\bar{L}/\bar{W}$ = 37:1) and have a length-to-spacing ratio of only 10:1. Relationships of dune widths to dune spacings in all these deserts are very similar.

(a) Mean dune measurements

Sand sea or desert	*Mean dune measurements, km*		
	$\bar{L}$	$\bar{W}$	$\bar{\lambda}$
Simpson (Australia)	24.0	0.22	0.90
Great Sandy (Australia)	22.7	.29	.90
Northern Arizona (United States)	3.65	.043	.15
Ar Rub' al Khālī (Saudi Arabia)	14.34	.38	1.41

(b) Comparison of pattern relationships

Sand sea or desert	*Ratios*		
	$\bar{L}/\bar{W}$	$\bar{L}/\bar{\lambda}$	$\bar{\lambda}/\bar{W}$
Simpson (Australia)	109.1	26.7	4.1
Great Sandy (Australia)	78.3	25.2	3.1
Northern Arizona (United States)	84.9	24.3	3.5
Ar Rub' al Khālī (Saudi Arabia)	37.7	10.2	3.7

(c) Comparison of scale ratios (from ref. 29)

Pairs of sand seas	$\bar{L}_1/\bar{L}_2$	$\bar{W}_1/\bar{W}_2$	$\bar{\lambda}_1/\bar{\lambda}_2$	*Maximum difference in scale ratios*	*Degree of similarity*[a]
Simpson/Great Sandy	1.06	0.76	1.0	0.30	Excellent
Simpson/Northern Arizona	6.58	5.12	6.0	1.46	Fair
Great Sandy/Northern Arizona	6.22	6.74	6.0	.74	Good
Ar Rub' al Khālī/Northern Arizona	3.93	8.84	9.4	5.47	Very poor
Simpson/Ar Rub' al Khālī	1.67	.58	.64	1.09	Fair
Great Sandy/Ar Rub' al Khālī	1.58	.76	.64	.94	Good

[a]The standard is subjective and is based on the maximum difference in scale ratios: 0.01 to 0.50 — excellent; 0.51 to 1.00 — good; 1.01 to 1.50 — fair; 1.51 to 2.00 — poor; over 2.10 — very poor.

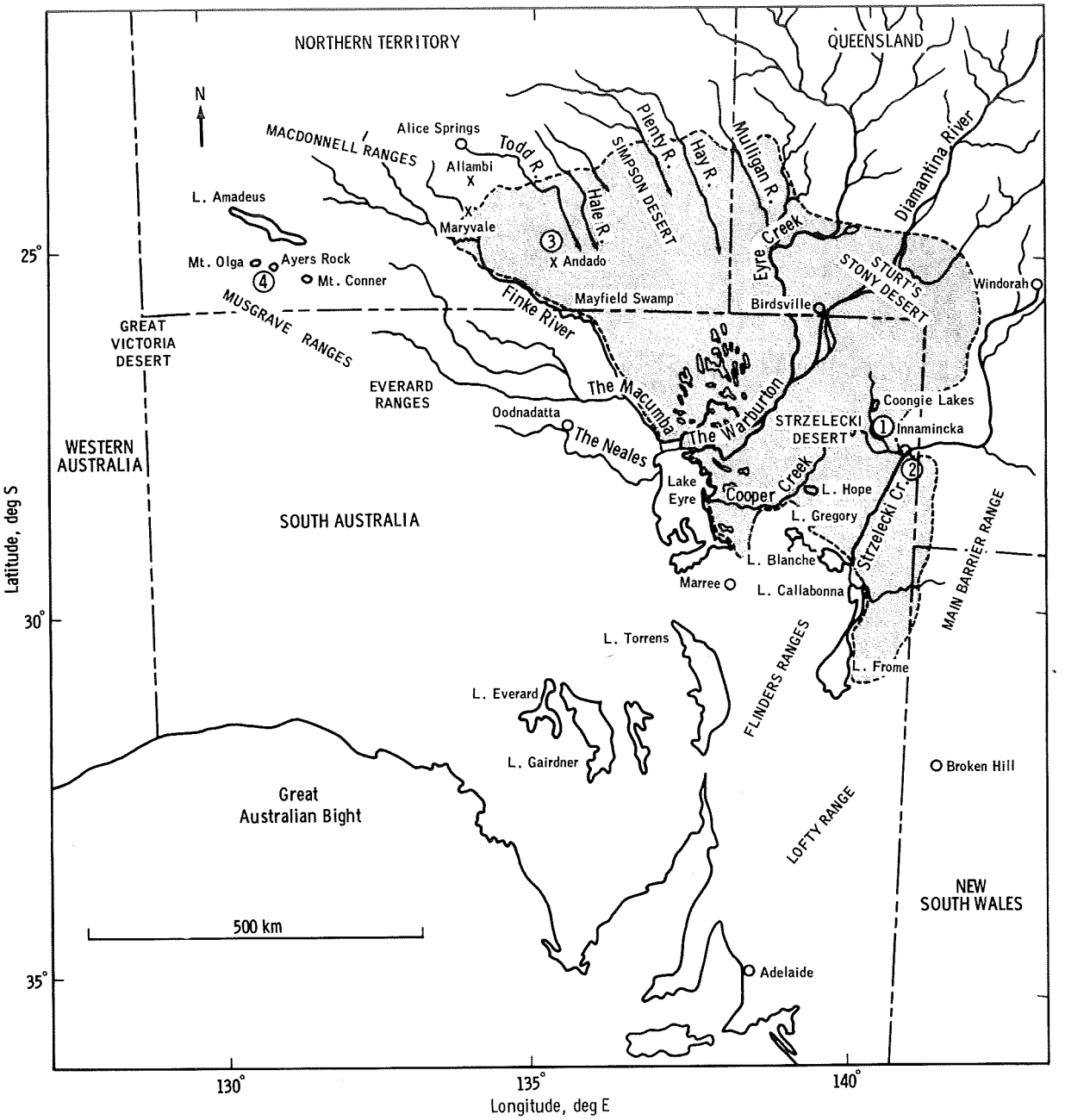


FIGURE 4.—Index map of localities visited in Central Australia (numbers 1 to 4). Approximate boundaries of the Simpson and Strzelecki sand seas (stippled area) are shown by the dashed line. All the streams are intermittent, and the lakes are normally dry.



FIGURE 5.—An ASTP photograph of Lake Eyre filled by the Kallakoopah and The Warburton distributary channels of the flooded Diamantina River, South Australia (AST-21-1726).

Lake Eyre

Lake Eyre (figs. 4 and 5) serves as the baselevel for internal drainage of nearly 1 300 000 km^2 of the Australian continent. Floodwaters on the Diamantina River system probably reach Lake Eyre only twice in a century (ref. 17, pp. 101-103). Between 1917 and 1946, floods on Cooper Creek reached only to Lake Hope (figs. 4 and 6), and the 1946 flood on Cooper Creek terminated on the Coongie Lakes (fig. 7) (ref. 8, p. 133; ref. 46, p. 55). Unique photographs of the filled lake were

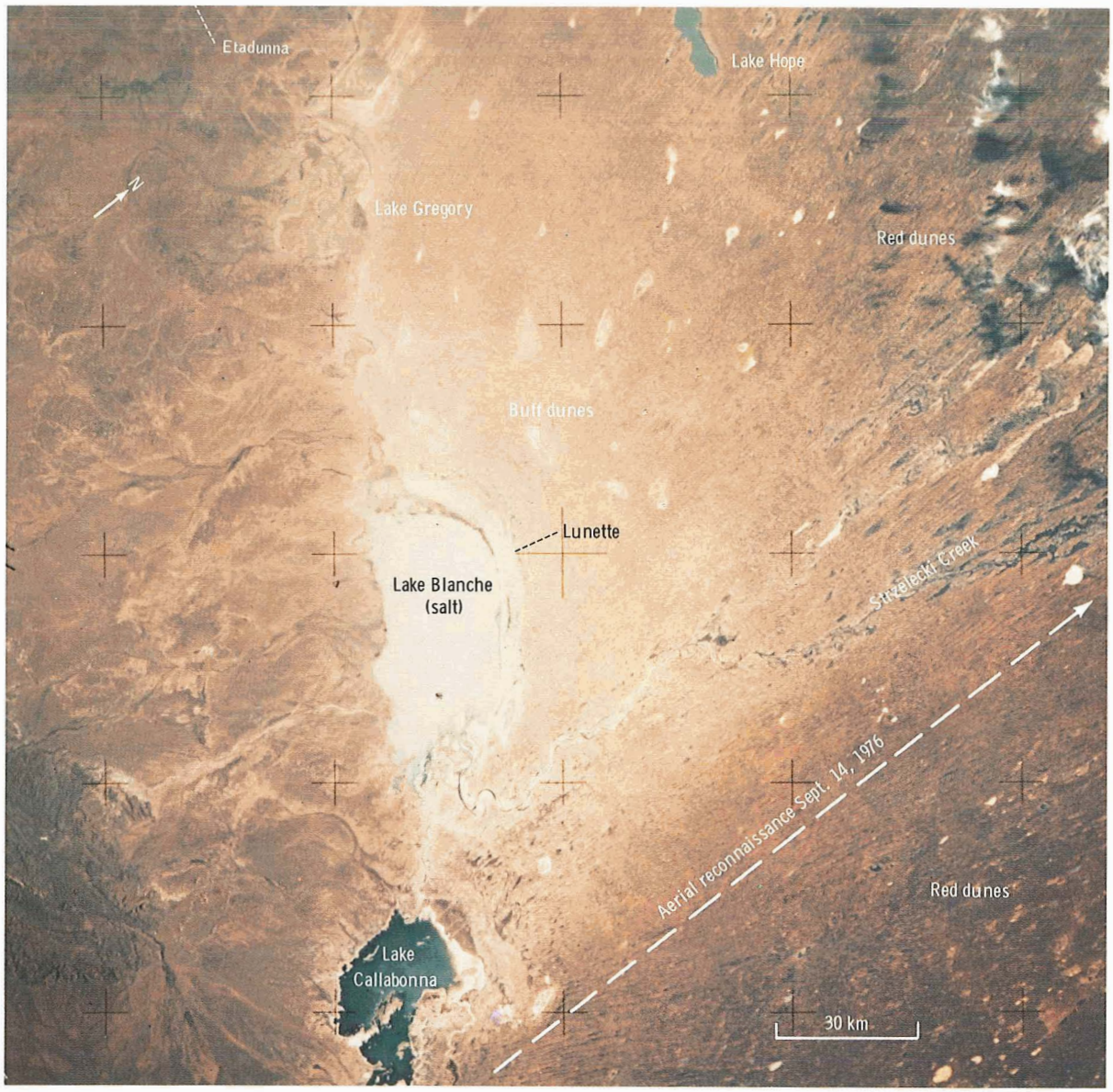


FIGURE 6.—An ASTP photograph of the upwind end of the Strzelecki Desert, South Australia. Dunes extend to leeward from the playas and grade in color from buff to red with increasing distance downwind (to the north) (AST-16-1133).

obtained by the ASTP crew in July 1975 (fig. 5). Sediments deposited in the Lake Eyre basin by floodwaters along the braided distributaries and playas associated with the Diamantina River and Cooper Creek to the east and the Finke-Macumba and Neales Rivers to the west are winnowed by the dominantly south, southeast, and southwest winds and blown northward into the sand seas of South Australia and the Northern Territory.



FIGURE 7.—A Landsat-1 image showing partly fluvial, partly eolian topography near Cooper Creek, at the border of the Strzelecki Desert with Sturt's Stony Desert, Australia. Dark areas are water-filled or heavily vegetated playas and channel remnants (billabongs); white areas are dry. The dull grayish areas are gravel plains (reg or "gibber" plains) or mesas. The bright linear features are sand dunes. The large arrow indicates the resultant direction of all winds recorded at Birdsville, approximately 90 km to the north along the Diamantina River (ref. 45, table 4).

Dunes in the Strzelecki Desert

Parts of the Strzelecki Desert, the lower Cooper Creek channel country, and Sturt's Stony Desert are shown on an ASTP photograph (fig. 6) and on a Landsat-1 image (fig. 7). From the lee sides of lakes Callabonna, Blanche, and Gregory (fig. 6), linear sand ridges extend downwind toward Cooper Creek. The change of dune color (from buff to deep red) with distance downwind from the supply of sand (the playa deposits) is clearly shown. In Australian sand seas as in other deserts of large-scale dunes, such as the Sahara (ref. 47), South West Africa (ref. 48), and southern California (ref. 49), increasing redness of dunes with distance from a uniform source of sand, in an area with uniform climatic conditions, is attributed to increasing oxidation of ferruginous clays and heavy minerals in the dune sediments with increasing time in a subaerial environment. Stages in the reddening process have recently been described by Folk (ref. 20) based on his observations in the Simpson Desert.

The ASTP crew described the color of dunes in the Innamincka-Birdsville region, at the downwind end of the sand sea in this region, as "very reddish," "really dark," and "really red" (ref. 3, pp. 138 and 148). However, the crew recognized here, over South Australia, that the color wheel aboard the spacecraft must be in sunlight to make valid comparisons with ground colors (ref. 3, p. 138). Color determinations based on field and laboratory comparisons of sand samples with the Munsell Soil Color Chart (ref. 50) are given in table II. The red dunes near Innamincka at the downwind end of the Strzelecki Desert are indeed very strong medium-dark reddish orange.

Figure 8 shows two sections exposed by gullying in the red dunes southeast of Innamincka (site 1 on the map, fig. 9). The dune shown in figure 8(a) is approximately 7 m high at the crest; its southeast-facing flank slopes very gently approximately 2° to 5°, and the northwest-facing flank slopes approximately 15°. Examination of the cut surface of the dune shown in figure 8(a) revealed an upper 75 cm of thin laminae dipping parallel to the surface slopes of the dune.

Beneath this surface set of very gently dipping laminae, the sand of the red dunes is structureless. The alluvial substrate is revealed at the base of the dune shown in figure 8(a), showing that this surface is continuous with that of the interdune corridors. The dunes seem to be eolian constructional features on the alluvial substrate rather than remnants (wind-rifts: refs. 10 and 11; ref. 36, pp. 129-130) left by wind erosion of a former sedimentary veneer. The interdune sediments are not as intensely red as the dune sediments; they are casehardened by gypseous cement and show deep desiccation cracks (fig. 8(a)).

The red dunes are heavily vegetated with spinifex and canegrass (*Triodia basedowii* and *Zygochloa paradoxa*), bushes (*Crotalaria* sp.), and even large trees (*Acacia* sp., *Grevillea nematophylla*, *Owenia* sp.). The interdune surfaces support an *Enneapogon avenacus* grassland that is quite different from the plant association that characterizes the dunes. The two different environments are thus easily identified by their different signatures on space and aerial photographs (figs. 6 and 10).

Grain size analysis of sand from the red dune shown in figure 8(a) is given in table II, and a frequency curve showing grain size distribution is given in figure 11(a). The dune is composed of moderately sorted, subangular to subrounded grains, mostly of quartz, which are coated with iron oxide. Mean size of the grains is 2.01ϕ (fine to medium sand), but the mode is medium sand. The distribution is leptokurtic and strongly fine-skewed. More than 5 percent of the sample consists of particles finer than 4ϕ (silts and clay).

The red dunes east of Innamincka are at the downwind end of an extensive sand sea that ends abruptly at Cooper Creek, as shown on the map (fig. 9) and on an aerial photomosaic (fig. 10). Near Innamincka, the trend of the red dunes is N10°E, unlike the N to N10°W trend of apparently modern buff dunes west of Innamincka (fig. 9). The intense oxidation of the red dune sand, the eroded appearance of the dune pattern, the heavy vegetative cover, and the lack of internal structures in the red dunes all suggest that they have been in place for a long period of time.

TABLE II.— Grain Size Analyses[a]

Site	Sample environment	Mean grain size, Mz in ϕ	Wentworth category	Percentage of pan-size sediments < 4ϕ	Sorting, σ_I in ϕ	Skewness, SK_I	Kurtosis, K_G	Munsell soil color, hue value/chroma	Color name (ref. 50)	Roundness (Powers scale)
					Innamincka, Australia					
1	Red dune	2.01	Fine to medium sand	5.6	0.91, moderate	+0.44, strongly fine-skewed	1.25, leptokurtic	2.5YR 4.5/6	Very strong medium-dark reddish-orange	2.5, subangular to subrounded
2	Buff dune	2.60	Fine sand	5.2	0.64, moderately well	+0.26, fine-skewed	1.26, leptokurtic	10YR 6/4	(Buff) strong light yellow-orange	2.5, subangular to subrounded
	Interdune	2.95	Fine sand	15.0	0.96, moderate	+0.16, fine-skewed	1.07, mesokurtic	10YR 6/4	(Buff) strong light yellow-orange	2.5, subangular to subrounded
					Andado, Australia					
A (main site)	Dune crest	2.15	Fine sand	0.8	0.80, moderate	+0.27, fine-skewed	0.81, platykurtic	10R 4/8	Intense dark red-orange	3.5, subrounded to rounded
	East-facing upper flank (windward)	2.39	Fine sand	4.3	0.98, moderate	+0.19, fine-skewed	0.66, very platykurtic	10R 4/8	Intense dark red-orange	3.5, subrounded to rounded
	West-facing upper flank (slipface)	2.44	Fine sand	1.7	0.79, moderate	−0.03, near symmetrical	0.81, platykurtic	10R 4/8	Intense dark red-orange	3.5, subrounded to rounded
	East-facing lower flank (toe)	2.35	Fine sand	3.9	0.97, moderate	+0.13, fine-skewed	0.68, very platykurtic	10R 4/8	Intense dark red-orange	3.5, subrounded to rounded
	West-facing lower flank (toe)	2.30	Fine sand	3.5	1.03, poor	+0.02, near symmetrical	0.72, platykurtic	10R 4/8	Intense dark red-orange	2.5, subangular to subrounded
	Interdune (surface)	2.30	Fine sand	0.9	1.03, poor	+0.02, near symmetrical	0.72, platykurtic	[b]10R 4/6 to [c]10R 4/8	Very strong to intense dark red-orange	2.5, subangular to subrounded
	Interdune (5-cm depth)	2.47	Fine sand	7.8	1.22, poor	−0.23, coarse-skewed	0.74, platykurtic	[b]10R 4/6 to [c]10R 4/8	Very strong to intense dark red-orange	2.5, subangular to subrounded
B (north)	Dune crest	2.72	Fine sand	2.1	0.53, moderately well	+0.05, near symmetrical	0.94, mesokurtic	2.5YR 4.5/8	Intense medium to dark reddish-orange	3, subrounded
	Dune flanks	2.63	Fine sand	2.5	0.57, moderately well	−0.02, near symmetrical	0.84, platykurtic	2.5YR 4.5/8	Intense medium to dark reddish-orange	2.5, subangular to subrounded
	Interdune	3.64	Very fine sand	37.3	1.37, poor	+0.23, fine-skewed	0.92, mesokurtic	7.5YR 5/5	Strong medium yellowish-brown	2.5, subangular to subrounded

TABLE II.—Concluded

Site	Sample environment	Mean grain size, Mz in ϕ	Wentworth category	Percentage of pan-size sediments $< 4\phi$	Sorting, σ_I in ϕ	Skewness, SK_I	Kurtosis, K_G	Munsell soil color, hue value/chroma	Color name (ref. 50)	Roundness (Powers scale)
					Andado, Australia					
C (north)	Dune crest	2.34	Fine sand	3.3	0.79, moderate	+0.25, fine-skewed	0.90, meso-kurtic	5YR 5/6	Very strong medium orange	2.5, subangular to subrounded
	East-facing flank (windward)	2.70	Fine sand	7.6	0.95, moderate	−0.05, near symmetrical	0.78, platykurtic	5YR 5/6	Very strong medium orange	2.5, subangular to subrounded
	West-facing flank (lee)	2.79	Fine sand	7.7	0.98, moderate	−0.18, coarse-skewed	0.96, meso-kurtic	5YR 5/6	Very strong medium orange	2.5, subangular to subrounded
	Interdune	2.02	Fine to medium sand	10.6	1.74, poor	−0.08, near symmetrical	0.79, platykurtic	[b]5YR 4/6 to [c]5YR 4/8	Very strong to intense dark orange	2.5, subangular to subrounded
					Moenkopi Plateau, Arizona					
1	Dune crest (active)	2.25	Fine sand	0.5	0.61, moderately well	+0.08, near symmetrical	0.85, platykurtic and bimodal	7.5YR 6/4	Strong light yellowish-brown	4.5, rounded
	Dune interior	3.09	Very fine sand	13.2	0.85, moderate	+0.33, strongly fine-skewed	1.93, very leptokurtic	7.5YR 5/4	Strong medium yellowish-brown	4.5, rounded (quartz); 2.5, subangular (ash)
3	Dune interior (inactive) (1-m depth)	3.00	Very fine sand	15.2	0.95, moderate	+0.36, strongly fine-skewed	1.59, very leptokurtic	5YR 5/4	Strong medium brown	4.5, rounded (quartz); 2.5, subangular (ash)

[a]Based on mechanical sieving of samples from fields of linear dunes (in one-fourth ϕ interval sieves for 15 minutes on a Ro-tap, by Kevin Horstman); graphic measures were obtained by the method of Folk (ref. 51); Mz = graphic mean, σ_I = inclusive graphic standard deviation, SK_I = inclusive graphic skewness, and K_G = graphic kurtosis.

[b]Coarse grains.

[c]Fine grains.

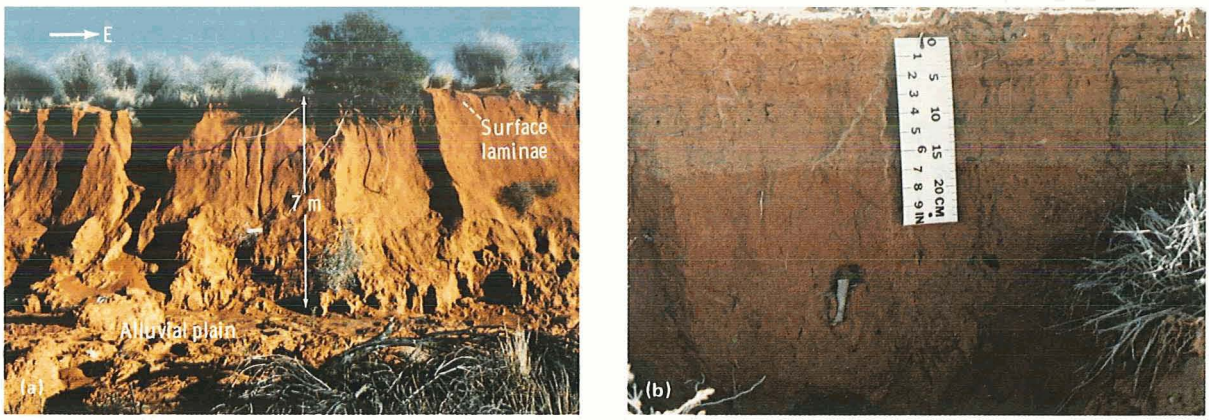


FIGURE 8.—Vertical cross-sections of fixed dunes exposed by gullying near Innamincka. The deep red hue and lack of structure beneath a surface veneer of gently dipping laminae are attributed to diagenetic changes that may be associated with long periods of stability in a subaerial, semiarid environment. (a) Red dune southeast of Innamincka. (b) Closeup of cross section.

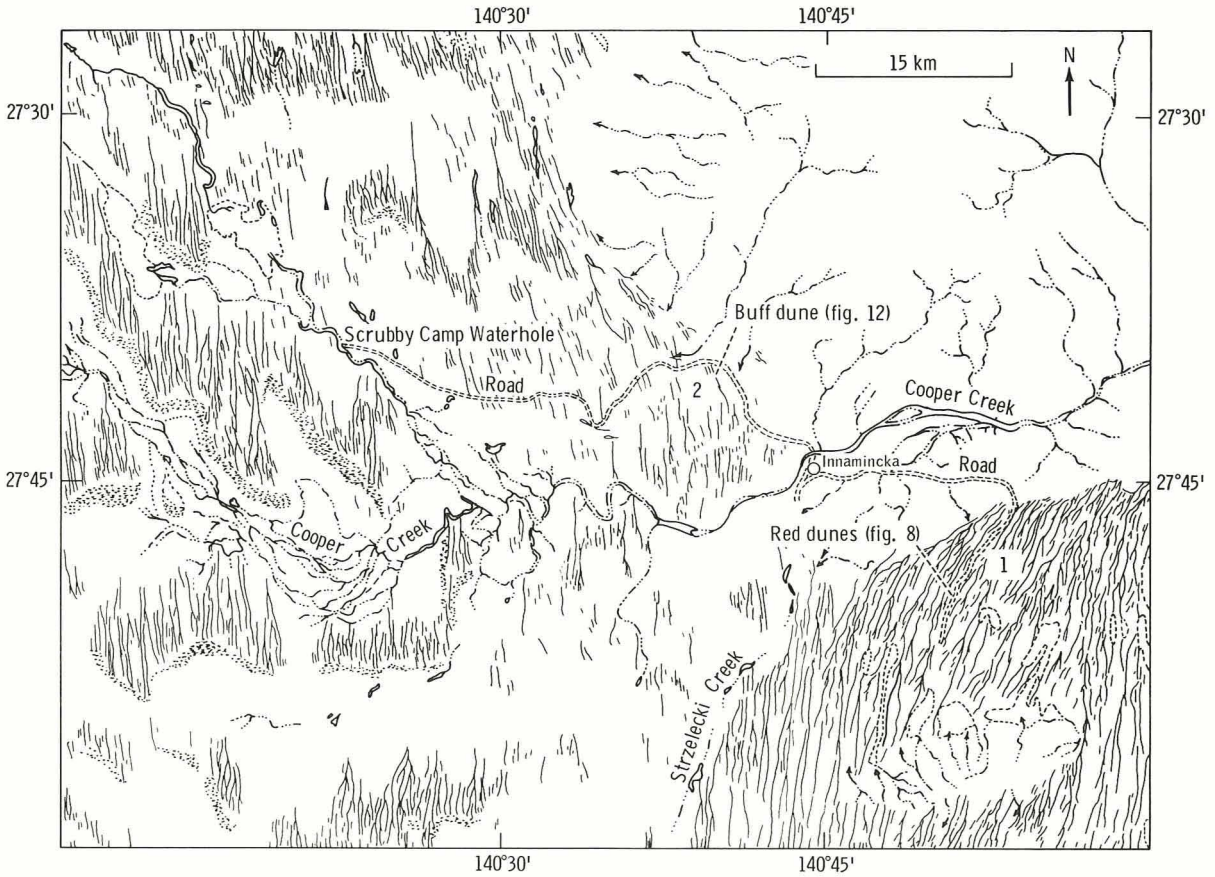


FIGURE 9.—Map traced from a section of the Innamincka, South Australia, topographic sheet SG 54-14, showing different distribution patterns of older red dunes (1) and more recent buff dunes (2). Dotted areas are leeside mounds (ref. 17) along playas and billabongs of the Cooper Creek system. Field examinations of dunes were made from area (1) to the vicinity of Scrubby Camp Waterhole.

In contrast, the buff dunes west of Innamincka have a much more youthful aspect. Figure 12 shows vertical cross-sections of one of these buff dunes that has been breached by recent gullying. The location is site 2 on figure 9, approximately 12 km northwest of Innamincka on the dirt road to Scrubby Camp Waterhole. This dune is approximately 1.5 km long and is sinuous and very broad (approximately 50 m) relative to its low height (approximately 3 m). The contact of the steeply dipping flank sediments with flat-bedded alluvium at the base (fig. 12(b)) shows that the dune is a wholly constructional feature lying on a surface that extends into the adjacent interdune corridors. Numerous other dunes of the same general color, shape, and orientation occur nearby.

The internal structure of the buff dune (fig. 12) consists of a few very broad, tabular sets of steeply dipping eolian cross-beds or laminae. The laminae are thin (approximately 1 to 3 cm) and dip northeast and southwest at angles of 22° to 32°. The northeast-dipping laminae are slightly thicker than those that dip to the southwest. The sets of laminae are 0.5 to 1 meter thick and are bounded by low-angle (3° to 8°) planar erosion surfaces. Thin laminae at the surface dip essentially parallel to the gentle side slopes of the dune.

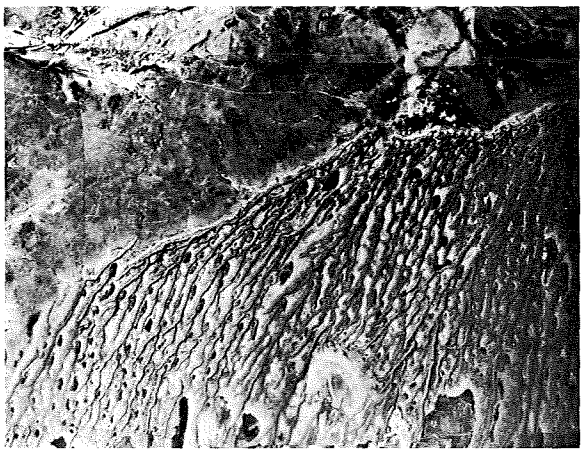


FIGURE 10.—Part of an aerial photomosaic (Innamincka Orthophotomap 7042) showing the eroded pattern of fixed red dunes and contrasting signatures of dunes and interdune swampy areas of the downwind end of the Strzelecki Desert east of Innamincka, South Australia. Note the abrupt downwind terminus of the sand sea near Cooper Creek. Photograph used by permission of the Department of Lands, South Australia. For scale, compare with area (1), figure 9.

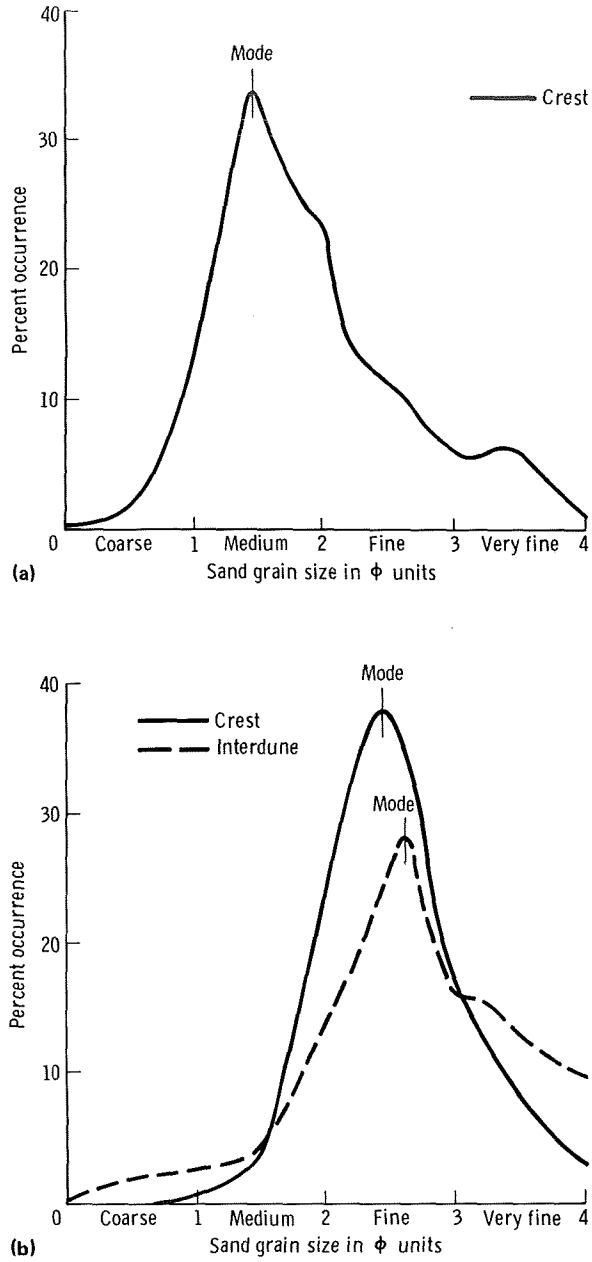


FIGURE 11.—Frequency curves showing grain size distributions in sediments from dune fields near Innamincka, South Australia. The crest sand of (b) shows a narrower range of grain sizes but almost the same mode as the interdune sediments. The crest sand has apparently been winnowed by wind from sediments similar to those in the interdune corridors. (a) Crest sand, fixed red dune. (b) Crest, interdune sands, buff dune.

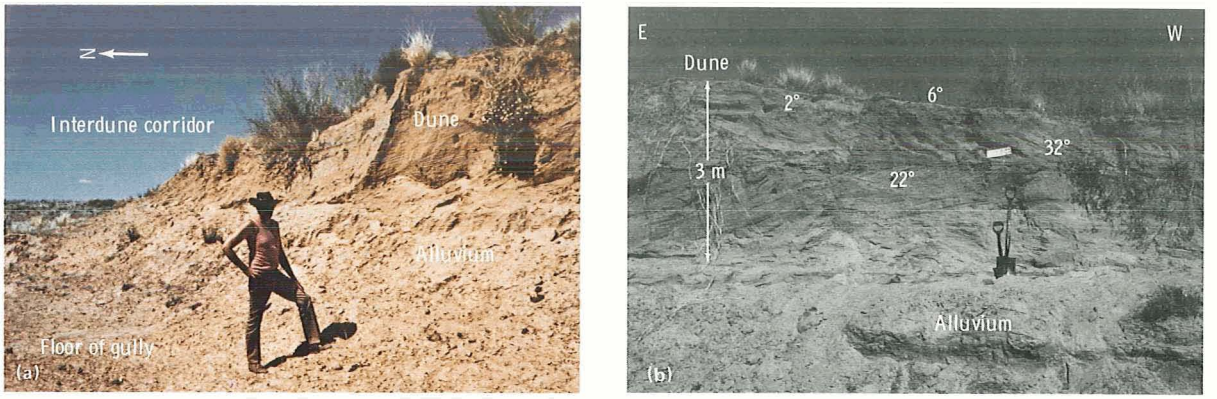


FIGURE 12.—Ground photographs showing structures in a field of buff dunes exposed by gullying west of Innamincka, South Australia. (a) Relation of the dune to underlying flat-bedded alluvium. (b) Tabular planar and wedge planar sets of eolian cross-beds in the center of the dune shown in (a). The scale above the shovel is 25 cm long.

Grain size distributions of dune and interdune sediments collected at this location are shown in table II and figure 11(b). Dune and interdune sediments consist mostly of fine-grained quartz sand, which is subangular to subrounded and is 10YR 6/4 (strong light yellow-orange) on the Munsell Soil Color Chart. Frequency curves of the size distributions of buff dune and interdune sediments (fig. 11(b)) show modes in the same size range (fine sand) and both distributions are fine-skewed; however, the curve for the dune sands is leptokurtic, whereas the distribution of the interdune sands is mesokurtic. The dune sand is moderately well sorted, in contrast to moderate sorting of the interdune sand, and the dune sediments contain a much lower proportion (5.2 percent) of particles smaller than 4ϕ (silt or clay) compared to 15 percent of these fines in the interdune sample. The grain size analysis suggests that the dune sand and interdune sediments are closely related to each other and to alluvial source materials from Cooper Creek. Selective winnowing by winds has narrowed the range of sediment sizes that have been carried upward onto the dune and has favored a slightly coarser mode for these sediments; otherwise, they are much alike.

A process by which modern dunes are presently growing downwind from lunettelike deposits or "lee-side mounds" in the Strzelecki Desert (figs. 6, 7, and 9) is proposed by Twidale (ref. 17, pp. 82-100). In his view, these ridges are essentially lee dunes (ref. 36, pp. 120-121), because they are deposited in zones of low wind velocity between vortices that are created as winds blow past obstacles (parts of the mounds themselves) on the plains. This process embodies some of the wind-rift theory of King (refs. 10 and 11), because the obstacles consisting of remnants of the lee-side mounds are, in effect, yardangs, and the dunes growing downwind from them are, in effect, sand tails.

Wind Data

Wind data are not recorded at Innamincka, but they can be extrapolated for the general area from data collected at Birdsville (refs. 45 and 52) in the Sturt's Stony Desert to the northwest (figs. 4 and 7). Strong winds at Birdsville are seasonally bimodal (see table 14c in ref. 52). In the fall, strong winds blow from the south, followed by winter winds from the northwest, spring winds from the south-southwest, and summer winds from the south-southeast. The prevailing wind at Birdsville, throughout all seasons, is from the south-southeast (ref. 45, p. 133 and table 4; ref. 52, tables 14b and 15). Orientations of the dunes west of Innamincka are nearly parallel to the annual resultant direction of all winds at Birdsville (fig. 7).

DUNE STUDIES IN THE NORTHERN TERRITORY

General Setting

The northern part of the Simpson Desert south of Alice Springs is extremely flat, sloping gradually from approximately 200 m above sea level north of Andado Station to 100 m above sea level at Oodnadatta and to 18 m below sea level at Lake Eyre (fig. 4). Bedrock outcrops consist of residual mesas of Mesozoic claystones, siltstones, sandstones, and conglomerates, which have been weathered to a resistant siliceous capping known in Australia as silcrete. These silcrete-capped mesas are surrounded by aprons of Quaternary alluvium that are commonly veneered by a lag gravel ("silcrete gibber"). One of the highest of these mesas is Mount Peebles, which rises 58 m above the 200-m elevation of the sand sea south of Andado Station (fig. 13).

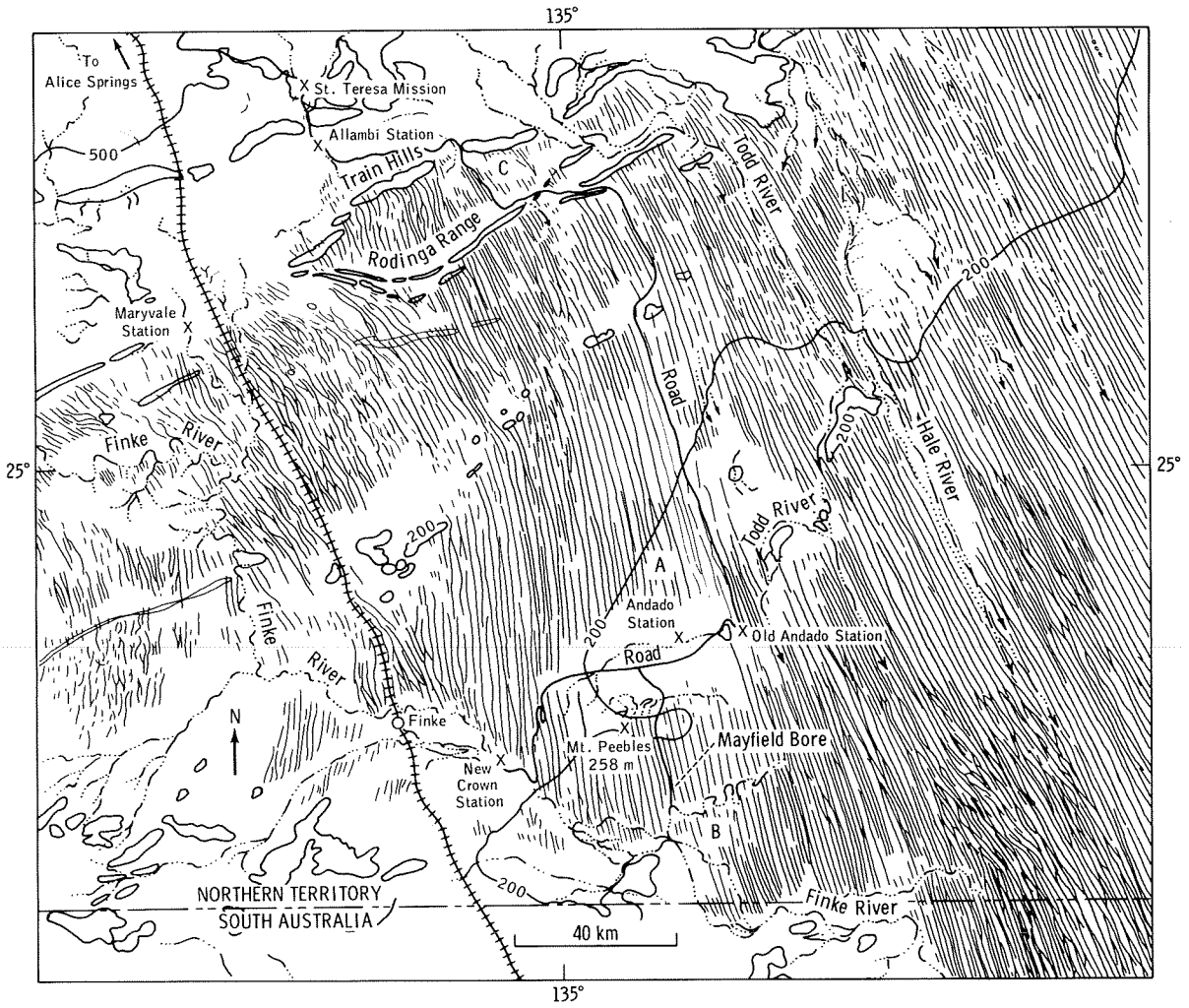


FIGURE 13.—Index map of the sand sea in the northwestern Simpson Desert, Northern Territory, Australia. Field examinations of dunes were made at sites A, B, and C.

The region lies within the 12.5 cm (5 in.) rainfall isohyet; however, rainfall is extremely variable, usually only 5 to 7.5 cm but as much as 25 to 30 cm in an occasional wet year. All the streams shown on the map (fig. 13) are normally dry, but they occasionally carry floodwaters into the sand sea. Vegetation is basically the *Zygochloa paradoxa-Triodia basedowii* (canegrass and spinifex) association described for the Simpson Desert sand sea by Crocker (ref. 53). Wiedemann (ref. 54, pp. 108, 111, 114, and 120) has determined that the distribution of plant habitat types in the sand sea north of Andado Station is controlled mainly by variations in the texture, compactness, and mobility of the dune and interdune sediments, and that an abrupt change of vegetation occurs on the dune slopes at the active sand margin.

The sand sea around the mesas and claypans consists of linear dunes as much as 35 m high and 80 km long, generally spaced approximately 0.5 to 1.5 km apart and separated by nearly flat interdune corridors. The sand in the Simpson Desert is as much as 30 m deep (see table 1 in ref. 40). A "pre-aeolian surface" lies at a depth of 70 cm in the interdune corridors north of Andado Station (ref. 16, pp. 483-485). In many places, the surfaces of the interdune corridors are veneered with desert-varnished lag gravels.

The classic descriptions of Australian sand-ridge dunes (refs. 6, 7, and 9) are based on observations in the Simpson Desert. Figure 14 is one of a series of ASTP photographs showing patterns of sand ridges typical of this part of central Australia. For ease of access into this remote region, dune study sites (fig. 13) were chosen near the area where Mabbutt and Sullivan (ref. 16) studied dune junctions and profiles and where Wiedemann (ref. 54) conducted his plant ecology studies. Site A is approximately 18 km north of Andado Station; site B is in an area of recently breached dunes near a "floodout" of the Finke River south of Mayfield Bore; and site C is in the low dune ridges at the northernmost (downwind) end of the sand sea, just south of the Train Hills.

Dunes Near Andado Station

The scale of the sand ridges at site A is shown in figure 15(a), which shows one of the authors at a dune crest comparing the color of the sand with a facsimile of the color wheel carried by the ASTP astronauts. The visual observation from ASTP (ref. 3, p. 150) evaluated the color of sand ridges in the Great Sandy Desert, approximately 2000 km west of the Simpson Desert, as about 9A, equivalent to 10R 4/8 on the Munsell Soil Color Chart. The ground test at site A (fig. 15(a)) and later laboratory comparison of sand samples from this site with the Soil Color Chart showed the same result: 10R 4/8 (intense dark red-orange). These dunes, deep in the main body of the Simpson Desert, have the reddest hue and most intense chroma of any of the dunes observed in Australia (table II). They are considerably redder than the reddish-orange dunes at site B to the south (fig. 16(a)) and the medium-orange dunes at the northern edge of the Simpson Desert at site C (fig. 16(b)). These color differences suggest differences in the sources of sands and/or different stages of dune development at these sites.

Ten test pits (fig. 15(b)) were dug from the interdune area across the dune at site A shown in the background of figure 15(a). Structures revealed are shown schematically in figure 17. For comparison, internal structures of seif dunes near Sabha, Libya (ref. 22), and structures inferred for seif dunes in the Egyptian sand seas (ref. 21) are shown in figure 18. The sets of cross-beds at site A are broad and are bounded by low-angle planar erosion surfaces. The steeply bounded sets typical of the seif dunes (fig. 18) are conspicuously absent. At this site and at site C (fig. 19), many of the cross-beds have low angles of dip.

At the crest of the dune at site A (fig. 17), sets of cross-beds are approximately 1 m thick, and the bedding in them is well preserved, at least to the depths of the trenches (1.5 m). Below the crest on the upper slopes of the dune, surface laminae dip parallel to the side slopes (approximately 25° on

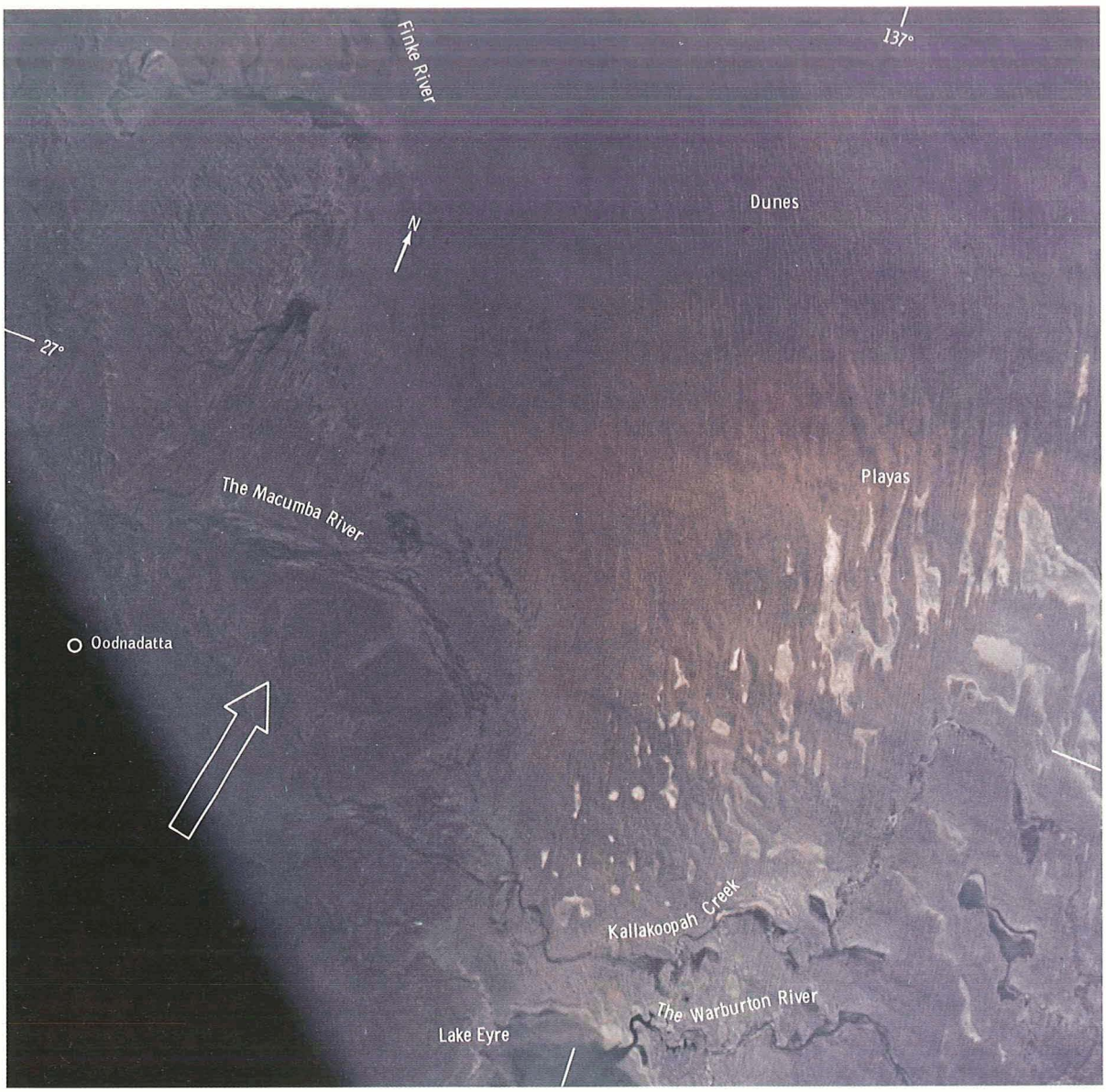


FIGURE 14.—An ASTP photograph showing the pattern of subparallel linear dunes typical of the Simpson Desert. The large arrow shows the resultant direction of sand-moving ("effective") winds calculated by S. G. Fryberger from surface winds recorded at Oodnadatta, South Australia (AST-19-1547).

the upper west-facing slope, 10° on the upper east-facing slope in September 1976). About midway down the flanks on both sides of the dune, the sand is structureless beneath the surface laminae. The lack of internal bedding in the main body of the dune is reminiscent of the lack of structure in the red dunes east of Innamincka (fig. 8).

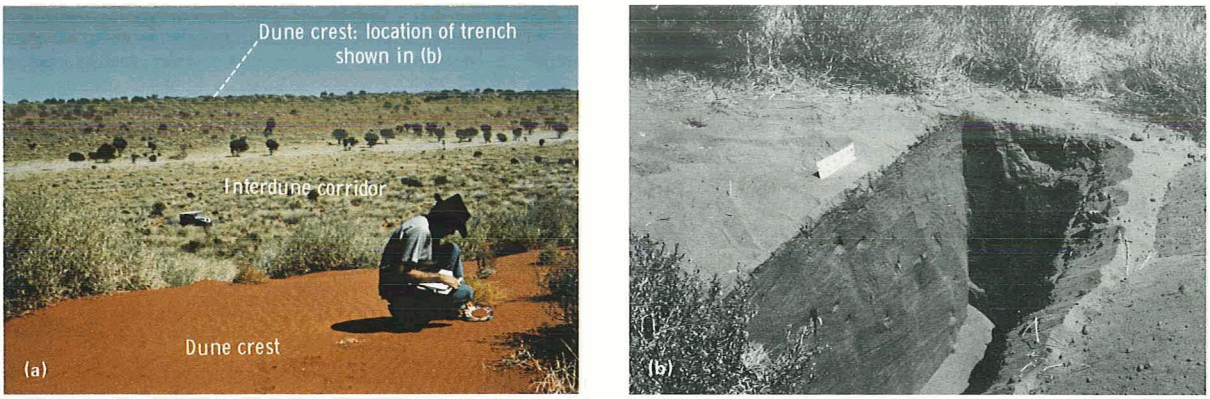


FIGURE 15.—Ground photographs at site A (fig. 13) near Andado Station, Northern Territory, Australia. (a) Ground test of ASTP color wheel with red dunes in the northern Simpson Desert; the dunes are 10R 4/8 (Munsell Soil Color Chart). (b) Trench in crest of dune shown in the background of (a). The scale beside the trench is 25 cm long.

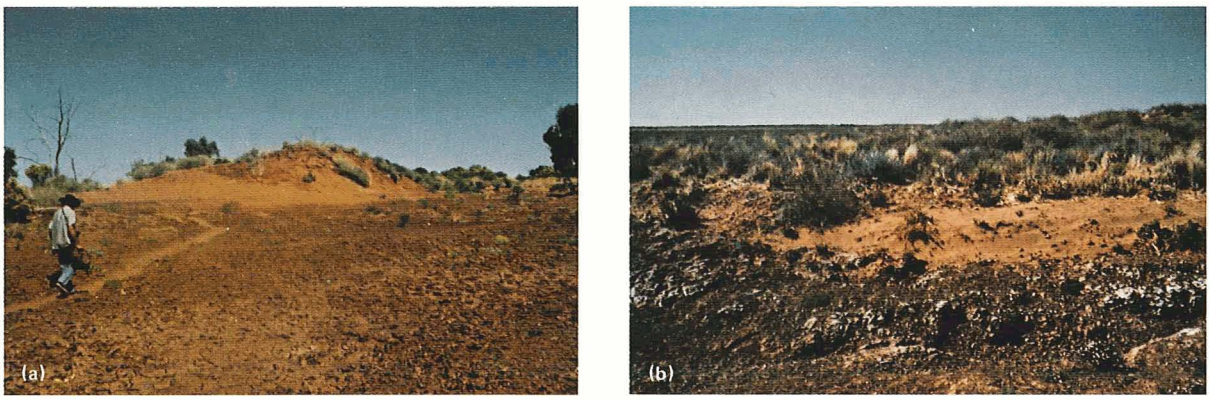


FIGURE 16.—Ground photographs showing typical profiles and colors of orange dunes at site B and near site C in the Simpson Desert. (a) North-facing end of a 5-m-high, 44-m-wide dune cut by a recent flood on a distributary of the Finke River at site B (fig. 13). Note distinct difference in color between the dune sand and the underlying brown alluvium with desiccation cracks. (b) Forward end (nose) of a dune just south of the Rodinga Range (fig. 13). The dune ends in a single layer of bright orange sand on the underlying brown desert pavement, encrusted with salts.

Avalanching obscured the lower part of the large dune breached by gullying at site B (figs. 16(a) and 19(a)), but structures were preserved throughout several smaller dunes nearby (fig. 19(b)). Significance of the structures is discussed in the interpretation part of this report.

Grain size analysis of samples from Andado sites A, B, and C are summarized in table II, and frequency curves showing the grain size distributions are given in figure 20. All the dunes are composed mostly of quartz grains with mean sizes in the fine sand range. Mean sizes of interdune sediments range from fine to medium sand at site C, at the northern end of the desert, to fine sand at site A and to very fine sand farthest south (site B). All the sites show progressively better sorting upwards from the interdune sediments to the crests of the dunes, but even the latter are only moderately sorted (sites A and C) to moderately well-sorted (site B).

Percentages of grains finer than 4ϕ (silt and clay fraction) generally increase from the crests of the dunes downward to the interdune sediments (fig. 21). An exception is the surface ripple sand from the interdune corridor at site A, which, like the crest sand there, includes less than 1 percent

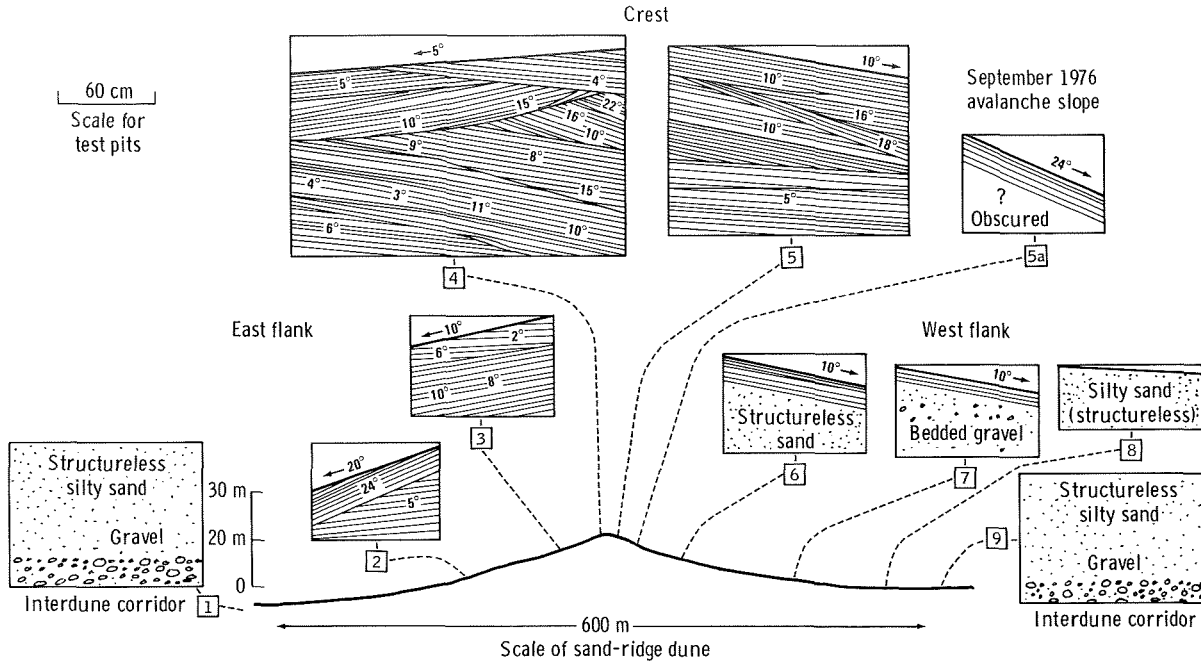


FIGURE 17.—Diagram showing measured profile of a dune at site A near Andado Station (fig. 13) and structures revealed in test pits dug at the locations shown. The pit near the east flank at the crest of the dune is shown in figure 15(b). Compare with figure 18.

silt or clay. Beneath this surface veneer of mostly coarse ripple sand is a typical, poorly sorted, bimodally distributed, coarse-skewed interdune sediment similar to that described by Folk (ref. 55). At sites A and B, crest sand is slightly more rounded than sand from dune flanks and interdune corridors, but no difference in roundness is seen among the sands from site C.

The frequency curves (fig. 20) show very different grain size distributions in sediments from sites A, B, and C. At site A, all the sands from the crest to the lower flanks of the dune are bimodally distributed; the bimodality also occurs in the interdune sediments beneath the surface ripple sand. It is suggested that the modes in the coarse-to-medium sand range may represent the traction load and the peaks in the fine-to-very-fine sand range may represent the saltation load, and that the sediments may have become bimodal through a "rectification" process proposed by Wood (ref. 56). Alternatively, the bimodalities may reflect differences in the competencies of seasonally changing winds.

A third possibility is that the sediments are not wholly eolian but represent a mixture of windblown sand and fluvio-lacustrine deposits. Aerial photographs shown to us by Mack Clark, owner of Andado Station, reveal the dunes in the northwestern part of the Simpson Desert around Andado as parallel, elongate islands in a vast inland lake caused by flooding on the Todd River (fig. 13). Some of the interdune areas were still swampy in September 1976, and thick deposits of silty sand left by the floodwaters are well-known hazards to road travel in the northwestern part of the Simpson Desert. As noted, the mean grain sizes of the interdune sediments become increasingly finer southward, away from the headwaters of the Todd and Finke Rivers, but in an upwind direction. If these sediments were entirely wind-deposited, one would expect the mean grain size to become finer, not coarser, in a downwind direction, as reported for Saharan dune fields by Alimen (ref. 47). Bedded pea-sized gravels exposed in a test pit on the lower flank of the trenched dune at site A (fig. 17) are considered ad-

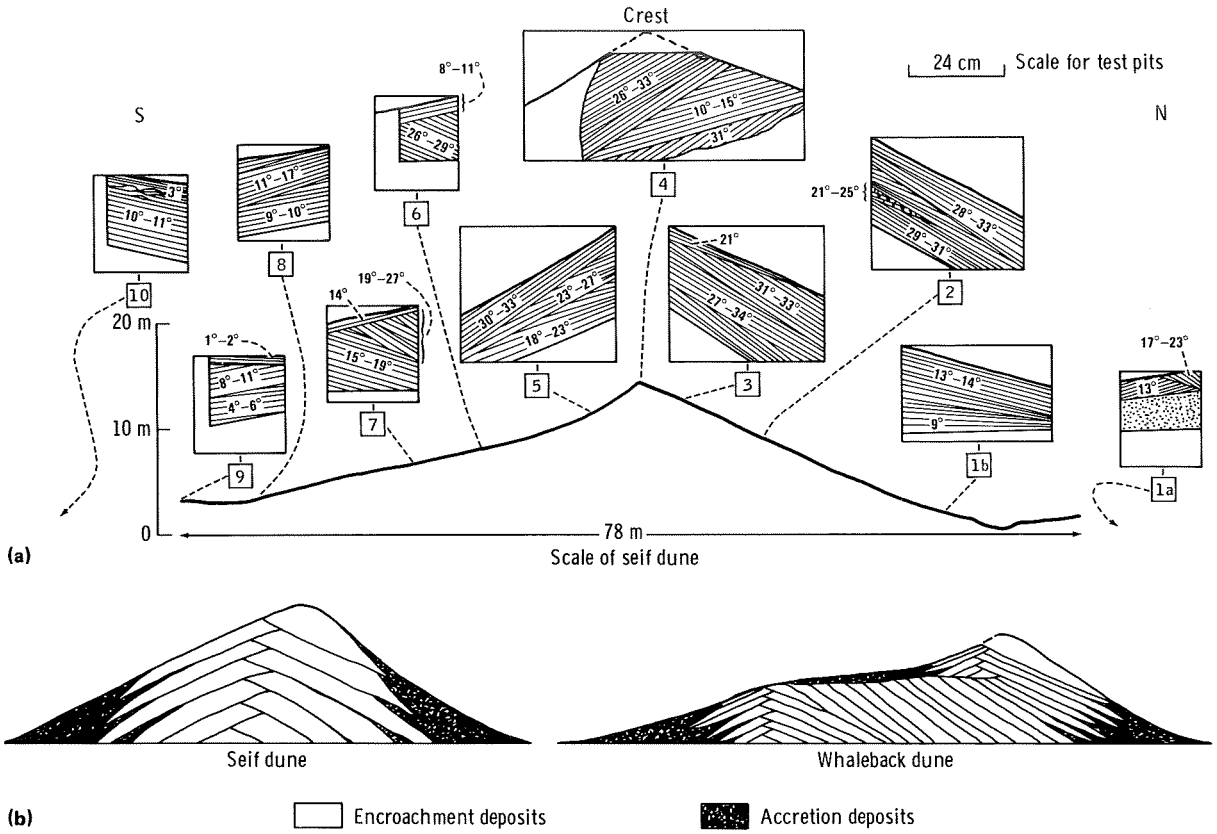


FIGURE 18.—Diagrams showing structures described as typical of seif dunes in north Africa. (a) From McKee and Tibbitts (ref. 22, fig. 6). (b) From Bagnold (ref. 21, figs. 83 and 84).

ditional evidence of noneolian deposition in the lower parts of the dunes. Similar gravels on the flanks of dunes near Maryvale Station (fig. 13) are reported by Folk (ref. 18, p. 19), who interprets them as evidence that at least some of the dunes are of the wind-rift type, with alluvial cores.

A mixture of eolian and fluvial sediment types in the sand sea is also suggested by the grain size distributions shown by the frequency curves for sediments from site C, nearest the headwaters of the Todd River (fig. 20(c)). The curve for the crest sand at site C seems similar to that of dune sands from other sites, but the flanks and interdune sediments seem to be unrelated to the crest sand and are believed to represent sediments that are not wholly eolian. Planned studies with a scanning electron microscope may help determine the sedimentological history of the grains in these sites.

If, as seems likely, some of the sediment below the crests of dunes in the northwestern Simpson Desert is deposited from floodwaters, rather than entirely by wind, then only the crests of these dunes should be considered purely eolian environments of deposition. Unusual wind regimes invoked to explain the coarser sand at the crests relative to finer sand at the flanks and in the interdune sediments in this desert (refs. 18, 53, and 57) may not be necessary.

Wind Data

Effective winds along the western edge of the Simpson Desert can be inferred from analysis of surface winds recorded at Oodnadatta (figs. 1 and 14). Sand roses calculated from the Oodnadatta surface wind data (fig. 22) show the potential



FIGURE 19.—Ground photographs showing details of internal structure in two dunes at site B, south of Andado Station (fig. 13). (a) Contact of steeply dipping (15° to 27°) cross-beds with a near-surface set of nearly horizontal laminae at the crest of the breached dune shown in figure 16(a). (b) Gently dipping strata on the flank of a smaller dune, 2.3 m high; the bedding is preserved throughout the full depth of this dune.

direction and amount of sand movement from each of 16 compass directions during each month of the year. Arrows extending from the center of each sand rose show the monthly resultant directions of sand drift, and the total wind energy available for sand transport in each month (drift potential) is indicated in vector units. The monthly resultant drift potentials, or net amount of energy available for sand transport in the resultant direction in any one month, is indicated by the length of the resultant arrow. Resolving these vectors into an annual resultant direction of potential sand movement near Oodnadatta gives the large arrow shown in figure 14.

Comparison of the monthly resultant arrows (length and direction) given in figure 22 indicates that the greatest potential net movement of sand at Oodnadatta is from the southwest and west-southwest in winter and early spring and from the southeast in midsummer (January and February in the Southern Hemisphere). Thus, the effective wind regime seems to be seasonally bimodal, swinging through approximately 95° of arc throughout each year.

Dune trends immediately to the northeast of Oodnadatta agree with the annual resultant of effective winds, but dunes farther east and north in the main body of the sand sea have a more northwesterly trend, in agreement with the southeast prevailing winds calculated for Oodnadatta, Finke, and Charlotte Waters by Brookfield (ref. 45, table 4; ref. 52, table 14). Unfortunately, most wind stations around the Simpson Desert do not provide wind data in the World Meteorological Organization (WMO) form suitable for the type of calculations made with the Oodnadatta data. For

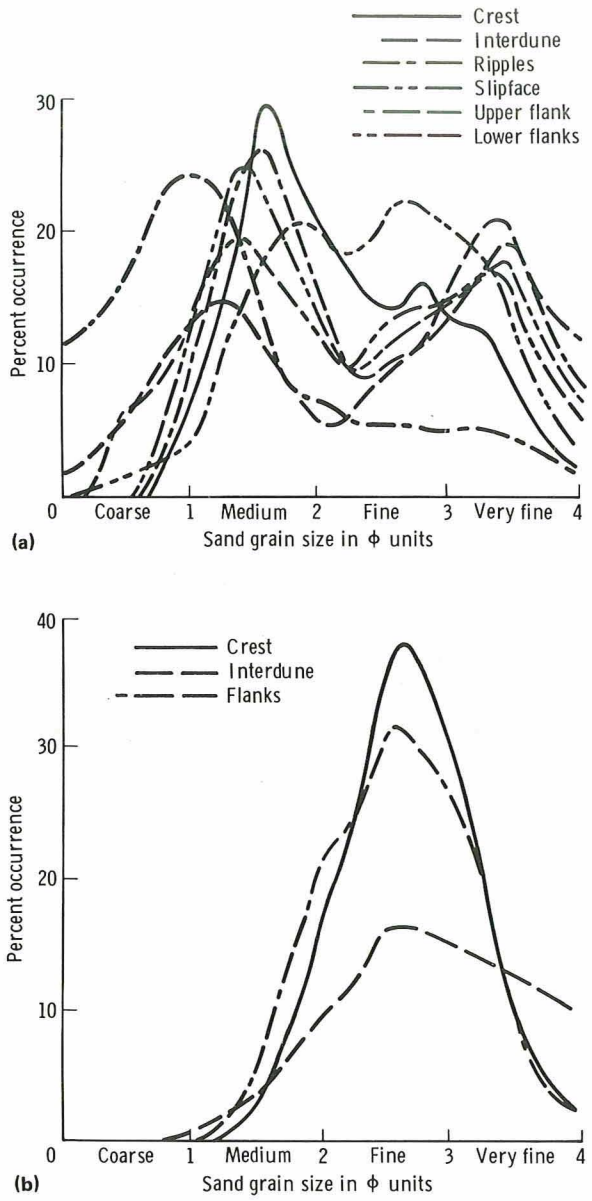


FIGURE 20.—Frequency curves showing grain size distributions in sediment samples from three sites in the northwestern Simpson Desert (fig. 13). (a) Site A near Andado Station. (b) Site B south of Mayfield Bore. (c) Site C south of the Train Hills.

example, direct comparison of the Oodnadatta sand roses with the wind roses plotted by Brookfield (refs. 45 and 52) for Birdsville (on the eastern side of the desert; fig. 4) is not feasible because different windspeed groups were recorded at the two stations and different weighting formulas were used to determine the potential rates of sand transport (ref. 52, pp. 1-20; ref. 58). According to Brookfield's analysis (ref. 52, tables 14 and 15), strongest seasonal resultant winds at Birdsville are from the south and southeast and occur in the fall. Sand-moving winds at Oodnadatta are also from the south or south-southeast in the fall, but the potential sand movement from that direction and in that season is not as great as the potential movement from the southwest in winter and from the southeast in summer, as shown in figure 22.

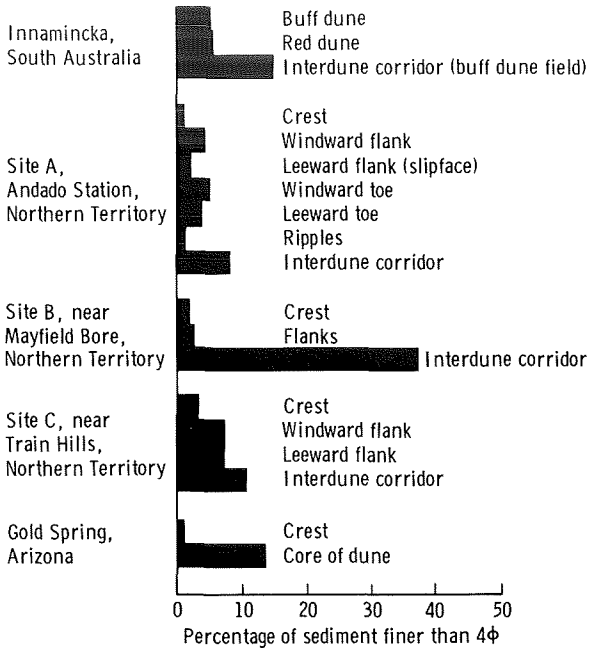


FIGURE 21.—Graphs showing percentages of pan-size ($<4\phi$ or 1/16 mm) sediments in different parts of dunes and in interdune corridors sampled in dune fields in Australia and Arizona.

Field evidence of the most recent sand-moving winds in the desert around Andado Station was found in September 1976 in the form of numerous arrays of wind-eroded ridges ("miniyardangs") preserved on the flanks of dunes and in the interdune corridors (fig. 23). These ridges were not eroded by running water, for they are oriented oblique to the downslope direction of dune flanks. Orientations of these wind indicators, measured with a Brunton compass, are superimposed on an aerial photograph of site A (fig. 24). The orientations range from N10°W in the interdune corridor to N55°W on the upper flank of the dune. No northeast-trending erosion forms were found, even on the west-facing flanks of the dunes, as might have been expected if the wind had been blowing in helical vortices down the interdune corridors, as proposed by Folk (ref. 18, pp. 20-21; ref. 19, figs. 4 and 5) and Glennie (ref. 23, fig. 73).

The arrows on figure 24 show the wind pattern inferred from the measured miniyardang orientations across two dunes and three interdune corridors at site A. Similar northwest-trending erosion features were found on dunes observed along the road between Old Andado Station and Allambi Station in the northwesternmost part of the Simpson Desert (fig. 13). The field evidence, although obviously only representative of the most recent sand-moving winds there, indicates that the winds in that area were blowing from the southeast. Windflow was apparently deflected westward up and over the dune crests, oblique to the general trend of the dunes, but resumed a general north-northwestward direction in the adjacent interdune corridors.

The occurrence of sand-moving winds from the southeast just before our investigations was corroborated by finding the loosest sand and steepest slopes on the west-facing upper flanks of all the dunes investigated at site A, north of Andado. The location of the most recent avalanche slopes on the west-facing flanks of the dunes is opposite to that reported by Madigan (refs. 6, 7, and 9) and most other workers in the Simpson Desert and suggests that some seasonal reversal of the slipfaces, from the east to the west flanks, occurs on these dunes.

Additional systematic measurements of wind erosion features formed during different seasons may be a reasonable method for studying patterns of sand-moving winds in dune fields. Similar changes in erosion features found on linear dunes of the Moenkopi Plateau in Arizona are currently being observed to test the correspondence of their seasonal orientations with the distribution of sand-moving winds calculated from the WMO wind data recorded at Winslow, Arizona.

WIND-STREAMLINED HILLS

South Australia

An aerial reconnaissance over some islands in the northern part of Lake Frome in the Strzelecki Desert (fig. 4) shows the presence there of streamlined hills with blunt prows facing south, into the prevailing wind (fig. 25). These hills are eroded in Quaternary sediments (ref. 59), and they have the flat, tapering crests and surrounding moats typical of many yardangs developed in

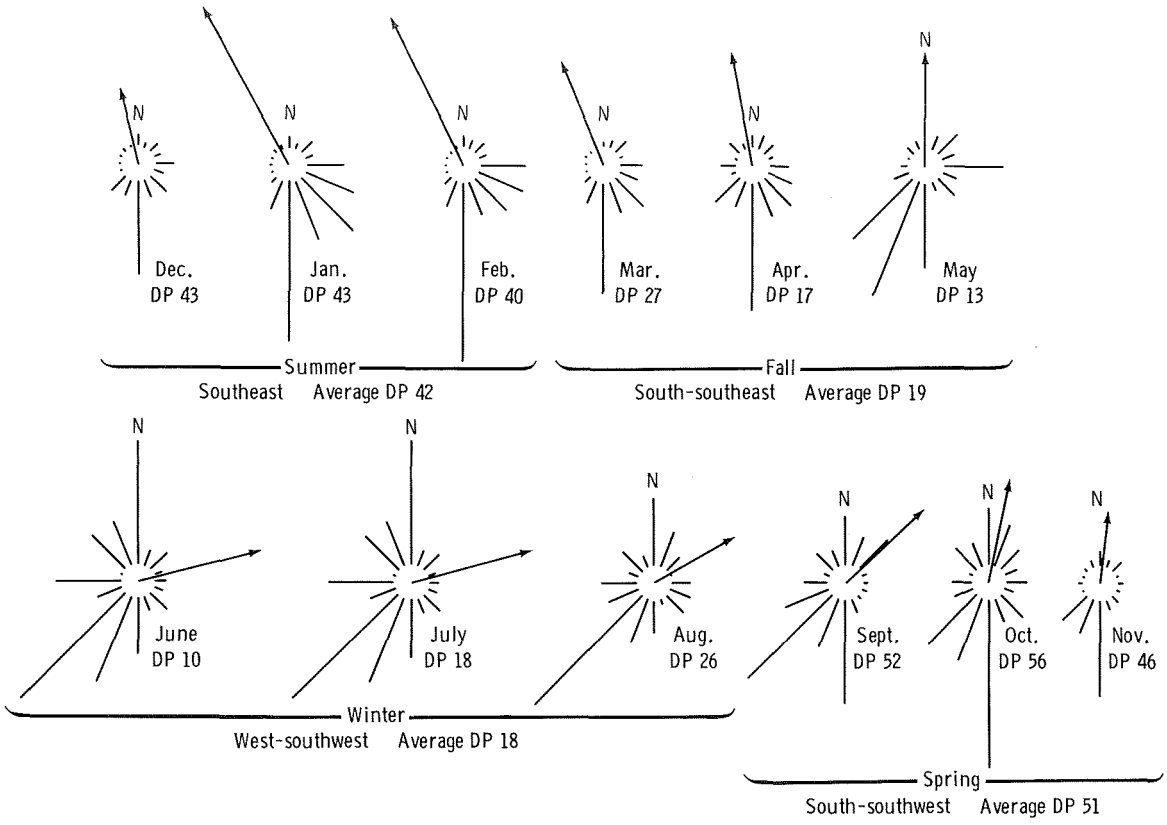


FIGURE 22.—Sand roses (circular histograms; calculated by S. G. Fryberger) showing the potential movement of sand by effective winds from each of 16 compass directions each month at Oodnadatta, South Australia (fig. 14). Arrows show the potential resultant direction of sand movement during each month, and the numbers show the magnitude of potential movement, in vector units (DP = drift potential: Fryberger, ref. 58).

similar sediments (lakebeds and old dune sands) described by numerous authors for other deserts and recently reviewed by McCauley, Grolier, and Breed (ref. 60).

Except for fluted terrain along the shore of Lake Eyre, illustrated by King (ref. 10, pl. 3) and noted by Twidale (in ref. 61, p. 1237), yardangs have not been described from Australia. However, eroded cores of old dunes in Sturt's Stony Desert, illustrated by Wopfner and Twidale (ref. 12, pl. 15B), are similar in form and type of material to yardangs described at Rogers Lake, California (refs. 60, 62, 63, and 64).

Bowler (ref. 44, pp. 297-299, fig. 5) describes one of the islands in the southern part of Lake Frome as an old dune (lunette) built of pelletal clays blown from the lake floor between approx-

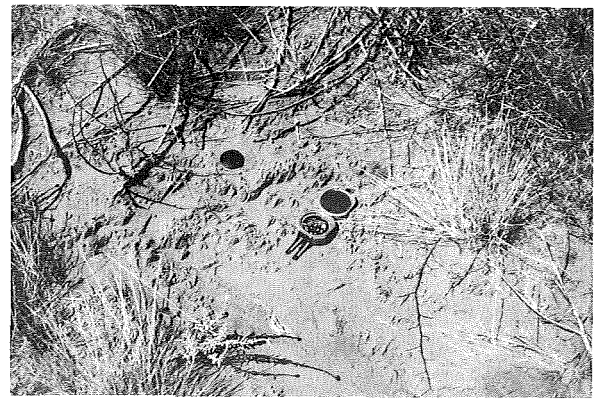


FIGURE 23.—Wind-eroded minor ridges ("miniyardangs") on the flank of a dune at site A, near Andado Station, Northern Territory. The measured orientations of these features are shown in figure 24, with wind directions inferred from their pattern of alinement on the dunes and interdune corridors.



FIGURE 24.—Vertical aerial photograph of dunes at site A, showing orientations of wind-eroded ridges (miniyardangs; fig. 23) on the dunes and in the interdune corridors. The arrows indicate the wind directions inferred from the miniyardang orientations, which are shown by the pattern of short parallel lines. This photograph has been made available by courtesy of the Director, Division of National Mapping, Department of National Resources, Canberra, Australia.

imately 15 000 and 20 000 years B.P. and wave-cut into island form during a rise in lake level since that time. David (ref. 65, pp. 58-59) states that Lake Frome probably receives some runoff every year. However, observations on Landsat images and the authors' aerial reconnaissance in 1976 indicate that the islands in Lake Frome remained dry even during the recent heavy floods in South Australia, which totally inundated Lake Eyre (fig. 5). Thus, the possibility that these streamlined hills are recent wave-cut features (lacustrine stacks) rather than wind-eroded features (yardangs) seems remote. Ground investigations of these hills, currently being conducted by John Douglas of the Ecological Survey of South Australia, should be definitive.

Northern Territory

Several domelike erosional remnants rise as inselbergs above the desert plains of central Australia. The best known is Ayers Rock, which is composed of steeply dipping massive beds of arkosic sandstone (fig. 26). Approximately 30 km to the northwest is a group of hills (including Mount Olga) composed of gently and variably dipping massive beds of boulder conglomerate; they are known collectively as the Olgas. Approximately 80 km to the southeast is Mount Conner, a semicircular mesa capped by nearly horizontal 100-m-thick beds of quartzite. The different shapes of these inselbergs have been attributed to different responses of the varying lithologies to processes of mechanical weathering (refs. 66 and 67).

The main monolith at Ayers Rock (fig. 26) is nearly 350 m high with a steep, blunt southeast end, and it tapers to a gentler slope at the lower northwest end. The arkose beds dip approximately 80° to the southwest, and their strike is parallel to the annual resultant of all winds recorded at Ernabella, approximately 160 km to the southeast (ref. 45, table 4). Ayers Rock, unlike the Olgas and Mount Conner, is composed mainly of readily transportable sand-sized grains, which weather out along upturned bedding planes alined parallel to the prevailing winds. Streamlining along these planes is evident in the main monolith

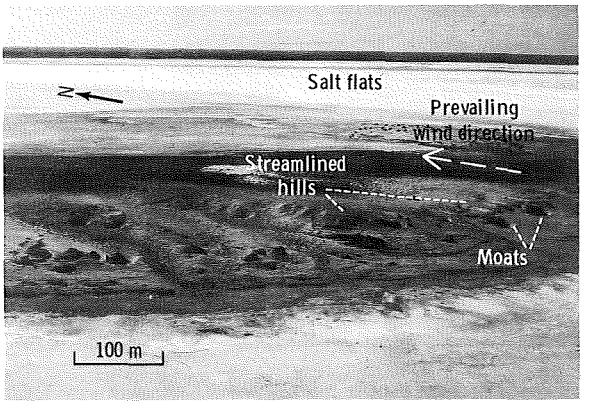


FIGURE 25.—Oblique aerial photograph, taken at approximately 3000 m altitude in September 1976, showing streamlined hills (yardangs?) on an island in Lake Frome.

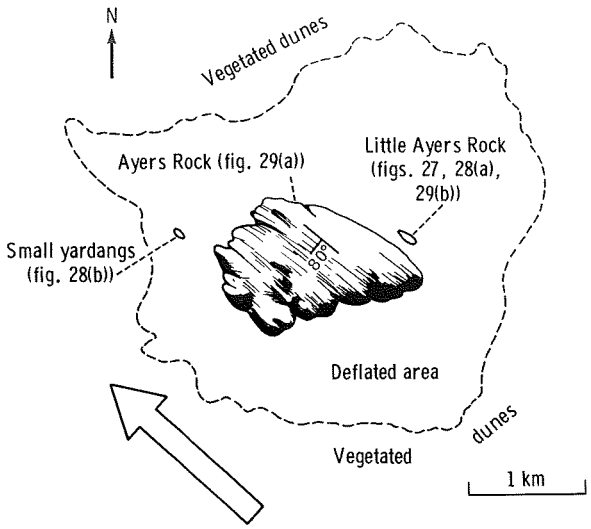


FIGURE 26.—Sketch drawn from a vertical aerial photograph showing the streamlined shapes of Ayers Rock and its outliers (shown in figs. 27 and 28). The large arrow shows the annual resultant direction of all winds recorded at Ernabella, approximately 160 km to the southeast (Brookfield, ref. 45, table 4).

(fig. 26) but is best developed in the smaller outliers, such as Little Ayers Rock and numerous smaller nearby hillocks (figs. 27 and 28).

The shape of Ayers Rock has most recently been described as a "sugarloaf," which is considered a relic of processes that operated in a former humid, tropical climate (ref. 68). However, Wellman and Wilson (ref. 69) attribute the forms of Ayers Rock and the Olgas to salt weathering. Ollier and Tuddenham (ref. 66) consider the main agent of weathering at Ayers Rock to be spalling, with subsequent removal of the detritus by winds. However, these authors state (p. 274) that "the wind is probably important in removing comminuted debris, but not as an agent of erosion." Clearly, these authors have not recognized the role of deflation as an important wind erosion process.

Recent studies, including field observations, modeling experiments, and a review of the literature on yardangs (refs. 60, 70, and 71), show that deflation is a major wind erosion process that produces yardangs in both soft sediments and in bedrock. Furthermore, yardangs can be meters to kilometers long (ref. 60, fig. 17; ref. 70, p. 37). Where structures such as bedding planes, joint systems, and fold axes are alined parallel to prevailing winds, large-scale streamlined hills, interpreted as yardangs, are observed even in Precambrian dolomites and crystalline rocks (ref. 60, figs. 16 and 20).

Both Ayers Rock and the Olgas are windy places. The aboriginal name for the gorge at the western end of the Olgas is "walpa," meaning windy, and Ollier and Tuddenham (ref. 66, p. 267) report that strong winds were experienced at the top of Ayers Rock. Weather pits, ridges, and furrows parallel to the strike there show evidence of deflation, and loose grains of sand were observed in sheltered crevices beneath the crusty plates that comprise the surfaces of Ayers and Little Ayers

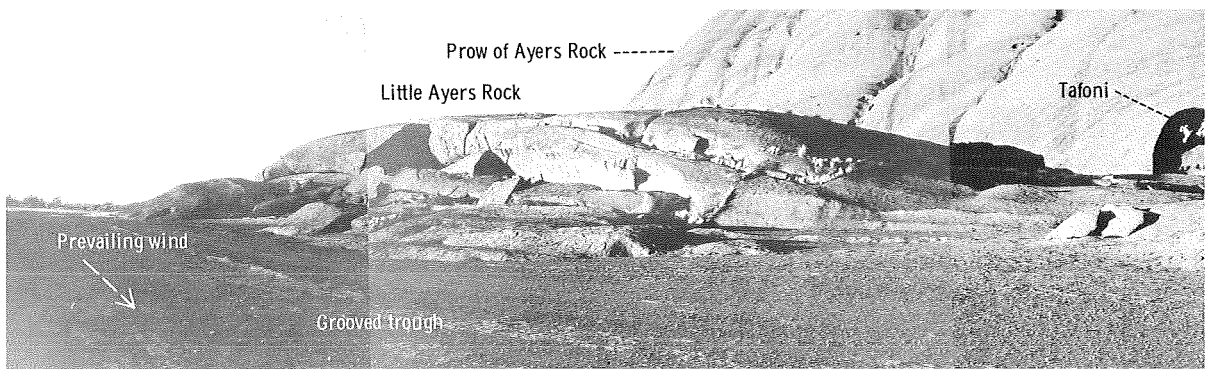


FIGURE 27.—Mosaic of three ground photographs showing the streamlined shapes of Little Ayers Rock and associated smaller arkose hillocks. The main part of Little Ayers Rock is approximately 200 m long, and the meter-sized hillocks extend another 100 m to leeward. One of the small hillocks is shown in detail in figure 28(a).

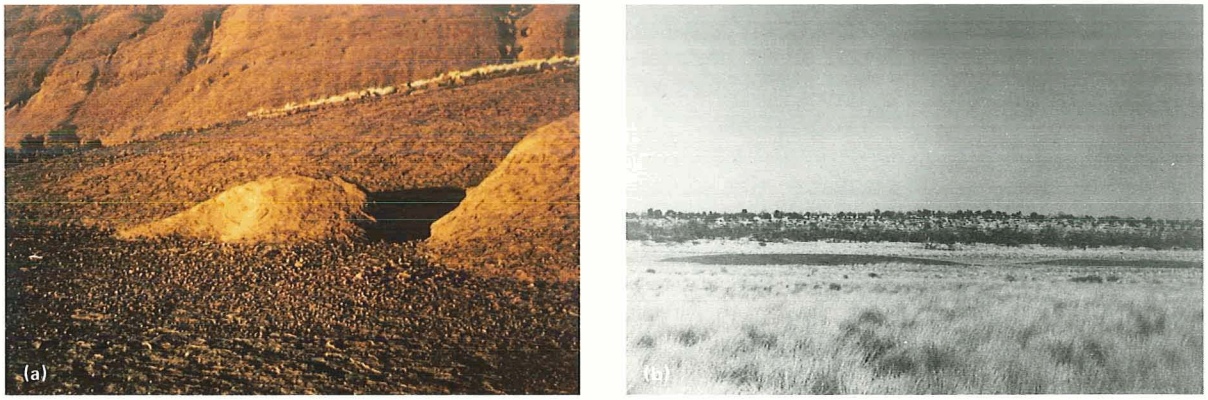


FIGURE 28.—Ground photographs showing the well-developed aerodynamic shapes of arkosic sandstone hillocks at Ayers Rock, Northern Territory, Australia. Prevailing winds are from the left in each photograph. (a) Meter-size yardang on the east side at the upwind end of Little Ayers Rock (fig. 27). (b) The low yardangs, each approximately 15 m long, in the lee of Ayers Rock (fig. 26).

Rock (fig. 29). Ollier and Tuddenham (ref. 66, p. 274) recognized that these "many thin and delicate exfoliation flakes would be destroyed by sand-blasting," but concluded, therefore, that "they could not possibly be formed by wind action." On the contrary, similar delicate platy textures, left by deflation of weathered detritus, are characteristic of yardang surfaces in the Peruvian desert (ref. 60, pp. 111-116 and 150-155).

Grooving of the wide troughs around Ayers Rock and Little Ayers Rock, and subparallel flutes along the length of Little Ayers Rock, resemble features seen in yardang fields in other deserts. Concave lower flanks, collapsed blocks, and tafoni (cavernous weathering) along the sides of Ayers Rock and Little Ayers Rock (fig. 27) are similar to features reported on yardangs of coastal Peru (ref. 60, pp. 140-143 and 146-153).

As in other deserts, the streamlined hills at Ayers Rock and the Olgas occur in groups, and the larger bodies are less well streamlined than the smaller mounds. At Ayers Rock, some of the outliers have developed almost perfectly streamlined aerodynamic forms (figs. 27 and 28). The streamlining of the main monolith, believed to be facilitated by the structural grain, is not so obvious but is pronounced in the vertical view (fig. 26). On the other hand, the different shapes of semi-

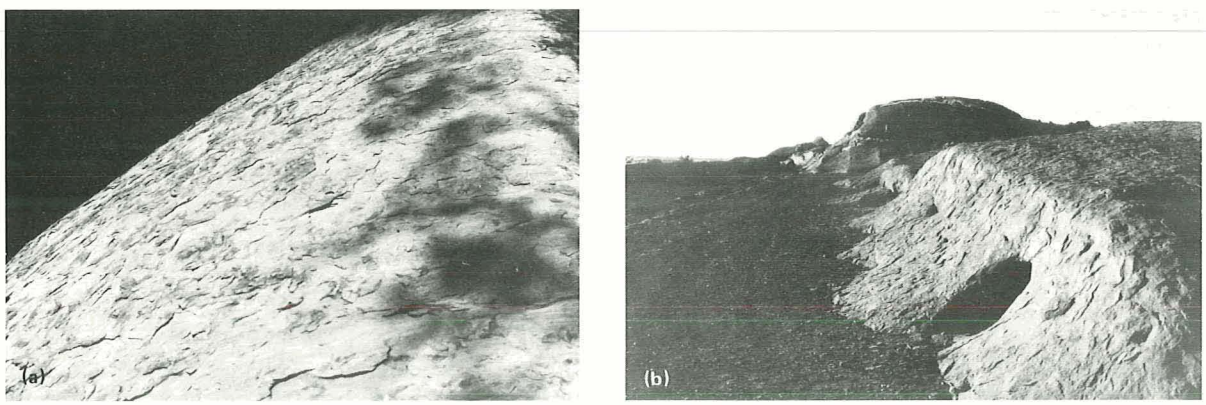


FIGURE 29.—Ground photographs showing the scabrous surface of Ayers Rock (a) and Little Ayers Rock (b). Grains of loose sand occur in crevices beneath the surface plates, which are a few millimeters thick. Similar platy surface textures, tafoni, and concave flanks (b) are found on yardangs in Peruvian deserts (McCauley, Grolier, and Breed, ref. 60, figs. 60, 61, and 69).

streamlined hills in the Olgas, and the apparent lack of streamlining at Mount Conner, are probably attributable to the different compositions and structural orientations of the rocks there.

The low parallel yardangs west of Ayers Rock are nearly obscured by vegetation (fig. 28(b)). Vegetation increases surface roughness and inhibits streamlined flow; therefore, its presence around the streamlined hills implies that, if deflation formed these hills, it occurred in an earlier, more arid period when such vegetation was absent. The deflated perimeter of Ayers Rock (fig. 26) and the surrounding sand sea of inactive, vegetated dunes also suggest past eolian activity. The long eolian history of this region has been discussed by numerous authors (ref. 13 and many others).

DUNE STUDIES ON THE MOENKOPI PLATEAU, ARIZONA

Extensive fields of linear dunes occur on the Colorado Plateau in western North America. A map showing the distribution of dune types in the southern part of this region, in northeastern Arizona, in southeastern Utah, and in northwestern New Mexico is given by Hack (ref. 72, fig. 2), and the distribution of eolian sand without regard to dune types is shown by Cooley et al. (ref. 73, pl. 3). An index map of a major dune area in northern Arizona is shown in figure 30, and the typical appearance of the linear dunes on the Moenkopi Plateau is shown in figure 31.

Hack (ref. 72, p. 243) described the linear dunes in this region as from 2 to 10 m high, 60 m to several kilometers long, and approximately 100 m apart, and he considered them to be similar to the longitudinal dunes of Australia. Earlier descriptions of the ridges as "lee dunes" (ref. 36, fig. 10) were considered erroneous by Hack because the dunes do not necessarily form in the lees of topographic obstacles but rather are located on flat plains.

In the area of northern Arizona studied by Hack, dunes of transverse (barchanoid), linear, and parabolic types are found in close geographic proximity. Hack (ref. 72, p. 240) considered that all three types of dunes are presently being formed and that the dune type formed depends on the relative resistance of the vegetative cover, in each locality, to the movement of sand by wind.

Recent space and aerial photographs of the area (such as the one shown in fig. 3) show that linear dunes can be traced from localities along the edge of the Moenkopi Plateau, where they are only slightly vegetated and where some ridge crests are active, into areas of high mesas where the ridges are inactive and are obscured, in ground view, by heavy vegetation. Beyond this immediate area, moreover, throughout 65 000 km^2 of the Colorado Plateau, wind-alined subparallel stream patterns are attributed (ref. 74) to confinement of drainages between ancient linear dunes. Based on the estimated rate of incision of some of these streams, Stokes (ref. 74, pp. 808, 815-816) concludes that some of the linear dunes on the Colorado Plateau were formed as many as 1 000 000 years ago.

Field observations and aerial reconnaissance of an area between Hogan View Point, west of Goldtooth, and Gold Spring, Arizona (fig. 30), indicate that active dunes there are mostly of the barchanoid type and are located mainly on the Ward Terrace, approximately 250 m below the Moenkopi Plateau. The linear dunes that cover the Moenkopi Plateau typically head several meters to kilometers downwind from the edge of the high Adeii Eechii Cliffs, which are marked by numerous deflation hollows. No dunes were observed climbing from the Ward Terrace to the level of the Moenkopi Plateau along these cliffs except in the low areas cut by Moenkopi Wash to the north, near Tuba City, and by Dinnebito Wash to the south, near Garces Mesa.

Sources of sand in the linear dunes on the high-level Moenkopi Plateau have not been established. Hack (ref. 72, p. 243) states that the dunes there generally extend downwind from "a narrow source of sand such as a furrow, a blowout, a gully head, or the crest of an active parabolic dune." However, such narrow sources seem inadequate to supply these dunes, which typically extend for 3 km or more in a downwind direction (fig. 3). The dunes may have originated as dunes of the source-bordering lee type described by Melton

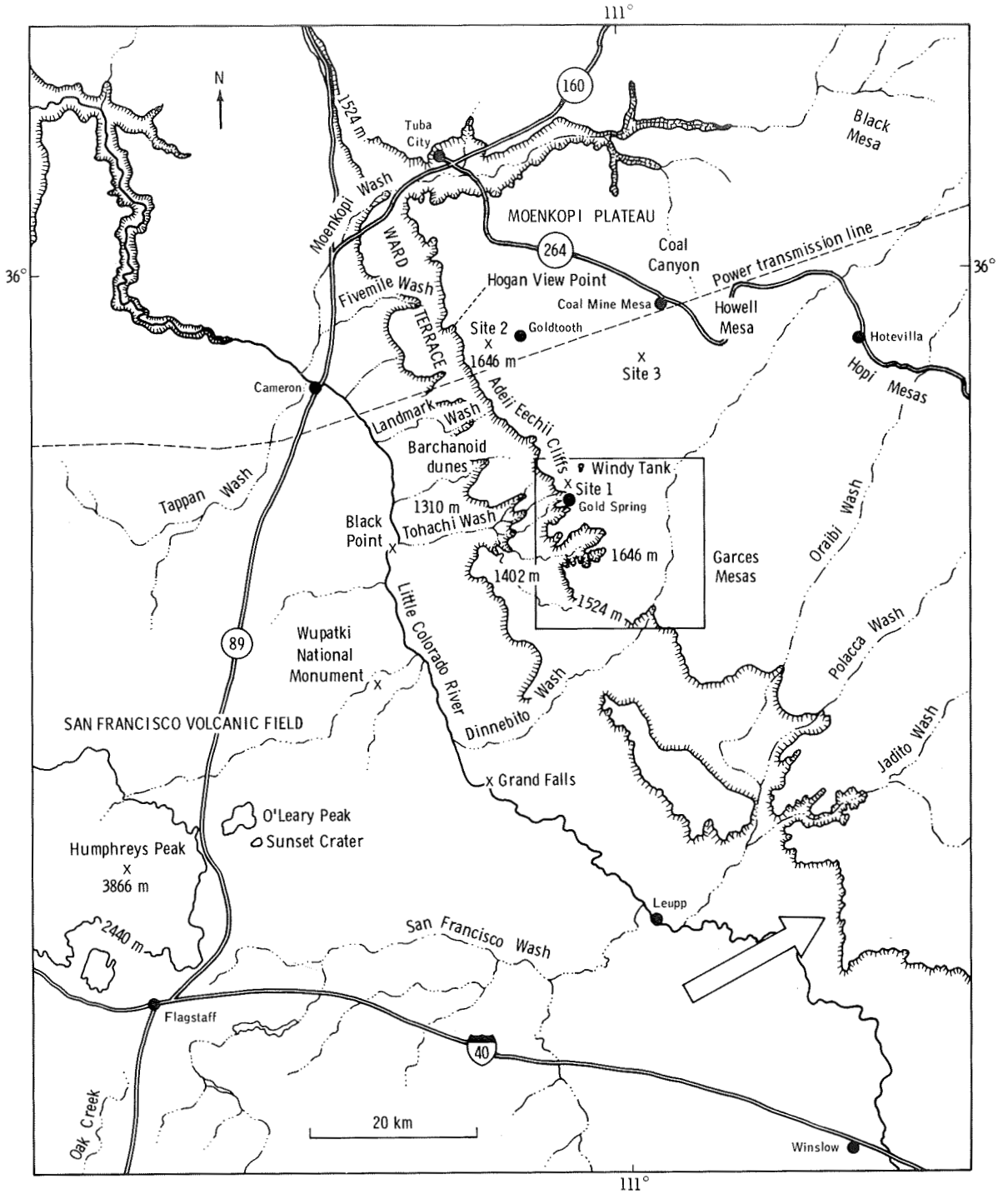


FIGURE 30.—Index map of localities where linear dunes are being investigated on the Moenkopi Plateau, Arizona. The large arrow shows the annual resultant direction of effective winds recorded at Winslow (shown in relation to the dunes in fig. 3). The outlined area is shown in figure 3.



FIGURE 31.—Oblique aerial photograph showing linear dunes on the Moenkopi Plateau, Arizona, near Gold Spring. View is to the north; the prevailing (southwest) wind is from the left. Photograph by John F. McCauley.

(ref. 36, pp. 122-123), supplied by alluvium of the Little Colorado River and its tributaries (fig. 30). At present, however, the linear dunes on the Moenkopi Plateau seem to be cut off from a source of replenishment except by deflation of the sandstones that cap the cliff edge. A veneer of whitish sand, apparently derived from this source, mantles the upwind ends of the dune ridges.

A trench in one of the linear dunes at site 1 near Gold Spring (fig. 32) reveals that sand at a 3-m depth at the base of the dune, though mostly typical quartz dune sand, includes at least one zone containing volcanic ash. Preliminary examination of the ash shows that they include delicate spindles, which suggests that they were deposited from a volcanic eruption in the nearby San Francisco Volcanic Field (fig. 30) and have not been secondarily transported to the dunes by saltation. Chemical analyses are planned to help resolve the age and source vent for the ash. In addition, scanning electron microscope studies are planned to help determine the recent sedimentological history of sand grains from the surface and interior parts of linear dunes at the upwind and downwind ends of the field on the Moenkopi Plateau. Similar studies of the apparently younger, presently active barchanoid dunes in the Ward Terrace fields below the Moenkopi Plateau are planned by C. K. McCauley.

Trenches cut by hand and by backhoe at several sites in the linear dunes on the Moenkopi Plateau (figs. 30, 32, and 33) reveal surface sets of bedded laminae down to depths of a few centimeters in inactive dunes and to a depth of approximately 1 m in a dune with an active crest. Below these surface sets, however, the dune sand is structureless. The structural relationships illustrated in figure 33 thus strongly resemble those of the red linear dunes at Innamincka, South Australia, and at site A near Andado Station, Northern Territory, both of which are believed to be old dunes.

Samples taken from an active crest and structureless interior (at a depth of 3 m) of a dune at the upwind end of the field near Gold Spring (site

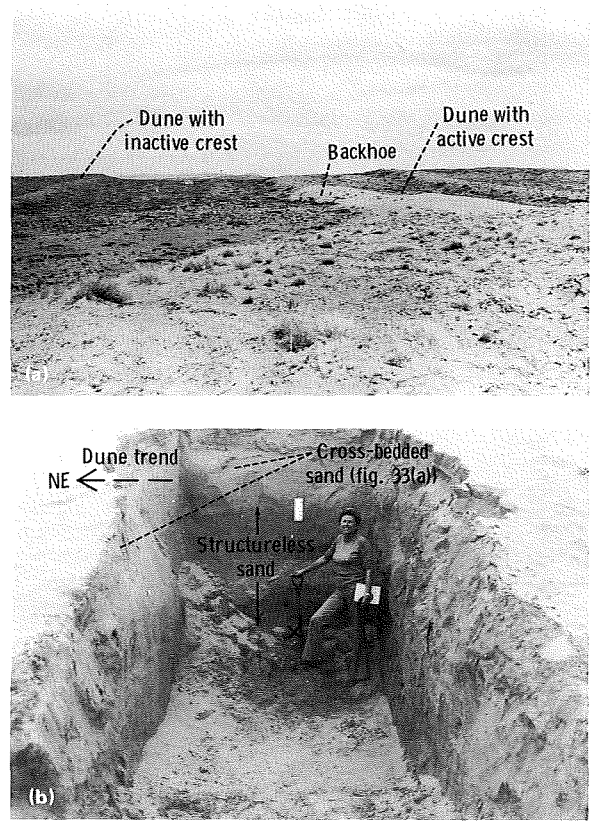


FIGURE 32.—Ground photographs showing linear dunes at site 1 on the Moenkopi Plateau, Arizona. (a) View toward the northeast showing trenching in two dunes, one with an active crest. (b) A 3-m-deep trench on the northwest side of the dune with the active crest shown in (a). The core of this dune consists of structureless sand, slightly calichified, with ash from a volcanic eruption collected at the level marked "X". The scale on the side of the trench is 25 cm long.

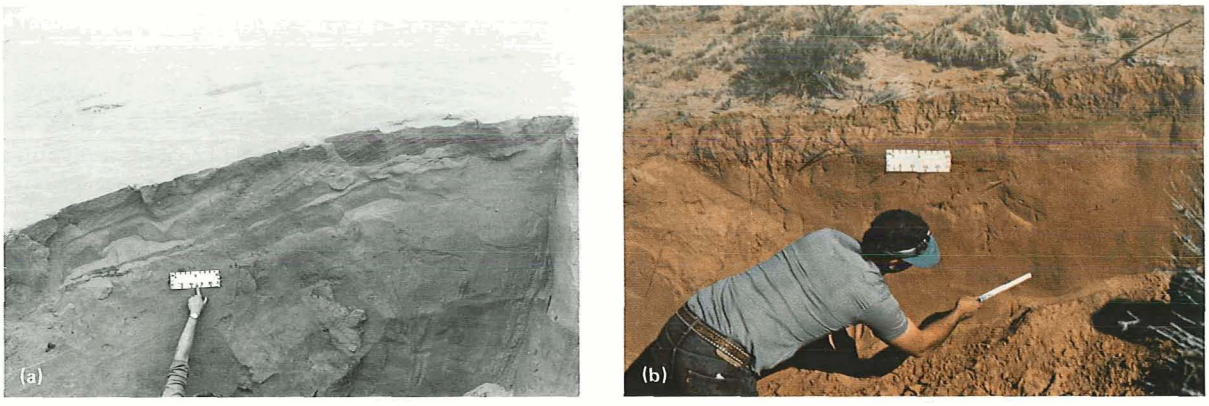


FIGURE 33.—Ground photographs showing details of dune structure at site 1, Moenkopi Plateau, Arizona. (a) View to the northeast, parallel to the dune trend, showing cross-bedding preserved in the upper 1 m of the dune with an active crest shown in figures 32(a) and 32(b). (b) View, with the same orientation, of a trench in the west side of the dune with an inactive crest shown in figure 32(a). Note the structureless sand beneath a thin set of surface laminae.

1) and from the eroded core of a linear dune at the downwind end of the field (site 3) were analyzed by Kevin Horstman, following the methods of Folk (ref. 51); results are shown in table II. As in Australia, samples from the dune cores at both sites show a much higher percentage of silt and clay (pan) sized sediments than does the sample from the dune crest, and the crest sand at site 1 has a coarser mean size and is better sorted than sand from the lower part of that dune. However, distribution of grain sizes in the crest sand is bimodal, whereas that of the interior sediments is not (fig. 34). A high clay content in the dune sand is indicated by the presence of desiccation cracks, which are common on these dunes, even on those with active crests (fig. 35).

A distinct difference in color is observed from the crest to the interior of the dunes at the upwind end of the Moenkopi Plateau (table II). The sand at the top and base of the dune at site 1 has the same hue and chroma (strong yellowish brown); however, even when dry, sand from the base is darker than sand from the crest. Moreover, sand from the downwind (northern) part of the dune field (at site 3) is redder than sand from the upwind end (at site 1). No differences in rounding of sand grains were seen in samples from the crest and base of the dune at site 1 or from dunes at the upwind and downwind parts of the field.

Field observations in July and November 1976 and in February 1977 confirm the occurrence of seasonal shifts in effective (sand-moving) winds as shown on the sand roses, which were constructed from surface wind data recorded at Winslow, Arizona, according to the method devised by S. G. Fryberger (ref. 58) (fig. 36). Southeast summer winds produce northwest-facing slipfaces on the active dune crests. These slipfaces are destroyed by northwest winter winds that produce southeast-facing slipfaces (figs. 37(a) and 37(b)). These seasonal shifts occur despite the general prevailing southwest winds. The calculated direction of potential net sand movement, however, is to the northeast, almost exactly parallel to the general trend of the dunes as shown in figure 3. Sand was observed saltating northeastward, parallel to the strike of the dunes, along an active crest at Gold Spring (site 1) in February 1977. Highest winds, with gusts greater than 40 knots (approximately 75 km/hr) are recorded from the south-southwest, southwest, west-southwest, and west in the spring and summer, which is also the dry season in northern Arizona, before onset of the summer monsoon.

Field observations and recorded wind data for the Arizona locality indicate that the seemingly unimodal wind regime (ref. 36, p. 121) actually has components that produce seasonally shifting sand deposits on opposing sides of the linear dunes. The straightness (lack of sinuosity) of the dunes may be due to the shepherding effect (ref. 18, p. 20) of the very strong prevailing winds from

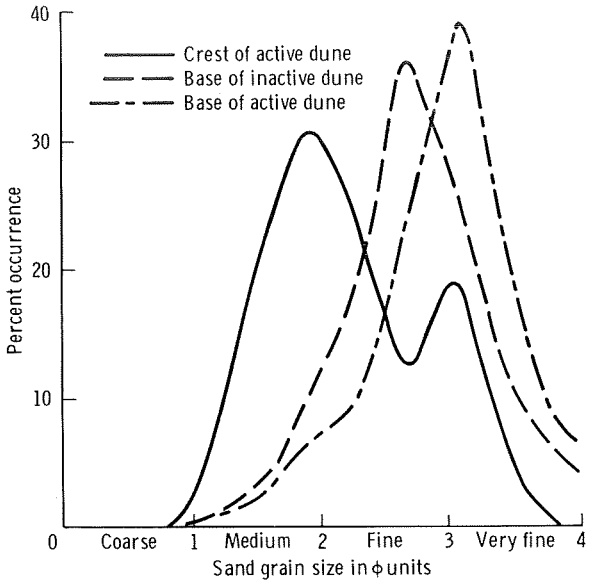


FIGURE 34.—Frequency curves showing grain size distributions of sand from two linear dunes on the Moenkopi Plateau, Arizona. Compare with grain size distributions in sands of Australian linear dunes (figs. 11 and 20).

the southwest quarter, which keeps the dunes on a constant course to the northeast despite the seasonal shifting of avalanche deposits from one side of the active crests to the other. This relationship seems more like that of the Australian dunes and wind regimes (fig. 24) than like that of Sabhā, Libya (ref. 22, fig. 3), where the dunes seem to be more sinuous and irregular in plan.

INTERPRETATION OF THE DUNE STUDIES

In general, bedding was seen only in active or what appeared to be recently active parts of linear dunes in Australia and in Arizona. In most cases, the bedding was not closely similar to that described as typical of seif dunes and thus thought to be common to all dunes of the "longitudinal" type. It seems likely that some of the observed structures, although obviously formed in dunes, might not be interpreted as dune structures if they were preserved in the geologic record (see, for example, ref. 75).

Several structural relationships that seem to be characteristic of the sand-ridge variety of linear dunes were noted in both Australia and Arizona. First, surface sets of accretion laminae were found over the entire surfaces of the dunes. The deposition of these surface layers of sand on the dunes may be aided by the presence of vegetation acting as baffles, as described by Goldsmith (ref. 76) for some coastal dunes at Cape Cod, Massachusetts. Second, steeply dipping surface laminae in wedge planar sets such as are typical of the peaked summits of seif dunes in Libya (ref. 22, pl. II, 8-F) were observed in only a few localized, active peaked crest areas on one of the Arizona dunes and were rarely seen in Australia. Sets of laminae in the Australian dunes and in a trench upwind of the active crest of a dune on the Moenkopi Plateau are typically truncated by low-angle, planar erosion surfaces.

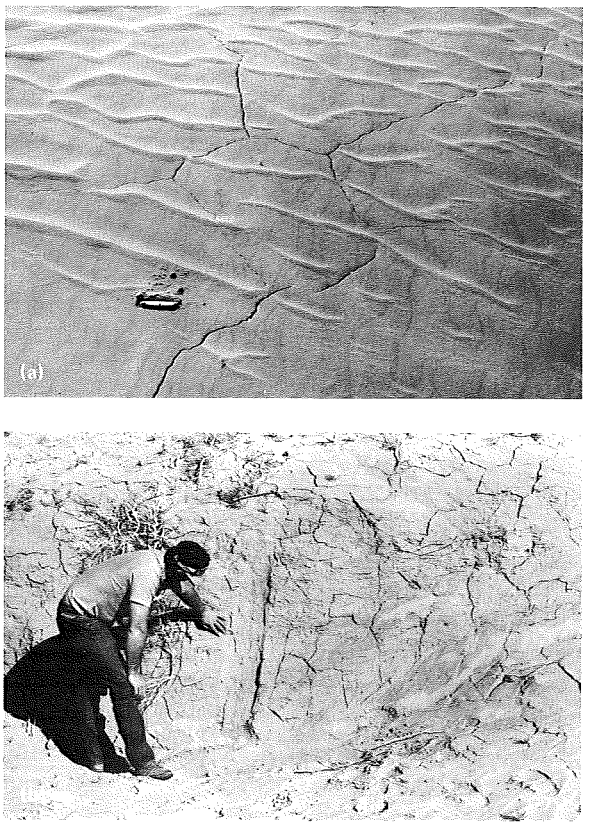


FIGURE 35.—Ground photographs showing desiccation cracks in a dune at site 1 on the Moenkopi Plateau, Arizona. (a) Active crest of the dune. (b) Eroded core of the same dune, near the upwind end.

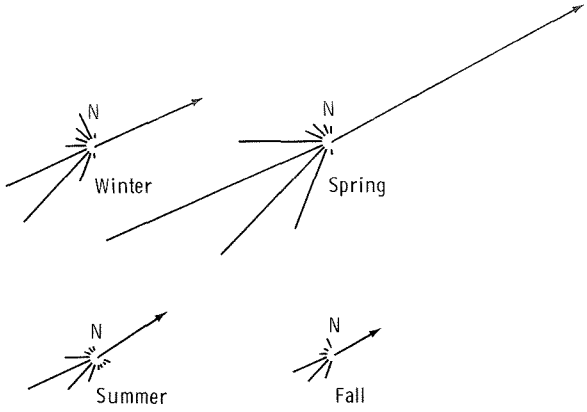


FIGURE 36.—Sand roses (circular histograms calculated from surface winds recorded at Winslow, Arizona) showing potential movement of sand from 16 compass directions during each season on the Moenkopi Plateau, Arizona. Effective winds range from northwest in winter to southeast in summer but are dominantly from the southwest and west-southwest at all seasons. The annual resultant of these winds is shown in figures 3 and 30.

Third, the cross-beds or laminae in the Australian dunes and in most parts of the Arizona dunes commonly have lower angles of dip than those associated with avalanche bedding. In this regard, the observed patterns fit the prediction of Yaalon and Laronne (ref. 77, p. 1062) that "seifs and other dunes subject to multidirectional winds" would have lesser proportions of avalanche bedding than dunes such as barchans, which are formed in unidirectional wind regimes.

Planar surfaces bounding sets of cross-beds in transverse dunes in Israel are attributed to limited drying out of the surface and its consequent deflation (ref. 77, p. 1063). An erosional surface of this type seems to have been in the making on the flank of the dune shown in figure 37(a). Bimodal components of the wind regime would seem to be essential to such a process. The time element may be important in determining whether the resulting sets are broad and tabular in cross-section as in Australia, or whether the sets terminate in wedges and are steeply bounded as at the crests of typical seif dunes (fig. 18). Certainly, the very broad sand ridges with rounded summits observed in Australia generally showed little evidence of the type of rapid depositional changes postulated for the Libyan seifs.

The linear dunes at Sabhā, Libya, reportedly grow southwestward, parallel to the resultant direction of bimodal winds, which are opposed at angles of approximately 90°. The change in direction of the effective winds at Sabhā is diurnal, from southeast in the mornings to northeast in the evenings (ref. 22, pp. 6-8 and 17). The dunes built by these winds at Sabhā characteristically have high, peaked summits with steep slipfaces at intervals along their lengths (ref. 22, pl. II, A). The surface shapes of the Libyan seifs seem quite unlike

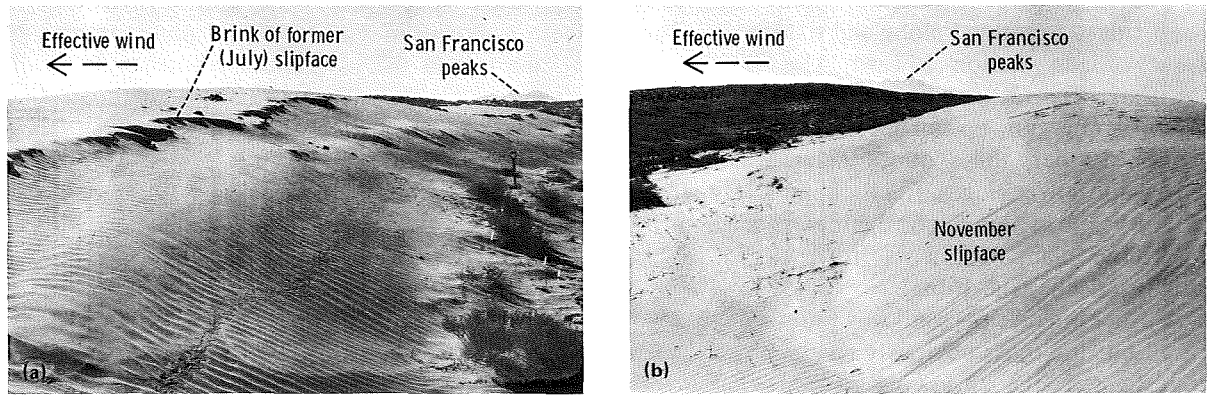


FIGURE 37.—Ground photographs (November 1976) showing seasonal reversal of slipfaces of linear dunes at site 1 on the Moenkopi Plateau, Arizona. View is to the southwest, toward the central peaks of the San Francisco Volcanic Field (fig. 30). (a) Remnants of the northwest-facing July slipface are wind-eroded into yardangs at the brink of the dune with an active crest. (b) The November slipface is developed on the southeast-facing dune slope, which was a windward slope in July.

the broad sand ridges with rounded summits and few slipfaces, which were observed near Innamincka in the Strzelecki Desert, in the northwestern Simpson Desert from Mayfield Bore to Allambi Station, and on the Moenkopi Plateau, Arizona. In all those areas, effective winds have seasonally bimodal components that are opposed at angles of as much as 131° (Birdsville, ref. 52, table 14c), 95° (Oodnadatta, fig. 25), and 210° (Winslow, summer and winter, fig. 36).

Quantitative data on actual amounts of sand moved by diurnally bimodal winds at Sabhā, Libya, and by seasonally bimodal winds in the Simpson Desert, Australia, and on the Moenkopi Plateau, Arizona, are not presently available. However, it seems reasonable to suppose that winds which persist in one direction for an entire season would deposit sand in sets of much broader lateral extent than would winds whose transporting effects are reversed on a daily basis. According to this idea, each season's winds would plane off the upwind slope and deposit broad, blanketlike sets of beds with uniform orientations across the top and down the lee slope of the dune ridge. Each season's deposit would be planed off and overlaid by a broad set deposited from a different direction during the following season. As in dunes built by diurnally opposing winds (ref. 22), the direction of growth of the dune would correspond to the mean vector of the effective winds. This concept is being tested by continuing studies in the linear dunes of the Moenkopi Plateau.

Fourth, downwind ends of "noses" of several sand ridges examined along the road north from Old Andado Station toward Allambi Station, Australia (fig. 13), and on the Moenkopi Plateau, Arizona (fig. 30), do not terminate in avalanche slopes. Rather, these dunes taper gradually to lower and lower ridges, finally ending in a single layer of sand, which can be distinguished from the interdune plain sediments in Australia by its bright red hue (fig. 16(b)).

Fifth, structureless sand was found in the cores of all but the most obviously recent linear dunes investigated (the buff dune at Innamincka and perhaps the large dune at site B, south of Andado). The structureless nature of the dune sand beneath the surface sets in the red dunes at Innamincka, beneath the active crest and slipface sands of the dunes at site A north of Andado, and on the Moenkopi Plateau, Arizona, raises many questions.

Processes that might account for the structureless interiors of these dunes include rising and falling ground-water levels in the dunes, percolation of rainwater (both of these with attendant clay illuviation and swelling of the clay minerals in the dune sediments), insect activity, freeze and thaw, and root growth. The last seems not to be an important factor because the structureless zone lies well beneath the zone of greatest root growth, not only at Innamincka and Andado but also in the dunes of the Moenkopi Plateau in northern Arizona. Vegetation, however, may play an essential role in trapping windblown dust for incorporation into the dune sediments, as suggested by Lutz (ref. 78, pp. 107 and 115).

The cohesiveness of the dune sediments, which permits preservation of miniyardangs in all but the loose crestal sand at Andado site A, is probably due to the high percentages, in dune flank and interdune sediments, of fine grains with diameters less than 4ϕ (1/16 mm). A progressively greater percentage of these grains (silts and clays) occurs in samples obtained from the crests to the flanks or interiors of the dunes at all sites in Australia and Arizona (table II).

Clay content in the cores of dunes at the upwind end of the Strzelecki Desert is reportedly as high as 5 percent, and clay illuviation has been invoked to explain it (ref. 12, p. 132). Wiedemann (ref. 54, p. 103) reports that clay content ranges from 1 percent in dune crest and slope samples to 5.5 percent in the interdune sediments north of Andado. Abundant clay in the dunes on the Moenkopi Plateau (fig. 33) can be inferred from the high percentages of fine-grained sediments (silts and clay) in the core samples of both active and inactive dunes (table II) and from the occurrence of desiccation cracks on the dunes there (fig. 35).

Clay illuviation by percolation of infrequent rains or by seepage into the dunes of floodwaters from intermittent streams, and attendant swelling and shrinkage of clay minerals, are suggested as likely causes of diagenetic destruction of bedding in dunes that remain largely inactive for long periods of time in a semiarid climate. Whitehouse

(ref. 46, pp. 23-27) describes periodic flooding of dunes in the Cooper Creek region, and it is similar to that which the authors have described around Andado. Present-day precipitation (rain and snow) on the Moenkopi Plateau in Arizona is approximately 20.5 to 26 cm (8 to 10 in.) annually. The trenched dunes at Andado in spring (September) and in Arizona in winter (February) were sufficiently damp so that the sides of most trenches did not collapse during the digging, even though they were not wetted down.

Insect activities (termites) were suggested to explain a lack of internal structures in red dunes of Pleistocene age in the Kalahari Desert in western Rhodesia (ref. 79, pp. 304-305). Termites, to the authors' knowledge, are not important insects in the Simpson or Strzelecki Deserts in Australia. Ant nests, however, abound in the dunes and in the interdune corridors around Andado, and an ant nest was excavated from one of the crest trenches at site A at a depth of approximately 1 m below the surface. Tenebrionid beetles are active to depths of approximately 1 m in the dunes on the Moenkopi Plateau, Arizona,[1] and observation of these insects' activities in the dunes continues at present.

Freeze and thaw may contribute to breakdown of dune structures, especially in northern Arizona where hard frosts occur throughout the late fall, winter, and spring. In various parts of central Australia, frosts occur as often as 65 days per year (ref. 37, p. 40). In parts of the Kalahari Desert (ref. 80, p. 191), "sharp frosts" are common.

The lack of bedding in some of the sand-ridge dunes neither supports nor refutes the idea that they may be, in part, wind-eroded remnants of alluvium rather than wholly eolian constructional features. Some evidence of this modified wind-rift hypothesis is the occurrence of bedded gravels in the lower flanks of dunes near Andado (and near Maryvale; ref. 18, p. 19) and the distribution of grain sizes in sediments from the Andado sites (fig. 20). Some wind-scouring of these sediments is quite likely, as postulated by King (refs. 10 and 11) and accepted, in part, by Folk (ref. 18, p. 18), Twidale (ref. 17, p. 81), and Worrall (ref. 81, p. 294). The presence of eolian cross-beds in the upper parts of the dunes does not rule out the lowering by wind erosion of the partly eolian, partly alluvial sediments in their lower parts and in the interdune corridors.

[1]Personal communication to W. Breed from C. A. Slobodchikoff, 1977.

ACKNOWLEDGMENTS

This work was performed under Smithsonian Institution Grant PC6-22324 as a subcontract of NASA contract NAS9-13831. The work was made possible by the helpful advice of numerous researchers in South Australia and Northern Territory. Their agreement with the authors' conclusions, however, is not implied. The authors are extremely grateful to John Douglas of the Ecological Survey of South Australia, without whose help their work in the Innamincka area would not have been feasible. Stan Culic of the South Australian Museum kindly identified the vegetation of that area. Logistical advice was also provided by Paul Lawson of the South Australian Museum in Adelaide, Professor C. R. Twidale of the University of Adelaide, Professor Ian Douglas of the University of New England, Dr. David Johnson of the University of New South Wales, and Dr. Neil MacDonald of the University of Canberra. The authors wish to especially thank Bob Millington of CSIRO, Alice Springs, and David Moore of the Northern Territory Geological Survey, Mines Branch, Alice Springs, for their help in obtaining maps and field equipment for work in the Northern Territory. Philip and Dulcie Clark of Old Andado Station were particularly helpful by kindly guiding the authors to an area of recently breached dunes (site B) near Mayfield Bore. The manuscript was reviewed by J. F. McCauley and J. P. Schafer of the U.S. Geological Survey, Flagstaff.

REFERENCES

1. Jennings, J. N.: A Revised Map of the Desert Dunes of Australia. Australian Geog., vol. 10, no. 5, 1968, pp. 408-409.

2. Wilson, Ian G.: The Erg Concept. Sed. Geol., vol. 10, no. 2, 1973, pp. 77-106.

3. El-Baz, Farouk: Astronaut Observations From the Apollo-Soyuz Mission. Vol. I of Smithsonian Studies in Air and Space, Smithsonian Institution Press (Washington, D.C.), 1977.

4. McKee, E. D.; and Breed, C. S.: Sand Seas of the World. ERTS-1, A New Window On Our Planet, R. S. Williams and W. D. Carter, eds., U.S. Geol. Survey Prof. Paper 929, 1976, pp. 81-88.

5. Breed, C. S.: Morphology and Distribution of Dunes in Sand Seas Observed by Remote Sensing. A Study of Global Sand Seas, E. D. McKee, ed., U.S. Geol. Survey Prof. Paper 1052, (in press).

6. Madigan, C. T.: The Australian Sand-Ridge Deserts. Geog. Rev., vol. 26, no. 2, 1936, pp. 205-227.

7. Madigan, C. T.: The Simpson Desert and Its Borders. Proc. Roy. Soc. New South Wales, vol. 71, pt. 2, Dec. 2, 1938, pp. 503-535.

8. Madigan, C. T.: The Simpson Desert Expedition, 1939, Scientific Reports, Introduction, Narrative, Physiography and Meteorology. Trans. Roy. Soc. South Australia, vol. 69, pt. 1, 1945, pp. 118-139.

9. Madigan, C. T.: The Simpson Desert Expedition, 1939, Scientific Reports, No. 6, Geology—The Sand Formations. Trans. Roy. Soc. South Australia, vol. 70, no. 1, 1946, pp. 45-63.

10. King, D.: The Quaternary Stratigraphic Record at Lake Eyre North and the Evolution of Existing Topographic Forms, Trans. Roy. Soc. South Australia, vol. 79, 1956, pp. 93-103.

11. King, D.: The Sand Ridge Deserts of South Australia and Related Aeolian Landforms of the Quaternary Arid Cycles. Trans. Roy. Soc. South Australia, vol. 83, 1960, pp. 99-109.

12. Wopfner, H.; and Twidale, C. R.: Geomorphological History of the Lake Eyre Basin. Landform Studies From Australia and New Guinea, J. N. Jennings and J. A. Mabbutt, eds., Cambridge Univ. Press, 1967, pp. 118-143.

13. Mabbutt, J. A.: Denudation Chronology in Central Australia; Structure, Climate, and Landform Inheritance in the Alice Springs Area. Landform Studies From Australia and New Guinea, J. N. Jennings and J. A. Mabbutt, eds., Cambridge Univ. Press, 1967, pp. 144-181.

14. Mabbutt, J. A.: Aeolian Landforms in Central Australia. Australian Geog. Studies, vol. 6, no. 2, 1968, pp. 139-150.

15. Mabbutt, J. A.; Wooding, R. A.; and Jennings, J. N.: The Asymmetry of Australian Desert Sand Ridges. Australian J. Sci., vol. 32, no. 4, 1969, pp. 159-160.

16. Mabbutt, J. A.; and Sullivan, M. E.: The Formation of Longitudinal Dunes: Evidence From the Simpson Desert. Australian Geog., vol. 10, no. 6, 1968, pp. 483-487.

17. Twidale, C. R.: Evolution of Sand Dunes in the Simpson Desert, Central Australia. Trans. Inst. British Geographers, vol. 56, 1972, pp. 77-109.

18. Folk, Robert L.: Longitudinal Dunes of the Northwestern Edge of the Simpson Desert, Northern Territory, Australia; 1. Geomorphology and Grain Size Relationships. Sedimentology, vol. 16, 1971, pp. 5-54.

19. Folk, Robert L.: Genesis of Longitudinal and Oghurd Dunes Elucidated by Rolling Upon Grease. Bull. Geol. Soc. America, vol. 82, no. 12, Dec. 1971, pp. 3461-3468.

20. Folk, Robert L.: Reddening of Desert Sands: Simpson Desert, N. T., Australia. J. Sediment. Petrol., vol. 46, no. 3, Sept. 1976, pp. 604-615.

21. Bagnold, R. A.: The Physics of Blown Sand and Desert Dunes. William Morrow & Co. (New York), 1941.

22. McKee, Edwin D.; and Tibbitts, Gordon C., Jr.: Primary Structures of a Seif Dune and Associated Deposits in Libya. J. Sediment. Petrol., vol. 34, no. 1, Mar. 1964, pp. 5-17.

23. Glennie, K. W.: Desert Sedimentary Environments. Developments in Sedimentology, vol. 14, Elsevier Publishing Co., 1970.

24. Breed, C. S.; and McKee, E. D.: Sand Dunes in Desert Areas. Proceedings of the Fourth Annual Conference on Remote Sensing in Arid Lands. Univ. Arizona Press (Tucson), 1973, pp. 160-171.

25. McKee, E. D.; Breed, C. S.; et al.: A Synthesis of Sand Seas Throughout the World. Type III Final Report, 1 July 1972-31 March 1974, ERTS-1, NASA CR-139226, 1974.

26. McKee, E. D.; and Breed, C. S.: Preliminary Report on Dunes. Sec. 9 of Skylab 4 Visual Observations Project Report, NASA TM X-58142, 1974.

27. McKee, Edwin D.; Breed, Carol S.; and Fryberger, Steven G.: Desert Sand Seas. Sec. 2 of Skylab Explores the Earth, NASA SP-380, 1977, pp. 5-47.

28. Breed, Carol S.: Terrestrial Analogs of the Hellespontus Dunes, Mars. Icarus, vol. 30, no. 2, Feb. 1977, pp. 326-340.

29. Strahler, A. N.: Dimensional Analysis Applied to Fluvially-Eroded Landforms. Bull. Geol. Soc. America, vol. 69, no. 3, Mar. 1958, pp. 279-300.

30. Price, W. Armstrong: Saharan Sand Dunes and the Origin of the Longitudinal Dune: A Review. Geog. Rev., vol. 40, no. 3, 1950, pp. 462-465.

31. McKee, E. D.: Primary Structures in Some Recent Sediments. Bull. American Assoc. Petr. Geol., vol. 41, no. 8, 1957, pp. 1704-1747.

32. McKee, E. D.: Structures of Dunes at White Sands National Monument, New Mexico (and a Comparison With Structures of Dunes From Other Selected Areas). Sedimentology, vol. 7, no. 1 (spec. issue), 1966.

33. McKee, Edwin D.: Primary Structures in Dune Sand and Their Significance (Abs.). Symposium on Geology of Libya, Univ. of Libya Faculty of Science, Tripoli, April 14-18, 1969, pp. 13-14.

34. Bagnold, R. A.: The Surface Movement of Blown Sand in Relation to Meteorology. Proceedings of International Symposium on Desert Research (Jerusalem, May 7-14, 1952), Res. Council of Israel Spec. Pub. No. 2, 1953, pp. 89-96.

35. Hanna, Steven R.: The Formation of Longitudinal Sand Dunes by Large Helical Eddies in the Atmosphere. J. Appl. Meteor., vol. 8, no. 6, Dec. 1969, pp. 874-883.

36. Melton, Frank A.: A Tentative Classification of Sand Dunes—Its Application to Dune History in the Southern High Plains. J. Geol., vol. 48, no. 2, 1940, pp. 113-174.

37. Gibbs, W. J.: The Climate and Meteorology of Australia. Bureau of Meteorology, Commonwealth of Australia, Official Year Book Bull. no. 1, 1965, pp. 26-68.

38. Johns, R. K.; and Ludbrook, N. H.: Investigation of Lake Eyre. Geol. Survey of South Australia, Rep. Inv. No. 24, pt. 1, The Sediments of the Lake Eyre Basin, 1962, pp. 1-68.

39. Krinsley, D. B.; Woo, C. C.; and Stoertz, G. E.: Geologic Characteristics of Seven Australian Playas. Playa Surface Morphology; Misc. Investigations, J. T. Neal, ed., Envir. Res. Paper No. 283, U.S. Air Force Cambridge Research Labs. (AFCRL)-68-0133, 1968, pp. 59-103.

40. Stewart, A. J.: McDills, Northern Territory; 1:250 000 Geological Series—Explanatory Notes. Sheet SG/53-7 (Int. Index) Bur. Min. Res., Geol., and Geophys., Canberra, 1968.

41. Shaw, R. D.: Hale River, Northern Territory; 1:250 000 Geological Series—Explanatory Notes. Bur. Min. Res., Geol., and Geophys., Canberra, 1968.

42. Twidale, C. R.: A Possible Late-Quaternary Change in Climate in South Australia. Quaternary Geology and Climate, H. E. Wright, ed., Proceedings of the Seventh Congress, International Association Quaternary Research, vol. 16, Nat. Acad. Sci. (Washington, D.C.), 1969, pp. 43-48.

43. Galloway, R. W.: Late Quaternary Climates in Australia. J. Geol., vol. 73, no. 4, 1965, pp. 603-618.

44. Bowler, J. M.: Aridity in Australia: Age, Origins and Expression in Aeolian Landforms and Sediments. Earth-Science Rev., vol. 12, no. 2-3, 1976, pp. 279-310.

45. Brookfield, Muriel: Dune Trends and Wind Regime in Central Australia. Z. Geomorph., vol. 10, 1970, pp. 121-153.

46. Whitehouse, F. W.: The Channel Country of Southwestern Queensland With Special Reference to Cooper's Creek. Bur. Inv. Tech. Bull. 1, Dept. Public Lands (Brisbane, Queensland, Australia), 1947, pp. 10-92.

47. Alimen, Marie-Henriette: Sables Quaternaires du Sahara Nord-Occidental. Service de la Carte Geologique de L'Algerie, Bull. No. 15, 1957.

48. Logan, R. F.: The Central Namib Desert, South West Africa, Natl. Acad. Sci./Natl. Res. Coun. Pub. 758, 1960.

49. Norris, Robert M.: Dune Reddening and Time. J. Sediment. Petrol., vol. 39, no. 1, Mar. 1969, pp. 7-11.

50. Folk, R. L.: Toward Greater Precision in Rock-Color Terminology. Bull. Geol. Soc. America, vol. 80, 1969, pp. 725-728.

51. Folk, R. L.: Petrology of Sedimentary Rocks. Hemphill's (Austin, Texas), 1968.

52. Brookfield, Muriel: Winds of Arid Australia. Commonwealth Scientific and Industrial Research Organization (CSIRO), Div. Land Res. Tech. Paper 30, 1970.

53. Crocker, R. L.: The Simpson Desert Expedition, 1939. Scientific Reports, No. 8, The Soils and Vegetation of the Simpson Desert and Its Borders. Trans. Roy. Soc. South Australia, vol. 70, 1946, pp. 235-258.

54. Wiedemann, A. M.: Vegetation Studies in the Simpson Desert, Northern Territory. Australian J. Bot., vol. 19, 1971, pp. 99-124.

55. Folk, R. L.: Bimodal Supermature Sandstones: Product of the Desert Floor. Sec. 8, Proceedings, Report of the 23rd International Geology Congress (Prague, Czechoslovakia), 1968, pp. 9-32.

56. Wood, William H.: Rectification of Wind-Blown Sand. J. Sediment. Petrol., vol. 40, no. 1, Mar. 1970, pp. 29-37.

57. Carroll, Dorothy: The Simpson Desert Expedition, 1939, Scientific Reports, No. 2, Geology—Desert Sands. Trans. Roy. Soc. South Australia, vol. 68, no. 1, 1946, pp. 49-59.

58. Fryberger, S. G.: Wind Regimes and Dune Types. A Study of Global Sand Seas, E. D. McKee, ed., U.S. Geol. Survey Prof. Paper 1052, (in press).

59. Callen, R. A.: Frome, South Australia, 1:250 000 Geological Quadrangle Map. South Australia Geological Atlas Series, Sheet SH 54-10, zone 6, 1975.

60. McCauley, J. F.; Grolier, M. J.; and Breed, C. S.: Yardangs of Peru and Other Desert Regions. U.S. Geol. Survey Interagency Report, Astrogeology 81, 1977.

61. Fairbridge, Rhodes W.: The Encyclopedia of Geomorphology. Encyclopedia of Earth Sciences Series, Vol. 3, Reinhold Book Corp. (New York), 1968.

62. Blackwelder, Eliot: Yardang and Zastruga. Science, vol. 72, Oct. 17, 1930, pp. 396-397.

63. Blackwelder, Eliot: Yardangs. Bull. Geol. Soc. America, vol. 45, no. 1, 1934, pp. 159-166.

64.. Ward, A. Wesley: The Yardangs at Rogers Playa, California. Abs., Geol. Soc. America 90th Annual Meeting (Seattle), 1977, p. 1216.

65. David, T. W. Edgeworth: The Geology of the Commonwealth of Australia. Vol. 2, Edward Arnold & Co. (London), 1950.

66. Ollier, C. D.; and Tuddenham, W. G.: Inselbergs of Central Australia. Z. Geomorph., vol. 5, no. 4, 1961, pp. 257-276.

67. Twidale, C. R.: A Contribution to the General Theory of Domed Inselbergs; Conclusions Derived From Observations in South Australia. Inst. of British Geographers, Pub. No. 34, 1964, pp. 91-113.

68. Bremer, Hannah: Ayers Rock. Z. Geomorph., vol. 9, 1965, pp. 249-284.

69. Wellman, H. W.; and Wilson, A. T.: Salt Weathering, a Neglected Geological Erosive Agent in Coastal and Arid Environments. Nature, vol. 205, no. 4976, Mar. 13, 1965, pp. 1097-1098.

70. Grolier, M. J.; Ericksen, G. E.; McCauley, J. F.; and Morris, E. C.: The Desert Land Forms of Peru; A Preliminary Photographic Atlas. U.S. Geol. Survey Interagency Report, Astrogeology 57, 1974.

71. McCauley, John F.; Ward, A. Wesley; et al.: Experimental Modeling of Wind Erosion Forms (Abs.). Reports of Planetology Geology Program, 1976-1977, NASA TM X-3511, 1977, pp. 150-152.

72. Hack, John T.: Dunes of the Western Navajo Country. Geog. Rev., vol. 31, no. 2, 1941, pp. 240-263.

73. Cooley, M. E.; Harshbarger, J. W.; et al.: Regional Hydrogeology of the Navajo and Hopi Indian Reservations, Arizona, New Mexico, and Utah. U.S. Geol. Survey Prof. Paper 521-A, 1969.

74. Stokes, William Lee: Incised, Wind-Aligned Stream Patterns of the Colorado Plateau. American J. Sci., vol. 262, June 1964, pp. 808-816.

75. Freeman, William E.; and Visher, Glenn S.: Stratigraphic Analysis of the Navajo Sandstone. J. Sediment. Petrol., vol. 45, no. 3, Sept. 1975, pp. 651-668.

76. Goldsmith, Victor: Internal Geometry and Origin of Vegetated Coastal Sand Dunes. J. Sediment. Petrol., vol. 43, no. 4, Dec. 1973, pp. 1128-1142.

77. Yaalon, D. H.; and Laronne, Jonathan: Internal Structures in Eolianites and Paleowinds, Mediterranean Coast, Israel. J. Sediment. Petrol., vol. 41, no. 4, Dec. 1971, pp. 1059-1064.

78. Lutz, Harold John: The Nature and Origin of Layers of Fine-Textured Material in Sand Dunes. J. Sediment. Petrol., vol. 11, no. 3, Dec. 1941, pp. 105-123.

79. Flint, Richard Foster; and Bond, Geoffrey: Pleistocene Sand Ridges and Pans in Western Rhodesia. Bull. Geol. Soc. America, vol. 79, Mar. 1968, pp. 299-314.

80. Grove, A. T.: Landforms and Climatic Change in the Kalahari and Ngamiland. Geog. J., vol. 135, pt. 2, 1969, pp. 191-212.

81. Worrall, G. A.: Observations on Some Wind-Formed Features in the Southern Sahara. Z. Geomorph., vol. 18, no. 3, 1974, pp. 291-302.

Determining Photograph Locations Over Oceans

S. McLafferty,[a] M. Pryslak,[a] and G. A. Maul[b]

ABSTRACT

To increase the scientific usefulness of Apollo-Soyuz Test Project ocean photographs, more precise definitions of their geographic locations are needed. The methods used in this report to quantitatively define the photo-locations are based on photogrammetry, on a knowledge of the groundtracks of the spacecraft and the times during which the photographs were taken, and on a comparison with satellite imagery. Latitudes and longitudes with an estimated error of ± 1 to ± 3 seconds are calculated for the center points of photographs taken during mapping passes that lack photo-support data. A method is developed for determining the center points for photographs containing two or more recognizable features on landmasses. Because the method of locating cloud features of Apollo-Soyuz open-ocean photographs on satellite images was largely unsuccessful, a map is provided which shows the Apollo groundtracks that correspond to the times when the photographs were taken.

INTRODUCTION

The Apollo-Soyuz Test Project (ASTP) ocean photographs can be grouped into four categories: (1) vertical mapping photographs, which are taken with 60 percent stereo-overlap and for which the exact coordinates of the center point and the four corners are known; (2) vertical mapping photographs for which the exact coordinates of the center point and the four corners are not known; (3) handheld-camera photographs containing a coastline and/or island(s); and (4) open-ocean photographs.

In the case of mapping passes with no photo-support data, the location of at least one photograph could be determined by accurately identifying a coast or an island, and the positions of the remaining photographs could therefore be determined by using equations to calculate the latitude and longitude of the Apollo spacecraft groundtrack. In the case of handheld-camera photographs containing an identifiable landmass, 1:1 000 000-scale Operational Navigation Charts (ONC's), published by the Defense Mapping Agency, were used; the main difficulty in this case was the obliquity of many of the photographs. In the last case, clouds in the open-ocean photographs were compared with clouds on weather-satellite images. The main problems were the low resolution of the satellite images and the difficulty in obtaining satellite imagery taken at the same time as the ASTP photographs.

MAPPING PASSES WITH PHOTO-SUPPORT DATA

The 70-mm Hasselblad data camera was used to acquire mapping photography. It was equipped with a glass reseau plate and would accept both a 60-mm and a 100-mm lens. The camera was bracket-mounted in one of the spacecraft windows, and the spacecraft was oriented so that the perspective center of the camera lens would point at nadir. An intervalometer controlled the opening of the shutter. At the exact instant the photo-

[a]National Air and Space Museum, Smithsonian Institution.

[b]Atlantic Oceanographic and Meteorological Laboratory, National Oceanic and Atmospheric Administration.

graph was taken, the time and the spacecraft position and orientation were recorded.

Through the use of a computer at the NASA Lyndon B. Johnson Space Center (JSC), the vectors for instrument pointing (one vector for the center of the photograph and one vector for each of the four corners) and spacecraft position were transformed into the geographic inertial coordinate system. This system is a Cartesian coordinate system, the origin of which is at the Earth's center, with the x-axis lying in the plane of the celestial equator of date through the Greenwich meridian, with the z-axis orthogonal to the celestial equator of date (the axis of rotation), and with the y-axis completing the right-handed system. The vectors were added together, and the resulting vector components were substituted in the following equations to obtain the latitude ϕ and the longitude λ:

$$\phi = \arctan \frac{z}{\sqrt{x^2 + x^2}}$$

for $-90° \leq \phi \leq 90°$, and

$$\lambda = \arctan \frac{y}{x}$$

for $0° \leq \lambda < 360°$. A detailed description of this method is given by Osburn et al. (ref. 1).

MAPPING PASSES WITHOUT PHOTO-SUPPORT DATA

Unfortunately, for several mapping passes, the photo-support data regarding time, spacecraft position, and orientation were not recorded. Thus, calculations for parameters essential in photogrammetry, such as the latitude and longitude of the center point and of the four corners of the photograph, could not be made. However, an approximation of the latitude and longitude could be made, although it was not as accurate as the photo-support data that were recorded.

The method used for the approximation was one that involved determining the subvehicle points for the times at which the photographs were taken. If the optical axis of the camera was at the vertical to the Earth (or nearly vertical), then the center point of the photograph would be on or very near the subvehicle point. If the center point of one photograph could be located by using "landmarks," then the center points of previous and subsequent mapping photographs could be determined because the interval at which they were taken was fixed by the intervalometer (a timing mechanism that automatically triggers the shutter at a predetermined interval).

Determination of Latitude

The latitude ϕ for a circular orbit is given by the following equation:[1]

$$\phi = \arcsin(\sin i \sin \sigma) \qquad (1)$$

where i = inclination of the orbit in degrees (51.77° for ASTP)

$$\sigma = \frac{360(t - t_o)}{\tau_n}$$

and where t represents time and τ_n represents the nodal period, or the interval between ascending nodes.

The value of σ from 0° to 360° represents a full cycle of latitude from ascending node to ascending node (the point at which the spacecraft crosses the Equator from the Southern to the Northern Hemisphere). For a circular orbit (i.e., the spacecraft altitude is constant), the value of σ is directly proportional to time. Thus, the $\Delta\sigma$ is constant for a given time interval.

[1]Personal communication from G. D. Griffith, JSC, 1974.

TABLE I.—Example of Three Latitudes and Corresponding Values of σ and $\Delta\sigma$

Day, 1975	*UT, hr:min*	*Latitude, deg (a)*	*σ, rad*	*$\Delta\sigma$, rad*
July 19	23:59	(a) 38.884 S	5.35733291	0.07100820
July 20	00:00	(b) 36.346 S	5.42834110	.07101589
July 20	00:01	(c) 33.682 S	5.49935700	Not applicable

[a]The letters "a, b, c" are designators used in the text.

The value of σ can be calculated—without knowing t, t_0, and τ_n—if a value of latitude is known.

$$\sigma = \arcsin \frac{\sin \phi}{\sin i} \qquad (2)$$

The values of $\Delta\sigma$ for a given time interval were calculated from the σ's of two known values of latitude. For example, table I contains three latitudes (taken from the postmission computer printout of the latitude and longitude of the subvehicle point at 1-minute intervals) and the corresponding calculated values of σ and $\Delta\sigma$; the times correspond to the beginning of mapping pass 6 on spacecraft revolution 64.

If the $\Delta\sigma$ between "a" and "b" in table I is added to the σ of "b," the result (5.4993493 rad) should equal the σ of "c." The result differs slightly, but when it is substituted in equation (1), the value of the latitude is still 33.682° S. Therefore, once the $\Delta\sigma$ for a 1-minute interval was calculated, the $\Delta\sigma$ for any time interval could be determined. The interval between frames taken with the 60-mm lens was 10.02 seconds.

After the latitude of one photograph was determined, the σ for that latitude was calculated from equation (2). By subtracting or adding increments of $\Delta\sigma$ to the original σ, latitudes for frames before or after the known photograph were calculated by substituting the new σ into equation (1). For example, during mapping pass 6 on revolution 64, photographs AST-16-1121 to AST-16-1123 were taken over the Great Australian Bight. The center point of AST-16-1123, which was located on Flinders Island, was plotted on an ONC; and a latitude of 33.72° S was obtained from the map. From equation (2), σ was calculated and found to be 5.49836471 rad. A $\Delta\sigma$ of 0.01185965 rad was used to calculate the σ's for AST-16-1122 and AST-16-1121 (table II). The latitudes (together with longitudes, altitudes, footprint sizes, and times) for all ocean mapping passes without photo-support data are listed in table III.

TABLE II.—Calculated σ's and Corresponding Latitudes for Three ASTP Photographs With No Support Data

[Mapping pass 6, revolution 64]

Photograph no.	*σ, rad*	*Latitude, deg*
AST-16-1123	5.49836471	33.72 S
AST-16-1122	5.48650506	34.17 S
AST-16-1121	5.47464541	34.62 S

TABLE III.—Geophysical and Temporal Parameters for All ASTP Ocean Mapping Passes Without Photo-Support Data

Photograph no.	*Latitude, deg*	*Longitude, deg*	*Altitude, km*	*Footprint size, km*	*Day, July 1975*	*UT, hr:min*
			Mapping pass 5, revolution 40			
AST-14-946	14.80 N	41.97 E	224	199	18	09:47
AST-14-947	15.32 N	42.38 E	224	199	18	09:47
AST-14-968	26.00 N	51.53 E	226	200	18	09:51
			Mapping pass 6, revolution 64			
AST-16-1121	34.62 S	133.53 E	229	203	20	00:01
AST-16-1122	34.17 S	133.93 E	229	203	20	00:01
AST-16-1123	33.72 S	134.30 E	229	203	20	00:01
AST-16-1151	20.14 S	148.13 E	225	199	20	00:06
AST-16-1152	19.63 S	148.56 E	225	199	20	00:06
AST-16-1153	19.12 S	148.98 E	225	199	20	00:06
AST-16-1154	18.60 S	149.41 E	225	199	20	00:07
AST-16-1155	18.09 S	149.82 E	225	199	20	00:07
AST-16-1156	17.57 S	150.25 E	225	199	20	00:07
AST-16-1157	17.05 S	150.66 E	225	199	20	00:07
AST-16-1158	16.54 S	151.07 E	224	199	20	00:07
AST-16-1159	16.02 S	151.48 E	224	199	20	00:07
AST-16-1160	15.50 S	151.89 E	224	199	20	00:08
AST-16-1161	14.97 S	152.30 E	224	199	20	00:08
AST-16-1162	14.45 S	152.70 E	224	199	20	00:08
AST-16-1163	13.93 S	153.10 E	224	199	20	00:08
AST-16-1164	13.40 S	153.50 E	224	199	20	00:08
AST-16-1165	12.88 S	153.89 E	224	199	20	00:08
AST-16-1166	12.35 S	154.30 E	224	199	20	00:09
AST-16-1167	11.83 S	154.68 E	224	199	20	00:09
AST-16-1168	11.30 S	155.08 E	224	199	20	00:09
AST-16-1169	10.77 S	155.48 E	224	199	20	00:09
AST-16-1170	10.25 S	155.86 E	223	198	20	00:09
AST-16-1171	9.72 S	156.26 E	223	198	20	00:09
AST-16-1172	9.19 S	156.53 E	223	198	20	00:10
AST-16-1173	8.66 S	157.03 E	223	198	20	00:10
AST-16-1174	8.13 S	157.41 E	223	198	20	00:10
AST-16-1175	7.60 S	157.80 E	223	198	20	00:10
AST-16-1176	7.07 S	158.18 E	223	198	20	00:10
AST-16-1177	6.53 S	158.57 E	223	198	20	00:10
AST-16-1178	6.00 S	158.95 E	223	198	20	00:11
AST-16-1179	5.47 S	159.33 E	223	198	20	00:11

TABLE III.—Concluded

Photograph no.	*Latitude, deg*	*Longitude, deg*	*Altitude, km*	*Footprint size, km*	*Day, July 1975*	*UT, hr:min*
			Mapping pass 6, revolution 64			
AST-16-1180	4.94 S	159.70 E	223	198	20	00:11
AST-16-1181	4.40 S	160.08 E	223	198	20	00:11
AST-16-1182	3.87 S	160.47 E	223	198	20	00:11
AST-16-1183	3.34 S	160.83 E	223	198	20	00:11
AST-16-1184	2.81 S	161.20 E	223	198	20	00:12
AST-16-1185	2.27 S	161.59 E	223	198	20	00:12
AST-16-1186	1.74 S	161.97 E	223	198	20	00:12
AST-16-1187	1.20 S	162.34 E	223	198	20	00:12
AST-16-1188	.67 S	162.72 E	223	198	20	00:12
AST-16-1189	.14 S	163.10 E	223	198	20	00:12
AST-16-1190	.40 N	163.48 E	223	198	20	00:13
AST-16-1191	.93 N	163.86 E	223	198	20	00:13
			Mapping pass 7, revolution 71			
AST-16-1262	33.29 N	32.93 E	226	200	20	10:46
AST-16-1263	33.75 N	33.46 E	226	200	20	10:46
AST-16-1264	34.20 N	34.05 E	226	200	20	10:46
			Mapping pass 9, revolution 72			
AST-17-1366	33.30 N	10.50 E	226	120	20	12:14
AST-17-1367	33.58 N	10.84 E	226	120	20	12:14
AST-17-1368	33.86 N	11.19 E	226	120	20	12:14
AST-17-1369	34.15 N	11.56 E	226	120	20	12:15
AST-17-1370	34.43 N	11.93 E	226	120	20	12:15
AST-17-1371	34.71 N	12.28 E	226	120	20	12:15
AST-17-1372	34.99 N	12.63 E	226	120	20	12:15
AST-17-1373	35.26 N	12.98 E	226	120	20	12:15
AST-17-1374	35.54 N	13.36 E	227	120	20	12:15
AST-17-1375	35.81 N	13.72 E	227	120	20	12:15
AST-17-1376	36.09 N	14.10 E	227	120	20	12:15
AST-17-1377	36.36 N	14.47 E	227	120	20	12:15
AST-17-1378	36.63 N	14.83 E	227	120	20	12:15
AST-17-1379	36.90 N	15.20 E	227	120	20	12:16

Determination of Longitude

Longitude λ for a circular orbit is given by the following equation:[2]

$$\lambda = \arctan(\cos i \sin \sigma) + \lambda_n - \left[\Omega_e(t - t_o)\right] - \left\{\frac{K_s}{R_o^{7/2}}\left[\cos i(t - t_o)\right]\right\} \quad (3)$$

where λ_n = longitude of the ascending node at t

Ω_e = rotation rate of the Earth (4.178074×10^{-3} deg sec^{-1})

K_s = super constant (4.654992784×10^8 deg n.mi.$^{7/2}$ sec^{-1})

R_o = circular radius of Earth

The longitude was difficult to accurately calculate because exact values for the ascending node and for the time factor $t - t_o$ were not known. When approximations of the ascending node, the time factors, and the σ (calculated from a known value of latitude) were substituted into equation (3), the results were off by as much as 0.1° when compared to the corresponding known value of longitude.

Because of this problem, a "graphic" solution was used for determining the longitude. The groundtrack was plotted on ONC's, and the longitude was obtained from the intersection of the calculated latitude and the groundtrack.

Discussion of Error

Three sources of error affected the accuracy of the calculations of latitude and longitude. First, the assumption was made that the orbit was perfectly circular. The altitude during each ASTP orbit varied by approximately 15 km, giving the orbit an eccentricity of 0.065. For this reason, the $\Delta\sigma$ varies somewhat throughout the orbit. However, the $\Delta\sigma$ did not vary significantly from minute to minute, as indicated in the previous discussion on latitude. The values of $\Delta\sigma$ were taken from the part of the groundtrack corresponding to the time the photographs were taken.

The second source of error was concerned with how accurately the initial photograph was located. On mapping pass 5 (revolution 40), mapping data were obtained for three isolated pictures taken over Saudi Arabia. These three frames were used as the initial frames so that the accuracy of the center-point locations was excellent. For mapping pass 6 (revolution 64) and mapping pass 9 (revolution 72), the center points of the initial frames coincided with distinct landmarks that could be located on ONC's with an accuracy of ± 1 second. On mapping pass 7 (revolution 71), the center point of the initial frame was located over the ocean so that the accuracy of location was approximately ± 3 seconds.

The third source of error resulted from the spacecraft's platform not being perfectly stable, and this characteristic caused the optical axis of the camera to wobble. Thus, the center point of the photograph would not necessarily coincide with the subvehicle point.

On mapping passes with photo-support data, the result of this spacecraft-platform phenomenon was expressed as the tilt angle and the tilt azimuth (ref. 1). The tilt angle of one particular mapping pass varied by as much as 0.7°, and the tilt azimuth varied in all directions. During the plotting of the center points of photographs with landmarks, the center point varied from the groundtrack by as much as 4 seconds of longitude.

Corner Points

Although a somewhat complex problem to solve, it is possible to calculate the latitudes and longitudes of the corner points. These calculations were not performed, for the following reasons: (1) exact altitude data, which were needed to determine accurate footprint size, were not available; (2) the lack of spacecraft-platform stability, which

[2] Ibid.

caused discrepancies in the expected values of the center points, would cause even larger discrepancies in the values of the corner points; and (3) it could not be assumed that the nose of the spacecraft was pointed in the direction of the groundtrack. On mapping pass 5 (revolution 40), the nose of the spacecraft was skewed by approximately 48° from the direction of the groundtrack, thus resulting in a tilt azimuth of similar magnitude.

Times, Altitudes, and Footprint Size

The times and altitudes were interpolated from the postmission computer printout of the groundtracks, which provided data at 1-minute intervals. The footprint size of the photograph can be calculated in one of two ways.

1. By using the flat-Earth approximation:

$$\text{Footprint size} = h\frac{f}{f_l}$$

where h = altitude above the Earth

f = format size (effectively 53.0 mm for the film in the Hasselblad cameras)

f_l = focal length of camera

2. By calculating the arc length A on the Earth (ref. 2, p. 1050):

$$A = R_o\theta$$

where R_o = circular radius of the Earth (6378 km)

$\theta = \arcsin[(R_o + h)/R_o]\sin\gamma - \gamma$

γ = half angle of lens

For a 60-mm lens, $\gamma = 23.82944942°$; for a 100-mm lens, $\gamma = 14.84222706°$.

The second method was used, and the results were rounded off to the nearest kilometer. (The result of the second method must be multiplied by 2 to obtain the full size of the footprint.) The results of the calculations for photographs taken on mapping passes with no photo-support data are given in table III.

PHOTOGRAPHS CONTAINING LANDMASSES

The remaining photographs were taken with a 70-mm Hasselblad reflex camera equipped to use both a 50-mm and a 250-mm lens. The camera was handheld, and the only data recorded were the approximate time when each photograph was taken, the lens size used, and some crewmember comments concerning the ocean scenes observed.

The ONC's were used to locate photographs that contained landmarks. In many instances, the scales of 180-mm-square prints of photographs taken with the 50-mm lens closely matched the 1:1 000 000-scale ONC's.

The first step in locating a handheld-camera ocean photograph was to obtain its approximate location from ASTP data provided by JSC.[3] A comparison was then made between the photograph and ONC's of the same area. When landmarks were recognized, an attempt was made to locate the center point and the corner points of the photograph. When landmarks fortuitously lay on one of these points, the latitude and longitude could be read directly from ONC's. But when landmarks were an appreciable distance from one of these points, the obliquity of the photograph had to be determined before the location of the center point could be interpolated.

Unfortunately, it is difficult to find the obliquity of a handheld-camera photograph. By using figure 22-1 in the "Manual of Photogrammetry" (ref. 2), it was found that

$$A = R\left[\arcsin(k\sin\alpha) - \alpha\right] \tag{4}$$

[3]The ASTP photographic data were documented by R. Underwood in a JSC publication entitled "ASTP Index to Onboard Photography," 1975.

where A = arc length on the Earth (km)

R = mean radius of the Earth (6367.475142 km)

h = altitude of camera (km)

$k = (R + h)/R$

α = nadir angle

Although α could not be solved explicitly in equation (4), it could be evaluated through an iterative method. The method involved finding two landmarks on the photograph that lay on the principal line (the line from the nadir point (NP) through the principal point (or center point) (PP)). (Refer to fig. 1 for a diagram of the terms used in this discussion.) Because the two landmarks were not always on opposite sides of the principal point, the distances between the landmarks and the principal point of the photograph were measured in the following manner. The distance d_c from landmark L_c to PP was measured positively in the direction away from PP toward NP. The distance d_f between landmark L_f and PP was measured positively in the direction away from NP toward PP.

The angles μ and γ (fig. 1) represent the angles formed by the optical axis (the line from the perspective center to the principal point) and the line from the perspective center to the landmark. The angles were calculated as follows.

$$\mu = \arctan \frac{d_c}{f_l} \qquad \gamma = \arctan \frac{d_f}{f_l}$$

where d_c = measured distance on the original photograph (70-mm film) between L_c and PP

d_f = measured distance on the original photograph (70-mm film) between L_f and PP

f_l = focal length of the camera lens

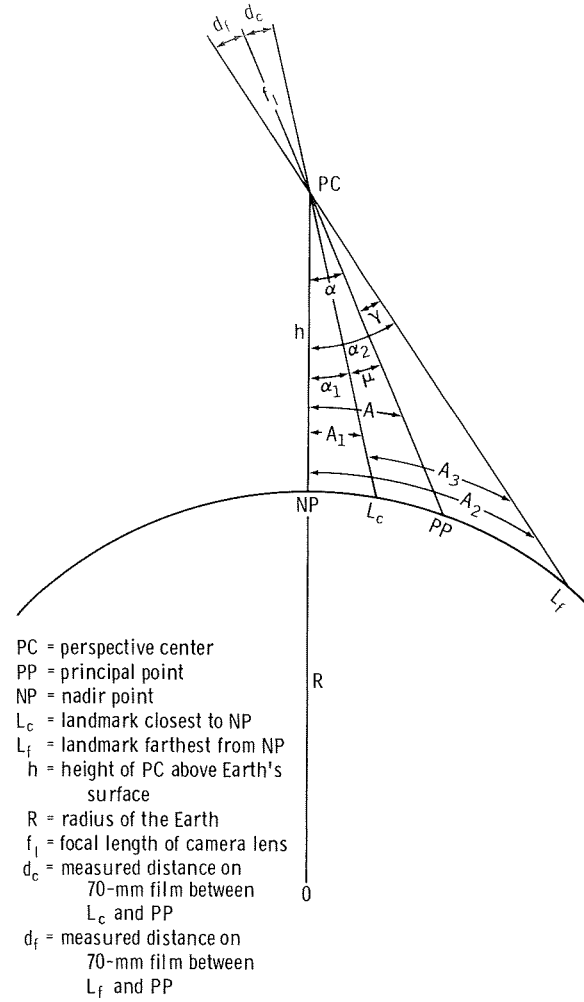


FIGURE 1.—Diagram illustrating the relationships between various arc lengths and angles discussed in the section concerning photographs containing landmasses (modified from fig. 22-1 of ref. 2).

Next, an estimate was made of the value of α (the obliquity of the photograph), and the angles α_1 and α_2 (fig. 1) were calculated.

$$\alpha_1 = \alpha - \mu \tag{5}$$

$$\alpha_2 = \alpha + \gamma \tag{6}$$

The arc lengths A_1 and A_2 were calculated from the values of α_1 and α_2 as in equation (4):

$$A_1 = R\left[\arcsin\left(k \sin \alpha_1\right) - \alpha_1\right] \quad (7)$$

$$A_2 = R\left[\arcsin\left(k \sin \alpha_2\right) - \alpha_2\right] \quad (8)$$

$$A_3 = A_2 - A_1 \quad (9)$$

The value A_3 was an approximation of A', the arc length between landmarks L_c and L_f, which was measured between the landmarks on the ONC's. If the approximated value A_3 was larger than A', then the estimate of α was too large. If A_3 was smaller than A', then the estimate of α was too small. A new estimate for α was made, and the calculations from equations (5) to (9) were repeated until A_3 matched A'.

With the final value of α, the latitude and longitude of the principal point were determined through a dead reckoning method. The arc length A_1, between landmark L_c and the nadir point, was calculated from equations (5) and (7); and the arc length A, between the nadir point and the principal point, was calculated from equation (4). Arc length A_1 was subtracted from arc length A to give the arc length d between landmark L_c and the principal point. Latitude and longitude were calculated from the following equations, which are based on the model of the Earth as a Mercator projection.

$$\phi = \phi_0 + \frac{d \cos C}{60(1.852)}$$

$$\lambda = \lambda_0 + \frac{180}{\pi}\left(\tan C\right)\left(\ln \frac{\tan 45 + \frac{\phi_0}{2}}{\tan 45 + \frac{\phi}{2}}\right)$$

for $C \neq 90°$ or $C \neq 270°$, and

$$\lambda = \lambda_0 - \frac{d \sin C}{60\left(\cos \phi_0\right)(1.852)}$$

for $C = 90°$ or $C = 270°$, where

ϕ_0 = latitude of landmark L_c

λ_0 = longitude of landmark L_c

d = distance in kilometers from landmark L_c to the principal point

C = course or direction from landmark L_c to the principal point in degrees (north = 0°)

The method for determining the obliquity of the photograph and the latitude and longitude of the principal point presented several difficulties. The first difficulty was that two recognizable landmarks had to be located on the principal line or this method could not be used. The second difficulty involved finding the location of the principal line on the photograph because this line was not always symmetrical with the format of the photograph. In the case of high-oblique photographs, which contained the horizon, the location of the principal line was perpendicular to the horizon line and intersected the principal point. In the case of low-oblique photographs, an iterative method was used. Many lines were chosen through the principal point and through the various pairs of landmarks. Respective values of α were calculated by using the iterative method described earlier. The line with the maximum α was closest to the principal line.

The third difficulty was that the entire process required a great deal of time. It was estimated that the principal points for only one or two photographs could be determined per day. Unfor-

tunately, although the time and funds were sufficient for developing this method, they were insufficient for the generation of data for specific photographs. It is hoped that this method will serve as a useful tool for persons interested in more specifically locating photographs that contain a coastline and/or islands.

PHOTOGRAPHS TAKEN OVER THE OPEN OCEAN

Photographs of the open ocean, of course, contained few or no landmarks from which to identify the geographical locations. However, the cloud pattern of a photograph acted as a temporary "fingerprint" of the Earth. Depending on weather conditions, this "fingerprint" might have remained for 15 minutes or longer in the atmosphere.

In an attempt to locate the area photographed over the open ocean, cloud patterns in the photographs were compared with the cloud patterns in satellite images. First, for each photograph, the revolution number and approximate time were obtained from the JSC photograph index.[4] This information, in conjunction with the groundtrack data, defined an area in which the photograph was taken. Then, a satellite image that was taken at approximately the same time and over the same area as the ASTP photograph was obtained. If the cloud patterns of the ASTP photograph could be matched with cloud patterns on the satellite image, then the location of the photograph was determined from the geographic coordinates on the satellite image.

For example, photographs AST-9-528, AST-9-529, and AST-9-530 were taken with a 50-mm lens over a highly cloud-covered area with a few points of exposed land. (A discussion of the ocean features seen in these photographs is given in the section entitled "Interpreting ASTP Photographs of the Ocean and Locating the Area Photographed (Case Study of the Gulf of Mexico).") The JSC photograph index listed the locations of the three photographs as Cuba, Cape San Antonio, and Yucatan Channel; Gulf of Mexico; and Gulf of Mexico, West of Florida, respectively. The photograph index listed the revolution number as 45 and the UT as between 199:18:41 and 199:18:55. During this time, the subvehicle point moved along the groundtrack from latitude 16.543° N and longitude 92.412° W to latitude 50.329° N and longitude 38.605° W. By limiting the area just to the Gulf of Mexico, the groundtrack was narrowed to a path between latitude 19.635° N, longitude 89.891° W at UT 199:18:42 and latitude 28.598° N, longitude 81.602° W at UT 199:18:45.

The Geostationary Operational Environmental Satellite 1 (GOES-1) images of the area were obtained from the National Oceanic and Atmospheric Administration (NOAA) National Environmental Satellite Service. The GOES-1 images were taken at 0.5-hour intervals; therefore, the appropriate images were chosen so that a time interval of 15 minutes or less existed between the acquisition of the satellite image and the acquisition of the ASTP photograph. The major cloud formations on the ASTP photographs were located on the GOES-1 images with little difficulty. After careful comparison between the ASTP photographs and the GOES-1 images, an outline of each photograph was drawn over the images. Using dominant landmarks on the GOES-1 images as a base, the latitude and the longitude of the principal point and the corner points of each ASTP photograph were interpolated across the GOES-1 images.

Unfortunately, the method of using satellite images only worked in the case of the three previously mentioned photographs over the Gulf of Mexico. Photographs taken with the 250-mm lens over the Gulf of Mexico were impossible to locate on the GOES-1 images because of the high resolution and large scale of the photographs as compared with the low resolution and small scale of the satellite images.

Data were obtained from the Defense Meteorological Satellite Program (DMSP) archive in Madison, Wisconsin, which contained two types of media: H channel (3.7-km (2 n. mi.) resolution) and V channel (0.6-km (0.33 n. mi.) resolution). The better data, the V channel, were found to be available only in coastal areas because the primary investigations using these data were

[4] Ibid.

usually land oriented. The H-channel data were found to be very difficult to use because of the large resolution and scale differences between the ASTP photographs and the satellite images. Because the orbital tracks of the DMSP satellite and the Apollo spacecraft crossed almost perpendicular to each other, comparison of the satellite data with the photographs was very difficult. Also, in most cases, the time interval between the acquisition of the DMSP data and the acquisition of the photographs was too large for the temporary pattern of clouds to be preserved.

The last set of data was received from the Nimbus Data Utilization Center at the NASA Goddard Space Flight Center. These data were also unusable for locating ASTP photographs because of their extremely low resolution.

As a final tool to more specifically locate ocean photographs, the map in figure 2 shows the portions of groundtrack along which ocean photographs were taken. The user should refer to appendix B to obtain the revolution number for a specific photograph and then locate the appropriate groundtrack on the map.

From the altitude of the Apollo spacecraft, the horizon would appear on the Earth's surface approximately 1600 km from the subvehicle point. Thus, the photograph is located somewhere within a 3200-km-wide swath divided by and parallel with the groundtrack. Although the swath defined by the groundtrack encompasses a large area, the swath does exclude substantial areas over the ocean where the photograph was not taken.

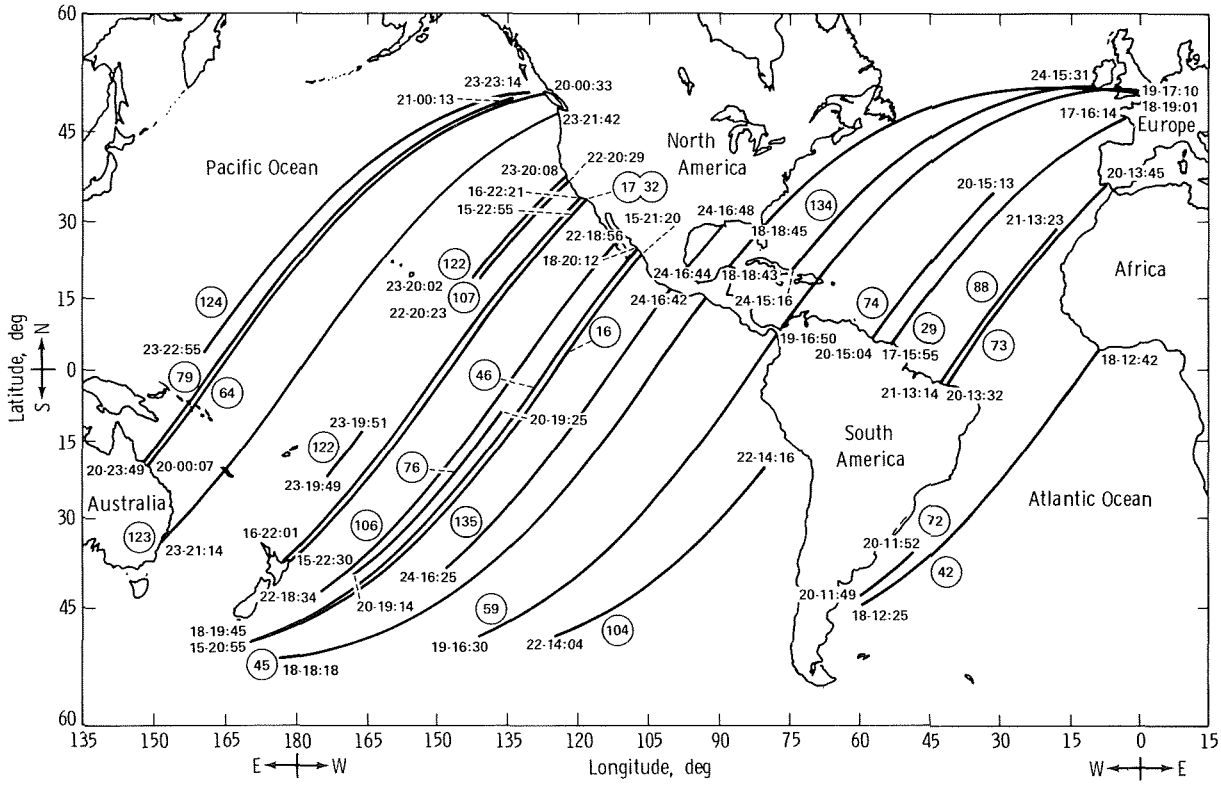


FIGURE 2.—Map of groundtracks along which ASTP photographs were taken; the user should obtain the time and/or revolution number for the particular photograph and find the corresponding groundtrack on the map. The two- and three-digit numbers are the revolution numbers. The six-digit numbers refer to the date in July (left of the dash) and the time (UT) in hours and minutes. The photograph will be somewhere within a 3200-km-wide swath divided by and parallel with the groundtrack.

SUMMARY AND SUGGESTIONS

The attempt to more specifically locate ASTP ocean photographs met with various degrees of success. Center points for mapping photographs with no photo-support data were estimated to ± 1 to ± 3 seconds of latitude and longitude. Footprint sizes were estimated to the nearest kilometer. Although a procedure for determining the principal point of handheld-camera oblique photographs containing a coastline and/or islands was developed, no data for specific photographs were generated. The use of satellite images in determining the location of the photographs taken over the open ocean met with very limited success because of the low resolution and the times of acquisition of the satellite imagery. Finally, a map was produced that shows the location of groundtracks during the times that photographs were taken over the ocean.

For future missions, the authors have two suggestions to greatly facilitate locating "ocean-looking" photographs.

1. Some type of timing device should be attached to the handheld camera to pinpoint the time of photoacquisition to seconds rather than minutes. Possibilities include attaching the handheld camera to a device similar to that used with the bracket-mounted camera of the ASTP mission, and placing a clock inside the camera as was done on the Earth terrain cameras of the Skylab missions.

2. Advance arrangements should be made for the acquisition of high-resolution satellite imagery over the same area and during the same time as photography planned for the mission.

REFERENCES

1. Osburn, R. K.; Barnett, Edward L.; Moore, Harry L.; and Ball, Jimmie R.: ASTP Experiment Support Data Processing. NASA CR-141915, 1975.

2. Thompson, Morris M.; Eller, Robert C.; Radlinski, William A.; and Speert, Julius L., eds.: Manual of Photogrammetry. Third ed., vol. II, American Soc. of Photogram. (Falls Church, Va.), 1966.

Interpreting ASTP Photographs of the Ocean and Locating the Area Photographed (Case Study of the Gulf of Mexico)

G. A. Maul[a]

ABSTRACT

Handheld-camera photographs, taken over the eastern Gulf of Mexico in July 1975, were evaluated for oceanic information. The areas photographed were located over the sea by comparing cloud formations in the photographs with the same formations in visible imagery acquired simultaneously by geostationary satellite. By using concurrently obtained ship data, patterns in the sunglint were interpreted as indicators of the cyclonic shear zone of the Gulf Loop Current. The study tested the hypothesis, based on Skylab experience, that frequently observed circular cloud features are indicators of mesoscale turbulence in ocean currents. It was found that the features could be consistently explained as being attributable entirely to atmospheric changes and that the features were not associated with cold-core ocean eddies.

INTRODUCTION

The importance of man's role as an ocean observer from space was recognized and discussed more than a decade ago (ref. 1). Astronauts have obtained photographs of ocean phenomena since the earliest space flights, and analyses of the Gemini and Apollo photographs have been made by Soules (ref. 2), Mairs (ref. 3), and others. During the Skylab 4 mission, the flightcrew was given special training in making visual observations and taking photographs of the Earth. The results of that effort and the variety of oceanic features observed and photographed are summarized in references 4 and 5.

During the Apollo-Soyuz Test Project (ASTP), the flightcrew received similar training, and the observational data have been cataloged by El-Baz (ref. 6). (No attempt is made here to review all the oceanographically interesting observations made during ASTP.) This report concerns some of the Skylab recommendations (refs. 4, 5, and 7) relative to the problem of locating the ocean area obtained in the handheld-camera photographs and the problem of interpreting data in the space photographs by comparison with shipboard observations that were acquired at approximately the same time.

The eastern Gulf of Mexico was chosen as a test site for the experiment. Near-simultaneous coverage from the Geostationary Operational Environmental Satellite (GOES) was available over the gulf; this was a key element in the technique to locate an ocean area in handheld-camera photographs. The eastern Gulf of Mexico is also a region of great oceanographic variability. Color boundaries are numerous; they result from the presence of Mississippi River sediments, the high productivity of marine organisms in regions such as the Campeche Bank, and the clear shallow areas such as the Florida Keys. A good potential signature in the visible part of the spectrum can be

[a]Atlantic Oceanographic and Meteorological Laboratories, National Oceanic and Atmospheric Administration.

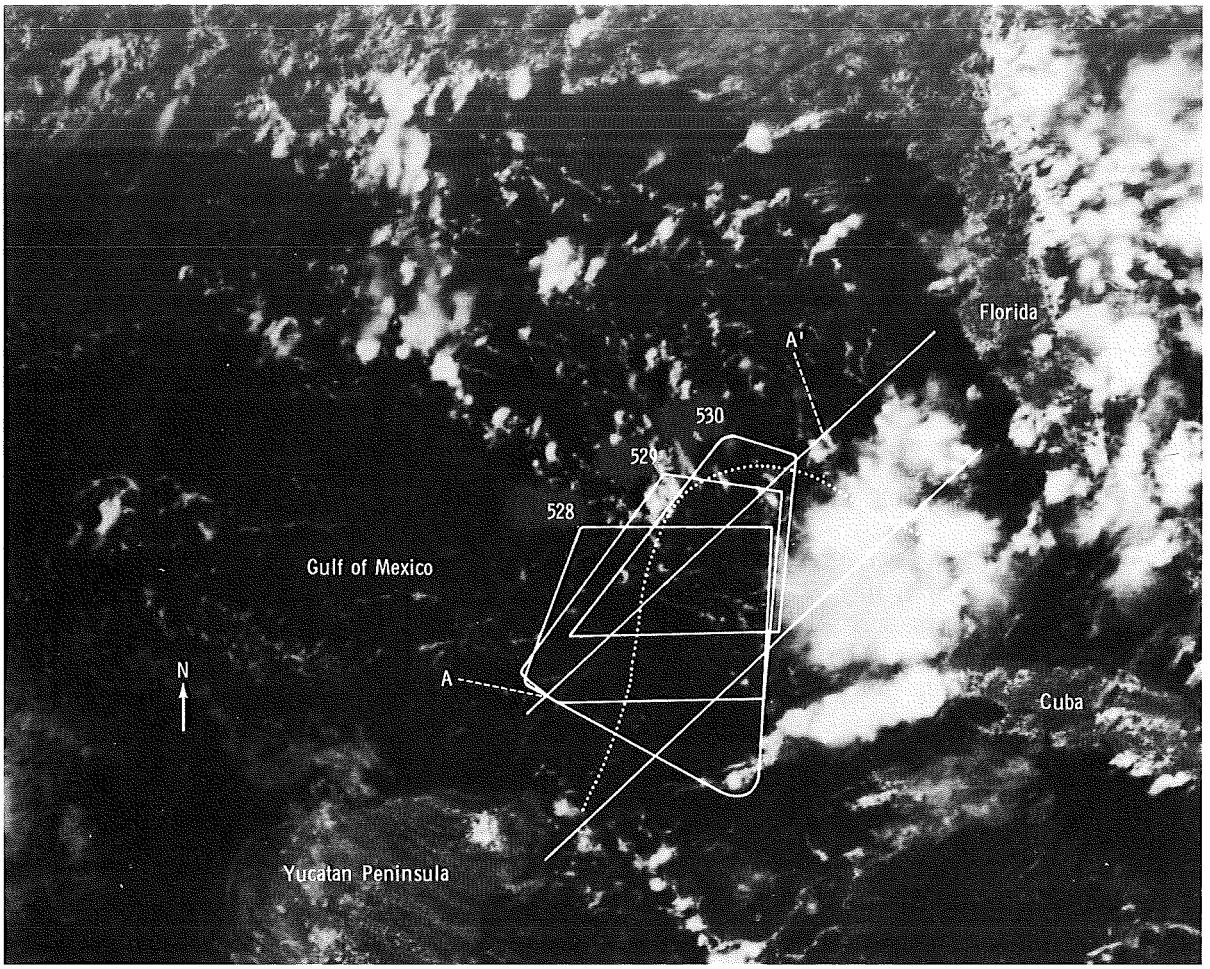
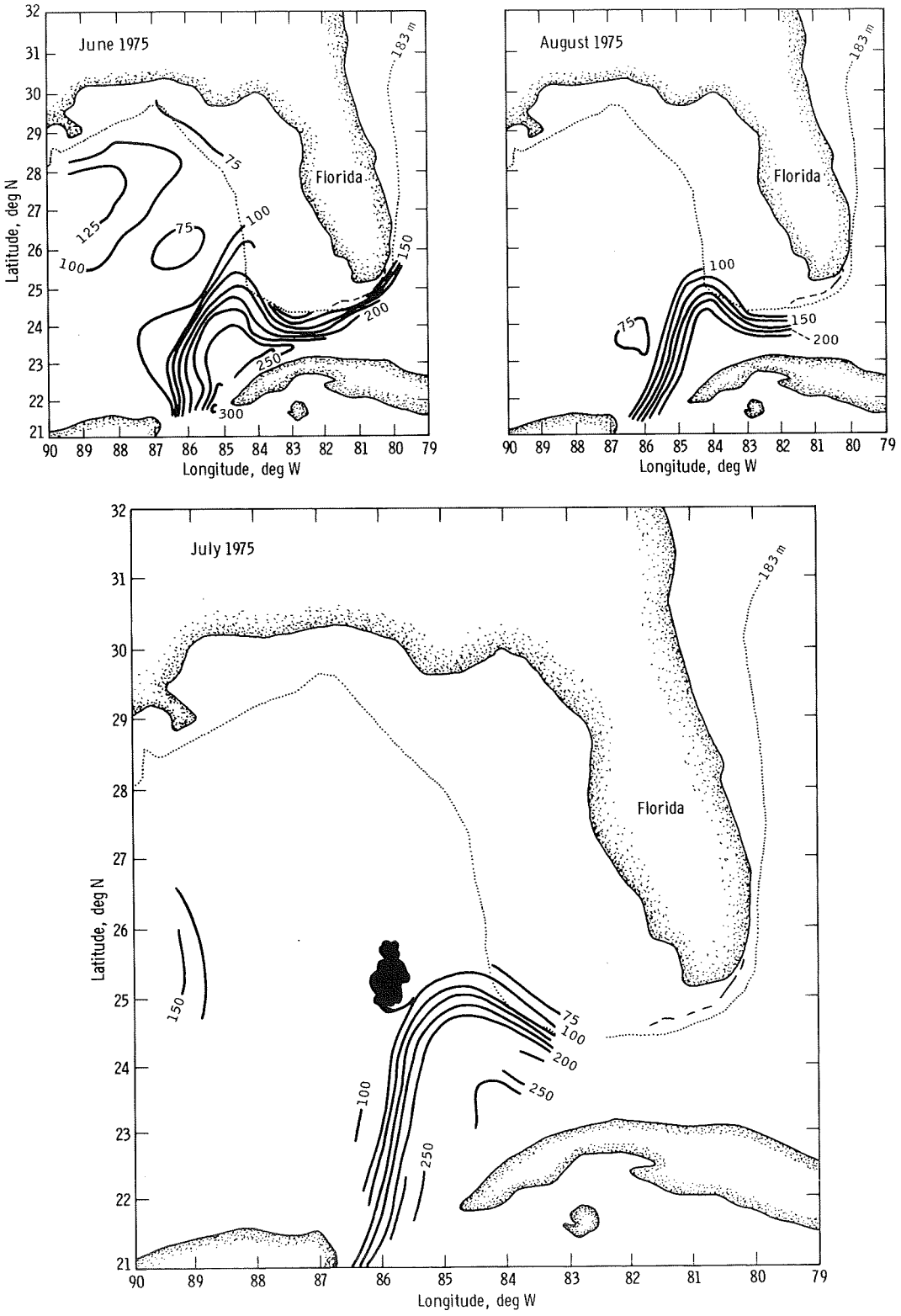


FIGURE 1.—The location of the test site in the eastern Gulf of Mexico is shown on this GOES 1-km-resolution visible-image taken at 19:00 UT on July 18, 1975. Northeast/southwest-trending lines are the surface tracks of the research vessel *Virginia Key*; the lines correspond to the suborbital tracks of the Apollo spacecraft. The three outlined areas represent the coverage of the handheld-camera photographs (frames AST-9-528 to AST-9-530) taken during the Apollo-Soyuz mission. (See also figs. 4(a) to 4(c).) The dotted line is the approximate locus of the cyclonic edge of the Gulf Loop Current as deduced from figure 2. The cross section in figure 3 is denoted by A-A'.

provided by current boundaries caused by the Gulf Loop Current and by the tidal currents through the Florida Keys. The National Oceanic and Atmospheric Administration (NOAA) research ship *Virginia Key* was assigned to this area for collecting oceanographic data "quasi-simultaneously" with the ASTP photographs taken from the Apollo spacecraft.

The test site is shown on the GOES image in figure 1. The two northeast/southwest-trending lines are the ship tracks, which are coincident with the groundtrack of the Apollo spacecraft. The

FIGURE 2.—Contours of the depth (in meters) of the 293-K (20° C) isothermal surface for June, July, and August of 1975, based on all data available from the National Oceanographic Data Center files. The dotted lines represent the outer limit of the Continental Shelf. Data in the region of the Gulf Loop Current were obtained between July 15 and 18 and are quasi-synoptic. The black sketch on the July map centered near latitude 25° N, longitude 86° W is the cloud feature imaged in figures 1 and 5(b), and photographed in figure 4(b). →


June 1975
August 1975
July 1975
Florida
183 m
75
100
125
150
200
250
300
Latitude, deg N
Longitude, deg W
32
31
30
29
28
27
26
25
24
23
22
21
90 89 88 87 86 85 84 83 82 81 80 79

southern line is revolution 15 (July 16, 1975), and the northern line is revolution 45 (July 18, 1975). Three handheld-camera photographs were taken by the spacecraft crew at approximately 18:43 UT on July 18; boundaries of the photographs are shown in figure 1. The dotted line is the locus of the 293-K (20° C) isotherm at a 100-m depth (fig. 2), which is approximately the left-hand edge of the Gulf Loop Current, facing downstream.

LOCATING AREAS IN THE PHOTOGRAPHS

Ocean photographs taken during ASTP can be divided into four groups: (1) vertical mapping photographs with exact data concerning latitude and longitude of the principal points, (2) mapping photographs with no data on the exact position of the principal point, (3) oblique photographs containing a coastline and/or islands, and (4) oblique photographs without any landmarks. In the second and third groups, routine photogrammetric techniques (ref. 8) can be used to locate the principal and corner points of most photographs. In the last group, clouds in the photographs were compared to clouds in near-simultaneous GOES visible imagery, and the clouds were used as reference points (fig. 1).

To properly interpret an oblique photograph, the nadir angle θ must be known. For a given camera altitude h, the arc length L on the Earth's surface from the nadir to the center point of the photograph is given by (ref. 8)

$$L = R \sin^{-1}[(K \sin \theta) - \theta]$$

where R is the mean radius of the Earth and K is defined as $(R + h)/R$. This is a transcendental equation in θ and can be solved quite readily. The solution requires finding the reference points on the photograph that lie on the principal line and measuring the distance from each reference point to the principal point. Then, by iteration, the angle θ is obtained and finally the latitude and longitude of the principal point.

With ocean photographs, several factors often make it difficult to find the principal line. First, the photograph is not annotated in a precise manner. Because the exact time of photoacquisition is often unknown, it is impossible to determine the nadir point; hence, the principal line is not defined. Second, locating clouds on a simultaneous GOES image has two pitfalls: (1) the best resolution of the visible imagery is 1 km, and (2) the geographical gridding of GOES imagery is not better than plus or minus several pixels. Not only are the scale and resolution of features on handheld-camera photographs not matched to the imagery, but the geographical positions of the features are poorly known. Third, GOES-type data are not available on a worldwide basis and special arrangements must be made in advance to ensure that 1-km-resolution images at 30-minute intervals are available. Other satellite data (available from NOAA, NASA, and the Department of Defense) were studied in this context, but they were found to have little value because of the time difference in observations (ref. 4).

The boundaries of the three photographs shown in figure 1 were located by comparing the major cloud features in the photographs with those in the 1-km-resolution GOES image. After careful comparison, an outline of each ASTP photograph was drawn over the GOES image. Then, by using dominant cloud features, the latitude and longitude of the principal point and of the corner points were interpolated across the photograph. It was not useful to calculate θ or to do any further quantification, because the exact time of photoacquisition was unknown.

EXAMPLE OF PHOTOINTERPRETATION

The ASTP mission provided an opportunity to supplement the visual observations from space by conducting a simultaneous research-ship cruise in the eastern Gulf of Mexico. The ship's southern trackline shown in figure 1 was quasi-synchronous with the Apollo spacecraft transit on July 16; the northern trackline was quasi-synchronous with transit on July 18. No photographs were taken on July 16; therefore, attention will be directed to the section from the Yucatan Peninsula to Florida observed on July 17 and 18, 1975. The temperature cross section as far as the west Florida platform is shown in figure 3.

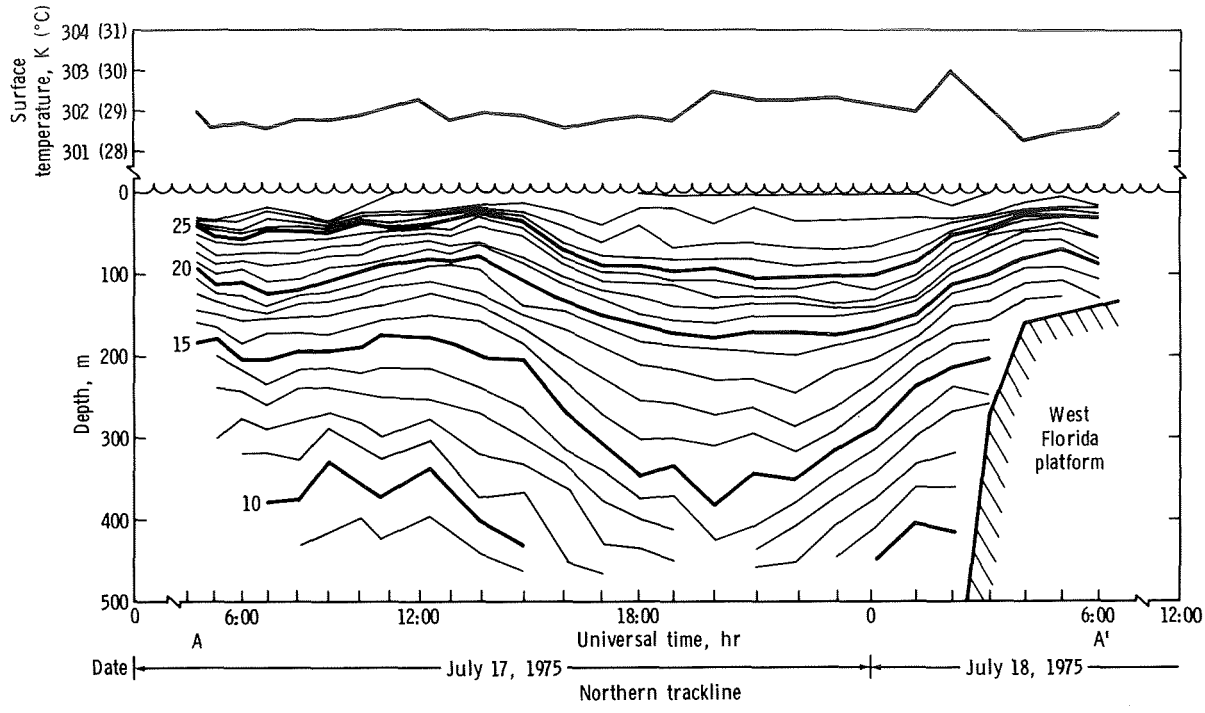


FIGURE 3.—Transect of water temperature and depth observed by the research vessel *Virginia Key* on July 17 and 18, 1975. This transect shows the part of the northern suborbital track sketched in figure 1 (A-A') between Campeche Bank and the Continental Shelf break of the west Florida platform. The sea-surface temperature profile was determined by means of a calibrated thermometer, which served as a control for the data. Eastern edge of the Gulf Loop Current occurs at approximately 14:00 UT, July 17, and the western edge at approximately 04:00 UT, July 18. (Isotherms are in Celsius (K = °C + 273.15).)

Temperature data were obtained from hourly (approximately 18-km spacing) expendable-bathythermograph (XBT) observations. In addition, hourly surface temperature and salinity observations were made, as well as continuous surface chlorophyll-*a* observations using Lorenzen's (ref. 9) method. The chlorophyll-*a* profile in the region covered in figure 3 was monotonic, thus suggesting that the edge of the Gulf Loop Current would not be indicated by a change in ocean color. Similarly, as expected for this time of the year, there is apparently no surface thermal indication of the current. From the many surveys into this area in the last 10 years (refs. 10 to 15 and others), the relation between the current and the thermal field is well known. The research vessel *Virginia Key* crossed into the Gulf Loop Current at approximately 14:00 UT on July 17 and left the current at approximately 04:00 UT on July 18 (fig. 3). In terms of the depth of the 293-K (20° C) isotherm, the cyclonic edge at the surface (left-hand side facing downstream) occurs just before the isotherm deepens to 100 m.

In figure 2, the areal distribution of the depth of the 293-K (20° C) isotherm, based on all available XBT and hydrographic station data for June, July, and August 1975, is plotted. The core of the Gulf Loop Current occurs in the thermal gradient region approximately bounded by the 125- and 200-m depths of the 293-K (20° C) isotherm. Also sketched on the July map is a significant cloud formation imaged in figure 1; this feature is discussed in later paragraphs. The position of the Gulf Loop Current changed very little during these 3 months. This suggests that the July shipboard data, spread over a 24-hour period, can be quasi-synoptically interpreted as satellite surface truth. Weather conditions over the eastern gulf were constant during the July data collection period; they were characterized by generally

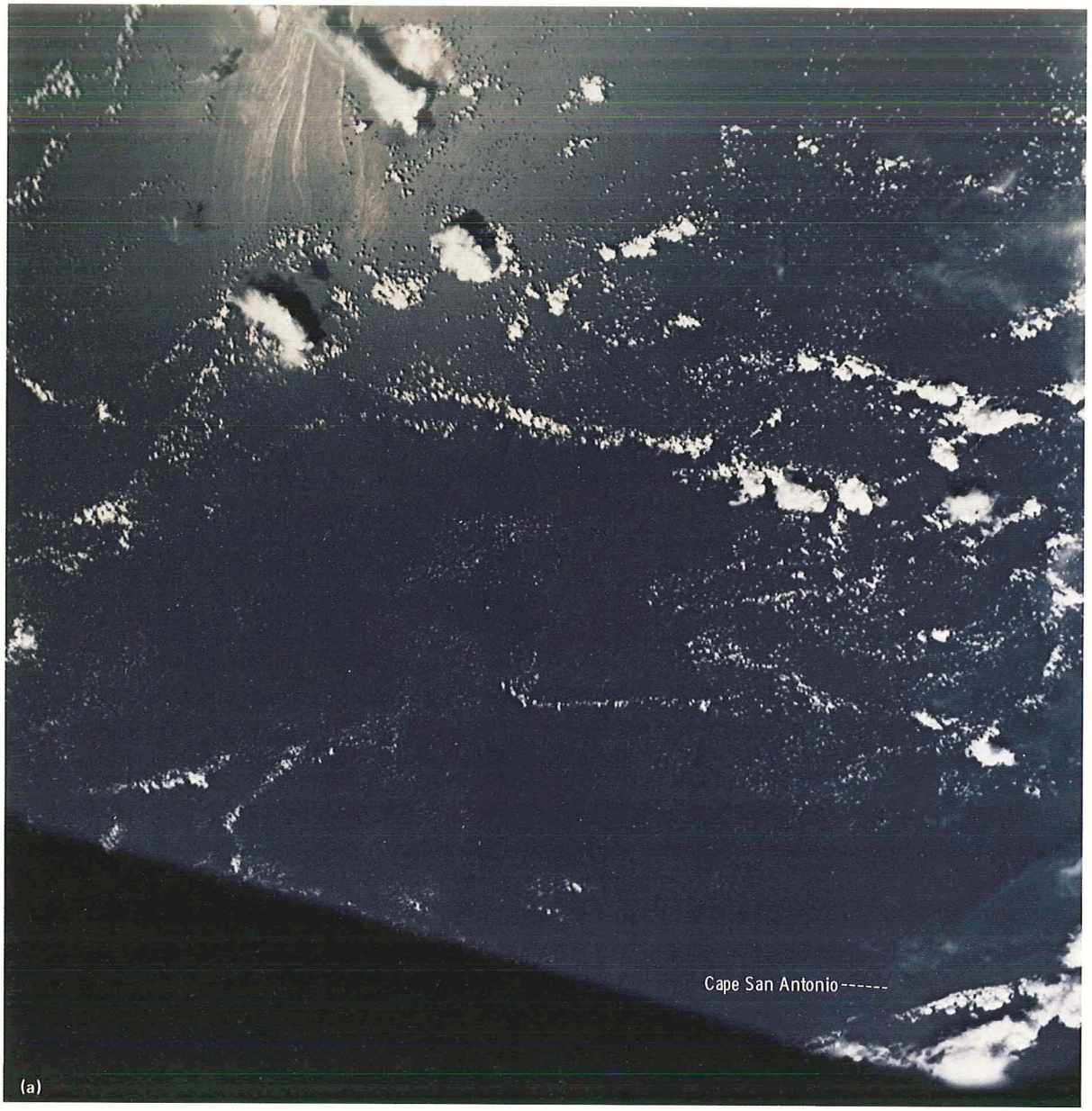


FIGURE 4.—Handheld-camera photographs over the eastern Gulf of Mexico taken by the Apollo crew at approximately 18:43 UT on July 18, 1975. Photographs were obtained with a 70-mm format camera using a 50-mm lens. The right-hand margin of each photograph is oriented approximately north-south, as shown in figure 1. The photographs were taken from the northeast, looking southwest. Clouds are easily differentiated from sea-surface features by comparing features in adjacent photographs or by their shadows. Approximate solar elevation is 77°, and approximate azimuth is 256° reckoned clockwise from north. (a) AST-9-528. (b) AST-9-529. (c) AST-9-530.

southeasterly winds at 2 to 3 m/sec interrupted by local thunderstorms.

The three ASTP photographs taken during this experiment are shown in figures 4(a) to 4(c). These are oblique 70-mm photographs taken with a 50-mm-focal-length lens. The black shadow in each photograph is the edge of a spacecraft window. Crew documentation and comments on

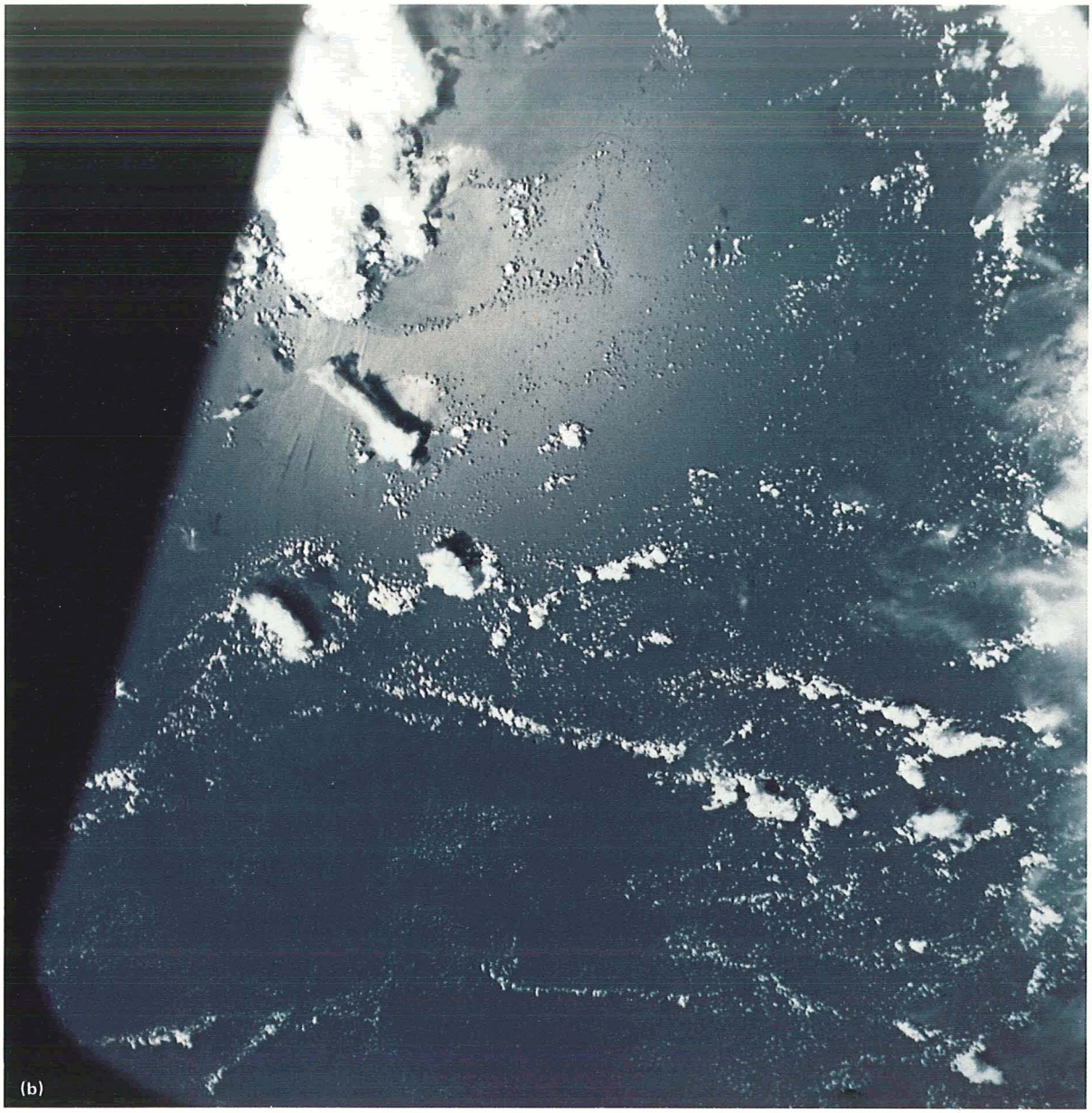


FIGURE 4.—Continued.

these photographs are minimal, and, except for knowing that they were taken over the gulf during revolution 45 (July 18), the only quantitative information was obtained by means of the location procedure discussed earlier. As can be seen by comparison with figure 1, the right-hand borders of figures 4(a) to 4(c) are oriented almost exactly north-south.

In figure 4(a), the western tip of Cuba can be seen in the lower right-hand corner and a series of streaks in the sunglint pattern appears near the upper left border. Water color patterns are quite evident near Cape San Antonio because of changes in bottom depth; but, in agreement with the ship data, there is no color evidence of the Gulf Loop Current. Because the streaks are to the

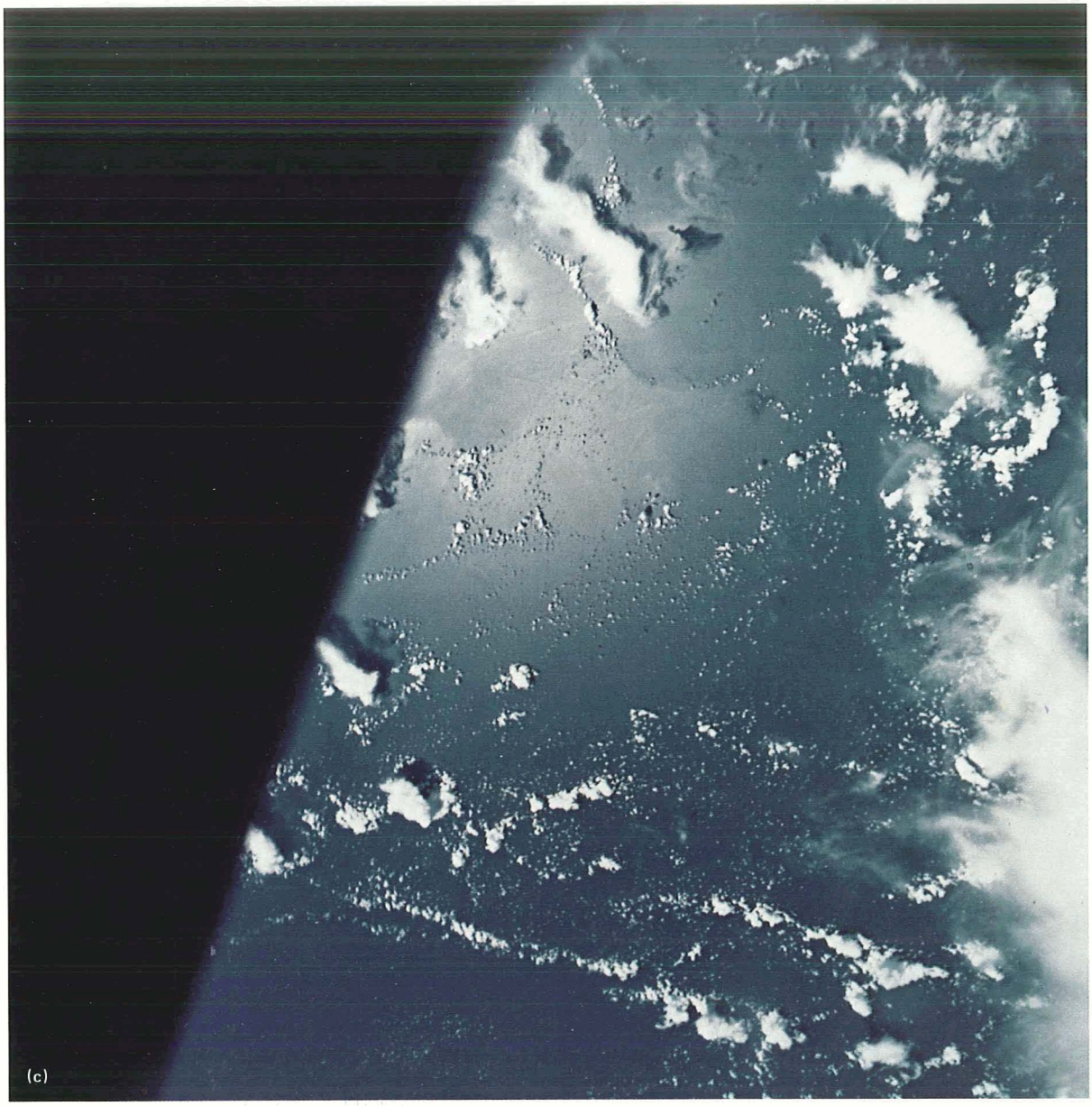


FIGURE 4.—Concluded.

west of the 293-K (20° C) isotherm at 100-m depth (fig. 1), it is likely that they are associated with the current's cyclonic edge. In figure 4(b), the streaks are again observable just to the right of the large cloud in the upper left corner of the photograph; this is the cloud sketched in figure 2. By comparing with figure 4(a), it is seen that the streaks in figure 4(b) are a continuation of those in figure 4(a) and can be followed through the sunglint into figure 4(c). The streaks show significant anticyclonic curvature in figures 4(b) and 4(c), in agreement with the ship data (fig. 2). Again, there is no color indication of the current in these last two photographs.

The interpretation of photographs showing slicks in sunglint has been reviewed by Soules (ref. 2). Because his photointerpretations were made without benefit of near-simultaneous shipboard observations, he was uncertain about the dynamic processes involved. Shipboard photographs (not shown) and logged observations indicate extensive areas of slicks in the time period 12:00 to 19:00 UT on July 17 (fig. 3); at 19:00 UT, the slicks were seen to be 20 to 30 m wide, separated by approximately 150 m. Judging from the wind conditions and following the discussion by McLeish (ref. 16), the slicks do not appear to be wind generated (particularly since they curve anticyclonically with the current). E. Mollo-Christensen and J. R. Proni[1] have proposed that horizontal shears (as inferred by the isotherms in fig. 3) can cause internal waves near the edge of the Gulf Stream; this would require a regularity in the slicks, which was not observed in figure 4. It appears then that an explanation for the slick pattern is the horizontal shear across the current. It has been observed elsewhere (ref. 17) that the horizontal velocity field can have a banded structure; i.e., bands of uniform current speed separated by a zone of very large shear. Such an explanation would be a horizontal analog of the vertical shear profile in the thermocline observed by Woods (ref. 18) and is consistent with other observations of layer quantization observed in the ocean (e.g., refs. 19 and 20).

The streaks in figure 4 show no indication of eddies embedded in the current such as those reported by Maul et al. (ref. 21) or by Maul (ref. 15). In the upper left corner of figure 4(b), however, is a cloud formation that is typical of what Stevenson (refs. 5 and 7) interpreted as a cold-core eddy embedded in the Yucatan Current. His interpretations were made from Skylab photographs, and there are several examples in figure 4. There is evidence to offer an alternative explanation for these data.

Scully-Power and Twitchell (ref. 22) gave a theoretical analysis of the conditions needed to form a cloud over a warm-core eddy. In contradistinction, a cold-core eddy should be characterized merely by a lack of cloud, much as observed in figure 4(b). Scully-Power and Twitchell found that for light wind conditions such as observed here, the height H of the convective condensation level (CCL) is given by

$$H = \tau/(\Gamma - \gamma) \tag{1}$$

where τ is the temperature excess (in degrees Celsius) of the warm waters relative to the surrounding waters, Γ is the dry adiabatic lapse rate (0.98° C/100 m), and γ is the observed lapse rate. Using the 12:00-UT Key West radiosonde data as input, the height of the CCL is 832 m and γ is 0.63° C/100 m. Solution of equation (1) requires $\tau = 2.9$ K (2.9° C), which is well beyond these or historical observations (ref. 23) of sea-surface temperature patterns in the Gulf of Mexico in July. In addition, careful examination of the streaks, especially in figures 4(b) and 4(c), shows that the streaks are continuous in their trend into and/or out of the circular feature. If the cloud feature was indeed an oceanic circulation feature, the streaks would show some indication of rotation. Also, the cloud feature in figure 4(b) is in the zone of maximum current shear, where streamline distortion due to the water's vorticity would be maximum. Third, the velocity of the feature, if it is as Stevenson (refs. 5 and 7) supposes, must be to the northeast at approximately 1 m/sec (i.e., with the current). Using the same image sequence technique employed by meteorologists to determine winds from cloud motion, the velocity of the main cloud feature was determined to be 5 m/sec to the west-southwest (i.e., against the current). Similar results were obtained with other cloud features (fig. 1); the analysis for the feature seen in figure 4 is given in figure 5, in which a sequence of GOES 1-km-resolution images is shown.

Gurka (ref. 24) offered an explanation of similar features that is consistent with the observations reported here. Gurka's analyses of GOES imagery and concurrent wind observations show that cloud features such as depicted in figure 4 are caused by strong wind zones accompanying thunderstorms. In a thunderstorm, circular bands of

[1] Personal communication, 1977.

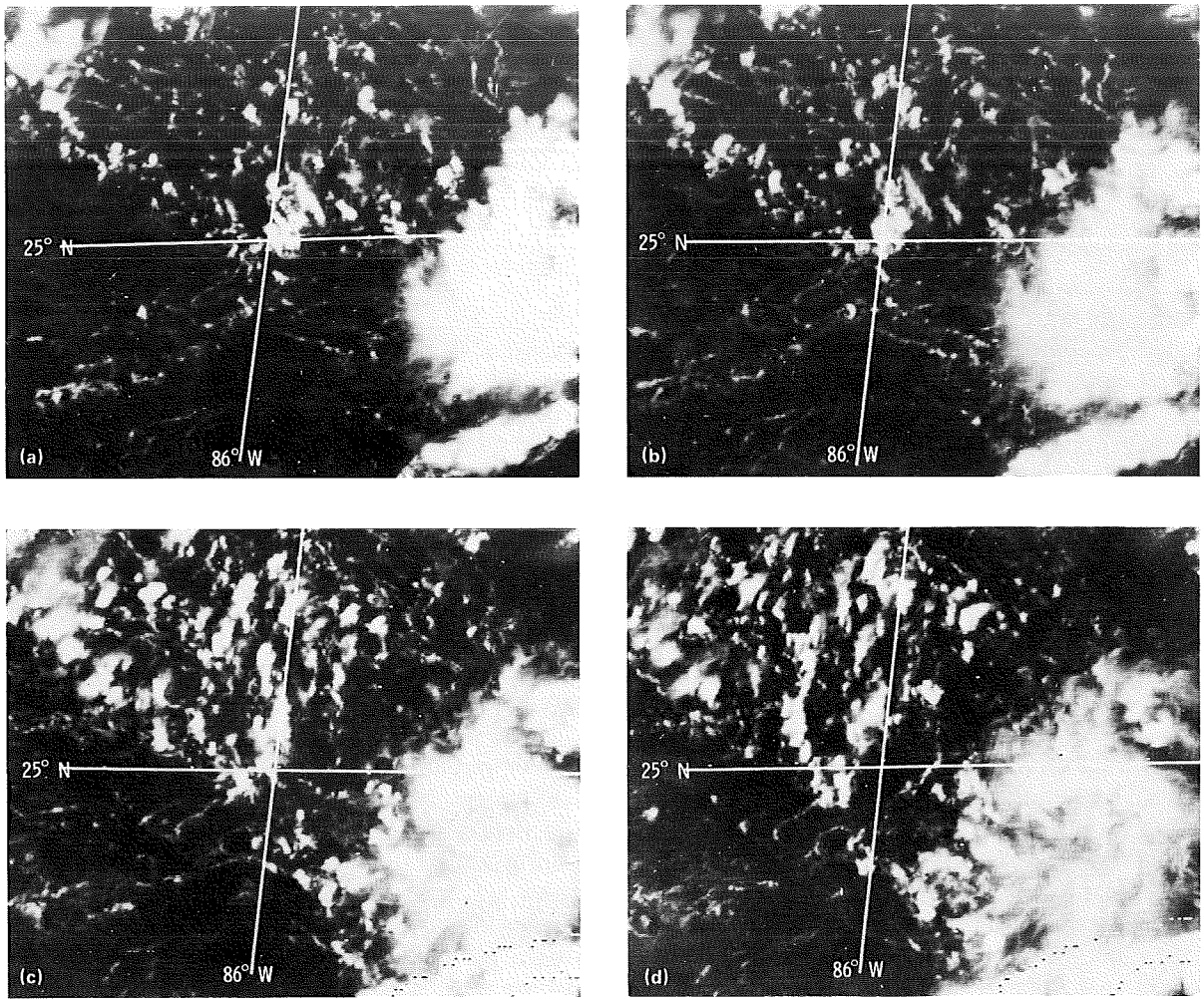


FIGURE 5.—Sequence of 1-km-resolution GOES visible images taken on July 18, 1975, centered at latitude 25° N, longitude 86° W. Evolution of the cloud feature noted in figures 1, 2, and 4(b) is seen to be toward the southwest. Dots in figures 5(c) and 5(d) are part of the electronic grid in the original images; the grid overlay was removed from figures 5(a) and 5(b) before final figure preparation. Data in figures 5(a), 5(c), and 5(d) were provided by the Environmental Data Service; figure 5(b) was specially imaged by the Miami Satellite Field Services Station, NOAA. (a) 18:00 UT. (b) 19:00 UT. (c) 20:00 UT. (d) 21:00 UT.

clouds (similar to those located southeast of the cumulonimbus in the upper left corner of fig. 4(b)) are caused by divergent winds that are orthogonal to the cloud ring. The clear area is an expression of dry air that has descended and diverged. Stevenson (refs. 5 and 7) noted that the color of the sea was often different in the center of the area; he ascribed this effect to cooler water. An alternate explanation based on the wind pattern is that the color change represents a change in reflectance, due to slopes caused by varying winds. Just such an abrupt change in sea state was seen from the research vessel *Virginia Key* during the morning of July 17. It was manifested as a marked change in ocean color from gray to blue after the passage of the wind front.

It is difficult to quantify the discussion in terms of wave-slope statistics (ref. 25) because the position of the spacecraft when the ASTP photographs were taken is not known. However, if the estimated photoacquisition time of 18:43 UT is nearly correct, the zenith angle Z and the azimuth

angle A of the Sun relative to sunglint can be calculated from the solar declination d, the latitude of the sunglint ϕ, and the local meridian angle t.

$$Z = \cos^{-1}[\sin d \sin \phi + \cos d \cos \phi \cos t]$$

$$= 13°$$

$$A = \sin^{-1}\left[\frac{\sin t \cos d}{\sin Z}\right]$$

$$= 256°$$

Then, using Snell's law, the position of the spacecraft can be estimated by dead reckoning to be latitude 25.1° N, longitude 84.5° W; i.e., the photographs in figure 4 were taken from the northeast looking southwest. Using this perspective, the mean-square wave-slope σ^2 equation of Cox and Munk (ref. 25)

$$\sigma^2 = 0.003 + 5.12 \times 10^{-3} W$$

where W is the windspeed in meters per second, can be employed to discuss varying reflectances in the sunglint pattern.

Strong and Ruff (ref. 26) showed that the radiance distribution from sunglint could be adequately modeled by assuming that σ^2 is independent of the wind direction and by using a Gaussian probability distribution. Assuming a probability function of the form

$$\frac{\exp\left[-\frac{\left(\frac{\partial z}{\partial x}\right)^2}{\sigma^2}\right]}{\pi\sigma^2}$$

where $\partial z/\partial x$ is the root-mean-square wave slope, the probability of a wave slope occurring for windspeeds of 0, 2, 5, and 10 m/sec was calculated and is shown in figure 6 for the viewing geometry deduced earlier. Isopleths of wave slope required to reflect the Sun for $Z = 13°$ describe an elliptical shape on the ocean surface. The diagram also shows how a sunglint pattern spreads over a larger area as a uniform windspeed increases. For the observer looking at the specular point ($\tan^{-1}(\partial z/\partial x) = 0°$), the probability that a photon will be reflected decreases rapidly with increasing windspeed; i.e., the radiance decreases. This condition is analogous to the situation in figure 4(b) in the southwestern corner of the ring-cloud area, where a higher windspeed would be manifested by a lower radiance. The opposite case, in which the wind vector from the thunderstorm and the mean wind field tend to cancel and result in a higher radiance, can easily be envisioned. Thus, a complicated wind field can be inferred from the radiance pattern.

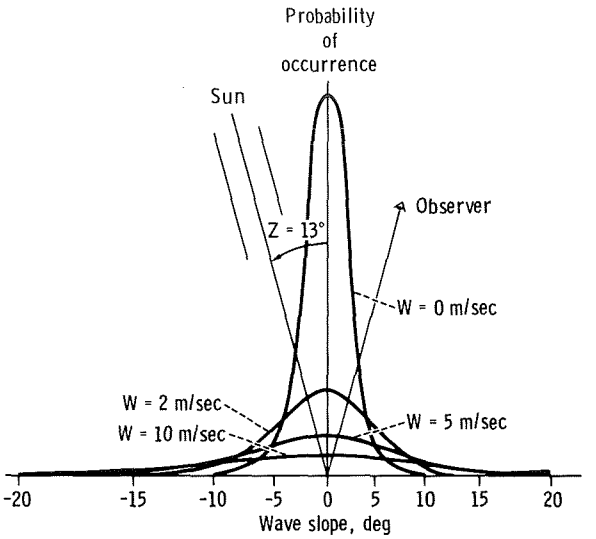


FIGURE 6.—Interpretation diagram for the sea-surface reflectance patterns seen in figure 4, neglecting the effects of upwelling diffuse radiance from beneath the sea and of atmospheric scattering. The probability that the Apollo observer would see specular return of the Sun is plotted for the range of windspeeds W and viewing geometry of figure 4. If an observer is looking at a point on the sea surface where a wave slope of +5° is required to reflect the Sun, the probability of reflection is much less for a 5-m/sec wind than for a 2-m/sec wind; this explains discontinuities in the reflectance pattern as spatial gustiness in the wind field.

DISCUSSION

The experiment described here was designed to evaluate the usefulness of ASTP handheld-camera photographs and visual observations over a

specific study site. The Apollo spacecraft crossed the eastern Gulf of Mexico several times during the mission, and three space photographs were obtained over the Gulf Loop Current boundary at the same time that the research vessel *Virginia Key* observed oceanic conditions. The most serious difficulties in using the satellite data were the lack of accurate time annotation on the photographs and the absence of voice comments at the time of transit. (The former problem can be solved by using crystal-controlled light-emitting-diode day/time displays along the sprocket holes in all future space-qualified cameras. The latter problem can be adequately solved by use of voice-activated recorders coupled to the camera system whereby the observer can note the frame number and time from the camera in the visual observations log.) Results from this experiment suggest that, for this mission, the 70-mm format camera using the 50-mm lens was the best combination of photographic equipment for oceanic viewing.

Location of the photographs was accomplished by comparison with near-simultaneous, 1-km-resolution GOES imagery. To fully exploit this technique, all full-disk 1-km-resolution imagery must be archived from the routine 30-minute observing schedule; only hourly data were available for this study. In addition, for specific experiments, special observing schedules should be followed to provide synoptic observations. During the Space Shuttle missions, worldwide geostationary imagery will be available; special planning will be required to fully exploit those data for handheld-camera photographic purposes.

Photographing the sunglint pattern proved to be the most valuable contribution to observing the current boundary. The shipboard data show that during the summer, there may be no color boundary to the Gulf Loop Current and that surface reflection patterns will be the only remotely sensed indicators of its location. This suggests that for experiments with the coastal zone color scanner to be flown on Nimbus-G, the instrument should be tilted to observe sunglint under certain conditions. In view of the pattern in sea-surface reflectance associated with the current, microwave techniques would appear to be a valuable sensing tool. However, there are high-frequency sea-state (capillary) fluctuations associated with meteorological conditions that would make microwave analysis difficult without ancillary measurements.

Circular features in cloud fields have been interpreted by Stevenson (refs. 5 and 7) as being caused by cold-water eddies in the current. From an investigation into this interpretation, the following conclusions were reached: (1) the surface temperature differences required to support the hypothesis were not observed, (2) streaks on the water showed no evidence of eddy-induced vorticity, (3) the cloud feature observed moved at 5 m/sec against the current, and (4) the sea-surface reflectance patterns could be explained on the basis of fluctuations of the wind field associated with the typical ring-cloud formations around thunderstorms. Because these facts are consistent with concurrent shipboard observations of the surface and subsurface thermal fields and with the ship's weather log, it is concluded that Stevenson's observation of mesoscale turbulence in ocean currents can be better explained as being entirely meteorological in nature, driven perhaps by a relatively uniform, warm sea-surface temperature field.

ACKNOWLEDGMENTS

Gratitude is expressed to M. Pryslak, S. McLafferty, and M. McCaslin for their assistance in data acquisition and analysis. Ocean temperature data for June and August 1975 were provided by R. L. Molinari (NOAA); the 19:00-UT GOES image was specially recorded by the Miami Field Services Station of the NOAA National Environmental Satellite Service.

REFERENCES

1. Ewing, G. C., ed.: Oceanography From Space. Ref. 65-10, Woods Hole Oceanographic Institution (Woods Hole, Mass.), 1965.

2. Soules, Stanley D.: Sunglitter Viewed From Space. Deep-Sea Res., vol. 17, Feb. 1970, pp. 191-195.

3. Mairs, Robert L.: Oceanographic Interpretation of Apollo Photographs. Photogram. Eng. vol. 36, Oct. 1970, pp. 1045-1058.

4. Maul, George A.; and McCaslin, Michael: An Assessment of the Potential Contributions to Oceanography From Skylab Visual Observations and Handheld-Camera Photographs. Sec. 12 of Skylab Explores the Earth, NASA SP-380, 1977.

5. Stevenson, Robert E.; Carter, L. David; Vonder Haar, Stephen P.; and Stone, Richard O.: Visual Observations of the Ocean. Sec. 11 of Skylab Explores the Earth, NASA SP-380, 1977.

6. El-Baz, Farouk: Astronaut Observations From the Apollo-Soyuz Mission. In vol. I of Smithsonian Studies in Air and Space, Smithsonian Institution Press (Washington, D.C.), 1977.

7. Stevenson, Robert E.: Observations From Skylab of Mesoscale Turbulence in Ocean Currents. Nature, vol. 250, no. 5468, Aug. 23, 1974, pp. 638-640.

8. Thompson, Morris M.; Eller, Robert C.; Radlinski, William A.; and Speert, Julius L., eds.: Manual of Photogrammetry. Third ed. American Soc. Photogram. (Falls Church, Va.), 1966.

9. Lorenzen, C. J.: A Method for the Continuous Measurement of in vivo Chlorophyll Concentration. Deep-Sea Res., vol. 13, no. 2, 1966, pp. 223-227.

10. Cochrane, J. D.: The Yucatan Current. Annual Report, Project 286, Texas A. & M. Univ. Ref. 65-17T, 1965, pp. 20-27.

11. Nowlin, W. D., Jr.; and McLellan, H. J.: A Characterization of the Gulf of Mexico Waters in Winter. J. Marine Res., vol. 25, no. 1, 1967, pp. 29-59.

12. Leipper, Dale F.: A Sequence of Current Patterns in the Gulf of Mexico. J. Geophys. Res., vol. 75, no. 3, Jan. 20, 1970, pp. 637-657.

13. Molinari, Robert L.; and Yager, Robert E.: Upper Layer Hydrographic Conditions at the Yucatan Strait During May, 1972. J. Marine Res., vol. 35, no. 1, 1977, pp. 11-20.

14. Morrison, John M.; and Nowlin, Worth D.: Repeated Nutrient, Oxygen, and Density Sections Through the Loop Current. J. Marine Res., vol. 35, no. 1, 1977, pp. 105-128.

15. Maul, George A.: The Annual Cycle of the Gulf Loop Current, Part I: Observations During a One-Year Time Series. J. Marine Res., vol. 35, no. 1, 1977, pp. 29-47.

16. McLeish, W. L.: On the Mechanisms of Wind-Slick Generation. Deep-Sea Res., vol. 15, 1968, pp. 461-469.

17. Maul, George A.; and Hansen, Donald V.: An Observation of the Gulf Stream Front Structure by Ship, Aircraft, and Satellite. Remote Sens. Environ., vol. 2, 1972, pp. 109-116.

18. Woods, John D.: An Investigation of Some Physical Processes Associated With the Vertical Flow of Heat Through the Upper Ocean. Meteorol. Mag., vol. 97, no. 1148, Mar. 1968, pp. 65-72.

19. Stommel, Henry; and Fedorov, K. N.: Small-Scale Structure in Temperature and Salinity near Timor and Mindanao. Tellus, vol. 19, no. 2, 1967, pp. 306-325.

20. LaFond, E. C.; and LaFond, K. G.: Vertical and Horizontal Thermal Structures in the Sea. Rep. NEL 1395, U.S. Navy Electronics Laboratory (San Diego, Calif.), July 1968.

21. Maul, G. A.; Norris, D. R.; and Johnson, W. R.: Satellite Photography of Eddies in the Gulf Loop Current. Geophys. Res. Letters, vol. 1, Oct. 1974, pp. 256-258.

22. Scully-Power, P.; and Twitchell, P.: Satellite Observation of Cloud Patterns over East Australian Current Anticyclonic Eddies. Geophys. Res. Letters, vol. 2, Mar. 1975, pp. 117-119.

23. Robinson, Margaret K.: Atlas of Monthly Sea Surface and Subsurface Temperature and Depth of the Top of the Thermocline, Gulf of Mexico and Caribbean Sea. Ref. 73-8, Scripps Inst. Oceanography (La Jolla, Calif.), 1973.

24. Gurka, James J.: Satellite and Surface Observations of Strong Wind Zones Accompanying Thunderstorms. Mon. Weather Rev., vol. 104, no. 12, 1976, pp. 1484-1493.

25. Cox, C.; and Munk, W.: Measurements of the Roughness of the Sea Surface From Photographs of the Sun's Glitter. J. Opt. Soc. America, vol. 44, no. 11, 1954, pp. 838-850.

26. Strong, Alan E.; and Ruff, Irwin S.: Utilizing Satellite-Observed Solar Reflections From the Sea Surface as an Indicator of Surface Wind Speeds. Remote Sens. Environ., vol. 1, 1970, pp. 181-185.

Visual Observations Over Oceans

R. D. Terry[a]

ABSTRACT

During the Apollo-Soyuz Test Project mission, visual observations of ocean features were successfully performed by the Apollo crewmen. Although three of the four ocean observation targets were cloud covered during the mission, observations of one scheduled target and of many targets of opportunity clearly demonstrated that astronauts could be trained to become excellent ocean observers. Previous space (but nonobservational) experience was found to be unimportant when compared with premission briefings and aircraft flyover exercises. Although the low spacecraft altitude (approximately 220 km) was excellent for Earth observations, the high relative velocity hampered target acquisition and created brief observational times of 5 to 20 seconds. The duration of the 9-day mission was insufficient to demonstrate any marked improvement in the "learning curve" of the crew.

Important factors in locating, identifying, describing, and photographing ocean features from space were (1) the presence or absence of sunglint, (2) water color, (3) clouds, (4) spacecraft altitude, (5) spacecraft attitude, (6) photographic equipment, (7) window fogging, (8) dual tasks, and (9) description as opposed to photography.

On the basis of crew comments and the findings of this author, the following recommendations can be made for Earth observations on Space Shuttle missions.

1. Flyover exercises must include observations and photography of both temperate and tropical/subtropical waters.

2. Sunglint must be included during some observations of ocean features.

3. Imaging remote sensors should be used together with conventional photographic systems to document visual observations.

4. Greater consideration must be given to scheduling Earth observation targets likely to be obscured by clouds.

5. An annotated photographic compilation of ocean features can be used as a training aid before the mission and as a reference book during space flight.

INTRODUCTION

The purposes of this specific investigation were (1) to evaluate the visual observation capabilities of spacecraft crews during a short-duration (9 day), low-altitude (220 km) orbital flight, (2) to contrast these capabilities with the capabilities developed during the 84-day Skylab 4 mission, and (3) to develop training techniques for making ocean observations and acquiring oceanographic data during orbital missions of the Space Shuttle and Spacelab vehicles. (Scientific results of oceanographic investigations are reported elsewhere in this volume.)

To achieve these purposes, observations and photographs of various ocean features were obtained during the Apollo-Soyuz Test Project (ASTP) as part of the Earth Observations and Photography Experiment. The simultaneous acquisition of ground-truth data by research vessels was also scheduled. Analyses of all these data helped answer the following questions.

1. What is the configuration of the "learning curve" for useful visual observations of the oceans

[a]Richard Terry & Associates/Environmental Science & Services, San Clemente, California.

by astronauts?

2. How do premission briefings contribute to observer performance as compared with previous space-flight experience?

3. What constraints are imposed upon visual observations by low-altitude, short-duration missions?

4. Is previous space (nonobservational) experience useful?

During the ASTP mission planning, four primary ocean targets were selected for observations and photography. These were the approaches to the English Channel and the Strait of Gibraltar, the Tasman Sea (off Australia), and the Kermadec Sea (off New Zealand). Many other visual observations of ocean features were planned in various parts of the world. However, this study will not include detailed analyses of the ocean targets, largely because other research, independent of this study, is being performed (ref. 1), and because this study is primarily concerned only with the answers to the four questions listed previously.

SOURCE MATERIALS

Visual Observation Comments

Visual observation comments made by the astronauts during ASTP are derived from the following NASA Lyndon B. Johnson Space Center (JSC) ASTP internal sources: (1) Technical Air-to-Ground Voice Transcription (JSC-09815), (2) Onboard Voice Transcription (JSC-09966), (3) onboard science tapes, (4) Visual Observations Debriefing (JSC-09920), and (5) Technical Crew Debriefing (JSC-09823). These five sources were compiled into a single document by El-Baz (ref. 2).

Photographs

A total of 2670 35-mm and 70-mm color photographs was taken during ASTP. Video-tape recordings were also made that included brief views of the ocean; however, these tapes were not examined as part of this study.

When 70-mm film was depleted, the crew used 35-mm film for Earth photography. Unfortunately, the 35-mm film was designated for indoor photography and was unsuitable for other purposes. Although color photographs on 35-mm film show clouds and gross features, subtle changes in ocean color and texture are undetectable.

Table I lists all ASTP photographs of the four targets established for ocean observations and concurrent surface investigations. Not all the photographs included in table I show the actual targets; they are listed because they are photographs taken near the targets. All photographs taken during ASTP are listed in the "Index to Onboard Photography," a JSC internal document prepared by Richard W. Underwood, and in NASA publication number TM 58218.

Ground-Truth Investigations

Ground-truth data were obtained during ASTP in four target areas. These are described in the following paragraphs.

Spanish Bight/Strait of Gibraltar

Ships and aircraft of the U.S. Navy acquired oceanographic data in the Spanish Bight/Strait of Gibraltar area. Included were P-3A *Orion* antisubmarine warfare (ASW) aircraft flying from the Azores. Air expendable bathythermograph (AXBT) instruments were dropped by these aircraft on July 19, 20, and 21, 1975. The oceanographic research vessel U.S.N.S. *Kane* obtained temperature/depth data along a northeasterly track toward the Spanish coast on July 21 and 22. The aircraft carrier U.S.S. *Kennedy* acquired Defense Meteorological Satellite Program (DMSP) imagery (visible and infrared) of the target on July 20. This imagery was sent to the U.S. Navy Weather Facility DMSP van, North Island, San Diego, California, for enhancement (ref. 1).

Tasman Sea

In the Tasman Sea, the Royal Australian Navy ship H.M.A.S. *Bombard* was stationed in the middle of one of the most intense warm-water eddies ever surveyed. The ANZUS eddy had a diameter of approximately 250 km and was nearly circular.

The *Bombard* was in the eddy, observing cloud and sea conditions, while making current speed and direction, temperature/depth, and sound-velocity measurements for 4 days. During the first 2 days, there were clear skies, with a well-developed formation of cumulus clouds over the eddy, and in the center were a dozen Japanese long-line tuna vessels. Unfortunately, a front moved through the area, making it impossible to see the eddy on the day of the ASTP observation. Previous researchers had identified the ANZUS eddy (refs. 3 to 5).

Kermadec Sea

The Royal New Zealand Air Force used P-3A *Orion* aircraft to observe and photograph conditions and to collect oceanographic and meteorological information along a 640-km (345 n. mi.) track extending from East Cape, New Zealand, northeastward toward the Kermadec Islands. The aircraft flew at an altitude of approximately 1500 m (5000 ft) on 3 consecutive days; the second was the day of the ASTP observation. In addition, the New Zealand Navy research vessel R/V *Tui* was in the same area, making a detailed survey of an eddy north of New Zealand. The eddy was identified by changes in sound velocities. On the day of the ASTP observation, oceans to the east of East Cape were obscured by clouds.

Approaches to the English Channel

To cover approaches to the English Channel, the Royal Air Force (RAF) flew *Nimrod* aircraft (converted *Comets*) westerly out of southern Ireland. The RAF dropped AXBT's along a 960-km (520 n. mi.) line. This area was also obscured by clouds during the visual observation experiment.

Scheduling of Events

Before the ASTP mission, a schedule of events, including Earth observations, was carefully planned, and an "ASTP Earth Observations

TABLE I.— ASTP Photographs of Ocean Test Sites

Geographic area	*Revolution*	*Photograph no., AST-*	*Film size, mm*
Spain/Gibraltar	73	27-2366, [a]27-2367, 27-2362 to 27-2365	70
	88	[a]24-1944	70
		11-684 to 11-688	35
Tasman Sea	123	20-1655 to 20-1659	70
Kemadec Sea	17	22-1776 to 22-1778, 1-036 to 1-040	70
	107	7-397 to 7-399	35
Approaches to English Channel	74	30-2541 to 30-2548	70
	119	20-1640 to 20-1644	70
	135	24-1948 to 24-1952	70
		10-599, 10-600	35

[a]Photograph of actual site, based on ASTP maps.

Book" was prepared for the astronauts. Ground-truth investigations were scheduled in accordance with the dates and times assigned for Earth observation passes. Although the spacecraft passed over or near each of the targets several times, additional visual observations were prevented because of scheduling conflicts. The first Earth observation pass was not completed until spacecraft revolution 17, approximately 33 hours after launch. Initially, only one crewmember was assigned to Earth observations during each pass; however, events occurred so quickly that eventually two or all three crewmembers became involved in Earth observations. In this way, it was considerably easier to obtain simultaneous visual observations and photographs.

For the Spanish/Gibraltar target, there were four possible opportunities to make visual observations: revolutions 43, 58, 73, and 88. Visual observation experiments were performed on revolutions 73 and 88, but the most important observation was made during revolution 73, when the site was in sunglint.

With the exception of the first 16 revolutions, there were at least 7 opportunities to observe the approaches to the English Channel (i.e., revolutions 44, 59, 74, 88, 104, 119, and 134). Earth observations were performed during 2 days on revolutions 74 and 134/135, but the areas were cloud covered.

The area of interest off the Australian coast was an eddy in the Tasman Sea near Sydney. Excluding early revolutions, there were only three possible passes (revolutions 108, 123, and 138) over the target; the Earth observation was attempted on revolution 123, but the area was obscured by clouds.

Off East Cape, New Zealand, the two possible revolutions for Earth observations were 17 and 32; one actual observation was made on revolution 17 when the site was cloud covered. The flightpaths of an additional seven or more revolutions passed over the target, at right angles to the flightpath of the P-3A *Orion* aircraft.

During the joint U.S.-U.S.S.R. operation, the Apollo spacecraft was at an altitude of approximately 183 km. After revolution 11, the altitude was increased, averaging approximately 220 km and varying between 165 and 237 km.

BACKGROUND

Since the Gemini flights, when the first ocean pictures were taken, there has been considerable interest in observing and photographing the world's oceans from space. During the early Apollo missions, emphasis was placed on obtaining photographs of ocean features, and some astronauts were briefed in oceanography before the Apollo 7 and 9 missions. However, few ground-truth investigations in support of orbital observations and photography were made before the Skylab 4 mission (refs. 6 and 7). The ASTP mission provided the second significant opportunity to perform visual observations of ocean features together with concurrent ground-truth investigations.

Ocean investigations on ASTP were planned through the efforts of Robert E. Stevenson, Office of Naval Research (ONR), Pasadena Branch Office, and Scientific Liaison Officer at the University of California, San Diego (La Jolla), California. The ocean observation project was directed by ONR in cooperation with the Smithsonian Institution; JSC; the Atlantic, Pacific, and Mediterranean units of the U.S. Navy; the RAF; the Royal Australian Navy; the New Zealand Defense Scientific Establishment; and the Royal New Zealand Air Force. Before and during ASTP, U.S. Navy Comdr. Robert F. Lawson (retired), also of the ONR Pasadena Office, coordinated all of the worldwide international military units gathering oceanographic data. An "Ocean Observations Desk" was set up at the JSC Mission Control Center during the critical days of the mission and was manned 24 hours a day by members of the Earth observations team.

As previously stated, four primary ocean targets were selected for observations and photography during the ASTP mission: the approaches to the English Channel and to the Strait of Gibraltar, the Tasman Sea, and the Kermadec Sea. There were several reasons for choosing these targets. First, they were on opposite sides of the world (antipodal) and large hydrodynamic features caused by the interaction of major ocean currents with landmasses could be examined. These areas had the following features in common: (1) a confluence of a major transoceanic cur-

rent and a continent, (2) islands influencing the flow of the current, (3) indigenous coastal currents, (4) a coastal ocean modified by dominating winds, and (5) large-scale turbulence resulting partly from the interference of the adjacent landmasses.

There were also the following major differences: (1) mid-latitude waters (Western Europe) compared to subtropical waters (Australia and New Zealand), (2) current flow toward the Equator (Europe) contrasted with flow toward the South Pole (Australia and New Zealand), (3) a small as opposed to a large inland sea (the Irish Sea and the English Channel in contrast with the Tasman Sea), and (4) a current modified by inflow from a major inland sea (Mediterranean) contrasted with a current modified by a large island complex (New Zealand). Furthermore, there is a seasonal difference between the European summer and the Australian winter, but this difference has no effect on the hydrodynamic similarities.

Astronaut observations of ocean areas were also planned for the Pacific Northwest, southern California, the western North Atlantic Ocean, the Caribbean and Mediterranean Seas, the northwest Indian Ocean, the Arabian Sea, the Arabian (Persian) Gulf, and targets of opportunity. In each case, the astronauts were asked to observe, describe, and photograph (1) ocean currents, (2) ocean fronts, (3) internal wave patterns, (4) eddies, and (5) combinations of features believed to exist in each area.

This particular study was focused on evaluating the visual observation capabilities of spacecraft crews during a short-duration, low-altitude orbital flight in contrast with the capabilities developed during the 84-day Skylab 4 mission, and on determining the applicability of the observations to the oceanography requirements of tactical fleet units. It should be strongly emphasized that the primary task of each astronaut was to describe the ocean scene in as much detail as possible, without making more than the most obvious evaluations and interpretations of observed features. In short, the crewman was to be an observer; he was not expected to be an oceanographer or a maritime meteorologist. The ASTP crewmen were given 16 hours of briefings in oceanography before the mission so that each crewmember would be able to recognize pertinent ocean features. Briefings included lectures on fundamentals of ocean current systems, ocean dynamics, air/sea interaction, and the visible sea-surface/marine-atmosphere manifestations of features of interest. (These discussions were conducted by George Maul, Atlantic Oceanographic Laboratory of the National Oceanic and Atmospheric Administration, and Robert E. Stevenson of the ONR.) Furthermore, the crew was involved in flyover exercises off the southern California coast, the Gulf of Mexico, and the eastern coast of the United States. The purpose of the flyovers was to give the crew practical experience in observing from the air features such as upwelling, bow waves, island wakes, internal waves, sediments (off river mouths, plumes, and indicators of water movement), wave refraction, gyres and eddies, scum lines, texture and water color, current boundaries (delineated by water color and/or texture), and sunglint. As a result of the briefings and flyovers, the ASTP crew had more oceanographic training than any other NASA flightcrew. However, only one of the astronauts, the Apollo commander (ACDR), had previous space experience. He had flown on the Gemini VI mission (25 hours 51 minutes), the Gemini IX mission (72 hours 21 minutes), and the Apollo 10 mission (192 hours 3 minutes), for a total of 290 hours 15 minutes, before the 9-day ASTP mission.

IMPORTANCE OF SPACE EXPERIENCE AND THE LEARNING CURVE

Introduction

The primary source of information used to determine the learning curve in making useful visual observations of ocean features was the transcript of astronaut comments made during the ASTP mission (ref. 2). The debriefing transcripts were less important because they did not accurately portray real-time learning. To gain a proper perspective of the learning progress, it seems worthwhile to summarize the astronauts' real-time comments, which can be found in reference 2. The following paragraphs summarize

longer comments made by the astronauts during the mission and omit short chats of no value. Specific and relevant comments are quoted; however, certain editorial liberties are used to make the commentaries more understandable.

Visual Observations

Revolution 17: During the first visual observation pass off East Cape, New Zealand, the land area was cloud covered, and there was little to observe in the water to the east, or between North and South Islands. The astronauts were uncertain about whether they were observing plankton, scum, or sea floor. The ACDR called the discolored water "plankton," although the command module pilot (CMP) thought it might be the bottom. However, a few seconds later, the CMP evidently had a different opinion and called it "scum," which could be plankton. Several photographs were taken of the area with the 70- and 35-mm cameras. Thus, NASA photograph AST-22-1777 (fig. 1) shows the coastline and a discoloration in the water. A second photograph, AST-1-037, shows similar features in the water, but the coastline is not visible. The structure of the discoloration is not typical of the sea floor, and it is therefore concluded that the features in the water are due to sediment or plankton. The onboard conversation suggests that possibly the two men were looking at different features at different times, and that the CMP had perhaps initially seen the sea floor and then had later seen the scum or plankton.

During this first visual observation pass, the crew quickly and accurately ascertained the problem inherent in using a color chart inside the spacecraft to determine water color. The color was decidedly different when viewed in shade and in sunlight.

Revolution 19: The ACDR indicated that it was possible to see much more detail at the current 177-km ASTP altitude than at the 225- to 300-km altitudes flown during Gemini missions. He also stated that everything appeared much closer and that everything moved much more quickly past him.

Revolution 39: The docking module pilot (DMP) gave a brief description of sediment plumes off the East African coast and even suggested that there were cold-water gyres spinning off currents.

Revolution 42: The DMP commented about large Bénard cells in the Atlantic Ocean and about the lack of eddies in the Mediterranean Sea: "It's a completely homogeneous surface down there."

Revolution 64: The CMP was looking for eddies in the Coral Sea and ended his Earth observations with the comment that he saw what appeared to be numerous eddies; he correlated cloud rings with eddies in this area and elsewhere in the southwestern Pacific Ocean (fig. 2).

Revolution 72: The DMP was unable to observe the Falkland Current, but he photographed the clouds because "the cloud patterns . . . may have been the current." Then, he added, "If that's typical of Gulf Stream operations, it could be the same down here."

As the spacecraft passed over the Libyan Desert, near Tripoli, the DMP observed: "Coming up on another very hazy area again. Ah, that's because we're right on the coastline." Then, ". . . there's some very light color along the coastline. I think that's probably due to shoals rather than any current flow . . . ." The DMP also mentioned an "unusual cloud pattern, that . . . probably defines a large current . . . ."

Revolution 73: The ACDR tried to locate a current boundary and noted that he could not see wakes around islands, or visible currents off the west coast of Africa.

As the spacecraft approached the observation target near the Spanish coast, the ACDR could see neither internal waves east of Gibraltar nor current boundaries to the west. But as the spacecraft got closer to Spain and the Sun angle changed so that the ocean was in the Sun's glitter, the ACDR recorded: "Oh, now I see these internal waves; there (they) are. All those waves and the boundary off the coastline . . . ." (fig. 3).

The plumes of the Rhône River, emptying into the Mediterranean, were noted but were not further described.

By revolution 74, the crew was seriously complaining about the spacecraft attitude for conducting Earth observations.

Revolution 78: The CMP commented: ". . . it

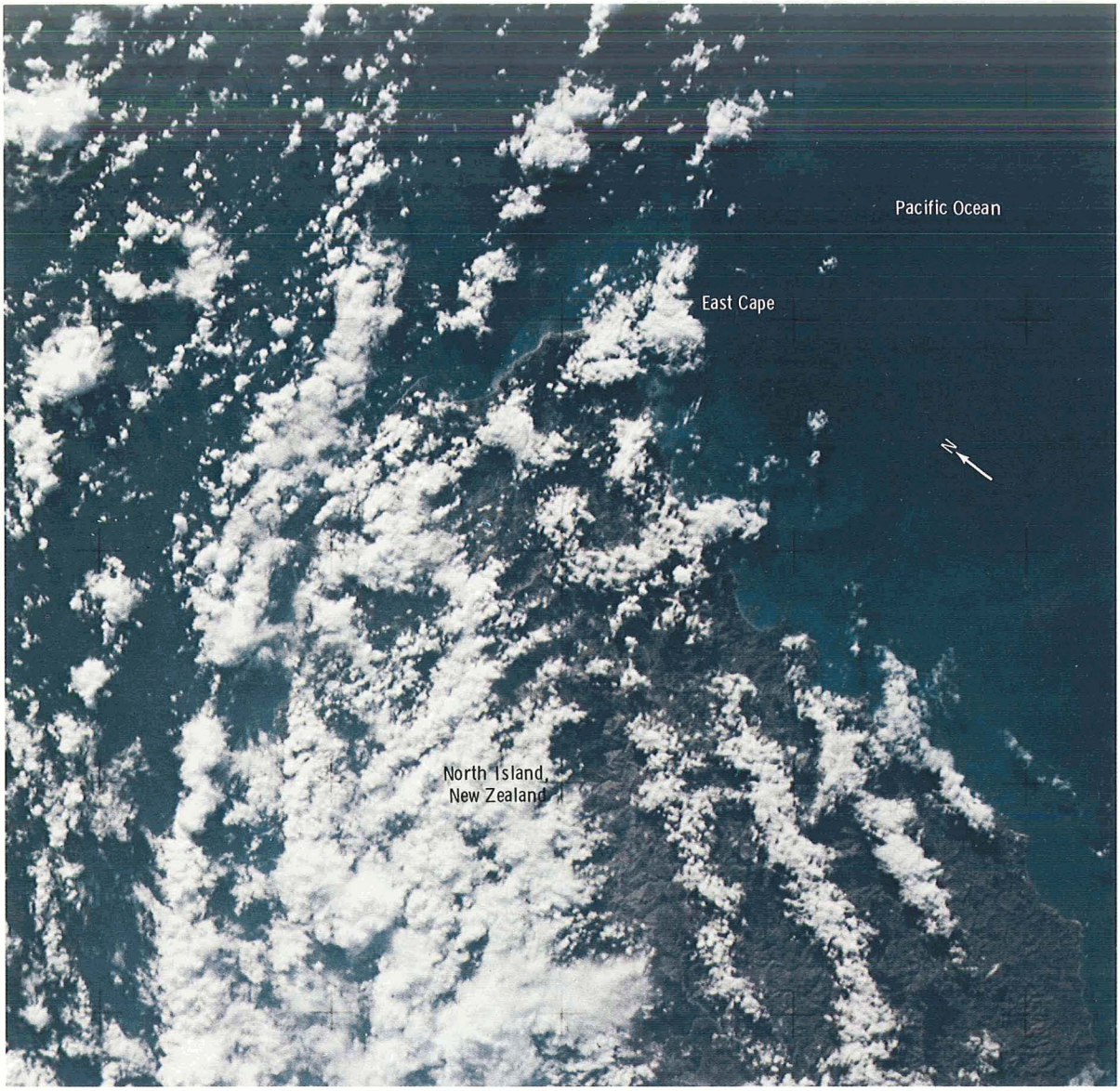


FIGURE 1.—East Cape, New Zealand. Discolored water, possibly caused by plankton or sediment (AST-22-1777).

looks like the Pacific is just full of eddies. Great big eddies . . . we think they are eddies because they are giant cloud-ringed areas that sort of make you think the water there is either hotter or colder than the rest . . . . They're all sizes." Later, the eddies were estimated to be 10 to 15 km in diameter, with some measuring tens of kilometers.

Revolution 79: Off Australia, the ACDR observed "some beautiful internal waves right off the coastline . . . . It's just like off Gibraltar. Certain Sun angles, you couldn't see . . ." (He could see nothing.)

Near the Marshall Islands, the DMP recorded: ". . . I'm passing a very distinctive cloud line laying off across the water which probably marks the



FIGURE 2.—Typical cloud-ring structure in the South Pacific Ocean, identified by the ASTP crew as an ocean eddy (AST-2-111).



FIGURE 3.—Oceanographic features off the Spanish coast. According to R. E. Stevenson, the features observable in this photograph are internal waves; the first sequence marks the boundary of the Huelva Front, and the roughened sea surface marks the straight current shear on the edge of the Tarif eddy. The shear, first seen by the ACDR (Maj. Gen. Thomas Stafford), is now known as the Stafford Shear (AST-27-2367).

edge of a current or an eddy, it's so distinct. However, it's not a convective cloud feature . . . ." The next day, they added to this observation as follows: ". . . there was a line of circles . . . running east-west. And it looked like a line of circles—like a chain . . . . And if you looked at one of those, and you could see them only because of the clouds, and it just made us wonder if maybe that was, perhaps, the boundary of a current . . . (they) must have been 100 to 200 miles long." Thus, cloud patterns were being used to draw major conclusions about ocean features. Unfortunately, the astronauts had little to say about ocean color or sea-surface texture on either side of the cloud lines. Later, when reminded of this, they agreed to look more closely.

Revolution 90/91: The DMP reported a series of small (12 km) eddies off Yucatán, "typical of the other eddies we see." He was unable to observe the Gulf Loop Current in the Gulf of Mexico; there was some cloud cover, "and it doesn't seem to be any particular pattern that would define a current."

Revolution 91: As they passed over the region between Norfolk, Virginia, and Cape Cod, Massachusetts, the DMP commented on muddy rivers, but he observed no gyres. The CMP and the DMP also observed "a cloud flow pattern coming over the tip of (an) island," and suggested, "cloud patterns may give a clue to the current." By revolution 91, after performing many Earth visual observations, the crew had concluded that Earth observation was at least a two-man job, and later they indicated that all three crewmembers were participating.

Revolution 104: The seaward limit of the muddy waters of the Orinoco River was determined on the basis of water-color changes.

Revolution 105/106: While over the New England coast during revolution 105/106, the DMP commented: "We're having trouble telling sunglint from red tide . . . . In addition to this highly important qualifying factor, the crew further decided that in the area where red tide was supposed to occur (i.e., near Boothbay Harbor, Maine), the water color was "obviously sediment . . . . And we're trying to differentiate if it's really a red tide or red sediment." They explained that some of the red coloration was obviously red river sediment because they could trace the same color clearly up the river. Both during the mission and during the debriefings, they refused to state categorically that they had seen red tide, stressing the influence of the reddish color in sunglint and the obviously sediment-laden waters of the river.

Revolution 112: The DMP commented on the enormous sediment plume of the Yangtze River and added: "And I think they showed pretty much how the current flows—rather, the coastal area or the area offshore." He also observed some outstanding internal waves in the Andaman Sea, off Thailand (fig. 4).

Revolution 123: For several days before the observations of ANZUS eddy, the Australian Navy reported that a large cumulus cloud was located directly over the eddy. Shortly before the Earth observation on revolution 123, a front moved through the area, and the ACDR reported that the area was "totally cloud covered." Approximately 320 km (175 n. mi.) east and south of the Hawaiian Islands, the crew observed "countless" eddies (as determined by rings of clouds), and the DMP observed the edge of a current and gyres. The crew also observed a small gyre or eddy with a cloud in the middle, along the edge of a current running east-west: "The cloud banners on both sides and clouds within it look a good deal like a Gulf Stream type of current."

Revolution 124: The CMP noted that, off the east coast of Australia, suspended sediments were always near shore, never extending to, or beyond, the Great Barrier Reef. A distinct island wake and a "boundary" near an island off Australia were noted conclusively by a change in water color. The CMP concluded, "that if I see sediments, I can't describe them too well." Following an earlier request to observe ocean texture where eddies were said to occur (i.e., eddies that were identified solely on the basis of linear or circular clouds), the CMP photographed an eddy in the Pacific Ocean in sunglint and tried to describe its texture as follows: "I see a slight textural change in (the) Sun, but it's so slight I can hardly describe it." He made a further observation that ". . . there were cumulus clouds emanating out of the side and sort of the interior of it . . . ."

By this time in the mission, the crew was ob-

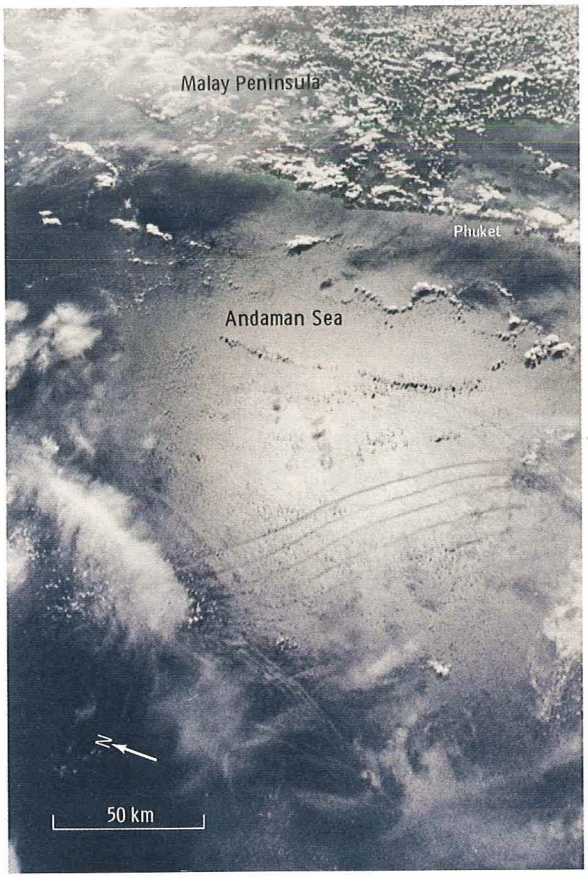


FIGURE 4.—Large internal waves in the Andaman Sea, off Thailand. Also note the linear, ribbonlike cloud patterns parallel to and near the shore. These are frequently considered to be boundaries of currents (AST-7-427).

viously on the "look out" for features observable in sunglint: "Got a picture of an island . . . (with) a lot of sunglint around it . . . you may be able to see some current patterns . . . ." In addition, they were equally observant of the good relationship between linear and circular cloud patterns, and current boundaries. Thus, the CMP said: "Typical, rather linear cloud patterns in the mid-Pacific oriented east-west. I see this quite a bit. Makes you think it might be associated with the water current . . . . These cloud patterns go sometimes for hundreds of miles."

Revolution 134/135: As they crossed the coast of Central America and moved over the Atlantic Ocean, the ACDR observed "a boundary layer," and photographed "internal waves and could even be some big upwellings." Onboard, the CMP inquired about the upwelling, and also agreed that "there is a thing that looks like an upwelling," approximately 30 km (15 n. mi.) offshore.

Later in the same revolution, the ACDR reported: "I just couldn't see a Gulf Stream boundary . . . or the Caribbean Current . . . . There's no differentiation in colors." A few moments later, he said, ". . . boundary right in the Atlantic Ocean . . . we have a boundary of (a) current from light blue to dark . . . ." This observation was made near Bermuda.

All three crewmembers observed the "tremendous sediment plumes" of the Danube Delta. The DMP remarked that the Danube water appeared to be "running right across the Black Sea."

Revolution 135/136: The crew was prepared for observing the Gulf Loop Current and/or internal waves. During revolution 135/136, the ACDR first noticed an eddy in the Gulf of Mexico; then, the DMP said that he thought he saw the Gulf Loop Current, but quickly added that there was a "total change in cloud pattern . . . ." The area off Monterrey, Mexico, was cloud covered, "but there's then a line of clouds that come right up around—almost follows the contour of the coast. I would guess it might very well be the Gulf Loop Current we're looking at. The problem is I can't see it off to the north." The ACDR commented again on the eddy, and he and the DMP then observed the eddies, but did not describe them further. They could see boat wakes off the Mississippi Delta, and they noted the water-color change in the delta area.

Farther up the east coast, suspended sediments, plumes, gyres, and pollution were briefly mentioned during flight over the Potomac River, Chesapeake Bay, and New York Harbor. The crew again attempted to identify red tide in the Boothbay Harbor region, but the DMP had to admit (after several passes) that he was uncertain about seeing red tide such as he had observed off the west coast during a flyover exercise. He also said that he had not seen any oil slicks, "And I think we probably wouldn't, generally, without having some sunglint." A little later, when over the Atlantic Ocean, the DMP added: "You know, (with) the combination of the cloud cover and the

Sun angle, we could have oil all over and we'd never know the difference."

Discussion

From these brief statements made by the crew, it is evident that extreme caution must be exercised in arriving at conclusions about the learning curve, the importance of previous space-flight (but nonobservational) experience, and other related factors. One reason for caution can be shown by the number of words spoken. The complete transcript of visual observation comments amounts to approximately 24 000 words, including technical discussions, air-to-ground transmissions, and so forth. Approximately 7500 words, totaling approximately 50 minutes of conversation, actually deal with visual observations of ocean features. This total averages approximately 17 minutes per crewman, which is quite insignificant. Another reason for caution is that three of the four targets established specifically for simultaneous ground-truth investigations and visual observations were obscured by clouds. This left only one brief visual observation supported with ground-truth data, i.e., the Spanish Bight/Strait of Gibraltar.

After the mission, Stevenson studied the ground-truth data and the visual observations and photographs of the Strait of Gibraltar. He indicated that the Atlantic Ocean west of the strait showed the following oceanographic features: (1) the Portuguese upwelling zone, (2) the Huelva Front, (3) warm surface water over the Spanish shelf, (4) a flow of warm water into the Mediterranean Sea, (5) upwelling off southern Spain with an associated sequence of warm-core eddies, (6) upwelling and turbulent eddies off the Atlantic coast of Morocco, and (7) an irregularly shaped area of warm water seemingly trapped west of Gibraltar.

In the Strait of Gibraltar area, the ACDR observed internal waves and a boundary off the coast of Spain (fig. 3). These features were visible only in the Sun's glitter; therefore, his field of view was significantly restricted. Because of the low altitude and the high groundspeed, the ACDR had only approximately 10 seconds to view the scene in sunglint; nevertheless, he did verify the presence of some of the ocean features that Stevenson (ref. 1) had described in considerable detail. It is important to note that the ASTP crew saw some of the features off Spain they had been trained to look for, and to recognize, during premission briefings and flyover exercises.

As discussed later, there were a number of constraints on good visual observations, but it should be emphasized that sunglint was the most important factor in observing the features off Spain. Although not all ocean features require Sun glitter in order to be visible, the ACDR's experience in observing the ocean features off the Strait of Gibraltar focuses attention on the necessity for pre-space-flight training that includes discussion of sunglint.

An effort was made to determine the learning curves of the ASTP crewmen by studying the changes in the observational capabilities of each crewmember as the mission progressed and by comparing the ACDR's learning curve with the curves for the other crewmembers to determine the importance of previous space experience. To do this, all Earth observation comments made by each crewmember were extracted. These extracts were examined first in a cursory manner for general impressions, then in detail for indications of improved learning. The extracts were also compared in detail for evidence of greater or less ability and/or improved Earth observation proficiency among the entire crew. Special attention was given to comparing the ACDR's learning curve with those of the other two crewmembers. Obvious inherent difficulties in making these comparisons include the following facts: (1) statistically, the data (for three men, during only 9 days) are meager, (2) evaluation may assume that the three men are identical in every respect—an illogical assumption, and (3) the brevity of Earth observation comments may make meaningful conclusions impossible.

During debriefings, the astronauts were asked if they felt more confident as the mission progressed. The CMP responded: "There's a learning curve." The DMP added that during the early part of the mission, the astronauts were "about four times busier than we really expected to be. We felt like we didn't really have time to prepare properly . . . ." With more experience,

and with all three men engaged in Earth observations, the DMP thought they obtained reasonably good results.

A combination of factors contributed to the learning curve. These included (1) an increase in crew involvement and cooperation, (2) a change in spacecraft attitude for easier viewing, (3) an improvement in the crew's ability to select the best camera/lens combination, (4) the use of sunglint to observe ocean features, and (5) an improvement in verbal descriptions as the crew learned to recognize features. The visual observation experience led the crew to make specific recommendations for a manned Earth observation ball, or turretlike module, equipped with sighting devices, quick reference navigational aids, and other items, for future space flights that include Earth observations.

Although quantitative evidence is lacking about the learning curve of the ASTP crew with respect to Earth observations, several possible scenarios may illustrate and encompass what is known.

First scenario: An untrained observer asked to look for ocean features off Spain might or might not have visually followed the entire sweep, from when the ocean waters off Spain first became visible in the distance until the ocean features became clear in a vertical view in the Sun's glitter. An untrained observer might have prematurely concluded that nothing was visible in the area because the water appeared uniformly blue in color. Thus, his attention might have wandered, or he might have been distracted for a few seconds, or he might have moved from the observation window. A few seconds would suffice since the scene in the Sun's glitter would last only a few seconds. Clearly, an untrained observer would not have understood air/sea interactions, and probably would not have known the significance of subtle changes in water color and texture. Similarly, the ACDR admitted that, before the ASTP ocean briefings, he was totally unaware of the meaning of the many ocean features that he had seen during previous space flights.

Second scenario: Assume an ASTP crew with more than 16 hours of premission oceanographic briefings and flyovers in which various ocean features were shown and explained. These training exercises demonstrated to the crew the importance of Sun glitter in accentuating certain features. Consequently, the trained observer did not let his eyes wander when a target was coming into view; therefore, when the ocean scene changed in sunglint, he was ready to verify whether the predicted ocean features were indeed present. Throughout ASTP, there were many such targets that tested the ability of the crewmen to recognize chance ocean features and air/sea interactions.

Third scenario: The ACDR had the same amount of Earth observations' training as the other two crewmembers, but he also had considerable space-flight experience. During Earth observations briefings, the ACDR indicated that during other space flights he had seen many of the features that were of interest to oceanographers, but he was unaware of their origin or importance. Thus, before the briefings, the ACDR was almost like the untrained observer depicted in the first scenario. Possibly, the ACDR was the first to recognize and learn about ocean features observed from space during the briefings, although there is no way of proving this advantage. However, it is evident that all members of the ASTP crew learned to recognize ocean features from briefings and flyovers.

Thus, there is no conclusive proof that nonobservational space experience is particularly beneficial. Certainly, the ACDR was the first crewmember to complain seriously about the spacecraft attitude for visual observation. Yet, the DMP, with no space experience, provided some of the longest descriptions of cloud systems. This could mean that the DMP had more experience in meteorology, or simply that he was more verbose.

It is impossible to judge quantitatively the oceanographic and observational abilities of each crewmember, because of the paucity of conversational ocean-feature discussions. Based on the transcripts, it appears that the most important factors are the quantity and quality of the briefings on ocean phenomena and of the flyover exercises. Throughout the 9-day ASTP mission, the astronauts' comments were similar and reflect similar learning from briefings and flyover exercises. For example, each crewmember showed heavy reliance on using circular and linear cloud patterns

to identify eddies and current boundaries; yet, they are not known to have seen differences in water color or texture on either side of the clouds to make a perfect cloud/ocean boundary correlation. They had to be asked during the mission to verify changes in water color and texture on either side of the clouds because of their total reliance on clouds to delineate water systems. In other words, during briefings, they had been trained to recognize linear clouds encompassing current boundaries and the circular cloud systems of eddies.

According to Stevenson et al., the Skylab 4 crew began to improve noticeably in Earth observation descriptions after approximately 2 weeks in space (ref. 6). Because of the higher altitude of the Skylab spacecraft, the acquisition/observation time at each target was approximately 40 to 45 seconds, compared with 5 to 20 seconds for ASTP. Longer visual observation times greatly enhanced the crewmen's ability to observe and learn. Another obvious factor was the much longer time spent in space by the Skylab 4 crew—84 days, compared to 9 days for ASTP. These two factors unquestionably had an important role in differences of learning curves for the two missions. The ASTP crew had an extremely short acquisition/observation time, which resulted in brief verbal descriptions; complete crew attention was focused on making the observation and/or photographing the target, and on the need to do this quickly. The short observation times, with one target quickly following another, left the crew little time to view, to study, and to reflect upon—or even to record—their observations or impressions. On the other hand, the Skylab 4 crew had much more time to prepare themselves mentally before and after target acquisition and observation. The importance of time cannot be overemphasized; it represents a major difference between a low-altitude, short-duration mission and one of long duration and high altitude. The evidence is conclusive: the ASTP crewmen were always pressed for time with no time to digest, describe, photograph, or evaluate what was seen.

Conclusions

Responses to the four questions posed in the introduction to this paper are presented in the following paragraphs.

On the basis of the experimental results, it does not appear that previous nonobservational spaceflight experience is as significant as premission briefings and flyovers. The assumption that the ACDR may have learned more rapidly during briefings cannot be proved. The three astronauts appear to have similar Earth observation capabilities, a strong indication that the 16 hours of briefings and the flyover experience were dominant factors in the learning process for performing useful visual observations.

Although it is difficult to depict quantitatively the configuration of the learning curve for useful visual observations of the oceans by the ASTP crewmen, it is suggested that it may resemble figure 5. Increasing experience and learning are shown by progressively heavier shading. Thus, "no prior space experience" is shown as blank. As learning increases and as more experience is

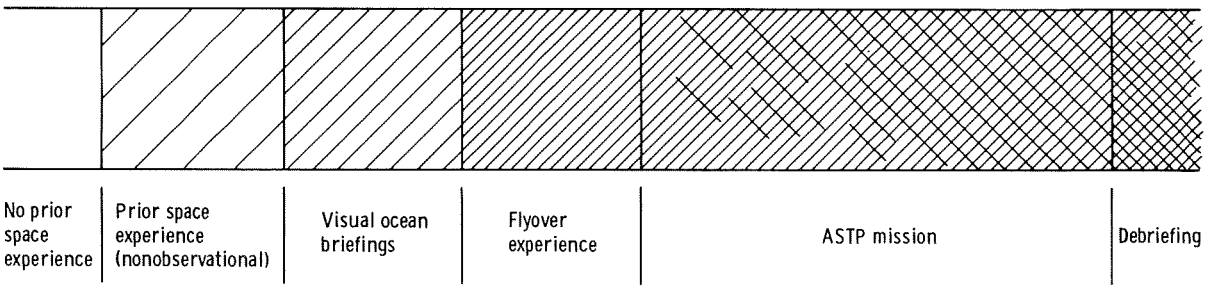


FIGURE 5.—Graph indicating increase in proficiency of ASTP crewmen for making visual observations of ocean features. The density of shading is directly proportional to the increase in proficiency, or "learning."

gained, including the actual space flight and, to some extent, during debriefings, the depth of experience and learning increases (shown by progressively heavier shading).

Space-flight experience exposes the inquiring mind to diverse and spectacular oceanic and atmospheric features. After a space flight, an astronaut might read or be told something about one or more of the features that he had observed and photographed. However, it is unlikely that most astronauts would have pursued the subject in depth. Hence, an untrained observer in space may be compared to a traveler who drives through spectacular scenery and appreciates the view, but does not delve too deeply into the natural history of the area such as the geology or the flora and fauna.

However, premission briefings, if well prepared and presented, can give the astronaut a broad background in oceanography and an understanding of the specific features or phenomena that are clearly discernible from space. Using the analogy of a traveler, briefings might incorporate a park ranger who provides lectures on sights observable from a highway or trails. He might describe the general geology and the principal animals, birds, and trees. This would give the traveler a much better insight into the scenery, but he would have no practical experience in testing and expanding this newly acquired knowledge.

For the astronauts, additional practical experience would be gained during high-altitude ocean flyovers. The traveler, experiencing the same type of learning, would engage in a field trip, carrying a geologic map and a small guidebook to identify common animals and plants. During the flyovers, the astronaut would see many ocean features to be observed later from space. Because he is in control of the aircraft, he can alter its course to make repeated observations of a specific feature, such as those that can only be seen in sunglint. Thus, he is able to observe and learn in a familiar, nonhostile environment. (The latter factor may have been of significant advantage to the ACDR with his 290 hours of space experience, because he would, perhaps, be more comfortable than the other two crewmen without space experience.) The traveler would be able to recognize major geologic features of scenery and to identify the larger animals, birds, and trees. Neither the astronaut nor the traveler would be considered a competent oceanographer or naturalist, but both would be able to carry out more profound observations in unexplored areas and to make important scientific contributions. Whatever was seen, reported, or described would be greatly influenced by information obtained during briefings (lectures) and flyover (field) experiences.

During space flight, additional learning occurs, primarily by (1) the experience gained by the application of newly acquired information in recognizing and describing features, (2) discussions among the crew, each sharing total knowledge and experience, by brainstorming, and (3) ground-to-air transmissions providing new or updated information, new targets and descriptions, and other data. All of these factors would contribute to a cumulative learning process.

It is known that after approximately 2 weeks in space, Skylab 4 astronauts showed a marked improvement in Earth observations. Apparently, 9 days in space, in a low-altitude mission, was not sufficient to demonstrate such a marked improvement.

FACTORS AFFECTING VISUAL OBSERVATIONS

The following items were identified as major factors in the location, identification, and photography of ocean features during ASTP.

Sunglint

Sunglint, or the reflection of sunlight off a water surface, was considered the most important factor in the identification of certain ocean features, particularly those not associated with distinctive cloud patterns. For example, during the ASTP debriefing, the ACDR talked about the importance of sunglint in observing ocean features during the California flyovers: ". . . you'd go one way and could see some of the (internal) waves and some gyres. If you turned around and (flew) down the other way with a different Sun angle, there would be nothing but

blue. I was looking for all these things and suddenly they popped out within a second, right there. Just suddenly when the Sun angle changed, everything was there; the waves and the boundary were all there . . . . But before that, there was nothing but just solid blue water—they just suddenly popped." Furthermore, during the ASTP mission, many ocean features were not visible in sunglint for more than approximately 5 to 10 seconds; therefore, it was mandatory to be prepared. The Sun glitter appears in the field of view "instantaneously" and disappears just as quickly. As soon as the Sun angle changes, the glitter pattern is lost.

On revolution 73, the ACDR was looking for the Huelva Front and for internal waves west of the Strait of Gibraltar. He dictated into the tape recorder as follows: "See no current boundaries west of Gibraltar, there." Visibility was good, and he could see the wakes of more than 15 ships in the Atlantic Ocean west of Gibraltar. Interestingly, the crewmen later said that they were able to see ship wakes with or without sunglint. Then, as they approached the target, the ACDR said: "Oh, now I see those internal waves; there (they) are! Right there! All those waves and the boundary off the coastline. The Sun angle changed. There they are, all of them. I couldn't see them before due to the Sun angle. Just got them, a whole series of them." Later, he recorded: "I could really see those internal waves from Gibraltar . . . right at the very last (minute) when the Sun angle changed. That's fantastic out there. You couldn't see them at all from a different Sun angle, though." Again, off the southern coast of Cuba, the ACDR commented: "Look at those big (internal waves) just suddenly pop up . . . ."

It was fortuitous that the target off the Spanish coast was observed in Sun glitter, because if it had not been highlighted in the glitter, it assuredly would not have been observed in the detail described. Instead, the target would probably have had the appearance of nothing more than blue water, with perhaps some indefinable features in the water. It follows that if the Earth observations for the Spanish site were scheduled on other spacecraft revolutions when the spacecraft passed near the site, the Sun angle might not have been optimum for visual observation of the site. This possibility emphasizes the need for careful planning of Earth observations.

Sun glitter may make it difficult to assess colors accurately. For example, while the ASTP crew was attempting to locate and observe red tide near Cape Cod, the DMP reported in an air-to-ground transmission: "We're having trouble telling sunglint from red tide . . . in this area." As a matter of fact, they could not accurately differentiate between red tide and muddy water, although they made an excellent evaluation about the source of the muddy water. The DMP also made the following comment about oil slick observations: "(with) . . . the combination of cloud cover and the Sun angle, we could have oil all over and we'd never know the difference." In addition, during crew debriefing, the crew mentioned problems in defining the seawardmost limit of muddy water from the Orinoco River, "because, in the sunglint, it does have a tendency to look a little tan or something."

Because sunglint is a rather local phenomenon, it cannot always be used to differentiate ocean features. The CMP commented: "In mid-ocean, you can plan on getting most of your data from clouds, and only once in a while getting it from sunglint—when you are especially lucky."

Water Color

Before the mission, a two-sided color wheel composed of carefully selected Munsell color chips was prepared to help the crewmen calibrate desert and ocean colors. According to the ASTP crew, it was difficult to determine ocean color with the color chart. When chart comparisons were made at the window, "the color chart had to be completely in the shade, with the same very bright (scene) out the window being contrasted. Your eye adapted to the bright thing and all the color chart colors tended to look very dark, and much the same because they were in the shadow. If you happen to have the Sun shining in the window, so that it's shining on the color chart just right, then you're in luck." On another occasion, the DMP commented: ". . . I don't have much luck with the color wheel because the wheel's in

the shade, and what I'm looking at is in the Sun, and I get absolutely no correlation at all . . . ." Later, the CMP said: "The standard problem we have been having with the color chart is that you have to have it somehow in light so you can compare it with what's on the ground. It's very dark in the cabin compared to outside."

As indicated in the previous discussion about Sun glitter, it was difficult to differentiate red tide, muddy water, and sunglint because of the brownish color of the water in the glitter pattern. But without distinct water-color changes, major current boundaries could not even be located. The ACDR reported: "I just couldn't see a Gulf Stream boundary down there . . . . There's no differentiation in colors."

Water color was also highly effective in determining distances of freshwater outflows from major rivers, such as the Orinoco. However, there was sometimes confusion as to whether a change in water color could be attributed to the ocean bottom, to current boundaries, or to plankton (red tide); such was the case off New Zealand.

Clouds

In some cases, clouds could be used to identify certain ocean features, but they also obscured the ocean surface. In the debriefing, the ACDR said: "As far as the eddies and gyres (are concerned), the big thing that outlined those to me—and I think to everybody else—were those little clouds right around the edges of them. You can really see that. And a current boundary too. The clouds define it often." In the mid-Pacific, the DMP recorded: ". . . I'm passing a very distinctive cloud line laying off across the water which probably marks the edge of a current or an eddy, it's so distinct. However, it's not a convective cloud feature . . . ."

Clouds are a serious problem in target acquisition and identification, particularly if there are only a few seconds available to locate, observe, and photograph a target. Thus, during the debriefing, the DMP said: "We were flying over cloud cover, and we didn't know where we were—as usual." Even if there are breaks in the clouds, say five-tenths cloud cover, the observer cannot see much of the Earth's surface, although it may be possible to identify some features and to make some limited definition or observation. Cloud shadows may also pose problems in target identification and in making rapid, accurate visual observations.

Some areas are cloud covered most of the year; therefore, visual observation and/or photography in these areas cannot be accurately scheduled. Other areas, such as hot desert regions (i.e., the Red Sea, Baja California, parts of Australia and South America, the Middle East, and north Africa) are usually cloud-free most of the year. For areas that are cloud covered most of the time, many opportunities for visual observation, photography, or both must be scheduled. Conversely, in cloud-free areas, few visual observation/photography opportunities need be assigned during mission scheduling. During short, low-altitude missions, this distinction is particularly important because (1) some sites may be cloud covered during all or most of the mission and (2) the crew has only a brief period for target acquisition, observation, and photography. Widely spaced targets, involving a "mix" of cloud-free and cloud-covered areas, would ensure optional opportunities—and time—for making visual observations.

Spacecraft Altitude

A low spacecraft altitude is excellent for visual observation, but this advantage must be balanced against extremely fast motion over the Earth's surface. Because of the high relative velocity, it is difficult to do several things simultaneously; e.g., visual observation and photography. During the ASTP mission, when a target came into view, only 5 to 20 seconds were available to point the camera and photograph the target. This time was insufficient for simultaneous visual observation and photography. If visual observations were desired, there was no time for making a photograph; conversely, if a good photograph was obtained, the observer did not see the scene clearly and therefore could not describe it.

At the ASTP altitude (approximately 220 km), it was possible to see clearly (". . . just like you can from 40 000 ft . . .") such phenomena as the

flaring of natural gas, grass fires, contrails, icebergs, snowcapped mountains protruding above clouds, ship wakes, large ocean swells, the stripe on Lake Bonneville salt flat, and hangars at an airport. The crew unanimously agreed that the human eye was adequate for visual observations at lower altitudes, and several observations proved that the eye could resolve small targets. However, the low altitude made it difficult to differentiate (and photograph) larger features, such as tropical storms. Thus, the crew was over a tropical storm and reported: "It doesn't look any different from a whole bunch of clouds . . . ." In other cases, it was necessary to take panoramic (multiple) photographs because the entire scene could not be depicted in one photograph.

The crew also found that at the ASTP altitude, the spotting scope (20×) "was of minimal value" because of the high spacecraft velocity. The same was true of high-power binoculars; 10× binoculars would have been quite adequate for the lower altitude and the high groundspeed. In addition, the crew often lamented that they did not know where they were because they were going too fast.

Because of the low altitude, the high speed, and the spacecraft attitude, with the extremely limited view from a window, the crew often commented that at least two men were required for visual observations.

Spacecraft Attitude

Although there were few complaints about the spacecraft attitude with respect to observing ocean features (perhaps because the sites could be readily located by reference to major landfalls), it was a serious problem when relatively small features had to be located on land. In the normal visual observation attitude, spacecraft window 3 (the hatch window) was oriented parallel to the Earth's surface at the subvehicle point, and the astronauts were seated upside down. A typical conversation regarding this attitude was: "Vance, you know we're upside down? If you're upside down, the Nazca Plain should be on the right. It says to shoot it upside down. No, I'd rather have it right side up so the spacecraft is . . . there's clouds . . . we're approaching the north coast of South America, Peruvian desert, trying to find the Nazca Plain . . . . This attitude is bad . . . . It's really bad when you try to keep your head back like that and look right and left. I'm going to change (it) . . . around . . . . There's no room to twist your head and look upside down" (for visual observation). After reorienting the spacecraft attitude for improving visual observation, the DMP commented: ". . . we're already past (the) site . . . . I guess headed southward to the right—or to the left. I'm confused about this attitude. The south should be the right. North should be to the left. It's got to be; we're traveling east." The CMP said: "We're heading east. We're upside down," and the DMP responded, "seems like it to me, it's got to be that way . . . ." The problem was particularly bad when the visual observation was made while leaving (retrograding) a target, because the view was different from that in the Earth Observations Book. It was much easier to get a lead into a target.

It was also difficult to locate a target when the spacecraft was oriented for near-vertical observation, largely because of the limited window field of view and the rapid groundspeed. After some experimentation, the crew found an attitude that permitted them to see farther ahead as well as to obtain vertical or near-vertical views. However, when they were looking for a specific target in a lead-in, upside down attitude, they found it "extremely difficult to think." For the lead-in to a target, they recommended right side up, pitched down. This attitude was especially important for target identification. "If you're upside down, all these years of training and living down here (on Earth) are certainly thrown out the window . . . . You have to think everything out. There is a 50:50 chance of being right, but we're usually wrong." Finally, only 5 to 20 seconds are available to do everything.

Another problem was target location when the spacecraft was oriented for optimal, near-vertical observation. Because of the limited field of view from the spacecraft window and the rapid groundspeed, it was exceedingly difficult to know the location of the target.

Spacecraft attitude and scheduling also had a role in attempts to observe bioluminescence. For example, the DMP was prepared to look for

bioluminescence on the Red Sea and reported: "But, unfortunately, what wasn't factored in here is that we're still in sunglint and I got the sunshine nice and bright right in the window." To conduct experiments on bioluminescence, a long dark-adaptation time is needed, and factors such as clouds and moonlight must be considered.

Spacecraft attitude was important in photography, and in some instances, visual observation was possible, but not photography. Thus, while attempting to perform visual observation in the Boston to New Brunswick ocean area, the DMP said the attitude "was okay for looking, I could see fairly well, but I couldn't get photography because it was a very oblique angle down through the window."

The effect of attitude with respect to Sun position on using the color wheel was described previously. A description of the effect of attitude on the long-focal-length lens follows.

Photography

The major complaints about cameras, lenses, and accessories were (1) the inability to see through long-focal-length (250- and 300-mm) lenses because of light loss; (2) the inability to see through an orange filter (however, during the debriefing it was determined that the problem was not the filter, but that the lens was out of focus); (3) the difficulty in using long-focal-length lenses to photograph small targets (some lenses were so long that the crew just pointed and shot); (4) the inadequacy of the 70-mm film budget (i.e., the crew had to use the 35-mm camera with indoor film when the supply of 70-mm film was exhausted); and (5) the impossibility of photographing a scene viewed from the spacecraft window at an oblique angle because the camera/lens could not be oriented properly.

Aside from obvious technical difficulties, the most important lessons concerning Earth observation are (1) that the film budget should be increased and (2) that more careful thought should be given to optimal lens sizes, because a long-focal-length lens places the observer far from the window, light loss through the lens is great, and at high groundspeeds it is difficult to pinpoint targets and photograph them. Moreover, the DMP said: "A lot of things that you can see with your eyeballs, you just can't see through that reflex (camera)." Although there was a considerable advantage in using the reflex camera because of the capability to frame a picture as the observer sees it, the high groundspeed (allowing, perhaps, 5 seconds to locate, frame, and photograph a picture) greatly affected other benefits adversely.

Window Fogging

The ASTP crew frequently complained about window fogging and the continual need to wipe the windows. Apparently, the fogging was caused by differences in cabin temperature. Thus, window 5 evidently did not fog up, but window 1 did. Earth observation and photography was hampered by this problem.

Dual Tasks

Crewmen complained about having to perform too many tasks in rapid succession. On one occasion, a microbial experiment was quickly followed by an Earth observation using television camera coverage and visual observation/photography: ". . . everybody in there was trying to do different things; it just wasn't very effective Earth obs, plus some cloud cover . . . ."

The crewmen seemed to agree that the best option was to obtain a photograph and then, if time permitted, to describe the target in as much detail as possible. During the debriefing, the DMP said that, most of the time, there was so much to do that "when you got through the pass, you were in the middle of something else. And you even have . . . to backtrack to pick that up. Early in the mission, things were happening too fast. We got very little good data out of it." The CMP concurred, adding: "I'd think, well, I'll have time right after this task to get it quickly on tape. And then, I didn't. The next site would come up and you would get five or six sites stacked up, and then it was all over. And then you would say that I'll debrief the whole thing. By that time, you have forgotten some pertinent parts, and then there wasn't time . . . to debrief the whole thing."

The crewmen reported that they needed repeated passes of a site and more time "because if you have one pass, there's a good chance that something will be bad. But if you have three or four passes, you've got a very good chance of getting a lot of data on it . . . and you shouldn't be very oblique . . . unless it's a major feature."

Because of the many joint operations tasks, it was mentally difficult to prepare adequately for a visual observation. This was especially true during the early part of the mission. Later on, when all three crewmembers worked together, conditions improved: "Once we got through the joint activity period, where we could all three work the problem together, help the guy that had the primary task by looking out the window, and we changed our attitude, I think we got reasonably good results from then on . . . prior to that, it was not very good." It seems reasonable, therefore, to conclude that during a low-altitude mission, involving many diverse tasks, there is simply insufficient time to do highly competent Earth observations.

Description as Opposed to Photography

The crewmen stated that they were able to see more than they could photograph, but that it was inherently difficult to scientifically describe many targets. Before the mission, the crewmen were briefed on the features designated for Earth observation. However, even when the feature was located, the crewmen had difficulty in providing detailed oral descriptions; consequently, they tended to rely on photography. In addition, attempts to sketch features in the Earth Observations Book were hampered by the difficulty of writing or drawing on glossy paper without a proper pen. A typical problem was explained by the CMP, who observed currents, gyres, and pollution in Puget Sound that were difficult to describe verbally. "Puget Sound is not a square tank, it's . . . rather complex . . . and I wanted to draw a picture of what I saw. So I took a pen . . . and I couldn't draw on the pictures; it was too dark anyway . . . . I feel that I lost some data there . . . after it was all over I cussed myself because I even tried to describe it. I should just have tried to take a picture."

During the debriefing, the crew commented that if "we got you good pictures (of a scene), we really didn't see it . . . . And comments may come easily one time and hard the next. For example, you may see something that you can describe very well. You may say, 'I see a circular cloud structure, and I see that it's 20 km across . . . the time I see it is such-and-such.' And you can describe the color maybe. The next time you come up on Sun glitter, you'll see a pattern, you'll see a gyre perhaps in there. And there's no way you can describe that, and you wish you had taken a picture, or you'll wish that you had a pad that you could draw on to fill in. For instance, if you had an outline of Puget (Sound) showing Seattle and two or three prominent landmarks and a pencil in your hand, you could draw in what you see. You need something like that." Thus, outline maps are needed for Earth observation.

GENERAL CONCLUSIONS AND RECOMMENDATIONS

A careful study of the ASTP transcripts and photographs leads to several general conclusions and impressions.

The primary purpose of the ocean observations was to determine whether nonoceanographers could be trained to recognize specific ocean features from space. The record shows that the 16 hours of training (briefings and flyovers) were instrumental in helping the crew recognize features, both as scheduled targets and, elsewhere, as targets of opportunity. The crewmen demonstrated an excellent response and application to their training. Any differences that experts may have in the interpretation of some features must be attributed to the difficulty in teaching complex subjects (oceanography and meteorology) in a few hours. Most oceanographic subjects could be treated only in a superficial manner. Therefore, during training, efforts were made to concentrate on a few ocean features and on air/sea interactions. From the transcript, it is evident what types of phenomena were emphasized in briefings, because all three crewmembers reported similar ocean features with apparently equal proficiency.

Furthermore, their observations went beyond the training. There are several examples. When the crewmen were asked to look for tsunamis (tidal waves) following strong earthquakes in the South Pacific, they quickly responded that it was unlikely they could see such waves from their altitude. The crewmen also made an excellent qualitative evaluation with regard to the source of red water near Boothbay Harbor, Maine; i.e., the origin of the discoloration was sediment carried in a river, rather than red tide. In another instance, the crew reported that water in sunglint had a brownish tint, and it was therefore difficult to distinguish true water color (such as might be caused by a red tide or sediment). This difficulty had been suspected but was not verified until the ASTP crew mentioned it in an unscheduled Earth observation.

Although three of the four targets were obscured by clouds on the day assigned for their visual observation, the observations off the Spanish coast, and many other visual observations embodying a wide range of ocean features (targets of opportunity), demonstrated that astronauts could be trained to recognize important ocean features and phenomena. However, insufficient information is available from this single mission to draw definite conclusions about such factors as the importance of previous space-flight (nonobservational) experience. Available information strongly suggests that nonobservational space experience is not as important as good premission briefings and flyover training.

Solutions to most of the problems affecting visual observations either are of a technical nature that can be solved without further comment or are so self-evident that they require no discussion here. During the debriefing, the ASTP crewmen made several general recommendations for improving visual observations, basically involving improvements in position location, tracking, and sighting devices. They indicated that Col. William R. Pogue was working on this general topic. Pogue, a Skylab 4 astronaut, reviewed the role of the trained observer in visual observations and made a number of useful recommendations for improving visual observations.[1] Stevenson et al. (ref. 7) made some valuable recommendations on visual ocean observations, covering many topics (e.g., sensors, sensor system control, onboard analysis, sensor payload control, and training). No attempt is made to review these important contributions. However, it seems worthwhile to make several recommendations on the basis of ASTP experience.

Flyover exercises should be scheduled for both temperate and tropical waters. The former would include, for example, the waters off southern California and the Baja California coast, and the waters near offshore islands. This area has a wide variety of temperate water and air/sea interactions, and the Baja California area is generally cloud-free. Within the tropical area (e.g., off the Florida coast, the Caribbean islands, and perhaps as far east as Bermuda) are marked changes in water color caused by a wide variety of conditions such as current boundaries, occasional red tides, complex eddies, gyres, and shallow sea floor. Air/sea interactions include tropical storms and many types of interesting cloud systems. An important addition would be the highly desirable inclusion of an oceanographer in the flyover crew, to act as an instructor and observer.

The ASTP crew proved the importance of Sun glitter in recognizing and accentuating features that would be undetected otherwise. Hundreds of photographs (taken since Gemini) have demonstrated the importance of making observations in the sunglint for some, but not all, ocean phenomena. As previously noted, it was fortunate that the Strait of Gibraltar was observed in Sun glitter; otherwise, the detailed features would have been missed by the observer. From a practical point of view, some consideration must be given to the scheduling of experiments to take advantage of sunglint. The position of the spacecraft with respect to the Sun's reflective position on the ocean surface can be calculated long before a mission starts, and where it seems important to view the ocean scene in Sun glitter, this position should be calculated; Earth observations, or photography, should be scheduled for such orbits. These points are especially important if there are military ap-

[1] W. R. Pogue: Assessment of Potential Roles for Space Transportation System Crewmen in Making Earth Observations. JSC memorandum to the Manager of the Earth Resources Program, 1976.

plications involving the use of observers in space to detect important oceanographic conditions.

Remote sensors, particularly infrared, would be exceedingly useful instruments for visual observations and photography. Recent research using data from the Defense Meteorological Satellite Program (DMSP), has demonstrated that many surface ocean features can be conclusively detected from infrared imagery. Stevenson (ref. 1) showed that DMSP imagery closely parallels features that can only be seen in the Sun glitter pattern off Spain. However, more research is needed in this important area.

Because successive orbital paths of the ASTP spacecraft precessed new paths over the Earth's surface, it was not simply a matter of waiting until the next orbit to take another photograph or make an observation of a selected site. There are two basic problems. First, each revolution moves approximately 23° of longitude farther west at the Equator. Except for the higher latitudes, where there is some overlap and more frequent repetitive paths over or near a site, it was necessary to wait a minimum of 15 revolutions, or approximately 23.25 hours, until the spacecraft was again near—but not over—the area of interest. If the scene must be viewed in sunglint, the number of possible observations is substantially reduced. Second, all experiments and tasks performed on the spacecraft are carefully scheduled months in advance to optimize available time during the mission. Thus, the tight, inflexible schedule does not allow for common intangibles (cloud cover), which cannot possibly be predicted months, or even a week, in advance. The problem is not restricted to low-altitude missions, but is particularly serious during short missions when only one opportunity is assigned for an Earth observation. The fact that three of the four ASTP ocean targets were "washed out" because of cloud cover on the day they were scheduled emphasizes the serious nature of this problem. For many targets in other fields, such as geology, for which conditions are static or for which no ground investigations are being simultaneously conducted, rescheduling is not a serious problem. But when experiments involve dynamic events, such as in oceanography or meteorology, with armadas of expensive ships and aircraft carrying out ground investigations, it would be beneficial if there was some flexibility in the schedule. The need for flexibility is more serious in short missions than in those of long duration.

If strictly formal Earth observation missions were conducted to provide information to military (or civil) ships, there are effective methods to deal with clouds in many but, perhaps, not all areas of the world. For example, visual and infrared imagery can be used to build a time-data base of ocean and cloud maps of a particular geographic area. Clouds often provide important clues to water conditions. Small breaks in clouds, in random parts of the area of interest, support constant updating of oceanographic conditions and correlations with clouds. However, such detailed ocean monitoring requires the dedication of manpower and equipment. During missions of short duration, combining many diverse tasks, there are high risks in restrictive scheduling of ocean targets, with no opportunity to reschedule should a target be obscured by clouds or not be enhanced by sunglint.

For various reasons, including cloud cover and the availability of time for Earth observations and scheduling of events, it is highly desirable to have several optimally spaced sites and/or repeated sites prearranged within the mission schedule. The problem is magnified on short-duration missions because, with so many tasks to perform on schedule, it is difficult for the observer to concentrate on Earth observations. If he does so, it is probably done "according to the book" or "mechanically" rather than using ingenuity and thought to record deep impressions. This topic needs further study because if the astronaut/observer's primary function is Earth observation, he must be able to concentrate on that one immutable assignment.

An annotated photographic record, or compilation, of ocean features would be useful in two forms. First, a significant compilation (using both aerial and previously acquired space photographs) could serve as a comprehensive training manual for all future Earth observers. Briefings could be organized around this compilation, which could also serve as an excellent onboard manual for flyover exercises. Second, a condensed version could be prepared for use during the mission, for

immediate reference purposes. Thus, during air-to-ground transmissions, the manual could be used to clarify instructions or to update Earth observation information. Both printed documents should precede the astronaut/observer ocean training programs (i.e., lectures and flyover exercises) as a means of ensuring an excellent, well-organized training program and of optimizing the crew's time. Information gathered from flyovers and subsequent space flights could be used to update the manuals. The smaller manual, or handbook, should be prepared immediately before the mission launch date, because it would be a synthesis of knowledge and would probably be specifically organized for the mission.

Although it has been demonstrated that non-oceanographers, with or without previous space-flight experience, can be trained to recognize features and to make Earth observations, it is also apparent that with additional training and experience, they can become even more proficient observers. The crewman can see subjective details that far exceed the resolution of cameras, lenses, and films currently available. This significant advantage needs to be further exploited. Personnel with this subjective insight should be used to the greatest advantage for mission accomplishments.

ACKNOWLEDGMENTS

Acknowledgments are given to Robert E. Stevenson, Office of Naval Research, who permitted the use of his extensive files, provided much information, and reviewed the final manuscript. James A. McShane critically edited the report and proofread the final manuscript. This work was performed under Smithsonian Institution Grant PC6-22373 as a subcontract of NASA contract NAS9-13831.

REFERENCES

1. Stevenson, R. E.: Huelva Front and Malaga, Spain, Eddy Chain as Defined by Satellite and Oceanographic Data. Deutschen Hydrographischen Zeitschrift, vol. 30, no. 2, 1977, pp. 51-53.

2. El-Baz, Farouk: Astronaut Observations From the Apollo-Soyuz Mission. Vol. I of Smithsonian Studies in Air and Space, Smithsonian Institution Press (Washington, D.C.), 1977.

3. Nysen, P. A.; Scully-Power, P.; and Bannister, R. W.: Project ANZUS Eddy: Acoustic Measurement of a Warm Core Ocean Eddy. Paper presented at 90th Meeting of the Acoustical Soc. Am. (San Francisco), Nov. 1975.

4. Scully-Power, Paul D.; Nysen, Paul A.; et al.: A Multisystem Technique for the Detection and Measurement of Warm Core Eddies. IEEE Ocean Conference, 1975, pp. 761-768.

5. Scully-Power, P.; and Twitchell, P.: Satellite Observation of Cloud Patterns Over East Australian Current Anticyclonic Eddies. Geophys. Res. Letters, vol. 2, no. 3, Mar. 1975, pp. 117-119.

6. Stevenson, R. E.; Carter, L. D.; and Vonder Haar, S. P.: Preliminary Report on Visual Observations of the Oceans From Skylab 4. Sec. 17 of Skylab 4 Visual Observations Project Report. NASA TM X-58142, 1974.

7. Stevenson, Robert E.; Carter, L. David; Vonder Haar, Stephen P.; and Stone, Richard O.: Visual Observations of the Ocean. Sec. 11 of Skylab Explores the Earth. NASA SP-380, 1977, pp. 287-338.

Antipodal Seas

Robert E. Stevenson[a]

ABSTRACT

The oceanographic experiment was conducted under the auspices of the Office of Naval Research to learn (1) whether or not astronauts could be trained to observe specific ocean features from space, (2) the variability of certain sea-surface conditions, in time and space, and (3) the role that these ocean features play in our understanding of synoptic oceanography. Sea-surface and subsurface data were collected by ships and aircraft from the military forces of Australia, Great Britain, New Zealand, and the United States. The areas of investigation were concentrated in the waters (1) east of Australia, (2) north of New Zealand, (3) east of Ireland, and (4) east of Spain.

From the analyses, it is clear that observations by man from orbiting space platforms have an important role in the development of synoptic oceanography.

INTRODUCTION

The Apollo-Soyuz Test Project (ASTP) came at a propitious time for oceanographers because it followed so closely the successful ocean observations during Skylab 4. Using photography together with visual observations, Skylab astronauts obtained information revealing remarkable ocean features, many of which had been unknown (if not in existence, at least unknown in scale) before the Skylab mission.

Of greatest importance to oceanographers, however, as well as to U.S. naval operations, were the remarkable eddies observed embedded in warm-water currents that flow poleward from equatorial oceans (ref. 1). These visual displays of mesoscale turbulence provided (1) a concept of the size and shape of such features, (2) an opportunity to examine the places of origin, (3) a feel for the rate at which they coalesce and grow downstream, and (4) an opportunity to ascertain their significance in the thermal energy regime of the oceans.

The author identified the eddies from photographs taken onboard Skylab 2 (May to June 1973) over the northwest Caribbean Sea (fig. 1). Such turbulence had been noted previously only in laboratory experiments; therefore, the continued observation of such features seemed logical and important.

Some detailed information on eddies came from the ANZUS eddy experiment in March 1975 when scientists from Australia, New Zealand, and the United States converged on a large warm-core eddy in the Tasman Sea to determine its oceanography and acoustic characteristics (ref. 2). This experiment was not suited, however, to check the concept of down-current eddy amalgamation which in the ocean must take place over distances of approximately 1500 km if it occurs at all. Therefore, the investigators looked forward to the joint U.S.-U.S.S.R. mission, which would offer an opportunity to perform observations covering great distances and an opportunity to gain a better understanding of eddies and their origins near the boundaries of the ocean.

The prime objective was to coordinate visual observations from the Apollo spacecraft with simultaneous measurements and observations of

[a]Scientific Liaison Office, Office of Naval Research, Scripps Institution of Oceanography, La Jolla, California.



FIGURE 1.—The northwestern Caribbean Sea, photographed in the summer of 1973, had linear cloud streets, oriented with the southeast trade winds, interrupted by oval-shaped clear patches of sky. Circular ocean eddies are clearly defined in the cloudless areas (SL2-10-072).

the ocean from military ships and aircraft. The team of investigators decided to concentrate on sea-surface features in (1) the approaches to the English Channel and the Strait of Gibraltar and (2) the Tasman and Kermadec Seas. These geographical areas were chosen primarily because they fit well in the mission schedule, and five offers of cooperation were received from military groups of the bordering countries. These ocean areas are on opposite sides of the Earth (antipodal); therefore, the experiment permitted the examination of large hydrodynamic features that

result from the interaction of major ocean currents with landmasses, both continental and insular, in two hemispheres at the same time (fig. 2).

In addition to the observations and measurements for the antipodal seas, routine data were to be collected elsewhere by surface units of the U.S. Navy while the Apollo crew observed from orbit. The areas of interest were

1. Western Pacific Ocean
2. Western part of North Atlantic Ocean including the Caribbean Sea
3. Mediterranean Sea
4. Northwestern Indian Ocean, Arabian Sea, and Persian Gulf

For each area, the astronauts were prepared to observe, describe, and photograph the following: (1) current boundaries, (2) ocean fronts, (3) internal wave patterns, and (4) eddies. The team of investigators designated the specific features or combinations of features to be observed.

EXPERIMENT

The basic purpose of this experiment was (1) to evaluate the visual observation capability of a spacecraft crew during a short-duration, low-altitude orbital flight, in contrast to the capability developed during the 84-day mission of Skylab and (2) to determine the applicability of the observations to the oceanography requirements of tactical fleet units. Although the ASTP mission was short and the Apollo spacecraft had limited facilities for sensing the Earth's surface, the flight was so similar to the mission envelope expected during the upcoming Space Shuttle flights that the investigators could test concepts which could be useful in the 1980's. It seemed necessary, for example, to determine whether astronauts could be trained to observe specific oceanographic features known to exist in specific areas, when only 15 to 25 seconds of observation time was allowed by the

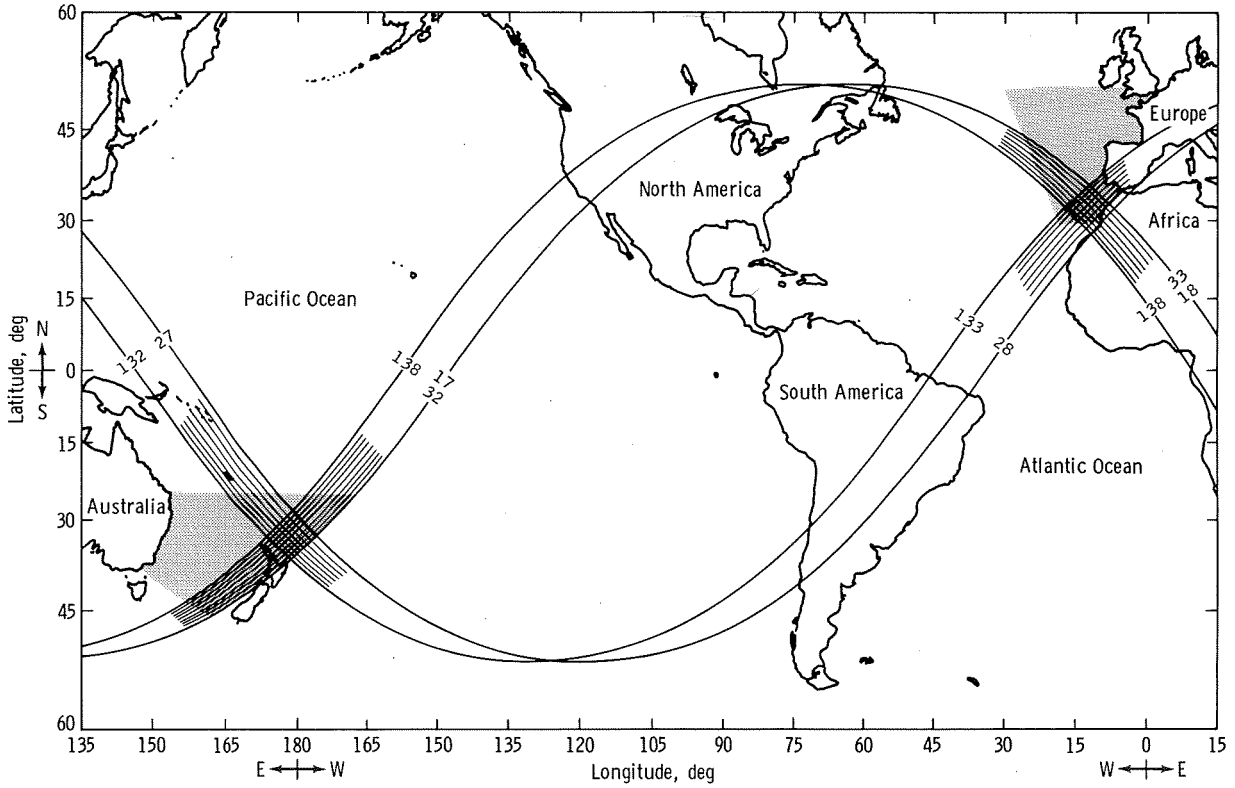


FIGURE 2.—Map showing antipodal sites (shaded areas) chosen for oceanographic study during the ASTP mission. Spacecraft revolutions for the test sites are given.

orbital profile. (The timespan for an observation at the low altitude of the Apollo flight would be the same as during a Space Shuttle mission.)

The Apollo crewmembers were expected to recognize pertinent features of the ocean surface. To this end, they had 14 hours of discussions covering the fundamentals of ocean current systems, ocean dynamics, air-sea interaction, and the visible sea-surface/marine-atmosphere manifestations of the features of interest. These discussions were conducted during the year preceding the ASTP flight. The U.S. astronauts received, therefore, the most extensive oceanographic training of any space-flight crew in history.

The task of the various military units was to acquire oceanographic and meteorologic data from the ocean surface and near surface, which would be applicable to the observations made from space. The gathering of these data was concentrated in the antipodal areas, as noted previously, and along the tracks of four specified orbits of the spacecraft (on four different days).

Nine aircraft missions were flown in 3-day sequences by British, New Zealand, and U.S. Navy patrol aircraft from which the following measurements and observations were made: (1) air and water temperatures, the latter from air expendable bathythermographs, (2) visual observations of sea-surface conditions, cloud types and their distribution, visibility, windspeed, and direction, and (3) radar imagery of cloud distribution and sea conditions whenever such equipment was available. Aircraft from the Royal Air Force (fig. 3) flew west from the southern coast of Ireland along a 960-km track. From the west coast of Spain, aircraft of the U.S. Navy flew along a northeast-southwest track immediately below the orbit of Apollo. From New Zealand, aircraft from their Defense Establishment flew from East Cape, New Zealand, northeast to the Kermadec Islands (fig. 4).

In the Tasman Sea, surface units of the Royal Australian Navy made observations of sea conditions, clouds, current speed and direction, and water temperatures around and through a large warm-core ANZUS eddy. Similar data were collected by the U.S.N.S. *Kane* (fig. 5), U.S. Naval Oceanographic Office, along the track flown by U.S. Navy aircraft southwest of Spain.



FIGURE 3.—The Royal Air Force used *Nimrod* patrol aircraft to acquire ocean temperatures of the northeast Atlantic Ocean southwest of Ireland.

Off the east coast of the United States, the U.S.S. *Preserver,* after first serving as the standby rescue vessel in the event of an aborted Apollo launch, deployed freely drifting buoys off the coast of Jacksonville, Florida. The buoys were tracked by the Nimbus 6 satellite as they floated northeasterly in the Gulf Stream. In the Mediterranean Sea, the U.S.S. *Kennedy* recorded 10 days of infrared and visible data from the Defense Meteorological Satellite Program (DMSP).



FIGURE 4.—The Royal New Zealand Air Force used P-3 *Orion* aircraft for observations and photographs along a track from East Cape, New Zealand, toward the Kermadec Islands.

All together, data collections were made by four military units of the United States, New Zealand, Australia, and Great Britain; from six ships; from three aircraft units; from satellites; and by weather centers in three of the four countries. Support from defense units was as follows:[1]

1. United States Forces

   a. Navy

      (1) U.S.S. *J. F. Kennedy,* CVA—Mediterranean Sea
      (2) U.S.S. *F. D. Roosevelt,* CVA—North Atlantic Ocean
      (3) U.S.N.S. *Kane,* RV—Approaches to Gibraltar
      (4) U.S.S. *Preserver,* ATS—Gulf Stream
      (5) Fleet ASW Squadron, Azores—Approaches to Gibraltar
      (6) Fleet Numerical Weather Central—Worldwide forecasts and data reduction

   b. Air Force

      (1) Defense Meteorological Satellite—Bird 29 (visual tapes)
      (2) Defense Meteorological Satellite—Bird 30 (infrared and visual tapes)

2. New Zealand Forces

   a. Royal New Zealand Air Force—Northeast Cape
   b. Defense Scientific Establishment, H.M.N.Z.S. *Tui*—Northwest Cape

3. Australian Forces

   a. Royal Australian Navy, H.M.A.S. *Bombard*—ANZUS eddy
   b. Royal Australian Navy Research Laboratory—Data analysis

[1]The terms are as follows: CVA = aircraft carrier, RV = research vessel, ATS = fleet tug, and ASW = Antisubmarine Warfare.



FIGURE 5.—The U.S.N.S. *Kane,* operated for the U.S. Naval Oceanographic Office, is shown here moving into the harbor of the Principe of Monaco.

4. British Forces

   a. Royal Air Force, ASW Squadron—Approaches to Ireland
   b. Royal Navy—Data support and analysis

TASMAN SEA AND THE WATERS WEST OF IRELAND

The H.M.A.S. *Bombard* (fig. 6) sailed in the Tasman Sea collecting data in the large warm-core ANZUS eddy for the 4 days prior to the visual observation to be made on July 23. The eddy was well defined; it had a diameter of approximately 250 km, similar to that reported by Scully-Power (fig. 7). However, on the day of the observation, a storm front moved across the Tasman Sea and as the Apollo docking module pilot (DMP) pointed out during his observation, ". . . it's totally cloud covered." "I'm not seeing nothing except clouds." As a consequence, no visual observation of the ANZUS eddy was made from the Apollo spacecraft. Data gathered by the H.M.A.S. *Bombard* are of interest only to the Royal Australian Navy and are not reported here.

A similar situation occurred off the western coast of Ireland. Royal Air Force aircraft flew on 3 successive days due west from the southern tip of

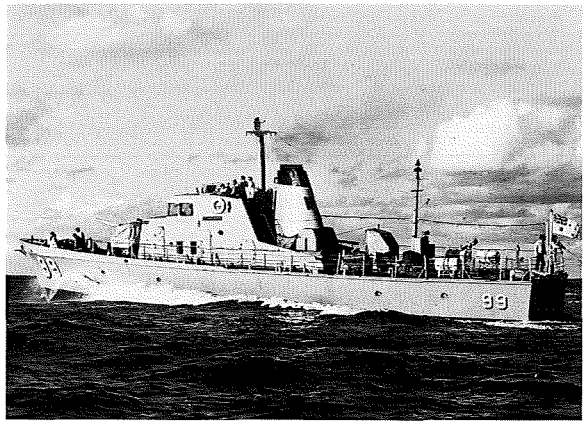


FIGURE 6.—The H.M.A.S. *Bombard* cruising in the waters of the Tasman Sea east of Australia. During the ASTP mission, the *Bombard* made observations of the ANZUS eddy.

Ireland, along a 960-km flightpath. These aircraft, *Nimrods,* deployed air expendable bathythermographs at regular intervals along the flightpath to obtain temperature data at the surface and at various depths for waters in the northeastern Atlantic Ocean. However, on the day of observation, again July 23, a large cold front moved across the flightpath and no visual observations could be made from the Apollo spacecraft. Again, the data gathered are primarily of use only to the British units and are not reported here.

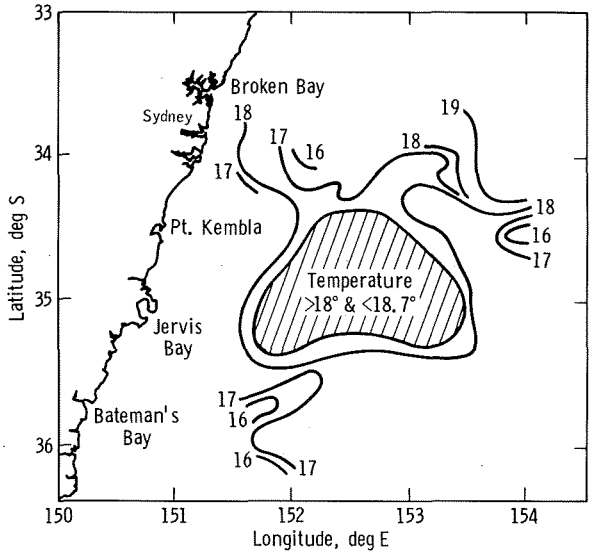


FIGURE 7.—Sea-surface temperature (in Celsius) of an ANZUS eddy, surveyed in September 1974 by Paul Scully-Power onboard the *Bombard* during research conducted under the auspices of the Royal Australian Naval Research Laboratory, the New Zealand Defense Establishment, and the U.S. Office of Naval Research. (K = °C + 273.15)

KERMADEC SEA

The joint experiment in the Kermadec Sea north of New Zealand (between units of the New Zealand Defense Establishment, the U.S. Navy, and the Apollo spacecraft) is a good example of the necessity for precise timing of the observation from space in attempting to detect an oceanographic feature that can be measured from the sea surface and observed from aircraft.

The waters north of East Cape, New Zealand, are dominated by the major flow of the ocean from west to east through the gap between New Zealand and the Kermadec Islands. This current, the East Auckland, flows southeastward along the coast of North Island between North Cape and East Cape. Near East Cape, the current flow divides, the main flow turns north, while the remainder continues southeast around East Cape to form the East Cape Current (fig. 8). As a result, an anticyclonic eddy occurs in the area northeast of East Cape. The presence of this eddy is shown by the horizontal variation of temperatures at a depth of 240 m, but is also well established in the surface temperatures and the surface salinity (figs. 9(a) and 9(b)). During observation from Apollo, the eddy was centered around latitude 37° S, longitude 179°30′ E. This position was confirmed by data from the air expendable bathythermograph of July 16 (fig. 10), which shows a pronounced subsurface temperature maximum at all depths where the groundtrack of revolution 17 crosses the 179°30′ E meridian.

Approximately 550 km north of the eddy, a shear in the major current system takes place apparently in response to the sea-floor topography in that area of the ocean. This shear is easily detected in the ocean temperatures (fig. 10) and is marked by both a cloud line (fig. 11) and a difference in sea-surface texture as seen from Royal New Zealand aircraft (figs. 12 and 13). On the northern side of the shear, the water temperatures rise to 290 K (63° F). On the southern side, the tem-

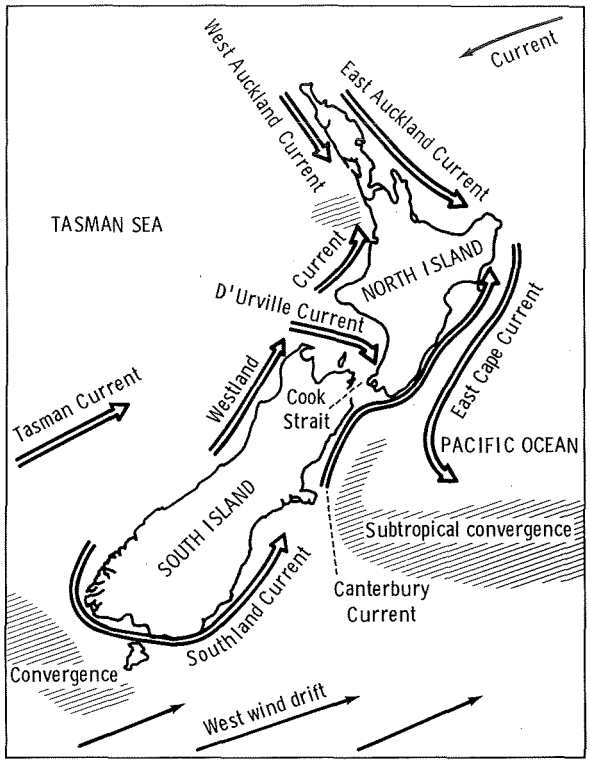


FIGURE 8.—Currents around the islands of New Zealand as depicted from studies reported by Jonathan Brodie.

peratures decrease to 288 K (58° F) and then become warmer again as the large anticyclonic eddy is approached north of East Cape.

Both the eddy immediately north of North Island and the shear and the currents between New Zealand and the Kermadec Islands were observed by the Apollo command module pilot (CMP). The CMP observed discolored water north of New Zealand and took a photograph of that water (fig. 14). He then observed what he called a "scum line" north of the discolored water, in the area of the shear observed from the aircraft. However, by the time the CMP was able to photograph the "scum line," the angle of the Sun's reflection had so changed that the shear was not visible in the photograph (fig. 15).

The lack of good photography of these two features is understandable considering that this was the first day of the Apollo mission. The entire onboard science and engineering program was

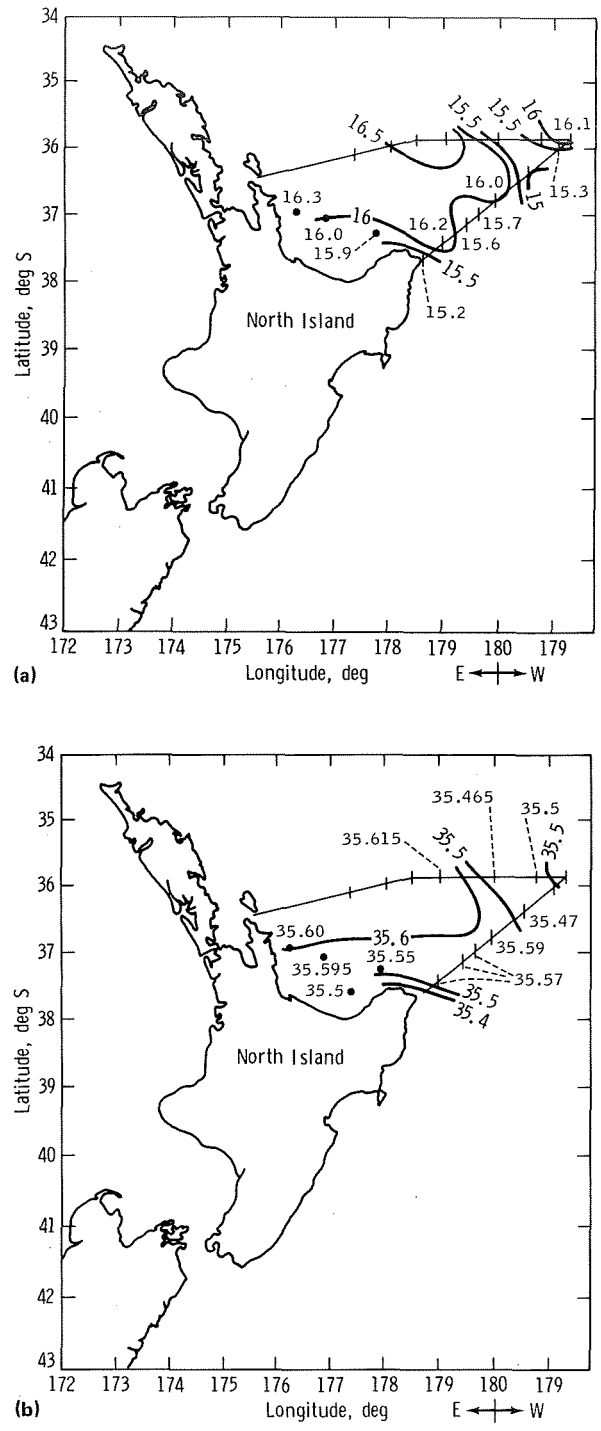


FIGURE 9.—Sea-surface data for an eddy north of North Island, New Zealand, drawn from information gathered onboard the New Zealand Navy research vessel *Tui* during the ASTP mission. (a) Surface temperatures (in Celsius). (b) Surface salinities.

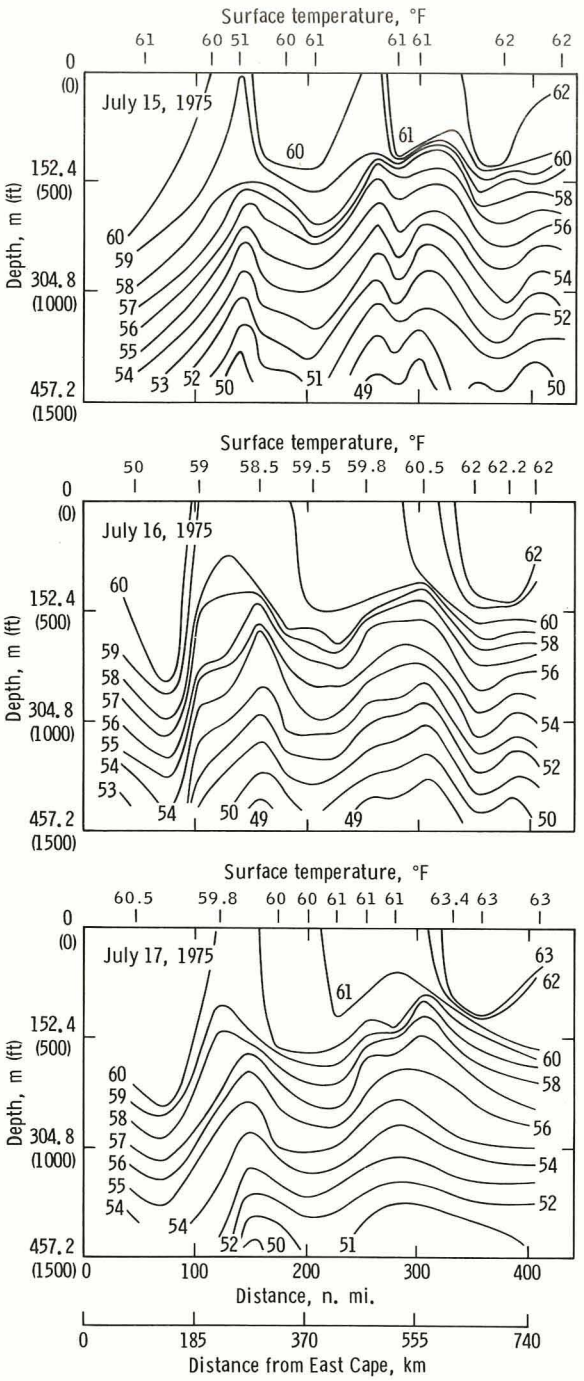


FIGURE 10.—Temperature profiles (in Fahrenheit) of the ocean between North Cape, New Zealand, and the Kermadec Islands on July 15, 16, and 17 of 1975 (New Zealand time). Drawn from data obtained from air expendable bathythermographs deployed by P-3 aircraft of the Royal New Zealand Air Force. (K = (5/9)(°F + 459.67))



FIGURE 11.—An oblique aerial photograph taken July 16, 1975, by Royal New Zealand Air Force personnel looking north at the east-west-trending cumulus cloud line marking temperature boundary of the major ocean-current shear.

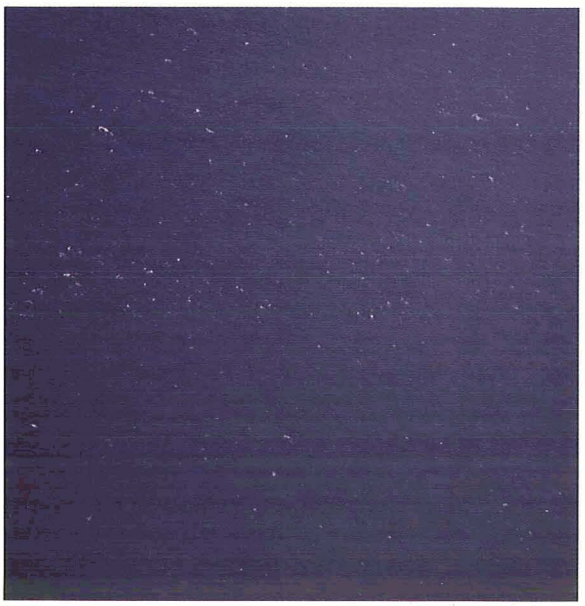


FIGURE 12.—An oblique aerial photograph taken a few minutes following that shown in figure 11. Photograph shows the greater number of whitecaps on the sea surface north of the current boundary than on the south side. Wind was from the west, thus blowing into the current flow north of the shear.



FIGURE 13.—An oblique aerial photograph taken a few minutes after that shown in figure 12. In this instance, photograph is looking west along the line of the current shear.



FIGURE 14.—ASTP photograph (AST-1-037) showing discolored water in the ocean north of North Island, New Zealand. Photographed from Apollo spacecraft on July 16, 1975, Cape Kennedy time.



FIGURE 15.—ASTP photograph (AST-1-038) of the Kermadec Sea taken from the Apollo spacecraft just seconds after that shown in figure 14. Although the current shear noted by the New Zealand air force pilots was visible to the Apollo CMP, in the few seconds between the CMP's observation and the photograph shown here the Sun angle had changed sufficiently for the scene to be lost to photography.

running behind schedule, and this was the first observation of the Earth's surface to be made by any of the crewmembers. The observational period went by exceedingly fast, with no more than 15 to 25 seconds available—depending upon the scene and how far ahead of the spacecraft the observer was able to pick up the particular feature to be observed. Consequently, to make the observation and to describe and photograph the scene in that short timespan was difficult on the first try. As a matter of fact, it was difficult on the first few tries, as noted in the section of this volume entitled "Visual Observations Over Oceans."

GULF OF CÁDIZ

The Gulf of Cádiz off the western coast of Spain was chosen as an area of interest for the U.S. Navy because of a possibly significant oceanographic feature that had been interpreted from a



FIGURE 16.—Skylab 2 photograph (SL2-5-370) provides magnificent view of southwestern Iberian Peninsula, parts of Morocco and Algeria, the Atlantic Ocean west of Gibraltar, and the western Alboran Sea. Note the straight-line feature imaged in the ocean west of Spain and the arc-shaped ocean eddies in the Alboran Sea.

photograph taken onboard Skylab 2, July 1973 (fig. 16). In that photograph, the subpoint of the Sun was in southwestern Spain. On the edge of the Sun's reflection, one could see (1) a north-south boundary in the ocean south of the town of Huelva, Spain, (2) an internal wave series over the Continental Shelf off western Spain, and (3) curved slicks in the surface waters of the Mediterranean Sea just east of Gibraltar, indicating the flow of large eddies. Because there were wavelike features at the sea surface west of the north-south front, with wavelengths of 3 to 5 km, the feature was interpreted as a warm/cold-water front, with warm water being on the western side and the internal waves broaching the sea surface along a rising thermocline.

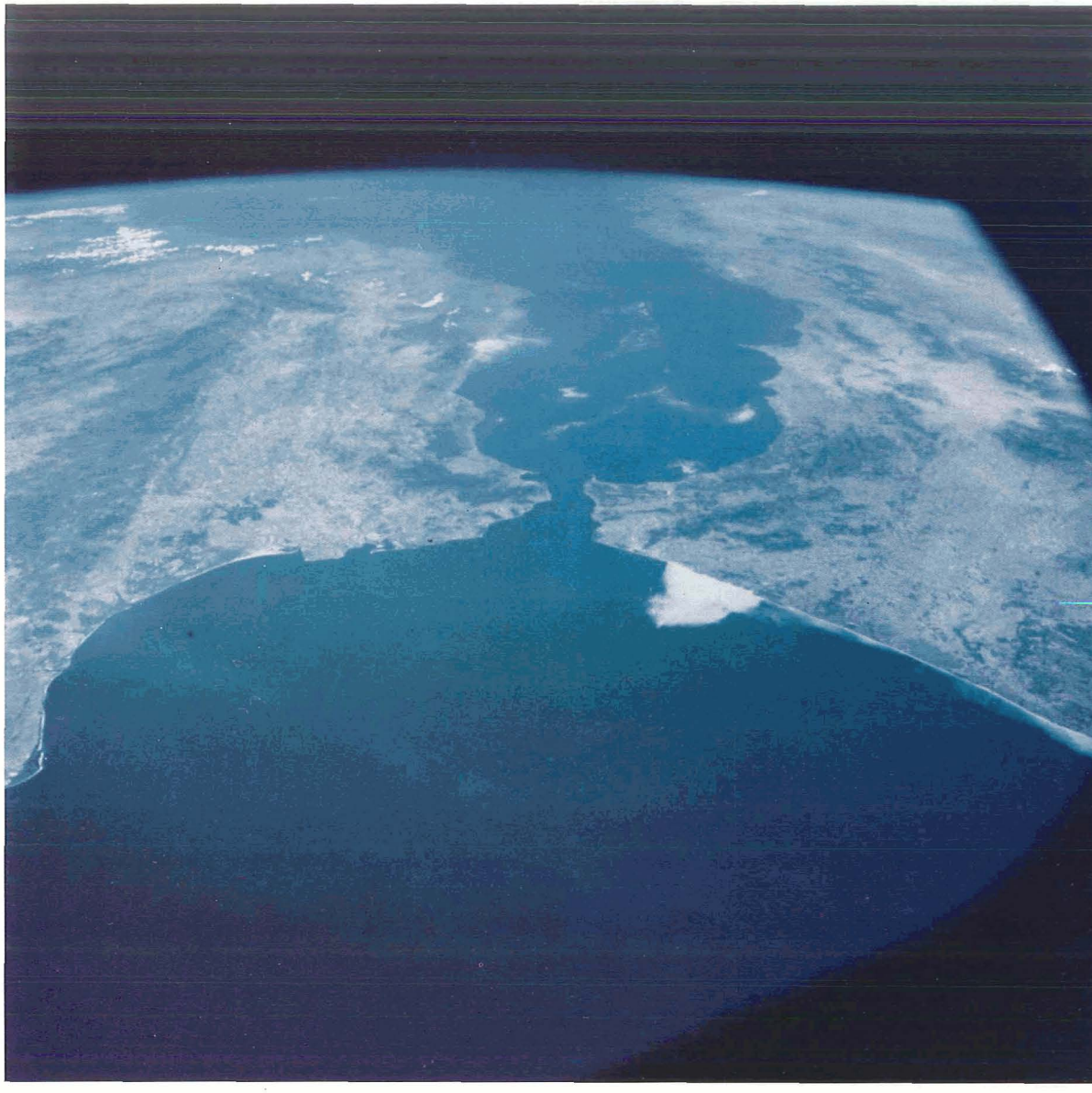


FIGURE 17.—ASTP photograph taken by the ACDR on July 20, 1975, as he and the spacecraft crew approached the Iberian Peninsula, Alboran Sea, and Morocco (AST-27-2364).

The existence of these features, both the front off the western coast of Spain and the apparent large eddies just east of the Strait of Gibraltar, created enough interest to establish this area as a prime experiment site. During the period July 19 to 22, 1975, ships and aircraft acquired oceanographic data along the Apollo groundtrack. On July 20, as the Apollo spacecraft approached Spain on an ascending orbit, the Apollo commander (ACDR) was the observer (fig. 17). Beneath him, the U.S.N.S. *Kane* sailed on a northeasterly track and a U.S. Navy P-3A flew southwesterly from the Spanish coast.

The ACDR saw nothing of the front nor the internal waves until the Apollo spacecraft was 10 seconds from Spain. At that instant, the Sun angle

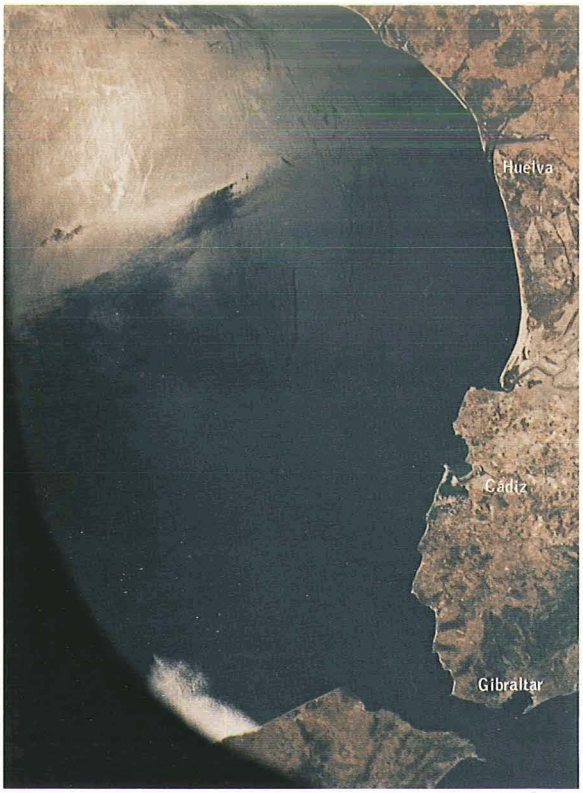


FIGURE 18.—ASTP photograph taken by the ACDR on July 20, 1975, of the Sun's glitter pattern on the sea surface off the western coast of Spain. The internal waves marking the Huelva Front and the straight-line Stafford Shear are clearly visible (AST-27-2367).

was perfect to permit visual observation and photography of the front and internal waves (fig. 18). The view was so spectacular in fact, that the ACDR noted, "There they are, there the bastards are," that is, the front and waves. Being prepared for the short period in which the scene would be in view, the ACDR had the camera available and took two quick photographs, both catching the internal wave and frontal sequence perfectly. During debriefing, the ACDR noted that he was so impressed with the scene, that he grabbed the DMP to draw him to the window to look at the reflection from the sea surface. But in just those few seconds required to reach the window, the scene was gone; the spacecraft being well over the coast of Spain.

The U.S.N.S. *Kane* obtained temperatures from expendable bathythermographs (fig. 19). The obvious features that can be detected from these data were (1) the warm-water trough approximately 75 km (40 n. mi.) from the coast, (2) a sharply rising thermocline between 37 and 75 km (20 and 40 n. mi.) offshore, and (3) an indication of cold water approximately 37 km (20 n. mi.) offshore. These data confirmed the interpretation made in 1973 from Skylab photographs.

Temperature profiles obtained from air expendable bathythermographs provided data through a 3-day sequence (fig. 20); the middle day was July 20, the day of the observation from Apollo. The temperature profiles of the water on those 3 days (fig. 21) correlate well with those taken on July 21 and 22 from the U.S.N.S. *Kane.* The configurations of the warm trough and the thermocline from both sets of data are the same. (Note that the temperatures taken from the aircraft were in Fahrenheit whereas those from the *Kane* were in Celsius.) Although there were differences from one day to the next, the basic ocean features were there each day.

From the aircraft profiles, a warm-cold-warm sequence between 275 and 460 km (150 and 250 n. mi.) from Spain is easily recognized. It remained for the analysis of data from DMSP to provide an understanding of the origin of this feature, a feature that was also caught in the ASTP photograph.

During the 9-day ASTP mission, meteorological personnel onboard the aircraft carrier U.S.S. *Kennedy,* then sailing in the Mediterranean Sea, taped all data (visual and infrared) transmitted from the DMSP satellites. These data provided a wealth of information, which confirmed all the analyses made from the Apollo visual observations and from the temperature data obtained by the *Kane* and U.S. Navy aircraft.

From DMSP infrared data, the warm/cold front near the Spanish coast was clearly depicted (fig. 22). It was evident that the front lay with a northwest-southeast orientation, approximately 90° to the direction of the bright linear feature observed by the ACDR and shown in the ASTP photograph (fig. 18). Huelva, Spain, lies at the juncture of the linear feature and the front; thus, the front was named after that town.

From the DMSP infrared data of July 18 (fig. 23), the following oceanographic features are

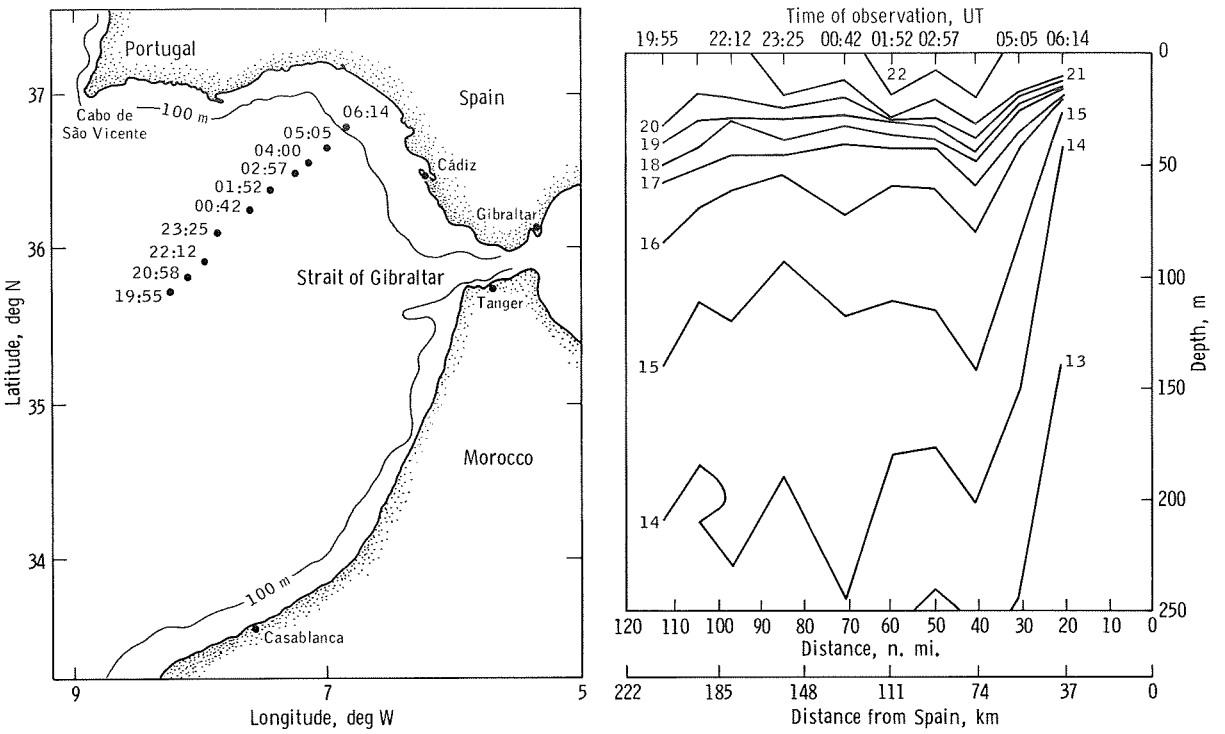


FIGURE 19.—Temperature profile (in Celsius) drawn from data gathered by expendable bathythermographs deployed by the U.S.N.S. *Kane* on July 21 and 22, 1975. Observations were along the Apollo groundtrack of July 20, 1975. Note the sharply rising isotherms at the nearshore end of the temperature profile.

easily detected: (1) Portuguese upwelling zone, (2) Huelva Front, (3) warm surface water over the Spanish shelf, (4) flow of warm water into the Mediterranean Sea through the Strait of Gibraltar, (5) upwelling off the coast of southern Spain and the associated sequence of warm-core eddies, (6) upwelling and turbulent eddies off the Atlantic coast of Morocco, and (7) an irregularly shaped area of warm water seemingly trapped west of Gibraltar.

The Spanish Bight had completely clear skies on July 20, which is indicated in figure 24. The result was the excellent observation by the ACDR and the good DMSP infrared scan in figure 22. (This sequence indicates the tremendous value of having both visual and infrared scans for a knowledgeful interpretation; it is not always simple to discriminate cold water from clouds in the infrared data).

The descending orbit by DMSP on July 20 was to the east, over the mid-Mediterranean, so the Spanish Bight appeared on the edge of the scan.

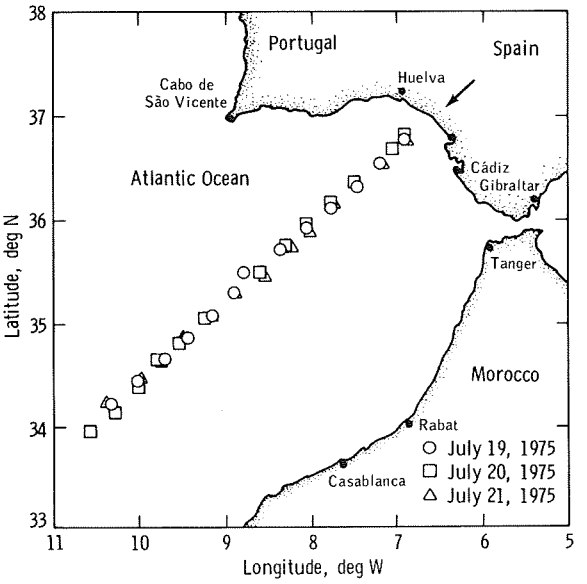


FIGURE 20.—Deployment positions of air expendable bathythermographs deployed by U.S. Navy P-3 aircraft on July 19, 20, and 21, 1975.

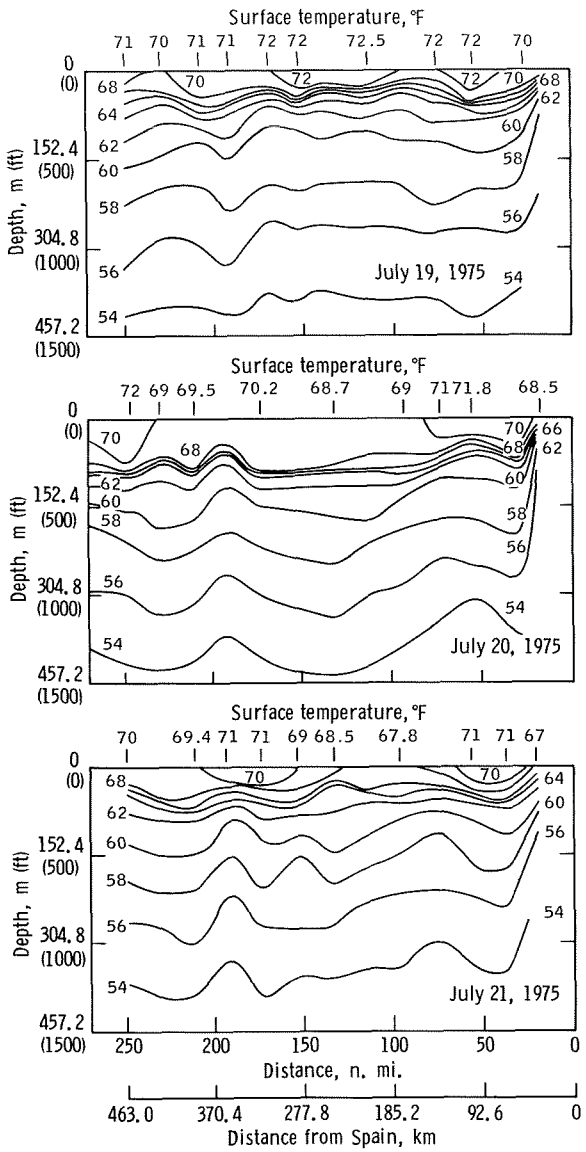


FIGURE 21.—Temperature profiles (in Fahrenheit) drawn from data gathered by U.S. Navy P-3 aircraft (fig. 20). Note the warm "bathtub" of water seaward of the nearshore cold front; also note the warm-cold-warm sequence of turbulence (eddies?) at the outer end of the temperature profile.

Nonetheless, the oceanographic features are readily recognizable and evident. In particular, note the cool boundary south of the Spain-Portugal border and the Huelva Front. Comparing these two boundaries with the photograph (fig. 25), it is apparent that the strong straight feature

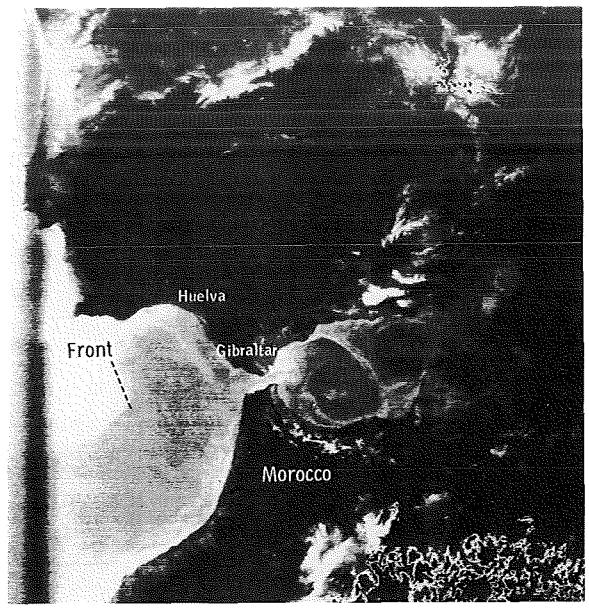


FIGURE 22.—DMSP infrared imagery of southwestern Spain and the adjacent ocean waters. Data gathered by the Defense Meteorological Satellite on July 20, 1975, and recorded on-board the U.S.S. *Kennedy*. The lighter grays depict the colder waters and the darker shades indicate warmer waters or land area. The range of sea-surface temperatures depicted in this image covers 6 K (6° C).

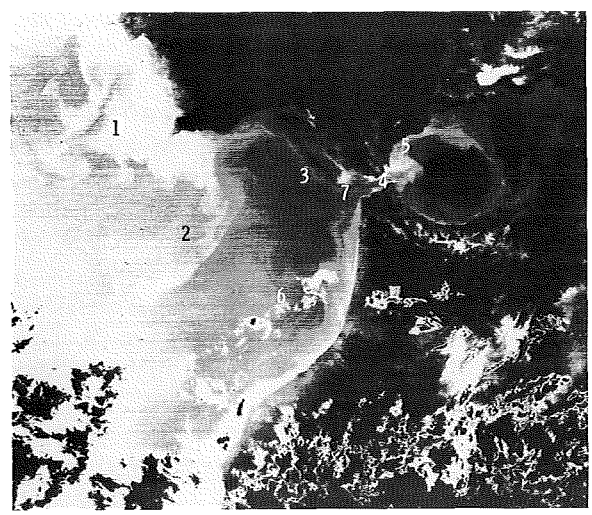


FIGURE 23.—DMSP infrared imagery of the western Iberian Peninsula and adjacent ocean waters (July 18, 1975). Note the greater definition of ocean features in this image than in figure 22. (Numbers are designators used in the text.)

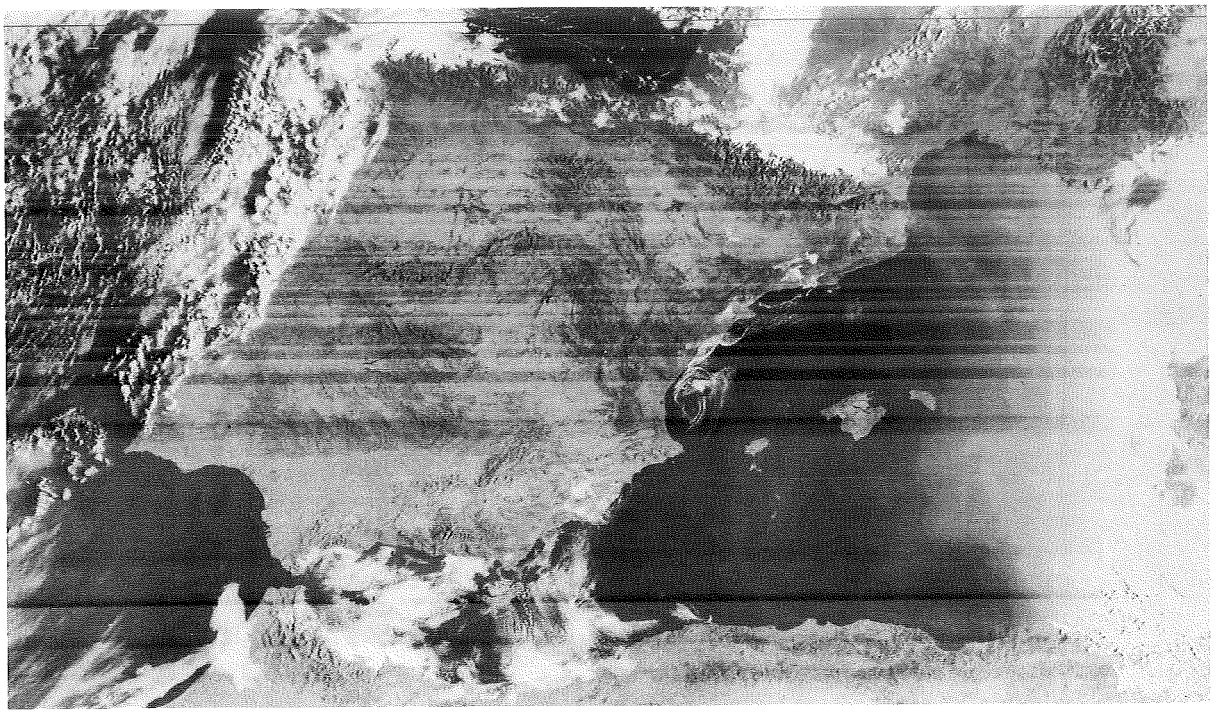


FIGURE 24.—DMSP visual imagery of the Iberian Peninsula and adjacent ocean (July 20, 1975).

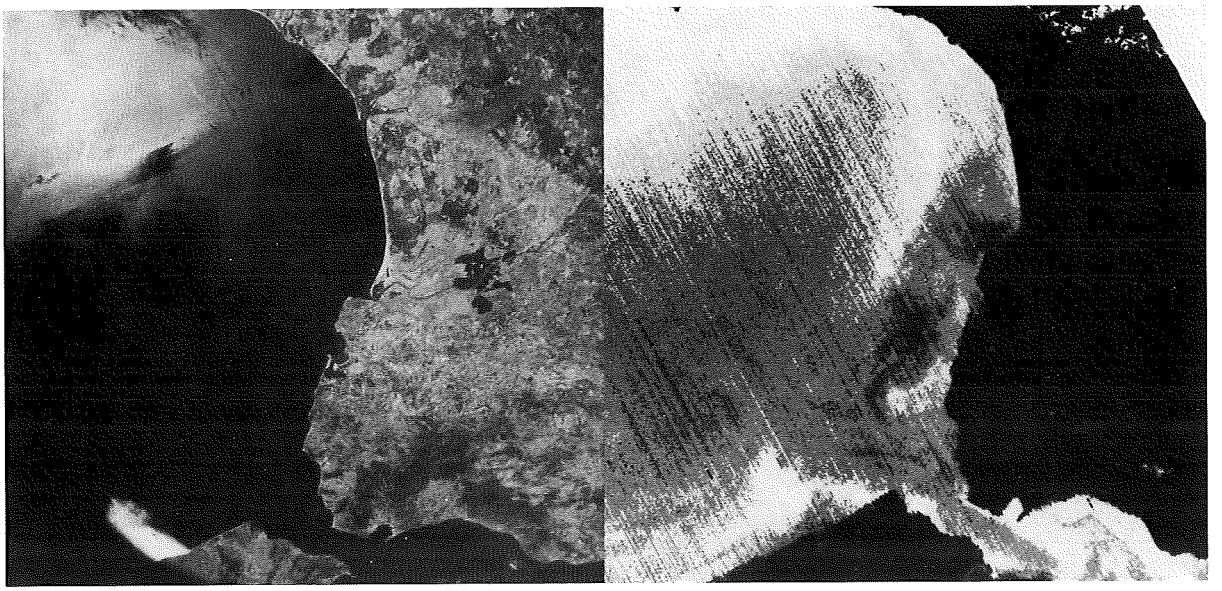


FIGURE 25.—DMSP infrared imagery (right) expanded and oriented to match as nearly as possible the ASTP photograph (left) taken by the ACDR of the waters in the Spanish Bight. Both the photograph and imagery were taken on July 20, 1975. The photograph, being earlier by approximately 1 hour, was taken near local noon.

in the Sun's reflective pattern is the cold/warm boundary to the northwest. (The Huelva Front is delineated by the strong internal wave sequence as it was in 1973.) The straight feature represents a strong current shear as well as a temperature boundary (note the *Kane's* track in fig. 26(a)). It has been named the Stafford Shear, after the succinct comment of Thomas P. Stafford, the Apollo commander, when he suddenly observed this feature.

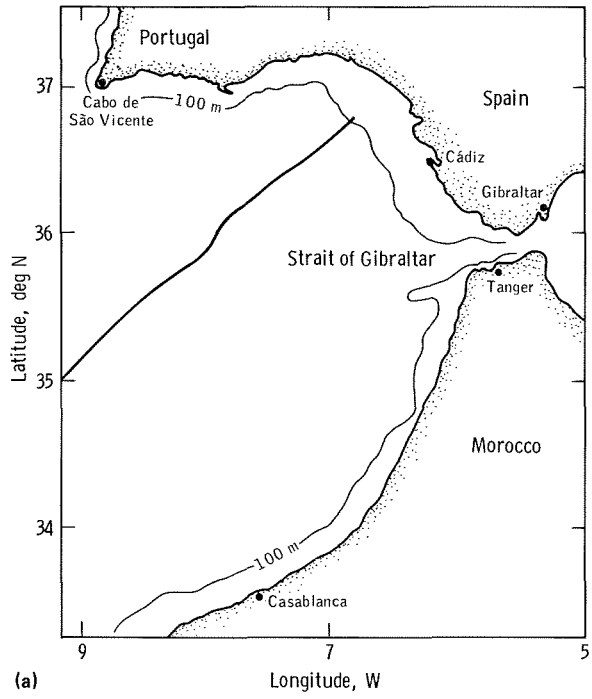
The warm-cold-warm sequence approximately 370 km (200 n. mi.) offshore (fig. 21) represents the subsurface expression of the boundary of the Portuguese upwelled water and what is recognized as a warm-core, shallow eddy off Gibraltar. Continuous surface temperatures taken from the U.S.N.S. *Kane* on July 21 and 22 (fig. 26(b)) show the eddy boundaries. On this day, the western edge was encountered approximately 200 to 220 km (110 to 120 n. mi.) from shore along the ship's track. The Stafford Shear carried the ship northward at that point. From there to the Huelva Front, the surface water became warmer, but in a manner indicating considerable turbulence within the eddy.

The eddy was well defined on July 24, as noted in the DMSP infrared data taken on that day (fig. 27). The turbulence in the Portuguese upwelling zone was also apparent.

Approximately 11 months later, in June 1976, personnel from the North Atlantic Treaty Organization's SACLANT[2] ASW Research Centre in La Spezia, Italy, cruised these same waters in the Gulf of Cádiz. Both temperature and salinity data were taken to determine the extent of the front. As indicated in figure 28, the Huelva Front existed (as depicted in the sea-surface temperatures) as well as the offshore shear (as shown by the deviation in the ship's track).

Although the ocean west of Spain was of primary interest during the ASTP mission, data were gathered also of a sequence of eddies from Gibraltar, east along the coast of Algeria (the Málaga Eddy Chain). The water temperatures in

[2]SACLANT is Strategic Allied Command, Atlantic.



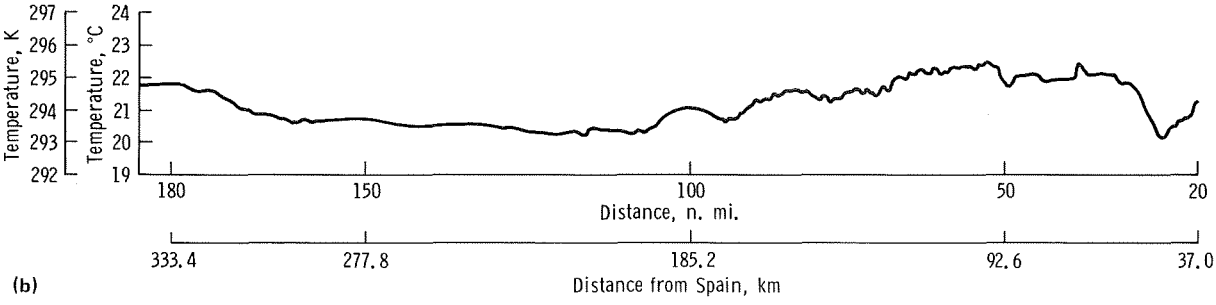


FIGURE 26.—Continuous sea-surface temperatures were collected from the *Kane* (July 21 and 22, 1975) along the track indicated here. Note the general, irregular increase in the water temperature across the Tarif Eddy; also the sharp fall at the Huelva Front. (a) Ship's track. (b) Sea-surface temperatures.

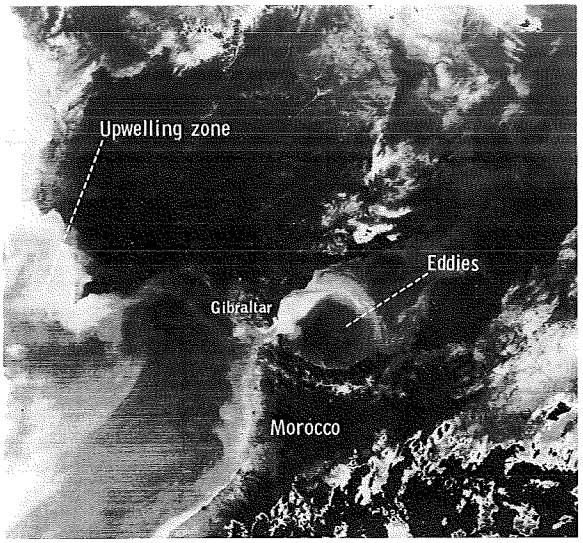


FIGURE 27.—DMSP infrared imagery (July 24, 1975) of the southwestern Iberian Peninsula and adjacent ocean.

these latter waters ranged from 293 to 301 K (20° to 28° C), in contrast to the 289 to 295 K (16° to 22° C) of the waters off Spain and Portugal. To analyze the DMSP data, therefore, it was necessary for personnel at the Navy Weather Service Facility to "drop" temperatures off the low end of the computer program and "add" temperatures to the top. By using this technique, the eddies in the Alboran Sea were clearly defined (fig. 29).

Data acquired by the U.S.N.S. *Kane* in the early days of August 1975 show the existence of a large anticyclonic circulation (fig. 30). However, the

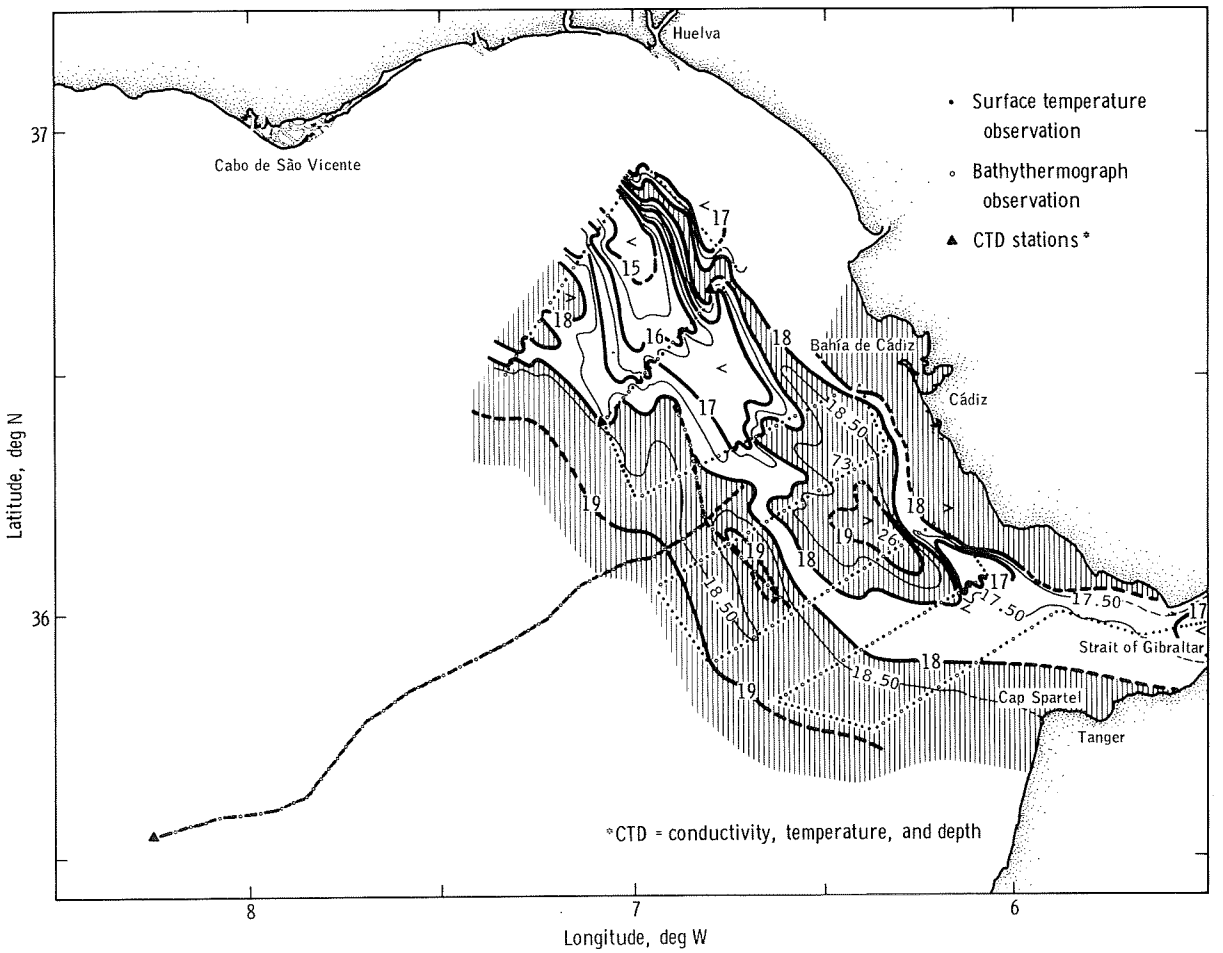


FIGURE 28.—Sea-surface temperatures (in Celsius) and ship tracks from the June 1977 cruise of SACLANT Research Centre (courtesy of James Cairns).

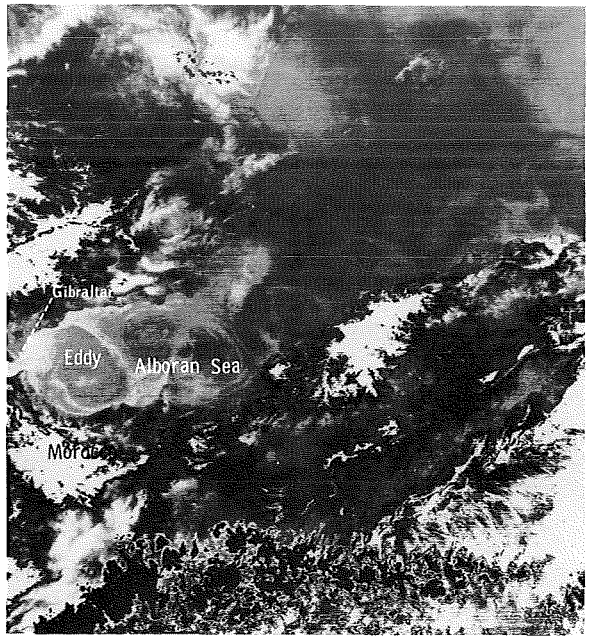


FIGURE 29.—DMSP infrared imagery (July 20, 1975) of the Alboran Sea and the western Mediterranean Sea. Note the eddy "chain" in the Alboran Sea and along the Algerian coast.

location of the hydrographic stations resulted in a definition of but one eddy, whereas three actually existed during the sampling period. Of course, personnel onboard the *Kane* were not aware then of the existence of three eddies. Consequently, they selected the hydrographic stations according to the oceanography known at that time.

Notice that the traverse to the east (the Albuñol line) cut through two eddies. Temperature and salinity profiles (fig. 31) indicate the existence of the two eddies, although it is unlikely that such an interpretation would be made without the accompanying satellite imagery.

From the temperature profiles, it is clear that the horizontal gradients of approximately 6 K (6° C) were present because of the summer season heating of the surface layers. This is especially obvious for the eddies east of Málaga, where the mixed layer and the thermocline were confined to the top 50 m of the sea.

The salinity profiles indicate the intrusion of low salinity water from the Atlantic Ocean and its concentration along the coast of Morocco and Algeria. As can be noted from the two profiles, the saline water spreads to a greater depth and diminishes in its salinity contrast with the Mediterranean water, as it reaches farther and farther into the Alboran Sea.

The origin of the coastal water along the southern coast of Spain, west of Málaga, is unknown at this time. It seems probable, however, that the water comes around Gibraltar from the shelf waters trapped behind the Huelva Front off western Spain. Future oceanographic studies conducted in this area by SACLANT ASW Research Centre will no doubt solve this particular problem.

All these data suggest that the Málaga eddy chain can be monitored easily during the warm months of the year (June to October) by the sea-surface temperature gradients. During the winter and spring, when the waters cool and become nearly isothermal at 286 to 287 K (13° to 14° C), the turbulent eddies can be followed by current measurements and by noting the distribution of salinity. It is further likely that the eddy chain, created by seasonal winds and upwelling, is less prominent in the winter-spring months than noted from the data presented here.

None of these data indicate that the eddies to the east of Gibraltar are actually spawned by the large circular eddy immediately inside the Strait and then progress eastward into the western Mediterranean Sea. Rather, it appears that the large eddy is a semipermanent feature of the

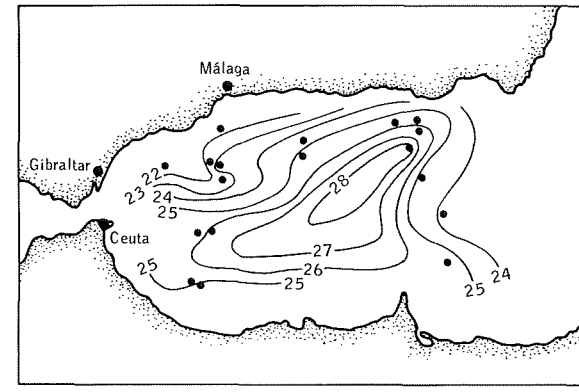


FIGURE 30.—Isotherms depicting sea-surface temperatures (in Celsius) in the Alboran Sea. Data gathered August 1975 from onboard the *Kane*.

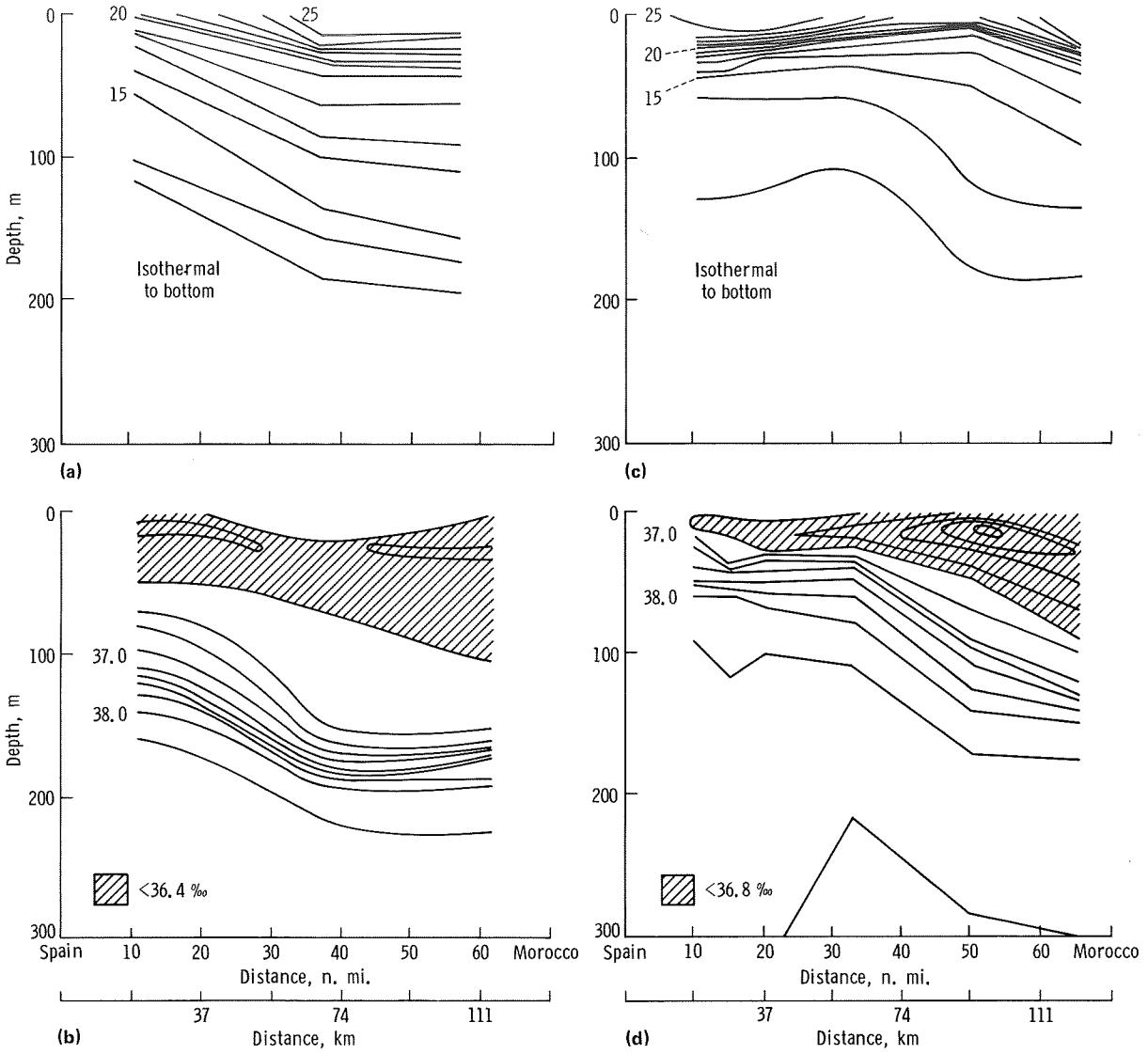


FIGURE 31.—Temperature (in Celsius) and salinity profiles along the two north-south transects cruised by the *Kane* in August 1975. (a) Málaga line, temperature. (b) Málaga line, salinity. (c) Albuñol line, temperature. (d) Albuñol line, salinity.

Alboran Sea, and the other eddies are determined by the strength of the air/sea interaction and by the currents spawned from the major eddy in the western Alboran Sea.

The data gathered off the western coast of Spain and in the Alboran Sea reveal, in a rather spectacular way, the results that can be obtained by a combination of multispectral remotely sensed data, visual observations from manned spacecraft, and ocean data gathered by ships and aircraft. From all these data, the oceanography southwest of Spain and in the Alboran Sea has been determined as never before (fig. 32). A strong ocean front has been defined and named (Huelva Front), a large (148 × 334 km (80 × 180 n. mi.)) shallow eddy has been recognized (Tarif Eddy) (fig. 33), and an eddy chain has been identified. Because of the interrelationship, information on the life history, origin, and physical characteristics of the fronts and eddies is not only of academic interest, but also of direct value to fisheries and all other marine activities.

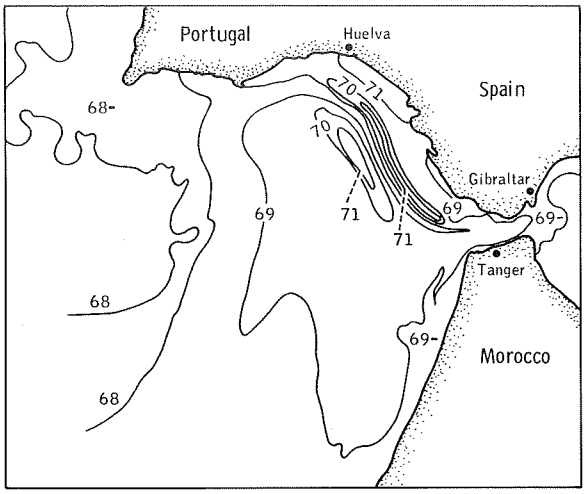


FIGURE 32.—Isotherms depicting sea-surface temperatures (in Fahrenheit) of the waters in the western approaches to Gibraltar. Compiled from data gathered July 15 to 26, 1975, from the U.S.N.S. *Kane*, the U.S. Navy P-3 aircraft, and the DMSP.

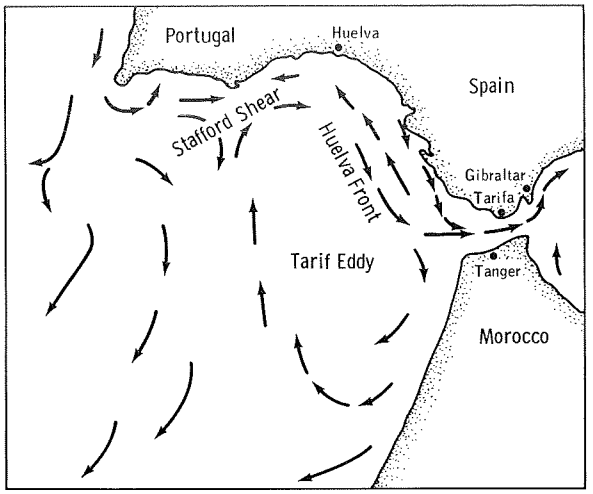


FIGURE 33.—Ocean currents in the western approaches to Gibraltar (July 15 to 26, 1975) as interpreted from DMSP infrared imagery.

CONCLUSIONS

In the experiment of visual observations of the ocean, conducted during ASTP by the Office of Naval Research, the aim was to carefully design an Earth observation program to fully evaluate the ability of man to contribute to a better understanding of oceanography. From the standpoint of the Navy's interest, it was important to learn whether astronauts could be trained to observe specific features that were of direct interest to the Navy—in specific areas at a specific time. In all aspects, the Office of Naval Research considers the experiment to have been highly successful, to have answered all the questions originally posed, and to have provided an excellent background for developing further observational programs during the Space Shuttle era.

By rejecting irrelevant information and concentrating on the particular feature for which they are looking, properly trained men have remarkable abilities to mentally process large amounts of data. Man's ability to select important features is large. Once a particular type of target is selected, he can make decisions on the specific qualitative measurements that should be made and on the importance of the data that will be received. The descriptive material, which man can provide, often places quantitative measurements in an overall framework that makes the observations more important.

It is always impossible to fully plan for all the observations that would be desirable from space. Disasters and natural phenomena (such as severe weather conditions, forest fires, volcanic eruptions, earthquakes, tsunamis, floods, and major oil spills) can all be observed from space, but cannot be preplanned for any given mission, whether manned or unmanned. The advantage of having a trained observer available in the spacecraft is that he can continuously modify "look directions" of the instruments, change the illumination angle, and select specific measurement devices for any unanticipated observation. This was clearly shown to be the case not only during the Apollo-Soyuz Test Project but also during earlier observations made during the Skylab 4 mission.

When looking ahead to the Space Shuttle observational program, one recognizes that the size, weight, capability, and power availability on the Space Shuttle makes it possible to carry a greater variety of observational instrumentation than is practical on all unmanned spacecraft. The utilization of the data returned from operating all these

instruments continuously would not be practical in terms of present, or anticipated, analysis capabilities. The ability to select and operate the "right instruments" at the "right time" for solving particular problems would be one of the greatest attributes of having trained observers present in the spacecraft. Decisions could be based on inferences made by looking ahead of the track of the spacecraft, by making observations on previous orbits, or from information transmitted from the ground to the orbiting Space Shuttle.

It is expected that, during the Space Shuttle Program, experiments will be planned so that data can be obtained from unmanned satellites by direct transmission with satellite to ground and to Shuttle, so that the manned and unmanned satellite systems can be evaluated and used in concert with each other. This capability would allow advance information on particular regions of the Earth where additional and more detailed observations should be obtained. The optimum observational tools could then be ready and operating when the Space Shuttle is in a proper position to function most effectively.

REFERENCES

1. Stevenson, Robert E.: Observations From Skylab of Mesoscale Turbulence in Ocean Currents. Nature, vol. 250, no. 5468, Aug. 23, 1974, pp. 638-640.

2. Nilsson, C. S.; Andrews, J. C.; and Scully-Power, P.: Observations of Eddy Formation off East Australia. J. Phys. Oceanogr., vol. 7, no. 5, 1977, pp. 659-699.

BIBLIOGRAPHY

Andrews, John C.; and Scully-Power, Paul: The Structure of a East Australian Current Anticyclonic Eddy. J. Phys. Oceanogr., vol. 6, no. 5, 1976, pp. 756-765.

Scully-Power, P.; and Twitchell, P.: Satellite Observation of Cloud Patterns Over East Australian Current Anticyclonic Eddies. Geophys. Res. Letters, vol. 2, no. 3, Mar. 1975, pp. 117-119.

Stevenson, R. E.: Huelva Front and Malaga, Spain, Eddy Chain as Defined by Satellite and Oceanographic Data. Deutschen Hydrographischen Zeitschrift, vol. 30, no. 2, 1977, pp. 51-53.

Stevenson, Robert E.; Carter, L. David; Vonder Haar, Stephen P.; and Stone, Richard O.: Visual Observations of the Ocean. Sec. 11 of Skylab Explores the Earth. NASA SP-380, 1977, pp. 287-338.

Maltese Front and Strait of Sicily Ocean Pattern Analysis

Daniel Jean Stanley [a]

ABSTRACT

Ocean-surface phenomena related to turbulence, including possible internal waves, are observed in Apollo-Soyuz Test Project (ASTP) color photographs of the eastern part of the Strait of Sicily between Djerba and the southeastern corner of Sicily. The convergence of the eastward-flowing, less-saline upper water of Atlantic origin and the denser "Intermediate Water" flowing underneath it in the opposite direction gives rise to the Maltese Front clearly visible off Cape Passero, Sicily. This investigation shows that the geographic position of these ocean-surface features is in part related, as previously suggested, to sea-floor topography. The vertical coverage made from an altitude of 226 km allows good definition of turbulence phenomena and serves to supplement earlier physical oceanographic observations made of the central region of the Mediterranean Sea.

INTRODUCTION

This study describes ocean-surface features recorded in a series of Apollo-Soyuz Test Project (ASTP) color photographs taken over the eastern part of the Strait of Sicily. The region examined is in the central Mediterranean Sea and extends between the southeastern coast of Tunisia and the southeastern tip of Sicily. The photographs cover a southwest-to-northeast (SW-NE) belt approximately 120 km wide and 720 km long (fig. 1). Water masses in this region flow through a relatively shallow (for the most part, less than 500 m deep) and geographically constrained area that is located between deep basins. The slope bordering the eastern part of the Strait of Sicily extends to a depth of approximately 3900 m in the Ionian Sea; the Malta Escarpment refers to the steepest part of this slope in the area off southeastern Sicily. The Ionian Sea is the part of the Mediterranean that occupies the region between Libya, southern Italy, and western Greece; it is contiguous with the Levantine Basin forming the easternmost Mediterranean. The western part of the Strait of Sicily is also bounded by steep slopes that extend northward into the Tyrrhenian Sea (approximately 3400 m deep) north of Sicily and that extend westward into the Algéro-Balearic Basin (approximately 2800 m deep) north of Tunisia. Thus, the Strait of Sicily is envisioned as a major sill that topographically separates several deep basins in the central part of the quasi-enclosed Mediterranean Sea.

The superposition of water layers that flow in opposite directions is one of the striking aspects of the Mediterranean circulation pattern, which has long attracted the attention of physical oceanographers. Less-saline water enters the Strait of Gibraltar from the Atlantic and can be traced hundreds of kilometers as it flows eastward along the African coast to the Levantine Basin. A denser water mass ("Intermediate" or "Levantine Water") lies beneath the "Atlantic Water" and flows toward the west; it eventually moves across the Strait of Sicily and Strait of Gibraltar sills, and flows into the Atlantic where it retains its saline warm water characteristics (fig. 2).

[a]Division of Sedimentology, Smithsonian Institution.

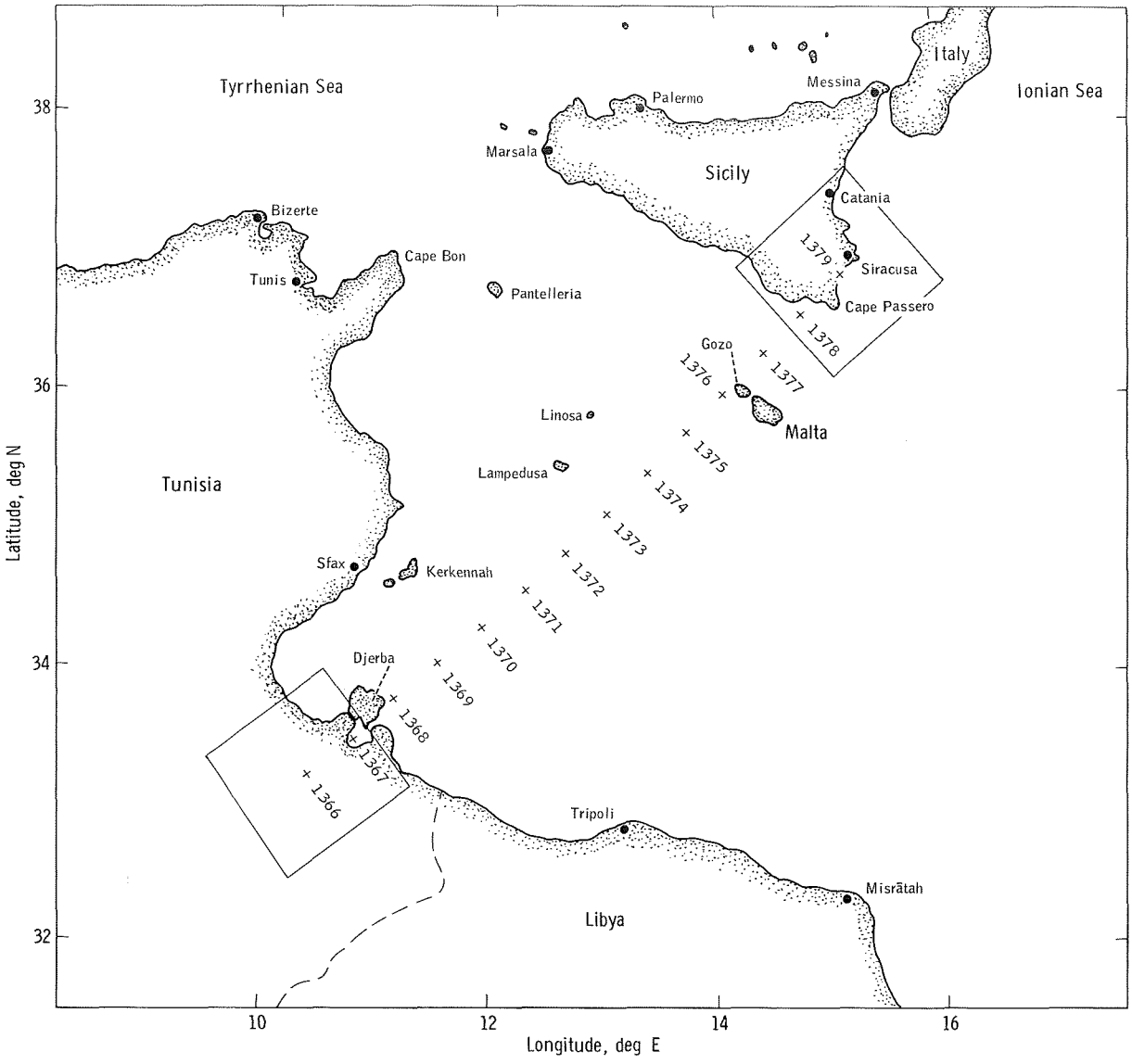


FIGURE 1.—Map showing locations of ASTP photographs taken over the eastern Strait of Sicily. (Numbers are the last digits in the ASTP photograph number, e.g., AST-17-1379.)

The driving force of this circulation system is usually discussed in terms of the overall balance between runoff, precipitation, and evaporation; i.e., the excess of evaporation (−1440 mm/yr) relative to rainfall and runoff (+469 mm/yr) that gives rise to a negative (−971 mm/yr) balance (values according to Gerges, ref. 1). The Atlantic Ocean provides a permanent source of water that is entrained into the Mediterranean to compensate for the loss of water by evaporation, thus maintaining the two-layer system. Generalized Mediterranean oceanographic patterns have been depicted by Lacombe and Tchernia (ref. 2, also see fig. 2) and Wüst (ref. 3); more detailed profiles of the water masses in this land-bound body are presented by Miller et al. (ref. 4).

This report evaluates the ASTP photographic data for the eastern Strait of Sicily, which bears on the problem of water mass convergence and associated turbulence in the central Mediterranean.

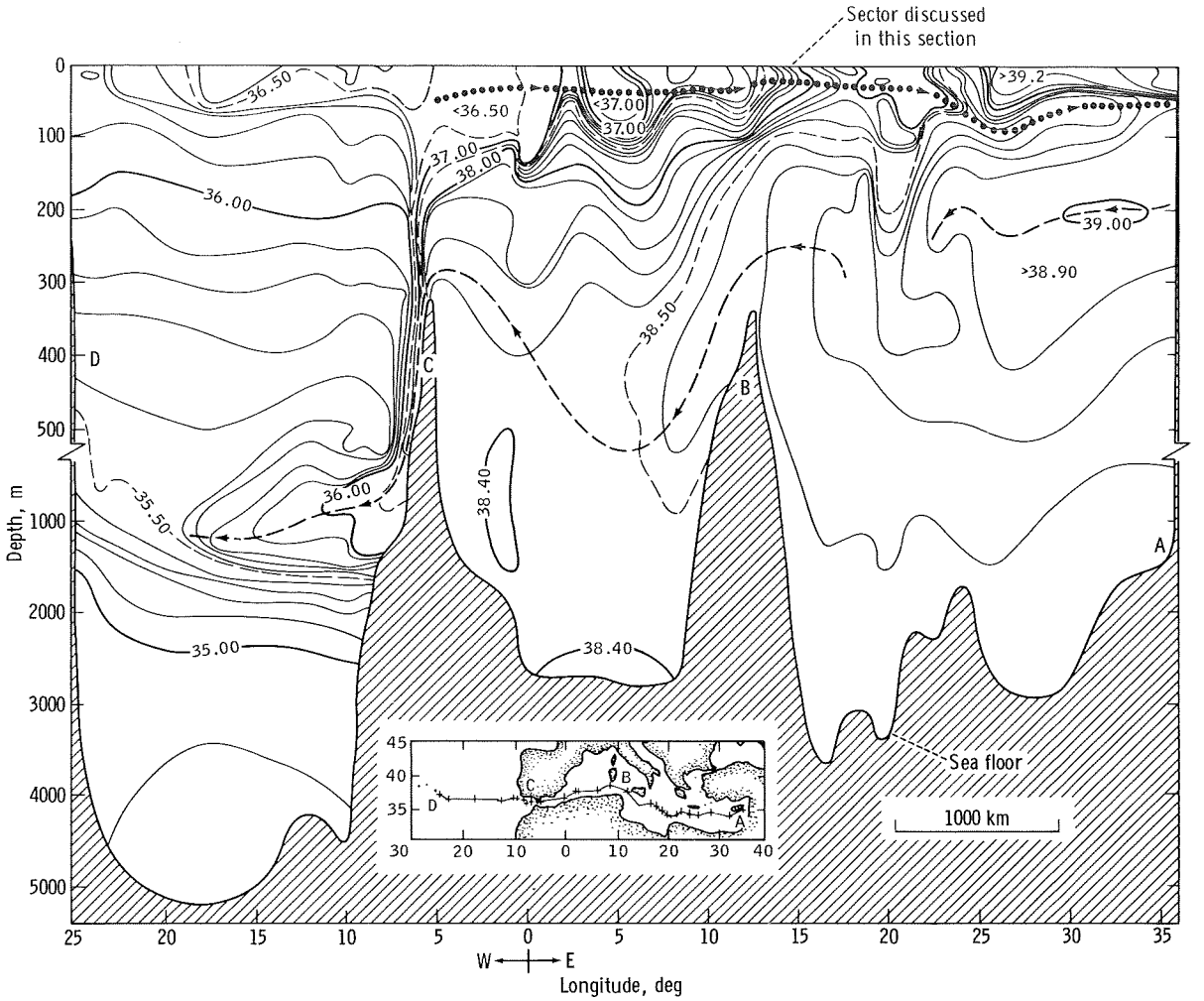


FIGURE 2.—Major water-mass circulation patterns (summer) in the Mediterranean Sea, after Lacombe and Tchernia (ref. 2). The profile shows "Atlantic Water" flowing eastward over westward-flowing "Intermediate Water" at the Strait of Sicily (point B). (Numbers are salinity in parts per thousand.)

MALTESE FRONT

Considerable attention has been given to the characteristic Mediterranean two-layer regime in the Strait of Gibraltar (ref. 5). More recently, investigations have begun to interpret the current flow and exchange patterns in the Strait of Sicily (ref. 6). This long, shallow platform acts as a sill partially separating the deep Mediterranean basin to the east (Ionian Sea) from the western basins (Algéro-Balearic Basin and Tyrrhenian Sea). As in the Strait of Gibraltar, it has been demonstrated that warm, saline (approximately 38.7 °/oo) "Intermediate Water" formed in the Levantine region flows from the Ionian Sea in a westerly direction through the Strait of Sicily underneath the east-

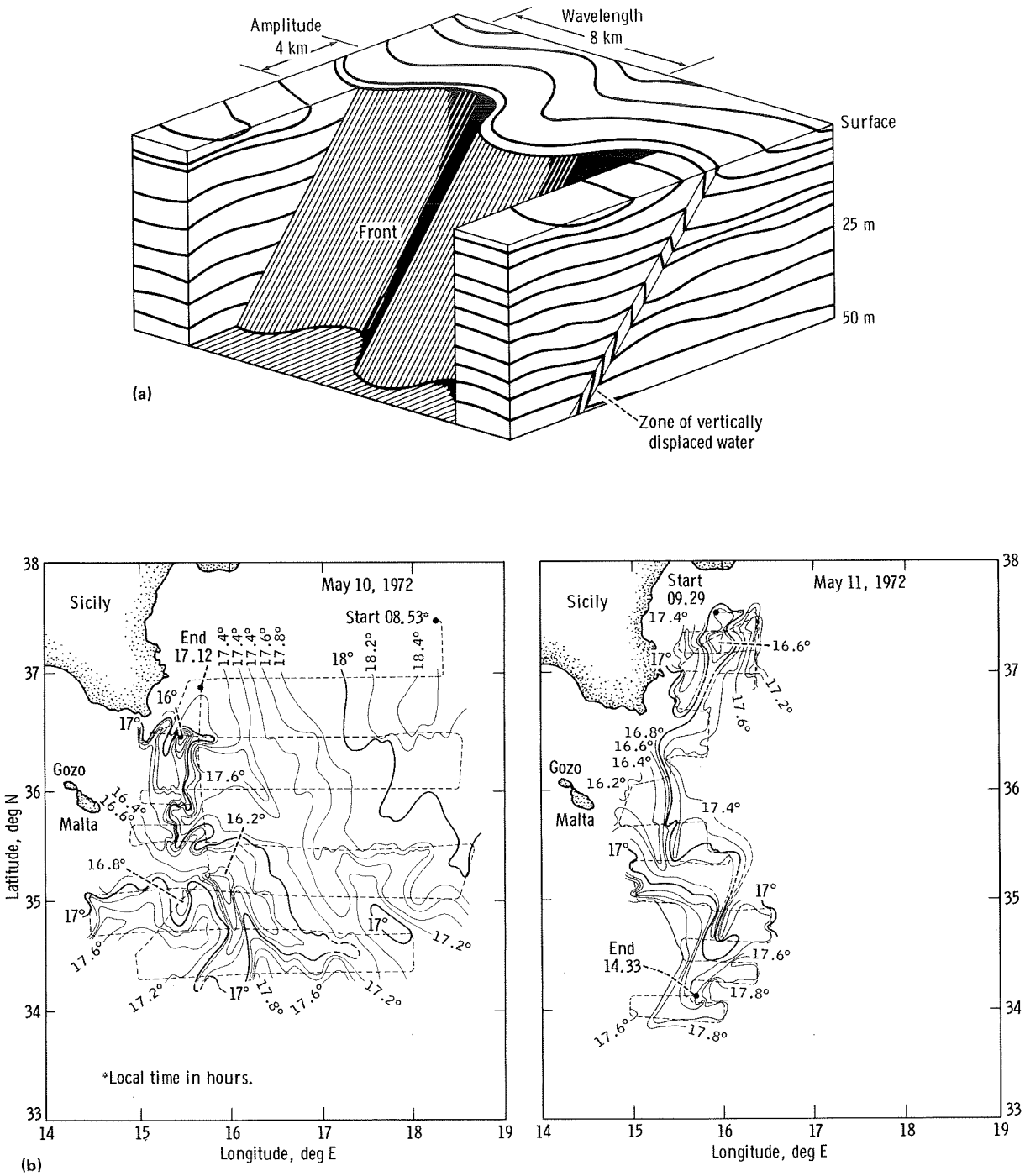


FIGURE 3.—Internal wave structure and sea-surface isotherms. (a) Diagram showing upwelling and downwelling and formation of waves on a front in the thermocline (from Woods, ref. 7). (b) Sea-surface isotherms from ART measurements off southeastern coast of Sicily in May 1972 (after Briscoe et al., ref. 9). Isotherms are in Celsius (K = °C + 273.15).

ward-flowing, less-saline (approximately 37.4 °/oo) water, mostly of Atlantic origin. Furthermore, it is postulated that the formation of large-amplitude internal waves results as one water mass flows above the other, also that turbulence should be expected at the water layer interfaces in the zone of convergence. (Theoretical considerations of this problem are presented in reference 7.) Of particular interest is the possibility of features at the ocean surface produced by upwelling and downwelling motions that occur as deep water is displaced upward and tongues of shallow water are entrained downward (fig. 3(a)).

Previous studies, in fact, have revealed an important north-south contact zone between two water masses at the ocean surface east of the island of Malta and off the southeasternmost tip of Sicily. This phenomenon was observed by shipborne expendable bathythermographs, towed shipborne temperature probes, and airborne infrared radiation thermometers (ART). This water mass boundary, identified by Woods and Watson (ref. 8) as the Maltese Front, appears to parallel the NNW-SSE trend of the eastern Strait of Sicily shelf break (fig. 3(b)). The shelf-to-slope break extends along the Malta Escarpment, from Siracusa, Sicily, at approximately 37° N, 15°20′ E southward to approximately 35°30′ N, 17°30′ E.

Briscoe et al. (ref. 9) suggest that the Maltese Front is in part related to the sea-floor topography, although its position is a mobile one; i.e., in winter the Maltese Front has been observed approximately 175 km east of Sicily, whereas in summer it is close to the shelf break and the island of Malta. Observations at sea indicate a salinity and temperature minimum west of a salinity-temperature jump and an inversion on bathythermograph profiles along the front. A series of high quality ASTP color photographs provides partial coverage of the eastern sector of the Strait of Sicily where this phenomenon has been identified, and the photographs show ocean-surface patterns related to circulation in this zone of convergence.

OBSERVATIONS

Fourteen photographs (AST-17-1366 to 1379) were obtained along a southwest to northeast tran-

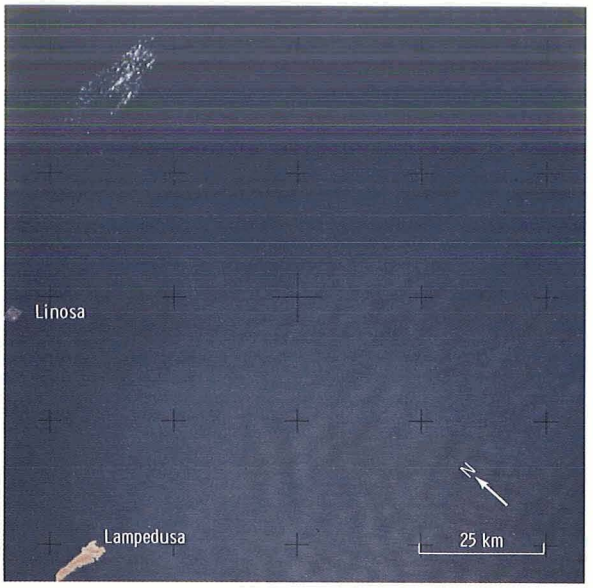


FIGURE 4.—An ASTP photograph showing intersection of large NE-SW waveforms (possible internal waves) and much smaller NW-SE trending surface waves. The islands of Linosa (3.5 km long) and Lampedusa (11 km long) provide a scale (AST-17-1374).

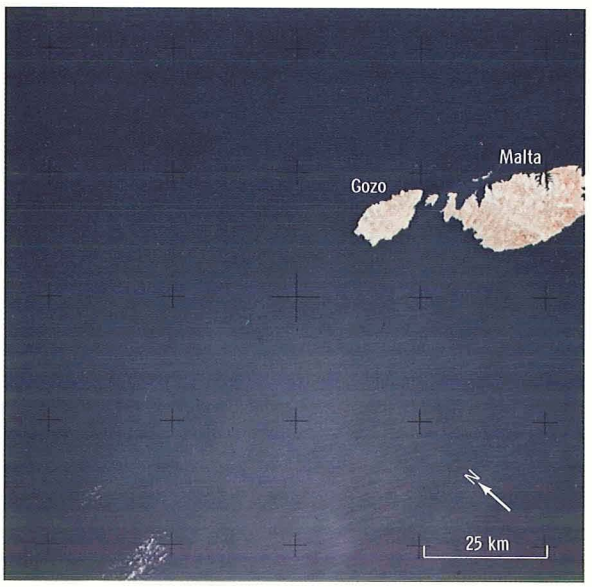


FIGURE 5.—This ASTP photograph shows the islands of Malta and Gozo and the predominant pattern of small wind-driven surface-wave patterns. Gozo, approximately 15 km in length, provides a scale (AST-17-1376).



FIGURE 6.—Truncation of wave patterns in ASTP photographs delineates the Maltese Front (large arrow) south of Cape Passero on Sicily's southeastern corner. The Maltese Front configuration is particularly well shown in the sunglint in part "a." Note the sliver of cloud cover coincident with the front. Small arrows show displacement of suspended sediment in the coastal sector. (a) Photograph AST-17-1379. (b) Photograph AST-17-1378.

sect passing over the islands of Djerba, Kerkennah, Lampedusa, Linosa, Gozo, Malta, and the southeastern part of Sicily. The near-vertical photographs were taken consecutively at an altitude of 226 to 228 km at 12:17 to 12:19 UT on July 20, 1975, on spacecraft revolution 72. The surface covered by each photograph is approximately 120 by 120 km (figs. 4 to 7). Lighting is such that physical oceanographic features are most clearly apparent in the lower half of each photograph (Sun angle = 70°). The ample overlap of photographic coverage permitted the investiga-



FIGURE 6.—Concluded.

tor to make a continuous and relatively detailed depiction of the wave patterns along the transect. The data, summarized in figure 8, reveal the following:

1. Long, broad waveforms trending SW-NE prevail along the transect from approximately 30 km northeast of Djerba to approximately 20 km south of Malta and Gozo. Their crest-to-crest measurements range from approximately 1 to 3 km (most often approximately 2 km); wave crests are gently sinuous and appear to anastomose locally (fig. 4).

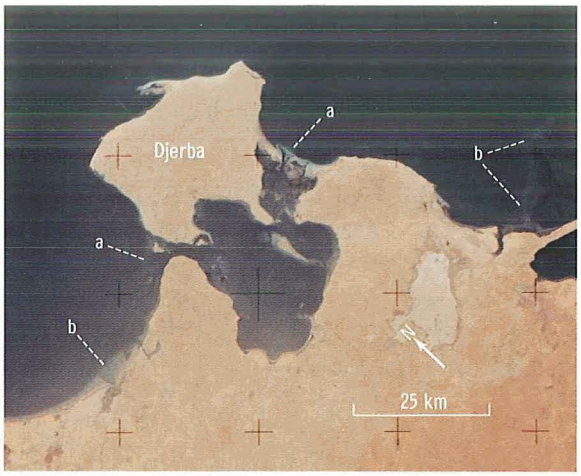


FIGURE 7.—Part of an ASTP photograph showing the island of Djerba off the southeastern coast of Tunisia. Points "a" indicate a series of channel and wash-over fan systems; points "b" indicate submarine bed forms (presumably sand) on the shallow inner Tunisian shelf (AST-17-1367).

2. A dense network of much smaller NW-SE oriented waves (crest-to-crest measurements of approximately 0.5 km or less) intersects the prominent set of broad SW-NE trending waveforms described in item 1 (fig. 4); these smaller waves become the dominant surface feature approximately 30 km south of the islands of Malta and Gozo (fig. 5).

3. The dense network of small surface-wave crests trends WNW-ESE between Malta/Gozo and Cape Passero on Sicily's southeast coast. This pattern is abruptly truncated by the SSE trending surface-wave patterns off Cape Passero that are clearly visible in photographs AST-17-1378 and AST-17-1379 (fig. 6). The sunglint in the latter photograph is particularly useful in revealing the details of this phenomenon (fig. 6(a)). Also noted is the narrow sliver of cloud cover coincident with the ocean-surface boundary.

4. Also visible is evidence of active coastal-sediment transport: (a) a series of channel and wash-over fan systems in the vicinity of Djerba (fig. 7, points "a"); (b) sediment (presumably sand of largely bioclastic origin, cf., ref. 10) entrainment and submarine bed forms on the shallow inner Tunisian shelf (fig. 7, points "b"); and (c) suspended sediment plumes off the southeastern coast of Sicily, displaced toward the east and the northwest (fig. 6, small arrows).

DISCUSSION

The remarkable variation in the configuration of ocean-surface features observed along the Djerba-to-Sicily transect indicates more than a simple wind-driven pattern. The large waveforms at and just below the surface with crests oriented SW-NE that prevail in the Sicily Strait proper (i.e., particularly between the islands of Kerkennah and Linosa) may represent internal waves. Such features would result from shear induced at the interface between the southeast flowing, less-saline, upper water mass and the deeper, northwest flowing "Intermediate Water," as the latter moves onto the shallow platform. In contrast, the small NW-SE oriented waves intersecting the SW-NE waveforms reflect the dominant wind pattern.

The change in wave flow pattern, observed in the vicinity of the island of Malta, indicates surface turbulence and shear produced at the convergence between the two superposed water masses that flow in opposite directions. The prevailing NW-SE wave-crest patterns south of Malta and Gozo may be related to the influence of submarine topography; that is, an alinement with the NW-SE trend of the southern margin of the shallow South Sicily Bank on which the islands lie. The even more obvious truncation of surface forms, along a NNW-SSE trending zone northeast of Malta and Gozo, occurs near the outer Strait of Sicily platform and closely parallels the Malta Escarpment (fig. 8). Based on the available information collected at sea, it is suggested that this truncation phenomenon indicates the surfacing of internal waves.

The ASTP photographs also provide evidence of active sediment displacement along both coastal margins, but the photographs provide no information on sediment transport in the more open sectors of the Strait of Sicily. The surficial sediment depositional patterns (ref. 11) indirectly suggest that material is being actively transported on the South Sicily and Medina Bank area east of Malta. Furthermore, it is conceivable that the dis-

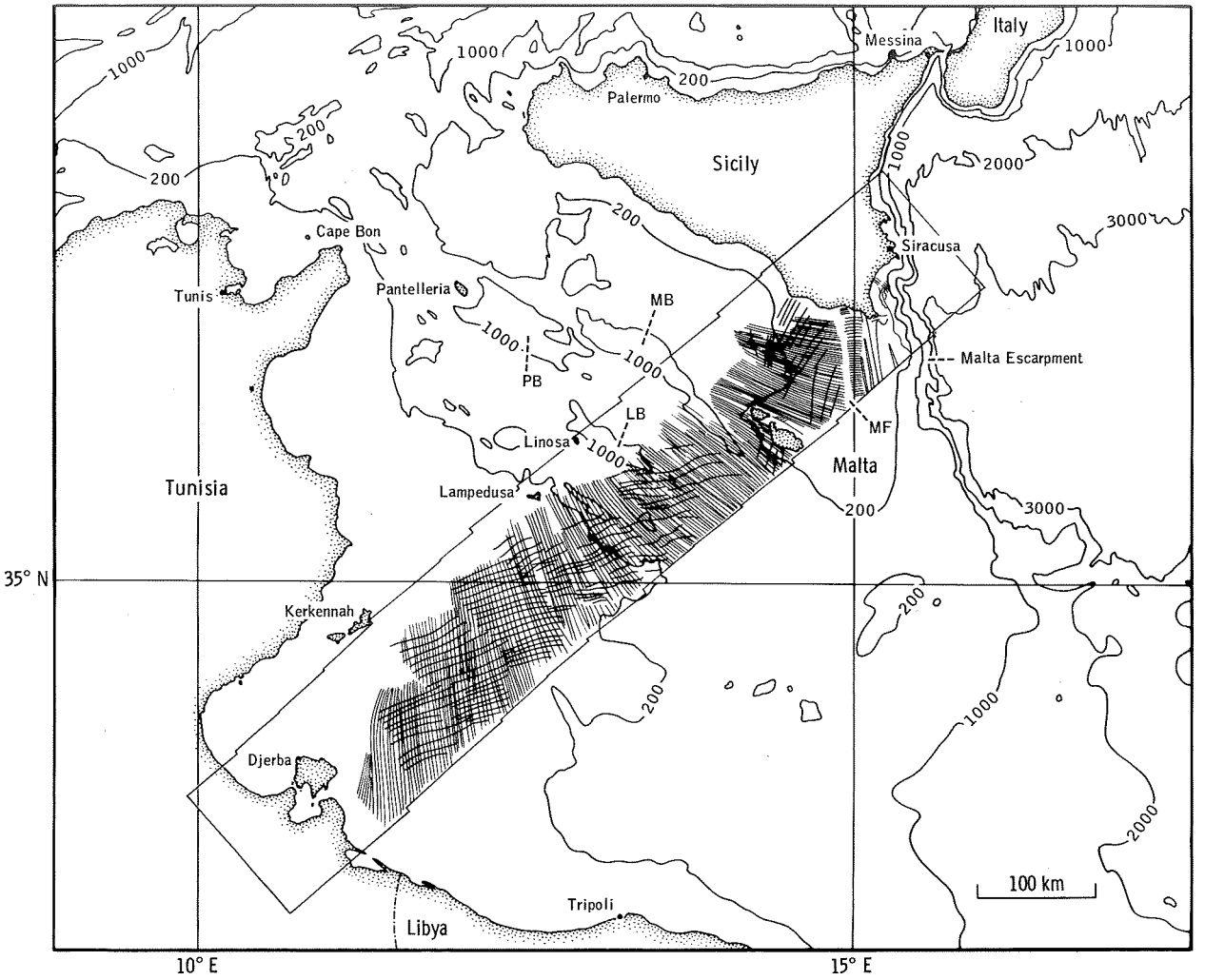


FIGURE 8.—Bathymetric chart of the eastern Strait of Sicily showing schematically the configuration of ocean-surface patterns described in the text and derived from ASTP photographs. Depth is given in meters. Note the position of the Maltese Front relative to the Malta Escarpment. (PB = Pantelleria Basin, LB = Linosa Basin, MB = Malta Basin, and MF = Maltese Front.)

tribution of major sediment types (sand, clayey mud, and calcareous ooze) in the eastern Strait of Sicily (as depicted by Akal, ref. 12, and Maldonado and Stanley, ref. 13) and the increased concentrations of suspensates in near-bottom waters (ref. 14) are related to the Maltese Front. The possible effects of turbulence and internal waves on sea-floor erosion and sediment transport in this region clearly require further study.

CONCLUSIONS

In summary, the color photographs record the presence of a zone of convergence and vertical mixing south of Sicily; they indicate that the position of this surface turbulence in July 1975 was relatively close to the position of the Maltese Front. The ASTP mission shows that the Maltese Front and related broad, regionally important

physical oceanographic patterns at, and near, the ocean surface can be successfully monitored from space. The use of multispectral photographic techniques is recommended on future missions to document more detailed patterns of the Maltese Front migration and evolution.

ACKNOWLEDGMENTS

This report is part of the Mediterranean Basin (MEDIBA) Project, which was funded in part by Smithsonian Research Foundation grant 71702120. Thanks are expressed to Dr. J. W. Pierce, U.S. National Museum of Natural History, Smithsonian Institution, for reviewing the manuscript.

REFERENCES

1. Gerges, M. A.: Analogy in the Oceanographic Processes in the Mediterranean Sea and Estuaries. (Processus de Formation des Eaux Océaniques Profondes, Paris, France, Oct. 4 to 7, 1972.) Colloq. int. Centre nat. Rech. Sci., No. 215, 1974, pp. 147-154.

2. Lacombe, H.; and Tchernia, Paul: Quelques traits généraux de l'hydrologie Méditerranéenne. Cahiers Océanog., vol. 12, 1960, pp. 528-547.

3. Wüst, Georg: On the Vertical Circulation of the Mediterranean Sea. J. Geophys. Res., vol. 66, no. 10, 1961, pp. 3261-3271.

4. Miller, A. R.; Tchernia, P.; and Charnock, H.: Mediterranean Sea Atlas. Woods Hole Oceanog. Inst. Atlas Series, vol. 3, 1970.

5. Lacombe, H.: Contribution á l'étude du régime de Détroit de Gibraltar. I, Etude dynamique. Cahiers Océanog., vol. 13, 1961, pp. 73-107.

6. Allan, T. D.; Akal, T.; and Molcard, R., eds.: Oceanography of the Strait of Sicily. SACLANTCEN Conf. Proc. 7, 1972, pp. 177-192.

7. Woods, J. D.: The Structure of Fronts in the Seasonal Thermocline. Oceanography of the Strait of Sicily, T. D. Allan, T. Akal, and R. Molcard, eds. SACLANTCEN Conf. Proc. 7, 1972, pp. 144-152.

8. Woods, J. D.; and Watson, N. R.: Measurement of Thermocline Fronts From the Air. Underwater Sci. Tech. J., vol. 2, 1970, pp. 90-99.

9. Briscoe, M. G.; Johannessen, O. M.; Vincenzi, S.; and Furnes, G.: The Maltese Oceanic Front: A Surface Description by Ship and Aircraft. Oceanography of the Strait of Sicily, T. D. Allan, T. Akal, and R. Molcard, eds. SACLANTCEN Conf. Proc. 7, 1972, pp. 153-175.

10. Poizat, Claude: Hydrodynamisme et sédimentation dans le Golfe de Gabès (Tunisie). Tethys, vol. 2, no. 1, 1970, pp. 267-296.

11. Blanc, J. J.: Sédimentologie sous-marine du Détroit Siculo-Tunisien: Campagnes de la Calypso. Résultats Scientifiques des Campagnes de la Calypso, Inst. Océanog. Annals, 1958, pp. 91-126.

12. Akal, T.: The General Geophysics and Geology of the Strait of Sicily. Oceanography of the Strait of Sicily, T. D. Allan, T. Akal, and R. Molcard, Eds. SACLANTCEN Conf. Proc. 7, 1972, pp. 177-192.

13. Maldonado, A.; and Stanley, D. J.: Late Quaternary Sedimentation and Stratigraphy in the Strait of Sicily. Smithsonian Contr. Earth Sciences, no. 16, 1976.

14. Pierce, J. W.; and Stanley, D. J.: Suspended-Sediment Concentration and Mineralogy in the Central and Western Mediterranean and Mineralogic Comparison With Bottom Sediment. Mar. Geol., vol. 19, no. 2, 1975, pp. M15-M25.

Ocean Color Observations

C. S. Yentsch,[a] W. Skea,[a] J. C. Laird,[a] and T. S. Hopkins[a]

ABSTRACT

Before the Apollo-Soyuz mission, the Apollo astronauts were briefed on four features that could alter ocean color: (1) phytoplankton chlorophyll, (2) dissolved yellow substance, (3) suspended sediments, and (4) bottom reflection. Photographs and observations of the Orinoco River Delta documented dissolved yellow substance and sediments in suspension. An example of discoloration by nonorganic sediments (red clays) was provided by photographs of a Canadian fjord. Photographs and observations of the Cape Cod area provided examples of data on the bathymetry in waters of average transparency.

Before and during the mission, the crew was alerted to the possibility of a red-tide occurrence along the coast of New England. However, they were unable to obtain useful photographs because of heavy fog and cloud cover.

The astronauts were successful in observing ocean discolorations, and the crew's verbal comments indicate that they were aware of the causes and sources of these color changes. Experience on this mission suggests that ground crews can work with astronauts in attempts to locate discolorations and to determine their extent and their sources.

INTRODUCTION

Some investigators have been skeptical about the usefulness of ocean color measurements obtained during Earth orbit, an opinion based largely on the difficulties relative to observations through the Earth's atmosphere. However, astronauts have consistently noted water discolorations; and, as a result of briefings with oceanographers, they have become aware of the causes of discoloration and have been alerted to the areas in which these discolorations occur.

The objectives of this study were to investigate the following questions.

1. Do astronauts see color changes in the oceans and can these changes be recorded on film?
2. Where are these color changes seen?
3. Can the cause of the discoloration be explained without the aid of ground inspection?
4. Are there other visual signals associated with color that can aid in the identification of discoloration?
5. Can the astronauts direct a ground investigation team in a manner that aids in determining the cause of the color or, conversely, can a ground observer direct the astronauts?

Before reviewing the photographic data obtained during the Apollo-Soyuz Test Project (ASTP) mission, the following section is presented to outline the factors affecting ocean color and to emphasize the problems associated with visual detection of ocean color.

PHYSICAL AND BIOCHEMICAL FACTORS INFLUENCING OCEAN COLOR

This section discusses "remote measurement" in which visible light returning from a water column is viewed by an airborne detector; in this case, the human eye. Included in this definition is the restriction that the eye is not seeing light scat-

[a]Bigelow Laboratory for Ocean Sciences, West Boothbay Harbor, Maine.

tered from the sea surface; it is seeing only light coming out of the water. This light is upwelling irradiance E_u and is the upward component of the total scattering within the body of water. The amount of E_u is equal to the amount of downwelling light E_d, minus light removed by absorption, plus that added by scattering.

$$E_u = E_d - (A_w + A_{p_o} + A_{p_i} + A_d) + (B_{p_o} + B_{p_i})$$

where A is attenuation and the subscripts w, p_o, p_i, and d designate water, phytoplankton, nonliving particles, and yellow substance, respectively. The term "yellow substance," or Gelbstoff, denotes dissolved organic material, usually carbohydrate-humic acids, formed by the decomposition of organic matter. It is distinguished from other dissolved organic material by light absorption at short wavelengths. The terms B_{p_o} and B_{p_i} represent scattering by phytoplankton and nonliving particles, respectively. The total reflectance R of the water column is the ratio E_u/E_d and is usually given as a percentage; e.g., for the open ocean, $R \approx 5$ percent.

The factors modifying the wavelengths of visible light can now be examined. In the open ocean, water is the dominant absorber. However, as one moves to coastal waters, both phytoplankton and yellow substances increase and thus change the water color by absorbing in the regions where water is the most transparent. Figure 1(a) is the attenuation curve for pure seawater, figure 1(b) is the curve for phytoplankton (cellular chlorophyll), and figure 1(c) is the curve for dissolved yellow substance. The other components of water color (A_{p_i} and B_{p_i}) are poorly defined and controversial. Most marine scientists agree that scattering *per se* is mostly nonselective in wavelength or, stated differently, wavelength selection is primarily by absorption.

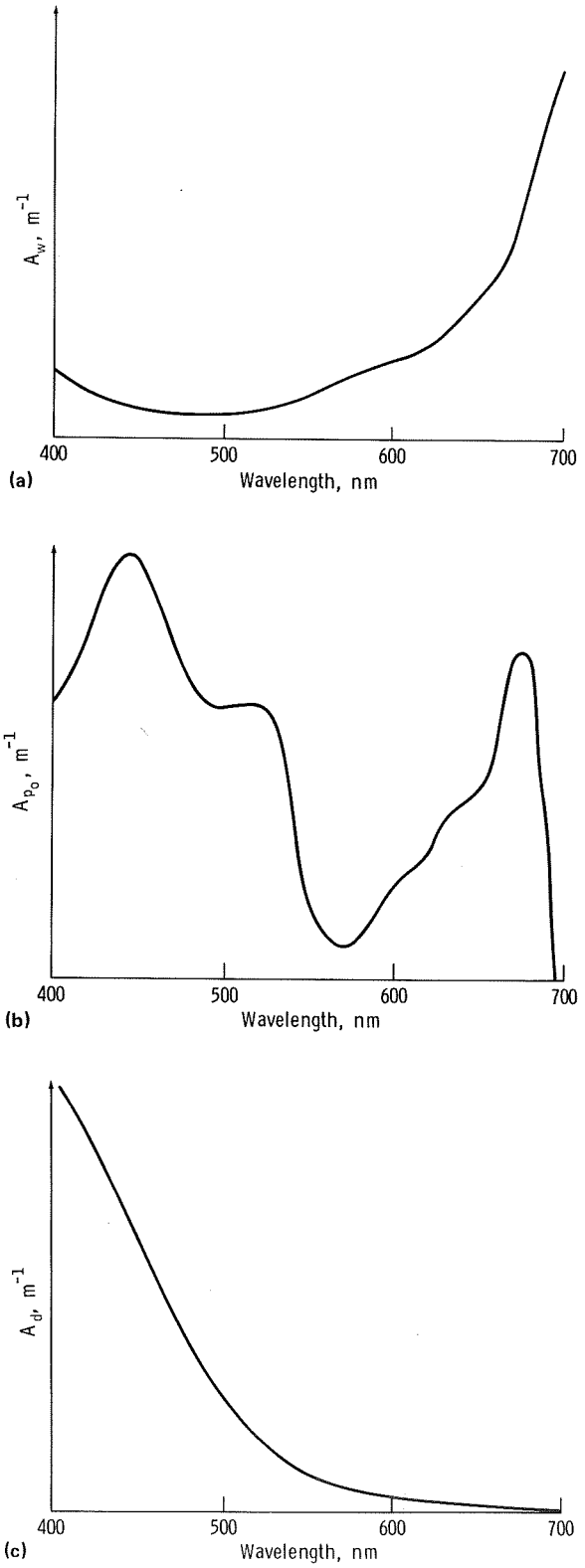


FIGURE 1.—Diagram of attenuation A per meter depth as a function of visible wavelength for ocean water illustrating the effect on water color of suspended and dissolved materials. Attenuation refers to the reduction of light by scattering plus absorption and increases with water depth. (a) Seawater. (b) Phytoplankton algae suspended in seawater. (c) Yellow substance dissolved in seawater.

The question of how well the eye sees changes in water color can now be addressed. Figure 2 shows curves characteristic of upwelling irradiance from blue open ocean water, slope water, and coastal waters that are green and turbid. Superimposed on this figure is the spectral sensitivity for the human eye. Figure 2 demonstrates that over a wide range of ocean color, the eye is a good detector. For example, between the wavelengths of maximum irradiance for the two ocean colors, there is a difference of approximately 150 nm. This difference lies in the region of maximum sensitivity for the human eye.

Next, is it possible for the eye to distinguish between the cause or causes of the total discoloration? The answer to this question is based on the absorbing characteristics of the components and on their relative concentrations. At best, one can say that it would be difficult to distinguish them, because all of the absorbers are strong in the blue, short-wavelength region, where water is the most transparent. Thus, one can conclude that color change arises because of a single occurrence or a combined mixture of phytoplankton and yellow substance, but the eye cannot distinguish between the different components of the discoloration.

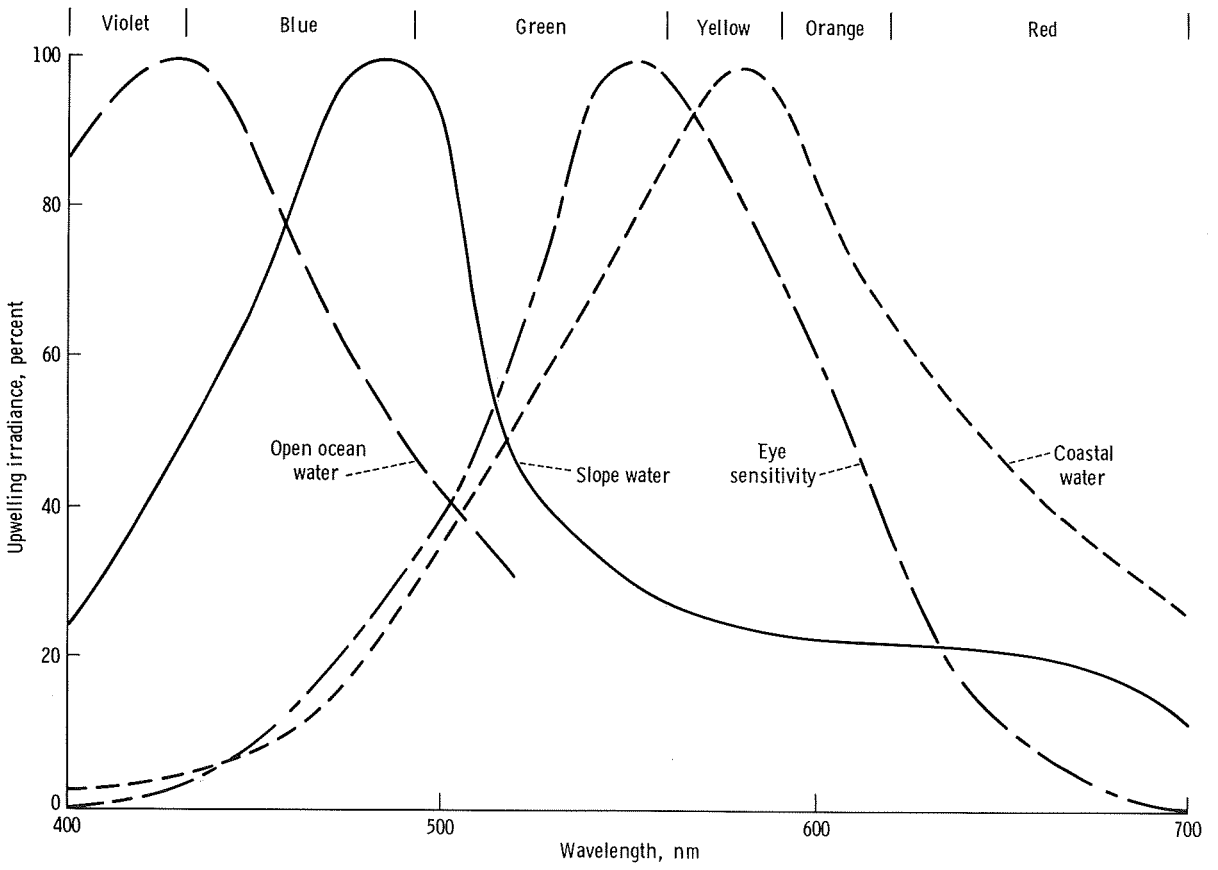


FIGURE 2.—Plot of upwelling irradiance of ocean water as a function of visible wavelength showing the spectral sensitivity of the human eye for comparison with the various water colors.

Bathymetry and Apparent Color

The high-altitude observer can also see water-color changes that, because of bottom reflection, can be termed "apparent color change." In very "pure" ocean water with a highly reflective bottom, the color of the water can be seen to change as a function of depth. In shallow water, the upwelling light (E_u) will be green; in deeper water, the color will shift to blue. This shift is accompanied by a decrease in total returning light, and the final disappearance of bottom reflection will appear to the observer as a distinct phenomenon. Some ASTP photographs show the influence of bottom reflection on water color.

As mentioned previously, the high-altitude observer sees an "apparent water color" due to the reflective characteristics of the bottom. In most areas of the world's oceans, the authors believe that these characteristics will not cause confusion with inherent water color for the following reasons.

1. Bottom reflection is distinctive, whereas that of real water-color substances, such as chlorophyll and yellow substance, are not.
2. In waters of low transparency, the signal from the suspended materials will greatly attenuate that from the bottom.
3. In the last analysis, photographic evidence can be checked against hydrographic relief.

With these points in mind, selected photographs taken by the Apollo crew have been used to demonstrate the influence of the ocean bottom on water color.

The astronauts photographed a section of the eastern coast of the United States starting from Rhode Island and ending north of the Canadian border. Photographs of some areas, because of heavy fog and mist, were unusable. However, a good series of photographs was obtained around Cape Cod (fig. 3) and Nantucket Shoals (fig. 4). In the photograph of Cape Cod (fig. 3), the contrast between the spit and the surrounding sea is largely due to the border of white sand beaches and dunes. The photograph suggests that the reflectance of the vegetation in the interior of the cape is about the same as the reflectance of the surrounding water. The major concentration of dunes is at the tip of the cape near Provincetown and off Barnstable Harbor (on Sandy Neck). Most of the shallow ocean-bottom area appears on the Massachusetts Bay side and gives this area a light-green cast. Some of the best examples can be seen in Provincetown Harbor, Wellfleet Harbor, and Barnstable Harbor. On the basis of known hydrographic data for the region, these depths (clearly visible) are on the order of 0.75 m.

Another example of the underwater topography of the area is Nantucket Shoals (fig. 4). At the northern end of Nantucket is a group of shoals known as Tuckernuck; many sailors have been baffled by their complexity. Their outlines in the photograph are delineated by the 0.75-m bottom contour. In the photograph, there is some suggestion that either the bottom is more reflective or that the water is more transparent than around Cape Cod.

Yellow Substance and Dissolved Organics

One of the most striking photographs taken by the Apollo crew is that of the Orinoco River region in Venezuela (fig. 5). Freshwater discharge from this region carries large concentrations of organic matter in both the suspended and the dissolved phase. The source of the organic materials is the jungle, specifically the vegetation. How this material gets into the rivers in the particulate form is not well understood. A possible mechanism for particulate formation upon entry into ocean waters could be changes in pH: on meeting alkaline ocean waters, acid-colored waters of the jungle would precipitate certain compounds. These compounds could absorb the yellow organics to produce particles that reflect long wavelengths but absorb short wavelengths. In any case, the photograph is remarkable for its contrasts. The heavy jungle appears to absorb most of the visible light as does the open ocean water. In contrast is the yellow coastal water that appears to reflect at least 10 times more radiation than the open ocean or jungle.

The ASTP photograph (fig. 5) reveals that the Orinoco River discharge influences the water color as far as 80 km (50 s. mi.) to sea; the water extends to Trinidad and appears to pass through the

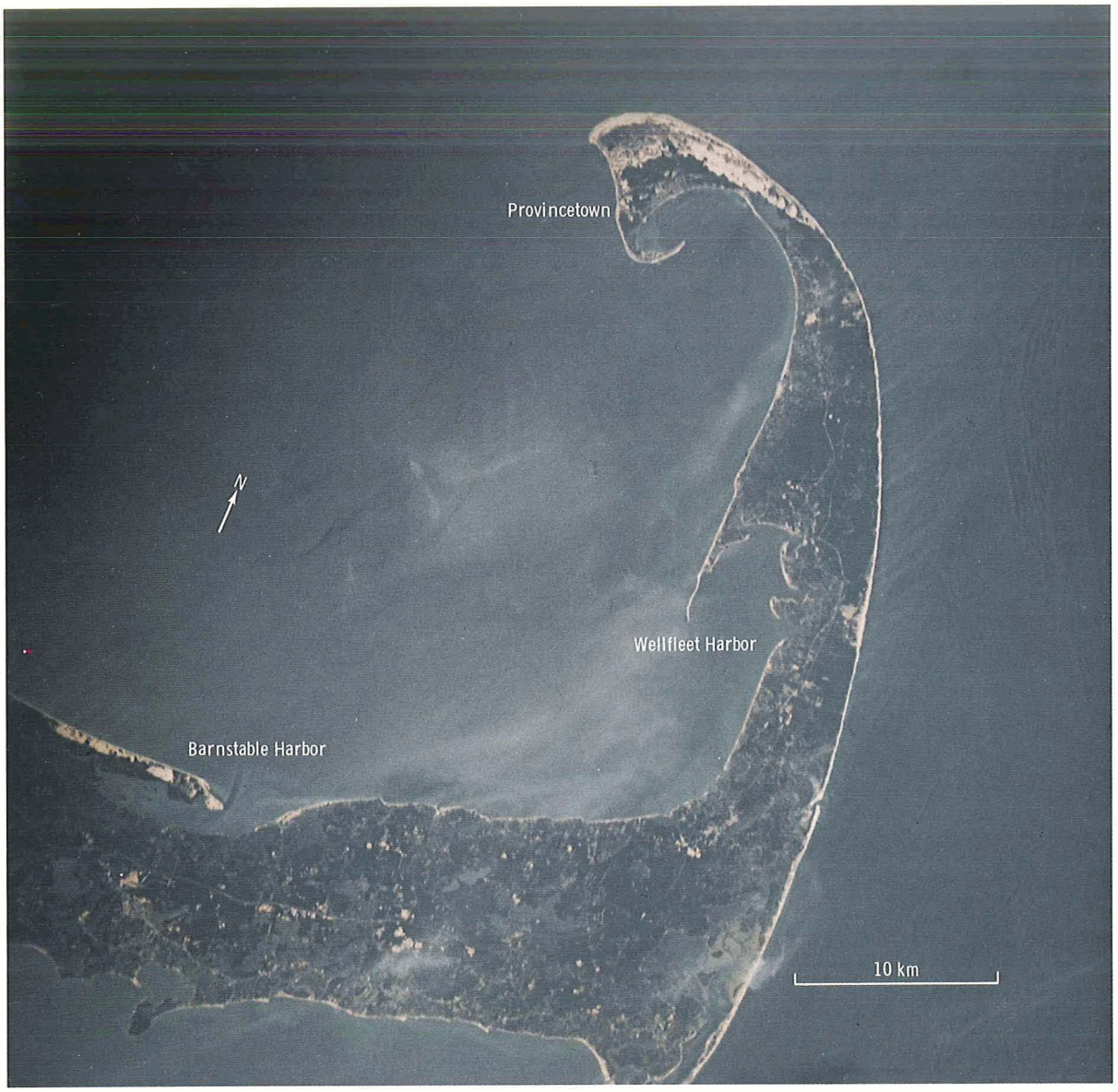


FIGURE 3.—Photograph of Cape Cod region taken on July 24, 1975 (AST-1-064).

Serpent's Mouth. Not confirmed by the photograph is the report by the astronauts that the water color was affected as far as Barbados Island; film sensitivity may be the reason for this discrepancy.

Along the eastern Canadian coast, a red discoloration was observed in several fjordlike indentations (fig. 6). In contrast to the Orinoco River photograph (fig. 5), this photograph shows more reddish water (rust red) and suggests less total reflectance. The in-flight tapes suggested that the astronauts thought this was a red tide. In reality, however, the material is "nonorganic" red clay that is characteristic of the region and that is easily washed into the sea by wave and tidal action. Because of a low settling velocity, this material will stay in suspension for a long time.



FIGURE 4.—Photograph of Nantucket Shoals taken on July 24, 1975 (AST-1-063).

Red-Tide Observations

In conjunction with the Apollo overflight, two research vessels working out of Boothbay Harbor covered New England waters in search of patches of red-tide dinoflagellates. The research vessel *Challenge* cruised the New England coast from Cape Ann, Massachusetts, north to Jonesport, Maine (figs. 7(a) and 7(b)). This vessel continually monitored the chlorophyll content (figs. 8(a) and 8(b)), the temperature (figs. 9(a) and 9(b)), and the salinity (figs. 10(a) and 10(b)) of the surface waters. At selected stations, dissolved yellow substance (fig. 11), backscattered irradiance, and other optical properties were measured. The research vessel *Bigelow*, also out of Boothbay Harbor, concentrated on sampling the near-shore inlets along this coast.

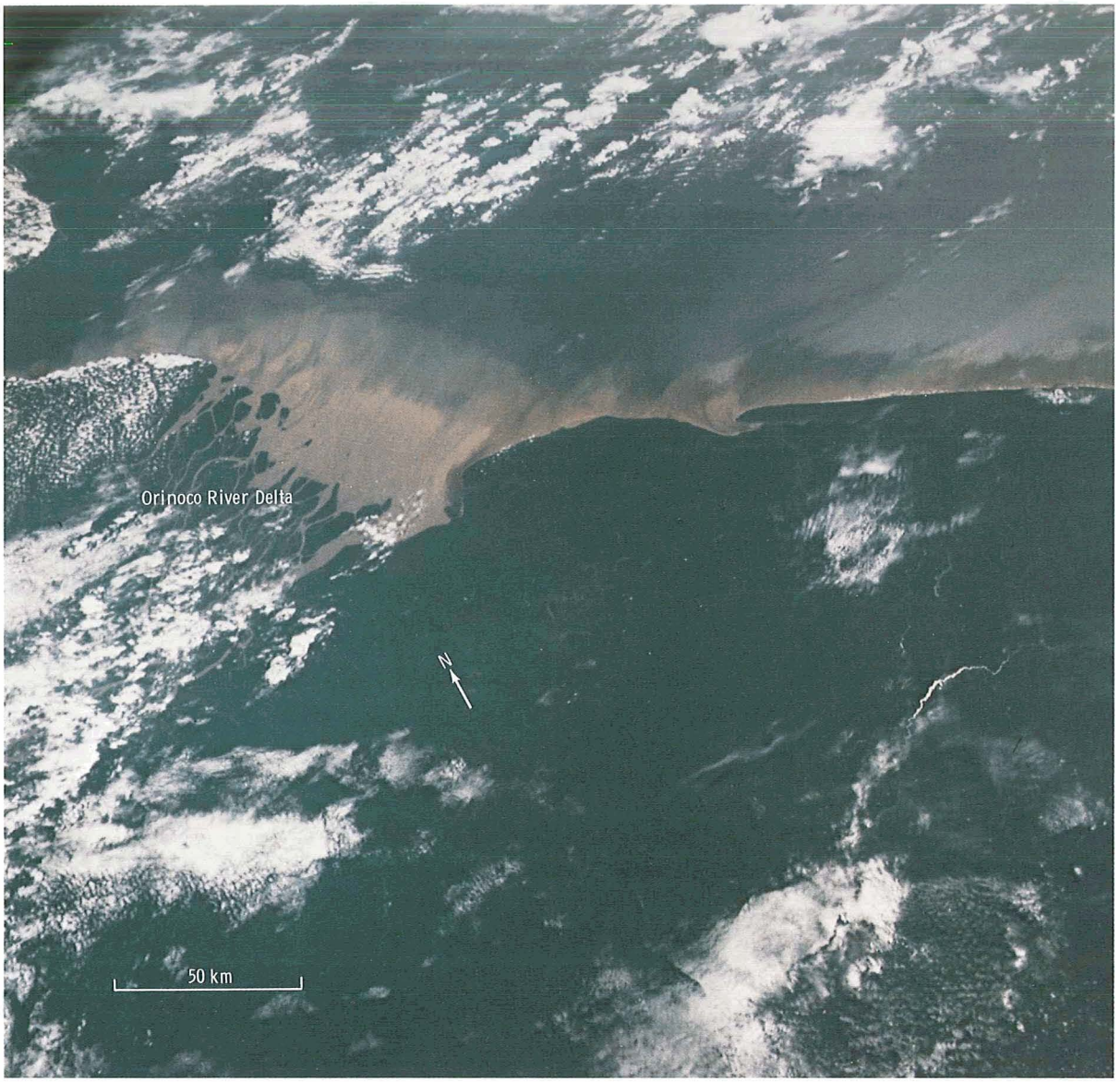


FIGURE 5.—Photograph showing the mouth of the Orinoco River taken on July 22, 1975 (AST-21-1683).

Between Cape Ann and Boothbay Harbor, the largest concentrations of chlorophyll fluorescence occurred near shore, generally in pockets restricted to the mouths of estuaries. North of Boothbay Harbor, chlorophyll distribution was comparatively uniform and the values generally were lower than those in the southern sections.

Water temperatures greater than 291 K (18° C) were observed in the southern section approximately 20 km offshore. Between Cape Ann and Boothbay Harbor, several cold near-shore pockets were observed. These pockets exhibited high chlorophyll fluorescence suggesting that they were the result of upwelled waters. North of Boothbay Harbor, temperatures greater than 288 K (15° C) were not encountered. Lowest temperatures (282 K (9° C)) were encountered off Jonesport.

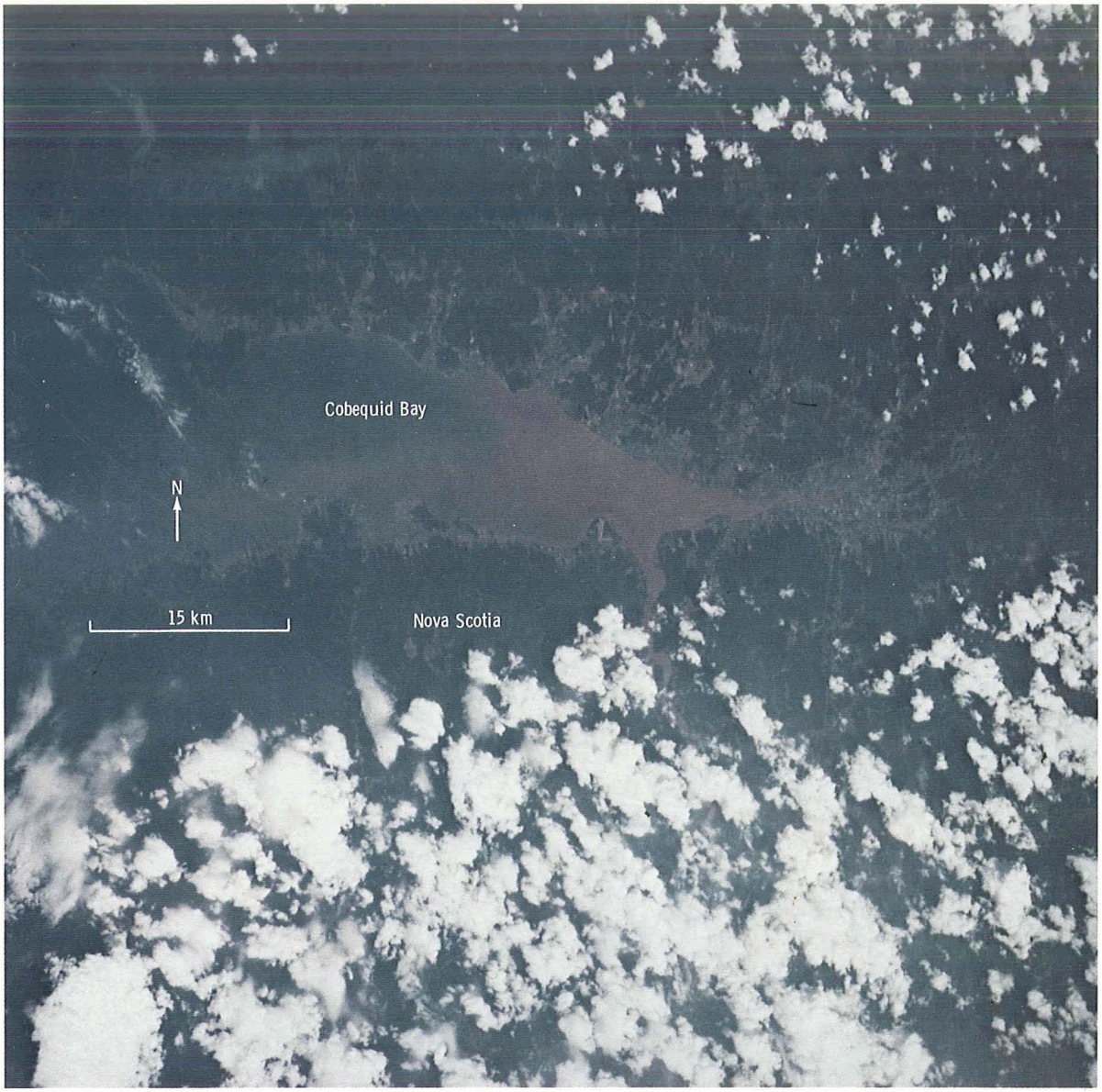


FIGURE 6.—Photograph of eastern Canada taken on July 24, 1975 (AST-1-067).

Between Cape Ann and Boothbay Harbor, the surface salinities ranged between 28 and 31.5 °/₀₀. Lowest salinities were found off the Merrimack and Plum Island Estuaries, just north of Cape Ann. High salinities occurred offshore. North of Boothbay Harbor, the salinity range was much less and the mean centered around 31.5 °/₀₀.

At the onset, it seemed unlikely that any major bloom of red tide would be encountered because it was very early in the season. To compound the problem, the New England coast could be shrouded with heavy fog during July. This condition certainly existed for most of the northern sections covered by *Challenge*. However, with the ex-

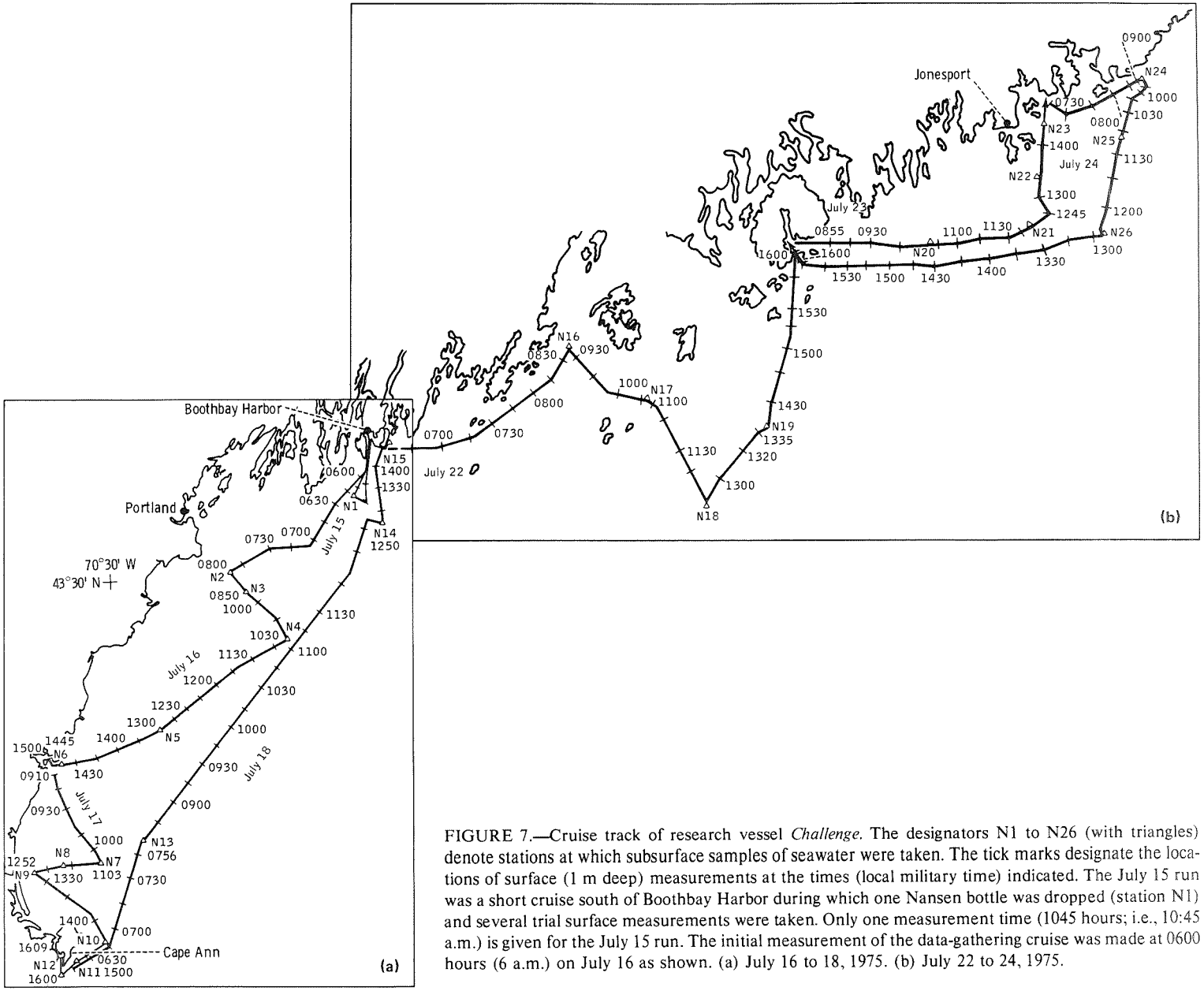


FIGURE 7.—Cruise track of research vessel *Challenge*. The designators N1 to N26 (with triangles) denote stations at which subsurface samples of seawater were taken. The tick marks designate the locations of surface (1 m deep) measurements at the times (local military time) indicated. The July 15 run was a short cruise south of Boothbay Harbor during which one Nansen bottle was dropped (station N1) and several trial surface measurements were taken. Only one measurement time (1045 hours; i.e., 10:45 a.m.) is given for the July 15 run. The initial measurement of the data-gathering cruise was made at 0600 hours (6 a.m.) on July 16 as shown. (a) July 16 to 18, 1975. (b) July 22 to 24, 1975.

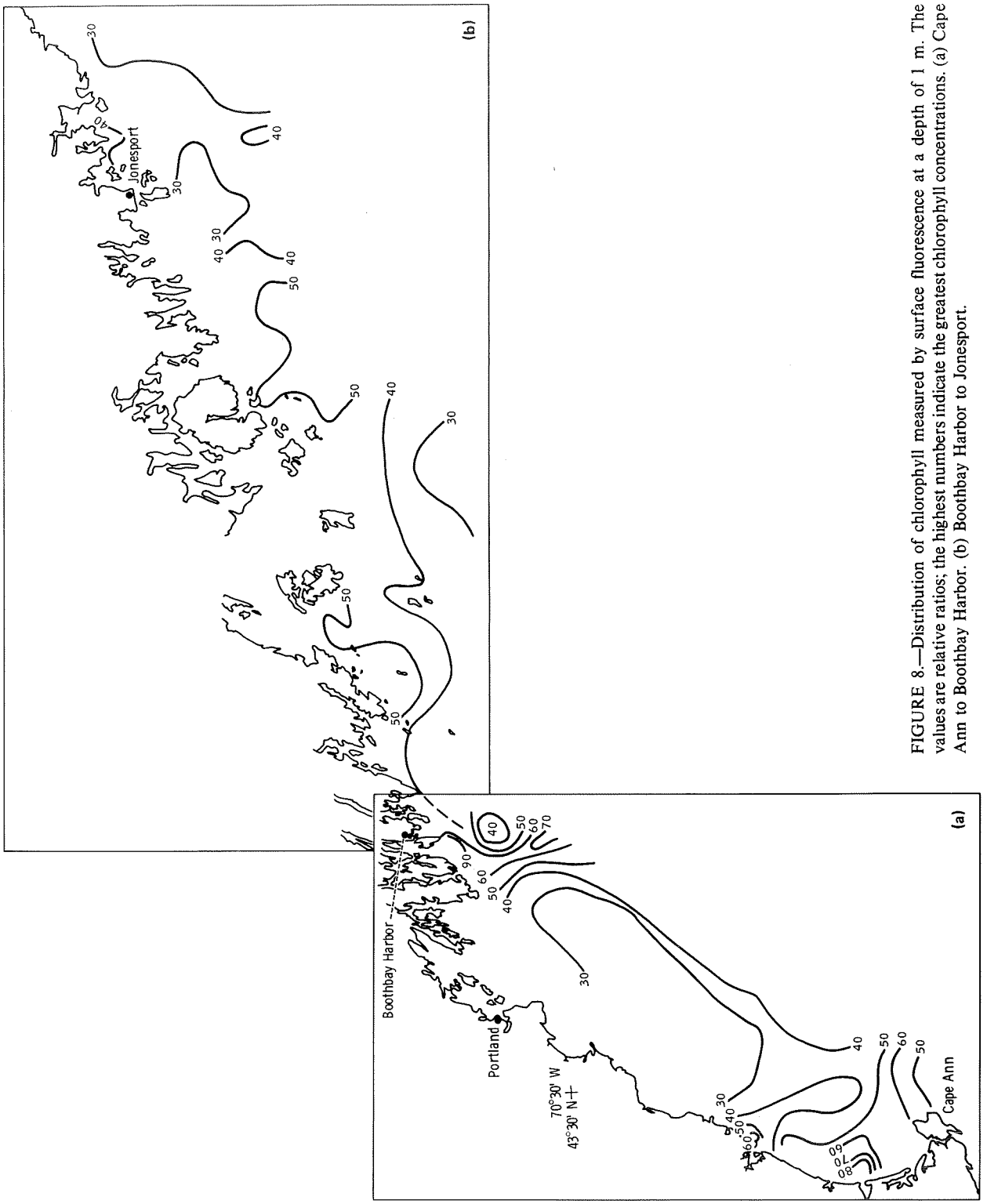


FIGURE 8.—Distribution of chlorophyll measured by surface fluorescence at a depth of 1 m. The values are relative ratios; the highest numbers indicate the greatest chlorophyll concentrations. (a) Cape Ann to Boothbay Harbor. (b) Boothbay Harbor to Jonesport.

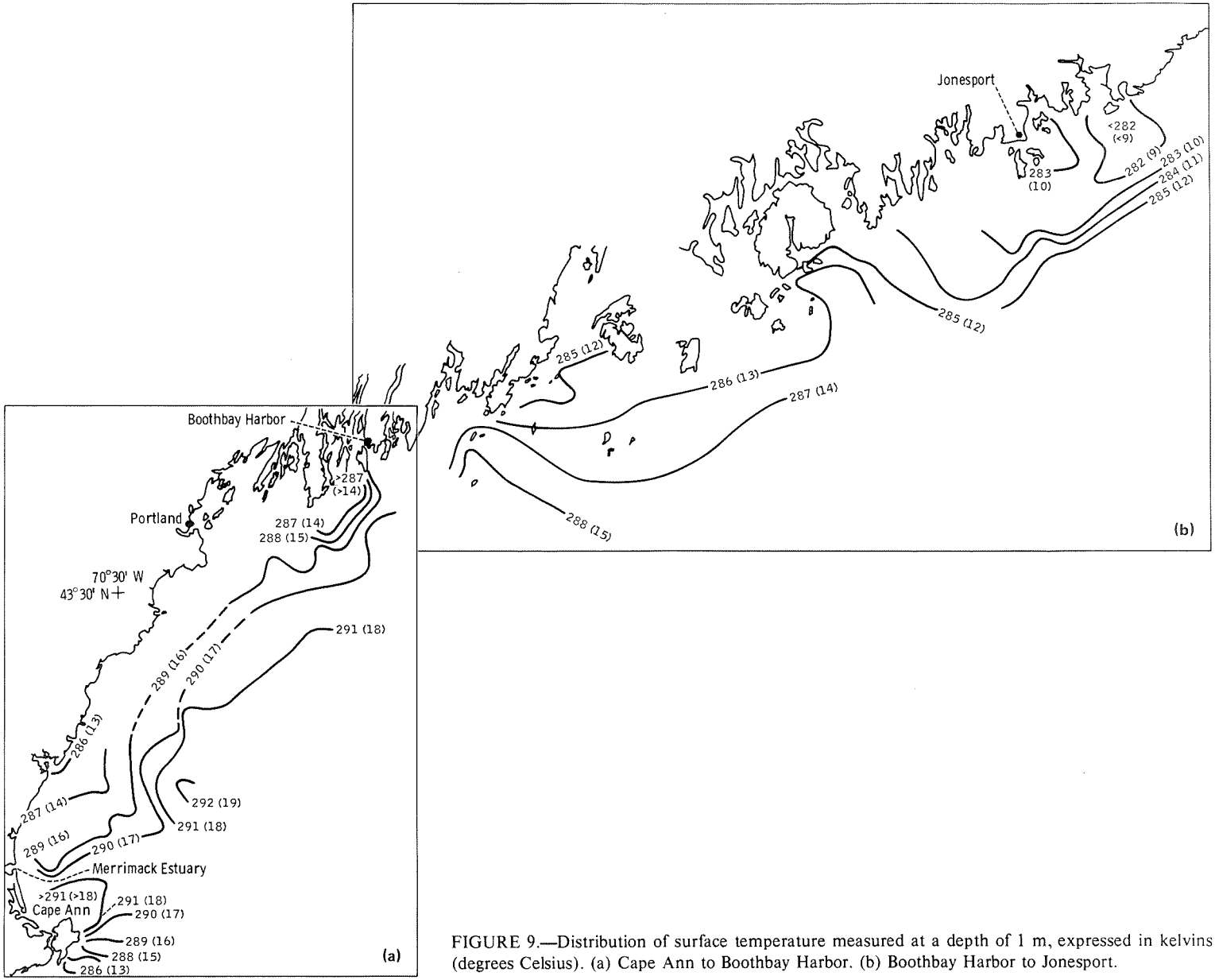


FIGURE 9.—Distribution of surface temperature measured at a depth of 1 m, expressed in kelvins (degrees Celsius). (a) Cape Ann to Boothbay Harbor. (b) Boothbay Harbor to Jonesport.

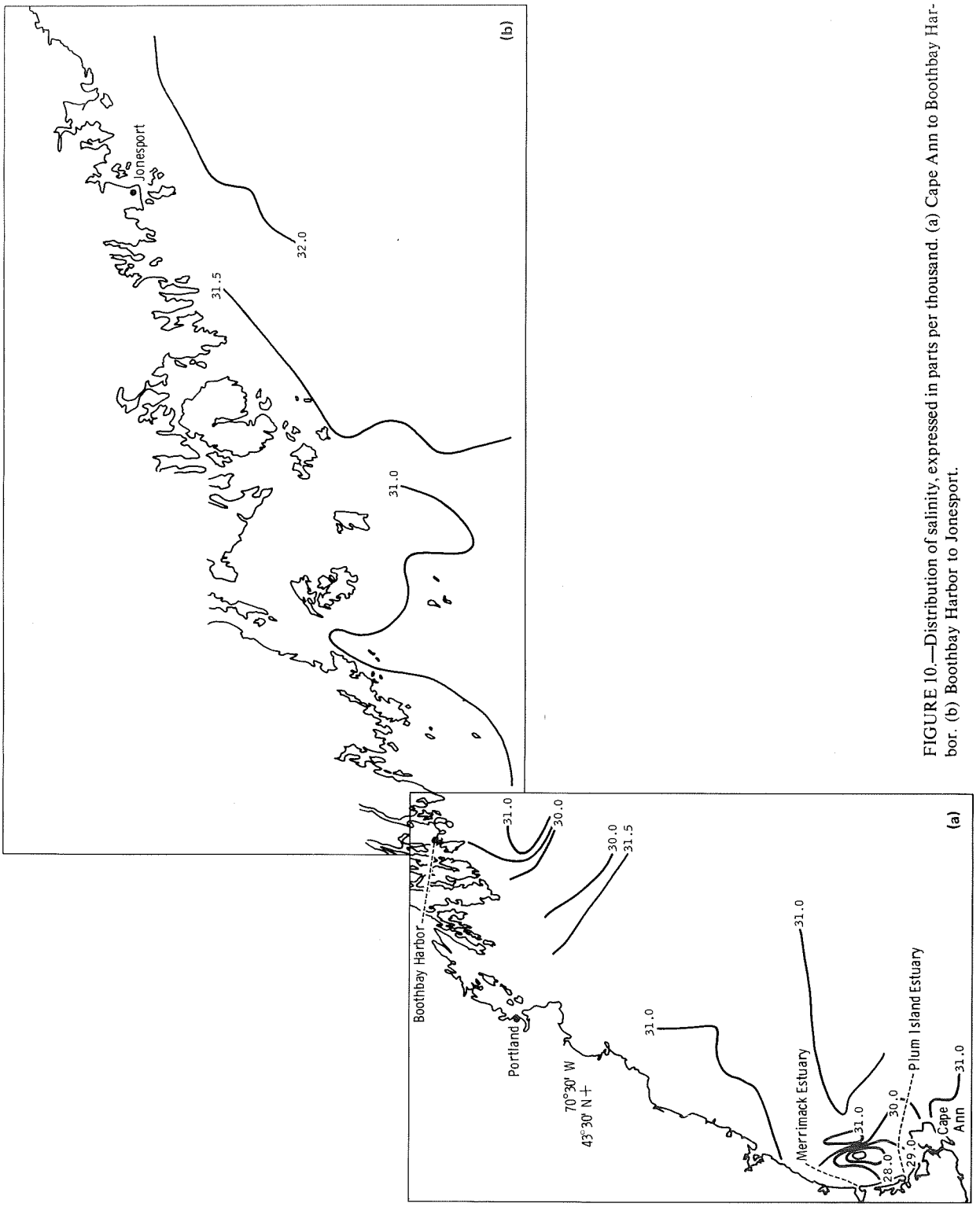


FIGURE 10.—Distribution of salinity, expressed in parts per thousand. (a) Cape Ann to Boothbay Harbor. (b) Boothbay Harbor to Jonesport.

tensive coverage given to this area, it can be said that, even if atmospheric conditions had been perfect, no large red-tide patches would have been available as photographic targets. The only major area of ocean discoloration occurred around the mouth of the Merrimack Estuary (figs. 9(a) and 10(a)). The outflow of the Merrimack River can be easily seen at least 10 km from the shore. This river is heavily polluted and contains large amounts of dissolved yellow substances. Thus, the discoloration of the ocean waters upon entry by the river is the summation of color contribution by an intense bloom of algae as well as by yellow substance.

In anticipation of the possibility of photographing this discoloration, a series of optical measurements was performed in the discolored plume. The peak of backscattered irradiance was near 580 nm. (The irradiance of clear seawater peaks between 450 and 480 nm.) Total, backscattered irradiance was 10 percent of the incoming irradiance; this value is about twice as high as that for clear water. Other optical data indicated a marked reduction in light penetration and a high particle count in plume waters. The algae in the plume (measured by chlorophyll) were in bloom proportions and consisted almost entirely of diatoms belonging to the genus *Skeletonema.*

Before launch, the Apollo crewmen were alerted to the possibility of observing the Merrimack discoloration, but they were unable to obtain photographs because of the hazy atmosphere. Several days into the mission, the research vessel *Bigelow* did encounter a patch of dinoflagellates at the mouth of the Sheepscot Estuary, just west of Boothbay Harbor. This encounter was unexpected, and the position of the bloom was relayed to the astronauts by way of the Mission Control Center in Houston. On several successive passes through the area, the astronauts reported seeing this patch and attempted to photograph the area. Because of visibility limitations, none of the photographs obtained were usable. However, the exercise demonstrated the ease with which a ground observer and astronauts can work together.

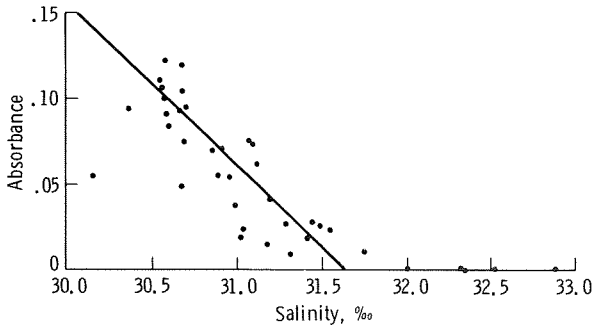


FIGURE 11.—Relationship between dissolved yellow substance (Gelbstoff) and salinity of water in the Gulf of Maine, July 16 to 24, 1975. The ordinate represents spectral absorbance by Gelbstoff at a wavelength of 260 nm.

CONCLUSIONS

At the beginning of this report, it was predicted that the following four features, which alter ocean color, could be observed from space:

1. Phytoplankton chlorophyll
2. Dissolved yellow substance
3. Sediments in suspension
4. Bottom reflection

The photograph of the Orinoco River (fig. 5) is a good example of points 2 and 3. In this case, there is short-wavelength absorption of the incoming irradiance plus backscattered reflectance from particles. This is probably the case for any body of water carrying a heavy organic load. In contrast, the photograph of the Canadian fjords (fig. 6) is an example of discoloration by nonorganic sediments. Here, the color is dominated by long-wavelength reflectance.

The photographs around Cape Cod (figs. 3 and 4) are excellent examples of what can be seen of the bathymetry in waters of average transparency. If the estimate of depths for these features ($\approx$1 m) is accurate, then a case could be made for viewing the bottom at a depth of 20 to 30 m in waters of more than average transparency.

To state that no photographs of phytoplankton chlorophyll were obtained is not completely accurate: the total photographic coverage of the mission shows ocean waters of different color. Waters off New England photograph green. Waters in the open South Atlantic Ocean photograph blue. These differences can be explained in part by the low phytoplankton productivity in the South

Atlantic and the high productivity in New England waters.

As predicted, the answers to the questions posed in the introduction are now obvious: astronauts do see ocean discolorations, and their verbal comments indicate that they are aware of the causes and sources. Finally, and this is a positive comment on logistics, experience suggests that it is rather easy for ground crews to work with astronauts in attempts to locate discolorations and to determine their extent and sources.

ACKNOWLEDGMENTS

This work was performed under Smithsonian Institution Grant PC6-20013 as a subcontract of NASA Contract NAS9-13831, NASA Contract NAS5-22948, and Energy Research and Development Administration Contract E(11-1)2538.

Analysis of Water Color as Seen in Orbital and Aerial Photographs of Cape Cod, Nantucket, and Martha's Vineyard, Massachusetts

Tracey Tisdall[a] *and Farouk El-Baz*[a†]

ABSTRACT

This paper includes a detailed analysis of coastal water color as seen in two Apollo-Soyuz photographs of Cape Cod, Nantucket, and Martha's Vineyard, Massachusetts. The natural color of the photographs enabled the recognition of light, blue-green areas marking shoals and suspended sediments; patterns that delineate sediment transport by longshore drift; light-colored striations on the water surface that are interpreted as wind streaks; and several series of crests and troughs with 3-km wavelengths that are believed to be manifestations of internal ocean waves, particularly off Cape Cod.

High-altitude NASA aircraft obtained color and multispectral photographs of the same area at the time of acquisition of the orbital photographs. The aircraft data were compared with the spacecraft photographs as well as with available bathymetric charts. These comparisons showed that the high-altitude photographs are necessary for detailed analyses, whereas the spacecraft photographs are useful in a comprehensive study of a large area.

The resolution of high-altitude photographs enabled detailed comparisons with bathymetric charts. These comparisons resulted in the recognition of numerous changes in the coastlines since the charts were made. The rates of change per year were calculated; these agreed with published data where ground-truth studies were made. In general, the bathymetric charts of this region were found to be good, and their features correspond well to those on the aerial photographs. However, greater detail was seen in the photographs because of the size of the chart contour intervals.

An attempt was made to quantify the reflectance values of coastal waters in the region. This was done through the use of a "Datacolor/Edge Enhancer System." Relative intensity profiles were made in which peaks represented bright beach sand and troughs corresponded to vegetated land and/or deep ocean water. Between these two extremes, lighter colored coastal waters generated distinctive peaks. However, without ground-truth data, this scale remains relative. Absolute reflectance values of shoal areas, chlorophyll concentrations, sediment-laden waters, etc. could be roughly estimated, but not accurately determined.

INTRODUCTION

Concurrent orbital and aerial photographs of the coastal regions of New England were taken during the Apollo-Soyuz Test Project (ASTP) mission to study red tide blooms (ref. 1). These photographs were in support of studies conducted by the Bigelow Laboratory, Boothbay Harbor, Maine, and the Department of Public Health of the Commonwealth of Massachusetts. Although a high chlorophyll concentration was recorded throughout this area (ref. 1), no red tides were present when the ASTP photographs were taken.

[a]National Air and Space Museum, Smithsonian Institution.

[†]Principal Investigator.

However, both the orbital and the aerial photographs document many other marine and coastal zone features that are discussed here.

Orbital photographs are particularly well suited to the study of marine and coastal environments because of the large areal coverage of a single frame. Natural color provides the necessary tool to note and map variations representing different water conditions over a broad region. These color variations may represent bottom topography, sediments or substances such as chlorophyll and pollutants in the water, currents and their boundaries, and internal ocean waves. In addition, changes in shoreline shape and position may be easily monitored using space photographs taken at different times (ref. 2). Also, orbital photographs are useful in the accurate determination of boundaries to resolve questions of ownership rights of natural resources such as oil deposits and fisheries (ref. 3).

This study was performed using two ASTP photographs taken on July 24, 1975, over the peninsula of Cape Cod and the islands of Nantucket and Martha's Vineyard in Massachusetts (fig. 1). These photographs exhibit color variations, subsurface topography, evidence of longshore drift, a band of wind streaks, and internal ocean waves. In addition to the ASTP coverage, the concurrent high-altitude aerial photographs, taken of the area by NASA aircraft to supplement the information gained from orbit, are included in this study.

The aims of this study are threefold: (1) to demonstrate the usefulness of space photographs in the study of marine and coastal features, (2) to extract as much information as possible about coastal and marine environments from the orbital and aerial photographs, and (3) to test the various analytical techniques used in determining the causes of brightness and color variations in coastal photographs.

METHODS

The first step in the analysis of the photographs is to examine them visually. According to Gierloff-Emden (ref. 3), more insight and information about a photograph may be obtained by a human interpreter than by a computer because of man's superior ability to discriminate. The usefulness of this technique depends on the conditions at the time of photography. In ocean studies, these conditions are determined by such factors as water turbidity (ref. 3), water transparency, Sun-elevation angle, bathymetry, wavelength of light (ref. 4), sea state, and atmospheric conditions. Visual examination of the ASTP photographs revealed a number of easily identifiable features and color variations as well as several subtle and questionable features requiring further study and documentation.

To support the results of this visual analysis of the photographs, comparisons were made between the ASTP data and several other sources of information. These included a Skylab 3 photograph, 11 high-altitude aerial photographs, and 4 bathymetric charts (refs. 5 to 8). The most illuminating comparison was that made between the aerial photographs and the charts because of their comparable scales. These comparisons were facilitated by a Bausch and Lomb zoom transfer scope, which enabled one to match the scales and to superimpose two sources of information.

A Datacolor/Edge Enhancer System was used to analyze color variations and brightness in the studied photographs. First, this machine enhanced color variations of features in the photographs by "slicing" the density of the film (i.e., the color intensity) into a number of divisions and assigning each division a color. This process emphasized subtle color variations and made them easier to study. Second, the machine was used to generate density profiles, which portrayed variations in intensity along a line. These profiles were compared with each other to determine whether a consistent relationship existed between the density of various surfaces. An attempt was made to fit a numerical scale to these profiles to quantify the comparisons. The scale is based on reflectance values that theoretically are directly related to color intensities in the photographs.

ASTP PHOTOGRAPHS

Cape Cod is a peninsula that extends into the Atlantic Ocean from the southeastern corner of

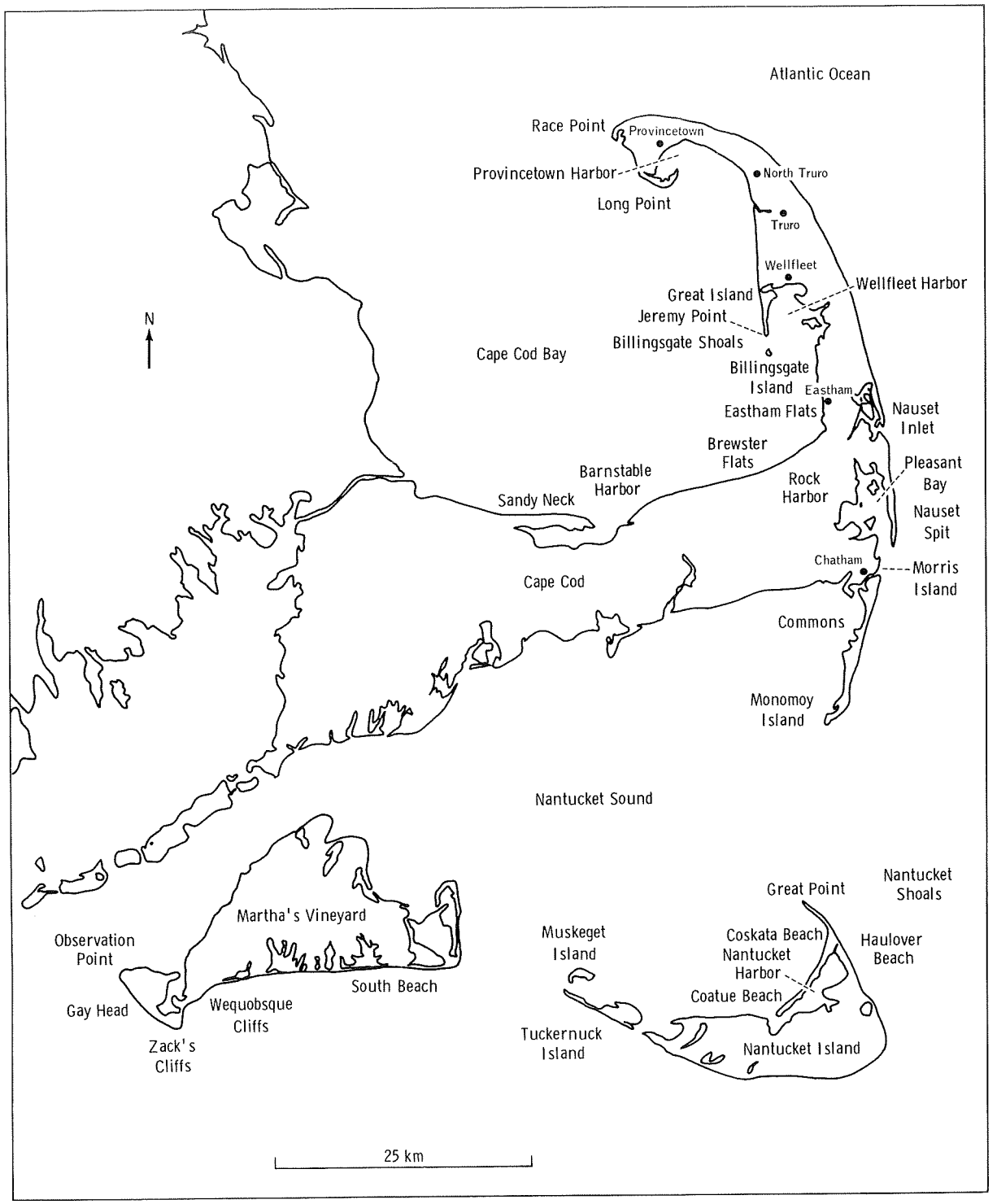


FIGURE 1.—Index map of Cape Cod, Nantucket, and Martha's Vineyard, Massachusetts.

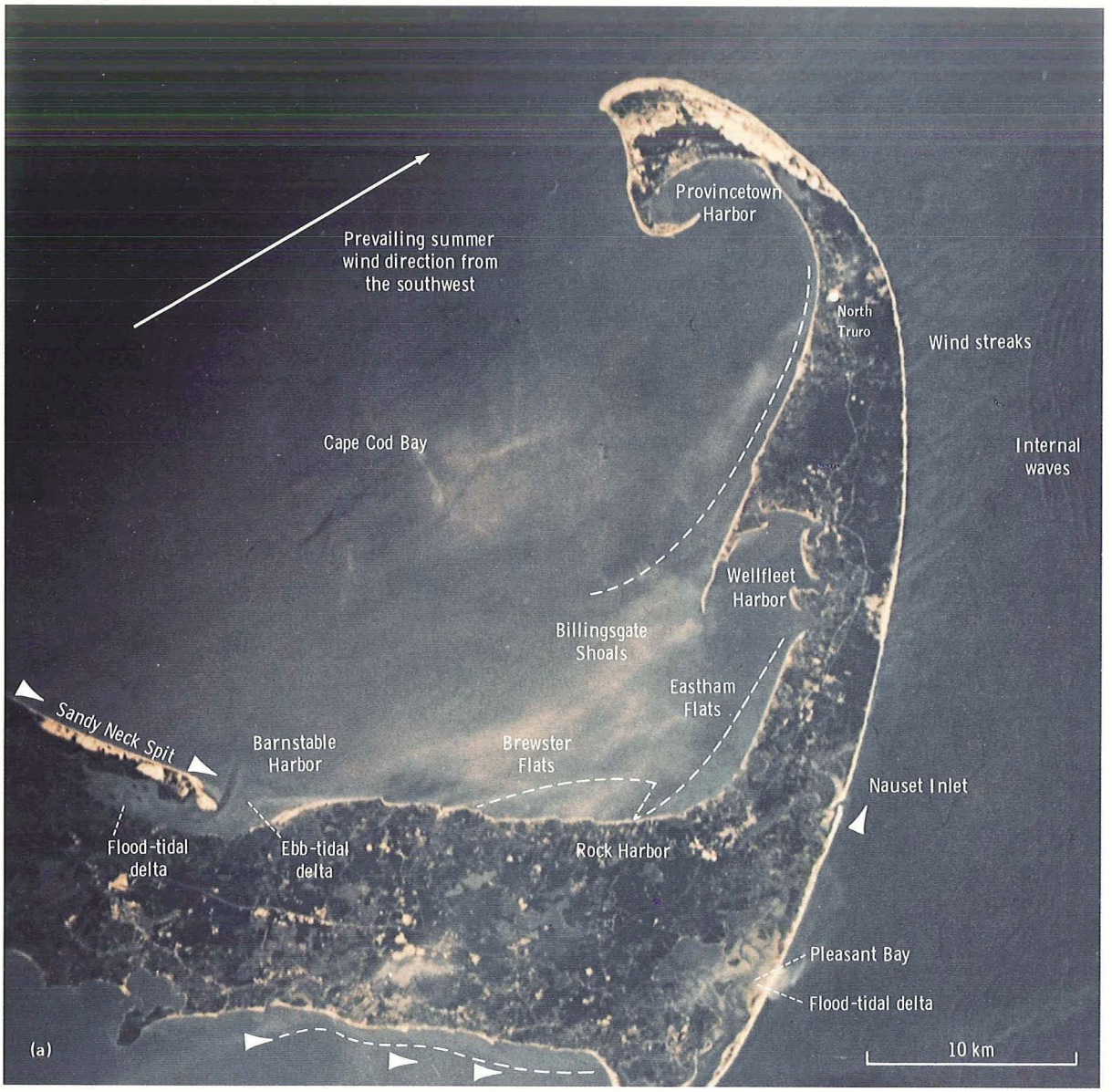


FIGURE 2.—ASTP photographs of the study area. Dashed lines indicate boundaries of light-colored water. Triangles mark locations of evidence for and directions of longshore drift. (a) Cape Cod (AST-1-64). (b) Nantucket, Monomoy Island, and part of Martha's Vineyard (AST-1-63).

Massachusetts. Nantucket and Martha's Vineyard are two islands south of Cape Cod. These landmasses were formed from the terminal moraines and outwash deposits of Pleistocene continental glaciers. Their rough, irregular shorelines were subsequently modified by storm waves and currents to become the smooth coasts of today.

The ASTP photographs (figs. 2(a) and 2(b)) give a regional view of this area showing not only the general morphology but also the specific local features that will be discussed in the following sections.



FIGURE 2.—Concluded.

Shoals and Suspended Sediments

In the coastal waters surrounding Cape Cod, the ASTP photographs show several light-colored areas (figs. 2(a) and 2(b)). These areas may represent bottom topography, concentrations of substances such as chlorophyll, and/or sediment-laden water, which in some cases is generated by turbulent current or wave action over a shoal.

Tidal deltas are found in several locations in the area. The bars and channels that compose ebb-tidal deltas are evident outside Barnstable Harbor (fig. 2(a)) and Chatham and Nantucket Harbors (fig. 2(b)). In the flood-tidal deltas in Pleasant Bay

and Barnstable Harbor (fig. 2(a)), the light brownish areas denote shoals and the darker blue, slightly sinuous forms denote channels. Monomoy Island, the southernmost extension of Cape Cod, is visible in the upper right corner of figure 2(b). Light-colored water surrounds the island. One area in particular is the Commons, an old flood-tidal delta, the result of a past break through the island (ref. 9). The delta is evident at the top margin of the figure.

Along the southeastern Cape Cod Bay shoreline, there is a fairly continuous zone of light blue water (fig. 2(a)). A series of flats extends from slightly east of Barnstable Harbor along the southeastern bight of the bay to North Truro. These shoals are composed of multiple parallel and oblique bars (refs. 9 and 10). They coincide with the color bands on the photographs. The flats can be distinguished from clouds by the former's bluish tint. In contrast to these regular shoals are the nonlinear shoals in the vicinity of Tuckernuck and Muskeget Islands at the western end of Nantucket (fig. 2(b)). These shoals and troughs are quite variable in shape (ref. 11).

Other apparent shoals are evident in Nantucket Sound between the islands and southern Cape Cod (fig. 2(b)). These are very subtle and somewhat blurred in the photograph. It appears that sediment is being entrained at the crests of the shoals and suspended above them. A similar combination of shoals and sediment exists in Provincetown and Wellfleet Harbors (fig. 2(a)), although the bathymetry in these locations is not as complex as in Nantucket Sound.

A sediment plume is visible off Great Point, Nantucket (fig. 2(b)). The plume and the light-colored area around it mark the location of the remnants of a glacial hummock, which originally provided the material for Coskata Beach and cusps (ref. 9). Farther east of Nantucket, the Nantucket Shoals are barely visible as light-colored streaks. In most of the aforementioned cases, the individual bars and troughs that compose the shoals are not discernible in the two ASTP photographs.

Longshore Drift

Results of longshore drift are evident in the ASTP photographs. Longshore drift is one of the most important agents of sediment transport on Cape Cod, Nantucket, and Martha's Vineyard. It is the mechanism by which the many spits and beaches that make up these areas are maintained and extended. The dynamic nature of this process is illustrated by the dramatic rate of change of these spits. Two examples on Cape Cod are Nauset Spit with an extreme migration rate of 90 m per year and Sandy Neck Spit with a rate of 2 m per year (ref. 12). Both of these spits are visible in figure 2(a). Their growth directions can be determined by the trends of the sequential arcs on the spits marking their former terminations and by comparisons between recent and older photographs and/or charts, as will be discussed later. The direction of spit growth is the same as the drift direction.

The trend of longshore drift is also obvious along the southern shore of Cape Cod (fig. 2(a)). Here, the evidence includes sediment accumulation on the updrift side of jetties, groins, and similar barriers, and regions of scour, which are indicated by darker color patches downdrift of the structures. A previously published longshore drift map (refs. 9, 13, and 14) corroborates the drift directions determined from the ASTP photograph (fig. 3).

Wind Streaks

A curious pattern of patchy, northeast-southwest oriented, light-colored streaks are visible in a narrow band across the forearm of Cape Cod in figure 2(a). The nature of these features cannot be absolutely determined because of the lack of ground data. However, there are three interpretations, the third of which is most likely. First, these features could be a cloud phenomenon, especially considering the cloudiness of the day on which the photographs were taken. They are oriented

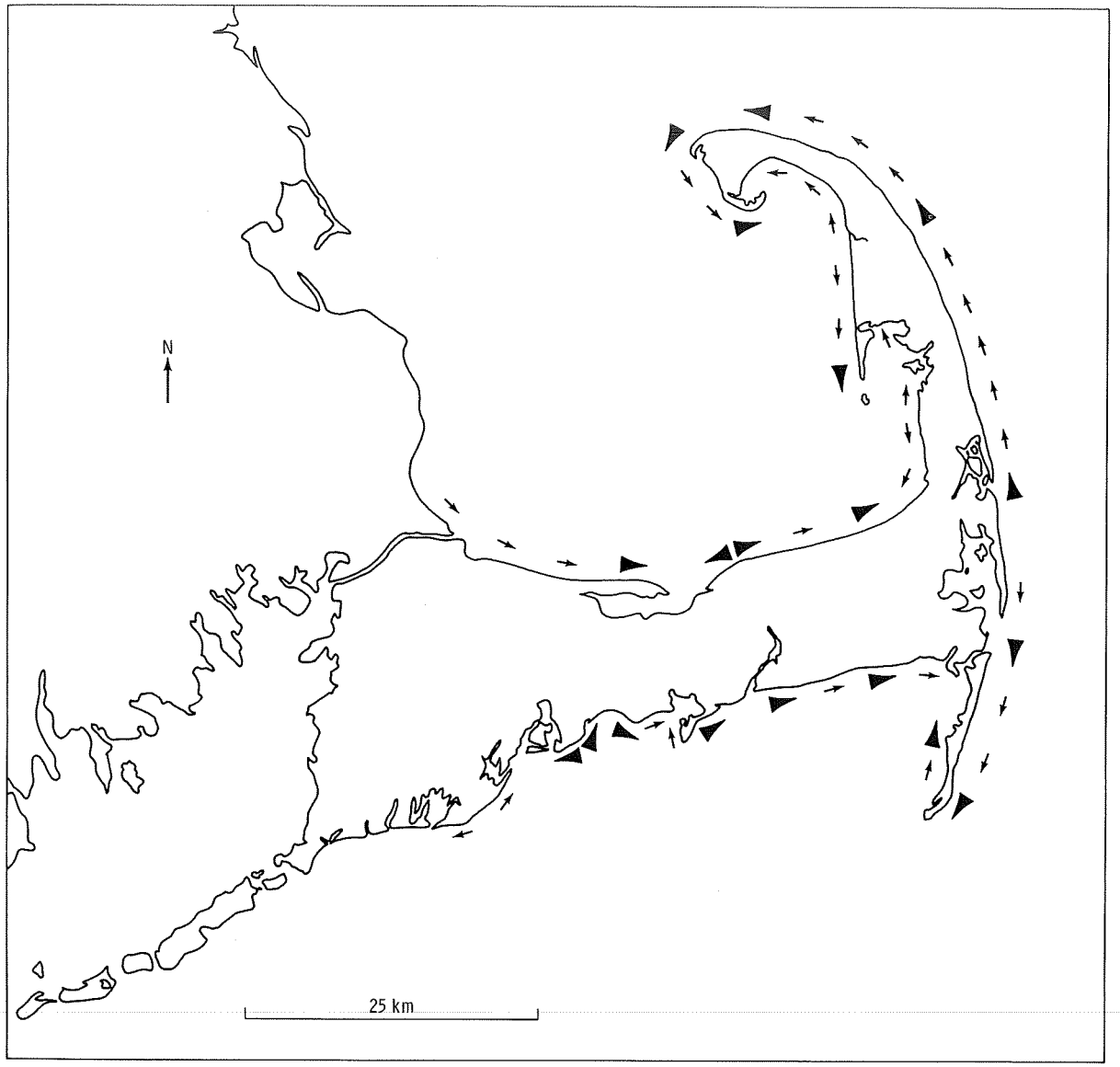


FIGURE 3.—Map showing longshore drift directions around Cape Cod, Massachusetts. Arrows indicate directions from Strahler, 1966, and Leonard et al., 1976 (refs. 13 and 9). Triangles mark directions determined from ASTP and high-altitude aerial photographs.

parallel to the prevailing wind direction from the southwest (ref. 9) and are present over the ocean, Cape Cod Bay, and inland ponds. However, there does not appear to be a continuation of these patterns over any land area. Also, there is a definite interaction between this pattern and the oceanside beach areas and shallow shoals and bars on Cape Cod, which would not be present in a cloud pattern. Finally, sunglint seems to have an effect on the visibility of the streaks since they can be seen only on a narrow band. These factors cast doubt on an atmospheric origin for this phenomenon.

Second, Gierloff-Emden (ref. 3), in his study of a Skylab 3 photograph of the eastern Gulf of Venezuela and the Caribbean Sea off the Península de Paranquaná in Venezuela, interprets streaks, whose form is similar to those in question, as a sandstorm. The facts that the streaks are parallel to the wind direction and are found over all water bodies support this explanation. Also, sunglint could enhance a dust or sand pattern like this. However, several factors make this possibility inapplicable to the study area. These include the facts that (1) the sandstorm is larger and more distinct than the ASTP streaks, (2) the sandstorm does not fade out with distance from the coast and does not exhibit any interaction with the shore, and (3) a sandstorm would require a source of sand and would continue over land. None of these conditions are satisfied in Cape Cod. Therefore, although the patterns are similar, the causes must be different.

The third and most reasonable explanation for these features is based on a combination of suspended sediment in the water and rough sea state due to wind action. The orientation of the streaks is a clue that they are wind related. Waves breaking on the southwestern side of the shoals in the high-altitude aerial pictures provide evidence of a northeast-southwest wind direction. The streaks do not extend over the land; therefore, they are probably a water phenomenon, which would be influenced by sunglint as these features are. On the eastern shore, it appears that sand is being entrained and suspended as breaking waves hit the beach. Also, the sandbars offshore have an indistinct appearance that may be due to entrained sediment from their crests resulting from turbulence. Suspended sand would increase the reflectance of the water as would rougher seas. On the bay shore and in ponds, the streaks are less prominent. This might be explained by the less turbulent environment of the bay and the inland waters despite the fact that the brightness of the water over the Eastham Flats (fig. 2(a)) indicates that sediment is being entrained at the top of the shoals.

Internal Waves

In figure 2(a), long linear features are present in the water offshore. They appear to be a series of crests and troughs, the crests being lines of higher reflectance. These features occur only on the oceanside of Cape Cod and are thought to be the surface manifestations of internal ocean waves.

Internal ocean waves are the result of the interactions between two bodies of different densities (refs. 15 and 16). (See also the paper by John R. Apel entitled "Observations of Internal-Wave Surface Signatures in ASTP Photographs" in this volume.) The density difference depends on the temperature and/or the salinity of the water. Internal ocean waves can be distinguished from surface waves and other phenomena by their large dimensions. The waves in figure 2(a) have wavelengths of approximately 3 km. Visibility of such waves depends on the accumulation of a surface slick or scum line of high or low reflectance resulting from the circulation pattern of waves. Conditions that emphasize the slick such as light wind, which roughens the surrounding water, and sunglint are helpful in viewing the waves (ref. 15 and Apel, this volume).

There is no absolute explanation for the occurrence of internal waves, although several theories on the subject have been put forth. One popular interpretation involves a transformation of a current of uniform density into baroclinic tidal waves at the Continental Shelf. The waves thus generated are then refracted as they move shoreward (ref. 15 and Apel, this volume). A study performed in Massachusetts Bay agrees that topographical variations have an important role in creating the density and temperature variations that generate and modify these waves. According to this study, the waves are found in the vicinity of the shallow seasonal thermocline (ref. 16).

The internal waves off Cape Cod are formed in discrete sets, some of which intersect each other. Because the waves are not consistently oriented parallel to the shoreline, the effect of the underlying bathymetry must be considered. The region

surrounding Cape Cod is composed of glacial moraine and outwash and has been modified by waves and currents into irregular shoals. It is reasonable to assume that these topographic highs and lows have as great an effect on the direction of internal waves as they would on shallow surface waves. The large dimensions of these waves can be seen in figure 2(a). The fact that these lineations are present only on the oceanside of Cape Cod would point to a source area in deeper water, possibly at the edge of the Continental Shelf.

From this discussion, it is evident that a great deal of information can be gained from such a visual examination of orbital photographs. Despite the less than perfect viewing conditions, particularly a light haze and partial cloudiness, many different features are distinguishable in the ASTP photographs of the study region.

COMPARISON OF ASTP PHOTOGRAPHS WITH OTHER DATA

The ASTP photographs of Cape Cod, Nantucket, and Martha's Vineyard were taken on July 24, 1975, at 12:53 eastern daylight time. The camera used was a handheld 70-mm Hasselblad reflex camera that was used by the astronauts to support their visual observations. The photographs were taken from an altitude of 226 km with a 250-mm lens (ref. 1). The scale of these near-vertical photographs is approximately 1:300 000.

The ASTP photographs show many interesting features. However, because of the scale of the photographs and especially the hazy conditions during which they were taken, it was thought that comparisons with other types of data would amplify the information contained in the ASTP photographs. Therefore, features noted in these two photographs were examined further using a Skylab 3 photograph, a Landsat image, high-altitude aerial photographs, and bathymetric charts.

Skylab 3 Photograph

A Skylab 3 photograph taken during September 1973 was included in this study to demonstrate how various orbital photographs can differ. The Skylab photograph, SL3-86-313 (fig. 4), covered approximately the same area as the ASTP photographs, and it was also taken at approximately the same time of day. This photograph is much sharper and has greater resolution than the two ASTP photographs.

The superior clarity and resolution of the Skylab photograph is due in part to the fact that it was taken with an Earth terrain camera (ETC). This instrument has a very high resolution capacity as opposed to the less sophisticated Hasselblad used on ASTP. Unlike the Hasselblad, the ETC was mounted in the scientific airlock of the Skylab orbital workshop; this location eliminated the effects of the spacecraft window glass on the resolution and quality of the photographs. The ETC also contained a mechanism by which compensation for the forward motion of the spacecraft was accomplished by reorienting the camera to produce a sharper image. Another differing factor was the focal length of the respective lenses. The Hasselblad had a 250-mm lens, and the ETC had a 450-mm (18 in.) lens (ref. 17).

Although good resolution is necessary in a photograph, the temporary conditions and features present during the time of photography are also important. In the present case, the weather conditions were better in the Skylab photograph. However, wind streaks are only seen in the ASTP photographs. This indicates that the usefulness of a photograph depends on the conditions at the time of photography as well as the quality of the photograph.

Throughout the Nantucket Shoals, individual troughs and bars are visible in the Skylab photograph (fig. 4). The shoals surrounding Muskeget and Tuckernuck Islands and those along the bight of Cape Cod Bay can be seen, and many of the individual bars and troughs that compose them are distinct. The brightness of the water of Nantucket



FIGURE 4.—Skylab 3 photograph of southeastern Cape Cod, Nantucket, and part of Martha's Vineyard (SL3-86-313).

Sound is probably due to sand on the crests of shoals, which has been entrained and carried into suspension. This same condition exists in the ASTP photograph of this area (fig. 2(b)), although it is not so clearly defined. Internal wave patterns are visible on both ASTP and Skylab photographs.

Landsat Image

A Landsat false-color composite image of the study area taken on July 17, 1974, was found to be less useful than originally expected. Bathymetric features are clearer in the Landsat image than in the ASTP photographs. However, the scale is too small for one to be able to see individual sandbars within the shoals. Also, wind streaks that are present in the ASTP photographs are absent in the Landsat image.

An interesting comparison was made between the Landsat image and the Skylab photograph. The shoals around Cape Cod, in Nantucket Sound, and east of Nantucket are more distinct in the Skylab photograph. This difference is probably due to the high-resolution Earth terrain camera and the larger scale of the Skylab photo-

graph. The advantage of the Landsat image is that greater water penetration at depth is facilitated by spectral bands 4 and 5. Despite the small scale, this penetration is evidenced by the lighter blue water patches adjacent to the very dark blue areas, especially northeast of Cape Cod.

High-Altitude Aerial Photographs

Eleven photographs from the two high-altitude aircraft flights over New England during the ASTP mission were compared to the ASTP photographs. Table I contains the pertinent information for each flight. Each aerial photograph covers approximately 1000 km^2, one-third of the area encompassed by one ASTP photograph. The aerial photographs taken during the ASTP mission have enough overlap to be viewed stereoscopically. This capability is useful in the determination of surface relief. The weather conditions over the study area were very good during both flights, and the pictures are quite clear. This fact helped to clarify some of the subtle or obscured features in the ASTP photographs. One multispectral photograph (wavelength band 475 to 575 nm) was used to study sediment and chlorophyll in the water.

In comparison to the ASTP photographs, the aerial photographs are much more detailed. Specific local features may be examined more closely than is possible using an orbital photograph. Individual bars and troughs are defined in many shoal areas seen in the aerial photographs. Wind streaks and internal waves are also more clearly defined than in the ASTP photographs. Orbital photographs are important in amplifying the studies done on a detailed level using aerial photographs and in giving these studies more credence by documenting features and trends over a large expanse. They also call attention to large and continuous features that might otherwise be overlooked or misinterpreted in a photograph that encompasses a smaller area. The use of orbital photographs with complementary aerial photographs provides the best results.

COMPARISON OF AERIAL PHOTOGRAPHS WITH BATHYMETRIC CHARTS

Comparisons were made between the high-altitude aerial photographs and the bathymetric charts (refs. 5 to 8) of the region. These comparisons were made (1) to better define the nature of features in both ASTP and aerial photographs, (2) to test the accuracy and detail of recent bathymetric charts, and (3) to determine the amount of change that has occurred since publication of the charts. This comparison was accomplished through the use of a zoom transfer scope.

TABLE I.—Data on High-Altitude Aerial Photographs of Coastal Massachusetts

Parameter	*Flyover 1*	*Flyover 2*
Date	July 19, 1975	Aug. 20, 1975
Camera	Zeiss	RC-10
Lens focal length, cm (in.)	15.24 (6)	15.24 (6)
Film type	SO-397	SO-242
f-stop	5.6	4.0
Shutter speed, sec	1/250	1/125
Filter	KL[a]	2.2 AV
Altitude, km (ft)	≈18.3 (60 000)	19.8 (65 000)
Approx. scale	1:135 000	1:135 000

[a]36 percent.

To simplify the discussion of features seen in these photographs, the study region was divided into five areas (fig. 5). From north to south, these areas are (1) northern Cape Cod including Provincetown and Wellfleet Harbors, the southeastern bight of Cape Cod Bay, and the northeastern shore of Cape Cod; (2) Nauset Beach and Monomoy Island encompassing Nauset Inlet, Pleasant Bay, and Chatham Harbor; (3) Barnstable Harbor including Sandy Neck Spit; (4) Nantucket Island; and (5) Martha's Vineyard.

Northern Cape Cod

The tip of Cape Cod is essentially a recurved spit, as is Long Point (fig. 1). Compared to the chart (ref. 5), the aerial photographs indicate that Long Point has curved farther inland since 1970. A light-colored area is visible in the photographs offshore between Race and Long Points. According to the chart, this area corresponds to a shallow submarine shelf beyond which the bottom drops off sharply. A question raised here is whether this light-colored area also represents some concentration of chlorophyll. It seems to differ texturally from some of the areas that are obviously bottom topography. In general, topography tends to be well defined, whereas the margins of an area of high chlorophyll concentration are more vague. (See the paper by C. S. Yentsch et al. entitled "Ocean Color Observations" in this volume.)

In Provincetown Harbor between Provincetown and Long Point, there is a region of sediment-laden water where bottom topography is visible. The linear feature spanning this area is a dike.[1]

The narrow beach connecting Provincetown and Long Point marks a zone of overwash that has probably helped to partly fill the basin landward of the dike and create the linear shoals that are situated seaward of the dike. These features, seen as color changes on the photographs, are roughly shown on the chart. There is a 15-m drop into Provincetown Harbor marked by the outer color boundary. This light-colored area is also noticeable on the ASTP photograph.

The shoals in Cape Cod Bay off North Truro, which are visible in the photographs, are not depicted on the chart. This chart has a contour interval of 5 m, which is too large to pick up depth variations such as these. Some of the multiple parallel bars that characterize the area can be discerned in the photographs.

The shoals that extend from Truro to Great Island are visible in the photographs and are fairly accurately outlined on the chart (ref. 6) by the 1.8- and 3.7-m (1 and 2 fathom) contour lines. The individual multiple bars that compose the shoals are easily distinguished in the photographs but not on the chart. The bars are essentially parallel to the north shore of Great Island except at Truro, where an effluent stream interrupts them. In this area, it appears that sediment is being entrained from the tops of the bars and suspended. This explains the murkiness of the water and the faintness of the bars. The area may also be rich in chlorophyll because high concentrations of chlorophyll due to heavy rains were reported around Cape Cod during the ASTP mission (ref. 1). Waves breaking over the bars off North Truro indicate a wind direction from the southwest, which is compatible with the prevailing summer wind direction.

The Billingsgate Shoals off Jeremy Point are made up of both parallel and oblique bars (fig. 6). Some depressions between the bars are noted on the chart. The presence of multiple bars is due to several factors: a low-energy environment, a gradually sloping sea bottom, and an abundance of sand-sized material (refs. 9 and 10). These conditions are all satisfied in the southeastern corner of Cape Cod Bay. The prevailing wind directions are northwest and west in the winter and southwest in the summer (ref. 9). However, because of the short fetch of the bay, waves do not get very large. An irregular glacial outwash plain underlies the bay. This gently sloping surface provides abundant grains for reworking and deposition in shoals and flats.

The comparison between the photographs and the chart shows that Jeremy Point has lengthened approximately 500 m since 1967. Billingsgate Island, now intertidal, can be seen on the photograph (fig. 6) and is indicated on the chart, north

[1]Personal communication (1978), J. J. Fisher, Dept. of Geology, University of Rhode Island, Kingston, R.I.

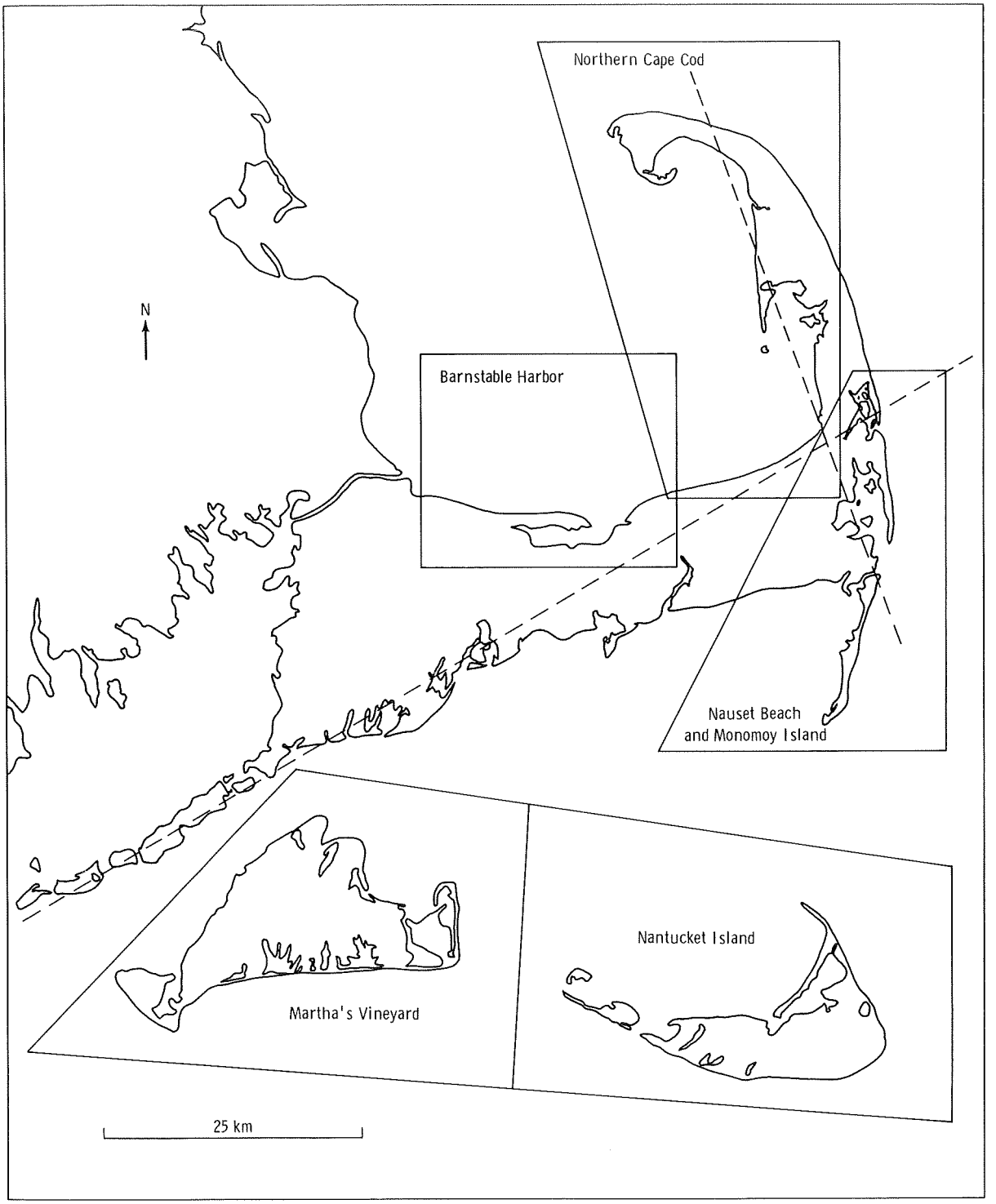


FIGURE 5.—Map showing the location of the five areas where bathymetric charts and high-altitude aerial photographs were compared. Dashed lines indicate paths of high-altitude aerial flights.

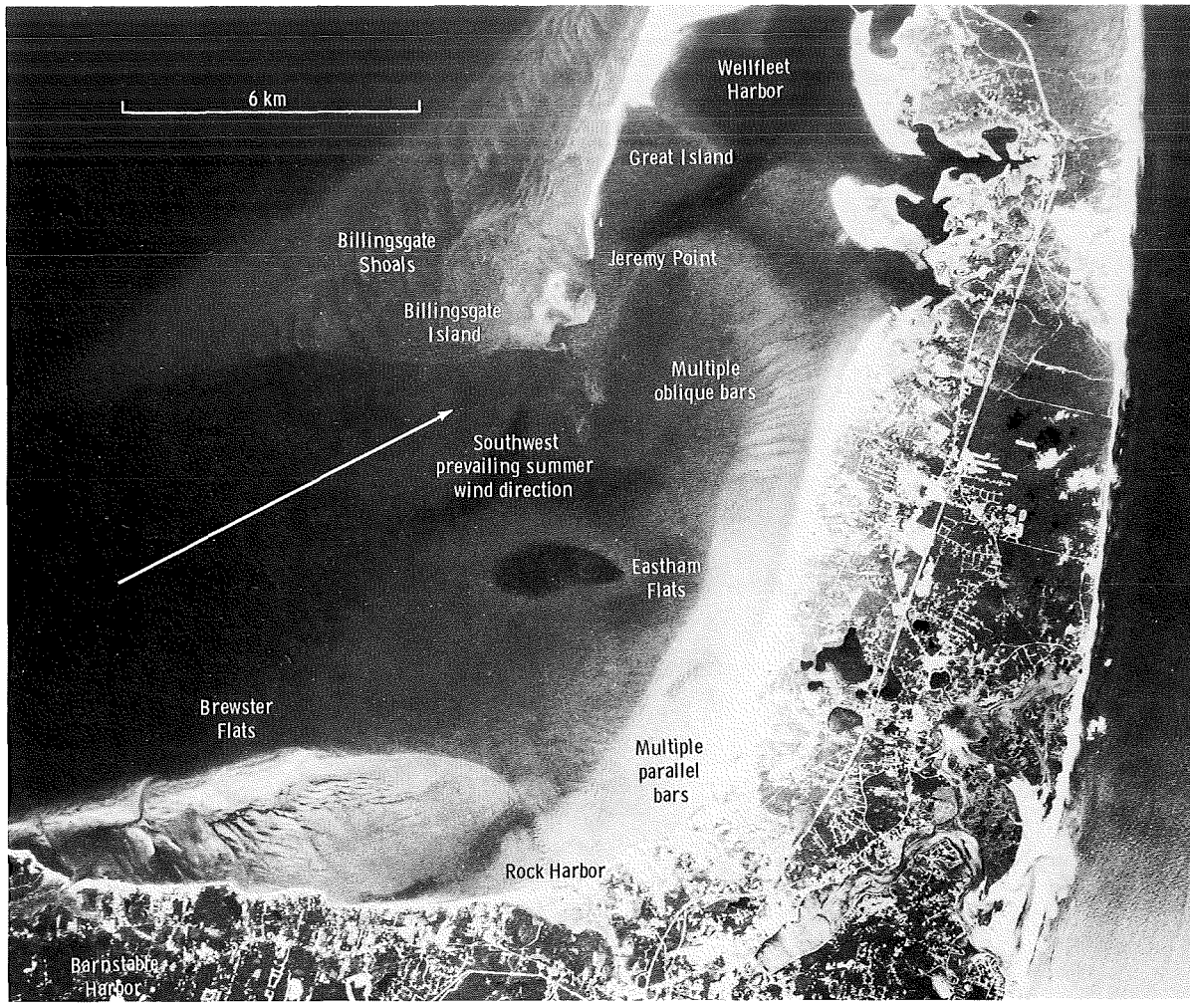


FIGURE 6.—Green-band, high-altitude aerial photograph of the southeastern bight of Cape Cod Bay showing Brewster and Eastham Flats and Billingsgate Shoals.

of its actual position on the photograph. The Eastham Flats are located along the shore south of Wellfleet Harbor to Rock Harbor (fig. 6). To the south, they are composed of extremely regular multiple bars that are parallel to the shore. Farther north, oblique bars intersect the parallel bars. These are thought to be the products of tidal currents in the harbor (ref. 9).

The Brewster Flats (fig. 6), which are visible in the photographs along the shore between Rock Harbor and Barnstable Harbor, are somewhat more complex than either the Eastham Flats or the Billingsgate Shoals. This characteristic is probably due to the original irregularity of the underlying glacial deposits (ref. 9). Individual bars and channels can be discerned in the photograph but not on the chart.

All the flats in Cape Cod Bay are formed by similar processes. They are the result of wave action and have different configurations depending on the fetch and the orientation of the shoreline. Winter winds generating waves out of the west are responsible for bars parallel to the shore. These are also influenced by summer winds from the southwest. However, the primary effect of summer winds occurs north of Eastham Flats and

Brewster Flats because of increased fetch. In this area, oblique bars formed by southwest waves are also prevalent (ref. 9).

Storm waves and longshore currents acting on the eastern shore of Cape Cod have sculpted a smooth, mature shoreline out of irregular glacial deltaic deposits (ref. 11). Beyond the shore, two parallel bars are evident on the photographs. These bars are documented on the charts (refs. 5 and 6) to the extent that several depressions are noted, which mark the troughs between the two bars and between the near bar and the shore. A comparison shows that some of these depressions conform to the present location of the troughs. Throughout the development of Cape Cod, the fulcrum point separating zones of erosion and deposition along the eastern shore has been shifting northwest because of the action of longshore drift. To the north of the fulcrum, the two offshore bars may represent future positions of the shoreline, and to the south, they may mark past positions (ref. 11).

Nauset Beach and Monomoy Island

On the southeastern shore of Cape Cod, a fine example of change through time is seen at Nauset Inlet. By comparison with the 1967 chart, it can be shown that the inlet has shifted approximately 875 m in 8 years (fig. 7). This change has been documented by Strahler (ref. 13), who postulated the northward growth of the spit. Since the time of the ASTP mission, the spit has been broken through and the inlet is presently south of its position on the 1975 photographs and the 1967 chart.[2] Careful examination of the photographs reveals that the breakthrough point at that time was a narrow zone in the spit, probably due to erosion by tidal currents and depletion of source material for the spit.

The section of Nauset Spit across Pleasant Bay has grown southward approximately 375 m since 1967, and the arcuate scars representing former spit terminations are evident on the photographs (figs. 7(a) and 7(b)). Similar features are better illustrated on the southern end of Monomoy Island, which has grown and been further recurved since 1967. Also, from the comparison with the chart, the island has become more narrow in the central region and wider at the southern tip due to deposition of sediment from the center by longshore drift (figs. 7(a) and 7(b)).

The major alteration in this area is the change in Monomoy Island from a landmass connected with southern Cape Cod to an independent island as it is shown on both the aerial (fig. 7(a)) and the orbital photographs. According to Leonard et al. (ref. 9), the breakthrough occurred in 1960, although this is not evident on the 1967 chart (fig. 7(b)). The breakthrough was triggered by the construction of a causeway, visible in figure 7(a) between Monomoy and Morris Islands, which were then connected, and Chatham. The breach occurred between the two islands. The large flood- and ebb-tidal deltas resulting from this break are quite obvious in the photographs and, of course, are not on the chart (figs. 7(a) and 7(b)).

The Commons, which is readily distinguishable on both the photograph (fig. 7(a)) and the chart (fig. 7(b)), is an old tidal delta, which was produced during a break in Monomoy Island approximately 150 years ago (ref. 9). The break occurred at the narrow point in the island, about one-third of the distance from the northern end. A temporary breakthrough took place in 1974, and the smaller delta created at that time can also be seen in the photograph.

A considerable amount of modification to the coastal region surrounding Monomoy Island has occurred because of longshore drift, tidal current patterns, and wave refraction patterns. Wave refraction in particular is thought to have a strong genetic effect on the offshore topography of the area (ref. 9). The resulting northeast-trending shoals are evident to the east of Monomoy, both on the photograph and on the chart (figs. 7(a) and 7(b)).

The channels, islands, and shoals within Pleasant Bay that are visible on the photographs clearly coincide with the chart contours. These features and those discussed previously are also visible on the ASTP photograph of Cape Cod (fig. 2(a)). The light-colored areas along the southern shore of

[2]Personal communication (1978), J. J. Fisher, Dept. of Geology, University of Rhode Island, Kingston, R.I.



FIGURE 7.—Nauset Beach and Monomoy Island. (a) High-altitude aerial photograph showing areas of change on Nauset Spit and Monomoy Island. Triangles indicate direction of longshore drift. (b) 1967 bathymetric chart (ref. 6) showing changes in Nauset Spit and Monomoy Island. Dashed lines indicate positions on 1975 photographs. Contour interval is 1 fathom (1.8 m).

Cape Cod, evident on the ASTP photograph, are seen in detail on the high-altitude aerial photographs. The results of longshore drift are well illustrated in this region (fig. 7(a)). Along the shore, there is a significant buildup of sediment on the western side of all the jetties. This buildup indicates a drift direction from the west, which correlates with Strahler's figure (ref. 13; fig. 3).

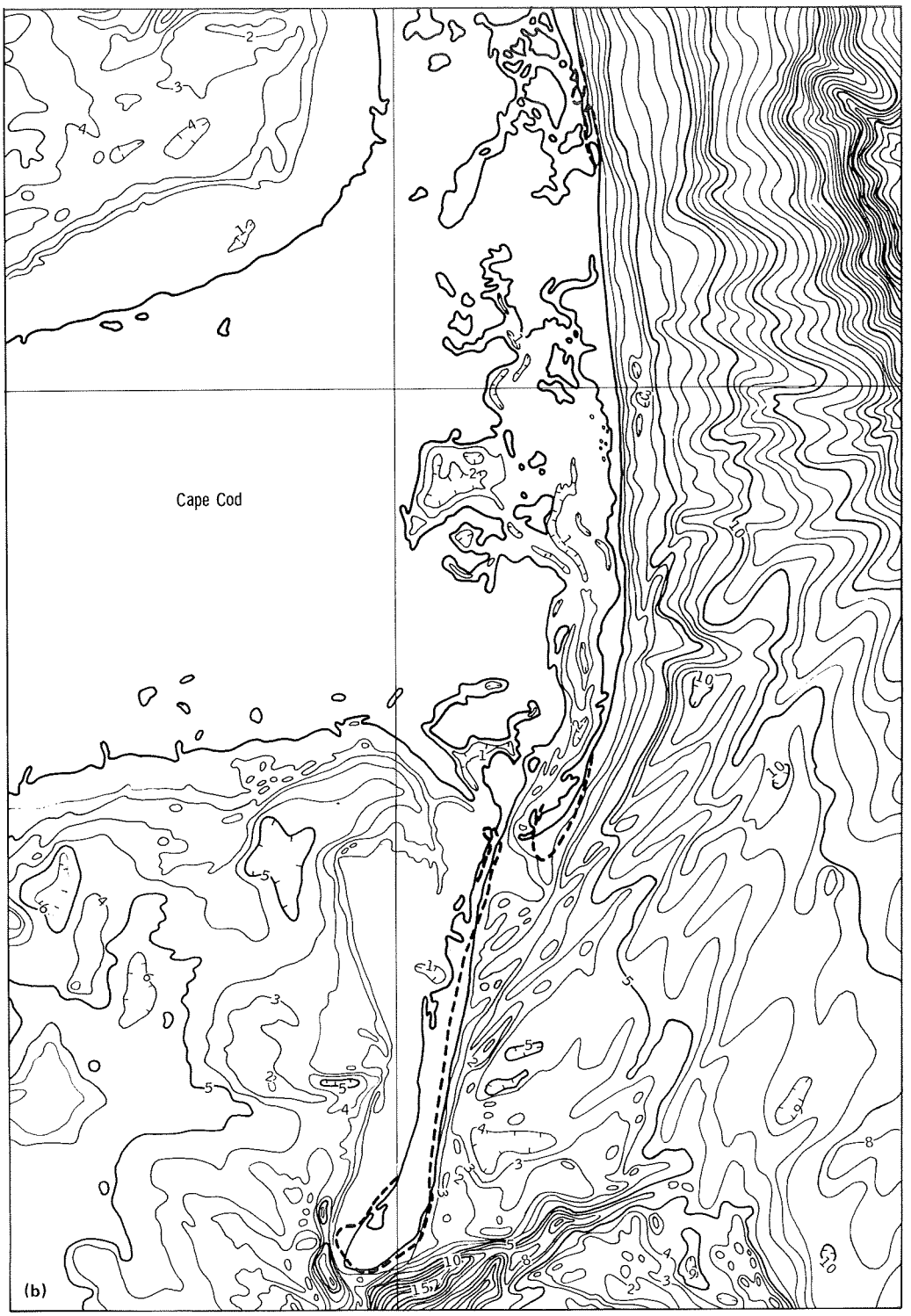


FIGURE 7.—Concluded.

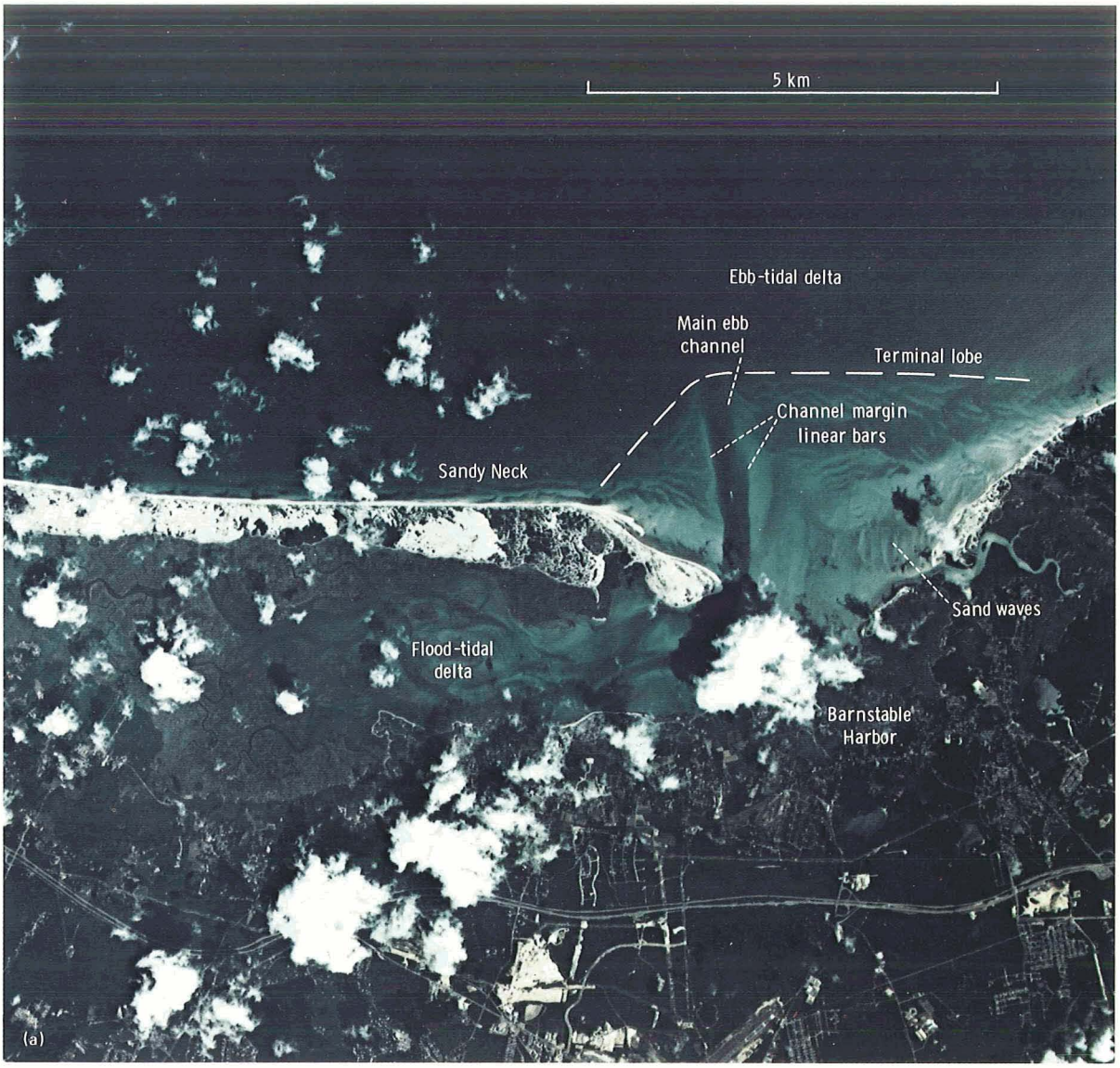


FIGURE 8.—Barnstable Harbor. (a) High-altitude aerial photograph showing components of the ebb-tidal delta. (b) Bathymetric chart of the area (ref. 5). Contour interval is 5 m.

Barnstable Harbor

The comparison between the charts and the photographs of the Barnstable Harbor shows that like Nauset Spit and Monomoy Island, Sandy Neck Spit has been extended since 1970 because of the local direction of longshore drift across Barnstable Harbor (figs. 8(a) and 8(b)). The amount of change is approximately 12 m, which approximately agrees with Hayes and Kana's postulated growth rate of 2 m per year (ref. 12). The previous positions of the spit can be seen as arcuate lines across its length.

The shoals seaward of Barnstable Harbor are an example of an ebb-tidal delta as described in Hayes and Kana (ref. 12). Various parts of the delta including the main ebb channel, terminal lobe, channel margin linear bars, and swash bars

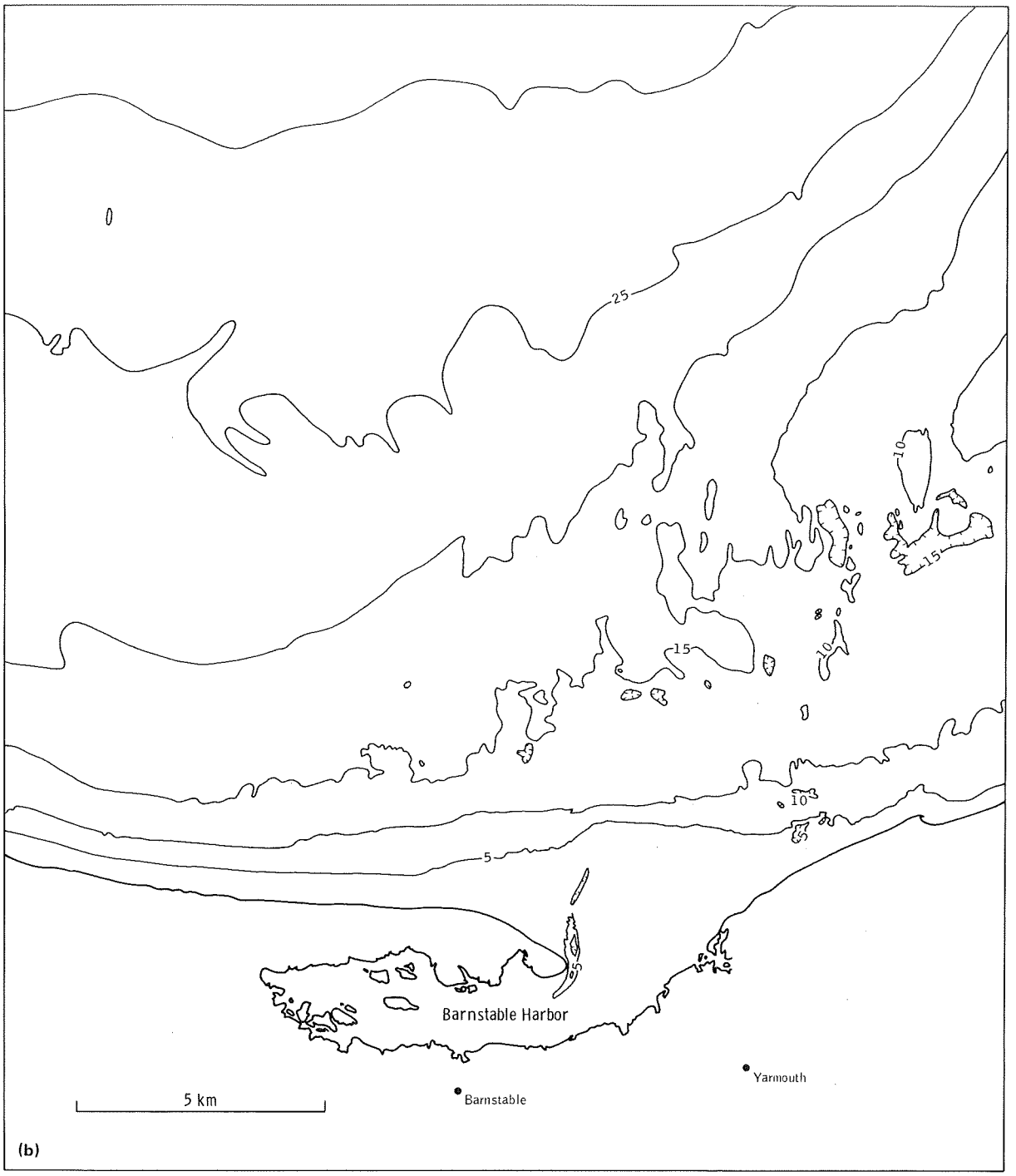


FIGURE 8.—Concluded.

are visible in the aerial photographs (fig. 8(a)). Sand waves, which indicate the current direction in the flood channels that flank the ebb-tidal delta, are also visible, although none of these forms are marked on the chart. The contour interval of the chart is too large to pick up detailed topographic variations such as individual bars and troughs. Landward of the ebb-tidal delta is a flood-tidal delta that also fits Hayes and Kana's model well.

Nantucket Island

A prominent ebb-tidal delta outside Nantucket Harbor is quite evident on the aerial photographs (fig. 9). There is also a flood-tidal delta inside the harbor inlet (ref. 9). However, the specific features of the flood-tidal delta are difficult to distinguish in the photographs. The chart outlines the interior of the harbor well, but the ebb-tidal delta features are not depicted at this contour interval.

The most intriguing feature in these photographs is the cuspate shoreline in Nantucket Harbor (fig. 9). The origin and mode of formation of these cusps have been disputed for some time. The following model is the most plausible. Essentially, the process requires a source of material to build these rhythmic features (ref. 18). In this case, the source material was a glacial hummock (ref. 9), which is presently represented by Coskata Beach and Great Point (fig. 9). Offshore, on the photographs and on the chart, there is further evidence of this topographic high (fig. 9). Coatue and Coskata Beaches and Haulover Beach (fig. 9) formed as a spit and a tombolo, respectively, connecting the hummocky terrain and the island (refs. 9 and 11).

From this beginning, the shore was modified by the wind system particular to the area. The harbor is oriented parallel to the prevailing wind direction from the southwest and the dominant storm wind direction out of the northeast. It is primarily the action of these opposing winds at high angles to the beach that has produced the cuspate configuration. However, the effect of factors such as currents, bathymetry, and coarseness of material cannot be neglected (ref. 18). According to Leonard et al. (ref. 9, p. 234), "longshore processes act in both directions, each eroding sediment from the center of each of the concavities between the cuspate spits and transporting it to the spit ends, where it is deposited as subaqueous bars. The upwind half of each concavity falls in the lee of the upwind spit, preventing longshore drift before the center of the concavity." This process creates the symmetry of the cusps, and the spit lengths are determined by the relative strengths of the currents. The distance between cusps is thought to depend on harbor width (ref. 18). This formation has been stabilized for some time (ref. 9).

At one point, an inlet was created at Haulover Beach, the very narrow stretch of land between the harbor and the ocean (fig. 9). During this period, the decreased tidal flow in the harbor upset the balance between accretion on the spit and erosion by tidal currents. Because of this imbalance, the spits grew large enough to reach the opposite shore (refs. 9 and 11). Now that the inlet is closed, equilibrium between deposition and erosion is maintained.

The shoals that appear in the photographs off Great Point to the north and east are very accurately designated on the chart. They are part of the Nantucket Shoals, which extend east of the island (fig. 9). Not all the shoals marked on the chart are observable in the photographs.

Several linear features south of Nantucket match up with shoals on the chart. Features that appear on both the photographs and the chart include a bar that runs along the shore and a subtidal feature, probably a glacial remnant that extends seaward in one spot. Breakers visible on the photograph indicate the presence of shoals. Their position as well as that of the light-colored water in these areas agree with the chart. There are also sediment plumes along the southern shore, which indicate a westward longshore current (fig. 9).

The northwestern end of Nantucket is an area of extremely variable bathymetry (fig. 9). Some of the shoals in the photograph correspond to the charts. In general, the area is roughly outlined by the 1.8-m (1 fathom) contour line, although individual shoals and depressions have less than 1.8 m (1 fathom) of relief as they are not apparent on the chart. In some places, there is a spit that extends northward from Tuckernuck Island (ref.

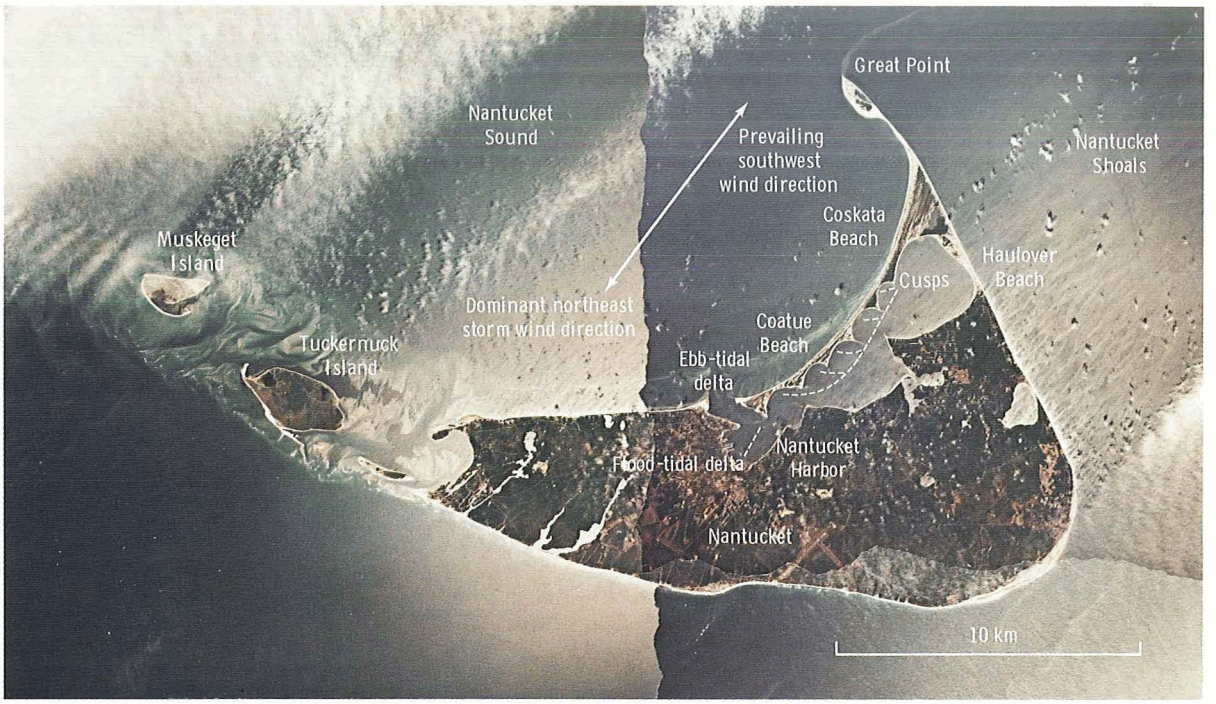


FIGURE 9.—Mosaic of the high-altitude aerial photographs of Nantucket Island.

11). However, at the time of the ASTP mission, the only evidence of this spit consisted of a long, northward-trending line of breakers and a few small linear islands. These latter features are easily discernible on the photograph (fig. 9).

Martha's Vineyard

The aerial photographs point to the importance of longshore drift in the erosion, transportation, and deposition of sediment along the shores of Martha's Vineyard (fig. 10). Conveniently for illustration purposes, there are several areas of landsliding along the coast (ref. 13). The clay-rich glacial tills that compose the sea cliffs are good markers to indicate the sediment drift direction. For example, at Zack's and Wequobsque Cliffs, south and east of Gay Head, respectively, the landslide debris is observable in the photograph (fig. 10). Waves break over the debris, and plumes of sediment can be traced to the east all along the southern shore. The chart only broadly defines this area. Evidence for the drifted landslide debris also occurs along the northwestern and northeastern coasts. Here, sediment accumulation occurs on the updrift side of jetties, and scour areas occur on the downdrift side. Occasionally, plumes of sediment that have been deflected seaward by the jetties are present.

At Observation Point on Gay Head, the landslide material contains a large amount of red clay, which shows up clearly on the photograph as plumes (fig. 10). A fulcrum point dividing northeasterly and southeasterly drift directions also occurs. The point is readily distinguishable because of the differing colors of the drifting sediments.

Longshore drift has a large role in the modification of the southern coast of Martha's Vineyard. As on Nantucket, there are many cutoff bays, which were formed when glacial source waters dried up and water flow through the bays was no longer strong enough to inhibit the flow and deposition of sand across the bay mouth due to longshore drift (fig. 10). These bays are terminated by a long, straight sand beach. The erosion

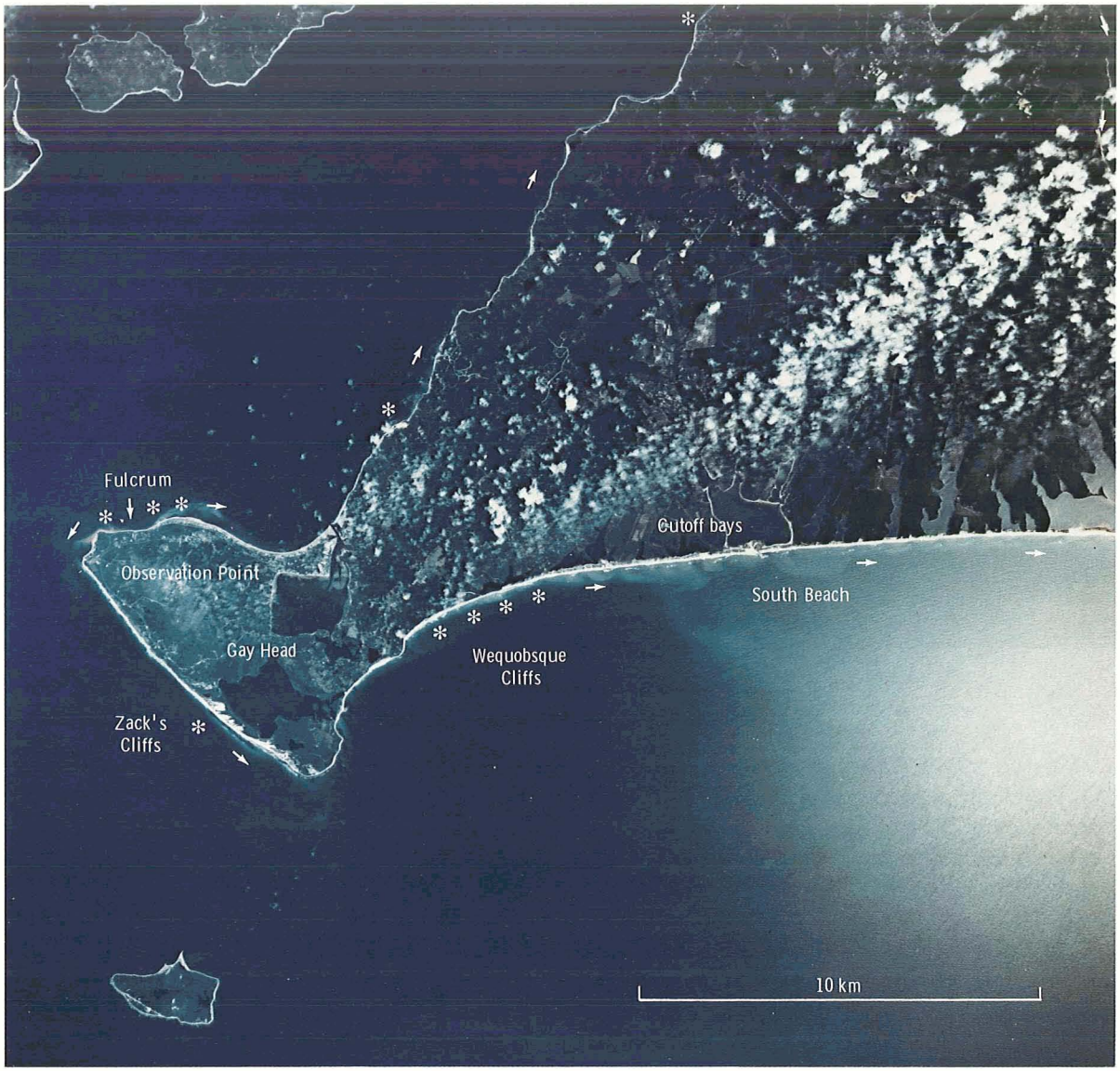


FIGURE 10.—High-altitude aerial photograph of Martha's Vineyard. Arrows indicate direction of longshore drift. Asterisks mark areas of landsliding.

and change along South Beach is enormous. The Kaye map (ref. 14) shows that the shore has retreated since the survey of 1776. Comparison with the 1949 shoreline indicates even further retreat on the order of 12 m.

From the comparisons, it is obvious that both large- and small-scale aerial photographs are exceedingly useful in making charts. Many detailed features of importance to chart users can be accurately mapped using aerial photographs. The incorporation of photographic data into mapmaking increases the accuracy and value of the products. It is also important to recognize the possibility that features have changed since the charts were made. In this case, photographs may be used to update the charts.

COLOR/EDGE ENHANCEMENT OF THE PHOTOGRAPHS

To determine the relationship between the water color observed in the ASTP and aerial photographs and the type of surface features, a Datacolor/Edge Enhancer System was used to enhance, "slice," and profile the photographs. The density of film, which is measured by this machine, is directly related to the color intensity, which is also related to the surface reflectance of the scene. Therefore, information about the reflectance values of the photographed surfaces is gained through the use of this machine.

The density slicer, which sliced the film thickness and assigned each slice a color, helped to clarify land/water interfaces and especially boundaries between waters of varying characteristics. The image density is related to depth and/or sediment content as well as sea state (ref. 19). The peaks marking lighter areas (higher reflectance) and the troughs marking darker areas (lower reflectance) along the profiles were identified and labeled according to the types of surfaces they represented.

A comparison of these profiles (figs. 11(a) and 11(b)) shows a correlation between the height of a profile and a particular surface. For example, the height of the peaks that represent sandy areas such as dunes or beaches is similar in all profiles. However, not all surfaces have a unique signature. Some peaks or troughs of corresponding amplitude represent completely different surfaces; for example, land regions and areas of deep water.

The terrain types or surfaces that are distinguished in this manner include beach sand, shoals and troughs, sediment-laden water, shallow bay and harbor water, and shallow nearshore regions. It is impossible without ground-truth data to accurately designate areas of chlorophyll concentration. However, it is known that plankton blooms are common in this region (refs. 1 and 20), and it is likely that some amount of chlorophyll is present, probably mixed with suspended sediments. The reflectance of such an area would be increased over that of pure chlorophyll because of the scattering effect of the sediment.

It would be possible to fit a scale of reflectance values to these profiles if ground-truth data and accurate knowledge, not only of the morphology of the sea bottom but also the genesis of the features, were available. This was not possible in this study because of the lack of such data in some areas. However, it may be assumed that the range of values would be between 5 percent for deep ocean water (Yentsch and El-Baz, "Estimate of Total Reflectance From the Orinoco River Outflow," this volume) and 40 to 60 percent for light sand (ref. 21).

There are several drawbacks in using the densitometer for accurate determination of the type of surface or terrain in question. One of these is the effect of sunglint on the photographs. If the Sun-elevation angle is medium, this problem is not as critical. However, a high Sun angle often produces a very bright patch of reflection on the water surface which distorts the actual brightness range of the area. Another distortion is created by poor weather conditions. A covering of haze such as that found in the ASTP photographs masks the actual brightness and therefore the reflectance of the surfaces in the photographs. Finally, the lack of ground-truth data eliminates the possibility of definitive identification of a surface. From the air, one can determine the morphology of a feature but not its mode of formation; therefore, accurate identification is inhibited. However, this technique has proved to be a valid tool in the clarification of the nature of various water body characteristics. Also, it provides a basis for comparison between profiles from photographs of unstudied areas or areas that otherwise may be difficult to investigate.

CONCLUSIONS

This analysis of ASTP photographs has demonstrated the importance of orbital photographs in the study of marine and coastal regions. The use of these photographs has facilitated the examination of features, processes, and phenomena such as shoals, sediment plumes, longshore drift, wind streaks, and internal waves. It has shown that the ability to view such features over broad areas per-

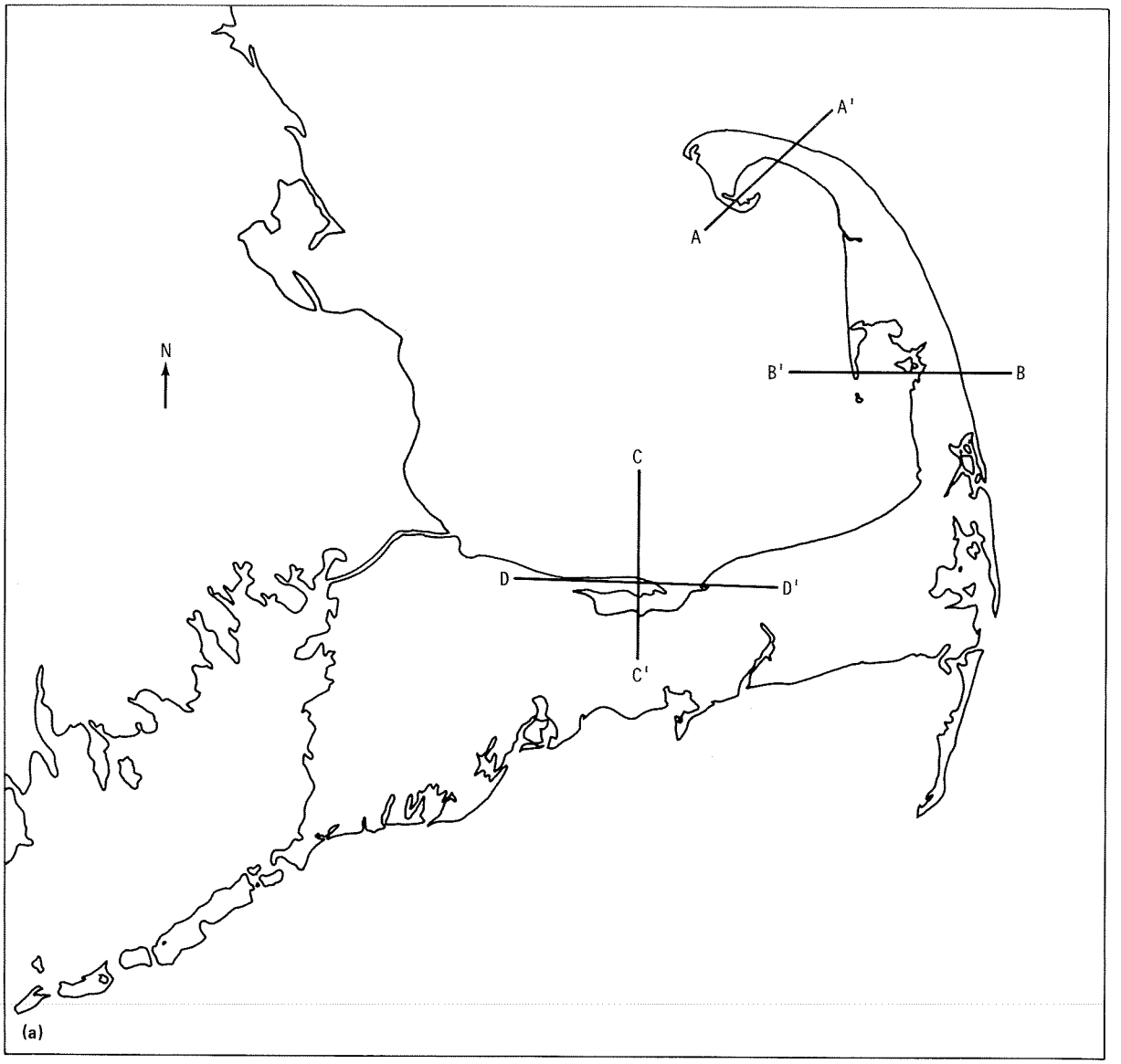


FIGURE 11.—Density profiles generated by the Datacolor/Edge Enhancer System. (a) Map of Cape Cod showing locations of profiles. (b) Color intensity profiles with peaks representing bright surfaces, such as sand, and troughs representing open ocean water and/or vegetated land. (Reference lines are shown under each curve.)

mits a more thorough and far-reaching investigation than is possible from ground data alone. This conclusion was confirmed by the comparisons with recent bathymetric charts. Although the charts were reasonably accurate, the photographs provided much more detail, especially around shoals. This result illustrates the usefulness of orbital and aerial photographs in clarifying and updating charts.

The use of concurrent high-altitude aerial photographs contributed enormously to the amount of information gained from this study. It is obvious that the combination of orbital and aerial photographs with ground-truth data in an

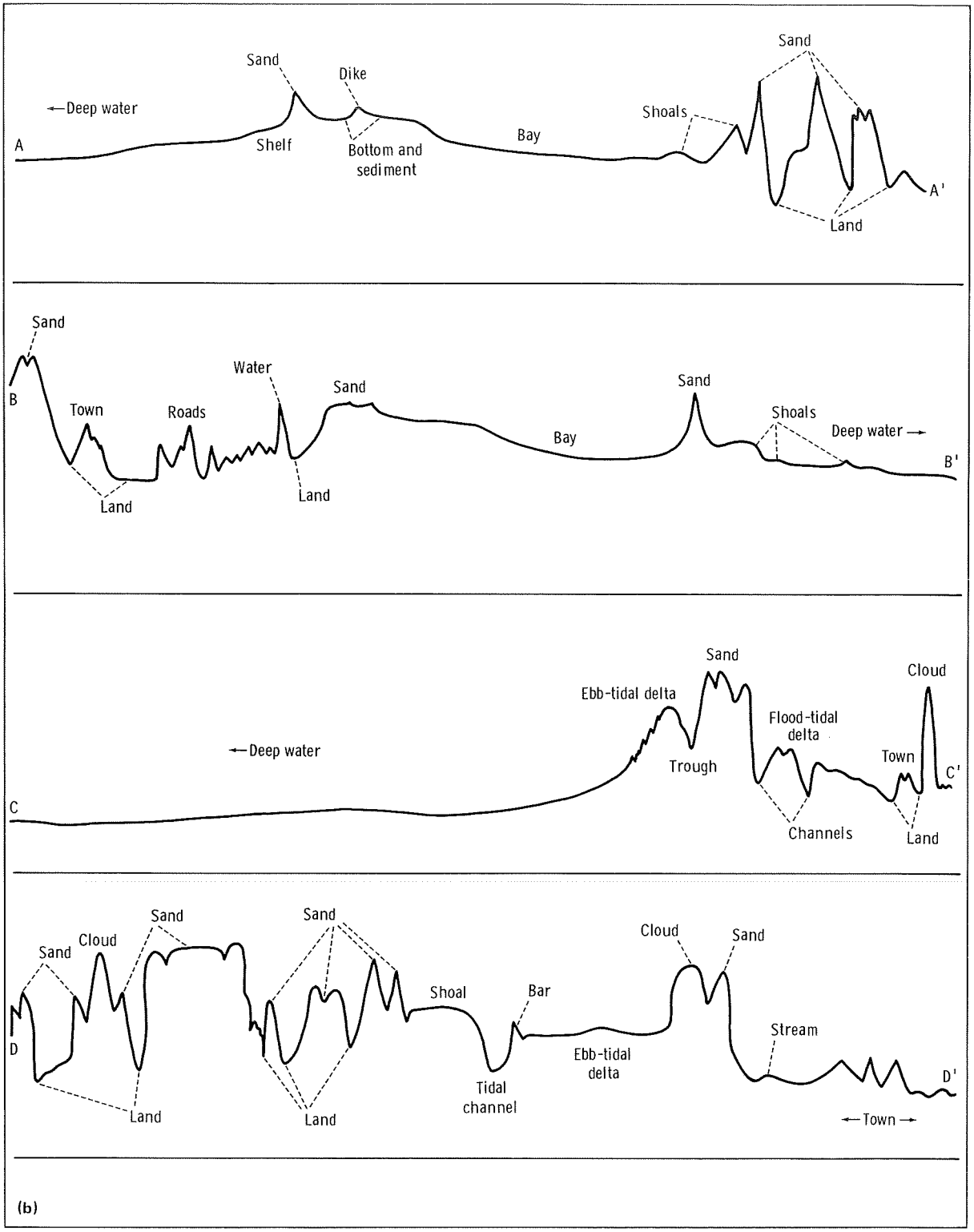


FIGURE 11.—Concluded.

investigation would provide the most complete and accurate results. The use of a Datacolor/Edge Enhancer System or a similar photographic analysis aid may be very helpful in adding a further dimension to such an investigation.

ACKNOWLEDGMENTS

The authors thank Elizabeth Simpson, whose contribution of expertise was invaluable throughout this study. Also, the assistance and advice of William Philpot and John Knight were greatly appreciated.

REFERENCES

1. El-Baz, Farouk: Astronaut Observations From the Apollo-Soyuz Mission. Vol. I of Smithsonian Studies in Air and Space, Smithsonian Institution Press (Washington, D. C.), 1977, pp. 16-19, 72-75.

2. Dolan, Robert; Hayden, Bruce; Heywood, Jeffrey; and Vincent, Linwood: Shoreline Forms and Shoreline Dynamics. Science, vol. 197, no. 4298, July 1, 1977, pp. 49-51.

3. Gierloff-Emden, H. G.: Manual of Interpretation of Orbital Remote Sensing Satellite Photography and Imagery for Coastal and Offshore Environmental Features (Including Lagoons, Estuaries and Bays). Intergovernmental Oceanographic Commission, IOC-UNESCO Contract SC/RP 600/341, 1976, pp. 17-26, 45-51.

4. Dietz, R. A.: Aerial Photographs in the Geologic Study of Shore Features and Processes. Air Photography and Coastal Problems, M. T. El-Ashry, ed., Dowden, Hutchinson and Ross, Inc. (Stroudsburg, Pa.), 1977, pp. 23-31.

5. Bathymetric Map, Cape Cod to Cape Ann, Massachusetts; Scale 1:125 000. U. S. Coast and Geodetic Survey 0808N-50, 1970.

6. Bathymetric Map, Nantucket Sound and Approaches; Scale 1:125 000. U. S. Coast and Geodetic Survey 0708N-51, 1967.

7. Bathymetric Map, Nantucket Shoals; Scale 1:125 000. U. S. Coast and Geodetic Survey 0708N-52, 1967.

8. Bathymetric Map, Block Island and Rhode Island Sounds; Scale 1:125 000. U. S. Coast and Geodetic Survey 0808N-51, 1967.

9. Leonard, J. E.; Fisher, J. J.; et al.: Coastal Geology and Geomorphology of Cape Cod; An Aerial and Ground View. Geology of Southeastern New England; A Guidebook for Fieldtrips to the Boston Area and Vicinity, Barry Cameron, ed., Science Press (Princeton, N. J.), 1976, pp. 224-264.

10. Nilsson, Harold D.: Multiple Longshore Sandbars: Occurrence and Origin Along a Low-Energy Shoreline in Cape Cod Bay, Massachusetts. Abstracts with Programs, Geol. Soc. America, vol. 10, no. 2, 1978, p. 78.

11. Johnson, Douglas: The New England-Acadian Shoreline. Hafner Publishing Co. (New York), 1967, pp. 119-123, 402-405, 415-416, 424-457, 458-465, 492, 494-497, 505-507, 514.

12. Hayes, M. O.; and Kana, T. W., eds.: Terrigenous Clastic Depositional Environments, Some Modern Examples. Coastal Research Division, Dept. of Geology, University of South Carolina, Technical Report No. 11-CRD, 1976, pp. I-55 to I-71.

13. Strahler, Arthur N.: A Geologist's View of Cape Cod. The Natural History Press (Garden City, N. Y.), 1966.

14. Kaye, C. A.: Map Showing Changes in Shoreline of Martha's Vineyard, Massachusetts, During the Past 200 Years. U. S. Geol. Survey Geomorphic Map MF-534, scale 1:48 000, 1973.

15. Apel, John R.; Byrne, H. Michael; Proni, John R.; and Charnell, Robert L.: Observations of Oceanic Internal and Surface Waves From the Earth Resources Technology Satellite. J. Geophys. Res., vol. 80, no. 6, Feb. 2, 1975, pp. 865-881.

16. Halpern, David: Semidiurnal Internal Tides in Massachusetts Bay. J. Geophys. Res., vol. 76, no. 27, Sept. 20, 1971, pp. 6573-6584.

17. Skylab Earth Resources Data Catalog. NASA Rep. JSC 09016, U. S. Government Printing Office (stock no. 3300-00586) (Washington, D. C.), 1974, pp. 8-11.

18. Zenkovitch, V. P.: On the Genesis of Cuspate Spits Along Lagoon Shores. J. Geol., vol. 67, no. 3, 1959, pp. 269-277.

19. Reeves, Robert G., ed.: Manual of Remote Sensing, vols. 1 and 2. American Soc. Photogram. (Falls Church, Va.), 1975.

20. Clarke, George L.; and Ewing, Gifford C.: Remote Spectroscopy of the Sea for Biological Production Studies. Optical Aspects of Oceanography, N. G. Jerlov and E. Steeman Nielsen, eds., Academic Press (New York), 1974, pp. 389-413.

21. Smith, John T., Jr., ed.: Manual of Color Aerial Photography. American Soc. Photogram. (Arlington, Va.), 1968, p. 77.

ASTP at Barbados: Mesoscale Pools of Amazon River Water in the Western Tropical Atlantic

G. Borstad[a]

ABSTRACT

Surface data at Barbados suggest successive passage of pools of brackish Amazon River water until late August. A review of the literature supports this hypothesis and makes it very unlikely that the discolored water observed east of Barbados by the Apollo crew during the Apollo-Soyuz Test Project was due to Orinoco River water. The expansive freshening of the western tropical Atlantic by brown-colored Amazon water in July will mask any effect by the smaller Orinoco.

INTRODUCTION

The western tropical Atlantic annually receives large inputs of fresh water from rain over oceanic areas and from runoff of two of the world's largest rivers, the Amazon and the Orinoco. Both rivers drain extensive inland areas having heavy seasonal rainfall, and oceanographic atlases show a progressive freshening of the neighboring Atlantic, which corresponds seasonally with the discharge of each river (ref. 1). The influence of these riverine discharges has been studied by many investigators (refs. 2 to 7), but single ship surveys of such large and dynamic regions do not provide very accurate descriptions.

During the Apollo-Soyuz Test Project (ASTP) in July 1975, the Apollo astronauts made a number of scientific visual observations from space. Over the western tropical Atlantic, they photographed and observed the Orinoco River Delta and the surrounding ocean to provide information regarding the ocean area influenced by that river. The Apollo flight provided a unique and valuable opportunity to obtain direct synoptic observations of the river plume over a wide area, the hydrology of which is quite complicated. This section is a report on the near-synoptic sea-surface observations made near Barbados to provide ocean-surface data for the observations from space.

SEA-SURFACE DATA

The research ship *Martlet* of the Bellairs Research Institute made three short cruises on July 21, 22, and 23, 1975, and acquired data at 64 stations. Bucket samples for sea-surface temperature, salinity, and chlorophyll-*a* concentration were obtained at all 64 stations. At alternate stations, bathythermograph casts were made to 75 m and seawater transparency or clarity recordings were made with the Secchi disk. As the Secchi disk was lowered into the water, the color of the surface waters was also measured by comparing the color of the Secchi disk, just as it disappeared in the water, with a series of colored solutions prepared according to the Forel-Ule scale (ref. 8). This series of 10 standards ranged from blue to green, and although they were not identical to the Munsell color comparators used by the astronauts, they did match the observed sea-colors very well.

[a]Marine Science Centre, McGill University, Montreal, Quebec, Canada.

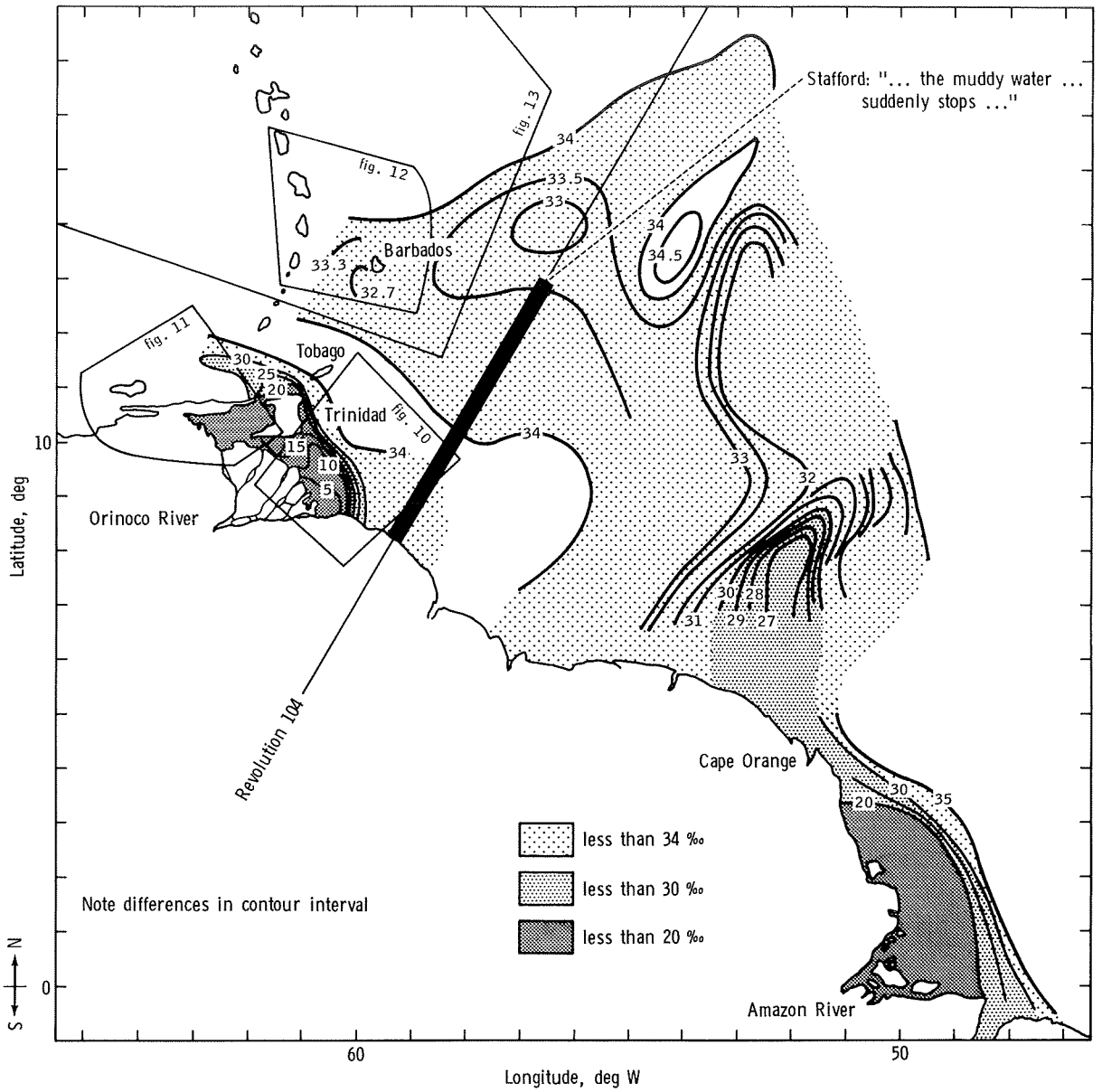


FIGURE 1.—Summer surface salinity (°/₀₀) in the western tropical Atlantic (June to August). The Orinoco area is after Gade (ref. 2), the Amazon area after Gibbs (ref. 6), and the oceanic area after Mazeika (ref. 11). The approximate area of photographs, groundtrack of revolution 104, and "the edge of the brown water" observed by the Apollo crew are indicated.

Several bucket samples were taken for cell counts of the planktonic cyanophyte, *Oscillatoria* (*Trichodesmium*), and its phycoerythrin pigment. Zooplankton collections were made at the stations most distant from the island on each cruise and over the bank south of the island. These collections were by means of surface tows using 0.5-m plankton nets of 0.24-mm mesh. Drift bottles were released over the entire area at closely spaced intervals.

In the laboratory, salinity was measured by an inductively coupled salinometer; chlorophyll-*a* measurements were made with a fluorometer equipped with a "blue" lamp and Corning 5-60

and 2-64 filters (ref. 9). Phycoerythrin was also measured fluorometrically (ref. 10). *Oscillatoria* cell counts were by the Untermöhl method after filtration through a 1-μm-pore filter to concentrate the sample.

Subsequent figures indicate the approximate locations of sampling stations. Raw data will not be included here but will be archived at the Marine Environmental Data Service, Ottawa, Ontario, Canada, and are available on request.

ASTP-DERIVED DATA

During space flight over the western tropical Atlantic, the Apollo astronauts photographed and observed the Orinoco River Delta and the sea surface north to Barbados. The ASTP-derived data were obtained during revolution 104 on July 22, 1975. For the surface waters between South America and Barbados, the crew tasks included descriptions of the sediment-plume boundaries of the Orinoco River and descriptions, using a Munsell color comparator, of the color of surface waters. Figure 1 shows the study area and indicates the areas and orientation of ASTP photographs; the figure also shows the groundtrack of revolution 104 and the brown-water boundary observed by the Apollo crew. Photographs were taken with handheld cameras on improved SO-368 film.

RESULTS

Meteorological Conditions

Synoptic weather maps issued by the Venezuelan meteorological office (ref. 12) show a simple pattern of isobars over the eastern Caribbean during most of July 1975, with a mean easterly wind of 2.5 to 7.7 m/sec (5 to 15 knots) (fig. 2). This regime was disturbed temporarily by the passage of two weak tropical waves. A small high-pressure anticyclone that developed over northern South America was responsible for some cloud cover over the Orinoco River Delta during ASTP and for a period of light and variable winds between Barbados and South America.

Winds observed at Seawell Airport, Barbados, and from the *Martlet* remained easterly with velocities less than 3 m/sec (6 knots) on July 21 and 22, and became northeasterly near 7.7 m/sec (15 knots) on July 23. At Trinidad, easterly winds became northwesterly on July 20, southwesterly on July 21 and 22, returning to easterly by July 23. Velocities dropped appreciably during this period with values for "number of miles run by the anemometer per day" decreasing from near 100 to near 40 (160 to 64 km).[1]

Very calm seas with a 0.5-m swell accompanied the period of low winds in the cruise area. With the retreat of the high-pressure system to the west, windspeed increased on July 23, and seas returned to normal with 1- to 2-m waves and swell.

Only widely scattered cumulus clouds were present over the western Atlantic during the mission, thus providing good conditions for observations of the sea from space.

Sea Surface Temperature

Surface "bucket" temperatures varied between 300 and 301 K (27° and 28° C) in the study area. Bathythermograph casts showed changes in stratification of approximately 20 m, which may imply that the low-salinity surface water was rotating anticyclonically. Johannessen (ref. 13) and Sander (ref. 14), however, have recorded vertical fluctuations of the thermocline of as much as 35 to 40 m resulting from internal waves and tidal oscillations. It is unlikely, therefore, that the trend was significant.

Surface Drift Currents

The residual drift during late July 1975, as inferred from drift bottle returns, was to the northwest at approximately 30 km/day (fig. 3). Different symbols are used to point out the grouping of returns, which suggests an absence of large-scale deformation of the water mass that may have resulted if either semipermanent eddies were

[1]Personal communication: P. Roachford, Caribbean Meteorological Institute, Barbados.

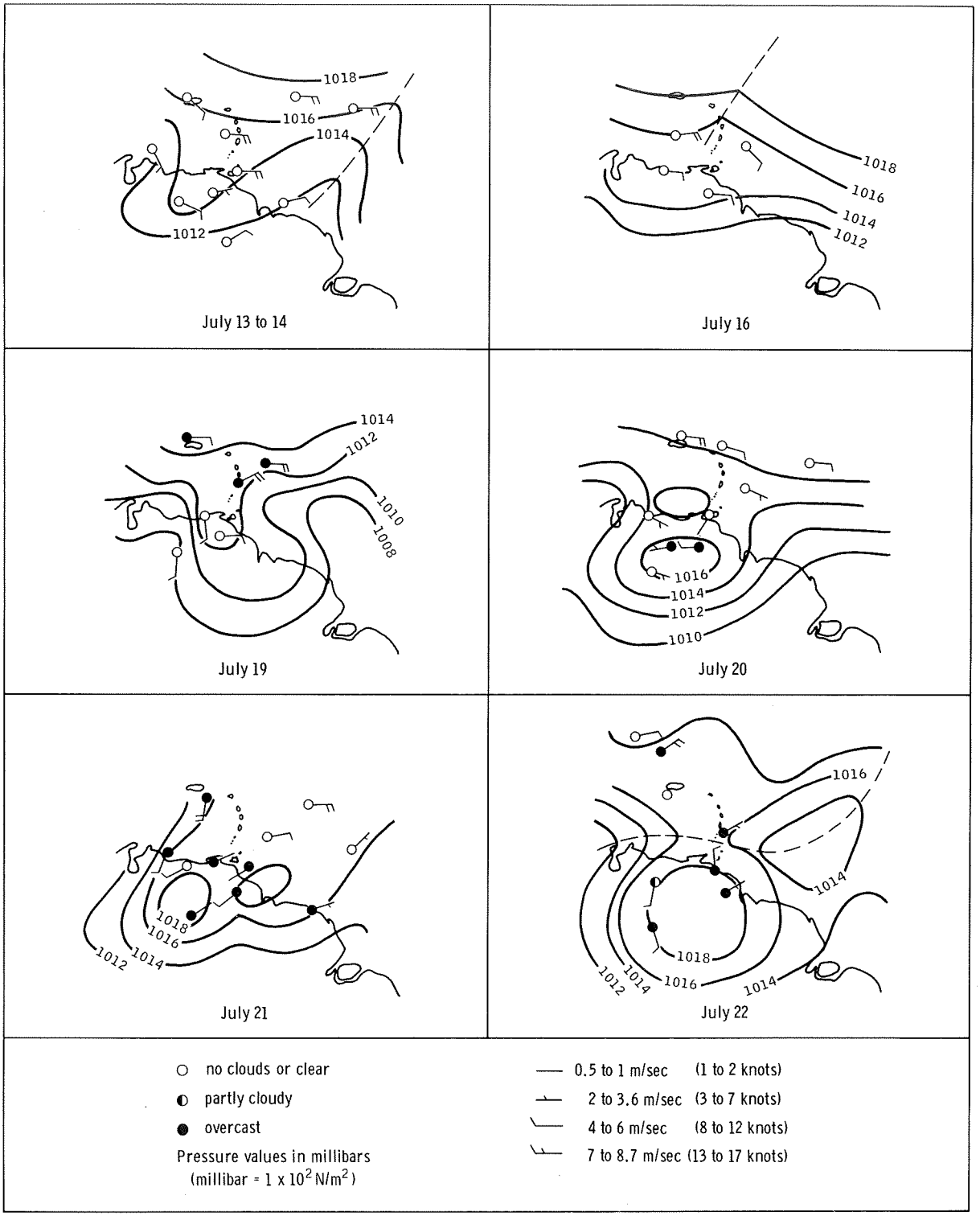


FIGURE 2.—Meteorological conditions over the western tropical Atlantic, July 13 to 22, 1975 (ref. 12).

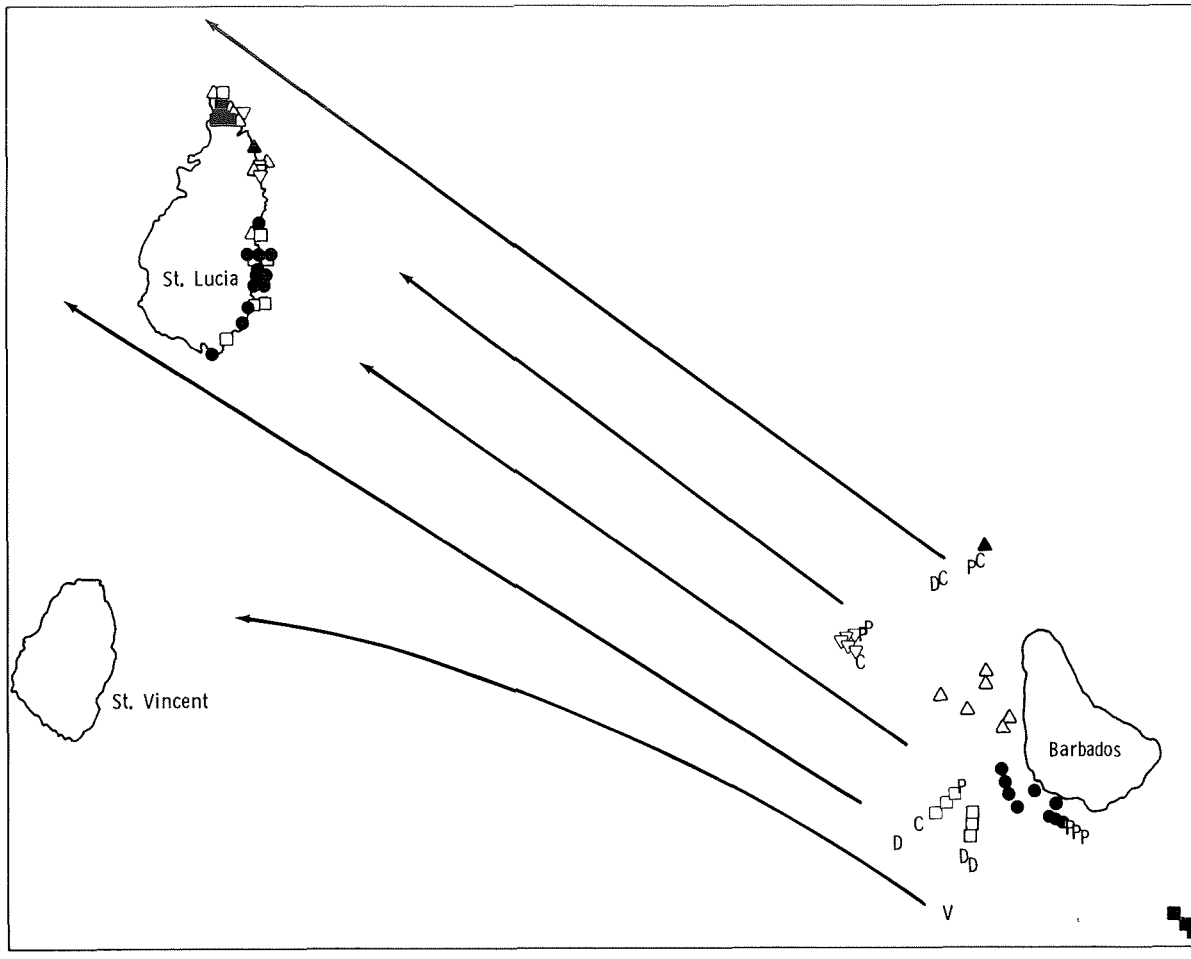


FIGURE 3.—Surface drift conditions inferred from drift bottle returns. The different symbols illustrate the original grouping and the grouping of returns from St. Lucia. (Letters represent returns from other islands: V, St. Vincent; P, Puerto Rico; C, St. Croix; D, Dominican Republic.) Calculated drift velocity was approximately 30 km/day.

present behind this island or if the water mass "seeded" with bottles was rotating.

The drift indicated in figure 3 is in good agreement with that calculated for July by Emery (ref. 15) and by the National Oceanographic Data Center in Washington from ships' drift (ref. 16).

Salinity

A consistent decrease in surface salinities was observed toward the south along the southeast track. Two days later, on the northwest track, a similar gradient was detected; and it is evident that, with a northwestward drift of some 30 km/day, the water mass sampled the first day in the southeast was the water mass sampled again on the second and third day. Figure 4(a) shows the location of stations and their observed salinities on each day; figure 4(b) shows the inferred salinity pattern "pseudosynoptically" when surface drift is accounted for. Other data, to be discussed later, provide evidence that this water mass was in fact the center of a larger body of low-salinity water, pools of which are common near Barbados in spring and summer.

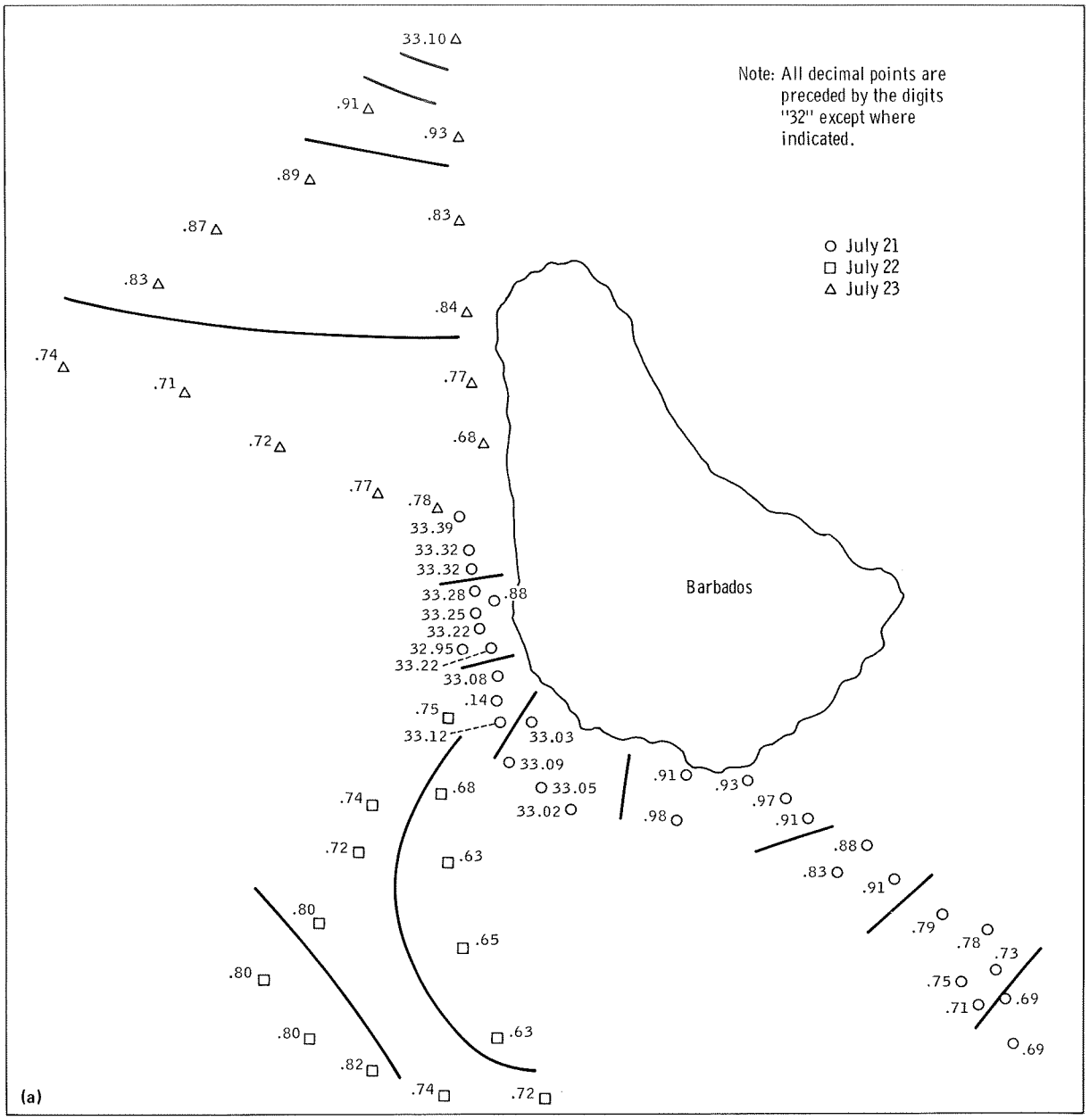


FIGURE 4.—Surface salinity (°/₀₀) for Barbados study area. (a) Empirical surface salinity for July 21, 22, and 23, 1975. (b) Inferred surface salinity for July 23, 1975, accounting for surface drift.

Water Color

Distinct differences in apparent color of the surface water were observed, and they correlated well with salinity as shown in figure 5. The lower salinity water appeared greener, a characteristic which in lakes is attributable to dissolved organic material and humic materials (ref. 8). There was no correlation of color with surface chlorophyll-*a*, with *Oscillatoria* cell numbers, or with Secchi transparency.

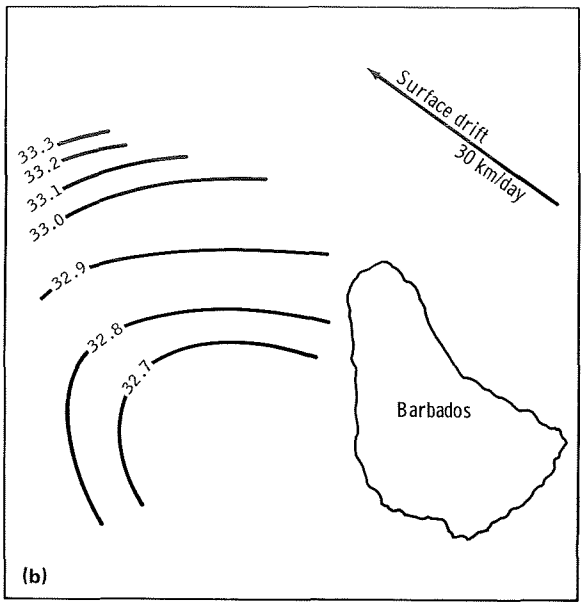


FIGURE 4.—Concluded.

Surface Chlorophyll-a and Phytoplankton Concentrations

Surface chlorophyll-*a* concentrations are shown in figure 6. There is no correlation with salinity and therefore no correlation with the presence of the brackish water mass passing the island; but there is evidence that the phytoplankton responded to the presence of the island. The apparent increase in the lee of the island is as much as 300 percent. This island-mass effect is well known (refs. 17 and 18) and is thought to be a result of varying degrees of fertilization of the water column because of a number of factors, including shoaling of internal waves on the island platform, mixing due to turbulence near the island, and runoff. Runoff will not be important at Barbados because the island has no rivers.

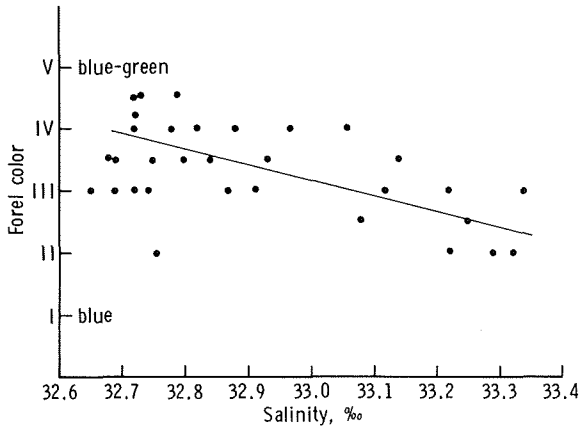


FIGURE 5.—Relation between sea surface salinity and Forel color.

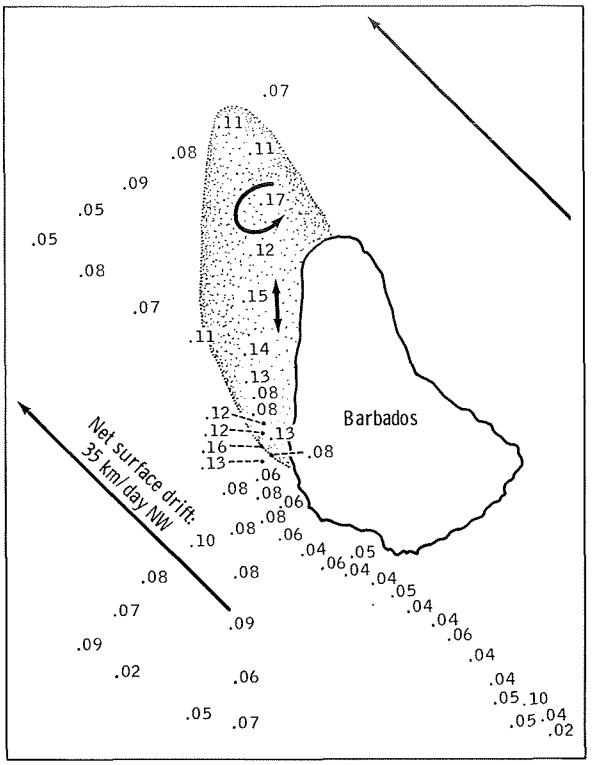


FIGURE 6.—Surface chlorophyll-*a* concentrations near Barbados (μg chlorophyll-*a*/liter) July 21 to 23, 1975. Arrows indicate surface drift pattern in July 1973.

At the time of this study, the effect observed was not great, and the increase in phytoplankton as they passed through the island lee did not persist for long. In the area of weak and variable currents close to the lee shore (ref. 19), the phytoplankton apparently have time to respond to the fertilization that occurs. As the water mass and the phytoplankton it contains move away from the island, the effect is removed and the phytoplankton population quickly diminishes to a nutrient-limited level similar to that east of the island.

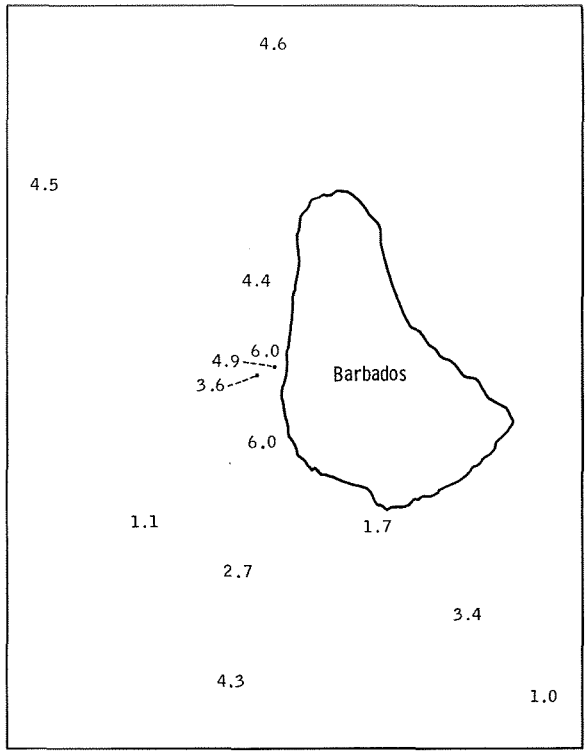


FIGURE 7.—Surface *Oscillatoria* concentrations (cells/liter × 10^4), July 21 to 23, 1975.

Cell counts of the planktonic blue-green algae *Oscillatoria* (*Trichodesmium*) were made at several stations as part of another study. These data indicated a trend similar to that of chlorophyll-*a*, with a population increase in the island lee but not correlated with surface salinity (fig. 7). Qualitative study of other phytoplankton and other data (Borstad, unpublished) indicate that all phytoplankton responded to the presence of the island, and the increase in chlorophyll-*a* concentrations should not be ascribed to *Osciliatoria* alone.

The cyanophycean pigment phycoerythrin was also measured at some stations, but the data were considered unreliable and are not included here. There was no relation between these measurements and *Oscillatoria* concentration.

Zooplankton

Surface zooplankton were studied at some stations; also as part of another study.[2] The data presented in figures 8(a) and 8(b) show an increase in total numbers and biomass in the low-salinity pool. Wet volume and dry weight show a constant trend; total zooplankton and copepods show the same trend except for station 55, which was the extreme northern station. This area may have been receiving small zooplankters swept out of the island littoral zone.

There may have been, therefore, a doubling of zooplankton population within the low-salinity water similar to that observed by Calef and Grice (ref. 4) off Cape Orange. Unfortunately, other data on zooplankton collections at Barbados during 1975 were not available at the time of writing.

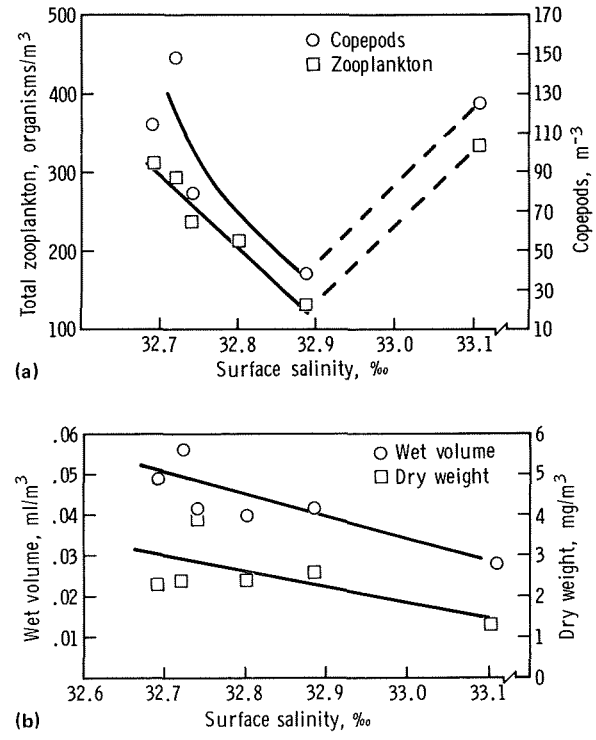


FIGURE 8.—Surface zooplankton data (R. Kidd, unpublished). (a) Relation between surface total zooplankton, copepods, and salinity. (b) Surface zooplankton biomass as measured by wet volume (ml/m³) and dry weight (mg/m³) compared to surface salinity.

[2]Personal communication: R. Kidd, Bellairs Research Institute, St. James, Barbados.

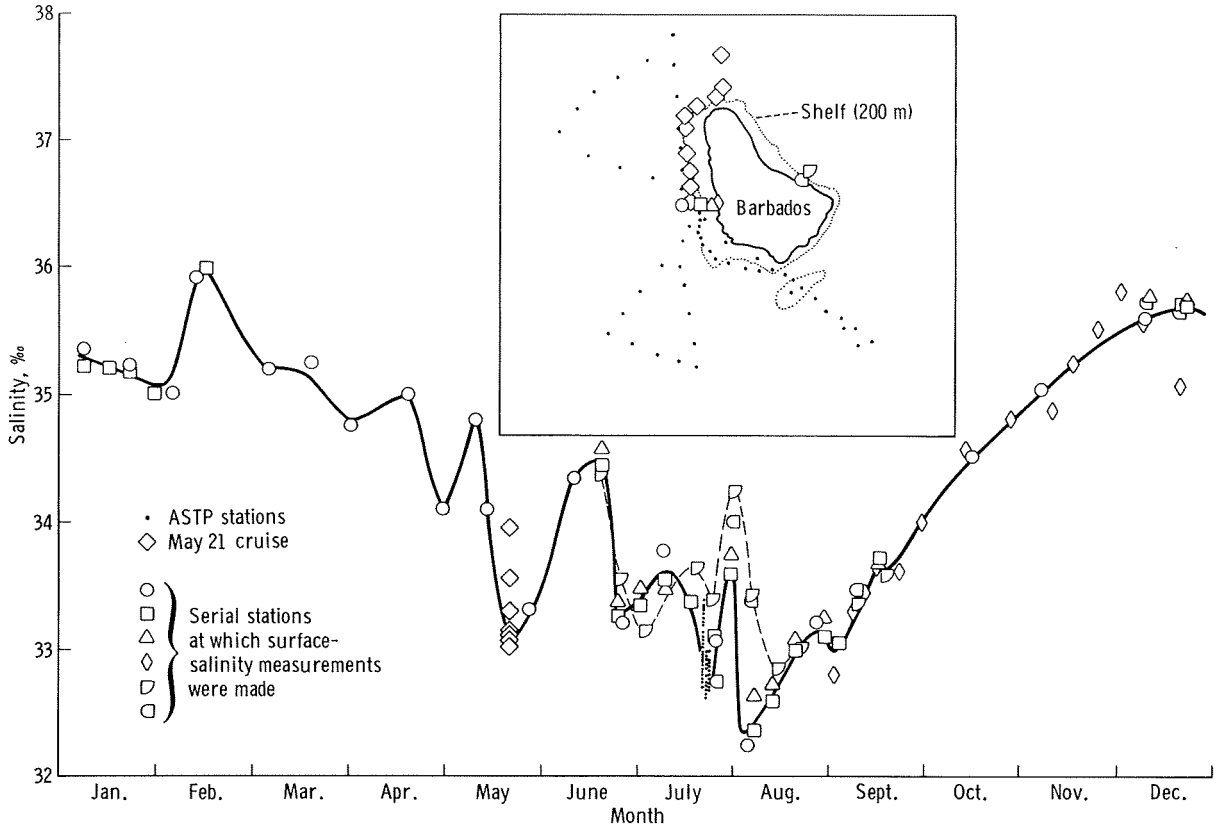


FIGURE 9.—Temporal variations of sea surface salinity at a number of stations around Barbados, 1975. (Borstad, Hawkins and Kidd, unpublished). Points alined vertically indicate different salinities measured at different locations on the same day (horizontal variability). The continuous line indicates inferred salinity at a point 8 km off the west coast. The broken line indicates inferred salinity at a station 4 km off the east coast.

DISCUSSION

The low-salinity surface water mass described earlier, which was passing through the area during ASTP, was in fact the center of a large pool of low-salinity water, as shown by salinity data from several stations in the vicinity of Barbados during 1975 (fig. 9). Beginning in early spring, the onset of freshening of the surface waters was accompanied by a series of short-term fluctuations suggesting a succession of pools of brackish water. Surface salinity is negatively correlated with silicate concentration at Barbados (ref. 20), and several investigators (refs. 20 and 21) have concluded that this characteristic indicates that freshening of surface waters is largely a result (approximately 65 percent) of the presence of Amazon River water.

The temporal pattern of surface salinities for 1975 at Barbados is similar to data from previous years, with large fluctuations about a decreasing mean from January to August, then a constant increase during the fall and winter. Elliott (ref. 22) reported that sea-surface salinity in the Barbados Oceanographic and Meteorological Experiment (BOMEX) area, 300 km east of Barbados, also fluctuated a great deal during May, June, and July; he suggested that horizontal advection was the most active mechanism producing these changes in that area. It is possible, therefore, that the mesoscale pools of low-salinity "Amazon Water" are also present in the BOMEX area, and that they

follow a route from Cape Orange north to near latitude 12° or 13° north then west past Barbados.[3] Very little research has been conducted with sampling intervals small enough to detect these features, but most studies show this tongue of low salinity, which suggests that the movement of the brackish water is governed mainly by wind stress (ref. 11). The geostrophic calculations for the area imply considerably different circulation for the lower layers.

There is little evidence that these pools of fresh water are rotating eddies; however, eddies have been observed in the region before. Emery (ref. 15) hypothesized the presence of semipermanent eddies in the lee of Barbados as an explanation for the distribution of returns of tagged flying fish. Brucks (ref. 24) inferred a complex pattern of eddies in the area from time-averaged geostrophic data; so have several other investigators (refs. 11, 25, and 26). Stalculp and Metcalf (ref. 27), however, found that geostrophically calculated currents near the Antilles bore little resemblance to directly measured currents, because of interference of internal waves and tidal oscillations. Johannessen (ref. 13) pointed out similar problems between Barbados and Trinidad but was still able to detect, from expendable bathythermograph data, a cyclonic eddy just south of Barbados.

The periodic reversals of currents recorded by current meters moored in the BOMEX area (ref. 11) suggest passage of rotating water masses; and, if fluctuations in salinity accompany these changes, they would provide direct evidence for passage of low-salinity eddies along the axis of the tongue extending north from Cape Orange (fig. 1).

It would appear that pools of brackish water are generated near the Amazon River Delta. Gibbs (ref. 6) reported direct airborne observations of the shedding of small eddies of turbid water from the Amazon plume near the delta, and he hypothesized that these small isolated masses of river water could be the sources of larger pools. Cadée (ref. 28) also observed great fluctuations of surface salinity near Cape Orange, which can be interpreted as evidence of pools or eddies of fresher water in that area. To Metcalf (ref. 29, p. 242) "the whole picture suggest(ed) a series of meanders and recurvings of parts of the Coastal Current, with successive pools of Amazon outflow moving offshore amongst them."

Summarizing, it appears that pools of Amazon water, perhaps rotating, leave the South American coast near Cape Orange and travel north to near 13° north latitude and then west under the influence of the zonal winds. The summer freshening of the surface waters at Barbados and east of the island is due, to a large extent, to the presence of this Amazon water. These pools are of different color than the high-salinity oceanic waters because of the presence of humic compounds; they also exhibit differences in zooplankton content.

The question remains as to whether the Orinoco River has a significant role in freshening the surface waters near Barbados. Gade (ref. 2) concluded this river's effect is quite local and is of relatively minor importance in determining the sea-surface salinity in the eastern Caribbean (fig. 1). The U.S. Navy Hydrographic Office "Atlas of Surface Currents of the North Atlantic Ocean" (ref. 30) shows the North Brazilian Coastal Current (ref. 29) and the Amazon plume north of Cape Orange beginning to recurve in July. The surface salinities at Barbados begin to increase 4 to 5 weeks later, at the same time the Orinoco River attains its maximum discharge. Any possible influence of Orinoco water near Barbados will more likely be detectable when the supply of Amazon water is cut off and when light and variable winds make the distribution of low-salinity surface water near the Orinoco Delta variable (ref. 2). (At least one apparent "reversal" of surface drift was reported by merchant seamen: an estimated 0.25- to 0.4-m/sec (0.5 to 0.75 knot) "current" to the east southeast between St. Vincent and Barbados during the week ending October 31, 1975. Winds recorded at Barbados were westerly for a short period that week, which may account for the observed drift. It is also possible that these ships crossed the periphery of a rotating water mass.)

[3]More nearly synoptic surface salinity data for the Guiana Current area between Tobago and Cape Orange have been presented by Urosa and Rao (ref. 23). These data show essentially the same pattern as reconstructed in figure 1, but the low-salinity surface water of Amazon origin is closer to the Guiana coast in the west. The Orinoco outflow is, however, separated from the low-salinity waters offshore by a narrow band of higher salinities.

The constant rate of increase in salinity values after August indicates that Orinoco water did not appear at Barbados in 1975.

The brackish water along the coasts of Trinidad and Venezuela, and in the Gulf of Paria is definitely of Orinoco origin and is distinguishable from oceanic waters by its color, usually being separated from it by a visible front (ref. 2). According to merchant seamen interviewed at Bridgetown, Barbados, the "green water" in the Gulf of Paria and near Trinidad is never visible north of Tobago. Their reports of the extent of this discoloration coincide well with the tongue of brackish water reported by Gade (ref. 2 and fig. 1). Most merchant captains agreed that the seasonal wandering of this boundary was only 15 to 25 km, with the maximum northward extension during the fall rainy season in Venezuela, corresponding with the Orinoco maximum discharge in early September. These observations are supplemented by information from R. Jones, Barbados Assistant Fisheries Officer, onboard the United Nations Development Program/Food and Agricultural Organization (UNDP/FAO) fisheries research vessel *Calamar*, who observed "a gradual change from oceanic blue to green water just north of Tobago"[4] on September 13, 1975. According to the captain of the *Calamar*, "the green water which was present between Trinidad and Tobago at that time was not present at all 6 weeks before."[5] This implies that the waters of the Orinoco plume were confined to the Gulf of Paria and near the delta during the ASTP, not having reached their maximum geographical extent until near the middle of September. This very obvious discoloration, due primarily to fine clays in suspension, was observed from space and appears on the photographs of the delta (fig. 10) and the Gulf of Paria.

During revolution 104, however, the Apollo commander (ACDR) marked "the spot where the muddy water from the Orinoco suddenly stops" at 170:06:06 GET, which would make it at 12.0° north latitude and 56.5° west longitude, or approximately 3° east of Barbados.

When questioned during the experiment debriefings regarding the extent of the "brown water," both the ACDR and command module pilot (CMP) mentioned that one could detect a brown color in sunglint, but they repeatedly insisted it was discolored water they had observed (ref. 31, p. 202). The ACDR, CMP, and docking module pilot (DMP) described the location as follows.

ACDR — We gave you a mark. It goes way out in the Atlantic.

CMP — Let me qualify one thing. You know we were talking about it all the way out there, to where the end of the brown water was; but later I kept watching and I decided that maybe we said it was a little too far out because you can detect a little bit of brown in sunglint . . .

DMP — Oh, yes. Barbados was in fairly close, but I sure agree with Vance (CMP), because in the sunglint it does have a tendency to look a little tan or something. In any place, the Pacific or the Atlantic. But you could look out to the side and it even went way past Barbados.

The Apollo crew may have observed brown colors at the sea surface north of Barbados, or they may have been disoriented and considered themselves north of the island after having "passed" it during revolution 104, which was angled northeasterly. It is difficult to identify the "edge of the brown water" precisely, especially since sunglint interfered with the observations; but it is obvious that a very large part of the western tropical Atlantic was receiving discolored water.

The sea color visible from onboard the *Martlet* was distinctly blue or blue green, with no brown hues, but this may have been due to the obvious differences in observation technique. Where clear oceanic waters are observed from high altitudes, the light emerging from the sea will be a relatively small part of the total to be seen (ref. 32). The tan color observed may have been due to atmospheric interference by airborne Saharan dust, which may be great at times over Barbados (ref. 33).

[4]Personal communication: R. Jones, Barbados Assistant Fisheries Officer.

[5]Ibid.

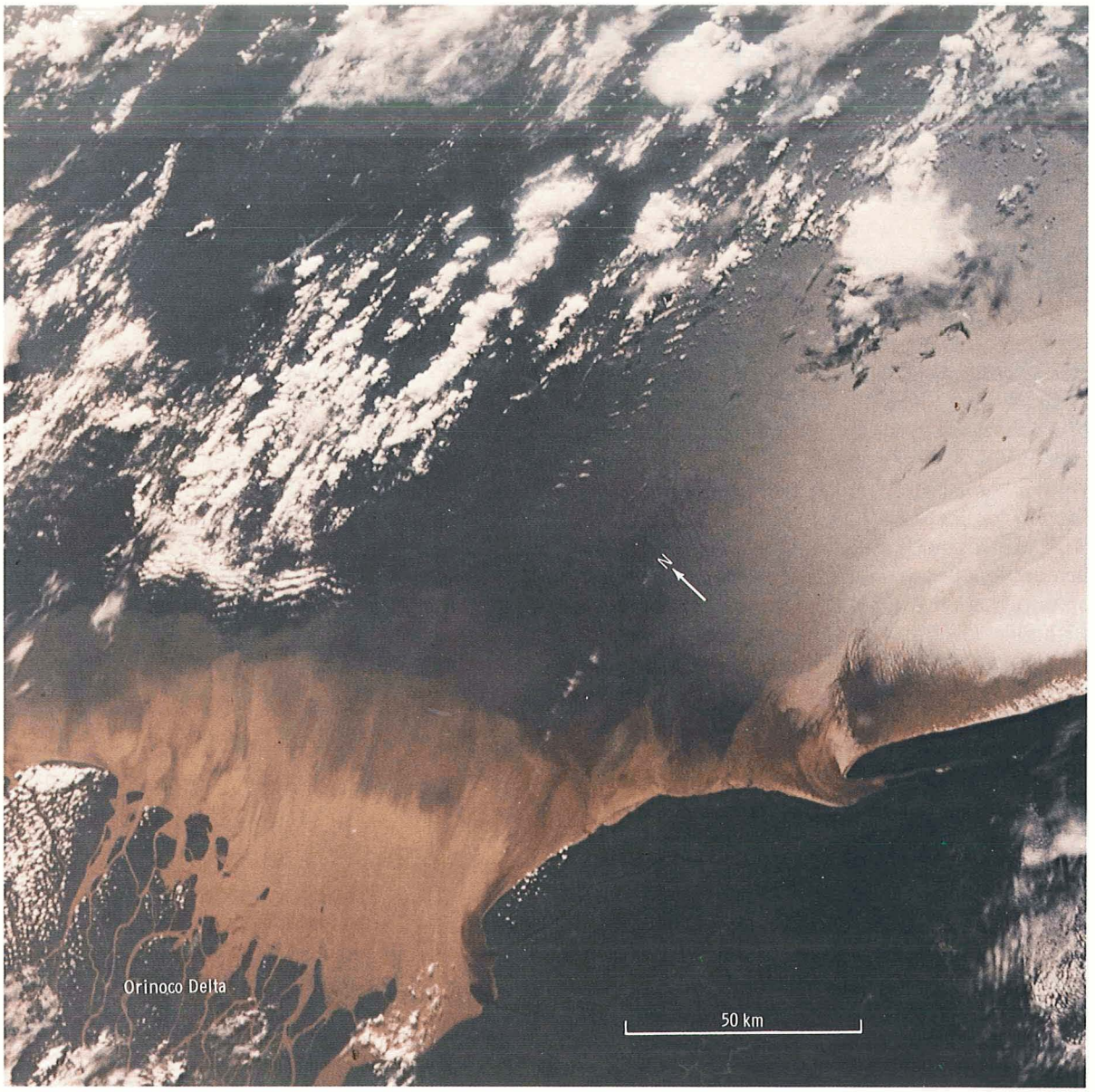


FIGURE 10.—The Orinoco Delta area showing local discoloration due to suspended sediment brought down by the river (AST-21-1685).

The most likely explanation is that the brownish hues observed from space were in fact caused by humic compounds of riverine origin, but that they were due to the expansive freshening of the entire western tropical Atlantic known to be attributable to the Amazon River and partially described earlier in this section. Indeed Ryther, Menzel, and Corwin (ref. 3) stated that, "In contrast with the turbid waters of the (Amazon) estuary and near the river mouth, the water in the fresh-water region (north of Cape Orange) was extremely clear and almost devoid of solids, though it retained a characteristic *brownish-black discoloration.*" If this discoloration is retained as long as the salinity signatures of the water mass, then the boundary observed by the Apollo crew is

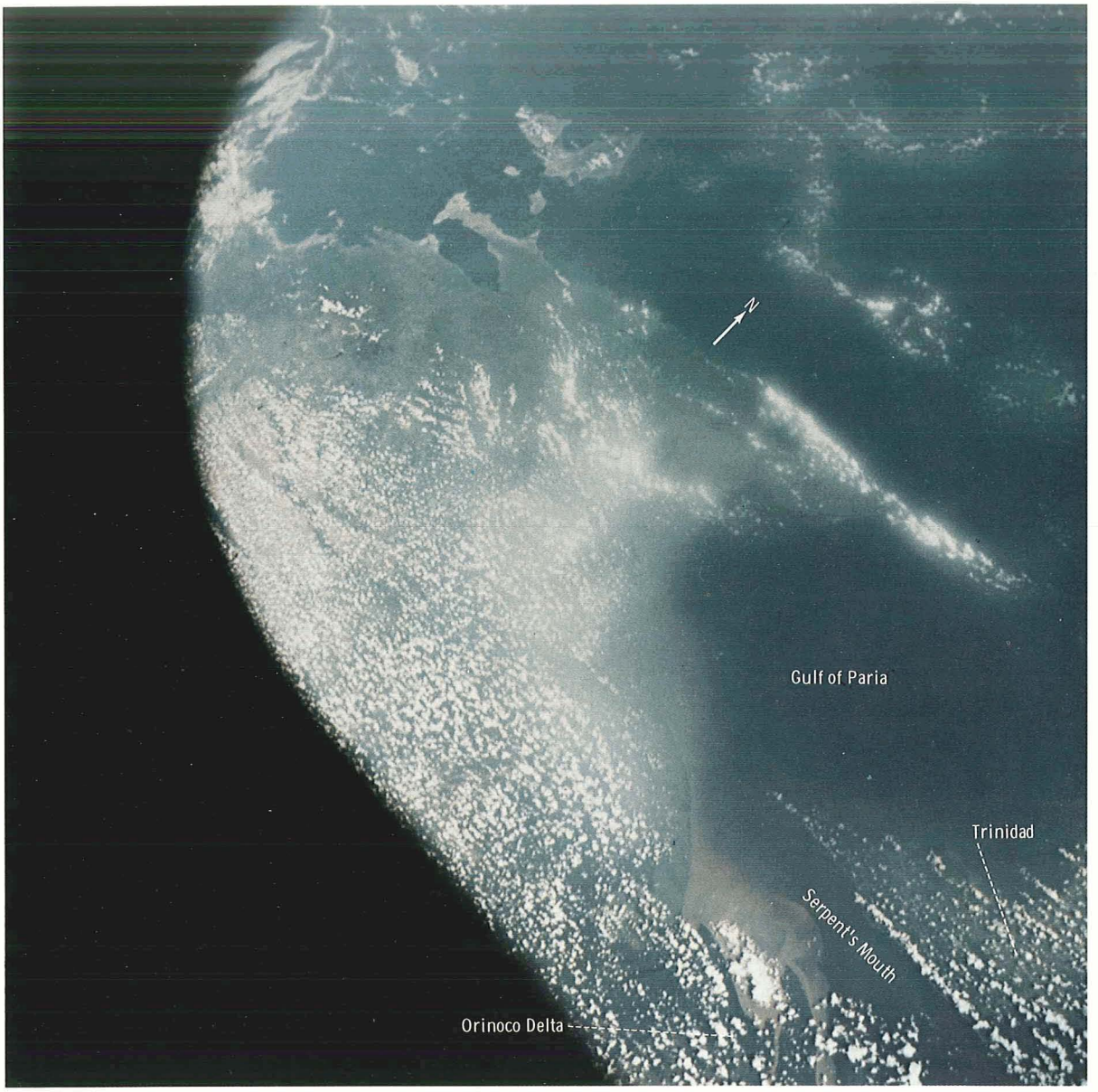


FIGURE 11.—The Gulf of Paria, showing discoloration of nearshore waters (AST-19-1575).

almost certainly the northern extent of Amazon waters, not those of the Orinoco. The Amazon plume is at its maximum extent in late July, whereas the much smaller Orinoco did not reach its discharge maximum until September (ref. 2 and comments of R. Jones, quoted earlier).

Photographs of the Orinoco Delta taken by the Apollo crew show the heavy sediment load of the nearshore waters, and they show a zoning similar to merchant seamen's descriptions of the ocean color of this area (fig. 10). A large lobe of the plume extends north along the coast toward Trinidad. (Note also a series of internal waves at the right of this photograph.) A photograph over the Gulf of Paria during an earlier revolution (fig. 11) also shows discoloration only near the

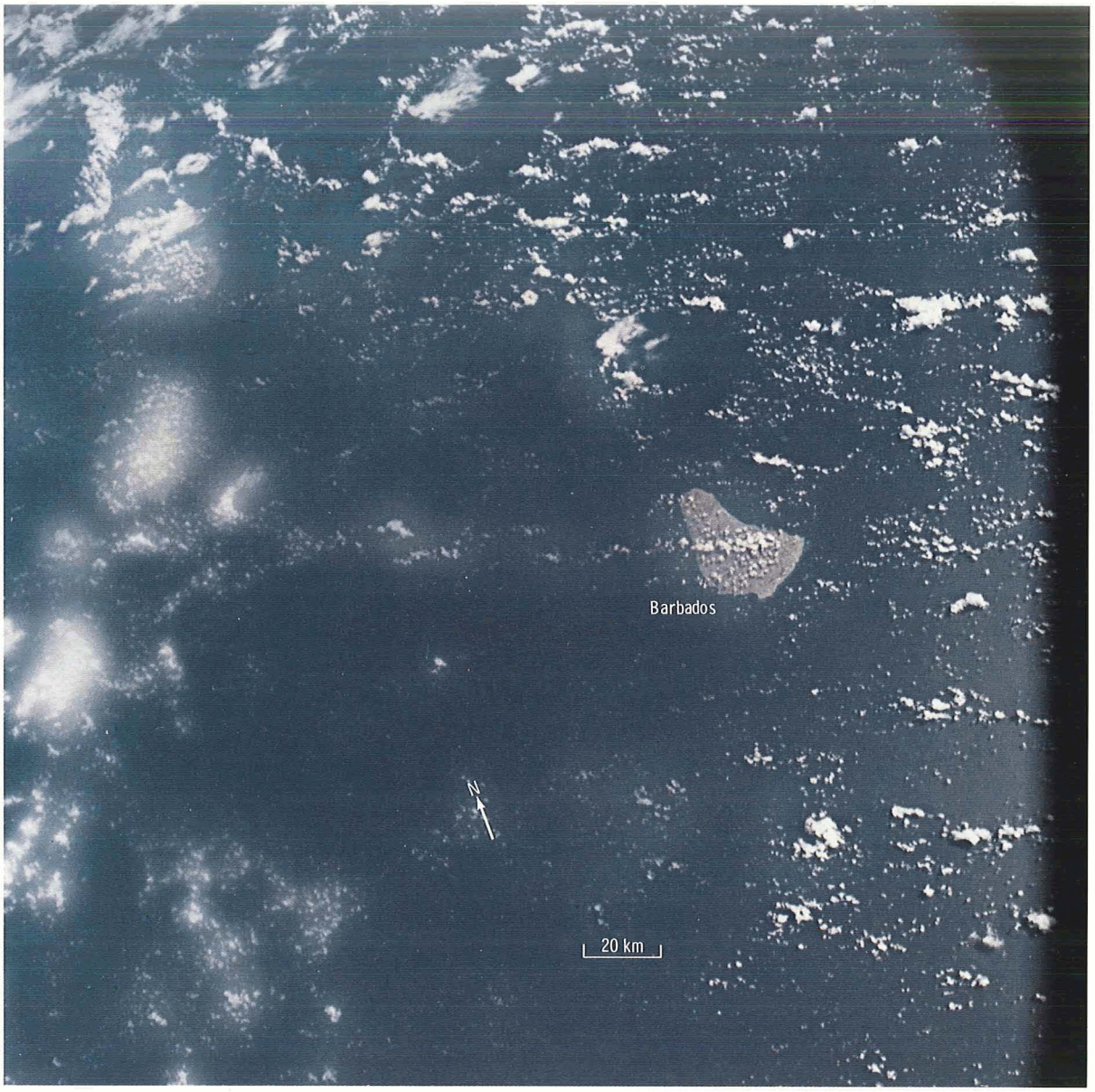


FIGURE 12.—Near-vertical photograph over Barbados. Lesser Antilles islands are out of focus under orographic cloud at the left. Note greenish coloration of sea surface to the right (AST-19-1576).

Venezuelan coast. There is considerable aberration associated with clouds both over the land and with the small patches north of the Paria Peninsula. The next photograph taken on that revolution (fig. 12), a near-vertical image over Barbados, also shows the problem; parts of the image are out of focus, especially where orographic cloud cover is present over the islands of the Lesser Antilles. The sea surface does have a greenish or brownish cast to it in the eastern part of the photograph, with some patchiness on this coloration to the west of Barbados. Whether or not this is the discoloration observed by the Apollo crew is difficult to say. Salinity observations, however, (fig. 8) indicate that the pool of green, brackish water sampled during the *Martlet* cruises was nearing

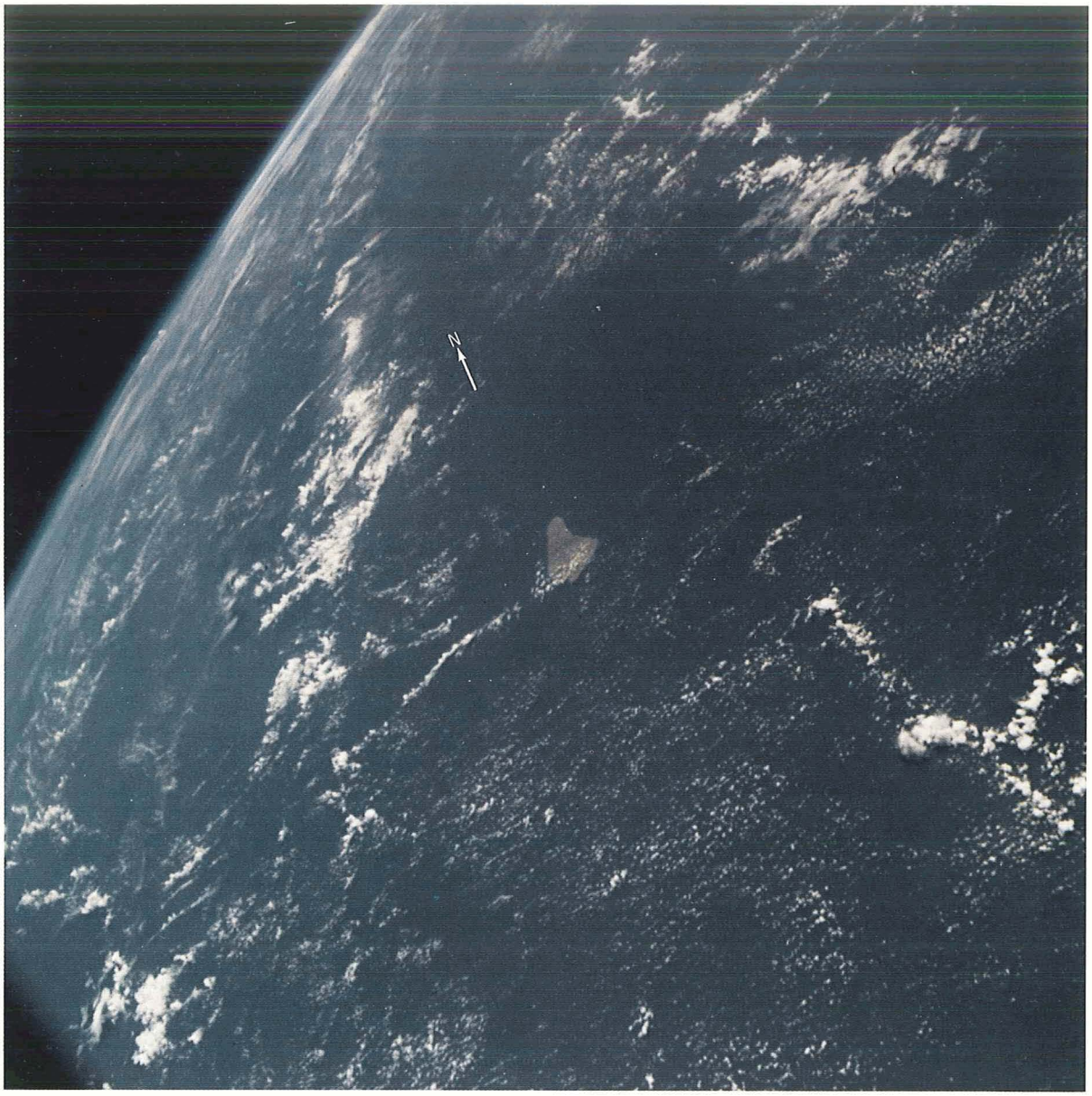


FIGURE 13.—Oblique photograph over Barbados (AST-21-1686).

the island from the east when this photograph (fig. 12) was taken. This pool may correspond to the greenish discoloration on the photograph. Oblique photographs of the area during revolution 104 (AST-21-1686 (fig. 13), AST-21-1687, and AST-21-1688) do not show this green color. These photographs do show a line of "puffball clouds" extending from Barbados to the west, similar to the features Stevensen (refs. 34 and 35) has demonstrated to be associated with cold-water eddies. The pool of brackish water described earlier would have been almost in that position when the photograph was taken, but it seems to have had a warm center not a cold one.

The photographs, therefore, are interesting but are of little use in resolving the question as to

which river was responsible for the discoloration observed from space. The author concludes, by the reasoning described here, that the Amazon River was responsible for the brown hues, which are a result of dissolved organic compounds similar to the fulvic and humic acids found in river waters. The larger flow of the Amazon and the extension of this river's water over the entire western tropical Atlantic under the influence of the wind and geostrophic currents, probably masked any effect of the Orinoco River that may have occurred in July 1975.

ACKNOWLEDGMENTS

This work was supported by the National Research Council of Canada in the form of a Postgraduate Scholarship to G. Borstad and an operating grant to F. Sander. The author acknowledges the unpublished data and assistance from R. Kidd and C. Hawkins, as well as cooperation and aid from all the staff and students of Bellairs Research Institute of McGill University, St. James, Barbados.

REFERENCES

1. Deutsches Hydrographisches Institut: Monatskarten für den Nordatlantischen Ozean (Hamburg), 1956.

2. Gade, H. G.: On Some Oceanographic Observations in the Southeastern Caribbean Sea and the Adjacent Atlantic Ocean With Special Reference to the Influence of the Orinoco River. Boletin de la Institute Oceanográfico de Universidad de Oriente, vol. 1, Dec. 1961, pp. 287-342.

3. Ryther, J. H.; Menzel, D. W.; and Corwin, Nathaniel: Influence of the Amazon River Outflow on the Ecology of the Western Tropical Atlantic. I. Hydrography and Nutrient Chemistry. J. Marine Res., vol. 25, 1967, pp. 69-83.

4. Calef, George W.; and Grice, George D.: Influence of the Amazon River Outflow on the Ecology of the Western Tropical Atlantic. II. Zooplankton Abundance, Copepod Distribution, With Remarks on the Fauna of Low-Salinity Areas. J. Marine Res., vol. 25, 1967, pp. 84-94.

5. Hulbert, E. M.; and Corwin, Nathaniel: Influence of the Amazon River Outflow on the Ecology of the Western Tropical Atlantic. III. The Planktonic Flora Between the Amazon River and the Windward Islands. J. Marine Res., vol. 27, 1969, pp. 55-72.

6. Gibbs, Ronald J.: Circulation in the Amazon River Estuary and Adjacent Atlantic Ocean. J. Marine Res., vol. 28, 1970, pp. 113-123.

7. Okuda, T.; Benitz, J.; et al.: Revisión de los Datos Oceanográficos en el Mar Caribe Suroriental, Especialmente el Margen Continental de Venezuela. Cuadernos Azules. Vol. 15, Organizing Committee of the Third United Nations Conference on Law of the Sea (Caracas), 1974.

8. Hutchinson, George Evelyn: A Treatise on Limnology. Vol. 1, Geography, Physics, and Chemistry. John Wiley and Sons, Inc., 1957, pp. 415-417.

9. Strickland, J. D. H.; and Parsons, T. R.: A Practical Handbook of Seawater Analysis. Bull. Fish. Res. Bd. Canada, vol. 167, 1968, pp. 201-203.

10. Moreth, C. M.; and Yentsch, C. S.: A Sensitive Method for the Determination of Open Ocean Phytoplankton Phycoerythrin Pigments by Fluorescence. Limnol. Oceanogr., vol. 15, no. 2, 1970, pp. 313-317.

11. Mazeika, P. A.: Circulation and Water Masses East of the Lesser Antilles. Deutsche. Hydrogr. Z., vol. 26, no. 2, 1973, pp. 49-73.

12. Ministerio de la Defensa, Republica de Venezuela: Boletin Meteorologico Diario. Ano XXVI, 1975.

13. Johannessen, O. M.: Preliminary Results of Some Oceanographical Observations Carried Out Between Barbados and Tobago, March/April 1968. Marine Sciences Manuscript Report No. 8, McGill Univ., 1968.

14. Sander, Finn: Internal Waves as Causative Mechanism of Island Mass Effects. Caribb. J. Sci., vol. 13, no. 3/4, 1973, pp. 179-182.

15. Emery, A. R.: Eddy Formation From an Oceanic Island: Ecological Effects. Caribb. J. Sci., vol. 12, no. 3/4, 1972, pp. 121-128.

16. National Oceanographic Data Center: Surface Current Data System (SCUDS). Washington, D.C.

17. Doty, M. S.; and Oguri, M.: The Island Mass Effect. (Int. Council for Exploration of the Sea.) J. du Conseil, vol. 22, 1956, pp. 33-37.

18. Sander, Finn: Organic Productivity of Inshore and Offshore Waters of Barbados. A Study of the Island Mass Effect and Its Causes. Ph. D. dissertation, McGill Univ. (Montreal), 1971.

19. Murray, S. P.; Roberts, H. H.; Conlon, D.; and Rudder, G. M.: Nearshore Current Fields Around Coral Islands: Control of Sediment Accumulation and Reef Growth. Proceedings of the Third International Coral Reef Symposium, Volume 2—Geology, Rosenstiel School of Marine and Atmospheric Science, Univ. of Miami, May 1977, pp. 53-59.

20. Steven, D. M.; and Brooks, A. L.: Identification of Amazon River Waters at Barbados, W. I., by Salinity and Silicate Measurements. Mar. Biol., vol. 14, 1974, pp. 345-348.

21. Froelich, P. N.; and Atwood, D. K.: Dissolved Silicate and Salinity Structure of the Upper Waters of the Venezuelan Basin: Caribbean Sea. CICAR-11 Symposium (July 1976, Caracas, Venezuela).

22. Elliott, G. W.: Precipitation Signatures in Sea-Surface-Layer Conditions During BOMEX. J. Phys. Oceanogr., vol. 4, no. 3, 1974, pp. 498-501.

23. Urosa, L. J.; and Rao, T. S.: Distributión de Quetognatos y Biomasa del Zooplancton en la Parte Occidental del Atlántico Tropical, Durante Julio y Agosto de 1968. Boletin de la Institute Oceanográfico de Universidad de Oriente, vol. 13, 1974, pp. 53-66.

24. Brucks, J. T.: Oceanographic Studies in the Lesser Antilles Region: II. Antilles Current East of the Windward Islands. Symposium on Investigations and Resources of the Caribbean and Adjacent Regions (CICAR-I), UNESCO, 1968.

25. Glombitza, R.: Geostrophic Currents in the Region of the Lesser Antilles. M. Sc. Thesis, McGill Univ. (Montreal), 1971.

26. Ortega, G. F.; and Herrara, L. E.: Circulation and Water Mass Transport in the Southeastern Caribbean. CICAR-11 Symposium (July, 1976, Caracas, Venezuela).

27. Stalculp, Marvel C.; and Metcalf, William G.: Current Measurements in the Passages of the Lesser Antilles. J. Geophys. Res., vol. 77, no. 6, 1972, pp. 1032-1049.

28. Cadée, G. C.: Primary Production off the Guyana Coast. Netherlands J. Sea Res., vol. 9, no. 1, 1975, pp. 128-143.

29. Metcalf, William G.: Shallow Currents Along the Northeastern Coast of South America. J. Marine Res., vol. 26, 1968, pp. 232-243.

30. U.S. Navy Hydrographic Office: Atlas of Surface Currents, North Atlantic Ocean. H. O. Publ. No. 571, 1st ed. (Washington, D.C.), 1947.

31. El-Baz, Farouk: Astronaut Observations From the Apollo-Soyuz Mission. Vol. I of Smithsonian Studies in Air and Space, Smithsonian Institution Press (Washington, D.C.), 1977.

32. McCluney, W. R.: Ocean Color Spectrum Calculations. Appl. Opt., vol. 13, no. 10, Oct. 1974, pp. 2422-2429.

33. Prospero, J. M.: Atmospheric Dust Studies on Barbados. Bull. Am. Meteorol. Soc., vol. 49, no. 6, June 1968, pp. 645-659.

34. Stevenson, Robert E.: Oceanographic Data Requirements for the Development of an Operational Satellite System. Proc. Princeton Univ. Conf. on Aerospace Methods for Revealing and Evaluating Earth's Resources, 1970, pp. 12.1-12.12.

35. Stevenson, Robert E.: Observations From Skylab of Mesoscale Turbulence in Ocean Currents. Nature, vol. 250, no. 5468, Aug. 23, 1974, pp. 638-640.

Estimate of Total Reflectance From the Orinoco River Outflow

C. S. Yentsch[a] and Farouk El-Baz[b†]

ABSTRACT

The Apollo astronauts photographed the Orinoco River Delta in eastern Venezuela. The photographs show discrete water-color zones that reflect the mixing of the sediment-laden Orinoco outflow with the water of the tropical Atlantic. One transparency was analyzed with a Datacolor/Edge Enhancer System to estimate the range of light reflectance in the scene. Based on this analysis, and assuming a 5-percent reflectance value for the open ocean water, the reflectance of the area studied was found to vary between 4 percent for the jungle and approximately 13 percent for sediment-laden river outflow. These values approximate those obtained by direct measurements of the Mississippi River Delta water. The results confirm that the reflectance from coastal waters will not be so high as to saturate instruments onboard unmanned satellites such as the Coastal Zone Scanner.

INTRODUCTION

The Orinoco River in northern South America, with a drainage area of approximately 841 750 km^2, delivers much organic sediment to its mouth at latitude 9° N, longitude 61° W. These sediments and associated dissolved organic compounds have been known to "discolor" the Atlantic Ocean water as far as 80 km from the Venezuela coastline. To aid in the study of this phenomenon, the Orinoco River Delta was selected as an observation target for the Apollo-Soyuz Test Project (ASTP) (ref. 1).

The ASTP photographs, which were taken with a highly color-sensitive film, provide new data on river discharge. The extent of the discolored Atlantic Ocean water due to the Orinoco outflow is the subject of another paper in this volume. This report, however, deals with the reflectance characteristics of the outflow in the immediate vicinity of the Orinoco River Delta.

One ASTP photograph of this delta (fig. 1) reveals numerous variations in water color. The brownish-tan river water directly impinges on the bluish water of the tropical Atlantic. The discoloration is also segmented into discrete color zones with the brownish-tan color decreasing outward from the delta. Although color variations in this case are extreme, the phenomenon is characteristic of most coastal areas near major river deltas.

Even though the range of reflectance of open ocean waters is well known (ref. 2), little information is available on sediment-laden water such as the Orinoco River outflow. Therefore, in this report, an attempt is made to estimate the reflectance characteristics as an aid in the evaluation of data obtained by unmanned satellites.

Existing Earth-viewing satellite systems that sense variations in visible-light surface reflectance must accept some compromise in sensitivity over areas of the Earth where the dynamic range in

[a]Bigelow Laboratory for Ocean Sciences, West Boothbay Harbor, Maine.

[b]National Air and Space Museum, Smithsonian Institution.

[†]Principal Investigator.

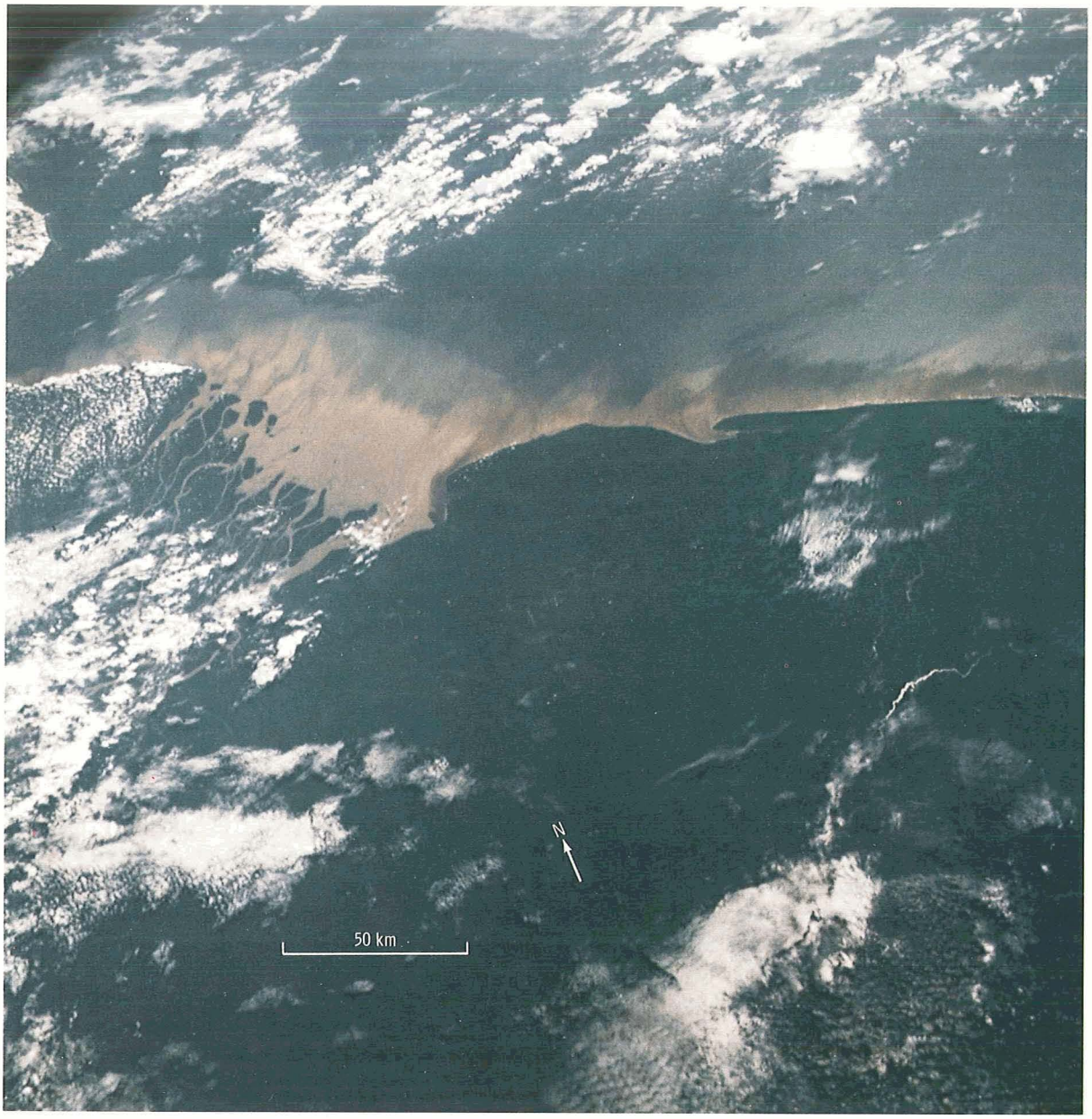


FIGURE 1.—ASTP photograph (AST-21-1683) of the Orinoco River Delta of northern South America.

reflectance is large. This is not a problem over open ocean areas, where the dynamic range is small. However, in the case of the latest Nimbus satellite (the G-series Coastal Zone Scanner), the channels must be capable of sensing water color derived from a wide range of concentrations of absorbing and reflecting substances. Highly reflective features, such as sand dunes, bottom topography, and certain sediment loads, could saturate the detectors with light and thereby create a "white out" in the imagery. The ASTP photograph of the Orinoco River outflow was used to estimate the reflectance of very bright, sediment-laden water.

METHOD

The ASTP photograph (fig. 1) was analyzed using a Datacolor/Edge Enhancer System by Spatial Data Systems. This enhancer, at the Smithsonian Institution's Center for Earth and Planetary Studies, is capable of producing color enhancements of film transparencies. The film is illuminated and scanned by a vidicon phototube. The density gradient seen by the scanner can be divided into as many as 12 equal bands, and each band is shown on a color television monitor as one of 12 colors. Borders between color bands may be considered as contour intervals, because all points lying along one contour represent the same film density. This "color slicing" allows the observer to view (in marked contrast) the density differences recorded on film.

The ASTP photograph was only "sliced" into six film densities (table I). The range in densities varied between the low reflectance of jungle and open ocean areas and the high reflectance of sediment loads and clouds. To delineate the film density steps, the color presentation was photographed on black-and-white film using a Polaroid camera (fig. 2). Each film density was emphasized by successively blackening out the areas of least reflectance. This procedure demonstrated that the lowest reflectance was associated with jungle areas (fig. 2(a)). The next lowest reflectance (fig. 2(b)) included almost all of the jungle and some of the open ocean. The next level of reflectance (fig. 2(c)) contained all of the jungle and all of the ocean water. Most of the reflected light was coming from the brown area seen in the ASTP color photograph (figs. 1 and 2(d)). However, one part of this area (fig. 2(e)) was more highly reflective.

TABLE I.— Color Density Analysis

Color slice	*Area*	*Figure no.*	D_i	B_i, *percent*
Violet	Jungle	2(a)	0.35	4.3
Magenta	Open ocean	2(b)	.30	5.0
Dark red	Delta water	2(c)	.25	6.0
Light red	Delta water	2(d)	.21	7.1
Green	Delta water	2(e)	.12	12.5
White	Clouds	2(f)	0	

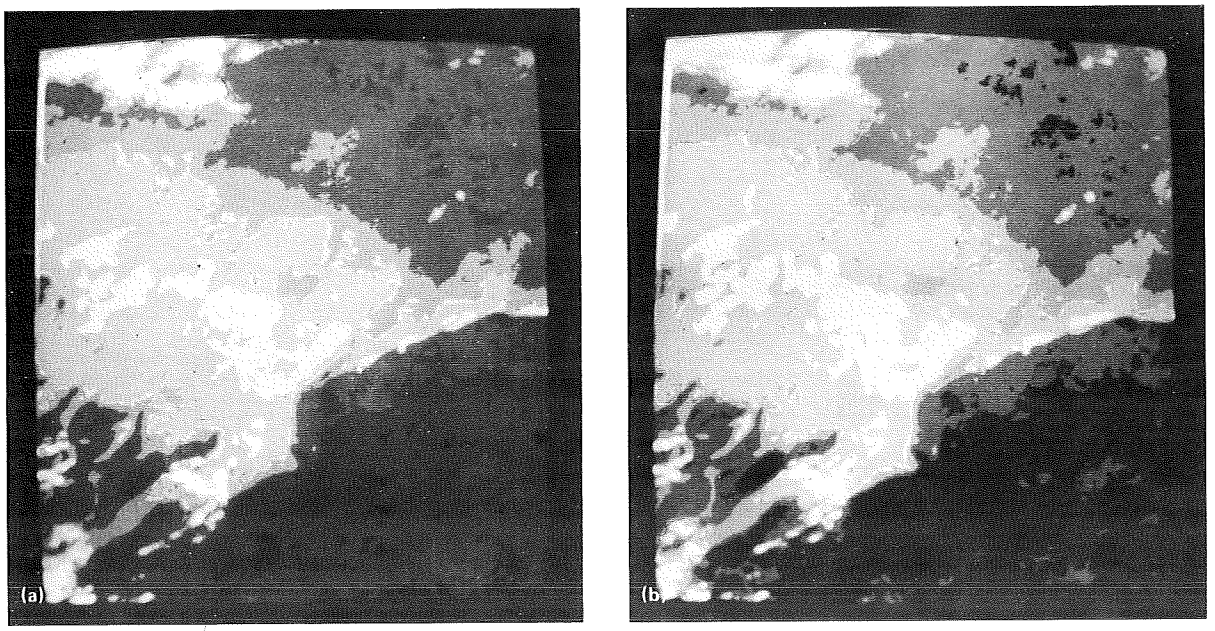


FIGURE 2.—Black-and-white Polaroid prints of color slicing of ASTP photograph showing successive blackening out of areas of least reflectance. (a) Violet. (b) Magenta. (c) Dark red. (d) Light red. (e) Green. (f) White.

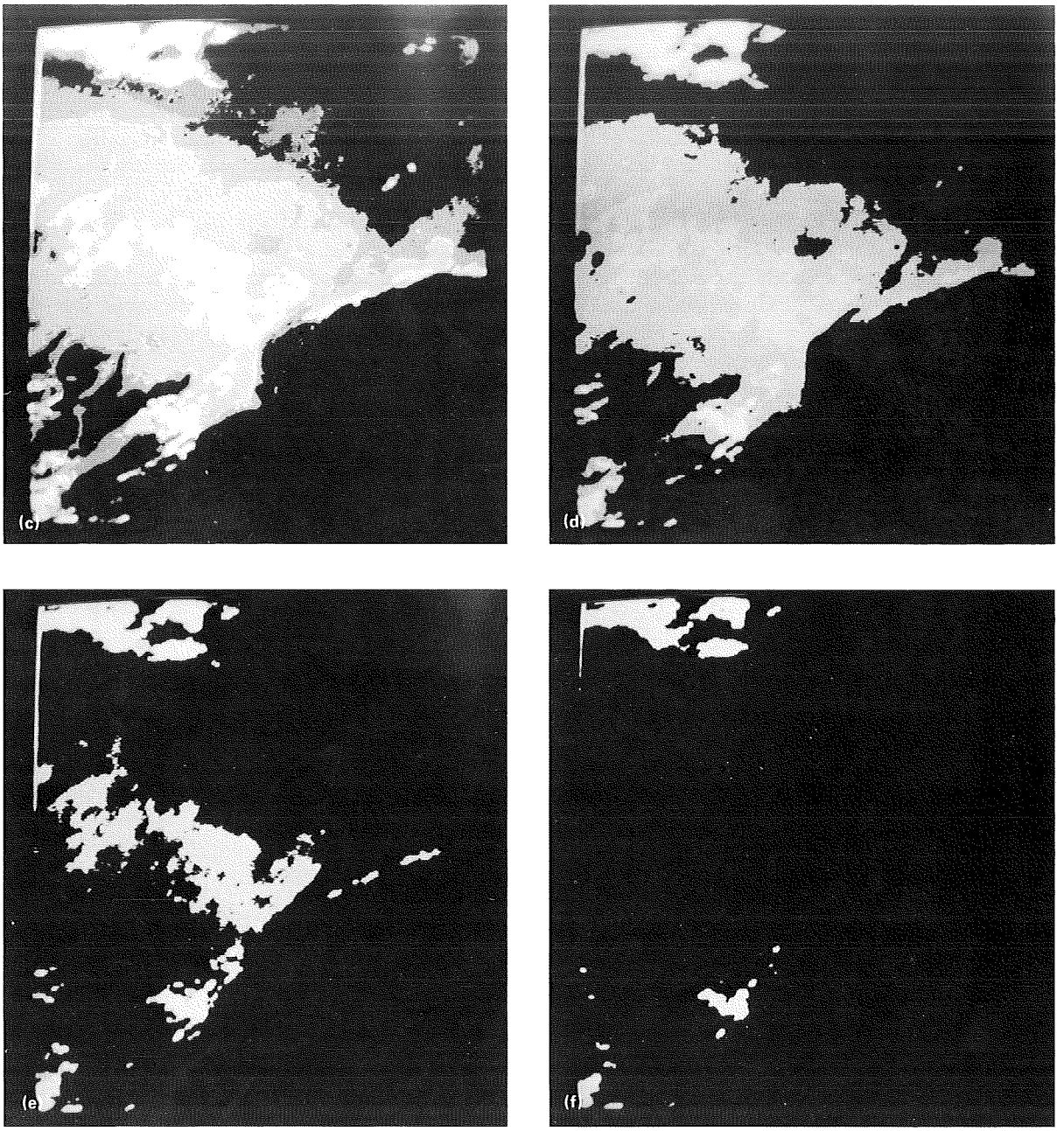


FIGURE 2.—Concluded.

The final step demonstrated that the clouds in the photograph were the most reflective objects in the scene.

The color slicing showed that incoming waters from the many streams feeding the delta were not carrying as much sediment as is found in the central region of the delta. This result leads one to suspect that wave and tidal action may be strong enough to place much of the sediment in suspension.

To estimate the amount of reflectance, it is understood that an increase in film density D for a positive transparency corresponds to a decrease in backscattering B. The backscattering is assumed to be inversely proportional to the film density and is normalized to the value commonly ascribed to the open ocean: $B_o = 5.0$ percent. The corresponding film density over the open ocean was measured to be $D_o = 0.30$. Then, B_i was determined for other areas by measuring D_i:

$$B_i = \frac{D_o B_o}{D_i}$$

$$= \frac{(0.30)(5.0)}{D_i}$$

$$= \frac{1.5}{D_i}$$

The range in B_i (table I) is from approximately 4 percent for the jungle to approximately 13 percent for the heavy sediment areas.

CONCLUSION

Because of the color sensitivity of the ASTP photograph of the Orinoco River outflow, it was possible to estimate the reflectance values of the bright, sediment-laden water. Although this method does not produce absolute reflectance values, the values obtained do approximate those which have been observed in other highly turbid waters. For example, in the coastal canals around Florida, the first author has observed (by direct measurement) that B_i is 10 to 15 percent. Similar values have been calculated for the Mississippi Delta waters (ref. 3).

Based on these findings, and if the values given in table I are representative of the reflectance range of coastal waters, then sedimentary loads will probably not saturate the Coastal Zone Scanner.

ACKNOWLEDGMENTS

The edge-enhancer work was done with the assistance of Fred J. Anders. This work was performed under Smithsonian Institution Grant PC6-22376, NASA contracts NAS9-13831 and NAS5-22948, and Energy Research and Development Administration contract E(11-1)2538.

REFERENCES

1. El-Baz, Farouk; and Mitchell, D. A.: Earth Observations and Photography, Experiment MA-136. Sec. 10 of Apollo-Soyuz Test Project Preliminary Science Report. NASA TM X-58173, 1976.

2. Jerlov, N. G.: Optical Oceanography. Elsevier Pub. Co. (Amsterdam-London-New York), 1968.

3. Wiseman, W. J., Jr.; Bane, J. M.; Murray, S. P.; and Tubman, M. W.: Small-Scale Temperature and Salinity Structure Over the Inner Shelf West of the Mississippi River Delta. Mem. Soc. R. Sci. Liege 8° (Belgium), vol. 10, 1976, pp. 277-285. (7th Liege Colloquium on Ocean Hydrodynamics, Liege, Belgium, 5-9 May 1975.)

Observations of Internal-Wave Surface Signatures in ASTP Photographs

John R. Apel[a]

ABSTRACT

At least three Apollo-Soyuz Test Project photographs have shown clear indications of oceanic internal gravity waves; the features are indicated by periodic changes in the optical reflectivity of the ocean surface overlying the waves. Two packets (or groups) of waves seen off Cádiz, Spain, have characteristics similar to internal waves seen in satellite images taken off the U.S. eastern coast. In the Andaman Sea off the Malay Peninsula, several groups were observed having wavelengths of 5 to 10 km and interpacket separations on the order of 70 to 115 km. If these are indeed surface signatures of internal waves, the waves are among the longest and fastest observed to date. Earlier shipboard measurements have shown that large-amplitude internal waves exist in the area.

INTRODUCTION

Internal gravity waves are very slow, progressive oscillations of constant density surfaces within the ocean; they occur as a result of a variety of geophysical forces such as tides, wave-wave interactions, and atmospheric disturbances. Although the oscillations may typically have amplitudes of 10 m or more, the associated surface elevations are very small, on the order of 10 cm or less. The period of a "high-frequency" internal wave may be 15 minutes, its wavelength is 500 m, and its characteristic phase speed is approximately 50 to 75 cm/sec.

Although such internal waves have very small surface elevations, the horizontal cellular currents that accompany them are of the same order as the wave phase speeds. Therefore, these circulating currents, where near the surface, may alter the short-length surface gravity and capillary waves by means of a periodic modulation that results in a characteristic surface signature of the underlying internal-wave field.

The existence of such surface signatures has been recognized for more than a generation, and various theories have been advanced to explain them. The usual explanations either cite formation of narrow surface slicks or stripes, which then accompany the waves (refs. 1 and 2), or else concentrate on the periodic focusing of capillary and ultragravity surface wave energy by the internal-wave currents (refs. 3 and 4). In either case, quasi-periodic surface features or signatures will be produced under light wind conditions, and such effects are often seen at sea.

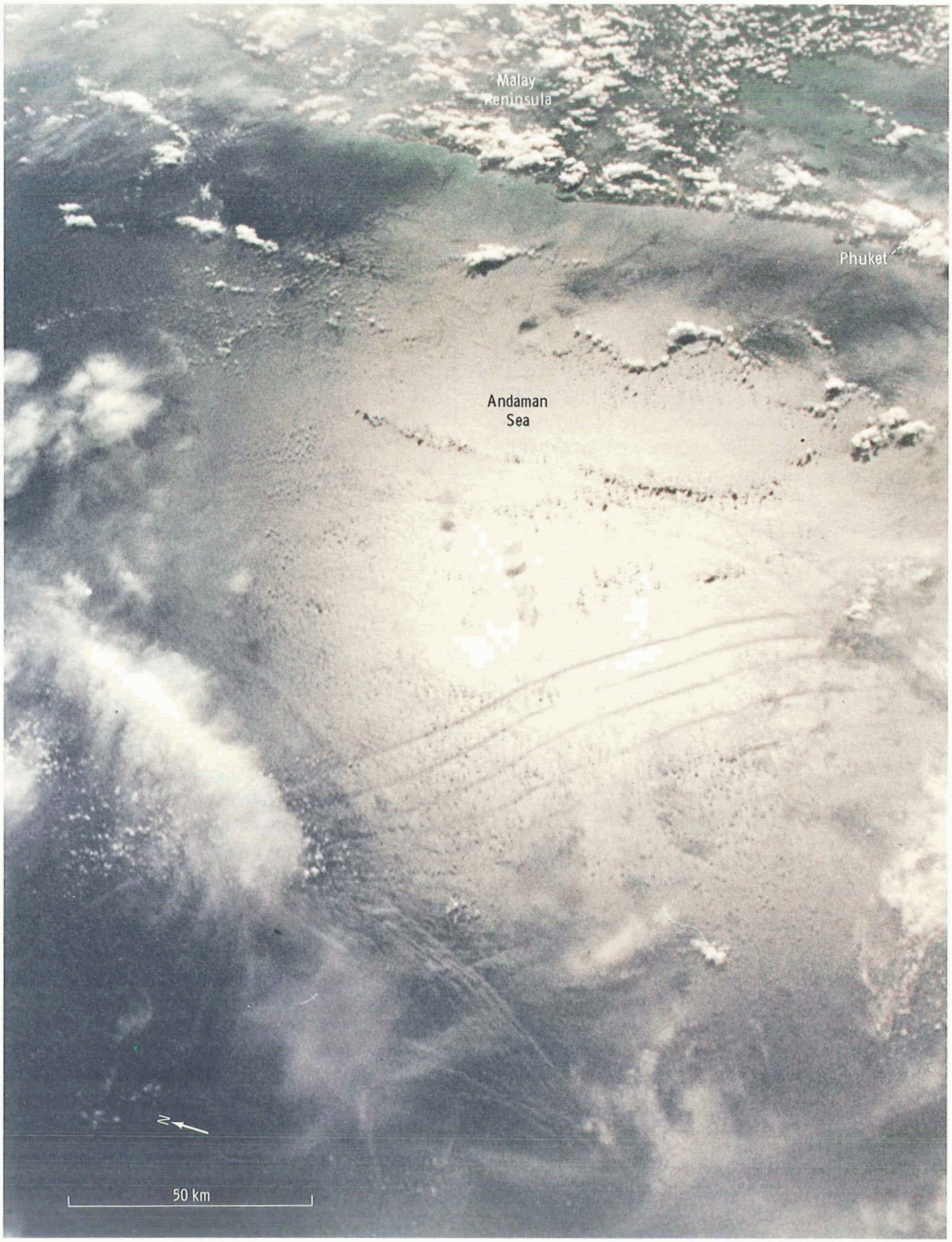
Data from the multispectral scanner subsystem (MSS) on the Landsat 1 and 2 satellites, as well as from a wide variety of other imaging sensors flown on many other spacecraft and aircraft (including optical and radar imaging devices), have shown that such surface signatures are readily seen in high-resolution images (refs. 4 to 7). Shipboard measurements have verified that such signatures often accompany coherent internal waves on the continental shelf under conditions of light winds.

[a]Pacific Marine Environmental Laboratory, Environmental Research Laboratories, National Oceanic and Atmospheric Administration, Seattle, Washington.



FIGURE 1.—Atlantic Ocean west of Cádiz, Spain, showing sunglint and two packets thought to be internal-wave surface signatures (AST-27-2367).

FIGURE 2.—Andaman Sea west of Phuket on the Malay Peninsula, showing four packets of very long linear features (AST-7-427). →


Malay
Peninsula
Phuket
Andaman
Sea
N
50 km

ANALYSIS

The theoretical explanation for the formation of the internal waves is that a large-scale current-shear condition arises from the scattering of the barotropic (i.e., uniform in depth) tide into baroclinic tidal modes, whose currents then vary with depth. The shear, when sufficiently intense, excites a high-frequency internal wave near the edge of the continental shelf for a few hours during the maximum tidal flow. This oscillation then propagates as a free wave even after the shear flow conditions are eliminated by reversal of the tide, and the wave thus generated lives an independent existence until attenuated or otherwise destroyed. This theory offers quantitative explanations for the intermittent, packet-like nature of the waves observed in satellite images, as well as explanations of their wavelength, period, and amplitudes (ref. 8).

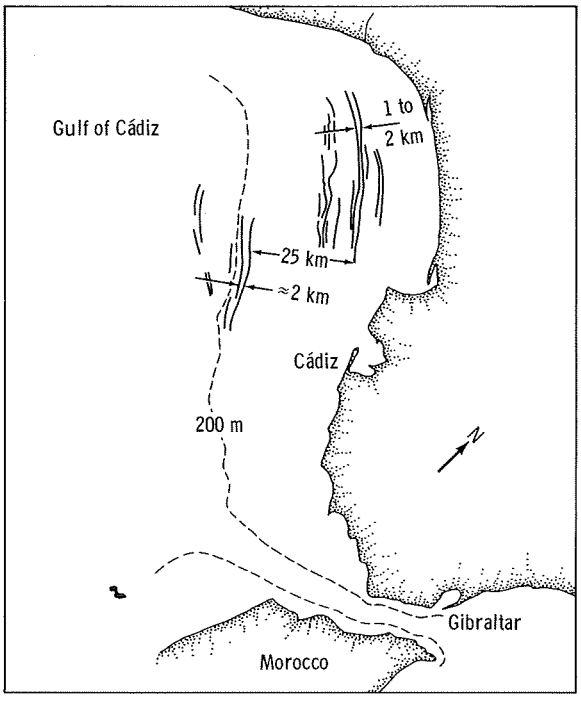


FIGURE 3.—Line drawing interpretation of AST-27-2367 (fig. 1), showing a packet of waves at the edge of the continental shelf (200-m contour) and another approximately 25 km shoreward. The wavelengths are approximately 2 km.

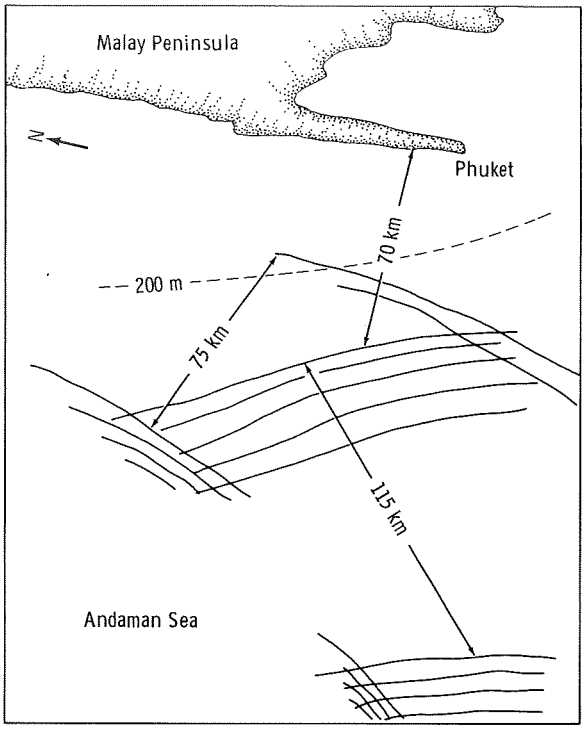


FIGURE 4.—Line drawing interpretation of AST-7-427 (fig. 2) and AST-7-426, suggesting there are four packets of waves having lengths of 5 to 10 km and interpacket separations of roughly 75 to 115 km. The wave generation regions may be to the west and south.

Because the surface signatures of the internal waves are most readily seen near the edge of Sun glitter on the sea surface, the Apollo-Soyuz Test Project (ASTP) crewmembers were instructed to be alert for periodic stripes on the surface, especially near the limits of the Sun's reflection. They were successful in photographing such stripes on at least two occasions in two widely separated parts of the world: in the eastern Atlantic west of Cádiz, Spain (fig. 1), and in the Andaman Sea west of the Malay Peninsula (fig. 2).

Interpretative line drawings of these two photographs are presented in figures 3 and 4. Figure 3 shows two packets of waves off Cádiz. The waves have wavelengths of approximately 2 km, and the packets are separated by approximately 25 km. This interpacket interval, when a phase speed of 50 cm/sec is assumed (estimated from historic oceanic density data for this place and season),

suggests a semidiurnal origin, as has been deduced from the spacing of packets in many other images. The position of the initial packet at the edge of the continental shelf (i.e., the 200-m contour) argues for the onset of the instability at the shelf break.

West of Cádiz (figs. 1 and 3), only two packets are observed; in the Andaman Sea (figs. 2 and 4), however, two sets of crossing packets, each consisting of several waves, may be seen. Here the wavelengths (distance between stripes) are estimated to be 5 to 10 km and the interpacket separations are 75 to 115 km. If these are indeed internal waves of semidiurnal tidal origin, their phase speeds must be on the order of 220 cm/sec and their periods near 40 to 80 minutes, which are extraordinarily high values. If the waves have a diurnal repetition interval, the phase speeds would be halved and the periods doubled. According to the theory cited in reference 8, such waves could be generated by an intense semidiurnal or diurnal tidal current shear developed in a deep, weakly stratified upper ocean.

Shipboard observations made during the *Pioneer* Indian Ocean Expedition (ref. 9) in 1964 have established the existence of similar long-length waves in the Andaman Sea; these waves have peak-to-trough amplitudes of approximately 80 m. Such waves would most likely have characteristics similar to the periodic stripes of figures 2 and 4; however, to the author's knowledge, no other supporting data are available to assist in this interpretation. If these stripes are indeed associated with internal waves, they then constitute the largest and fastest wave groups observed to date.

In summary, the ASTP photographs both reinforce and extend the other spacecraft and aircraft data on surface signatures of internal waves. Acquisition of these photographs was based on predictions of the phenomenon that served to alert the crewmembers; therefore, the photographs add significantly to the rapidly expanding body of space-acquired knowledge of the sea.

REFERENCES

1. Ewing, G.: Slicks, Surface Films and Internal Waves. J. Marine Res., vol. 9, 1950, pp. 161-187.

2. Shand, J. A.: Internal Waves in the Georgia Strait. EOS, vol. 34, 1953, pp. 849-856.

3. Gargett, A. E.; and Hughes, B. A.: On the Interaction of Surface and Internal Waves. J. Fluid Mech., vol. 52, 1972, pp. 179-191.

4. Apel, John R.; Byrne, H. Michael; Proni, John R.; and Charnell, Robert L.: Observations of Oceanic Internal and Surface Waves From the Earth Resources Technology Satellite. J. Geophys. Res., vol. 80, no. 6, 1975, pp. 865-881.

5. Apel, J. R.; Proni, J. R.; Byrne, H. M.; and Sellers, R. L.: Near-Simultaneous Observations of Intermittent Internal Waves From Ship and Spacecraft. Geophys. Res. Letters, vol. 2, Apr. 1975, pp. 128-131.

6. Apel, J. R.; Byrne, H. M.; Proni, J. R.; and Sellers, R. L.: A Study of Oceanic Internal Waves Using Satellite Imagery and Ship Data. Remote Sens. Environ., vol. 5, no. 2, 1976, pp. 125-135.

7. Sawyer, C.; and Apel, J. R.: An Atlas of Oceanic Internal-Wave Signatures Seen From Satellite. U.S. Dep. of Commerce, NOAA S/T 2401.

8. Tsai, J.; and Apel, J. R.: Tidally-Induced Shear-Flow Instability as a Source of Internal Waves on the Continental Shelf. EOS, vol. 58, 1977, p. 1167.

9. Perry, Richard B.; and Schimke, Gerald R.: Large-Amplitude Internal Waves Observed Off the Northwest Coast of Sumatra. J. Geophys. Res., vol. 70, no. 10, 1965, pp. 2319-2324.

Detection of a Probable Ancestral Delta of the Nile River

Mohamed A. Abdel-Rahman[a] *and Farouk El-Baz*[b†]

ABSTRACT

Interpretation of a near-vertical Apollo-Soyuz color photograph of northern Egypt revealed a dark-colored and finely textured zone partially overlapped by the present Nile Delta. Extrapolation of the identified zone beyond the Apollo-Soyuz photographic coverage, using a false-color Landsat mosaic, indicated that this zone forms a part of a deltalike pattern. Review of the literature on the geology of the area indicated that its outcropping and subsurface rocks are of terrigenous types. In addition, all its deposits belong to fluvial, deltaic, prodeltaic, estuarine, and fluvio-marine facies.

Examination of the size, form, and extension of the identified pattern revealed that it is most probably the late Eocene to early Miocene ancestral delta of the Nile River. This supports the theory that the Nile originated in late Eocene time. From the southern borders of Egypt to the city of Asyût, the river followed a course similar to that of the present-day Nile. At the end of the early Miocene time, a sudden lengthening of its course occurred, and the river ceased depositing its sediments in the ancestral delta northwest of Asyût. Probably guided by faults, the river flowed northward to its present-day position. This change in the course of the Nile was probably associated with a regional uplift that affected Egypt during middle Miocene time.

[a]Ain Shams University, Cairo, Egypt.

[b]National Air and Space Museum, Smithsonian Institution.

[†]Principal Investigator.

INTRODUCTION

Orbital photographs and images can furnish invaluable information on the geological attributes of the Earth's surface. In areas where knowledge is scant, examination of orbital photographs may emphasize regional patterns. Photointerpretation of such patterns may lead to the formulation of hypotheses regarding their nature and origin. The synoptic view of these photographs also provides a basis for extending geological information from well-studied areas to the surrounding less-known regions.

When studying exposed surface materials, it is noteworthy that true color photographs are superior to Landsat false-color images because of two reasons: (1) True colors can be interpreted on their merits (absolute scale) whereas false-color composities should be interpreted on the basis of assumptions or mentally translated true colors (relative scale). (2) Color photographs reveal, by virtue of color tone, considerable information on the textural characteristics of the sediments whereas Landsat images, which are made up of pixels,[1] are less reliable in studying textural characteristics.

Apollo-Soyuz Test Project (ASTP) photographs reveal true color zones in the Nile Delta region. West of the Nile Delta, three parallel color zones with sharp and straight-line boundaries have been identified (ref. 1). The boundaries of these zones are mainly oriented N85°E. The southernmost zone, which is the subject of detailed examination in this study is described by

[1]Pixels are spatially limited resolution elements.

El-Baz and El-Etr in another section of this volume (section entitled "Color Zoning in the Western Desert of Egypt").

ASTP PHOTOINTERPRETATION

Visual examination of the aforementioned southernmost color zone reveals the following:

1. The southernmost color zone can be traced west of the Nile Delta and possibly to the eastern side of the Suez Canal.

2. Differences between the southernmost zone and the intermediate zone are not only in color but are also in texture. The southernmost zone is characterized by very coarse to coarse texture as compared with the medium to fine texture of the intermediate zone. This textural variation is reflected in the field description by El-Baz and El-Etr of the southernmost zone as "a desert pavement composed of sand mixed with dark pebbles." The intermediate zone, however, was described as sand "which appears to be active, forming ripples and sand shadows behind desert brush."

3. Assuming that a qualitative scheme of color classification is applied to identify color zones, the total variation of color in the photograph can be divided into two categories: (a) color variance between zones and (b) color variance within zones. If category "a" is more predominant than category "b," the scheme of classification becomes valid. Qualitatively applying this concept to the southernmost and intermediate color zones reveals that the boundary between the two zones is defined by minimum variation within each zone and maximum differences between the zones. Figure 1 shows that the southernmost zone is characterized by abundant east-west-trending strips of different color and texture. This is in contrast to the intermediate zone, which appears to be homogeneous except for subtle and gradual color variations. The east-west-trending strips are examples of the "within zone variance," as described by El-Baz and El-Etr's field examination of that southernmost zone: "the topography of this zone is not flat but rather rolling or undulating. The amount of gravel increases on higher areas, and the low areas are covered mostly with sand." (See section entitled "Color Zoning in the Western Desert of Egypt.") The east-west-trending strips (fig. 1) are interpreted as areas covered with Pliocene deposits or Quaternary sand. This interpretation is based partly on the geological map of Egypt (ref. 2) and partly on using photograph characteristics for areal extrapolation.

4. The southernmost zone discussed in this paper shows a clear east-west grain (fig. 1), which is reflected in the alinement and orientation of the northern and southern boundaries of the zone; the east-west-trending strips of Pliocene deposits and Quaternary sands; and the basaltic extrusions.

5. The Abu Rawâsh dome, of white Cretaceous limestone and chalk, crops out in this southernmost zone (fig.1). Outcrops of this Cretaceous rock contribute to the within-zone color and textural variance. In addition, the outcropping of these Cretaceous rocks within predominantly lower Miocene rocks indicates a structural high (ref. 3) and supports the prevalence of structural control.

6. East of the Nile Delta and west of the Suez Canal, east-west extension faults are known to exist widely and to predominate the structural grain of that area (refs. 3 and 4). Faults of similar trend are also known to cut across the present Nile Delta (ref. 5).

These observations clearly indicate that the structural pattern of the eastern part of this zone can be extrapolated through the present Nile Delta and to the west of it. Therefore, structural control by faults and/or megafractures (undifferentiated and labeled lineaments in fig. 1) should explain the development of the east-west-trending depressions in which Pliocene and Quaternary deposits are accumulated. The predominance of extension faults should also explain the widespread occurrence of basaltic extrusions in this zone. The northern boundary of the zone (fig. 1) with its straight-line appearance and its persistence for more than 400 km may reflect a fault line. The southern boundary of the zone that lies east of the Nile Delta coincides with a group of east-west-trending faults mapped by Abdel-Rahman and El-Etr. (See section entitled "Structural Pattern of the Northern Part of the Eastern

Desert of Egypt.") In addition, most parts of the southern boundary of the western part of the zone coincide with faults on the geological map of Egypt (ref. 2).

COLOR ZONE EXTRAPOLATION

To amplify their understanding of the nature of the study zone, the authors extrapolated beyond ASTP photographic coverage and compared these data with all available geological information.

A false-color mosaic of Landsat images of Egypt was used for the extrapolation. Zone extrapolation resulted in the recognition that the study zone forms part of a much larger pattern. The pattern is delta-shaped and lies mostly in the Western Desert of Egypt (fig. 2). The identified pattern is darker in color than the surrounding mass and is well defined by easily mappable boundaries. This deltalike pattern occupies approximately 55 000 km^2, which is much larger than the area occupied by the present Nile Delta, which is 18 000 km^2. Approximately 5000 km^2 of the identified pattern lie to the east of the present Nile Delta, whereas 5000 km^2 lie below the present delta in the Western Desert of Egypt.

The V-shaped tip of the identified pattern lies to the northwest of Asyût and widens gradually to form the base of a triangle at the northern edge. The western boundary of the pattern truncates the present-day Qattara Depression and suddenly terminates on a straight line oriented N85°E that follows the northern slope of the Qattara Depression. This N85°E line delimits the northern boundary of the identified pattern and can be traced eastward until it passes the Suez Canal near Ismailia where it suddenly terminates. The eastern edge of the deltalike pattern curves around the Faiyûm Depression where the middle Eocene limestone rocks are exposed. This boundary crosses the Nile Valley south of Cairo and extends eastward terminating just east of the Suez Canal (fig. 2).

Examination of color variations over this deltalike pattern indicates the following: (1) Colors are generally deeper in the southern part of the pattern than in the northern part (eastward, however, color intensity decreases remarkably). (2) Longitudinal chains of lighter-colored sand dunes are superposed on this pattern.

The shape, position, and size of the identified deltalike pattern suggest the possibility that the detected pattern may reflect an ancient (fossil) delta of the Nile River.

GEOLOGIC DISCUSSION

The hypothesis that the identified deltalike pattern represents an old Nile Delta is tested on the basis of the available literature on this area including the works of Beadnell (refs. 5 to 16). Figure 3 shows the time-rock units of the area as presented on the geological map of Egypt (ref. 2). The area is composed of Eocene, Oligocene, and lower Miocene rocks. The Eocene rocks probably belong to the late Eocene time except for a few isolated outcrops that formed topographic highs during the deposition of the upper Eocene, Oligocene, and lower Miocene.

The upper Eocene rocks have relatively limited exposures in the area. These are composed of brown sandy limestone, sand, and shale beds (ref. 3). The upper Eocene rocks in the subsurface consist of clay, shale, siltstone, and marl (ref. 15). However, upper Eocene rocks elsewhere in the Western Desert constitute the Qasr el Sagha Formation, which is characterized by numerous vertebrate remains with few marine shells.

The Oligocene rocks of the area constitute the Qatrani Formation. They are composed of cross-bedded sandstone and gravel with interbeds of shale and limestone. Most of these sediments contain mixed fluvio-marine mollusks whereas others contain huge tree trunks some of which are silicified, forming "petrified forests." In addition, numerous beds of the Qatrani Formation contain remains of various land animals, crocodiles, tortoises, and turtles. Said's description (ref. 3) of the Oligocene deposits leaves no doubt that they were formed by "rivers of considerable size." The Oligocene rocks attain their maximum thickness (250 m) in the Widan el Faras hills almost halfway between the Baharîya Oasis and the Faiyûm Depression (fig. 3). East and west of that location,

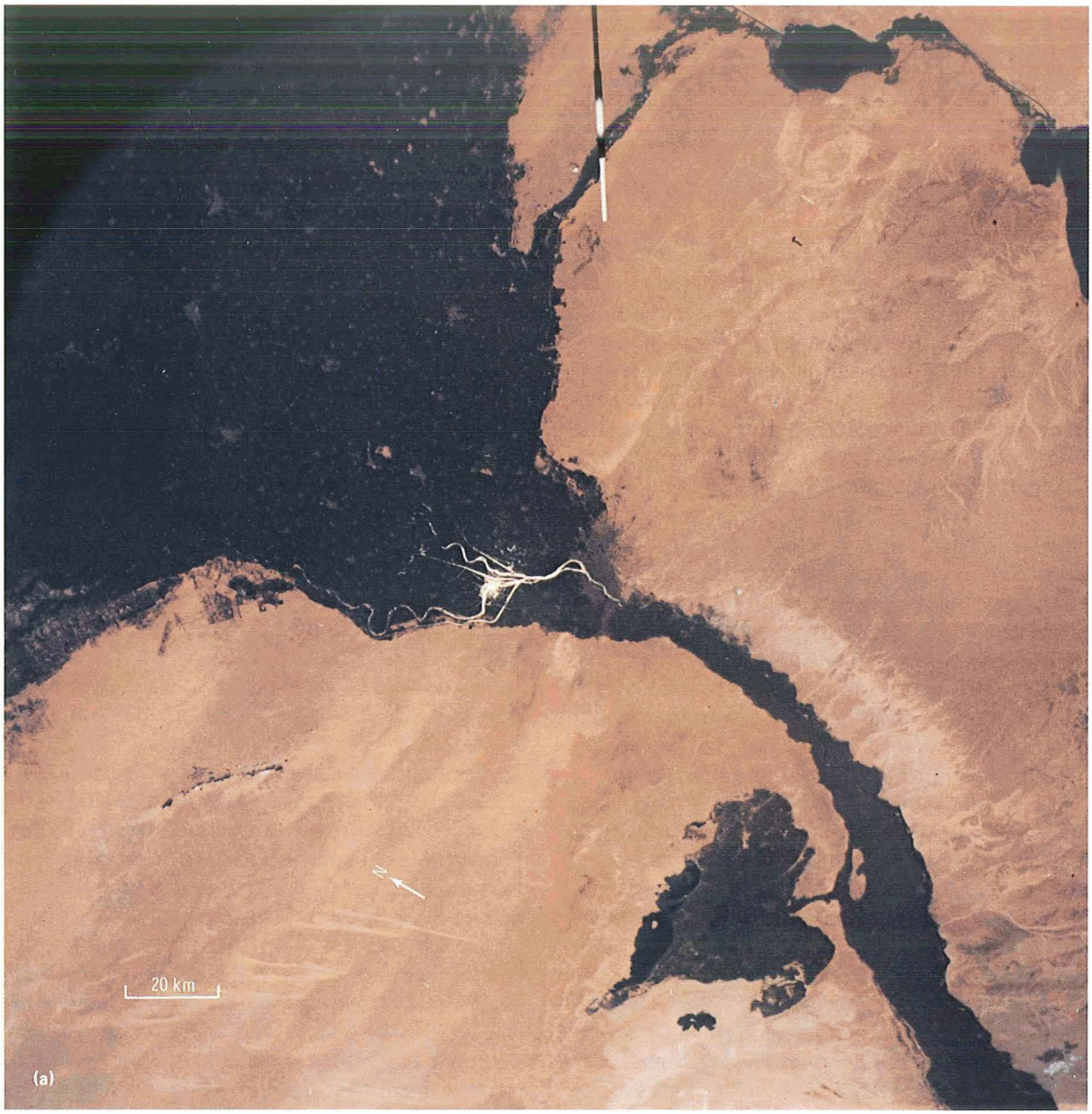


FIGURE 1.—ASTP photograph and sketch map of the zone east and west of the present Nile Delta. (a) Photograph AST-9-556 showing the color and textural photograph characteristics. (b) Sketch map of same area showing structural characteristics of the zone.

the Qatrani Formation thins out gradually (ref. 3). The lenticular shape displayed by the thickness of the Oligocene sediments adds more support to their fluvio-marine origin. The southernmost extension of the Oligocene deposits is represented by an extensive sand and gravel plain (fig. 3). According to Said (ref. 3), these deposits include pebbles of quartz, chert, flint, quartzite, and jasper derived mainly from the Nubia Sandstone and Eocene rocks to the south.

East of Cairo, the Oligocene rocks (also described by Said, ref. 3, as fluviatile) have a very

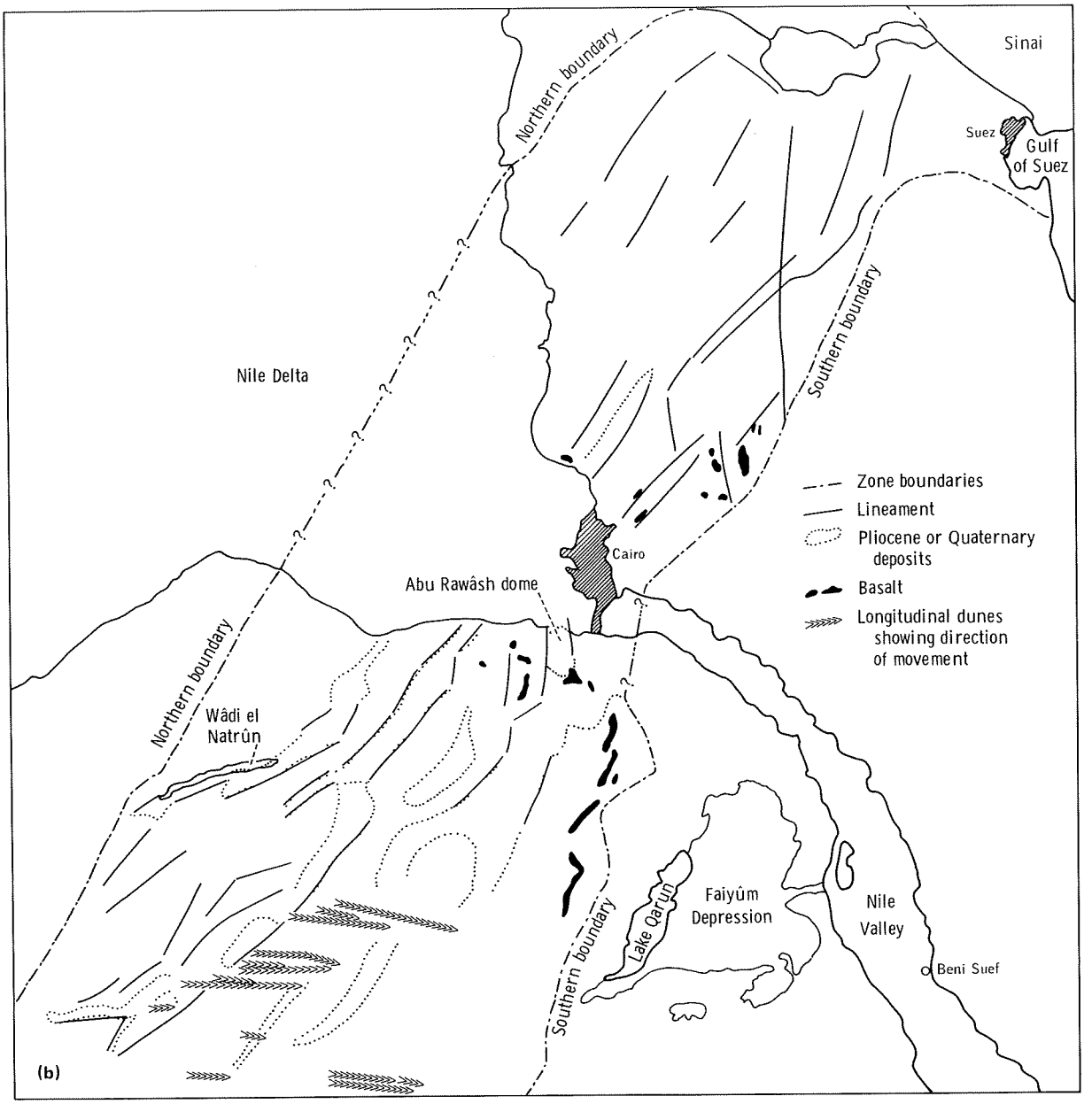


FIGURE 1.—Concluded.

similar composition to those west of Cairo. Shukri and Ayouty (ref. 13), however, have noted that sillimanite is abundant in these deposits in contrast to those of the Western Desert. A likely source rock for this mineral is the metamorphic terrain west of the Gulf of Suez.

Based on field study, relationships of the basaltic extrusions in Baharîya Oasis indicate that two phases of volcanic eruptions may have occurred during the Oligocene time (authors' observations). The age of the earliest phase is not well established, whereas the later phase marks the late



FIGURE 2.—False-color Landsat mosaic of Egypt showing the boundaries, shape, size, and location of the probable ancestral delta of the Nile River.

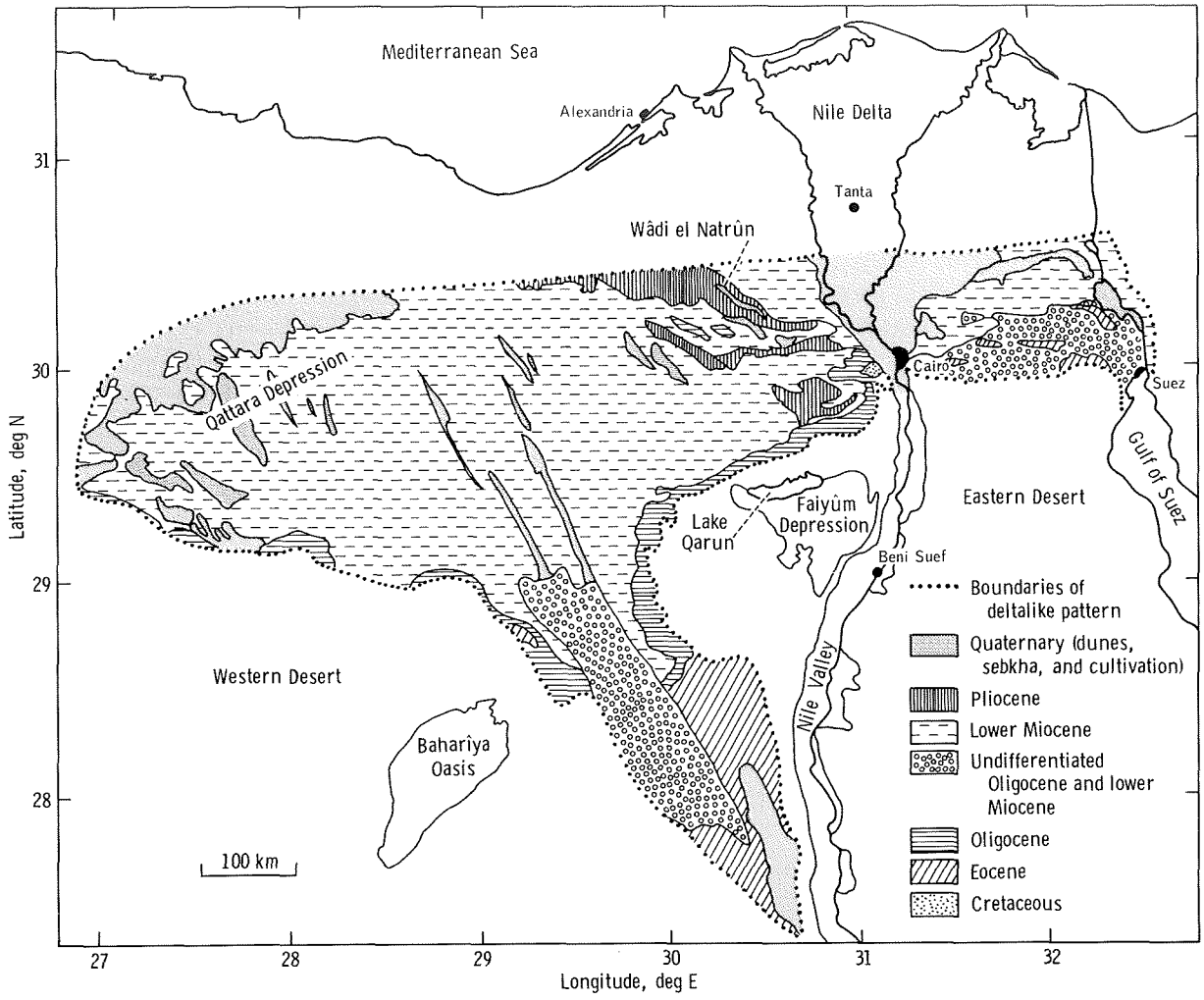


FIGURE 3.—Geological sketch map of the probable ancestral delta of the Nile. This map is based on the geological map of Egypt (ref. 2) and is modified east of Wâdi el Natrûn (based on Said, ref. 3) and simplified east of Cairo. Fault lines are not shown for simplicity; some are shown in figure 1(b).

Oligocene time and forms the unconformity surface between the Oligocene and the overlying lower Miocene rocks.

The lower Miocene deposits in the deltalike pattern occupy extensive areas in both the Western and Eastern Deserts. The type locality of these deposits is near Moghra Oasis where the section is exposed along the northern slope of the Qattara Depression. The sediments of the lower Miocene (Moghra Formation) are very similar to the previously described Oligocene strata except for their much lighter colors. They are composed of sand and gravel containing silicified wood, vertebrate remains, and freshwater fossils. Locally, these clastics may be found interbedded with their marine marl beds, indicating limited sea-level fluctuations during deposition.

Similar to the Oligocene deposits, the lower Miocene deposits attain their maximum thickness along the axis of the deltalike pattern. They attain

a thickness of 615 m approximately 100 km southwest of Wâdi el Natrûn. The northern boundary of the deltalike pattern (fig. 3) corresponds to the boundary of facies change of the lower Miocene deposits; west, northwest, and north of the Qattara Depression, marine deposits of lower Miocene age predominate. It is also noteworthy that the northern boundaries of the deltalike pattern correspond to the northern boundary of the Qattara Depression. This may indicate that the northern boundary of the Qattara Depression is, in fact, a fault line and a boundary of marked facies change. The lower Miocene rocks to the north of that boundary are predominantly marine and those to the south are predominantly sandy. The distribution of sand dunes in the Qattara Depression (fig. 2) indicates that all the dunes originate south of the northern Qattara boundary; i.e., all the dunes are derived from the lower Miocene Moghra Formation.

The Miocene rocks that crop out east of Cairo are not fully understood. However, according to Said (ref. 3, p. 223) "it seems possible to correlate the lower sandy beds of the Miocene of the Cairo-Suez district with the lower Miocene Moghra Formation described from the Western Desert. There is no conclusive paleontological proof that the former beds are of lower Miocene age."

CONCLUDING REMARKS

From the previous discussion, it is clear that the upper Eocene, Oligocene, and lower Miocene deposits present in the area indicate very similar facies. The large area covered by the deltalike pattern, the huge thickness of sediments that belong to similar facies, and the continuity of the facies indicate that these deposits were laid down by a single continuous event and not by intermittent events. The unanimous agreement, in the literature, on describing these sediments as fluvial, estuarine, prodeltaic, deltaic, and fluviomarine leaves no doubt as to their origin. The position of the identified deltalike pattern (fig. 3), the position of its V-shaped tip in the proximity of the Nile Valley northwest of Asyût, and the similarity of the northwest orientation of the axis of this pattern to the orientation of the Nile Valley south of Asyût, lead the authors to believe that the identified deltalike pattern is in fact an ancestral delta of the Nile.

The pear-shaped pattern that is interpreted here as an ancestral Nile Delta appeared with less clarity on a visible image (0.5 to 0.7 μm) taken by the NOAA 2 VHRR (National Oceanic and Atmospheric Administration 2 very-high-resolution radiometer) of the Nile Valley on October 23, 1974. The pattern was tentatively interpreted as an "old Nile Delta" (ref. 17), based on the hypothesis of Hantar (ref. 14). However, the present study of ASTP photographs and Landsat images provides new evidence and makes the interpretation more valid.

The ancestral Nile appears to have followed a similar course to that of the present Nile from Asyût and southward. It must have originated in late Eocene and lasted until the deposition of lower Miocene sediments (approximately 28 million years). Early in the middle Miocene time, the Nile ceased dumping its deposits in its delta. Instead, it lengthened its course flowing northward where it occupied a course similar to the present one. The reason for such a sudden change in course and length of the Nile is likely related to a major uplift that started in the Oligocene time and continued until the early Miocene. This phase of uplift is the same phase that caused the extensive rifting tectonics of the Gulf of Suez region and the extrusion of basalts. It is noteworthy that the majority of the exposed Oligocene basalts in Egypt lie within the ancestral Nile Delta or delimit parts of its boundaries. It is also important to note that the southern tip (V-shaped end) of the ancestral Nile Delta has two large basaltic outcrops (ref. 2) suggesting a possible partial role of volcanic extrusives in blocking the course of the Nile.

The abandonment of the ancestral Nile Delta is beyond doubt related to tectonics. Periodic changes that occur in the distributary patterns of deltas involve a variety of geomorphic reasons (ref. 16), and their effects lead mainly to facies changes. Quaternary changes in the depositional regimes of the present Nile Delta are documented by Said (ref. 5).

The northern boundary of the ancestral Nile Delta (figs. 1 to 3) is straight and continuous for

approximately 500 km. This may indicate that the northern boundary represents a fault line whose downthrown side is to the north. As indicated earlier, this fault line was probably marking the shelf margin during the deposition of the Oligocene/lower Miocene rocks.

Color and textural variations observed within the identified delta are related to either the patchy occurrence of overlapping younger sediments (e.g., Pliocene and Quaternary deposits) or to the characteristics of the discontinuous and patchy lithofacies of the deltaic sedimentation pattern.

The eastward decrease in color intensity (fig. 1) may partly be due to the thinning out of these deltaic deposits east of Cairo because of increasing distance away from the source. The offset of the ancestral Nile Delta to the east may be explained by a longshore current acting along the shorelines of Egypt from west to east (ref. 15).

The detailed mineralogy and geochemistry of the upper Eocene, Oligocene, and lower Miocene rocks may vary locally. Such variations may specifically be noticeable in that part of the delta east of Cairo, because of the influence of tributary drainage lines that drain the basement rocks of the Gulf of Suez area.

The present study should end a long-lasting debate on two theories concerning the origin of the Nile (ref. 14). Blanckenhorn (refs. 8 and 9) believed that there was an older Nile (Ur-nil) that flowed to the west of the present Nile. He obtained support for his theory from the presence of deltaic deposits west of Faiyûm. Arguments against his hypothesis, however, included the absence of a river channel south of that delta. Ball (refs. 10 and 11) and Hume (ref. 12), on the other hand, maintained that the present-day Nile had existed since the early Miocene-Oligocene time and that it followed a course very similar to the present Nile course.

The present study has identified the limits, shape, position, and age of the ancestral Nile Delta; therefore, the authors believe that the two parts of the Nile have different ages. The part of the Nile south of Asyût dates back to the late Eocene time and its delta is the ancestral Nile Delta identified in the present study. The part of the Nile to the north of Asyût is younger because it was cut in "post" early Miocene time after the deposition of the lower Miocene terrigenous deposits. This finding is in agreement with Salem (ref. 15) but is in contradiction with Said (ref. 5). According to Salem (ref. 15, p. 46), "the Nile apparently changed its course dramatically in middle Miocene time and debouched its sediments near the present Nile delta. This change most probably resulted from faulting. Thus, deltaic deposition started near its present site at least as early as middle Miocene time." Said (ref. 5, p. 9), however, maintains that "the cutting of the valley of the Nile seems to have taken place during the Messinian (Upper Miocene)."

The authors disagree with Salem (ref. 15, p. 34) on two issues:

1. According to Salem, "progradation during the Oligocene and Miocene was from southwest to northeast" . . . and . . . "longshore currents aided in the redistribution of sediments in an easterly direction toward the present Nile delta." The present study has defined the full extent and shape of the ancestral Nile Delta and its point of junction with the Nile; therefore, it is pertinent that the progradation of the deltaic sedimentation occurred from southeast to northwest and that the effects of the longshore currents (from west to east) resulted in the offset of the ancestral Nile Delta (fig. 2).

2. Despite the fact that Salem (ref. 15, p. 54) has identified a sedimentological pattern that coincides with the central and northern parts of the ancestral Nile Delta identified in the present study (fig. 2), he attributed the deltaic deposits to "ancestral Nile deltas near the present Nile delta" (ref. 15, p. 34). Therefore, he did not consider the whole pattern as one delta. This shows the importance of the synoptic view provided by space photographs. Probably the reason that Salem (ref. 15) did not identify a "one delta" pattern is that his study area did not extend far enough south for him to identify the southernmost extension of the deltaic pattern and its relationship with the Nile Valley. However, the fact that Salem's model was based entirely on sedimentological and stratigraphic analysis demonstrates beyond doubt the validity of ASTP photographs and Landsat images, if properly used, in depicting regional depositional patterns.

The history of the river Nile is an unfinished

story. Despite the fact that Egypt is the gift of the Nile, published work on that river is scarce and its geology is still far from being well understood. This study may have added just a sentence to the unfinished story of the Nile.

REFERENCES

1. El-Baz, Farouk: The Meaning of Desert Color in Earth Orbital Photographs. Photogramm. Eng. & Remote Sens., vol. 44, no. 1, pp. 69-75.

2. Geological Map of Egypt, Scale 1:2 000 000. Geological Survey of Egypt, 1971.

3. Said, Rushdi: The Geology of Egypt. Elsevier Pub. Co. (Amsterdam), 1962.

4. Youssef, Mourad I.: Structural Pattern of Egypt and Its Interpretation. Bull. American Assoc. Petr. Geol., vol. 52, no. 4, Apr. 1968, pp. 601-614.

5. Said, Rushdi: The Geologic Evolution of the River Nile. Problems of Prehistory: North Africa and the Levant, Fred Wendorf and Anthony E. Marks, eds., Southern Methodist University Press (Dallas, Tex.), 1975, pp. 7-44.

6. Beadnell, H. J. L.: The Geological Survey of Egypt. Geol. Mag., vol. 7 (decade 4), 1900, pp. 46-48.

7. Beadnell, H. J. L.: The Topography and Geology of the Fayum Province of Egypt. Egypt. Survey Dept. (Cairo), 1905.

8. Blanckenhorn, M.: Neues zur Geologie und Paläontologie Aegyptens. II: Das Palaeogen (Eocän und Oligocän). Z. deut. geol. Ges., vol. 52, 1900, pp. 403-479.

9. Blanckenhorn, M.: Neues zur Geologie und Paläontologie Aegyptens. III: Das Miozän Z. deut. geol. Ges., vol. 53, 1901, pp. 52-132.

10. Ball, J.: On the Origin of the Nile Valley and the Gulf of Suez. Cairo Sci. J., vol. 3, 1909, pp. 250-252.

11. Ball, J.: Contributions to the Geology of Egypt. Egypt. Survey Dept. (Cairo), 1939.

12. Hume, W. F.: The Origin of the Nile Valley in Egypt. Geol. Mag., vol. 7 (decade 5), 1910, pp. 385-389.

13. Shukri, N. M.; and Ayouty, M. K.: The Mineralogy of Eocene and Later Sediments in the Anqabia Area, Cairo-Suez District. Bull. Fac. Sci. Cairo Univ., no. 32, 1954, pp. 47-61.

14. Hantar, G.: Contribution to the Origin of the Nile Delta. Ninth Arab Petrol. Congress, United Arab Emirates-Dubai, paper no. 117 (B-3), Mar. 1975.

15. Salem, R.: Evolution of Eocene-Miocene Sedimentation Patterns in Parts of Northern Egypt. Bull. American Assoc. Petr. Geol., vol. 60, no. 1, 1976, pp. 34-64.

16. Rice, R. J.: Fundamentals of Geomorphology. Longman (London), 1977.

17. Allison, Lewis J.: Geological Applications of Nimbus Radiation Data in the Middle East. NASA TM X-71207, 1976.

Suspended-Sediment Dispersal Patterns of River Deltas Photographed by ASTP

Ted A. Maxwell[a]

ABSTRACT

Orbital photographs of five major river deltas reveal the presence of distinctive suspended-sediment plume patterns that can be related to models of sedimentation in a deltaic environment. By using both delta geometry and plume pattern, the relative effects of river inertia, buoyancy of suspended matter, and turbulent bed friction can be evaluated. Although long-term delta development is affected by numerous factors, the study of plumes from orbital photographs indicates the short-term processes that dominate deltaic sedimentation. Photographs of the Fraser and Rhône Rivers suggest river-inertia domination, whereas those of the Orinoco and Yangtze Rivers suggest the importance of both frictional turbulence and buoyancy. The major process operating at the mouth of the Danube River is buoyancy.

INTRODUCTION

As part of the Earth Observations and Photography Experiment of the Apollo-Soyuz Test Project (ASTP), several sites of present-day deltaic sedimentation were chosen for visual observations and photography. Information on cameras, film types, and photographic support data are in reference 1. The intent of this study is to investigate the sediment plume patterns emanating from deltas with respect to (1) shore morphology, (2) deltaic pattern of the river, and (3) models of deltaic sedimentation.

Much of the world's supplies of oil and gas has been found in ancient deltaic sediments and, consequently, many studies have been made of both recent and ancient deltas (reviewed in refs. 2 and 3). These studies have dealt mainly with the distribution of sediments and the depositional environment, and only recently have they made use of aerial photographs and space images to define the distribution of suspended sediment plumes (refs. 4 and 5). Recent studies of Landsat images have shown the importance of longshore currents, prevailing winds, and turbulence in distributing the sediment input by rivers. However, the relationship of color zones within the plumes can be studied only through the use of a continuous-tone color film, such as that used on ASTP.

Five major river deltas were photographed during the mission: the Danube, Fraser, Orinoco, Rhône, and Yangtze (fig. 1). Although numerous photographs of the Nile Delta were taken, there are no pronounced sediment discharge plumes and, consequently, the Nile is not included in this study. Sediment plumes are visible at the mouths of all the other rivers studied, and may be classified according to the relative effects of river and receiving-basin energy levels. Plume patterns of the Orinoco and Yangtze are most affected by longshore currents and by the effects of wave and tidal energy, whereas patterns of the Rhône and Fraser Rivers are influenced by outflow inertia (ref. 6). Based on present models of deltaic deposition, it may be possible to estimate the geometry of subaqueous bar development based on plume pattern. Consequently, this paper will first review

[a]National Air and Space Museum, Smithsonian Institution.

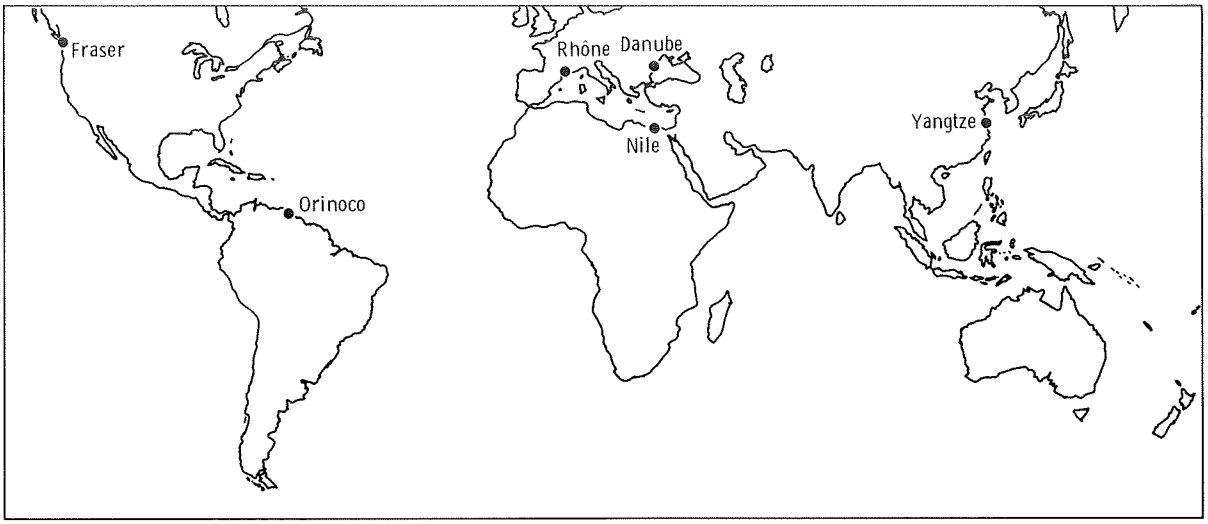


FIGURE 1.—Locations of major deltas photographed by ASTP crewmembers.

models of distributary-mouth bar development, and then discuss plume patterns photographed by ASTP in terms of their dominant controlling mechanisms.

CONTROLS OF SEDIMENT DISTRIBUTION PATTERN

Although long-term deposition and delta evolution are controlled by climate more than by any other single factor (ref. 3), the instantaneous nature of sediment plumes revealed in space photographs is more a function of short-term daily (or even hourly) weather and tidal conditions. However, the deltaic processes that give the plume its characteristic shape are time-independent, and the study of plumes can therefore be used to estimate the relative importance of each process. The significance of each process is subject to daily variations in weather, tides, discharge, and receiving-basin conditions; therefore, detailed interpretations cannot be made on the basis of a single photograph. However, for purposes of this study, the basic factors of delta and shore geometry will be considered static.

Based on a synthesis of deltaic studies, three dominant processes have been proposed for the evolution of sediment dispersal patterns (refs. 3, 6, and 7). With the exception of coastal processes, sediment discharge can be viewed as a function of (1) outflow inertia, (2) turbulent bed-friction seaward of the mouth, and (3) outflow buoyancy (ref. 7). Depositional patterns resulting from these three mechanisms are summarized in figure 2. Although these processes were proposed partially on the basis of depositional patterns, they are also applicable to sediment plumes in ASTP photographs. The following summary of river mouth processes is based on studies by Coleman and Wright (refs. 3 and 7).

River inertia effects on sediment dispersal take place through turbulent jet diffusion at the boundary of the river and receiving basin (fig. 2, sketch A). This process is enhanced by steep river gradients, the lack of bottom interference, and small differences in buoyancy between the river and basin water. A river mouth dominated by this process is characterized in plan view by a lunate bar that is further distinguished by sediment sorting; the coarsest material is deposited at the landward margin of the bar. With this process dominating, the sediment plume would have relatively sharp margins with the basin water, and its length would be the direct result of river velocity.

When continuous deposition at the mouth of the river results in decreased water depth, an in-

crease in the dominance of bed friction occurs. High bed friction contributes to increased deposition. Eventually, channelization will occur, localized by subaqueous levees, and a triangular-shaped bar will develop at the mouth of the river (fig. 2, sketch B). The resulting plume pattern will be broader than an inertia-dominated river mouth, although a subaqueous channel may be marked by a concentrated zone of suspended sediment.

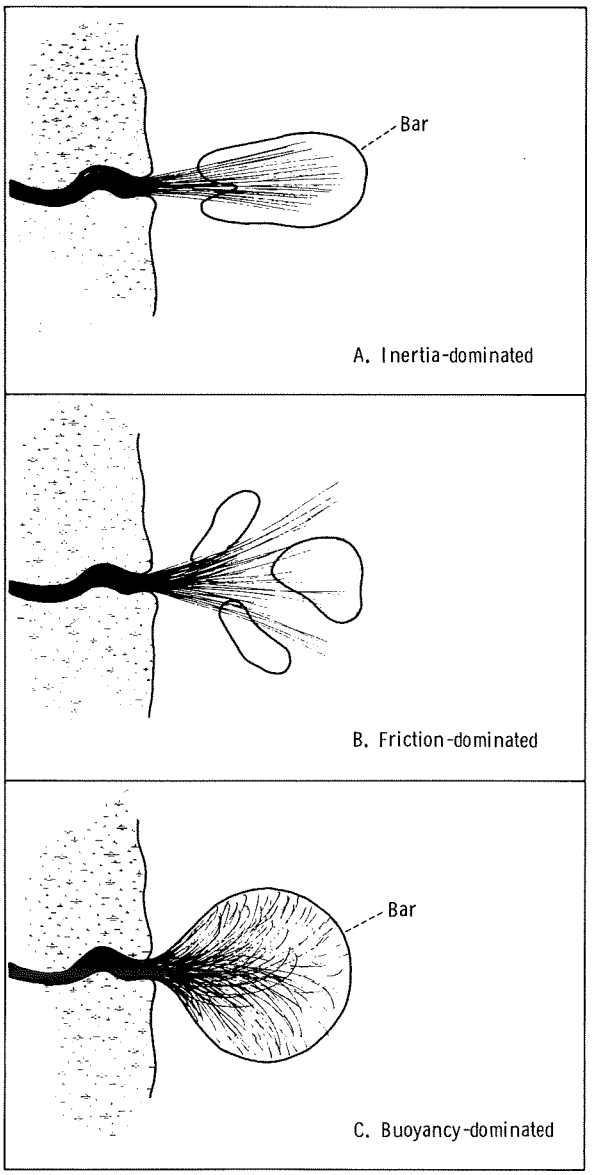


FIGURE 2.—Patterns of sediment dispersal and distributary-mouth bar formation for three processes of sedimentation (modified from Coleman, ref. 3).

Because the density of seawater is greater than that of river water (even with admixed sediment), the suspended sediment of a coastal delta will be buoyantly supported. The process of turbulent diffusion is not as significant as is the spreading of the river water above the more dense basin water. Consequently, the bar of the river mouth extends radially away from the mouth, and sediment deposits will be laterally sorted. Depending on the magnitude of discharge and the difference between river and basin water density, this process may also occur within the river, where straight distributaries would be flanked by subaqueous levees (fig. 2, sketch C). The sediment plumes resulting from this mechanism will appear more symmetrical than those of inertial or frictional processes.

Although these factors are the primary controls on the outflow pattern of sediments, forces active in the receiving basin will redistribute suspended matter. Active wave and tidal regimes will produce rapid mixing of the sediment, and may offset the effects of buoyancy through vertical mixing of freshwater and seawater (ref. 7). Because these processes can fluctuate rapidly with local tidal and weather conditions, interpretation of plumes seen in ASTP photographs will be considered only with respect to the primary depositional processes.

PLUME CHARACTERISTICS

Danube River

The Danube Delta occupies an area of 2740 km^2 (ref. 3) on the western margin of the Black Sea. Sediment plumes emanate from all three major branches of the river, although the central and northern branches (Sulina and Chilia) join at the coast and together are responsible for the most dense portion of the plume (fig. 3(a)). North of these river mouths, sediment is distributed uniformly along the coast, but it has a sharp boundary with clearer basin water approximately 8 km from the shore.

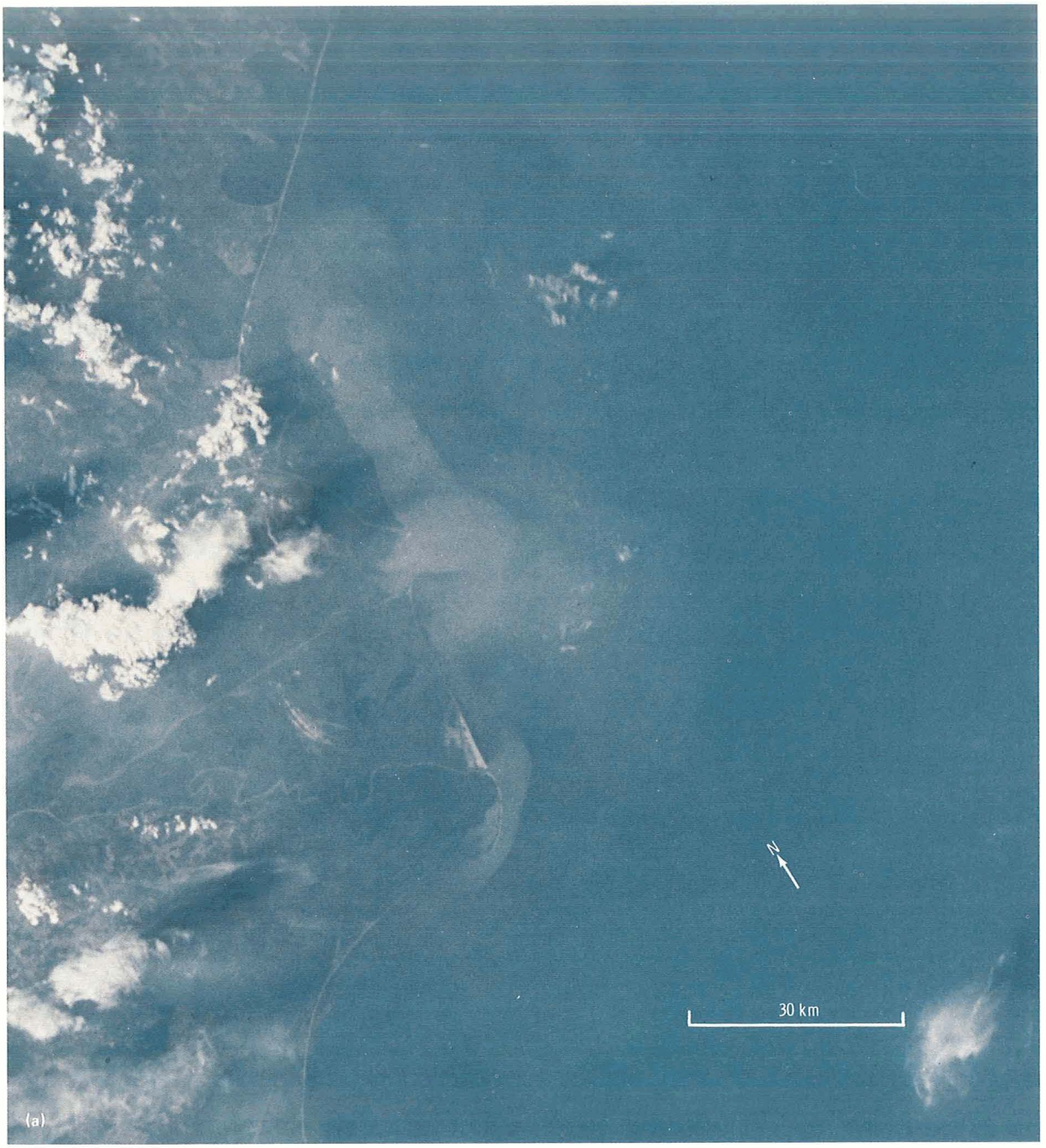


FIGURE 3.—The Danube Delta on July 24, 1975. (a) On this ASTP photograph, the northern distributary indicates redistribution by longshore currents, but the southern distributary indicates effects of buoyancy (AST-24-1965). (b) The Landsat band 5 image, taken on same day as figure 3(a), shows change of drift direction, although the basic patterns are similar (E-2183-08071).

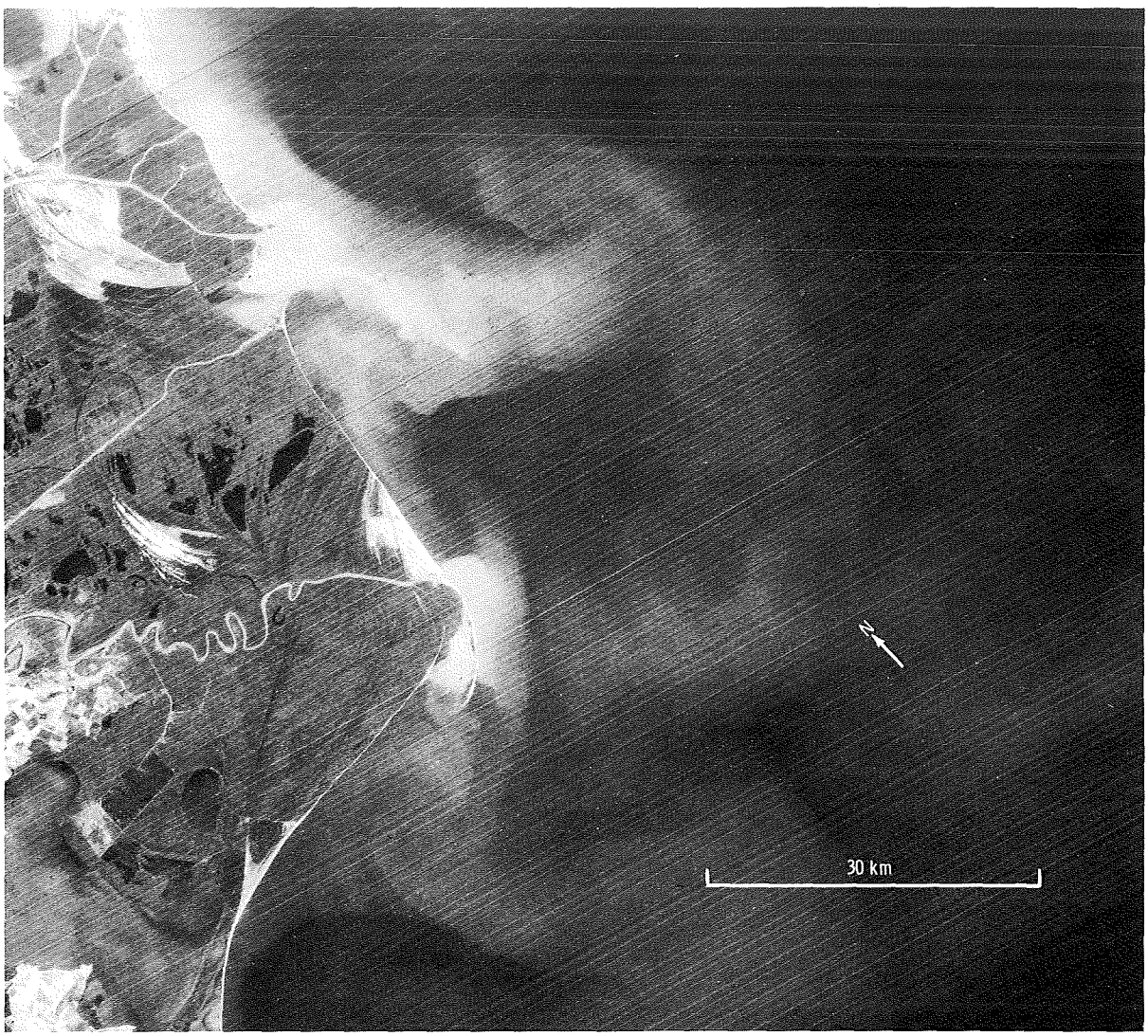


FIGURE 3.—Concluded.

Although offshore wave and current activity has distributed sediment along the coast, the effect of buoyant support of river sediment has previously been noted for the Danube Delta (ref. 6). The southern mouth of the river shows the sediment distribution pattern that is expected from a buoyancy-dominated system (fig. 3(a)). Both the large extent and color of the Danube effluent were observed by Apollo crewmembers (ref. 8): "Coming up to the Danube Delta, there's tremendous sediment plumes there . . . . Man, that's really flooding out into the Black Sea; turning it brown. . It looks like the Danube's . . . water running right across the Black Sea."

The extension of the plume to the south shows the effect of local longshore currents; however, the variability in both size and pattern of sediment distribution within the same day is emphasized by figure 3(b). Although the major plume pattern remains the same, the plume seen on the Landsat image extends farther into the basin, and is influenced more by the southward current.

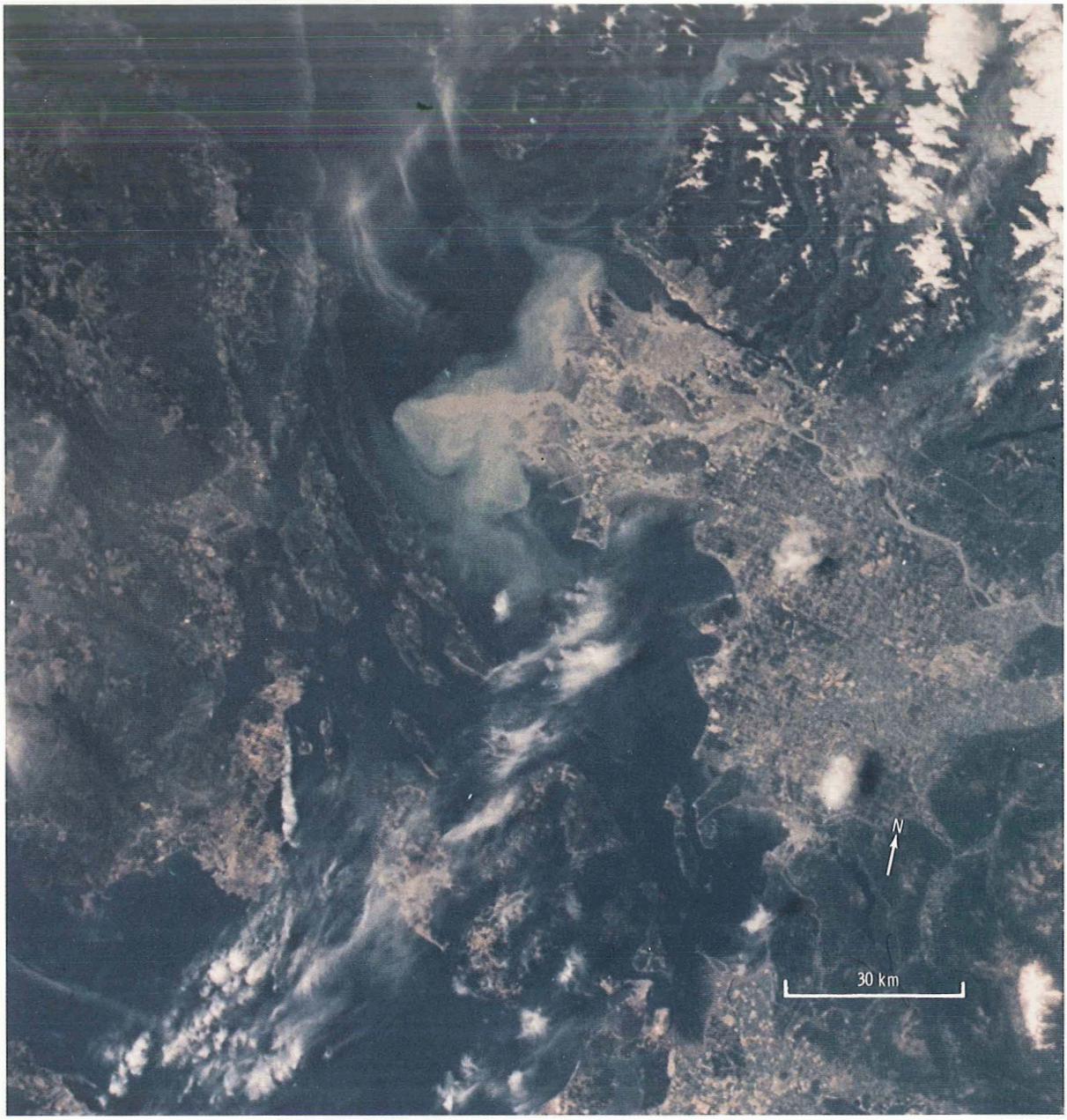


FIGURE 4.—The Fraser River Delta, near Vancouver, British Columbia. The straight, jetlike appearance of the sediment plume indicates the dominance of river inertia (AST-19-1538).

Fraser River

The mouth of the Fraser River is in a more protected environment than that of the Danube. As expected, therefore, the sediment plume is less diffuse. It extends 18 km into the Strait of Georgia, approximately 75 percent of the width of the strait (fig. 4). The main part of the plume is light brown and extremely dense, as is the nearshore water to the south.

As a result of the sheltered receiving basin, inertial force of the river is the dominant cause of

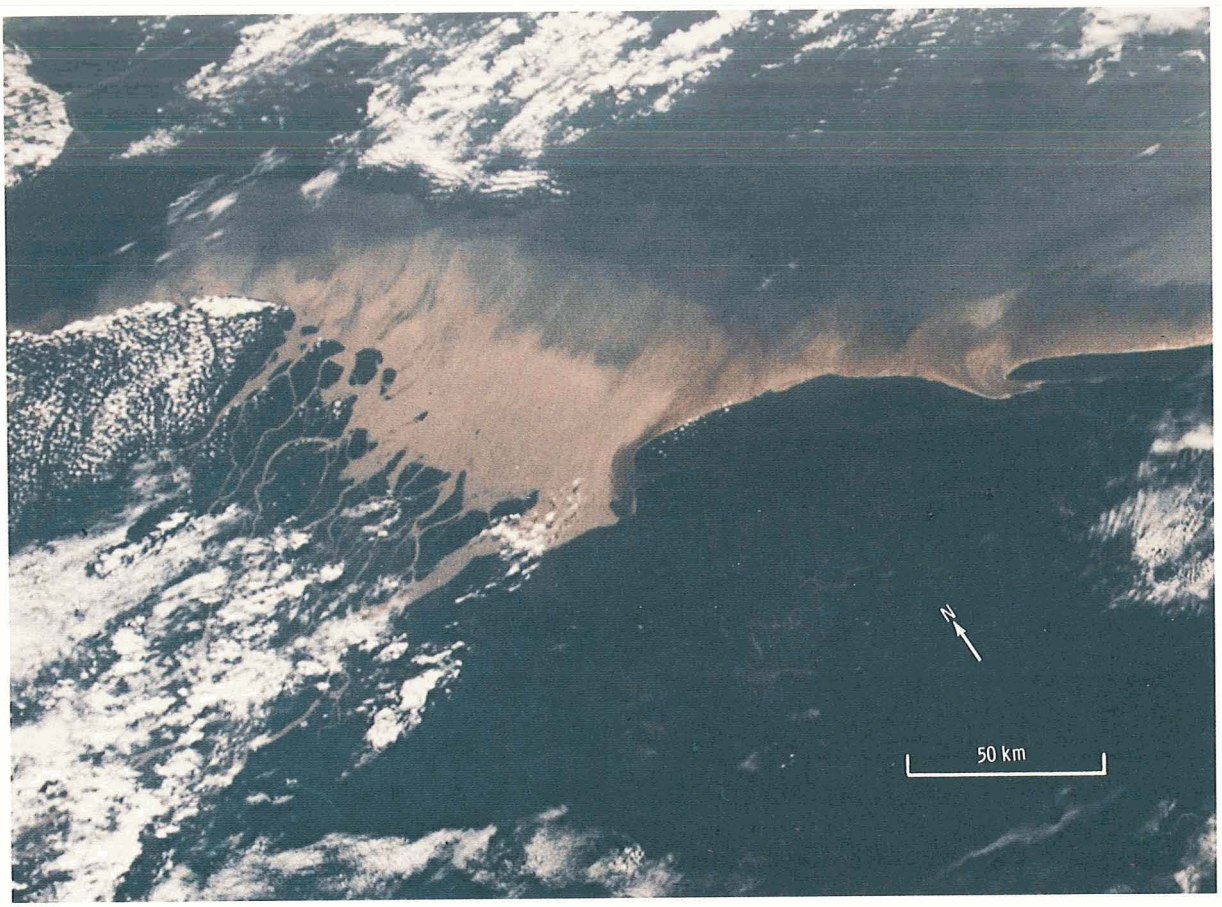


FIGURE 5.—Three distinct zones of sediment density are present in this ASTP view of the Orinoco Delta. Note longshore drift to the east (AST-21-1683).

the plume pattern. Although some southward drift has occurred, the more diffuse parts of the plume do not occur next to the shore as is the case with deltas open to the ocean. The lack of effective longshore redistribution of sediment has resulted in protrusion of the present delta into the strait. Consequently, it is likely that river inertia has played the dominant role throughout formation of the delta.

Orinoco River

On the basis of field studies, Van Andel (ref. 9) has shown that the Orinoco Delta is a zone of rapid coastal accretion, with a large volume of sediment contributed by longshore transport from nearby rivers. The nearshore pattern of sediment seen in ASTP photographs, however, suggests that the major contribution of suspended sediment comes from the Orinoco River itself.

Three distinct zones of sediment density are present in the Orinoco plumes (fig. 5). The zone nearest the distributary mouths has the highest sediment concentration. It is light tan in color, similar to the water of the Orinoco distributaries. Approximately 30 km from the distal end of the delta, there is a sharp boundary with darker basin water. In this zone (30 to 55 km), the dark tan color of the effluent matches the color of nearshore water along the coast. A third zone of brown-tinted seawater occurs in a band 5 to 17 km wide at the outmost edge of the sediment plume. This color zone is present elsewhere on the coast

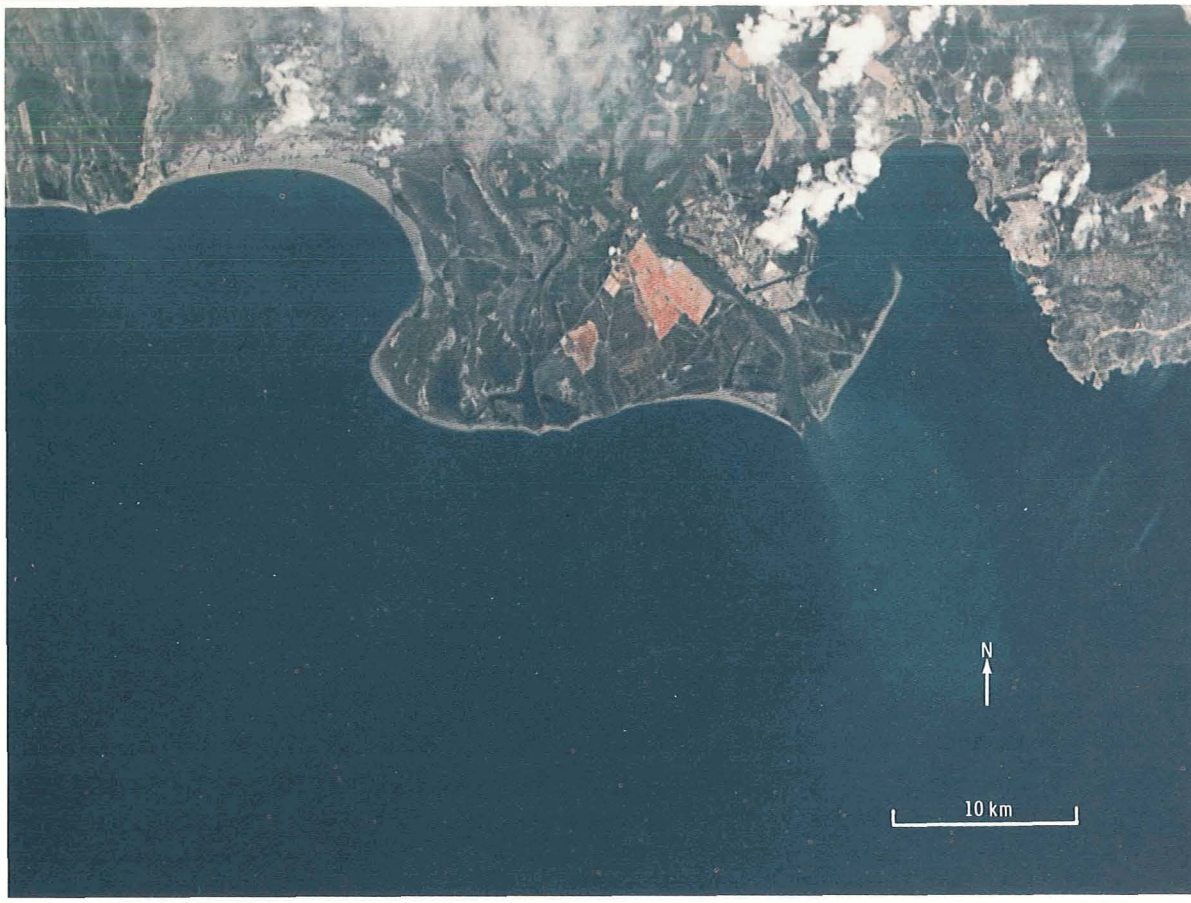


FIGURE 6.—The delta pattern of the Rhône River indicates the result of inertia-dominated formation, which is also reflected in the faint sediment plumes (AST-23-1945).

where it is gradational with the dark tan nearshore sediment; however, this zone is most clearly delineated at the outer Orinoco plume.

Both the depth and slope of the sea floor are shallow at the mouth of the Orinoco (ref. 9); therefore, frictional processes of sedimentation would be expected to dominate. Within 40 km from the delta, the depth of seawater is less than 10 m, which corresponds to the most dense portion of the sediment plume. However, studies of bottom topography reveal no major subsequent channels; this may be due to either redistribution by longshore currents or to buoyant support of sediment. Consequently, the major primary processes of sediment support in the Orinoco Delta region are a combination of both frictional turbulence and buoyancy. The effects of longshore currents, although evident elsewhere along the coast, are not prominent in ASTP photographs.

Rhône River

The delta pattern of the central Rhône distributary is geometrically similar to models of delta growth presented by Komar (ref. 10) in which river sediments were provided to an initially straight shoreline with waves moving directly onshore. The slight curvature of the shoreline on either side of the distributary mouth, and the larger-scale irregular nature of the shoreline both suggest that longshore sediment transport and redistribution have not been active processes in development of the Rhône Delta. Consequently,

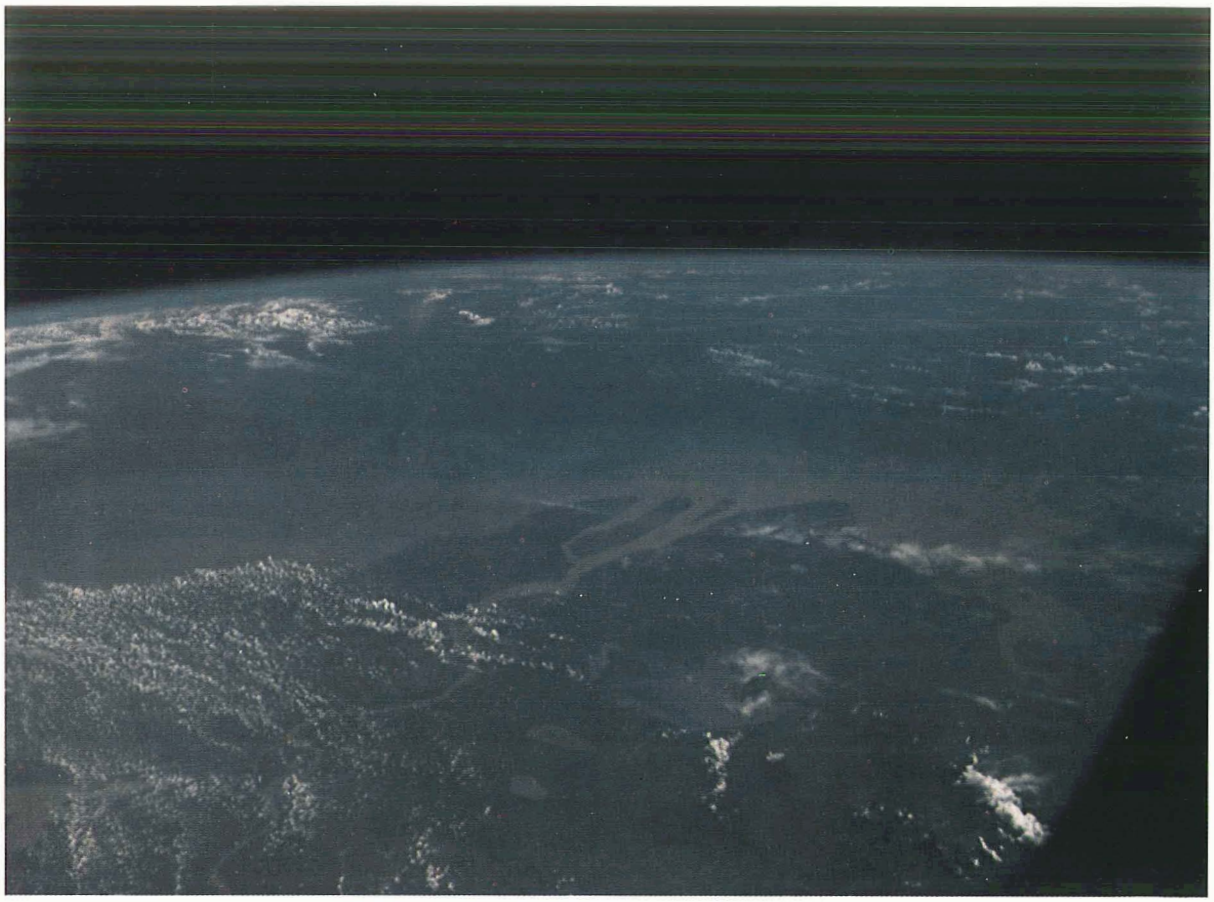


FIGURE 7.—High-oblique view of the Yangtze River Delta (AST-21-1738). Light tan suspended sediment is distributed along the coast, indicating the prevalence of longshore drift.

delta growth is primarily the result of accretion of river sediments to form beaches, and the consequent formation of intervening strand flats (ref. 9).

As would be expected from the delta pattern, a river-dominated sediment plume is generated at the mouth of the Rhône. This faint plume extends 12 to 15 km into the Gulf of Lions, and is only slightly affected by a current to the east (fig. 6). Although river inertia is the dominant factor controlling the shape of the sediment plume, the low density of the effluent can be attributed to a lack of fine-grained sediment entrained by the river. Consequently, the interpretation of a river-dominated sediment plume for the Rhône River can be made equally on the basis of deltaic and effluent patterns.

Yangtze River

High-oblique ASTP photographs of the Yangtze River Delta indicate the presence of both nearshore and fluvial suspended sediment. Nearshore surface water is lighter tan than that of the river mouth, although considerable reworking of river sediment is suggested by streaks of brown-tinted water in the coastal zone (fig. 7). The dark tan color of Yangtze River water is continuous in tone from the upper reaches of the river (within the delta) to the mouths of the distributaries. Although these photographs are too oblique to indicate well-defined zones of sediment density, the mixing of river water with basin water is not gradational. A light blue zone of mixed sediment and basin water occurs continuously along the coast.

Because several distributary channels are responsible for the influx of suspended sediment, the effects of either bed friction or effluent buoyancy dominate over river inertia, and these effects are most likely responsible for the plume pattern. Turbulent bed friction is the most probable mechanism, on the basis of the mixing pattern, but the influence of other factors is difficult to judge because of the effective longshore redistribution.

CONCLUSIONS

On the basis of three models for deltaic deposition, the use of orbital photographs from ASTP allows classification of plumes and deltas as a function of the dominant sedimentary process. River-inertia-dominated plumes are represented by the Fraser and Rhône Rivers, and buoyant support of suspended sediment is represented by the Danube River. Both the Orinoco and Yangtze Rivers owe their characteristic sediment patterns to a combination of frictional turbulence and buoyancy.

Because of rapidly changing coastal conditions (as indicated by comparison of the ASTP photograph and Landsat image of the Danube Delta), these observations of delta development are valid only for short-term investigations of the deltaic environment. For longer-term observations of delta development, the effects of tides, currents, and local weather conditions on plume patterns should be related.

REFERENCES

1. El-Baz, Farouk; and Mitchell, D. A.: Earth Observations and Photography Experiment MA-136. Sec. 10 of Apollo-Soyuz Test Project Preliminary Science Report, NASA TM X-58173, 1976.

2. Broussard, M. L., ed.: Deltas, Models for Exploration. Houston Geol. Soc. (Houston, Tex.), 1975.

3. Coleman, J. M.: Deltas: Processes of Deposition and Models for Exploration. Continuing Education Publ. Co. (Champaign, Ill.), 1976.

4. Wiesnet, Donald R.: Suspended Sediment in Great Slave Lake, Northwest Territories, Canada. ERTS-1, A New Window on Our Planet, U. S. Geol. Survey Prof. Paper 929, Richard S. Williams, Jr., and William D. Carter, eds., 1976, pp. 162-163.

5. Pluhowski, Edward J.: Dynamics of Suspended-Sediment Plumes. ERTS-1, A New Window on Our Planet, U. S. Geol. Survey Prof. Paper 929, Richard S. Williams, Jr., and William D. Carter, eds., 1976, pp. 157-158.

6. Wright, L. D.: Sediment Transport and Deposition at River Mouths: A Synthesis. Bull. Geol. Soc. America, vol. 88, no. 6, 1977, pp. 857-868.

7. Coleman, J. M.; and Wright, L. D.: Modern River Deltas: Variability of Processes and Sand Bodies. Deltas, Models for Exploration, M. L. Broussard, ed., Houston Geol. Soc. (Houston, Tex.), 1975, pp. 99-150.

8. El-Baz, Farouk: Astronaut Observations From the Apollo-Soyuz Mission. Vol. I of Smithsonian Studies in Air and Space, Smithsonian Institution Press (Washington, D.C.), 1977.

9. Van Andel, Tj. H.: The Orinoco Delta. J. Sediment. Petrol., vol. 37, 1967, pp. 297-310.

10. Komar, Paul D.: Computer Models of Delta Growth Due To Sediment Input From Rivers and Longshore Transport. Bull. Geol. Soc. America, vol. 84, July 1973, pp. 2217-2226.

Use of Apollo-Soyuz Photographs in Coastal Studies

M. T. El-Ashry[a]

ABSTRACT

The coastal zone is a dynamic system in which sediment is in continuous motion. The position and configuration of a shoreline in a given coastal area and at a given time is determined by the balance between sediment contribution and sediment removal. An air photograph (conventional aircraft, satellite, and spacecraft) provides an excellent record of the pattern of coastal features at the time the photograph is taken.

Apollo-Soyuz photographs of the Maryland, Delaware, and Virginia coasts including the Chesapeake Bay; of the Nile Delta and adjacent areas in Egypt; and of the Rhône Delta in France provided valuable information regarding coastal zones and demonstrated various areas of application in coastal studies. These include shoreline features such as barrier islands, beach ridges, salt marshes, tidal inlets, and tidal deltas; shoreline changes including identification of major areas of erosion or accretion and prediction of future changes along rapidly changing shorelines; and information regarding littoral drift. Because coastal engineering planning considers knowledge of long-term trends in shoreline changes, Earth-orbital photographs, especially when combined with conventional aerial photographs, can be instrumental in providing such information.

INTRODUCTION

A coastline represents a dynamic and fragile, physical and biological environment that is constantly changing in response to natural processes and human activities. Field measurements and observations as well as laboratory modeling are the major activities for collecting and interpreting data from coastal areas. Nautical charts and topographic maps are used for gathering information regarding the configuration of the coasts and the changes that take place along them. However, aerial and orbital photographs, and other sensors, have proved valuable in showing the larger features and circulation patterns that do not normally appear on photographs taken from ground levels. Over shallow and clear waters, aerial images indicate shoals and channels that exist along many shorelines; and they provide accurate means for revising and updating maps and nautical charts.

In the 1970's, the supply of remotely sensed data and the importance of remote sensing greatly increased with the launching on July 23, 1972, of the first unmanned Earth Resources Technology Satellite, now known as Landsat-1, into a near-polar orbit 900 km above the Earth. The Landsat-1 operational period was overlapped by the manned Skylab missions in 1973 and 1974, and followed by the Apollo-Soyuz mission in July 1975.

The literature contains a large number of papers and a few books that emphasize the value of air photography (conventional aircraft, satellite, and spacecraft) as a tool in coastal studies. A current review of the literature is included in El-Ashry (ref. 1).

[a]Environmental Defense Fund, Inc., Denver, Colorado.

An aerial photograph provides an excellent record of the pattern of coastal features at the time the photograph is taken. The size and spacing of waves, the direction of wave fronts, the direction of littoral drift, and the distribution of shallow water sediment accumulations to depths of approximately 7 m may easily be determined. In addition, more details of the configuration of coastal and nearshore features are discernible on aerial photographs than are usually recorded in careful field surveys of a coastline.

During the last 40 years, repetitive aerial coverage of coastal areas has made it possible to observe changes in beaches, sand dunes, and inlets as well as the effects of severe storms and man-made structures. Published topographic maps and coastal charts, as well as field sketches from coast surveys, enable observation and comparison of changes occurring before the availability of aerial photographs. From sequential aerial photography, it is possible to measure changes resulting from sediment shift during the interval between dates of photography.

In the last decade, valuable information on coastal zones has been obtained from orbital photographs. Numerous studies have demonstrated the various areas of application of such photographs (for example, refs. 2 and 3). Shoreline features, including barrier islands, beach ridges, dunes, salt marshes, tidal flats, tidal inlets, and deltas, are portrayed clearly on orbital photographs. Changes in shoreline configuration can be determined and major areas of erosion or deposition can be identified from orbital photographs. Because considerable underwater penetration is possible, orbital photographs can be used in water depth determination. Information regarding littoral drift direction can be obtained from certain shoreline features or changes as well as from sediment plumes discharged from river mouths and bays. The possibility of widespread offshore movement of nearshore sediments was appreciated after orbital photographs became available. In addition, sequential orbital photographs will prove to be of great help in studying rapidly changing shorelines.

Based on the experience obtained in previous manned space missions, an Earth Observations and Photography Experiment was designed for the Apollo-Soyuz Test Project (ASTP) mission of July 1975. One of the objectives of the experiment was to acquire photographs related to geology, oceanography, hydrology, and meteorology (ref. 4). Most ASTP photographs were taken with a bracket-mounted 70-mm Hasselblad data camera. For this camera, an intervalometer established a 60-percent overlap between successive frames. Other ASTP photographs were taken with a handheld 70-mm Hasselblad reflex camera.

For the purpose of illustrating the value of ASTP photographs in coastal studies, two contrasting coastal regions have been chosen. These are (1) the U. S. Atlantic coast between Cape Henlopen, Delaware, and Cape Charles, Virginia, including the Chesapeake Bay and (2) the Nile Delta coastline and adjacent areas in Egypt including a comparison with the Rhône Delta in France.

CHESAPEAKE BAY AREA

The Chesapeake Bay area is illustrated by photographs AST-13-797 and AST-13-798. The photographs were taken on July 24, 1975, with a 50-mm lens from an altitude of 225 km. They were taken with the camera axis near vertical and at a Sun angle of 80°.

The map reproduced in figure 1 shows the coastal locations described in this area. Most of the basic information on these locations was derived from Shepard and Wanless (ref. 5). In their book, Shepard and Wanless used a large number of low- and high-altitude aerial photographs to illustrate coastal features and coastal changes in selected areas of the U. S. Atlantic coast. Supplementing space photographs with aerial photographs proved to be a valuable tool in studying coastal features and their changes, including the distribution of shallow water sediment accumulations, direction of littoral drift, and exchange of sediment-laden water between lagoons and the open seas through inlets (ref. 6).

The Chesapeake Bay is a drowned river valley system that includes the lower valleys of the Susquehanna, Potomac, Rappahannock, York, and James Rivers. It extends inland for more than 260 km. The bay is more than 40 km wide in its central part and approximately 21 km wide at its mouth

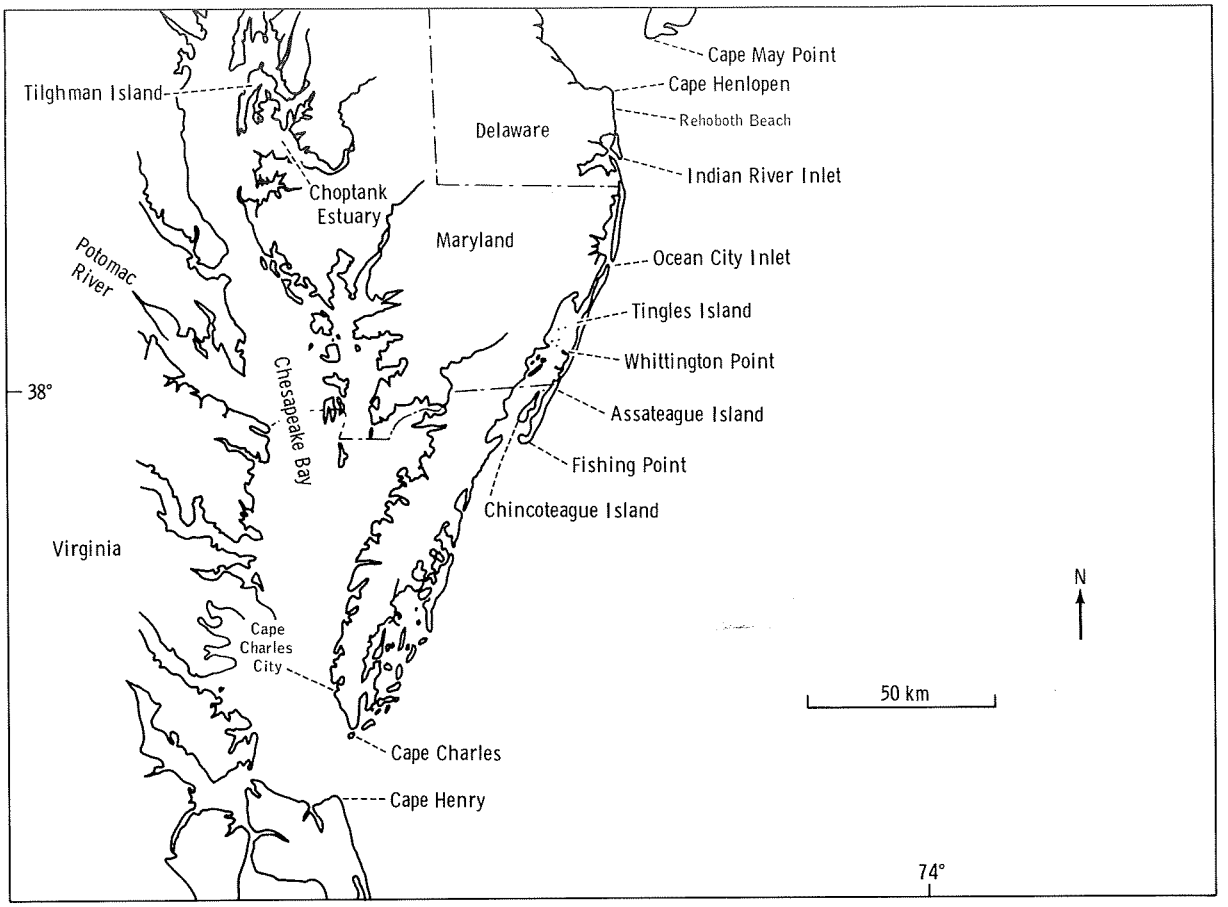


FIGURE 1.—Index map showing coastal locations described between Delaware Bay and Chesapeake Bay, U.S.A.

between Cape Charles and Cape Henry. The channel ranges in depth from 6 to 25 m and leaves the bay near Cape Henry on the southern shore. Generally, winds in the Chesapeake Bay area are from the west or the northwest and result in wave heights that are usually larger along the eastern side of the bay. The consequence has been a surprisingly fast rate of erosion along the eastern side of the bay as well as on the northern and western sides of the islands within the bay. According to Jordan (ref. 7), the eroded sediments have partly filled depressions in the bay and have formed shoals on the lee sides of the eroded islands. Such shoals are clearly displayed in the ASTP photograph (fig. 2). In addition to the shallow underwater sediment accumulations, beach features include baymouth bars, recurved spits, and cuspate forelands. There are also well-developed sand waves near the southern side of the bay entrance that seem to have been formed by tidal action. Tidal currents tend to flow in on the northern side of the Chesapeake Bay and out on the southern side.

The eastern flank of the Chesapeake Bay is in the form of a long, narrow peninsula, which Shepard and Wanless (ref. 5) designated "Delmarva Peninsula," a name used by National Geographic because of the three states involved. To the east, the area is largely marsh and lagoons with a chain of barrier islands along the seaward margin. On the western side, the land is higher and mostly well drained (ref. 5). The barrier islands are separated by tidal inlets maintained by tidal scour. Sediment plumes discharging from the

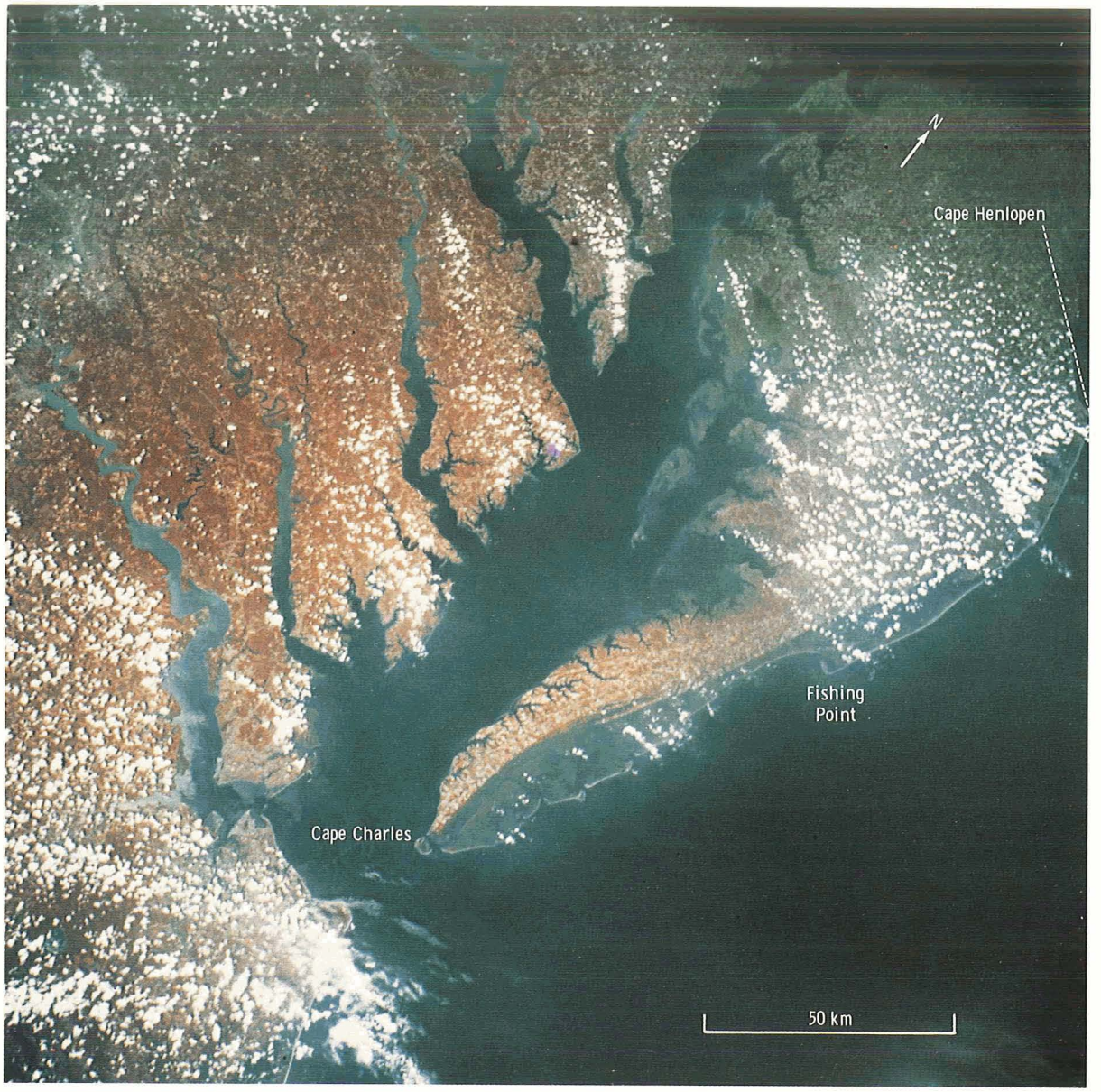


FIGURE 2.—Apollo-Soyuz color-infrared photograph of the Chesapeake Bay area including Cape Henlopen, Fishing Point, and Cape Charles, U.S.A. (AST-13-797).

inlets are clearly visible in the ASTP photograph (fig. 2). The recurved spits built into the inlets, the pronounced offset at the inlets, and a cuspate foreland suggest that the predominant direction of littoral drift along this section of the coast is to the northeast. The higher western side of the peninsula is marked by several well-defined beach ridges, which indicate different stages in its growth and development.

Between Cape Henlopen, on the southern side of Delaware Bay, and Fishing Point, the shoreline is in the form of a barrier island that extends for more than 100 km and is interrupted only by two inlets, Indian River Inlet and Ocean City Inlet. Indian River Inlet was artificially opened and its location can only be identified on the ASTP



FIGURE 3.—Apollo-Soyuz photograph showing Delaware Bay, Cape Henlopen, Ocean City (Maryland), Assateague Island, and Fishing Point (Virginia) (AST-13-798).

photograph (fig. 3) by the tidal delta inside the bay between Rehoboth Bay to the north and Indian River Bay to the south. Ocean City Inlet is located almost halfway between Cape Henlopen and Fishing Point. The ASTP photograph (fig. 3) clearly shows the offset of the barrier on both sides of the inlet. This offset is due to sediment accumulation, from a strong littoral current that flows southward against the jetty constructed on the northern side of the inlet and from erosion along the southern side of the inlet.

South of Ocean City Inlet to Fishing Point, the barrier island is known as Assateague Island. The lagoon side of the island is quite irregular as a result of washovers formed during major storms and old tidal deltas inside inlets that no longer

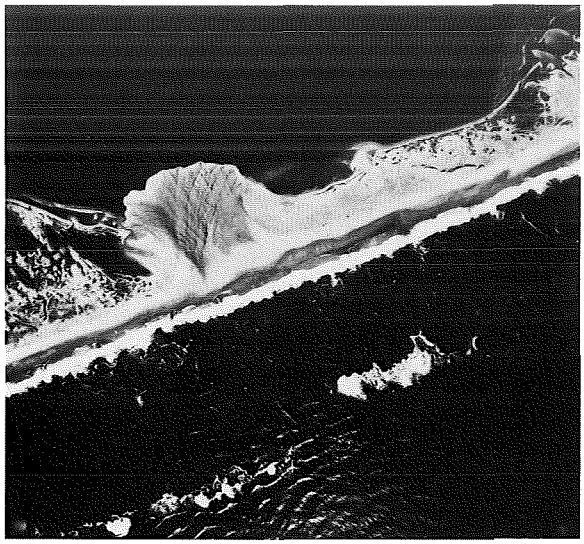


FIGURE 4.—Aerial photograph of Assateague Island, Maryland, after the great Atlantic coast storm of March 1962, showing a washover fan with reticulate bars (U.S. Coast and Geodetic Survey photograph).

exist (fig. 3). Aerial photographs of the island (fig. 4) show dunes, sluiceways, washover fans, sand plains, and washarounds; this variety of features makes Assateague Island one of the most spectacular areas along the Atlantic coast (ref. 5). However, most of these details cannot be easily identified on the ASTP photographs without prior knowledge of their existence from examination of aerial photographs. On the other hand, the capability of an ASTP photograph (fig. 3) to portray a large coastal area in a single exposure clearly illustrates how an uneven coastline (exemplified by this section of the Atlantic coast) resulting from sea-level rise following glacial melt has been completely straightened by a combined process of erosion of promontories and deposition of a narrow continuous barrier island across the mouths of estuaries.

NILE DELTA AND RHÔNE DELTA

The Nile Delta is illustrated by photographs AST-9-558, AST-16-1257, and AST-16-1258. Photograph AST-9-558 was taken on July 19, 1975, with a 50-mm lens from an altitude of 226 km, with the camera axis near vertical, and at a Sun angle of 60°. Photographs AST-16-1257 and AST-16-1258 were taken on July 20, 1975, with a 60-mm lens from an altitude of 225 km and at a Sun angle of 75°.

The Nile Delta is the classic example that led Herodotus, nearly 2500 years ago, to apply the Greek letter delta as a geomorphological term. The Nile Delta is a lobate delta (fig. 5), where the supply of fluvial sediment is abundant and wave and current scour have not been excessive (ref. 8). Several distributaries of the Nile once existed. All but two are now defunct. The two remaining are the Rosetta Branch to the west and the Damietta Branch to the east. This is in contrast to the Rhône Delta, a river with wandering and intermittent outlets (fig. 6), in which the old main outlet is now the relatively unimportant Petit Rhône and the present river discharges through the larger Grand Rhône channel farther east (fig. 7 in ref. 8). Following the decay of the Vieux Rhône (fig. 7) and the diminished outflow from the Petit Rhône, sediments deposited by these distributaries were eroded by waves and transported westward by littoral currents to build the forelands at Pointe de Beauduc and Pointe de l'Espiquette (ref. 8 and fig. 7). Pointe de Beauduc is shown on photograph AST-23-1945 (fig. 6), which was taken on July 21, 1975, with a 250-mm lens from an altitude of 226 km, with the camera axis near vertical, and at a Sun angle of 85°. Beach ridges mark former shorelines of the foreland and depict the successive stages of its growth. A large lagoon still exists between the oldest of the beach ridges and the mainland, and relatively smaller water bodies still remain in the depressions between the other major ridges (fig. 6). The former shorelines were probably formed as barrier islands during major storms, in which storm waves scoured bottom sediments under conditions of high storm tides. The barrier islands were built later by material carried westward by means of littoral drift; thus, the lagoon was enclosed behind the deposited sediment. A wide beach was also built in the embayment developed on the western side of the foreland.

The Rhône Delta is a cuspate delta (fig. 6). It covers a large part of the shore of the Gulf of Lions. To the southwest of the delta, a long stretch

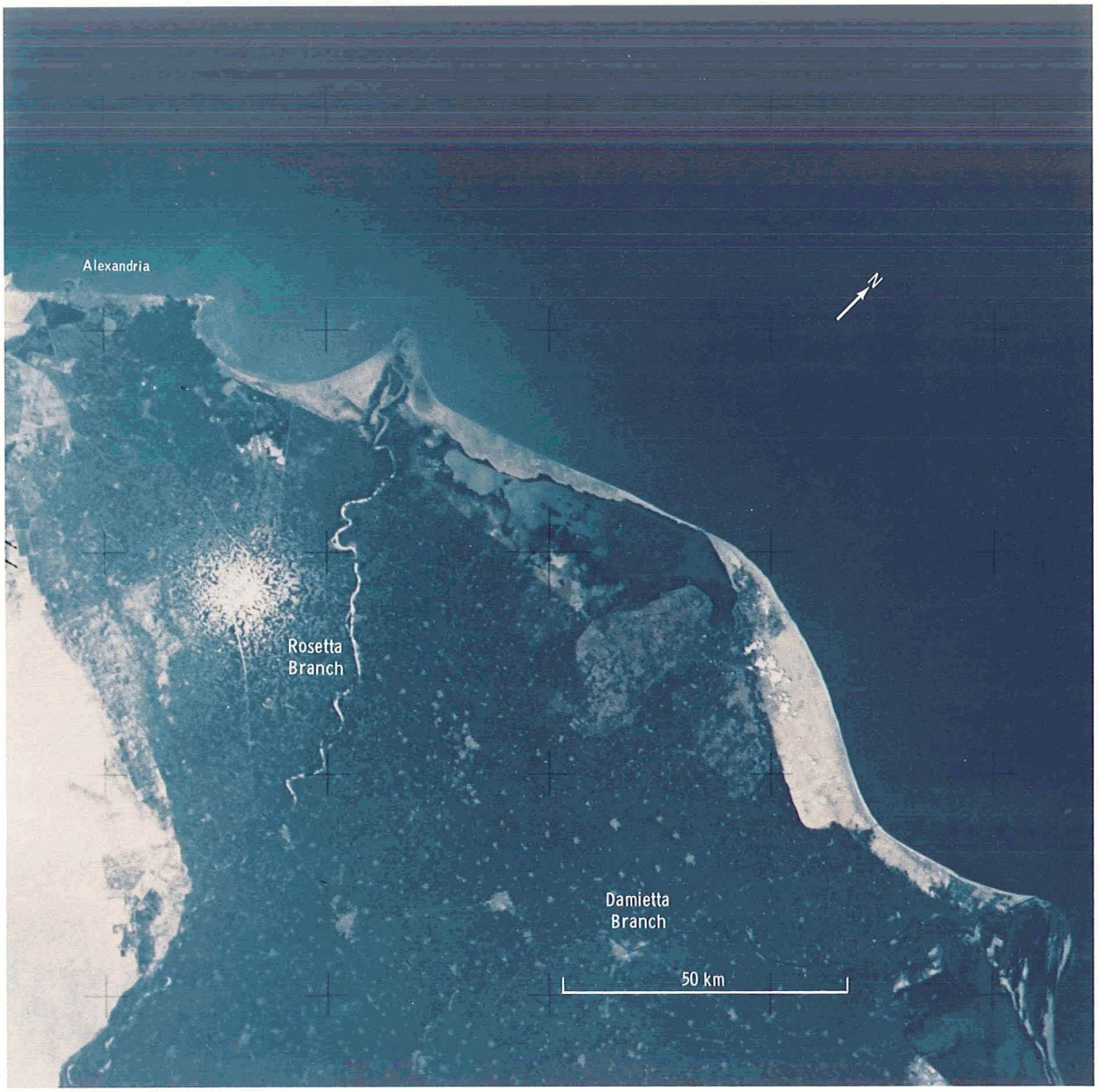


FIGURE 5.—Photograph of the Nile Delta, Egypt (AST-16-1258).

of sandy beaches of varying widths extends; to the east, the deltaic coast merges abruptly into a rocky coastline (ref. 9). The southwestern side of the delta clearly exhibits a recurved spit, which indicates a localized reversal in littoral current direction toward the apex of the delta. On the eastern side of the Gulf of Lions, there is clear indication of a copious discharge from the land. However, neither the source nor the chemical composition of this sediment can be verified at this time.

The foreland at Pointe de Beauduc is similar in general configuration to the foreland along the Nile Delta shoreline immediately east of the Damietta outlet at Râs el Barr (figs. 5 and 8). However, the foreland at Râs el Barr seems to have been formed by a series of recurved spits

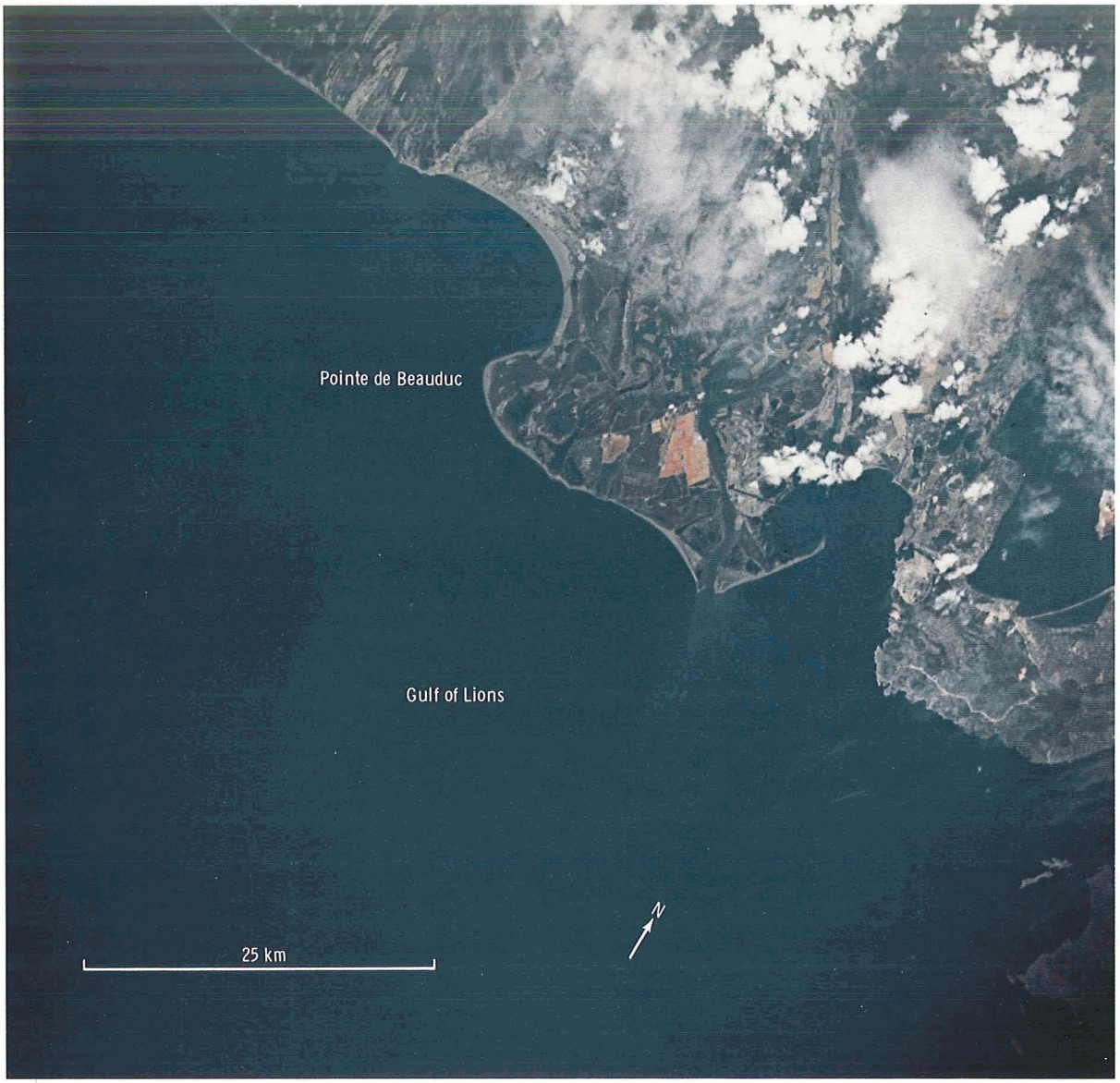


FIGURE 6.—Photograph of the Rhône Delta, Gulf of Lions, and Pointe de Beauduc, France (AST-23-1945).

built by fluvial sediment introduced in the nearshore zone by the Damietta outlet and carried eastward by longshore currents.

In the moderate wave energy environment of the Mediterranean Sea along the Nile Delta shores, sand contributed by the two branches of the Nile or eroded from the delta shore is built into beaches, spits or barriers enclosing lagoons along the delta margin, and forelands (figs. 5, 9, and 10). The map reproduced in figure 8 was taken from reference 10 and shows the major coastal locations described in the Nile Delta area.

The shoreline of the Nile Delta has undergone severe changes during the last 100 years. Erosion has occurred at several important locations along the coast: (1) El Gamil between Port Said and Râs el Barr, (2) Râs el Barr, (3) Burullus and Baltîm, (4) El Burg, (5) Rosetta, (6) Abu Qîr, and

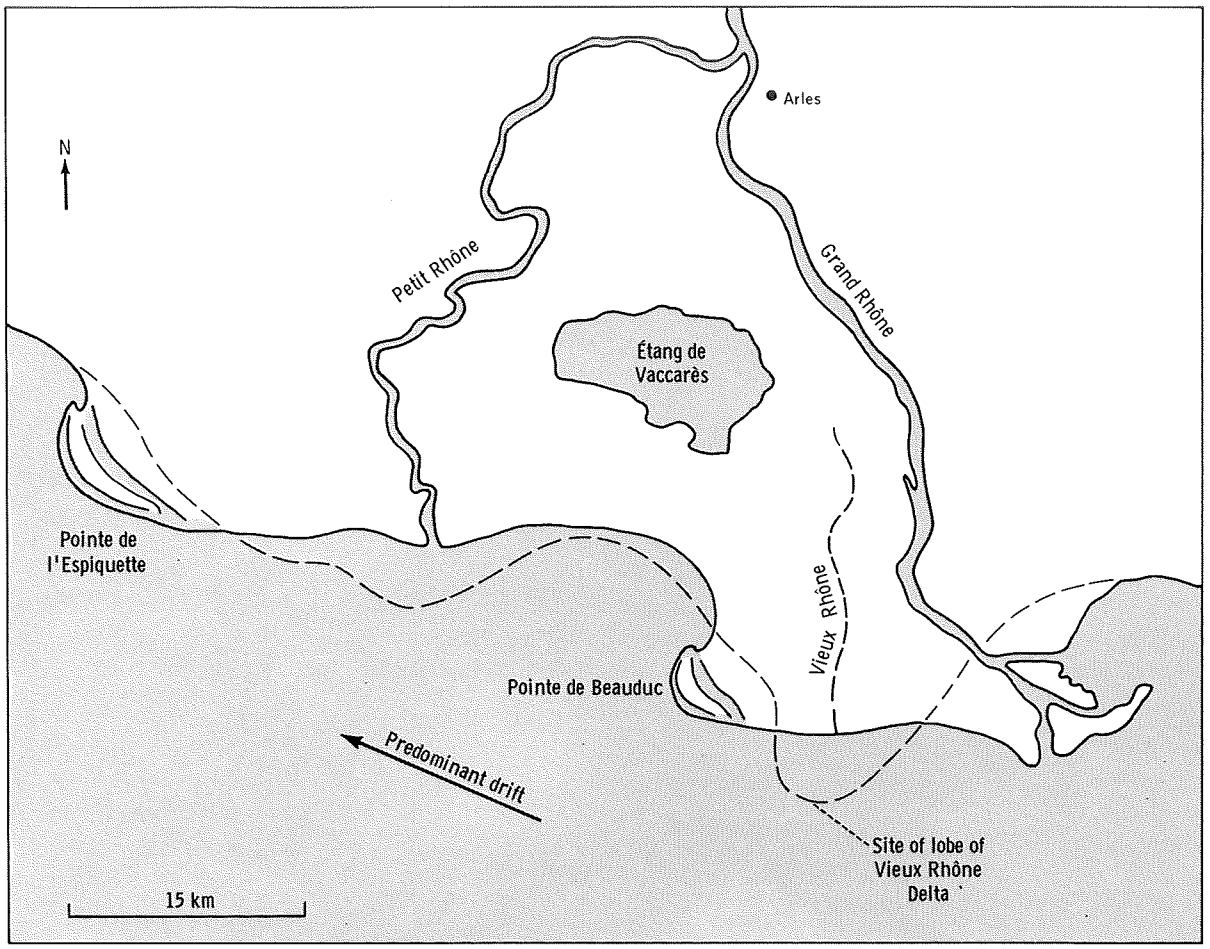


FIGURE 7.—Map of the Rhône Delta, France.

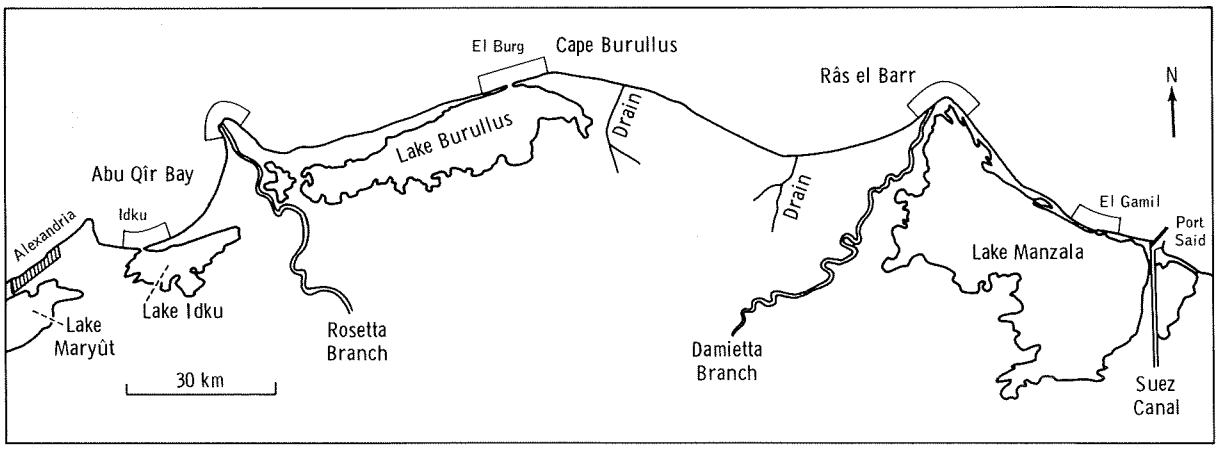


FIGURE 8.—Index map showing coastal locations described along the Nile Delta coastline, Egypt.

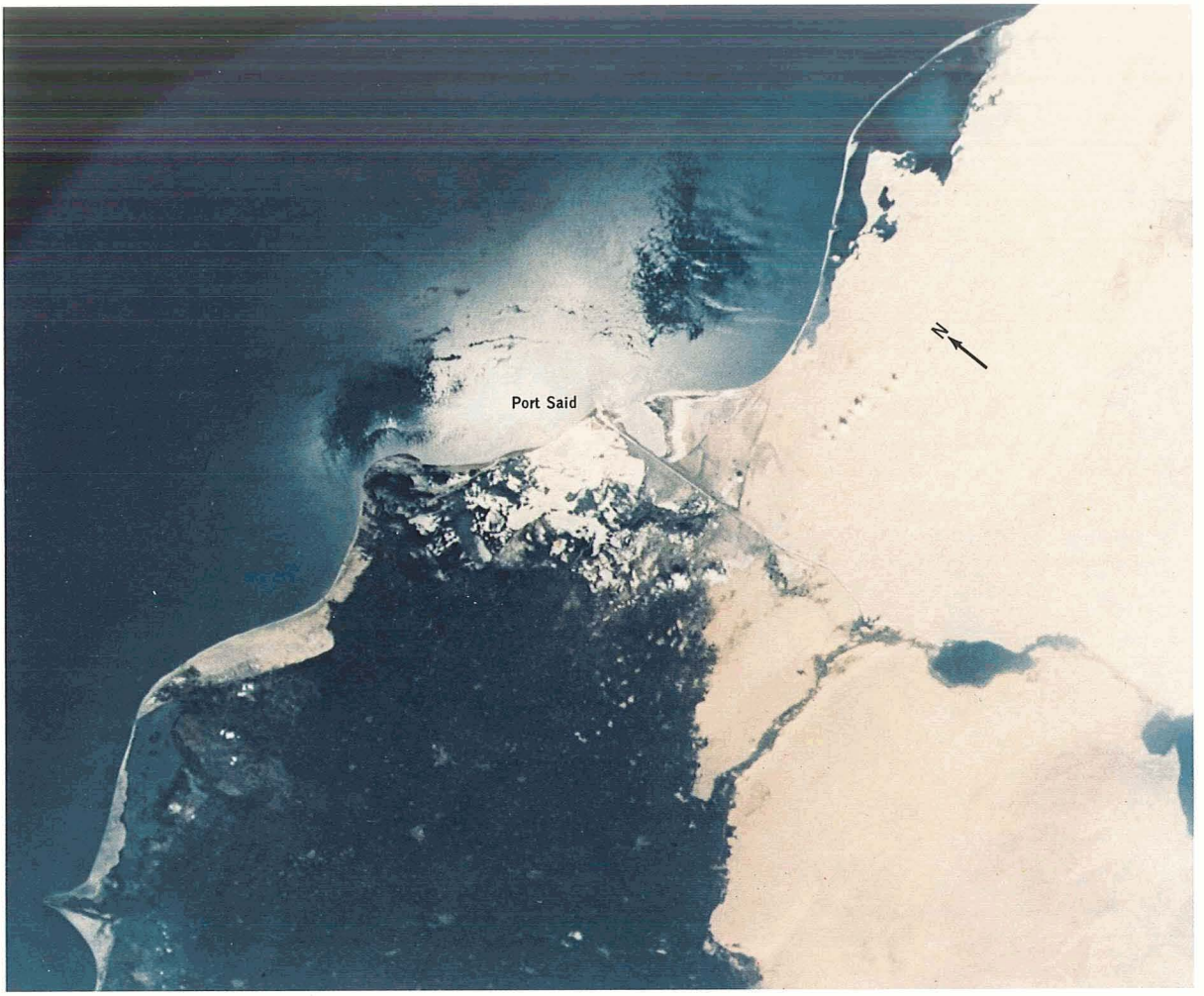


FIGURE 9.—Photograph of the eastern half of the Nile Delta showing the Suez Canal, Egypt (AST-9-558).

(7) Alexandria. At the same time, accretion is occurring near the entrance of the Suez Canal, in front of the Port Said breakwater (fig. 9), causing navigational problems and requiring dredging at great expense. It is well known that a delta shoreline continues to prograde as long as the rate of supply of sediment, mainly from the river, exceeds the rate of removal by waves and currents. In the case of the Nile Delta, the process of reservoir development on the Nile (for example, the Delta Barrages completed in 1881 and the Aswân Dam completed in 1902) has gradually decreased the sediment load brought by the river to the delta. In addition, the construction of the high dam at Aswân (completed in 1968) has brought the Nile in Egypt under full control and has reduced the outflow and sediment load of the river to insignificant quantities (ref. 11). This has resulted in severe erosion problems along the Nile Delta shoreline, where the current rate of retreat has been reported by Kassas (ref. 11) to be several meters per year.

El Burg, near the Lake Burullus outlet (figs. 5 and 8), is one of the most exposed locations of all the delta. The shoreline is straight for a long distance and is oriented obliquely to the prevailing wave direction. In addition, the slope of the nearshore zone is relatively steep (ref. 10) and thus allows the waves to reach the shore without being completely transformed or their energy dis-

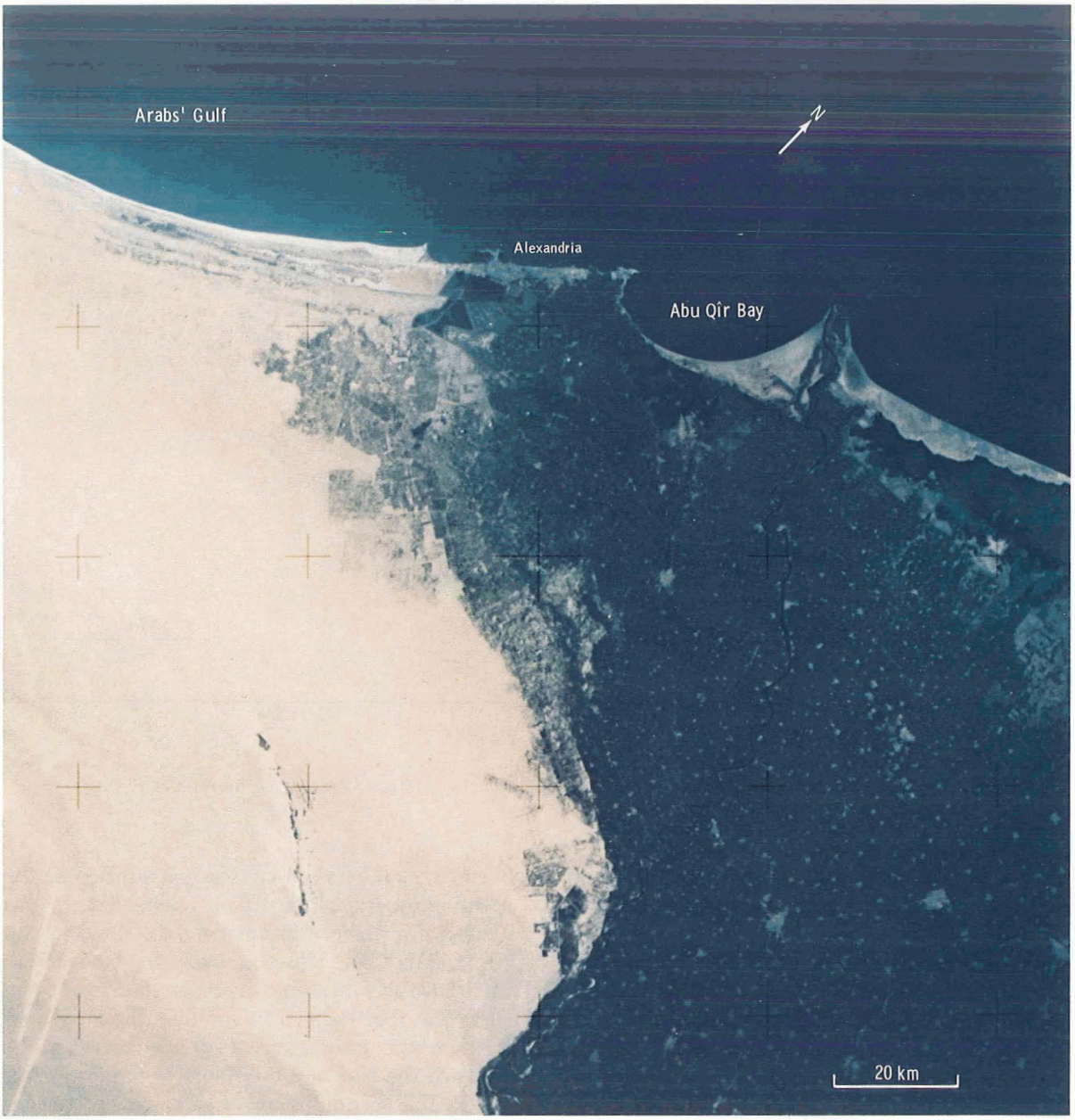


FIGURE 10.—Photograph of the western half of the Nile Delta showing Abu Qîr Bay, Alexandria, and ancient shorelines of Arabs' Gulf, Egypt (AST-16-1257).

sipated. Accordingly, beach erosion has occurred along this section for a long time and some serious property damage has been incurred.

In addition to the serious beach erosion at El Burg, the fate of the sandbar or sandspit that separates Lake Burullus from the sea is a matter for concern in view of its continuous retreat landward. Examination of the ASTP photograph (fig. 5) reveals that the features on the western two-thirds of the bar near the Rosetta outlet have been produced by a process of washover whereby materials eroded by waves from the sea side are

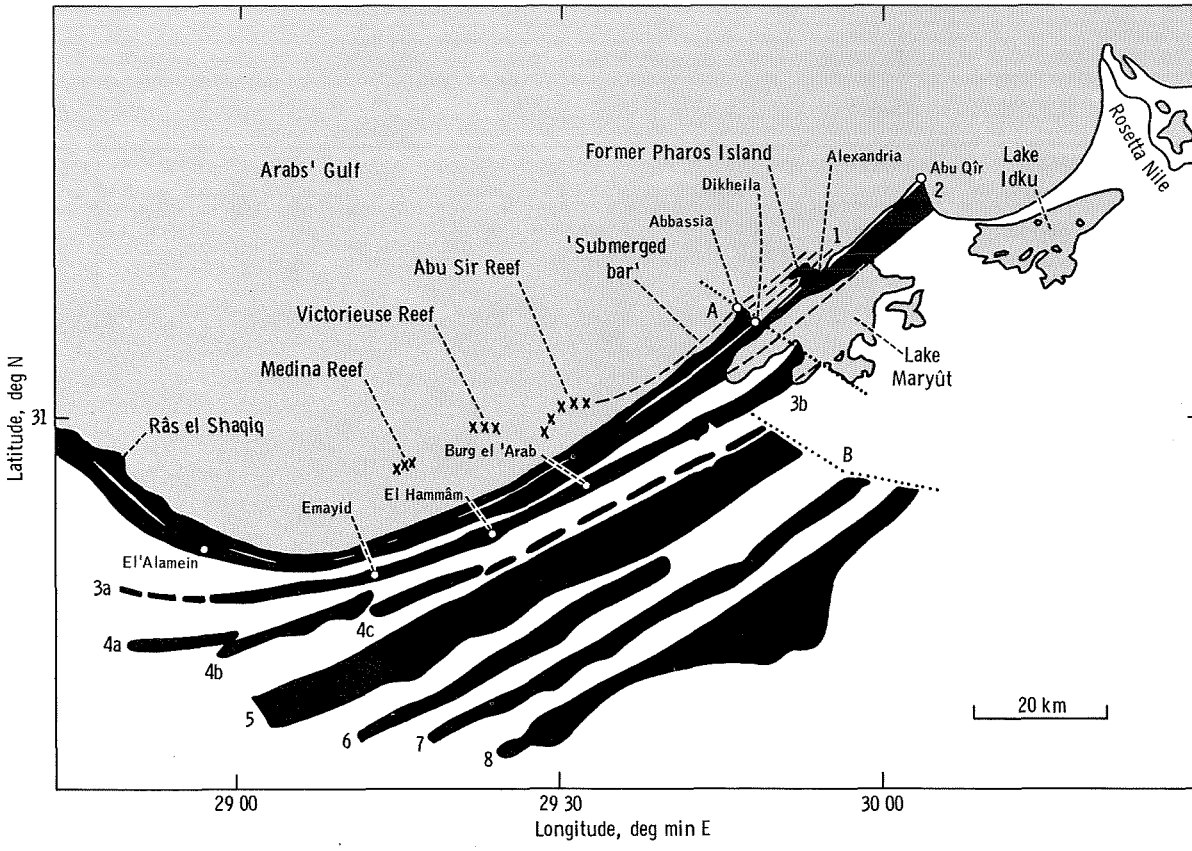


FIGURE 11.—Outline map of the Pleistocene bars and lagoons of Arabs' Gulf west of Alexandria, Egypt.

washed over the bar and deposited on the lagoon side. Such a process, if continued, will result in the eventual merger of the bar with the southern shore of the lake. On the other hand, the eastern end of the bar near the Lake Burullus outlet is very narrow and, eventually, storm waves may succeed in opening new inlets across low areas at that end. However, in view of the fact that Lake Burullus is quite shallow, new inlets might not remain open for any considerable length of time.

A very interesting feature that shows clearly on the ASTP photograph (fig. 10) is the sequence of ancient shorelines along the Arabs' Gulf west of Alexandria. These features represent fossil offshore bars and lagoons. Butzer (ref. 12), through detailed field work, identified and mapped eight such bars (fig. 11) corresponding to at least eight transgressions above modern mean sea level during the Pleistocene epoch. At least five of Butzer's eight bars can be clearly identified on the ASTP photograph (fig. 10): 1, coastal bar; 2, Abu Sir bar; 3a, Gebel Maryût bar; 3b, Sanakra and Habbub bar; 4a, Ruweisat bar; 4b, Gebel Bein Gabir bar; 4c, Khashm el Eish bar; and 5, 'Alam el Halfa bar. (See fig. 11.) In addition, the tonal contrast on the photograph (fig. 10) between the crests of the bars and the floors of the lagoons is due to the accumulation of salts on the former lagoon floors by evaporation. This salt deposit produces very light tones in contrast to the darker tones attributable to vegetative cover on the former offshore bars. Such vegetative cover seems to decrease with distance from the shore because of a decrease in available moisture and may explain the inability to identify the rest of the bars on the photograph since the tonal contrast between the sand of the bars without substantial vegetative cover and that of the surrounding

desert sand will be negligible from an orbital altitude.

SUMMARY AND CONCLUSIONS

The three examples of the use of ASTP photography in coastal studies have demonstrated that valuable information regarding the coastal zone can be obtained from such photography. The major advantage of these photographs over conventional aerial photographs is that the area of the land or water surface covered in a single exposure is many times larger, which helps in studying and mapping large regional features and their interrelationships. On the other hand, the ASTP photographs have the disadvantage of not showing the minute details that may appear on aerial photographs. This suggests that attempts should be made in future space missions to obtain high-resolution, color photographs for use in coastal studies. In the meantime, ASTP photographs when supplemented with aerial photographs can become an excellent tool in studying coastal features and their changes.

The three examples used in this study have demonstrated the various areas of application of ASTP photography in coastal studies. Shoreline features, including barrier islands, beach ridges, salt marshes, tidal inlets, tidal deltas, and river deltas, are portrayed clearly on the photographs. Detection of changes in shoreline configuration and identification of major areas of erosion or accretion were possible from such photography. Information regarding littoral drift direction was obtained from certain shoreline features such as recurved spits and offsets at coastal inlets as well as from sediment plumes discharged from river outlets and tidal inlets.

REFERENCES

1. El-Ashry, Mohamed T., ed.: Air Photography and Coastal Problems. Benchmark Papers in Geology, Vol. 38, Academic Press (New York), 1977.

2. Nichols, M. M.: Coastal Processes From Space Photography. Proc. Twelfth Coastal Engineering Conf., Vol. 2, American Society of Civil Engineers (New York), 1970, pp. 641-649.

3. Magoon, O. T.: Use of ERTS-1 in Coastal Studies. Proc. NASA/Goddard Space Flight Center ERTS-1 Symp., 1973, pp. 108-116.

4. El-Baz, Farouk; and Mitchell, D. A.: Earth Observations and Photography Experiment MA-136. Sec. 10 of Apollo-Soyuz Test Project Preliminary Science Report, NASA TM X-58173, 1976.

5. Shepard, F. P.; and Wanless, H. R.: Our Changing Coastlines. McGraw-Hill Book Co. (New York), 1971.

6. El-Ashry, M. T.: An Example of Coastal Studies From Space and Aerial Photographs. J. Geol. Educ., vol. 21, no. 2, 1973, pp. 75-78.

7. Jordan, G. F.: Erosion and Sedimentation, Eastern Chesapeake Bay at the Choptank River. U. S. Coast and Geodetic Survey Tech. Bull. 16, 1961.

8. Bird, E. C. F.: Coasts. An Introduction to Systematic Geomorphology, Vol. 4, The M.I.T. Press (Cambridge, Mass.), 1969.

9. Oomkens, Eppo: Depositional Sequences and Sand Distribution in the Postglacial Rhône Delta Complex. Deltaic Sedimentation—Modern and Ancient, J. P. Morgan, ed., Soc. of Economic Paleontologists and Mineralogists (Tulsa, Okla.), Spec. Pub. 15, 1970, pp. 198-212.

10. Zenkovitch, V. P.: Report and Some Recommendations on Nearshore Investigations and Protection of the Nile Delta Shores. UNESCO (Paris), 1964.

11. Kassas, M.: Impacts of River Control Schemes on the Shoreline of the Nile Delta. The Careless Technology—Ecology and International Development, M. T. Farvar and J. P. Milton, eds., Natural History Press (Garden City, N. Y.), 1972, pp. 179-188.

12. Butzer, Karl W.: On the Pleistocene Shore Lines of Arabs' Gulf, Egypt. J. Geol., vol. 68, no. 6, 1960, pp. 626-637.

South American River Morphology and Hydrology

R. K. Holz,[a] V. R. Baker,[a] S. M. Sutton, Jr.,[a] and M. M. Penteado-Orellana[b]

ABSTRACT

Color photographs taken over Brazil during the Apollo-Soyuz mission were studied in an analysis of South American river morphology and hydrology. The Amazon Basin was examined on five photographs that reveal a remarkable variation in the sizes and morphologies of various rivers. Three major river types were distinguished on the basis of sinuosity P and other properties.

1. The Rio Solimões (western Amazon River) has $P = 1.2$ to 1.5 and has developed a prominent flood plain (*varzea*) with scroll topography, abandoned meanders, and marginal lakes.

2. The Rio Japurá, like the Solimões, has Andean sources in its basin, resulting in a low sinuosity ($P = 1.1$) and a relatively high solid load.

3. The Rio Juruá drains only the tropical lowlands. Impoverished in its solid load, the Juruá has a tortuous pattern ($P > 2.5$).

Channel widths, meander wavelengths, and other variables were measured from space photographs of rivers in the Amazon Basin. Various empirical formulas were evaluated for estimating the hydrologic properties of these rivers.

The results indicate that the excellent empirical formulas derived from studies of humid-temperate and semiarid streams do not explain the regime behavior of these complex tropical rivers. The low-sinuosity Amazon Basin streams are much less dominated by relatively coarse-grained sediments than are streams of equivalent sinuosity described for semiarid regions. Discharge variability and bank stability (related to both vegetation and lithology) appear to be the dominant factors in accounting for channel pattern variations in the Amazon Basin.

The Paraguay River was photographed at three sites along its upper course; the sites occur within a large Quaternary alluvial plain known as the "Pantanal." The Pantanal is a sparsely settled complex of abandoned channels (*vazantes*), depressions (*baias*), abandoned levees (*cordilheiras*), and swamps. All these features were easily mapped from space imagery. The maps derived from these photographs distinguish perennially wet and frequently flooded bottomlands from seasonally flooded zones and from more rarely flooded zones. The zones are recognized by their distinctive landforms and by their characteristic vegetation assemblages. The Pantanal is flooded in February by the intense tropical precipitation in the northern headwaters of the Paraguay River. The slow return flow of water from the flooded swamplands to the river sustains the flow through the dry season. Remote sensing from space has obvious advantages for monitoring this highly dynamic hydrologic environment.

INTRODUCTION

Premission site selection for the Apollo-Soyuz Test Project (ASTP) orbital photography included the headwaters of the Rio Paraná in southwestern Brazil. This area was selected because of the planned large-scale river basin project that is similar to the Tennessee Valley Authority. The goal of the suggested study was to obtain information for (1) assessing land use, (2) determining the extent of present river basin development, and (3) mak-

[a]The University of Texas at Austin.

[b]Fundaçao Universidade de Brasília.

ing general estimates of population in the region. To accomplish this goal, extensive and systematic photographic coverage of the region was requested. Because of mission constraints and cloud cover, however, such systematic coverage was not produced. Consequently, emphasis was placed on general studies of stream regimes, including analyses of meander wavelengths, flood-plain development, and basin morphology, instead of land use. The areas photographed for this study are shown in figure 1.

Problems and Opportunities for Study

The measurements described in this report constitute a guide to the hydrologic properties of streams in the Amazon and Paraguay Basins. The measurements and other variables are incorporated into a hydrologic reconnaissance that includes the weathering characteristics of rocks exposed in the basins, vegetation types and density, climatic factors, and terrain variability. These factors were used to generate a hydrologic assessment of specific sites.

The photographs were analyzed for adjustments or changes in river morphology caused by altered water and sediment discharges and by Quaternary climatic changes. The authors believe the artificial straightening of rivers for navigation, flood control, hydroelectric developments, or other development purposes would induce severe downstream consequences by altering a presently stable hydraulic regime. Examination of river paleochannels, plainly visible on some photographs, offers some insight into problems associated with the practical application of river development.

In a number of ASTP photographs, clear-water marginal lakes can be observed along stream courses. Some of these lakes are abandoned meanders of the river. In other cases, the lakes appear to be *cienagas*, or places where overbank flow or tributary streamflow is trapped outside the stream course by the development of natural levees; some of these lakes cover large areas. The photographs indicate that these lakes are subject to large expansion and contraction; they pose a serious barrier to the development of settlements and land transportation. Their development is not completely understood, but they seem to provide a natural mechanism for flood-hazard management. Surplus water could be diverted to *cienagas* from stream channels during times of flood and then returned to the river during normal or low-water stages.

Finally, by use of the ASTP photographs, there is some potential for identifying critical river reaches where agricultural development or newly constructed roads and towns could markedly affect sediment yields carried into nearby rivers and thus induce a river metamorphosis that might not be desirable.

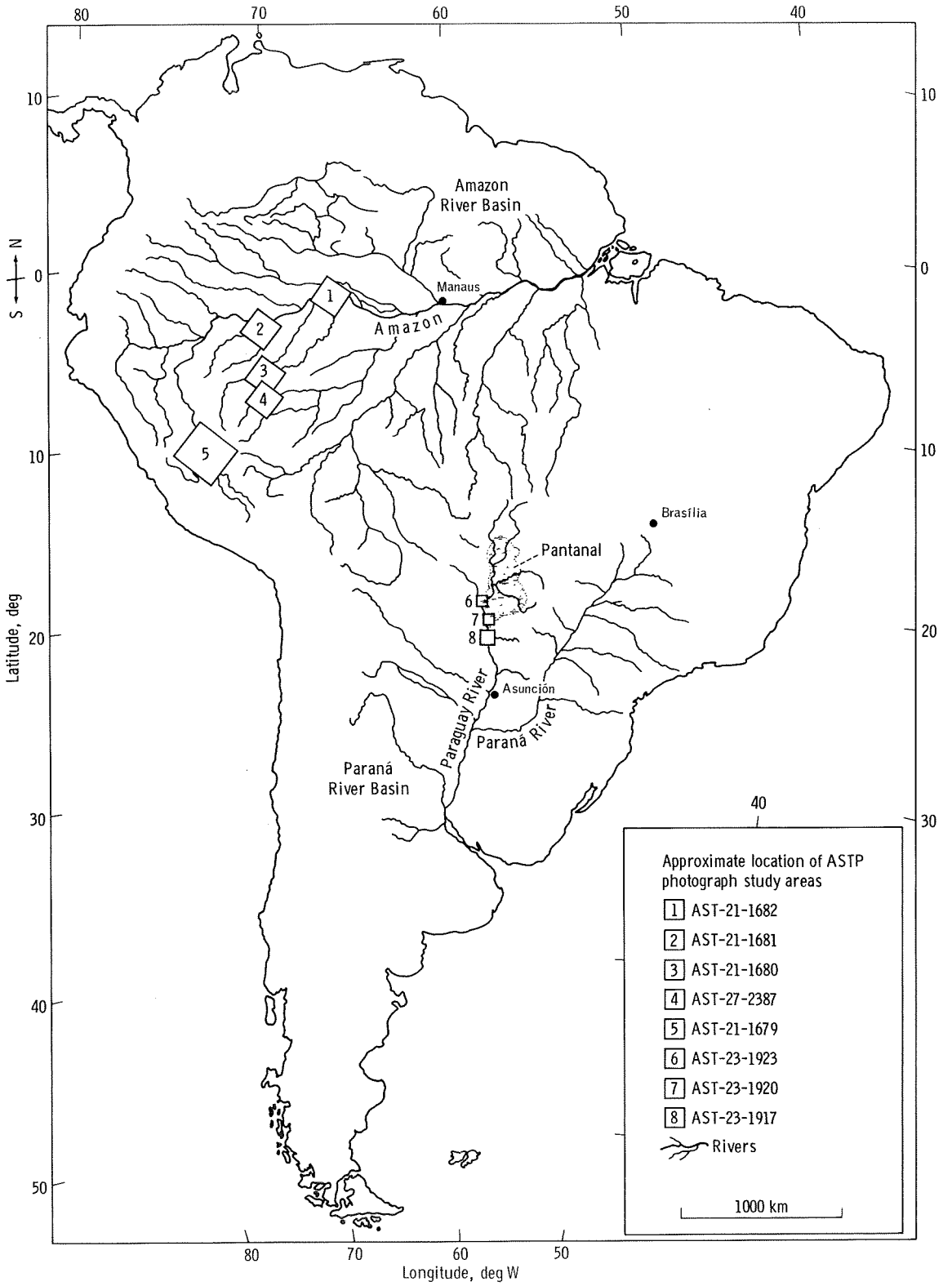
Rationale of Study

Baker et al. (ref. 1) have proved the feasibility of using space photographs for studying small-basin drainage networks. The study reported here expands this research to larger streams and into a different environment. Also, a more regional approach is adopted that involves studying selected stream segments covered by the photographs with emphasis on suggesting areas critical for development.

Space photographs of the rain-forest environment of northwestern Brazil contain little information for a photointerpreter other than the continuous tone of forest, broken only by streams, lakes, and slight changes in the vegetation pattern as a result of differences in flood-plain morphology and modest activity by man. Photographs of the Pantanal region in southwestern Brazil are more varied and offer more possibilities, but the hydrographic phenomena are still the dominant features for interpretation.

The development of these sparsely settled, relatively unknown areas should be preceded by detailed, systematic studies using remote-sensing techniques. Basin size, drainage network density, flood-plain width and general morphology, meander wavelength, relative sediment load, general stream conditions, vegetation, and land use are all interpretable and in some cases

FIGURE 1.—The location of study sites.


Amazon
River Basin
Manaus
Amazon
Brasília
Pantanal
Asunción
Paraguay River
Paraná River
Paraná
River Basin
Approximate location of ASTP
photograph study areas
1 AST-21-1682
2 AST-21-1681
3 AST-21-1680
4 AST-27-2387
5 AST-21-1679
6 AST-23-1923
7 AST-23-1920
8 AST-23-1917
Rivers
1000 km
Latitude, deg
Longitude, deg W
S
N

measurable from remotely sensed imagery. As a group, these variables describe the river regime at any instant in time. Recording them provides a benchmark for measuring change and permits predictions concerning the problems associated with development and land use change.

PURPOSE

The general purpose of this research is to examine ASTP photographs of Brazil to extract from them broad patterns of stream morphology and land use. More specifically, the intent is to evaluate present landscapes in regard to development and to assess the usefulness of color orbital photography for such landscape evaluations.

Evaluation of Prior and Present Landscapes

Without detailed onsite field investigations, it is difficult to evaluate existing landscapes from space photographs alone. Eastern Brazil from Pôrto Alegre in northern Rio Grande do Sul to the flood plain of the Amazon near Fortaleza in Ceará is a very old, stable landmass of predominantly hard crystalline rock. It is part of the so-called Amazonian Shield. Much of the rock of this shield is of Precambrian age (more than 570 million years old) with some mildly disturbed sedimentary and volcanic rocks. This landmass is highest in the east with a steep escarpment facing eastward along the Atlantic coast and a more gentle dip slope toward the west. Drainage from the shield is northward and westward into the lowland of the Amazon Basin and southward and westward into the Rio Paraná Basin and the Paraguay River Basin.

To the west of these basins, outside the national territory of Brazil, are the Andes Mountains. These mountains are much higher, younger, and less stable than are the highlands of eastern Brazil. Generally, the Andes are thought to be of late Mesozoic or early Cenozoic age, or approximately 60 to 65 million years old. Drainage from the humid, east-facing slopes of the Andes is into the Amazon Basin or, farther to the south (south of the Mato Grosso region of Brazil and Bolivia), into the Paraguay River Basin.

These two interior lowland basins are separated by the Mato Grosso, and both receive runoff from the contrasting highlands to the east and west. Through the years, streams discharging into the basins have built up successive, thick layers of sediments washed down from the surrounding highlands. These existing alluvial-basin landscapes constitute the sites for this study.

The Value of Color Orbital Photography

Much has been written about the value of color versus black-and-white photographs for the purposes of photointerpretation. A review of this literature, plus discussion with currently active photointerpreters and the authors' own earlier work, suggests that probably any signature appearing on a color photograph would also appear on a simultaneously generated black-and-white photograph. However, because the human eye can distinguish hundreds of subtle color tonal contrasts but only a few (9 to 12) gray-scale values, most interpreters agree that it is easier to extract data from color photographs than from black-and-white photographs. It is doubtful whether some of the clear-water meander lakes, *cienagas*, or smaller streams discussed in this paper would have been detected on black-and-white photographs. The value, or amount, of light reflected by these water bodies is quite low, and because the signature of such water bodies is very similar to the signature of surrounding forests, it probably would have been overlooked by an interpreter of black-and-white photographs. On a color photograph, the small lakes and streams are (barely) discernible from the surrounding forest.

The ASTP color photographs also provide the subtle tonal contrasts necessary to distinguish flood-plain limits, abandoned stream channels, minor changes in land use and vegetation, settlements, and other features that are important to this study. In general, the authors feel that many of the details on the maps that follow in this study would have been overlooked if color photographs had not been available.

SITE CHARACTERISTICS

The regions selected for study were the western Amazon River Basin and the upper Paraguay River Basin (the Pantanal). The general characteristics of the natural environment given in tables I and II, respectively, provide background information for photointerpretation. Rainfall and temperature data for two selected stations in the Amazon Basin are given in table III.

RIVERS OF THE AMAZON BASIN

The ASTP photographs of the Amazon Basin reveal rivers that are distinguishable by their size and morphology. These rivers have been classified by Gibbs (ref. 2) according to the environment of their drainage basins. They can also be classified according to sedimentological data gathered by Gibbs (ref. 2). Characteristics of the photographed rivers are summarized in tables IV

TABLE I.—General Characteristics of Amazon Basin

Characteristic	*Description*
	General
Drainage area	6×10^{12} m^2 (2.3×10^6 s. mi^2)
Slope	<0.1 m/km (0.5 ft/s. mi.) (easterly)
Basin width	Widest near Andes; narrows to 160 km (100 s. mi.) between Guianan Shield and Amazonian (Brazilian) Shield; widens again east of Rio Xingu junction into broad, low plain at mouth of Amazon River
	Climate
Type	Equatorial; characterized by heavy rains produced from penetration of warm, humid Atlantic Ocean air through Intertropical Convergence Zone
Midbasin temperature	
Average	300 K (27.2° C)
Deviation	1.7 K (1.7° C)
Rainfall	>200 cm (80 in.) in highland and coastal areas; wettest January to June; characterized by violent showers that compact or erode exposed soils and produce local flooding
	Geology and Physiography
General	Basin receives runoff from older highlands to north, east, and south and from younger mountains to west; surface composed of intermixed layers of unconsolidated gravel, sand, clay, and silt; few older rock outcrops
Sediments	Cambrian, Silurian, Devonian, Carboniferous, and Cenozoic; thickest (>460 m (>1500 ft)) Devonian; evidence of intrusion by Recent diabase dikes
Streams	Wide variation in type and quantity of sediments carried; downstream from Rio Negro, Amazon flood plain 80 to 95 km (50 to 60 s. mi.) wide, bordered by steep valley bluffs 45 to 60 m (150 to 200 ft) high; main channel characterized by meander scars, oxbow lakes, levees, and back swamps and by very low gradient (< 3 cm/km (< 2 in/s. mi.)) from midbasin to mouth

TABLE I.—Concluded

Characteristic	*Description*
	Land Use
Historical	Confined primarily to stream courses because of water access; large-scale agriculture generally not successful because concentration of crops composed of single plant type results in insect infestations and plant diseases, and clearing results in soil infertility; rubber, banana, cacao, and date and oil palm crops have been attempted commercially, generally without success, although native rubber trees were exploited successfully from the 1850's to 1900
Recommended	Best use of basin lands probably extensive, selective gathering of forest products
	Vegetation and Soils
Vegetation	Largest existing area of tropical rain forest (*selva*); forest dominant; in some highlands, forest replaced by grassy savanna with scattered trees reaching to edge of flood plain; flood plain has grassy openings, usually marshy areas where coarse grass (wet savanna) replaces forest; some area cleared for cultivation or settlement; *selva* composed of very tall (38 to 45 m (125 to 150 ft)) trees representing many species; dense canopy blocks out sunlight and prevents plant growth on forest floor; lack of pure stands and accessibility makes systematic harvesting difficult
Soils	Not generally fertile, especially for agriculture; most nutrients held in existing vegetation; soil nutrients leached periodically by heavy rainfall, which leaves only coarse, insoluble, and generally infertile iron and aluminum compounds at surface; thin organic layer at surface replenished constantly by falling leaves, twigs, and other plant matter when protected by forest canopy; most fertile soils occur on flood plains, but frequent and sustained flooding makes use difficult

and V. Although these rivers are typical of the rivers in the Amazon Basin, they do not encompass the full range of river characteristics found in this region.

Rio Solimões (Amazon River)

The main course of the Amazon River is given various names in different countries and along various parts of its course. In North America, the entire stream is known as the Amazon, but the Peruvians call it the Rio Marañón. From the border with Peru to the Rio Negro, the Brazilians refer to it as the Rio Solimões. From that point downstream to its mouth, it is known as the Rio Amazonas. The Amazon has the largest volume of flow of the world's rivers. It averages approximately 215 000 m^3/sec (3.4×10^9 gal/min), or about 10 to 11 percent of all the freshwater runoff from the continents (ref. 3). The Amazon has not built a delta into the Atlantic, but its yellowish, silt-filled waters can be identified as far as 322 km (200 s. mi.) from shore.

Headwaters

The headwaters of the Solimões River reach high into the Andes Mountains (fig. 2). The Amazon River in Peru begins with the confluence of the Ucayali and Marañón Rivers, which have mountainous environments (ref. 2). Four other major tributaries of the Solimões River head in mountainous regions but flow through significant, tropical lowland reaches before discharging into the Solimões River. These mixed mountainous- to tropical-environment rivers are the Napo, Içá,

TABLE II.—General Characteristics of Pantanal Basin

Characteristic	*Description*
	General
Location	In southern Mato Grosso; upper basin of Paraguay River, along the western border of Brazil adjacent to Paraguay and Bolivia
Status	Wet, swampy lowland covered by savanna with scattered palm trees; entire area can be flooded by high water; very complex in geologic history, soils development, climate, vegetation, and drainage patterns; ineffectively developed, sparsely populated frontier
	Climate
Type	Tropical; characterized by year-round hot temperatures with a well-developed dry season
Northern; tropical monsoon forest	
General	Transitional climate; rainy season from October to April; rainfall associated with convection-cell development in equatorial airmasses over Amazon Basin; dry season results from domination of equatorial Atlantic airmasses bringing stable, warm weather conditions; sometimes broken by tongue of dry, cold polar air (polar outburst) penetrating, characterized by reduced humidity, clearing, and strong southerly winds; polar outbursts may bring heavy rains along zone of contact between airmasses
Temperature	
Mean	297 K (24° C)
Deviation	5 K (5° C)
Mean rainfall	200 cm (78.7 in.)
Southern; tropical savanna	
General	Characterized by an accentuated dry season in winter; more than 80 percent of precipitation occurs during spring and summer; hottest month October
Temperature	
Mean	300 K (26.7° C)
Highest recorded	316 K (42.8° C)
Rainfall for driest month	6 cm (2.4 in.)
	Geology and Physiography
Geologic history	
General	Basin originated as subsiding tectonic valley created upstream by fault lines developed perpendicular to Paraguay River's main direction of flow; subsidence of middle and upper portion of valley resulted in deposition of huge alluvial plain during Pleistocene and Holocene and still occurring; during middle Tertiary, very low base level, which controlled drainage evolution of the Pantanal, was established in the center of the basin; Rio Paraná was captured by Paraguay River in the Posadas region of Paraguay; current basin subsidence is indicated

TABLE II.—Continued

Characteristic	*Description*
	Geology and Physiography
Pantanal Formation	Quaternary formation consisting of sandy-clayish material overlying conglomerate cemented by limonite; evidence of block faulting seen; in southern basin, relief created by old tectonic depression and uplift (graben faults) reactivated during Tertiary that affected Paraguay Basin morphology and drainage network; basin is subsequent to faulting and follows meridian (north-south) vector of main fault lines lying between Andes and basaltic scarp of Paraná Basin
Physiography	
General	Pleistocene sediments are fluvial and lacustrine and are composed of limes and clays with top layer of water-worked sands; deposits average ≈80 m (262 ft) thick and were transported mostly by tributary streams draining from Brazilian highlands; metamorphic basement rock and overlying sediment outcrops (mostly sandstone, siltstone, quartzite, shales, limestone, granite, and mica schist), belonging to several formations dating from the Precambrian and Lower Silurian, occur around edge of basin, to the east, west, and north
Paraná Basin (east of the Pantanal)	Nearly separate Paleozoic-Mesozoic basin essentially represented by units of cross-bedded red sandstone, conglomerate, siltstone, shale, coarse-grained sandstone, and basalt lava flows that constitute past and present source of Rio Paraguay sediments; beds dip eastward 10° to 15°; homoclinal structure (plus difference in bed resistance) results in differential erosion (especially since post-Cretaceous times) and creates geomorphic series of steps and cuesta landforms with escarpments facing westward toward main course of Paraguay River; escarpments and gentle slopes descend from 800 m (2625 ft) to 300 m (984 ft) from east to west and terminate in the "Pantanal edge"; from plateau cliffs, streams that have established obsequent drainage (e.g., Rios Itiquira, Taquari, Coxim, Jauru, Negro, Negrinho, Taboco, and Apa) flow as tributaries to Paraguay River left bank; because of steep gradient profiles, erosion is extensive and silt and sand load of rivers is large
West of the Pantanal	Rock outcrops in Bolivia and Paraguay represented by metamorphic basement of Precambrian age; sediment from these formations insignificant because west side of basin is dry and has poorly organized drainage system
	Vegetation and Soils
Vegetation	
Equatorial forest (*hileia*)	Humid, dense evergreen forest, stratified with great variety of trees
Transitional (equatorial semi-deciduous forest)	Characterized by variety of small (15 to 20 m) trees that lose their leaves during dry season; crown cover not dense
Tropical forest (*mata galeria*)	Generally associated with hot, wet summers and dry winters; found in more humid valleys; trees 15 to 30 m (50 to 100 ft) tall

TABLE II.—Concluded

Characteristics	*Description*
	Vegetation and Soils
Cerrado	Surrounds Paraguay Basin at elevations of 100 to 1000 m (328 to 3280 ft); covers about one-half of the Mato Grosso; characterized by small, widely spaced trees trending to open grassland; grass dries to loose straw mat during dry season; dominant processes of hillslope development are sheet flood, rill erosion, and rain wash
Stunted forest	Consists of gnarled, xerophytic trees 8 to 12 m (26 to 39 ft) tall and widely spaced
Dense to open brushland	Consists of 2- to 3-m (6.6 to 9.8 ft) tall trees and small shrubs widely spaced
Grassland meadow (*campos limpos*)	Consists of brush, grass, and herbaceous cover; has appearance of steppe grassland where brush is absent
Pantanal complex (*complesco do Pantanal*)	A floristic subregion of the Chaco complex vegetation of Mato Grosso swamplands; found in main valley lowlands at elevations of 100 to 110 m (328 to 361 ft); appearance changes with lithologic and topographic location; represents a continuation of the Bolivian and Paraguayan Chaco vegetation; predominant feature is *campos limpos*; also associated with acid soils developed on lime-clay, sand-free deposits
Soils	Soils on uplands developed from sediments eroded from surrounding highlands, in which five principal soil groups are recognized; two main soil types are recognized in the lowlands; the main difference between the two is attributed to different drainage characteristics; soils in upper Pantanal Basin generally not well developed; new alluvium deposited and reworked by runoff continues the soil-forming processes
	Land Use
Status	Isolated; sparsely settled; has few towns, roads, or other developments; heavy seasonal rainfall, general geologic structure, and low stream gradient produce seasonal flooding on vast scale; some areas remain swampy throughout year; poor drainage, variability of flood levels, and unhealthy conditions discourage settlement; large cattle ranches abound; low-productivity farming, designed to meet local needs, tends to be more subsistent than commercial; people and economy generally self-sufficient
Attitude of territorial claimants	
Brazil	Area cut off by Rio Paraná and rugged cuesta topography on eastern edge
Bolivia	Hot, tropical lowland not desirable in contrast to cool mountain environment; access possible only after difficult passage across high Andes
Paraguay	Located too far north for easy land access; erratic flow of Rio Paraguay discourages water access
Possibilities	Multinational development project needed to bring Pantanal effectively into national milieu of three controlling nations; series of dams could control flooding, produce hydroelectric power, and provide storage of surplus water for use during dry season

Japurá, and Madeira Rivers (ref. 2). Although they comprise only 12 percent of the total Amazon Basin area, the mountainous headwater regions of the Solimões River contribute 82 percent of the total suspended sediment and 85 percent of the total dissolved sediment carried by the Solimões River at its mouth (ref. 2).

During the ASTP mission, the Ucayali River was photographed where it originates at the confluence of the Tambo and Urubamba Rivers in Peru (photograph AST-21-1679, fig. 3(a)). This photograph illustrates the mountainous environment. The Tambo and Urubamba Rivers have low to moderately sinuous channels. The Urubamba River contains several vegetated islands and many nonvegetated channel deposits. These deposits are not associated with point bars. Approximately 130 km (81 s. mi.) of the upper Ucayali River is apparent on this photograph. Within this reach, over several tens of kilometers, the channel pattern changes drastically. For about the first 50 km (31 s. mi.), the pattern of the Ucayali River is a complex of anastomosing channels, meanders, elongate and irregularly shaped vegetated islands, and abundant nonvegetated channel deposits. Downstream, the channel becomes broadly meandering. With the exception of one large island, islands are less prominent. Nonvegetated channel deposits are less abundant and occur primarily as point bars. No major tributaries enter the Ucayali River in this reach. The

FIGURE 2.—The Amazon Basin and study sites. →

TABLE III.—Climatic Data for Selected Stations in the Amazon Basin

Month	*Manaus (interior)*[a]		*Belém (coastal)*[b]	
	Rainfall, cm	*Temperature, K (°C)*	*Rainfall, cm*	*Temperature, K (°C)*
January	23.4	299.8 (26.6)	19.3	298.8 (25.6)
February	22.9	299.9 (26.7)	33.8	298.4 (25.2)
March	24.4	299.7 (26.5)	43.2	298.6 (25.4)
April	21.6	299.8 (26.6)	45.2	298.8 (25.6)
May	17.8	299.9 (26.7)	30	299.2 (26.0)
June	9.1	299.9 (26.7)	23.1	299.2 (26.0)
July	5.6	300.2 (27.0)	5.8	299.1 (25.9)
August	3.6	300.8 (27.6)	7.1	299.2 (26.0)
September	5.1	301.4 (28.2)	1.5	299.2 (26.0)
October	10.4	301.4 (28.2)	1.3	299.6 (26.4)
November	14	301.4 (28.2)	1.5	299.8 (26.6)
December	19.6	300.2 (27.0)	6.6	299.5 (26.3)
Total	177.5	—	218.4	—
Average	14.8	300.4 (27.2)	18.2	299.1 (25.9)

[a]Elevation, 45 m.

[b]Elevation, 10 m.

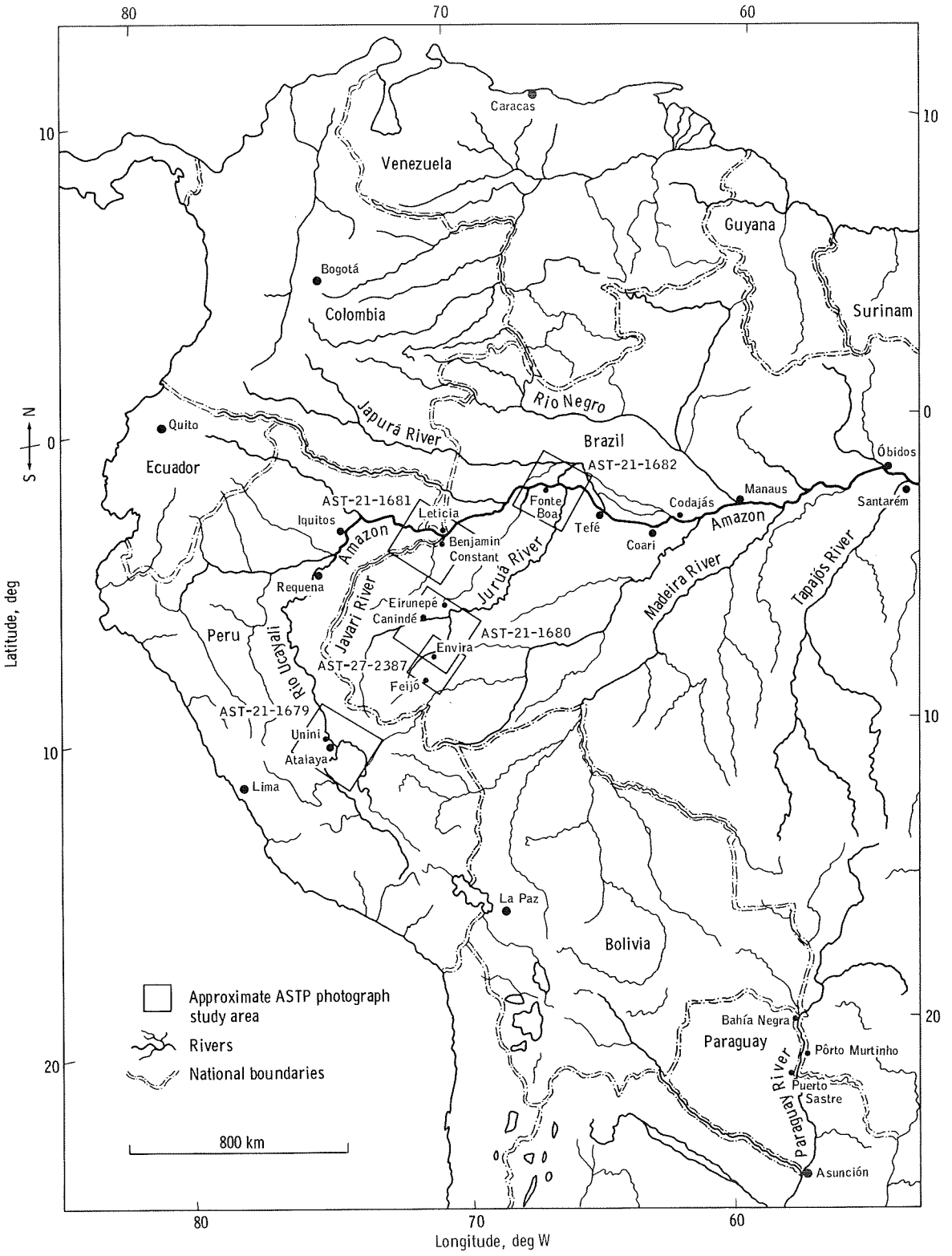

80
70
60
10
0
20
Caracas
Venezuela
Guyana
Surinam
Bogotá
Colombia
Rio Negro
Japurá River
Brazil
Quito
Ecuador
Óbidos
AST-21-1682
AST-21-1681
Fonte Boa
Manaus
Santarém
Iquitos
Leticia
Tefé
Codajás
Amazon
Benjamin Constant
Coari
Juruá River
Requena
Madeira River
Tapajós River
Eirunepé
Canindé
Javari River
Peru
Rio Ucayali
AST-21-1680
Envira
AST-27-2387
Feijó
AST-21-1679
Uniní
Atalaya
Lima
La Paz
Bolivia
Bahía Negra
Paraguay
Pôrto Murtinho
Puerto Sastre
Paraguay River
Asunción
Approximate ASTP photograph study area
Rivers
National boundaries
800 km
Latitude, deg
Longitude, deg W
S
N

TABLE IV.—Regional Drainage Characteristics for Amazon Basin Rivers

River and location	*Photograph*	*Basin environment (a)*	*Basin area, km² (a)*	*Discharge, m³/yr (a)*	*Channel morphology*
Ucayali near Rio Tambo	AST-21-1679	Mountainous	406×10^3	0.301×10^{12}	Braided to moderately sinuous
Solimões (Amazon) near Leticia	AST-21-1681	Primarily mountainous	1041	.905	Low-sinuosity, anastomosing channel with prominent elongate to lenticular, vegetated islands
Solimões (Amazon) near Fonte Boa	AST-21-1682	Mixed tropical and mountainous	1263	1.161	Moderate-sinuosity, anastomosing channel with prominent elongate to lenticular, vegetated islands; meanders typically simple
Javari near Benjamin Constant	AST-21-1681	Tropical	106	.116	Moderate-sinuosity channel; many meander forms compound
Japurá near Japurá	AST-21-1682	Mixed tropical and mountainous	289	.351	Low-sinuosity channel with elongate islands; less anastomosing than Rio Solimões
Juruá near Eirunepé	AST-21-1680	Tropical	—	—	Moderate to tortuous sinuosity; meander forms typically compound
Juruá near Rio Solimões	AST-21-1682	Tropical	217	.197	Moderate to tortuous sinuosity; meander forms typically compound
Amazon at mouth	None	Mixed	6300	5.5	Not established from space photographs

[a]From Gibbs (ref. 2).

change in channel pattern of the Ucayali River is probably governed by changes in channel and valley slope and by sediment sorting along the channel.

A change in flood-plain character accompanies the change in channel pattern of the Ucayali River (fig. 3(b)). Where the channel pattern is complex, the flood plain is not clearly developed. It is marked by no distinctive morphology and can be discerned on the photograph only through subtle changes in the color of vegetation. Where the channel begins to meander, the flood plain is well developed. Abandoned meanders are preserved adjacent to the river, and the general tone of

vegetation on the flood plain is distinctly lighter than that of surrounding forest. Photograph AST-21-1679 (fig. 3(a)) shows numerous minor tributaries to the Ucayali River. Those that descend from the highlands to the west tend to be relatively closely spaced and have low-sinuosity channels. The tributaries that flow from the lowlands to the east are more widely spaced and have moderately to highly sinuous channels.

TABLE V.—Sediment-Load Characteristics for Rivers in the Amazon Basin

River	Sediment load (a)		Basin suspended-sediment yield rates, g/km²/yr
	Bed load,[b] percentage of solid load	Percentage of total load	
Amazon[c]	5	32	79.0×10^6
Ucayali	5 to 10	33	307.1
Japurá	2.3	48	120.2
Javari	Low (<1)	14	68.3
Juruá	Low (<1)	40	49.4

[a]After Gibbs (ref. 2).

[b]Generalized, based on environment.

[c]At mouth.

Midreaches: Channel

The Solimões River was photographed in two reaches in western Brazil. Both sites are typical of the central Amazon Basin. Landscapes with less than 200 m (656 ft) of relief are developed on Tertiary sediments (ref. 4), and broadleaf evergreen forests flourish under annual rainfall of at least 200 cm (79 in.) and, in places, more than 300 cm (118 in.) (ref. 5). Photograph AST-21-1681 (fig. 4(a)) shows the Solimões River in the vicinity of Leticia and its confluence with the Javari River (fig. 2). At this point, less than 30 percent of the major tributary discharge to the river is derived from tropical or mixed environments (ref. 2). Photograph AST-21-1682 (fig. 5(a)) shows the Solimões River in the vicinity of Fonte Boa and the Juruá and Japurá Rivers. This location is approximately 350 km (217 s. mi.) downstream of the Javari River. Approximately 45 percent of the major tributary discharge to the Solimões River at Fonte Boa is derived from mixed- and tropical-environment rivers (ref. 2).

The channel pattern of the Solimões River in western Brazil is anastomosing and meandering. The degree of meandering, or the sinuosity, of a channel has been related to the channel width-to-depth ratio, the channel gradient, the proportion of bed load to suspended load in the solid-sediment load of the stream, and the proportion of silt and clay in channel-bed and channel-bank deposits (ref. 6). These parameters depend on a complex of geologic, pedologic, physiographic, climatic, and other variables. Sinuosity is typically defined as the ratio of channel length to valley or flood-plain length for a given reach. This definition requires that sinuosity be measured for a single channel. To accommodate the anastomosing Solimões River to this definition, three sinuosity measurements were made for each photographed site. The channel was measured along the longest, the shortest, and the widest courses over a given flood-plain length. No channel was measured unless it comprised at least 20 percent of the composite channel width at that cross section. Sinuosity measurements for the Solimões River are summarized in table VI. Sinuosity in the vicinity of Leticia is low, approximately 1.2. Sinuosity downstream in the vicinity of Fonte Boa is approximately 1.5. This increase in sinuosity may reflect the increasing contribution of tropical streams to the Solimões River.

These sinuosity values should be considered estimates rather than precise values. Measurements were made from slightly oblique photographs. Image rectification was inhibited by the paucity of stable landmarks visible from orbital platforms over this part of the world and by the general lack of detailed correspondence between ASTP photographs and available regional maps. Measurements were made from the most vertical photographs available.

Although sinuosity has been studied extensively in single-channel rivers, the significance of sinuosity for anastomosing channels has not been

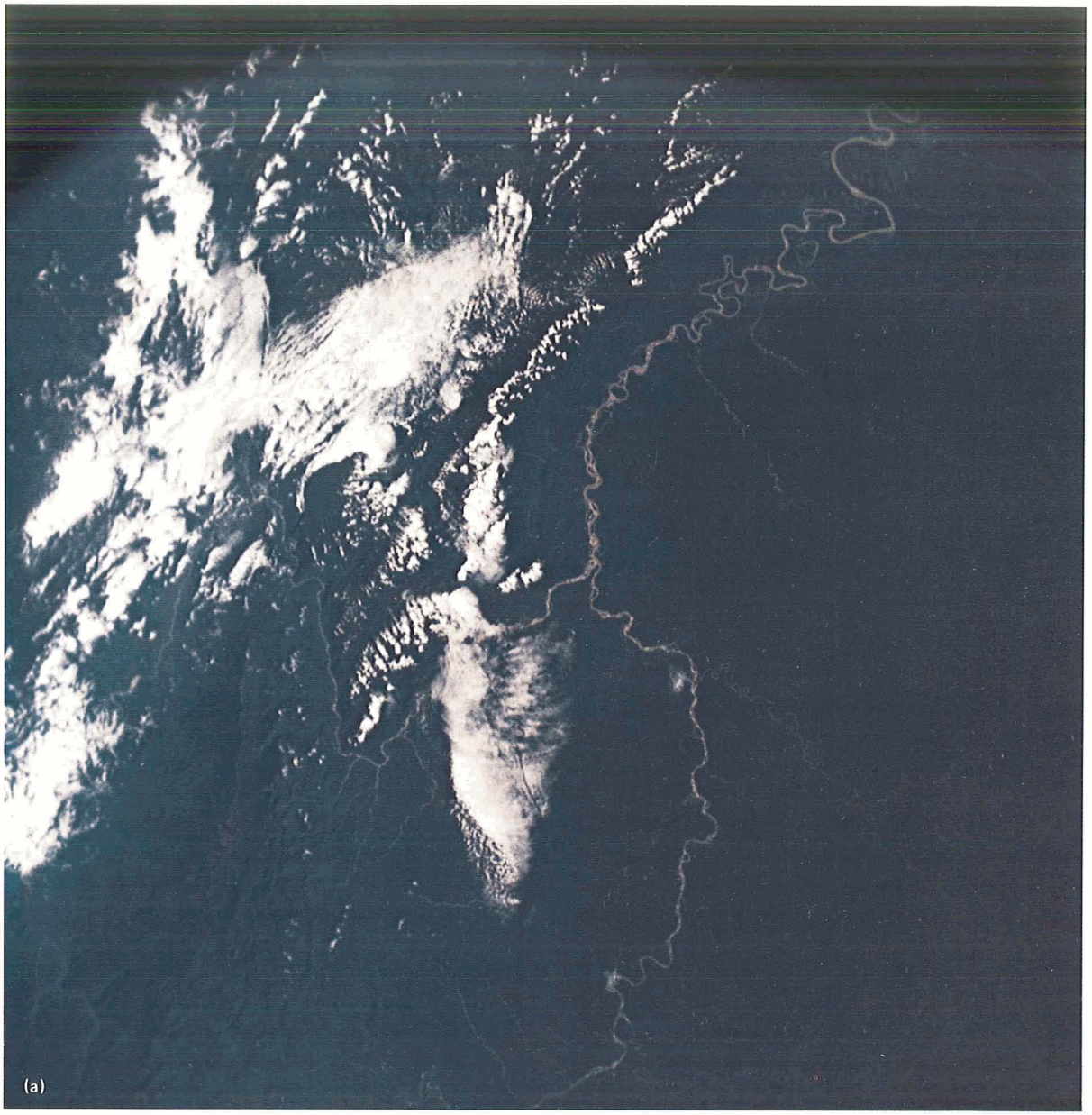


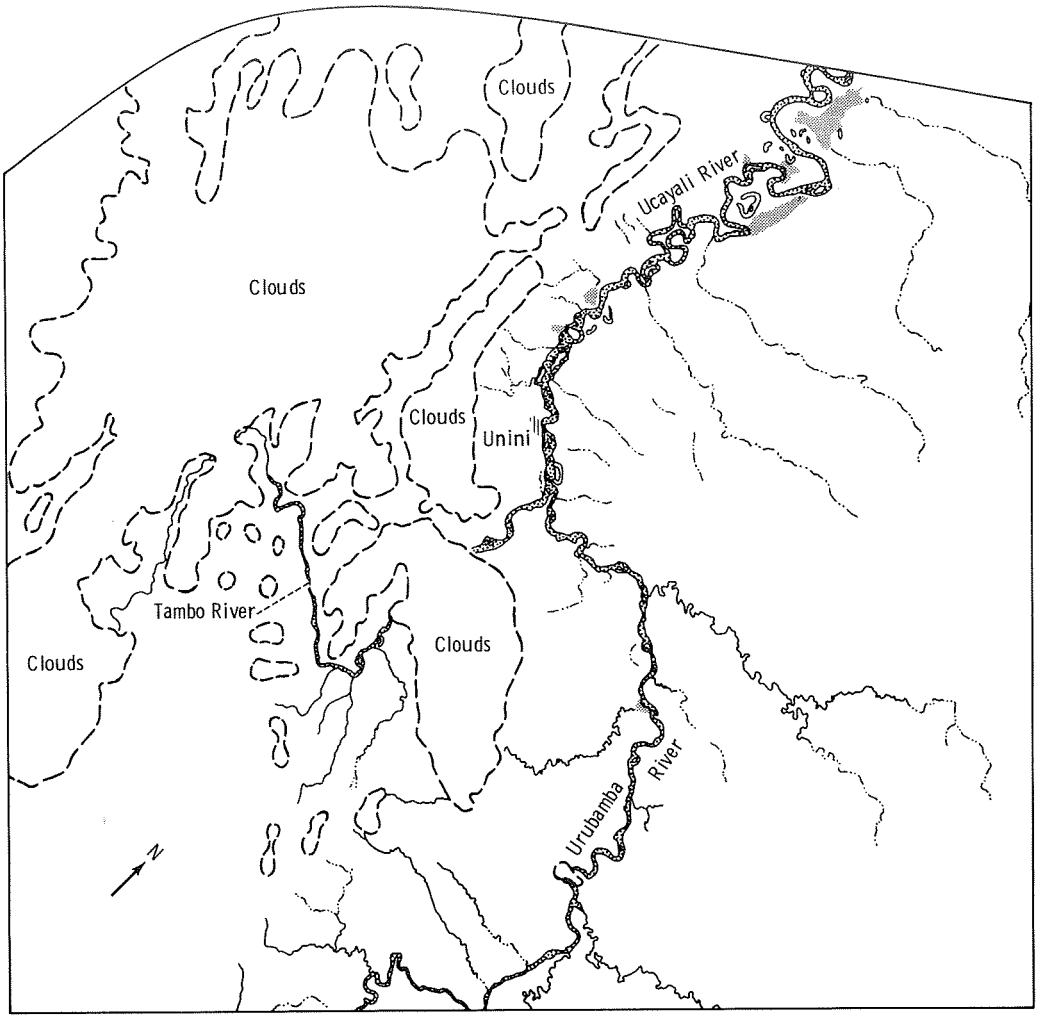
FIGURE 3.—The Ucayali River in Peru. (a) Photograph (AST-21-1679). (b) Sketch map.

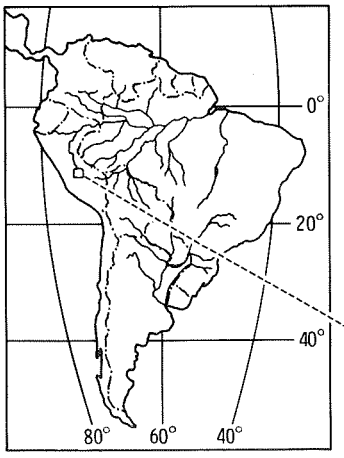
explored. Schumm (refs. 6 and 7) has related sinuosity P to the channel width-to-depth ratio F and to the percent of silt and clay M in channel deposits, as follows.

$$P = 3.5F^{-0.27}$$

$$P = 0.94M^{0.25}$$

These are empirical relationships derived from data drawn from single-channel reaches of the Great Plains of the United States. This semiarid environment is significantly different from the predominantly tropical environment of the Amazon Basin. Stream discharge tends to be much more regular in tropical than in semiarid regions, and vegetation is much more abundant in





(b)

FIGURE 3.—Concluded.

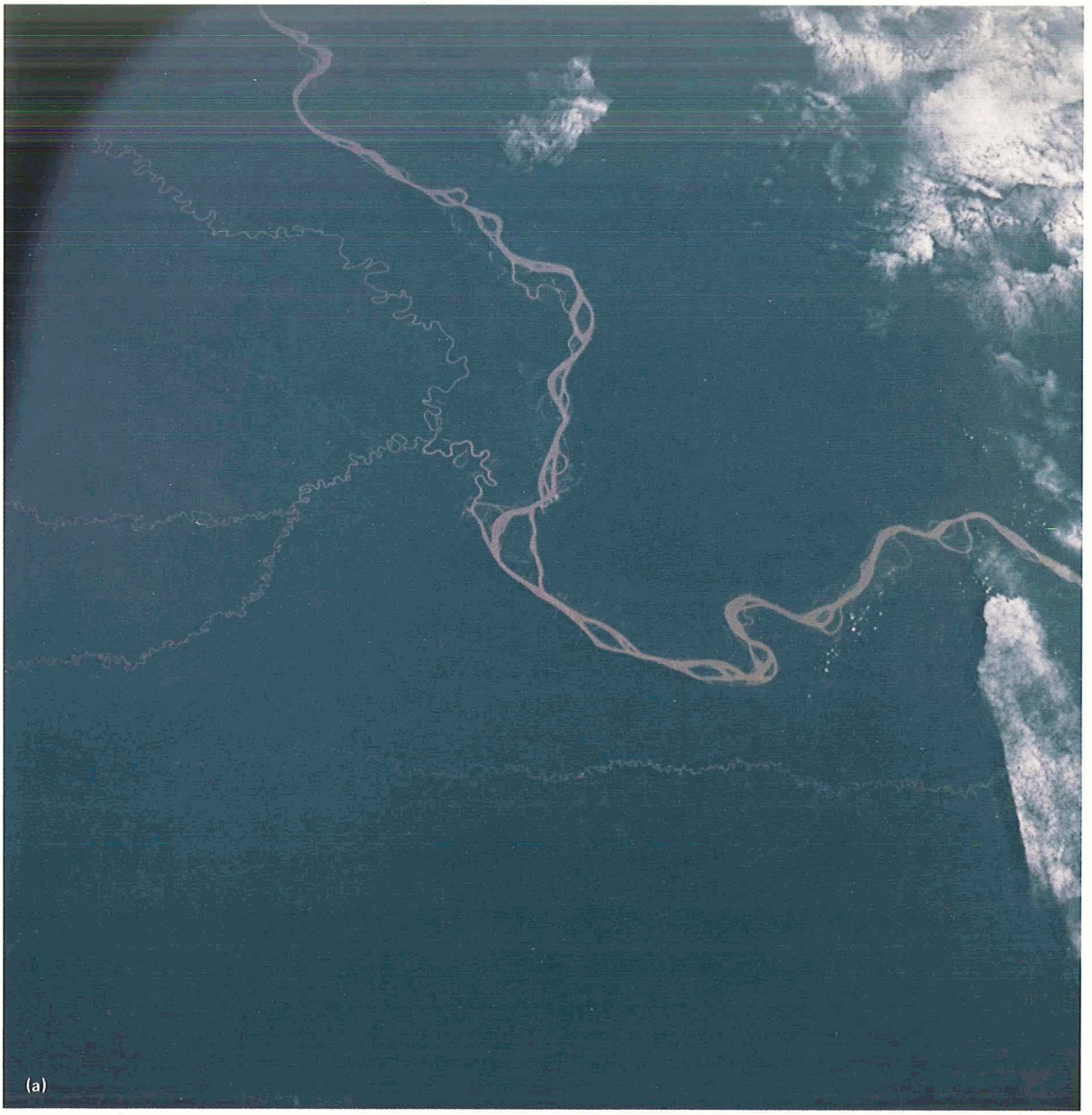
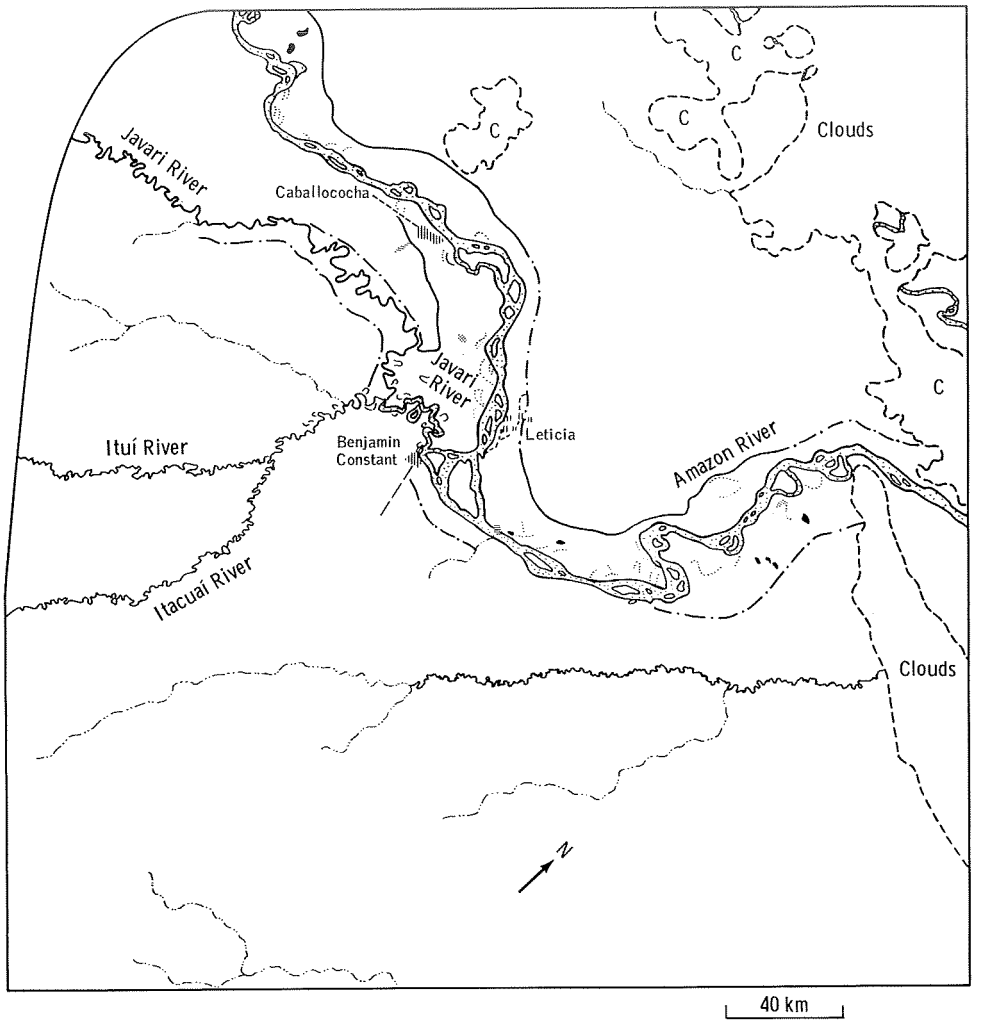
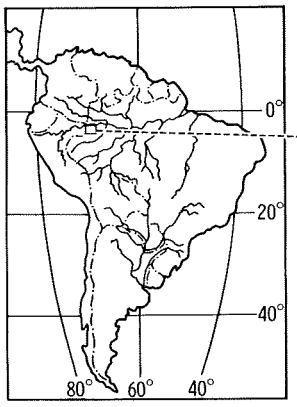


FIGURE 4.—The Solimões River near Leticia. (a) Photograph (AST-21-1681). (b) Sketch map.

tropical than in semiarid environments. Savat (ref. 8) has noted the strong influence of vegetation on bank stability of rivers in the Zaire Basin of equatorial Africa. The effects of environmental factors on the relationships recognized by Schumm (ref. 6) have not been investigated. Dense, tropical vegetation probably increases the resistance of streambanks to erosion while not affecting channel-bed scour resistance. Thus, tropical streams may have lower width-to-depth ratios than do semiarid streams that are comparable in other respects. Dense, tropical vegetation may protect meanders from cutoff by chuting, but it may inhibit sinuosity development by slowing





(b)

Rivers
Indistinct river channels
Abandoned meanders
Swales
Clear lakes
Flood-plain margins
Projected flood-plain margins
Other areas of high reflectivity
Settlement
Road
C Clouds

FIGURE 4.—Concluded.

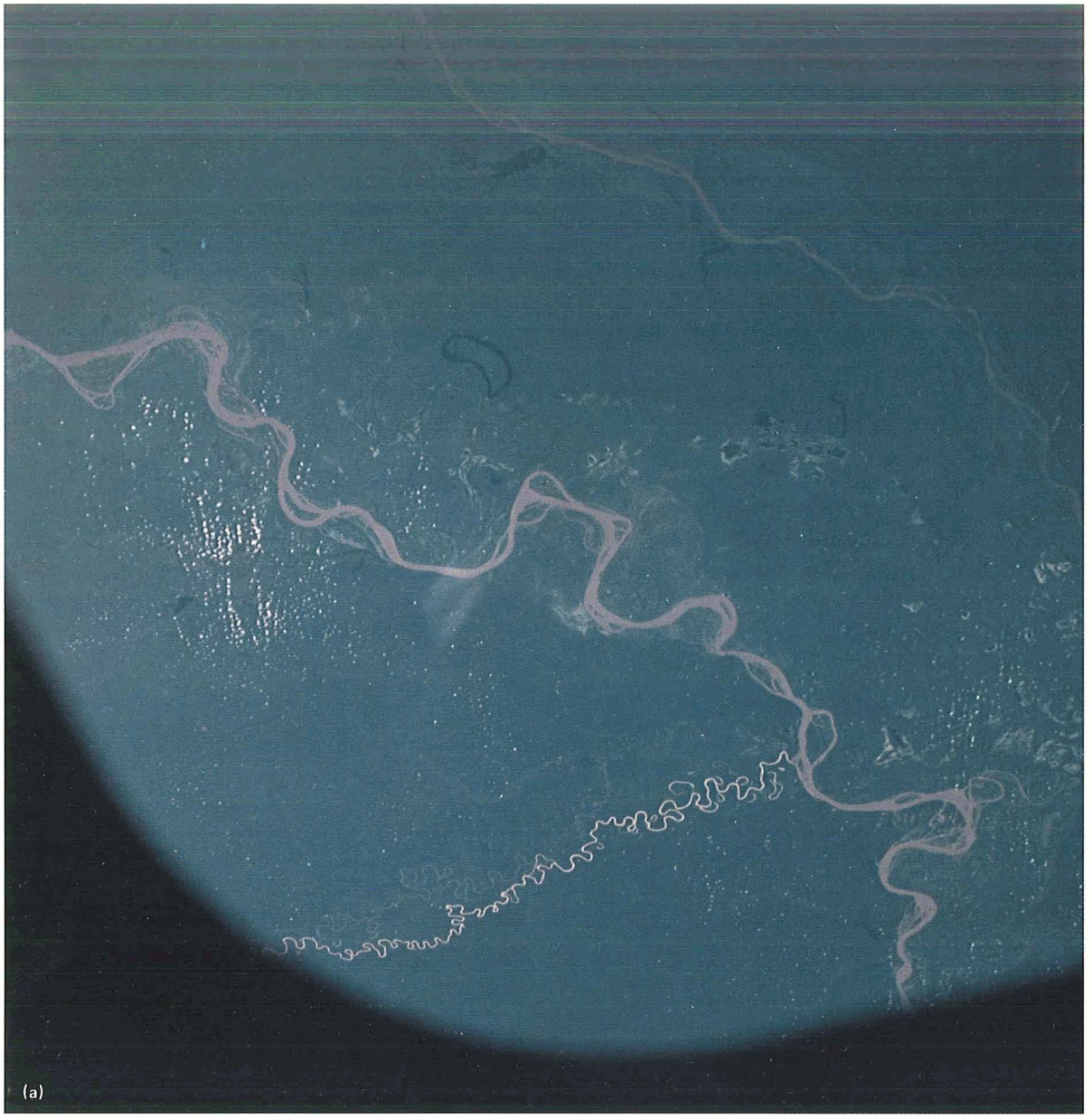


FIGURE 5.—The Solimões River near Fonte Boa with its tributaries, the Juruá and Japurá Rivers. (a) Photograph (AST-21-1682). (b) Sketch map. Average scale computed along Solimões River.

channel migration. However, where rivers are significantly large, as is probably the case with the Solimões River, vegetation may have a minimal effect on channel stability. The effect of vegetation would be most pronounced on smaller rivers. Given these qualifications, values of F and M calculated from Schumm's (refs. 6 and 7) relationships are presented in table VI. These values indicate the general character of the river and the tendency of trends along it. Until more is known about tropical fluvial environments, however, these characterizations should be understood

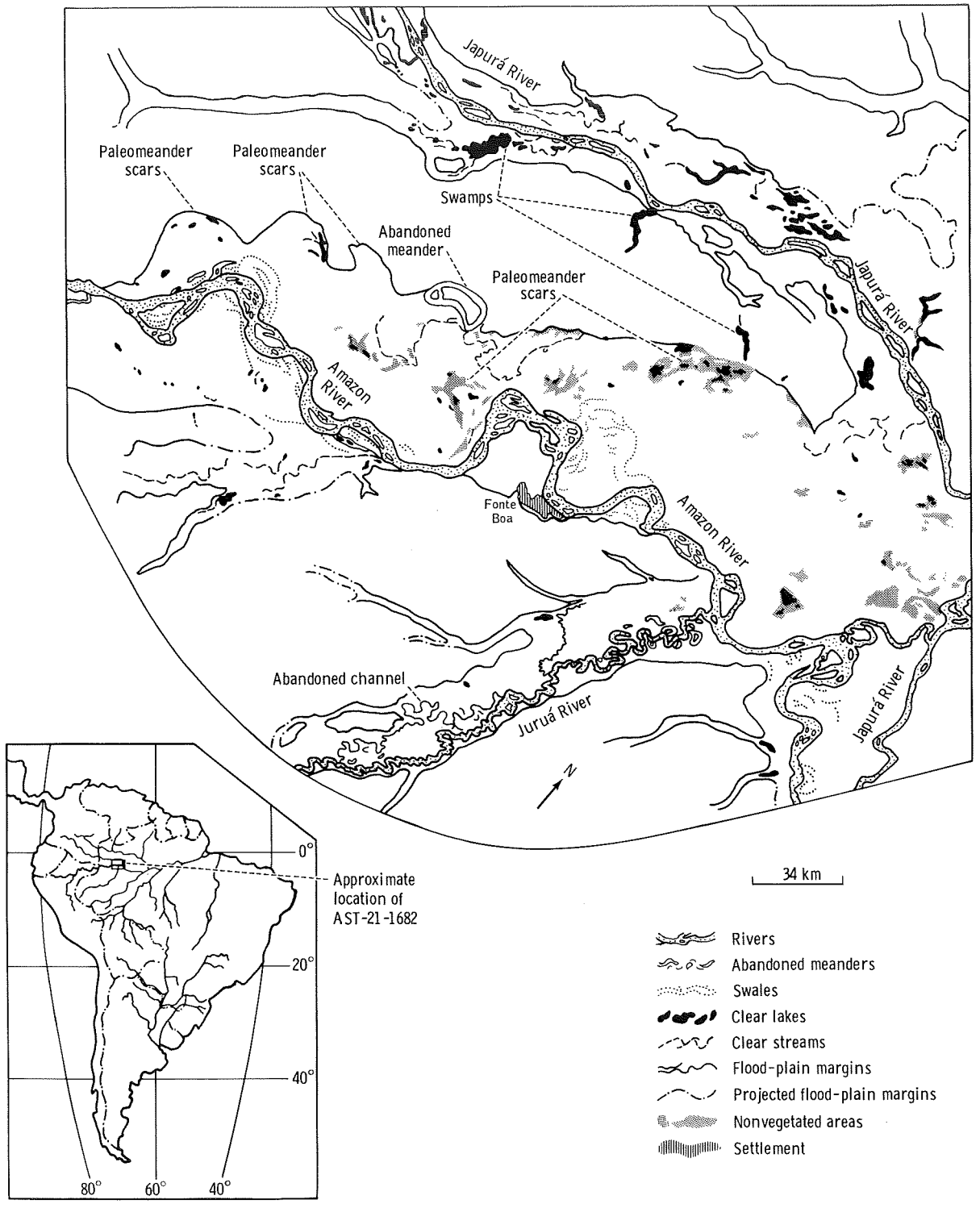


FIGURE 5.—Concluded.

qualitatively rather than quantitatively.

Meander wavelength for the Solimões River can be determined without distortion due to photograph obliqueness. The length of a channel reach can be determined from a map, and the number of meanders in that reach can be counted on the photograph. (Often, the small-scale maps necessary to cover the large areas photographed from space do not accurately depict the details of river channel patterns.) Because of low sinuosity and the anastomosing channel in the vicinity of Leticia, a realistic count of meanders on photograph AST-21-1681 (fig. 4(a)) is not possible. The channel pattern is simpler in the vicinity of Fonte Boa. Nine meander waves occur in the approximately 260-km (162 s. mi.) reach on photograph AST-21-1682 (fig. 5(a)). Although these meanders vary widely in form, they have been counted as equivalent. The average meander wavelength in this reach is approximately 29 km (18 s. mi.). The channel pattern is complicated by smaller meanders superposed on the nine larger meanders. The smaller meanders give rise to multiple channel reaches and incipient compound meanders. The significance of the smaller meanders is not understood. More highly oblique photographs of the Solimões River downstream of Fonte Boa, in the vicinity of Coari and Codajás (fig. 2) (i.e., frames AST-27-2393 and AST-27-2391, not shown in this report), reveal that, here also, the great complexity of the channel pattern prevents determination of a meander wavelength appropriate to the whole reach.

The width of the Solimões River can only be estimated subject to image distortion due to tilt. In addition, measurements can only be made of the width of flow at the particular river stage at the time of the photograph. The ASTP photographs were taken on July 19, 1975, in the early part of the "dry," or less rainy, season in the Amazon Basin (ref. 5). At this time of year at Manaus, the Solimões River has just passed but is still very near its annual peak stage (fig. 6). Upstream, near Fonte Boa, the peak stage should pass somewhat earlier, but in mid-July, the stage should still be well above average. Because the discharge of the Solimões River at Fonte Boa is only about one-third that at Manaus (ref. 2), the annual variation in stage may be significantly less at Fonte Boa than the 10-m (33 ft) variation at Manaus (fig. 6). Nevertheless, a stage variation of only a few meters will have a significant effect on the lateral spread of flow across flat flood-plain topography. Thus, flow widths at Fonte Boa are probably subject to large annual variations. On photograph AST-21-1682 (fig. 5(a)), it appears that flood-waters have recently receded, leaving swales and other flood-plain depressions filled with muddy water. Considering this and the pattern of annual stage variation, it is a reasonable assumption that

TABLE VI.—Channel Morphology for River Reaches in the Amazon Basin as Estimated From ASTP Photographs

Photograph	*River and channel*	*Sinuosity* P	*Percentage silt and clay* M	*Width-to-depth ratio* F
AST-21-1681	Solimões (Amazon)			
	Widest	1.2	2.6	53
	Longest	1.3		
	Shortest	1.2		
AST-21-1682	Solimões (Amazon)			
	Widest	1.5	6.5	23
	Longest	1.5		
	Shortest	1.4		
AST-21-1682	Japurá	1.1	1.9	73

the flow width photographed on July 19 approximates or slightly exceeds the bankfull channel width. Based on average image scale, the average flow width of the Solimões River near Fonte Boa is approximately 2.4 km (1.5 s. mi.), and it ranges between 1.6 and 3.2 km (1 and 2 s. mi.), for both single- and composite-channel reaches.

Channel width and meander wavelength may be used to estimate river discharge. Two relationships include bankfull channel width w:

$$w = kQ_m^{0.5} \quad (1)$$

$$w = kQ_m^{0.4}/M^{0.4} \quad (2)$$

where k is an arbitrary constant, Q_m is mean annual discharge, and M is as defined previously. (Units are feet and cubic feet per second.) These are empirical relationships derived from data taken from the Great Plains, Rocky Mountains, and Colorado Plateau of the United States (ref. 10), and the Riverine Plain of Australia (ref. 11). The relationships are of the same questionable applicability to tropical environments as the sinuosity relationships discussed previously. The effect of tropical vegetation on channel-bank stability may significantly affect the response of channel width to stream discharge. Harvey (ref. 12) has demonstrated for three streams in England that channel size is adjusted to different frequency flows in base-flow reaches and in flood-

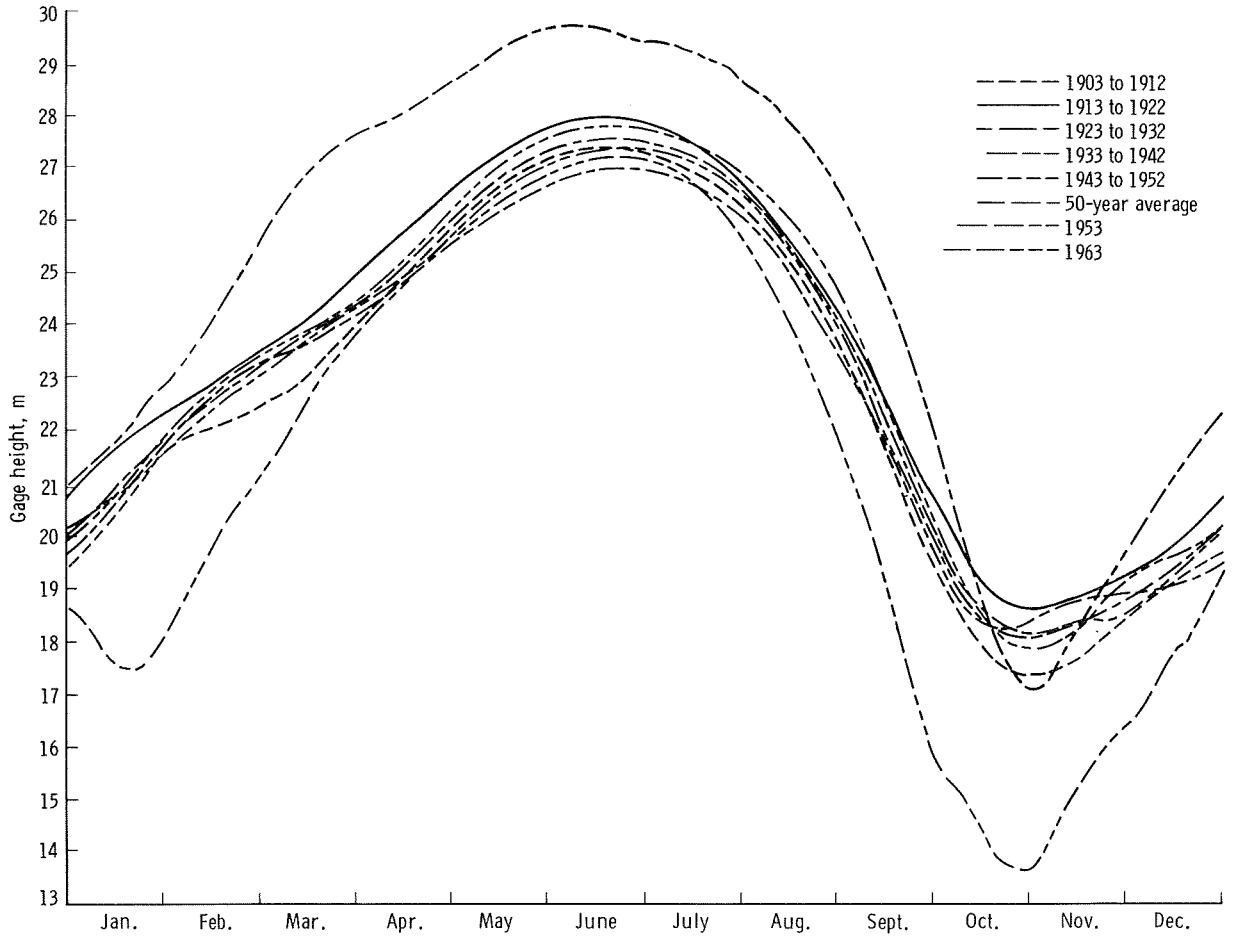


FIGURE 6.—Daily river stages for the Amazon River at Manaus. Years of maximum flow (1953) and minimum flow (1963) are shown as well as averages. (From Sternberg, ref. 9.)

regime reaches; in other words, that channel size adjusts differently to different time patterns of discharge. Significant differences exist in the time patterns of discharge for tropical and semiarid streams, and these differences may affect the adjustment of channel size to mean annual discharge. In addition to these difficulties, the equations relating channel width to discharge cannot be applied to rivers of the Amazon Basin until the constant term in these equations is known. Relationships of this form can be used to estimate the relative discharge of rivers based on the relative size of channels when the constant is unknown. Schumm's (ref. 11) equation (eq. (2)) considers the influence of stream sediment character, as well as discharge, on channel width. In this regard, it is a more sophisticated relationship than Leopold and Maddock's (ref. 10) equation (eq. (1)), but lack of knowledge concerning channel sediment types for Amazon Basin rivers makes Schumm's (ref. 11) equation more difficult to apply. Until more is known of tropical rivers, channel width will remain a poor indicator of river discharge.

Three equations relate meander wavelength λ to various discharges:

$$\lambda = 30Q_p^{0.5} \tag{3}$$

$$\lambda = 106Q_m^{0.5} \tag{4}$$

$$\lambda = 1890Q_m^{0.34}/M^{0.74} \tag{5}$$

where Q_p is the discharge of the most probable flood, and Q_m and M are as defined earlier. (Units are feet and cubic feet per second.) These relationships (eq. (3) from ref. 13; eq. (4), ref. 14; eq. (5), ref. 11) are subject to the same general qualifications as all empirical relationships based on semiarid environments but applied to tropical environments. The percent of silt and clay in channel deposits (M) is understood to be an indicator of channel-bank stability (ref. 15). Savat (ref. 8) has observed that tropical vegetation increases the stability of clayey channel banks in the Zaire Basin. If an increase in channel-bank vegetation is effectively the same as an increase in the proportion of fine-grained sediments in the bank, then Schumm's (ref. 11) equation (eq. (5)) suggests that the meander wavelength should be less for a heavily vegetated tropical stream than for a relatively nonvegetated but otherwise comparable semiarid channel. The difficulty of evaluating M for rivers in the Amazon Basin has already been discussed. The relationship between the temporal distribution of discharge and meander wavelength has not been established, and the manner in which the relatively regular flow of tropical rivers might affect meander wavelength is unclear.

Estimates of Solimões River discharge in the vicinity of Fonte Boa are presented in table VII. Mean annual discharge estimates based on formulas derived from semiarid environment data range from 22 823 m^3/sec (8.06×10^5 ft^3/sec) (based on λ alone) to 758 890 m^3/sec (2.68×10^7 ft^3/sec) (based on λ and M). The latter value is higher than that predicted for the most probable flood (based on λ alone). Solimões River discharge summed from estimates of major tributary discharge is 36 812 m^3/sec (1.30×10^6 ft^3/sec) (ref. 2); this value would be slightly higher if minor tributary discharge were included. The estimate based on Gibbs data (ref. 2) is lower than those predicted by the empirical equations including estimates of M. This difference suggests either that the empirical relationships including M are not valid for the Solimões River or that M does not relate to channel sinuosity and bed-load discharge in tropical rivers as it does in semiarid rivers.

The definition of bed load may lead to additional complications in the estimates shown here. Schumm (ref. 15) defines bed-load material as sediment coarser than 0.074 mm. Gibbs (ref. 2) defines bed-load material as all sediment that travels within 50 cm of the channel bottom. Gibbs' data (ref. 2) show that for the Marañón River, a mountainous stream, approximately 4 percent of the suspended load is coarser than 0.074 mm, and that all of the suspended load for the Xingu River, a tropical stream, is less coarse than 0.008 mm. Near the mouth of the Amazon River, less than 1 percent of the suspended load is coarser than 0.074 mm. Based on the variability of suspended-sediment size distribution, it seems reasonable to assume that the material traveling

within 50 cm of channel bottoms in Amazon Basin rivers bears no relation to sediment size class. Because Schumm's equation ($\lambda = 1890 Q_m^{0.34}/M^{0.74}$) is predicated on a functional relationship between sediment size and the mode of sediment transport, it may not be valid for the Amazon Basin. Intense physical and chemical weathering in the Amazon Basin produces sediments of a more limited physical character than those generated in semiarid or humid environments.

Midreaches: Flood Plain

The flood plain of the Solimões River is clearly distinguishable on ASTP photographs. Vegetation on the flood-plain surface is more variable than in the surrounding rain forests. Ridge-and-swale topography, abandoned meanders, and associated lakes and channels are found on the flood plain but not in the uplands. Flood-plain margins are also marked by clear-water lakes that occur adjacent to the flood plain. These lakes probably form where streams flowing onto the flood plain are dammed by fluvial deposits, probably natural levees. In the vicinity of Fonte Boa, the Solimões River flows along the southern part of its flood plain. Near Leticia, the Solimões River wanders across its flood plain.

TABLE VII.—Estimates of Solimões River Discharge in the Vicinity of Fonte Boa

Basis of estimate	Q, *m³/sec (ft³/sec)*
Equation (3) (ref. 13)	[a]286 000 (1.01×10^7)
Equation (4) (ref. 14)	[b]22 823 (8.06×10^5)
Equation (5) (ref. 11), [c]M=6.4	[b]167 635 (5.92×10^6)
Equation (5) (ref. 11), [d]M=13	[b]758 890 (2.68×10^7)
Gibbs (ref. 2)	[be]36 812 (1.30×10^6)
Equation (5) (ref. 11), [f]M=3	[b]72 774 (2.57×10^6)

[a] Q_p.

[b] Q_m.

[c] Based on sinuosity.

[d] Based on sediment-load estimates from Gibbs (ref. 2) and Schumm's (ref. 15) classification of alluvial channel types.

[e] Q_m is the sum of major tributary discharge to this point. Contributions from minor tributaries will raise this value. According to Gibbs' estimates for the whole basin, minor tributaries account for approximately 10 percent of the total mean annual discharge.

[f] According to Schumm (ref. 15), this value of M would require a sediment discharge of more than 11 percent bed load of particle size ≥0.074 mm.

Many segments of prior courses of the Amazon are apparent on the flood plain near Fonte Boa. The flood plain contains no abandoned meanders that are the size of the present river channel. One relatively small, abandoned meander occurs at the northern margin of the flood plain, northwest of Fonte Boa (fig. 5(b)). This meander is more sinuous than are meanders along the present channel, and its channel is narrower than the present channel. It is the only abandoned meander on the flood plain that has not been plugged by sediment. (It is now a clear-water lake.) Its preservation may have been favored by a sudden cutoff at its narrow neck. Large, arcuate forms along the northern flood-plain margin may mark the site of large ancient meanders (fig. 5(b)). These approximate the size of the largest of the present river meanders. The complex pattern of the present river channel and of associated ridge-and-swale topography suggests that large meander forms may result from the compounding of smaller meanders. Because of this possibility, and the lack of visible morphologic detail in the areas of paleomeander forms, no firm conclusions can be drawn about the size of paleomeanders.

The most impressive evidence of prior channel courses is the abundant scroll topography along the present channel. These features are probably more closely related to the modern channel than are any other features on the flood plain. Typically, the scroll topography roughly parallels the modern channel, but it also marks the course of former meanders. The size and shape of the former meanders are similar to those of existing channel meanders. The superposition of scroll patterns is similar to the pattern of anastomosing channels along the present river. Indeed, many swales appear to become an active part of the anastomosing channel complex at times of high flow. Although the intervening ridges are vegetated, the swales are not, probably because of frequent flooding. Many swales adjacent to the channel appear on photograph AST-21-1682 (figs. 5(a) and 5(b)) to contain muddy water from recent

flooding of the Solimões River. Some swales appear unaffected by flooding. On the photograph, they are whitish in contrast to the blue-green of the surrounding rain forest. These swales may be subjected either to less frequent flooding by the Solimões River or to seasonal flooding from local drainage or rising ground water during wet periods.

Although no single prior Solimões River course is apparent on ASTP photographs, the abundant traces of prior channels permit some limited conclusions. The relative narrowness of the single oxbow lake suggests that the river of which it was a part carried a lower mean annual discharge than does the present river. Otherwise, the flood-plain morphology indicates prior channels with meanders of roughly similar size and shape to present meanders. Field investigation will be necessary to resolve potential differences between older and present channel morphology. The limited observations presented here suggest that the bulk of the present flood-plain surface was formed by a river regime approximately similar to the present regime.

Garner (ref. 16) associates anastomosing river patterns with changing climatic conditions and, hence, with changing fluvial regimes. There is good reason to believe that the Amazon Basin has undergone climatic change (ref. 17). An accurate characterization of the Solimões River channel pattern is therefore crucial to understanding the development of the river and its associated morphology. Sternberg (ref. 9, p. 18) noted that the Solimões River does not have a meandering course, but that the pattern is one in which "waters fork and come together again, embracing lenticular islands." The Solimões River is anastomosing, but to characterize its course only as anastomosing is an oversimplification. Some essentially single-channel (i.e., non-anastomosing) reaches of the river follow meander forms; in other reaches, the relatively small-scale anastomosing channel network follows a larger meandering pattern that may be prominently outlined by the main channel (figs. 4(b) and 5(b)). The islands around which the channels anastomose are located primarily at bends in the meandering pattern. The islands are lenticular or teardrop shaped and elongated more or less parallel with the river. Typically, one side of an island is grossly convex, whereas the other side is straight or concave (fig. 5(b)). The broadest flow path may follow either side of the island.

Because of their shape and position, many islands appear to be former point bars that have become islands, either through active chuting and channelization across their bends or by more passive submergence during a rise in river stage. The islands are as vegetated as the surrounding flood plains, and they bear the same ridge-and-swale, washboard topography that characterizes much of the land adjacent to the river. These islands are probably relatively stable features because of the vegetation they support. Archeological materials lying on or near the surface of one island in the Solimões River have been dated to 2050 $\pm$ 120 years before present (ref. 18).

A variety of lakes and channels characterizes the flood plain of the Solimões River. Clear-water lakes are formed where rain-forest streams are ponded at flood-plain margins. These may be so small as to be barely noticeable on ASTP photographs (figs. 4(a) and 5(a)), or they may be very large, such as Lago de Coari (AST-27-2391). Gibbs (ref. 2) has shown that the suspended-sediment concentration of the Coari River increases markedly during the dry season; thus, Lago de Coari and similar features may not always appear as blue as they do on ASTP photographs taken shortly after the flood crest of the wet season. Clear-water lakes also occupy swales, abandoned meanders, and other depressions on the flood plain. These may derive their water from local surface drainage or regional subsurface drainage. Many swales appear to have been flooded shortly before they were photographed. Floodwaters are an alternative source of lake water, but they would require some time to clear as the suspended sediment settled in the lakes.

Several active channels cross the Solimões River flood plain. The most prominent connects the Solimões and Japurá Rivers, creating Ilhas Macuapanim. This channel follows a highly sinuous course and has abandoned segments associated with it. The large size of this channel's meanders relative to its width suggests some control of the channel pattern by something other than the present channel discharge, perhaps relict

features associated with the larger rivers. The direction of flow in this channel probably depends on the relative stage of the two rivers it connects. Other, smaller channels connecting flood-plain water bodies and the large rivers are not clearly visible on photograph AST-21-1682 (figs. 5(a) and 5(b)). These are more apparent on photographs that catch more direct reflections from the Sun (e.g., AST-8-477). Near the major rivers, these channels appear to contain abundant sediment, but at some distance from the rivers, their water is clear. The longest channel apparent on frames AST-21-1682 (fig. 5(a)) and AST-8-477 follows a broadly meandering course that is probably in part controlled by flood-plain morphology. Smaller meanders along the larger meanders are attributable to the flow regime of the channel.

Rio Japurá

The Rio Japurá heads on the eastern front of the Cordillera Oriental. Photograph AST-21-1682 (fig. 5(a)) shows the river just upstream from the Solimões River flood plain. This is the tropical portion of a mixed tropical-mountainous drainage basin (ref. 2). The sinuosity of the channel is low (1.1), but it increases across the Solimões River flood plain. According to Schumm's (ref. 6) relationships derived from semiarid environments, this low sinuosity indicates a low percentage of silt and clay in channel banks ($M = 1.9$) and a high width-to-depth ratio ($F = 73$). According to Schumm (ref. 15), if a semiarid-environment stream has $M = 1.9$, then the total sediment load is more than 11 percent bed load. However, Gibbs (ref. 2) believes that only 2 to 3 percent of the total sediment load of the mixed-environment streams is bed load. The difference between Schumm's (ref. 15) and Gibbs' (ref. 2) definitions of bed load has been discussed. It does not seem possible that more than approximately 6 or 7 percent of the sediment load of the Japurá River could be coarse enough to meet Schumm's (ref. 15) criterion of bed load. Only about 4 percent of the suspended load of Rio Marañón, a mountain stream, is coarser than 0.074 mm (ref. 2). This percentage should be higher than that in the mixed-environment Japurá River. If no more than 4 percent of the Japurá River suspended sediment is coarser than 0.074 mm, then even if all of the 2 to 3 percent of the total load that Gibbs (ref. 2) considers to be bed load is coarser than 0.074 mm, no more than 7 percent of the total load is that coarse. Thus, Gibbs' data indicate that the amount of sediment coarser than 0.074 mm in the Japurá River may be less than half that indicated by Schumm's (ref. 15) relationship. If Gibbs' (ref. 2) data are accurate, then the sinuosity of the Japurá River must be strongly influenced by a factor other than sediment-load character. This premise raises further questions about the applicability of empirical relationships from semiarid environments to tropical environments.

The channel pattern of the Japurá River is slightly anastomosing but not as much as the pattern of the Solimões River. The Rio Japurá islands are typically more elongate than those in the Solimões River. The Japurá River islands are vegetated; the channel does not appear to contain significant nonvegetated sedimentary deposits. Such deposits, indicative of channel braiding, might be expected in a semiarid stream channel of such low sinuosity. Their absence may be in part attributable to the generally fine caliber of sediment transported by the river. Braided channel deposits are typically sand and gravel; the intense weathering conditions of mountainous and tropical environments in the Amazon Basin (ref. 2) probably restrict the amount of coarse sediment available for such deposits.

The average channel width of the Japurá River is approximately 1.4 km. Although the Japurá River is about half as wide as the Solimões River in typical reaches just upstream of their confluence, the sinuosity of the Japurá River indicates that it should be proportionally shallower than the Solimões River. Thus, relative width is not an accurate indicator of relative discharge. Based on Gibbs' (ref. 2) tributary discharge estimates, the discharge of the Solimões River is at least 3.3 times greater than the discharge of the Japurá River at their confluence.

Meander wavelength is a parameter that is probably not applicable to the low-sinuosity, anastomosing channel of the Japurá River. Also, the Japurá River bends over a wide range of distances. Some of these bends may not be meanders,

and no single distance typifies the "wavelength" of all bends. Because the appropriate measurements cannot be made, it is not possible to make estimates of river discharge based on the empirical formulas used for the Solimões.

The flood plain of the Japurá River is apparent on ASTP imagery primarily because the vegetation it supports appears different from the surrounding rain forest. The Japurá River flood plain displays a less varied and distinctive morphology than does the Solimões River flood plain. Because of the low sinuosity of the Japurá River, its flood plain bears no apparent abandoned meanders or ridge-and-swale topography. The most prominent features on the flood plain are clear-water lakes and streams. Several streams emerging from the rain-forest uplands are ponded at flood-plain margins. This ponding suggests that overbank deposition is as prominent along the low-sinuosity Japurá River as it is along any of the more sinuous tropical rivers. Overbank deposition is usually a relatively minor process along low-sinuosity semiarid streams because it requires fine-grained sediment. If the Japurá River carries abundant fine-grained sediment in suspension, then, despite the low sinuosity of the river, this sediment would be subject to overbank deposition during floods.

Tropical Tributary Rivers

The tropical-environment rivers photographed during the ASTP mission are among the smaller major tributaries to the Solimões River, although some tropical rivers (not photographed) are among the largest tributaries to the Solimões River (ref. 2). Photographed tropical Solimões River tributaries include the Javari, Jandiatuba, and Juruá Rivers. Photographed rivers in the Javari River Basin include the Ituí and Itacuaí Rivers. Photographed rivers in the Juruá River Basin include the Gregório, Jurupari, Envira (Embira), and Tarauacá Rivers. Many smaller rivers are visible on the photographs, but because the detail of their channel patterns is not clear, they were not studied.

The headwaters of the tropical rivers rise to relatively low elevations. The headwaters of the Juruá River, for example, rise to only approximately 600 m (2000 ft), as compared to elevations greater than 6000 m (20 000 ft) for the headwaters of the Ucayali River. The tropical rain-forest environment of the Amazon Basin is very humid. Much of the interior Amazon Basin receives more than 200 cm of precipitation in a year, and many areas receive more than 300 cm of rain each year. Streamflow in the interior tropical environments may be much more regular than in the marginal humid and semiarid environments. The seasonal regularity of the Solimões River is illustrated in figure 6. Although precipitation in the Amazon Basin is seasonally distributed, rainfall is abundant throughout the year. Many environmental factors probably act to moderate stream discharge. Tropical-environment relief is only low to moderate (ref. 4). Dense rain-forest vegetation and some of the deepest soil profiles in the world retard precipitation runoff into streams. Well-developed flood plains along tropical rivers provide overbank storage of peak discharges. Saturation of the environment may decrease the retardation effect of some environmental elements, but an even precipitation distribution in a given season may maintain status and stream discharges whether environmental runoff retardation is relatively high or low.

The sinuosity of tropical streams tributary to the Solimões is typically moderate to high. Sinuosity estimates based on the least tilted images are listed in table VIII. The percent silt and clay in channel sediments (M) and channel width-to-depth ratio (F) have been calculated for selected sinuosity values representative of the tropical rivers (table IX). No measured sinuosity was less than 1.7. The highest measured values were approximately 3. Most sinuosity measurements range between 1.8 and 2.2. Meanders on the tropical rivers are typically compound and asymmetrical (according to the classification of Brice, ref. 19), and many channel reaches have irregular and tortuous patterns (according to the classification of Schumm, ref. 6).

Highly sinuous rivers are subject to greater distortion from photograph tilt than are less sinuous rivers. Photograph tilt has the effect of foreshortening apparent distance in the direction of tilt. If photograph tilt is in the direction of the stream valley, the apparent valley length is foreshortened

TABLE VIII.—Tropical River Sinuosity

Photograph	*River*	P
AST-21-1680	Juruá	[a]2.2 to ≈3.0
	Tarauacá	[a]1.9 to 2.2
	Jurupari	1.7
	Embira	1.8
AST-21-1681	Javari	[a]2.0 to 2.2
	Itacuaí	[a]2.2 to 2.5
	Ituí	[a]2.0 to 2.2
AST-21-1682	Juruá	[a]1.8 to 2.2
	Abandoned channel of Juruá	2.7
	Reach of Juruá downstream of abandoned channel, including lengths of recently abandoned meanders	≈3.2

[a]Range of sinuosities measured along different reaches of river.

more than the apparent channel length because a part of the channel is not alined in the foreshortened direction. The resulting apparent sinuosity is higher than the actual sinuosity. If photograph tilt is alined perpendicular to the stream valley, parts of the channel will be foreshortened but the valley length is not. The result is an apparent sinuosity that is lower than actual. Because low-sinuosity channels deviate little from the orientation of their valleys, the potential for differential distortion of apparent channel and valley lengths is less than for high-sinuosity stream courses that deviate significantly from the orientation of their valleys. For ASTP photographs, the apparent sinuosity of the same reach on different photographs varied by as much as 30 percent for highly sinuous streams but varied by only 5 to 10 percent for the lower sinuosity Solimões River. In table X, measurements of apparent sinuosity on more and less tilted photographs of the same area are compared. These measurements show no systematic variation between photographs. The apparent sinuosity of reaches on the more highly tilted photographs is greater than, equal to, and less than the apparent sinuosity of the corresponding reaches on the less tilted photographs. Sinuosity trends along a channel, and above and below river confluences, are distorted.

The sinuosity of the tropical-environment streams suggests that they are relatively narrow, deep, suspended-load streams (ref. 6). Gibbs' (ref. 2) analysis of the tropical Xingu River shows that its suspended load is made up entirely of particles finer than approximately 8 μm. Gibbs' data suggest that less than 1 percent of the solid sediment load of the tropical rivers is bed load (by his definition). If the suspended-sediment load is an indication of the total sediment load of tropical rivers, then much less than 1 percent of the total solid load of these rivers may meet Schumm's (ref. 15) criterion for bed loads (coarser than 0.074 mm).

The ASTP photographs enable the study of the distribution of sinuosity along tropical rivers. Typically, sinuosity varies across the confluences of these rivers, but, probably because of the dependence of sinuosity on a variety of factors, including stream sediment-load character and valley slope, this variability is not systematic. These factors may not vary systematically across channel confluences.

Sinuosity along the Juruá River seems to vary without dependence on tributary contributions. The Juruá River on AST-21-1680 (figs. 7(a) and 7(b)) can be divided into two reaches of relatively high sinuosity that alternate with two reaches of lower sinuosity. Although the absolute value of sinuosity in these reaches may be slightly dis-

TABLE IX.—Calculated Values of M *and* F *Based on Selected Sinuosities Representative of Tropical Rivers*

Sinuosity	M, *percent*	F
1.8	13.5	12.0
2.2	30.0	5.6
2.6	59.0	3.0
3.0	100.0	1.8

TABLE X.—Comparison of Apparent Sinuosities on Tilted Photographs of the Same Area

Photograph	*River and reach*	*Relative tilt*	P
AST-21-1680	Envira (Embira), upstream	Low	1.8
AST-27-2387	Envira (Embira), upstream	High	1.8
AST-21-1680	Envira (Embira), downstream	Low	1.8
AST-27-2387	Envira (Embira), downstream	High	2.4
AST-21-1680	Jurupari	Low	1.7
AST-27-2387	Jurupari	High	1.8
AST-21-1680	Tarauacá	Low	2.0
AST-27-2387	Tarauacá	High	1.7

torted by photograph tilt, the pattern of relative sinuosity distribution is real, because the angular relationship between the river course and the direction of photograph tilt is virtually constant. The low-sinuosity reaches contain meanders that were cut off after the compilation of the Carto do Brasil, whereas the high-sinuosity reaches have evolved to the verge of cutoff since that time. This distribution of sinuosity suggests that the river adjusts sinuosity at least semi-independently within apparent reaches. If the factors affecting sinuosity within any reach are relatively uniform, the meander development should take place uniformly in rate and style in that reach. When a critically high sinuosity develops in any reach, an avulsion may occur in which several meanders are cut off during a relatively short period. Consequently, sinuosity in the reach decreases to a lower value from which it can once again increase. For some reason, reaches of a channel may be at various stages of meander development, but all reaches may be oscillating about a similar steady state. In other words, the average sinuosity over time for one reach of river may be the same as the overall sinuosity of many similar reaches at one particular time. Meander cutoff occurs primarily across highly convoluted meander forms with locally narrow necks. This characteristic suggests that meander cutoff may be governed by the degree of development of either individual meanders or neighboring groups of meanders, rather than by the overall sinuosity through the reach.

The Juruá River on photograph AST-21-1682 (fig. 5(a)) shows two modes of sinuosity adjustment. The upstream portion of the river flows beside a channel that appears to be virtually abandoned. Neither channel has many associated abandoned meanders. Downstream of the confluence of these two channels, the single channel is surrounded by many abandoned meanders. The sinuosity of the present channel is relatively low in both reaches. Relatively high sinuosities (table XI) characterize both the abandoned channel and the present channel with recently abandoned meanders included. The upstream portion of the Juruá River on photograph AST-21-1682 (fig. 5(a)) appears to have been reduced in sinuosity by avulsion. No meander cutoffs occurred along the avulsed reach, and probably none have had time to develop along the new channel. The downstream portion of the Juruá River recaptured the avulsion where flow was forced back into the channel by the flood-plain margin. Downstream of this point, river sinuosity was decreased by numerous abandoned cutoffs. Differences in the sinuosity of the avulsion channel and of the reach straightened by meander cutoff may be caused by the different modes of sinuosity reduction. Whereas the new channel was probably relatively restricted in its development, the reach characterized by meander cutoffs may have been limited by residual high-sinuosity elements.

The apparent sinuosity of the Juruá River on photographs AST-21-1680 (fig. 7(a)) and AST-21-1682 (fig. 5(a)) ranges from about 2 to about 3. This is a large variation, photographic distortion notwithstanding. According to Schumm (ref. 6), for this range of sinuosity, channel width-to-depth ratios should range from about 10 to less than 1, and the percent of silt and clay in channel-bank sediments (M) should range from about 20 to about 100. For this range of M, the proportion of bed load in the total sediment load should range from about 3 percent to virtually nothing. The

suggested range of these variables is quite large, especially in light of environmental constraints on the character of sediment available to this river. It is likely that the actual variance of the channel width-to-depth ratio, of the amount of silt and clay in channel sediments, and of the proportion of bed load in the total sediment load is actually less than is suggested by the variance of sinuosity. If so, a wide range of sinuosities may result from a relatively small range of environmental parameters. The particular sinuosity of a reach may also depend on the stage of channel development in that reach.

The photographic evidence suggests that the range of sinuosity associated with these tropical rivers is greater than that associated with a typical semiarid stream. The standard error for both of Schumm's (ref. 6) equations

$$P = 3.5F^{-0.27}$$

$$P = 0.94M^{0.25}$$

(where P, F, and M are as defined previously) is between 11 and 12 percent. If one assumes relatively uniform values of F and M for the Juruá River and an average sinuosity of approximately 2.5, then the regular variation of the Juruá River sinuosity for these values of F and M is approximately 20 percent. The high variance of sinuosity in the Juruá River may be attributable to stability factors in the tropical environment: the probable relative regularity of tropical streamflow as compared to semiarid streamflow and the abundance of fine-grained sediments and dense vegetation in the tropical environment. Meander cutoff seems to occur through narrow meander necks resulting from highly evolved, convoluted meander forms. This suggests that the cutoff occurs when meanders develop under ordinary conditions to the point at which cutoff will occur during a relatively frequent discharge event. Although the cutoff discharge occurs frequently, many such discharges may have to pass before conditions are such that the meander will be cut off. Thus, it may be an infrequent event in comparison to the discharge that effects the cutoff. Channel-bank stability, provided by fine sediments and dense vegetation,

TABLE XI.—Sinuosity of the Juruá River, Past and Present

[From photograph AST-21-1682]

River reach	*Sinuosity*
Present channel; reach spanned by abandoned channel	1.9
Abandoned channel	2.7
Present channel downstream of confluence with abandoned channel	2.2
Present channel downstream of confluence with abandoned channel, including lengths of recently abandoned meanders	≈3.0

may reduce the effectiveness of low and moderate floods with regard to cutting off meanders. The probable regularity of tropical-stream discharges may reduce the frequency of high-magnitude floods that could potentially cut off meanders regardless of their form. Relatively high-magnitude floods may occur frequently enough in humid-temperate and semiarid environments to exert a significant control over channel morphology (ref. 20). This control may include limits on the upper values of channel sinuosity. In tropical environments, where relatively high-magnitude events are less frequent than in humid and semiarid environments, more frequent events will determine channel morphology. These events should not have the limiting effect on channel sinuosity that high-magnitude events have, and the effective upper limit of channel sinuosity may be the complexity of the channel pattern itself.

The channel width of the tropical rivers photographed during the ASTP mission varies from river to river. The calculated width of the Juruá River, the largest of the photographed rivers, is approximately 0.3 km. The meander wavelength of these rivers is difficult to assess because of irregular meander patterns and compound meander forms. Little can be concluded about discharge based on the meander wavelength of these rivers until the relationship of complex meander forms to discharge is better understood.

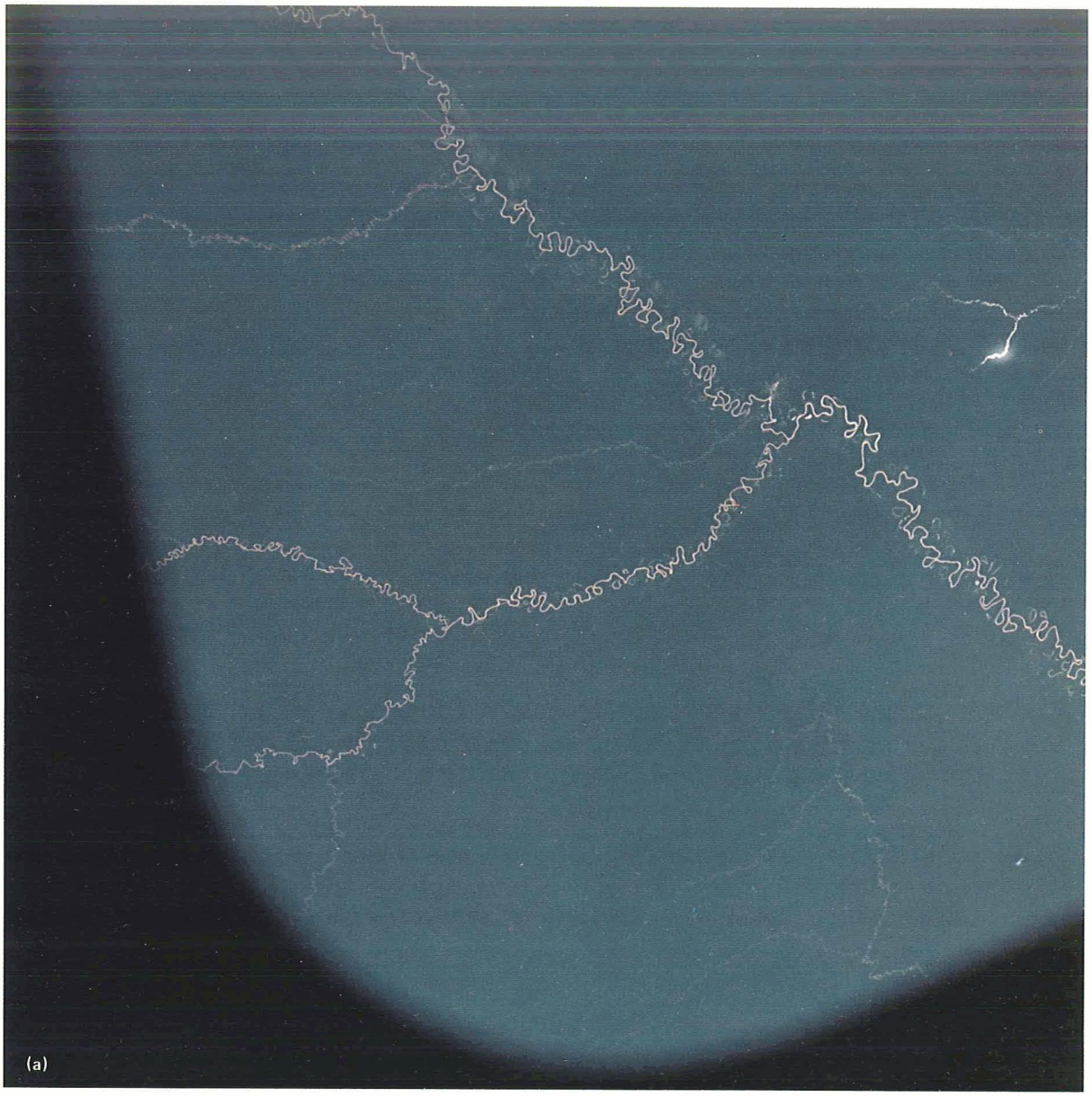
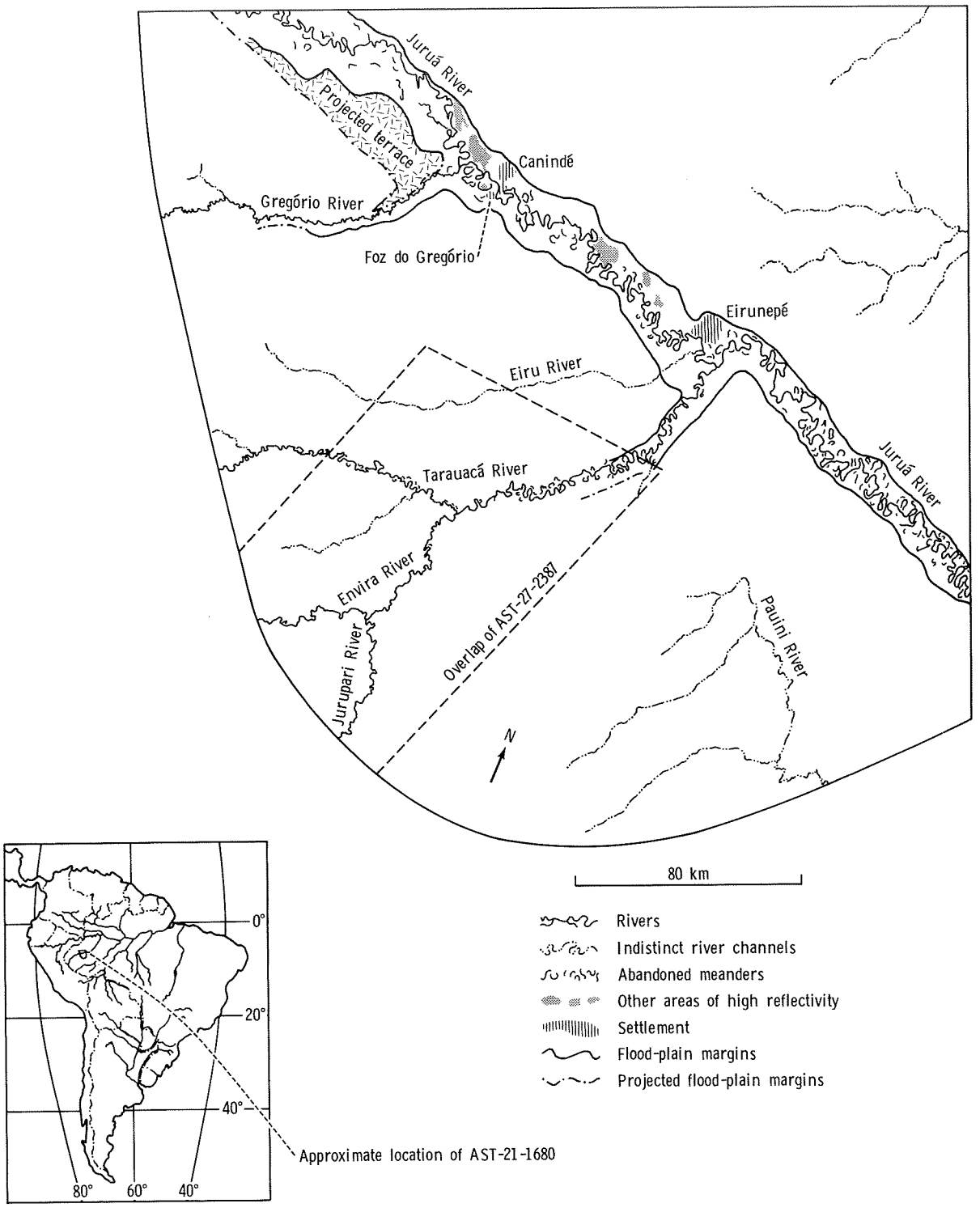


FIGURE 7.—The upper Juruá River. (a) Photograph (AST-21-1680). (b) Sketch map.

The flood plains of the tropical Amazon Basin rivers photographed by ASTP do not appear to be as varied as the flood plain of the Solimões River. Some small streams are ponded at the flood-plain margins, but this ponding does not occur as frequently on a large scale as it does for the nontropical rivers. It may be that the amount of overbank deposition is limited on the tropical rivers by the low erosion rates within this environment (ref. 2). Abandoned meanders are the most prominent flood-plain features. The relatively high-resolution photographs indicate that abandoned meanders may reach the maximum probable spatial density along some river reaches (fig. 8(b)).



(b)

FIGURE 7.—Concluded.

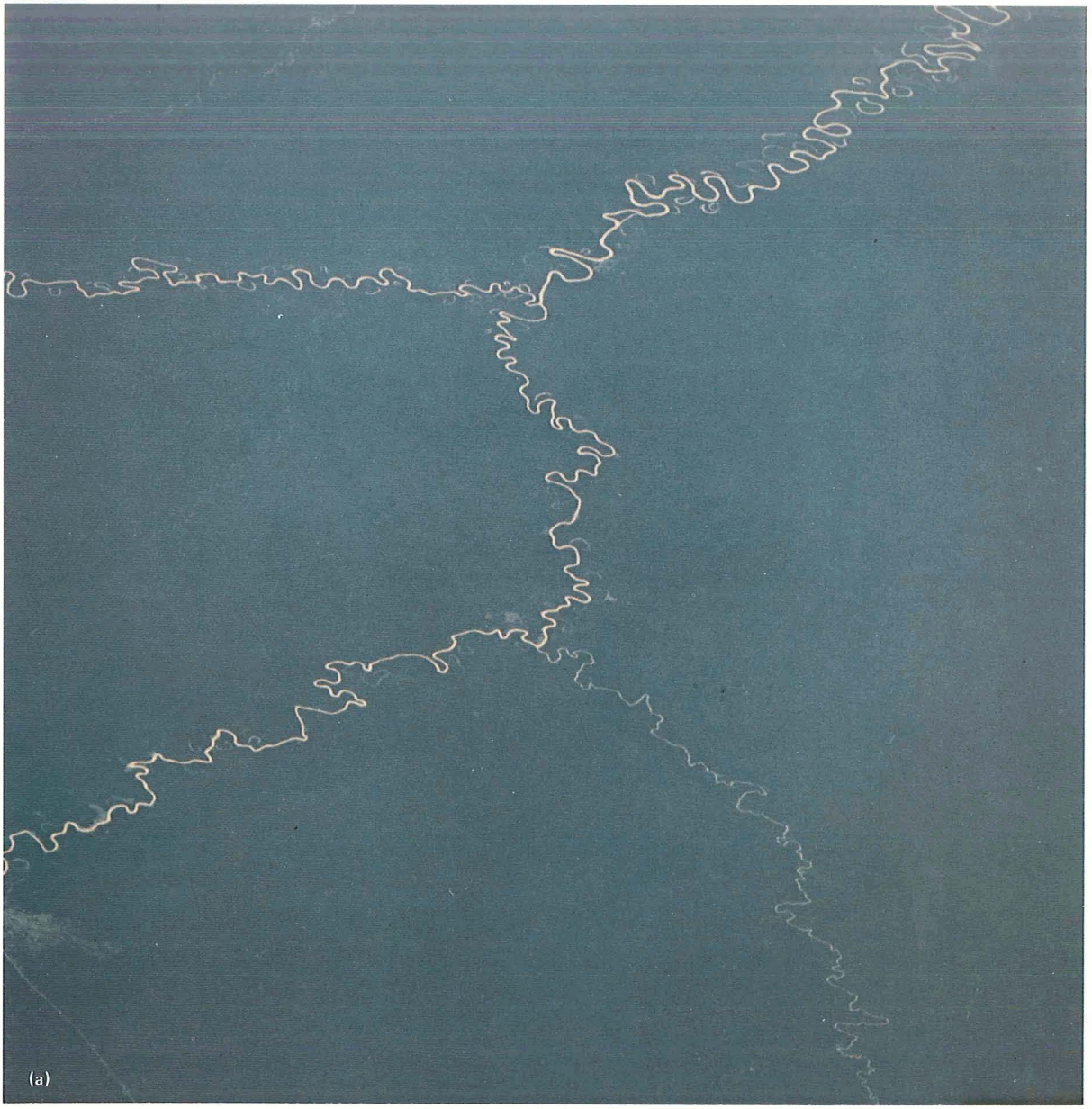
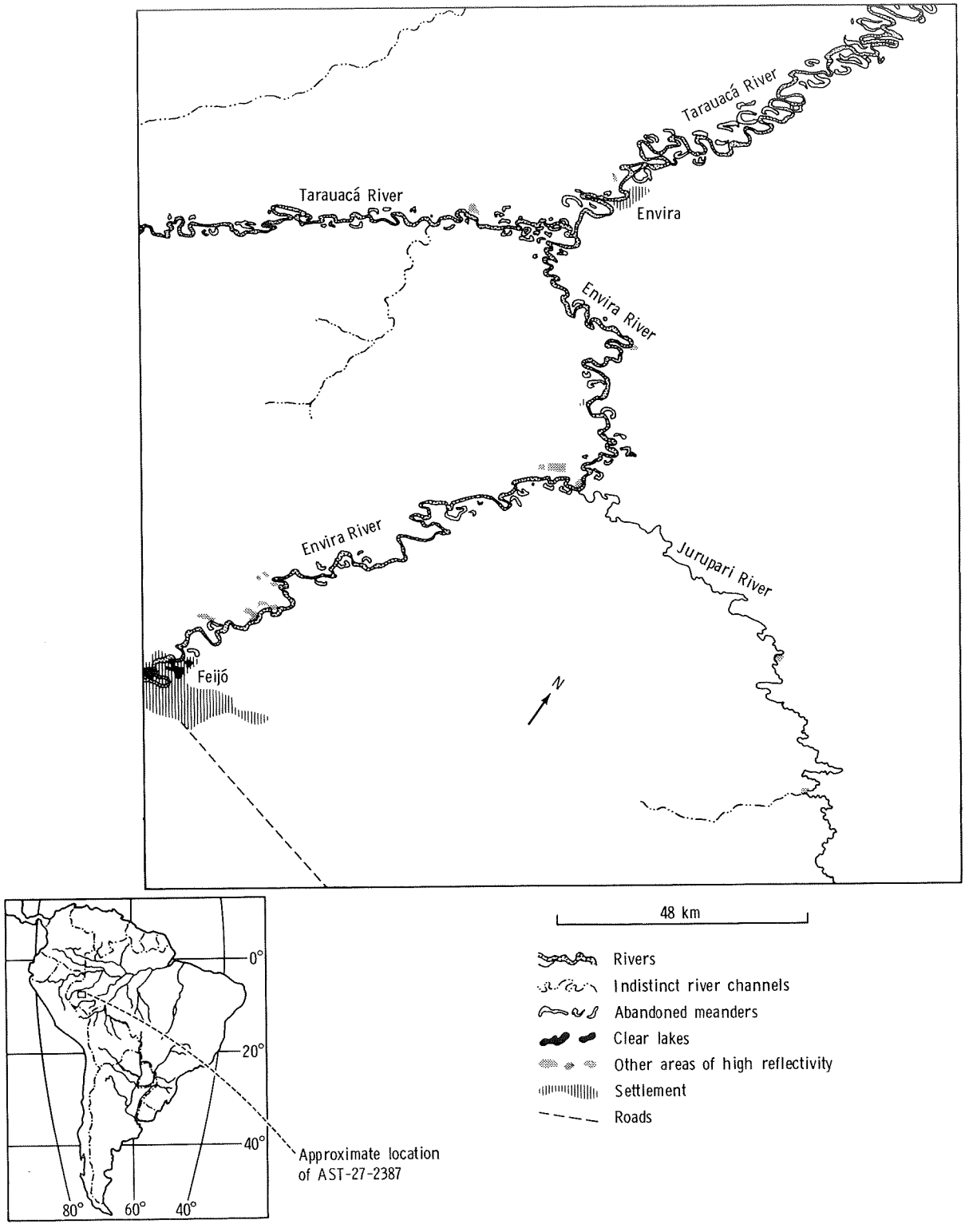


FIGURE 8.—The confluence of the Tarauacá and Envira Rivers near Feijó. (a) Photograph (AST-27-2387). (b) Sketch map.

Ridge-and-swale topography, common along the Solimões River, is not apparent along the tropical rivers. The tropical rivers seem to cross over their flood plains with a greater spatial frequency than does the Solimões River, and their flood plains are probably young and active.

PARAGUAY RIVER

The Paraguay River drainage basin lies almost entirely within a tropical climatic zone with 100 to 125 cm of precipitation and 60 to 120 cm of potential evaporation annually. Some headwater por-



(b)

FIGURE 8.—Concluded.

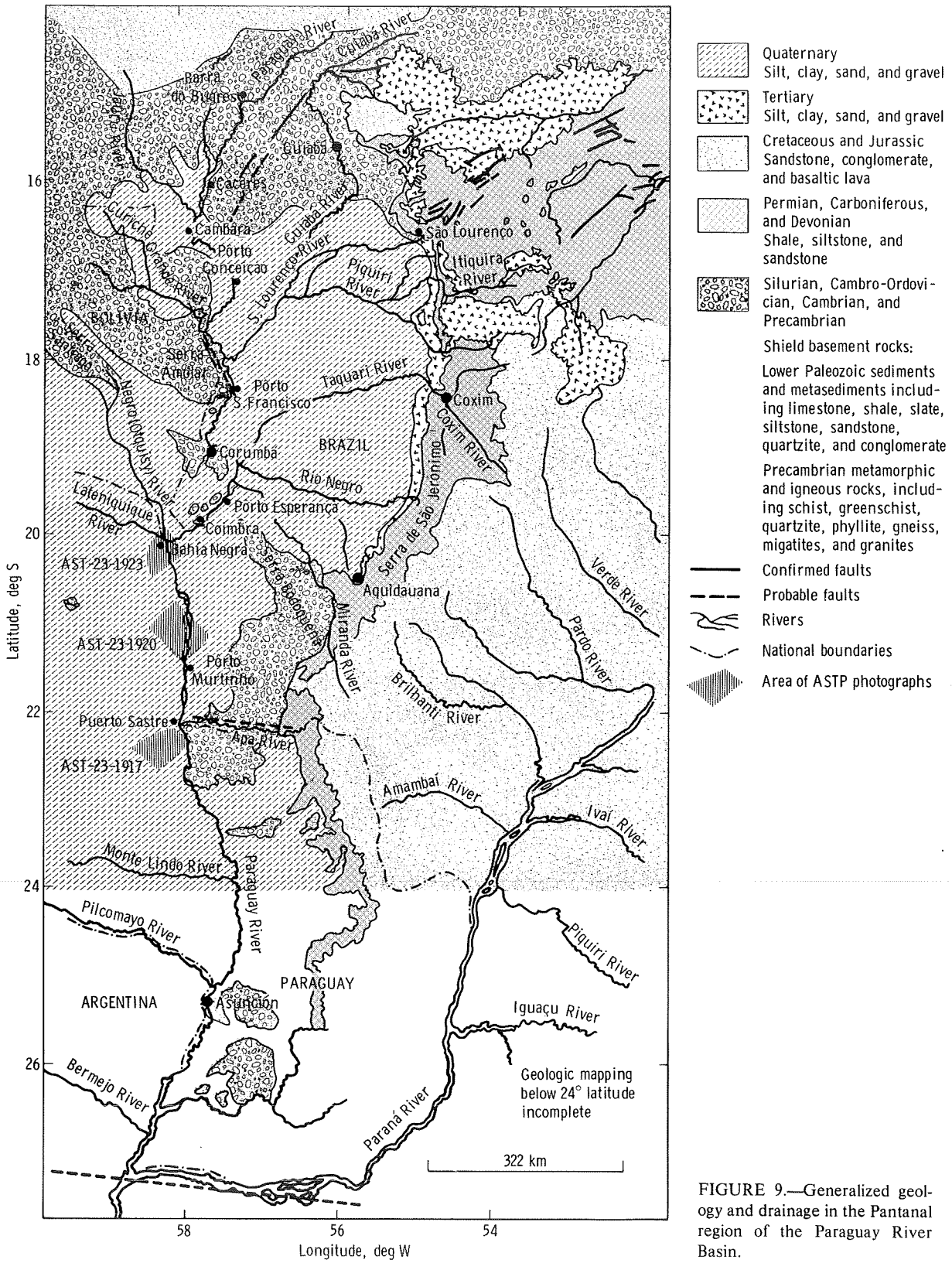


FIGURE 9.—Generalized geology and drainage in the Pantanal region of the Paraguay River Basin.

tions of the basin receive more than 200 cm of precipitation annually. For a major portion of its course, the Paraguay River flows through the Pantanal Basin, a Pleistocene-Holocene alluvial plain that covers almost 100 000 km^2 in Brazil alone (fig. 9). The elevation of the Pantanal Basin is generally less than 200 m; relief is generally low. Pantanal Basin morphology consists of a complex network of old meanders, abandoned channels, depressions, lakes, swamps, low ridges, and isolated highlands. The northern end of the basin has undergone tectonic subsidence, whereas the southern end has been uplifted.

Geomorphology

Various highland geomorphic provinces surround the Pantanal Basin. To the east, step, plateau, and cuesta landforms rise 200 to 800 m. On these eastern slopes, the Devonian sandstone of the western Paraná sedimentary basin contributes coarse sand to large alluvial cones filling the eastern Pantanal Basin. North of the basin lies the high Paraguay peneplain, a well-developed erosion surface that cuts metasedimentary quartzite and phyllite at an elevation of approximately 250 m. Drainage has incised this surface to depths of 50 m. The high Paraguay peneplain was rejuvenated in the Tertiary, before Pantanal Basin deposition. South of the Pantanal Basin, Ordovician dolomite units form the Serra da Bodoquena, a range of hills 600 m high linking the Paraná Plateau to the Chiquitos Mountains of the Bolivian Chaco. West of the Pantanal Basin, a westward-dipping erosion surface cuts crystalline rocks. This surface is surrounded by higher, residual quartzite hills.

Pantanal Basin lowlands enclose isolated highlands that rise 30 to 100 m above the surrounding plain. These are erosional remnants from late Tertiary, Andean orogenic fault blocks. They are composed of Paleozoic and Precambrian rocks.

The alluvial deposits of the Pantanal Basin are almost 100 m thick. In the tectonically uplifted southern part of the basin, the deposits are only approximately 36 m thick. These deposits are mostly coarse sand but include fine sand, silt, and clay. In the eastern part of the basin, coarse-grained sand is derived from Devonian sandstone units. Toward the center of the basin, the sand is typically fine grained. The upper 10 to 12 m of the alluvial deposits cover an iron duricrust, which probably formed in the middle Quaternary. The sedimentary section as a whole is permeable, and both alluvial deposits and basement rock yield abundant ground water.

The Pantanal Basin can be divided into hydrogeomorphic regions on the basis of the extent and frequency of flooding. The two principal hydrogeomorphic types are permanently flooded land and intermittently flooded land. Some higher landforms are rarely flooded.

Typical Pantanal Basin topography consists of alternating depressions and slightly higher ground. These depressions (*baias*) are circular, elliptical, and crescentic in plan view, and may be hundreds of meters to tens of kilometers long. The depressions probably result from abandoned (Pleistocene) meanders and channels, possibly augmented by differential subsidence of compacting alluvium. The depressions are often separated from one another by belts of higher ground typically 1 to 2 km long and 5 to 10 m higher than intervening *baias*. Many of these ridges are natural levee deposits along abandoned channels. The ridges are called *cordilheiras* (mountain ranges) because, despite their low relief, they rarely flood. The *cordilheiras* support subxerophytic vegetation and provide shelter for cattle during the flood season.

Lakes and swamps occupy the *baias*, and many of these support vegetation. During the dry season, many of the *baias* are not interconnected by surface drainage, but during the flood season, water flows between them through a network of generally poorly formed, vegetated channels. Depending on relative flood stages, these channels carry flow in either direction. Two principal types of drainage paths connect *baias*. *Vazantes* are broad, vegetated troughs without a well-formed channel. They may be kilometers wide, and are probably abandoned river channels. Their gradients are very low, typically comparable to the slope of the surrounding plain. *Corixos* are well-developed channels. These may contain perennial or intermittent flow. They include reactivated abandoned channels and new channels that have

formed within *vazantes*. Where the *corixo* is an abandoned channel, it will have the slope and pattern, usually meandering, of that channel. *Corixos* that have developed within *vazantes* are usually straighter and steeper than those that have reactivated prior channels. Flow in *vazantes* and *corixos* typically reverses with the rise and fall of floods.

The Paraguay River crosses the Pantanal Basin in a migrating, sinuous channel with many alluvial islands. Natural levees along the channel rise above the surrounding flood plain. These marginal sandy dikes are only 1 to 2 m high, but they prevent many tributary streams from entering the river directly. Many tributaries flow through long reaches parallel to the river before entering it. The Paraguay River is 1270 km long, with an average slope of 3.3 cm/km. At Corumbá Harbor, the Pantanal Basin is 110 m above sea level and 2000 km from the Paraná River mouth.

The gradient of the Paraguay River is low and decreases downstream. From Cáceres to Pôrto Conceição, the average river gradient is 6.1 cm/km; from Pôrto Conceição to Forte Coimbra, the gradient ranges from 2.6 to 2.0 cm/km; and downstream of Forte Coimbra, the gradient varies from 1.75 to 1.03 cm/km. The gradients of tributary rivers vary depending on the morphology of their basins. Tributaries that enter the Pantanal Basin from the eastern highlands have steep gradients. The mean gradient of the São Lourenço River is 17.6 cm/km. Between São José do Borireu and the Cuiabá River, the gradient of the São Lourenço River is 21.2 cm/km. The Taquari River has a gradient of 26.7 cm/km at Pôrto Rolon. The Cuiabá River, which enters the Pantanal Basin from the lower highlands to the north, has an average gradient of 10.2 cm/km between Cuiabá and Retiro Biquacal. The Aquidauana and Miranda Rivers, which enter the Pantanal Basin from the southeast, have gradients of 6.6 cm/km in the lowlands. This gradient is greater than the general flood-plain slope in the region, which has been affected by tectonic uplift. These rivers are sinuous but carry a large sediment load of sand.

General Hydrology

The eastern tributaries of the Paraguay River contribute much of their sandy sediment load to large alluvial cones that are common along the eastern edge of the Pantanal Basin. These rivers have broad, shallow cross sections and beds of migrating sand. So much of the bed load of the eastern tributary rivers is deposited on the alluvial cones that little reaches the Paraguay River. If much of this sand reached the Paraguay River, its channel might be braided rather than meandering.

The margins of the Pantanal Basin are subject to floods from highland terrains. Much of the runoff from highland floods infiltrates the alluvial deposits rimming the basin, and does not penetrate the basin as surface runoff. High evapotranspiration during the dry season depletes soil moisture; thus, almost all of the rainfall of the first months of the rainy season is absorbed. During this interval, only high-intensity storms create significant flooding along streams. Ground-water flow penetrates far into the basin; interflow surfaces near the base of scarps and alluvial cones along the basin margins. Because of the prominence of subsurface drainage in this region, few well-formed streams are found in the basin close to the highlands. Interflow provides water to *baias* and *vazantes*.

Pardé (ref. 21) classified the Paraguay River as a river of complex transitory regime because of the successive regime changes along its course. In the upper portions of the river basin, the regime is tropical with maximum discharge in February and low flows in July. Precipitation in this region may exceed 200 cm each year, and streamflow pattern coincides with the seasonal precipitation pattern. At Corumbá, the high-water stage occurs in June, and the low stage occurs in December and January. At Asunción, two high-water stages occur annually. One flood period occurs between February and April; the other occurs in May and June. The peak discharge of the Paraguay River occurs during the dry season because physiographic factors control the river stage. During the wet season, floodwaters are lost to the extensive flood plains of the Pantanal Basin. During the dry season, river floodwater and other subsurface and surface water, which has accumulated in the basin, flows slowly into the Paraguay River. The cumulative flow produces the highest stages on the river.

Pantanal Basin morphology not only affects the occurrence of peak stages along its rivers but also

influences seasonal flow recession because rivers in the basin receive discharge from different sources. The Paraguay River at Pôrto São Francisco and the Cuiabá River at Cuiabá derive a large portion of their discharge from accumulated water in swamps (pantanals) and lakes. The Paraguay and Cuiabá Rivers lose 49.8 percent and 34.5 percent, respectively, of their initial discharges in the 90 days preceding their minimum discharges. These rivers also receive substantial ground-water discharge. Other rivers, including Taquari, Coxim, Piquiri, and São Jerônimo, are primarily base-flow streams fed by subsurface water drained from highlands. The Taquari and Piquiri Rivers lose 24.5 and 28 percent, respectively, of their initial discharges in the 90 days preceding their minimum discharges.

Evaporation, transpiration, infiltration, and overflow cause the Paraguay and Cuiabá Rivers to lose discharge progressively downstream. Intermittent tributary subsurface discharge does not completely compensate for this loss. At the northern end of the Pantanal Basin, the specific discharges of the Paraguay River at Cáceres and of the Cuiabá River at Auaba, averaged over the entire drainage area, are approximately 8 to 10 liters sec^{-1} km^{-2} (ref. 21). To the south at Puerto Sastre, the specific discharge is only 6.7 liters sec^{-1} km^{-2}. In the relatively dry years of 1968 to 1971, only 16 to 24 percent of the rainfall on the 33 860 km^2 of the Paraguay Basin upstream of Barra do Bugres left the basin as river discharge. Discharge losses upstream of Puerto Sastre range from 1 to 5 liters sec^{-1} km^{-2}. The total loss is greater in wet years than in dry years because losses increase with increasing overflow.

The low slope of the Paraguay River and of its lowland tributaries creates a variety of flood phenomena. These depend on the relative stages of the Paraguay River and its tributaries. Relative flood crests along the Paraguay River extend far upstream along tributary rivers, and tributary flood waves similarly affect the Paraguay River. This produces backwater, still-standing floods called *remansos*. Increasing discharges upstream on one river may not produce significant flood stages downstream on the same river because of the distribution of floodwater upstream along other rivers. These rivers have flood crests, although their discharges do not increase, and negative discharge may occur. Thus, it is possible for the peak discharge and peak stage effects of a single flood to occur along several different rivers.

Although a *remanso* may create very low or even negative flow velocities along rivers in the Pantanal Basin, river velocities are not generally low. The mean maximum velocities of the Paraguay River at a number of cross sections throughout its length range from 0.46 to 0.97 m/sec.

Despite the seasonal and spatial variation of discharge within the Pantanal Basin, the variability of discharge at a given station along the Paraguay River is not great. For example, the minimum recorded discharge at Puerto Sastre is 3 liters sec^{-1} km^{-2}. The regularity of the Paraguay River discharge is attributable to the moderating effect of Pantanal Basin morphology. Flood waves entering the basin from surrounding highlands are reduced by infiltration into the thick sedimentary deposits rimming the basin. Much of this water is discharged as base flow to the major rivers of the region. Some of the absorbed highland floodwater emerges onto the Pantanal Basin surface, where it is stored for possible slow release through the poorly developed drainage network of the Pantanal Basin.

Flood crests along the major rivers are dissipated by flood-plain storage of overflow discharges. The low relief and numerous depressions of the Pantanal alluvial surface provide a vast storage area for floodwaters. Water stored on the Pantanal surface is returned slowly to the rivers through a poorly developed drainage network of *vazantes* and *corixos*. *Corixo* flow velocities are typically only 5 to 20 cm/sec. Flow in *vazantes* is even slower, typically 1 to 10 cm/sec: Flow across the Pantanal surface is inhibited by poor channel form, low gradients, and obstructing vegetation. Floodwater return to the major rivers is also retarded by natural levees along the rivers. The levees force ponding of small tributaries until the water level rises sufficiently to breach the levees. Water stored on the Pantanal surface is subject to infiltration and evapotranspiration, which further reduce the amount of floodwater available to the rivers.

Suspended-sediment data were collected at

Pôrto Esperança during 1964 and 1965. These data suggest that suspended-sediment concentration in the Paraguay River depends not only on the main river discharge but also on the discharge of tributary rivers. High concentrations of suspended sediment in February, March, July, August, and September indicate that the tributaries from the west and southeast (such as the Miranda and Taquari Rivers) contribute more to the suspended-sediment concentration of the Paraguay River than do the principal northern and eastern tributaries, which lose much of their sediment to alluvial cones.

Apollo-Soyuz Photographs

Three sites along the Paraguay River were photographed during the ASTP mission (photographs AST-23-1923 (fig. 10(a)), AST-23-1920 (fig. 11(a)), and AST-23-1917 (fig. 12(a)). Maps of these sites are presented in figures 10(b), 11(b), and 12(b). Large-scale map data were available for the photographed area within Brazil. These were not available for the photographed area west of the Paraguay River, including Bolivia and Paraguay. Thus, maps constructed from ASTP photographs represent a significant extrapolation of existing morphologic and phytological-ecological data.

The northernmost portion of the Paraguay River photographed during the ASTP mission is the region around Bahía Negra (fig. 10(a)). The Brazilian portion of the photographed region is generally swampy and includes many *corixos* and *vazantes*. In the Bolivian portion of the photographed area, abandoned meanders are common. The shape and size of these meanders suggest that they belonged to the Paraguay River rather than to the smaller Rio Negro. The sinuosity of the Paraguay River in this region is 1.4. This value indicates that the channel sediments contain approximately 5 percent silt and clay, and that 11 percent of the total solid-sediment load of the river is bed load (ref. 22). This composition reflects the sandy sediment contribution of tributaries draining the sandstone terrain of the sedimentary Paraná Basin to the east. The portion of the Paraguay River apparent on photograph AST-23-1923 (figs. 10(a) and 10(b)) consists of two reaches of low-sinuosity and small-amplitude meanders, with an intervening reach of high-sinuosity and large-amplitude meanders.

The phytological-ecological environments represented on the maps of this region reflect edaphological-morphological conditions developed on Quaternary fluvial and lacustrine deposits. Three major types of environments can be distinguished. The first environment consists of river flood plains, *vazantes, corixos,* abandoned meanders, lakes, *baias*, and swamps that are perennially wet. In this environment, gramineous-herbaceous vegetation is established on acid, impermeable, sandy-clayey soils. Halophytic vegetation grows in saline, clayey soils that are flooded seasonally but are wet most of the year. Acid, clayey lime soils support gramineous vegetation and thorny bushes (*campo chaqueno*). The second major environment consists of slightly higher terrain that is flooded annually. Under these conditions, alluvial tropical forests grow on acid terrace soils (*bosque de que bracho*). The third major environment consists of the highest, least flooded terrain, including terraces, the natural levees of abandoned channels (*cordilheiras*), and flat watersheds. These features rise 2 to 10 m above the adjacent lowlands. Savanna (*cerrado*) vegetation is typical of the relatively high terrain. A variety of *campo chaqueno* grows in drier areas, but thorny bushes are more prominent than in the annually flooded *campo chaqueno.* A mixed forest (*bosque chaqueno*) grows on flat watersheds with silty lime soils. The lowest areas within the relatively high ground are depressions filled with fine sand. These support a variety of savanna vegetation (*cambara*). These depressions are usually floored with clayey soils that originally supported grasses. Overgrazing has induced the erosion of sand that has collected in the depressions. These general environments persist among the photographed areas, although the prominence of any environment or vegetation type varies from region to region. In the photographed area around Bahía Negra, *campo chaqueno* is prominent on acid lime-clay soils of the lowland, and *bosque chaqueno* is developed on the less frequently flooded, sandy-clay soils of the low terraces between the Paraguay River and the Rio Negro.

The longest ASTP-photographed reach of the Paraguay River centers around Barranco Branco (figs. 11(a) and 11(b)). The river flows through the southern portion of the Brazilian Pantanal Basin within the zone of uplifted fault blocks. The sinuosity of the Paraguay River in this photographed reach is 1.4. Although this sinuosity is similar to that of the river near Bahía Negra, it is lower than the general sinuosity of the Paraguay River in the northern Pantanal Basin. Differences in Paraguay River sinuosity may be attributable to changing tributary sediment contribution and to tectonic influences. In the central portion of the reach shown on frame AST-23-1920, abandoned meanders appear to indicate a prior river course. This apparent prior course has a sinuosity of 2.0. The present channel through this reach has a sinuosity of only 1.1. In a pattern similar to that of the Paraguay River channel apparent on photograph AST-23-1923, the present channel shown on photograph AST-23-1920 has alternating large-meander-amplitude, high-sinuosity reaches, and small-meander-amplitude, low-sinuosity reaches. In response to regional tectonic uplift, the river has cut 1- to 2-m-high terraces (fig. 11(b)).

Overall, the landscape of photograph AST-23-1920 is less swampy than is typical of the Pantanal Basin to the north. This difference is probably because tectonic uplift and river downcutting have generally raised the landscape relative to the regional water table.

Frame AST-23-1917 is the southernmost ASTP photograph of the Paraguay River (fig. 12(a)). This is the shortest reach of the river photographed. The area is also the least flooded of any of those photographed. It coincides with an uplifted fault block that trends east-west across the Paraguay Valley. The sinuosity of the reach shown on this photograph is 1.4. The reach is too short to show a significant variation in pattern along its length. Human settlement is denser in this region than in the others photographed along the Paraguay River. This population density is probably attributable to the relative prominence of higher landforms in the southern Pantanal Basin. The map of this area (fig. 12(b)) was constructed entirely by extrapolation from the other maps because no other data were available for this area.

DISCUSSION OF ENVIRONMENTAL CHANGE

The detailed analysis of ASTP photographs in this report constitutes an environmental reconnaissance. In this section, the consequences of environmental change, both natural and man-induced, are considered. The natural changes were induced by Quaternary climatic oscillations that left their legacy in relict river channels. The man-induced changes are mostly yet to come. Brazil is encouraging its populace to migrate westward into the areas discussed in this report. As new towns and roads are constructed, they will alter water and sediment yields. The new settlers will have to adjust to the flood regimen of the rivers and to any changes that they induce in the activities of the rivers.

Implications for Quaternary Sedimentation Patterns

The differing Amazon Basin channel morphologies have some important implications for Quaternary sedimentation on the Amazon continental margin. Milliman and others (ref. 23) note that during interglacial (high sea level) phases, most of the sediment contributed by the Amazon accumulated along the coastline. The sediment of the full-glacial Amazon, however, was channeled directly to the deep sea. This full-glacial sediment is arkosic and little weathered. Damuth and Fairbridge (ref. 17) speculated that the source of the sands was the Brazilian and Guianan Shields, which are now covered with forest and contribute almost no sediment. Contribution of sediment from these areas would require extensive aridity throughout the Amazon Basin.

Milliman and others (ref. 23) pose a different model for the full-glacial Amazon. They suggest that the Andes tributaries of the Amazon were the source of the arkosic sands that were deposited in the western equatorial Atlantic during glacial times. They further suggest that the eastern slopes of the Andes may have been less favorable to chemical weathering during the full-glacial phase, either because of decreased temperature or



FIGURE 10.—The Paraguay River near Bahía Negra. (a) Photograph (AST-23-1923). (b) Hydrogeomorphic map. Explanation of map units is given immediately following figure 12(b).

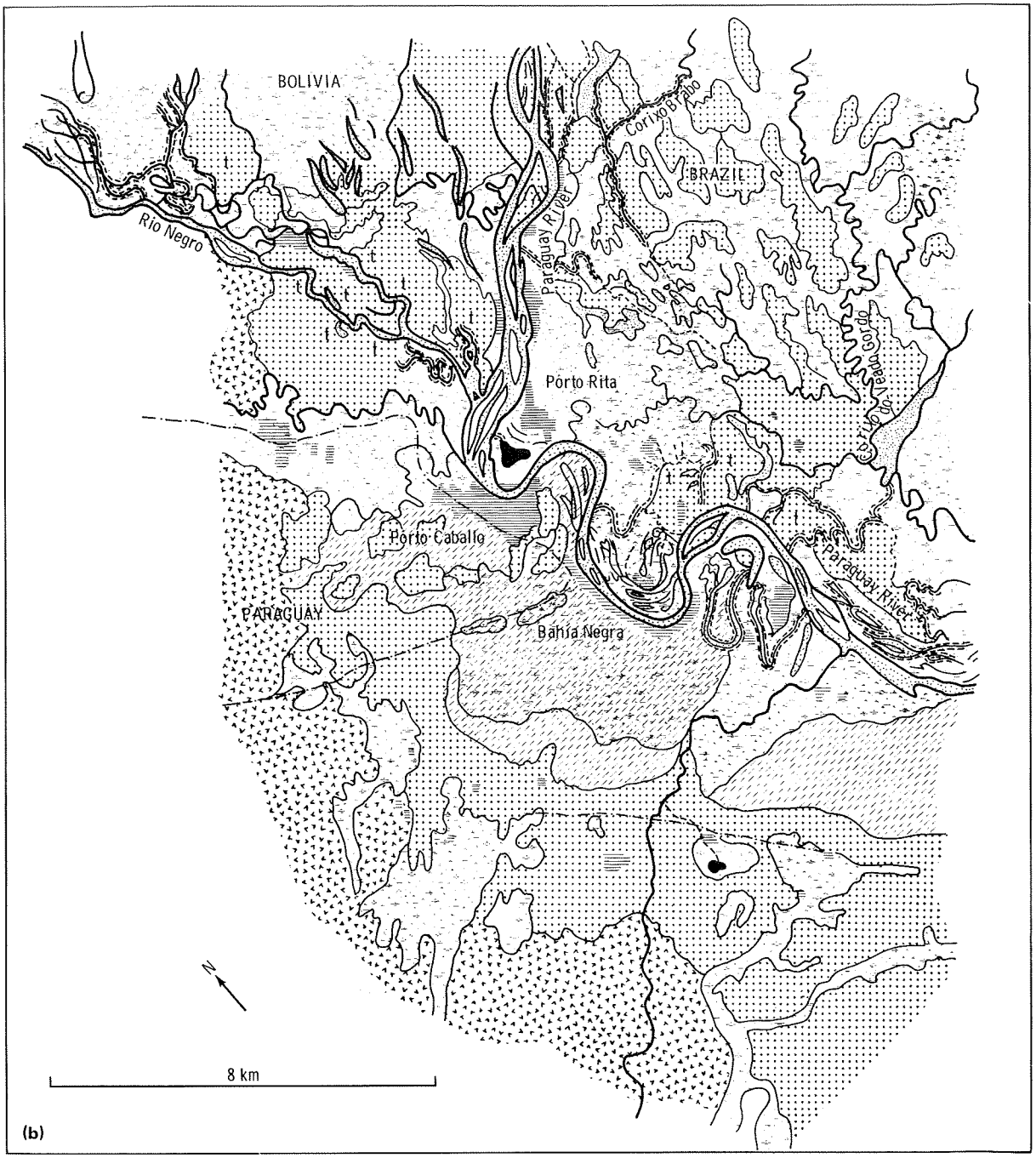


FIGURE 10.—Concluded.

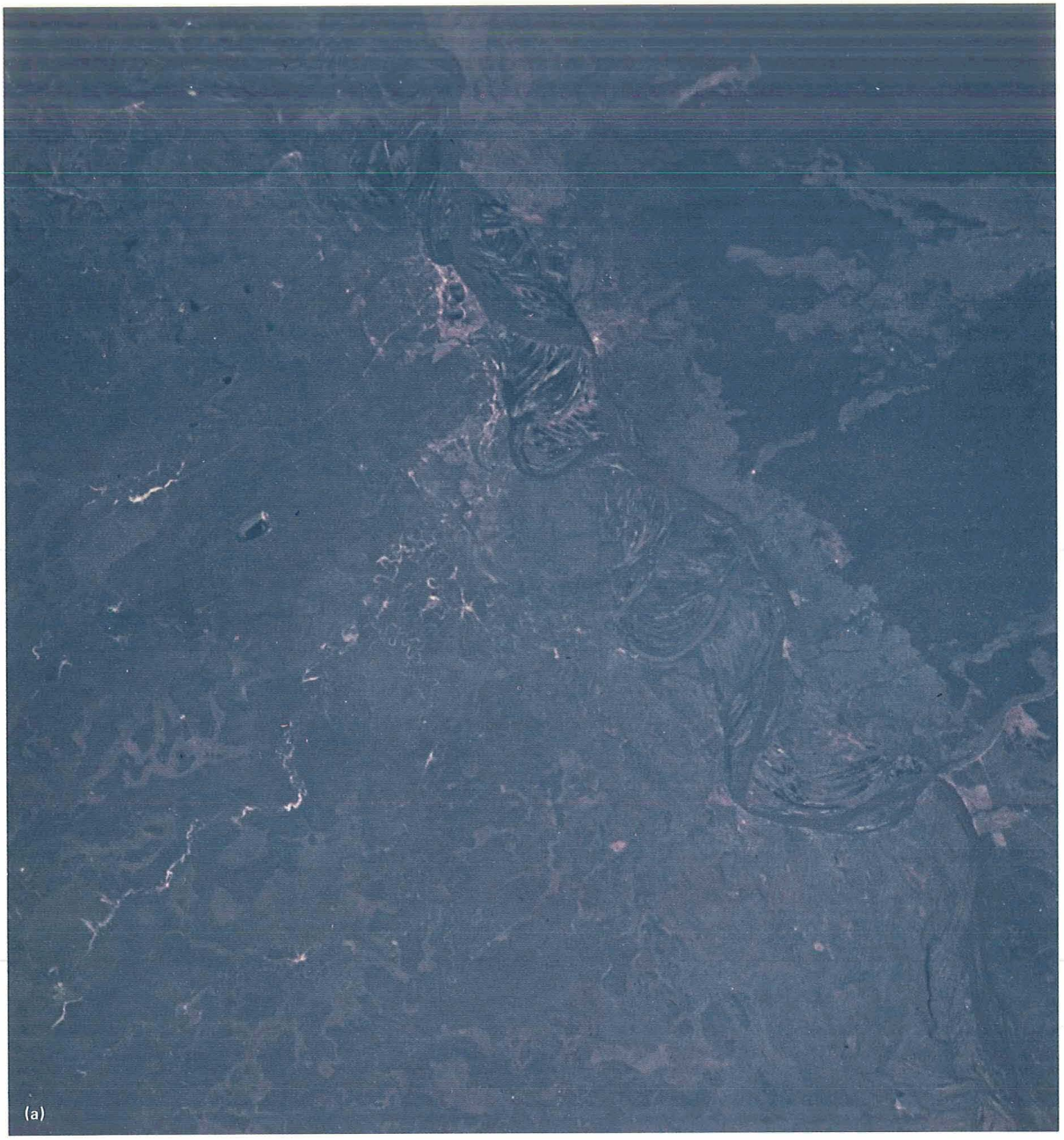
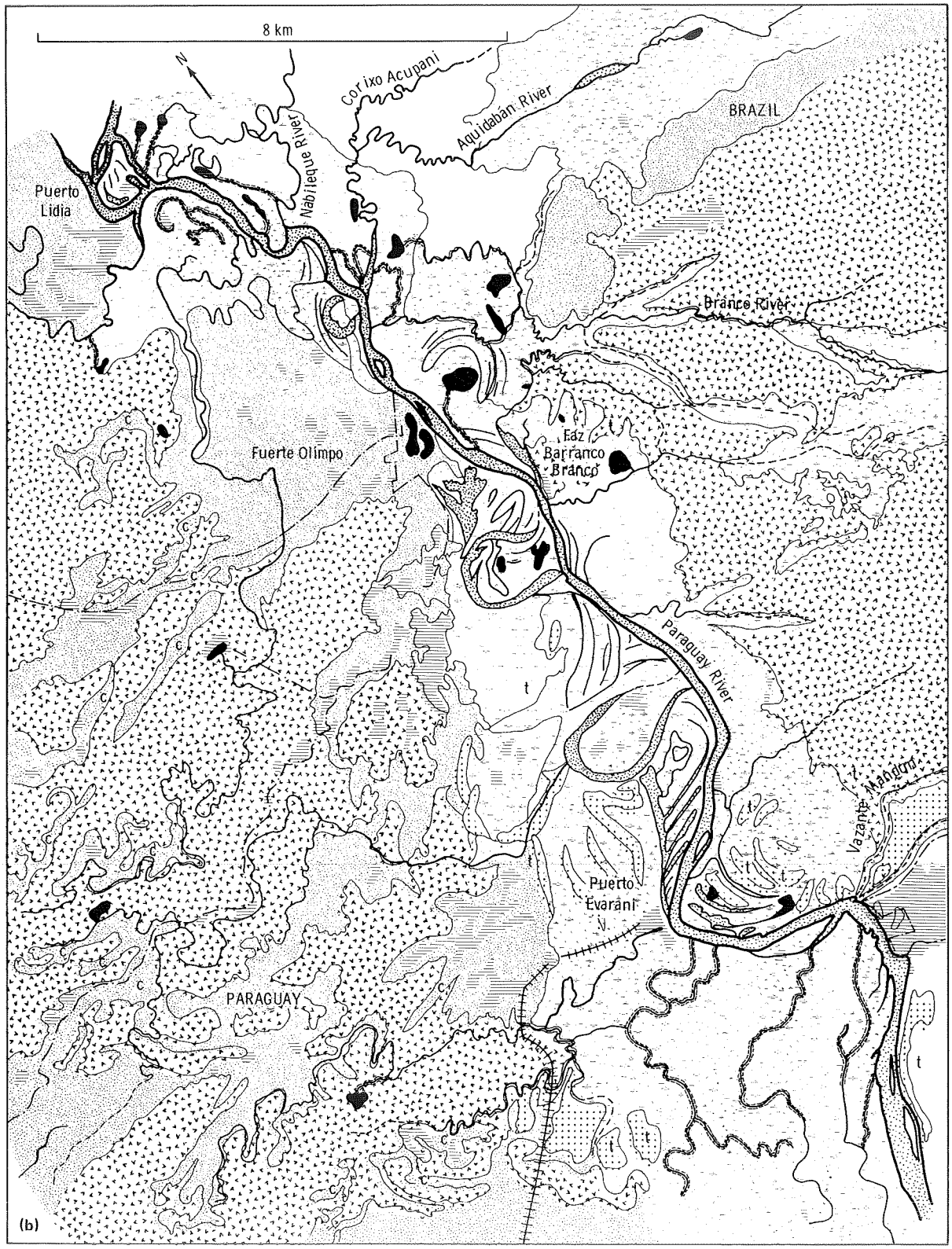


FIGURE 11.—The Paraguay River near Barranco Branco. (a) Photograph (AST-23-1920). (b) Hydrogeomorphic map. Explanation of map units is given immediately following figure 12(b).


8 km
N
Corixo Acupani
Aquidabán River
Nábileque River
BRAZIL
Puerto Lidia
Branco River
Faz Barranco Branco
Fuerte Olimpo
Paraguay River
Vazante Mandiroré
Puerto Evaristo
PARAGUAY
(b)

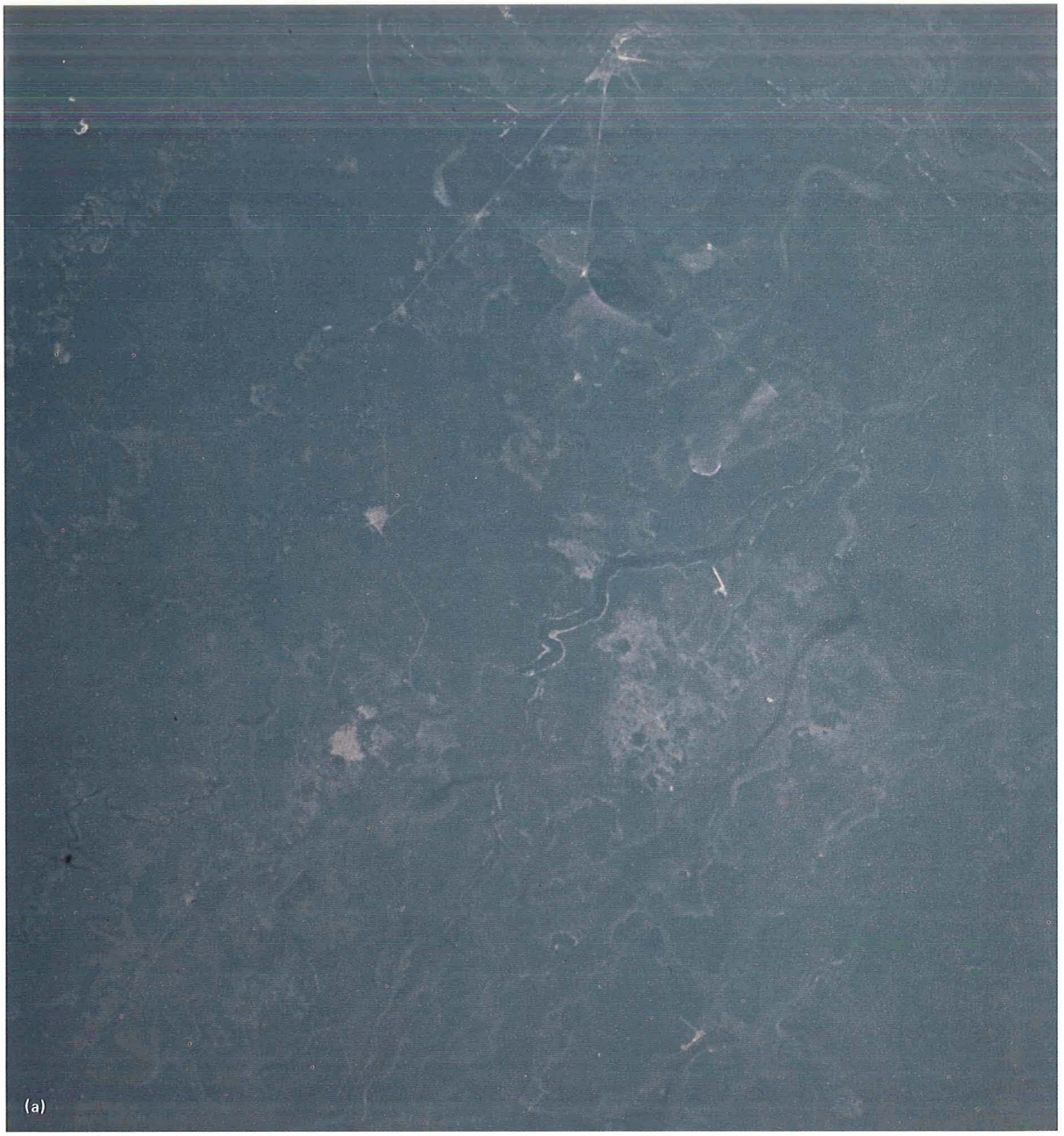


FIGURE 12.—The Paraguay River south of the Pantanal Basin. (a) Photograph (AST-23-1917). (b) Hydrogeomorphic map. Explanation of map units is given immediately following part (b).

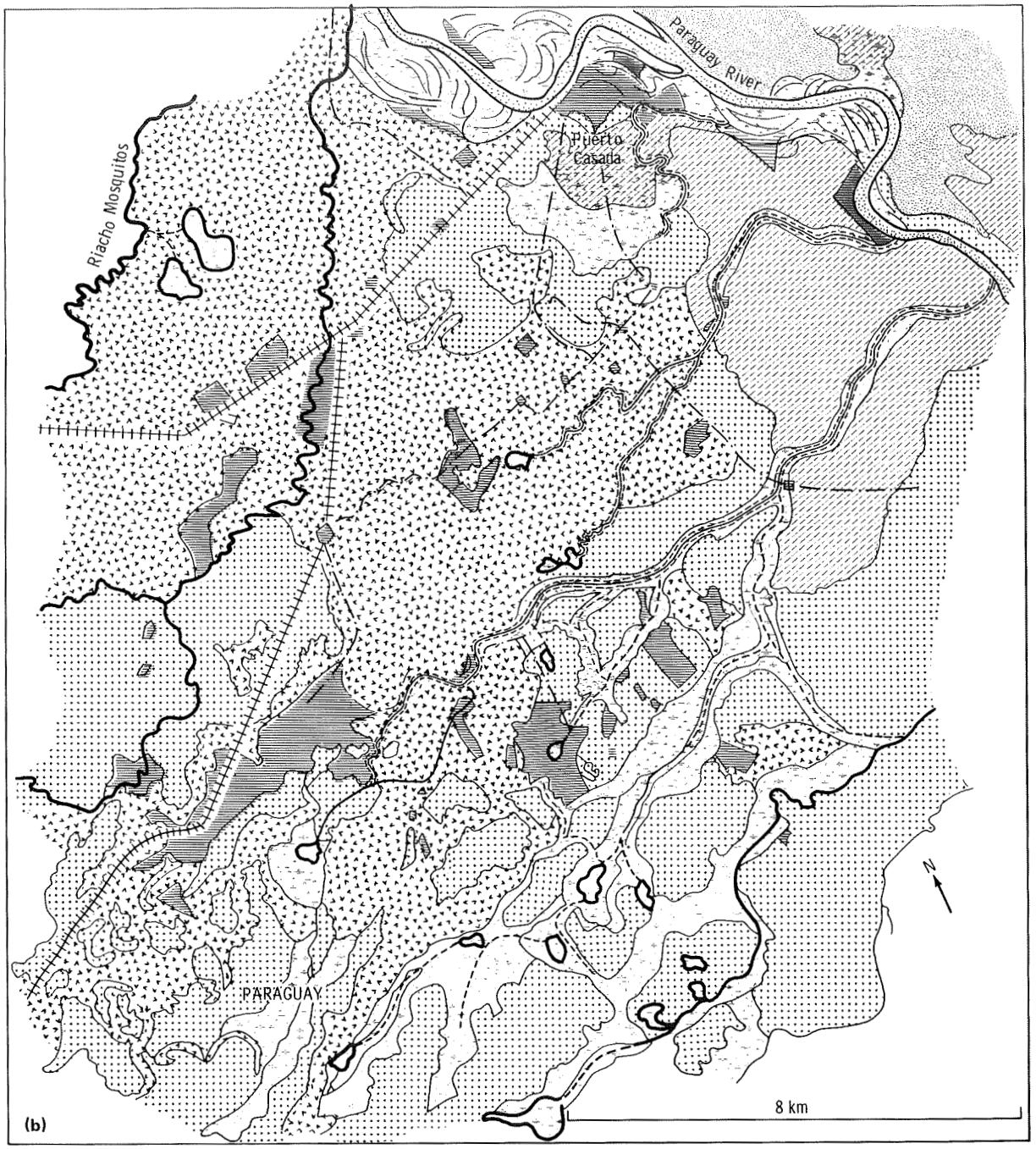


FIGURE 12.—Concluded.

Hydrogeomorphic map units

(figs. 10(b), 11(b), and 12(b))

	Physical environment	Vegetation
Perennially wet or frequently flooded bottomlands	"Baias," small lakes and marshes often located along relict channelways; salty and alkaline soils	Halophytes and sedges
	"Corixos" and "corixoês" (large corixos); sand channelways filled with stagnant water	Gramineous vegetation on channel edges
	"Vazantes," relict channelways temporarily flooded during rainy season	"Campos" (meadows) of gramineous vegetation and sparse savanna trees
	Other perennially wet bottomlands; clay soils	"Campos" (meadows) of gramineous vegetation
Seasonally flooded zones	Lower sand-clay terraces and abandoned levees; acid soils	Campo chaqueño: mixed gramma grass and thorny bushes
	Lower silty-clay terraces and abandoned levees	Basque chaqueño: mixed tropical forest and taller thorny trees
	Lower sand-clay terraces obscured by dense forest	Tropical forest or dense thorny forest
More rarely flooded zones (2 to 10 m above bottomlands)	Higher sandy terraces and cordilheiras (abandoned levees). The cordilheiras (indicated by C) are most safe from flooding	Cerrado (savanna)
	"Cambará" parks, relict sand-filled depressions that are perennially wet spots on the terraces	Savanna dominated by cambará trees
	t Terraces	
Other features	Rivers	Abandoned meanders
	Roads	Railroads
	Areas of cultural activity including urban and agricultural features	

because of aridity. The channel pattern studies presented in this report support the latter interpretation. The margins of the Amazon Basin almost certainly became drier during full-glacial phases. However, the interior tropical rain-forest zone probably remained as such during the full-glacial phase. In the investigation reported here, no evidence of low-sinuosity relict channels for rain-forest rivers like the Juruá was found. The Solimões, in contrast, may have undergone a slight expansion in discharge since the early Holocene. During the Wisconsinan, this and other Andes tributaries like the Japurá probably contributed the arkosic sediment that moved through the lower reaches of the Amazon to the sea. It is possible that relict, arid-phase alluvium is preserved beneath the lateritic soil profiles of the *terra firme*. Dense forest cover over these regions

prevented an assessment of their character from ASTP photographs.

No appreciable photographic evidence was found for Quaternary alterations in water and sediment discharges to the rivers in the west-central Amazon Basin that had been expected from the descriptions of Amazon Basin margins by Garner (ref. 16), Damuth and Fairbridge (ref. 17), and Bigarella and others (ref. 24). The Solimões River may have had a slightly reduced discharge prior to its present phase, but paleochannel morphology of its flood plain suggests a stream of approximately the same discharge as today. From ASTP data, it is concluded that the tropical rain-forest climatic zone did not disappear in full-glacial periods as suggested by Damuth and Fairbridge (ref. 17). Instead, relative aridity on the Amazon Basin margins may have enhanced the contributions of coarse sediment to Andean streams (e.g., Japurá River) while not affecting the tropical rain-forest streams (e.g., Juruá River). The major trunk stream, the Amazon, either did not undergo major morphological change or does not show that change on ASTP photographs. The possibility of complex sea-level controls on the flood plain is also unresolved. Of course, times of low sea level would cause downstream incision of the Amazon system at the precise time when aridity at the basin margins was introducing the coarse sediment. The coarse Wisconsinan sediment of the Amazon is probably buried beneath its Holocene flood plain.

Changing Land Use and River Morphology

Inhabitants of the Amazon Basin must contend with two general environments: (1) the *terras firmes* (uplands and terraces above the flood-plain margins) and (2) the *varzeas* (flood plains) (ref. 9). Both environments are easily recognized on ASTP photographs (fig. 5(a)).

The *varzeas* contain most of the potentially arable land in the Amazon Basin. Unlike the *terras firmes*, which are underlain by deeply leached laterites, the *varzeas* have relatively fertile soils. Overbank sedimentation along the Amazon and its mountain tributaries introduces sediment containing a variety of nutrients. Sediments in the smaller tributaries heading in nonmountain areas are depleted in nutrients, and the rivers are impoverished in aquatic life (ref. 9).

Farmers cultivating the *varzeas* will have to contend with the dynamic processes that occur in those areas. These include overbank deposition building natural levees (*restingas*), bank caving associated with discharge changes (*terras caidas*), and the development of back swamps (*igapos*). The river patterns visible on ASTP imagery imply differing degrees of river stability. The anastomosing Solimões River is remarkably stable. The alluvial islands split the river into a master channel and one or more secondary channels, called *paranas*. These accommodate discharge variations as does the back-swamp area flooded through natural breaks in the levees. In contrast to the relatively low-sinuosity Solimões, the high-sinuosity tropical tributaries, like the Juruá, migrate rapidly as evidenced by their numerous oxbow lakes and avulsions (figs. 5(a) and 5(b)).

The *varzeas* are important in damping flood peaks by collecting and temporarily storing overbank flows. This is the main reason for the great similarity in annual water-level fluctuations from maximum to minimum flow years (fig. 6). The great variety of lakes and depressions that were mapped from ASTP photographs are very important in this process. The most important types include the following: (1) clear lakes marginal to the flood plain and extending into the *terras firmes* caused by the damming of tributaries by mainstream deposition (termed *cienagas* in Colombia by Van Es and others (ref. 25)) and (2) a variety of *varzea* lakes formed as abandoned meander loops (oxbows) and irregular depressions (possibly related to subsidence). A complex network of second-order channels (called *vazantes* and *corixos* in the Pantanal) links these lakes and depressions to the main (first order) channel. Water flows out of the main channel into this network during rising flood stage, filling the depressions and inundating the entire back swamp during larger floods. During flood recession on the main stream, flow direction reverses in the second-order channels slowly carrying water from the *varzea* back to the river. A similar effect is produced by the *vazantes* and *corixos* of the Pantanal.

The dynamic nature of the *varzeas* as flood storage basins poses a dilemma for their possible agricultural or other economic development. Present land use is based on the variation in river flow. Expansion of development on the flood plain would have to involve protection of parts of the *varzea* from its normal flooding cycle. Such protection might involve construction of drainage ditches or dikes to divert or hold back floodwaters. In addition to the potential ecological damage caused by such manmade drainage ditches and dikes, the presence of restricted, small areas for temporary storage of floodwater on the natural *varzea* could increase flooding downstream. Levee construction on the Mississippi River has produced precisely this change (ref. 26).

A more imminent change in the rivers is posed by the projected highway network. Sternberg (ref. 9) notes that current plans call for 17 855 km of trunk roads. Adjacent to these roads, strips of land cleared for agriculture and urbanization will promote changes in the runoff and sediment yields into the river systems. Eckholm (ref. 27) notes that migrant farmers are already moving from the coast to accept 100-hm^2 plots of land under government jurisdiction adjacent to the new roads. Data from the Amazon cited previously show that a broad range of river morphologies is delicately adjusted to different environmental parameters, especially discharge and sediment type. The clearing of large areas of forest for transport or agriculture can only lead to an upset in this balance with attendant downstream changes. Moreover, this change will mainly affect *varzeas*, which constitute all of the 4 percent of Amazon Basin land estimated to be potentially capable of high agricultural productivity (ref. 27).

The streams most likely to respond drastically to man-induced change are the small, high-sinuosity, wholly tropical rivers like the Juruá. The larger, low-sinuosity streams like the Solimões and Japurá are transenvironmental and appear to have undergone much less natural adjustment on their Holocene flood plains than have these tropical rivers. The marked variations in sinuosity of the lower Juruá (figs. 5(a) and 5(b)) point to a critical reach that could be easily affected by construction projects upstream in the basin.

Artificial straightening of rivers for navigation and hydroelectric development are additional actions that could affect the rivers studied in this report. Navigational modification is unlikely considering the trend to abandon the traditional waterborne transport of the region in favor of highways (ref. 9). Hydroelectric development is a possibility for the upstream portions of rivers in the southern Amazon Basin. This resource is immense and is being considered to support mining and railroads in the area (ref. 9, pp. 60-61). Dams on these rivers are likely to produce immense downstream changes through their alteration of flow variability and sediment load. A dam on a Japurá-type stream, for example, would result in gradual adjustment of reaches downstream to a Juruá-type stream. Thus, the variability of channel morphologies revealed regionally on ASTP photographs provides a very general guide to the fluvial changes that can be induced temporally by highways, land clearance, dams, and other human works.

CONCLUSIONS

Data from the ASTP Earth Observations and Photography Experiment were found useful in providing a variety of fluvial morphological measurements. In the Amazon Basin, the authors were able to distinguish three major river types on the basis of sinuosity P and other properties. Representatives of each type include the Solimões with sinuosity increasing downstream from $P = 1.2$ to $P = 1.5$, the Japurá ($P = 1.1$) with headwaters in the Andes, and the Juruá ($P = 2.5+$) with headwaters in the Amazon Basin lowlands. Channel widths and meander wavelengths were also easily determined.

Various empirical formulas were evaluated for estimating the hydrologic properties of Amazon Basin rivers. Formulas based on morphology alone (e.g., eqs. (3) and (4)) proved to be more successful than formulas that incorporated esti-

mates of sediment type (e.g., eqs. (2) and (5)). From Carlston's equation (eq. (4)), a mean annual discharge of 22 650 m^3/sec (800 000 ft^3/sec) was predicted for the Solimões at Fonte Boa. The reason for poorer results with Schumm's equations (eqs. (2) and (5)) probably arises from the complex nature of bank resistance in tropical rivers. Besides sediment type, these streams have banks that are indurated with clay and stabilized by the roots of tropical vegetation.

The study revealed the lack of precise understanding of regime behavior in tropical rivers. Much more work has been done on rivers of humid-temperate and semiarid regions. Results presented here show that low-sinuosity Amazon Basin streams (e.g., Japurá and Solimões) are much more dominated by relatively fine-grained sediment than are streams of equivalent sinuosity described for semiarid regions by Schumm. Vegetation appears to be an important, though incompletely understood, factor in bank stabilization in these rivers.

In the Pantanal Basin (Paraguay River), the authors considered the detailed interaction of many environmental variables. In addition to hydrology, the authors examined weathering characteristics, vegetation types and densities, climatic factors, and terrain roughness and relief. Hydrogeomorphic maps produced from the ASTP photographs show an amazing amount of detail. Such maps can be used for (1) inventorying land resources of the region, (2) guiding future land use of the area, and (3) monitoring land use changes as the region is developed.

An important result implied by this analysis, but requiring verification in the field, is that a relatively wide range of river morphological types can be produced in this region by changing a relatively small range of environmental parameters (sediment type, discharge variations, and vegetation). This result is especially critical for the rivers with drainages wholly in the rainforest zone (e.g., the Juruá River). Parts of the projected Amazonia highway network extend across the headwaters of the Juruá River and similar streams. Land cleared for agricultural development around this highway system could pose a threat to the valuable *varzea* soils of these streams by altering the fluvial regime.

ACKNOWLEDGMENTS

The work was performed under Smithsonian Institution Grant PC6-22305 as a subcontract of NASA Contract NAS9-13831.

REFERENCES

1. Baker, Victor R.; Holz, Robert K; et al.: Stream Network Analysis and Geomorphic Flood Plain Mapping From Orbital and Suborbital Remote Sensing Imagery—Application to Flood Hazard Studies in Central Texas, Final Report. NASA CR-144354, 1975.

2. Gibbs, Ronald J.: The Geochemistry of the Amazon River System: Part 1, The Factors That Control the Salinity and the Composition and Concentration of the Suspended Solids. Bull. Geol. Soc. America, vol. 78, 1967, pp. 1203-1232.

3. Oltman, R. E.; Sternberg, H. O'R.; Ames, F. C.; and Davis, L. C., Jr.: Amazon River Investigations, Reconnaissance Measurements of July 1963. U.S. Geol. Survey Circular 486, 1964.

4. Jenks, William J., ed.: Handbook of South American Geology: An Explanation of the Geologic Map of South America. Mem. Geol. Soc. America, Memoir 65, 1956.

5. Guerra, A. T., compiler: Geografia do Brasil. Grande Regiao Norte: Instituto Brasileiro de Geografia e Estatistica (Rio de Janeiro), 1959.

6. Schumm, S. A.: Sinuosity of Alluvial Channels on the Great Plains. Bull. Geol. Soc. America, vol. 74, Sept. 1963, pp. 1089-1100.

7. Schumm, S. A.: The Shape of Alluvial Channels in Relation to Sediment Type. U.S. Geol. Survey Prof. Paper 352-B, 1960, pp. 17-30.

8. Savat, J. L.: Some Morphological and Hydraulic Characteristics of River Patterns in the Zaire Basin. Catena, vol. 2, 1975, pp. 161-180.

9. Sternberg, Hildegard O'Reilly: The Amazon River of Brazil. Franz Steiner Verlag GmbH (Wiesbaden), 1975.

10. Leopold, L. B.; and Maddock, Thomas, Jr.: The Hydraulic Geometry of Stream Channels and Some Physiographic Implications. U.S. Geol. Survey Prof. Paper 252, 1953.

11. Schumm, S. A.: River Adjustment to Altered Hydrologic Regimen, Murrumbidgee River and Paleochannels, Australia. U.S. Geol. Survey Prof. Paper 598, 1968.

12. Harvey, A. M.: Channel Capacity and the Adjustment of Streams to Hydrologic Regime. J. Hydrology, vol. 8, no. 1, May 1969, pp. 82-98.

13. Dury, G. H.: Theoretical Implications of Underfit Streams. U.S. Geol. Survey Prof. Paper 452-C, 1965.

14. Carlston, Charles W.: The Relation of Free Meander Geometry to Stream Discharge and Its Geomorphic Implications. American J. Sci., vol. 263, Dec. 1965, pp. 864-885.

15. Schumm, Stanley A.: River Metamorphosis. J. Hydraulics Div., Proc. American Soc. Civil Engrs., HY 1, 1969, pp. 255-273.

16. Garner, H. F.: The Origin of Landscapes; A Synthesis of Geomorphology. Oxford University Press (New York), 1974.

17. Damuth, John E.; and Fairbridge, Rhodes W.: Equatorial Atlantic Deep-Sea Arkosic Sands and Ice-Age Aridity in Tropical South America. Bull. Geol. Soc. America, vol. 81, 1970, pp. 189-206.

18. Broecker, W. S.; Kulp, J. L.; and Tucek, C. S.: Lamont Natural Radiocarbon Measurements III. Science, vol. 124, no. 3213, 1956, pp. 154-165.

19. Brice, James: Meandering Pattern of the White River in Indiana — An Analysis. Fluvial Geomorphology, Proceedings of the Fourth Annual Geomorphology Symposium, Marie Morisawa, ed. Publications in Geomorphology, State Univ. of New York at Binghamton, 1973, pp. 178-200.

20. Gupta, A.; and Fox, H.: Effects of High-Magnitude Floods on Channel Form; A Case Study in Maryland Piedmont. Water Resources Res., vol. 10, no. 3, 1974, pp. 499-509.

21. Pardé, Maurice: Fleuves et Rivieres. Librairie Armand Colin (Paris), 1964.

22. Schumm, S. A.: Fluvial Geomorphology: Channel Adjustment and River Metamorphosis. River Mechanics, Hsieh Wen Shen, ed. and publisher, Fort Collins, Colo., vol. 1, 1971, pp. 5.1-5.22.

23. Milliman, John D.; Summerhayes, Colin P.; and Barretto, Henyo T.: Quaternary Sedimentation on the Amazon Continental Margin: A Model. Bull. Geol. Soc. America, vol. 86, May 1975, pp. 610-614.

24. Bigarella, J. J.; Mousinho, M. R.; and Da Silva, J. X.: Processes and Environments of the Brazilian Quaternary. Cold Climate Processes and Environments, VII INQUA Conf. Symp. (Fairbanks, Alaska), Universidade de Paraná (Curitiba, Brazil), 1965.

25. Van Es, Eduard; Gomez, Hernán; and Soeters, Robert: An Inundation Study of the Lower Magdalena-Cauca River Basin. Proceedings NASA Earth Resources Survey Symposium, NASA TM X-58168, 1975, pp. 2295-2297.

26. Belt, C. B., Jr.: The 1973 Flood and Man's Construction of the Mississippi River. Science, vol. 189, no. 4204, 1975, pp. 681-684.

27. Eckholm, Erik P.: Losing Ground: Environmental Stress and World Food Prospects. W. W. Norton & Co. (New York), 1976.

Snow Hydrology Studies

M. D. Smallwood,[a] C. J. Bowley,[a] and J. C. Barnes[a]

ABSTRACT

One of the objectives of the Earth Observations and Photography Experiment of the Apollo-Soyuz Test Project (ASTP) was to observe and photograph snow cover in specified areas, primarily in the northwestern United States and Canada. To this end, ASTP crewmen were able to obtain high-quality color photographs of snow cover on the Cascades and Olympic Mountains in Washington State, and on the Canadian Rockies in British Columbia and Alberta. The crewmen were also able to observe and photograph snow cover in the Chilean Andes and in the Southern Alps of New Zealand.

The results of the experiment substantiate the earlier results of the Skylab 4 Visual Observations Project by demonstrating that astronauts can make unique observations compared with those obtained by unmanned satellite systems. The most accurate snowline determination was made using the ASTP photographs taken with the 250-mm lens; and the availability of color, stereo photography greatly facilitated the interpretation of the snow-cover extent, particularly with regard to delineating the very irregular snowline that is characteristic of the summer season. The photographs analyzed revealed a tendency for the snowline elevations to be lower in the areas surrounding the permanent snowfields and glaciers than in areas of seasonal snowpack.

[a]Environmental Research and Technology, Inc., Concord, Massachusetts.

INTRODUCTION

Purpose of ASTP Study

The Earth Observations and Photography Experiment of the Apollo-Soyuz Test Project (ASTP) provided an opportunity to continue investigations on the use of spacecraft data in mapping the Earth's snow cover. One of the objectives of the experiment, therefore, was for the crewmen to observe and photograph various snow-covered areas. The late July time of the mission limited northern-hemisphere snow observations to the higher-elevation mountain ranges in Washington State and to the Canadian Rockies. However, it was possible for the crewmen to observe and photograph snow cover during the southern-hemisphere winter season.

The ASTP data sample analyzed in this report consisted of 70-mm color transparencies and 20- by 25-cm (8 by 10 in.) enlarged color prints taken with a Hasselblad camera equipped with 50-mm and 250-mm lenses. Stereo photography was acquired for most of the sites. In addition, 35-mm Nikon photographs were obtained over some areas. The comments of the crewmen as they observed snow-covered terrain were also available.

As with the Skylab 4 Visual Observations Project, the ASTP mission illustrated the advantages of manned space flight for Earth observations. The value of man-in-space lies in his unique ability to observe and photograph specific "targets of opportunity" that may well be missed by the programed observations of unmanned satellite platforms. Many Earth resources indicators, such as color, texture, and spatial orientation, are often better observed by the human eye than by a

camera lens. Also, the unique viewing angles and film/filter combinations made possible with handheld-camera photographs can add significantly to the interpretation of many Earth resource features.

Review of Previous Studies

In much of the western United States, snowmelt accounts for a large percentage of the total streamflow. Therefore, the importance of snow data as input to runoff models is obvious. The 1972-73 winter season offered an excellent example of the impact of snow on the economy of the western part of the United States; in central Arizona, exceptional winter snowfall resulted in replenished groundwater and a summer of abundant water supplies, whereas in the Pacific Northwest a winter of well below normal snowfall produced a power-generation crisis later in the year. More recently, the reduced water supply in California, a result of the snow drought during the 1975-76 and 1976-77 winters, has had severe economic impact.

Since the time of the first pictures from the Television and Infrared Observation Satellite (TIROS) more than 15 years ago, use has been made of remote sensing from satellites to map snow cover and the rate of retreat of mountain snowpacks. Studies have demonstrated that valuable information on snow distribution could be derived even from the relatively poor-resolution data of the earlier meteorological satellites. Investigations carried out in the past few years have shown that snow cover can be mapped in more detail from Landsat and Skylab imagery than is depicted on aerial-survey snow charts.

A summary report on the status of satellite snow mapping was prepared in 1973 by an international committee for the World Meteorological Organization (ref. 1). More recently, a handbook of techniques for satellite snow mapping has been prepared for the National Aeronautics and Space Administration (ref. 2). Results of the investigations to apply data from the Skylab Earth Resources Experiment Package (EREP) to snow hydrology are described in a report by Barnes, Smallwood, and Cogan (ref. 3).

In addition to the Skylab EREP data, the Skylab 4 Visual Observations Project provided a substantial number of observations with applications to snow mapping studies. Some 300 handheld-camera photographs were taken over snow-covered areas of North America and of other parts of the world. The results of the snow mapping experiment are reported in detail by Barnes (ref. 4) and Barnes et al. (ref. 5).

The crewmen of Skylab 4 could readily identify snow. They reported that, because of the contrast in reflectance and color, they had no doubt in their minds as to where the snow was; moreover, the crewmen could discern no significant differences in the appearance of snow cover from one mountain range to another and could, in most instances, distinguish snow from clouds with little difficulty. The crewmen were able to detect unusual snow patterns and dynamic changes in snow cover, and to monitor changes in snow cover as melting took place; changes were strikingly evident in urban areas where the snow rapidly became contaminated with pollutants and melted more quickly than did the snow in the surrounding countryside.

The results of the Skylab 4 experiment indicated that man-in-space is better at identifying snow than is possible through the interpretation of satellite photographs alone. The crewmen could obtain useful information in the presence of partial cloud cover, although the same amount of cloud cover would make interpretation of a photograph difficult. The ability of astronauts to identify snow and to point an observing system at a specific target, together with orbital characteristics that enable greater repetitive coverage than is currently possible from unmanned satellites providing high-resolution data, leads to more frequent and more reliable observations of a specific drainage basin during a critical snowmelt period. It is conceivable that there may be situations where high data rates, limited field-of-view, and data processing considerations may make it imperative to point sensors at targets, taking advantage of breaks in the clouds, rather than providing continuous operation and coverage. Rather than fabricate complex, ground-controlled means for doing this, a manned, multipurpose Earth resources space laboratory may be advantageous.

The Skylab experiment also indicated that it was possible for the crewmen to make observations at various viewing angles and at various Sun angles, using a variety of camera film/filter combinations. As a consequence, features that might not be visible in vertical photographs may become detectable in oblique photographs, even when lighting conditions are the same. This flexibility has particular application for observing geological structures enhanced by snow-cover and vegetation patterns, where a unique combination of viewing angle and solar illumination may permit the discovery of an important new feature.

DESCRIPTION OF SITES

Northern Hemisphere

In the northern hemisphere, the sites selected for analysis were considered prime targets because of the high probability of snow cover at the time of the ASTP mission (July 15 to 24, 1975). These sites are described as follows:

1. Cascades and Olympic Mountains (Washington): The Cascades and the Olympic Mountains are densely forested regions, except for some lower-elevation grassland and farmland. These regions are characterized by mountain ranges intersected by numerous river valleys, and only isolated areas exceed 3000 m (10 000 ft) in elevation. The snowfall of this region is relatively consistent and is distributed over a prolonged season with maximum depths often exceeding 250 cm. On many of the broader, higher-elevation ridges permanent snowfields are found, consisting of dense snow, ice, and alpine glaciers.

2. Canadian Rockies (British Columbia and Alberta): The ASTP crewmen also observed snow in the Canadian Rockies. The site, located in the Blackwater Mountains, consists of river-dissected ranges with many glacier-covered ridges that are more than 3000 m (10 000 ft) in elevation. In late July, most of the remaining snow cover in this area is confined to the more permanent snowfields located above the 2400 m (8000 ft) elevation.

Southern Hemisphere

The late July time-frame of the ASTP mission occurred during the southern-hemisphere winter season. Therefore, extensive snow cover was found in the ASTP photographs of New Zealand and the Andes. In the Andes, an isolated mountain range 1500 to 2100 m (5000 to 7000 ft) in elevation, located just south of Santiago, Chile, was photographed. Similarly, substantial snow cover was visible along New Zealand's Southern Alps during the mission, and high-resolution, stereo color photographs were acquired. Many of the higher peaks in the southern Alps reach elevations of 2100 to 2800 m (7000 to 9000 ft), and glacial activity is indicated on topographic maps. However, much of this area was cloud covered at the time of the overpass, so only a portion of a lower-elevation ridge was mapped for this report.

DATA SAMPLE AND ANALYSIS PROCEDURES

Description of Spacecraft Data

The photographs taken by the ASTP crewmen were analyzed and compared with data from other spacecraft systems including Landsat, Skylab, and the National Oceanic and Atmospheric Administration (NOAA) very-high-resolution radiometer (VHRR) satellites. The characteristics of each of these satellite systems are described in the following paragraphs.

ASTP Photography

During the ASTP mission a rather extensive 70-mm color, photographic data base was acquired by the crew using a Hasselblad reflex camera with both 50-mm and 250-mm lenses. Also available to the crew was a Nikon 35-mm camera. The approximate photographic scale for the designated study areas ranged from 1:1 300 000 for the vertical-viewing photographs with the 50-mm lens to 1:500 000 for the photographs with the 250-mm lens.

The photographs selected for analysis were received in both 70-mm color transparency and 20- by 25-cm (8 by 10 in.) color print formats. Most of the analyses were performed using the hard-copy color prints.

Many of the photographic strips provided stereo coverage of the test sites. The three-dimensional perspective was found to facilitate the analysis of snow cover and glacial conditions and was especially valuable for distinguishing between snow and clouds. The stereo photography over the Canadian Rockies is discussed later.

Landsat Imagery

The Landsat multispectral scanner subsystem (MSS) views a swath 185-km wide, with coverage of the same area occurring every 18 days. Some orbital overlap occurs on two consecutive days (greater overlap occurs at higher latitudes). Features greater than approximately 70 m in width can be identified in the MSS imagery and can be mapped accurately to a scale of at least 1:250 000. The MSS senses in four spectral bands: MSS-4 (0.5 to 0.6 μm), MSS-5 (0.6 to 0.7 μm), MSS-6 (0.7 to 0.8 μm) and MSS-7 (0.8 to 1.1 μm).

Landsat direct readout coverage of North America is provided by three receiving stations in the United States and one in Canada. The data can be obtained by the user in various formats, primarily 70-mm (scale 1:3 million) and 18.5-cm (7.3 in.) (1:1 million) imagery. Color composite imagery, processed by combining the different spectral bands, and digitized computer tapes can also be obtained. The overall accomplishments of the Landsat program are summarized in the proceedings of the second and third Landsat symposia (refs. 6 and 7). The particular application of Landsat data to snow mapping is evaluated in reports by Barnes, Bowley, and Simmes (ref. 8) and Bowley and Barnes (ref. 9).

Skylab Photography

Considerable photography over snow-covered areas within the United States was collected on the Skylab missions, both as part of the EREP experiment and the Skylab 4 Visual Observations Project. Although these data were not intended for operational snow mapping use, the S190A and S190B cameras did provide photographs with higher resolutions than even the data from Landsat.

The S190A is a six-camera multispectral system with a resolution of 30 to 70 m (as compared to 70 to 100 m for Landsat). The S190B camera is equipped with a 46-cm (18 in.) lens and has a resolution of 15 to 30 m. The application of the S190A and S190B photographs to snow mapping is discussed in a report by Barnes et al. (ref. 10).

In the Skylab 4 Visual Observations Project, approximately 300 handheld-camera photographs of snow-covered areas were taken by the crew. Although the resolution of the handheld-camera photographs is generally not as good as that of the S190A and S190B, these photographs taken at various viewing angles have been found to be very useful for research purposes (refs. 4 and 5).

NOAA VHRR Imagery

The primary snow mapping sensor on the NOAA satellites is the VHRR, a dual-channel scanner that is sensitive in the visible (0.6 to 0.7 μm) and thermal infrared (10.5 to 12.5 μm) spectral regions. The spatial resolution of the VHRR is approximately 1 km. In the direct readout mode, a VHRR data swath about 2200 km wide and more than 5000 km long can be received. The VHRR also has a limited stored data capability; 8 minutes of data can be stored on each orbital pass yielding an image approximately 2200 km wide and 2200 km long.

The VHRR imagery is available from the National Environmental Satellite Service in a standard 25- by 25-cm (10 by 10 in.) format (scale approximately 1:10 million). The VHRR data are also available in digitized format and in enhanced imagery that can be processed from the digitized tapes.

Photointerpretation Techniques

Conventional photointerpretation techniques and equipment were used in analyzing the ASTP photographs. The techniques for identifying snow cover in the ASTP and other satellite data were

developed in earlier studies and are discussed in detail in the Handbook of Techniques for Satellite Snow Mapping (ref. 2); these techniques are briefly summarized in the following paragraphs. It should be pointed out that the interpretation of spacecraft photography to identify snow involves a considerable amount of subjective analysis; therefore, for coping with the problems of forest effects, mountain shadows, or identifying partial snow cover, it is essential that the analyst be thoroughly familiar with the geographic area in question.

Distinguishing Snow From Clouds

In satellite photography, snow cover and clouds both have high reflectances. Differentiating between the two is perhaps the greatest problem in the use of satellite observations for snow-cover mapping. Snow can be distinguished from clouds, however, by the following interpretive keys.

1. Recognition of terrestrial features: Natural terrestrial features (such as coastlines, lakes, rivers, and boundaries between forested and nonforested areas) and such manmade features as roads, powerline swaths, timber cuts, urban areas, and cultivated fields are detectable in the ASTP photographs.

2. Pattern recognition: Mountain snowpacks cover the higher elevation terrain and, thus, are directly related to the geologic structure. The configuration of the geologic structure of typical mountain ranges is quite different from the patterns of clouds as viewed from space; therefore, the snow cover can be readily recognized. Also, the snowline is generally well defined and forms a sharper boundary than is characteristic of most cloud edges.

3. Uniformity of reflectance: Typically, snow cover in areas that are not forested has a more uniform reflectance than clouds and is usually smooth textured while clouds are often rough or lumpy in appearance.

4. Shadows: Occasionally, the shadows of narrow cloud bands are observed on an underlying snow surface. Most common, however, is the detection of cloud shadows during the spring season when cumuliform clouds tend to develop over mountain ranges.

5. Pattern stability: Clouds seldom retain the same shape for more than a few hours; therefore, stable patterns of high reflectivity viewed by satellite are indicative of snow cover. Naturally, to use this technique, observations at least several hours apart are required.

Forest Effects

Forested areas composed of dense coniferous growth remain distinctly darker than areas of deciduous forest, sparse vegetation, or nonforested terrain. Such areas remain dark even with substantial snow cover, because dry snow tends to filter through and not remain fast to conifers. Small lakes, timbercuts, or open land within these areas do, however, appear highly reflective, indicating the existence of snow cover. Areas of sparse coniferous growth display a slightly higher reflectivity (grayer tone).

Mountain Shadow Effects

During the midwinter period, low Sun angles produce mountain shadows that can cause ambiguity in locating the snowline. In spacecraft imagery, the reflectance of a north-facing ridge that is partially or totally snow covered may appear the same as the reflectance of terrain that is completely snow free. The processing of enlarged prints, using various exposure times to bring out more detail in the dark shadow areas, aids considerably in alleviating the mountain shadow problem. Later in the winter and spring, the snow distribution may be even less, and the analyst must account for the possibility of there being more snow on the north-facing than on the south-facing slopes. Fortunately, because of higher Sun angles, the shadow problem is not as severe in the spring.

Effects of Urban Areas

In nonforested regions, urban areas can be readily identified when snow is on the ground. The albedo rapidly decreases after a snowfall because of snow removal from roads and highways, contamination of a snow surface by pollutants, and the increased rate of snowmelt as a

result of the higher temperatures associated with heated buildings, industry, and the close-knit structure of the urban core. Though in many instances substantial snow depth measurements are reported within these urban areas, they appear in the satellite imagery as small pockets of little or no snow cover because of their lower albedo.

Partially Snow-Covered Terrain

In the late spring and early summer, patchy snow may be difficult to distinguish from highly reflective bare rock surfaces. It may be necessary to refer to several observations to establish that a pattern is actually snow rather than bare rock.

Mapping Procedures

Once snowlines have been interpreted from the photographs or other types of imagery it is necessary to transfer the snowline to a topographic base map so that contour elevations may be determined. The two primary methods of data transfer in this study were (1) the use of the Bausch and Lomb zoom transfer scope (ZTS) and (2) the use of a fine mesh grid transfer system.

The ZTS is a device that allows optical matching of two different scales, as well as rectification of slight photographic distortion. In using the ZTS, the image (either a print or a transparency) is superimposed optically onto a base map. Through adjustment of the image projection size and through stretching of the image along either axis, the original image is rectified to fit the exact scale of the base map. Once these procedures have been completed, it is possible to transfer information from the image directly onto a base map of desired scale.

A more tedious method for measuring the snowline elevation in mountainous terrain is to transfer the snow pattern mapped from photographs or imagery directly onto elevation contour charts. Charts from the National Topographic Map Series (scale: 1:250 000) are useful for matching the amount of detail detectable in the ASTP photographs. In the procedure used, an accurate half-degree latitude-longitude grid overlay is prepared on a transparent overlay using landmark references. Then, by use of a variable scale, a fine mesh grid is drawn within each half-degree square on the transparent overlay. The snow boundaries are traced onto the gridded overlay and transferred to an identical (fine mesh grid) transparent overlay on the corresponding topographic chart, which has an elevation contour interval of 60 m (200 ft). The mean snowline elevation is then determined by measurements at a large number of points along the snow boundary.

In some instances, a "Houston Fearless" Variscan was also used to analyze and map snow-cover extent. The Variscan provides magnifications ranging from 3× to 30× and will view transparencies ranging in size from 16-mm film to 23- by 23-cm (9 by 9 in.) photographs. The Variscan allows the operator to manipulate the data by using rotation and scanning controls and, in addition, has a drive motor capability for the viewing of roll film. Through experience, it has been demonstrated that, by slightly modifying the existing optics in the Variscan, it is possible to achieve "scale matching" between various topographic maps and the original photographs, which greatly expedites the task of transferring detail to a base map.

ANALYSIS OF SNOWLINE ELEVATION

Olympic Mountains

The snow extent for the Olympic Mountains in northwest Washington State was mapped by using ASTP photographs taken on July 23, 1975 (AST-19-1537, fig. 1). The interpreted snowline was then transferred to a 1:250 000 scale topographic sheet using the ZTS. The snowline superimposed on the map is shown in figure 2. As indicated by the elevation figures, the snowline varies with different parts of the Olympic Mountains; however, when averaged together, the snowline elevation is approximately 1405 m (4610 ft).

It appears that all the mountain ranges except for the immediate area of Mount Olympus are exhibiting a higher elevation snowline, 1400 to 1645 m (4600 to 5400 ft). Most of these ranges are

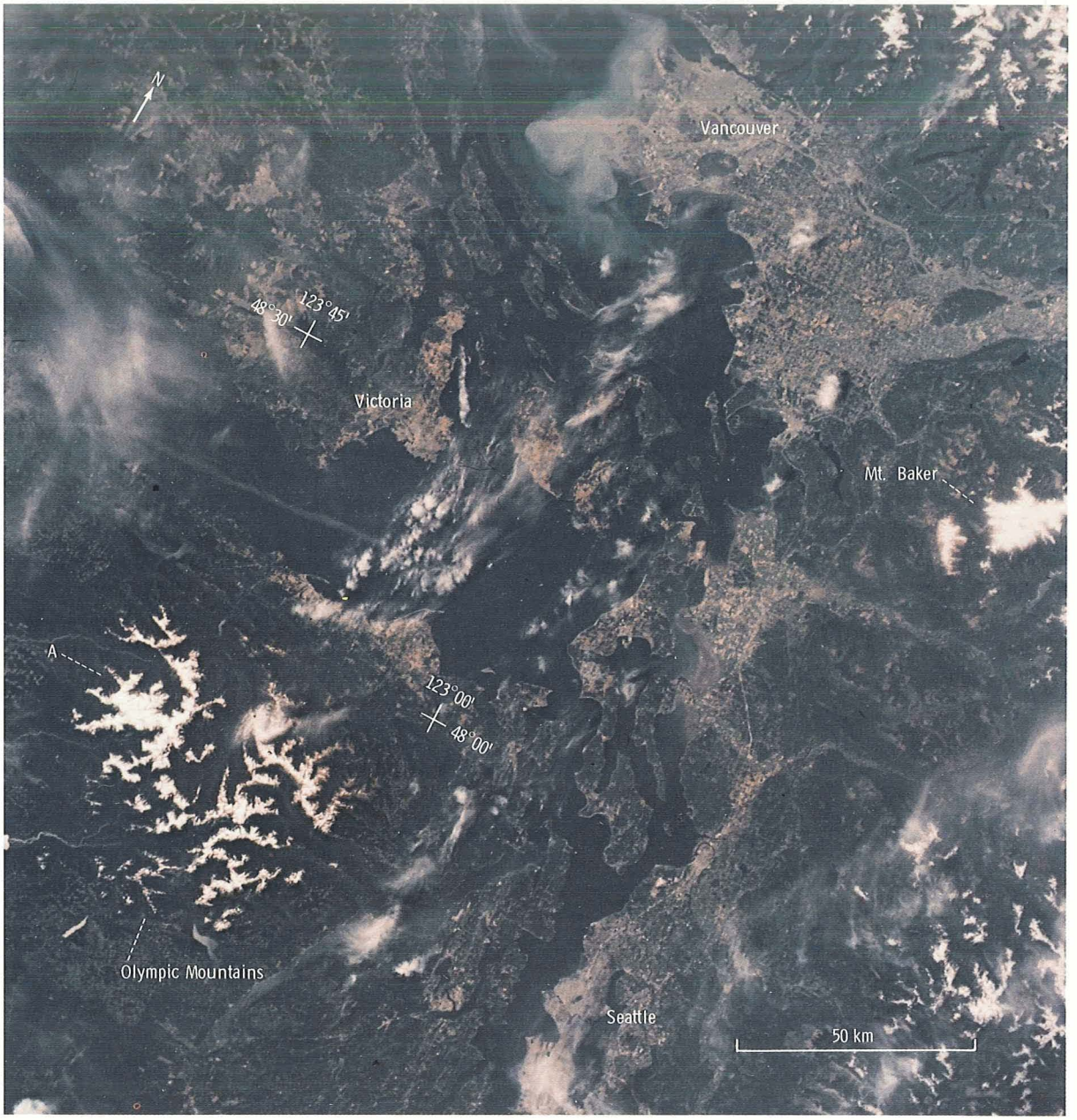


FIGURE 1.—An ASTP photograph (AST-19-1537) showing snow cover on the Olympic Mountains in Washington State, July 23, 1975. The Mount Olympus area (A) exhibits a significantly lower snowline elevation than other areas in the region.

covered by seasonal snowfall that would be expected to melt more rapidly than the multiyear, permanent snowpack such as that found in the Mount Olympus area. This permanent snowpack consists of numerous alpine glaciers and very dense snow and ice that would tend to endure melting temperatures longer than seasonal snowfall, resulting in a lower snowline elevation, 1280 to 1310 m (4200 to 4300 ft).

The Olympic Mountains and Cascade Range were also observed during the Skylab 2 mission in the spring of 1973. Analysis of a Skylab 2

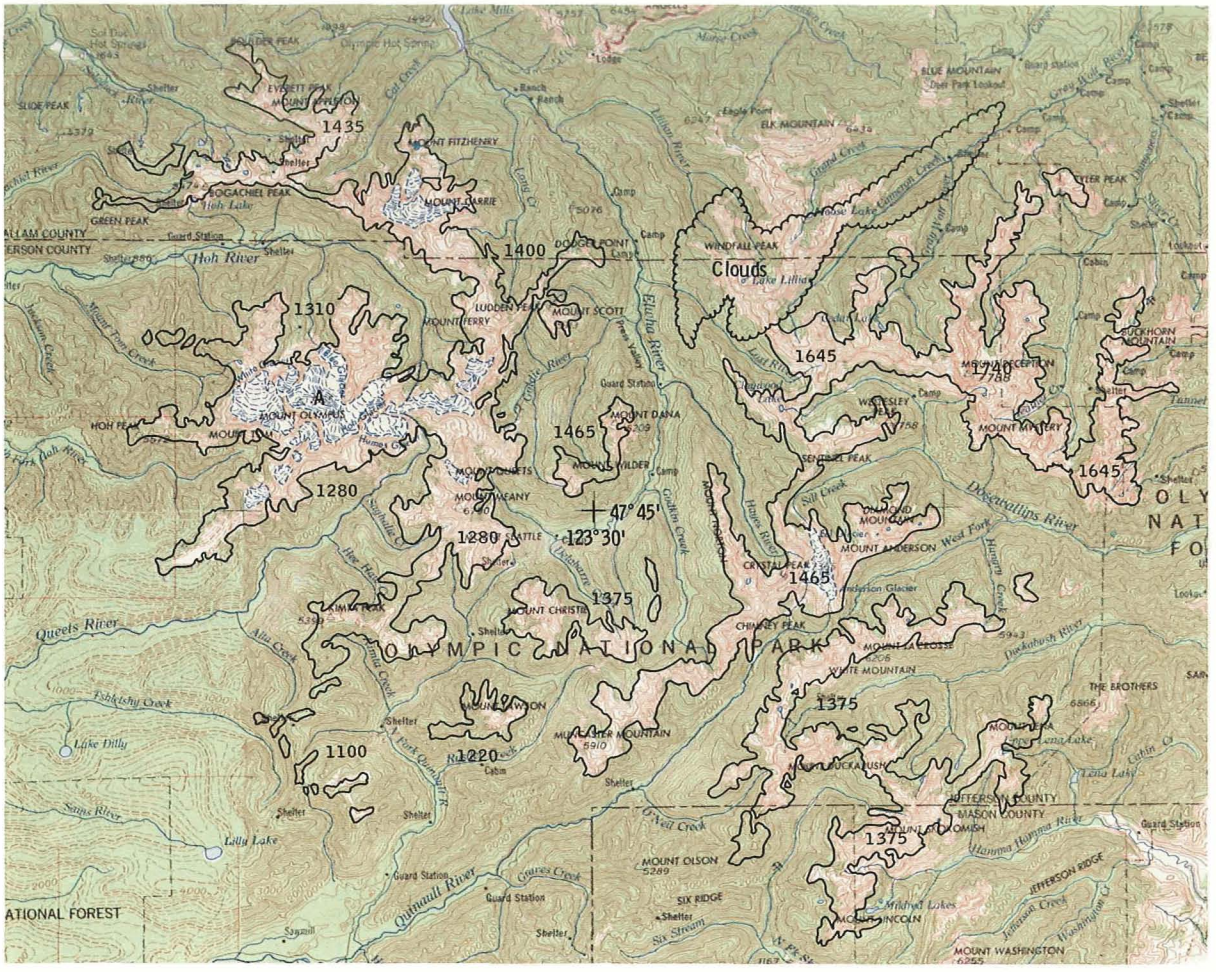


FIGURE 2.—Part of a 1:250 000 USGS topographic map for the Olympic Mountains area. The ASTP-derived snowline and mean elevations in meters are superimposed. Mount Olympus is at "A."

handheld-camera, oblique photograph (fig. 3) of early June 1973 indicated a mean snowline elevation of approximately 1525 m (5000 ft) on the Olympic Mountains. The scale and viewing angle of this oblique photograph restricted the analysis of the snowline to a comparison of the snow limit with the 305-m (1000 ft) elevation contours displayed on the U.S. Geological Survey (USGS) base map (scale 1:250 000) to obtain a best fit.

Unlike the substantial variation detected in the snowline elevations of individual ridges in the ASTP photograph discussed here (AST-19-1537), the Skylab image displays a nearly uniform snow extent. The variations in snowline elevation, therefore, appear to be associated with the more rapid summertime melting conditions.

Mount Baker Region (Cascade Range)

The Mount Baker region of the Cascades has been the subject of several recent investigations (ref. 11) concerning the nature and dynamics of geothermal activity in areas such as Sherman Crater. Historical records indicate that Mount Baker, a moderately eroded stratovolcano, has

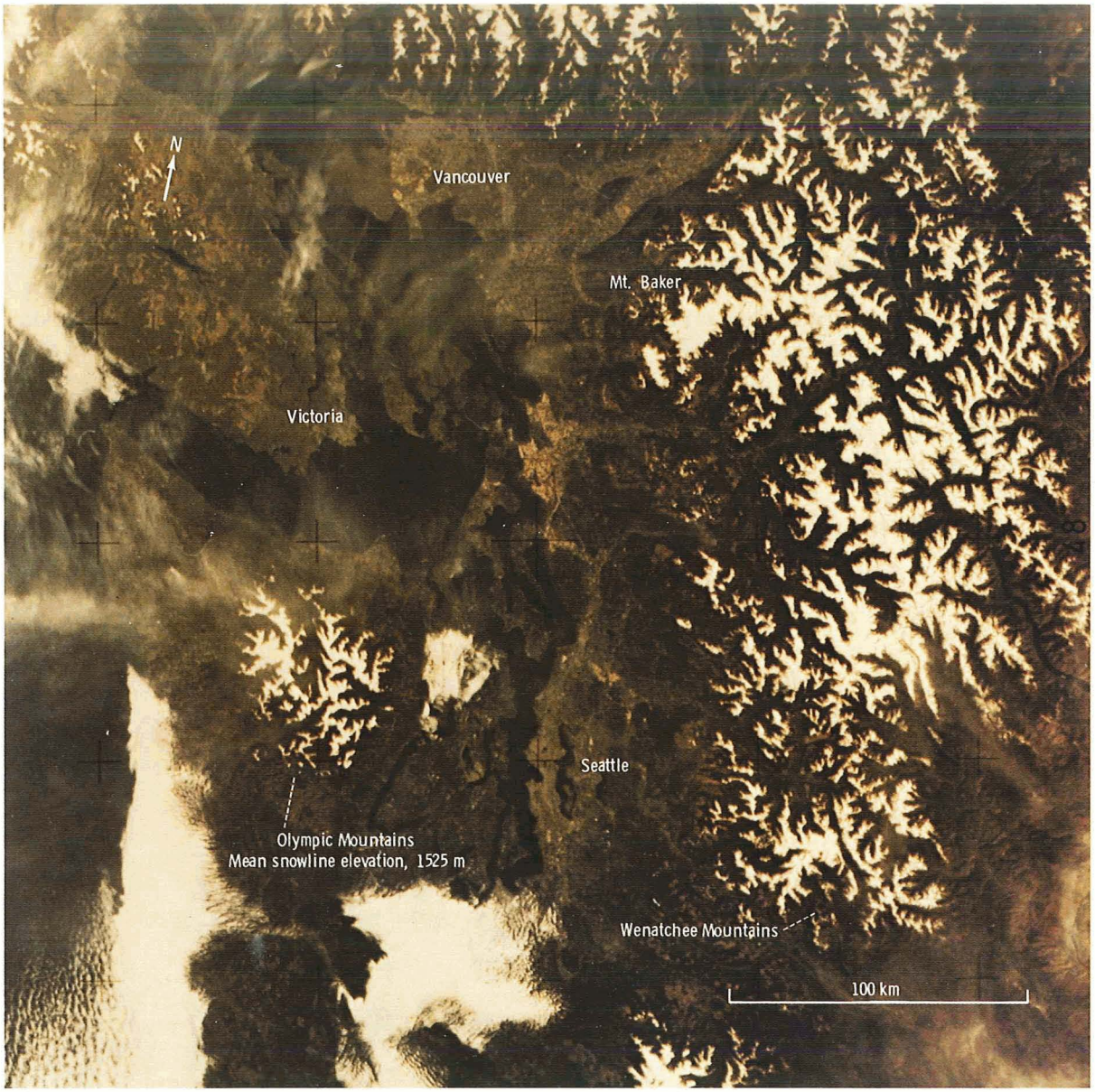


FIGURE 3.—Skylab 2 photograph of Olympic Mountains and Cascade Range taken early June of 1973 (SL2-5-458).

been the scene of apparent fumarolic activity in the past; and, more recently, it is exhibiting the largest known thermal increase at one of the Cascade volcanoes since the Lasser Peak eruptions of 1914 to 1917 (ref. 12). The culmination of this activity could be the formation of a crater lake retained by an ice dam; should this ice dam fail, the lake outburst would have a significant destructive potential in the Boulder Creek Valley. Analysis of ASTP photographs did not indicate any features that could be definitely associated with the recent geothermal activity; it appears that the camera resolution is not sufficient to identify such features.

The ASTP photographs depicting the Mount Baker region of the Cascade Range were acquired on July 23, 1975, and one of these photographs taken with the 50-mm lens (AST-19-1540) was used to determine the snowline elevation for this area. Although portions of the region exhibit varying snowline elevations, it was possible to measure an average snowline of 1405 m (4615 ft).

The ASTP photograph was enlarged and compared to a Landsat image of the same area of the Cascades (No. 2182-18195) acquired on the same day. The snowlines as mapped from ASTP photographs and Landsat imagery are shown in figure 4. It is apparent from this figure that the ASTP photograph has a reasonably accurate snowline when compared to the Landsat-derived snowline. The overall pattern and positioning of the snowpack is relatively accurate even though much of the finer detail along the edge of the snow is not discernible on the ASTP enlarged photograph taken with the normal 50-mm lens.

This comparison of mapping accuracy of the ASTP photographs can be further supplemented by a quantitative comparison of snowline elevations. The elevation figures for various parts of the area are also indicated in figure 4. Though some significant variations in snowline elevation are observed for parts of the Cascades, it should be noted that the average snowline elevation (1405 m) from the ASTP compares favorably with the average Landsat-derived snowline elevation (1395 m).

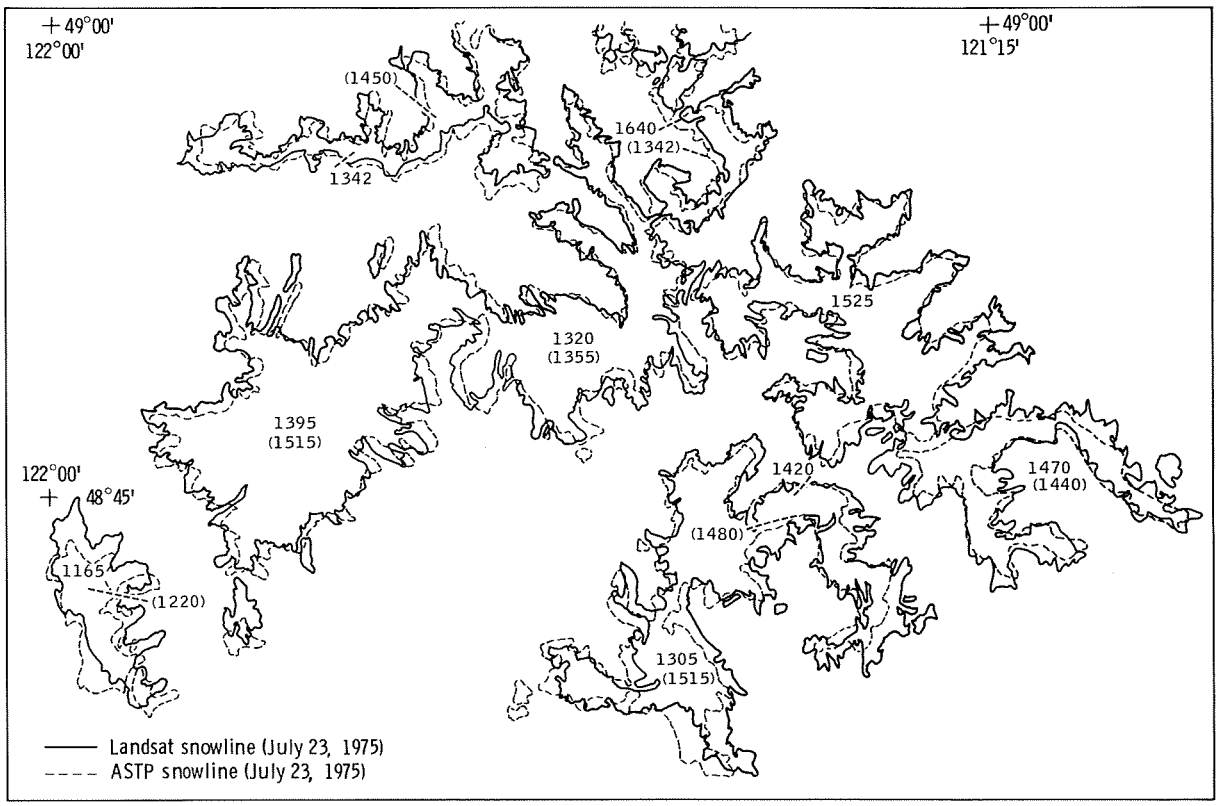


FIGURE 4.—Comparison of snowlines derived from ASTP photograph (dotted line) and a Landsat image (solid line). The elevations in meters refer to the mean snowline elevation derived for each mountain area. (Elevations for the ASTP snowline are in parentheses.)

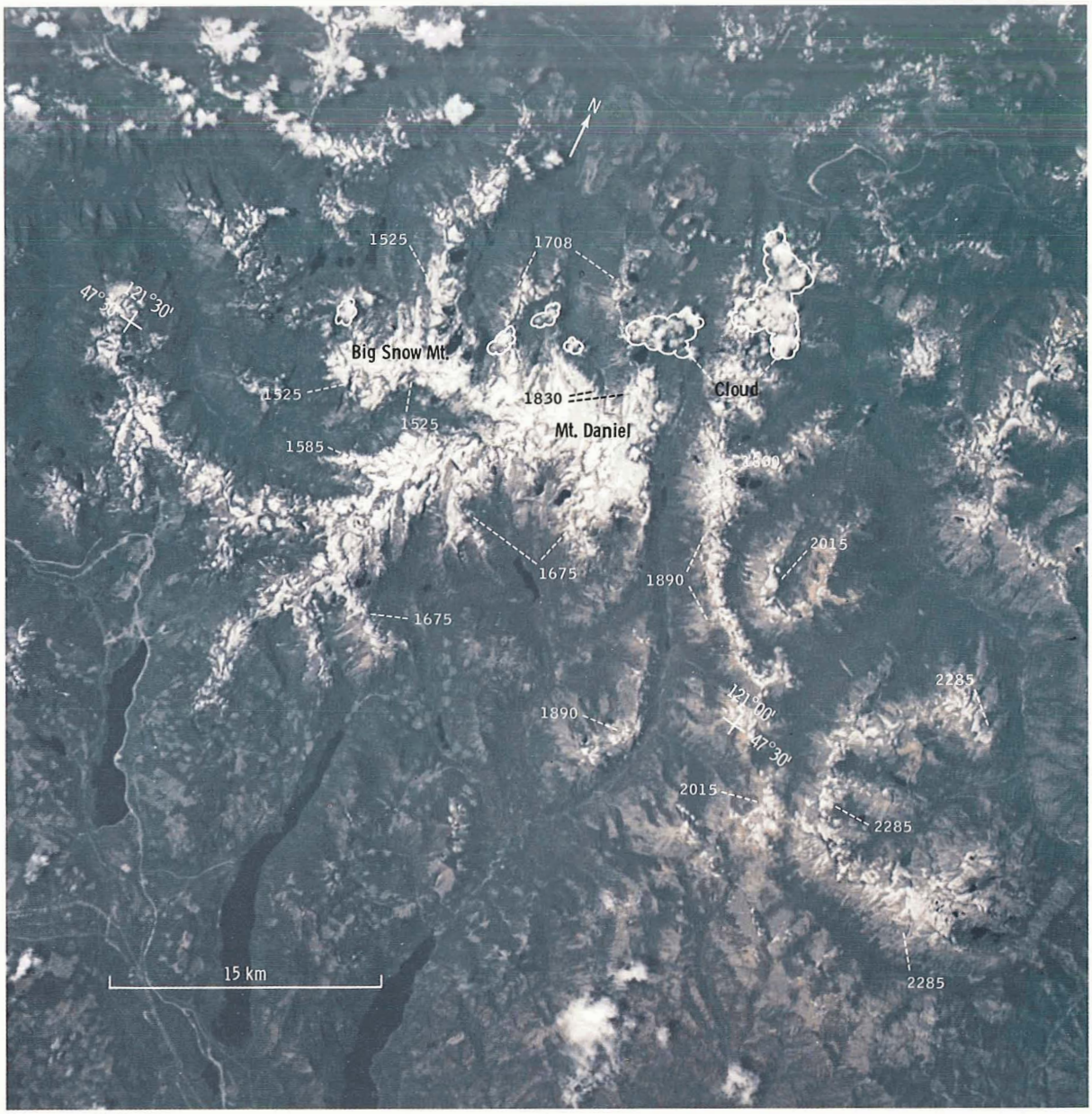


FIGURE 5.—High-resolution (250-mm lens) ASTP photograph of the Wenatchee Mountains (AST-30-2601), July 20, 1975. Snowline elevations (in meters) for various parts of the mountain range are indicated.

Wenatchee Mountains (Cascade Range)

An ASTP photograph (fig. 5) of the Wenatchee Mountains on July 20, 1975, taken with the high-resolution 250-mm camera lens, shows considerable detail in the remaining mountain snow cover. The snowline elevation derived from this photograph varies by as much as 760 m (2500 ft) across individual ridges and peaks. The snowline elevation surrounding the broader, more permanent snowfields in the area of Mount Daniel (47°35′ N, 121°10′ W) ranges between 1675 and 1830 m (5500

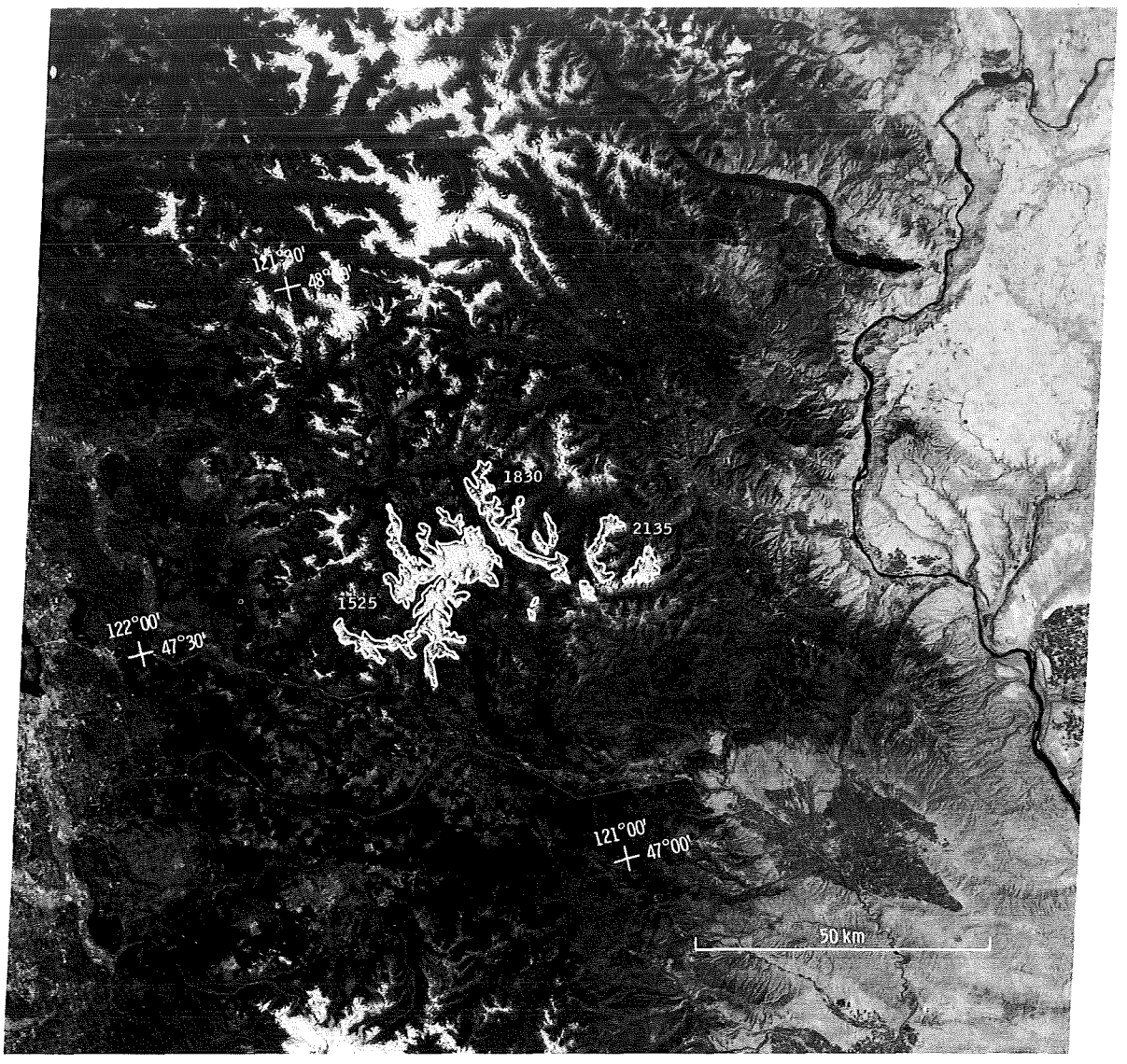


FIGURE 6.—Landsat-2 image (No. 2181-18143) of the Wenatchee Mountains, July 22, 1975. This Landsat image shows less snowline detail than the ASTP photograph in the previous figure. Snowline elevations are in meters.

and 6000 ft), whereas the peaks of Big Snow Mountain and Summit Chief Mountain (the westernmost peaks along the same ridge) have a mean snowline elevation of 1525 to 1675 m (5000 to 5500 ft). The ranges located just to the east of the permanent snowfields have significantly higher snowline elevations, between the 1830- to 2285-m (6000 to 7500 ft) level.

This area was also studied with a Landsat-2 image (fig. 6) taken 2 days later. This image reveals noticeably less detail in the mountain snow cover; however, variations of as much as 610 m (2000 ft) were determined in the mean snowline elevations across this same area. Analysis of the observed snow-cover extent shows a range of from 1525 to 2135 m (5000 to 7000 ft) in the same west to east comparison described for these areas by using the ASTP photograph.

Clearly, the high-resolution (250-mm lens) ASTP photograph displays significantly more

detail in the mountain snow cover than is observed in the standard Landsat imagery. Also, it is evident that, because the ASTP photograph is a color product, the snow limit can be more accurately defined. The snow-free, bare rock surfaces that appear as a high reflectance in the black-and-white Landsat imagery can very easily be misinterpreted as snow cover. In the ASTP color imagery, however, they appear in distinct color tones of dark gray, light brown, or beige, in contrast to the white snow.

Canadian Rockies

The ASTP stereo photography of July 23, 1975, (fig. 7) viewing an area of the Canadian Rockies (near 52° N and 117° W) shows substantial snow cover on the higher elevations of the Mount Columbia region. The stereo effect aids in distinguishing snow from clouds, helps to define glacial activity, and enhances topographic relief, all of which results in a more accurate interpretation of snow-cover extent. Analysis of the snowline elevation observed in these photographs shows that, by late July, the majority of the observed snowfields are the more permanent ones generally ranging between the 2440- and 2745-m (8000 to 9000 ft) contours. However, smaller isolated patches of snow observed at the highest peaks and ridges east of the Athabasca River were found to be more closely associated with the 2745- to 3050-m (9000 to 10 000 ft) contours.

In a search for correlative snow data, an inquiry was made to personnel in the Department of Civil Engineering at the University of British Columbia, who have developed a runoff model for the Mount Columbia region. Records on file at the university show that the period between July 1 and 12, 1975, was relatively warm, whereas the period from July 12 to 23 had unsettled weather with rainfall. The runoff model predicted an average snowline elevation of 2440 m (8000 ft) by July 23. The British Columbia group concludes that, because the previous winter accumulation of snow in the Mount Columbia region had been substantially reduced by July, the summer melt progressed into the more permanent snowfields above 2440 m. This agrees remarkably well with the snowline elevations determined from analysis of the ASTP photographs.

During the ASTP visual observations debriefing, the command module pilot reported that he had easily seen a firn line on one of the big glaciers in the area of the Alberta and British Columbia border. Firn is defined as old snow that has recrystallized into a dense material. Unlike snow, the particles are to some extent joined together, but, unlike ice, the air spaces still connect with each other. A distinct boundary of much lower reflectance is observed in the photographs of the Saskatchewan Glacier located immediately north of Mount Columbia. It appears likely that this may be the firn line mentioned in the debriefing, for which the ASTP crew reported a distinct textural and color gradation where the ice went from white to gray.

Analysis of a Landsat-1 image (No. 1004-18185), shown in figure 8, viewing a portion of this same mountain region on approximately the same date 3 years earlier (July 27, 1972), shows a considerably lower snowline elevation more closely associated with the 1830- to 2440-m (6000 to 8000 ft) contour.

An NOAA-4 VHRR nighttime infrared image (fig. 9) viewing the area of the Canadian Rockies on July 23, 1975, shows the snow cover of the larger permanent snowfields near 52° N and 117° W. However, most smaller areas of patchy snow observed in the ASTP photographs are not discernible in the poorer resolution VHRR imagery. Comparison of these figures clearly shows the different scales of the manned and unmanned spacecraft observations.

ANALYSIS OF APPARENT CHANGE IN SNOW-COVER EXTENT

One of the unique advantages of man-in-space is his ability to photograph "targets of opportunity" utilizing various combinations of film, filters, lenses, and viewing angles. Often the information from vertical-viewing photography can be supplemented by the utilization of oblique photography. An example of a comparison between vertical-viewing and oblique photography is presented in figures 10 and 11. Both photographs

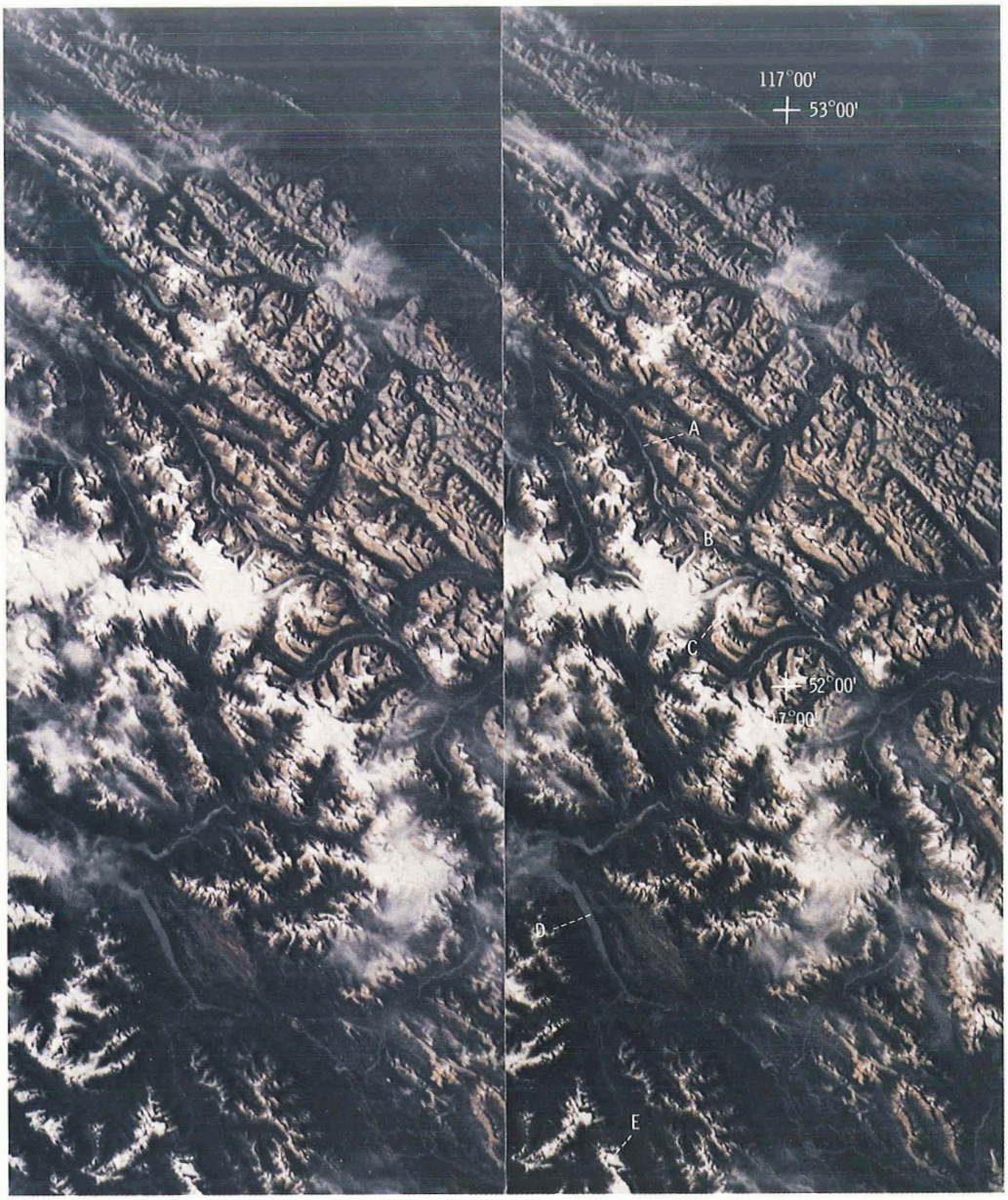


FIGURE 7.—Stereopair (AST-19-1570 and 19-1571) of the Canadian Rockies, July 23, 1975. Features visible include the Athabasca River (A); a possible firn line on Saskatchewan Glacier (B); Mount Columbia (C); the Columbia River (D); and Mount Dawson (E).

view the same area of the Olympic Mountains in northwest Washington State.

The photograph in figure 10 (AST-30-2597) was taken on July 20, 1975, and that in figure 11 (AST-6-328) was taken on July 23, 1975. In comparing these two photographs, a significant variation in snow-cover extent becomes obvious. Since there appears to be much less snow on the earlier date, climatic data were reviewed to determine if snowfall had occurred between July 20 and 23.



FIGURE 8.—Landsat-1 image (No. 1004-18185) viewing a portion of same mountain region shown in figure 7; July 27, 1972.

The results of this review indicate above-freezing temperatures (275 to 276 K (2° to 3° C)) and virtually no precipitation even at the higher elevations.

Since climatic conditions indicate no new snowfall between July 20 and 23, it is assumed that the apparent difference in snow-cover extent is due to the viewing angle of the oblique photograph. Patchy summertime snow-cover appears to be uniformly distributed in vertical-viewing photographs, whereas the oblique view more accurately portrays the distribution of snow within the watershed. It appears that, during periods of rapid snowmelt, a combination of mapping photography and oblique photography may afford a more accurate determination of snow-cover extent than either vertical or oblique photography alone.

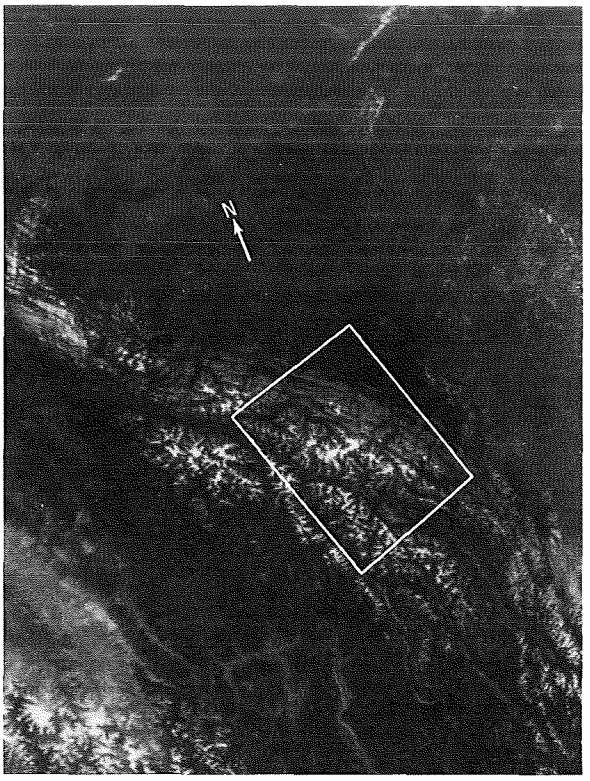


FIGURE 9.—An NOAA-4 VHRR infrared image viewing the Canadian Rockies, July 23, 1975. By comparing the designated area with figures 7 and 8, one can discern similarities in the snowpack even at the 1-km resolution of this sensor.

INTERPRETATION OF SNOW COVER IN THE SOUTHERN HEMISPHERE

Chilean Andes

An oblique view of the Chilean Andes (AST-23-1908) southwest of Santiago was acquired on July 21, 1975. Because of the low oblique camera angle and lack of photogrammetric control, it was not practical to map the snowline for this area; however, the areal extent of snow cover is indicated on the photograph shown in figure 12. This photograph shows snow-covered mountain peaks (elevation 1525 to 2135 m (5000 to 7000 ft)) rising above a stratus cloud deck. Although an accurate determination of snowline elevation was not made, it was possible to compare the photograph to a base map and to estimate the elevation to be between 915 and 1220 m (3000 and 4000 ft) for this portion of the Andes.

It is interesting to note, of course, that the south-facing slopes are shadowed in the southern hemisphere, whereas the north-facing slopes are shadowed in the northern hemisphere. This difference required a slight perceptual reorientation when mapping the snowlines.

New Zealand

On July 16, 1975, the crewmen obtained high-resolution (250-mm lens) photographs over the Southern Alps of New Zealand. Although much of the area was cloud covered, it was possible to map a small portion of the snowline for the mountains west of Lake Wanaka by using ASTP photographs (AST-1-028 and AST-1-029). The ASTP-derived snowline is shown superimposed on a 1:2 188 800 scale base map in figure 13. At the time of the photography, the southern hemisphere was well into its winter season, so that snow covered many of the higher elevations. By using the small-scale photographs and base maps, it was possible to place an estimated snowline elevation at 1180 m (3870 ft) for this area.

SUMMARY OF RESULTS

A review of the ASTP photographs resulted in the selection of 16 color photographs for analysis of mountain snow cover. These photographs taken late in July 1975 showed snow cover on the Olympic Mountains and Cascades, in the Pacific Northwest, and on an area of the Canadian Rockies; snow was also observed and photographed on the Chilean Andes and the Southern Alps of New Zealand.

Analysis of the ASTP photographs indicated that the 250-mm lens system provides photographs with the greatest detail of mountain snow cover. For snow cover on the Wenatchee Mountains (Cascade Range), comparison of an ASTP photograph at this scale (1:500 000) with Landsat

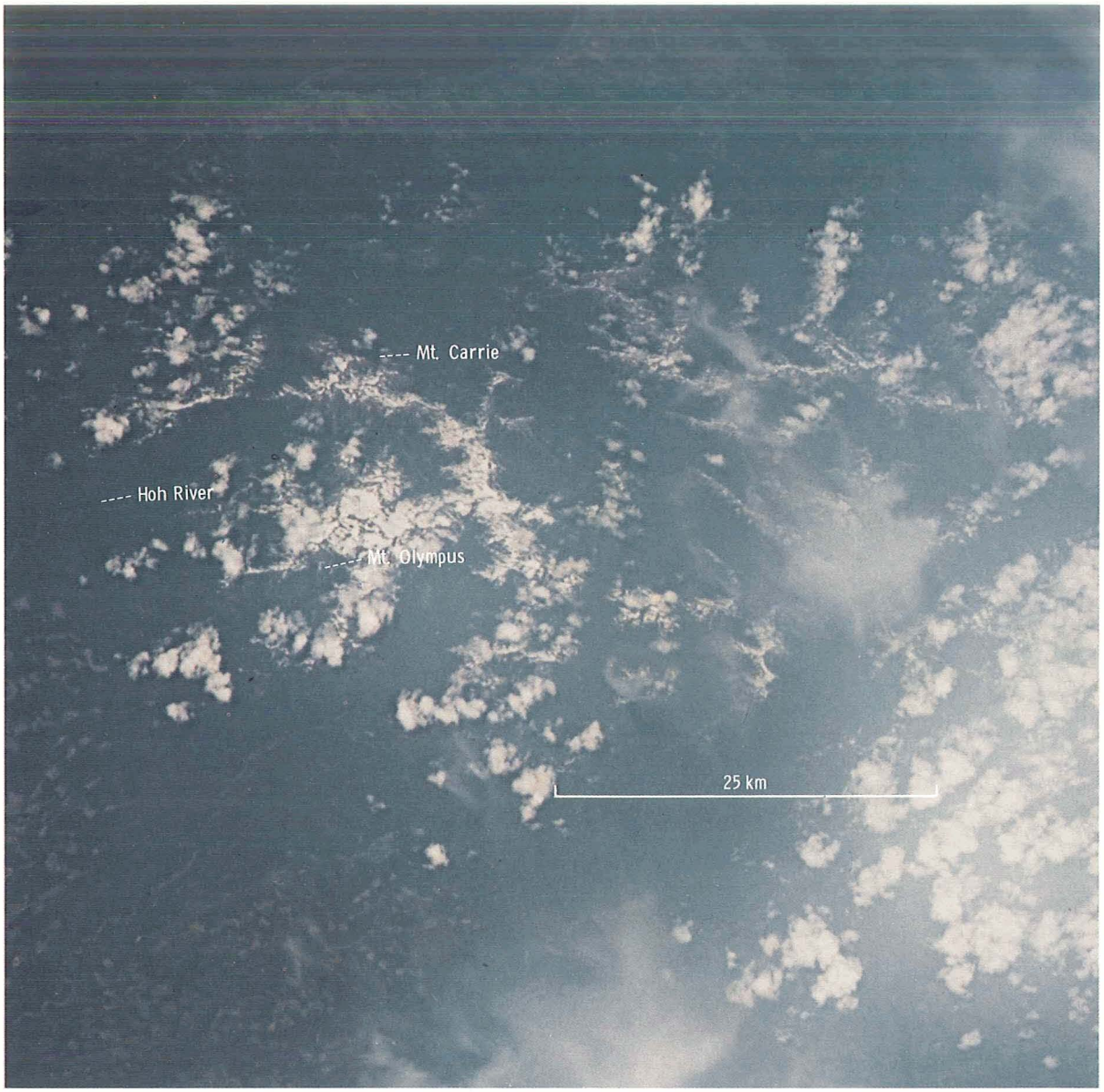


FIGURE 10.—An ASTP high-resolution (250-mm lens) oblique photograph (AST-30-2597) of the Olympic Mountains, July 20, 1975.

imagery taken 2 days later showed that the ASTP photograph displayed considerably more detail in the areal snow-cover extent. Also, because the ASTP photograph was a color product, the snow-free, bare rock surfaces appeared in distinct color tones of dark gray, light brown, or beige, thus allowing easy identification. However, these bare rock surfaces in the Landsat black-and-white imagery displayed a high reflectance adjacent to the snow cover, and they could easily have been misinterpreted as snow cover.

Examination of the ASTP photographs, viewing large glaciers in the Canadian Rockies near Mount Columbia, showed the possible existence

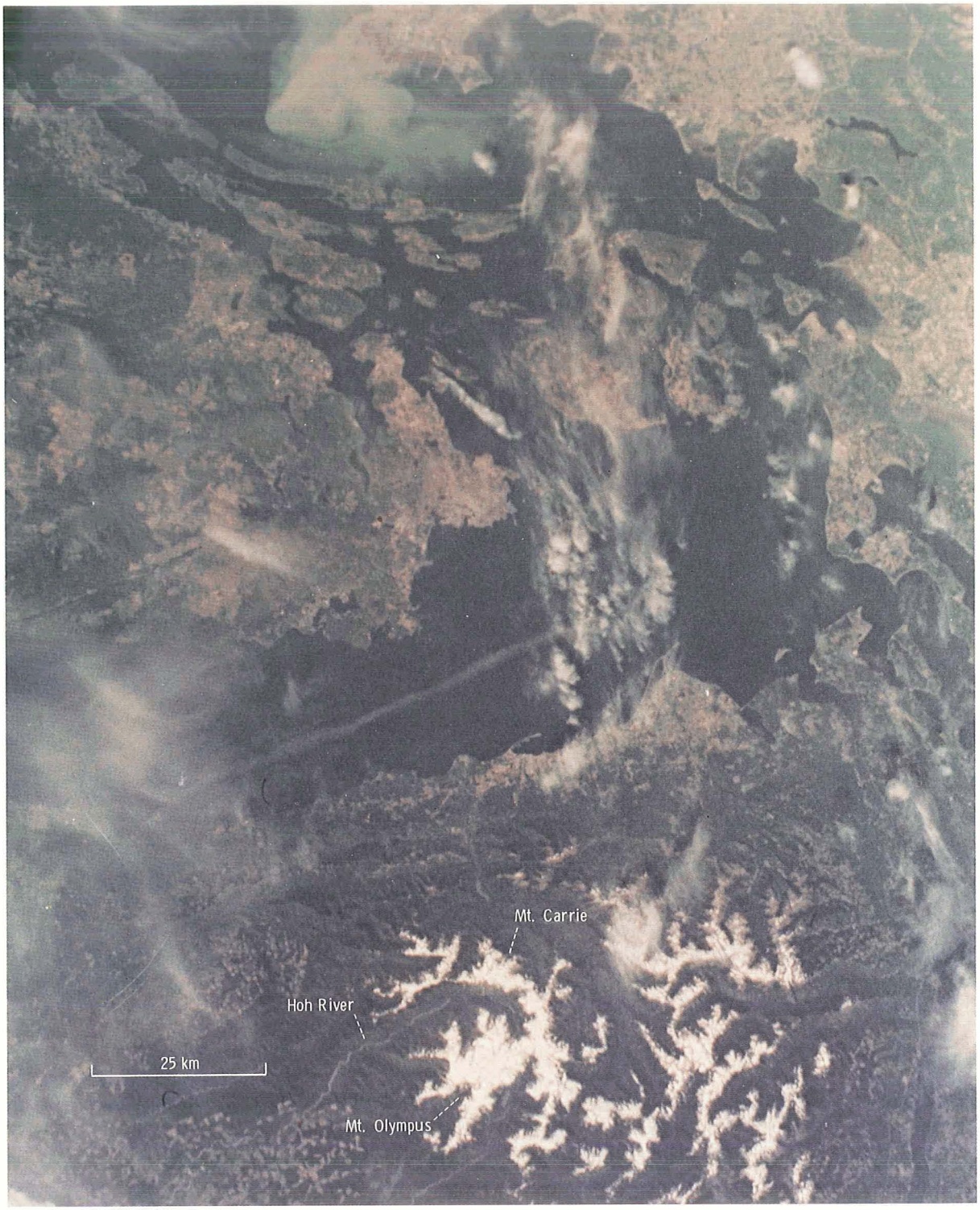


FIGURE 11.—An ASTP vertical-viewing photograph (AST-6-328) showing snow cover in the Olympic Mountains, July 23, 1975. Note the apparent difference in snow cover between this photograph and the photograph in figure 10 taken 3 days earlier.



FIGURE 12.—An ASTP oblique photograph (AST-23-1908) of the Chilean Andes, southwest of Santiago, July 21, 1975. The snow-covered peaks are seen rising above a stratus cloud deck.

of a firn line on the Saskatchewan Glacier. In the debriefing on visual observations (ref. 13), the ASTP crewmen reported that they had easily seen a firn line on a glacier in the Canadian Rockies near Mount Columbia. Their interpretation was based on a distinct textural and color gradation where the ice went from white to gray. Especially at this site, stereo photography was very beneficial to snow-cover interpretation. The three-dimensional view added significantly to the identification and delineation of snow-cover extent and glaciofluvial activity.

One of the most significant findings from the ASTP photographs was that, in each of the areas examined, the snowline elevations showed a definite tendency to remain lower in areas surrounding the permanent snowfields and glaciers. Analysis of snowline elevations on the Olympic Mountains, Cascade Range, and Canadian Rockies revealed that the snowline elevations

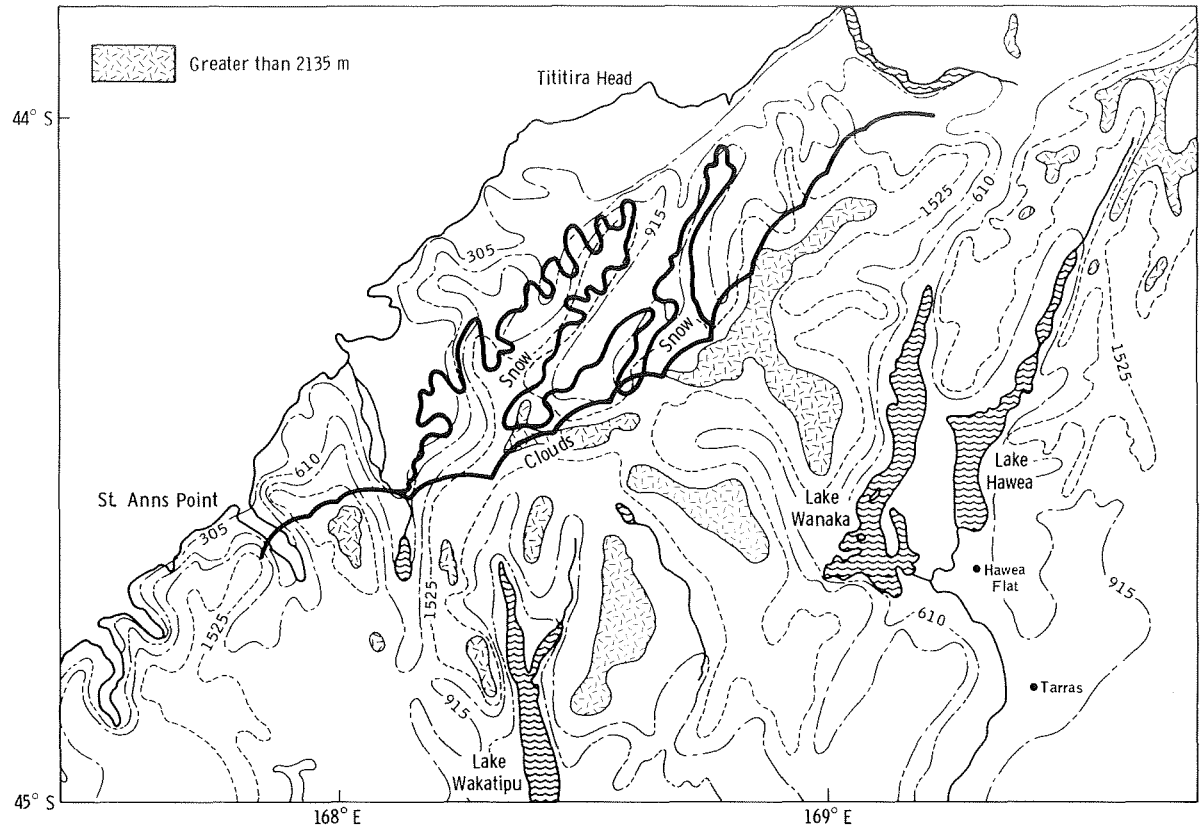


FIGURE 13.—The ASTP-derived snowline for a portion of New Zealand's Southern Alps superimposed on an air navigation chart (scale 1:2 188 800).

were from 305 to 762 m (1000 to 2500 ft) lower in the areas surrounding the broad permanent snowfields and glaciers, compared to the snowlines found on some narrower, higher elevation ridges and peaks.

One explanation may be that the melting occurs at a much slower rate because of the greater density of the older snowfields on the glaciers. Also, the air temperatures may remain significantly lower across the broader regions of permanent snow and ice. This would be especially true during nighttime hours when synoptic conditions are such that radiational cooling would occur.

Another influencing factor may be the east-west orientation of each of the permanent snowfields examined, whereas the narrower ridges and peaks showing higher-elevation mean-snowlines tend to be oriented more north-south. The snowfall amounts induced by orographic effect during regimes of moist, southerly airflow would probably be greater over the broader mountain ranges oriented east-west. In addition, there appeared to be less melt on north-facing slopes, probably the effect of mountain shadow.

CONCLUSIONS

The results of the ASTP snow hydrology studies substantiate the earlier results of the Skylab 4 Visual Observations Project. The ASTP crewmen were able to identify and photograph snow-covered areas, even with the very limited midsummer snowpack. In interpreting the ASTP photographs, the identification of the irregular snow cover and permanent snowfields, typical of the summertime, was greatly facilitated by the color and by stereo-viewing. In one instance, an

oblique view using the higher resolution lens (250 mm) showed considerably more detail in the snow cover than was observed in a vertical-viewing photograph or in a Landsat image.

Snow cover is a resource that requires monitoring over much of the world. The monitoring can only be accomplished by satellites, and operational monitoring can only be accomplished economically by unmanned satellite systems. As was true with the Skylab mission, however, the Apollo-Soyuz Test Project has shown that man-in-space can acquire unique observations that can provide additional information related to snow hydrology. The flexibility of manned space flights in the forthcoming Space Shuttle era will undoubtedly enable the collection of data to augment that obtained from unmanned satellite systems.

ACKNOWLEDGMENTS

This research was performed under Smithsonian Institution Grant PC6-22331 as a subcontract of NASA contract NAS9-13831.

REFERENCES

1. McClain, E. P.: Snow Survey From Earth Satellites. World Meteorological Organization, pub. no. 353, Geneva, Switzerland, 1973.

2. Barnes, J. C.; and Bowley, C. J.: Handbook of Techniques for Satellite Snow Mapping. (Final report, NASA contract 5-21803, Environmental Research and Technology, Inc., Concord, Mass.) 1974.

3. Barnes, J. C.; Smallwood, M. D.; and Cogan, J. L.: Study to Develop Improved Spacecraft Snow Survey Methods Using Skylab/EREP Data. (Final report, NASA contract 9-13305, Environmental Research and Technology, Inc., Concord, Mass.) NASA CR-144388, 1975.

4. Barnes, J. C.: Snow-Mapping Experiment. Sec. 15 of Skylab 4 Visual Observations Project Report. NASA TM X-58142, 1974.

5. Barnes, James C.; Bowley, Clinton J.; Parr, J. Thomas; and Smallwood, Michael D.: Snow-Mapping Experiment. Sec. 7 of Skylab Explores the Earth. NASA SP-380, 1977.

6. Freden, S. C.; Mercanti, E. P.; and Witten, D. E., eds.: Symposium on Significant Results Obtained From ERTS-1, Vol. II, Summary of Results. NASA TM X-66283, 1973.

7. Freden, Stanley C.; Mercanti, Enrico; and Friedman, David B., eds: Third Earth Resources Technology Satellite Symposium, Vol. II, Summary of Results. NASA SP-356, 1974.

8. Barnes, James C.; Bowley, Clinton J.; and Simmes, David A.: The Application of ERTS Imagery to Mapping Snow Cover in the Western United States. (Final report, NASA contract 5-21803, Environmental Research & Technology, Inc., Concord, Mass.) NASA CR-137223, 1974.

9. Barnes, J. C.; and Bowley, C. J.: The Application of ERTS Imagery to Mapping Snow Cover in the Western United States. (Supplemental report, NASA contract 5-21803, Environmental Research and Technology, Inc., Concord, Mass.) NASA CR-142680, 1975.

10. Barnes, James C.; Bowley, Clinton J.; and Smallwood, Michael D.: A Study To Develop Improved Spacecraft Snow Survey Methods Using Skylab/EREP Data; Demonstration of the Utility of the S190 and S192 Data. (Interim report, NASA contract 9-13305, Environmental Research & Technology, Inc., Concord, Mass.) NASA CR-138687, 1974.

11. Meier, M. F.: Applications of ERTS Imagery to Snow and Glacier Hydrology. Paper presented at Symposium on Approaches to Earth Survey Problems Through the Use of Space Techniques, 16th COSPAR Plenary Meeting, Konstanz, West Germany, May 23 to June 5, 1973.

12. Malone, Stephen D.; and Frank, David: Increased Heat Emission From Mount Baker, Washington. EOS, vol. 56, no. 10, Oct. 1975, pp. 679-685.

13. El-Baz, Farouk: Astronaut Observations From the Apollo-Soyuz Mission. Vol. I of Smithsonian Studies in Air and Space, Smithsonian Institution Press (Washington, D.C.), 1977.

Mesoscale Cloud Patterns Revealed by ASTP Photographs

P. G. Black[a]

ABSTRACT

Complicated internal-wave patterns are revealed in Apollo-Soyuz Test Project (ASTP) photographs of marine fog patches. Evidence for the reflection of atmospheric wave packets at water-land boundaries is present in these patterns.

Photographs of "arc" or "ring" clouds show that these clouds are associated with decaying maritime thunderstorms. The cloud-free inner ring delineates cold air that has been transported from aloft by thunderstorm downdrafts, thus inhibiting cumulus cloud development. There is no evidence to indicate that this clear inner ring is a result of cold-core eddies in the ocean.

Other interesting cloud patterns revealed by ASTP photographs include: (1) linear trails created in low stratocumulus cloud decks by passing ships and (2) dome-shaped anvil clouds created by vigorous thunderstorms.

INTRODUCTION

Photographs of cloud patterns can very often provide information concerning the dynamics of meteorological processes. For example, time-lapse photography of convective clouds has led to new information regarding the life cycles of these clouds. The vantage point from which cloud photographs are taken is also very important. For instance, ground-based cloud photography can reveal information about vertical cloud growth, whereas geostationary-satellite cloud photography can reveal information about horizontal cloud growth and about the areal extent of large-scale convergence patterns that are precursors to severe weather conditions.

The vantage point of manned and unmanned satellites has given a whole new perspective to cloud patterns. Island cloud wakes and Bénard-type cellular convection patterns become immediately evident from satellite altitudes, although previously, from ground and airborne vantage points, no coherent pattern was apparent. With a manned satellite platform, an astronaut observer is able to distinguish chaotic cloud patterns from interesting cloud patterns that result from some organized process. Also, an observer in space can point a camera in any direction, not only at some predetermined angle. Furthermore, manned space flights usually occur at lower altitudes (approximately 200 to 500 km) than unmanned satellites (approximately 700 to 40 000 km), allowing greater resolution of small-scale cloud patterns.

The Apollo-Soyuz Test Project (ASTP) presented an opportunity to obtain detailed photographs of cloud patterns revealing interesting meteorological phenomena. Two major classes of cloud patterns are discussed in this article: (1) wave patterns in layers of fog and (2) so-called "arc" clouds. The dynamic processes associated with these patterns are also discussed.

[a]National Hurricane and Experimental Meteorology Laboratory, National Oceanic and Atmospheric Administration (NOAA).

WAVE PATTERNS IN FOG PATCHES

Figures 1 to 3 are a series of ASTP photographs showing complicated wave patterns in the fog at the head of the Bay of Fundy in Canada. Over Minas Basin, Minas Channel, and Chignecto Bay, wave packets that appear to result from multiple reflections of the wave packet at the water-land boundaries are particularly evident (fig. 4(a)). These bodies of water are bounded by steeply rising hills more than 200 m high in places. The ASTP photographs were taken on July 22, 1975, at approximately 11:30 a.m. local (Atlantic) standard time. The water temperatures at that time of year were approximately 285 to 288 K (12° to 15° C). The air temperature over land for that day was approximately 295 K (22° C); winds were from the west-southwest at less than 5 m/sec. These conditions gave rise to a thin layer of cold air, less than 100 m thick, over the water. Within this layer, the air temperature was nearly equal to the water temperature, the humidity was near 100 percent (equal to 100 percent in fog patches), and the wind was nearly calm. An inversion existed at the top of this layer where the air temperature increased 10 K (10° C) in approximately 10 m of height. Just above this transition layer, the air temperature was 295 K (22° C), and the wind was from the west-southwest at 5 m/sec. Recalling that the hills surrounding the bays rose to 200 m, which was well above the height of the inversion, one could conclude that the cold air layer was not only bounded on the top but on the sides also.

This situation favors the existence of internal waves in the boundary layer with a maximum amplitude at the height of the inversion. All that is needed to initiate the waves is some disturbance or perturbation at the inversion surface. The source of this disturbance in the present case is uncertain. It is not inconceivable, however, that the rapidly changing tide of 10 m in 6 hours could induce a sufficient change in the depth of the marine layer to act as a "trigger" for the waves at the inversion surface.

The wave fronts are sketched more clearly in figure 4(a). From the shape of the wave fronts and from the apparent refraction of the wave fronts at the edges of the bay, one can infer that the waves are moving southward down the bay and against the wind at the top of the inversion. The

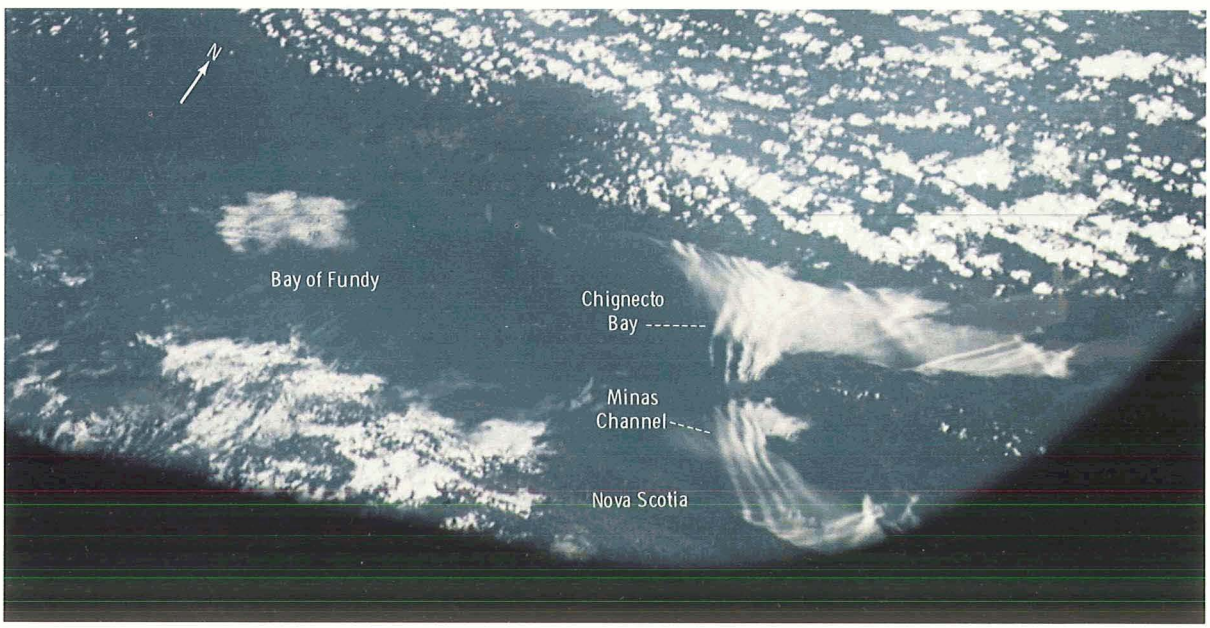


FIGURE 1.—Complicated wave patterns in a fog bank at the head of the Bay of Fundy. This ASTP photograph (AST-21-1702) was taken at 13:30 UT, July 22, 1975. A handheld 70-mm Hasselblad camera with a 50-mm lens was used.

wavelength of the leading few waves is approximately 4 km. Figure 4(b) illustrates schematically the refraction process to be expected when the denser (colder) fluid is constrained between two walls (hills). Note that a concave wave front will become convex when it is refracted from the shore; this appears to be the case in figure 4(a), especially in Minas Channel.

Other striking examples of internal-wave motion in fog patches capped by a strong inversion are shown in figures 5 and 6, which are Landsat-1 images of the western shore of Lake Michigan (fig. 5) and the western part of Lake Superior including Isle Royale (fig. 6). Figure 5, taken on April 18, 1973, shows multiple-wave packets propagating at random over Lake Michigan, which at this time had a water temperature of 281 to 283 K (8° to 10° C). Southerly airflow was bringing warmer air (293 K (20° C)) over the lake creating a strong inversion. The cold air was typically less than 50 m thick and was bounded by cliffs and hills on the western shore. This situation is quite similar to that in the Bay of Fundy. The wave pattern is also quite similar to that produced by oceanic internal-wave packets observed off the U.S. east coast in Landsat images (ref. 1). The mixed-layer depths in both the atmospheric and the oceanic cases are approximately 50 m.

Figure 6, taken on May 21, 1974, shows very long wave fronts in Lake Superior fog. Cumulus cloud streets indicate a southerly wind direction bringing warm air over the cold water. In addition to the internal waves, note the finer scale waves in the fog, oriented perpendicular to the wind direction just off the Ontario shore. These appear to be Kelvin-Helmholtz waves, which are caused by a

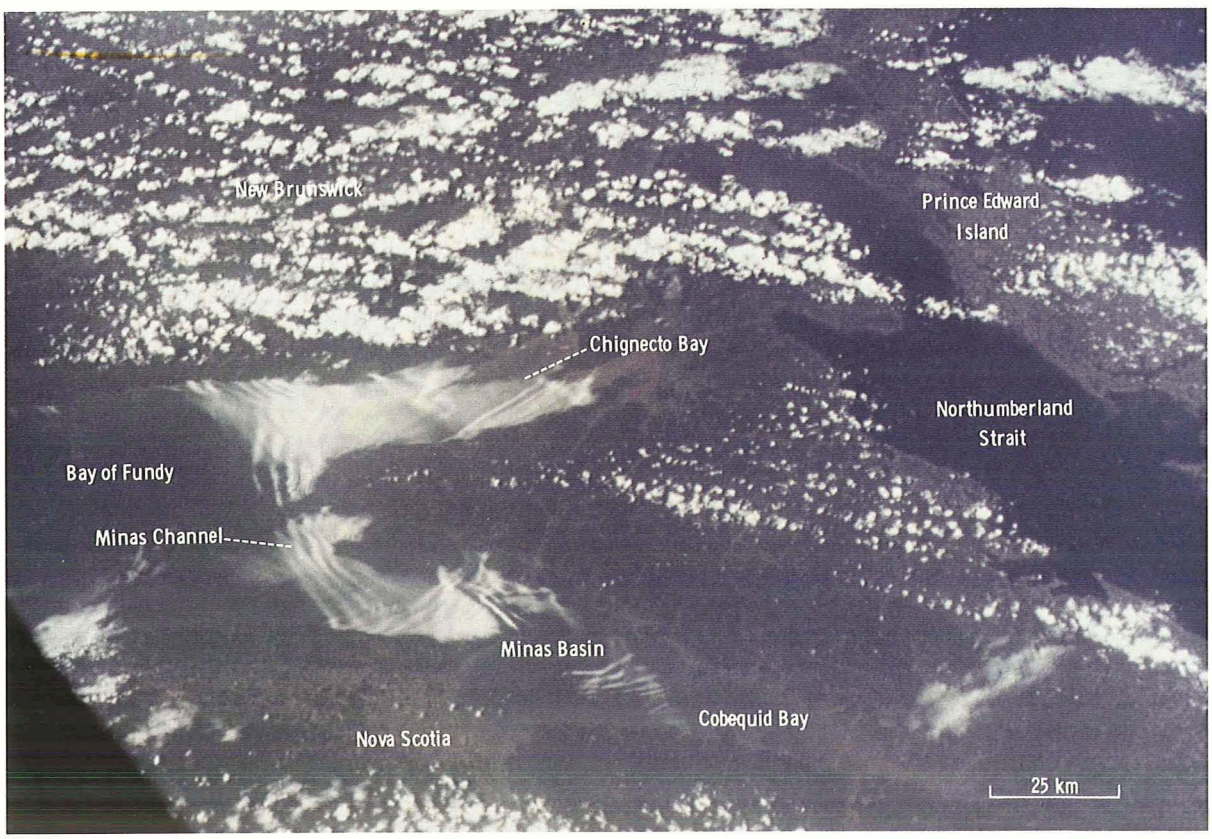


FIGURE 2.—An ASTP photograph (AST-8-495) showing same scene as figure 1, but taken with a 35-mm Nikon camera with a 300-mm lens.

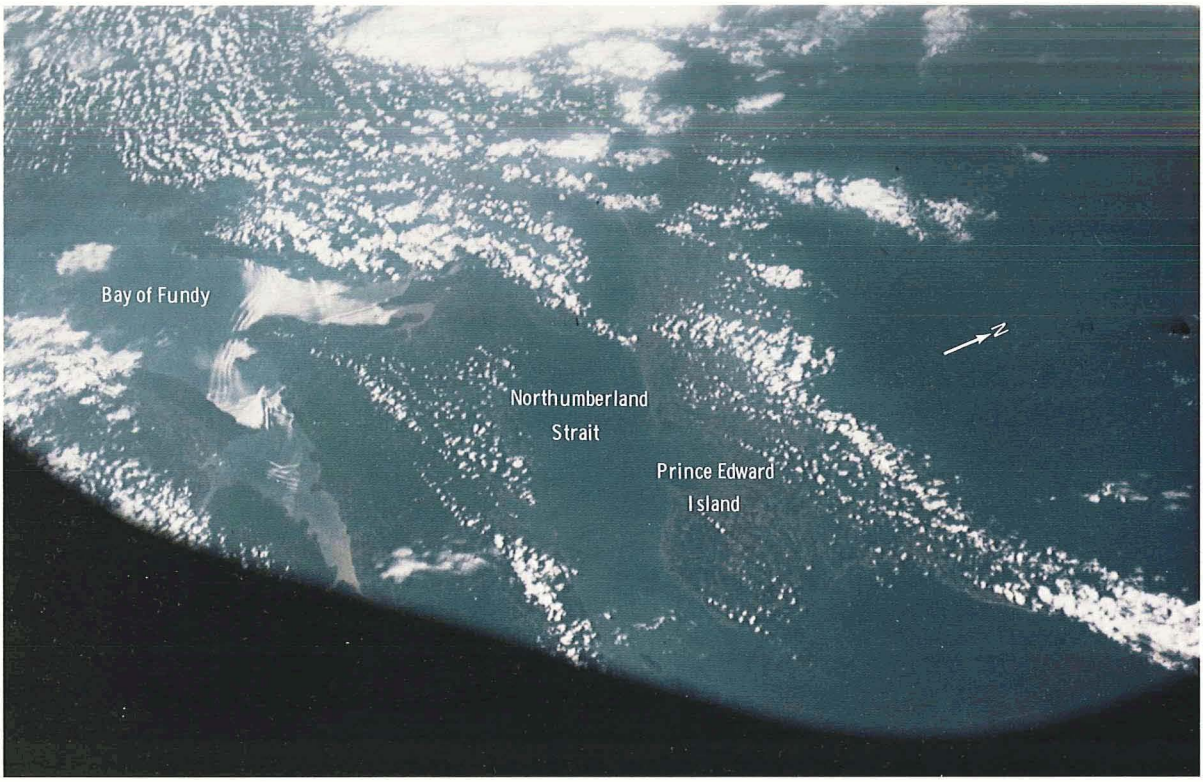


FIGURE 3.—Atmospheric wave patterns over the Bay of Fundy (AST-21-1705).

strong vertical wind shear across the inversion surface.

Other interesting wave patterns in the fog are shown in figures 7 to 10. Figure 7 shows an ASTP photograph taken on July 24, 1975, of the French Islands, St. Pierre and Miquelon, just offshore from the Burin Peninsula, Newfoundland. The ocean area is covered with fog and its temperature is approximately 283 K (10° C). A bow wave is formed around the southernmost part of Miquelon Island by the southwesterly winds. Flow around these islands appears to be responsible for the clear wakes downwind where turbulent mixing destroys the inversion layer. Airflow around the Burin Peninsula appears to be responsible for the waves in the fog adjacent to the Burin Peninsula.

Several minutes later, a photograph was taken that shows extensive wave motion in a fog bank several hundred kilometers east of St. John's, Newfoundland (fig. 8). The wavelengths for these waves are approximately 4 km.

Another example of a wave field generated by an island is shown in figure 9. This ASTP photograph looks west with the southwest tip of Newfoundland in the foreground, the Magdalen Islands in the center, and the Gaspé Peninsula and New Brunswick in the distance. It has been shown by Fujita (ref. 2), who used several Skylab photographs as examples, that an island protruding above a strong, shallow inversion can produce a wake similar in appearance to that left by a speedboat moving over a water surface, provided the windspeed is strong. This wake appears as a series of waves that fan out in a V-shaped pattern behind the obstacle, with the wave fronts parallel to the sides of the "V." In the case illustrated in figure 9, the orientation of the cumulus cloud streets indicates the wind is blowing from the southwest. Note that a few wave fronts oriented

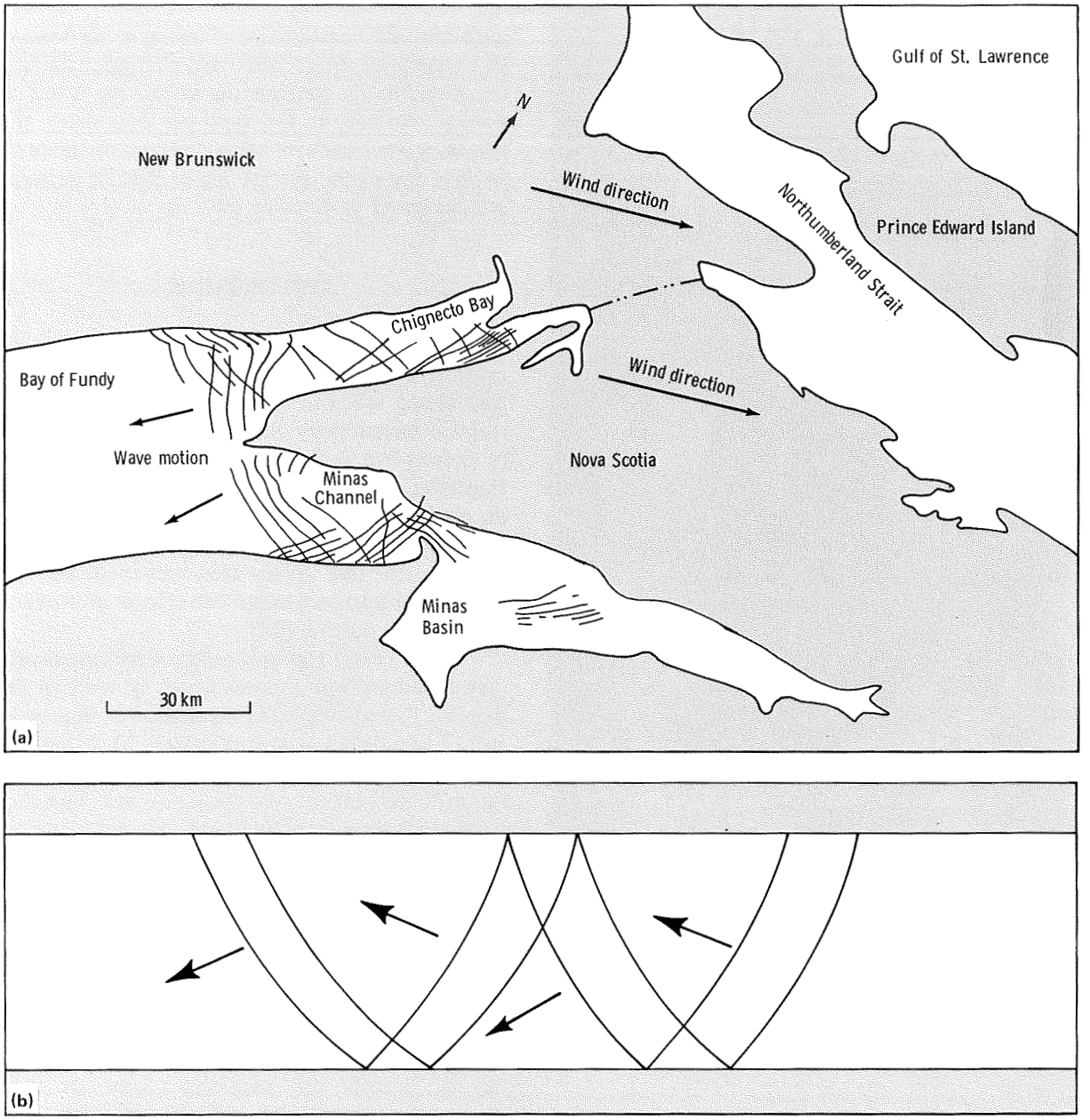


FIGURE 4.—Sketch of wave pattern in figure 2 and schematic of wave reflection from a boundary. (a) Sketch of wave pattern. (b) Wave reflection from a boundary.

roughly north-south are evident to the north of the northwestern coast of Newfoundland. Note also the series of wave fronts oriented roughly east-west that are south of the southern coast of Newfoundland. If these sets of wave fronts are extrapolated on a map to the apex of the "V," one finds St. Paul Island in the Cabot Strait just northeast of Cape North on Cape Breton Island, Nova

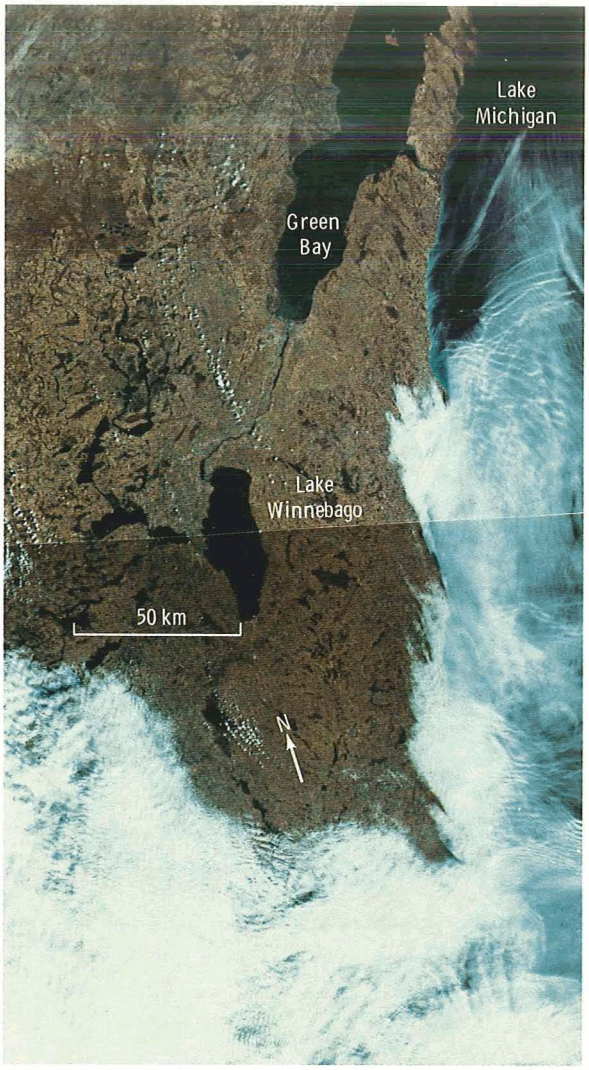


FIGURE 5.—Landsat-1 false-color composite (E-1269-6101 and E-1269-16104) of wave patterns in fog over Lake Michigan, April 18, 1973.

Scotia. Thus, it appears that these waves are a result of the airflow past an island and are similar to those observed on Skylab photographs.

Figure 10 shows a series of waves at the land-fog boundary all along the south shore of Nova Scotia. These waves appear to be triggered close to coastline irregularities such as jagged points of land and hills. The southwest wind indicated by the orientation of the cloud streets is blowing parallel to the coastline. Air flowing along this jagged coastline, where hills rise sharply from the sea, could easily generate perturbations in the inversion surface at the land-sea boundary; the resulting wave pattern is made visible by the presence of fog in the marine layer. Similar patterns are discussed by Ormsby (ref. 3).

ARC CLOUDS

In the general circulation of the Earth's atmosphere, a significant role is played by convective cloud systems. An important question in tropical meteorology at present concerns the role of convective downdrafts in the mechanics of tropical weather systems. Many numerical models do not consider the effects of downdrafts. It appears that downdraft effects may be considerable because of the large area covered by the downdrafts and because of the effects of interacting adjacent downdrafts.

Figures 11 to 13 are examples of arc clouds produced by maritime thunderstorm systems in the tropics. The photographs illustrated in figures 11 and 12 were taken at approximately 10° N latitude in the middle of the tropical Atlantic, and that in figure 13 was taken over the Coral Sea. The convective systems in both figures 11 and 12 are in their decaying stage with the system in figure 11 being slightly younger than the one in figure 12. In order to generate this system, a cluster of cumulonimbus clouds supported by strong updrafts had existed before these photographs were taken. The cloud cluster was characterized at the time of the photographs by heavy rain and a well-developed downdraft. The downward moving air parcels will evaporate some of their moisture, assuming they are not saturated. This cools the air parcels and accelerates them downward. It appears from upper-air maps[1] for this time period that these clouds are embedded in deep easterly flow extending from near the surface to the tropopause, and weak wind shear is

[1]Maps prepared by the World Meteorological Organization (WMO) Regional Center for Tropical Meteorology, Miami, Florida.

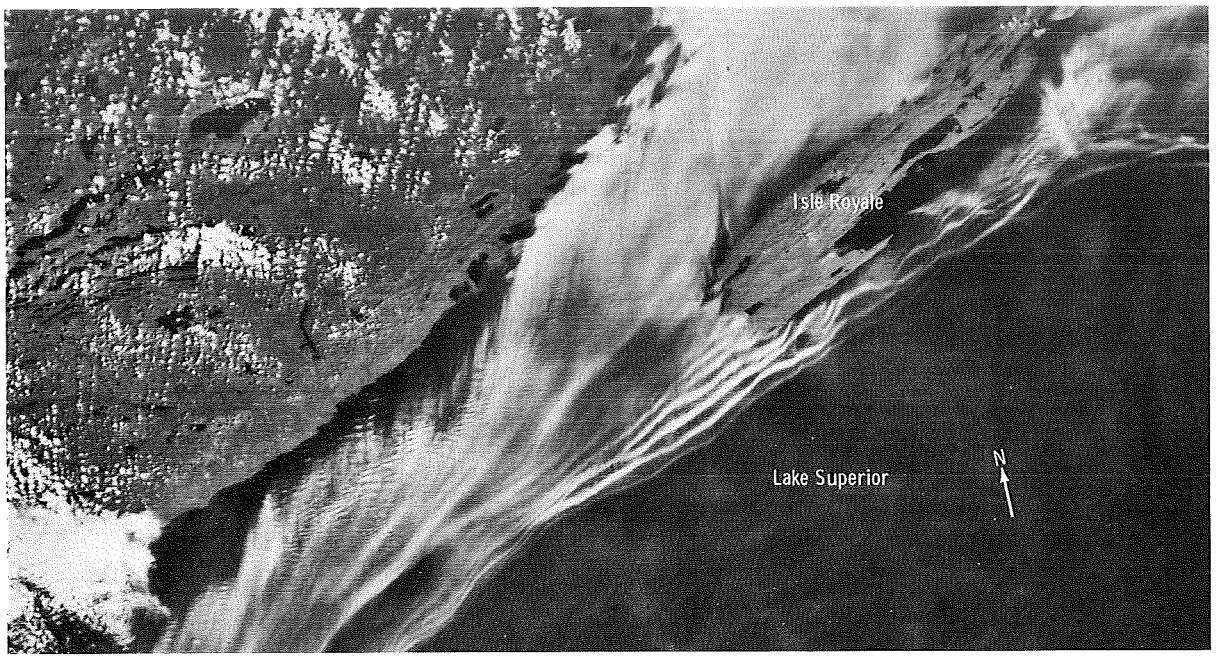


FIGURE 6.—Band 7 Landsat-1 image of waves in fog over Lake Superior, May 21, 1974 (E-1667-16134).

present. Therefore, the downward accelerating air will tend to spread out uniformly in all directions from the center of the rain shaft. Because of the acceleration induced by evaporation, the air will be moving outward from the rain area at a speed much greater than the low-level wind. The air that moves out ahead of the system (downwind or toward the west) will thus be moving faster than the surrounding air and will be moving into a region of fresh moist tropical air. The moist tropical air will be pushed upward over the top of downdraft air and will create an arc of ascending air and hence a line of towering cumulus clouds. Sometimes, adjacent cumulus cloud arc lines intersect; this produces very strong ascending motions and generates a new thunderstorm complex, which starts the whole process over again.

The downdraft air that spreads out behind the thunderstorm (upwind) is entering a region that has already been cooled by preceding downdraft air as the system moves toward the west. Thus, no collision with warm, moist tropical air occurs, and no arc cloud is formed on the downwind side of the cloud.

After several hours have passed, the parent cloud and debris clouds may evaporate entirely leaving only the cold pool of downdraft air. Such a case is illustrated in figure 13, where only a thin wisp of cirrus cloud remains of the thunderstorm complex. The cooler downdraft air is evident because the development of small cumulus clouds is inhibited in this area. After several more hours, mixing processes will warm the air and return the area to normal.

The cold downdraft pools enclosed by the arc clouds in figures 11 and 12 are on the order of 225 km in diameter. The one in figure 13 is perhaps 100 km in diameter.

Clear patches such as those in figure 13 have been interpreted by some oceanographers as manifestations of cold-core ocean eddies. It is believed that in the tropics this is almost never the case for the reasons cited by Maul (see section entitled "Interpreting ASTP Photographs of the Ocean and Locating the Area Photographed"). Cloud rings around cold eddies have yet to be documented by concurrent oceanic and atmospheric observations.

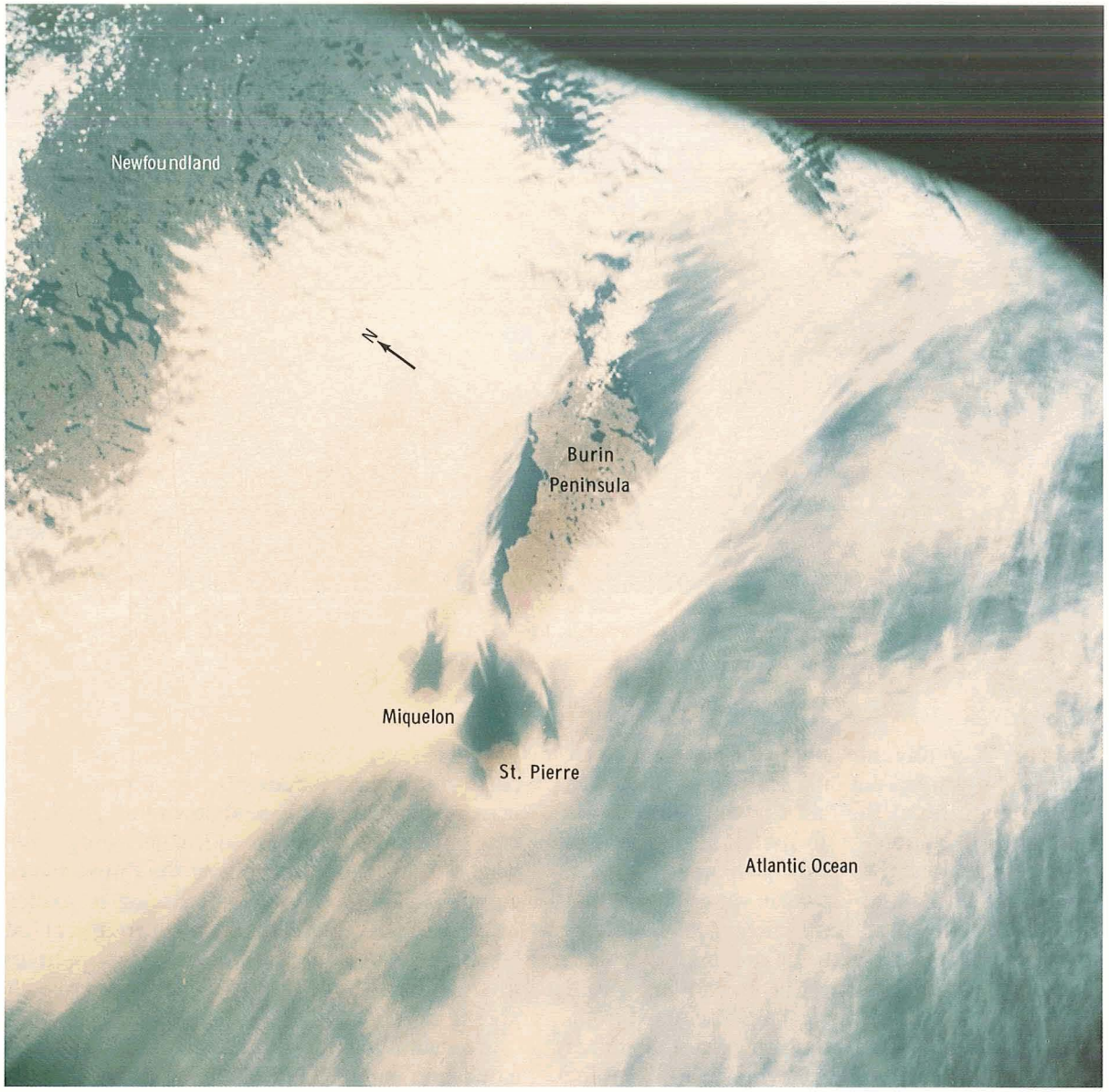


FIGURE 7.—Airflow around the islands of St. Pierre and Miquelon and the Burin Peninsula, Newfoundland, revealed in the fog pattern. This ASTP photograph (AST-13-806) was taken with a 70-mm Hasselblad camera with a 50-mm lens.

Almost every well-developed thunderstorm will produce its own pool of cold air. If the thunderstorm cloud is surrounded by a field of small cumulus clouds, its evaporation leaves a clear circular region, which remains until the residual cool air is warmed sufficiently by contact with the sea surface to allow the cumulus clouds to redevelop. The rate of evaporation depends on the atmospheric structure. Sometimes, the cloud evaporation is so slow that the cold air it produces is warmed again before all the remaining cloud debris evaporates.

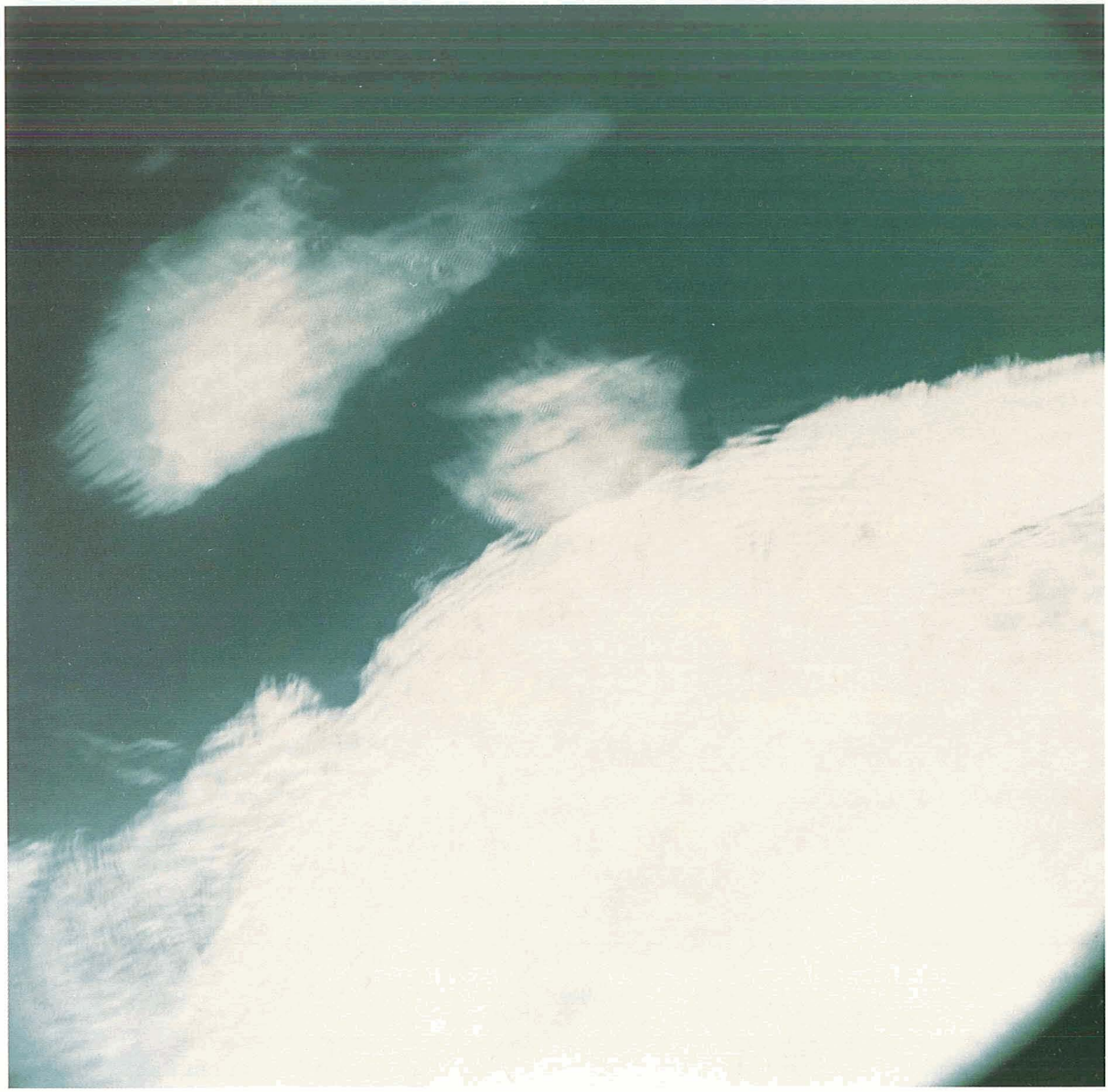


FIGURE 8.—Waves in fog bank east of Newfoundland. Hasselblad 70-mm camera with 50-mm lens (AST-13-813).

ANOMALOUS CLOUD LINES

Figure 14 is an intriguing photograph of intersecting linear cloud features located in the Pacific Ocean just off the southern California coast. The cloud lines are interesting in that they gradually broaden from their apparent point of origin. In addition, the enhanced cloudiness in the center of the line is flanked on either side by a clear moat.

It appears that these patterns are ship wakes. The effluent from a ship's stack in the form of aerosols, moisture, and heat will enhance conden-

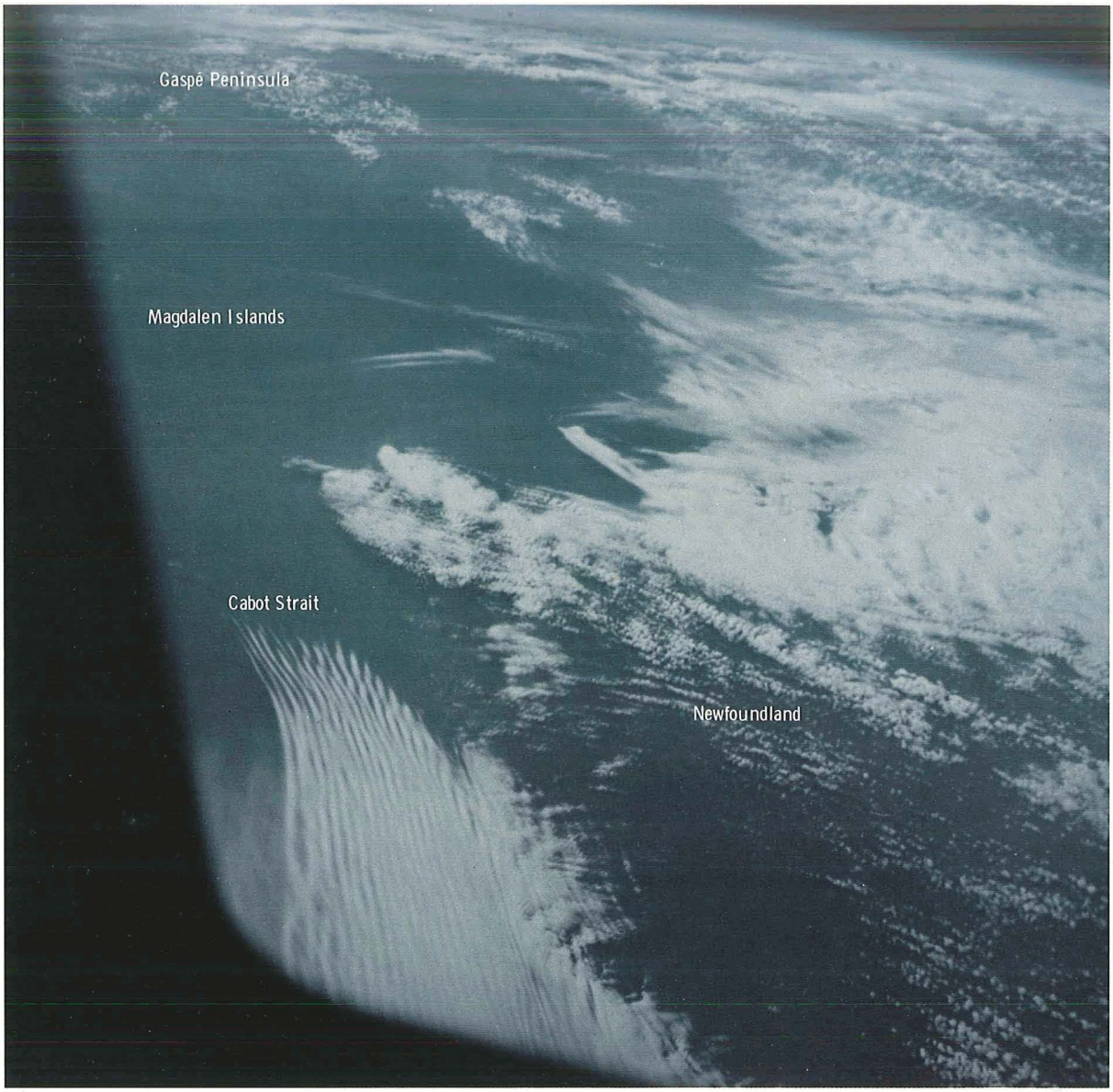


FIGURE 9.—Island wake and wave pattern in fog patch along the southern shore of Newfoundland, downwind from St. Paul Island in the Cabot Strait. Magdalen Islands and the Gaspé Peninsula can be seen in the distance. Hasselblad 70-mm camera with 50-mm lens (AST-30-2574).

sation at the top of the marine layer, capped by an inversion. The existence of the scattered stratocumulus cloud field indicates that condensation is just barely occurring naturally (i.e., the layer below the inversion is saturated or slightly supersaturated). The stack effluent could thus lead to enhanced condensation along the ship's path, which in turn could lead to a slight enhancement of the vertical motion along the track. Rising motion would occur along the track, with compensating sinking motion immediately adjacent to the track. This would create a thicker cloud along the ship's track and evaporate the clouds adjacent to the track. Diffusion processes would account



FIGURE 10.—The south shore of Nova Scotia is the land mass on the right in the photograph; the Atlantic Ocean is to the left of the land mass. Hasselblad 70-mm camera with 50-mm lens (AST-2-100).

for the horizontal broadening of the pattern downstream from the apparent source.

Figure 15 shows an NOAA-satellite view of ship trails similar to those in figure 14, but covering an extensive area of the eastern North Pacific between latitude 25° to 35° N and longitude 125° to 135° W, an area of approximately 1.23×10^6 km^2. At least 10 ship trails are evident in the stratocumulus cloud field. Their widths range from 15 to 25 km, approximately 3 times wider than the 3- to 7-km widths in figure 14.

This phenomenon is consistent with earlier observations first described by Conover (ref. 4) and referred to as "anomalous cloud line." It has since

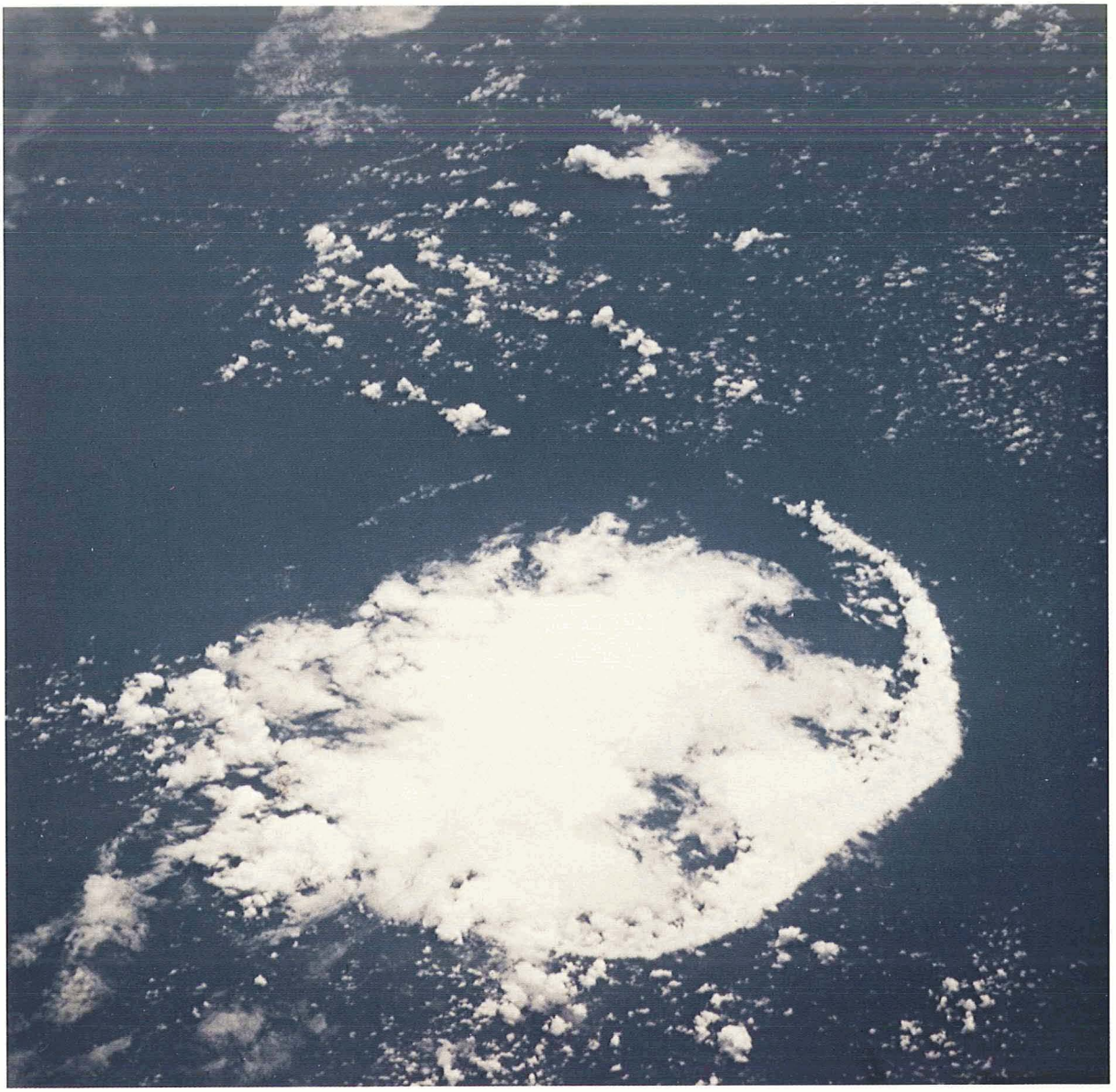


FIGURE 11.—Thunderstorm complex with arc cloud over central Atlantic near latitude 10° N on July 20, 1975, at approximately 15:00 UT. Hasselblad 70-mm camera with 50-mm lens (AST-27-2399).

been referred to as ship contrail, ship trail, or ship wake. Conover documented 16 cases of ship wakes observed by Tiros satellites and described the meteorological conditions under which they occurred. Bowley (ref. 5) later added five more cases. These cases were all located in the North Pacific between latitude 35° to 55° N and in regions dominated by high-pressure areas and generally light winds (less than 5 m/sec). These features appear to be frequently observed in the North Pacific and are long lived (a day or longer), based on geostationary-satellite imagery (ref. 6).

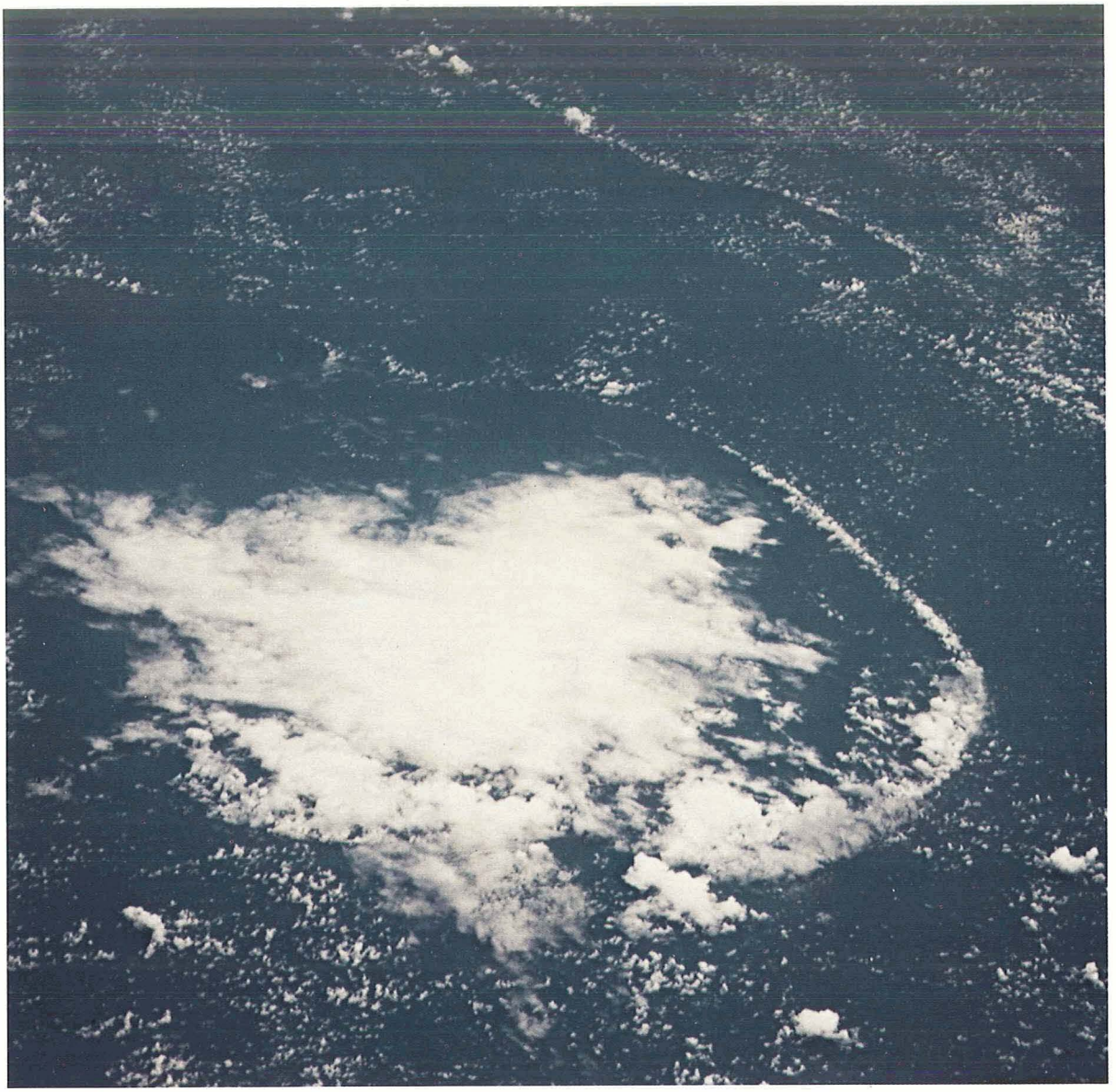


FIGURE 12.—Same as figure 11, except slightly farther southeast (AST-27-2396).

Aircraft observations linking the presence of a ship with the "anomalous cloud line" have been reported by Conover (ref. 7) and Parmenter (ref. 6). Recently, Randerson (ref. 8) reported on a Skylab observation of a ship wake bearing a strong similarity to that shown in figure 14.

Conover (ref. 4) gave an explanation for the ship wakes which is, in essence, the same as that described above. However, Twomey et al. (ref. 9) gave credence to the explanation by describing observations of very low cloud condensation nuclei levels in the subcloud layer beneath the inversion

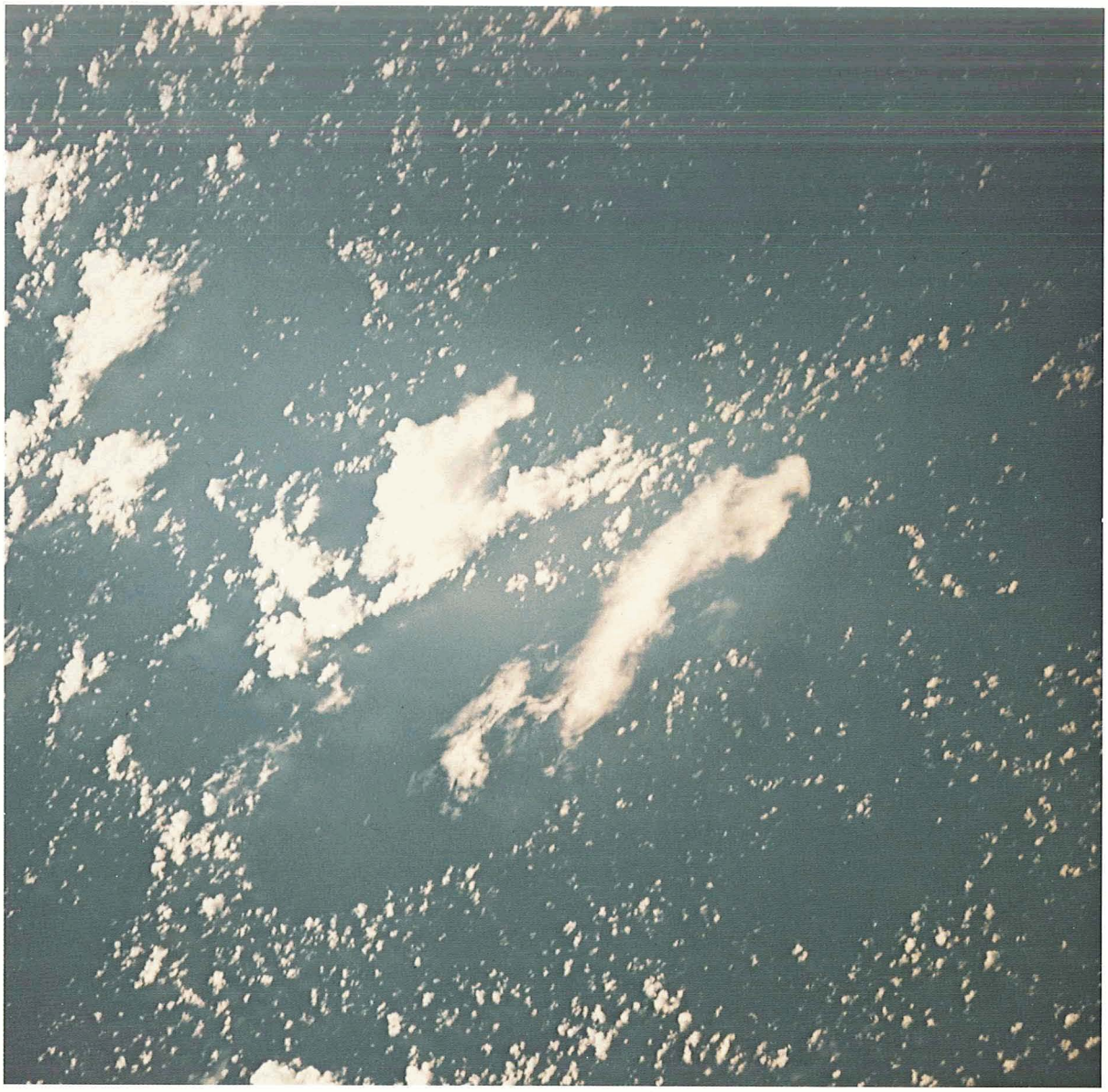


FIGURE 13.—Cloud-free hole in cumulus cloud field created by dissipating thunderstorm over the Coral Sea on July 20, 1975, 00:00 UT. Hasselblad 70-mm camera with 50-mm lens (AST-2-106).

in the areas where ship wakes had been observed. This would allow for saturated and supersaturated conditions to exist with very little condensation taking place. The aerosols released from the stacks of passing ships would thus act as cloud condensation nuclei, triggering enhanced cloud formation.

OVERSHOOTING CONVECTIVE CLOUDS

Figure 16 is a photograph of convective turrets overshooting a thunderstorm anvil near Yerevan, Soviet Armenia, taken from the Apollo spacecraft prior to its linkup with the Soyuz spacecraft,



FIGURE 14.—Stratocumulus cloud field with apparent ship trails in the Pacific off the coast of southern California, July 16, 1975, 22:30 UT. Hasselblad 70-mm camera with 250-mm lens (AST-1-42).

which is shown in the upper left at a distance of 34 m. The photograph was taken looking southeastward with the sunset terminator in the background. West is to the right and east is to the left. The anvil is approximately 200 km long and approximately 50 km wide at its western end. Shading of the anvil top indicates that it is dome shaped with the overshooting turrets protruding above the dome. The strong anvil outflow toward the west opposing the strong westerly flow over the anvil top is apparently responsible for the shear-induced Kelvin-Helmholtz waves that ema-

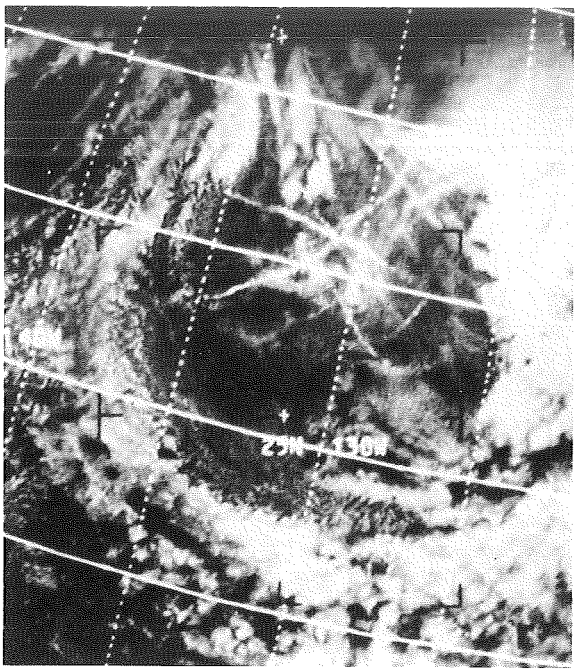


FIGURE 15.—An NOAA polar-orbiting satellite image of the eastern North Pacific, just off the U.S. west coast. A stratocumulus cloud field is shown to be crisscrossed by brighter, linear cloud features. These features appear to be generated by ships and are a larger scale view of the type of cloud feature in figure 14.

nate from each of the turrets in the westerly and northwesterly direction. These waves are similar to the waves observed in hurricane and typhoon circular convective clouds by Black (ref. 10) using Skylab imagery.

RECOMMENDATIONS FOR SHUTTLE ERA

One of the shortcomings of manned space photography has been the lack of coordination with ground-based measurements. This has not always been possible in the past because many of the interesting photographs were made in a discovery mode of operation. Earth-science investigators are still learning what interesting phenomena can be observed from space. In the future, however, much more can be learned about certain phenomena if photographs from space are linked with quantitative observations from the ground.

For instance, if vertical profiles of temperature and moisture had been available coincident with the acquisition of the photograph in figure 2, models of internal-wave motion could have been tested by comparing the predictions of excited wavelengths to be expected in such a situation.

If an aircraft had been able to obtain meteorological data through the arc clouds in figures 11 or 12, various energy budgets and diagnostic parameters concerning the role of convective-scale updrafts and downdrafts and their interaction with the tropical general circulation could have been calculated. Aircraft data sometimes suffer from a lack of perspective, and satellite data sometimes suffer from not being quantitative enough. Therefore, the two can complement one another if coordinated.

The Space Shuttle offers a great opportunity to coordinate space photography with ground-based measurements. A number of global-scale meteorological experiments are being planned for the 1980's, the decade when the Space Shuttle will be operational. A global-scale geosynchronous-satellite network will be in operation in addition to the implementation of the World Weather Watch, a World Meteorological Organization plan to standardize global meteorological observations.

Handheld-camera photographs, taken by Space Shuttle crews on a target of opportunity basis, offer great opportunity to add to the data sets presently being planned. A visual observations project similar to the one conducted during Skylab and ASTP does not presently exist. Valuable resources will be wasted if investigators do not take advantage of this opportunity to obtain photographs of meteorological events in areas of the world where meteorological experiments are being conducted at the same time as Space Shuttle flights.

It is recommended, therefore, that a complement of handheld cameras be carried for crew use in photographing meteorological targets as time and orbital constraints permit. A program of crew training should be established. Most important, a communications link between ground-based or airborne observation teams and the Space Shuttle crews should be established to ensure coordination of observations on the targets of interest.

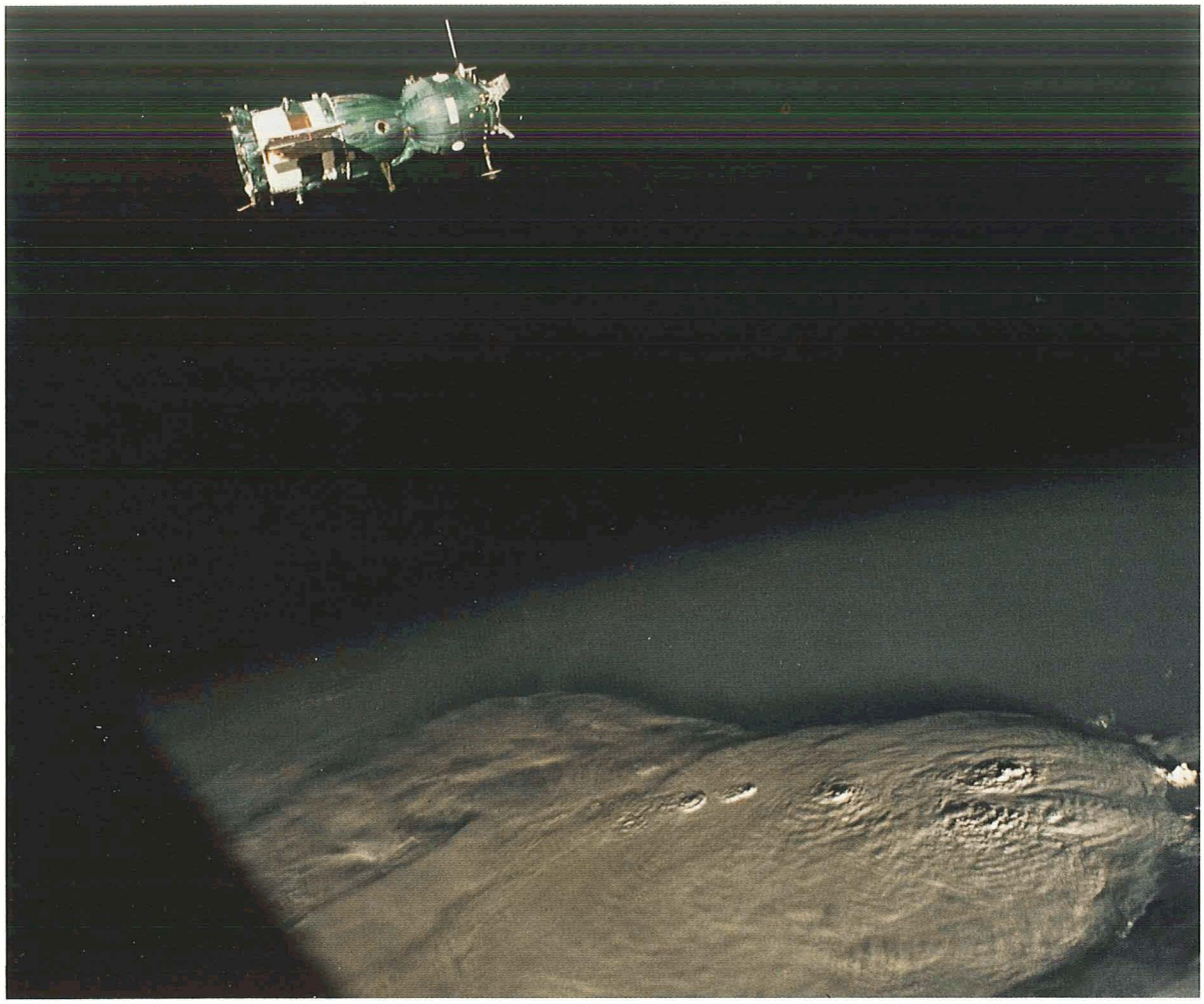


FIGURE 16.—Overshooting convective turrets in a thunderstorm anvil near Yerevan, Soviet Armenia, July 19, 1975, 18:00 UT. Soyuz spacecraft is in foreground at a range of approximately 34 m. Hasselblad 70-mm camera with 50-mm lens (AST-2-94).

The advantages of Space Shuttle for this type of program are as follows:

(1) It can serve as an experimental platform for integrating remote-sensing observations from various other platforms; i.e., polar-orbiting Sun-synchronous satellites, geostationary satellites, aircraft, and surface platforms. The integrated approach does not exist at present.

(2) One can take advantage of a lower orbit and obtain higher resolution data than can be obtained by other means in order to enhance interpretation of other data, especially time histories. A low-orbit unmanned satellite is uneconomical. Shuttle crews can serve as calibrators and interpreters.

(3) It can be used as a "test bed" for feasibility studies.

(4) It makes use of man's unique observational and judgmental capabilities.

(5) One can optimize orbital parameters for solving a specific problem.

(6) One can design sequential experiments of increasing complexity.

ACKNOWLEDGMENTS

Photographs in figures 5 and 6 were brought to the author's attention by Walter Lyons, University of Minnesota.

REFERENCES

1. Apel, John R.; Byrne, H. Michael; Proni, John R.; and Charnell, Robert L.: Observations of Oceanic Internal and Surface Waves From the Earth Resources Technology Satellite. J. Geophys. Res., vol. 80, no. 6, 1975, pp. 865-881.

2. Fujita, T. Theodore; and Tecson, Jaime J.: Mesoscale Wake Clouds in Skylab Photographs. Sec. 17 of Skylab Explores the Earth, NASA SP-380, 1977, pp. 463-477.

3. Ormsby, J. P.: Mesoscale Cloud Phenomena Observed by Landsat. NASA TN D-8494, 1977.

4. Conover, John H.: Anomalous Cloud Lines. J. Atmos. Sci., vol. 23, no. 6, Nov. 1966, pp. 778-785.

5. Bowley, Clinton J.: Comments on Atmospheric Requirements for the Genesis of Anomalous Cloud Lines. J. Atmos. Sci., vol. 24, no. 5, Sept. 1967, pp. 596-597.

6. Parmenter, Frances C.: Ship Trails or Anomalous Cloud Lines. Mon. Wea. Rev., vol. 100, no. 8, Aug. 1972, pp. 646-647.

7. Conover, John H.: New Observations of Anomalous Cloud Lines. J. Atmos. Sci., vol. 26, no. 5, Part II, Sept. 1969, pp. 1153-1154.

8. Randerson, Darryl: Quantitative Analysis of Atmospheric Pollution Phenomena. Sec. 14 of Skylab Explores the Earth, NASA SP-380, 1977, pp. 381-405.

9. Twomey, S.; Howell, H. B.; and Wojciechowski, T. A.: Comments on "Anomalous Cloud Lines." J. Atmos. Sci., vol. 25, no. 2, Mar. 1968, pp. 333-334.

10. Black, Peter G.: Some Aspects of Tropical Storm Structure Revealed by Handheld-Camera Photographs From Space, Sec. 16 of Skylab Explores the Earth, NASA SP-380, 1977, pp. 417-461.

Comparison of Astronaut Visual Color Observations With ASTP Photographs

Farouk El-Baz,[a†] Delia M. Warner,[a] and Fred J. Anders [a]

ABSTRACT

Visual observations of the color of both desert and ocean scenes, made by the U.S. astronauts on the Apollo-Soyuz mission, were analyzed and compared to photographs of the same regions. During the mission, use of Munsell color chips on a specially developed "color wheel" made the comparison possible. Colors on photographs never exactly match those observed from space; available films are less color sensitive than the human eye and do not capture the true Earth colors. Determination of a color correction factor for use with the photographs was not possible because of the inconsistent variations in measured colors and because of the meager statistical basis. It is recommended that additional observations be made from Earth orbit utilizing uniformly illuminated color chips. This would allow meaningful correlations between natural colors as seen from space and those depicted on orbital photographs.

INTRODUCTION

Astronauts of the Gemini, Apollo, and Skylab missions consistently reported that Earth colors observed from space were not captured accurately on film. As a result, visual color observations were planned as part of the Earth Observations and Photography Experiment (refs. 1 and 2) on the Apollo-Soyuz Test Project (ASTP). An attempt was made to quantify the color observations by the use of standard color chips. In addition to the knowledge of actual Earth color, it was hoped that astronaut visual color observations could be used to calibrate the colors on the photographs.

It was recently realized that color is an important parameter in studying orbital photographs. For example, in oceanography, measurements of water color are important in identifying distinct ocean currents, eddies, and areas of biological productivity (ref. 3). Also, in desert regions, a study of color variations could supply information on sand sources and the relative ages of sand seas (ref. 4).

WHAT IS COLOR?

Color is a phenomenon of light that depends on wavelength, specifically as seen by the eye. Light waves have different wavelengths; monochromatic light has its energy concentrated in a single wavelength, and white light or sunlight has an even distribution of energy throughout the visible spectrum (wavelength ranges from 380 to 720 nm). The latter is the band of light that develops when light passes through a prism and is broken down into its component colors composed of red, orange, yellow, green, blue, indigo, and violet. Red light has the longest wavelengths, and violet the shortest. When light falls on an object, some of the light is absorbed and some is reflected. An object observed in daylight appears in the color of the reflected waves.

The ability to discriminate light on the basis of its wavelength composition is called color vision. The eye is assumed to have visual receptors that

[a]National Air and Space Museum, Smithsonian Institution.

[†]Principal Investigator.

respond differently to the various wavelengths of the visible light. As far as human vision is concerned, the commonly accepted view is that there are three or more types of receptors that possess pigments, which selectively absorb light from a particular region of the visible spectrum.

Colors in nature usually occur in an infinite number of mixtures; one seldom encounters a surface whose color is narrowly tuned to a single wavelength of light. The human eye is a very sensitive color sensor; it is more sensitive to subtle color variations than any instrument or film. Under laboratory conditions, the eye is estimated to be able to distinguish 7.5 million color surfaces, a precision that is two to three times better than most photoelectric spectrophotometers (ref. 5).

ASTP COLOR WHEEL

An important objective of the Earth Observations and Photography Experiment was to quantify desert and water colors observed by the astronauts during orbit. This was achieved through the use of a two-sided color wheel composed of carefully selected colors (fig. 1). Numerous versions of the color wheel were used by the crew during flyover exercises to obtain data on land and water colors. Actually, the colors of the wheel were selected on the basis of experience gained during the flyovers.

The color wheel, fabricated at NASA Lyndon B. Johnson Space Center (JSC),[1] was in a "doughnut" shape with a 20.3-cm (8 in.) diameter and a 12.7-cm (5 in.) central hole. It was constructed of 3-mm (1/8 in.) thick aluminum with double rows of Munsell standard color chips fastened to both sides. Each color chip was identified with a row identifier ("A" or "B") and a number that established its position in the row. A total of 108 different color chips were fastened onto the wheel; 54 color chips for desert colors on one side and an equal number for ocean colors on the other. The doughnut configuration allowed the crewmembers to conveniently hold the device and to rotate it until the proper color in either row "A" or "B" matched the scene on the Earth's surface.

Each color chip on the wheel corresponds to a color of the Munsell system (ref. 6). In this system, every color is identified by three basic attributes: hue, value, and chroma. These three properties form a three-dimensional balance, which the human eye perceives as a single color. Hue can be defined as the name of a color. It is that quality by which we distinguish one color family from another, as red from yellow, or green from blue (ref. 6, p. 15). There are five principal hues: red, yellow, green, blue, and purple. Five additional hues are formed by their intermediate combinations, YR, GY, BG, PB, RP, forming a continuous spectrum. Value is the lightness or darkness of a color. A light gray would have a high value, and black would have a very low value. Chroma is defined as the intensity, saturation, or strength of a color. A weak red has a lower chroma than a vibrant, strong red. Variation in either of these three attributes changes the exact color that is perceived.

Notation of color in the Munsell system takes the following form: Hue Value/ Chroma (H V/C). Hue is noted first by the initials of one of the 10 principal hues. A finer division of hue is obtained by dividing each hue into four subdivisions: 2.5, 5, 7.5, and 10. A 2.5YR is closer to the red end of the spectrum and a 10YR is closer to the yellow. However, both are yellow-red in hue. Value is noted next. It ranges from 1 (very dark, black) to 10 (very light, white). On the color wheel most chips range between values of 3 to 8. Chroma is the last color attribute to be noted. Each color chip on the wheel represents an even increment of chroma ranging between 4 and 12. Thus, any numbered chip on the color wheel can be put into Munsell notation; for example, color 16A on the wheel is 5YR 6/6 in the Munsell system (fig. 1).

VISUAL COLOR OBSERVATIONS

As previously stated, one of the principal objectives of the Earth Observations and Photography Experiment involved the use of a color wheel to quantify the visual observations of desert and ocean colors. During the mission, the ASTP

[1]Robert Wolfe of the Smithsonian Institution assisted James Regan of JSC in the preparation of the color wheel.

crewmembers held the color wheel up to the spacecraft window and noted the number of the Munsell color chip that best matched the color of the scene below. A total of 13 color comparisons were made in this manner.

Observations of desert areas included the Gran Desierto (16A); the Simpson Desert (6A); the Sahara Desert north of Lake Chad (25A); and Western Australia (9A). (For identification of desert colors see fig. 1(a).)

Ocean color observations were made over the Pacific Ocean northeast of New Zealand (47B); the Pacific Ocean east of Hawaii (47B); the Pacific Ocean off the coast of San Francisco (47B); the Mediterranean Sea between Tripoli and Sicily (36); the Caribbean Sea southeast of Jamaica (42A); current boundaries in the north Atlantic (37 to 41); and the Gulf of Mexico near the Mississippi coast (47B to 45B). (For identification of ocean colors see fig. 1(b).)

During some visual observation passes, viewing conditions were excellent, as clearly indicated by the following comments between the Apollo commander (ACDR), command module pilot (CMP), and capsule communicator (CAPCOM) (ref. 2, p. 149-150):

CMP — Hey, we're going over the Simpson Desert right now. And it's just fantastic. It's got dunes in it. It looks like they are very long, and they look like road tracks there are so many of them—like hundreds of parallel road tracks. And we'll comment on it in our usual fashion with the onboard tape recorder . . . .

ACDR — Yeah, and the long red streaks are matching about color 10, I would say, on Farouk's (color) wheel.

CAPCOM — Thanks a lot for the input; wish I could see it myself. Beano and I are whipping out our color chart and seeing what color it is ourselves.

CMP — This is one of those cases where there was light coming in the window, falling on the color chart. And that made it easy to use. Sometimes when it's in the shadow, it's hard.

CAPCOM — Roger. Understand. Incidentally if you ever do have a question about the chart or any comment on it, we've got one here at the console that's just about identical to yours, I think.

ACDR — And some of those long streaks, those long sand streaks, could have either gone between 9 and 10.

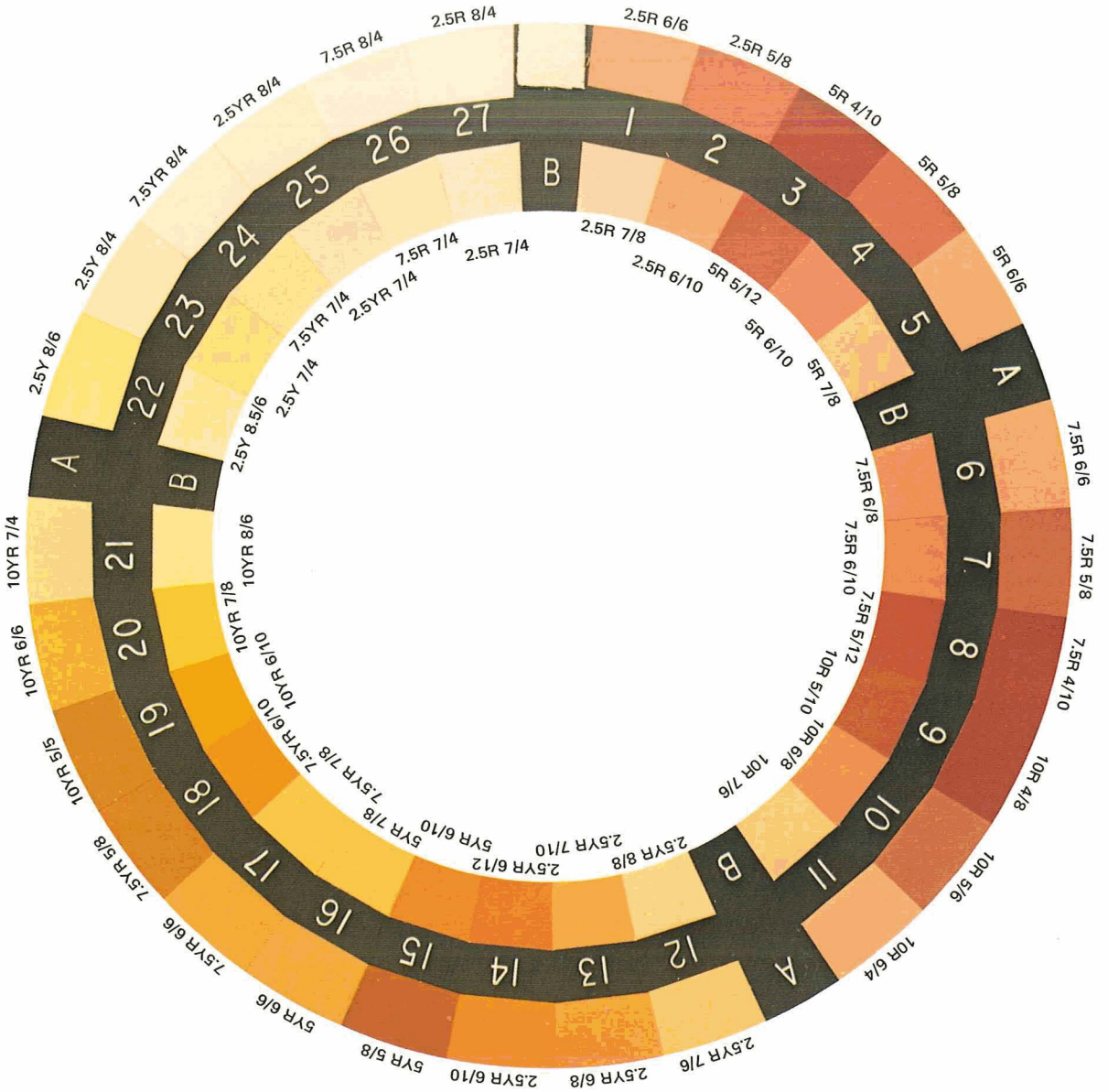
CAPCOM — Okay, thanks, Tom. Could you differentiate 9 or 10-A or B? Are they dark or light?

ACDR — Now that the sun gets on the wheel where I can see it, it was more like 9. Oh, I'm sorry. Okay. Be about like 9-A.

However, the ASTP color observations were not always made under the best possible viewing conditions. A number of factors, including spacecraft attitude, Sun angle, and atmospheric conditions, influenced the color comparisons and perhaps even affected their validity. The astronauts were aware of these problems, and early in the mission, they informed the Earth observations support team of the difficulties they sometimes encountered in using the color wheel.

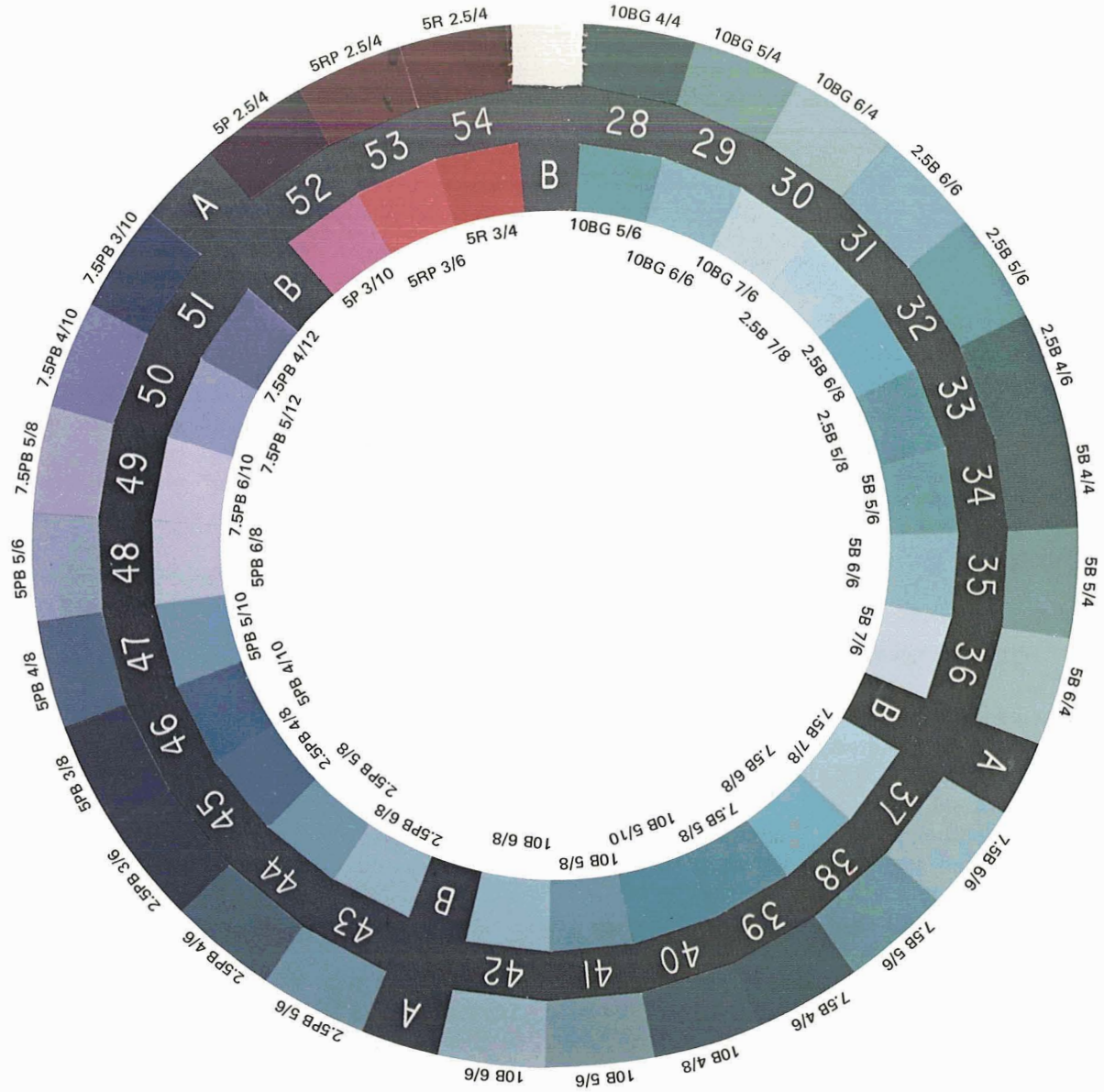
The main problem involved the varying lighting conditions within the spacecraft cabin. The astronauts found it difficult to compare the colors of a sunlit target with the Munsell color chips when the color wheel was shaded from the Sun. After the mission, this problem was discussed during the technical crew debriefings. The docking module pilot (DMP) and CMP commented as follows (ref. 2, p. 182):

DMP — But it (the color wheel) worked pretty good in the airplane where you get lighting behind it which corresponds with the lighting you're seeing on the ground. And in the spacecraft, you're always in the shade with the color wheel, but you are looking at (something) in the sunshine and trying to compare the two is like comparing apples with oranges. And the only way I could



(a)

FIGURE 1.—The two-sided color wheel used by Apollo astronauts for visual comparison with colors of observed Earth scenes. Color chips were given numbers arranged in two rows, "A" and "B." Munsell color notations are given near the corresponding chips. (a) Desert colors. (b) Ocean colors.



(b)

FIGURE 1.—Concluded.

DMP Concluded: come up with anything even close, I'd look out the window and then I'd come back in the cockpit and get the color wheel in the light, and look at that and say, I think that was close to what I was looking at.

CMP: My technique was to hold the color wheel sideways in the window and hope some light would shine on it.

Because of the viewing problems they encountered, the crew recommended the development of a handheld optical color comparator. If developed, this device would be about the size of a pair of binoculars. Through one half of the instrument the Earth could be viewed; the other half would "contain a uniformly lighted color screen, which could be varied to obtain ground/screen color comparisons" (ref. 2, p. 119).

COLOR OF ASTP PHOTOGRAPHS

The conventional interpretive procedures used with aerial photographs are different for Earth orbital photographs, largely because of the latter's greater regional coverage and frequent obliquity. For orbital photographs, photointerpreters find that color and texture are the most important recognition elements. Color is especially significant because natural colors are meaningful and are often important indicators of the identity of surface features. The human eye is able to distinguish significantly more color surfaces than gray tones. Because of this, most photointerpreters agree that color photographs are more useful and more informative than black-and-white photographs.

The geologist uses color variations to detect features such as boundaries between geological formations and to make gross lithological discriminations for thematic mapping. Studies of regional tectonic patterns, which include detection of faults, fractures, and folds, are also facilitated by the use of color orbital photographs.

Desert specialists use orbital photographs to study variations in the colors of desert sands. These color variations are meaningful and could provide information on the chemical makeup and relative ages of sand bodies. Desert sands often contain iron compounds, and the red color of many sand seas is due to the presence of iron oxide (hematite) coatings on individual grains. The degree of reddening in sands of uniform aridity, and derived from the same source, could be used to determine the relative ages of the sands (for example, ref. 4).

In the Western Sahara, the ASTP crewmembers noted the occurrence of reddened sands in a large expanse of the Algerian Desert (ref. 2, pp. 77 and 141) (fig. 2):

DMP: Oh, there's some really heavy clouds of sand blowing down there; some darker rock hills sticking out. . . . Some very red sand to the north. In fact, it looks almost like a massive parabolic sand dune, black with red sand behind it. And we're coming up on a large band of very black barren-looking hills with great red areas interspersed between them . . . .

The astronauts also noticed that in the Sahara the colors of desert sands were generally lighter along the Mediterranean coast. This sequence of the redder and presumably older sands accumulating inland away from the brighter and more yellow sands along the coastline is duplicated in the Namib Desert of southwestern Africa (refs. 2 and 7).

Color variations are also important to oceanographers, and accurate measurements of water color can help identify distinct ocean currents, eddies, and areas of biological productivity (ref. 3). On orbital photographs, a body of water may exhibit a wide variation in color, which could be a function of a number of factors such as Sun angle, water surface roughness, suspended sediments, and bottom topography (ref. 8, p. 1487). Theories concerning the optical properties of water suggest that a pure, deep body of water would be blue. Discoloration of water would occur as a result of the presence of (1) organic or nonorganic particles, such as suspended river sediments discharged into the ocean; (2) life forms such as red tide phytoplankton; and (3) bottom



FIGURE 2.—ASTP photograph showing various hues of reddened sands in part of the Algerian Desert (AST-17-1339).

topography in shallow water (ref. 8, p. 1488). For example, figure 3 illustrates the differences in water color between shallow and deep water bodies. In this ASTP photograph of Aitutaki Atoll in the Cook Islands, the triangular-shaped atoll is distinguished by the light blue color of the shallow lagoonal waters enclosed by a coral reef. The surrounding ocean waters are a deeper, darker blue.

It is difficult for a color film to reproduce a scene with total color fidelity, largely because available films are less color sensitive than the human eye and do not capture the true Earth colors. In addition, a number of other factors, such as Sun angle, atmospheric conditions, and film processing procedures, will influence the colors recorded on film. From the authors' own

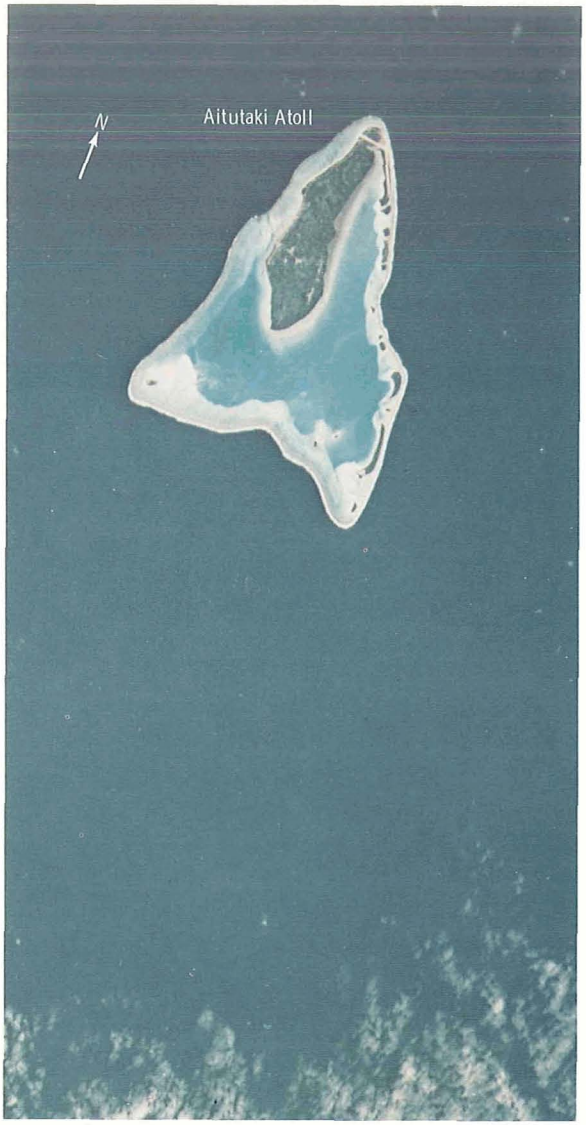


FIGURE 3.—ASTP photograph of Aitutaki Atoll in the Cook Islands. Note the differences in water color between the shallow lagoonal waters and the surrounding deep ocean waters (AST-1-39).

experience they have found that the color prints made from the same negative can differ greatly if processing conditions are not strictly controlled.

The effects of Sun angle and atmospheric conditions are illustrated in figure 4. These three photographs were taken over different sections of the Great Barrier Reef, which extends more than 2000 km along the eastern coast of Australia. Figure 4(a) is overexposed, which darkens and deepens water color and suppresses the brighter hues of the shoals. Figure 4(b) was taken under haze conditions, which reduces contrast at the land/water interface and gives the whole photograph a blurry appearance. Figure 4(c) was taken at a low Sun-illumination angle, which drastically changes water color but, in the meantime, enhances water surface texture. This particular photograph was taken with a Sun azimuth angle which allowed direct reflection that simulated sunglint conditions. These three photographs clearly show how ocean colors can drastically vary with variation in Sun illumination conditions.

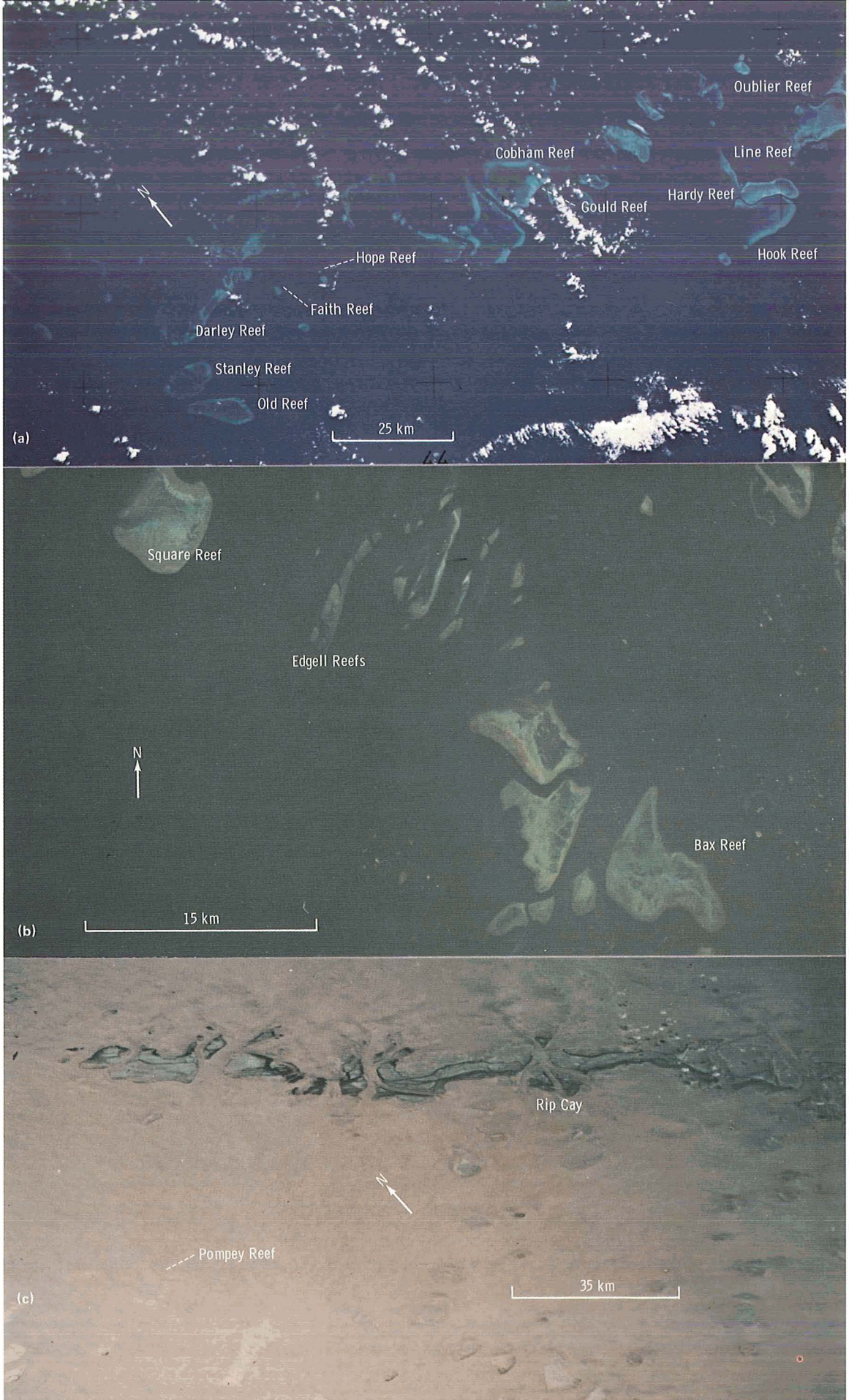
CONCLUSIONS

Visual color observations from Earth orbit complement photographic data. Color photographs, although they can depict subtle color changes in the photographed scene, do not faithfully capture natural colors. For this reason, the human eye can be efficiently used to add significant data in support of photointerpretation.

The observation aids used on ASTP fell short of achieving valid color comparisons. It is recommended that, for future space missions, particularly Shuttle flights, a better color-comparison aid be developed. This aid should have consistent internal lighting and should also permit the observer to mix various colors to achieve the best match.

Perhaps this type of observation aid could be achieved with a device resembling binoculars. Through one eyepiece the Earth could be viewed; the other half could contain an internally illuminated color screen. This device would provide a simultaneous view of the color screen and the target.

FIGURE 4.—Three ASTP photographs over parts of the Great Barrier Reef, Australia, illustrating how the ocean colors captured on film are affected by variations in Sun illumination conditions. (a) Overexposure (AST-16-1153). (b) Hazy atmospheric conditions (AST-2-103). (c) Low Sun-illumination angle (AST-1-46). →


Oublier Reef
Cobham Reef
Line Reef
Hardy Reef
Gould Reef
Hope Reef
Hook Reef
Faith Reef
Darley Reef
Stanley Reef
Old Reef
25 km
(a)
Square Reef
Edgell Reefs
N
Bax Reef
15 km
(b)
Rip Cay
Pompey Reef
35 km
(c)

REFERENCES

1. El-Baz, Farouk; and Mitchell, D. A.: Earth Observations and Photography Experiment MA-136. Sec. 10 of the Apollo-Soyuz Test Project Preliminary Science Report, NASA TM X-58173, 1976.

2. El-Baz, Farouk: Astronaut Observations From the Apollo-Soyuz Mission. Vol. I of Smithsonian Studies in Air and Space, Smithsonian Institution Press (Washington, D. C.), 1977.

3. Jerlov, N. G.; and Nielson, E. S.: Optical Aspects of Oceanography. Academic Press (New York), 1974.

4. El-Baz, Farouk: The Meaning of Desert Color in Earth Orbital Photographs. Photogramm. Eng. & Remote Sens., vol. 44, no. 1, 1978, pp. 69-75.

5. Committee on Colorimetry: The Science of Color. Opt. Soc. America (Washington, D. C.), 1963.

6. Munsell, A. H.: A Color Notation. Twelfth ed. Munsell Color Company, Inc. (Baltimore, Md.), 1975.

7. McKee, Edwin D.; Breed, Carol S.; and Fryberger, Steven G.: Desert Sand Seas. Sec. 2 of Skylab Explores the Earth, NASA SP-380, 1977, pp. 5-47.

8. Reeves, Robert G.; Anson, Abraham; and Landen, David, eds.: Manual of Remote Sensing. American Soc. Photogram. (Falls Church, Va.), 1975.

Film Selection for the Earth Observations and Photography Experiment

N. T. Lamar,[a] H. E. Lockwood,[b] and R. E. D'Alli[c]

ABSTRACT

Four color-reversal positive-transparency films were evaluated for use in the Earth Observations and Photography Experiment on the Apollo-Soyuz mission: Ektachrome MS SO-368 (normal color), Aerial Color SO-242 (normal color), Aerochrome Infrared 2443 (false color), and High Definition Aerochrome Infrared SO-127 (false color). Film SO-127 was eliminated because of its low speed. Aerochrome Infrared 2443, selected for use in discriminating vegetation, required exposure through a Wratten 12 filter. An equivalent lens filter (520-nm cutoff) was in the approved flight-hardware inventory. Aerial Color SO-242 was found to be suitably fast for use as a high-resolution, normal-color film; it required no special filter. However, Ektachrome MS SO-368, a medium-resolution, normal-color film, required exposure through the equivalent of a Wratten 2A filter. This item was not in the flight-hardware inventory and could neither be acquired nor approved in time for launch. Eastman Kodak Company was awarded a contract to manufacture a special version of SO-368 with a yellow dye overcoat whose absorption characteristics matched those of a 2A filter. In laboratory tests conducted at the Lyndon B. Johnson Space Center, the new film (designated QX-807 and delivered in March 1975) performed in every respect the same as SO-368 used with a 2A filter. Film QX-807 processing was compatible with other flight film and was done in the model 1811 Versamat Processor with EA-5 chemistry.

INTRODUCTION

Color photography of the Earth was one of two principal objectives of the Earth Observations and Photography Experiment on the Apollo-Soyuz Test Project (ASTP). This experiment was designed to evaluate the performance of astronauts in making scientific Earth observations from space. The value of a human observer in space lies in his ability to distinguish subtle "ground color" differences and to select and photograph targets of opportunity. To exploit these uniquely human faculties, 55 targets in the flightpath of the Apollo spacecraft were selected for visual study. Space photographs constituted a documentation of astronaut observations. Therefore, the response of the color film was tantamount to the success of the experiment. Selection and manufacture of the photographic film were the critical links in the chain of events from mission planning to the final reduction of ASTP experiment data.

Photographing the Earth's surface from space poses a few problems not encountered by ground-based amateurs and professionals. Just as incoming sunlight is most strongly scattered (by atmospheric gases and aerosols) in the blue region of the spectrum (thus, the blue sky), the light reflected from a photographic subject is similarly scattered on its way to the camera. Taking pictures through great thicknesses of the Earth's at-

[a]NASA Lyndon B. Johnson Space Center.

[b]Technicolor Graphic Services, Houston, Texas.

[c]National Air and Space Museum, Smithsonian Institution.

mosphere results in a bluish cast in an uncorrected photograph (refs. 1, 2, and 3). This phenomenon, well known to aerial photographers, is usually circumvented by using a haze filter such as the Wratten 2A in front of the lens. A haze filter is pale to light yellow in appearance, is opaque to blue light or shorter wavelengths, but is transparent to the other colors in the visible spectrum.

Beyond the problem of color correction, the high rates of speed maintained by orbiting spacecraft introduce another problem to space photography, that of image motion. (The Apollo spacecraft races over more than 7 km of its groundtrack every second of flight.) However, a combination of high shutter speeds and an appropriately designed shutter eliminate any blurring or image distortion due to motion.

CAMERA SYSTEM

The Hasselblad 70-mm camera system, workhorse of manned space-flight photography, was chosen for use in the experiment. One Hasselblad camera (called the "black camera" during the mission) was bracket-mounted to a spacecraft window and motor-driven to provide 60-percent overlap of consecutive frames; it was the mapping camera. The other Hasselblad (called the "silver camera") was a handheld single-lens reflex camera. Four interchangeable Zeiss lenses (table I) completed the system.

FILM SELECTION

Past experience led to the selection of four Eastman Kodak films for the experiment; the film characteristics are listed in table II. All four products are positive-transparency films. Ektachrome MS (SO-368) and Aerial Color (SO-242) are normal-color films. Aerochrome Infrared (2443) and High Definition Aerochrome Infrared (SO-127), both of which are false-color film, are suitable when desiring to discriminate vegetation from other features.

The properties of each film are important factors in choosing the appropriate lens and exposure values for the photographic targets. Ektachrome MS SO-368 is a special order version of the standard Aerochrome MS 2448 film. Aerochrome MS is a very-fine-grain, multilayer, color-reversal film balanced for daylight exposure. Its Estar base provides good dimensional stability, making it suita-

TABLE I.—Zeiss Lenses Used With the Hasselblad Cameras

Lens	*Focal length, mm*	*Maximum aperture*	*Best system performance achieved when —*	
			Used with: (a)	*Shutter speed is:*
Distagon	50	f/4.0	High-resolution film Medium-resolution film	Greater than 1/125 sec Less than 1/125 sec
Biogon	60	f/5.6	High-resolution film Medium-resolution film	Greater than 1/125 sec Less than 1/125 sec
Planar	100	f/3.5	High-resolution film Medium-resolution film	Greater than 1/250 sec Less than 1/250 sec
Sonnar Superachromat	250	f/5.6	Medium-resolution film	At least 1/500 sec

[a]High-resolution film refers to SO-242 or SO-127, medium resolution to SO-368 or 2443 (table II). High-resolution film cannot be used with the telephoto Sonnar Superachromat lens, because this film is too slow for the shutter speeds required to prevent image motion from dominating system performance; the 250-mm lens should be used at 1/500 sec.

ble as a medium-altitude aerial mapping and reconnaissance film, for which it was originally designed.

The effective aerial film speed of 32, listed in table II, is not equivalent to the familiar ASA rating of amateur films. For color and infrared-sensitive aerial film, it is an empirically determined value based upon rather specific exposure and development conditions. A typical exposure for Aerochrome MS at a 1.5-km altitude on a clear day is 1/500 second at f/4.7, assuming that the Sun is 40° above the horizon. An equivalent ASA speed can, however, be calculated.

In fact, the ASA rating of any film depends entirely upon processing. Just as amateur films can be "pushed" in speed by assuming a higher-than-normal ASA and increasing development times, the equivalent ASA rating of SO-368 flight film depends upon the speed of operation of the automated processing equipment. A model 1811 Versamat Ektachrome RT Processor using Kodak EA-5 chemistry was chosen to develop SO-368. Based upon the operating characteristics of the Versamat, the following ASA ratings can be given to SO-368: for a machine speed of 2.1 m/min (7 ft/min), the equivalent ASA is 101; for 2.7 m/min (9 ft/min), ASA is 71; and for 3.4 m/min (11 ft/min), ASA is 57. These speeds assume the use of a Wratten HF-3, 2A, or equivalent filter recommended by Kodak to reduce the effects of atmospheric haze.

Aerial Color SO-242 film is an extremely fine-grain, high-definition, daylight emulsion coated on a thin, but strong and flexible, polyester base. The film was designed for high-altitude stabilized-platform aerial cameras with high-quality optics. At 2.5 times the resolving power of Ektachrome MS, its only drawback is its low speed, nearly 2.5 f/stops slower than SO-368. Even though the Earth is very bright from orbit, the use of high shutter speeds requires large apertures with SO-242, somewhat of a handicap with the available lenses as described in table I.

Aerochrome Infrared 2443 film was designed for camouflage detection, agricultural and forestry work, and other applications in which infrared discrimination is required. To capitalize on the shift toward the infrared in sensitivity of the three

TABLE II.—Selected Characteristics of Four Candidate Films

Film (a)	*Marketing name*	*Film type*	*Base thickness*	*Effective aerial film speed*	*Process*	*Maximum resolving power, lines/mm*
SO-368 (same as 2448)	Ektachrome MS (Aerochrome MS)	Color reversal, normal color	Estar/4.0 mil[b]	32 (no filter)	EA-5	80
SO-242	Aerial Color	Color reversal, normal color	Estar thin base/ 2.5 mil	6 (no filter)	ME-4 or EA-5	200
2443	Aerochrome Infrared	Color reversal, false color	Estar/4.0 mil	40 (with Wratten 12 filter)	EA-5	63
SO-127	High Definition Aerochrome Infrared	Color reversal, false color	Estar/4.0 mil	6 (no filter)	EA-5	160

[a]The SO designation by Kodak signifies a "special order" film. These films are usually either newly developed products or products not manufactured on any regular production schedule. These may later become standard "off-the-shelf" products, regularly listed and stocked, such as type 2443.

[b]Film specifications are given in mils (1 mil = 2.54×10^{-5} m).

emulsion layers, it is necessary to filter out the blue region of the solar spectrum to which infrared film is also sensitive. The manufacturer recommends the use of a Wratten 12 deep-yellow (minus blue) filter, which is essentially opaque to light whose wavelength is shorter than about 500 nm. A typical exposure on a clear day for 2443 film behind a Wratten 12 filter from a 3-km altitude is 1/500 second at f/5.6. It is the fastest of all film considered for the ASTP flight, and consequently the grainiest. Before and after exposure, false-color film also requires special handling, such as refrigeration. Until they were loaded into the cameras during the flight, the magazines of 2443 film were maintained as closely as possible to the environment in which they left the factory.

The last film considered for ASTP use was High Definition Aerochrome Infrared, SO-127, an improvement over 2443 in spectral sensitivity as well as in resolution and grain size. Film SO-127 permits better false-color differentiation than 2443 and does not require the use of a filter. A special coating whose absorption characteristics match the deep-yellow filter is applied directly to the color-sensitive emulsions in the final step of manufacturing. This extremely accurate film was designed for the same uses as SO-242 and suffers from the same problem of slow speed.

Since the film, camera shutter, and lens must act as a unit during an exposure, the final image quality is a function of the quality of all three components. To quantify the film-shutter-lens sharpness, a system modulation transfer function (MTF) is calculated. An MTF is essentially a measure of the crispness in transition across a boundary between different brightness or color levels on the image. In evaluating the MTF calculations, guidelines for the use of each lens, as outlined in table I, were drawn up. The choice of lenses for each target was determined by matching the desired area of coverage with the field-of-view of the lens. As it turned out, the 250-mm telephoto lens was selected for each target where vegetation discrimination was required. Thus, High Definition Aerochrome Infrared SO-127 film was eliminated from mission planning because of its unsuitably low speed.

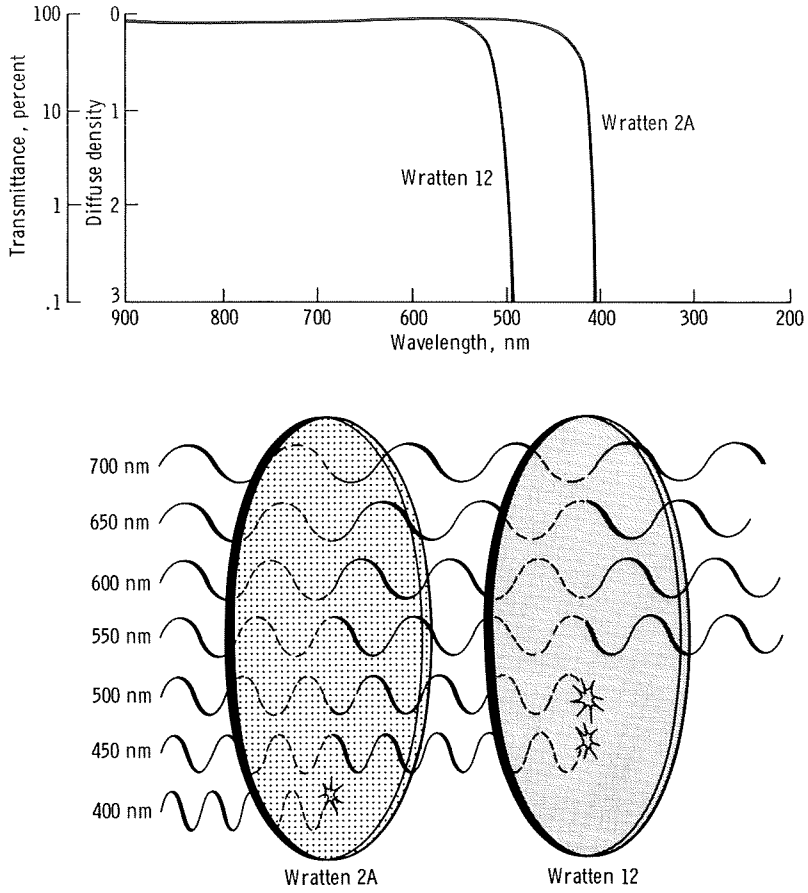
Having decided the film assignments for each target, ASTP planners allotted 14 magazines of 70-mm film to the experiment: 7 magazines at 70 frames per magazine of SO-368; 5 magazines at 150 frames per magazine of SO-242; and 2 magazines at 70 frames per magazine of 2443. Constraints placed on the experiment by flight procedures generally required that SO-242 be used for mapping passes and that SO-368 be used for visual observations.

FILTER SELECTION

As mentioned earlier, each film selected for the flight can benefit in terms of color rendition from the use of a blue-absorbing filter. To optimize the interlayer sensitivity of Aerochrome Infrared film, the use of such a filter should cause a sharp drop in light transmission from a maximum to nearly zero within a 50-nm window centered on 520 nm (fig. 1). This is precisely what a Wratten 12 filter does. All equipment used during the mission was subjected to lengthy checkout procedures and approval as flight hardware. A 520-nm filter, equivalent to the Wratten 12, was available in the approved flight-hardware inventory, thus clearing the way for the proper use of 2443.

The normal-color film types, on the other hand, have a higher threshold of sensitivity to blue light. The wavelengths that should be filtered out begin for SO-368 and SO-242 in the vicinity of 420 nm, characteristic of a Wratten 2A (fig. 1) or 2E filter. The manufacturer has conveniently solved the problem for SO-242 by building in the equivalent of a 2E filter as an overcoating on the film (fig. 2). However, SO-368 is not supplied in this way.

The equivalent of a 2A (420 nm) filter was not an item in the approved flight-hardware inventory; and the procurement, checkout, and approval of such a filter would have presented serious, if not insurmountable, scheduling difficulties. The photographic laboratory at the Lyndon B. Johnson Space Center (JSC) proposed a reasonable alternative to the camera filter: prepare SO-368 for flight by overcoating it with the equivalent of a 2A filter in exactly the same manner as SO-242. The following section describes how this alternative was implemented.



Wavelength, nm	Percent transmittance	
	No. 2A	No. 12
400	–	–
10	4.0	–
20	42.0	–
30	74.0	–
40	82.7	–
50	85.6	–
60	87.0	–
70	88.1	–
80	88.8	–
90	89.4	–
500	89.7	1.5
10	90.0	17.3
20	90.2	55.0
30	90.3	77.8
40	90.4	86.0
50	90.5	88.4
60	90.6	89.4
70	90.6	89.7
80	90.7	90.1
90	90.7	90.3
600	90.8	90.4
10	90.8	90.5
20	90.9	90.7
30	90.9	90.8
40	90.9	90.9
50	91.0	91.0
60	91.0	91.1
70	91.0	91.2
80	91.1	91.2
90	91.1	91.2
700	91.1	91.3

FIGURE 1.—Spectrophotometric curves for Wratten 2A and 12 filters. These filters effectively block blue or shorter wavelength radiation from reaching the film when they are placed in front of a camera lens. The 12 filter is used with 2443 Aerochrome Infrared film to remove radiation whose wavelength is shorter than approximately 520 nm. The 2A filter, recommended for use with the normal-color Ektachrome film, was coated directly onto the SO-368 film during manufacture as described in the text. The coating was a yellowish dye that blocked radiation shorter than approximately 420 nm in wavelength.

MANUFACTURING AND TESTING QX-807

There are essentially two techniques for coating a photographic film with a filter layer: (1) add a light-absorbing dye to the emulsion side of existing stock film or (2) add a light-absorbing dye to the film as the final step in manufacturing. The latter technique was selected because of a significant cost saving and because of confidence in the filter-coating technology as demonstrated with SO-242, which was used extensively in the Skylab and Earth Resources Aircraft programs.

The new film was designated type QX-807, indicating that it differed from SO-368 by virtue of its special 2A filter overcoating. The JSC photographic laboratory prepared a series of tests for the new QX-807 film, not only to verify its performance, but also for ASTP certification. Sample rolls for the tests were selected at random from each batch of 16-mm, 35-mm, and 70-mm film widths. The standard to which the QX-807 samples were compared was an uncoated roll of SO-368 film. The tests and their results are summarized in table III. Figure 3 shows the results of a cross-section analysis on QX-807. Figure 4 qualitatively demonstrates the match in spectral sensitivity between QX-807 and SO-368.

Characteristic curves for SO-368 and QX-807 are shown in figure 5. As indicated in table III, the testing of QX-807 film for process compatibility

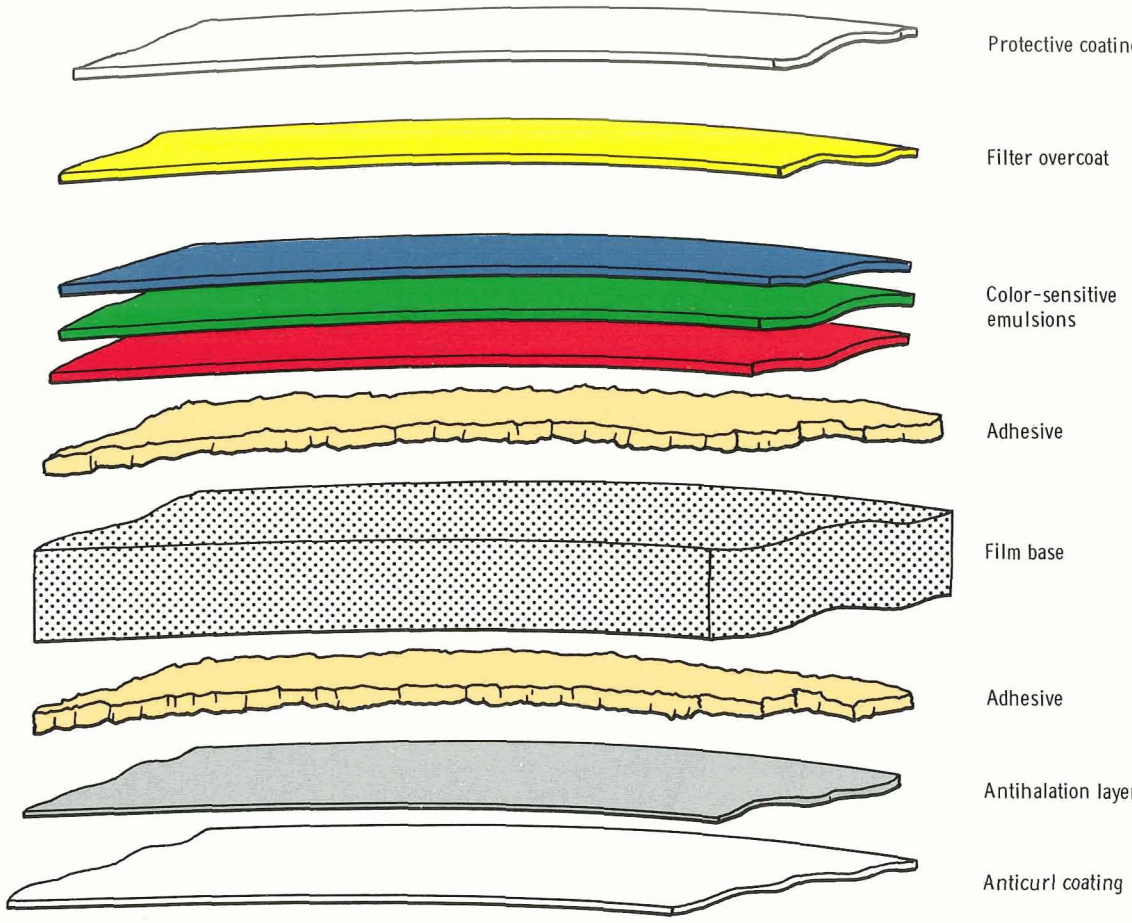


FIGURE 2.—Schematic drawing of the typical construction of a color-reversal transparency film with a filter overcoat. A typical photographic color film consists of three color-sensitive layers bonded to a polyester film base. The antihalation coating prevents light from reflecting back through the emulsion to cause halos around bright parts of the picture (ref. 4). The protective overcoat prevents scratches on the emulsion layers below. Standard thickness of the film base is either 2.5 mils (Estar thin base) or 4.0 mils (Estar base).

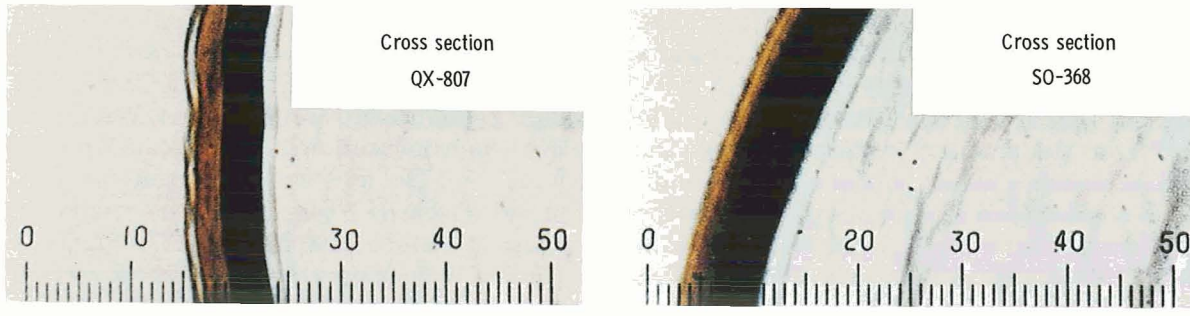
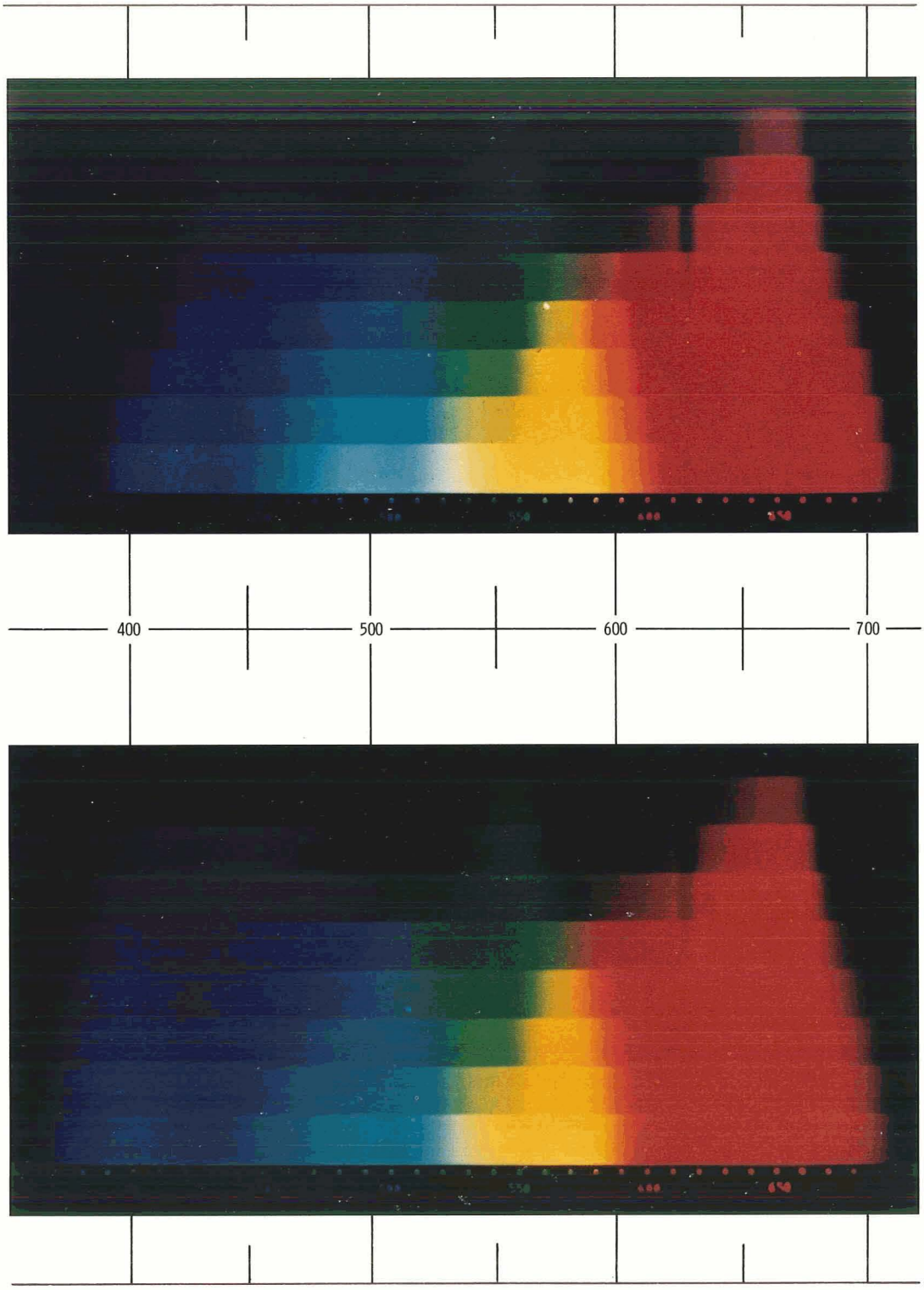


FIGURE 3.—Photographic cross sections of QX-807 and SO-368. The three color layers of the emulsion, the base, and the filter overcoat of QX-807 are all clearly visible. The scale is a relative one and shows the thicknesses of both films to be very similar.

TABLE III.— Summary of Test Results on QX-807 Film (SO-368 With Special 2A Overcoat)

Test	*Purpose*	*Procedure*	*Results*
Physical inspection	Check for manufacturing defects	Visual inspection	Single pinhole defect in one 70-mm roll; otherwise, clean, scratch free, smooth, defect free
Process capability	Evaluate JSC Ektachrome Film Processor (ME-4 chemistry) and 1811 Versamat Ektachrome RT Processor (EA-5 chemistry)	Develop test roll in each unit; compare sensitometry	The 1811 Versamat Processor considered superior with EA-5 chemistry (see figure 5)
Effective sensitivity	Derive an equivalent ASA rating for QX-807	Make calibrated exposures, process in Versamat and JSC processors at varying speeds; calculate ASA	See text for equivalent ASA rating (same as for SO-368); also see figure 5
Color balance	Evaluate interlayer sensitivity	Measure densities of each layer of developed QX-807	Red and green sensitivity approximately equal with good balance; blue layer approximately 1/2 stop slower indicating 2A overcoat effectiveness (see figure 5)
Cross-section analysis	Compare thickness of layers of QX-807 with SO-368	Cut thin sections of film with microtome; microscopic inspection	No significant difference in construction of films
Resolution	Determine resolving power	Expose film to U.S. Air Force 1951 resolution target	QX-807: 63 lines/mm, SO-368: 71 lines/mm
Spectral sensitivity	Measure color response of film across visible spectrum	Expose film to JSC Mead Spectrum spectral sensitometer	Subjective comparison of films indicated similar response above 400 nm; filter overcoat effective below 400 nm (see figure 4 and compare figure 1)
Consistency of results	Measure reproducibility of response	Identically expose at 16 areas along 30-m strip of QX-807; read film densities	Results consistent within ± 0.02 density units (very acceptable)
Picture sample analysis	Subjective evaluation of photography	Expose film to actual ground targets at ground level and from aircraft altitude; develop and evaluate	Slight yellow color balance when shot at ground level; less-than-normal blue levels when shot from aircraft



QX-807

SO-368

FIGURE 4.—Spectral sensitometry of QX-807 and SO-368. Results of this test were evaluated subjectively, because density conversion data for SO-368 were not available at JSC. Note the obvious cutoff in response of QX-807 below approximately 400 nm attributable to the 2A overcoat (cf. fig. 1).

involved exposing and developing it under the identical conditions to which a standard roll of SO-368 had been subjected. The sensitometric curves for the three color-sensitive layers of each film are shown in figure 5, and the shape of the curves demonstrates the nearly identical performance of QX-807 and SO-368. Notice that the red and green layers of both films are well balanced. The curve for the blue layer of QX-807 is offset from the family of curves by approximately 1/2 f/stop. This characteristic is indicative of the operation of the 2A overcoat, "slowing" the response of the blue layer by absorbing radiation shorter than approximately 420 nm in wavelength. The curves for the SO-368 standard were redrawn from the Aerochrome MS 2448 curves derived from a model 31A Eastman Electronic Densitometer (ref. 5). The QX-807 curves were derived by using a MacBeth TD-504 densitometer. Both films were exposed to a daylight source (5500 K) for 1/50 second through blue-absorbing filters; they were developed in EA-5 chemistry.

Sophisticated bench-testing notwithstanding, the real proof of a color film may very well be the subjective evaluation of the photographs it produces. To this end, QX-807 was loaded in Hasselblad cameras and exposed to a variety of targets, both on the ground by JSC laboratory personnel and in the air by astronauts flying T-38 aircraft. As could be predicted, the ground-target pictures had a slightly yellow color balance, and the aerial shots displayed a less-than-normal blue saturation. In the event that ASTP photographs other than ground targets were taken and the full effect of the 2A overcoat filter was unnecessary, the photographic laboratory could use conventional laboratory color-balancing techniques to "print out" the yellowing produced by the filter.

Following the completion of all tests, QX-807 was certified for the ASTP mission. Sensitometry indicated superior characteristics of the emulsion.

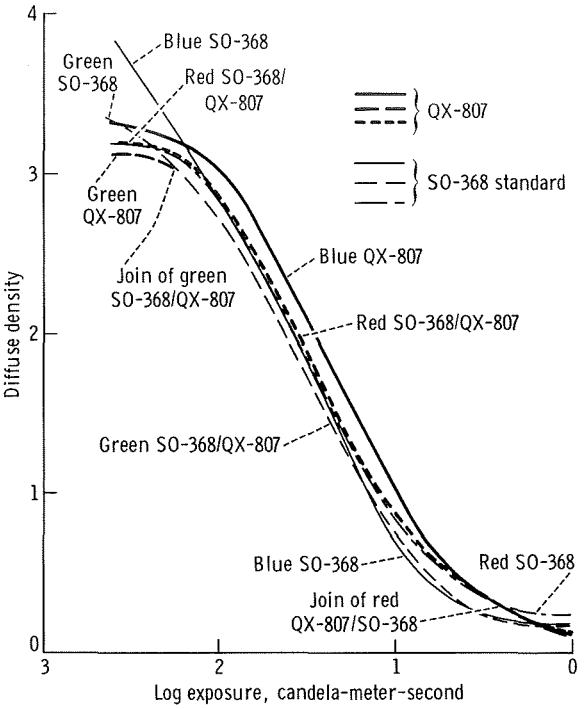


FIGURE 5.—Characteristic curves for SO-368 and QX-807 film.

Its relatively high ASA rating made QX-807 an excellent choice for normal-color photography for which film speed is important.

REFERENCES

1. Electro-Optics Handbook. Radio Corp. of America, TCA, Commercial Engineering (Harrison, N.J.), 1968.

2. Thomas, W.: SPSE Handbook of Photographic Science and Engineering. Wiley-Interscience (New York), 1973.

3. Wyszecki, Gunter; and Stiles, W. S.: Color Science: Concepts, Methods, and Quantitative Data and Formulae. Wiley-Interscience (New York), 1967.

4. Life Library of Photography: Light and Film. Time-Life Books (New York), 1970.

5. Eastman Kodak: Kodak Data for Aerial Photography. Fourth ed., book M-29. Eastman Kodak Co. (Rochester, N.Y.), 1976.

Film Exposure Calculations

H. E. Lockwood,[a] Lincoln Perry,[a] and R. W. Wolfe[b]

ABSTRACT

The determination of camera shutter and aperture settings to produce consistently high-quality aerial and orbital photographs is a task complicated by numerous variables. Presented in this paper are (1) brief discussions of these variables and (2) specific data that may be used to systematically control them. The variables discussed include sunlight, atmospheric effects, subject and season, film speed, and optical system.

Data that may be used as a base reference are included. The data encompass sensitometric specification for two film-chemistry processes together with parameters that have been established and used to produce good exposures for Apollo-Soyuz Test Project photography. Information contained here may be used to design and implement an exposure determination system for other orbital photography missions.

INTRODUCTION

Scientists, aerial photographers, and processing-laboratory personnel at the NASA Lyndon B. Johnson Space Center (JSC) in Houston, Texas, have accumulated extensive experience in the determination of camera exposure settings for aerial and orbital photography. The JSC is responsible for photography on major projects including the Earth Resources Aircraft Program (ERAP) and manned-space-flight missions. The ERAP uses aircraft flown as low as 305 m and as high as 18.3 km over thousands of subject areas both inside and outside the continental United States. Space flights, of course, have enabled photography of sites around the world; the largest collection of orbital photographs was obtained during the three manned Skylab missions.

Exposure determinations for these projects are made at JSC, where the ERAP imagery and the space-flight original imagery are processed, duplicated, and distributed. Correct exposure settings must receive high priority. The photographic laboratory strives to either control or compensate for the many variables that affect in-camera film exposures. Discussed here are the variables that affect film exposure and the steps taken to control those variables on the Apollo-Soyuz Test Project (ASTP).

CORRECT EXPOSURE

Proper exposure is critical to obtain the maximum information and ground resolution from orbital photographs. Correct exposure can be defined as that particular combination of shutter speed and lens aperture (f-stop) that, together with proper development of the film, will produce a photographic record of the scene in which contrast and density lie within the linear portion of the characteristic curve for the film. Furthermore, the color balance of the image should be acceptable over the entire scene reflectance-image density range. The optimum imagery placement on the characteristic curve of Kodak type SO-242 (special order) aerial color film is shown in figure 1.

It is obvious from this curve that only a narrow subject brightness range (10:1 to 20:1) may be accommodated with a linear density relationship by

[a]Technicolor Graphic Services, Houston, Texas.

[b]National Air and Space Museum, Smithsonian Institution.

these film types. However, in most aerial photographs taken from altitudes above a few thousand meters, the contrast range is typically only 4:1 or 5:1. A goal for correct exposure, then, may be specified as placement of imagery in the optimum recording range of the film to be used. This optimum range usually means placement of maximum scene reflectances (in a positive image) at the low-density end of the straight line of the film-process characteristic curve. The density range of imagery obtained at orbital altitudes is even lower because of contrast attenuation due to the atmosphere.

The reflectance of some scenes frequently produces images with densities higher or lower than the optimum range, but exposures should be centered about the optimum area. The images of most scenes will lie in the optimum density range with specular highlights and dense shadows lying outside that range.

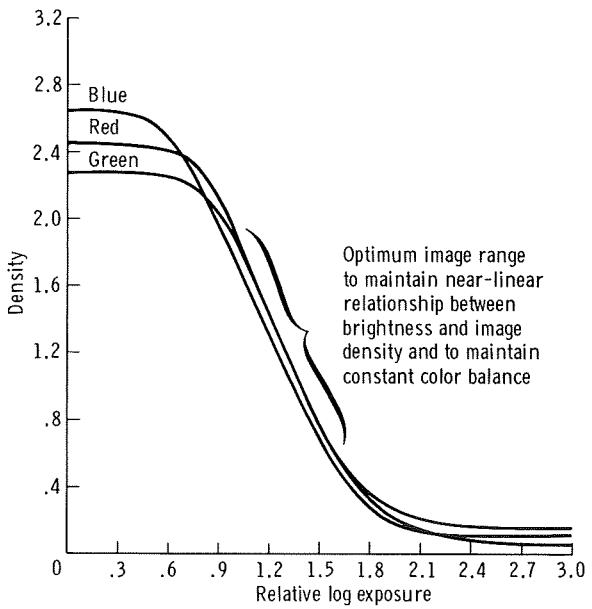


FIGURE 1.—The characteristic curve of type SO-242 aerial color film showing the optimum imagery placement. A Versamat 1811 processor was used with EA-5 chemistry.

FACTORS AFFECTING FILM EXPOSURE

Several factors affect film exposures in orbital photography and can create considerable confusion and poor results if each is not considered and controlled where possible. These factors include the Sun angle, atmospheric effects, the nature of the scene, the type of film, and the optical system. Most of these factors can result in a minimum exposure change of 0.5 f-stop, and some may require compensation of as much as 3 f-stops to obtain the correct exposure.

Attention to the factors affecting film exposure is especially critical in orbital photography. In a typical aerial photographic mission, most of these factors would remain constant or would change only slightly during the mission. In orbital photography, however, the Sun angle, the nature of the scene, and the atmospheric effects are constantly changing. Within minutes, the proper exposure may change by several f-stops.

Sun Angle and Atmospheric Effects

The Sun elevation angle best describes the gross amount of light illuminating the scene to be photographed. However, attenuation and scattering of sunlight by the Earth's atmosphere can cause a large loss of light at the scene. It will be seen that the interrelationship of the influence of Sun angle and atmospheric effects prevents separate treatment of these factors. In the following paragraphs, taken from Harris (ref. 1, pp. 76-77), this complex interplay is clearly explained.

> Beginning with the total solar illumination that reaches the upper side of the earth's atmosphere, sunlight is divided into the following components:
>
> (a) Direct sunlight or that portion which reaches the surface of the earth without being scattered or absorbed.
>
> (b) Skylight and cloud light or that portion which reaches the earth after being scattered by the atmosphere and reflected or scattered by clouds.
>
> (c) Non-image forming atmospheric haze or cloud reflected light which does not

reach the earth, but is received by the aerial camera.

(d) Absorbed sunlight or that portion which neither reaches the earth or the camera.

The sum of these four components is equal to the essentially constant total solar illumination which reaches the upper surface of the earth's atmosphere, but the relative amounts of the components are dependent upon a theoretically infinite set of atmospheric conditions.

The relative amounts of the four components are also dependent upon the altitude angle of the sun which is explicitly defined for a horizontal surface by the geographic latitude of the area to be photographed, the time of year and the time of day.

Sun elevation angles for the date, July 21 are shown in table I as a function of latitude and local solar time.

Light reflected by the scene must pass through the atmosphere before reaching the orbital

TABLE I.—Sun Elevation Angle as a Function of Latitude and Local Solar Time

[July 21]

Latitude, deg	*Sun elevation angle, deg, at local time*[a] —																
	2000 0400	1930 0430	1900 0500	1830 0530	1800 0600	1730 0630	1700 0700	1630 0730	1600 0800	1530 0830	1500 0900	1430 0930	1400 1000	1330 1030	1300 1100	1230 1130	1200
60 N	4	7	10	14	17	21	25	29	32	36	39	42	45	47	48	49	50
50 N	NA[b]	NA	6	11	15	20	25	30	35	39	44	48	52	55	58	59	60
40 N	NA	NA	2	7	13	18	24	30	36	41	47	52	58	62	67	68	70
30 N	NA	NA	NA	NA	10	16	23	29	35	42	48	55	61	67	73	77	80
20 N	NA	NA	NA	NA	7	14	20	27	34	41	48	55	62	69	76	81	90
10 N	NA	NA	NA	NA	3	10	17	25	32	39	46	53	60	65	73	77	80
0	NA	NA	NA	NA	NA	7	14	21	27	35	42	49	53	58	63	67	70
10 S	NA	NA	NA	NA	NA	NA	10	17	24	30	37	42	48	53	57	59	60
20 S	NA	NA	NA	NA	NA	NA	6	13	19	24	30	35	41	44	48	49	50
30 S	NA	NA	NA	NA	NA	NA	NA	6	13	19	24	28	33	35	38	39	40
40 S	NA	NA	NA	NA	NA	NA	NA	NA	8	12	16	20	24	26	29	29	30
50 S	NA	NA	NA	NA	NA	NA	NA	NA	NA	3	9	12	15	17	18	19	20
60 S	NA	NA	NA	NA	NA	NA	NA	NA	NA	NA	NA	3	6	7	9	9	10

[a]0400 = 4 a.m., 1200 = noon, 2000 = 8 p.m., etc.

[b]NA = not applicable; refers to elevation angles less than 0°, or depression angles.

camera. Harris (ref. 1, p. 77) describes the components into which this light is divided by atmospheric effects as follows.

(a) Terrain reflected light which is absorbed by the atmosphere.

(b) Terrain reflected light which is scattered by the atmosphere in such a manner that it does not reach the camera.

(c) Terrain reflected light that is scattered by the atmosphere but does reach the camera as non-image forming haze light.

(d) Useful image forming light from the terrain which reaches the camera without being scattered.

Some light, both sunlight and light reflected by the scene, is scattered by the atmosphere and reaches the camera as haze, or non-image-forming light. Haze increases the exposure of the film, lowers the contrast of the image, and diminishes color saturation.

Unless corrective filtration is provided, orbital photographs will generally have a blue color balance due to atmospheric effects. In general, the atmosphere transmits less light in the shorter wavelength (blue) region than in the longer visible wavelength (red) region of the spectrum (fig. 2; ref. 2). The major factor influencing color balance in orbital photographs, however, is the scattering of light by the atmosphere. The scattering effect of the atmosphere as a function of wavelength for a minimum haze condition (Rayleigh atmosphere) is shown in figure 3 (ref. 3). Rayleigh scattering is inversely proportional to the fourth power of wavelength. In other words, scattering in the 450-nm wavelength region (blue) is significantly greater than in the 700-nm wavelength region (red). A comparison of figures 2 and 3 clearly indicates that the influence of atmospheric scattering on color balance is greater than that of atmospheric transmittance.

A typical remedy for the blue color balance is the addition of a filter that absorbs short-wavelength light and reduces the problem. The equivalent of a Wratten 2A filter (fig. 4; ref. 4) has been found to be most satisfactory.

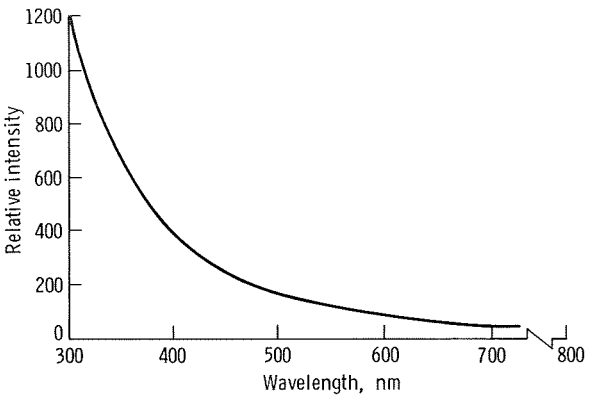


FIGURE 3.—Atmospheric scattering as a function of wavelength for Rayleigh atmosphere (after ref. 3).

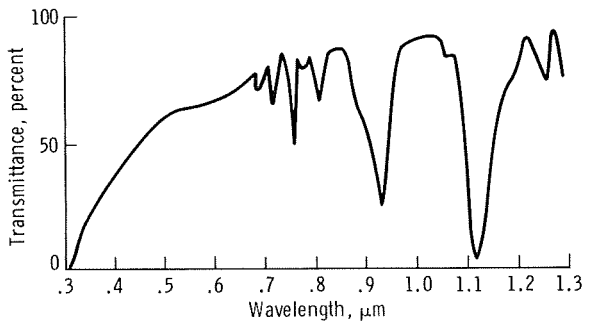


FIGURE 2.—Atmospheric transmittance as a function of wavelength (after ref. 2).

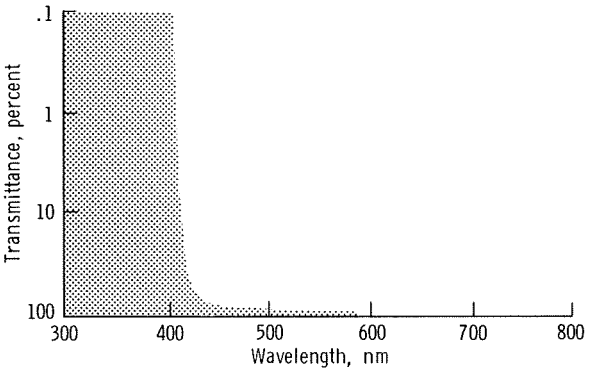


FIGURE 4.—Transmittance of Wratten 2A filter used for short-wavelength correction (after ref. 4). The shaded area represents absorbed light.

Nature of the Scene

Light reflected from the surface of the Earth forms the useful image in orbital photography. The amount of light that is reflected affects the proper exposure and is a function of the nature of the scene. Materials at the Earth's surface can be divided into two classes on the basis of their reflective properties: specular (mirrorlike) reflectors and diffuse reflectors. Water and ice are the most common specular reflectors. When the angle of reflection directs most of the light from a specular reflector toward the camera, a "Sun spot" or "sunglint" of very high brightness is formed on the image. The land areas of Earth are diffuse reflectors. The reflectivities of materials range widely (table II).

TABLE II.— Reflectivities of Various Materials

[From ref. 1]

Material	*Reflectivity*	*Material*	*Reflectivity*
Asphalt	0.02 to 0.05	Soils	0.10 to 0.30
Dark trees	0.04 to 0.08	Concrete	0.25 to 0.35
Deep water	0.04 to 0.06	Dark sand	0.25 to 0.40
Light trees	0.06 to 0.12	Light sand	0.40 to 0.60
Grassland	0.10 to 0.15	Snow	0.65 to 0.80

Many scenes may have different reflectivities, depending on the season. The presence of snow is obviously related to the season. Often overlooked, however, are the seasonal changes in vegetation. The most profound effect is that, in the summer, light is reflected from vegetation (reflectivity = 0.06 to 0.15) and in the winter from bare ground (reflectivity = 0.10 to 0.50). The effect may be even more pronounced when films having a wide spectral sensitivity are used. A vegetated scene has an average reflectivity in the visible wavelengths and a high reflectivity in the infrared. In the winter, the same area may have a high reflectivity in the visible region of the spectrum and a low reflectivity in the infrared.

Type of Film and Processing

A vital part of any exposure determination is the effective sensitivity or speed of the photographic film on which the subject is to be imaged. Wide variability will be encountered not only between different film types but sometimes between emulsion batches of the same film type. Changes of 0.5 f-stop in effective film speed have been encountered with different emulsion batches of the same film.

Considerable differences in effective film speed may arise as a function of the processing chemistry or of the speed of processing (for gamma control). For example, figure 5 illustrates potential variability between processes with the same SO-022 Panatomic-X aerial film. A variability equivalent to 1.75 f-stops at a density of 0.3 is apparent. Figure 6 shows the effect of process gamma on effective speed measured at a density of 0.4. A difference of 1.25 f-stops between the slowest and fastest process rates for Plus-X Aerographic type 2402 film is apparent.

Orbital photographs of consistently high quality are possible only if the film speed "varia-

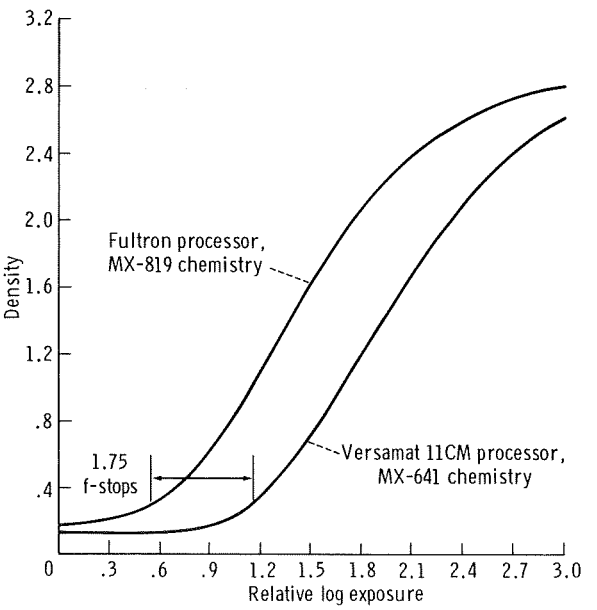


FIGURE 5.—Plot of effective speed as a function of processing, using Panatomic-X type SO-022 aerial film.

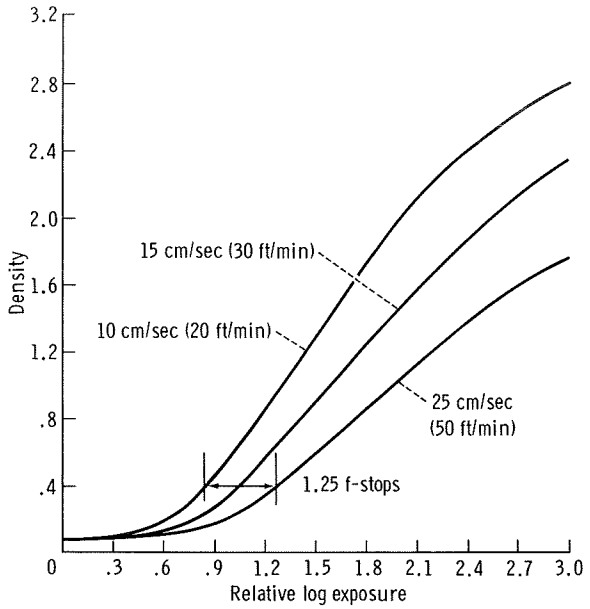


FIGURE 6.—Plot of effective speed change with gamma. Plus-X Aerographic type 2402 film, a Fultron processor, and MX-641 chemistry were used.

ble" is controlled. It is imperative, therefore, that a close working relationship be established between the photographer or person responsible for exposing the film and the processing laboratory that is responsible for processing the exposed films. For this reason, the following procedures should be established: (1) evaluate all emulsion batches of every film type for effective sensitivity and make adjustments, if required, in exposure index to compensate for changes in emulsion sensitivity and (2) establish process control curves for laboratory use in maintaining process consistency to ensure minimal variance in effective film speed due to processing.

Test Emulsion Batch

Each emulsion batch should be tested by the laboratory before use. Sensitometric exposures can be made both on the emulsion under test and on one in current use; then, the two sample films are processed together. A density analysis of the results will show differences in speed, color balance, gamma, maximum density, and minimum density. In most instances, corrective actions are possible. Film should also be tested with commonly used filters to determine any gross problems with spectral sensitivity. The JSC photographic laboratory certifies every emulsion batch received using these methods, and in the case of type 2443 Aerochrome Infrared film, every cut of every emulsion batch is certified. Records are maintained and the film is recertified if the emulsion remains in use for 6 months or if the film is subjected to any questionable environment. Stored with each emulsion are pertinent notes regarding use, such as "one-half stop faster than standard" or "for high-altitude use only."

Process Control Standards

Process control standards are established for each film type and are maintained by a laboratory process control group. Before processing any exposed orbital imagery, the process is sampled and evaluated to meet the standards established. The photographic laboratory maintains standards for each color film process and three standards for each black-and-white film process (one each for red, green, and blue filters) with the exception of type 2424 Infrared Aerographic film, which has a single standard for each process (with infrared-transmitting filter). If these standards are followed, film-process variables will be minimized.

Optical System

Camera lenses, filters, and spacecraft windows are the components of the optical system in orbital photography. Their characteristics may influence the determination of correct exposures.

Camera lens data either may be available from the manufacturer or may be determined in the optical laboratory. Transmission should be measured at all wavelengths that may be recorded on the film. It is not uncommon, for example, for lens transmission at shorter wavelengths (400 nm) to be one-half the lens transmission at longer wavelengths (700 nm).

Camera filters (for spectral correction or spectral isolation) and antivignetting filters should be calibrated or checked so that the exposure or filter factor is known. Antivignetting filters may be labeled as to percent transmission of center compared to edge (e.g., 40 percent) or as to the exposure factor required (e.g., 2.2) to correct for the center density of the filter. Filters alone can result in the addition of more than 3 f-stops to the exposure required. In the case of unknown spectral filters, a sensitometric comparison with a known filter of similar wavelength may be made to determine the exposure factor.

Although spacecraft windows are of high-quality, high-transmission glass, their transmission characteristics should be determined. The most severe problem related to spacecraft windows is likely to be condensation.

EXPOSURE CALCULATIONS FOR ASTP

The exposures calculated for the ASTP Earth Observations and Photography Experiment were based on data obtained from (1) previous experience with similar photographic tasks including Skylab, (2) high-altitude RB-57 aircraft photographic data, (3) simulation aircraft flights using the ASTP films, and (4) sensitometric test data.

Base Exposures

Base exposures were determined by evaluating Skylab 4 exposure data and imagery and by performing dynamic film tests using various cameras and lenses.

Evaluation of Skylab 4 Exposure Data and Imagery

Skylab 4 photographs taken with type 2443 Aerochrome Infrared film were evaluated, and a normal exposure for this film was determined to be 1/200 second at f/9.5. The ASTP 2443 emulsion 206-1 was 0.5 f-stop slower than the Skylab-4 2443 emulsion 166-3 as determined by cross-sensitometric tests. The normal 2443 exposure for ASTP was 1/500 second at f/5.6 (i.e., 1/500 second was selected for compatibility with the Hasselblad shutter settings).

The SO-242-43-1 film selected for ASTP was approximately equal in speed to the Skylab-4 SO-356 film. On the basis of Skylab data, the normal SO-242 exposure for ASTP was determined to be 1/250 second at f/4.0.

Camera Checks

Films QX-807 and SO-242 were tested using ASA 64 and ASA 10, respectively, to establish exposures. Results confirmed the speeds as correct. Film QX-807 is 2.5 f-stops faster than film SO-242. A normal ASTP exposure for QX-807 was 1/500 second at f/8.0.

A simulation flight for the ASTP mapping photography was flown on April 28, 1975, using the C-130 aircraft over New Mexico (Truth or Consequences, Elephant Butte Reservoir, and Cibola National Forest) at a 7.6-km altitude. Films QX-807 and SO-242 were exposed using 250-mm, 100-mm, 60-mm, and 50-mm lenses on Hasselblad cameras. It was found that QX-807 produced an exaggerated effect when overexposed because of a lower contrast toe of the characteristic density as a function of log exposure.

The QX-807 curve has a relatively long straight line, which gives a wide exposure latitude. Therefore, the normal exposure for QX-807 was made 0.5 f-stop less, or 1/500 at f/8.0, to minimize potential overexposure.

By means of these procedures, the following base exposures for the three ASTP films were established.

Film	*Exposure*
SO-242	1/250 second at f/4.0
QX-807	1/500 second at f/8.0
2443	1/500 second at f/5.6

Exposure Corrections

Factors to correct these base exposures for Sun angle, atmospheric effects, and scene characteristics were calculated.

Sun Angle

The following data for Sun elevation angle (i.e., angle measured from subject, reference horizontal as 0°) were used successfully on the final Skylab mission. These same data were programed for ASTP to compensate for scene brightness due to solar illumination.

Sun elevation angle	*Exposure*
90° to 35°	Normal
35° to 22°	Plus 0.5 f-stop
22° to 15°	Plus 1 f-stop
15° to 10°	Plus 1.5 f-stops
10° to 5°	Plus 2 f-stops
5° to 0°	Plus 2.5 f-stops

Scene Characteristics

Experience with RB-57 photography taken from an altitude of 18.3 km and an analysis of Skylab photographic projects resulted in the following data on providing compensation for varying subject reflectances.

Subject	*Exposure*
Vegetation and mountains	Normal
Coastal and shallow water	Normal
Sandy soil or high desert	Minus 0.5 f-stop
Bright desert (sand dunes)	Minus 1 f-stop
Snow	Minus 1.5 f-stops
Clouds	Minus 2 f-stops
Deep ocean water	Plus 1 f-stop
Heavy vegetation (jungle)	Plus 1 f-stop

Atmospheric Effects

Training flights were flown by the ASTP crew numerous times including March 1 over the east coast from Houston to Florida to Massachusetts, March 15 and 16 over the same area, and mid-June over the Western United States. Film exposed by astronauts during training flights in aircraft flown at 12.2 km was analyzed together with Skylab handheld-camera photographs. Oblique photographs are effectively overexposed because of atmospheric haze. For ASTP oblique photography, the following compensations were made to minimize overexposure effects caused by haze.

Lens	*Exposure*
250 mm	Normal
100 mm	Minus 0.5 f-stop
50 mm	Minus 0.5 f-stop

REFERENCES

1. Harris, W. D.: Aerial Photographic Exposure. Manual of Color Aerial Photography. First ed. John T. Smith and Abraham Anson, eds., American Society of Photogrammetry (Falls Church, Va.), sub-chapter 2.3, 1968, pp. 76-93.

2. Electro-Optics Handbook. Radio Corp. of America, TCA, Commercial Engineering (Harrison, N.J.), 1968.

3. Jenkins, Francis A.; and White, H. E.: Fundamentals of Optics. Third ed. McGraw-Hill, 1957.

4. Kodak Filters for Scientific and Technical Uses. Revised ed. Book B-3, Eastman Kodak Co. (Rochester, N.Y.), 1972.

ASTP Photographic Film Processing and Sensitometric Summary

H. E. Lockwood [a]

ABSTRACT

The procedures used for processing the camera film exposed during the Apollo-Soyuz Test Project resulted from extensive testing of each film type, and the procedures were verified in numerous simulations before the mission. Exposure control curves for both visual density and tricolor densities were established for each film type before the mission. Sensitometrically exposed control strips of film were retained during the mission for comparisons with the flight film. Processing of all film conformed to preestablished standards, and no difficulties were experienced during the film processing.

INTRODUCTION

Film for the Earth Observations and Photography Experiment of the Apollo-Soyuz Test Project (ASTP) was processed at the NASA Lyndon B. Johnson Space Center (JSC). Extensive preflight tests of flight-film stock and of processing methods were made to ensure optimum results with the flight film. Both broadband and spectral sensitometry exposures and measurements were made on the film stock and on the flight film. All film was processed according to premission guidelines; standard Eastman Kodak Company chemicals and procedures were used.

Detailed information regarding film handling, laboratory procedures, sensitometric control, and postprocessing sensitometric data is available in references 1 and 2.[1] The following summary of processing methods is presented for ASTP photographic investigations and for future planning.

FILM HANDLING PROCEDURES

A summary of film handling procedures is presented in figure 1. The amount and type of film to be used was jointly determined by the Principal Investigators and the ASTP Program Office. Because of its intended use, all film of the same type had to be from the same emulsion batch, or as specified on the purchase request. After receipt of the film at JSC, a sample of film from each lot was chosen and measurements were made of the following film characteristics: sensitivity, color balance for color films, thickness, width, length, and emulsion integrity.

Following these film-certification procedures (manufacturer's specifications were used as criteria), more extensive testing of each film type was performed to determine (1) the usable range of photographic response and (2) the optimum processing methods. All sensitometric calibrations were exposed onto the film with a precision Eastman 1-B Intensity Scale Sensitometer; filtration simulated the spectral characteristics of the primary radiation expected during the mission. Final process control curves for each film type and specified photographic objective were supplied to the ASTP Program Office.

[a]Technicolor Graphic Services, Houston, Texas.

[1]Film handling procedures were documented in the JSC report entitled "Film Handling Procedures for Apollo-Soyuz Test Project," JSC-09650, 1975.

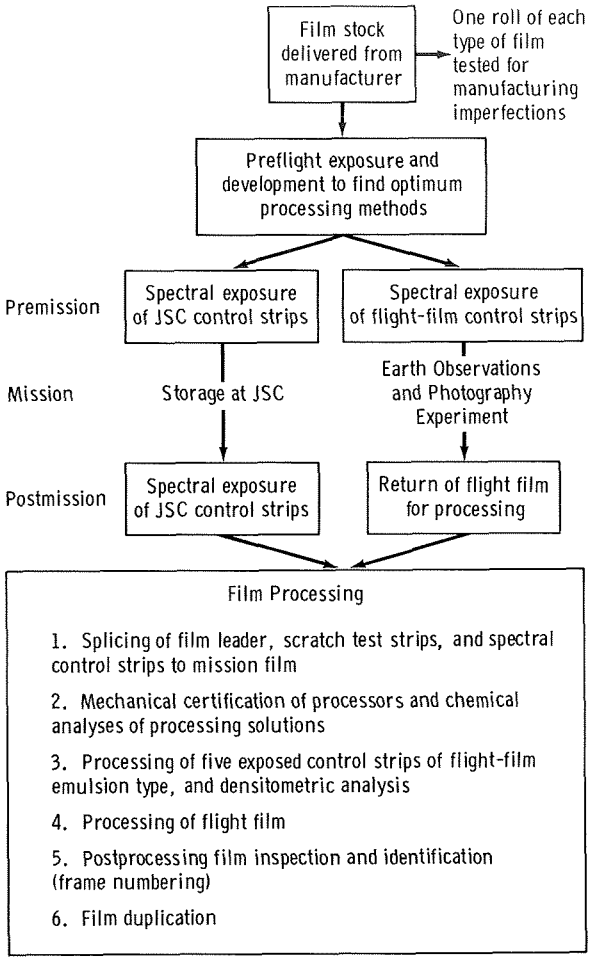


FIGURE 1.—Flow chart for processing and control of ASTP photographic film.

Mission flight and backup film was prepared at JSC for transportation to the NASA John F. Kennedy Space Center. Film preparation included shortening of standard length rolls, spooling from bulk film, application of sensitometric calibration exposures, film roll canning, loading of magazines, and preparation of JSC control film stock.

PROCESSING

Standards for the sensitometric response of each film type, the processing machine configuration (speed and temperature), and the chemicals used for processing were determined before flight-film processing. Eleven different types of sensitometric exposures were used for calibration and control of film processing (table I). All exposures were made with a 2850-K light source, and broad-

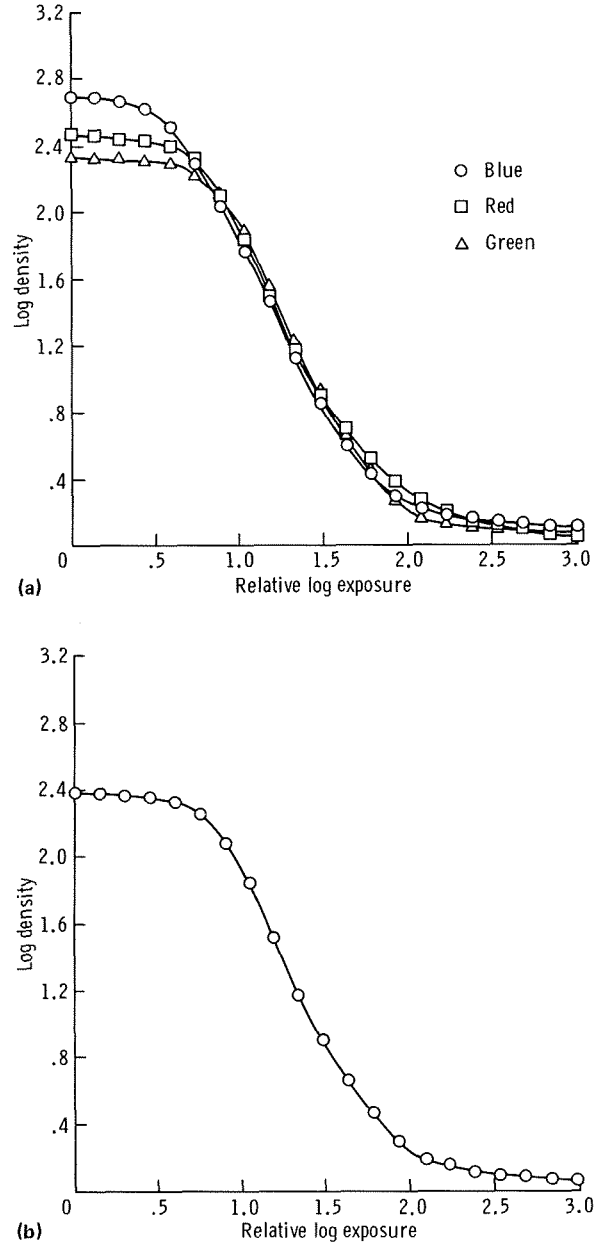


FIGURE 2.—Process control curves (log exposure compared to densities) for film type SO-242. (a) Spectral process control curve (tricolor). (b) Broadband process control curve (visual density).

TABLE I.—Sensitometry Applications to ASTP Photographic Film[a]

Exposure	*Designation*	*Use*
Broadband	Certification	Five exposures made on strips of each film type to test processing methods
Broadband	Original[b] premission	Exposure made on head of flight film premission
Broadband	Original postmission	Exposure made on head of flight film postmission
Broadband	JSC control premission	Exposure made on film stock control strips premission
Broadband	JSC control postmission	Exposure made on film stock control strips postmission
Broadband	Head	Spliced to flight-film head for processing control
Broadband	Tail	Spliced to flight-film tail for processing control
Spectral	Original premission	Exposures made on one roll of each type of 70-mm color film
Spectral	Original postmission	Exposures made on three designated rolls postmission
Spectral	JSC premission	Exposures made on JSC control strips premission
Spectral	JSC postmission	Exposures made on JSC control strips postmission

[a]The sensitometric exposures provide radiometric calibrations of the original film that are traceable through the various stages of film duplication. When the mission sensitometry is evaluated and compared with the JSC control exposures, measurement of the effects of mission radiation and environment can be determined.

[b]Laboratory designation for flight film.

band exposures were made with a 5500-K filter. The JSC control exposures may be useful in assessing the effects of space-flight environments when the processed JSC control imagery is compared to the "first generation" space-flight imagery. Samples of sensitometric control curves established for one film type are shown in figure 2.

Machine processing configuration was tested by using sensitometric exposures of the film types as well as simulation imagery. Once an acceptable result was achieved, the sensitometric curves were established as standards for flight-film processing. A chemical analysis of each processing solution (table II) was also performed following the tests of film types.

Before the flight film was processed, each processing machine to be used was cleaned and mechanically certified. Chemicals were added and aged by processing either simulation films or other films. Immediately preceding flight-film processing, the chemicals were analyzed and compared to the predetermined standard.

CONCLUSIONS

The processing of each roll of flight film included processing of sensitometric control strips, testing of the machines for process-induced scratches, and careful leadering to prevent damage to the film (fig. 3).

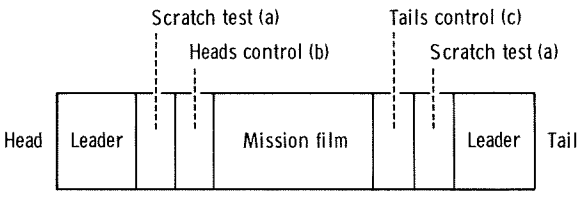


FIGURE 3.—Processing configuration for ASTP flight film: section a: approximately 15 m (50 ft) of blank film to test for processing-induced scratches; section b: freshly exposed control strip plus preexposed JSC control strip; section c: freshly exposed control strip.

TABLE II.—ASTP Earth Observations and Photography Film Processing Summary

Magazine no.	*Film type*[a]	*Film width, mm*	*Process chemistry*[a]
IF-02	2443	70	EA-5
CI-14	SO-168	35	ME-4
CI-15	SO-168	35	ME-4
CI-18	SO-168	35	ME-4
CI-20	SO-168	35	ME-4
CS-03	QX-806	35	ME-4
CT-02	SO-242	70	EA-5
CT-03	SO-242	70	EA-5
CT-04	SO-242	70	EA-5
CT-05	SO-242	70	EA-5
CX-06	QX-807	70	EA-5
CX-07	QX-807	70	EA-5
CX-08	QX-807	70	EA-5
CX-09	QX-807	70	EA-5
CX-10	QX-807	70	EA-5
CX-11	QX-807	70	EA-5
CX-12	QX-807	70	EA-5
CX-13	QX-807	70	EA-5
CX-14	QX-807	70	EA-5
CX-16	QX-807	70	EA-5
CX-17	QX-807	70	EA-5
CX-18	QX-807	35	ME-4

[a]All film and processing types are Eastman Kodak Company designations.

REFERENCES

1. Lockwood, H. E.: Apollo-Soyuz Test Project Photographic Processing Control Plan. NASA CR-141859, 1975.

2. Lockwood, H. E.: Apollo-Soyuz Test Project Photographic Film Processing and Sensitometric Summary. NASA CR-144631, 1975.

Photogrammetric Analysis of ASTP Earth Observations Experiment Data

C. W. Baker [a]

ABSTRACT

Apollo-Soyuz Test Project (ASTP) photographs of the Earth were used in photogrammetric triangulations to evaluate the spacecraft position data, the calibration of two camera lenses, and the orientation of the principal axis for each lens system. Photogrammetric triangulations were performed using 100-mm focal length photographs of California and 60-mm focal length photographs of Egypt, Syria, and Turkey. Spacecraft positions determined in the triangulation over California were within 100 m of their predicted values. However, those over Egypt, Syria, and Turkey were biased by approximately 2 km in latitude, 1.4 km in longitude, and 0.7 km in altitude. Only one element of camera calibration, radial lens distortion, could be determined. In this case, both lenses were essentially free of distortion. Errors in camera orientation angles were approximately 1.19° as predicted. However, it was possible to compute and apply a misalinement matrix to all orientation data and to reduce the error to approximately 0.33°. A correction for each sequence of photographs could be applied to reduce the error to less than 0.01°.

INTRODUCTION

The Earth Observations and Photography Experiment of the Apollo-Soyuz Test Project (ASTP) provided color stereographic photographs of the Earth during several spacecraft revolutions. The photographs were taken with a Hasselblad 70-mm camera (Model 500 EL) with a 1-cm reseau grid mounted in the film plane. Two different camera lenses were used. One was a Biogon 60-mm f/5.6 and the second was a Planar 100-mm f/3.5. The scales of the resulting photographs ranged from 1:2 000 000 to 1:3 750 000 (for a 55-by 55-mm image size) depending on the orbital altitude and the camera lens used. The photogrammetric analysis described in this section was necessary for preparing the geometrically controlled photomosaics that were used in the scientific data analysis.

By using the Apollo-Soyuz Experiment Parameter (ASEP) computer program, the tracking data, telemetry data, and camera shutter times were processed and merged to provide spacecraft-position, spacecraft-velocity, and camera-attitude data at the time of each exposure. The ASEP processing was by NASA Lyndon B. Johnson Space Center and TRW, Inc. (JSC/TRW); the resulting experiment support data (output on magnetic tapes and microfilm) were available to the various users. A more detailed explanation of the experiment support data is given in reference 1.

A series of analytical photogrammetric triangulations was performed using sequential overlapping photographs, which were part of photographic mapping passes covering selected test areas. Parameters provided with the experiment support data were used as initial approximations for camera positions and orientations. These test triangulations provided a means for evaluating experiment support data defining camera position and attitude. Analysis of the photo-measure-

[a]Defense Mapping Agency, Aerospace Center, St. Louis, Missouri.

ment residuals computed in the least-squares triangulation solutions reflects the mensuration capability and the metric stability of the camera system and provides a means for performing a limited postflight camera calibration.

PHOTOGRAMMETRIC TRIANGULATIONS

Photographic Materials

A total of 14 photographs was selected to provide stereographic coverage over three geographical areas (table I). These three filmstrips provided reasonably cloud-free photographic coverage over areas of available photo-identifiable map control. Revolution 17 photographs were taken with the 100-mm focal length lens, and revolution 71 photographs were taken with the 60-mm lens (fig. 1).

Ground Control

Map control was used to provide absolute positioning and leveling of the photogrammetric triangulation. The primary sources for control in the California area were U.S. Geological Survey (USGS) maps at 1:24 000 and 1:62 500 scales; U.S. Army Map Service (AMS) maps at a scale of 1:50 000 were the primary control sources in the

TABLE I.—Photographs Selected for Photogrammetric Triangulation

Revolution number	*Photograph numbers of filmstrip*	*Geographical area*
17	AST-14-880 to AST-14-884	California
71	AST-16-1256 to AST-16-1259	Egypt
71	AST-16-1266 to AST-16-1270	Syria/Turkey

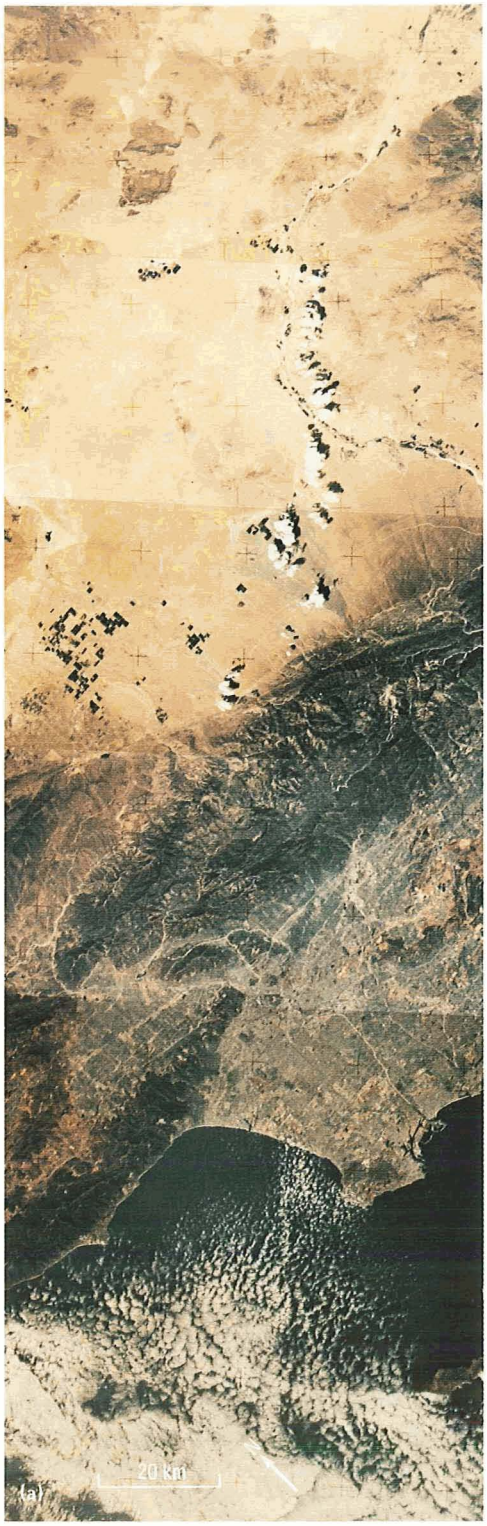




FIGURE 1.—Photomosaics prepared from the ASTP mapping photographs selected for photogrammetric triangulation. (a) Southern California (AST-14-880 to AST-14-884). (b) Egypt (AST-16-1256 to AST-16-1259). (c) Syria and Turkey (AST-16-1266 to AST-16-1270).

Egypt and Syria/Turkey areas. A pattern of ground features that could be identified on both the ASTP photographs and the maps was selected for absolute control in all three test areas. Additional sea-level points along the coastlines in each area were selected for vertical control to aid in leveling the photographic models. Pass points of common photographic images were selected to complete a pattern of approximately 25 points for each two-photo model area.

Data Acquisition and Reduction

All image points were measured by using 400-percent enlargements of the contact film. A three-stage stereocomparator with a 1-μm least count was used to accomplish the measurements. The 25 reseau intersections (which were a part of the Hasselblad camera system) were measured on each photograph at the same time they were measured on the detail images. A least-squares nonconformal cubic polynomial adjustment of the measured comparator coordinates to the known camera system coordinates for the 25 reseau intersections was performed for each photograph. The resulting coefficients were used to transform the image point comparator coordinates to camera system coordinates and to correct for film deformation.

The computer program used for the analytical triangulations was based on a simultaneous least-squares solution of the colinearity condition equations. Approximations for the camera positions and orientations and for the ground coordinates of selected points were treated as observations and were assigned variance-covariance estimates to reflect the statistical assurance associated with each parameter in the least-squares solution. In addition, parameters modeling interior camera calibration and systematic corrections to camera orientation approximations were determined in the least-squares solution.

An indication of the mensuration capability was obtained from preliminary relative analytical triangulations of each test strip. For these relative triangulations, ground control was not constrained. Camera position and orientation parameters were given enough freedom to adjust in order to obtain an optimum relative model constraining only the interior camera geometry. The resulting photograph image residuals indicated no unusual systematic patterns. The unweighted mean error of the measurement residuals (which

TABLE II.—Corrections to Spacecraft Positions in Experiment Support Data

Photograph number	*Change in latitude, m*	*Change in longitude, m*	*Change in altitude, m*	*In-track correction, m*	*Cross-track correction, m*	*Radial correction, m*
AST-14-880	2	68	−10	53	46	−10
881	3	56	8	44	36	8
882	1	40	26	31	24	26
883	29	56	44	64	13	44
884	11	21	62	23	5	62
AST-16-1256	2178	1193	626	2467	738	620
1257	2189	1228	631	2496	736	624
1258	2163	1228	636	2468	735	629
1259	2142	1233	640	2448	732	634
AST-16-1266	2047	1338	676	2397	719	670
1267	2036	1359	682	2397	715	675
1268	2008	1362	688	2369	712	681
1269	2012	1401	693	2392	710	688
1270	1999	1423	699	2390	708	693

is a measure of the one-sigma mensuration accuracy) was approximately 5.0 μm for the California strip and 6.5 μm for the Egypt and Syria/Turkey strips.

EVALUATION OF SPACECRAFT POSITION DATA

The experiment support data gave no specific accuracy statements on the spacecraft positions for the photographs used in this test. In general, the nominal errors were expected to be approximately 3 km at the three-sigma level with a range from 600 m to as much as 10 km. Controlled triangulation solutions were performed in the three test areas. The camera station positions were assigned large *a priori* standard deviations to permit complete freedom in the adjustment. Scaled geographic coordinates of the selected control points were input and assigned standard deviations of 50 m (one sigma) to provide absolute positioning and leveling of the photogrammetric triangulations. Table II lists the corrections to the spacecraft positions in the experiment support data, which were required to obtain the best least-squares fit to ground control. The corrections indicate that the trajectory data and time data for revolution 17 over California are quite good. However, the data for revolution 71 show errors approaching or exceeding the expected nominal error of 3 km. It should be noted that the ground-control coordinates in the three triangulation solutions were referenced to the local geodetic datums (European and North American Datum of 1927) with elevations referenced to mean sea level. The corrections shown in table II, therefore, include the biases between the local geodetic datums and the ephemeris reference system. Part of the systematic corrections is also caused by any camera calibration errors in focal length and principal point offset.

CAMERA CALIBRATION

Only a very limited postflight camera calibration could be achieved. Because of the large uncertainties in exposure-station positions and ground-control identification, it was impossible to isolate model translation and scale biases caused by errors in camera focal length, principal point offset, and lens decentering. However, the three coefficients modeling symmetric radial lens distortion are determinant to some degree with a good pass-point pattern and sufficient vertical control for model leveling. Table III lists the computed radial lens corrections as functions of radial distance from the principal point for the two lenses involved. The indicated corrections are quite small (less than 8 μm at the maximum radial distance) and are not significant in relation to the associated one-sigma error bounds based on the error propagation from the triangulation solutions.

TABLE III.—Computed Radial Lens Corrections

Radial distance, mm	*Correction, μm*	*Standard deviation, μm*
AST-14-880 to AST-14-884 (focal length: 100.57 mm)		
0	0.0	0.0
3	.0	.1
6	.0	.1
9	.1	.8
12	.4	1.6
15	.8	3.5
18	1.5	6.7
21	2.7	11.5
24	4.5	18.9
27	7.2	29.0
AST-16-1256 to 1259 and AST-16-1266 to 1270 (focal length: 61.17 mm)		
0	0.0	0.0
3	.0	.1
6	.0	.1
9	.0	.7
12	.1	1.4
15	.2	3.0
18	.6	4.2
21	1.2	10.8
24	2.5	17.2
27	4.7	26.5

EVALUATION OF CAMERA ORIENTATION DATA

For each exposure time, the experiment support data include a rotation matrix defining the relationship between the camera coordinate system and the Earth-fixed coordinate system. This nominal camera orientation matrix is actually the product of a series of rotation matrices relating various reference coordinate systems. The rotation matrix, defined as $[F]$, relates the camera coordinate system to the rigid body of the Apollo spacecraft or the navigation-base coordinate system. The $[F]$ matrix is constant and is defined by preflight determined parameters. The navigation base can be related to the nominal inertial measurement unit (IMU) reference platform by the rotation defined by the matrices $[D]$ and $[G]$. The $[G]$ matrix relates the actual IMU system to the navigation base system and is computed from the spacecraft gimbal angles. The $[D]$ matrix relates the nominal and actual IMU systems and accounts for observed platform misalinements and/or drift. The nominal IMU system is related to the Earth-fixed system through a rotation matrix $[R]$. (The various reference coordinate systems and their relationship are discussed in reference 1.)

The product rotation matrix $[FGDR]^T$ defines the relationship between the camera and the Earth-fixed coordinate systems at the time a particular photograph was taken. There are, of course, several sources of error affecting the accuracy of the camera orientations provided in the experiment support data. The major error sources and the three-sigma error magnitudes as estimated by JSC/TRW are listed in table IV.

Sources 5, 6, 7, and 8 are all involved in the transformation from the navigation base system to the camera system described by the $[F]$ matrix, and they represent the largest error source in the camera orientation computations. The total root-sum-square expected three-sigma error magnitude for camera orientation in the experiment support data is approximately 1.19°. However, a major part of these error sources is accounted for by systematic errors that are constant for any one sequence of photographs and to some extent constant for the entire ASTP mission.

TABLE IV.—Sources of Error Affecting Accuracy of Camera Orientations in the Experiment Support Data

Source	*Magnitude, deg*
1. IMU platform misalinement	0.03
2. Platform drift	[a](0.02)(Δt)
3. Navigation base misalinement	.05
4. Gimbal angle errors	.02
5. Camera alinement	.50
6. Mounting hole accuracy	.25
7. 1- to zero-g structural deflections	1.00
8. Structural thermal variations	.33

[a]Δt is the time, in hours, from the latest platform alinement to the time of exposure.

A major objective of the photogrammetric triangulations was to determine an indication of the magnitude of the orientation errors and to determine to what extent the systematic misalinement errors could be recovered and modeled. The computer program used for the test triangulations permits solving for three angles which define a single rotation matrix that models any systematic orientation errors common to all photographs in the solution. Two separate triangulation solutions were performed for orientation evaluation. One solution used data for the five photographs over the California area, which were taken during revolution 17 with the 100-mm focal length lens. The other solution combined the photographs from the two areas of revolution 71 (Egypt and Syria/Turkey), taken with the 60-mm lens.

For the experiment support data, the computed systematic corrections to the photograph orientations, in terms of Eulerian angles, for the California area were

$\omega = -1°9'50.0''$
$\phi = -0°43'57.4''$
$\kappa = 0°15'2.7''$

Comparable systematic corrections to the nine photographs for the Egypt and Syria/Turkey areas were

$\omega = -0°35'0.3''$
$\phi = -0°45'53.7''$
$\kappa = 0°11'17.8''$

Table V presents the additional residual orientation errors of the individual photograph orientation angles based on photogrammetric triangulation solutions to known ground control. These orientation angle residuals represent errors in addition to the systematic errors defined by the Eulerian angles.

Although these results are based on a small sample of the ASTP Earth Observations Experiment photographs, they do provide an indication of the accuracy of photograph orientations in the experiment support data. The magnitudes of the computed systematic orientation corrections support the expected three-sigma uncertainty of 1.19°. The two sets of systematic angle corrections are quite similar, but the differences between them (particularly in the ω angle) indicate that using one rotation matrix to model camera misalinement for the entire ASTP mission would still result in orientation angle errors of at least 0.33°. However, the orientation residuals listed in table V indicate that a systematic orientation correction could be computed for any one sequence of photographs, which would reduce the magnitude of orientation errors to less than 0.01°. Additional testing would be required to determine how frequently this orientation misalinement must be computed to maintain adequate orientation accuracies.

TABLE V.—Angle Residuals for Camera Orientation in Experiment Support Data

[*Values represent residuals in arcsec after corrections for systematic camera misalinement*]

Photograph number	$\Delta\omega$, *arcsec*	$\Delta\phi$, *arcsec*	$\Delta\kappa$, *arcsec*
AST-14-880	−1	−9	1
881	0	11	0
882	2	−1	−2
883	−2	7	0
884	1	−7	1
AST-16-1256	−3	−10	4
1257	−3	−5	−3
1258	1	11	4
1259	3	4	0
AST-16-1266	0	−4	1
1267	0	−1	−3
1268	4	22	6
1269	0	−7	−8
1270	−3	−9	−2

CONCLUSIONS

Results of the photogrammetric triangulation tests using ASTP photographs in the Earth Observations and Photography Experiment indicate the following:

1. The metric qualities of the Hasselblad photographs are adequate for photogrammetric triangulation. (Photograph mensuration accuracies of 5 to 6 μm (one sigma) were obtained with the selected test photographs; however, the small scale (approximately 1:3 500 000) and generally poor contrast of the photographs make point identification difficult, with identification errors generally exceeding 50 m at ground scale.)
2. There was no indication that significant lens-distortion errors were present with either the 60- or 100-mm focal length lenses.
3. Errors in the spacecraft positions approach the nominal expected error of 3 km; however, the positions for the photographs over the California test area are significantly more accurate than the minimum expected error of 600 m (see table II).
4. Observed errors in the orientation angles of the experiment support data agree with the predicted 1.19° error. (The triangulation results from the small test sample indicate that a camera misalinement matrix could be computed and applied to all the orientation data to reduce the expected error to approximately 0.33°, and a separate camera misalinement matrix for each sequence of photographs could be computed to reduce the expected orientation errors to less than 0.01°.)

REFERENCE

1. Osburn, R. K.; Barnett, Edward L.; Moore, Harry L.; and Ball, Jimmie R.: ASTP Experiment Support Data Processing. NASA CR-141915, 1975.

Appendix A—Glossary

adiabatic—occurring without gain or loss of heat

agglomerate—a rock composed of coarse, angular, pyroclastic fragments

albedo—the percentage of incident radiation that is reflected by a surface or a body

allochthon—(1) a mass of rocks that has been moved from its original site by tectonic forces; for example, a thrust sheet or nappe (2) a mass of sedimentary materials transported and redeposited far away from the place of origin

allochthonous—formed or occurring elsewhere than in place

alluvium—a deposit of clay, silt, sand, gravel, or similar detrital material that was transported and deposited by flowing water

Alpides—a name given to the great system of young, folded mountains that extends from Spain into southern Asia and that includes the Alps and the Himalayas. The term "Alpide" is also used in a stricter sense to refer to the north flank of the orogenic belt; for structures on the south flank, the term "Dinarides" is used.

Alpine facies—name given to a facies of the European Triassic that is characterized predominantly by marine sediments deposited in an open, shallow sea

anastomosing channels—interlacing, branching, and reuniting channels; braided streams

andesite—an extrusive, usually dark-grayish, fine-grained igneous rock consisting primarily of plagioclase feldspar

anemometer—any instrument used to measure windspeed

anorthosite—a plutonic granular igneous rock composed almost entirely of plagioclase feldspar, which is usually labradorite

anticline—a fold of rock strata in which older rocks are found at the core

anticlinorium—an anticlinal structure of regional extent composed of lesser folds

anticyclone—a horizontal motion system of winds circulating around a region of high atmospheric pressure, clockwise in the Northern Hemisphere, counterclockwise in the Southern Hemisphere

antiform—an anticlinal-type structure in which the chronologic succession of the rock strata is not known

anvil—name given to the anvil-shaped upper part of an expanding cumulonimbus cloud; usually considered a feature of a growing thunderstorm

Archeozoic—the earlier part of Precambrian time

arenaceous—(1) said of a sediment or sedimentary rock resembling, made of, or containing sand or sand-sized particles (2) growing in sandy places

arkose—a sedimentary rock of granular texture composed primarily of angular to subangular grains of quartz and feldspars

asthenosphere—the layer of the Earth, tens of kilometers below the surface, that is a region of weakness where plastic movements take place to permit isostatic adjustments

astrobleme—a geologically ancient scar on the Earth's surface, formed by the impact of a meteor or a comet

autochthon—a mass of rocks localized at its site of origin; autochthonous rocks, although not moved from their site of original formation, may be deformed

avulsion—the sudden removal or separation of land by a flood or by a change in a river's course

bankfull stage—the elevation of the water surface of a stream that is flowing at the maximum its channel can carry without overflowing its banks

bar—an elongate ridge or mound of unconsolidated sand, gravel, or other material, submerged or nearly submerged below the surface of a body of water

barchan—a moving, isolated, crescent-shaped sand dune in which the horns point downwind

baroclinity—a condition of a fluid (or an airmass) in which surfaces of constant pressure (isobaric) intersect surfaces of constant density (isosteric)

barotropy—the state of zero baroclinity; a condition of a fluid (or an airmass) in which surfaces of constant density are coincident with those of constant pressure

basalt—a dark-gray to black, dense, fine-grained, commonly extrusive, mafic igneous rock composed primarily of calcic plagioclase and clinopyroxene

base/height ratio—the ratio between the aerial base (the length of the line joining two air stations) and the flight height of a stereoscopic pair of photographs

batholith—a large, irregular mass of igneous rock that has more than 100 km^2 in surface exposure and has melted or forced its way into surrounding strata

bathymetry—concerning the distribution of water depths in a water body

bathythermograph—a device that records the temperature and depth of seawater and lets one map the temperature structure of the upper layers of the sea

bedload—the bottom load; that part of the stream load moved along the streambed by traction or saltation

Bénard cells—standard convection cells formed over oceans when surface water temperatures are evenly distributed over large areas, windspeeds are less than 7.7 m/sec (15 knots), and sufficient nuclei for water vapor condensation exist

bight—a curve, a bend, or an indentation in the shoreline of a sea or a bay

bimodal distribution—a frequency distribution with two modes, each occurring with greater frequency than the immediately adjacent values

bioluminescence—the emission of light from living organisms

biomicrite—a limestone consisting of skeletal debris and carbonate mud

block mountains (fault-block mountains)—mountains bounded by one or more faults and produced by block faulting, a type of normal faulting in which the crust is divided into relatively elevated and depressed blocks

blowout—in geomorphology, a general term for a trough- or saucer-shaped hollow formed by wind erosion in a preexisting dune or sand deposit

bolsón—a geomorphic term used to describe a basin or a depression nearly or entirely surrounded by mountains. Drainage is centripetal, and a playa often occupies the lowermost part of the basin.

Bouguer anomaly—a gravity anomaly calculated by taking into account the attraction effect of topography but not that of isostatic adjustment

braided stream—a stream with an interwoven, intricate pattern of several branching and reuniting shallow channels separated from each other by branch islands

breccia—a clastic rock consisting of large, angular rock fragments embedded in a fine-grained matrix

buoyancy—the resultant of upward forces exerted by a fluid on a body placed in it, equal to the weight of the fluid displaced by the body

caldera—a large, basinlike depression whose diameter is many times larger than that of the included vent(s) and that is formed by an explosion removing the upper part of the volcanic cone or by collapse of the roof of a magma chamber

Cambrian—the earliest geologic time period of the Paleozoic era occurring between 500 and 600 million years ago

Campanian—a geologic-time unit in the Upper Cretaceous (above Santonian and below Maestrichtian)

capillary waves—waves of short wavelength (less than 1.7 cm) whose restoring force is surface tension

Carboniferous—the Mississippian and Pennsylvanian periods combined; occurring from 270 to 350 million years ago; also known as the age of coal

cargneule—a carbonate sedimentary rock with cavities that are filled with soft evaporitic material, which easily dissolves or falls out

Cartesian coordinate system—a system for locating points in space by reference to three intersecting planes (coordinate planes). These three planes are represented by three straight lines that intersect at a common point called the origin

casehardening—the process by which the surface layer of a porous rock is hardened by being coated with a cement left by the evaporation of mineral-bearing solutions

causeway—a raised road or path crossing low ground or water

Cenomanian—a geologic-time unit in the lowermost Upper Cretaceous (above Albian, below Turonian)

Cenozoic—of, or pertaining to, the present geologic era beginning about 70 million years ago and marked by the appearance of mammals

chert—a rock resembling flint and consisting dominantly of cryptocrystalline silica

chlorophyll—the principal photosynthetic pigment of plants; the green coloring of leaves and plants

chlorophyll-*a*—a pigment in phytoplankton

cienaga—(1) a name given to a marshy area, which may contain standing water, where the ground is wet because of seepage or the presence of springs (2) places where overbank flow or tributary streamflow is trapped outside the streamcourse by the development of natural levees

cinder cone—a cone-shaped hill formed by the accumulation of cinders thrown out by a volcano

claypan—a term used in Australia for a shallow depression or playa with a hard clay surface

color intensity—characteristic determined by the amount of light reflected by a surface; less reflection produces a more intense color

complex dune—a large-scale accumulation of eolian sand formed by the combination of two or more different types of dunes

continental shelf—the submerged, gently sloping edge of a continent between the shoreline and the continental slope

copepods—minute crustaceans of the subclass Copepoda; the most abundant crustacean organisms in the ocean

cordillera—a system of mountain ranges consisting of more or less parallel chains of mountains

Coriolis force—an apparent force that causes, as a result of the Earth's rotation, a deflection of projectiles and winds to the right in the Northern Hemisphere and to the left in the Southern Hemisphere

crescentic dune—see barchan

Cretaceous—the last period of the Mesozoic era, occurring between 136 and 65 million years ago

cross-bed—a single, more than 1-cm-thick, often lenticular cross-stratum of uniform or gradational lithology, which was deposited at an angle to the original surface and was separated from adjacent beds by surfaces of erosion, nondeposition, or abrupt changes in lithology

cross-lamina—cross-bed; used in a stricter sense to refer to a cross-stratum less than 1 cm thick

crush zone—an area of fault breccia, formed by the crushing or shearing of rocks during fault movement, or of fault gouge; a slippery, clayey, or claylike material coating the fault surface or cementing the fault breccia

crust—the solid, exterior shell of the Earth

cuesta—a hill or a ridge with a long gentle slope on one side and a steep face or escarpment on the other

cusps—a series of wave-built triangular projections of beach material separated by crescent-shaped depressions. These forms have varying sizes.

Cyanophyta—blue-green algae in which photosynthetic pigments are distributed through the cytoplasm and not localized in chromatophores, and nuclear substances are not organized in definite nuclei

cyclone—a system of winds rotating around a center of low atmospheric pressure, clockwise in the Southern Hemisphere and counterclockwise in the Northern Hemisphere

dacite—quartz andesite; a fine-grained extrusive rock having almost the same composition as andesite but with a less calcic feldspar

Decke—the German equivalent of "nappe"

décollement—detachment; used to describe a structural discordance that results in independent styles of deformation in the rocks above and below it; usually used to refer to a discordance over which an allochthonous rock mass has moved

deflation—the sorting, lifting, and removal of fine-grained sediment by the wind; the erosion of soil by the wind

delta, river— a nearly flat plain of alluvial deposits occurring at the mouth of a river

dendritic—branching irregularly in all directions and at all angles

densitometry—the measurement of the optical density of a material, especially a photographic film

deranged drainage—drainage whose original flow pattern has been disrupted by agents other than streams, such as wind deposition, glaciation, volcanism, or crustal movements

desert varnish—a glossy surface stain or coating composed mostly of iron oxide with traces of manganese oxide and silica, which coats many exposed rock surfaces in deserts

detritus—loose rock and mineral material that results directly from disintegration or abrasion

Devonian—a period of the Paleozoic era occurring 350 to 400 million years ago; known as the age of fishes

diabase—In the United States, a dark, intrusive igneous rock whose main mineral components are labradorite and pyroxene

diagenesis—(1) recombination or rearrangement of a mineral resulting in a new mineral (2) basically, the conversion of a sediment into a rock

diapir—a dome or an anticlinal fold in which a mobile core has broken through overlying rocks

diatoms—microscopic, unicellular, marine or freshwater algae with siliceous cell walls

diatreme—a pipe through which magmatic materials have passed that is now filled with breccia

dike—(1) a long, narrow igneous intrusion that cuts across the planar structures of the surrounding rock; also, a similar mass composed of other types of material such as sandstone (2) an artificial embankment for controlling or containing floodwaters

dinoflagellates—numerous, chiefly marine, motile organisms of the order *Dinoflagellata,* usually possessing two flagella. Some dinoflagellates, such as the variety that causes the "red tide," are poisonous to fish and to man.

dip slope—a slope of the land surface that roughly conforms with the direction and angle of dip of the underlying rock strata

discharge—for a stream, the rate of flow at a given moment in time, expressed as volume per unit of time

disharmonic fold—a fold whose form is modified by the varying strata through which it passes

distal—remote or far from the point of origin

distributary—a river branch flowing away from the main stream and not returning to it, as in a delta or on an alluvial plain

dolerite—diabase

dolomite—a carbonate sedimentary rock rich in magnesium carbonate or consisting chiefly of the mineral dolomite

draa—a large-scale accumulation of eolian sand

drainage basin—the whole area drained by a particular river and all its tributaries

drainage pattern—the actual arrangement in plan view of all the stream courses in a given area

duricrust—a general term referring to a hard crust on the surface layer of soil in a semiarid climate; formed by the accumulation of soluble minerals left by the evaporation of mineral-bearing waters

ebb-tidal delta—particular deltaic deposit formed by the dominant ebb-tidal current leaving a tidal inlet; composed of a main ebb channel,

channel-margin linear bars, a terminal lobe, swash platforms, and marginal flood channels

eddies—currents of air or water differing from a main current, especially those having circular motion; small whirlpools

effluent—flowing forth or out

electromagnetic radiation (EMR)—energy propagated as electromagnetic waves through space or material media

eluviation—the downward movement of soluble or suspended material in soil by the movement of water when rainfall exceeds evaporation

endoreic—said of a depression or basin with internal drainage

entrain—to pick up and transport, as sand taken up and put into suspension by a current

Eocene—an epoch of the Tertiary period

eolian—pertaining to the wind; especially said of deposits whose constituents were transported and deposited by the wind, or of landforms produced or eroded by the wind

epeirogeny—the deformation of the Earth's crust by which the larger features of continents and oceans are produced

epicontinental—lying upon a continent or a continental shelf; for example, an epicontinental sea is a sea on the continental shelf or within a continent

epidermis—in geology, a term referring to the sedimentary part of the Earth's crust

estuary—the part of the lower course of a river that is affected by the mixing of freshwater and saltwater

evapotranspiration—the loss of water from a land area through direct evaporation from the soil and transpiration from plants

exfoliation—the process by which scales, layers, or flakes of rock are split off, peeled, spalled, or stripped from a larger rock mass

extrusive—said of an igneous rock formed by the crystallization of lava poured out at the Earth's surface

facies—a rock or group of rocks that differs from comparable rocks in aspects such as mineral composition, age, fossil content, and type of bedding

fathom—a nautical unit of length equal to 1.8 m (6 ft)

fault—a fracture in the Earth's crust along which displacement has occurred

ferruginous—(1) of, pertaining to, or containing iron (2) said of a rock having a rusty color because of the presence of ferric oxide

fetch—the area of water over which wind blows in essentially a constant direction and thereby generates waves; also called generating area

field of view—the entire angular expanse through which an instrument is sensitive to radiation

firn line—on a glacier, the highest level to which winter snow cover retreats; the snowline on a glacier

flint—a massive, hard, somewhat impure variety of cryptocrystalline quartz that breaks with a conchoidal fracture and that produces a spark when struck by steel

flood plain—a nearly flat plain adjacent to a river channel that is naturally subject to flooding

flood-tidal delta—particular deltaic deposit formed by dominant flood-tidal currents entering a tidal inlet; composed of a flood ramp, flood channels, ebb shields, ebb spits, and spillover lobes

fluorescence—the emission of radiation by a substance exposed to external radiation; this emission ceases when the external stimulus ceases

fluorometer—an instrument for measuring fluorescence

flysch—a marine sedimentary facies characterized by a thick and extensive sequence of thinly bedded, graded deposits composed largely of marls and shales interbedded with conglomerates, coarse sandstones, and graywackes

focal length—the distance between the focal point of a lens and the focal plane

fold—a curve or a bend in rock strata or any planar structure

fold belt—an orogenic belt; a linear region that has been subjected to folding and other deformation

foreland—a stable area bordering a fold belt (an orogenic belt), toward which the rocks of the fold belt were thrust or overfolded

Forel-Ule scale— a color scale consisting of 22 different prepared solutions which are compared to the color of seawater observed against a white Secchi disk to obtain a crude determination of ocean color

front—the generally linear outermost slope of a mountain range that rises above a plain or a plateau

f-stop—an expression used to represent the speed of a lens; defined by the ratio of the camera focal length to the diameter of the lens opening

fulcrum—a point or zone on a coast which divides a region of sediment accretion from a region of erosion

fumarole—a vent from which vapors and gases arise; often associated with the late stages of volcanic activity

gabbro—a group of dark-colored, basic intrusive igneous rocks composed primarily of monoclinic pyroxene and calcic plagioclase

gamma—a numerical measure of the processing conditions under which a film negative has been developed

geanticline—a regionally extensive mobile upwarping of the Earth's crust (antonym: geosyncline)

geostationary satellite—a satellite that maintains a constant position relative to the Earth's surface by orbiting at the speed of Earth rotation

geostrophic—of, or pertaining to, the balance between the horizontal pressure force in the atmosphere and the Coriolis force

geosynclinal couple—an orthogeosyncline; a geosyncline containing both miogeosynclinal (nonvolcanic) and eugeosynclinal (volcanic) furrows linked by geanticlinal ridges

geosyncline—an extensive mobile downwarping of the Earth's crust, which is subsiding with the accumulation of sedimentary and volcanic rocks thousands of meters thick

Germanic facies—a sedimentary facies of the European Triassic system that is characterized predominantly by continental deposits (mostly red beds) and occasionally by deposits of an inland sea (evaporites)

gibber—a faceted pebble or stone, especially those composing a desert pavement

gibber plain—a rock-floored desert plain; a desert pavement covered with gibbers

glacier—a large mass of ice slowly creeping downslope, formed, in part, on land by the compaction and recrystallization of snow

glauconite—an authigenic mineral of the mica group, found in the form of green pellets; formed in a marine environment, occurring in greensand and in many Paleozoic or younger sandstones and limestones

graben—an elongate and depressed crustal block bounded by faults on its long sides

gramineous—grasslike

granite—a plutonic rock composed essentially of quartz and orthoclase or microcline

gravity fault—a normal fault; a fault in which the rocks on the overlying side or "hanging wall" appear to have moved downward relative to rocks on the underlying side or "footwall"

graywacke—a coarse-grained, usually dark (gray or greenish gray) sandstone composed of poorly sorted angular to subangular fragments of quartz and feldspar all firmly bound together by a clayey matrix, which is sometimes partly metamorphosed

greenstone—(1) any of numerous usually altered, dark-green, compact, basic to ultrabasic igneous rocks commonly found in folded mountain ranges. The dark-green color is attributed to the presence of epidote, chlorite, and hornblende. (2) the mineral nephrite; a compact, fine-grained amphibole (tremolite or actinolite) that is the more common and less valuable type of jade

groin—a low protective structure of stone, steel, or other sturdy material built to prevent erosion or to contain sand for forming a beach

ground truth—supporting data collected on the ground to aid in the interpretation of photographs and other remotely sensed data; also called ground data

gypsum—a common sulfate mineral, often associated with anhydrite and halite in evaporite deposits; also frequently found interstratified with limestones and shales

halophyte—a plant that grows in salty or alkaline soil

hematite—a common iron mineral constituting an important iron ore (Fe_2O_3)

Hercynian orogeny—the late Paleozoic orogenic era of Europe that reached its principal mountain-building culmination toward the end of the Carboniferous

hinge zone—the boundary between a stable region and a region affected by upward or downward movement

hinterland—a region bordering or lying within the internal side of an orogenic belt, away from the direction in which rocks of the fold belt were thrust or overfolded

Holocene—an epoch of the Quaternary period, from the end of the Pleistocene to the present

homocline—a rock unit in which all strata dip in the same direction

hornblende—a very common mineral of the amphibole group, found primarily in igneous rocks, which varies in composition and may be black, dark green, or brown

horst—an elongate and uplifted crustal block bounded by faults on its long sides

hummock—a mound or rise, usually round in shape

illuviation—the process by which soluble or suspended material that was transported from an upper horizon by the process of eluviation, is accumulated in a lower soil horizon

imbricated—overlapping (as in the overlapping pattern of scales)

imbricated fault zone—a zone of closely spaced, nearly parallel, overlapping thrust faults

indurated—descriptive of a compact rock or soil hardened by the action of heat, pressure, or cementation

inertia—a property of matter by which a mass offers resistance to a change of its translational motion

inselberg—a prominent, isolated hill or mountain rising abruptly from a plain

interfluve—the area between rivers; the interstream area

intermediate—term used to describe an igneous rock that has a silica content between 54 and 65 percent and is transitional between basic (low silica content) and silicic (high silica content)

intermittent stream—a stream that only flows part of the time

internal waves—subsurface waves formed within fluids exhibiting vertical density gradients or between layers of different density. Wavelengths, heights, and periods of internal waves are usually large. At the surface, slicks and scum lines often provide visible evidence of internal wave flow.

intertidal—pertaining to the area between the high-water line and the low-water line

Intertropical Convergence Zone (ITCZ)—zone popularly known as the doldrums, occurring along the meteorological equator where trade winds from the Northern and Southern Hemispheres meet; characterized by a slow updraft of air, with frequent thunderstorms associated with rising, unstable air

intervalometer—a timing mechanism used for automatically triggering the shutter of a camera at any predetermined interval

intrasparite—a limestone composed of at least 25 percent intraclasts, a cement of coarse-grained calcite crystals, and a less abundant carbonate-mud matrix

intrusive—said of an igneous rock formed by emplacement of magma in preexisting rock; also pertaining to the process of intrusion

inversion—a reversal of a normal gradient; in meteorology, an increase of temperature with height rather than a decrease; in oceanography, an increase in water temperature with depth

irradiance—a measurement of light energy; the incident radiant power per unit area at an intercepting surface

island wake—atmospheric or oceanic waves occurring in the lee of an island and presenting a pattern morphologically similar to that formed by a ship moving through water

isobar—a line on a weather map or chart along which the pressure has a constant value

isogram—a general term for any line on a map or a chart that connects points of equal value with respect to a given physical quantity

isohyet—a line on a map connecting points of equal rainfall

isotherm—a line drawn on a map connecting points of equal temperature

jasper—a slightly translucent cryptocrystalline quartz of any of several colors

jet—a sudden and usually forceful rush of fluid discharged through a narrow opening

jetty—a low protective structure perpendicular to the shore built to modify the local area by erosion, by prevention of deposition, or by deflection of currents; often constructed at harbors

kaolin—a group of common clay minerals characterized by a two-layer hydrous aluminum-silicate crystal lattice

katabatic wind—a local wind that flows downward along a slope; a gravity wind

Kelvin-Helmholtz wave—an unstable wave in a system of two homogeneous fluids with a velocity discontinuity at the surface

kurtosis—a measure of the peakedness or flatness of the graphic representation of a frequency distribution

lacustrine—of, relating to, produced by, or growing in a lake or lakes

lamina—a sedimentary layer less than 1 cm thick, differing from other layers in color, composition, or grain size

Landsat—an NASA unmanned, Earth-orbiting remote-sensing satellite; formerly designated Earth Resources Technology Satellite (ERTS)

laterite—a highly weathered, reddish, ferruginous soil usually formed in tropical regions

leach—to remove soluble constituents from a rock, an ore body, or an upper soil horizon by the action of percolating water

lee—the side sheltered from the wind

lens (or lense)—term used to describe a feature shaped like a double-convex optical lens; e.g., a geologic deposit that is thick in the middle and thins out toward the edges, or a lenticular layer of freshwater lying above denser, more saline water

leptokurtic—pertaining to a narrow frequency distribution curve more peaked than the corresponding normal distribution curve

Libyan Desert glass—silica glass found over an extensive area of Libya centered at approximately latitude 25°25′ N and longitude 25°30′ E. Silica glass is a hard, brittle, noncrystalline substance produced by fusion and consisting predominantly of silica (SiO_2). The Libyan Desert glass occurs as lumps, chips, or fragments with colors ranging from greenish yellow to greenish black.

lignite—a usually brownish-black coal intermediate between peat and bituminous coal

limestone—a sedimentary rock consisting mainly of calcium carbonate

limonite—a brown, amorphous, hydrous ferric oxide of variable composition

lineament—a straight or gently curved feature on the Earth's surface; usually the expression of fractures or faults

lithofacies—a horizontal, mappable subdivision of a particular stratigraphic unit, distinguished from other subdivisions on the basis of lithologic characteristics

lithology—(1) the study and description of rocks on the basis of such characteristics as color, particle size, mineral content, and structure (2) the physical character of a rock

lithosphere—the solid part of the Earth; the Earth's crust

littoral—intertidal; pertaining to the shore zone between high water and low water

longitudinal dune—a long, narrow sand dune, more or less symmetrical in cross profile, that is oriented parallel with the direction of the dominant wind

longshore current—littoral current; an ocean current flowing parallel to and near the shore and caused by the approach of waves to the shore at an angle

longshore drift—the movement of sediment along a coastline by a current caused by the angular approach of waves to the shore

lunate—crescent shaped

lunette dune—a broad, low crescentic mound usually developed just downwind from a blowout or a pan

maar—a low-relief, coneless volcanic crater produced by a violent explosion and often containing a small lake

Maestrichtian—a geologic-time unit of the Upper Cretaceous (above Campanian, below Danian of Tertiary)

mantle—the zone of the Earth below the crust and above the core

marl—a loose, crumbly, unconsolidated deposit that contains a substantial amount of calcium carbonate mixed with clay; used as a fertilizer for soils deficient in lime

meander—pertaining to a stream, one of a series of sinuous curves, turns, or windings in the course of a stream

melange—a mixture of rock materials; specifically, a body of deformed rocks consisting of a fine-grained matrix mixed with angular, poorly sorted rocks of different geologic origins and ages

meseta—an extensive plateau or tableland forming the central physical feature of a region

mesokurtic—said of a distribution curve that closely resembles a normal frequency distribution in that it is neither very peaked nor very flat across the top

Mesozoic—of, or pertaining to, an era of geologic time lasting from the end of the Paleozoic to the beginning of the Cenozoic, or approximately 150 million years; characterized by the appearance of flowering plants and the appearance and extinction of dinosaurs; also known as the age of reptiles

metamorphic—a term used to describe rocks that have formed in the solid state as a result of pronounced changes in temperature, pressure, and chemical environment

microwave—the region of the electromagnetic spectrum characterized by comparatively short wavelengths, especially those between 100 cm and 1 cm

migmatite—a composite rock that is composed of igneous or igneous-looking and/or metamorphic materials

Miocene—an epoch of the upper Tertiary period between the Oligocene and the Pliocene

mobile belt—orogenic belt; fold belt

molasse—(1) a sedimentary facies that is partly marine, partly continental or deltaic and that consists of a thick sequence of ungraded, cross-bedded, fossiliferous conglomerates, sandstones, shales, and sometimes coal deposits (2) an extensive postorogenic sedimentary formation of coarse material that is derived through the wearing down of an emergent high mountain chain and that is normally not folded

monocline—a unit of strata that dips in one direction only and is not part of an anticline or a syncline

monzonite—a plutonic rock containing almost equal amounts of orthoclase and plagioclase

moraine—a ridge or mound of unsorted glacial debris including clay, sand, gravel, and boulders

morphotectonic—pertaining to the tectonic relations and origins of the present-day topographic features of the Earth's crust

multispectral scanner—a remote-sensing device that is capable of detecting energy in the ultraviolet, visible, and infrared portions of the spectrum. The radiation recorded by the scanner is converted by a detector element into an electrical signal, which provides image information on the viewed scene.

Munsell color system—a system devised by A. H. Munsell in which three parameters, hue, value, and chroma, are used to standardize color description

Muschelkalk—stage of the Germanic facies of the European Triassic characterized by deposits of an inland sea

nappe— an allochthonous rock mass that has been thrust over other rock

natron—a mineral ($Na_2CO_3 \cdot 10H_2O$) used in ancient Egypt in embalming, in manufacturing glass and glaze, and as a cleansing agent

Neogene—an interval of time incorporating the upper Tertiary including the Miocene and Pliocene epochs; one of two periods (with the Paleogene) of the Tertiary era

Nubian sandstone—a sedimentary formation consisting of almost horizontal beds of coarse- to fine-grained sandstones with occasional shale and quartzite beds that is widely distributed over the southern part of Egypt and the northern Sudan

Oligocene—an epoch of the lower Tertiary period between the Eocene and the Miocene

oölite—a sedimentary rock chiefly made up of oöliths, which are small, round accretionary bodies usually formed of calcium carbonate by inorganic precipitation

ophiolite—a suite of essentially mafic and ultramafic igneous rocks whose origin is believed to be related to the early development of a geosyncline; the "ophiolite belt" refers to such a suite of ultramafic rocks found in the Tethyan mountain system

Ordovician—a period of the Paleozoic era believed to have occurred between 500 and 430 million years ago

orocline—a fold belt (orogenic belt) with a curvature or sharp change in trend

orogeny—the process of mountain formation; specifically, the process by which structures within mountain areas were formed

outwash—the stratified debris, primarily gravel and sand, deposited by melt waters beyond the margin of a glacier

oxbow—(1) a closely looping, bow-shaped bend in a river, or the land embraced by it (2) a bow-shaped lake occupying an abandoned channel of a meander

paleomagnetism—the intensity and direction of residual magnetic polarization in ancient rocks

paleontology—the science that deals with the life of past geological periods as deduced from fossil remains

Paleozoic—an era of geologic time from the end of the Precambrian (approximately 600 million years ago) to the beginning of the Mesozoic (approximately 225 million years ago). The Paleozoic era consists of the Cambrian, Ordovician, Silurian, Devonian, Mississippian, Pennsylvanian, and Permian periods.

palinspastic—of, or pertaining to, the inferred original geographic positions of landmasses before extensive deformational movements

pan—playa

parabolic dune—a long, U- or V-shaped sand dune with horns pointing upwind and resembling the form of a parabola in plan view

parautochthonous—of, or pertaining to, a rock body that is intermediate in tectonic character between autochthonous and allochthonous

pediment—a broad, flat or gently sloping rock-floored erosion surface with low relief that is situated at the base of a steeper slope in an arid or semiarid region; sometimes thinly covered with alluvial gravel and sand

pediplain—an extensive erosion surface consisting of a series of coalescing pediments and representing the penultimate stage of the arid erosion cycle

pedology—soil science

Peléan cloud—nuée ardente; a swiftly flowing gaseous cloud erupted from a volcano. The nuée ardente is a characteristic type of eruption of Mount Pelée on the island of Martinique.

peneplain—a low, gently undulating land surface that has presumably been reduced almost to a plain by erosion

peralkaline—descriptive of an igneous rock in which the molecular proportion of alumina is less than that of soda and potash combined

peridotite—a coarse-grained plutonic rock composed of ferromagnesian minerals and especially olivine

Permian—the last period of the Paleozoic occurring 280 to 225 million years ago

phi—an expression of particle-size diameter as the negative logarithm to the base 2 of the diameter in millimeters; as phi increases, particle size decreases

photogrammetry—the science of obtaining reliable measurements by means of photographs

photon—a quantum of radiant energy

phreatic—said of a volcanic explosion of steam or other nonincandescent material that was produced by an underlying magma coming in contact with ground water, resulting in heating and expansion

phycoerythrin—the red coloring matter which is combined with chlorophyll in certain algae

phyllite—an argillaceous, metamorphic rock with lustrous cleavage due to minute mica crystals

phytoplankton—passively floating or drifting unicellular, microscopic plant cells in the ocean

planar crossbedding—crossbedding that is bounded on the lower side by planar erosion surfaces

plankton bloom—a high concentration of aquatic algae which discolors the local water

plate tectonics—the branch of geology that examines the movements and interrelationships of plates thought to make up the Earth's crust

platform zone—that part of a continent which is overlain by flat-lying or gently tilted strata and which overlies basement rocks

playa—a flat-floored, vegetation-free area of thin sheets of clay and silt in the lowermost portion of a desert lake basin; formed when temporary lakes quickly evaporate leaving deposits of fine sediment and soluble salts

Pleistocene—an epoch forming the earlier part of the Quaternary period; the "Great Ice Age"

plutonic—said of igneous rocks formed at a great depth within the Earth

polymict breccia—a brecciated meteorite in which the fragments have differing compositions

porphyrite—porphyry; any igneous rock that contains large, conspicuous crystals (phenocrysts) in a fine-grained interstitial material (ground mass)

Precambrian—all geologic time before the beginning of the Paleozoic

principal line—the line through the principal point and the nadir point (for aerial and space photographs)

Proterozoic—the more recent division of the Precambrian; i.e., the interval between the Archeozoic and the Paleozoic

provenance—the place of origin

pyroclastic—pertaining to fragmented rock material formed by a volcanic explosion

quaquaversal—(1) of, or pertaining to, strata that dip in all directions away from a central point (2) a geologic structure with a quaquaversal dip, such as a dome

quartzite—(1) a metamorphic rock composed chiefly of quartz and formed by recrystallization of sandstone (2) a very hard, unmetamorphosed sandstone composed mainly of quartz and solidly cemented with secondary silica

Quaternary—the geological period forming the latter part of the Cenozoic era, which covers the last 2 or 3 million years and consists of the Pleistocene and Holocene epochs

radiometer—an instrument for detecting and measuring electromagnetic radiation (EMR)

radiosonde—an airborne device, usually attached to a balloon, that is used to gather and to transmit meteorological data as it travels upward

ramp—a high-angle thrust fault

Rayleigh scattering—scattering by atmospheric particles that are small in size compared with the wavelengths being scattered

real time—during the mission or event

Recent—Holocene

recess—an indentation; for folds, this term refers to the area in which the surface axes of folds are concave toward the outer edge of the folded belt

red tide—a general term given to patches of planktonic organisms whose pigments impart a reddish discoloration to the water

reflectance—the ratio of the radiant energy reflected by a surface to that incident on it

refraction—in oceanography, the change in direction of a wave due to the influence of bottom topography

regmatic—of, or pertaining to, regional strike-slip displacements along fault planes

regolith—the unconsolidated rock material, either residual or transported, that overlies the Earth's solid rock. It includes soils, eolian deposits, glacial drift, loess; mantle rock.

remote sensing—the acquisition and interpretation of data obtained by a sensor that is physically remote from the object under study

reseau plate—a glass plate on which an accurately ruled grid is etched. It is placed immediately in front of the film plane of a camera to improve geometric accuracy.

resolution—the capability to differentiate between two very closely spaced objects

reverse fault—a fault in which rocks on the overlying side (hanging wall) appear to have moved upward relative to rocks on the underlying side or footwall

revolution—in astrodynamics, one complete cycle of the movement of a spacecraft in its orbit; measured with respect to a specific point on the Earth through return to the same longitude

rheid—(1) of, or pertaining to, a body of rock showing flow structure (2) a substance (below its melting point) that is deformed by viscous flow during the time of applied stress at an order of magnitude significantly greater than that of elastic deformation

rhyolite—an extrusive igneous rock that is the equivalent of granite

rift zone—a network of crustal fractures

ripple—a very small ridge of sand produced by the action of wind, a current of water, or waves

rose diagram—a circular or semicircular, star-shaped graph in which values are plotted as radii in several directions of bearing from a point of origin

Ro-Tap—a mechanical device used to sieve disaggregated particles

sabkha—see sebkha

salient—something that projects outward from its surroundings; for folds, this term refers to the area in which the surface axes of folds are convex toward the outer edge of the folded belt

saltation—a mode of sediment transport in which particles move by bouncing or short intermittent leaps

sand ridge—a long, low ridge of sand believed to be the eroded stump of a former longitudinal sand dune

sand rose—circular histogram that shows the potential movement of sand at a given location by winds of certain speed groups in various compass directions

sand wave—a large ridge of sand formed on the surface of a stream or on the sea bottom by a strong water current

Santonian—a geologic-time unit of the Upper Cretaceous (above Coniacian, below Campanian)

saprolite—a soft, earthy, disintegrated, and decomposed rock formed in place by chemical weathering of igneous and metamorphic rocks

savanna—a grassland region with scattered trees usually occurring on the margins of the tropics where rainfall is seasonal

scanner—any device that produces an image by scanning

scatter—the irregular refraction or diffraction of visible light or other electromagnetic radiation in many directions

schist—a strongly foliated metamorphic crystalline rock that can be split up in thin, irregular plates

scree—(1) broken rock fragments (2) an accumulation of rocky debris lying on a slope or at the base of a hill or cliff (3) talus

scroll—a crescentic deposit built by a stream on the inner bank of a shifting channel

sea-floor spreading—the process by which new crustal material is created at a mid-ocean ridge and adjacent crustal plates are moved laterally away from the ridge

sea state—the smoothness or roughness of the sea surface

sebkha—(1) a smooth, flat saline plain sometimes occupied by a temporary lake after a rainfall; a playa (2) a salt marsh

Secchi disk—a white disk used to measure the transparency of seawater; i.e., the depth at which the disk is no longer visible when lowered in water is measured to give a rough estimate of the optical purity of seawater

sediment plume—an elongate band of material held in suspension in water, often found at the mouth of a river

seif dune—a variety of longitudinal dune or chain of sand dunes; a large, sharp-crested, tapering dune oriented parallel with the direction of the prevailing wind; from the Arabic word for sword

seismic—of, subject to, or produced by earthquakes or Earth vibration

selva—tropical rain forest

serpentine—a group of rock-forming minerals that consists essentially of hydrous magnesium silicates

serpentinite—a rock composed almost entirely of serpentine-group minerals

shale—a fine-grained sedimentary rock formed by the consolidation of clay, silt, or mud and having a finely stratified structure

shatter cone—a structure produced by shear planes outlining a conical fragment of rock several centimeters in diameter; generally believed to have been formed by shock waves caused by meteorite impact

sheetflood—a broad expanse of moving water spread out in a thin sheet over a large area in an arid region during periods of exceptional rainfall

shelf—a submerged rock ledge or sandbank which extends seaward from the shore

shield volcano—a volcano with a broad, low, domelike shape that was built by low-viscosity basaltic lava flows

shoal—(1) a shallow area in a body of water (2) a submerged sandbar or sandbank

sierra—a high range of hills or mountains, especially one with a serrated or irregular outline

silcrete—indurated layers consisting of surficial sand and gravel cemented by silica

silex—(1) silica or siliceous material, especially a finely ground form used as a filler in paints or wood, or as a dental material (2) the French term for flint

siliceous—of, pertaining to, or containing silica (SiO_2)

sillimanite—an aluminum silicate mineral (Al_2SiO_5) usually occurring in orthorhombic crystals

Silurian—a period of the Paleozoic era occurring 400 to 440 million years ago

sinuosity—the ratio of channel length to valley or flood-plain length for a given river reach

skewness—(1) the state of being unsymmetrical or distorted (2) in statistics, the deviation of a frequency distribution curve from a symmetrical form (3) a measure of the degree of asymmetry of the grain-size frequency curve; the sign (+ or −) indicates whether the curve has an asymmetrical tail on the left or on the right of the curve

slicks—smooth glassy patches or streaks on an otherwise rippled water surface, commonly occurring in lakes, coastal waters, or bays. The lack of ripples in slicks is caused by monomolecular layers of organic materials, which reduce surface tension.

slipface—the steep face on the lee side of a dune, standing at or near the angle of repose of sand (32° to 34°)

snowfield—a large and relatively permanent area of snow cover

snowline—(1) a transient line marking the area or altitude with complete snow cover (2) an imaginary line on land above which there is perpetual snow cover

snowpack—the extensive annual accumulation of packed snow at higher elevations that melts slowly and provides water for irrigation and power generation

spatter cone—a low, steep-sided cone consisting of small pyroclastic fragments and built up on a vent or fissure

specific discharge—discharge per unit area

spectrum—(1) in physics, an array of energies ordered according to wavelength or frequency (2) the series of colors produced by the dispersion of radiant energy

spilite—a group of rocks that are closely related to basalts in chemical composition but are very different in mineral composition; often occurs as submarine lava flows

spit—a narrow bank of land composed of sand deposited by longshore currents extending from the shore into a body of water; may curve back upon itself: a recurved spit

star dune—a stationary, isolated hill of sand resembling in plan view a star, and having sharp-crested radial ridges extending in many directions; usually formed in an area where the wind blows from all directions

steppe—an extensive, usually level, treeless grassland tract normally found in the semiarid midlatitudes

stereoscope—an optical instrument for blending into one image two overlapping photographs from slightly different points of view, so as to produce a mental impression of a three-dimensional image

stratification—the act or process of stratifying (forming, accumulating, or depositing material in layers); the state of being stratified

stratovolcano—a volcano characterized by alternating layers of lava and pyroclastics

stress—in a solid, the force per unit area acting on any surface within it

strike-slip fault—a fault that is characterized by movement parallel to the strike of the fault

subangular—free from sharp angles but not smoothly rounded

subaqueous—below the surface of water

subrounded—partly rounded

sunglint—the Sun's reflection off a water surface; Sun glitter

swale—a shallow, sometimes swampy depression

swash bar—a bar formed by the swash action of waves; a component of an ebb-tidal delta

syenite—a plutonic rock composed chiefly of feldspar

syncline—a fold whose core contains stratigraphically younger rocks. The beds of a syncline dip toward each other from either side, and the fold is concave upward.

synclinorium—a synclinal structure of regional extent composed of lesser folds

synform—a synclinal-type structure in which the chronologic succession of the rock strata is not known

tectonic—of, or relating to, the deformation of the Earth's crust; also to the forces involved in and the resulting structures of such deformation

terminal lobe—the margin of a section of a glacier

Tertiary—the first period of the Cenozoic era thought to have occurred between 65 and 3 to 2 million years ago

thermocline—a layer of water with an intensive vertical negative gradient in temperature

thrust fault—a high-angle reverse fault with a dip of 45° or less

till—a glacial deposit composed of unsorted boulders, gravel, sand, and clay

tillite—a sedimentary rock formed by lithification of glacial till

time-rock unit—time-stratigraphic unit; a stratigraphic subdivision based solely on time of origin or geologic age

tombolo—a sandbar which joins an island to the mainland or to another island

trachyte—a usually light-colored volcanic rock consisting chiefly of alkalic feldspar and minor amounts of biotite, hornblende, or pyroxene

traction load—the bedload of a stream that is moved by traction

transform fault—a strike-slip fault that is characteristic of mid-oceanic ridges and along which ridges are offset

transverse dune—a symmetrical dune ridge oriented normal (perpendicular) to the dominant direction of sand-moving winds

triangular facet—the truncated end of a mountain spur, characterized by a triangular shape with the apex pointing upward. Triangular facets often characterize fault scarps at the base of block mountains.

Triassic—the first period of the Mesozoic era occurring between 225 and 195 to 190 million years ago

tuff—a compacted pyroclastic deposit composed primarily of ash and dust

turbulence—turbulent flow; a fluid flow in which flow lines are disordered and heterogeneously mixed

Turonian—a geologic-time unit of the Cretaceous (above Cenomanian, below Coniacian)

unconformity—a break or gap in the geologic record such as a lack of continuity in deposition between rock strata in contact; results from a period of nondeposition, erosion, or weathering

upwellings—areas in the sea where cold, heavy subsurface water rises upward

vertical tectonics—refers to vertical movements of crustal units of varying specific gravity

vidicon—a television camera tube using the principle of photoconductivity

vignetting—a gradual decrease in film density usually from the edge to the center of a photograph caused by the blocking of some rays entering the lens

vitric—of, or pertaining to, a pyroclastic material that is more than 75 percent glass

vuggy—said of a rock having numerous small cavities (vugs)

wadi—a usually dry watercourse

watershed—(1) a drainage basin; the area drained by a river and all its tributaries (2) a drainage divide; the line or ridge separating two drainage basins

wave refraction—the process by which a wave moving in shallow water and approaching the shore at an angle is deflected from its original direction

wind-rift dune—a sand dune produced on the lee side of blowout areas by a strong wind of constant direction

Wisconsinan—the fourth and last glacial stage of the Pleistocene epoch in North America

wrench fault—a nearly vertical fault characterized by movement parallel to the strike of the fault; a strike-slip fault

xeric—of, or pertaining to, a dry environment

xerophyte—a plant adapted for growth under dry conditions

yardang—a long, irregular ridge bounded by round-bottomed troughs formed by eolian erosion and oriented parallel to the direction of the dominant wind

yellow substances—the general term given to dissolved organic substances in river or ocean waters which absorb light at short wavelengths

zooplankton—all passively floating or drifting minute animal organisms in the ocean

Appendix B—Acronyms

ACDR	Apollo commander
AMS	U.S. Army Map Service
Aramco	Arabian American Oil Company
ART	airborne infrared radiation thermometers
ASEP	Apollo-Soyuz Experiment Parameter
ASTP	Apollo-Soyuz Test Project
ASW	antisubmarine warfare
ATS	U.S. Navy fleet tug
AXBT	air expendable bathythermograph
BOMEX	Barbados Oceanographic and Meteorological Experiment
B.P.	before the present
CAPCOM	capsule communicator
CCL	convective condensation level
CMP	command module pilot
CPRM	Companhia de Pesquisa de Recursos Minerals (Brazil's national mineral resources company)
CSIRO	Commonwealth Scientific and Industrial Research Organization
CVA	U.S. Navy aircraft carrier
DMP	docking module pilot
DMSP	Defense Meteorological Satellite Program
ERAP	Earth Resources Aircraft Program
EREP	Earth Resources Experiment Package
ETC	Earth terrain camera
GOES	Geostationary Operational Environmental Satellite
GTI	ground-truth investigation
HDC	Hasselblad data camera
HRIR	high resolution infrared
IMU	inertial measurement unit
INPE	Instito de Pesquisas Espacias (Brazil's space agency)
JSC	NASA Lyndon B. Johnson Space Center
MFZ	Marda Fault zone
MSS	multispectral scanner subsystem
MTA	Maden Tetkik Arama Enst. of Ankara, Turkey
MTF	modulation transfer function
NA	not applicable
NOAA	National Oceanic and Atmospheric Administration
ONC	Operational Navigation Chart
ONR	Office of Naval Research
RADAM	radar mapping of the Amazon
RAF	Royal Air Force
RV	research vessel
SEM	scanning electron microscope
SLAR	side-looking airborne radar

TIROS	Television and Infrared Observation Satellite
TVZ	Transverse Volcanic Zone
U.A.E.	United Arab Emirates
UNDP/FAO	United Nations Development Program/Food and Agricultural Organization
USGS	U.S. Geological Survey
UT	universal time
VHRR	very-high-resolution radiometer
WMO	World Meteorological Organization
XBT	expendable bathythermograph
ZTS	zoom transfer scope